Methods in Molecular Biology 2419

Springer Protocols

Dipak P. Ramji *Editor*

Atherosclerosis

Methods and Protocols

Humana Press

METHODS IN MOLECULAR BIOLOGY

Series Editor
John M. Walker
School of Life and Medical Sciences
University of Hertfordshire
Hatfield, Hertfordshire, UK

For further volumes:
http://www.springer.com/series/7651

For over 35 years, biological scientists have come to rely on the research protocols and methodologies in the critically acclaimed *Methods in Molecular Biology* series. The series was the first to introduce the step-by-step protocols approach that has become the standard in all biomedical protocol publishing. Each protocol is provided in readily-reproducible step-by-step fashion, opening with an introductory overview, a list of the materials and reagents needed to complete the experiment, and followed by a detailed procedure that is supported with a helpful notes section offering tips and tricks of the trade as well as troubleshooting advice. These hallmark features were introduced by series editor Dr. John Walker and constitute the key ingredient in each and every volume of the *Methods in Molecular Biology* series. Tested and trusted, comprehensive and reliable, all protocols from the series are indexed in PubMed.

Atherosclerosis

Methods and Protocols

Edited by

Dipak P. Ramji

Cardiff School of Biosciences, Cardiff University, Cardiff, UK

Humana Press

Editor
Dipak P. Ramji
Cardiff School of Biosciences
Cardiff University
Cardiff, UK

ISSN 1064-3745 ISSN 1940-6029 (electronic)
Methods in Molecular Biology
ISBN 978-1-0716-1923-0 ISBN 978-1-0716-1924-7 (eBook)
https://doi.org/10.1007/978-1-0716-1924-7

© The Editor(s) (if applicable) and The Author(s), under exclusive license to Springer Science+Business Media, LLC, part of Springer Nature 2022
This work is subject to copyright. All rights are solely and exclusively licensed by the Publisher, whether the whole or part of the material is concerned, specifically the rights of translation, reprinting, reuse of illustrations, recitation, broadcasting, reproduction on microfilms or in any other physical way, and transmission or information storage and retrieval, electronic adaptation, computer software, or by similar or dissimilar methodology now known or hereafter developed.
The use of general descriptive names, registered names, trademarks, service marks, etc. in this publication does not imply, even in the absence of a specific statement, that such names are exempt from the relevant protective laws and regulations and therefore free for general use.
The publisher, the authors and the editors are safe to assume that the advice and information in this book are believed to be true and accurate at the date of publication. Neither the publisher nor the authors or the editors give a warranty, expressed or implied, with respect to the material contained herein or for any errors or omissions that may have been made. The publisher remains neutral with regard to jurisdictional claims in published maps and institutional affiliations.

This Humana imprint is published by the registered company Springer Science+Business Media, LLC, part of Springer Nature.
The registered company address is: 1 New York Plaza, New York, NY 10004, U.S.A.

Dedication

This book is dedicated to Professor Sampath Parthasarathy who passed away on 1 December 2020. Prof. Parthasarathy published over 250 articles on atherosclerosis and other diseases. His research was instrumental in the development of a key concept that oxidized low-density lipoprotein is involved in the initiation and progression of atherosclerosis. The world has lost not only a dedicated scientist of great intellect who made tremendous contributions in the field of cardiovascular research but also a kind and considerate human being.

Preface

Atherosclerosis and its clinical complications, such as myocardial infarction and cerebrovascular accident, are the major cause of global morbidity and mortality. The disease is an enormous economic burden, and it is anticipated that this will worsen in the future because of the prevalence of risk factors such as hypercholesterolemia, hypertension, diet rich in saturated fats, sedentary lifestyle, obesity, and diabetes. Current therapies are not fully effective and associated with various adverse side effects. It is therefore essential to increase our understanding of the molecular basis of atherosclerosis as this will not only reveal novel targets for therapeutic intervention but ultimately improve diagnosis, prevention, and treatment of this disease. The use of *in vitro* and *in vivo* model systems coupled with techniques that probe atherosclerosis-associated processes in such models has been instrumental in advancing our knowledge of the genetic, molecular, and cellular mechanisms underlying the disease and will continue to do so in the future.

This book provides a comprehensive and up-to-date coverage of methods used in atherosclerosis research. The first part of the book addresses the pathogenesis of atherosclerosis, model systems employed to probe the disease, and emerging concepts in the field. This is followed by in-depth coverage of *in vitro and in vivo* model systems together with current and emerging methods in the field. Each methods chapter includes introduction to the topic, list of materials and reagents required, detailed step-by-step laboratory protocols, and invaluable notes based on the authors' personal experiences. The book will be an invaluable resource for those engaged in research on atherosclerosis and cardiovascular disease, those that are planning to move into the field, those working on other inflammatory disorders that predispose to atherosclerosis (e.g., obesity, diabetes, arthritis, etc.), and students at both the undergraduate and postgraduate levels.

Cardiff, UK ***Dipak P. Ramji***

Contents

Part III In Vivo Model Systems for Atherosclerosis Research

Contributors

Ali Abdelfattah • *Department of Medical Laboratory Sciences, Faculty of Applied Medical Sciences, Hashemite University, Zarqa, Jordan*

Aaron D. Aguirre • *Wellman Center for Photomedicine, Harvard Medical School and Massachusetts General Hospital, Boston, MA, USA; Cardiovascular Research Center, Division of Cardiology, Massachusetts General Hospital, Harvard Medical School, Boston, MA, USA*

Ramzi Ajjan • *Leeds Institute of Cellular & Metabolic Medicine, Faculty of Medicine & Health, University of Leeds, Leeds, UK*

Sulaiman Al Alawi • *Cardiff School of Biosciences, Cardiff University, Cardiff, UK*

Ahmed Al-Aufi • *Leeds Vascular Institute, Faculty of Medicine & Health, University of Leeds, Leeds, UK*

Basmah Al-Sayejh • *Leeds Institute of Cellular & Metabolic Medicine, Faculty of Medicine & Health, University of Leeds, Leeds, UK*

Alaa Alahmadi • *Cardiff School of Biosciences, Cardiff University, Cardiff, UK*

Mazen S. Albaghdadi • *Cardiovascular Research Center, Division of Cardiology, Massachusetts General Hospital, Harvard Medical School, Boston, MA, USA*

Alhomidi Almotiri • *College of Applied Medical Sciences-Dawadmi, Shaqra University, Dawadmi, Saudi Arabia*

Reem Alotibi • *Cardiff School of Biosciences, Cardiff University, Cardiff, UK*

Fahad Alradi • *Cardiff School of Biosciences, Cardiff University, Cardiff, UK*

Nouf Alshehri • *Cardiff School of Biosciences, Cardiff University, Cardiff, UK*

Chandrakala Aluganti Narasimhulu • *Burnett School of Biomedical Sciences, College of Medicine, University of Central Florida, Orlando, FL, USA*

G. M. Anantharamaiah • *Department of Medicine, UAB Medical Centre, Birmingham, AL, USA*

Vicente Andrés • *Laboratory of Molecular and Genetic Cardiovascular Pathophysiology, Vascular Biology Area, Centro Nacional de Investigaciones Cardiovasculares (CNIC), Madrid, Spain; Centro de Investigación Biomédica en Red de Enfermedades Cardiovasculares (CIBERCV), Madrid, Spain*

Ananth Annapragada • *E.B. Singleton Department of Radiology, Texas Children's Hospital & Baylor College of Medicine, Houston, TX, USA*

Andrew Badachhape • *E.B. Singleton Department of Radiology, Texas Children's Hospital & Baylor College of Medicine, Houston, TX, USA*

Andrew H. Baker • *BHF Centre for Cardiovascular Sciences (CVS), University of Edinburgh, Edinburgh, UK; Department of Pathology, Maastricht University Medical Center (MUMC), Cardiovascular Research Institute Maastricht (CARIM), Maastricht, The Netherlands*

Ana Barettino • *Laboratory of Molecular and Genetic Cardiovascular Pathophysiology, Vascular Biology Area, Centro Nacional de Investigaciones Cardiovasculares (CNIC), Madrid, Spain; Centro de Investigación Biomédica en Red de Enfermedades Cardiovasculares (CIBERCV), Madrid, Spain*

Tobias Becher • *Laboratory of Molecular Metabolism, The Rockefeller University, New York, NY, USA; First Department of Medicine (Division of Cardiology), University Medical*

Center Mannheim, Mannheim, Germany; DZHK (German Centre for Cardiovascular Research), Partner Site Heidelberg/Mannheim, Mannheim, Germany

Ignacio Benedicto • *Laboratory of Molecular and Genetic Cardiovascular Pathophysiology, Vascular Biology Area, Centro Nacional de Investigaciones Cardiovasculares (CNIC), Madrid, Spain*

Jacob F. Bentzon • *Department of Clinical Medicine, Heart Diseases, Aarhus University, Aarhus, Denmark; Centro Nacional de Investigaciones Cardiovasculares (CNIC), Madrid, Spain*

Juan A. Bernal • *Centro Nacional de Investigaciones Cardiovasculares (CNIC), Madrid, Spain*

Rohan Bhavane • *E.B. Singleton Department of Radiology, Texas Children's Hospital & Baylor College of Medicine, Houston, TX, USA*

Martin Mæng Bjørklund • *Department of Clinical Medicine, Heart Diseases, Aarhus University, Aarhus, Denmark; Centro Nacional de Investigaciones Cardiovasculares (CNIC), Madrid, Spain*

Bethan A. Brown • *Department of Translational Health Sciences, Bristol Medical School, University of Bristol, Bristol, UK*

Úrsula Catalán Santos • *Facultat de Medicina i Ciències de la Salut, Departament de Medicina i Cirurgia, Grup Nutrició Funcional, Oxidació i Malalties Cardiovasculars (NFOC-Salut), Universitat Rovira i Virgili, Reus, Spain; Eurecat, Centre Tecnològic de Catalunya, Unitat de Nutrició i Salut, Reus, Spain*

Yee-Hung Chan • *Cardiff School of Biosciences, Cardiff University, Cardiff, UK*

Jing Chen • *Cardiff School of Biosciences, Cardiff University, Cardiff, UK*

Yajie Chen • *Department of Molecular Pathology, Faculty of Medicine, Interdisciplinary Graduate School of Medicine, University of Yamanashi, Chuo, Japan; School of Biotechnology and Health Sciences, Wuyi University, Jiangmen, China*

Jingyi Chi • *Laboratory of Molecular Metabolism, The Rockefeller University, New York, NY, USA*

Mohammed M. Chowdhury • *Cardiovascular Research Center, Division of Cardiology, Massachusetts General Hospital, Harvard Medical School, Boston, MA, USA; Division of Vascular Surgery, Department of Surgery, Addenbrooke's Hospital, University of Cambridge, Cambridge, UK*

Paul Cohen • *Laboratory of Molecular Metabolism, The Rockefeller University, New York, NY, USA*

Patrick A. Coughlin • *Division of Vascular Surgery, Department of Surgery, Addenbrooke's Hospital, University of Cambridge, Cambridge, UK*

Stephen J. Cross • *Department of Translational Health Sciences, Bristol Medical School, University of Bristol, Bristol, UK*

Gary A. Cuthbert • *Leeds Vascular Institute, Faculty of Medicine & Health, University of Leeds, Leeds, UK*

Thomas Q. de Aguiar Vallim • *Department of Medicine, Cardiology, University of California Los Angeles, Los Angeles, CA, USA; Department of Biological Chemistry, David Geffen School of Medicine at UCLA, University of California Los Angeles, Los Angeles, CA, USA; Molecular Biology Institute, David Geffen School of Medicine at UCLA, University of California Los Angeles, Los Angeles, CA, USA; Jonsson Comprehensive Cancer Center, David Geffen School of Medicine at UCLA, University of California Los Angeles, Los Angeles, CA, USA*

Marco De Giorgi • *Department of Molecular Physiology and Biophysics, Baylor College of Medicine, Houston, TX, USA*
Alba de Juan • *Institut Curie, PSL Research University, INSERM, U932, Paris, France*
Anuradha Dhanasekaran • *Centre for Biotechnology, Anna University, Chennai, Tamil Nadu, India*
Charles Drummer IV • *Cardiovascular Research Center, Lewis Katz School of Medicine at Temple University, Philadelphia, PA, USA*
Christopher P. Durant • *La Jolla Institute for Immunology, La Jolla, CA, USA*
Ali Ertürk • *Institute for Stroke and Dementia Research, Klinikum der Universität München, Ludwig-Maximilians-University (LMU), Munich, Germany; Helmholtz Zentrum München, Deutsches Forschungszentrum für Gesundheit und Umwelt, Neuherberg, Germany*
Joan Carles Escolà-Gil • *Institut de Recerca de l'Hospital de la Santa Creu i Sant Pau, Institut d'Investigacions Biomèdiques (IIB) Sant Pau, Barcelona, Spain; CIBER de Diabetes y Enfermedades Metabólicas Asociadas, CIBERDEM, Madrid, Spain; Departament de Bioquímica i Biologia Molecular, Universitat Autònoma de Barcelona, Barcelona, Spain*
Jianglin Fan • *Department of Molecular Pathology, Faculty of Medicine, Interdisciplinary Graduate School of Medicine, University of Yamanashi, Chuo, Japan; School of Biotechnology and Health Sciences, Wuyi University, Jiangmen, China*
Sara Fernández-Castillejo • *Facultat de Medicina i Ciències de la Salut, Departament de Medicina i Cirurgia, Grup Nutrició Funcional, Oxidació i Malalties Cardiovasculars (NFOC-Salut), Universitat Rovira i Virgili, Reus, Spain; Eurecat, Centre Tecnològic de Catalunya, Unitat de Nutrició i Salut, Reus, Spain*
Benjamin Förstera • *Institute for Stroke and Dementia Research, Klinikum der Universität München, Ludwig-Maximilians-University (LMU), Munich, Germany; Helmholtz Zentrum München, Deutsches Forschungszentrum für Gesundheit und Umwelt, Neuherberg, Germany*
Sarah J. George • *Department of Translational Health Sciences, Bristol Medical School, University of Bristol, Bristol, UK*
Godfrey S. Getz • *Department of Pathology, The University of Chicago, Chicago, IL, USA*
Ketan B. Ghaghada • *E.B. Singleton Department of Radiology, Texas Children's Hospital & Baylor College of Medicine, Houston, TX, USA*
Kayleigh Griffiths • *Institute of Cardiovascular Sciences, College of Medical and Dental Sciences, University of Birmingham, Birmingham, UK*
Andreas Habenicht • *Institute for Cardiovascular Prevention (IPEK), Klinikum of the University of Munich (KUM), Ludwig-Maximilians-University (LMU), Munich, Germany; German Center for Cardiovascular Research (DZHK), Partner site Munich Heart Alliance, Munich, Germany*
Magda R. Hamczyk • *Centro de Investigación Biomédica en Red de Enfermedades Cardiovasculares (CIBERCV), Madrid, Spain; Departamento de Bioquímica y Biología Molecular, Instituto Universitario de Oncología (IUOPA), Universidad de Oviedo, Oviedo, Spain*
Michael A. Harrison • *School of Biomedical Sciences, University of Leeds, Leeds, UK*
Catherine C. Hedrick • *La Jolla Institute for Immunology, La Jolla, CA, USA*
Shervanthi Homer-Vanniasinkam • *Leeds Vascular Institute, Faculty of Medicine & Health, University of Leeds, Leeds, UK*
Alaa Ismail • *Cardiff School of Biosciences, Cardiff University, Cardiff, UK*

Farouc A. Jaffer • *Cardiovascular Research Center, Division of Cardiology, Massachusetts General Hospital, Harvard Medical School, Boston, MA, USA; Wellman Center for Photomedicine, Harvard Medical School and Massachusetts General Hospital, Boston, MA, USA*

Philip E. James • *Cardiff School of Sport and Health Sciences, Cardiff Metropolitan University, Cardiff, UK*

Kelsey E. Jarrett • *Department of Medicine, Cardiology, University of California Los Angeles, Los Angeles, CA, USA*

Xiaohua Jiang • *Cardiovascular Research Center, Lewis Katz School of Medicine at Temple University, Philadelphia, PA, USA; Metabolic Disease Research, Departments of Pharmacology, Microbiology and Immunology, Lewis Katz School of Medicine at Temple University, Philadelphia, PA, USA*

Jason L. Johnson • *Department of Translational Health Sciences, Bristol Medical School, University of Bristol, Bristol, UK*

Josep Julve • *Institut de Recerca de l'Hospital de la Santa Creu i Sant Pau, Institut d'Investigacions Biomèdiques (IIB) Sant Pau, Barcelona, Spain; CIBER de Diabetes y Enfermedades Metabólicas Asociadas, CIBERDEM, Madrid, Spain; Departament de Bioquímica i Biologia Molecular, Universitat Autònoma de Barcelona, Barcelona, Spain*

Mohamad B. Kassab • *Cardiovascular Research Center, Division of Cardiology, Massachusetts General Hospital, Harvard Medical School, Boston, MA, USA*

Yoichiro Kawamura • *Cardiovascular Research Center, Division of Cardiology, Massachusetts General Hospital, Harvard Medical School, Boston, MA, USA*

Katie Lacey • *School of Molecular & Cellular Biology, University of Leeds, Leeds, UK*

William R. Lagor • *Department of Molecular Physiology and Biophysics, Baylor College of Medicine, Houston, TX, USA*

Begoña Lavin Plaza • *School of Biomedical Engineering and Imaging Sciences, King's College London, London, UK; Department of Biochemistry and Molecular Biology, School of Chemistry, Complutense University, Madrid, Spain*

Klaus Ley • *La Jolla Institute for Immunology, La Jolla, CA, USA; Department of Bioengineering, University of California San Diego, La Jolla, CA, USA*

Yuanfang Li • *Institute for Cardiovascular Prevention (IPEK), Klinikum of the University of Munich (KUM), Ludwig-Maximilians-University (LMU), Munich, Germany*

Yutao Li • *Institute for Cardiovascular Prevention (IPEK), Klinikum of the University of Munich (KUM), Ludwig-Maximilians-University (LMU), Munich, Germany*

Jonathan R. Lindner • *Oregon Health & Science University, Portland, OR, USA*

Enqi Liu • *Research Institute of Atherosclerotic Disease and Laboratory Animal Center, Xi'an Jiaotong University School of Medicine, Xi'an, China*

George Liu • *Institute of Cardiovascular Sciences, Key Laboratory of Molecular Cardiovascular Sciences, Ministry of Education, School of Basic Medical Sciences, Peking University, Beijing, China*

Ronan Lordan • *Department of Biological Sciences, University of Limerick, Limerick, Ireland; Health Research Institute, University of Limerick, Limerick, Ireland*

Shu Lu • *Institute for Cardiovascular Prevention (IPEK), Klinikum of the University of Munich (KUM), Ludwig-Maximilians-University (LMU), Munich, Germany*

Yifan Lu • *Cardiovascular Research Center, Lewis Katz School of Medicine at Temple University, Philadelphia, PA, USA*

Melanie Madhani • *Institute of Cardiovascular Sciences, College of Medical and Dental Sciences, University of Birmingham, Birmingham, UK*

Manousos Makridakis • *Center of Systems Biology, Biomedical Research Foundation, Academy of Athens (BRFAA), Athens, Greece*
Keiichiro Matoba • *Division of Diabetes, Endocrinology and Metabolism, Department of Internal Medicine, The Jikei University School of Medicine, Tokyo, Japan*
Remco T. A. Megens • *Institute for Cardiovascular Prevention (IPEK), Klinikum of the University of Munich (KUM), Ludwig-Maximilians-University (LMU), Munich, Germany; Cardiovascular Research Institute Maastricht (CARIM), Maastricht University, Maastricht, The Netherlands*
Juan Bautista Menendez-Gonzalez • *Department of Stem Cell and Regenerative Biology, Harvard Stem Cell Institute, Harvard University, Cambridge, MA, USA; Center for Regenerative Medicine, Massachusetts General Hospital, Boston, MA, USA*
Melissa A. Meyer • *La Jolla Institute for Immunology, La Jolla, CA, USA*
Sarajo K. Mohanta • *Institute for Cardiovascular Prevention (IPEK), Klinikum of the University of Munich (KUM), Ludwig-Maximilians-University (LMU), Munich, Germany; German Center for Cardiovascular Research (DZHK), Partner site Munich Heart Alliance, Munich, Germany; Munich Cluster of Systems Neurology (SyNergy), Ludwig-Maximilians-University Munich, Munich, Germany*
Claude Motta • *Facultat de Medicina i Ciències de la Salut, Departament de Medicina i Cirurgia, Grup Nutrició Funcional, Oxidació i Malalties Cardiovasculars (NFOC-Salut), Universitat Rovira i Virgili, Reus, Spain*
Jan Nagenborg • *Pathology Department, Cardiovascular Research Institute Maastricht (CARIM), Maastricht University Medical Center (MUMC), Maastricht, The Netherlands*
Jamie Nash • *Cardiff School of Sport and Health Sciences, Cardiff Metropolitan University, Cardiff, UK*
Rosa M. Nevado • *Centro Nacional de Investigaciones Cardiovasculares (CNIC), Madrid, Spain; Centro de Investigación Biomédica en Red de Enfermedades Cardiovasculares (CIBERCV), Madrid, Spain*
The Anh Nguyen • *Oregon Health & Science University, Portland, OR, USA*
Manabu Niimi • *Department of Molecular Pathology, Faculty of Medicine, Interdisciplinary Graduate School of Medicine, University of Yamanashi, Chuo, Japan*
Marco Orecchioni • *La Jolla Institute for Immunology, La Jolla, CA, USA*
Mayakonda Palgunachari • *Department of Medicine, UAB Medical Centre, Birmingham, AL, USA*
Sampath Parthasarathy • *Burnett School of Biomedical Sciences, College of Medicine, University of Central Florida, Orlando, FL, USA*
Anna Pedret Figuerola • *Facultat de Medicina i Ciències de la Salut, Departament de Medicina i Cirurgia, Grup Nutrició Funcional, Oxidació i Malalties Cardiovasculars (NFOC-Salut), Universitat Rovira i Virgili, Reus, Spain; Eurecat, Centre Tecnològic de Catalunya, Unitat de Nutrició i Salut, Reus, Spain*
Zhonglie Piao • *Wellman Center for Photomedicine, Harvard Medical School and Massachusetts General Hospital, Boston, MA, USA*
Sreenivasan Ponnambalam • *School of Molecular & Cellular Biology, University of Leeds, Leeds, UK*
Dipak P. Ramji • *Cardiff School of Biosciences, Cardiff University, Cardiff, UK*
Catherine A. Reardon • *Ben May Department, The University of Chicago, Chicago, IL, USA*
Lien M. Reolizo • *Department of Translational Health Sciences, Bristol Medical School, University of Bristol, Bristol, UK*

Dario F. Riascos-Bernal • *Department of Medicine (Cardiology Division), Wilf Family Cardiovascular Research Institute, Albert Einstein College of Medicine, Bronx, NY, USA; Department of Developmental and Molecular Biology, Wilf Family Cardiovascular Research Institute, Albert Einstein College of Medicine, Bronx, NY, USA*

Andrea Rivas-Urbina • *Institut de Recerca de l'Hospital de la Santa Creu i Sant Pau, Institut d'Investigacions Biomèdiques (IIB) Sant Pau, Barcelona, Spain*

Neil P. Rodrigues • *European Cancer Stem Cell Research Institute, School of Biosciences, Cardiff University, Cardiff, UK*

Anne Roivainen • *Turku PET Centre, University of Turku and Turku University Hospital, Turku, Finland; Turku Center for Disease Modeling, University of Turku, Turku, Finland*

Barnaby W. R. Roper • *School of Molecular & Cellular Biology, University of Leeds, Leeds, UK*

Noemi Rotllan • *Institut de Recerca de l'Hospital de la Santa Creu i Sant Pau, Institut d'Investigacions Biomèdiques (IIB) Sant Pau, Barcelona, Spain; CIBER de Diabetes y Enfermedades Metabólicas Asociadas, CIBERDEM, Madrid, Spain*

James H. F. Rudd • *Division of Cardiovascular Medicine, Addenbrooke's Hospital, University of Cambridge, Cambridge, UK*

Fatma Saaoud • *Cardiovascular Research Center, Lewis Katz School of Medicine at Temple University, Philadelphia, PA, USA*

Ryosuke Saigusa • *La Jolla Institute for Immunology, La Jolla, CA, USA*

Jose Luis Sanchez-Quesada • *Institut de Recerca de l'Hospital de la Santa Creu i Sant Pau, Institut d'Investigacions Biomèdiques (IIB) Sant Pau, Barcelona, Spain; CIBER de Diabetes y Enfermedades Metabólicas Asociadas, CIBERDEM, Madrid, Spain; Departament de Bioquímica i Biologia Molecular, Universitat Autònoma de Barcelona, Barcelona, Spain*

David Santos • *Institut de Recerca de l'Hospital de la Santa Creu i Sant Pau, Institut d'Investigacions Biomèdiques (IIB) Sant Pau, Barcelona, Spain; CIBER de Diabetes y Enfermedades Metabólicas Asociadas, CIBERDEM, Madrid, Spain*

Antti Saraste • *Turku PET Centre, University of Turku and Turku University Hospital, Turku, Finland; Heart Center, Turku University Hospital and University of Turku, Turku, Finland*

Jessica P. Scanlon • *BHF Centre for Cardiovascular Sciences (CVS), University of Edinburgh, Edinburgh, UK*

Ying Shao • *Cardiovascular Research Center, Lewis Katz School of Medicine at Temple University, Philadelphia, PA, USA*

Nicholas E. S. Sibinga • *Department of Medicine (Cardiology Division), Wilf Family Cardiovascular Research Institute, Albert Einstein College of Medicine, Bronx, NY, USA; Department of Developmental and Molecular Biology, Wilf Family Cardiovascular Research Institute, Albert Einstein College of Medicine, Bronx, NY, USA*

Judith C. Sluimer • *Pathology Department, Cardiovascular Research Institute Maastricht (CARIM), Maastricht University Medical Center (MUMC), Maastricht, The Netherlands; BHF Centre for Cardiovascular Sciences (CVS), University of Edinburgh, Edinburgh, UK*

Rosa Solà • *Facultat de Medicina i Ciències de la Salut, Departament de Medicina i Cirurgia, Grup Nutrició Funcional, Oxidació i Malalties Cardiovasculars (NFOC-Salut), Universitat Rovira i Virgili, Reus, Spain; Hospital Universitari Sant Joan de Reus, Reus, Spain*

Alexandros Somos • *Department of Translational Health Sciences, Bristol Medical School, University of Bristol, Bristol, UK*
Mia Ståhle • *Turku PET Centre, University of Turku and Turku University Hospital, Turku, Finland*
Karen Stanic • *Institute for Stroke and Dementia Research, Klinikum der Universität München, Ludwig-Maximilians-University (LMU), Munich, Germany; Helmholtz Zentrum München, Deutsches Forschungszentrum für Gesundheit und Umwelt, Neuherberg, Germany*
Sabine Steffens • *Institute for Cardiovascular Prevention (IPEK), Klinikum of the University of Munich (KUM), Ludwig-Maximilians-University (LMU), Munich, Germany; German Center for Cardiovascular Research (DZHK), Partner site Munich Heart Alliance, Munich, Germany*
Jianxin Sun • *Department of Medicine, Sidney Kimmel Medical College, Thomas Jefferson University, Philadelphia, PA, USA*
Ting Sun • *Institute for Cardiovascular Prevention (IPEK), Klinikum of the University of Munich (KUM), Ludwig-Maximilians-University (LMU), Munich, Germany*
Yu Sun • *Cardiovascular Research Center, Lewis Katz School of Medicine at Temple University, Philadelphia, PA, USA*
Vasantika Suryawanshi • *La Jolla Institute for Immunology, La Jolla, CA, USA*
Ritsuko Suzuki • *Admission Center, University of Yamanashi, Kofu, Japan*
Eric Tanifum • *E.B. Singleton Department of Radiology, Texas Children's Hospital & Baylor College of Medicine, Houston, TX, USA*
Guillermo J. Tearney • *Wellman Center for Photomedicine, Harvard Medical School and Massachusetts General Hospital, Boston, MA, USA; Department of Pathology, Harvard Medical School and Massachusetts General Hospital, Boston, MA, USA*
Darren C. Tomlinson • *School of Molecular & Cellular Biology, University of Leeds, Leeds, UK*
Alexandros Tsoupras • *Department of Biological Sciences, University of Limerick, Limerick, Ireland; Health Research Institute, University of Limerick, Limerick, Ireland; Bernal Institute, University of Limerick, Limerick, Ireland*
Kim van Kuijk • *Pathology Department, Cardiovascular Research Institute Maastricht (CARIM), Maastricht University Medical Center (MUMC), Maastricht, The Netherlands; Institute of Experimental Medicine and Systems Biology, Faculty of Medicine, RWTH Aachen University, Aachent, Germany*
Selvaraj Vimalraj • *Centre for Biotechnology, Anna University, Chennai, Tamil Nadu, India*
Antonia Vlahou • *Center of Systems Biology, Biomedical Research Foundation, Academy of Athens (BRFAA), Athens, Greece*
Kerry S. Wadey • *Department of Translational Health Sciences, Bristol Medical School, University of Bristol, Bristol, UK*
Hong Wang • *Metabolic Disease Research, Departments of Pharmacology, Microbiology and Immunology, Lewis Katz School of Medicine at Temple University, Philadelphia, PA, USA*
Yuhui Wang • *Institute of Cardiovascular Sciences, Key Laboratory of Molecular Cardiovascular Sciences, Ministry of Education, School of Basic Medical Sciences, Peking University, Beijing, China*
Zhihua Wang • *Institute for Cardiovascular Prevention (IPEK), Klinikum of the University of Munich (KUM), Ludwig-Maximilians-University (LMU), Munich, Germany*

Christian Weber • *Institute for Cardiovascular Prevention (IPEK), Klinikum of the University of Munich (KUM), Ludwig-Maximilians-University (LMU), Munich, Germany; German Center for Cardiovascular Research (DZHK), Partner site Munich Heart Alliance, Munich, Germany; Cardiovascular Research Institute Maastricht (CARIM), Maastricht University, Maastricht, The Netherlands; Munich Cluster of Systems Neurology (SyNergy), Ludwig-Maximilians-University Munich, Munich, Germany*

Cass Whelan • *Cardiff School of Sport and Health Sciences, Cardiff Metropolitan University, Cardiff, UK*

C. Roger White • *Department of Medicine, UAB Medical Centre, Birmingham, AL, USA*

Helen Williams • *Department of Translational Health Sciences, Bristol Medical School, University of Bristol, Bristol, UK*

Jessica O. Williams • *Cardiff School of Sport and Health Sciences, Cardiff Metropolitan University, Cardiff, UK*

Georg Wissmeyer • *Cardiovascular Research Center, Division of Cardiology, Massachusetts General Hospital, Harvard Medical School, Boston, MA, USA*

Paul Wolkowicz • *Department of Medicine, UAB Medical Centre, Birmingham, AL, USA*

Xunde Xian • *Institute of Cardiovascular Sciences, Key Laboratory of Molecular Cardiovascular Sciences, Ministry of Education, School of Basic Medical Sciences, Peking University, Beijing, China*

Keman Xu • *Cardiovascular Research Center, Lewis Katz School of Medicine at Temple University, Philadelphia, PA, USA*

Xiaofeng Yang • *Cardiovascular Research Center, Lewis Katz School of Medicine at Temple University, Philadelphia, PA, USA; Metabolic Disease Research, Departments of Pharmacology, Microbiology and Immunology, Lewis Katz School of Medicine at Temple University, Philadelphia, PA, USA; Centers for Cardiovascular Research, Inflammation & Lung Research, Metabolic Disease Research, and Thrombosis Research, Lewis Katz School of Medicine at Temple University, Philadelphia, PA, USA*

Changjun Yin • *Institute for Cardiovascular Prevention (IPEK), Klinikum of the University of Munich (KUM), Ludwig-Maximilians-University (LMU), Munich, Germany; German Center for Cardiovascular Research (DZHK), Partner site Munich Heart Alliance, Munich, Germany; Munich Cluster of Systems Neurology (SyNergy), Ludwig-Maximilians-University Munich, Munich, Germany*

Jun Yu • *Metabolic Disease Research, Departments of Pharmacology, Microbiology and Immunology, Lewis Katz School of Medicine at Temple University, Philadelphia, PA, USA*

Stephanie Yu • *Northeastern University, Boston, MA, USA*

Arif Yurdagul Jr • *Department of Molecular and Cellular Physiology, LSU Health Shreveport, Shreveport, LA, USA*

Ioannis Zabetakis • *Department of Biological Sciences, University of Limerick, Limerick, Ireland; Health Research Institute, University of Limerick, Limerick, Ireland*

Chuankai Zhang • *Institute for Cardiovascular Prevention (IPEK), Klinikum of the University of Munich (KUM), Ludwig-Maximilians-University (LMU), Munich, Germany*

Xi Zhang • *Institute for Cardiovascular Prevention (IPEK), Klinikum of the University of Munich (KUM), Ludwig-Maximilians-University (LMU), Munich, Germany*

Part I

Atherosclerosis: Pathogenesis, Model Systems and Emerging Concepts

Chapter 1

Atherosclerosis: Pathogenesis and Key Cellular Processes, Current and Emerging Therapies, Key Challenges, and Future Research Directions

Yee-Hung Chan and Dipak P. Ramji

Abstract

Atherosclerosis is the principal cause of cardiovascular disease that continues to be a substantial drain on healthcare systems, being responsible for about 31% of all global deaths. Atherogenesis is influenced by a range of factors, including oxidative stress, inflammation, hypertension, and hyperlipidemia, and is ultimately driven by the accumulation of low-density lipoprotein cholesterol within the arterial wall of medium and large arteries. Lipoprotein accumulation stimulates the infiltration of immune cells (such as monocytes/macrophages and T-lymphocytes), some of which take up the lipoprotein, leading to the formation of lipid-laden foam cells. Foam cell death results in increased accumulation of dead cells, cellular debris and extracellular cholesterol, forming a lipid-rich necrotic core. Vascular smooth muscle cells from the arterial media also migrate into the intima layer and proliferate, taking up the available lipids to become foam cells and producing extracellular matrix proteins such as collagen and elastin. Plaque progression is characterized by the formation of a fibrous cap composed of extracellular matrix proteins and smooth muscle cells, which acts to stabilize the atherosclerotic plaque. Degradation, thinning, and subsequent rupture of the fibrous cap leads to lumen-occlusive atherothrombosis, most commonly resulting in heart attack or stroke. This chapter describes the pathogenesis of atherosclerosis, current and emerging therapies, key challenges, and future directions of research.

Key words Atherosclerosis, Cardiovascular disease, Inflammation, Macrophages, Vascular smooth muscle cells

1 Introduction

Atherosclerosis is the major cause of cardiovascular disease (CVD) which persists as a top cause of global morbidity and mortality [1, 2], being responsible for 17.9 million deaths annually according to the World Health Organization (WHO). In the UK alone, 7.4 million people are living with CVD according to the British Heart Foundation. CVD is a broad term that describes conditions of the heart and circulation; these include coronary artery disease (CAD), peripheral vascular disease (PVD), angina pectoris and

Dipak P. Ramji (ed.), *Atherosclerosis: Methods and Protocols*, Methods in Molecular Biology, vol. 2419,
https://doi.org/10.1007/978-1-0716-1924-7_1,
© The Author(s), under exclusive license to Springer Science+Business Media, LLC, part of Springer Nature 2022

cerebrovascular accidents. The high prevalence of CVD in modern society is attributed to rising obesity and diabetes [1], predisposing to the development of atherosclerosis and its sequelae. A chronic inflammatory disorder of the vasculature, atherosclerosis is largely asymptomatic until the late stages of the disease, occurring decades later, where plaque rupture and thrombosis may trigger a range of clinical manifestations, with myocardial infarction (heart attack) and cerebrovascular accident (stroke) being the most common [3]. Atherosclerosis and its associated adverse cardiovascular events hence remain a significant health and socioeconomic burden, driving much of past and current research into delineating its etiology/pathogenesis and uncovering potential therapeutic avenues. The repertoire of methods and model systems developed and applied in atherosclerosis research is hence extensive. Standardization of in vitro and preclinical atherosclerosis research methods is vital to enable robust data interpretation and comparisons between studies.

2 Atherogenesis

Atherosclerosis is characterized by the formation of fibrous plaques within the walls of medium and large arteries, arising from lipid deposition and accumulation within the arterial subendothelial space that stimulates an inflammatory response. Key risk factors of atherosclerosis include hypercholesterolemia, hypertriglyceridemia, oxidative stress, hypertension, and inflammation [4]. Within the vasculature, sites of bifurcations and inner curvatures associated with incessant low-grade inflammation, are especially prone to disease development [5]. Endothelial cells (ECs) form a continuous monolayer lining in most blood vessels and have key functions, including regulating vascular tone, as well as anti-inflammatory, antioxidative, and homeostatic responses. The ECs are constantly subject to different types of shear stress that results from the flow of circulating blood [6]. They contain various mechanosensing molecules/complexes on their membranes, which sense changes in blood flow patterns (mechanosensors), transducing the mechanosignal to the ECs [7]. When these mechanosensors have altered expression or structure, this changes mechanotransduction, leading to endothelial dysfunction/activation [8]. Endothelial dysfunction is the key initiating step of atherogenesis; ECs can also become "activated" as part of the immune response to cholesterol accumulation within the arterial intima [9]. Changes include endothelial hyperpermeability, increased expression of adhesion molecules (such as vascular cell adhesion molecule (VCAM)-1 and intercellular adhesion molecule (ICAM)-1), and release of proinflammatory mediators. These changes ultimately enhance leukocyte–endothelial adhesion, vascular smooth muscle cell (VSMC) proliferation

and migration, foam cell formation and platelet activation [10]. Low-density lipoprotein (LDL) is the major carrier of cholesterol in the bloodstream (*see* [11] for a detailed review of the role of cholesterol metabolism in atherosclerosis). Elevated circulating LDL levels increase the risk of its accumulation within the arterial wall (with LDL delivery facilitated by scavenger receptor (SR) class B type 1 [12]) and subsequent atherogenesis. Apolipoprotein (apo) B (apoB) contained within the lipoproteins encourages their retention and aggregation within the subendothelial space [13], where they are prone to modification, in particular oxidation by locally produced reactive oxygen species (ROS), forming oxidized LDL (oxLDL) [14]. OxLDL is immunogenic [15] and also stimulates the activation of surrounding ECs and the infiltration of circulating immune cells, including monocytes and T-lymphocytes to the region. Moreover, oxLDL may also promote necroptosis activation, a nonapoptotic, programmed cell death pathway, as well as inflammation within the surrounding tissues [16]. Therefore, sustained elevations in ROS not only increase oxidation of lipoproteins but can induce oxidative stress and oxidative damage to the cells and their components, promoting cellular dysfunction and pathogenesis. High-density lipoprotein (HDL) facilitates the clearance of excess cholesterol effluxed from cells via transportation from peripheral tissues to the liver for excretion via reverse cholesterol transport (RCT). This pathway involves the efflux of intracellular cholesterol by the ATP-binding cassette transporters (e.g., ABCA1, ABCG1), packaging of this cholesterol by apoA-I into nascent HDL particles, and subsequent release of cholesterol from the plasma membrane [14, 17, 18]. Additional HDL lipidation and maturation in the plasma is followed by eventual hepatic uptake (SR-B1 binds the mature HDL) and cholesterol removal via catabolism and excretion [19, 20]. Although considered as the "good," atheroprotective cholesterol, strategies focused on elevating levels of HDL cholesterol (HDL-C) have not produced the promising, anti-atherogenic/atheroprotective effects as hoped, despite studies demonstrating an inverse relationship between plasma HDL-C levels and CVD risk [21–25]. This suggests that the atheroprotective functions of HDL (i.e., its cholesterol efflux activity) are more important than its concentration.

3 Foam Cell Formation

Increased endothelial permeability combined with the expression of adhesion molecules and cytokines/chemokines promotes the recruitment and migration of circulating immune cells to the subendothelial space via endothelial adhesion ("rolling and adherence") and subsequent transendothelial diapedesis. For example, monocyte chemoattractant/chemotactic protein (MCP)-1 (also

known as C-C motif chemokine ligand 2 (CCL2)), produced by monocytes/macrophages, ECs and VSMCs, is a key chemokine responsible for summoning circulating monocytes to the lesion [26]. MCP-1 is highly expressed in atherosclerotic lesions and critically involved in the initiation and amplification of monocyte recruitment to the arterial wall [27, 28]. Macrophage colony-stimulating factor (M-CSF) and granulocyte–macrophage colony-stimulating factor (GM-CSF) induce the monocytes to differentiate into macrophages, which can be polarized into various subsets depending on the local environment. At the broadest and simplest level, macrophages are classified as M1 (classically activated, pro-inflammatory) or M2 (alternatively activated, anti-inflammatory), but various subsets of these classes exist and have been reviewed in detail by [26]. Both M1 and M2 macrophages are prominent throughout human atherosclerosis [29]. Activities of M1 macrophages include contributing to T helper 1 cell (Th1) responses, and mediating pro-inflammatory and disruptive reactions, while M2 macrophages manifest Th2-associated effector functions, expressing IL-10 (anti-inflammatory cytokine), SRs and mannose receptors [30, 31]. Cytokines originating from M1 macrophages can induce endothelial dysfunction via dampening endothelial nitric oxide synthase (eNOS) expression and enhancing oxidative stress by increasing ROS and reactive nitrogen species (RNS) production [32]. Resident macrophages also undergo local proliferation resulting in increased macrophage numbers independent of monocytes recruited from the bloodstream [33]. Initially, the presence of macrophages is beneficial and vital for the phagocytosis and clearance of the accumulated cholesterol [34]. However, these cells can undergo metabolic reprogramming as a result of exposure to the different stresses within the atherosclerotic microenvironment due to their heterogeneity and plasticity [35]. Changes include enhanced proliferation and production of pro-inflammatory mediators; both these pro-atherogenic processes exacerbate inflammation and increase the availability of macrophages for foam cell formation, promoting disease progression.

Macrophage cholesterol uptake is facilitated by various receptor- and non-receptor-mediated mechanisms (e.g., macropinocytosis and phagocytosis) [14]. Increased cholesterol uptake and decreased cholesterol efflux facilitate the retention of abnormally high levels of cholesterol within the cell, resulting in the formation of lipid-laden foam cells. Hence, LDL-C has been widely used as a key marker and predictor of CVD risk in clinical practice over the years [36]. The initial accumulation of foam cells is responsible for the early lesion formation (referred to as a “fatty streak”). Cholesterol efflux from the cell is mediated by a number of efflux transporters, including ABCA1 and ABCG1. Macrophages have increased expression of SRs (e.g., cluster of differentiation (CD) 36 and SR-A1), which facilitate the unregulated and excessive

uptake of modified LDL [37], resulting in the formation of lipid-laden foam cells. Contrary to LDL uptake via its cognate receptor (LDL receptor; LDLR), SR-mediated uptake of oxLDL is not regulated by intracellular cholesterol levels via negative feedback. This enables the accumulation of excess intracellular cholesterol, which is also furthered by impaired cholesterol efflux out of the cell. Cholesterol crystals within macrophages can trigger activation of the nucleotide oligomerization domain (NOD) leucine-rich repeat (LRR) and pyrin domain (PYD) containing protein 3 (NLRP3) inflammasome to result in caspase-1-mediated cleavage and secretion of potent pro-inflammatory cytokines, interleukin (IL)-1β and IL-18 [38]. These are only a few of a plethora of cytokines expressed in atherosclerotic plaques and implicated in atherosclerosis; others include tumor necrosis factors (TNFs) (e.g., TNF-α) and interferons (IFNs) (e.g., IFN-γ). Pro-inflammatory cytokines are involved in all stages of the disease, being master regulators of numerous atherogenic processes (*see* [11, 39] for detailed reviews).

Abnormal/excess intracellular cholesterol loading leads to cell death via apoptosis, necrosis and other mechanisms, resulting in the release of an array of pro-inflammatory/atherogenic mediators that perpetuate chronic inflammation and dysfunction. Macrophages and macrophage-derived foam cells are hence key cell types that constitute atherosclerotic plaques, having a major impact on plaque burden and chronic inflammation. More recently however, VSMCs are also being increasingly recognized as a key cell type of atherosclerotic plaques that possess much more heterogeneity and plasticity than previously believed. VSMCs can also adopt phenotypes akin to those of macrophages, foam cells, mesenchymal stem cells and osteochondrogenic cells, and can have both positive and negative effects on atherosclerosis progression [2]. Results of lineage-tracing studies have demonstrated that VSMCs and VSMC-derived cells have a more complex and prominent role in the disease than previously thought [2], providing a major source of plaque cells and extracellular matrix (ECM) proteins throughout atherosclerosis. These studies have broadened the view of the roles that VSMCs play in atherosclerosis, which were largely underestimated in their plasticity, heterogeneity and contribution to disease progression [2].

4 Plaque Progression and Rupture

Continued cell death results in the formation of a necrotic core as dead cells, cellular debris and extracellular cholesterol amass in the arterial wall. Defective efferocytosis promotes the retention of these materials within the intima layer and growth of the necrotic core, while the increasingly necrotic environment promotes pro-inflammatory signaling to amplify inflammation [26]. As the

atherosclerotic plaque progresses, a fibrous cap forms which encapsulates and stabilizes the plaque. Fibrous cap formation coincides with the infiltration of VSMCs (from the tunica media) to the intima; the VSMCs undergo a phenotypic shift from a quiescent state to become proliferative, synthetic cells that produce ECM proteins. These include collagens, elastins, and proteoglycans, which become major constituents of the fibrous cap [40]. In the later stages of atherosclerosis, lesional macrophages and other cells produce matrix metalloproteinases (MMPs) and other proteases which degrade this protective fibrous cap, increasing plaque vulnerability, destabilization, and, ultimately, risk of rupture [14, 41, 42]. Degradation and thinning of the fibrous cap are also expediated by suppressed expression of tissue inhibitor of MMP (TIMP) and sustained inflammation, which reduce VSMC proliferation and encourages VSMC death by apoptosis. It is well known that vulnerable plaques possess a large, lipid-rich necrotic core bound by a fine, unstable, and substantially inflamed fibrous cap rich in monocytes, macrophages and T-lymphocytes [43]. Plaque rupture results in thrombosis; the specific anatomical location of the thrombus within the vascular bed dictates the clinical manifestation, which includes angina pectoris, PVD and CAD [2]. A diagrammatic overview of the key processes and cytokines implicated in atherosclerosis pathogenesis is shown in Fig. 1.

5 Current and Emerging Therapeutic Strategies

Currently available therapeutic strategies for atherosclerosis/CVD are mainly targeted to manipulating lipid metabolism combined with lifestyle changes to modify plasma lipoprotein profile and combat hyperlipidemia. The current, gold standard preventative and therapeutic strategy widely used is statins (3-hydroxy-3-methyl-glutaryl Coenzyme A (HMG-CoA) reductase inhibitors). Statins work by inhibiting the key, rate-limiting step of endogenous cholesterol synthesis which is catalyzed by HMG-CoA reductase [45]. Statins hence lower cholesterol levels while also having other pleiotropic effects, including anti-inflammatory activities [46]. Statins have had significant impact on lowering morbidity and mortality from atherosclerosis and its associated major adverse cardiovascular events (MACE) since its widespread application in clinical practice. However, it is important to note that clinical trials have also identified significant residual cardiovascular risk after statin therapy [47–49]. Furthermore, statins are known to have adverse side effects (e.g., myalgias and hepatic abnormalities), some of which can be severe although rare (e.g., rhabdomyolysis), resulting in compromised patient compliance. Furthermore, disappointing results from trials on numerous agents developed against established targets [50–52] has fueled the exploration of alternative

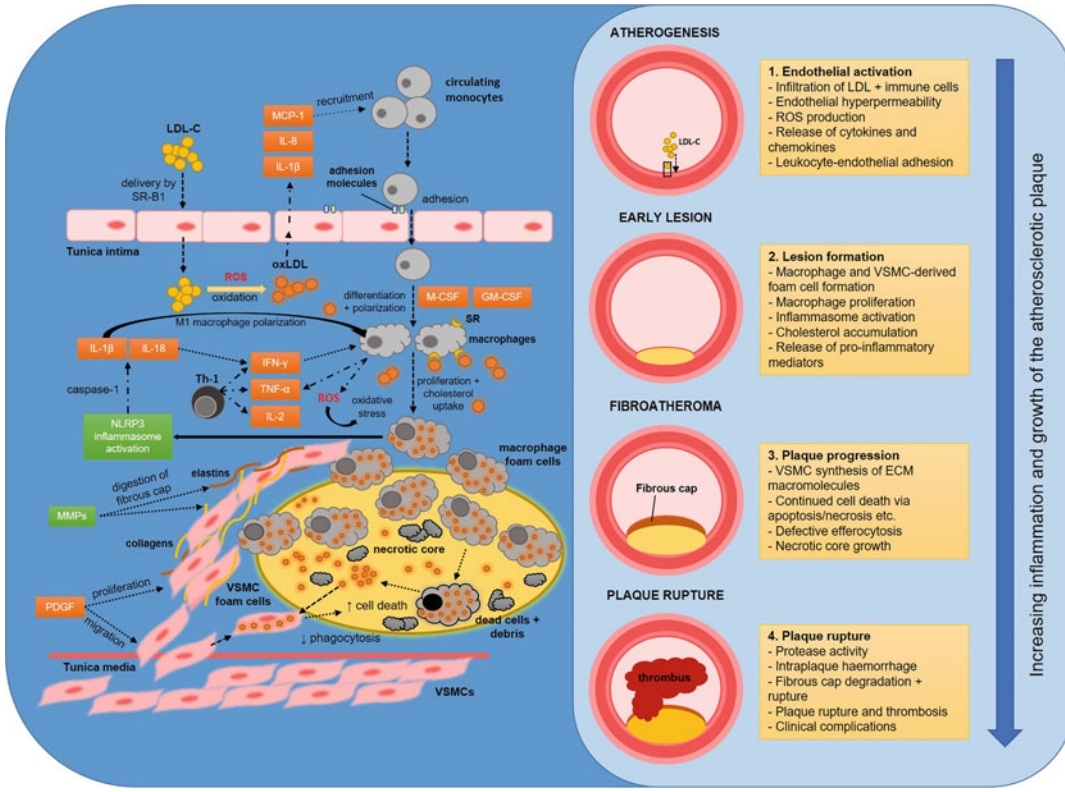

Fig. 1 Diagrammatic representation of pathogenesis of atherosclerosis. Key cellular processes and cytokines are illustrated (adapted from [44]). LDL, low-density lipoprotein; SR-B1, scavenger receptor-B1; MCP-1, monocyte chemotactic protein-1; IL-1β, interleukin-1β; IL-8, interleukin-8; ROS, reactive oxygen species; oxLDL, oxidized LDL; M-CSF, macrophage colony-stimulating factor; GM-CSF, granulocyte–macrophage colony-stimulating factor; SR, scavenger receptor; IL-18, interleukin-18; IFN-γ, interferon-γ; TNF-α; tumor necrosis factor-α; IL-2, interleukin-2; Th1, T-helper 1 cell; NLRP3, nucleotide oligomerization domain (NOD) leucine-rich repeat (LRR) and pyrin domain (PYD) containing protein 3; MMPs, matrix metalloproteinases; PDGF; platelet-derived growth factor; VSMC, vascular smooth muscle cell

therapeutic avenues. Cholesteryl ester transfer protein (CETP) inhibitors for example, appeared to be promising agents for atherosclerosis due to their ability to increase HDL-C and reduce LDL-C levels based on studies using animal models [53–56]. This is as CETP mediates the transfer of esterified cholesterol from HDL to LDL and very-low density lipoprotein (VLDL) particles in exchange for triglycerides (TGs) [57]. However, large-scale clinical trials have yielded largely disappointing results; where benefit was obtained, it was modest at best and derived with an agent whose pharmacokinetic issues prevented regulatory approval [58].

A promising alternative to statin therapy is the inhibition of proprotein convertase subtilisin/kexin type-9 (PCSK9) to prevent PCSK-9-mediated degradation of the LDLR and increase LDL-C absorption by the liver [59]. PCSK-9 binds to LDLR to stimulate

its degradation by intracellular lysosomes to limit its availability on the cell surface [60, 61]. PCSK-9 inhibition can be achieved via monoclonal antibodies or gene silencing using small-interfering RNA (siRNA). The only two licensed human monoclonal antibodies of PCSK9 are evolocumab and alirocumab, which have been shown to reduce LDL-C levels by more than half in two phase III trials [62]. SiRNA is a type of noncoding RNA (ncRNA) which acts on one specific gene, contributing to gene silencing and degradation to prevent translation. Inclisiran inhibits hepatic PCSK-9 synthesis and has recently been shown to reduce LDL-C levels by approximately 50% in atherosclerotic CVD (or equivalent) patients receiving subcutaneous injections every 6 months in two phase III clinical trials (ORION-10 and ORION-11) [63]. However, their high cost and sub-optimal cost effectiveness, due to the requirement of repeated subcutaneous injection, continues to restrict widespread application in clinical practice. As with any drug that requires subcutaneous injection, appropriate management of injection site adverse events is also required. Another promising agent is ezetimibe, which lowers LDL-C by inhibiting cholesterol absorption at the brush border of the small intestine [64]. Clinical studies have reported a maximum of 22% reduction in LDL-C after ezetimibe monotherapy and their results provide evidence supporting its use as a secondary therapy for patients unsuited to statins [43, 65]. Therefore, there is an increasing demand for low cost, effective therapeutic strategies for patients unsuitable for statins and those at risk of secondary MACE, post-statin therapy. Another potential avenue showing promise is bempedoic acid which inhibits a key enzyme involved in endogenous cholesterol synthesis upstream of HMG-CoA reductase [66] without the adverse side effects as seen with statins [67, 68]. This agent has been combined with ezetimibe to successfully reduce LDL-C in high-risk CVD patients [69], although how this translates to reduction in cardiovascular risk is yet to be established.

Recently, focus has switched more to the use of anti-inflammatory strategies (e.g., anti-inflammatory/cytokine therapies) to dampen levels of key pro-inflammatory cytokines (e.g., IL-1β and IL-6) and combat persisting inflammation, especially since results of the breakthrough Canakinumab Anti-Inflammatory Thrombosis Outcomes Study (CANTOS) were published in 2017 [70]. This trial showed that targeted reduction in IL-1β levels is effective in combating the residual cardiovascular risk that persists post-statin therapy. The broad-spectrum anti-inflammatory agent, colchicine, is another promising avenue which has demonstrated comparable success to canakinumab in terms of cardiovascular risk reduction [71–73], which may also be attributed to its inhibitory actions on NLRP3 inflammasome activation [74] and subsequent generation of IL-1β [75]. Therefore, given the key role of IL-1β in driving pathogenesis and chronic inflammation in atherosclerosis, targeting

the IL-1 pathway of inflammation is a logical and seemingly effective strategy.

Another potential avenue beyond strategies modifying cholesterol metabolism but in the much more earlier stages of development, is blood flow mimetic compounds targeted to ameliorating endothelial dysfunction, the rate-limiting step of atherogenesis. Emerging studies have shown that pharmacological modulators of mechanosensors, transcription factors (TFs) and associated enzymes, attenuate endothelial dysfunction and reduce the occurrence of experimental atherosclerosis [4]. This is since flow-induced biomechanical signals modulate the gene expression and/or activity of mechanosensitive TFs, epigenetic modification enzymes and ncRNAs to regulate endothelial function by stimulating biological responses. Examples include agonists of transient receptor potential cation channel subfamily V member 4 (TRPV4; an EC mechanosensor) to improve endothelium-dependent vasodilation (e.g., GSK1016790A), which has shown to be capable of activating eNOS-dependent vasodilation and attenuating endothelial dysfunction and atherosclerosis in *ApoE*-deficient ($ApoE^{-/-}$) mice fed Western-type diet (WD) [76], and activators of Kruppel-like factor 2 (KLF2) (a master regulator of flow-induced endothelial gene expression with downstream genes critically involved in regulating vascular homeostasis and remodeling) (e.g., tannic acid), which has demonstrated atheroprotective actions in hyperlipidemia $ApoE^{-/-}$ mice fed WD [77, 78]. Importantly, KLF2 is also a key molecular target of statins, which induce activation of KLF2 expression and activity via two distinct pathways [79, 80]. Furthermore, evidence suggests that statin therapy can reduce hepatic expression of *Apoc3*, the gene coding for apoC-III, which inhibits lipoprotein lipase (LPL) and is a key regulator of TG metabolism. LPL is the main enzyme responsible for the hydrolysis of TG in TG-rich lipoproteins (TRLs) [81]. Strategies targeted to lowering apoC-III levels has demonstrated potential for the management of hypertriglyceridemia and subsequent CVD prevention in individuals with elevated plasma TG concentrations [81]. Loss-of-function mutation in *Apoc3* and subsequent deficiency in apoC-III has been associated with rapid lipolysis of plasma TRLs [82, 83]. Trials exploiting emerging gene-silencing technologies demonstrate that intervention markedly lowers apoC-III levels and plasma TG [81], outcomes from recent clinical trials indicate effective reduction of plasma TGs is achieved via inhibition of apoC-III [84, 85].

Nutraceuticals, food constituents with additional health benefits beyond their nutritional value, represent promising alternative preventative/therapeutic avenues that can be combined with current pharmacological therapies. Armed with a plethora of cardiovascular health benefits, including anti-inflammatory and antioxidative properties, they demonstrate potential in attenuating atherogenesis and disease progression at a cheaper cost compared

to other pharmaceutical agents. Particular examples include omega-3 polyunsaturated fatty acids ($n-3$ PUFAs) [86–88] (e.g., eicosapentaenoic acid (EPA) and docosahexaenoic acid (DHA)), green tea catechins [89–91] and olive oil polyphenols [92–94] (e.g., hydroxytyrosol). The Reduction of Cardiovascular Events with Icosapent Ethyl-Intervention Trial (REDUCE-IT) demonstrated that daily intake of 4 g of icosapent ethyl (IPE; a purified EPA ethyl ester) by patients with established CVD/diabetes/other risk factors already on statin therapy significantly reduced the incidence of total cardiovascular events by 32% [95]. More recently, the Effect of Icosapent Ethyl on Progression of Coronary Atherosclerosis in Patients with Elevated TGs on Statin Therapy (EVAPORATE) trial showed that the same dose of IPE significantly decreased the volume of low attenuation plaques (unstable plaques with high risk of rupture) and other associated parameters together with subsequent plaque burden at 18 months in CAD patients with no effect on TG [96]. Together, these studies emphasize the promising potential of exploiting nutraceutical agents as cotherapies with statins for the prevention and treatment of atherosclerosis and atherosclerotic CVD. However, further research is required to fully characterize their beneficial actions and associated underlying mechanisms to identify more potential candidates.

6 Challenges of Atherosclerosis Treatment and Research

Prevention and treatment of atherosclerosis and its associated MACE poses a major clinical challenge, in part due to the complexity of its etiology and pathophysiology. Furthermore, this is compounded by the fact that, while tremendous progress has been made in developing understanding of the disease, the comprehensive role of all atherogenic mediators and underlying mechanisms still require full characterization. Some mediators may also have more ambiguous effects on disease and may be considered as both pro-atherogenic and anti-atherogenic. A number of key cellular processes implicated in atherosclerosis have been recapitulated in vitro and there are a number of animal models available to study disease development and progression and even, regression. Over the years, research has largely relied upon using animal models of atherosclerosis to understand its etiology and key processes, and to gain insights into the underlying mechanisms. Mouse models have provided the majority of mechanistic insights into atherosclerosis over the past three decades. Since mice are naturally resistant to atherosclerosis, inducing atherogenesis requires genetic or other modifications to alter their normal physiological cholesterol metabolism. The two principal mouse models of atherosclerosis are *Apoe*$^{-/-}$- and *Ldlr*-deficient mice (*Ldlr*$^{-/-}$) [97],

although the different mouse models available today have greatly expanded beyond these. In both mouse models, atherosclerosis is driven by modification of their normal lipoprotein profile to increase levels of circulating LDL-C. The benefits of using mice include their cost-effectiveness combined with ease of genetic manipulation and cross-breeding [97, 98], as well as the ability to induce atherosclerosis in a matter of months compared to the decades it requires to develop in humans. Therefore, it is easy to see why mice are the most used animals for studying atherosclerosis [99]. However, differences exist between mouse and human atherosclerotic plaques; mice lack a thick fibrous cap [100], have less coronary plaque formation, and plaque rupture is rare [98]. Moreover, there are differences in lipoprotein and immune cell profiles between humans and mice [98]. Nonetheless, the continued efforts to develop atherosclerosis model systems have advanced our knowledge and understanding of the disease, playing vital roles in drug discovery and development by bridging the gap between in vitro and clinical studies. Disease heterogeneity contributed by the involvement of a multitude of factors that are inextricably linked is another reason for the difficulty in the development of accurate atherosclerosis models, with disparity of atherosclerotic plaques between different individuals. Even in the $Ldlr^{-/-}$ mouse model, female $Ldlr^{-/-}$ mice develop larger, more severe plaques compared to their male counterparts [101–104]. This heterogeneity is also present between plaques of different locations and vascular beds within the same individual [105, 106]. Therefore patient-dependent efficacy will likely be a persisting hurdle in any therapeutic strategy for atherosclerosis and CVD.

CVD is the largest cause of mortality worldwide and the major contributor to pathology is atherosclerosis. Being responsible for such a high proportion of all deaths, therapeutic strategies for CVD must have low cost and be readily available to enable extensive application on the frontline of cardiovascular medicine. Several pharmaceutical agents beyond statins able to effectively reduce circulating plasma cholesterol levels have been developed in recent years. However, their expense and/or limited cost effectiveness continues to restrict their use to high-risk patients. Furthermore, the pathophysiology of atherosclerosis is driven by much more than hyperlipidemia/hypercholesterolemia alone. While statins have had significant positive impact on CVD mortality rates, it is incapable of eliminating cardiovascular risk altogether, fueling the search into alternative therapeutic avenues beyond hypercholesterolemia attenuation. While atherosclerosis has been widely accepted and well known to be a disorder with an inflammatory component, anti-inflammatory strategies were largely unsuccessful until canakinumab was shown to significantly reduce risk of secondary MACE in MI patients in the CANTOS trial [70]. This breakthrough phase III clinical trial has encouraged research into agents capable of

modulating inflammation to suppress levels of potent pro-inflammatory cytokines involved in atherosclerosis. It is important to also note that another clinical trial exploiting low-dose methotrexate was unsuccessful at reducing cardiovascular risk [107] (despite the drug being associated with fewer cardiovascular events in arthritic patients [108–110]), and so further research on inflammation as a therapeutic target is needed. However, as with any therapy targeting mediators of the immune system, issues and challenges will be with compromising immune function and suitability of treatment for those already immunocompromised. Beyond this, issues will likely be surrounding cost-effectiveness and overall price, to identify agents that can be manufactured at a low cost and maximize cost effectiveness to enable widespread use on the frontline of medical practice.

7 Future Research Directions

Development of more accurate models of atherosclerosis and other research techniques in the field is increasingly important despite advances in knowledge over the years. This will no doubt increase the rate and efficiency of developing potential therapies, as well as help elucidate underlying mechanisms responsible for driving pro-atherogenic processes. When exploring the preventative/therapeutic potential of emerging agents/avenues, it would be highly beneficial to adopt a standardized approach for conducting experiments moving forward to improve consistency, which we hope to facilitate with methods-based resources. This will enable direct and meaningful comparisons between studies and help accelerate the research and development process. Furthermore, the complexity, heterogeneity, and multifaceted nature of atherosclerosis pathophysiology underpinned by various interlinking mechanisms has helped encourage a lean toward high-throughput research methods in order to gain a deeper mechanistic understanding of the disease. Examples being RNA-sequencing (RNA-seq) on disease-relevant tissues (e.g., different layers of the arteries such as aorta, and liver), and single-cell RNA-seq to gain more meaningful and deeper insights on global gene expression changes at the tissue and cellular level respectively. It is hoped that resources like these will facilitate the progression of atherosclerosis research to the next level by elucidating the underlying mechanisms and assist in the targeted research and development of novel therapies for atherosclerosis, and CVD prevention and treatment in the future.

Acknowledgments

We thank the British Heart Foundation for financial support (grants PG/16/25/32097 and FS/17/75/33257).

References

1. Moss JWE, Ramji DP (2016) Nutraceutical therapies for atherosclerosis. Nat Rev Cardiol 13(9):513–532. https://doi.org/10.1038/nrcardio.2016.103
2. Basatemur GL, Jørgensen HF, Clarke MCH, Bennett MR, Mallat Z (2019) Vascular smooth muscle cells in atherosclerosis. Nat Rev Cardiol 16(12):727–744. https://doi.org/10.1038/s41569-019-0227-9
3. Virani SS et al (2021) Heart disease and stroke statistics - 2021 update. Circulation 143(8):e254–e743
4. Xu S (2020) Therapeutic potential of blood flow mimetic compounds in preventing endothelial dysfunction. Pharmacol Res 155:104737. https://doi.org/10.1016/j.phrs.2020.104737
5. Jongstra-Bilen J, Haidari M, Zhu SN, Chen M, Guha D, Cybulsky MI (2006) Low-grade chronic inflammation in regions of the normal mouse arterial intima predisposed to atherosclerosis. J Exp Med 203(9):2073–2083
6. Rajendran P, Rengarajan T, Thangavel J et al (2013) The vascular endothelium and human diseases. Int J Biol Sci 9(10):1057–1069
7. Fang Y, Wu D, Birukov KG (2019) Mechanosensing and mechanoregulation of endothelial cell functions. Compr Physiol 9(2):873–904
8. Niu N, Xu S, Xu Y et al (2019) Targeting mechanosensitive transcription factors in atherosclerosis. Trends Pharmacol Sci 40(4):253–266
9. Sitia S, Tomasoni L, Atzeni F, Ambrosio G, Cordiano C, Catapano A, Tramontana S, Perticone F, Naccarato P, Camici P, Picano E, Cortigiani L, Bevilacqua M, Milazzo L, Cusi D, Barlassina C, Sarzi-Puttini P, Turiel M (2010) From endothelial dysfunction to atherosclerosis. Autoimmun Rev 9:830. https://doi.org/10.1016/j.autrev.2010.07.016
10. Wang D, Yang Y, Lei Y et al (2019) Targeting foam cell formation in atherosclerosis: therapeutic potential of natural products. Pharmacol Rev 71(4):596–670
11. Buckley ML, Ramji DP (2015) The influence of dysfunctional signaling and lipid homeostasis in mediating the inflammatory responses during atherosclerosis. Biochim Biophys Acta 1852(7):1498–1510. https://doi.org/10.1016/j.bbadis.2015.04.011
12. Huang L, Chambliss KL, Gao X, Yuhanna I, Behling-Kelly E, Bergaya S, Ahmed M, Michaely P, Luby-Phelps K, Darehshouri A, Xu L, Fisher EA, Ge WP, Mineo C, Shaul PW (2019) SR-B1 drives endothelial cell LDL transcytosis via DOCK4 to promote atherosclerosis. Nature 569(7757):565–569
13. Tabas I, Williams KJ, Boren J (2007) Subendothelial lipoprotein retention as the initiating process in atherosclerosis: update and therapeutic implications. Circulation 116:1832–1844
14. McLaren JE, Michael DR, Ashlin TG et al (2011) Cytokines, macrophage lipid metabolism and foam cells: implications for cardiovascular disease therapy. Prog Lipid Res 50:331–347
15. Zhang J, Wang D, Shenghu H (2015) Roles of antibody against oxygenized low density lipoprotein in atherosclerosis: recent advances. Int J Clin Exp Med 8(8):11922–11929
16. Ruan Z-H, Xu Z-X, Zhou X-Y, Zhang X, Shang L (2019) Implications of necroptosis for cardiovascular diseases. Curr Med Sci 39(4):513–522
17. Michael DR, Ashlin TG, Davies CS et al (2013) Differential regulation of macropinocytosis in macrophages by cytokines: implications for foam cell formation and atherosclerosis. Cytokine 64(1):357–361
18. Phillips MC (2014) Molecular mechanism of cellular cholesterol efflux. J Biol Chem 29:24020–24029
19. Trigatti BL, Rigotti A, Braun A (2000) Cellular and physiological roles of SR-B1, a lipoprotein receptor which mediates selective lipid uptake. Biochim Biophys Acta 1529(1–3):276–286
20. Trigatti BL, Rigotti A, Krieger M (2000) The role of the high-density lipoprotein receptor SR-B1 in cholesterol metabolism. Curr Opin Lipidol 11(2):123–131

21. Kwiterovich PO (1998) The antiatherogenic role of high-density lipoprotein cholesterol. Am J Cardiol 82(9A):13Q–21Q
22. Boden WE (2000) High-density lipoprotein cholesterol as an independent risk factor in cardiovascular disease: assessing the data from Framingham to the Veterans Affairs high-density lipoprotein intervention trial. Am J Cardiol 86(12A):19L–22L
23. Harper CR, Jacobson TA (1999) New perspectives on the management of low levels of high-density lipoprotein cholesterol. Arch Intern Med 159(10):1049–1057
24. Libby P (2001) What have we learned about the biology of atherosclerosis? The role of inflammation. Am J Cardiol 88(7B):3J
25. Di Angelantonio E, Sarwar N, Perry P, Kaptoge S, Ray KK, Thompson A, Wood AM, Lewington S, Sattar N, Packard CJ, Collins R, Thompson SG, Danesh J (2009) Major lipids, apolipoproteins, and risk of vascular disease. JAMA 302(18):1993–2000
26. Shirai T, Hilhorst M, Harrison DG et al (2015) Macrophages in vascular inflammation - from atherosclerosis to vasculitis. Autoimmunity 48(3):139–151
27. Gerszten RE, Garcia-Zepeda EA, Lim YC et al (1999) MCP-1 and IL-8 trigger firm adhesion of monocytes to vascular endothelium under flow conditions. Nature 398:718–723
28. Colonnello JS, Hance KA, Shames ML et al (2003) Transient exposure to elastase induces mouse aortic wall smooth muscle cell production of MCP-1 and RANTES during development of experimental aortic aneurysm. J Vasc Surg 38:138–146
29. Stoger JL, Gijbels MJ, van der Velden S et al (2012) Distribution of macrophage polarization markers in human atherosclerosis. Atherosclerosis 225:461–468
30. Fenyo IM, Gafencu AV (2013) The involvement of the monocytes/macrophages in chronic inflammation associated with atherosclerosis. Immunobiology 218:1376–1384
31. Mantovani A, Garlanda C, Locati M (2009) Macrophage diversity and polarization in atherosclerosis: a question of balance. Arterioscler Thromb Vasc Biol 29:1419–1423
32. Simionescu M (2009) Cellular dysfunction in inflammatory-related vascular disorders' review series. The inflammatory process: a new dimension of a 19 century old story. J Cell Mol Med 13:4291–4292
33. Robbins CS, Hilgendorf I, Weber GF, Theurl I, Iwamoto Y, Figueiredo JL, Gorbatov R, Sukhova GK, Gerhardt LM, Smyth D, Zavitz CC, Shikatani EA, Parsons M, van Rooijen N, Lin HY, Husain M, Libby P, Nahrendorf M, Weissleder R, Swirski FK (2013) Local proliferation dominates lesional macrophage accumulation in atherosclerosis. Nat Med 19(9): 1166–1172
34. Kzhyshkowska J, Neyen C, Gordon S (2012) Role of macrophage scavenger receptors in atherosclerosis. Immunobiology 217(5): 492–502
35. Koelwyn GJ, Corr EM, Erbay E, Moore KJ (2018) Regulation of macrophage immunometabolism in atherosclerosis. Nat Immunol 19(6):526–537
36. Wadhera RK, Steen DL, Khan I, Giugliano RP, Foody JM (2016) A review of low-density lipoprotein cholesterol, treatment strategies, and its impact on cardiovascular disease morbidity and mortality. J Clin Lipidol 10(3):472–489. https://doi.org/10.1016/j.jacl.2015.11.010
37. Glass CK, Witztum JL (2001) Atherosclerosis. The road ahead. Cell 104(4):503–516
38. Duewell P, Kono H, Rayner KJ, Sirois CM, Vladimer G, Bauernfeind FG, Abela GS, Franchi L, Nuñez G, Schnurr M, Espevik T, Lien E, Fitzgerald KA, Rock KL, Moore KJ, Wright SD, Hornung V, Latz E (2010) NLRP3 inflammasomes are required for atherogenesis and activated by cholesterol crystals. Nature 464(7293):1357–1361. https://doi.org/10.1038/nature08938
39. Moss JWE, Ramji DP (2016) Cytokines: roles in atherosclerosis disease progression and potential therapeutic targets. Future Med Chem 8(11):1317–1330
40. Adiguzel E, Ahmad PJ, Franco C et al (2009) Collagens in the progression and complications of atherosclerosis. Vasc Med 14:73–89
41. Michael DR, Ashlin TG, Buckley ML et al (2012) Macrophages, lipid metabolism and gene expression in atherogenesis: a therapeutic target of the future? J Clin Lipidol 7:37–48
42. Silvestre-Roig C, De Winther MP, Weber C et al (2014) Atherosclerotic plaque destabilization: mechanisms, models, and therapeutic strategies. Circ Res 114:214–226
43. Bergheanu SC, Bodde MC, Jukema JW (2017) Pathophysiology and treatment of atherosclerosis: current view and future perspective on lipoprotein modification treatment. Neth Hear J 25(4):231–242
44. Chan Y-H, Ramji DP (2020) A perspective on targeting inflammation and cytokine actions in atherosclerosis. Future Med Chem 12(7): 613–626

45. Haslinger-Löffler B (2008) Multiple effects of HMG-CoA reductase inhibitors (statins) besides their lipid-lowering function. Kidney Int 74(5):553–555. https://doi.org/10.1038/ki.2008.323
46. Antonopoulos AS, Margaritis M, Lee R, Channon K, Antoniades C (2012) Statins as anti-inflammatory agents in atherogenesis: molecular mechanisms and lessons from the recent clinical trials. Curr Pharm Des 18(11): 1519–1530. https://doi.org/10.2174/138161212799504803
47. Campbell CY, Rivera JJ, Blumenthal RS (2007) Residual risk in statin-treated patients: future therapeutic options. Curr Cardiol Rep 9(6):499–505. https://doi.org/10.1007/bf02938395
48. Libby P, Ridker PM, Hansson GK (2011) Progress and challenges in translating the biology of atherosclerosis. Nature 473(7347):317–325. https://doi.org/10.1038/nature10146
49. Sampson UK, Fazio S, Linton MF (2012) Residual cardiovascular risk despite optimal LDL cholesterol reduction with statins: the evidence, etiology, and therapeutic challenges. Curr Atheroscler Rep 14(1):1–10. https://doi.org/10.1007/s11883-011-0219-7
50. Weber C, Noels H (2011) Atherosclerosis: current pathogenesis and therapeutic options. Nat Med 17:1410–1422
51. Ladeiras-Lopes R, Agewall S, Tawakol A et al (2015) Atherosclerosis: recent trials, new targets and future directions. Int J Cardiol 192: 72–81
52. Moss JWE, Williams JO, Ramji DP (2018) Nutraceuticals as therapeutic agents for atherosclerosis. Biochem Biophys Acta Mol Basis Dis 1864:1562–1572
53. Morehouse LA, Sugarman ED, Bourassa P-A et al (2007) Inhibition of CETP activity by torcetrapib reduces susceptibility to diet-induced atherosclerosis in New Zealand White rabbits. J Lipid Res 48:1263–1272
54. Rittershaus CW, Miller DP, Thomas LJ et al (2000) Vaccine-induced antibodies inhibit CETP activity in vivo and reduce aortic lesions in a rabbit model of atherosclerosis. Arterioscler Thromb Vasc Biol 20:2106–2112
55. Okamoto H, Yonemori F, Wakitani K et al (2000) A cholesteryl ester transfer protein inhibitor attenuates atherosclerosis in rabbits. Nature 406:203–207
56. Sugano M, Makino N, Sawada S et al (1998) Effect of antisense oligonucleotides against cholesteryl ester transfer protein on the development of atherosclerosis in cholesterol-fed rabbits. J Biol Chem 273(9): 5033–5036
57. Barter PJ, Chapman MJ, Hennekens CH et al (2003) Cholesteryl ester transfer protein. A novel target for raising HDL and inhibiting atherosclerosis. Arterioscler Thromb Vasc Biol 23:160–167
58. Nicholls SJ (2018) CETP-inhibition and HDL-cholesterol: a story of CV risk or CV benefit, or both. Clin Pharmacol Ther 104(2):297–300
59. Scherer DJ, Nelson AJ, Psaltis PJ, Nicholls SJ (2017) Targeting low-density lipoprotein cholesterol with PCSK9 inhibitors. Intern Med J 47(8):856–865. https://doi.org/10.1111/imj.13451
60. Leren TP (2014) Sorting an LDL receptor with bound PCSK9 to intracellular degradation. Atherosclerosis 237:76–81
61. Lambert G, Sjouke B, Choque B et al (2012) The PCSK9 decade. J Lipid Res 53: 2515–2524
62. Hadjiphilippou S, Ray KK (2017) PCSK9 inhibition and atherosclerotic cardiovascular disease prevention: does reality match the hype? Heart 103(21):1670–1679. https://doi.org/10.1136/heartjnl-2016-310844
63. Ray KK, Wright S, Kallend D et al (2020) Two phase 3 trials of inclisiran in patients with elevated LDL cholesterol. N Engl J Med 382(16):1507–1519
64. Jia L, Betters JL, Yu L (2011) Niemann-pick C1-like 1 (NPC1L1) protein in intestinal and hepatic cholesterol transport. Annu Rev Physiol 73:239–259. https://doi.org/10.1146/annurev-physiol-012110-142233
65. Catapano AL, Graham I, De Backer G et al (2016) ESC/EAS Guidelines for the management of dyslipidaemias: the task force for the management of dyslipidaemias of the European Society of Cardiology (ESC) and European Atherosclerosis Society (EAS). Developed with the special contribution of the European Association for Cardiovascular Prevention & Rehabilitation (EACPR). Eur Heart J 37(39):2999
66. Pinkosky SL, Filippov S, Srivastava RA et al (2013) AMP-activated protein kinase and ATP-citrate lyase are two distinct molecular targets for ETC-1002, a novel small molecule regulator of lipid and carbohydrate metabolism. J Lipid Res 54:134–151
67. Laufs U, Banach M, Mancini GBJ et al (2019) Efficacy and safety of bempedoic acid in

patients with hypercholesterolemia and statin intolerance. J Am Heart Assoc 8:e011662

68. Ballantyne CM, Banach M, Mancini GBJ et al (2018) Efficacy and safety of bempedoic acid added to ezetimibe in statin-intolerant patients with hypdercholesterolemia: a randomized, placebo-controlled study. Atherosclerosis 277:195–203
69. Ballantyne CM, Laufs U, Ray KK et al (2020) Bempedoic acid plus ezetimibe fixed-dose combination in patients with hypdercholesterolemia and high CVD risk treated with maximally tolerated statin therapy. Eur J Prev Cardiol 27(6):593–603
70. Ridker PM, Everett BM, Thuren T, MacFadyen JG, Chang WH, Ballantyne C, Fonseca F, Nicolau J, Koenig W, Anker SD, Kastelein JJP, Cornel JH, Pais P, Pella D, Genest J, Cifkova R, Lorenzatti A, Forster T, Kobalava Z, Vida-Simiti L, Flather M, Shimokawa H, Ogawa H, Dellborg M, Rossi PRF, Troquay RPT, Libby P, Glynn RJ (2017) Antiinflammatory therapy with canakinumab for atherosclerotic disease. N Engl J Med 377(12):1119–1131. https://doi.org/10.1056/NEJMoa1707914
71. Nidorf SM, Eikelboom JW, Budgeon CA et al (2013) Low-dose colchicine for secondary prevention of cardiovascular disease. J Am Coll Cardiol 61(4):404–410
72. Tardif J-C, Kouz S, Waters DD et al (2019) Efficacy and safety of low-dose colchicine after myocardial infarction. N Engl J Med 381(26): 2497–2505
73. Nidorf SM, Fiolet ATL, Mosterd A et al (2020) Colchicine in patients with chronic coronary disease. N Engl J Med 383(19): 1838–1847
74. Nidorf SM, Eikelboom JW, Thompson PL (2014) Targeting cholesterol crystal-induced inflammation for the secondary prevention of cardiovascular disease. J Cardiovasc Pharmacol Therapeut 19(1):45–52
75. Martinez GJ, Celermajer DS, Patel S (2018) The NLRP3 inflammasome and the emerging role of colchicine to inhibit atherosclerosis-associated inflammation. Atherosclerosis 269:262–271
76. Xu S, Liu B, Yin M et al (2016) A novel TRPV4-specific agonist inhibits monocyte adhesion and atherosclerosis. Oncotarget 7(25):37622–37635
77. Xu Y, Liu P, Xu S et al (2017) Tannic acid as a plant-derived polyphenol exerts vasoprotection via enhancing KLF2 expression in endothelial cells. Sci Rep 7(1):6686
78. Do GM, Kwon EY, Ha TY et al (2011) Tannic acid is more effective than clofibrate for the elevation of hepatic beta-oxidation and the inhibition of 3-hydroxy-3-methyl-glutaryl-CoA reductase and aortic lesion formation in apo E-deficient mice. Br J Nutr 106(12): 1855–1863
79. Parmar KM, Nambudiri V, Dai G et al (2005) Statins exert endothelial atheroprotective effects via the KLF2 transcription factor. J Biol Chem 280(29):26714–26719
80. Sen-Banerjee S, Mir S, Lin Z et al (2005) Kruppel-like factor 2 as a novel mediator of stain effects in endothelial cells. Circulation 112(5):720–726
81. Taskinen M-R, Packard CJ, Boren J (2019) Emerging evidence that apoC-III inhibitors provide novel options to reduce the residual CVD. Curr Atheroscler Rep 21:27
82. Blood I, Crosby J, Peloso GM et al (2014) Rare mutations that disrupt APOC3 function were associated with lower levels of plasma triglycerides and APOC3. Carriers of these mutations were found to have reduced risk of coronary heart disease. N Engl J Med 371(1):22–31
83. Jorgensen AB, Frikke-Schmidt R, Nordestgaard BG et al (2014) Loss-of-function mutations in APOC3 were associated with low levels of triglycerides and a reduced risk of ischemic cardiovascular disease. N Engl J Med 371(1):32–41
84. Gouni-Berthold I (2017) The role of antisense oligonucleotide therapy against apolipoprotein-CIII in hypertriglyceridemia. Atheroscler Suppl 30:19–27
85. Blom DJ, O'Dea L, Digenio A et al (2018) Characterizing familial chylomicronemia syndrome: baseline data of the APPROACH study. J Clin Lipidol 12(5):1234–1243
86. Lavie CJ, Milani RV, Mehra MR, Ventura HO (2009) Omega-3 polyunsaturated fatty acids and cardiovascular diseases. J Am Coll Cardiol 54(7):585–594. https://doi.org/10.1016/j.jacc.2009.02.084
87. Mozaffarian D, Wu JHY (2011) Omega-3 fatty acids and cardiovascular disease: effects on risk factors, molecular pathways, and clinical events. J Am Coll Cardiol 58(20): 2047–2067. https://doi.org/10.1016/j.jacc.2011.06.063
88. Calder PC (2013) Omega-3 polyunsaturated fatty acids and inflammatory processes: nutrition or pharmacology? Br J Clin Pharmacol 75(3):645–662. https://doi.org/10.1111/j.1365-2125.2012.04374.x

89. Babu PVA, Liu D (2008) Green tea catechins and cardiovascular health: an update. Curr Med Chem 15(18):1840–1850
90. Bhardwaj P, Khanna D (2013) Green tea catechins: defensive role in cardiovascular disorders. Chin J Nat Med 11(4):345–353. https://doi.org/10.1016/S1875-5364(13)60051-5
91. Mangels DR, Mohler ER (2017) Catechins as potential mediators of cardiovascular health. Arterioscler Thromb Vasc Biol 37(5):757–763. https://doi.org/10.1161/ATVBAHA.117.309048
92. Covas M-I, Konstantinidou V, Fitó M (2009) Olive oil and cardiovascular health. J Cardiovasc Pharmacol 54(6):477–482. https://doi.org/10.1097/FJC.0b013e3181c5e7fd
93. Estruch R, Ros E, Salas-Salvadó J, Covas M-I, Corella D, Arós F, Gómez-Gracia E, Ruiz-Gutiérrez V, Fiol M, Lapetra J, Lamuela-Raventos RM, Serra-Majem L, Pintó X, Basora J, Muñoz MA, Sorlí JV, Martínez JA, Fito M, Gea A, Hernan MA, Martínez-González MA (2018) Primary prevention of cardiovascular disease with a Mediterranean diet supplemented with extra-virgin olive oil or nuts. N Engl J Med 378(25):e34–e47. https://doi.org/10.1056/NEJMoa1800389
94. Luque-Sierra A, Alvarez-Amor L, Kleemann R, Martín F, Varela LM (2018) Extra-virgin olive oil with natural phenolic content exerts an anti-inflammatory effect in adipose tissue and attenuates the severity of atherosclerotic lesions in ldlr−/− Leiden mice. Mol Nutr Food Res 62(13):e1800295–e1800328. https://doi.org/10.1002/mnfr.201800295
95. Bhatt DL, Steg PG, Miller M, Brinton EA, Jacobson TA, Ketchum SB, Doyle RT, Juliano RA, Jiao L, Granowitz C, Tardif J-C, Ballantyne CM (2019) Cardiovascular risk reduction with icosapent ethyl for hypertriglyceridemia. N Engl J Med 380(1):11–22. https://doi.org/10.1056/NEJMoa1812792
96. Budoff MJ, Bhatt DL, Kinninger A, Lakshmanan S, Muhlestein JB, Le VT, May HT, Shaikh K, Shekar C, Roy SK, Tayek J, Nelson JR (2020) Effect of icosapent ethyl on progression of coronary atherosclerosis in patients with elevated triglycerides on statin therapy: final results of the EVAPORATE trial. Eur Heart J 41:3925–3932. https://doi.org/10.1093/eurheartj/ehaa750
97. Getz GS, Reardon CA (2012) Animal models of atherosclerosis. Arterioscler Thromb Vasc Biol 32(5):1104–1115
98. Lee YT, Lin HY, Chan YWF et al (2017) Mouse models of atherosclerosis: a historical perspective and recent advances. Lipids Health Dis 16:12
99. Mukhopadhyay R (2013) Mouse models of atherosclerosis: explaining critical roles of lipid metabolism and inflammation. J Appl Genet 54:185–192
100. Rosenfeld ME, Averill MM, Bennett BJ et al (2008) Progression and disruption of advanced atherosclerotic plaques in murine models. Curr Drug Targets 9:210–216
101. Cheng J, Cheng A et al (2020) MicroRNA-144 silencing protects against atherosclerosis in male, but not female mice. Arterioscler Thromb Vasc Biol 40(2):412–425
102. Zabalawi M, Bhat S, Loughlin T et al (2003) Induction of fatal inflammation in LDL receptor and apoA-I double knockout mice fed dietary fat and cholesterol. Am J Pathol 163(6):1201–1213
103. Mansukhani NA, Wang Z, Shively VP et al (2018) Sex differences in the LDL receptor knockout mouse model of atherosclerosis. Artery Res 20:8–11
104. Zhang Y, Wang X, Vales C et al (2006) FXR deficiency causes reduced atherosclerosis in *Ldlr*$^{-/-}$ mice. Arterioscler Thromb Vasc Biol 26(10):2316–2321
105. Vanderlaan PA, Reardon CA, Getz GS (2003) Site specificity of atherosclerosis. Arterioscler Thromb Vasc Biol 24(1):12–22
106. Kayashima Y, Maeda-Smithies N (2020) Atherosclerosis in different vascular locations unbiasedly approached with mouse genetics. Genes (Basel) 11(12):1427
107. Ridker PM, Everett BM, Pradhan A et al (2018) Low-dose methotrexate for the prevention of atherosclerotic events. N Engl J Med 380(8):752–762
108. Choi HK, Hernan MA, Seeger JD et al (2002) Methotrexate and mortality in patients with rheumatoid arthritis: a prospective study. Lancet 359(9313):1173–1177
109. Micha R, Imamura F, Wyler Von Ballmoos M et al (2011) Systematic review and meta-analysis of methotrexate use and risk of cardiovascular disease. Am J Cardiol 108(9):1362–1370
110. Westlake SL, Colebatch AN, Baird J et al (2010) The effect of methotrexate on cardiovascular disease in patients with rheumatoid arthritis: a systematic literature review. Rheumatology 49(2):295–307

Chapter 2

Key Roles of Inflammation in Atherosclerosis: Mediators Involved in Orchestrating the Inflammatory Response and Its Resolution in the Disease Along with Therapeutic Avenues Targeting Inflammation

Yee-Hung Chan and Dipak P. Ramji

Abstract

Inflammation is a critical driver of all stages of atherosclerosis, from lesion development to plaque rupture. Cytokines are mediators of the immune response and in atherosclerosis, the balance of anti- and pro-inflammatory cytokines is tipped in favor of the latter, resulting in persistent and unresolved inflammation. Although reducing plasma cholesterol levels mainly via the use of statins has positively impacted patient outcomes and reduced mortality rates, the presence of significant residual inflammation and cardiovascular risk posttherapy emphasizes the prevailing risk of primary and secondary events driven by inflammation independently of hyperlipidemia. Given the dominant role of inflammation in driving pathogenesis, alternative therapeutic avenues beyond targeting lowering of plasma lipids are required. This chapter will discuss the role of inflammation and pro-inflammatory cytokines in driving atherogenesis and disease progression, the therapeutic potential of targeting cytokines for atherosclerosis and promising avenues in this area.

Key words Atherosclerosis, Inflammation, Cytokines, Macrophages, IL-1β, Inflammasome

1 Introduction

The immune system is vital for tissue repair and regeneration, combating infections caused by invading pathogens, and establishing immunity against these via the production of antibodies. Cytokines are the master regulators of both the innate and adaptive immune responses [1]. They are a large group of proteins subdivided into several classes that include interleukins (IL), chemokines, tumor necrosis factors (TNF) and interferons (IFN) [2, 3]. Both pro- and anti-inflammatory cytokines and perhaps more importantly, the balance of these, have vital roles in the maintenance of normal physiological cardiovascular health. An abundance of evidence, both experimental and clinical, supports

Dipak P. Ramji (ed.), *Atherosclerosis: Methods and Protocols*, Methods in Molecular Biology, vol. 2419,
https://doi.org/10.1007/978-1-0716-1924-7_2,
© The Author(s), under exclusive license to Springer Science+Business Media, LLC, part of Springer Nature 2022

the fundamental involvement of inflammation in driving atherosclerosis through to the onset of clinical manifestations [3, 4]. Key potent pro-atherogenic and pro-inflammatory cytokines include IL-1β, TNF-α, and IFN-γ, which are implicated in various processes that drive inflammation and disease progression. In atherosclerosis, the levels of pro-inflammatory cytokines are elevated and exceed those of anti-inflammatory cytokines; this imbalance ultimately results in persistent and unresolving inflammation. These pro-inflammatory cytokines are hence fundamental drivers of atherosclerosis, being implicated in persisting inflammation, foam cell formation, lesion development, plaque progression and rupture [3, 4]. A plethora of pro-inflammatory cytokines are expressed in atherosclerotic plaques and the surrounding tissues. Cytokines often act synergistically, mediating the cross talk between different cells, and are produced by almost all cells with key roles in atherosclerosis pathogenesis [5, 6]. All cell types implicated in the disease are capable of both secreting and responding to these cytokines [7], and increasing inflammation is positively correlated to the risk of plaque rupture [8–11]. While inflammation itself does not necessarily elicit atherogenesis initially, it is more the facilitatory link between classical risk factors and disease initiation. Therefore, comprehensive understanding of how these cytokines influence atherogenesis and plaque progression through to rupture can hence open up therapeutic avenues for atherosclerosis and other pathologies fueled by chronic inflammation.

2 Inflammation in Atherosclerosis

Several chronic inflammatory and autoimmune diseases, such as rheumatoid arthritis, gout, and systemic lupus erythematosus, have been associated with elevated cardiovascular risk [12], emphasizing the detrimental role of systemic inflammation, regardless of its origin, in CVD. In atherosclerosis, the deposition, accumulation and retention of circulating low-density lipoprotein (LDL) cholesterol (LDL-C) within the arterial cell wall instigates an immune response by surrounding endothelial cells (ECs). The LDL is subject to modification by locally produced reactive oxygen species (ROS), mainly via oxidation, to become immunogenic oxidized LDL (oxLDL). Other risk factors can also encourage endothelial activation/dysfunction and subsequent atherogenesis; these including hypertension, disturbed blood flow and toxins from cigarette smoke [13]. Activated ECs release an array of chemokines and cytokines which result in the recruitment of circulating leukocytes, in particular monocytes and T lymphocytes [13]. Monocyte chemoattractant/chemotactic protein-1 (MCP-1; also known as C-C motif chemokine ligand 2 (CCL2)) is generated by monocytes/macrophages, ECs and vascular smooth muscle cells

(VSMCs) and recruits circulating proinflammatory monocytes to the site of dysfunction. ECs also express adhesion proteins, including intercellular adhesion molecule-1 (ICAM-1) and vascular cell adhesion molecule-1 (VCAM-1), which facilitate leukocyte-endothelial adhesion and subsequent *trans*-endothelial diapedesis of the recruited immune cells. The recruited monocytes are subject to various signals that influence their differentiation into macrophages and their subsequent activation/polarization and production of inflammatory mediators. Their plasticity and heterogeneity render them highly sensitive to changes in the microenvironment. Macrophages are capable of polarizing into numerous subsets now appreciated to go far beyond the most basic M1 (classically activated, proinflammatory) and M2 (alternatively activated, anti-inflammatory) classes [14]. During early atherosclerosis, macrophages engulf the oxLDL via scavenger receptors (SRs), such as SR-A1 and cluster of differentiation (CD)36, which induces the release of several pro-inflammatory cytokines (e.g., IL-1β and TNF-α) [15]. This results in their transformation into lipid-laden foam cells which are characteristic of, and abundant in, atherosclerotic lesions. In the later stages of atherosclerosis, the release of matrix metalloproteinases (MMPs) from monocytes/macrophages and other cells promotes plaque destabilization via breakdown of the fibrous cap components synthesized by VSMCs (including collagens and elastins). Plaque rupture results in clinical manifestations in the form of CVDs; most commonly, myocardial infarction (MI) and cerebrovascular accident.

Although the mechanisms underlying chronic, unresolving vascular inflammation in atherosclerosis are not completely understood, it is generally accepted that the accumulated mediators within the atherosclerotic plaque induces chronic low-grade inflammation to promote pathogenesis. In atherosclerosis, the deposited lipids within the arterial wall are taken up by macrophages and VSMCs to become lipid-laden foam cells, a key hallmark of the disease. Excess intracellular cholesterol retention triggers endoplasmic reticulum stress; eventual death of these foam cells leads to the formation of a core consisting of necrotic materials and cholesterol. Such materials are retained and amass within the vessel wall, helped by defective efferocytosis, generating an inflammatory environment that encourages cellular dysfunction and further pro-inflammatory signaling [14]. This becomes a continuous cycle, as intracellular cholesterol retention and accumulation promotes proinflammatory signaling, and activated immune cells favor cholesterol accumulation by impairing its efflux from the cells [16]. Dyslipidemia and inflammation are hence interlinked, and so it is important to target both underlying, chronic inflammation and hypercholesterolemia that perpetuates atherogenesis to improve clinical outcomes.

2.1 Role of IL-1β and the Inflammasome

The IL-1 family of cytokines are comprised of various pro-inflammatory cytokines, including IL-1α/β, IL-18, and IL-36α/β/γ [17], that play essential roles in the differentiation, polarization, and function of innate and adaptive lymphocytes [18]. Most innate immune cells express these cytokines, their receptors or both, and so are susceptible to the effects of IL-1 signaling. IL-1 has manifold effects on various cell types, including inducing cyclooxygenase (COX)-2-mediated prostaglandin production, amplifying nitric oxide (NO) production by increasing the levels of inducible isoform of nitric oxide synthase (iNOS), enhancing the expression of leukocyte adhesion molecules and thrombogenic mediators, and activating innate immune cells [19]. IL-1β, a distinct isoform of IL-1, has multiple pro-atherogenic effects, and its production and release can be stimulated by a range of factors typically present within atherosclerotic plaques. Cells in atherosclerotic lesions generate IL-1 as a response to inflammatory stimuli typically present within the atheroma [20, 21]. Examples of processes modulated by IL-1β include inducing pro-inflammatory M1 macrophage polarization [22–24], as well as autocrine production of platelet-derived growth factor (PDGF), which stimulates VSMC proliferation [25]. M1 macrophage polarization can also be activated by lipopolysaccharide (LPS) and IFN-γ [4, 26], which is produced via T helper-1 (T_{h1})-driven responses [27]. These M1 macrophages produce pro-inflammatory mediators such as IL-6, IL-12 and TNF-α, which stimulates ROS production, promoting oxidative stress and further endothelial dysfunction [3, 28]. Cytokines can also have direct effects on endothelial permeability; IFN-γ and TNF-α, for example, can induce reorganization of actin and tubulin cytoskeletons of endothelial cells, increasing the space between adjacent cells [29], thereby facilitating the infiltration of circulating immune cells. Macrophages, lymphocytes, natural killer (NK) cells, and VSMCs are all capable of secreting TNF-α, IL-1, and IL-6 [6]. TNF-α and IL-1 signaling promotes atherogenesis by augmenting the expression of other cytokines and adhesion molecules to facilitate interaction between circulating leukocytes and the activated endothelium, as well as the migration and mitogenesis of VSMCs and ECs [5].

An abundance of experimental and clinical evidence supports the fundamental involvement of inflammation in driving atherosclerosis through to the onset of clinical manifestations [8–10]. IL-1β is a particularly important pro-inflammatory mediator that contributes to both local vascular and systemic inflammation [30]. Cells within the normal arterial cell wall and lesional leukocytes can both generate and respond to IL-1β. A major activator of innate immunity, IL-1β is capable of inducing self-expression (via

an "autoinduction" amplification loop) in various cell types [31, 32], and its production and release can be stimulated by a number of factors. IL-1β mainly acts extracellularly as a soluble mediator in comparison to the α isoform (which only acts short distances via juxtacrine or paracrine signaling) [7]. However, the IL-1β precursor is not constitutively expressed and so requires induction by signals that activate nuclear factor kappa-light-chain-enhancer of activated B cells (NF-κB)-mediated transcription [33]. IL-1β requires processing by the proteolytic enzyme, caspase-1, to be activated [7]. Human atherosclerotic lesional macrophages possess caspase-1 [34], which is activated by the nucleotide oligomerization domain (NOD) leucine-rich repeat (LRR) and pyrin domain (PYD) containing protein 3 (NLRP3) inflammasome (an innate immune supramolecular signaling complex) [33, 35]. Inflammasome assembly and action requires "danger" signals, which activate pattern recognition receptors that include scavenger receptors (SRs), Toll-like receptors (TLRs), and NOD-like receptors (NLRs) by macrophages and other immune cells [36, 37]. These signals can be produced in response to LDL modification and foam cell lysis [38]. Example "danger" signals include oxLDL and crystalline cholesterol [39] which are common within the center of atherosclerotic plaques, linking arterial cholesterol deposition and vascular inflammation. Lysosomal destabilization, ROS release, and action of the caspase-1 protease results in cleavage and secretion of mature IL-Iβ and IL-18 [40].

Macrophages are phagocytic cells which, in the early lesion, are vital for clearing various kinds of particulate matter, notably aggregated/crystalline cholesterol [38]. However, this causes phagolysosomal rupture, ROS production and NLRP3 inflammasome activation [37], ultimately promoting oxidative stress and the propagation of IL-1-mediated vascular inflammation. Therefore, as well as forming the characteristic foam cells that are abundant in atherosclerotic lesions, macrophages also contribute greatly to the pro-inflammatory phenotype within plaques. The NLRP3 inflammasome is hence a key driver of the IL-1 family-mediated inflammatory signaling in atherosclerosis. IL-1β stimulation can also induce VSMCs and various other cells to elaborate IL-6, a stimulator of the acute phase response that leads to increased hepatic C-reactive protein (CRP) production, as well as enhanced expression of atherothrombosis mediators. In humans, clinical studies have shown that unstable angina patients have elevated serum IL-6 levels, which is considered as an independent risk factor for coronary artery disease [6, 41]. IL-6 and high-sensitivity CRP (hsCRP) are hence markers of IL-1β-mediated inflammation and subsequently of cardiovascular risk. Actions of IL-6 are mediated by its receptor and the signal transducing protein, glycoprotein 130 (gp130), resulting in activation of Janus kinase 1 (JAK1) and signal transducer and activator of transcription (STAT)-1 and -3 [2]. While plasma LDL-C was previously the main factor used to determine cardiovascular risk, other markers associated with

amplified inflammation are increasingly being recognized and employed in this regard.

3 Therapeutic Approaches Targeting Hyperlipidemia

Atherosclerotic development in blood vessels is ultimately fueled by dyslipidemia and incessant vascular inflammation; eventual plaque rupture can lead to a range of clinical presentations. CVD deaths are mainly attributed to major cardiovascular events (MACE), such as myocardial infarction (MI) and cerebrovascular accident (stroke), which are mainly caused by lumen occlusive atherothrombosis of blood vessels. Current therapeutic approaches for atherosclerosis and associated CVDs are focused on lowering plasma LDL-C to moderate hypercholesterolemia; this is mainly via the use of 3-hydroxy-3-methyl-glutaryl-coenzyme-A reductase inhibitors (statins). Statins have inhibitory effects on endogenous cholesterol synthesis [42] and promote hepatocyte LDL receptor (LDLR) expression to reduce plasma cholesterol [43] while also having other anti-inflammatory and pleiotropic activities [44]. Although statins have demonstrated efficacy at attenuating hyperlipidemia and subsequent cardiovascular risk, issues include variable tolerability among patients and adverse side effects [45], a key contributing factor to noncompliance. More importantly, previous clinical trials have identified significant residual cardiovascular risk post-statin therapy, despite successful alleviation of hypercholesterolemia [46–48]. This has hence fueled the search for alternative therapeutic approaches to expand available strategies in cardiovascular medicine.

Alternative therapeutic avenues include proprotein convertase subtilisin kexin 9 (PCSK9) inhibition via monoclonal antibodies (evolocumab and alirocumab) or gene silencing via small interfering RNA (inclisiran) to prevent PCSK9-mediated LDLR degradation and enhance liver LDL-C absorption. Inclisiran is capable of conferring approximately 50% reduction in LDL-C in atherosclerotic CVD (or equivalent) patients after biannual subcutaneous injection in two phase III clinical trials (ORION-10 and ORION-11) [49]. Another avenue is ezetimibe which inhibits cholesterol absorption at the intestinal brush border to reduce LDL-C [50]. Both strategies have demonstrated therapeutic potential and efficacy in reducing plasma cholesterol and subsequent cardiovascular risk in various clinical trials either as monotherapy or cotherapy with statins [51–53]. More recently, the adenosine triphosphate-citrate lyase (ACL) inhibitor, bempedoic acid, has been combined with ezetimibe to successfully lower LDL-C and hsCRP in a phase III clinical trial involving hypercholesterolemic, high CVD risk patients [54]. ACL is a cytosolic enzyme critically involved in the endogenous cholesterol synthesis pathway that acts

upstream of HMG-CoA reductase [55]. In contrary to statins, bempedoic acid is selectively activated in the liver rather than skeletal muscle [56], and so has not been associated with muscle-related side effects, even in statin-intolerant patients [57, 58]. It will hence be interesting to see the effect of this fixed dose combination therapy on cardiovascular risk. Although demonstrating promise, the expense and limited cost-effectiveness of these alternative agents, especially in comparison to statins, has greatly restricted their widespread application given the high prevalence of CVD. Furthermore, it is important to note that MI and strokes can also occur in patients with persistent vascular inflammation devoid of hyperlipidemia [59]. In accordance with this, increased levels of CRP have been identified in patients receiving statins [60, 61], suggesting that residual cardiovascular risk is driven by persisting inflammation and drawing more attention to anti-inflammatory approaches.

4 Targeting the IL-1/6 Pathway of Inflammation

Given the potent role of inflammation in driving pro-atherogenic processes, controlling levels of pro-inflammatory cytokines that are critically involved in pathogenesis may hence delay onset of clinical complications associated with atherosclerosis. Cytokines have previously been recognized as promising therapeutic targets for atherosclerosis, and a number of preclinical studies have shown that dampening levels of several different pro-inflammatory cytokines attenuates disease progression [3, 4], supporting the critical role of cytokines in lesion formation and development. Advances in bespoke pharmaceutical design have enabled the manufacture of highly specific antibodies against mediators with crucial roles in propagating the inflammatory cascade [5]. The main methods for targeting individual pro-inflammatory cytokines, besides developing specific knockout (KO) models, is via recombinant antibodies or receptor antagonists, and the effect of these on animal models of atherosclerosis have been widely explored.

A plethora of preclinical studies have demonstrated the therapeutic potential of inhibiting the actions of key pro-inflammatory cytokines in atherosclerosis. IL-1 has been shown to exert effects on various cells typically present in human atheroma, such as enhanced endothelial expression of adhesion molecules and MCP-1 production [62, 63], and VSMC proliferation [25]. Moreover, human atherosclerotic coronary arteries have enhanced levels of IL-1β, which was positively associated with disease burden compared to their normal counterparts [64]. In animal studies, prolonged IL-1β administration led to arterial intimal thickening in pigs [65] and spontaneous atherosclerotic lesion development was reduced in IL-1β deficient *apolipoprotein E* KO ($ApoE^{-/-}$) mice

[66]. A major source of control for IL-1-mediated inflammatory signaling is the IL-1 receptor (IL-1R) antagonist (IL1Ra), as both the α and β isoforms signal via this receptor. In animals, IL-1Ra administration or IL-1 deficiency generally results in favorable changes to atherosclerotic lesions with reduced disease severity. For example, IL-1Ra administration attenuated neointima formation after vessel wall injury in a porcine coronary artery model [67] and inhibited fatty streak formation in $ApoE^{-/-}$ mice [68]. In addition, IL-1Ra overexpression decreased diet-induced atherogenesis in $Ldlr^{-/-}$ mice [69], and IL-1Ra deficiency enhanced spontaneous atherosclerotic lesion development in $ApoE^{-/-}$ mice [70] and gave rise to transmural arterial inflammation leading to lethal aneurysms [71]. Furthermore, the development of diet-induced atherosclerotic plaques was attenuated in both $Ldlr^{-/-}$ and $ApoE^{-/-}$ mice after transplantation of IL-1-deficient bone marrow [39] and/or administration of the monoclonal antibody for IL-1β [72] respectively. However, it is important to note that although IL-1R deficiency reduced lesion size in $ApoE^{-/-}$ mice, impaired outward vessel remodeling was observed (decreased lumen size) along with signs of plaque instability (e.g., reduced plaque VSMC and collagen content) [73]. This suggests that IL-1 may be pro-atherogenic in early atherosclerosis but have atheroprotective actions in advanced disease, by encouraging lesion stability by facilitating fibrous cap formation due to its profibrotic and proliferative actions on VSMCs. Indeed, this is also true for other cytokines, which may contribute both positively and negatively to atherosclerosis depending on the stage of disease, along with various other factors.

Due to the biological and structural similarities of IL-18 to IL-1β, it has been proposed that IL-18 is also involved in autoinflammatory pathologies mediated by inflammasome-activated caspase-1 [5]; however, both cytokines can also be produced independently of this protease [37]. This may in part explain why deficiency in NLRP3 or caspase-1 did not inhibit macrophage infiltration and subsequent atherosclerosis progression [74]. However, IL-1β deficiency decreased disease severity [66] and monoclonal antibodies targeting IL-1β inhibited plaque formation [72] in $ApoE^{-/-}$ mice. $ApoE^{-/-}$ mice also lacking IL-1R type-1 had reduced lesion size and aortic expression of CD68, VCAM-1, ICAM-1 and MCP-1 [75]. IL-1α deficiency in bone marrow derived cells also inhibited atherogenesis in $ApoE^{-/-}$ mice and wild-type mice fed atherogenic diet [76, 77]. Therefore, given the influential role of IL-1-driven inflammatory processes in atherogenesis, direct targeting of the potent pro-inflammatory cytokine IL-1β is hence an appealing and promising anti-inflammatory strategy.

Although controlling inflammation by targeting key pro-inflammatory signaling pathways has previously been

hypothesized to reduce disease burden and improve clinical outcomes, it was not until the breakthrough Canakinumab Anti-Inflammatory Thrombosis Outcomes Study (CANTOS) [78] that this was successfully achieved. This was a large-scale phase III clinical trial involving just over 10,000 MI-surviving patients with a hsCRP level above 2 mg/dL, that were given three doses (50, 150, and 300 mg) of the IL-1β monoclonal antibody, canakinumab. The two highest doses conferred a 17% reduction in occurrence of MACE after IL-6 and hsCRP levels were lowered by approximately 35–40% after 12 months and 48 months respectively. This was despite canakinumab having no significant effects on plasma LDL-C. Therefore, the CANTOS trial not only demonstrated the effectiveness of dampening IL-1β-mediated pro-inflammatory signaling to reduce cardiovascular risk, but the influence of hyperlipidemia-independent inflammation in fostering this risk. This emphasizes the importance of targeting chronic inflammatory signaling to further diminish risk of MACE post-hypercholesterolemia management.

5 Other Anti-inflammatory Agents Under Investigation

Since the breakthrough CANTOS trial especially, there has been a shift in focus to anti-inflammatory therapies and targeting actions of key, pro-inflammatory cytokines to prevent primary and secondary MACE. In contrast to the success of the canakinumab, the Cardiovascular Inflammation Reduction Trial (CIRT) revealed that broad-spectrum anti-inflammatory, low-dose methotrexate had no effect on IL-1β, IL-6, or hsCRP and thus did not confer any cardiovascular protection to previous CVD patients with type 2 diabetes/metabolic syndrome [79]. This is despite low-dose methotrexate use being associated with less cardiovascular events in arthritic patients in prior observational studies [80–82]. Although low-dose methotrexate has various anti-inflammatory actions, it does not specifically affect the IL-1/6 pathway, which may explain the lack of effect on hsCRP levels. Therefore, specific targeting of key, pro-inflammatory signaling pathways, such as IL-1β, may be more efficacious. As such, various studies have investigated the short-term, anti-inflammatory effects of IL-1Ra therapy (100 mg/day anakinra) on cardiovascular outcomes in various phase II clinical trials [83–86] with progression onto phase III trials required to fully elucidate long-term safety and efficacy of anakinra. Beyond this, the efficacy of various other anti-inflammatory agents for atherosclerotic CVD have also been investigated in a number of phase III clinical trials [87–89], with only broad-spectrum anti-inflammatory agent, colchicine, conferring benefit to CVD patients. Colchicine has demonstrated efficacy in reducing risk of cardiovascular events in stable coronary disease

patients [87] and ischemic cardiovascular events in patients that had suffered MI within 30 days [90] at 0.5 mg/day, with comparable performance to canakinumab. In another randomized, controlled trial involving chronic coronary disease patients, the same dose of colchicine also significantly lowered risk of MACE [91]. The success of this broad-spectrum anti-inflammatory agent, which was not seen with low-dose methotrexate may be attributed to its ability to inhibit the action of the NLRP3 inflammasome (by preventing its assembly [92]) and hence generation of active IL-1β [93]. Therefore, anti-inflammatory strategies targeting the IL-1 pathway have demonstrated potential in attenuating residual cardiovascular risk that remains post-statin therapy, and further reducing CVD morbidity and mortality rates.

6 Other Potential Avenues

Other potential targets for anticytokine therapy include IL-6 and IL-18 (an inducer of IFN-γ), which are both associated with IL-1β. *ApoE*$^{-/-}$ mice that had received recombinant IL-6 injections displayed more severe atherosclerosis [94, 95] and IL-6 lentivirus induced plaque destabilization [96]. Fittingly, blocking IL-6 *trans*-signaling via soluble gp130 attenuated atherosclerosis via inhibition of multiple proatherogenic processes [97]. However, IL-6 deficiency in both *ApoE*$^{-/-}$ and *Ldlr*$^{-/-}$ mice actually promoted atherosclerosis [98]. Similarly, *ApoE*$^{-/-}$ mice receiving intraperitoneal injections of IL-18 exacerbated atherosclerosis in an IFN-γ-dependent manner [99]. In another study, *ApoE*$^{-/-}$ mice developed larger, more unstable plaques with increased expression of CD36 and matrix metalloproteinase-9 [100]. However, *ApoE*$^{-/-}$ mice deficient in IL-18 fed high-fat diet (HFD) for 12 weeks developed more plaques that were larger in size compared to *ApoE*$^{-/-}$ controls [101]. Taken together, this suggests that complete removal of certain cytokines may have detrimental effects on disease development, while dampening its levels in preexisting/advanced disease may elicit benefit. Therefore, any anticytokine approach must be carefully considered due to the complexity and ambiguity of cytokines/cytokine actions in health and disease.

TNF-α is another potential target cytokine; *TNF-α* and *ApoE* double KO mice and *ApoE*$^{-/-}$ mice treated with a recombinant soluble decoy receptor to inhibit TNF-α activity gave similar conclusions whereby atherogenesis, endothelial adhesion and inflammatory markers were attenuated [102, 103]. In another study, *ApoE*$^{-/-}$ mice lacking TNF-α also had reduced lesion size attributed to decreased lipid accumulation and expression of multiple proinflammatory cytokines and chemokines after 6 weeks [104]. These include IFN-γ, ICAM-1, VCAM-1, and CCL2, which were similarly reduced in *LDLR* and TNF receptor (p55)

double KO mice fed HFD; these mice also had reduced atherosclerotic lesions [105]. In humans, TNF-α facilitates the interaction between circulating immune cells and the endothelium via up-regulation of expression of adhesion molecules, including VCAM-1 [106]. Therefore, attenuating the levels and activity of TNF-α may protect against endothelial activation/dysfunction and attenuate atherogenesis.

Besides targeting general inflammation or specific key pro-inflammatory cytokines, augmenting levels of anti-inflammatory, atheroprotective cytokines has been proposed. Regulatory T cells (T_{regs}) have immunomodulatory activity facilitated in part via the secretion of anti-inflammatory, atheroprotective cytokines such as transforming growth factor (TGF)-β and IL-10 [2], as well as down regulation of TNF-α production [107] and endothelial ICAM-1 expression [108]. Furthermore, nutraceuticals (food constituents with health benefits beyond their nutritional value) represent promising preventative/therapeutic avenues that have a plethora of cardiovascular health benefits, including anti-inflammatory, anti-proliferative, and antioxidative activities. Promising candidates such as omega-3 and -6 polyunsaturated fatty acids (e.g., eicosapentaenoic acid (EPA) and dihomo-γ-linolenic acid respectively) have demonstrated promising antiatherogenic activities in vitro and in vivo [109, 110]. In clinical trials, daily intake of a purified EPA ethyl ester by CVD patients on statin therapy significantly decreased the occurrence of ischemic events [111] and reduced plaque burden in CVD (or equivalent) patients [112]. Therefore, nutraceuticals represent promising preventative and therapeutic avenues that can be combined with pharmaceutical agents, such as statins, as a cotherapy to offer additional protection against MACE.

7 Challenges and Future Perspectives

Previous clinical trials showing residual cardiovascular risk in statin-treated patients combined with the successful attenuation of this after previous MI patients were given canakinumab has emphasized the importance of targeting both inflammation and hyperlipidemia to improve patient outcomes. Conventional approaches focused on lowering LDL-C only are insufficient in completely removing residual cardiovascular risk. A dual strategy targeting both hypercholesterolemia and inflammation appears to be the best approach for improving patient outcomes via combinatory therapies, either with pharmacological agents or nutraceuticals. Given the potent role of inflammation in driving pro-atherogenic processes, controlling levels of pro-inflammatory cytokines that are critically involved in pathogenesis may hence delay the onset of clinical complications.

However, cytokines are highly complex and capable of exerting multiple effects affecting different cells, contributing to plaque development and driving dysfunction via different mechanisms. Additionally, the roles that cytokines play within the atherosclerotic microenvironment may not be strictly anti- or pro-atherogenic, and so disease progression/stage as well as specific risk factors/biomarkers should be evaluated carefully, supporting the need for a more personalized approach ("personalized medicine"). Indeed, modulating mediators of the immune response presents the challenge of balancing disease suppression with compromising immune function. This is further complicated by patients with comorbidities and those who are already immunocompromised. Thus minimizing undesirable systemic side effects that may result from immune suppression warrants further research into targeted drug delivery methods. Nevertheless, promising results obtained from clinical trials that exploit anti-cytokine/anti-inflammatory therapies for reducing residual cardiovascular risk in statin-treated patients will likely pave the way for further investigation into other target cytokines closely associated with IL-1β (e.g., IL-6, IL-18, and IFN-γ). Focus will likely shift to finding other effective anticytokine/anti-inflammatory agents that are cheap and cost-effective, and hence can be widely applied in cardiovascular medicine, especially due to the high prevalence of CVD.

Acknowledgments

We thank the British Heart Foundation for financial support (grants PG/16/25/32097 and FS/17/75/33257).

References

1. Banyer JL, Hamilton NH, Ramshaw IA et al (2000) Cytokines in innate and adaptive immunity. Rev Immunogenet 2(3):359–373
2. Ait-Oufella H, Taleb S, Mallat Z et al (2011) Recent advances on the role of cytokines in atherosclerosis. Arterioscler Thromb Vasc Biol 31:969–979
3. Ramji DP, Davies TS (2015) Cytokines in atherosclerosis: key players in all stages of disease and promising therapeutic targets. Cytokine Growth Factor Rev 26:673–685
4. Moss JWE, Ramji DP (2016) Cytokines: roles in atherosclerosis disease progression and potential therapeutic targets. Future Med Chem 8(11):1317–1330
5. Tousoulis D, Oikonomou E, Economou EK et al (2016) Inflammatory cytokines in atherosclerosis: current therapeutic approaches. Eur Heart J 37(22):1723–1732
6. Tedgui A, Mallat Z (2006) Cytokines in atherosclerosis: pathogenic and regulatory pathways. Physiol Rev 86:515–581
7. Libby P (2017) Interleukin-1 beta as a target for atherosclerosis therapy: the biological basis of CANTOS and beyond. J Am Coll Cardiol 70(18):2278–2289
8. Lichtman AH, Binder CJ, Tsimikas S et al (2013) Adaptive immunity in atherogenesis: new insights and therapeutic approaches. J Clin Invest 123:27–36
9. Nus M, Mallat Z (2016) Immune-mediated mechanisms of atherosclerosis and implications for the clinic. Expert Rev Clin Immunol 12:1217–1237

10. Hansson GK, Libby P, Tabas I (2015) Inflammation and plaque vulnerability. J Intern Med 278:483–493
11. Libby P, Ridker PM, Hansson GK (2009) Inflammation in atherosclerosis: from pathophysiology to practice. J Am Coll Cardiol 54: 2129–2138
12. Mason JC, Libby P (2015) Cardiovascular disease in patients with chronic inflammation: mechanisms underlying premature cardiovascular events in rheumatologic conditions. Eur Heart J 36:428–484
13. McLaren JE, Michael DR, Ashlin TG et al (2011) Cytokines, macrophage lipid metabolism and foam cells: implications for cardiovascular disease therapy. Prog Lipid Res 50: 331–347
14. Shirai T, Hilhorst M, Harrison DG et al (2015) Macrophages in vascular inflammation - from atherosclerosis to vasculitis. Autoimmunity 48(3):139–151
15. Stewart CR, Stuart LM, Wilkinson K et al (2010) CD36 ligands promote sterile inflammation through assembly of a Toll-like receptor 4 and 6 heterodimer. Nat Immunol 11(2): 155–161
16. Tall AR, Yven-Charvet L (2015) Cholesterol, inflammation and innate immunity. Nat Rev Immunol 15:104–116
17. Dinarello CA (2018) Overview of the IL-1 family in innate inflammation and acquired immunity. Immunol Rev 281:8–27
18. Garlanda C, Dinarello CA, Mantovani A et al (2013) The interleukin-1 family: back to the future. Immunity 39:1003–1018
19. Dinarello CA (2009) Immunological and inflammatory functions of the interleukin-1 family. Annu Rev Immunol 27:519–550
20. Libby P, Ordovas JM, Auger KR et al (1986) Endotoxin and tumor necrosis factor induce interleukin-1 gene expression in adult human vascular endothelial cells. Am J Pathol 124: 179–186
21. Libby P, Ordovas JM, Birinyi LK et al (1986) Inducible interleukin-1 expression in human vascular smooth muscle cells. J Clin Invest 78: 1432–1438
22. Wolfs IMJ, Donners MMPC, de Winther MPJ (2011) Differentiation factors and cytokines in the atherosclerotic plaque microenvironment as a trigger for macrophage polarisation. Thromb Haemost 106(5): 763–771
23. Chinetti-Gbaguidi G, Colin S, Staels B (2015) Macrophage subsets in atherosclerosis. Nat Rev Cardiol 12(1):10–17
24. Leitinger N, Schulman IG (2013) Phenotypic polarization of macrophages in atherosclerosis. Arterioscler Thromb Vasc Biol 33(6): 1120–1126
25. Libby P, Warner SJ, Friedman GB (1988) Interleukin 1: a mitogen for human vascular smooth muscle cells that induces the release of growth-inhibitory prostanoids. J Clin Invest 81:487–498
26. Khallou-Laschet J, Varthaman A, Fornasa G et al (2010) Macrophage plasticity in experimental atherosclerosis. PLoS One 5:e8852
27. Robertson AK, Hansson GK (2006) T cells in atherogenesis: for better or for worse? Arterioscler Thromb Vasc Biol 26:2421–2432
28. Zhang H, Park Y, Wu J et al (2009) Role of TNF-α in vascular dysfunction. Clin Sci 116: 219–230
29. Pober JS, Sessa WC (2007) Evolving functions of endothelial cells in inflammation. Nat Rev Immunol 7(10):803–815
30. Frostegard J (2013) Immunity, atherosclerosis and cardiovascular disease. BMC Med 11: 117. https://doi.org/10.1186/1741-7015-11-117
31. Dinarello CA, Ikejima T, Warner SJC et al (1987) Interleukin-1 induces interleukin-1. I. Induction of circulating interleukin-1 in rabbits in vivo and in human mononuclear cells in vitro. J Immunol 139:1902–1910
32. Warner SJC, Auger KR, Libby P (1987) Interleukin-1 induces interleukin-1. II. Recombinant human interleukin-1 induces interleukin-1 production by adult human vascular endothelial cells. J Immunol 139: 1911–1917
33. Patel MN, Carroll RG, Galvan-Pena S et al (2017) Inflammasome priming in sterile inflammatory disease. Trends Mol Med 23(2):165–180
34. Geng Y-J, Libby P (1995) Evidence for apoptosis in advanced human atheroma. Co-localization with interleukin-1 converting enzyme. Am J Pathol 147:251–266
35. Latz E, Xiao TS, Stutz A (2013) Activation and regulation of the inflammasomes. Nat Rev Immunol 13:397–411
36. Prochnicki T, Mangan MS, Latz E (2016) Recent insights into the molecular mechanisms of the NLRP3 inflammasome activation. F1000Res 5:1469
37. Grebe A, Hoss F, Latz E (2018) NLRP3 inflammasome and the IL-1 pathway in atherosclerosis. Circ Res 122:1722–1740
38. Zimmer S, Grebe A, Latz E (2015) Danger signaling in atherosclerosis. Circ Res 116: 323–340

39. Duewell P, Kono H, Rayner KJ et al (2010) NLRP3 inflammasomes are required for atherogenesis and activated by cholesterol crystals. Nature 464:1357–1361
40. Tschopp J, Schroder K (2010) NLRP3 inflammasome activation: the convergence of multiple signalling pathways on ROS production? Nat Rev Immunol 10(3):210–215
41. Biasucci LM, Liuzzo G, Fantuzzi G et al (1999) Increasing levels of interleukin(1L)-1Ra and IL-6 during the first 2 days of hospitalization in unstable angina patients are associated with increased risk of in-hospital coronary events. Circulation 99:2079–2084
42. Haslinger-Löffler B (2008) Multiple effects of HMG-CoA reductase inhibitors (statins) besides their lipid-lowering function. Kidney Int 74(5):553–555. https://doi.org/10.1038/ki.2008.323
43. Bergheanu SC, Bodde MC, Jukema JW (2017) Pathophysiology and treatment of atherosclerosis: current view and future perspective on lipoprotein modification treatment. Neth Hear J 25(4):231–242. https://doi.org/10.1007/s12471-017-0959-2
44. Antonopoulos A, Margaritis M, Lee R et al (2012) Statins as anti-inflammatory agents in atherogenesis: molecular mechanisms and lessons from the recent clinical trials. Curr Pharm Des 18(11):1519–1530
45. Calderon RM, Cubeddu LX, Goldberg RB et al (2010) Statins in the treatment of dyslipidemia in the presence of elevated liver aminotransferase levels: a therapeutic dilemma. Mayo Clin Proc 85(4):349–356
46. Campbell CY, Rivera JJ, Blumenthal RS (2007) Residual risk in statin-treated patients: future therapeutic options. Curr Cardiol Rep 9(6):499–505. https://doi.org/10.1007/BF02938395
47. Libby P, Ridker PM, Hansson GK (2011) Progress and challenges in translating the biology of atherosclerosis. Nature 473(7347):317–325. https://doi.org/10.1038/nature10146
48. Sampson UK, Fazio S, Linton MF (2012) Residual cardiovascular risk despite optimal LDL cholesterol reduction with statins: the evidence, etiology, and therapeutic challenges. Curr Atheroscler Rep 14(1):1–10. https://doi.org/10.1007/s11883-011-0219-7
49. Ray KK, Wright S, Kallend D et al (2020) Two phase 3 trials of inclisiran in patients with elevated LDL cholesterol. N Engl J Med 382(16):1507–1519
50. Jia L, Betters JL, Yu L (2011) Niemann-pick C1-like 1 (NPC1L1) protein in intestinal and hepatic cholesterol transport. Annu Rev Physiol 73:239–259. https://doi.org/10.1146/annurev-physiol-012110-142233
51. Cannon CP, Blazing MA, Giugliano RP et al (2015) Ezetimibe added to statin therapy after acute coronary syndromes. N Engl J Med 25:2387–2397
52. Tsujita K, Sugiyama S, Sumida H et al (2015) Impact of dual lipid-lowering strategy with ezetimibe and atorvastatin on coronary plaque regression in patients with percutaneous coronary intervention. J Am Coll Cardiol 66(5):495–507
53. Bohula EA, Giugliano RP, Leiter LA et al (2018) Inflammatory and cholesterol risk in the FOURIER trial. Circulation 138(2):131–140
54. Ballantyne CM, Laufs U, Ray KK et al (2020) Bempedoic acid plus ezetimibe fixed-dose combination in patients with hypercholesterolemia and high CVD risk treated with maximally tolerated statin therapy. Eur J Prev Cardiol 27(6):593–603
55. Pinkosky SL, Filippov S, Srivastava RA et al (2013) AMP-activated protein kinase and ATP-citrate lyase are two distinct molecular targets for ETC-1002, a novel small molecule regulator of lipid and carbohydrate metabolism. J Lipid Res 54:134–151
56. Pinkosky SL, Newton RS, Day EA et al (2016) Liver-specific ATP-citrate lyase inhibition by bempedoic acid decreases LDL-C and attenuates atherosclerosis. Nat Commun 7:13457
57. Ballantyne CM, Banach M, Mancini GBJ et al (2018) Efficacy and safety of bempedoic acid added to ezetimibe in statin-intolerant patients with hypercholesterolemia: a randomized, placebo-controlled study. Atherosclerosis 277:195–203
58. Laufs U, Banach M, Mancini GBJ et al (2019) Efficacy and safety of bempedoic acid in patients with hypercholesterolemia and statin intolerance. J Am Heart Assoc 8:e011662
59. Ridker PM, Libby P, MacFayden JG et al (2018) Modulation of the interleukin-6 signaling pathway and incidence rates of atherosclerotic events and all-cause mortality: analyses from the Canakinumab Anti-Inflammatory Thrombosis Outcomes Study (CANTOS). Eur Heart J 39(38):3499–3507
60. Ridker PM, Cannon CP, Morrow D et al (2005) C-reactive protein levels and outcomes after statin therapy. N Engl J Med 352(1):20–28

61. Puri R, Nissen SE, Libby P et al (2013) C-reactive protein, but not low-density lipoprotein cholesterol levels, associate with coronary atheroma regression and cardiovascular events after maximally intensive statin therapy. Circulation 128(22):2395–2403
62. Bevilacqua MP, Pober JS, Majeau GR et al (1984) Interleukin 1 (IL-1) induces biosynthesis and cell surface expression of procoagulant activity in human vascular endothelial cells. J Exp Med 160:618–623
63. Bevilacqua MP, Pober JS, Wheeler ME et al (1985) Interleukin 1 acts on cultured human vascular endothelium to increase the adhesion of polymorphonuclear leukocytes, monocytes, and related leukocyte cell lines. J Clin Invest 76:2003–2011
64. Galea J, Armstrong J, Gadsdon P et al (1996) Interleukin-1 beta in coronary arteries of patients with ischemic heart disease. Arterioscler Thromb Vasc Biol 16:1000–1006
65. Shimokawa H, Ito A, Fukumoto Y et al (1996) Chronic treatment with interleukin-1 beta induces coronary intimal lesions and vasospastic responses in pigs in vivo. J Clin Invest 97:769–776
66. Kirii H, Niwa T, Yamada Y et al (2003) Lack of interleukin-1β decreases the severity of atherosclerosis in ApoE-deficient mice. Arterioscler Thromb Vasc Biol 23(4):656–660
67. Morton AC, Arnold ND, Gunn J et al (2005) Interleukin-1 receptor antagonist alters the response to vessel wall injury in a porcine coronary artery model. Cardiovasc Res 68: 493–501
68. Elhage R, Maret A, Pieraggi MT et al (1998) Differential effects of interleukin-1 receptor antagonist and tumor necrosis factor binding protein on fatty-streak formation in apolipoprotein E-deficient mice. Circulation 97: 242–244
69. Devlin CM, Kuriakose G, Hirsch E et al (2002) Genetic alterations of IL-1 receptor antagonist in mice affect plasma cholesterol level and foam cell lesion size. Proc Natl Acad Sci U S A 99:6280–6285
70. Isoda K, Sawada S, Ishigami N et al (2004) Lack of interleukin-1 receptor antagonist modulates plaque composition in apolipoprotein E-deficient mice. Arterioscler Thromb Vasc Biol 24:1068–1073
71. Nicklin MJ, Hughes DE, Barton JL et al (2000) Arterial inflammation in mice lacking the interleukin 1 receptor antagonist gene. J Exp Med 191:303–312
72. Bhaskar V, Yin J, Mirza AM et al (2011) Monoclonal antibodies targeting IL-1 beta reduce biomarkers of atherosclerosis in vitro and inhibit atherosclerotic plaque formation in Apolipoprotein E-deficient mice. Atherosclerosis 216(2):313–320
73. Alexander MR, Moehle CW, Johnson JL et al (2012) Genetic inactivation of IL-1 signaling enhances atherosclerotic plaque instability and reduces outward vessel remodeling in advanced atherosclerosis in mice. J Clin Invest 122:70–79
74. Menu P, Pellegrin M, Aubert J-F et al (2011) Atherosclerosis in ApoE-deficient mice progresses independently of the NLRP3 inflammasome. Cell Death Dis 2(3):e137–e145
75. Shemesh S, Kamari Y, Shaish A et al (2012) Interleukin-1 receptor type-1 in non-hematopoietic cells is the target for the pro-atherogenic effects of interleukin-1 in apoE-deficient mice. Atherosclerosis 222(2): 329–336
76. Kamari Y, Werman-Venkert R, Shaish A et al (2007) Differential role and tissue specificity of interleukin-1alpha gene expression in atherogenesis and lipid metabolism. Atherosclerosis 195:31–38
77. Kamari Y, Shaish A, Shemesh S et al (2011) Reduced atherosclerosis and inflammatory cytokines in apolipoprotein-E-deficient mice lacking bone marrow-derived interleukin-1α. Biochem Biophys Res Commun 405(2): 197–203
78. Ridker PM, Everett BM, Thuren T et al (2017) Antiinflammatory therapy with canakinumab for atherosclerotic disease. N Engl J Med 377(12):1119–1131
79. Ridker PM, Everett BM, Pradhan A et al (2018) Low-dose methotrexate for the prevention of atherosclerotic events. N Engl J Med 380(8):752–762
80. Westlake SL, Colebatch AN, Baird J et al (2010) The effect of methotrexate on cardiovascular disease in patients with rheumatoid arthritis: a systematic literature review. Rheumatology 49(2):295–307
81. Choi HK, Hernan MA, Seeger JD et al (2002) Methotrexate and mortality in patients with rheumatoid arthritis: a prospective study. Lancet 359(9313):1173–1177
82. Micha R, Imamura F, Wyler Von Ballmoos M et al (2011) Systematic review and meta-analysis of methotrexate use and risk of cardiovascular disease. Am J Cardiol 108(9): 1362–1370
83. Morton AC, Rothman AM, Greenwood JP et al (2015) The effect of interleukin-1 receptor antagonist therapy on markers of inflammation in non-ST elevation acute coronary

syndromes: the MRC-ILA Heart study. Eur Heart J 36(6):377–384

84. Abbate A, Kontos MC, Abouzaki NA et al (2015) Comparative safety of interleukin-1 blockade with anakinra in patients with ST-segment elevation acute myocardial infarction (from the VCU-ART and VCU-ART2 pilot studies). Am J Cardiol 115(3):288–292
85. Abbate A, Kontos MC, Grizzard JD et al (2010) Interleukin-1 blockade with anakinra to prevent adverse cardiac remodeling after acute myocardial infarction (Virginia Commonwealth University Anakinra Remodeling Trial [VCU-ART] Pilot study). Am J Cardiol 105(10):1371–1377
86. Abbate A, Trankle CR, Buckley LF et al (2020) Interleukin-1 blockade inhibits the acute inflammatory response in patients with ST-segment-elevation myocardial infarction. J Am Heart Assoc 9:e014941
87. Nidorf SM, Eikelboom JW, Budgeon CA et al (2013) Low-dose colchicine for secondary prevention of cardiovascular disease. J Am Coll Cardiol 61(4):404–410
88. O'Donoghue ML, Braunwald E, White HD et al (2014) Effect of darapladib on major coronary events after an acute coronary syndrome: the SOLID-TIMI 52 randomized clinical trial. JAMA 312(10):1006–1015
89. O'Donoghue ML, Glaser R, Cavender MA et al (2016) Effect of losmapimod on cardiovascular outcomes in patients hospitalized with acute myocardial infarction: a randomized clinical trial. JAMA 315(15): 1591–1599
90. Tardif J-C, Kouz S, Waters DD et al (2019) Efficacy and safety of low-dose colchicine after myocardial infarction. N Engl J Med 381(26): 2497–2505
91. Nidorf SM, Fiolet ATL, Mosterd A et al (2020) Colchicine in patients with chronic coronary disease. N Engl J Med 383(19): 1838–1847
92. Nidorf SM, Eikelboom JW, Thompson PL (2014) Targeting cholesterol crystal-induced inflammation for the secondary prevention of cardiovascular disease. J Cardiovasc Pharmacol Therapeut 19(1):45–52
93. Martinez GJ, Celermajer DS, Patel S (2018) The NLRP3 inflammasome and the emerging role of colchicine to inhibit atherosclerosis-associated inflammation. Atherosclerosis 269:262–271
94. Huber SA, Sakkinen P, Conze D et al (1999) Interleukin-6 exacerbates early atherosclerosis in mice. Arterioscler Thromb Vasc Biol 19: 2364–2367
95. Schieffer B, Selle T, Hilfiker A et al (2004) Impact of interleukin-6 on plaque development and morphology in experimental atherosclerosis. Circulation 110:3493–3500
96. Zhang K, Huang XZ, Li XN et al (2012) Interleukin 6 destabilizes atherosclerotic plaques by downregulating prolyl-4-hydroxylase α1 via a mitogen-activated protein kinase and c-Jun pathway. Arch Biochem Biophys 528: 127–133
97. Schuett H, Oestreich R, Waetzig GH et al (2012) Transsignaling of interleukin-6 crucially contributes to atherosclerosis in mice. Arterioscler Thromb Vasc Biol 32:281–290
98. Madan M, Bishayi B, Hoge M et al (2008) Atheroprotective role of interleukin-6 in diet- and/or pathogen-associated atherosclerosis using an ApoE heterozygote murine model. Atherosclerosis 197:504–514
99. Whitman SC, Ravisankar P, Daugherty A (2002) Interleukin-18 enhances atherosclerosis in apolipoprotein E(-/-) mice through release of interferon-gamma. Circ Res 90: E34–E38
100. Bhat OM, Kumar PU, Giridharan NV et al (2015) Interleukin-18-induced atherosclerosis involves CD36 and NF-κB crosstalk in Apo E-/- mice. J Cardiol 66(1):28–35
101. Pejnovic N, Vratimos A, Lee SH et al (2009) Increased atherosclerotic lesions and Th17 in interleukin-18 deficient apolipoprotein E-knockout mice fed high-fat diet. Mol Immunol 47(1):37–45
102. Canault M, Peiretti F, Mueller C et al (2004) Exclusive expression of transmembrane TNF-alpha in mice reduces the inflammatory response in early lipid lesions of aortic sinus. Atherosclerosis 172:211–218
103. Ohta H, Wada H, Niwa T et al (2005) Disruption of tumor necrosis factor-alpha gene diminishes the development of atherosclerosis in apoE-deficient mice. Atherosclerosis 180: 11–17
104. Xiao N, Yin M, Zhang L et al (2009) Tumor necrosis factor-alpha deficiency retards early fatty-streak lesion by influencing the expression of inflammatory factors in apoE-null mice. Mol Genet Metab 96(4):239–244
105. Xanthoulea S, Thelen M, Pottgens C et al (2011) Absence of p55 TNF receptor reduces atherosclerosis, but has no major effect on angiotensin II induced aneurysms in LDL receptor deficient mice. PLoS 4(7):e6113
106. Mackesy DZ, Goalstone ML (2014) ERK5: novel mediator of insulin and TNF-stimulated VCAM-1 expression in vascular cells. J Diab 6:595–602

107. Rajasingh J, Bord E, Luedemann C et al (2006) IL-10-induced TNF-alpha mRNA destabilization is mediated via IL-10 suppression of p38 MAP kinase activation and inhibition of HuR expression. FASEB J 20: 2112–2114

108. Lisinski TJ, Furie MB (2002) Interleukin-10 inhibits proinflammatory activation of endothelium in response to *Borrelia burgdorferi* or lipopolysaccharide but not interleukin-1 beta or tumor necrosis factor alpha. J Leukoc Biol 72:503–511

109. Gallagher H, Williams JO, Ferekidis N et al (2019) Dihomo-γ-linolenic acid inhibits several key cellular processes associated with atherosclerosis. Biochem Biophys Acta Mol Basis Dis 1865(9):2538–2550

110. Takai S, Jin D, Kawashima H et al (2009) Anti-atherosclerotic effects of dihomo-gamma-linolenic acid in ApoE-deficient mice. J Atheroscler Thromb 16(4):480–489

111. Bhatt DL, Steg PG, Miller M et al (2019) Cardiovascular risk reduction with icosapent ethyl for hypertriglyceridemia. N Engl J Med 380(1):11–22

112. Budoff MJ, Bhatt DL, Kinninger A et al (2020) Effect of icosapent ethyl on progression of coronary atherosclerosis in patients with elevated triglycerides on statin therapy: final results of the EVAPORATE trial. Eur Heart J 41:3925–3932

Chapter 3

Survey of In Vitro Model Systems for Investigation of Key Cellular Processes Associated with Atherosclerosis

Dipak P. Ramji, Alaa Ismail, Jing Chen, Fahad Alradi, and Sulaiman Al Alawi

Abstract

Atherosclerosis progression is associated with a complex array of cellular processes in the arterial wall, including endothelial cell activation/dysfunction, chemokine-driven recruitment of immune cells, differentiation of monocytes to macrophages and their subsequent transformation into lipid laden foam cells, activation of inflammasome and pro-inflammatory signaling, and migration of smooth muscle cells from the media to the intima. The use of in vitro model systems has considerably advanced our understanding of these atherosclerosis-associated processes and they are also often used in drug discovery and other screening platforms. This chapter will describe key in vitro model systems employed frequently in atherosclerosis research.

Key words Atherosclerosis, Cardiovascular disease, Endothelial cell dysfunction, Foam cells, Macrophages, Smooth muscle cells

1 Introduction

The progression of atherosclerosis is associated with a complex array of processes involving multiple cell types, including endothelial cells, smooth muscle cells, monocytes/macrophages, and other immune cells [1]. The various risk factors for this disease, particularly increased levels of plasma low-density lipoprotein (LDL), cause endothelial cell activation or dysfunction that is characterized by marked changes in the functions of these cells associated with increased permeability, secretion of chemokines and expression of adhesion proteins on their surface [2, 3]. The increased permeability together with transcytosis causes infiltration of LDL into the subendothelial layer and its modification, particularly oxidation to oxidized LDL (oxLDL), under conditions of oxidative stress [1, 4]. In addition, increased secretion of chemokines together with the expression of adhesion proteins causes recruitment of

Dipak P. Ramji (ed.), *Atherosclerosis: Methods and Protocols*, Methods in Molecular Biology, vol. 2419,
https://doi.org/10.1007/978-1-0716-1924-7_3,
© The Author(s), under exclusive license to Springer Science+Business Media, LLC, part of Springer Nature 2022

immune cells such as monocytes and their infiltration into the subendothelial layer [1, 5]. The monocytes differentiate into macrophages, which is associated with increased expression of pattern recognition receptors such as scavenger receptors, which are involved in the uncontrolled uptake of oxLDL and other modified forms of this lipoprotein [5]. Other processes such as phagocytosis and macropinocytosis also contribute to LDL/modified LDL uptake by macrophages, leading ultimately to the formation of lipid laden foam cells [5]. Several macrophage polarization states exist that have potentially different functions and ability to uptake modified LDL and transform into foam cells [5–7]. Increased accumulation of lipids in foam cells initiates stress responses, including endoplasmic reticulum stress, that ultimately leads to the death of foam cells by apoptosis and necrosis [5]. This coupled with defective clearance of apoptotic cells (i.e., efferocytosis) results in the formation of a lipid-rich necrotic core that causes a state of chronic inflammation [1]. This involves activation of the inflammasome pathway, continuous recruitment of monocytes and other immune cells and production of proinflammatory factors, particularly cytokines, by different cells in the lesion [5, 8]. To counteract the various detrimental changes produced under inflammatory conditions, the normally quiescent smooth muscle cells proliferate, migrate from the media to the intima and produce extracellular matrix (ECM) proteins that form plaque stabilizing fibrous cap that covers the lipid-rich necrotic core [4, 5]. Excessive degradation of ECM proteins via proteases produced by various cells in the plaque under inflammatory conditions together with reduced proliferation and increased apoptotic death of smooth muscle cells causes plaque rupture and subsequent thrombotic cascade associated with platelet aggregation, which leads to clinical complications of the disease such as myocardial infarction.

A number of in vitro model systems that recapitulate various changes seen during atherogenesis, as detailed above, have been developed. In vitro model systems exist for endothelial cell dysfunction, chemokine-driven recruitment of immune cells, inflammasome activation and proinflammatory signaling, smooth muscle cell invasion, platelet aggregation, and several others [2, 9–12]. Although such in vitro models often do not reflect the complexity of the disease that occurs in vivo where there are interactions between multiple cells, contribution of ECM to the disease pathology together with total body and systemic impact, they have provided key mechanistic insights into the molecular basis of the disease and as an initial step in screening programs for drug discovery [2, 9, 10, 12–17]. In addition, in vitro model systems have other advantages in being relatively cheap and more amenable for applying advanced molecular biology techniques to understand disease-associated changes and refine experimental design for subsequent in vivo validation, thereby reducing the numbers of

animals used. This chapter will describe several in vitro model systems that are used in atherosclerosis research (*see* Table 1 for summary). The objective is to provide insights into key models and associated techniques and/or markers used to investigate particular changes rather than providing a comprehensive coverage of all the model systems employed. The choice of species in in vitro model systems is of importance given the existence of species-specific differences in several aspects in relation to atherosclerosis (e.g., metabolism, inflammatory responses) [18]. Ideally human in vitro models should be used unless the studies are intended for experimental design in mouse models in vivo.

2 Endothelial Cell Dysfunction

Endothelial cell dysfunction is an important early step in the pathogenesis of atherosclerosis and it is therefore not surprising that this has been the subject of numerous studies [9, 19]. Human umbilical cord endothelial cells (HUVEC) have been widely used since they were first described in the 1960s given their immense potential for high throughput studies on aspects such as oxidative stress, inflammation and cell signaling [19]. Several immortalized cell lines have also been established, some of which are based on HUVEC; for example, the EaHy926 is a hybridoma of the epithelial cell line A549 and HUVEC [20]. However, differences in cytokine actions associated with inflammation have been identified between such cell lines and primary HUVEC cultures [20]. Even with HUVECs, how they resemble arterial endothelial cells in vivo is often questioned given they are of venous and fetal origin [19]. Indeed, single cell RNA-sequencing (RNA-seq) has recently revealed considerable heterogeneity of endothelial cells across distinct vascular beds during homeostasis and inflammation [19]. Protocols now exist for the isolation of endothelial cells from a range of sources [21, 22] and many are available commercially (e.g., human aortic endothelial cells).

Endothelial cell dysfunction is typically initiated by stimulation of the cells with oxLDL or the cytokine tumor necrosis factor-α (TNF-α). This is followed by determination of several parameters associated with endothelial cell dysfunction, including (1) production of reactive oxygen species (ROS) (e.g., conversion of oxidant-sensitive dye such as dihydroethidine to fluorescent ethidium) or other parameters associated with oxidative stress (e.g., reduced glutathione levels); (2) apoptosis [e.g., terminal deoxynucleotidyl transferase dUTP nick end labeling (TUNEL) assay, flow cytometry following annexin V and propidium iodide staining]; (3) measurement of mitochondrial membrane potential (e.g., use of lipophilic cationic probe such as fluorochrome JC-1); (4) production of nitric oxide (NO) using Griess reagent and expression of

Table 1
In vitro model systems for atherosclerosis research

Cell type	Examples of cellular models	Processes
Endothelial cells	Human umbilical cord endothelial cells, EaHy926 cell line, human aortic endothelial cells	Endothelial cell dysfunction, angiogenesis, senescence
Monocytes	Primary monocytes, human THP-1 and U937 cell lines	Changes in gene expression in relation to LDL, modified LDL or inflammatory stimulus, differentiation to different polarized macrophage states, ability to transform into foam cells, migration and adherence to endothelial cells, trained immunity
Macrophages	Primary cultures such as human monocyte-derived macrophages, bone marrow-derived macrophages, peritoneal macrophages; cell lines such as differentiated THP-1 or U937, RAW264.7, J774.2	Polarization to different phenotypes, proliferation, foam cell formation and associated parameters (e.g., intracellular levels of cholesteryl esters, uptake of labeled, modified LDL, phagocytosis, macropinocytosis, cholesterol efflux), apoptosis, efferocytosis, inflammasome activation
Vascular smooth muscle cells	Rat A10 and A7r5 cell lines, human HITB5 cell line, primary cultures of human aortic smooth muscle cells	Proliferation, migration, expression of markers associated with phenotypic switching, senescence, foam cell formation and associated parameters, expression of ECM proteins, apoptosis, calcification

endothelial nitric oxide synthase (e.g., western blot analysis); (5) expression of markers such as monocyte chemotactic protein-1 (MCP-1), intercellular adhesion molecule-1 (ICAM-1) and vascular cell adhesion molecule 1 by real time-quantitative PCR (RT-qPCR), enzyme-linked immunosorbent assay (ELISA) or other approaches; and (6) adhesion of labeled monocytes/leukocytes under static or flow conditions [23–27]. Endothelial cell dysfunction is also associated with increased permeability, which is in part responsible for the accumulation of LDL in the subendothelial layer. Several assays are available for determining changes in endothelial cell permeability, including immunofluorescent staining for VE-cadherin, endothelial electric resistance measurement and investigation of permeability of labeled large molecules (e.g., carbon-14 labeled sucrose, fluorescein isothionate labeled dextran or albumin, horseradish peroxidase) [28]. The transcription factor nuclear factor kappa-light-chain-enhancer of activated B cells (NF-κB) is a key mediator of induced expression of several genes, such as MCP-1 and ICAM-1, seen during endothelial cell dysfunction [25]. Its activation is therefore often used as a potential

mechanism for the changes in parameters related to endothelial dysfunction by specific agents. NF-κB typically consists of the p50 and p65 subunits that are held in the cytoplasm complexed to inhibitory κB (IκB) subunit. Activation is associated with phosphorylation-triggered degradation of IκB, thereby allowing NF-κB to translocate to the nucleus, binding to its recognition sequences in target genes and induction of their transcription. NF-κB activation is often followed by monitoring degradation of IκB or accumulation of p65 subunit in the nucleus [25]. Alternatively, activation of plasmids containing NF-κB binding sites linked to a reporter gene in transfected cells is monitored [25, 29].

A major limitation of many studies on endothelial cells in vitro is that they are carried out under static flow conditions [30]. However, the flowing blood creates shear stress that has a major impact on endothelial cell function [30]. Thus, branches and bends of arteries are subject to complex flow pattens that are associated with athero-promoting low oscillatory shear stress [30]. On the other hand, higher shear stress elsewhere in the artery is protective [30]. It is hence best to carry out assays under conditions of different shear stress as these could provide new mechanistic insights [31, 32]. For example, endothelial reprogramming by disturbed flow has recently been revealed by single-cell RNA sequencing (scRNA-seq) and scATAC-seq [33].

Angiogenesis, a process by which new blood vessels are formed and expanded, has relevance to atherosclerosis and many other pathological conditions [34]. Angiogenesis is associated with proliferation, migration, and remodeling of endothelial cells and several assays have been employed to study these. Incorporation of tritiated thymidine or bromodeoxyuridine (BrDU) is often used to confirm changes in proliferation noted initially from more indirect approaches such as counting cell numbers or using nucleic acid intercalating dyes [35]. Migration can be followed horizontally using scratch assays and vertically in response to a chemotactic gradient (Boyden chamber) [34, 35]. Several 2D and 3D matrix tube formation assays are also available to investigate angiogenesis [34, 35].

Atherosclerosis development is associated with premature cellular senescence including those of endothelial cells, which then contribute to endothelial cell dysfunction [10]. There are generally two types of cell senescence that have been described: (1) replicative senescence, a characteristic of aging that is associated with shortened telomeres which then tends to trigger a DNA damage response; and (2) stress-induced premature senescence that is triggered by external stimuli and not usually characterized by telomere shortening [10, 36]. Several markers are often used to monitor cellular senescence, including those of endothelial cells, including altered expression of cell cycle regulators (e.g., p16, p21, p53, cyclin D1 by western blot analysis or immunostaining), the

lysosomal enzyme senescence-associated β galactosidase (SAβG; e.g., X-gal substrate followed by light microscopy, fluorogenic substrate followed by fluorescence microscopy), reduction in DNA replication [e.g., tritiated thymidine or BrDU incorporation assays, immunostaining or western blot analysis of proliferation markers such as Ki-67 and proliferating cell nuclear antigen (PCNA)] [10, 36]. Some markers such as SAβG may overestimate cellular senescence so it is advisable to use multiple markers [36].

Major advances in endothelial cell biology, including identification of endothelium derived relaxing factors such as NO, have emerged from ex vivo assays that allow investigation of vascular tone and other parameters [37]. The three most common methods employed are organ bath, wire myography, and pressurized arterial myograph [37]. Intravital microscopy has also been employed for evaluation of endothelial function, particularly leukocyte-endothelium interaction, in the microvasculature ex vivo [9].

3 Changes in Monocyte Function in Relation to Atherosclerosis

Monocytes represent the primary inflammatory cells that infiltrate atherosclerotic plaques and drive the inflammatory response [38, 39]. Monocytes in mice are generally divided into two major subsets: classical, inflammatory $CCR2^{hi}CX3CR1^{lo}Ly6C^{hi}$ monocytes (also called $Ly6C^{hi}$ subset) and nonclassical $CCR2^{lo}CX3CR1^{hi}Ly6C^{lo}$ monocytes (also called $Ly6C^{lo}$ subset) [38]. The monocyte subsets in humans are classified on the basis of their expression of CD14 and CD16 with three classes identified: classical $CD14^{++}CD16^{-}$ monocytes (recognized as being analogous to $Ly6C^{hi}$ subset in mice), nonclassical $CD14^{dim}CD16^{+}$ monocytes (regarded analogous to $Ly6C^{lo}$ subset in mice), and an intermediate $CD14^{+}CD16^{+}$ subset [38]. Studies on monocyte function in relation to atherosclerosis could involve the use of primary cultures [40, 41] or cell lines such as human monocytic leukemia cell line THP-1 and human myeloid leukemia cell line U937 [42, 43]. Commonly employed assays with monocytes in relation to atherosclerosis include: (1) impact of LDL, oxLDL, and inflammatory mediators (e.g., lipopolysaccharide [LPS], cytokines) on gene expression at the level of mRNA or protein together with other parameters relevant to the disease (e.g., differentiation to different macrophage subtypes (*see* Subheading 4), ability to transform into foam cells) [44, 45]; and (2) migration and recruitment to an activated endothelium under normal and different shear stress conditions together with probing of the potential mechanisms involved (e.g., expression of chemokines and their receptors, different classes of integrins, etc.) [46–50]. Substantial recent interest has also been generated in a form of memory associated with immune cells such as monocytes called trained immunity. This

refers to a long-term reprogramming by exogenous or endogenous insults that is associated with an altered response to a second challenge following return to a nonactivated state [51, 52]. In vitro models for trained immunity have been established [53] and it has been shown, for example, that oxLDL produces long-term pro-inflammatory cytokine production and foam cell formation via epigenetic reprogramming of monocytes [54].

4 Changes in Macrophage Function in Relation to Atherosclerosis

Macrophages play a pivotal role at all stages of atherosclerosis, including foam cell formation, inflammatory response, formation of lipid-rich necrotic core and plaque destabilization, and therefore represent excellent targets for therapeutic intervention [55]. Several macrophage/macrophage-like cells have been found in atherosclerotic plaques such as monocyte-derived macrophages, resident-tissue macrophages and vascular smooth muscle cell-derived macrophage-like cells [38]. In addition, macrophage proliferation has been found to play an important role in atherosclerosis, particularly in advanced plaques [56]. Several macrophage cell lines (e.g., differentiated human THP-1 or U937, murine RAW264.7, J774.2) and primary cultures (e.g., peritoneal macrophages, monocyte-derived macrophages, bone marrow-derived macrophages) have been used to investigate various macrophage processes associated with atherosclerosis [15, 42, 57].

Macrophages have classically been classified as proinflammatory M1, induced by T-helper 1 cytokines, and M2 that are produced by stimulation with T-helper 2 cytokines [7, 58]. Models using polarization of naïve macrophages into M1 phenotype using LPS and interferon-γ (IFN-γ) and M2 phenotype with interleukin (IL)-4 or IL-13 or combination have provided a wealth of information on these two subtypes [58, 59]. The effects of various agents to induce these phenotypes in the absence of polarizing stimulus or either inhibit or enhance the phenotypes in the presence of the polarizing stimulus have been investigated by monitoring the expression of specific markers at the mRNA or protein level, or on the cell surface (e.g., RT-qPCR, Western blot analysis, flow cytometry) [13, 60–62]. However, further studies of mouse and human atherosclerosis have revealed several other phenotypes, some of which can also be produced in vitro to investigate their properties and function [58, 59]. Thus, subtypes of M2 macrophages exist: M2a produced by IL-4 and IL-13; M2b induced by immune complexes and toll-like receptor (TLR) ligands or IL-1 receptor agonists; and M2c by IL-10 and glucocorticoids [58]. M4 macrophages are produced by the platelet chemokine (C-X-C motif) ligand 4 (CXCL4), whereas intraplaque hemorrhage-mediated release of free hemoglobin (Hb) causes polarization to M(Hb) (hemoglobin/haptoglobin)

and Mhem (heme) macrophages [58]. It must be emphasized that macrophage phenotype is an expanding field particularly with the application of more emerging technologies such as cytometry by time of flight (CyTOF) and scRNA-seq [63]. In addition to different phenotypes, macrophage proliferation is increasingly being found to play an important role in atherosclerosis, particularly during the latter stages of the disease [56]. This can be followed as described for endothelial cells (e.g. tritiated thymidine or BrDU incorporation assays) and correlation with markers of proliferation such as Ki67 and PCNA [56].

Macrophage foam cell formation is a critical early event in the pathogenesis of atherosclerosis responsible for the fatty streak seen in the disease [5]. It is therefore not surprising that in vitro assays are used routinely to investigate different parameters related to foam cell formation. Although acetylated LDL has not been found to be present in atherosclerotic lesions, it is avidly taken up by macrophages and hence often used along with oxLDL for conversion of macrophages into foam cells [14, 15, 64]. Foam cell formation is associated with increase in intracellular content of cholesteryl esters [5]. The effect of specific agents or genes on foam cell formation produced by modified LDL is often investigated by determining intracellular levels of cholesteryl esters using enzyme-based assays [14, 15]. A radioactive based assay that gives more detailed information is also often used [65, 66]. In such assays, macrophages are converted into foam cells with modified LDL in the presence of a tracer (e.g., ^{14}C-labeled acetate) followed by extraction of lipids, chromatographic separation (e.g., one dimensional thin layer chromatography) and determination of radioactivity in different classes (e.g., polar lipids, triacylglycerol, nonesterified fatty acids, free cholesterol, cholesteryl esters) [65, 66]. Oil red O staining has also been used to determine lipid accumulation in macrophages [67] though further assays detailed below are required to delineate exact processes that are involved in such lipid accumulation.

Foam cell formation is a balance between the uptake of modified LDL by the cells, its intracellular metabolism and efflux of cholesterol from foam cells to acceptors such as HDL for reverse cholesterol transport. Uptake of modified LDL by scavenger receptors is a key mechanism for foam cell formation where radiolabeled modified LDL was used in the past but has since been replaced by the use of a fluorescent tag (e.g., 1,1′-dioctadecyl-3,3,3′,3′-tetramethylindocarbocyanine perchlorate [Dil]-labeled oxLDL) [14–16, 65]. The changes in the uptake of Dil-labeled modified LDL are often correlated with the expression of key scavenger receptors such as SR-A and CD36 [15, 65]. Dil is also used as a label to monitor the uptake of other lipoproteins such as LDL and HDL. Other processes also contribute to foam cell formation such as phagocytosis and macropinocytosis

[5]. Macrophage phagocytic activity plays a critical role in the clearance of pathogens and apoptotic bodies; these are typically monitored using prelabeled cells/apoptotic bodies, bacteria or zymosan particles [68]. Aggregated oxLDL has also been found to be taken up by phagocytosis and studied by incubating cells with them followed by quantification by Oil Red O staining of foam cells [68]. Macropinocytosis, a form of fluid-phase endocytosis where the uptake of the solute is directly proportional to the volume of the internalized liquid and the concentration of the solute, also plays an important role in the uptake of LDL, oxLDL and cholesterol crystals [5, 17, 69]. This endocytic process involves actin-dependent ruffling of the plasma membrane and the subsequent fusion of the membrane to itself to form vacuoles called macropinosome [69]. Macropinocytosis is typically followed by the uptake of dyes (e.g., lucifer yellow) or Dil-labeled LDL or modified LDL [17, 69] coupled to where required, use of inhibitors of the process (e.g., cytochalasin-D, phosphoinositide 3-kinase inhibitors) [5, 17, 69].

Macrophage cholesterol efflux is an important anti-atherogenic process with the sterol then transported to the liver for biliary secretion (reverse cholesterol transport) [5]. Radioactive-based cholesterol efflux assays have been used extensively to study macrophage cholesterol efflux to HDL particles or its key apolipoprotein (A1); efflux activity of plasma HDL is now associated with its protective actions rather than absolute concentrations [5, 15, 65, 66]. In the assay, macrophages are first converted into foam cells via incubation with modified LDL (typically acetylated LDL) in the presence of radiolabeled ^{14}C-cholesterol. Efflux is stimulated via incubation with HDL or lipid-free ApoA1 and radioactivity in conditioned media and lysed cells determined [15, 65, 66]. The changes are correlated with the expression of key genes implicated in the control of macrophage cholesterol efflux such as ATP-binding cassette transporters (ABC)-A1 and G1 together with transcription factors such as liver X receptors [14, 15, 66]. More recently, nonradioactive assays have been developed to monitor cholesterol efflux [70].

Apoptosis, necrosis and other processes (e.g., necroptosis) of macrophages and foam cells results in the deposition of lipids and formation of lipid-rich necrotic core [5]. Several assays are available based on morphological and biochemical changes seen in these processes [71]. Efferocytosis is a process by which apoptotic cells are cleared by phagocytic cells and atherosclerosis progression is associated with defective efferocytosis [72]. In vitro efferocytosis assays typically involve incubation of macrophages with fluorescently labeled apoptotic cells (e.g., Jurkat cells made apoptotic by ultraviolet irradiation) and following uptake by flow cytometry, microscopy or immunocytochemical approaches [73].

Chronic inflammation drives atherosclerotic lesions and is orchestrated by a range of cytokines and other proinflammatory mediators [8]. Activation of NLR family pyrin domain containing 3 (NLRP3) inflammasome is associated with production of IL-1β and IL-18 by cleavage from their pro forms [74]. Activation of NLRP3 inflammasome requires two signals: priming (e.g., LPS, endogenous cytokines) and activation (e.g., cholesterol crystals, minimally modified LDL) and is followed by determination of secretion of IL-1β and IL-18 by ELISA and activation of caspase-1 (e.g., Western blot analysis) [74]. Production of other cytokines in macrophages can also be followed by ELISA. In addition, the impact of cytokines on atherosclerosis-associated macrophage processes detailed above or gene expression (e.g., RT-qPCR, RNA-seq) is investigated in the context of their roles in disease and on the effects of specific agents [13–15].

Atherosclerotic plaque stability is affected by the production of inflammatory mediators by macrophages and other immune cells together with proteases, particularly matrix metalloproteinases (MMPs), that destabilize plaques by degradation of the stabilizing ECM proteins of the fibrous plaques [8]. It is therefore not surprising that MMPs have been intensely studied in relation to expression at mRNA, protein and, particularly, activity not only in macrophages but VSMC (gelatin zymography) [75–77].

5 Changes in Vascular Smooth Muscle Cell Function in Relation to Atherosclerosis

VSMC play an important but complex role in atherosclerosis. The traditional view is that during the progression of atherosclerosis, VSMC migrate from the media to the intima and undergo phenotypic changes from contractile to proliferative synthetic state that produces ECM, which forms plaque stabilizing fibrous cap [10, 78]. However, VSMC have been demonstrated to be more plastic and can adapt several phenotypes, including those resembling foam cells, macrophages, mesenchymal stem cells and osteochondrogenic cells [10, 78]. Although cell lines (e.g., rat A10 and A7r5, human HITB5) have been used to probe smooth muscle cell function in relation to atherosclerosis, there has been a general shift to the use of primary cultures (e.g., human aortic smooth muscle cells) that can be obtained commercially or isolated using several excellent protocols that exist [79, 80].

Phonotypic switching of VSMC plays a critical role in atherogenesis and plaque stability [10]. Thus, VSMC in the media have a contractile phenotype and express a range of markers (e.g., α-smooth muscle cell actin [αSMA], smooth muscle cell myosin heavy chain, SM22-α/transgelin), the expression of which is reduced in atherosclerosis, where the cells have a synthetic phenotype. Such phenotypic switch is associated with increased

proliferation and migration, expression of markers such as osteopontin (OPN) and secretion of ECM proteins and cytokines [10]. αSMA and OPN are typically used initially to distinguish between contractile and synthetic phenotypes and expanded with other markers with more detailed characterization [81, 82] and more in-depth mechanistic insights (e.g., serum response factor [SRF] and myocardin [Myocd] forms an SRF-Myocd transcriptional activation complex that is required for αSMA expression and maintenance of a contractile phenotype with the SRF-Myocd complex negatively regulated by Msh homeobox 1 or 2 [Msx1/2]; microRNA-145 and p53 mitigate phenotypic switch from contractive to synthetic phenotype by regulating Myocd) [10, 78, 81]. As with other cells implicated in atherosclerosis, proliferation of VSMC in vitro is monitored by following tritiated thymidine or BrDU incorporation whereas migration is typically investigated by the use of modified Boyden chambers with platelet derived growth factor-BB as a chemoattractant or in vitro scratch assays [83, 84]. VSMC senescence can also be followed using similar approaches to those detailed above in relation to endothelial cells.

Recent studies have revealed that VSMC make a major contribution to foam cell formation in atherosclerosis [85]. VSMC foam cell formation can be investigated using the same techniques as described for macrophages (e.g., Oil Red O staining, Dil-oxLDL uptake, radioactive or nonradioactive-based cholesterol efflux assays) and correlated with the expression of key genes implicated in these processes. VSMC expression of plaque stabilizing ECM proteins (e.g., collagen-1 and -3, elastin) contributes to plaque stabilization and can be determined by Western blot analysis [77]. On the other hand, apoptosis of VSMC contributes to plaque destabilization and can be followed using approaches similar to that in macrophages and endothelial cells detailed above (e.g., flow cytometry following annexin V and propidium iodide staining) and correlated to markers such as caspase-3 [81]. Finally, vascular calcification plays a key role in advanced stages of atherosclerosis and in vitro assays on VSMC can be used to study the process in more detail (e.g., Alizarin Red S staining, correlation with osteogenic differentiation markers such as runt-related transcription factor 2 and alkaline phosphatase) [80, 81, 86].

6 Conclusions

This chapter has described some common in vitro models and approaches used for investigation of atherosclerosis-associated processes in some of the key, and extensively studied, cell types implicated in this disease; endothelial cells, monocytes/macrophages and VSMC. However, cell culture models are now available for virtually all the cell types implicated in atherosclerosis, including

those not addressed in this chapter (e.g., monocyte-derived dendritic cells, subtypes of T-cells) [87–93]. The use of induced pluripotent stem cells has increased the repertoire of in vitro models to probe atherosclerosis-associated processes with additional applications in regenerative medicine [94, 95]. In vitro models are generally simple and inexpensive, thereby ideal for high throughput analysis required for screening strategies or approaches that require large numbers of replicates and allows for more guided studies in animals and hence reduces their numbers in experimentations. In addition, such models are more amenable for detailed probing of mechanisms using advanced molecular biology techniques coupled with biochemical approaches. However, isolated cell culture models are oversimplification of the complex processes of atherosclerosis involving interactions between multiple cell types and key roles of components such as ECM. Cocultures, 2D, 3D, and ex vivo models have been developed recently though their use for the investigation of the molecular basis of atherosclerosis is still limited [35, 96–100]. The majority of research on atherosclerosis still tends to use a combination of more simple cell culture model systems with some manipulations (e.g., changes in flow conditions), as detailed above, coupled to in vivo model systems [101, 102].

Acknowledgments

We thank the British Heart Foundation for financial support (grants PG/16/25/32097 and FS/17/75/33257). AI and FA received PhD studentships from the Kingdom of Saudi Arabia; JC received PhD studentship from China Scholarship Council; and SA received PhD studentship from Oman Government.

References

1. Chan YH, Ramji DP (2020) A perspective on targeting inflammation and cytokine actions in atherosclerosis. Future Med Chem 12(7): 613–626. https://doi.org/10.4155/fmc-2019-0301
2. Gimbrone MA, García-Cardeña G (2016) Endothelial cell dysfunction and the pathobiology of atherosclerosis. Circ Res 118(4): 620–636. https://doi.org/10.1161/CIRCRESAHA.115.306301
3. Mundi S, Massaro M, Scoditti E, Carluccio MA, van Hinsbergh VWM, Iruela-Arispe ML, De Caterina R (2018) Endothelial permeability, LDL deposition, and cardiovascular risk factors-a review. Cardiovasc Res 114(1): 35–52. https://doi.org/10.1093/cvr/cvx226
4. Buckley ML, Ramji DP (2015) The influence of dysfunctional signaling and lipid homeostasis in mediating the inflammatory responses during atherosclerosis. Biochim Biophys Acta 1852(7):1498–1510. https://doi.org/10.1016/j.bbadis.2015.04.011
5. McLaren JE, Michael DR, Ashlin TG, Ramji DP (2011) Cytokines, macrophage lipid metabolism and foam cells: implications for cardiovascular disease therapy. Prog Lipid Res 50(4):331–347. https://doi.org/10.1016/j.plipres.2011.04.002
6. Barrett TJ (2020) Macrophages in atherosclerosis regression. Arterioscler Thromb Vasc Biol 40(1):20–33. https://doi.org/10.1161/ATVBAHA.119.312802

7. Yang S, Yuan HQ, Hao YM, Ren Z, Qu SL, Liu LS, Wei DH, Tang ZH, Zhang JF, Jiang ZS (2020) Macrophage polarization in atherosclerosis. Clin Chim Acta 501:142–146. https://doi.org/10.1016/j.cca.2019.10.034
8. Ramji DP, Davies TS (2015) Cytokines in atherosclerosis: key players in all stages of disease and promising therapeutic targets. Cytokine Growth Factor Rev 26(6):673–685. https://doi.org/10.1016/j.cytogfr.2015.04.003
9. Chia PY, Teo A, Yeo TW (2020) Overview of the assessment of endothelial function in humans. Front Med 7:542567. https://doi.org/10.3389/fmed.2020.542567
10. Bennett MR, Sinha S, Owens GK (2016) Vascular smooth muscle cells in atherosclerosis. Circ Res 118(4):692–702. https://doi.org/10.1161/CIRCRESAHA.115.306361
11. Moore KJ, Tabas I (2011) Macrophages in the pathogenesis of atherosclerosis. Cell 145(3):341–355. https://doi.org/10.1016/j.cell.2011.04.005
12. Lordan R, Tsoupras A, Zabetakis I (2020) Platelet activation and prothrombotic mediators at the nexus of inflammation and atherosclerosis: potential role of antiplatelet agents. Blood Rev 45:100694. https://doi.org/10.1016/j.blre.2020.100694
13. Moss JW, Davies TS, Garaiova I, Plummer SF, Michael DR, Ramji DP (2016) A unique combination of nutritionally active ingredients can prevent several key processes associated with atherosclerosis in vitro. PLoS One 11(3):e0151057. https://doi.org/10.1371/journal.pone.0151057
14. McLaren JE, Calder CJ, McSharry BP, Sexton K, Salter RC, Singh NN, Wilkinson GW, Wang EC, Ramji DP (2010) The TNF-like protein 1A-death receptor 3 pathway promotes macrophage foam cell formation in vitro. J Immunol 184(10):5827–5834. https://doi.org/10.4049/jimmunol.0903782
15. McLaren JE, Michael DR, Salter RC, Ashlin TG, Calder CJ, Miller AM, Liew FY, Ramji DP (2010) IL-33 reduces macrophage foam cell formation. J Immunol 185(2):1222–1229. https://doi.org/10.4049/jimmunol.1000520
16. Michael DR, Salter RC, Ramji DP (2012) TGF-beta inhibits the uptake of modified low density lipoprotein by human macrophages through a Smad-dependent pathway: a dominant role for Smad-2. Biochim Biophys Acta 1822(10):1608–1616. https://doi.org/10.1016/j.bbadis.2012.06.002
17. Michael DR, Ashlin TG, Davies CS, Gallagher H, Stoneman TW, Buckley ML, Ramji DP (2013) Differential regulation of macropinocytosis in macrophages by cytokines: implications for foam cell formation and atherosclerosis. Cytokine 64(1):357–361. https://doi.org/10.1016/j.cyto.2013.05.016
18. Michael DR, Ashlin TG, Buckley ML, Ramji DP (2012) Liver X receptors, atherosclerosis and inflammation. Curr Atheroscler Rep 14(3):284–293. https://doi.org/10.1007/s11883-012-0239-y
19. Le Brocq M, Leslie SJ, Milliken P, Megson IL (2008) Endothelial dysfunction: from molecular mechanisms to measurement, clinical implications, and therapeutic opportunities. Antioxid Redox Signal 10(9):1631–1674. https://doi.org/10.1089/ars.2007.2013
20. Lidington EA, Moyes DL, McCormack AM, Rose ML (1999) A comparison of primary endothelial cells and endothelial cell lines for studies of immune interactions. Transpl Immunol 7(4):239–246. https://doi.org/10.1016/s0966-3274(99)80008-2
21. Molina-Sánchez P, Andrés V (2015) Isolation of mouse primary aortic endothelial cells by selection with specific antibodies. Methods Mol Biol 1339:111–117. https://doi.org/10.1007/978-1-4939-2929-0_7
22. Kobayashi M, Inoue K, Warabi E, Minami T, Kodama T (2005) A simple method of isolating mouse aortic endothelial cells. J Atheroscler Thromb 12(3):138–142. https://doi.org/10.5551/jat.12.138
23. Bachar AR, Scheffer L, Schroeder AS, Nakamura HK, Cobb LJ, Oh YK, Lerman LO, Pagano RE, Cohen P, Lerman A (2010) Humanin is expressed in human vascular walls and has a cytoprotective effect against oxidized LDL-induced oxidative stress. Cardiovasc Res 88(2):360–366. https://doi.org/10.1093/cvr/cvq191
24. Hort MA, Straliotto MR, de Oliveira J, Amoêdo ND, da Rocha JB, Galina A, Ribeiro-do-Valle RM, de Bem AF (2014) Diphenyl diselenide protects endothelial cells against oxidized low density lipoprotein-induced injury: involvement of mitochondrial function. Biochimie 105:172–181. https://doi.org/10.1016/j.biochi.2014.07.004
25. Bao MH, Zhang YW, Lou XY, Cheng Y, Zhou HH (2014) Protective effects of let-7a and let-7b on oxidized low-density lipoprotein induced endothelial cell injuries. PLoS One 9(9):e106540. https://doi.org/10.1371/journal.pone.0106540

26. Jin X, Yi L, Chen ML, Chen CY, Chang H, Zhang T, Wang L, Zhu JD, Zhang QY, Mi MT (2013) Delphinidin-3-glucoside protects against oxidized low-density lipoprotein-induced mitochondrial dysfunction in vascular endothelial cells via the sodium-dependent glucose transporter SGLT1. PLoS One 8(7): e68617. https://doi.org/10.1371/journal.pone.0068617
27. Lawson C, Rose M, Wolf S (2017) Leukocyte adhesion under hemodynamic flow conditions. Methods Mol Biol 1591:85–100. https://doi.org/10.1007/978-1-4939-6931-9_7
28. Wang Y, Alexander JS (2011) Analysis of endothelial barrier function in vitro. Methods Mol Biol 763:253–264. https://doi.org/10.1007/978-1-61779-191-8_17
29. Varejckova M, Gallardo-Vara E, Vicen M, Vitverova B, Fikrova P, Dolezelova E, Rathouska J, Prasnicka A, Blazickova K, Micuda S, Bernabeu C, Nemeckova I, Nachtigal P (2017) Soluble endoglin modulates the pro-inflammatory mediators NF-κB and IL-6 in cultured human endothelial cells. Life Sci 175:52–60. https://doi.org/10.1016/j.lfs.2017.03.014
30. Souilhol C, Serbanovic-Canic J, Fragiadaki M, Chico TJ, Ridger V, Roddie H, Evans PC (2020) Endothelial responses to shear stress in atherosclerosis: a novel role for developmental genes. Nat Rev Cardiol 17(1):52–63. https://doi.org/10.1038/s41569-019-0239-5
31. Green JP, Souilhol C, Xanthis I, Martinez-Campesino L, Bowden NP, Evans PC, Wilson HL (2018) Atheroprone flow activates inflammation via endothelial ATP-dependent P2X7-p38 signalling. Cardiovasc Res 114(2): 324–335. https://doi.org/10.1093/cvr/cvx213
32. Russo TA, Banuth AMM, Nader HB, Dreyfuss JL (2020) Altered shear stress on endothelial cells leads to remodeling of extracellular matrix and induction of angiogenesis. PLoS One 15(11):e0241040. https://doi.org/10.1371/journal.pone.0241040
33. Andueza A, Kumar S, Kim J, Kang DW, Mumme HL, Perez JI, Villa-Roel N, Jo H (2020) Endothelial reprogramming by disturbed flow revealed by single-cell RNA and chromatin accessibility study. Cell Rep 33(11):108491. https://doi.org/10.1016/j.celrep.2020.108491
34. Zucchelli E, Majid QA, Foldes G (2019) New artery of knowledge: 3D models of angiogenesis. Vasc Biol 1(1):H135–H143. https://doi.org/10.1530/VB-19-0026
35. Fearon IM, Gaça MD, Nordskog BK (2013) In vitro models for assessing the potential cardiovascular disease risk associated with cigarette smoking. Toxicol in Vitro 27(1): 513–522. https://doi.org/10.1016/j.tiv.2012.08.018
36. Noren Hooten N, Evans MK (2017) Techniques to induce and quantify cellular senescence. J Vis Exp (123). doi:https://doi.org/10.3791/55533
37. Ko EA, Song MY, Donthamsetty R, Makino A, Yuan JX (2010) Tension measurement in isolated rat and mouse pulmonary artery. Drug Discov Today Dis Model 7(3–4):123–130. https://doi.org/10.1016/j.ddmod.2011.04.001
38. Flynn MC, Pernes G, Lee MKS, Nagareddy PR, Murphy AJ (2019) Monocytes, macrophages, and metabolic disease in atherosclerosis. Front Pharmacol 10:666. https://doi.org/10.3389/fphar.2019.00666
39. Woollard KJ, Geissmann F (2010) Monocytes in atherosclerosis: subsets and functions. Nat Rev Cardiol 7(2):77–86. https://doi.org/10.1038/nrcardio.2009.228
40. Plaisance-Bonstaff K, Faia C, Wyczechowska D, Jeansonne D, Vittori C, Peruzzi F (2019) Isolation, transfection, and culture of primary human monocytes. J Vis Exp (154). https://doi.org/10.3791/59967
41. Liu Y, Reynolds LM, Ding J, Hou L, Lohman K, Young T, Cui W, Huang Z, Grenier C, Wan M, Stunnenberg HG, Siscovick D, Psaty BM, Rich SS, Rotter JI, Kaufman JD, Burke GL, Murphy S, Jacobs DR, Post W, Hoeschele I, Bell DA, Herrington D, Parks JS, Tracy RP, McCall CE, Stein JH (2017) Blood monocyte transcriptome and epigenome analyses reveal loci associated with human atherosclerosis. Nat Commun 8(1):393. https://doi.org/10.1038/s41467-017-00517-4
42. Qin Z (2012) The use of THP-1 cells as a model for mimicking the function and regulation of monocytes and macrophages in the vasculature. Atherosclerosis 221(1):2–11. https://doi.org/10.1016/j.atherosclerosis.2011.09.003
43. Verhoeckx K, Cotter P, López-Expósito I, Kleiveland C, Lea T, Mackie A, Requena T, Swiatecka D, Wichers H (2015) The impact of food bioactives on health: in vitro and ex vivo models. Springer, Cham
44. Escate R, Padro T, Badimon L (2016) LDL accelerates monocyte to macrophage

differentiation: effects on adhesion and anoikis. Atherosclerosis 246:177–186. https://doi.org/10.1016/j.atherosclerosis.2016.01.002

45. Sieg SF, Bazdar DA, Zidar D, Freeman M, Lederman MM, Funderburg NT (2020) Highly oxidized low-density lipoprotein mediates activation of monocytes but does not confer interleukin-1β secretion nor interleukin-15 transpresentation function. Immunology 159(2):221–230. https://doi.org/10.1111/imm.13142
46. Tsubota Y, Frey JM, Tai PW, Welikson RE, Raines EW (2013) Monocyte ADAM17 promotes diapedesis during transendothelial migration: identification of steps and substrates targeted by metalloproteinases. J Immunol 190(8):4236–4244. https://doi.org/10.4049/jimmunol.1300046
47. Tsubota Y, Frey JM, Raines EW (2014) Novel ex vivo culture method for human monocytes uses shear flow to prevent total loss of transendothelial diapedesis function. J Leukoc Biol 95(1):191–195. https://doi.org/10.1189/jlb.0513272
48. Gerhardt T, Ley K (2015) Monocyte trafficking across the vessel wall. Cardiovasc Res 107(3):321–330. https://doi.org/10.1093/cvr/cvv147
49. Angelovich TA, Hearps AC, Maisa A, Kelesidis T, Jaworowski A (2017) Quantification of monocyte transmigration and foam cell formation from individuals with chronic inflammatory conditions. J Vis Exp (128). https://doi.org/10.3791/56293
50. de Gaetano M, Dempsey E, Marcone S, James WG, Belton O (2013) Conjugated linoleic acid targets β2 integrin expression to suppress monocyte adhesion. J Immunol 191(8):4326–4336. https://doi.org/10.4049/jimmunol.1300990
51. Netea MG, Domínguez-Andrés J, Barreiro LB, Chavakis T, Divangahi M, Fuchs E, Joosten LAB, van der Meer JWM, Mhlanga MM, Mulder WJM, Riksen NP, Schlitzer A, Schultze JL, Stabell Benn C, Sun JC, Xavier RJ, Latz E (2020) Defining trained immunity and its role in health and disease. Nat Rev Immunol 20(6):375–388. https://doi.org/10.1038/s41577-020-0285-6
52. Flores-Gomez D, Bekkering S, Netea MG, Riksen NP (2020) Trained immunity in atherosclerotic cardiovascular disease. Arterioscler Thromb Vasc Biol 41:62. https://doi.org/10.1161/ATVBAHA.120.314216
53. Bekkering S, Blok BA, Joosten LA, Riksen NP, van Crevel R, Netea MG (2016) In vitro experimental model of trained innate immunity in human primary monocytes. Clin Vaccine Immunol 23(12):926–933. https://doi.org/10.1128/CVI.00349-16
54. Bekkering S, Quintin J, Joosten LA, van der Meer JW, Netea MG, Riksen NP (2014) Oxidized low-density lipoprotein induces long-term proinflammatory cytokine production and foam cell formation via epigenetic reprogramming of monocytes. Arterioscler Thromb Vasc Biol 34(8):1731–1738. https://doi.org/10.1161/ATVBAHA.114.303887
55. Moore KJ, Sheedy FJ, Fisher EA (2013) Macrophages in atherosclerosis: a dynamic balance. Nat Rev Immunol 13(10):709–721. https://doi.org/10.1038/nri3520
56. Robbins CS, Hilgendorf I, Weber GF, Theurl I, Iwamoto Y, Figueiredo JL, Gorbatov R, Sukhova GK, Gerhardt LM, Smyth D, Zavitz CC, Shikatani EA, Parsons M, van Rooijen N, Lin HY, Husain M, Libby P, Nahrendorf M, Weissleder R, Swirski FK (2013) Local proliferation dominates lesional macrophage accumulation in atherosclerosis. Nat Med 19(9):1166–1172. https://doi.org/10.1038/nm.3258
57. Tengku-Muhammad TS, Hughes TR, Cryer A, Ramji DP (1996) Differential regulation of lipoprotein lipase in the macrophage J774.2 cell line by cytokines. Cytokine 8(7):525–533. https://doi.org/10.1006/cyto.1996.0071
58. Jinnouchi H, Guo L, Sakamoto A, Torii S, Sato Y, Cornelissen A, Kuntz S, Paek KH, Fernandez R, Fuller D, Gadhoke N, Surve D, Romero M, Kolodgie FD, Virmani R, Finn AV (2020) Diversity of macrophage phenotypes and responses in atherosclerosis. Cell Mol Life Sci 77(10):1919–1932. https://doi.org/10.1007/s00018-019-03371-3
59. Chinetti-Gbaguidi G, Colin S, Staels B (2015) Macrophage subsets in atherosclerosis. Nat Rev Cardiol 12(1):10–17. https://doi.org/10.1038/nrcardio.2014.173
60. Chang HY, Lee HN, Kim W, Surh YJ (2015) Docosahexaenoic acid induces M2 macrophage polarization through peroxisome proliferator-activated receptor γ activation. Life Sci 120:39–47. https://doi.org/10.1016/j.lfs.2014.10.014
61. Gao S, Zhou J, Liu N, Wang L, Gao Q, Wu Y, Zhao Q, Liu P, Wang S, Liu Y, Guo N, Shen Y, Yuan Z (2015) Curcumin induces M2 macrophage polarization by secretion IL-4 and/or IL-13. J Mol Cell Cardiol 85:

131–139. https://doi.org/10.1016/j.yjmcc.2015.04.025

62. Wang C, Dong C, Xiong S (2016) IL-33 enhances macrophage M2 polarization and protects mice from CVB3-induced viral myocarditis. J Mol Cell Cardiol 103:22–30. https://doi.org/10.1016/j.yjmcc.2016.12.010
63. Willemsen L, de Winther MP (2020) Macrophage subsets in atherosclerosis as defined by single-cell technologies. J Pathol 250(5):705–714. https://doi.org/10.1002/path.5392
64. Goldstein JL, Ho YK, Basu SK, Brown MS (1979) Binding site on macrophages that mediates uptake and degradation of acetylated low density lipoprotein, producing massive cholesterol deposition. Proc Natl Acad Sci U S A 76(1):333–337. https://doi.org/10.1073/pnas.76.1.333
65. Gallagher H, Williams JO, Ferekidis N, Ismail A, Chan YH, Michael DR, Guschina IA, Tyrrell VJ, O'Donnell VB, Harwood JL, Khozin-Goldberg I, Boussiba S, Ramji DP (2019) Dihomo-γ-linolenic acid inhibits several key cellular processes associated with atherosclerosis. Biochim Biophys Acta 1865(9):2538–2550. https://doi.org/10.1016/j.bbadis.2019.06.011
66. Taylor JM, Borthwick F, Bartholomew C, Graham A (2010) Overexpression of steroidogenic acute regulatory protein increases macrophage cholesterol efflux to apolipoprotein AI. Cardiovasc Res 86(3):526–534. https://doi.org/10.1093/cvr/cvq015
67. Xu S, Huang Y, Xie Y, Lan T, Le K, Chen J, Chen S, Gao S, Xu X, Shen X, Huang H, Liu P (2010) Evaluation of foam cell formation in cultured macrophages: an improved method with Oil Red O staining and DiI-oxLDL uptake. Cytotechnology 62(5):473–481. https://doi.org/10.1007/s10616-010-9290-0
68. Ganesan R, Henkels KM, Wrenshall LE, Kanaho Y, Di Paolo G, Frohman MA, Gomez-Cambronero J (2018) Oxidized LDL phagocytosis during foam cell formation in atherosclerotic plaques relies on a PLD2-CD36 functional interdependence. J Leukoc Biol 103(5):867–883. https://doi.org/10.1002/JLB.2A1017-407RR
69. Kruth HS (2013) Fluid-phase pinocytosis of LDL by macrophages: a novel target to reduce macrophage cholesterol accumulation in atherosclerotic lesions. Curr Pharm Des 19(33):5865–5872. https://doi.org/10.2174/1381612811319330005
70. Litvinov DY, Savushkin EV, Garaeva EA, Dergunov AD (2016) Cholesterol efflux and reverse cholesterol transport: experimental approaches. Curr Med Chem 23(34):3883–3908. https://doi.org/10.2174/0929867323666160809093009
71. Jiang L, Poon IKH (2019) Methods for monitoring the progression of cell death, cell disassembly and cell clearance. Apoptosis 24(3–4):208–220. https://doi.org/10.1007/s10495-018-01511-x
72. Doran AC, Yurdagul A, Tabas I (2020) Efferocytosis in health and disease. Nat Rev Immunol 20(4):254–267. https://doi.org/10.1038/s41577-019-0240-6
73. Proto JD, Doran AC, Gusarova G, Yurdagul A, Sozen E, Subramanian M, Islam MN, Rymond CC, Du J, Hook J, Kuriakose G, Bhattacharya J, Tabas I (2018) Regulatory T cells promote macrophage efferocytosis during inflammation resolution. Immunity 49(4):666–677.e666. https://doi.org/10.1016/j.immuni.2018.07.015
74. Duewell P, Kono H, Rayner KJ, Sirois CM, Vladimer G, Bauernfeind FG, Abela GS, Franchi L, Nuñez G, Schnurr M, Espevik T, Lien E, Fitzgerald KA, Rock KL, Moore KJ, Wright SD, Hornung V, Latz E (2010) NLRP3 inflammasomes are required for atherogenesis and activated by cholesterol crystals. Nature 464(7293):1357–1361. https://doi.org/10.1038/nature08938
75. Newby AC (2008) Metalloproteinase expression in monocytes and macrophages and its relationship to atherosclerotic plaque instability. Arterioscler Thromb Vasc Biol 28(12):2108–2114. https://doi.org/10.1161/ATVBAHA.108.173898
76. Toth M, Sohail A, Fridman R (2012) Assessment of gelatinases (MMP-2 and MMP-9) by gelatin zymography. Methods Mol Biol 878:121–135. https://doi.org/10.1007/978-1-61779-854-2_8
77. Watt V, Chamberlain J, Steiner T, Francis S, Crossman D (2011) TRAIL attenuates the development of atherosclerosis in apolipoprotein E deficient mice. Atherosclerosis 215(2):348–354. https://doi.org/10.1016/j.atherosclerosis.2011.01.010
78. Basatemur GL, Jørgensen HF, Clarke MCH, Bennett MR, Mallat Z (2019) Vascular smooth muscle cells in atherosclerosis. Nat Rev Cardiol 16(12):727–744. https://doi.org/10.1038/s41569-019-0227-9
79. Metz RP, Patterson JL, Wilson E (2012) Vascular smooth muscle cells: isolation, culture, and characterization. Methods Mol Biol 843:

169–176. https://doi.org/10.1007/978-1-61779-523-7_16

80. Villa-Bellosta R, Hamczyk MR (2015) Isolation and culture of aortic smooth muscle cells and in vitro calcification assay. Methods Mol Biol 1339:119–129. https://doi.org/10.1007/978-1-4939-2929-0_8
81. Zhao D, Li J, Xue C, Feng K, Liu L, Zeng P, Wang X, Chen Y, Li L, Zhang Z, Duan Y, Han J, Yang X (2020) TL1A inhibits atherosclerosis in apoE-deficient mice by regulating the phenotype of vascular smooth muscle cells. J Biol Chem 295(48):16314–16327. https://doi.org/10.1074/jbc.RA120.015486
82. Watanabe R, Watanabe H, Takahashi Y, Kojima M, Konii H, Watanabe K, Shirai R, Sato K, Matsuyama TA, Ishibashi-Ueda H, Iso Y, Koba S, Kobayashi Y, Hirano T, Watanabe T (2016) Atheroprotective effects of tumor necrosis factor-stimulated gene-6. JACC Basic Transl Sci 1(6):494–509. https://doi.org/10.1016/j.jacbts.2016.07.008
83. Huang J, Kontos CD (2002) Inhibition of vascular smooth muscle cell proliferation, migration, and survival by the tumor suppressor protein PTEN. Arterioscler Thromb Vasc Biol 22(5):745–751. https://doi.org/10.1161/01.atv.0000016358.05294.8d
84. Liang CC, Park AY, Guan JL (2007) In vitro scratch assay: a convenient and inexpensive method for analysis of cell migration in vitro. Nat Protoc 2(2):329–333. https://doi.org/10.1038/nprot.2007.30
85. Wang Y, Dubland JA, Allahverdian S, Asonye E, Sahin B, Jaw JE, Sin DD, Seidman MA, Leeper NJ, Francis GA (2019) Smooth muscle cells contribute the majority of foam cells in ApoE (Apolipoprotein E)-deficient mouse atherosclerosis. Arterioscler Thromb Vasc Biol 39(5):876–887. https://doi.org/10.1161/ATVBAHA.119.312434
86. Di Bartolo BA, Cartland SP, Harith HH, Bobryshev YV, Schoppet M, Kavurma MM (2013) TRAIL-deficiency accelerates vascular calcification in atherosclerosis via modulation of RANKL. PLoS One 8(9):e74211. https://doi.org/10.1371/journal.pone.0074211
87. Haka AS, Singh RK, Grosheva I, Hoffner H, Capetillo-Zarate E, Chin HF, Anandasabapathy N, Maxfield FR (2015) Monocyte-derived dendritic cells upregulate extracellular catabolism of aggregated low-density lipoprotein on maturation, leading to foam cell formation. Arterioscler Thromb Vasc Biol 35(10):2092–2103. https://doi.org/10.1161/ATVBAHA.115.305843
88. Salvatore G, Bernoud-Hubac N, Bissay N, Debard C, Daira P, Meugnier E, Proamer F, Hanau D, Vidal H, Aricò M, Delprat C, Mahtouk K (2015) Human monocyte-derived dendritic cells turn into foamy dendritic cells with IL-17A. J Lipid Res 56(6):1110–1122. https://doi.org/10.1194/jlr.M054874
89. Iborra S, González-Granado JM (2015) In vitro differentiation of naïve CD4$^+$ T cells: a tool for understanding the development of atherosclerosis. Methods Mol Biol 1339:177–189. https://doi.org/10.1007/978-1-4939-2929-0_12
90. Cochain C, Koch M, Chaudhari SM, Busch M, Pelisek J, Boon L, Zernecke A (2015) CD8+ T cells regulate monopoiesis and circulating Ly6C-high monocyte levels in atherosclerosis in mice. Circ Res 117(3):244–253. https://doi.org/10.1161/CIRCRESAHA.117.304611
91. Kyaw T, Tay C, Khan A, Dumouchel V, Cao A, To K, Kehry M, Dunn R, Agrotis A, Tipping P, Bobik A, Toh BH (2010) Conventional B2 B cell depletion ameliorates whereas its adoptive transfer aggravates atherosclerosis. J Immunol 185(7):4410–4419. https://doi.org/10.4049/jimmunol.1000033
92. Selathurai A, Deswaerte V, Kanellakis P, Tipping P, Toh BH, Bobik A, Kyaw T (2014) Natural killer (NK) cells augment atherosclerosis by cytotoxic-dependent mechanisms. Cardiovasc Res 102(1):128–137. https://doi.org/10.1093/cvr/cvu016
93. Tsoupras A, Lordan R, Harrington J, Pienaar R, Devaney K, Heaney S, Koidis A, Zabetakis I (2020) The effects of oxidation on the antithrombotic properties of tea lipids against PAF, thrombin, collagen, and ADP. Foods 9(4):385. https://doi.org/10.3390/foods9040385
94. Musunuru K, Sheikh F, Gupta RM, Houser SR, Maher KO, Milan DJ, Terzic A, Wu JC, Biology AHACoFGaT, Young CoCDit, Nursing aCoCaS (2018) Induced pluripotent stem cells for cardiovascular disease modeling and precision medicine: a scientific statement from the American Heart Association. Circ Genom Precis Med 11(1):e000043. https://doi.org/10.1161/HCG.0000000000000043
95. Klein D (2018) iPSCs-based generation of vascular cells: reprogramming approaches and applications. Cell Mol Life Sci 75(8):1411–1433. https://doi.org/10.1007/s00018-017-2730-7

96. Noonan J, Grassia G, MacRitchie N, Garside P, Guzik TJ, Bradshaw AC, Maffia P (2019) A novel triple-cell two-dimensional model to study immune-vascular interplay in atherosclerosis. Front Immunol 10:849. https://doi.org/10.3389/fimmu.2019.00849
97. Mallone A, Stenger C, Von Eckardstein A, Hoerstrup SP, Weber B (2018) Biofabricating atherosclerotic plaques: in vitro engineering of a three-dimensional human fibroatheroma model. Biomaterials 150:49–59. https://doi.org/10.1016/j.biomaterials.2017.09.034
98. Gu X, Xie S, Hong D, Ding Y (2019) An in vitro model of foam cell formation induced by a stretchable microfluidic device. Sci Rep 9(1):7461. https://doi.org/10.1038/s41598-019-43902-3
99. Robert J, Weber B, Frese L, Emmert MY, Schmidt D, von Eckardstein A, Rohrer L, Hoerstrup SP (2013) A three-dimensional engineered artery model for in vitro atherosclerosis research. PLoS One 8(11):e79821. https://doi.org/10.1371/journal.pone.0079821
100. Lebedeva A, Vorobyeva D, Vagida M, Ivanova O, Felker E, Fitzgerald W, Danilova N, Gontarenko V, Shpektor A, Vasilieva E, Margolis L (2017) Ex vivo culture of human atherosclerotic plaques: a model to study immune cells in atherogenesis. Atherosclerosis 267:90–98. https://doi.org/10.1016/j.atherosclerosis.2017.10.003
101. Getz GS, Reardon CA (2012) Animal models of atherosclerosis. Arterioscler Thromb Vasc Biol 32(5):1104–1115. https://doi.org/10.1161/ATVBAHA.111.237693
102. Emini Veseli B, Perrotta P, De Meyer GRA, Roth L, Van der Donckt C, Martinet W, De Meyer GRY (2017) Animal models of atherosclerosis. Eur J Pharmacol 816:3–13. https://doi.org/10.1016/j.ejphar.2017.05.010

Chapter 4

Survey of Approaches for Investigation of Atherosclerosis In Vivo

Dipak P. Ramji, Yee-Hung Chan, Alaa Alahmadi, Reem Alotibi, and Nouf Alshehri

Abstract

Although in vitro model systems are useful for investigation of atherosclerosis-associated processes, they represent simplification of complex events that occur in vivo, which involve interactions between many different cell types together with their environment. The use of animal model systems is important for more in-depth insights of the molecular mechanisms underlying atherosclerosis and for identifying potential targets for agents that can prevent plaque formation and even reverse existing disease. This chapter will provide a survey of such animal models and associated techniques that are routinely used for research of atherosclerosis in vivo.

Key words Atherosclerosis, Cardiovascular disease, Animal models, Approaches, Mice

1 Introduction

Cardiovascular disease (CVD) accounts for more global deaths than any other disease [1–3]. Atherosclerosis, an inflammatory disorder of the vasculature associated with deposition of lipids and cellular debris, is the principal underlying cause of CVD. The progression of atherosclerotic CVD involves: (1) endothelial cell dysfunction or activation by various risk factors associated with this disease such as high plasma levels of low density lipoprotein (LDL); (2) chemokine-driven recruitment of immune cells such as monocytes into the subendothelium where they differentiate into macrophages; (3) uptake of oxidized and other modified LDL by macrophages and their transformation into lipid laden foam cells; (4) death of foam cells by apoptosis and necrosis in response to stress responses triggered by increased intracellular accumulation of cholesterol leading to the formation of a lipid-rich necrotic core; (5) chronic inflammation due to activation of the inflammasome by lipids (e.g., cholesterol crystal) and other proinflammatory pathways;

Dipak P. Ramji (ed.), *Atherosclerosis: Methods and Protocols*, Methods in Molecular Biology, vol. 2419,
https://doi.org/10.1007/978-1-0716-1924-7_4,
© The Author(s), under exclusive license to Springer Science+Business Media, LLC, part of Springer Nature 2022

(6) migration of smooth muscle cells (SMC) from the media to the intima where they form a plaque stabilizing fibrous cap consisting of extracellular matrix (ECM) proteins that covers the lipid-rich necrotic core; (7) thinning of the fibrous cap because of reduced proliferation and increased apoptosis of SMC together with increased degradation of ECM by various proteases (e.g., matrix metalloproteinases) under inflammatory conditions; and (8) plaque rupture leading to thrombotic complications such as myocardial infarction and cerebrovascular accidents [1–5].

In vitro model systems have provided important mechanistic insights into several atherosclerosis-associated cellular processes (e.g., endothelial cell dysfunction, chemokine-driven monocyte migration, macrophage polarization, foam cell formation and SMC proliferation and migration) and have been useful in screening for specific drugs or agents [6–10]. However, such models represent a gross simplification of a complex process that occurs in vivo involving multiple cell types with key influences by interactions between them and with the ECM and the environment [6]. Animal models of atherosclerosis have therefore formed the foundation for defining atherosclerosis-associated mechanisms, investigation of the roles of specific genes in the disease and identifying potential targets for the prevention, treatment, and even regression of the disease [11–15]. This chapter will survey the various animal models used for atherosclerosis research together with the approaches employed with such models to gain deeper mechanistic insights (Table 1).

2 Animal Models of Atherosclerosis

Most animal models of atherosclerosis involve acceleration of disease development by feeding them a Western-type diet (WD) rich in cholesterol, modulation of key genes implicated in the regulation of cholesterol homeostasis or introduction of additional risk factors for the disease (e.g., diabetes) [11–14]. Rabbit model systems were used extensively until 2000 because they are relatively cheap, easy to breed and handle, have lipoprotein metabolism more similar to humans [e.g., express cholesterol ester transfer protein (CETP)] and display many similarities to human plaques [11–13]. Examples of rabbit models include New Zealand White rabbits fed diet rich in cholesterol and Watanabe heritable hyperlipidaemic rabbits which have defects in the LDL receptor (LDLr) [11–13]. However, there are several disadvantages associated with rabbit models such as differences in the localization of the plaques compared to humans and the abnormal diet required for long duration in such models can often cause substantial inflammation and hepatic toxicity [12].

Mice have therefore become the model of choice in the last 10–15 years because they are relatively cheap and easy to breed,

Table 1
Parameters frequently investigated for investigation of atherosclerosis in vivo

Models	Tissues/other sources	Examples of parameters analyzed
Rabbits (e.g., New Zealand White, Watanabe heritable hyperlipidemic)	General	Diet induced weight gain, weight of organs
Mice (e.g., ApoE$^{-/-}$, LDLr$^{-/-}$, ApoE$^{-/-}$LDLr$^{-/-}$, PCSK9-AAV, ApoE$^{-/-}$Fbn1$^{C1039G+/-}$ mice, Reversa mice, bone marrow transplantation approaches)	Blood/plasma	Lipid and lipoprotein profile (e.g., total cholesterol and triglycerides, LDL, HDL, VLDL); immune cell profile (e.g., monocyte subtypes); key cytokines; specific antibodies (e.g., oxLDL)
Pigs	Aorta	En face staining with Oil Red O for plaque burden; gene expression; RNA-sequencing and single cell RNA sequencing; flow cytometry of immune cells; laser capture microdissection followed by downstream analysis; mass cytometry in tandem with time-of-flight mass spectrometry
Hamsters	Sections from aortic root, brachiocephalic artery and other vascular beds	Staining with Oil Red O and hematoxylin and eosin or other stains for plaque burden; in-depth analysis of cellular and biochemical composition (e.g., immunostaining with antibodies against markers of specific cell types or processes; histological staining for collagen, calcification or connective tissue; in situ hybridization of noncoding RNA; in-depth analysis of parameters associated with plaque stability and rupture; near-infrared calcium imaging)
Nonhuman primates Others	Whole animal	Noninvasive approaches for monitoring plaque burden and associated parameters such as ultrasound, magnetic resonance imaging, positron emission tomography, computed tomography or combinations; in vivo macrophage-specific reverse cholesterol transport

represent low cost for pharmacological intervention studies, are amenable to genetic manipulation and have shorter time frame for atherosclerosis development [11–15]. Wild type mice are relatively resistant to atherosclerosis development because of

differences in their lipoprotein profile compared to humans (e.g., cholesterol is transported as HDL particles) and hence manipulation of cholesterol homeostatic mechanisms is required [11, 12]. Examples of mouse models in atherosclerosis include apolipoprotein E deficient ($ApoE^{-/-}$) mice, LDL receptor deficient ($LDLr^{-/-}$) mice, double $ApoE^{-/-}LDLr^{-/-}$ mice, single adeno-associated virus (AAV)-mediated gene transfer of mutant proprotein convertase subtilisin/kexin type 9 (PCSK9) in mice (PCSK9-AAV mice) and $ApoE^{-/-}Fbn1^{C1039G+/-}$ mice [12–16]. These models can also be adapted to investigate atherosclerosis associated with other diseases such as diabetes and chronic renal disease [11]. However, translation of findings from such mouse models to humans should be considered with caution because of the many differences that exist such as lipid metabolism (e.g., mice lack CETP), immune cells, inflammatory responses and vascular beds where lesions are seen [11, 12, 15, 17].

$ApoE^{-/-}$ and $LDLr^{-/-}$ mice have been used extensively [11, 12, 16]. The former model can develop atherosclerosis following long-term feeding of a normal diet but can be speeded up by the use of a WD diet (e.g., containing 21% saturated fat and 0.2% cholesterol) [11, 12]. However, the lipid profile in these mice in relation to atherosclerosis is different from humans with increase mainly in the very low density lipoprotein (VLDL) and chylomicron fractions [11, 12, 16]. In addition, ApoE is involved in the control of other processes such as inflammation, reverse cholesterol transport (RCT) from macrophages, oxidation and proliferation and migration of SMC [18], which may all impact plaque development in $ApoE^{-/-}$ mice [11, 12]. In contrast, $LDLr^{-/-}$ mice develop little or no atherosclerosis on a normal diet and require a WD for atherogenesis though plaque development is generally less rapid than in $ApoE^{-/-}$ mice [11, 12, 16]. However, the $LDLr^{-/-}$ mouse model has more human-like plasma lipid profile (e.g., increase in LDL), the deficiency of LDLr does not impact inflammation and also the model has several characteristics akin to human familial hypercholesterolemia due to deficiency of functional LDLr [11, 12, 16]. The double $ApoE^{-/-}LDLr^{-/-}$ mice develop atherosclerosis on normal diet with marked progression compared to deficiency of $ApoE^{-/-}$ alone [12]. This model is therefore of particular use in investigation of antiatherosclerotic agents as there is no need for the use of an atherogenic diet [12].

The use of PCSK9-AAV mice has been increasing in the last few years as no germ line deficiency or genetic modification is required [12, 16, 19, 20]. The protease PCSK9 interacts with the LDLr on the cell surface and increases its endosomal and lysosomal degradation, thereby reducing hepatic uptake of LDL [21]. A D344Y gain-of-function mutation leads to hypercholesterolemia so many studies have employed infection of AAVs carrying this human mutation or its mouse equivalent mutation (D377Y) in C57BL/6 mice

[22]. However, a WD is required for plaque formation [12, 16]. ApoE3-Leiden was described in a large Dutch family and was associated with a dominantly inherited form of hyperlipidemia [12]. The ApoE3-Leiden transgenic mice carry a genomic 27 kb DNA construct from the original ApoE3 Leiden proband [12]. These mice develop atherosclerosis on a WD with a more human-like lipid profile and have a functional ApoE gene [12, 23, 24].

Atherosclerotic plaque rupture is critical for the clinical complications of the disease [1, 4]. Unfortunately, the models detailed above such as $ApoE^{-/-}$ or $LDLr^{-/-}$ mice, have limitations in relation to studies on plaque rupture where this only occurs sporadically or after a long time in certain vascular beds (e.g., brachiocephalic artery) or following mechanical injury with reproducibility often on the lower side [12]. Some promise has been seen recently with the development of $ApoE^{-/-}Fbn1^{C1039G+/-}$ mice; $ApoE^{-/-}$ mice containing a heterozygous mutation ($C1039G^{-/-}$) in the fibrillin-1 (Fbn1) gene that is associated with Marfan syndrome and characterized by the fragmentation of elastic fibers [12, 16, 25–27].

The above models are extensively used for functional studies (e.g., deficiency of specific genes, knockin approaches, tissue specific or temporal conditional knockout, expression of genes to generate transgenic mice) or to study the effects of a particular agent/treatment strategy on the development of atherosclerosis [11, 22]. Typically, the models that employ WD involve feeding for 8–12 weeks, which allows for monitoring of several parameters associated with the development of atherosclerosis, though it is recommended that at least two time points be used (e.g., early and advanced lesions) to delineate differences that could potentially be missed by the use of a single point [11–13, 16]. Bone marrow transplantation approaches in such models have also been useful in delineating the roles of leukocytes, or deficiency of specific genes in such cells, on atherosclerosis and thereby differentiate from endothelial cells or SMC that would not be possible in the case of germ line deficiency [11, 22, 28, 29]. The approach involves adoptive transfer of bone marrow cells from control or test mice into irradiated recipients. $LDLr^{-/-}$ are preferred in such approaches because the expression of LDLr on bone marrow cells of the recipient does not have any major impact on plasma lipid levels or atherosclerosis [11, 28]. In contrast, the expression of ApoE in recipient bone marrow impacts plasma lipid levels and atherosclerosis in $ApoE^{-/-}$ mice so the recipient bone marrow cells also have to be deficient in this apolipoprotein [11, 28]. It should however be noted that radiation could potentially impact atherosclerosis [30–32]. For example, a recent study has shown the effect of radiation on early atherosclerosis via the suppression of intimal LDL accumulation [32]. Thus, radiation exposure caused LDL uptake by

endothelial cells to be diverted to lysosomal degradation and RCT, thereby reducing the intimal levels of lipids that then impacted lesion initiation and growth [32].

Mouse models of atherosclerosis are not just useful for studies on the progression of the disease but can be adapted to investigate plaque regression [33–36]. Such approaches for plaque regression include dietary intervention (e.g., switching from a WD to a standard chow diet), aortic transplant (transplantation of lesion containing aortic segments from an atherosclerotic animal to normolipidemic host), overexpression approaches (e.g., human apolipoprotein A-I, liver-specific expression of ApoE) and the use of the Reversa mouse ($Ldlr^{-/-}$ $ApoB^{100/100}Mttp^{fl/fl}$ $Mx1Cre^{+/+}$) [11, 35, 37]. In the case of the Reversa model, these mice develop severe hypercholesterolemia because of deficiency in LDLr and the presence of the apoB100-only allele; however, this can be reversed by the expression of the Mx1-Cre transgene that inactivates the gene coding for microsomal triglyceride transfer protein (Mttp) [37].

Other animal models that have been used to probe atherosclerosis include pigs and nonhuman primate [11, 12]. Pigs demonstrate many similarities to human plaques but are relatively expensive and difficult to handle [11, 12]. In addition, other approaches such as selection of natural mutants, mechanical damage, introduction of other risk factors, or genetic engineering approaches are required for advanced lesions [11, 12]. While nonhuman primates display similar plaque formation as humans, including in the coronary arteries, they are expensive, highly regulated and require specialized training [11, 12]. Advances in gene editing tools such as CRISPR (clustered regularly interspaced short palindromic repeats) gene editing are increasing the repertoire of animal models available for atherosclerosis research and include minipigs, rats, hamsters, and guinea pigs [12, 14].

3 Approaches for Investigation of Plasma/Blood Parameters Together with Plaque Burden and Cellular Content

Because mouse models are extensively used for atherosclerosis research, the survey of approaches addressed here will be restricted to this species. Specific recommendation now exists for the design, execution, and reporting of atherosclerosis studies in animals [17]. Some standard parameters are routinely measured in animals before the assessment of plaque and include diet induced weight gain, weight of organs and plasma lipid profile. The plasma lipid profile is particularly important for mechanistic insights and include determination of the total concentration of cholesterol and triglycerides using calorimetric assays together with key lipoproteins,

such as LDL, VLDL and HDL via ultracentrifugation, precipitation-based methods that provides a measure of concentration of cholesterol in HDL particles and apoB containing lipoproteins or size exclusion chromatography (e.g., fast protein liquid chromatography) [17]. More detailed analysis of lipoprotein size, subtypes and numbers can also be carried out if required for mechanistic insights [38]. Other parameters associated with blood or plasma can also be analyzed for further mechanistic insights, including levels of key cytokines (multiplex assays), immune cells (e.g., monocyte subtypes by flow cytometry), and antibody titers and antibodies against specific antigens [e.g., oxLDL via enzyme-linked immunosorbent assay (ELISA)] [39–42].

The en face technique is often used to determine plaque burden in some studies and involves the removal of the entire length of the aorta from the heart to iliac bifurcation, staining for neutral lipids (e.g., Oil Red O) and image analysis [17, 43–45]. However, most studies use Oil Red O and hematoxylin and eosin or Verhoeff van Gieson staining of sections (usually ~10 μm) from the aortic root, though it is recommended to confirm findings by using sections from other vascular beds (e.g., brachiocephalic artery) for more informed analysis [17, 43].

Plaque size and lipid content in sections detailed above are accompanied by more in-depth analysis of cellular and biochemical composition, which can provide further mechanistic insights. These include sterol content (e.g., ratio of unesterified to esterified cholesterol), immunostaining and histological staining [17]. Immunostaining of sections for specific markers is routinely used to determine the cellular content of the atherosclerotic plaques (e.g., macrophages/foam cells, endothelial cells, specific polarized macrophages, T cells and various subtypes, dendritic cells, SMC and several others) [10, 17, 39]. Markers that are often used include Mac-2 (galectin-3) or F4/80 for macrophages, CD3 for T-lymphocytes, α-actin for smooth muscle cells, von Willebrand factor, platelet/endothelial cell adhesion molecule 1 (PECAM-1) or vascular endothelial cadherin for endothelial cells [7, 10, 17, 39]. Immunostaining is also useful for analysis of other markers that can then provide more detailed mechanistic insights (e.g., Ki67 for proliferation, adhesion proteins) [24, 46]. Several approaches are also available to evaluate apoptosis, including number of pyknotic/fragmented nuclei, immunohistochemistry (IHC) for cleaved poly (ADP-ribose) polymerase-1 and terminal deoxynucleotidyl transferase dUTP nick-end labeling [47–51]. The last decade has also seen an explosion of studies on noncoding RNA (e.g., microRNAs, long noncoding RNAs) and hence techniques of in situ hybridization have been developed for determining their levels and localization in atherosclerotic plaques [52, 53].

Histological stains such as Oil Red O and hematoxylin and eosin have been described above. Others include Picrosirius red

for collagen; Alizarin red or Von Kossa for calcification; and Verhoeff–Van Gieson, Masson's trichrome, or modified Movat's for connective tissue components such as collagen, elastin and proteoglycans [17, 39, 54, 55]. Such histological stains together with other approaches are often useful for more in-depth analysis of plaque instability and potential for rupture (e.g., levels of macrophages, presence of large necrotic core, encapsulation of necrotic areas and presence of connective tissue as an indicator of fibrosis) [47–51]. Thus, sections are typically analyzed for: fibrous cap thickness; acute plaque rupture (disruption of fibrous plaque with intrusion of blood products into the core); buried fibrous layers (structures invested with collagen and elastin and usually overlain with foam cells); necrotic cores [matrix-poor, acellular regions below a fibrous cap (smooth muscle α-actin-rich) region with often the presence of cholesterol crystals and calcification]; leukocyte ingress into plaques (IHC using monocyte chemotactic protein-1 and vascular cell adhesion molecule-1) and presence of intraplaque thrombus or hemorrhage with, if required, use of specific stains (e.g., Dunn Thompson for hemoglobin, Perls' Prussian Blue iron for iron) [17, 47–51]. More recently, near-infrared calcium imaging has also been used for molecular imaging and quantification of the calcification process [22, 56].

Several noninvasive approaches, which have been previously employed for the diagnosis, localization and characterization of human plaques, have also been used and/or are being refined to determine the size and characteristics of atherosclerotic lesions in animal models [17]. These include ultrasound, magnetic resonance imaging, positron emission tomography (PET), and computed tomography, either individually or in combination (e.g., PET/magnetic resonance imaging). However, their use at present is not widespread because of issues relating to resolution though refinements are allowing novel insights to at least some parameters [17, 22, 57, 58]. For example, because macrophages have high glycolytic activities and fluorodeoxyglucose (^{18}F-FDG) is a marker for cellular glucose uptake, ^{18}F-FDG-PET has been used to probe macrophage accumulation in atherosclerotic plaques and combined with ^{14}C-glutamine to investigate macrophage heterogeneity [22, 59]. In addition, fluorescence molecular tomography/X-ray computed tomography after injections of an elastase-targeted fluorescent agent has been used to probe endothelial dysfunction and neutrophil accumulation in early atherosclerosis [60]. Thus, combination of histological analysis with other imaging modalities (e.g., PET with different labels) will improve characterization of atherosclerotic lesions in the future.

4 Other Approaches in Investigation of Atherosclerosis In Vivo

Macrophage cholesterol efflux and RCT plays a critical antiatherogenic role [5]. An in vivo approach for determining macrophage specific RCT has been used in many studies [61–63]. This assay involves preparation of [^{3}H]-cholesterol-loaded macrophages (e.g., using mouse J774.1 cell line), intraperitoneal injection of these radiolabeled foam cells into mice, collection of feces and blood at timed intervals and at the end of the experimental period (e.g., 48 h) and determination of radioactivity in serum, high density lipoprotein (HDL) particles, liver, feces and faecal bile acids [61–63].

Because immunostaining has limitations in quantification of cell numbers, flow cytometry of atherosclerotic mouse aorta has been carried out in some studies [64, 65]. This involves digestion of ECM of mouse aortas and quantification of released cells using fluorescent antibodies [66]. Laser capture microdissection has also been used to study specific cell types from particular locations in atherosclerotic plaques [17, 67–69]. The most common approach involves identification of cells of interest by light microscopy, use of laser beam to safely remove cells, lysis of the cells, and purification of components for subsequent analysis (e.g., RNA for gene expression studies) [68].

Recruitment of leukocytes is a critical event not only at the start of atherosclerosis during endothelial dysfunction but throughout the disease and represents a promising therapeutic target [70]. Intravital microscopy has been used to delineate the molecular mechanisms underlying such leukocyte recruitment in atherosclerosis [70–72]. In addition, state-of-the art intravital two photon microscopy has recently been employed to visualize monocyte/macrophage dynamics in real time in live animals [22, 73, 74].

Despite the major contribution that flow cytometry has made in atherosclerosis research, the technique is able to quantify only a limited number of markers. Many recent studies have therefore used mass cytometry, which quantifies abundance of proteins at single-cell resolution using antibodies conjugated with heavy metal, in tandem with time-of-flight mass spectrometry [75–77].

Single cell RNA sequencing (scRNAseq) often combined with flow cytometry, mass cytometry and other approaches are revolutionizing our understanding of the molecular basis of atherosclerosis [75, 76, 78–86]. ScRNAseq has identified new cell types, delineated heterogeneity in populations previously considered to be homogenous, revealed cellular plasticity and intercellular communications and provided new insights into progression from normal to diseased phenotype [78, 80–82]. Such approaches have allowed transcriptome-based cellular landscape of atherosclerotic plaques, defined immune cell landscapes, including macrophage

and T-cell subsets, and cell atlas of atherosclerosis progression and regression in mouse model systems [78, 80–82].

5 Conclusions

The use of animal models of atherosclerosis has advanced our understanding of the molecular basis of the disease. Mouse model systems remain the most popular because of ease of genetic manipulation and breeding, short time frame for disease development and cost-effectiveness. The application of such models with plasma lipid profile coupled with plaque burden and cellular content have provided important insights into the roles of key genes and cell types in this disease. The application of scRNAseq is providing new insights and opening up new avenues for research such as functional relevance of new cell types that have been identified (e.g., immunological mechanisms, cell-type specific pathways), mechanisms underlying intercellular communications and novel tailored interventional strategies. However, mice differ from humans in two key aspects related to disease, lipoprotein metabolism and immune/inflammatory responses, and have limitations as far as studies on plaque rupture are concerned. Thus, caution needs to be exerted in terms of extrapolating findings to humans. However, gene editing approaches are allowing development of new animal model systems that should hopefully be more similar to disease development in humans, and scRNASeq is not only providing insights into cells during progression and regression of disease in animal models but also more precise information regarding similarities and differences with plaques in humans. Overall, continued advances in in vivo approaches addressed here will allow identification of new therapeutic targets and development of new drugs for the treatment of this disease, which still accounts for a third of all global deaths.

Acknowledgments

DPR and Y-HC thank the British Heart Foundation for financial support (grants PG/16/25/32097 and FS/17/75/33257). AA, RA, and NA received PhD studentships from Kingdom of Saudi Arabia.

References

1. Chan YH, Ramji DP (2020) A perspective on targeting inflammation and cytokine actions in atherosclerosis. Future Med Chem 12(7): 613–626. https://doi.org/10.4155/fmc-2019-0301
2. Moss JWE, Ramji DP (2016) Nutraceutical therapies for atherosclerosis. Nat Rev Cardiol 13(9):513–532. https://doi.org/10.1038/nrcardio.2016.103
3. Moss JWE, Williams JO, Ramji DP (2018) Nutraceuticals as therapeutic agents for atherosclerosis. Biochim Biophys Acta 1864(5 Pt A):1562–1572. https://doi.org/10.1016/j.bbadis.2018.02.006
4. Buckley ML, Ramji DP (2015) The influence of dysfunctional signaling and lipid homeostasis in mediating the inflammatory responses during atherosclerosis. Biochim Biophys Acta 1852(7):1498–1510. https://doi.org/10.1016/j.bbadis.2015.04.011
5. McLaren JE, Michael DR, Ashlin TG, Ramji DP (2011) Cytokines, macrophage lipid metabolism and foam cells: implications for cardiovascular disease therapy. Prog Lipid Res 50(4):331–347. https://doi.org/10.1016/j.plipres.2011.04.002
6. Fearon IM, Gaça MD, Nordskog BK (2013) In vitro models for assessing the potential cardiovascular disease risk associated with cigarette smoking. Toxicol in Vitro 27(1):513–522. https://doi.org/10.1016/j.tiv.2012.08.018
7. McLaren JE, Michael DR, Salter RC, Ashlin TG, Calder CJ, Miller AM, Liew FY, Ramji DP (2010) IL-33 reduces macrophage foam cell formation. J Immunol 185(2): 1222–1229. https://doi.org/10.4049/jimmunol.1000520
8. Gallagher H, Williams JO, Ferekidis N, Ismail A, Chan YH, Michael DR, Guschina IA, Tyrrell VJ, O'Donnell VB, Harwood JL, Khozin-Goldberg I, Boussiba S, Ramji DP (2019) Dihomo-γ-linolenic acid inhibits several key cellular processes associated with atherosclerosis. Biochim Biophys Acta 1865(9): 2538–2550. https://doi.org/10.1016/j.bbadis.2019.06.011
9. Gao S, Zhou J, Liu N, Wang L, Gao Q, Wu Y, Zhao Q, Liu P, Wang S, Liu Y, Guo N, Shen Y, Yuan Z (2015) Curcumin induces M2 macrophage polarization by secretion of IL-4 and/or IL-13. J Mol Cell Cardiol 85:131–139. https://doi.org/10.1016/j.yjmcc.2015.04.025
10. Zhao D, Li J, Xue C, Feng K, Liu L, Zeng P, Wang X, Chen Y, Li L, Zhang Z, Duan Y, Han J, Yang X (2020) TL1A inhibits atherosclerosis in apoE-deficient mice by regulating the phenotype of vascular smooth muscle cells. J Biol Chem 295(48):16314–16327. https://doi.org/10.1074/jbc.RA120.015486
11. Getz GS, Reardon CA (2012) Animal models of atherosclerosis. Arterioscler Thromb Vasc Biol 32(5):1104–1115. https://doi.org/10.1161/ATVBAHA.111.237693
12. Emini Veseli B, Perrotta P, De Meyer GRA, Roth L, Van der Donckt C, Martinet W, De Meyer GRY (2017) Animal models of atherosclerosis. Eur J Pharmacol 816:3–13. https://doi.org/10.1016/j.ejphar.2017.05.010
13. Lee YT, Laxton V, Lin HY, Chan YWF, Fitzgerald-Smith S, To TLO, Yan BP, Liu T, Tse G (2017) Animal models of atherosclerosis. Biomed Rep 6(3):259–266. https://doi.org/10.3892/br.2017.843
14. Zhao Y, Qu H, Wang Y, Xiao W, Zhang Y, Shi D (2020) Small rodent models of atherosclerosis. Biomed Pharmacother 129:110426. https://doi.org/10.1016/j.biopha.2020.110426
15. von Scheidt M, Zhao Y, Kurt Z, Pan C, Zeng L, Yang X, Schunkert H, Lusis AJ (2017) Applications and limitations of mouse models for understanding human atherosclerosis. Cell Metab 25(2):248–261. https://doi.org/10.1016/j.cmet.2016.11.001
16. Oppi S, Lüscher TF, Stein S (2019) Mouse models for atherosclerosis research-which is my line? Front Cardiovasc Med 6:46. https://doi.org/10.3389/fcvm.2019.00046
17. Daugherty A, Tall AR, Daemen MJAP, Falk E, Fisher EA, García-Cardeña G, Lusis AJ, Owens AP, Rosenfeld ME, Virmani R, American Heart Association Council on Arteriosclerosis TraVB, Sciences aCoBC (2017) Recommendation on design, execution, and reporting of animal atherosclerosis studies: a scientific statement from the American Heart Association. Arterioscler Thromb Vasc Biol 37(9):e131–e157. https://doi.org/10.1161/ATV.0000000000000062
18. Greenow K, Pearce NJ, Ramji DP (2005) The key role of apolipoprotein E in atherosclerosis. J Mol Med 83(5):329–342. https://doi.org/10.1007/s00109-004-0631-3
19. LeBlond ND, Ghorbani P, O'Dwyer C, Ambursley N, Nunes JRC, Smith TKT, Trzaskalski NA, Mulvihill EE, Viollet B, Foretz M, Fullerton MD (2020) Myeloid deletion and therapeutic activation of AMPK do not alter atherosclerosis in male or female mice. J Lipid

Res 61(12):1697–1706. https://doi.org/10.1194/jlr.RA120001040

20. Goettsch C, Hutcheson JD, Hagita S, Rogers MA, Creager MD, Pham T, Choi J, Mlynarchik AK, Pieper B, Kjolby M, Aikawa M, Aikawa E (2016) A single injection of gain-of-function mutant PCSK9 adeno-associated virus vector induces cardiovascular calcification in mice with no genetic modification. Atherosclerosis 251:109–118. https://doi.org/10.1016/j.atherosclerosis.2016.06.011
21. Preiss D, Mafham M (2017) PCSK9 inhibition: the dawn of a new age in cholesterol lowering? Diabetologia 60(3):381–389. https://doi.org/10.1007/s00125-016-4178-y
22. Wu C, Daugherty A, Lu HS (2019) Updates on approaches for studying atherosclerosis. Arterioscler Thromb Vasc Biol 39(4): e108–e117. https://doi.org/10.1161/ATVBAHA.119.312001
23. Lutgens E, Daemen M, Kockx M, Doevendans P, Hofker M, Havekes L, Wellens H, de Muinck ED (1999) Atherosclerosis in APOE*3-Leiden transgenic mice: from proliferative to atheromatous stage. Circulation 99(2):276–283. https://doi.org/10.1161/01.cir.99.2.276
24. Gijbels MJ, van der Cammen M, van der Laan LJ, Emeis JJ, Havekes LM, Hofker MH, Kraal G (1999) Progression and regression of atherosclerosis in APOE3-Leiden transgenic mice: an immunohistochemical study. Atherosclerosis 143(1):15–25. https://doi.org/10.1016/s0021-9150(98)00263-9
25. De Wilde D, Trachet B, Van der Donckt C, Vandeghinste B, Descamps B, Vanhove C, De Meyer GR, Segers P (2015) Vulnerable plaque detection and quantification with gold particle-enhanced computed tomography in atherosclerotic mouse models. Mol Imaging 14:9. https://doi.org/10.2310/7290.2015.00009
26. Kurdi A, Roth L, Van der Veken B, Van Dam D, De Deyn PP, De Doncker M, Neels H, De Meyer GRY, Martinet W (2019) Everolimus depletes plaque macrophages, abolishes intraplaque neovascularization and improves survival in mice with advanced atherosclerosis. Vasc Pharmacol 113:70–76. https://doi.org/10.1016/j.vph.2018.12.004
27. Roth L, Schrijvers DM, Martinet W, De Meyer GR (2016) Angiotensin II increases coronary fibrosis, cardiac hypertrophy and the incidence of myocardial infarctions in $ApoE^{-/-}$ $Fbn1^{C1039G+/-}$ mice. Acta Cardiol 71(4): 483–488. https://doi.org/10.2143/AC.71.4.3159703
28. Aparicio-Vergara M, Shiri-Sverdlov R, de Haan G, Hofker MH (2010) Bone marrow transplantation in mice as a tool for studying the role of hematopoietic cells in metabolic and cardiovascular diseases. Atherosclerosis 213(2): 335–344. https://doi.org/10.1016/j.atherosclerosis.2010.05.030
29. Sreeramkumar V, Hidalgo A (2015) Bone marrow transplantation in mice to study the role of hematopoietic cells in atherosclerosis. Methods Mol Biol 1339:323–332. https://doi.org/10.1007/978-1-4939-2929-0_22
30. Schiller NK, Kubo N, Boisvert WA, Curtiss LK (2001) Effect of gamma-irradiation and bone marrow transplantation on atherosclerosis in LDL receptor-deficient mice. Arterioscler Thromb Vasc Biol 21(10):1674–1680. https://doi.org/10.1161/hq1001.096724
31. Patel J, Douglas G, Kerr AG, Hale AB, Channon KM (2018) Effect of irradiation and bone marrow transplantation on angiotensin II-induced aortic inflammation in ApoE knockout mice. Atherosclerosis 276:74–82. https://doi.org/10.1016/j.atherosclerosis.2018.07.019
32. Ikeda J, Scipione CA, Hyduk S, Althagafi MG, Atif J, Dick SA, Rajora MA, Jang E, Emoto T, Murakami J, Ikeda N, Ibrahim HM, Polenz CK, Gao X, Tai K, Jongstra-Bilen J, Nakashima R, Epelman S, Robbins C, Zheng G, Lee WL, MacParland SA, Cybulsky MI (2021) Radiation impacts early atherosclerosis by suppressing intimal LDL accumulation. Circ Res 128:530. https://doi.org/10.1161/CIRCRESAHA.119.316539
33. Feig JE (2014) Regression of atherosclerosis: insights from animal and clinical studies. Ann Glob Health 80(1):13–23. https://doi.org/10.1016/j.aogh.2013.12.001
34. Rahman K, Fisher EA (2018) Insights from pre-clinical and clinical studies on the role of innate inflammation in atherosclerosis regression. Front Cardiovasc Med 5:32. https://doi.org/10.3389/fcvm.2018.00032
35. Burke AC, Huff MW (2018) Regression of atherosclerosis: lessons learned from genetically modified mouse models. Curr Opin Lipidol 29(2):87–94. https://doi.org/10.1097/MOL.0000000000000493
36. Williams KJ, Feig JE, Fisher EA (2008) Rapid regression of atherosclerosis: insights from the clinical and experimental literature. Nat Clin Pract Cardiovasc Med 5(2):91–102. https://doi.org/10.1038/ncpcardio1086
37. Chistiakov DA, Myasoedova VA, Revin VV, Orekhov AN, Bobryshev YV (2017) The phenomenon of atherosclerosis reversal and regression: lessons from animal models. Exp Mol

Pathol 102(1):138–145. https://doi.org/10.1016/j.yexmp.2017.01.013

38. Véniant MM, Withycombe S, Young SG (2001) Lipoprotein size and atherosclerosis susceptibility in Apoe(-/-) and Ldlr(-/-) mice. Arterioscler Thromb Vasc Biol 21(10): 1567–1570. https://doi.org/10.1161/hq1001.097780
39. Miller AM, Xu D, Asquith DL, Denby L, Li Y, Sattar N, Baker AH, McInnes IB, Liew FY (2008) IL-33 reduces the development of atherosclerosis. J Exp Med 205(2):339–346. https://doi.org/10.1084/jem.20071868
40. Cardilo-Reis L, Gruber S, Schreier SM, Drechsler M, Papac-Milicevic N, Weber C, Wagner O, Stangl H, Soehnlein O, Binder CJ (2012) Interleukin-13 protects from atherosclerosis and modulates plaque composition by skewing the macrophage phenotype. EMBO Mol Med 4(10):1072–1086. https://doi.org/10.1002/emmm.201201374
41. Lindskog Jonsson A, Caesar R, Akrami R, Reinhardt C, Fåk Hållenius F, Borén J, Bäckhed F (2018) Impact of gut microbiota and diet on the development of atherosclerosis in Apoe-/- mice. Arterioscler Thromb Vasc Biol 38(10):2318–2326. https://doi.org/10.1161/ATVBAHA.118.311233
42. Bijnen M, van de Gaar J, Vroomen M, Gijbels MJ, de Winther M, Schalkwijk CG, Wouters K (2019) Adipose tissue macrophages do not affect atherosclerosis development in mice. Atherosclerosis 281:31–37. https://doi.org/10.1016/j.atherosclerosis.2018.12.010
43. Andrés-Manzano MJ, Andrés V, Dorado B (2015) Oil red O and hematoxylin and eosin staining for quantification of atherosclerosis burden in mouse aorta and aortic root. Methods Mol Biol 1339:85–99. https://doi.org/10.1007/978-1-4939-2929-0_5
44. Lloyd DJ, Helmering J, Kaufman SA, Turk J, Silva M, Vasquez S, Weinstein D, Johnston B, Hale C, Véniant MM (2011) A volumetric method for quantifying atherosclerosis in mice by using microCT: comparison to en face. PLoS One 6(4):e18800. https://doi.org/10.1371/journal.pone.0018800
45. Tangirala RK, Rubin EM, Palinski W (1995) Quantitation of atherosclerosis in murine models: correlation between lesions in the aortic origin and in the entire aorta, and differences in the extent of lesions between sexes in LDL receptor-deficient and apolipoprotein E-deficient mice. J Lipid Res 36(11): 2320–2328
46. Lhoták Š, Gyulay G, Cutz JC, Al-Hashimi A, Trigatti BL, Richards CD, Igdoura SA, Steinberg GR, Bramson J, Ask K, Austin RC (2016) Characterization of proliferating lesion-resident cells during all stages of atherosclerotic growth. J Am Heart Assoc 5(8):e003945. https://doi.org/10.1161/JAHA.116.003945
47. Stoneman V, Braganza D, Figg N, Mercer J, Lang R, Goddard M, Bennett M (2007) Monocyte/macrophage suppression in CD11b diphtheria toxin receptor transgenic mice differentially affects atherogenesis and established plaques. Circ Res 100(6): 884–893. https://doi.org/10.1161/01.RES.0000260802.75766.00
48. Johnson JL, George SJ, Newby AC, Jackson CL (2005) Divergent effects of matrix metalloproteinases 3, 7, 9, and 12 on atherosclerotic plaque stability in mouse brachiocephalic arteries. Proc Natl Acad Sci U S A 102(43): 15575–15580. https://doi.org/10.1073/pnas.0506201102
49. Johnson JL, Fritsche-Danielson R, Behrendt M, Westin-Eriksson A, Wennbo H, Herslof M, Elebring M, George SJ, McPheat WL, Jackson CL (2006) Effect of broad-spectrum matrix metalloproteinase inhibition on atherosclerotic plaque stability. Cardiovasc Res 71(3):586–595. https://doi.org/10.1016/j.cardiores.2006.05.009
50. Johnson JL, Baker AH, Oka K, Chan L, Newby AC, Jackson CL, George SJ (2006) Suppression of atherosclerotic plaque progression and instability by tissue inhibitor of metalloproteinase-2: involvement of macrophage migration and apoptosis. Circulation 113(20):2435–2444. https://doi.org/10.1161/CIRCULATIONAHA.106.613281
51. Johnson JL, Devel L, Czarny B, George SJ, Jackson CL, Rogakos V, Beau F, Yiotakis A, Newby AC, Dive V (2011) A selective matrix metalloproteinase-12 inhibitor retards atherosclerotic plaque development in apolipoprotein E-knockout mice. Arterioscler Thromb Vasc Biol 31(3):528–535. https://doi.org/10.1161/ATVBAHA.110.219147
52. Nazari-Jahantigh M, Wei Y, Noels H, Akhtar S, Zhou Z, Koenen RR, Heyll K, Gremse F, Kiessling F, Grommes J, Weber C, Schober A (2012) MicroRNA-155 promotes atherosclerosis by repressing Bcl6 in macrophages. J Clin Invest 122(11):4190–4202. https://doi.org/10.1172/JCI61716
53. Hung J, Scanlon JP, Mahmoud AD, Rodor J, Ballantyne M, Fontaine MAC, Temmerman L, Kaczynski J, Connor KL, Bhushan R, Biessen EAL, Newby DE, Sluimer JC, Baker AH (2020) Novel plaque enriched long noncoding RNA in atherosclerotic macrophage regulation (PELATON). Arterioscler Thromb Vasc Biol

40(3):697–713. https://doi.org/10.1161/ATVBAHA.119.313430

54. O'Rourke C, Shelton G, Hutcheson JD, Burke MF, Martyn T, Thayer TE, Shakartzi HR, Buswell MD, Tainsh RE, Yu B, Bagchi A, Rhee DK, Wu C, Derwall M, Buys ES, Yu PB, Bloch KD, Aikawa E, Bloch DB, Malhotra R (2016) Calcification of vascular smooth muscle cells and imaging of aortic calcification and inflammation. J Vis Exp (111). https://doi.org/10.3791/54017
55. Li P, Wang Y, Liu X, Liu B, Wang ZY, Xie F, Qiao W, Liang ES, Lu QH, Zhang MX (2020) Loss of PARP-1 attenuates diabetic arteriosclerotic calcification via Stat1/Runx2 axis. Cell Death Dis 11(1):22. https://doi.org/10.1038/s41419-019-2215-8
56. Ceneri N, Zhao L, Young BD, Healy A, Coskun S, Vasavada H, Yarovinsky TO, Ike K, Pardi R, Qin L, Tellides G, Hirschi K, Meadows J, Soufer R, Chun HJ, Sadeghi MM, Bender JR, Morrison AR (2017) Rac2 modulates atherosclerotic calcification by regulating macrophage interleukin-1β production. Arterioscler Thromb Vasc Biol 37(2):328–340. https://doi.org/10.1161/ATVBAHA.116.308507
57. Joshi FR, Lindsay AC, Obaid DR, Falk E, Rudd JH (2012) Non-invasive imaging of atherosclerosis. Eur Heart J Cardiovasc Imaging 13(3):205–218. https://doi.org/10.1093/ehjci/jer319
58. Gan LM, Grönros J, Hägg U, Wikström J, Theodoropoulos C, Friberg P, Fritsche-Danielson R (2007) Non-invasive real-time imaging of atherosclerosis in mice using ultrasound biomicroscopy. Atherosclerosis 190(2):313–320. https://doi.org/10.1016/j.atherosclerosis.2006.03.035
59. Tavakoli S, Downs K, Short JD, Nguyen HN, Lai Y, Jerabek PA, Goins B, Toczek J, Sadeghi MM, Asmis R (2017) Characterization of macrophage polarization states using combined measurement of 2-deoxyglucose and glutamine accumulation: implications for imaging of atherosclerosis. Arterioscler Thromb Vasc Biol 37(10):1840–1848. https://doi.org/10.1161/ATVBAHA.117.308848
60. Glinzer A, Ma X, Prakash J, Kimm MA, Lohöfer F, Kosanke K, Pelisek J, Thon MP, Vorlova S, Heinze KG, Eckstein HH, Gee MW, Ntziachristos V, Zernecke A, Wildgruber M (2017) Targeting elastase for molecular imaging of early atherosclerotic lesions. Arterioscler Thromb Vasc Biol 37(3):525–533. https://doi.org/10.1161/ATVBAHA.116.308726
61. Escolà-Gil JC, Lee-Rueckert M, Santos D, Cedó L, Blanco-Vaca F, Julve J (2015) Quantification of in vitro macrophage cholesterol efflux and in vivo macrophage-specific reverse cholesterol transport. Methods Mol Biol 1339:211–233. https://doi.org/10.1007/978-1-4939-2929-0_15
62. Huang L, Fan B, Ma A, Shaul PW, Zhu H (2015) Inhibition of ABCA1 protein degradation promotes HDL cholesterol efflux capacity and RCT and reduces atherosclerosis in mice. J Lipid Res 56(5):986–997. https://doi.org/10.1194/jlr.M054742
63. Srivastava N, Cefalu AB, Averna M, Srivastava RAK (2018) Lack of correlation of plasma HDL with fecal cholesterol and plasma cholesterol efflux capacity suggests importance of HDL functionality in attenuation of atherosclerosis. Front Physiol 9:1222. https://doi.org/10.3389/fphys.2018.01222
64. Galkina E, Kadl A, Sanders J, Varughese D, Sarembock IJ, Ley K (2006) Lymphocyte recruitment into the aortic wall before and during development of atherosclerosis is partially L-selectin dependent. J Exp Med 203(5):1273–1282. https://doi.org/10.1084/jem.20052205
65. Galkina E, Harry BL, Ludwig A, Liehn EA, Sanders JM, Bruce A, Weber C, Ley K (2007) CXCR6 promotes atherosclerosis by supporting T-cell homing, interferon-gamma production, and macrophage accumulation in the aortic wall. Circulation 116(16):1801–1811. https://doi.org/10.1161/CIRCULATIONAHA.106.678474
66. Gjurich BN, Taghavie-Moghadam PL, Galkina EV (2015) Flow cytometric analysis of immune cells within murine aorta. Methods Mol Biol 1339:161–175. https://doi.org/10.1007/978-1-4939-2929-0_11
67. Trogan E, Feig JE, Dogan S, Rothblat GH, Angeli V, Tacke F, Randolph GJ, Fisher EA (2006) Gene expression changes in foam cells and the role of chemokine receptor CCR7 during atherosclerosis regression in ApoE-deficient mice. Proc Natl Acad Sci U S A 103(10):3781–3786. https://doi.org/10.1073/pnas.0511043103
68. Feig JE, Fisher EA (2013) Laser capture microdissection for analysis of macrophage gene expression from atherosclerotic lesions. Methods Mol Biol 1027:123–135. https://doi.org/10.1007/978-1-60327-369-5_5
69. Trogan E, Choudhury RP, Dansky HM, Rong JX, Breslow JL, Fisher EA (2002) Laser capture microdissection analysis of gene expression in macrophages from atherosclerotic lesions of apolipoprotein E-deficient mice. Proc Natl

Acad Sci U S A 99(4):2234–2239. https://doi.org/10.1073/pnas.042683999

70. Megens RT, Soehnlein O (2015) Intravital microscopy for atherosclerosis research. Methods Mol Biol 1339:41–60. https://doi.org/10.1007/978-1-4939-2929-0_3
71. Eriksson EE (2011) Intravital microscopy on atherosclerosis in apolipoprotein e-deficient mice establishes microvessels as major entry pathways for leukocytes to advanced lesions. Circulation 124(19):2129–2138. https://doi.org/10.1161/CIRCULATIONAHA.111.030627
72. Döring Y, Noels H, Mandl M, Kramp B, Neideck C, Lievens D, Drechsler M, Megens RT, Tilstam PV, Langer M, Hartwig H, Theelen W, Marth JD, Sperandio M, Soehnlein O, Weber C (2014) Deficiency of the sialyltransferase St3Gal4 reduces Ccl5-mediated myeloid cell recruitment and arrest: short communication. Circ Res 114(6):976–981. https://doi.org/10.1161/CIRCRESAHA.114.302426
73. Li W, Luehmann HP, Hsiao HM, Tanaka S, Higashikubo R, Gauthier JM, Sultan D, Lavine KJ, Brody SL, Gelman AE, Gropler RJ, Liu Y, Kreisel D (2018) Visualization of monocytic cells in regressing atherosclerotic plaques by intravital 2-photon and positron emission tomography-based imaging-Brief Report. Arterioscler Thromb Vasc Biol 38(5):1030–1036. https://doi.org/10.1161/ATVBAHA.117.310517
74. Williams JW, Martel C, Potteaux S, Esaulova E, Ingersoll MA, Elvington A, Saunders BT, Huang LH, Habenicht AJ, Zinselmeyer BH, Randolph GJ (2018) Limited macrophage positional dynamics in progressing or regressing murine atherosclerotic plaques-Brief Report. Arterioscler Thromb Vasc Biol 38(8):1702–1710. https://doi.org/10.1161/ATVBAHA.118.311319
75. Winkels H, Ehinger E, Vassallo M, Buscher K, Dinh HQ, Kobiyama K, Hamers AAJ, Cochain C, Vafadarnejad E, Saliba AE, Zernecke A, Pramod AB, Ghosh AK, Anto Michel N, Hoppe N, Hilgendorf I, Zirlik A, Hedrick CC, Ley K, Wolf D (2018) Atlas of the immune cell repertoire in mouse atherosclerosis defined by single-cell RNA-sequencing and mass cytometry. Circ Res 122(12):1675–1688. https://doi.org/10.1161/CIRCRESAHA.117.312513
76. Winkels H, Wolf D (2020) Heterogeneity of T cells in atherosclerosis defined by single-cell RNA-sequencing and cytometry by time of flight. Arterioscler Thromb Vasc Biol 41:549. https://doi.org/10.1161/ATVBAHA.120.312137
77. Cole JE, Park I, Ahern DJ, Kassiteridi C, Danso Abeam D, Goddard ME, Green P, Maffia P, Monaco C (2018) Immune cell census in murine atherosclerosis: cytometry by time of flight illuminates vascular myeloid cell diversity. Cardiovasc Res 114(10):1360–1371. https://doi.org/10.1093/cvr/cvy109
78. Iqbal F, Lupieri A, Aikawa M, Aikawa E (2021) Harnessing single-cell RNA sequencing to better understand how diseased cells behave the way they do in cardiovascular disease. Arterioscler Thromb Vasc Biol 41:585. https://doi.org/10.1161/ATVBAHA.120.314776
79. Depuydt MAC, Prange KHM, Slenders L, Örd T, Elbersen D, Boltjes A, de Jager SCA, Asselbergs FW, de Borst GJ, Aavik E, Lönnberg T, Lutgens E, Glass CK, den Ruijter HM, Kaikkonen MU, Bot I, Slütter B, van der Laan SW, Yla-Herttuala S, Mokry M, Kuiper J, de Winther MPJ, Pasterkamp G (2020) Microanatomy of the human atherosclerotic plaque by single-cell transcriptomics. Circ Res 127(11):1437–1455. https://doi.org/10.1161/CIRCRESAHA.120.316770
80. Willemsen L, de Winther MP (2020) Macrophage subsets in atherosclerosis as defined by single-cell technologies. J Pathol 250(5):705–714. https://doi.org/10.1002/path.5392
81. Hajkarim MC, Won KJ (2019) Single cell RNA-sequencing for the study of atherosclerosis. J Lipid Atheroscler 8(2):152–161. https://doi.org/10.12997/jla.2019.8.2.152
82. Williams JW, Winkels H, Durant CP, Zaitsev K, Ghosheh Y, Ley K (2020) Single cell RNA sequencing in atherosclerosis research. Circ Res 126(9):1112–1126. https://doi.org/10.1161/CIRCRESAHA.119.315940
83. Fernandez DM, Rahman AH, Fernandez NF, Chudnovskiy A, Amir ED, Amadori L, Khan NS, Wong CK, Shamailova R, Hill CA, Wang Z, Remark R, Li JR, Pina C, Faries C, Awad AJ, Moss N, Bjorkegren JLM, Kim-Schulze S, Gnjatic S, Ma'ayan A, Mocco J, Faries P, Merad M, Giannarelli C (2019) Single-cell immune landscape of human atherosclerotic plaques. Nat Med 25(10):1576–1588. https://doi.org/10.1038/s41591-019-0590-4
84. Gu W, Ni Z, Tan YQ, Deng J, Zhang SJ, Lv ZC, Wang XJ, Chen T, Zhang Z, Hu Y, Jing ZC, Xu Q (2019) Adventitial cell atlas of wt (wild type) and ApoE (apolipoprotein E)-deficient mice defined by single-cell RNA sequencing. Arterioscler Thromb Vasc Biol

39(6):1055–1071. https://doi.org/10.1161/ATVBAHA.119.312399

85. Lin JD, Nishi H, Poles J, Niu X, Mccauley C, Rahman K, Brown EJ, Yeung ST, Vozhilla N, Weinstock A, Ramsey SA, Fisher EA, Loke P (2019) Single-cell analysis of fate-mapped macrophages reveals heterogeneity, including stem-like properties, during atherosclerosis progression and regression. JCI Insight 4(4): e124574. https://doi.org/10.1172/jci.insight.124574
86. Cochain C, Vafadarnejad E, Arampatzi P, Pelisek J, Winkels H, Ley K, Wolf D, Saliba AE, Zernecke A (2018) Single-cell RNA-seq reveals the transcriptional landscape and heterogeneity of aortic macrophages in murine atherosclerosis. Circ Res 122(12):1661–1674. https://doi.org/10.1161/CIRCRESAHA.117.312509

Chapter 5

Exploring the Associations Between Clonal Hematopoiesis of Indeterminate Potential, Myeloid Malignancy, and Atherosclerosis

Juan Bautista Menendez-Gonzalez and Neil P. Rodrigues

Abstract

Outgrowth of a mutated hematopoietic stem/progenitor clone and its descendants, also known as clonal hematopoiesis, has long been considered as either a potential forerunner to hematologic malignancy or as a clinically silent phase in leukemia that antedates symptomatic disease. That definition of clonal hematopoiesis has now been expanded to encompass patients who harbor specific genetic/epigenetic mutations that lead to clonal hematopoiesis of indeterminate potential (CHIP) and, with it, a relatively heightened risk for both myeloid malignancy and atherosclerosis during aging. In this review, we provide contemporary insights into the cellular and molecular basis for CHIP and explore the relationship of CHIP to myeloid malignancy and atherosclerosis. We also discuss emerging strategies to explore CHIP biology and clinical targeting of CHIP related malignancy and cardiovascular disease.

Key words Clonal hematopoiesis, CHIP, Stem cells, Myeloid, Leukemia, Atherosclerosis

1 Introduction

Rare, self-renewing tissue-specific stem cells (hereafter stem cells) support the maintenance of individual tissues for a lifetime. Stem cells are the master cell within a tissue that divide into precursors, termed progenitors, which on further division, or differentiation, supply cell types with specialized functions. With somatic mutations occurring routinely throughout life, it has become abundantly clear that stem cell function is inextricably linked to the maintenance of genomic integrity, which is scrutinized during cell cycle progression and by immunosurveillance mechanisms. If these safeguards go awry, as they can during aging, a mutation originating in a single stem cell may hypothetically be able to propagate through their progeny and compromise tissue integrity. This so-called clonal stem cell and/or their progeny could confer a competitive "fitness" advantage and outpace growth of their nonmutated counterparts.

Dipak P. Ramji (ed.), *Atherosclerosis: Methods and Protocols*, Methods in Molecular Biology, vol. 2419,
https://doi.org/10.1007/978-1-0716-1924-7_5,
© The Author(s), under exclusive license to Springer Science+Business Media, LLC, part of Springer Nature 2022

In the hematopoietic system, clonal expansion of mutated blood cell populations, or clonal hematopoiesis, has long been recognized as a feature of several clinical conditions. For example, monoclonal gammopathy of undetermined significance (MGUS) in a small (~1%) fraction of patients leads to multiple myeloma, Waldenström macroglobulinemia, light chain amyloidosis and lymphoma [1]. In contrast, a larger fraction of patients (~75%) diagnosed with Clonal Cytopenia of Undetermined Significance (CCUS) develop myelodysplastic syndrome/myeloproliferative neoplasms [2]. Chronic myeloid leukemia, acute myeloid leukemia (AML), and childhood acute lymphoblastic leukemia are each known to have a clinically silent phase, in association with clonal expansion that precedes symptomatic disease [3–5].

Historically, clonal hematopoiesis has therefore been broadly labeled as a prelude to malignancy characterized by clonal expansion. However, recent studies from three laboratories who conducted exome sequencing of blood DNA from patients without hematologic malignancy has painted a more complex portrait of clonal hematopoiesis and its relationship with blood cancer as well as other nonmalignant disease [6–8]. Importantly, analysis of blood DNA in these studies has permitted an assessment of clonal expansion descending directly from stem cells. Age-related loss-of-function mutations at a variant allele frequency (VAF) of at least 2% was identified in epigenetic regulators (e.g., Tet Methylcytosine dioxygenase [TET2] and DNA Methyltransferase 3 alpha [DNMT3A]), splicing factors (e.g., U2 Small Nuclear RNA Auxiliary Factor 1 [U2AF1]), Serine and Arginine Rich Splicing Factor 2 [SRSF2], and Splicing Factor 3B Subunit 1 [SF3B1]), tumor suppressors (e.g., Protein Phosphatase Mg^{2+}/Mn^{2+} Dependent 1D [PPM1D] and Tumor Protein 53 [TP53]), signal transducers (e.g., Janus Kinase 2 [JAK2]), and chromatin regulators (e.g., ASXL Transcriptional Regulator 1 [ASXL1]). Reflecting the hitherto uncertainty of what these mutations mean for onset and prognosis of hematologic malignancy and to distinguish it from clinically recognized clonal conditions such as MGUS and CCUS, the term clonal hematopoiesis of indeterminate potential (CHIP) has now been coined for specific mutation driven clonal hematopoiesis that occurs in the absence of overt hematologic malignancy and abnormal blood counts.

As alluded to above, CHIP-related mutations in HSPCs could drive the expression of mutations in all downstream blood and immune cells, as supported by the finding that DNMT3A preleukemic mutations in HSPCs are found in both their myeloid and lymphoid progeny [4]. For mutated blood cells, as they are liberated into the circulation to perform their many physiologic functions that include inflammatory responses and immunosurveillance, this may profoundly alter their biology leading to detrimental clinical consequences. Supporting this notion, CHIP has been

linked to increased all-cause mortality, including heightened risk of atherosclerosis and chronic obstructive pulmonary disease, which are both conditions linked to perturbed inflammatory processes [5, 9, 10].

2 CHIP in Hematologic Malignancy

While CHIP itself is not a disease nor is it associated with clinically significant alterations in blood parameters, the most commonly seen mutations in CHIP are also known drivers of myeloid malignancies. In fact, in large population-based cohorts that underwent exome sequencing, the presence of CHIP was associated with an approximately tenfold increased relative risk of developing de novo MDS/AML over several years of follow-up [11, 12]. Importantly, the risk of malignancy in carriers of CHIP was directly proportional to the size of the mutant clone, with those who went on to develop malignancy having a substantially larger clone size than those who did not.

The most prevalent mutations observed in CHIP are DNMT3A, TET2 and ASXL1 [8]. Knock-out (KO) mouse models show that the lack of these genes alters hematopoietic stem cell (HSC) self-renewal, impairs differentiation, and, in some instances, facilitates progression to malignancy. However, cell-intrinsic properties alone do not explain CHIP progression to MDS/AML in humans. Because most people will harbor HSCs with somatic mutations in CHIP-related genes by the age of 50, but only in a fraction of individuals will these HSCs expand sufficiently by age 70 years to be classed as CHIP (VAF $>$ 2%), it is likely that additional extrinsic factors drive mutant clones to expand to various degrees in different individuals [13]. Therefore, the current impetus in CHIP research is focused on understanding the environmental cues that foment the expansion of mutant clones.

DNMT3A, accounting for approximately 50% of all CHIP mutations, is responsible for de novo methylation of cytosines, an epigenetic mark known to influence gene expression [14, 15]. Most DNMT3A mutations are heterozygous and lead to loss of protein function via different mechanisms [16, 17]. DNMT3A KO HSCs have increased self-renewal and impaired differentiation [18] and are able to continuously propagate in transplantation assays [19]. Recently, a pivotal study found that IFN-γ signaling induced during chronic mycobacterial infection drives the expansion of DNMT3A mutant HSCs [20]. Transcriptome analysis revealed an infection-induced reduction of differentiation and apoptosis of DNTMT3A mutant clones driven, at least in part, by Fos/Jun (Fos/Jun protooncogene, AP1 transcription factor subunit) downregulation. Expansion of mutant DNMT3A clones was also seen after treatment with interleukin (IL)1β but not with

lipopolysaccharide (LPS), tumor necrosis factor (TNF)α or pIpC, indicating that selective pressure of DNTM3A mutant clones only arises under a specific inflammatory milieu [20].

TET2 is responsible for catalyzing the oxidation of 5-methylcytosine to 5-hydroxymethylcytosine leading to demethylation [21]. Mouse models harboring loss-of-function *Tet2* alleles show an HSC competitive advantage in vivo as well as a myeloproliferative phenotype [22, 23]. Several studies demonstrated that *Tet2* mutant HSPCs as well as mature lineage-derived cells are particularly responsive to changes in levels of proinflammatory cytokines. While chronic exposure to proinflammatory cytokines such as TNFα and IL-6 are detrimental to normal HSC functionality, *Tet2* mutant HSCs are refractory to these signals, imparting them with a competitive advantage in an inflammatory setting [24, 25]. In fact, *Tet2* mutant macrophages exhibit an increased nucleotide-binding domain-like receptor protein 3 (NLRP3) inflammasome-mediated IL-1β secretion [26] as well as in IL-6 secretion, which in turn favor *Tet2*-deficient HSPCs over its normal counterparts, constituting a feed-forward loop. Another source of inflammation that may be germane to CHIP comes from harmful products released in the microbiota, which can reach circulation including the bone marrow (BM) [27]. To this end, a recent report found that dysfunction of the small intestinal barrier leads to bacterial-mediated increase in IL-6 production contributing to the expansion of *Tet2*-mutant HSPCs. This phenotype could be reversed by antibiotic treatment, and fails to develop in pathogen-free mice [27].

ASXL1 is involved in various histone modifications to regulate gene expression, and function as a scaffold for epigenetic regulators [28, 29]. *Asxl1* KO mice closely recapitulate the pathology of human MDS and the expression of mutant ASXL1 in mice also induces the development of MDS-like disease [30–32]. In humans, most mutations in ASXL1 are frameshift or nonsense mutations in the N-terminal region of the last exon, generating a C-terminally truncated form of ASXL1 that may result in dominant-negative or gain-of function mutations [33], thus careful consideration must be taken when evaluating loss-of-function ASXL1 mouse models to study CHIP. ASXL1 mutations are strongly correlated with smokers [34] and therefore employing conditions that mimic smoking [35] may help to understand ASXL1 pathogenesis in the context of CHIP.

As alluded to above, TET2 and DNMT3A mutation driven CHIP leads to a HSPC growth advantage that increases the susceptibility of these mutations to myeloid leukemia. Similarly, JAK2 mutations activate proliferative pathways related to constitutive activation of JAK/signal transducer and activator of transcription (STAT) signaling [36] and TP53 mutations allow for the avoidance of corrective DNA damage response mechanisms, resulting in cell

cycle progression [37]. Taken together with the increased proliferative status of aging HSCs [38], these data support the postulate that an aging CHIP HSPC clone may register enhanced proliferation, cell survival or other prooncogenic attributes, driven by inflammatory signals, that facilitate acquisition of further mutations with potential for malignant transformation. However, the behavior of some CHIP related mutations, like ASXL1, where mouse models have indicated decreased HSPC function [39], challenge the simple concept of clonal expansion driven by CHIP related mutations, and rather suggest that they can also act as enablers of clonal selection. Underlying this, it is possible that these types of mutations have a variety of complex opposing pro- and antioncogenic functions dependent on cell context, which govern growth, survival, and overall probability for expansion of individual dysplastic and neoplastic clones within the heterogeneous HSPC compartment [31].

Therapy-related myeloid neoplasms (t-MNs) include MDS/AML arising in patients treated with chemotherapy for a previous cancer and has a 5-year prognosis below 10% [40], highlighting that use of traditional chemotherapeutic regimens has a carcinogenic impact on the blood system. Before the expansion of the genomic era, t-MNs was suspected to solely come from mutations that occur during chemotherapy treatment. However, exome sequencing analysis showed that cases of t-MN have a higher frequency of CHIP prior to treatment compared to age-matched healthy individuals [41]. More recently, an analysis of 21,146 patients with different types of cancer from the Memorial Sloan Kettering-Integrated Mutation Profiling of Actionable Cancer Targets (MSK-IMPACT) found that CHIP was present in 30% of patients at a median VAF of 5% [42]. In particular, mutations in DNA damage response (DDR) genes such as TP53, PPM1D and Checkpoint Kinase 2 (CHEK2) were strongly associated with prior chemotherapy. It is therefore plausible that cancer treatment favors and selects for preexisting CHIP lesions in a cell autonomous manner. Independently, such selection may be further facilitated by changes to the niche that are induced following chemotherapy.

Deeper sequencing of TP53-mutated samples demonstrated subclonal chromosome 5 and 7 copy number variations many years prior to the diagnosis of t-MN, suggesting that TP53 mutant clones are the first mutational hit in t-MN [43]. These clones are generally resistant to chemotherapy and, in turn, have a selective advantage after chemotherapy [44]. In particular, TP53 mutant clones are linked to platinum, radiation, and taxane exposure [42]. The selective pressure in these specific environments is thought to be mediated by a TP53-related immune escape mechanism, whereby TP53-mutant progeny is rich in regulatory T cells and myeloid-derived suppressor cells [45].

PPM1D mutations accounts for 20% of t-MN cases, and in striking contrast to TP53, it is more prevalent after treatment with DNA-damaging agents such as cisplatin [42]. PPM1D mutants are mostly frameshift and nonsense truncating mutations within exon 6 [46] that generates a gain-of-function mutant protein that prevents activation of p53-dependent pathways [46]. Mouse studies corroborated that PPM1D-mutant HSPCs have a growth advantage after cisplatin, etoposide and doxorubicin treatment, but not vincristine or total body irradiation treatment [47, 48]. PPM1D mutant conferred apoptosis resistance to HSPCs. This competitive advantage was abolished after administration of a PPM1D small molecule inhibitor (GSK2830371), opening the possibility for targeted therapies in cancer patients that receive cisplatin treatment [48].

HSC transplantation is the only curative option for many hematologic malignancies, some solid tumors and nonmalignant diseases. Donor-derived AML, together with relapse, cardiovascular events, and graft-versus-host disease (GvHD), are the main causes of morbidity in patients undergoing HSC transplantation. It would seem that CHIP clones would thrive and outgrow their normal counterparts in this scenario, although so far the association between CHIP in donors and survival outcome is still unclear [49, 50] and longer follow-up is needed. A study of 500 allogeneic hematopoietic cell transplant related donors aged 55 years or above showed that CHIP was present in 16% of donors and was linked with more chronic graft-versus-host disease and higher nonrelapse mortality, though at the same time lower relapse was observed [51]. Bearing in mind that CHIP progeny are more proinflammatory, it is likely that this could be beneficial for enhancing the graft-versus-leukemia (GVL) setting while diminishing graft-versus-host disease. Developing new therapies to modulate CHIP mutant clones to enhance GVL will offer new avenues to treat relapse in hematopoietic malignancies.

3 CHIP and Atherosclerosis

Given the level of interaction of the blood and immune system with other tissues within the body, it is unsurprising that outgrowth of CHIP mutant clones in mature blood cells, which can constitute about a fifth of the peripheral blood, can cause clinical manifestations. Correlative studies have confirmed the association of CHIP to atherosclerosis, an inflammation led process that causes lipid plaque deposition in medium and large arteries and restricts blood flow; ischemic stroke, coronary heart disease and myocardial infarction are consequences of atherosclerosis [9]. Notably, the risk of ischemic stroke and myocardial infarction in CHIP patients with DNM3TA, TET2 and ASXL1 mutations is more elevated in

younger adults than is normally observed irrespective of standard traditional cardiovascular disease risk factors such as hypertension and LDL cholesterol level [9]. Furthermore, DNM3TA and TET2 mutations have also been correlated with increased hospitalization and mortality following myocardial infarction [52].

While these elegant exome sequencing studies have highlighted the correlation between CHIP mutations and atherosclerosis in patients, the causative roles of CHIP mutations on atherosclerosis have relied on experimental mouse models that have largely focused on mimicking TET2 mutations [9, 53]. Bone marrow from mice engineered to be deficient in *Tet2* and engrafted into low-density lipoprotein receptor (*Ldlr*) KO recipient mice, which have the propensity to develop atherosclerosis when fed a high fat diet, developed larger atherosclerotic lesions compared to those recipients receiving normal bone marrow. Further analysis of *Tet2*-deficient macrophages—the central innate immune cell driving foam cell production during atherosclerotic plaque deposition—unveiled a proinflammatory chemokine and cytokine environment that includes chemokines C-X-X motif chemokine ligand (Cxcl)1, Cxcl2, Cxcl3 and cytokines IL-1β and IL-6. The potential therapeutic importance of the TET2–IL-1β axis has been further highlighted in other experimental *Tet2*-deficient mouse models of aortic constriction, chronic ischemia, or angiotensin II administration-induced heart failure that causes increased IL-1β level, which can be obviated by an NLRP3 inflammasome inhibitor of IL-1β secretion [26, 54].

$JAK2^{V617}$ mutations leading to myeloproliferative neoplasms have also been associated with CHIP [55, 56]. As well as reaffirming the central role of the IL-1β pathway in macrophages of CHIP driven atherosclerosis, $JAK2^{V617}$ mutations in macrophages alter glycolytic metabolism, which leads to DNA replication stress and activation of the AIM2 (absent in melanoma 2) inflammasome. Further work will be needed to decipher the metabolic dependencies of $JAK2^{V617}$ mutations and, indeed other CHIP mutations, in driving atherosclerosis.

While knowledge about the causality of CHIP mutations in atherosclerosis has been gleaned through myeloid-specific deletion (e.g. LysM-Cre) or monocyte/macrophage specific analysis [26], the impact on other lymphoid effectors is less well established. As clonal mutations occurring in HSCs will be transmitted to both myeloid and lymphoid progeny, it will be important to address this question comprehensively. To this end, one study has conducted single cell RNA-sequencing to capture the inflammatory landscape in DNM3TA mutation driven clonal hematopoiesis in heart failure patients [57]. DNMT3A mutational status in these patients was associated with a molecular signature consistent with increased monocyte-T cell activation including cluster of differentiation (CD)300LB, CD83, sialic acid-binding Ig-like lectin

12 (SIGLEC12), the CD2 ligand and cell adhesion molecule CD58, and expression of the T-cell alpha receptor constant chain and alterations in T helper cell subsets, $CD8^+$ effector, $CD4^+$ memory, and regulatory T-cells, thus highlighting that cross-talk between the innate and adaptive immune system is pivotal to sustaining inflammation in atherosclerosis [58].

In atherosclerotic *Ldlr* and Apolipoprotein E (*ApoE*) KO mouse models, extensive hematopoietic stem cell proliferation and leukocytosis has been observed [59, 60], which suggests that proinflammatory signals emanating from atherosclerotic lesions could stimulate quiescent HSCs into proliferation and alter mature blood lineage fates derived from HSCs, inducing leukocytosis. In support of this notion, it is established that inflammatory signals, including IFNs, TNF, and toll like receptors (TLRs), drive proliferation of HSC and their direct descendants, lineage specific multipotent progenitors (MPPs), with expansion of megakaryocyte/erythroid (Meg/E)-biased MPP2 and myeloid-biased MPP3 and concomitant suppression of lymphoid biased MPP4, which translates to an overall myeloid bias. In the context of CHIP, the extent of myeloid bias could be mutation dependent. It was recently illustrated that HSC proliferation doubled in atherosclerotic prone mice and patients with atherosclerosis, yet increased HSC proliferation was not caused by hyperlipidemia per se [61]. By analyzing VAF in progressively aged healthy blood donors and incorporating these data into mathematical models of HSC fate decisions, it was suggested that expansion of CHIP related mutations is a direct consequence of HSC proliferation. This model was confirmed experimentally in two settings known to increase HSC proliferation: following transplantation into mice engineered to be deficient in *Ldlr* with recipients maintained on a high-fat diet, or, alternatively, following transplantation in a model of sleep fragmentation; in both settings Tet2-deficient donor hematopoietic cells, including both HSPCs and leukocytes, expanded markedly.

Current data therefore suggest an intimately linked, reciprocal and cyclical model of atherosclerosis, through which proinflammatory mediated mechanisms force increased hematopoietic stem cell proliferation leading to clonal expansion and leukocytosis, which further exacerbates atherosclerosis. Yet such studies raise important further questions about the association of CHIP to atherosclerosis. What are the other biological and clinical manifestations of HSC proliferation and clonal expansion driven by atherosclerosis? Does atherosclerosis bias MPP subpopulations toward increasing the myeloid pathway and what are the biological traits of leukocytes derived by clonal hematopoiesis? For example, leukocytes in clonal hematopoiesis have shorter telomeres, presumably as a consequence of HSC proliferation [61], and it will be of interest to investigate the impact of shorter telomeres on myeloid leukemic transformation and disease progression, which has been evidenced

in other hematologic malignancies [61, 62]. It is tempting to speculate that enhanced HSC proliferation mediated by atherosclerosis increases the vulnerability of expanded CHIP mutant clones to acquire secondary mutations that drive myeloid malignancy, shaping the course of disease progression. Therapeutic targeting efforts for CHIP and atherosclerosis must be refined in order to take into account reciprocal causality of atherosclerosis and clonal hematopoiesis, with a focus on disentangling the contrasts and commonalities between CHIP driven inflammatory mechanisms and atherosclerosis driven inflammatory mechanisms.

4 Future Directions

4.1 Experimental Models of CHIP

Several models to study the biology of CHIP have been described so far. The first approach uses CRISPR-Cas9 (clustered regularly interspaced short palindromic repeats-CRISPR associated protein 9) to disrupt genes frequently mutated in CHIP in human HSPCs followed by transplantation into immunodeficient (NSG) mice [63]. Another approach is based in the generation of engineered mouse models that express specific mutations found in CHIP [64]. However, NSG mice lack a fully functional BM microenvironment and immune system, which are key players in mediating the stressors that dictate cell competition of mutated and normal HSCs clones. Engineered mouse models overcome this limitation but so far the studies published have employed conditional KO mice that express mutations in all HSC clones, hence restraining the interactive effect that normal HSCs and their progeny may have with mutated clones. Transplantation assays using chimeras with reduced frequency of mutated HSCs solves this issue, though this setting may not reflect steady-state conditions to study CHIP progression due to myeloablative conditioning of recipient mice. Alternative approaches using nonirradiated mice transplanted with a high dose BM cells may provide a more homeostatic environment [65]. Aside from mouse models, human induced pluripotent stem cells (iPSCs) and genome editing technology offers an attractive model to study clonal evolution of AML. This system allows the stepwise introduction of CHIP mutations followed by additional secondary mutations to assess its progression to MDS and AML, that can be assessed in vitro via hematopoietic differentiation assays and in vivo transplantation assays [66]. Using this approach, a recent study identified an intrinsic dysregulation of inflammatory signaling in ASXL1 mutant iPSCs that could be exploited therapeutically during incipient stages of disease [67].

One of the most important factors to consider when studying CHIP is the genetic model employed. In the last decade, accumulating evidence in hematological and solid malignancies has underscored that specific gene mutations often have a distinct phenotype

than complete loss-of-gene function. In CHIP, different heterozygous DNMT3A mutants have different protein stabilities and overall DNMT3A protein levels, highlighted by the dominant-negative role of R882H, leaves roughly 20% net DNMT3A protein levels [17, 68]. Mutation-specific effects have also been described in ASXL1, P53, and PPM1D [69–71] and it is possible that this phenomenon is more common than currently acknowledged. Thus, while KO mouse models have been useful to understand HSC biology, future studies should be directed at CHIP mouse and iPSC models using specific gene mutations.

To study progression of CHIP clones, models need to incorporate cell-extrinsic factors, such as the bone marrow microenvironment, the microbiome, or diet, that has shown to play a role in clonal expansion. Despite the fact that additional mutations unequivocally contribute to transformation potential, the order by which mutations are acquired is another factor to consider when creating a CHIP model. As a case in point, a study showed that the longer the latency period between DNMT3A and NPM1 mutation, the shorter is the onset to AML [64]. Newer DNA-sequencing technologies have recently provided a better picture of clonal history and mutational order in AML patients [72], which can then be used to generate models that more faithfully recapitulate CHIP progression to AML.

4.2 How Should Information on CHIP in the Clinic Be Used to Predict and Treat Hematological Malignancy and Cardiovascular Disease?

Many people with CHIP will experience no clinical consequences, and the absolute risk for progression to MDS/AML is estimated at between 0.5% and 1% per year [11, 12]. As there is currently no established intervention to halt or eradicate mutant clones, there is an ethical conundrum as to whether ostensibly healthy people should be tested or informed of their CHIP status, especially bearing in mind the potential psychological impact. Until there are more accurate predictive models to narrow down and pinpoint the relative risk for developing cancer or cardiovascular complications, it is generally not beneficial to notify patients of their CHIP status. Nevertheless, individuals that are found to have CHIP with additional features associated with higher risk of hematologic malignancy, such as high red blood cell distribution width (RDW) parameter, high VAF, or more than one CHIP mutation, especially in higher risk genes such as isocitrate dehydrogenase (IDH)1/2, TP53, or spliceosome genes [11, 12], may benefit from a more in-depth hematological evaluation and routine follow-up. Furthermore, notification of CHIP status in patients with high risk of cardiovascular disease could be advantageous, especially in individuals harboring TET2 and JAK2 mutations [53, 55]. The highest-priority patients to notify of CHIP would be those with detectable TP53 or PPM1D mutations following treatment of a solid tumor, given the substantial risk of progression to therapy-related MDS/AML [42]. Importantly, this is crucial for follow-up after

treatment and to refine and tailor specific treatments that will address the primary cancer and reducing the chances of expanding preexisting CHIP mutant clones (e.g., the avoidance of platinum-based therapies in the case of finding PPM1D mutant clones).

4.3 Proof-of-Concept Therapeutic Targeting of CHIP

Prevention of evolution of CHIP to overt myeloid malignancy and cardiovascular disease is critically important. We still lack the tools to address how and when to intervene, a problem further confounded by emerging evidence of reciprocal causality between atherosclerosis and clonal hematopoiesis. Some evidence from the literature indicates that the blockade of downstream inflammatory pathways may be feasible. In particular, targeting of the IL1β/NLRP3 pathway in TET2 mutant monocytes/macrophages could prove beneficial for patients with risk to develop cardiovascular disease. TET2 mutant myeloid progeny have an increase in NLRP3 inflammasome that mediates the production of IL1β [53]. Preclinical studies using a selective NLRP3 inhibitor protected against the development of heart failure and improve all cardiac parameters in *Tet2*-deficient mice [26, 53]. Furthermore, a randomized placebo-controlled trial CANTOS (Canakinumab Anti-inflammatory Thrombosis Outcomes Study) of the anti-IL1β antibody canakinumab in patients with a history of myocardial infarction, canakinumab prevented recurring cardiovascular events and stroke [73]. Analysis of pretreated samples from nearly half the patients enrolled in the trial found that this benefit was mostly restricted to subjects with TET2-mutant CHIP [73]. In addition, ASXL1 mutant clones may be targeted with interleukin-1 receptor-associated kinase (IRAK)1/4 or ubiquitin conjugating enzyme E2 N (UBE2N) inhibitors [67] while modulation of the interferon (IFN)-γ signaling pathway could lead to a reduction of DNMT3A mutant clones [20].

Alternatively, small molecule inhibitors that have the ability to suppress mutant clones directly, could potentially lessen the risk of both myeloid malignancy and cardiovascular disease. With respect to direct targeting of CHIP clones, inhibitors for splicing factors or IDH1/2 proteins used in MDS/AML patients are attractive, especially since these mutations predict a higher relative risk of developing MDS/AML [11, 12]. Because the residual activity of TET2 is still required for survival of normal and mutant HSCs, a recent study found that transient selective targeting of TET2 restricted the clonal advantage of TET2 mutants in mouse and human cells, whilst their effect on normal HSC was reversible [74]. The opposite intervention is to restore TET2 activity with high concentrations of vitamin C, which is able to restore its function and constrain the self-renewal of leukemic stem cells in preclinical models [75, 76]. Oral vitamin C does not achieve the required concentration to restore TET2 function significantly [75]. However, clinical trials with modulation of dosing of intravenous vitamin C

represents a potentially promising approach for successful therapy for cancer and cardiovascular disease.

4.4 Implications of CHIP for Other Tissues

Several studies have found that CHIP is associated with 30–40% increased mortality risk [8], and this is mostly due to the development of hematological cancer and cardiovascular disease. CHIP is also associated with many other age-related diseases in epidemiological studies; however, it is still unclear whether this association is causative or correlative. CHIP could simply be another biomarker of ageing, with no direct involvement in other tissues, excepting the already proven role in cardiovascular system. This caveat notwithstanding, blood is present in every tissue in the body. Notably, those blood cell effectors in tissues, such as resident monocyte/macrophages and T cells, are known key players of steady-state tissue homeostasis and in disease states including cancer or autoimmune disease. A clear indicator for this hypothesis is that the negative effect of CHIP on atherosclerosis is mediated by mutant monocytes/macrophages. Therefore, any mutant HSC will give rise to mutant progeny that will patrol other tissues and, at the very least, will deregulate inflammatory signaling pathways. It is this inflammatory phenotype that raises the possibility that CHIP partakes in the initiation or outcome of many age-related diseases where inflammation predominates, such as Alzheimer's and neurodegenerative diseases, diabetes, autoimmune disease, and other solid tumors. In support of this hypothesis is an initial causative role for *Tet2* mutant progeny in insulin resistance and type II diabetes [77]. Transplant of *Tet2* KO BM cells in mice leads to increased blood glucose over time due to the presence of inflammatory macrophages in epidermal white adipose tissue that secrete IL1β. Similar to its effects on coronary *Tet2* macrophages, inhibitors of the NLRP3 inflammasome abolished exacerbated levels of IL1β and ameliorated blood glucose levels in mice [77].

Finally, the CHIP paradigm can be applied to other solid tissues, where somatic mutations have also been identified in healthy individuals [78, 79]. Interestingly, genotoxic stress-based competition has been described in TP53 mutant stem cells in esophageal and skin cancer [80, 81]. Understanding the causes and consequences of CHIP may therefore provide a framework to comprehend aging processes across other tissues.

Acknowledgments

The Rodrigues laboratory is supported by the Leukemia Cancer Society, Leukaemia Research Appeal for Wales, and the Saudi Arabian Cultural Bureau.

References

1. van Nieuwenhuijzen N, Spaan I, Raymakers R, Peperzak V (2018) From MGUS to multiple myeloma, a paradigm for clonal evolution of premalignant cells. Cancer Res 78: 2449–2456. https://doi.org/10.1158/0008-5472.CAN-17-3115
2. Steensma DP (2019) The clinical challenge of idiopathic cytopenias of undetermined significance (ICUS) and clonal cytopenias of undetermined significance (CCUS). Curr Hematol Malig Rep 14:536–542. https://doi.org/10.1007/s11899-019-00547-3
3. Hong D, Gupta R, Ancliff P et al (2008) Initiating and cancer-propagating cells in TEL--AML1-associated childhood leukemia. Science 319:336–339. https://doi.org/10.1126/science.1150648
4. Shlush LI, Zandi S, Mitchell A et al (2014) Identification of pre-leukaemic haematopoietic stem cells in acute leukaemia. Nature 506: 328–333. https://doi.org/10.1038/nature13038
5. Holyoake TL, Vetrie D (2017) The chronic myeloid leukemia stem cell: stemming the tide of persistence. Blood 129:1595–1606. https://doi.org/10.1182/blood-2016-09-696013
6. Xie M, Lu C, Wang J et al (2014) Age-related mutations associated with clonal hematopoietic expansion and malignancies. Nat Med 20: 1472–1478. https://doi.org/10.1038/nm.3733
7. Genovese G, Kähler AK, Handsaker RE et al (2014) Clonal hematopoiesis and blood-cancer risk inferred from blood DNA sequence. N Engl J Med 371:2477–2487. https://doi.org/10.1056/nejmoa1409405
8. Jaiswal S, Fontanillas P, Flannick J et al (2014) Age-related clonal hematopoiesis associated with adverse outcomes. N Engl J Med 371: 2488–2498. https://doi.org/10.1056/nejmoa1408617
9. Jaiswal S, Natarajan P, Silver AJ et al (2017) Clonal hematopoiesis and risk of atherosclerotic cardiovascular disease. N Engl J Med 377:111–121. https://doi.org/10.1056/nejmoa1701719
10. Zink F, Stacey SN, Norddahl GL et al (2017) Clonal hematopoiesis, with and without candidate driver mutations, is common in the elderly. Blood 130:742–752. https://doi.org/10.1182/blood-2017-02-769869
11. Abelson S, Collord G, Ng SWK et al (2018) Prediction of acute myeloid leukaemia risk in healthy individuals. Nature 559:400–404. https://doi.org/10.1038/s41586-018-0317-6
12. Desai P, Mencia-Trinchant N, Savenkov O et al (2018) Somatic mutations precede acute myeloid leukemia years before diagnosis. Nat Med 24:1015–1023. https://doi.org/10.1038/s41591-018-0081-z
13. King KY, Huang Y, Nakada D, Goodell MA (2020) Environmental influences on clonal hematopoiesis. Exp Hematol 83:66–73. https://doi.org/10.1016/j.exphem.2019.12.005
14. Chen T, Ueda Y, Dodge JE et al (2003) Establishment and maintenance of genomic methylation patterns in mouse embryonic stem cells by Dnmt3a and Dnmt3b. Mol Cell Biol 23: 5594–5605. https://doi.org/10.1128/mcb.23.16.5594-5605.2003
15. Okano M, Bell DW, Haber DA, Li E (1999) DNA methyltransferases Dnmt3a and Dnmt3b are essential for *de novo* methylation and mammalian development. Cell 99:247–257. https://doi.org/10.1016/S0092-8674(00)81656-6
16. Sandoval JE, Huang YH, Muise A et al (2019) Mutations in the DNMT3A DNA methyltransferase in acute myeloid leukemia patients cause both loss and gain of function and differential regulation by protein partners. J Biol Chem 294:4898–4910. https://doi.org/10.1074/jbc.RA118.006795
17. Khrabrova DA, Loiko AG, Tolkacheva AA et al (2020) Functional analysis of DNMT3A DNA methyltransferase mutations reported in patients with acute myeloid leukemia. Biomolecules 10:1–16. https://doi.org/10.3390/biom10010008
18. Challen GA, Sun D, Jeong M et al (2012) Dnmt3a is essential for hematopoietic stem cell differentiation. Nat Genet 44:23–31. https://doi.org/10.1038/ng.1009
19. Jeong M, Park HJ, Celik H et al (2018) Loss of Dnmt3a immortalizes hematopoietic stem cells *in vivo*. Cell Rep 23:1–10. https://doi.org/10.1016/j.celrep.2018.03.025
20. Hormaechea-Agulla D, Matatall KA, Le DT et al (2021) Chronic infection drives Dnmt3a-loss-of-function clonal hematopoiesis via IFNγ signaling. Cell Stem Cell 28: 1428–1442.e6. https://doi.org/10.1016/j.stem.2021.03.002
21. Tahiliani M, Koh KP, Shen Y et al (2009) Conversion of 5-methylcytosine to 5-hydroxymethylcytosine in mammalian DNA

by MLL partner TET1. Science 324:930–935. https://doi.org/10.1126/science.1170116

22. Li Z, Cai X, Cai CL et al (2011) Deletion of Tet2 in mice leads to dysregulated hematopoietic stem cells and subsequent development of myeloid malignancies. Blood 118:4509–4518. https://doi.org/10.1182/blood-2010-12-325241
23. Abdel-Wahab O, Mullally A, Hedvat C et al (2009) Genetic characterization of TET1, TET2, and TET3 alterations in myeloid malignancies. Blood 114:144–147. https://doi.org/10.1182/blood-2009-03-210039
24. Abegunde SO, Buckstein R, Wells RA, Rauh MJ (2018) An inflammatory environment containing TNFα favors Tet2-mutant clonal hematopoiesis. Exp Hematol 59:60–65. https://doi.org/10.1016/j.exphem.2017.11.002
25. Cai Z, Kotzin JJ, Ramdas B et al (2018) Inhibition of inflammatory signaling in Tet2 mutant preleukemic cells mitigates stress-induced abnormalities and clonal hematopoiesis. Cell Stem Cell 23:833–849.e5. https://doi.org/10.1016/j.stem.2018.10.013
26. Sano S, Oshima K, Wang Y et al (2018) Tet2-mediated clonal hematopoiesis accelerates heart failure through a mechanism involving the IL-1β/NLRP3 inflammasome. J Am Coll Cardiol 71:875–886. https://doi.org/10.1016/j.jacc.2017.12.037
27. Meisel M, Hinterleitner R, Pacis A et al (2018) Microbial signals drive pre-leukaemic myeloproliferation in a Tet2-deficient host. Nature 557:580–584. https://doi.org/10.1038/s41586-018-0125-z
28. Abdel-Wahab O, Adli M, LaFave LM et al (2012) ASXL1 mutations promote myeloid transformation through loss of PRC2-mediated gene repression. Cancer Cell 22:180–193. https://doi.org/10.1016/j.ccr.2012.06.032
29. Fisher CL, Pineault N, Brookes C et al (2010) Loss-of-function additional sex combs like 1 mutations disrupt hematopoiesis but do not cause severe myelodysplasia or leukemia. Blood 115:38–46. https://doi.org/10.1182/blood-2009-07-230698
30. Abdel-Wahab O, Gao J, Adli M et al (2013) Deletion of Asxl1 results in myelodysplasia and severe developmental defects *in vivo*. J Exp Med 210:2641–2659. https://doi.org/10.1084/jem.20131141
31. Wang J, Li Z, He Y et al (2014) Loss of Asxl1 leads to myelodysplastic syndrome-like disease in mice. Blood 123:541–553. https://doi.org/10.1182/blood-2013-05-500272
32. Yang H, Kurtenbach S, Guo Y et al (2018) Gain of function of ASXL1 truncating protein in the pathogenesis of myeloid malignancies. Blood 131:328–341. https://doi.org/10.1182/blood-2017-06-789669
33. Schnittger S, Eder C, Jeromin S et al (2013) ASXL1 exon 12 mutations are frequent in AML with intermediate risk karyotype and are independently associated with an adverse outcome. Leukemia 27:82–91. https://doi.org/10.1038/leu.2012.262
34. Dawoud AAZ, Tapper WJ, Cross NCP (2020) Clonal myelopoiesis in the UK Biobank cohort: ASXL1 mutations are strongly associated with smoking. Leukemia 34:2660–2672. https://doi.org/10.1038/s41375-020-0896-8
35. Morales-Mantilla DE, Huang X, Erice P et al (2020) Cigarette smoke exposure in mice using a whole-body inhalation system. J Vis Exp (164):e61793. https://doi.org/10.3791/61793
36. Vainchenker W, Constantinescu SN (2013) JAK/STAT signaling in hematological malignancies. Oncogene 32:2601–2613. https://doi.org/10.1038/onc.2012.347
37. Dutta S, Pregartner G, Rücker FG et al (2020) Functional classification of tp53 mutations in acute myeloid leukemia. Cancers 12:1–16. https://doi.org/10.3390/cancers12030637
38. Kirschner K, Chandra T, Kiselev V et al (2017) Proliferation drives aging-related functional decline in a subpopulation of the hematopoietic stem cell compartment. Cell Rep 19:1503–1511. https://doi.org/10.1016/j.celrep.2017.04.074
39. Marshall A, Kasturiarachchi J, Datta P et al (2020) Mir142 loss unlocks IDH2R140-dependent leukemogenesis through antagonistic regulation of HOX genes. Sci Rep 10:1–13. https://doi.org/10.1038/s41598-020-76218-8
40. Kuendgen A, Nomdedeu M, Tuechler H et al (2021) Therapy-related myelodysplastic syndromes deserve specific diagnostic sub-classification and risk-stratification—an approach to classification of patients with t-MDS. Leukemia 35:835–849. https://doi.org/10.1038/s41375-020-0917-7
41. Takahashi K, Wang F, Kantarjian H et al (2017) Preleukaemic clonal haemopoiesis and risk of therapy-related myeloid neoplasms: a case-control study. Lancet Oncol 18:100–111. https://doi.org/10.1016/S1470-2045(16)30626-X
42. Bolton KL, Ptashkin RN, Gao T et al (2020) Cancer therapy shapes the fitness landscape of

clonal hematopoiesis. Nat Genet 52: 1219–1226. https://doi.org/10.1038/s41588-020-00710-0

43. Bernard E, Nannya Y, Hasserjian RP et al (2020) Implications of TP53 allelic state for genome stability, clinical presentation and outcomes in myelodysplastic syndromes. Nat Med 26:1549–1556. https://doi.org/10.1038/s41591-020-1008-z
44. Chen S, Gao R, Yao C et al (2018) Genotoxic stresses promote clonal expansion of hematopoietic stem cells expressing mutant p53. Leukemia 32:850–854. https://doi.org/10.1038/leu.2017.325
45. Sallman DA, McLemore AF, Aldrich AL et al (2020) TP53 mutations in myelodysplastic syndromes and secondary AML confer an immunosuppressive phenotype. Blood 136: 2812–2823. https://doi.org/10.1182/blood.2020006158
46. Kleiblova P, Shaltiel IA, Benada J et al (2013) Gain-of-function mutations of PPM1D/Wip1 impair the p53-dependent G1 checkpoint. J Cell Biol 201:511–521. https://doi.org/10.1083/jcb.201210031
47. Kahn JD, Miller PG, Silver AJ et al (2018) PPM1D-truncating mutations confer resistance to chemotherapy and sensitivity to PPM1D inhibition in hematopoietic cells. Blood 132:1095–1105. https://doi.org/10.1182/blood-2018-05-850339
48. Hsu JI, Dayaram T, Tovy A et al (2018) PPM1D mutations drive clonal hematopoiesis in response to cytotoxic chemotherapy. Cell Stem Cell 23:700–713.e6. https://doi.org/10.1016/j.stem.2018.10.004
49. Gibson CJ, Lindsley RC (2020) Stem cell donors should not be screened for clonal hematopoiesis. Blood Adv 4:789–792. https://doi.org/10.1182/bloodadvances.2019000395
50. DeZern AE, Gondek LP (2020) Stem cell donors should be screened for CHIP. Blood Adv 4:784–788. https://doi.org/10.1182/bloodadvances.2019000394
51. Frick M, Chan W, Arends CM et al (2019) Role of donor clonal hematopoiesis in allogeneic hematopoietic stem-cell transplantation. J Clin Oncol 37:375–385. https://doi.org/10.1200/JCO.2018.79.2184
52. Dorsheimer L, Assmus B, Rasper T et al (2019) Association of mutations contributing to clonal hematopoiesis with prognosis in chronic ischemic heart failure. JAMA Cardiol 4:25–33. https://doi.org/10.1001/jamacardio.2018.3965
53. Fuster JJ, MacLauchlan S, Zuriaga MA et al (2017) Clonal hematopoiesis associated with TET2 deficiency accelerates atherosclerosis development in mice. Science 355:842–847. https://doi.org/10.1126/science.aag1381
54. Sano S, Oshima K, Wang Y et al (2018) CRISPR-mediated gene editing to assess the roles of TET2 and DNMT3A in clonal hematopoiesis and cardiovascular disease. Circ Res 123:335–341. https://doi.org/10.1161/CIRCRESAHA.118.313225
55. Sano S, Wang Y, Yura Y et al (2019) JAK2V617F-mediated clonal hematopoiesis accelerates pathological remodeling in murine heart failure. JACC Basic Transl Sci 4: 684–697. https://doi.org/10.1016/j.jacbts.2019.05.013
56. Fidler TP, Xue C, Yalcinkaya M et al (2021) The AIM2 inflammasome exacerbates atherosclerosis in clonal haematopoiesis. Nature 592: 296–301. https://doi.org/10.1038/s41586-021-03341-5
57. Abplanalp WT, Cremer S, John D et al (2021) Clonal hematopoiesis-driver DNMT3A mutations alter immune cells in heart failure. Circ Res 128:216–228. https://doi.org/10.1161/CIRCRESAHA.120.317104
58. Medzhitov R, Janeway CA (1997) Innate immunity: impact on the adaptive immune response. Curr Opin Immunol 9:4–9. https://doi.org/10.1016/S0952-7915(97)80152-5
59. Murphy AJ, Akhtari M, Tolani S et al (2011) ApoE regulates hematopoietic stem cell proliferation, monocytosis, and monocyte accumulation in atherosclerotic lesions in mice. J Clin Invest 121:4138–4149. https://doi.org/10.1172/JCI57559
60. Feng Y, Schouteden S, Geenens R et al (2012) Hematopoietic stem/progenitor cell proliferation and differentiation is differentially regulated by high-density and low-density lipoproteins in mice. PLoS One 7:1–12. https://doi.org/10.1371/journal.pone.0047286
61. Heyde A, Rohde D, McAlpine CS et al (2021) Increased stem cell proliferation in atherosclerosis accelerates clonal hematopoiesis. Cell 184:1348–1361.e22. https://doi.org/10.1016/j.cell.2021.01.049
62. Ventura Ferreira MS, Crysandt M, Ziegler P et al (2017) Evidence for a pre-existing telomere deficit in non-clonal hematopoietic stem cells in patients with acute myeloid leukemia. Ann Hematol 96:1457–1461. https://doi.org/10.1007/s00277-017-3049-z

63. Tothova Z, Krill-Burger JM, Popova KD et al (2017) Multiplex CRISPR/Cas9-based genome editing in human hematopoietic stem cells models clonal hematopoiesis and myeloid neoplasia. Cell Stem Cell 21:547–555.e8. https://doi.org/10.1016/j.stem.2017.07.015
64. Loberg MA, Bell RK, Goodwin LO et al (2019) Sequentially inducible mouse models reveal that Npm1 mutation causes malignant transformation of Dnmt3a-mutant clonal hematopoiesis. Leukemia 33:1635–1649. https://doi.org/10.1038/s41375-018-0368-6
65. Wang Y, Sano S, Yura Y et al (2020) Tet2-mediated clonal hematopoiesis in nonconditioned mice accelerates age-associated cardiac dysfunction. JCI Insight 5:1–16. https://doi.org/10.1172/jci.insight.135204
66. Spyrou N, Papapetrou EP (2021) Studying leukemia stem cell properties and vulnerabilities with human iPSCs. Stem Cell Res 50:1–9. https://doi.org/10.1016/j.scr.2020.102117
67. Wang T, Pine AR, Kotini AG et al (2021) Sequential CRISPR gene editing in human iPSCs charts the clonal evolution of myeloid leukemia and identifies early disease targets. Cell Stem Cell 28:1–16. https://doi.org/10.1016/j.stem.2021.01.011
68. Russler-Germain DA, Spencer DH, Young MA et al (2014) The R882H DNMT3A mutation associated with AML dominantly inhibits wild-type DNMT3A by blocking its ability to form active tetramers. Cancer Cell 25:442–454. https://doi.org/10.1016/j.ccr.2014.02.010
69. Boettcher S, Miller PG, Sharma R et al (2019) A dominant-negative effect drives selection of TP53 missense mutations in myeloid malignancies. Science 365:599–604. https://doi.org/10.1126/science.aax3649
70. Dudgeon C, Shreeram S, Tanoue K et al (2013) Genetic variants and mutations of PPM1D control the response to DNA damage. Cell Cycle 12:2656–2664. https://doi.org/10.4161/cc.25694
71. Inoue D, Matsumoto M, Nagase R et al (2016) Truncation mutants of ASXL1 observed in myeloid malignancies are expressed at detectable protein levels. Exp Hematol 44:172–176.e1. https://doi.org/10.1016/j.exphem.2015.11.011
72. Miles LA, Bowman RL, Merlinsky TR et al (2020) Single-cell mutation analysis of clonal evolution in myeloid malignancies. Nature 587:477–482. https://doi.org/10.1038/s41586-020-2864-x
73. Ridker PM, Everett BM, Thuren T et al (2017) Antiinflammatory therapy with canakinumab for atherosclerotic disease. N Engl J Med 377:1119–1131. https://doi.org/10.1056/nejmoa1707914
74. Guan Y, Tiwari AD, Phillips JG et al (2021) A therapeutic strategy for preferential targeting of TET2 -mutant and TET dioxygenase–deficient cells in myeloid neoplasms. Blood Cancer Discov 2:146–161. https://doi.org/10.1158/2643-3230.bcd-20-0173
75. Cimmino L, Dolgalev I, Wang Y et al (2017) Restoration of TET2 function blocks aberrant self-renewal and leukemia progression. Cell 170:1079–1095.e20. https://doi.org/10.1016/j.cell.2017.07.032
76. Agathocleous M, Meacham CE, Burgess RJ et al (2017) Ascorbate regulates haematopoietic stem cell function and leukaemogenesis. Nature 549:476–481. https://doi.org/10.1038/nature23876
77. Fuster JJ, Zuriaga MA, Zorita V et al (2020) TET2-loss-of-function-driven clonal hematopoiesis exacerbates experimental insulin resistance in aging and obesity. Cell Rep 33:1–9.e5. https://doi.org/10.1016/j.celrep.2020.108326
78. García-Nieto PE, Morrison AJ, Fraser HB (2019) The somatic mutation landscape of the human body. Genome Biol 20(298):1–20. https://doi.org/10.1186/s13059-019-1919-5
79. Franco I, Helgadottir HT, Moggio A et al (2019) Whole genome DNA sequencing provides an atlas of somatic mutagenesis in healthy human cells and identifies a tumor-prone cell type. Genome Biol 20(285):1–22. https://doi.org/10.1186/s13059-019-1892-z
80. Murai K, Skrupskelyte G, Piedrafita G et al (2018) Epidermal tissue adapts to restrain progenitors carrying clonal p53 mutations. Cell Stem Cell 23:687–699.e8. https://doi.org/10.1016/j.stem.2018.08.017
81. Fernandez-Antoran D, Piedrafita G, Murai K et al (2019) Outcompeting p53-mutant cells in the normal esophagus by redox manipulation. Cell Stem Cell 25:329–341.e6. https://doi.org/10.1016/j.stem.2019.06.011

Chapter 6

Peptides as Therapeutic Agents for Atherosclerosis

C. Roger White, Mayakonda Palgunachari, Paul Wolkowicz, and G. M. Anantharamaiah

Abstract

More than three decades ago, as a test for the amphipathic helix theory, an 18 amino acid residue peptide and its analogs were designed with no sequence homology to any of the exchangeable apolipoproteins. Based on the apolipoprotein A-I (the major protein component of high density lipoproteins, HDL) mimicking properties, they were termed as ApoA-I mimicking peptides. Several laboratories around the world started studying such de novo-designed peptides for their antiatherogenic properties. The present chapter describes the efforts in bringing these peptides as therapeutic agents for atherosclerosis and several lipid-mediated disorders.

Key words Atherosclerosis, LDL, HDL apoA-I, apoE, Apolipoprotein mimetic peptides

1 Introduction

Cardiovascular disease remains the major cause of death in the United States despite changes in lifestyle and the use of new pharmacological approaches. Atherosclerosis is an inflammatory disease, which is characterized by abnormal accumulation of cholesterol and oxidized lipids in the arterial wall. The formation of fatty streaks is an early event in the development of atherosclerosis, which is due to the uptake of oxidized LDL by macrophage scavenger receptors and subsequent accumulation of lipid-laden macrophages under the endothelium. A variety of pharmacotherapies has been developed in order to treat lipid disorders in humans. Unfortunately, tolerance issues and undesirable side effects frequently occur. The phenomenon of statin resistance is relatively common and may arise in response to gene polymorphisms and/or upregulation of proprotein convertase subtilisin/kexin type 9 (PCSK9). In these subjects, LDL receptor degradation is associated with increased

In Memory of Dr. Geeta Datta, who left us in January 2020.

Dipak P. Ramji (ed.), *Atherosclerosis: Methods and Protocols*, Methods in Molecular Biology, vol. 2419,
https://doi.org/10.1007/978-1-0716-1924-7_6,
© The Author(s), under exclusive license to Springer Science+Business Media, LLC, part of Springer Nature 2022

coronary disease risk. Subjects with homozygous familial hypercholesterolemia also have reduced LDL receptor function and show a limited response to statin or PCSK9 inhibitor therapy. Treatment options for these individuals are therefore limited. This review considers the therapeutic potential of synthetic peptides based on the structures of apolipoproteins (apo) A-I and E.

2 HDL and Atherosclerosis

Among circulating plasma lipoproteins, higher levels of apoB-containing lipoproteins (very low density and low-density lipoproteins, VLDL and LDL) are considered proatherogenic due to the presence of higher amounts of cholesterol and cholesterol esters. These lipoproteins are modified due to oxidation and taken up by macrophages. High density lipoproteins (HDL) act as protective agents by inhibiting such oxidation and facilitate the clearance of VLDL and LDL via their receptor-mediated uptake by the liver.

The clinical treatments for atherosclerosis have largely focused on the control of the traditional Framingham Risk factors especially LDL cholesterol levels and hypertension. Serum HDL levels are another major independent risk factor for atherosclerosis. Treatments that target HDL have not been successfully developed or incorporated into the armamentarium of antiatherosclerotic therapies. Despite strong evidence for a direct atheroprotective role of HDL, recent findings indicate that the relationship between serum HDL and atherosclerosis is complex [1]. Unraveling how HDL protects against atherosclerosis and designing new therapeutics based on this knowledge may ameliorate the ongoing medical challenge of heart disease in more affluent cultures [2].

A direct protective effect of HDL against the development of atherosclerosis has been demonstrated in animals infused with HDL or in transgenic mice overexpressing human apoA-I [3, 4]. Similarly, infusion of $apoAI_{Milano}$–phospholipid complexes into human subjects resulted in a reduction in their coronary atheroma volume as measured by intravascular ultrasound (IVUS) [5]. Erickson et al. [6] reported that intravenous treatment of humans with pro-apoA-I liposomal complexes resulted in increased fecal sterol content without an increase in cholesterol synthesis, suggesting a significant increase in reverse cholesterol transport (RCT), the process by which cellular cholesterol is transferred from extrahepatic sites to the liver for clearance. Other human infusion studies have also shown a significant increase in pre-β HDL levels, evidence of enhanced RCT [7], and a significant reduction in the inflammatory LDL [8]. While lower HDL levels need not be associated with increased cardiovascular risk [9], serum LDL levels consistently relate to coronary artery disease and myocardial infraction. These data indicate that HDL may modify the

atherogenicity of LDL. Thus, there remains a strong demand for new therapeutics capable of reducing serum LDL levels and improving the antiatherogenic properties of HDL. The failure of torcetrapib, an inhibitor of cholesterol ester transfer protein (CETP), to reduce endpoint death from myocardial infarction calls the importance of HDL levels in reducing CVD risk into question [10]. This lack of support for serum HDL as a cardioprotective variable is further supported by the early observation in the original Framingham study that 44% of coronary events in men and 43% of such events in women occurred in individuals with normal levels of HDL [11]. However, HDL can be either anti-inflammatory [12] or proinflammatory under the conditions of an acute phase response [13]. Thus, one potential resolution of these two distinct sets of clinical data is that certain HDL constituents or HDL subtypes may predict cardiovascular disease better than simple measurement of gross levels of serum HDL.

3 Apolipoproteins and the Amphipathic Helix Theory

Lipoproteins are in general spherically shaped, water-soluble complexes of proteins and lipids that circulate in the blood. Phospholipids, free cholesterol, and proteins are present at the surface of lipoproteins, while neutral lipids such as cholesterol ester and triglycerides form the core of lipoproteins. The protein present on the surface of lipoproteins is referred to as apolipoprotein. Distinct apolipoproteins interact with water-insoluble lipids to create the complexes that form the external shell of all lipoproteins, including VLDL, LDL, and HDL.

The atherogenic lipoproteins LDL and VLDL possess relatively large amounts of lipid. Apolipoprotein B (apo B-100) is the major protein component of LDL and VLDL. Substantial experimental evidence supports the idea that apoB more accurately measures the atherogenic risk of VLDL and LDL [14]. In contrast, HDL is the smallest of the lipoproteins and possesses approximately a 1:1 ratio by weight of protein and lipid. Thus, HDL is the densest lipoprotein. The major HDL protein is apoA-I. Since epidemiological studies support the idea that HDL is atheroprotective, how apoA-I might regulate this clinically important outcome has been extensively studied [15, 16].

For a long time, the mechanism by which apo A-I associates with phospholipid was not known. The first clue for a structural motif responsible for lipid association came from model building [17]. Specifically, the primary amino acid sequences of apoA-I were found to possess distinct tandem repeating 22mer amino acid sequences separated by a Pro residue [18]. Folding of each of these 22mers into an α-helix produced a helical structure in which charged residues resided largely on one face of the helix while

hydrophobic amino acids populated the other face. This secondary structural pattern is known as the amphipathic helical motif. It is present in all of the exchangeable HDL apolipoproteins. This peptide amphipathic structure compliments phospholipids, which also possess charged or nonpolar head groups and hydrophobic acyl chains. Thus, these amphipathic helical peptide structures can interact well with amphipathic phospholipids to form protein–lipid complexes which are water-soluble. Through this structural mirroring of polar and nonpolar regions, insoluble lipids can be made soluble in water.

4 Apolipoprotein Mimetic Peptides That Support the Amphipathic Helix Theory

We set out to test the following theory: if the amphipathic helix motif is responsible for the formation of lipoprotein protein–lipid complexes, shorter primary amino acid sequences, particularly those capable of forming amphipathic helices, should interact with phospholipids to form lipoprotein-like peptide–lipid complexes. First, we designed a peptide consisting of the primary amino acid sequence Asp-Trp-Leu-Lys-Ala-Phe-Tyr-Asp-Lys-Val-Ala-Glu-Lys-Leu-Lys-Glu-Ala-Phe. The 18 amino acid peptide, designated 18A, has no sequence homology to any of the naturally occurring amphipathic helical domains found in apolipoproteins [19]. When folded as an α-helix, this peptide is amphipathic with all of its positively charged Lys residues at the polar–nonpolar interface and its negatively charged Asp and Glu residues at the center of the polar face. The opposite face of this putative helix contains all hydrophobic Val, Leu, Tyr, and Phe residues while a Trp residue resides near the polar–nonpolar interface. Analysis of apolipoprotein amphipathic helices showed a preponderance of such [polar–nonpolar–interfacial] structural motifs in which (1) positively charged residues reside at the polar–nonpolar interface, (2) negatively charged residues reside at the center of the polar face, and (3) a hydrophobic face is found opposite to the polar face. This type of tripartite structure was termed a Class A amphipathic helix.

Next, we designed a peptide sequence denoted as Reverse-18A, which has a primary amino acid sequence of Lys-Trp-Leu-Asp-Ala-Phe-Tyr-Lys-Asp-Val-Ala-Lys-Glu-Leu-Glu-Lys-Ala-Phe. In contrast to peptide 18A, the negatively charged Asp and Glu residues of Reverse-18A lie at the polar–nonpolar interface while again in contrast to peptide 18A, the positively charged residues of Reverse-18A are found at the center of the polar face and negatively charged residues at the polar–nonpolar interface. The hydrophobic face is identical in both peptides Reverse-18A and 18A. That is, the positive and negative charge distribution alone is altered in Reverse-18A compared to peptide 18A.

Since human apoA-I spontaneously forms protein–lipid complexes with 1,2-dimyristoyl-*sn*-glycero-3-phosphocholine (DMPC), we mixed peptide 18A, Reverse-18A and ApoA-I solutions in phosphate buffered saline solution at a weight ratio of 1:1 with multilamellar DMPC vesicles (MLVs) to compare the ability of our model peptides and human apo-A1 to clarify these turbid DMPC suspensions. While both apoA-I and 18A spontaneously cleared the turbid DMPC suspension, indicating fragmentation of DMPC MLVs, the Reverse-18A peptide did not clear DMPC MLV suspensions. Upon examination of the 18A/Reverse-18A/Apo-A1:DMPC complexes present in these solutions by negatively stained electron microscopy (EM), both apoA-I and peptide 18A formed similarly sized and shaped discoidal complexes. These results showed two things. First, the segregation of charges in the polar–nonpolar faces is important in peptide–lipid complex formation. Second, positively charged Lys and Arg residues found at the polar–nonpolar interface of the amphipathic helix contributes to enhanced hydrophobicity of the amphipathic helix. This is likely due to their increased side-chain length compared to the shorter Asp and Glu side chains. Computer analyses of apolipoprotein amphipathic helical domains showed the presence of Class A motifs in their domains that associate with lipids. Thus, peptide 18A was termed an apoA-I mimetic peptide.

5 Platform for the Design of Amphipathic Helical Peptides

The original 18A peptide was unblocked at the N- and C-termini which imparts charge/polarity to both ends of this Apo-A1 mimetic. To test whether end terminal charge affects peptide–lipid interaction, we blocked the N- and C-termini of 18A with acetate and amide groups to produce the peptide Ac-18A-NH_2. It had more helicity than 18A and clarified suspensions of both 2-oleoyl-1-palmitoyl-*sn*-glycero-3-phosphocholine (POPC) and egg PC. In contrast, apoA-I does not spontaneously clarify POPC and egg PC suspensions but requires the detergent cholate to form lipid complexes with apoA-I [20]. Thus, the synthetic peptides were more effective than any of the apolipoproteins in their ability to interact with phospholipids. Subsequently, Ac-18A-NH_2 was systematically modified to incorporate an increasing number of aromatic residues at the nonpolar face (Table 1). We measured the exclusion pressure at the lipid monolayer to assess the affinity of these various Apo-A1 mimetic peptides with lipid membranes. The initial surface pressure of egg PC monolayers was adjusted to values in the range of 5–40 dynes/cm, and the peptide solutions were injected beneath the lipid monolayer. Increase in the surface pressure due to the peptide penetrating the egg PC monolayer surface was recorded, and the exclusion pressure values ($\Delta\pi$) are

Table 1
Arrangement of aromatic residues at the center of the nonpolar face but not lipid affinity or number of aromatic residues determines antiatherogenic potency

Sequence	Abbreviated name	Exclusion Pressure (dynes/cm)	Effect on lesion (Ref)
Human apoA-I		34	
Baseline peptide			
DWLKAFYDKVAEKLKEAF	18A	30	Not tested
Pro-linked dimer of 18A			
18A-Pro-18A	37pA	41	Not tested
Protected 18A			
Ac-18A-NH_2	2F	38	No inhibition (99)
2F with 3F residues on NP face			
Ac-DKWKAVYDKFAEAFKEFL-NH_2 (aromatics at the center of nonpolar face)	3F-1	38	Reduces lesion (98)
Ac-[F^3]18A-NH_2	3F^3 (L^3 in 2F >F)	38	No inhibition (98)
2F with 4F residues on NP face			
Ac-[$F^{3,14}$]18A-NH_2	4F ($L^{3,14}$ in 2F >F)	40	Reduces lesion (25)
2F with 5F residues on NP face			
Ac-[$F^{11,14,17}$]18A-NH_2	5F ($L^{3,14}$ A^{17} in 2F >F)	45	Reduces lesion (24)
2F with 6F residues on NP face			
Ac-[$F^{10,11,14,17}$]18A-NH_2	6F ($A^{11,17}$ V^{10} L^{14} in 2F >F)	46	Not tested[a]
2F with 7F residues on NP face			
Ac-[$F^{3,10,11,14,17}$]18A-NH_2	7F ($L^{3,14}$ V^{10} $A^{11,17}$ in 2F >F)	45	Not tested[a]

Design of apoA-I mimetic peptides with increasing lipid affinity as measured by increase in the surface pressure. The initial surface pressure of egg PC monolayer was adjusted to values in the range of 5–40 dyne/cm and the peptides were injected beneath the monolayer. Increase in surface pressure ($\Delta\pi$) due to penetration of the peptide into the egg PC monolayer was recorded. The exclusion surface pressure values represent the pressure at which the peptide is unable to penetrate into the egg PC monolayer. > denotes substitution. NP face = nonpolar face

[a]Peptides 6F and 7F not tested due to solubility problems

the pressures at which the peptide is unable to penetrate into the egg PC monolayer. As can be seen in Table 1, other than 18A which shows a lower surface pressure than apoA-I, all of the other peptides exhibited surface pressure values far beyond that of apoA-I. Thus, modified 18A peptides have much superior 'membrane penetrating potential' compared to apo A-I.

These initial studies were performed using normal phospholipids. We also compared the ability of apo A-I and the 4F peptide to associate with membranes containing oxidized phospholipids, a key component of atherogenic lipoproteins. The binding of apoA-I to membranes was similar in bilayers containing normal and oxidized phospholipids [21]. Indeed, we found that the binding of arachidonic and linoleic acid to apoA-I decreased significantly after their oxidation. In contrast, the binding affinities of the antiatherogenic 4F and 3F-2 peptides for oxidized phospholipid membranes increased compared to membranes containing only nonoxidized phospholipids. Interestingly, the binding of oxidized and nonoxidized free fatty acids to the 4F peptides was of equally high affinity, with Kd values ranging between 1025 and 10,210 M [21]. The significance of these results will be further discussed later in this chapter.

6 First In Vivo Experiment Showing Inhibition of Atherosclerosis

The ability of apoA-I to inhibit atherosclerotic lesion formation in humans make it an attractive therapeutic candidate. HDL and apoA-1 possess other functional properties, which add to their attractiveness as potential human therapies. HDL and apoA-I inhibit LDL-induced monocyte chemotaxis [22]. HDL particles also carry enzymes that attenuate LDL oxidation, including paraoxonase (PON), platelet-activating factor acetyl-hydrolase (PAFAH) and lecithin-cholesterolacyltransferase (LCAT) [23]. These enzymes degrade proinflammatory oxidized phospholipids, thereby limiting their accumulation in LDL [23]. An in vitro assay was developed to measure LDL-induced monocyte chemotaxis in which cocultures of human aortic endothelial and smooth muscle cells were incubated in the absence of LDL for 24 h. The culture medium was then removed, the cell layers were washed at 37 °C, fluorescently labeled human monocytes were added and monocyte chemotaxis was quantitated [22]. The 18A analogs Ac-18A-NH_2 (2F), $3F^3$, $3F^{14}$, 4F, 5F, 6F, and 7F were studied for their ability to inhibit LDL-induced monocyte chemotaxis using this assay. While peptide 2F was not very effective in inhibiting LDL-induced monocyte chemotaxis, peptides 4F, 5F and 6F potently inhibited LDL-induced monocyte chemotactic activity. The 5F peptide was the most effective and also exhibited the maximum ability to activate the plasma enzyme LCAT. While

peptides 6F and 7F exhibited similar exclusion pressure values, they were not easily soluble. Therefore, peptide 5F was selected to study the effect of apoA-I mimetic peptides on atherosclerosis. Here we used a C57BL/6J mice fed a cholate containing Paigen diet as a model of atherosclerotic lesion formation [24]. The 5F peptide (20 μg in 200 μL PBS) was administered once daily by intraperitoneal injection for 16 weeks. Mouse apoA-I (50 μg in 200 μL) was also administered for a separate set of mice on the Paigen diet. Due to the poor solubility of peptide 5F, we had to restrict the dosage administered to 20 μg/mouse. There was no change in the levels of plasma cholesterol or lipoproteins in any of the groups compared to the control groups. No toxicity or antibodies to the administered peptide were observed in any of the groups. Importantly, administration of the 5F peptide showed significantly less aortic atherosclerotic lesion area, whereas there was no difference between the control mice and mice treated with apoA-1. To elucidate one potential mechanism for the antiatherogenic effect of the ApoA-I mimetic peptide 5F, human or mouse apoA-I (50 μg) or 5F (20 μg/mouse) were injected into C57BL/6J mice on the Paigen diet and after 16 weeks after the start of diet, their HDL fractions were isolated and tested for their ability to inhibit LDL-induced monocyte chemotaxis and Auerbach lipid hydroperoxide formation [22]. Control mouse HDL and HDL isolated from mice given apoA-I had similar efficacies in these two assays. Importantly, HDL isolated from either 5F or human apoA-I administered group showed a reduction in lipid hydroperoxides and LDL-induced monocyte chemotaxis. Peptide 2F was unable to inhibit monocyte chemotaxis and inhibit diet-induced atherosclerosis [24, 25]. As shown in Table 1, peptide 5F exerts enhanced exclusion pressure compared to peptide 2F. These results for the first time demonstrate a major effect of these ApoA-1 mimetic peptides in improving the antiatherogenic function of HDL. These observations support the idea that HDL function rather than HDL levels may determine the antiatherogenic property of HDL. That is, peptide 5F converted a proinflammatory HDL into an anti-inflammatory HDL. It is also clear from Table 1 that arrangement of aromatic residues and not number or the lipid affinity determines the ability of the peptide to inhibit atherosclerosis. For example, two peptide containing three Phe residues exhibit equal surface pressure but differ in their ability to inhibit lesion formation.

7 Studies in Several Laboratories

Several criticisms of apoA-1 mimetic peptides were raised. Two major critiques were (1) a peptide with only 18 amino acid residues cannot mimic all of the properties of native apoA-I, and (2) the

specificity of apoA-I for activating antioxidant enzymes such as LCAT, PON-1, PAH-AH, and hemoxygenase-1 (HO-1) or for participating in ATP-binding cassette transporters (ABCA-1)-mediated cholesterol efflux does not exist in these short amphipathic peptides. However, since progress in science depends on observable facts and not on suppositions, the first in vivo mouse experiments showing that the 5F peptide inhibits atherosclerosis clearly swayed opinion as evidenced by the large increase in the number of publications utilizing the 18A, the 5F and other, similar apoA-1 mimetic peptides designed by other laboratories, as will be described later. Due to the exceeding number of published confirmatory results of the antiatherogenic nature of all of these peptides (Table 2), several important studies that lead to Phase I clinical trials will be discussed.

In collaboration with our laboratory, the group headed by Alan Fogelman published several papers using the 18A peptides and shorter ones such as a 10-residue peptide from apoJ sequence and a tetrapeptide. Data acquired in these studies led to eight conclusions: (1) Apo-mimetic peptides can be orally active in inhibiting lipid-mediated inflammatory disorders [23, 25]; (2) lesion regression can occur in the presence of statins [32]; (3) reagents such as niclosamide can protect all L-amino acid containing peptides making them orally active [52]; (4) certain peptides with increased aromatic residues on their nonpolar face associate with oxidized lipids with very high affinity compared to human apoA-I, thus making them superior to apoA-I in their ability to ameliorate lipid-mediated inflammatory disorders [21]; (5) peptide administration converts inflammatory HDL into anti-inflammatory HDL [24, 53]; (6) administration of peptide improves cognition, inhibits amyloid deposition, improves insulin resistance in diabetic animal models and inhibits tumor in several animal models [31, 34, 45, 54, 55]; (7) a peptide expressed transgenically in tomatoes is orally active as it inhibits atherosclerosis and inflammatory bowel disease in animal models [56]; and (8) peptide treatment can change macrophage phenotype, resulting in amelioration of inflammatory disorders [57].

Several studies show that D-4F is orally effective [25, 58]. Furthermore, treating apoE null mice subjected to the bypassed vein graft model of atherosclerosis with peptide for 4 weeks significantly reduced evolving atherosclerosis and decreased intraplaque lipid and macrophages [58]. The Remaley group modified the 18A peptide with proline such that one end of 18A became less hydrophobic compared to the original peptide [59, 60]. This modification was designed to reduce the detergent effect of the peptide 18A, thus rendering the resulting peptide less toxic. However, the same authors have not compared the original 37pA peptide with their modified analogs in in vivo studies. The 18A-Pro-18A peptide was shown by Mendez et al. to enhance cellular cholesterol efflux

Table 2
Direct and indirect effects of the peptide can explain beneficial effects of ApoA-I mimetic peptides in different dyslipidemic and inflammatory diseases

Study description	References
ApoA-I mimetic peptides inhibit atherosclerosis in several atherosclerosis susceptible animal models	[24, 25]
4F inhibits inflammation and monocyte infiltration mediated by influenza virus and reduces caspase expression in pneumocytes	[26]
ApoA-I mimetic peptides inhibit LPS mediated inflammatory responses	[27, 28]
4F reduces arterial intima smooth muscle cell proliferation	[29]
A-I mimetic peptides induce HO-1 and extracellular SOD; decreases endothelial sloughing and improves vascular function	[29, 30]
4F administration decreases arteriole inflammation and improves cognitive performance	[31]
4F synergistically regresses lesion formation	[32]
4F administration restores NO and superoxide anion balance	[33]
Oral D-4F reduces Alzheimer's plaque formation	[34]
4F administration reduces chronic rejection of transplanted hearts	[35]
4F administration reduces airway inflammation	[36]
D-4F/Pravastatin inhibit collagen-induced arthritis	[37]
4F treatment reduces adiposity, increases adiponectin levels and improves insulin sensitivity in obese mice	[38–42]
4F administration ameliorates tissue injury in sepsis	[27, 43]
4F ameliorates hyperlipidemia and sickle cell-induced vascular dysfunction	[44]
ApoA-I mimetic peptides reduce tumor formation in animal models of cancer	[45]
4F ameliorates hyperlipidemia-induced platelet aggregation inhibition	[46]
Tg-6F mitigates inflammation in Cox-2 dependent inflammatory bowel disease	[47]
4F administration reduces age-related macular degeneration in mice and monkeys	[48]
Peptide 5F promotes endothelial differentiation of bone marrow stem cells	[49, 50]
4F attenuates monocyte activation and adverse remodeling to limit tissue injury in hyperglycemia and myocardial infarction	[51]

via ABCA-1 [61]. They also showed that this peptide binds to the high affinity HDL binding sites on cholesterol-loaded cells. In these and other studies, 18A-Pro-18A was found to be nontoxic to cells [61].

The laboratory led by Abraham reported that apoA-I mimetic peptides ameliorate diabetes, obesity and the metabolic syndrome [38–41]. Administration of the apoA-I mimetic peptide 4F in the obese mouse model resulted in decreased insulin resistance, weight loss, and increased adiponectin levels. However, no major changes

in HDL and LDL levels were observed. These investigations showed that one of the factors affecting the improved quality of HDL is heme oxygenase (HO-1). Specifically, that 4F induces HO-1 has been supported by several subsequent studies [41, 42]. Additional studies by Liu et al. and Ou et al. supported that L-4F improved vasodilatation in hypercholesterolemic and sickle cell mice and restored endothelial cell nitric oxide and superoxide anion balance by recoupling endothelial nitric oxide synthase (eNOS) [29, 33].

Recently, [4F:lipid] complexes have been used as nanodisc "traps" of microsomal cytochrome P450, a hydrophobic membrane protein [62]. These data are the first evidence that a biomimetic compound can induce the formation of CYP2B4 raft domains in the endoplasmic reticulum. The results from these investigations showed that the peptide-induced lipid raft formation effectively and increased the thermal stability of P450 in addition to dramatically altering its binding kinetics for the hydrophilic ligand butylated hydroxytoluene (BHT). Thus, these peptide-based nanodisc traps may act as drug carriers.

In a systematic study, Wool et al. showed that 37pA, a peptide in which two 18A strands are connected by a Pro residue is more effective than 4F as studied by in vivo HDL binding and mediation of HDL anti-inflammatory properties [63]. These investigators also showed that administration of peptide 4F into apoE null mice induces natural antibody production, resulting in the reduction of nascent atherosclerotic lesions [63].

Bielicki et al. reported a synthetic α-helix peptide ATI-5261 using the C-terminal domain of apoE (216–299), which forms a class A α-helix [64]. Intraperitoneal injections of either a peptide solution or a peptide–lipid complex into LDL-R null mice on Western diet or into apoE null mice inhibited atherosclerosis by 30–45% respectively. Additional extensive investigations on the therapeutic potential have not been reported [64]. Yokoyama and colleagues designed a 22mer peptide with an ELK sequence arranged in the form of the class A amphipathic helix [65, 66]. The sequence (PKLEELKEKLKELLEKLKEKLA) is designed based on the 22mer tandem repeating sequence from apoA-I. This ELK peptide associated with 1,2-dimyristoyl-*sn*-glycero-3-phosphocholine (DMPC). Whether this peptide, analogous to 18A analogs, also associates with POPC has not been studied. POPC complexes with this peptide were prepared using cholate dialysis, similar to the preparation of human apoA-I:POPC complexes. ID peptides are another group that consist of fewer negatively charged residues in the center of the hydrophilic face of the helical peptides [67]. Most charged amino acids are located along the edge of the helix and are susceptible to forming salt bridges with residues of an antiparallel helix. These peptides were also shown to associate with DMPC spontaneously but required cholate

to form complexes with POPC. These peptides cause efflux of cellular cholesterol but do not activate plasma LCAT. In vivo studies have not been reported either with ELK peptides or ID peptides. Based on these published studies, only analogs of 18A have undergone extensive studies for various lipid-mediated inflammatory diseases in different animal models [*see* Table 2].

8 Phase I Studies of ApoA-I Mimetic Peptide

As shown in Fig. 1, the amphipathic helical peptide 4F exhibits different retention times in hypercholesteremic animals compared to normal animals. In support of this, it has been shown that regardless of the mode of administration, the intestine is the major site of action [68]. Given that 4F interacts with oxidized lipids with high affinity [21], it follows that the plasma residence time of the 4F peptide in dyslipidemic mice, which possess high levels of lipid hydroperoxides, is very short. Therefore, plasma levels should not be one of the factors for determining the in vivo efficacy of apoA-I mimetics. Garber et al. established that the peptides synthesized using D-amino acids, such as D-4F, were not degraded in vivo [69]. Since D-4F was highly effective in animal models of atherosclerosis, Phase I clinical studies were conducted initially using D-4F. The first clinical trial was carried out to determine the toxicity of orally active D-4F [70]. A single oral dose of D-4F was administered (0.43–7.14 mg/kg or placebo) to high-risk cardiovascular patients. At doses of 4.3 mg/kg or 7.14 mg/kg, the ability of HDL to inhibit LDL-induced monocyte chemoattractant protein 1 (MCP-1) activity in cultures of human aortic endothelial cells was significantly improved compared to the placebo. The maximum plasma concentration achieved with the higher doses was 8.13 ± 5.66 ng/mL and 15.9 ± 6.53 ng/mL respectively. In another study [71], daily doses of D-4F at 1.43 mg/kg, 4.3 mg/kg or 7.14 mg/kg together with placebo were administered to high-risk cardiovascular patients over a 13-day period. Doses of 4.3 mg/kg and 7.14 mg/kg significantly improved HDL function in the cell-based assay compared to the placebo. The lower dose peptide was ineffective in improving HDL function. Again, importance was given to the plasma concentration of the peptide, which was in the ng/kg range. Despite observing a positive effect on HDL function and no toxicity with a single dose, further studies with D-4F were abandoned due to lack of clearance of D-amino acid containing peptides and the thinking that the peptide may accumulate in vivo.

Additional studies were performed using 4F synthesized using L-amino acids. The aim was to maximize the plasma concentration of the peptide [72]. L-4F peptide was administered by subcutaneous injection or by intravenous infusion at doses ranging between 0.042 and 1.43 mg/kg. As expected, based on the turnover studies

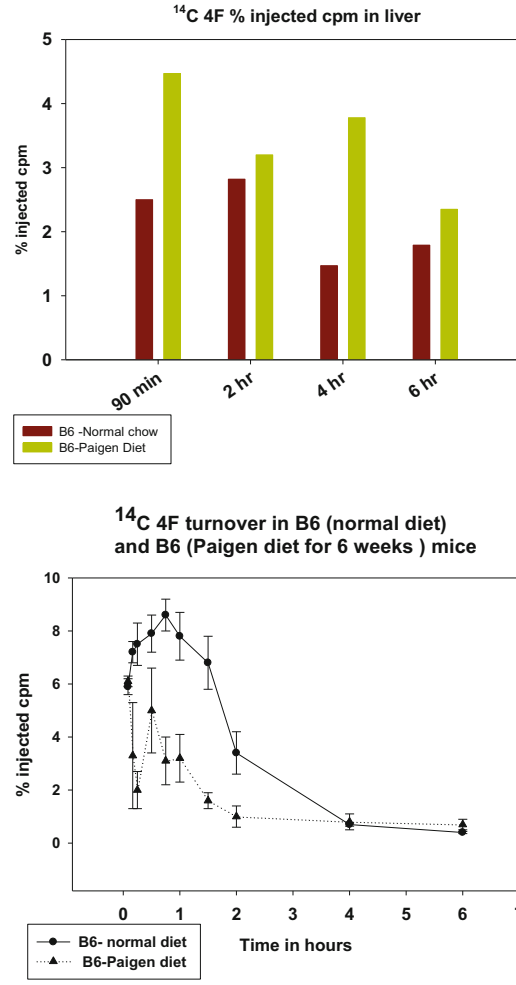

Fig. 1 Turnover of 4F from plasma is faster in C57BL/6 (B6) mice on Paigen diet compared to the same mice on normal diet. ^{14}C-4F (20 μg/mouse) was administered intraperitoneally and radioactivity was followed in plasma samples at various time points (●, Paigen diet; ▲, normal diet; $n = 3$). Enhanced hepatic uptake of 4F in Paigen diet-administered mice may be due to cholate-induced inflammation in the liver compared to control

performed in a hypercholesteremic animal model, plasma concentration of the test peptide was very low (3255 ± 640 ng/mL). HDL functional improvement was not observed at any of the doses administered. Knowledge that these active peptides target intestine and that the plasma concentration does not provide any information on the efficacy of the peptides was obtained as a result of these phase I clinical studies. These studies also revealed the need for additional methods to assay HDL function.

Studies have been performed to develop transgenic tomatoes capable of producing apoA-I mimetic peptides. It is thought that this will reduce the cost of production and provide hope that apoA-

I mimetic peptides may still be a viable mode of therapy [56]. Based on the results obtained in mice and monkey models, synthetic peptide 4F is undergoing clinical studies for age related macular degeneration and has shown promise in a monkey model [48, 49]. It should be emphasized that these 18A based peptide analogs have been shown to be superior to even apoA-I in their antioxidant and anti-inflammatory properties and in their ability to efflux cellular cholesterol. Even though some peptides shorter than 18 amino acids have been shown to reduce atherosclerosis in animal models, lack of further studies on these peptides and different peptides designed by other investigators to the extent of 18A analogs in various inflammatory models provide compelling support for the apoA-I mimetic peptides as future drugs for lipid-mediated inflammatory diseases.

9 Design and Studies of apoE Mimetics

Most reports indicate that apoA-I mimetics exhibit beneficial effects without changing plasma cholesterol or lipid levels. Other than apoA-I, the major protein component of HDL, apoE present in HDL and VLDL has also been shown to be atheroprotective [73]. ApoE is a 299 amino acid residue protein that possesses a two-domain structure. One domain is the LDL-receptor binding site and is contained in an N-terminal four-helix bundle. A second domain associates with lipids and is a 64 residue long amphipathic helix (203–266). Our initial studies identified the cytosolic and the cytolytic domains of apoE [74]. In these studies, we showed that peptides in the region of residues 130–149 and 130–155 of apoE inhibited cell proliferation without cytolysis whereas dimeric peptides 141–155 and 141–149 were cytotoxic [75]. Based on these initial observations, Nikoulin and Curtiss showed that a dimeric peptide of residues 141–155 of apoE targets to lipoproteins in plasma and mediates both cellular lipoprotein interactions in vitro and acute clearance of cholesterol-rich lipoproteins in vivo [24].

We designed a dual domain peptide to mimic the dual domain motif structure with the amino terminal consisting of residues 141–150 of human apoE (LRKLRKRLLR) covalently attached on the carboxyl end to the well-studied lipid associating peptide 18A instead of the long 64 residue lipid associating domain from apoE [76]. This peptide was referred to as hE18A, with the h signifying human apoE. In vivo administration of this peptide reduced plasma cholesterol dramatically in several hypercholesteremic animal models [77]. In addition to demonstrating antioxidant properties, hE18A decreased both plasma cholesterol and lipid hydroperoxides [78]. As shown in Fig. 2, administration of hE18A in apoE null mice dramatically reduced cholesterol and increased levels of the antioxidant enzyme paraoxonase (PON-1).

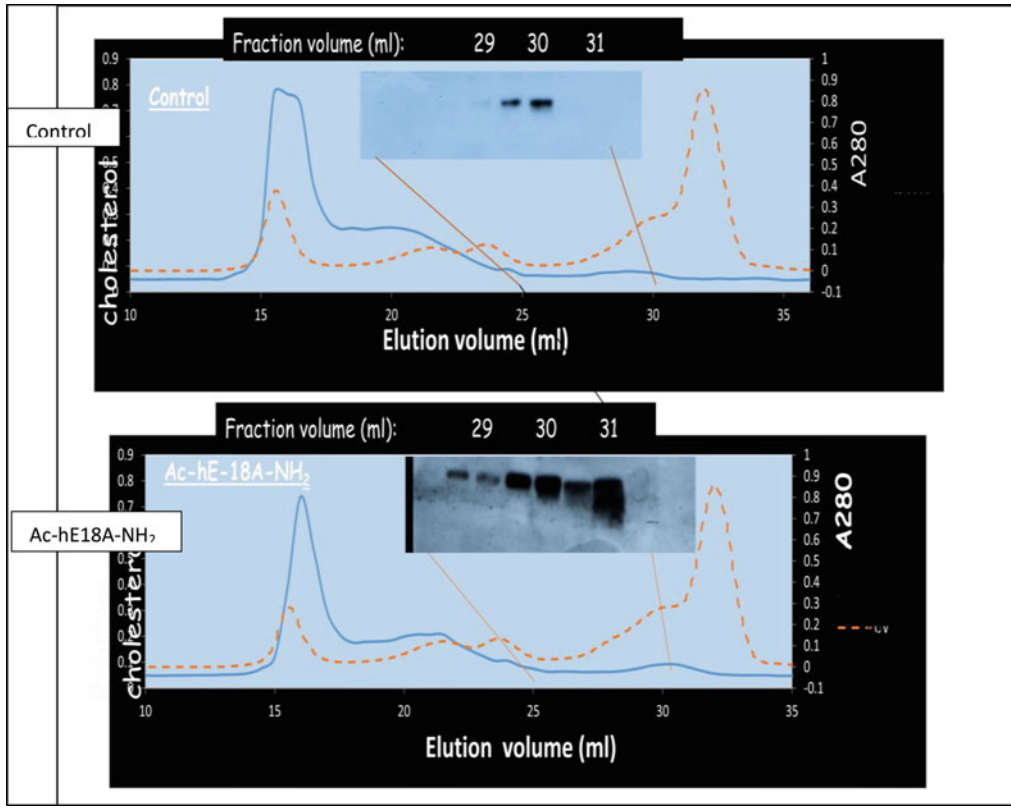

Fig. 2 Ac-hE18A-NH_2 dramatically increases PON-1 levels in HDL fractions (after gel filtration) in apoE null mice. Peptide administration (50 μg/mouse) decreases plasma cholesterol (blue line), A280 (orange line) and shows decrease in VLDL content

The Western blot shows differential protein expression for PON-1 in isolated gel filtration fractions from HDL. This apoE mimetic peptide has also been shown to reduce Alzheimer's plaque formation in a mouse model of Alzheimer's disease [79].

Modification of the N-terminal protecting group with either fatty acyl chains of different lengths or Ac-Aha (where Aha = -α-amino hexanoic acid) dramatically improved the cholesterol reducing abilities of these peptide analogs [80]. For example, a single administration of Myr-Ac-[R]hE18A-NH_2 (where R represents LRRLRRRLLR instead of LRKLRKRLLR in hE region) at 7.4 mg/kg in monkeys fed a Western diet reduced plasma cholesterol and plasma LDL levels by 64% and 74%, even after 7 days of administration, whereas it required 12 mg/kg of Ac-hE18A-NH_2 to elicit similar response [80]. While peptide Ac-hE18A-NH_2 has already undergone Phase I clinical trials [81], the highly active acyl peptides have not yet been tested in clinical trials. While the dual domain peptides have to be administered as injections, an 18-residue cationic peptide called mR18L can be orally administered and has been found to reduce plasma cholesterol and inhibit atherosclerosis in a mouse model of the disease [82].

The apoE mimetic peptides Ac-hE18A-NH_2 and mR18L have also been shown to reduce amyloid deposition and inhibit LPS-mediated inflammation [78, 83–86]. The COG peptides designed by Vitek et al. utilized the apoE sequence of residues 133–149 fused with a 17 amino acid prefix derived from the protein transduction domain (PTD) known as antennapedia. These peptides were also effective anti-inflammatory agents and reduced Alzheimer's plaque formation in experimental animal models [87]. A review of the of the CoG apoE mimetic peptides by Vitek and coworkers has been published [88]. However, these peptides have not been studied for their effect on plasma cholesterol.

Lipoprotein apheresis has been shown to affect lipoprotein-particle subclasses more efficiently compared with the PCSK-9 inhibitor evolocumab [89]. Since apoE mimetics designed by us have been shown to enhance PON-1, reduce plasma lipid hydroperoxides, exert potent antioxidant properties and dramatically reduce plasma cholesterol, the acylated apoE mimetics may provide an alternative to plasma apheresis, a procedure not well tolerated in all patients. The main advantage of apoE mimetic therapy is that it bypasses the highly specific LDL-receptor, thus reducing plasma cholesterol even in the presence of nonfunction LDL receptor.

10 Conclusions

The schematic diagram of apolipoprotein-mimetic peptide action in cholesterol metabolism and apolipoprotein–lipoprotein modulation is shown in Fig. 3. Peptides designed to clear oxidized lipids either on LDL or in the plasma appear to be most effective in mitigating lipid-mediated disorders such as atherosclerosis. These 18 residue anti-inflammatory peptides adopt an amphipathic α-helical structure when they associate with lipid or in the lipid environment. The fact that the kinetics of clearance of anti-inflammatory peptides is faster in dyslipidemic mice supports the idea that these peptides associate with oxidized lipids with high affinity and clear them more efficiently than the normal lipids. As electron-rich oxidized lipids reside closer to the polar interface compared to normal lipids, this atypical location aids a strong interaction of peptides with oxidized lipids and especially favors the interaction of oxidized lipids with the π-electron containing aromatic residues (F, W, and Y). This interaction of oxidized lipids with free radical quenching aromatic residues may convert proinflammatory HDL into an anti-inflammatory platform, inhibiting LDL-induced chemotaxis. Based on the structural characteristics of biologically active peptides that we delineated, it may be possible to design peptides shorter than 18 amino acids with antiatherogenic and anti-inflammatory properties. ApoE-mimetic peptides discovered in our laboratory clear atherogenic lipoproteins which possess larger amounts

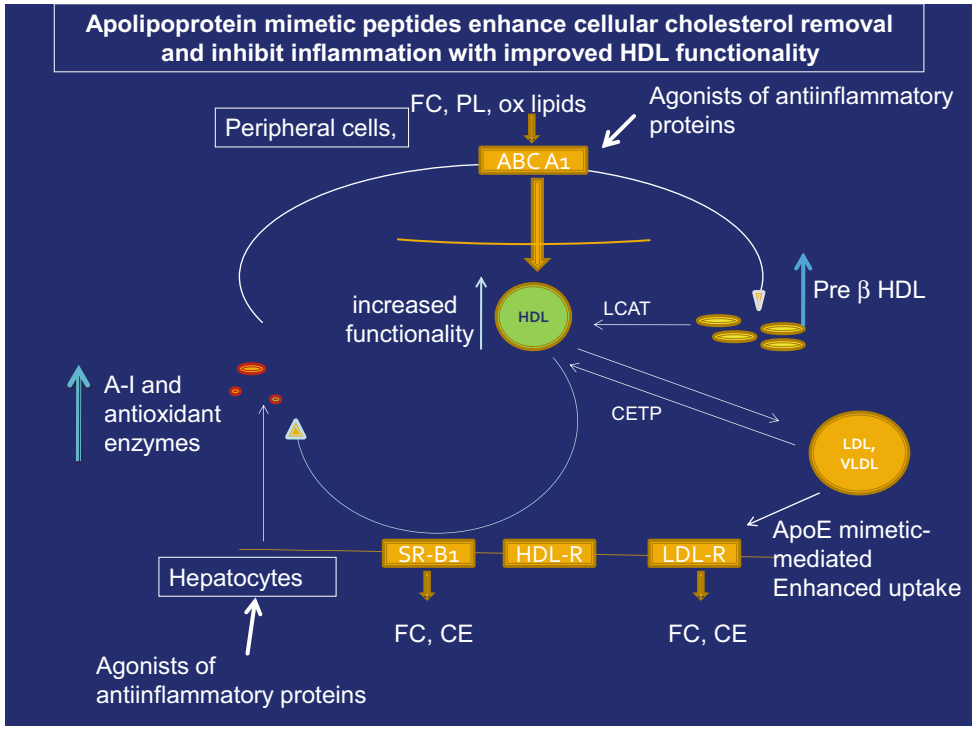

Fig. 3 Schematic diagram of apolipoprotein–mimetic peptide action in cholesterol metabolism and apolipoprotein–lipoprotein modulation. Orange arrows indicate lipid (FC, CE, PL) movements; blue arrows indicate increase in protein levels; white arrows indicate apo-mimetic mediated conversions; and yellow dots on LDL (⬭) represents LOOH present on ox-LDL. ApoA-I mimetic peptides act as agonists of anti-inflammatory proteins such as PON-1, PAF-AH, and HO-1 in hepatocytes, which increase the functionality of HDL. In peripheral cells, they clear free cholesterol and ox-lipids to enhance HDL function, and clear CE via HDL receptors. They also produce increased amounts of pre-beta-HDL which enhances cholesterol efflux from peripheral cells. ApoE mimetic peptides enhance clearance of atherogenic lipoproteins, which also cause increase in antioxidant enzymes, thus improving HDL function

of neutral lipids such as cholesterol esters or triglycerides. Rapid clearance of these lipoproteins also clears their lipid hydroperoxides. This decrease in oxidized lipids could rapidly change cell signaling mechanisms, inhibiting the uptake of cholesterol by cells and changing macrophage phenotype from inflammatory to non-inflammatory, thus ameliorating atherosclerosis and other lipid-mediated disorders.

References

1. Kontush A, Chapman J (2006) Functionally defective high-density lipoprotein: a new therapeutic target at the crossroads of dyslipidemia, inflammation and atherosclerosis. Pharmacol Rev 58:342–374
2. Hulley SB, Cohen R, Widdowson G (1977) Plasma high-density lipoprotein cholesterol level. Influence of risk factor intervention. JAMA 238:2269–2271
3. Badimon JJ, Badimon L, Fuster V (1990) Regression of atherosclerotic lesions by high

density lipoprotein plasma fraction in the cholesterol-fed rabbit. J Clin Invest 85:1234–1241

4. Rubin EM, Krauss RM, Spangler EA, Verstuyft JG, Clift SM (1991) Inhibition of early atherogenesis in transgenic mice by human apolipoprotein AI. Nature 353:265–267
5. Nissen S, Tusnoda T, Tuzcu EM, Schoenhagen P, Cooper CJ, Yasin M, Eaton GM, Lauer MA, Sheldon WS, Grines CL, Halpern S, Crowe T, Blankenship JC, Kerensky R (2003) Effect of apoA-I Milano on atherosclerosis in patients with acute coronary syndromes. A randomized controlled trail. JAMA 290:2292–2300
6. Erickson M, Carson LA, Miettinen TA, Angelin B (1999) Stimulation of fecal excretion after infusion of recombinant proapolipoproteinA-I. *Circulation* 100:594–598
7. Nanjee MN, Doran JE, Lerch PG, Miller NE (1999) Acute effects of intravenous infusion of ApoA-I/phosphatitylcholine discs on plasma lipoproteins in humans. Atheroscler Thromb Vasc Biol 19:979–989
8. Kunitake ST, Jarvis MR, Hamilton RL, Kane JP (1992) Binding of transition metals by apolipoprotein A-I–containing plasma lipoproteins: inhibition of oxidation of low density lipoproteins. Proc Natl Acad Sci U S A 89:6993–6997
9. Futterman LG, Lemberg L (2005) Apo A-I Milano. Am J Crit Care 14:244–247
10. Nissen SE, Tardif J-C, Nicholls SJ, Revkin JH, Shear CL, Duggan WT, Ruzyllo W, Bachinsky WB, Lasala GP, Tuzcu EM (2007) Effect of Torcetrapib on the progression of coronary atherosclerosis. NEJM 356:1304–1316
11. Castellini WP (1996) Lipids, risk factors and ischaemic heart disease. Atherosclerosis 124: S1–S9
12. Barter PJ, Nicholls S, Rye KA, Anantharamaiah GM, Navab M, Fogelman AM (2004) Antiinflammatory properties of HDL. Circ Res 95:764–772
13. Navab M, Anantharamaiah GM, Reddy ST, Van Lenten BJ, Ansell BJ, Hama S, Hough G, Wagner AC, Shaposhnik Z, Fogelman AM (2005) The double jeopardy of HDL. Anals Med 37:173–178
14. Sniderman AD, Thanassoulis G, Glavinovic T, Navar AM, Pencina M, Catapano A, Ference BA (2019) Apolipoprotein B containing particles and cardiovascular risk. JAMA Cardiol 4:1287–1295
15. Shah PK, Kaul S, Nilsson J, Cercek B (2001) Exploiting the vascular protective effects of high-density lipoprotein and its apolipoproteins: an idea whose time for testing is coming, part I. Circulation 104:2376–2383
16. Murphy AJ, Westerterp M, Yvan-Charvel L, Tall AR (2012) Anti-atherogenic mechanisms of high density lipoprotein: effects on myeloid cells. Biochim Biophys Acta 182:513–521
17. Segrest JP, Jackson RL, Morrisett JD, Gotto AM Jr (1974) A molecular theory of lipid-protein interactions in plasma lipoproteins. FEBS Lett 38:247–253
18. Segrest JP, Brouillette CG, Garber DW, Harvey S, Anantharamaiah GM (1994) The amphipathic α-helix: a multifunctional and structural motif in plasma lipoproteins. Adv Protein Chem 45:303–309
19. Anantharamaiah GM, Jones JL, Brouillette CG, Schmidt CF, Chung BH, Hughes TA, Bhown AS, Segrest JP (1985) Studies of synthetic peptide analogs of the amphiphatic helix. Structure of complexes with dimyristoyl phosphatidylcholine. J Biol Chem 260:10248–10255
20. Arnulphi C, Sanchez SA, Tricerri A, Gratton E, Jonas A (2005) Interaction of human apolipoprotein A-I with model membranes exhibiting lipid domains. Biophys J 89:285–295
21. Van Lenten BJ, Wagner AC, Jung CL, Ruchala P, Waring AJ, Lehrer RI, Watson AD, Hama S, Navab M, Anantharamaiah GM, Fogelman AM (2008) Anti-inflammatory apoA-I-mimetic peptides bind oxidized lipids with much higher affinity than human apoA-I. J Lipid Res 49:2302–2311
22. Navab M, Imes SS, Hama SY, Hough GP, Lori A, Ross LA, Bork RW, Valente AJ, Berliner JA, Drinkwater DC, Lakas H, Fogelman AM (1991) Monocyte transmigration induced by modification of low density lipoprotein in cocultures of human aortic wall cells is due to induction of monocyte chemotactic protein 1 synthesis and is abolished by high density lipoprotein. J Clin Invest 88:2039–2046
23. Mackness MI, Durrington PN (1995) HDL, its enzymes and its potential to influence lipid peroxidation. Atherosclerosis 115:243–253
24. Garber DW, Datta G, Chaddha M, Palgunachari MN, Hama SY, Navab M, Fogelman A, Segrest JP, Anantharamaiah GM (2001) A new synthetic class A amphipathic peptide analogue protects mice from diet-induced atherosclerosis. J Lipid Res 42:545–552
25. Navab M, Anantharamaiah GM, Reddy ST, Hama S, Hough G, Grijalva VR, Mishra VK, Palgunachari MN, Fogelman AM (2005) Oral small peptides render HDL antiinflammatory

in mice and monkeys and reduce atherosclerosis in ApoE null mice. Circ Res 97:524–532

26. Van Lenton BJ, Wagner AC, Navab M, Anantharamaiah GM, Hui K-W, Nayak DP, Fogelman AM (2004) D-4F, an apolipoprotein A-I mimetic peptide, inhibits the inflammatory response induced by influenza A infection of human type II pneumocytes. Circulation 110:3252–3258
27. Sharifov OF, Xu X, Gaggar A, Grizzle WE, Mishra VK, Honavar J, Litovsky SH, Palgunachari MN, White CR, Anantharamaiah GM, Gupta H (2013) Anti-inflammatory mechanisms of apolipoprotein A-I mimetic peptide in acute respiratory distress syndrome secondary to sepsis. PLoS One 8(5):e64486
28. Gupta H, Dai L, Datta G, Garber DW, Grenett H, Lee Y, Mishra VK, Palgunachari MN, Handattu S, Gianturco SH, Bradley W, Anantharamaiah GM, White CR (2005) Inhibition of lipopolysaccharide-induced inflammatory responses by an apolipoprotein AI mimetic peptide. Circ Res 97:236–243
29. Liu D, Ding Z, Wu M, Xu W, Qian M, Du Q, Zhang L, Cui Y, Zheng J, Chang H, Huang C, Lin D, Wang Y (2017) The apolipoprotein A-I mimetic peptide, D-4F, alleviates ox-LDL-induced oxidative stress and promotes endothelial repair through the eNOS/HO-1 pathway. J Mol Cell Cardiol 105:77–88
30. Kruger AL, Peterson S, Turkseven S, Kaminski PM, Zhang FF, Quan S, Wolin MS, Abraham NG (2005) D-4F induces heme oxygenase-1 and extracellular superoxide dismutase, decreases endothelial cell sloughing, and improves vascular reactivity in rat model of diabetes. Circulation 111:3126–3134
31. Buga GM, Frank JS, Mottino GA, Hendizadeh M, Hakhamian A, Tillisch JH, Reddy ST, Navab M, Anantharamaiah GM, Ignarro LJ, Fogelman AM (2006) D-4F decreases brain arteriole inflammattion and improves cognitive performance in LDL receptor-null-mice on a Western diet. J Lipid Res 47:2148–2160
32. Navab M, Anantharamaiah GM, Hama S, Hogh G, Reddy ST, Frank JS, Garber DW, Handattu S, Fogelman A (2005) D-4F and statins synergize to render HDL anti-inflammatory in mice and monkeys and cause lesion regression in old apolipoprotein E-null mice. Arterioscler Thromb Vasc Biol 25:1426–1432
33. Ou Z, Ou J, Ackerman A, Oldham KT, Prichard KA Jr (2003) L-4F, an apolipoprotein A-1 mimetic, restores nitric oxide and superoxide anion balance in low-density lipoprotein-treated endothelial cells. Circulation 107:1520–1524
34. Handattu SP, Garber DW, Monroe CE, van Groen T, Kadish I, Nayyar G, Cao D, Palgunachari MN, Li L, Anantharamaiah GM (2009) Oral apolipoprotein A-I mimetic peptide improves cognitive function and reduces amyloid burden in a mouse model of Alzheimer's Disease. Neurobiol Dis 34:525–534
35. Schnickel GT, Hsieh GR, Kachikwu EL, Garcia C, Shefizadeh A, Fishbein M, Ardehali A (2006) Cytoprotective gene HO-1 and chronic rejection in heart transplantation. Transplant Proc 38:3259–3262
36. Nandedkar SD, Weihrauch D, Xu H, Shi Y, Feroah T, Hutchins W, Rickaby DA, Duzgunes N, Hillery CA, Konduri KS, Pritchard KA Jr (2011) D-4F, an apoA-1 mimetic, decreases airway hyperresponsiveness, inflammation, and oxidative stress in a murine model of asthma. J Lipid Res 252:499–508
37. Charles-Schoeman C, Banquerigo ML, Hama S, Navab M, Park GS, Van Lenten BJ, Wagner AC, Fogelman AM, Brahn E (2008) Treatment with an apolipoprotein A-1 mimetic peptide in combination with pravastatin inhibits collagen-induced arthritis. Clin Immunol 127(2):234–244
38. Cao J, Puri N, Sodhi K, Bellner L, Abraham NG, Kappas A (2012) ApoA-I mimetic rescues the diabetic phenotype of HO-2 knockout mice via an increase in HO-1 adiponectin and LKBI signaling pathway. Int J Hypertens 2012:628147
39. Peterson SJ, Kim DH, Li M, Positano V, Vanella L, Rodella LF, Piccolomini F, Puri N, Gastaldelli A, Kusmic C, L'Abbate A, Abraham NG (2009) The L-4F mimetic peptide prevents insulin resistance through increased levels of HO-1, pAMPK, and pAKT in obese mice. J Lipid Res 50:1293–1304
40. Vecoli C, Cao J, Neglia D, Inoue K, Sodhi K, Vanella L, Gabrielson KK, Bedia D, Paolocci N, L'abbate A, Abraham NG (2011) Apolipoprotein A-I mimetic peptide L-4F prevents myocardial and coronary dysfunction in diabetic mice. J Cell Biochem 112:2616–2626
41. Marino JS, Peterson SJ, Li M, Vanella L, Sodhi K, Hill JW, Abraham NG (2012) ApoA-1 mimetic restores adiponectin expression and insulin sensitivity independent of changes in body weight in female obese mice. Nutr Diab 12:e33
42. Vanella L, Li M, Kim D, Malfa G, Bellner L, Kawakami T, Abraham NG (2012) ApoA1: mimetic peptide reverses adipocyte dysfunction in vivo and in vitro via an increase in

hemoxygenase (HO-1) and Wnt10b. Cell Cycle 11:706–714

43. Dai L, Datta G, Zhang Z, Gupta H, Patel R, Honavar J, Modi S, Wyss JM, Palgunachari M, Anantharamaiah GM, White CR (2010) The apolipoprotein A-I mimetic peptide 4F prevents defects in vascular function in endotoxemic rats. J Lipid Res 51:2695–2705
44. Ou Z, Jones DW, Holzhauer S, Hartoum OA, Ackerman AW, Gutternan DD, Guice K, Oldham KT, Hillery CA, Prichard KA Jr (2003) L-4F, an apolipoprotein A-1 mimetic, dramatically improves vasodilation in hypercholesterolemia and sickle. Cell Dis 107:2337–2341
45. Su F, Kozaka KR, Imaizumib S, Gao F, Amneusa MW, Grijalva V, Ng C, Wagner A, Hough G, Farias-Eisner G, Anantharamaiah GM, Van Lenten BJ, Mohamad M, Fogelman AM, Reddy ST, Farias-Eisner R (2010) Apolipoprotein A-I (apoA-I) and apoA-I mimetic peptides inhibit tumor development in a mouse model of ovarian cancer. Proc Natl Acad Sci U S A 107:19997–12000
46. Buga GM, Navab M, Imaizumi S, Reddy ST, Yekta B, Hough G, Chanslor S, Anantharamaiah GM, Fogelman AM (2010) 4F ameliorates hyperlipidemia-induced platelet aggregation inhibition L-4F alters hyperlipidemic (but not normal) mouse plasma to reduce platelet aggregation. Arterioscler Thromb Vasc Biol 30(2):283–292
47. Meriwether D, Sulaiman D, Volpe C, Dorfman A, Grijalva V, Dorreh N, Solorzano-Vargas RS, Wang J, O'Connor E, Papesh J, Larauche M, Trost H, Palgunachari MN, Anantharamaiah GM, Herschman HR, Martin MG, Fogelman AM, Reddy ST (2019) Apolipoprotein A-I mimetics mitigate intestinal inflammation in COX2-dependent inflammatory bowel disease model. J Clin Invest 129:3670–3685
48. Rudolf M, Curcio C, Schlötzer-Schrehardt U, Mir A, Sefat M, Tura A, Aherrahrou Z, Brinkmann M, Grisanti S, Miura Y, Ranjbar M (2019) Apolipoprotein A-I mimetic peptide L-4F removes Bruch's membrane lipids in aged nonhuman primates. Invest Ophthalmol Vis Sci 60:461–472
49. Rudolf M, Mir Mohi Sefat A, Miura Y, Tura A, Raasch W, Ranjbar M, Grisanti S, Aherrahrou Z, Wagner A, Messinger JD, Garber DW, Anantharamaiah GM, Curcio CA (2018) ApoA-I mimetic peptide 4F reduces age-related lipid deposition in murine Bruch's membrane and causes its structural remodeling. Curr Eye Res 43:135–146
50. Zhang J, Cui Y, Li X, Xiao Y, Liu L, Jia F, He J, Xie X, Parthasarathy S, Hao H, Fang N (2020) 5F peptide promotes endothelial differentiation of bone marrow stem cells through activation of ERK1/2 signaling. Eur J Pharmacol 876:173051–173060
51. Hamid T, Ismahil MA, Bansal SS, Patel B, Goel M, White CR, Anantharamaiah GM, Prabhu SD (2020) The apolipoprotein A-I mimetic L-4F attenuates monocyte activation and adverse cardiac remodeling after myocardial infarction. Int J Mol Sci 21:3519–3534
52. Navab M, Ruchala P, Waring AJ, Lehrer RL, Hama S, Hough G, Palgunachari MN, Anantharamaiah GM, Fogelman AM (2009) A novel method for oral delivery of apolipoprotein mimetic peptides synthesized from all L-amino acids. J Lipid Res 50:1538–1547
53. Navab M, Anantharamaiah GM, Reddy ST, Hama S, Hough G, Grijalva VR, Wagner AC, Frank JS, Datta G, Garber D, Fogelman AM (2004) Oral D-4F causes formation of pre-β high-density lipoprotein and improves high-density lipoprotein-mediated cholesterol efflux and reverse cholesterol transport from macrophages in apolipoprotein E-null mice. Circulation 109:3215–3220
54. Sahoo BR, Genjo T, Cox SJ, Stoddard AK, Anantharamaiah GM, Fierke C, Ramamoorthy AJ (2018) Nanodisc-forming scaffold protein promoted retardation of amyloid-beta aggregation. Mol Biol 430:4230–4244
55. Peterson SJ, Drummond G, Kim DH, Li M, Kruger AL, Ikehara S, Abraham NG (2008) L-4F treatment reduces adiposity, increases adiponectin levels, and improves insulin sensitivity in obese mice. J Lipid Res 49:1658–1669
56. Chattopadhyay A, Navab M, Hough G, Gao F, Merriweather D, Grijalva V, Springstead JR, Palgnachari MN, Namiri-Kalantari R, Su F, Van Lenten BJ, Wagner AC, Anantharamaiah GM, Frais-Eisner R, Reddy ST, Fogelman AM (2013) A novel approach to apoA-I mimetic therapy. J Lipid Res 54:995–1010
57. Smythies LE, White CR, Maheshwari A, Palgunachari MN, Anantharamaiah GM, Chaddha M, Kurundkar AR, Datta G (2010) Apolipoprotein A-I mimetic 4F alters the function of human monocyte-derived macrophages. Am J Phys Cell Physiol 298: C1538–C1548
58. Li X, Chyu K-Y, Faria JR, Yano J, Nathwani N, Ferreira C, Dimayuga PC, Cercek B, Kaul S, Shah PK (2004) Differential effects of apolipoprotein A-I-mimetic peptide on evolving and established atherosclerosis in apolipoprotein E-null mice. Circulation 110:1701–1705
59. Remaley AT, Thomas F, Stonik JA, Demosky SJ, Bark SE, Neufeld EB, Bocharov AV, Vishnyakova TG, Patterson AP, Eggerman TL,

Santamarina-Fojo S, Brewer B (2003) Synthetic amphipathic helical peptides promote lipid efflux from cells by an ABCA1-dependent and an ABCA1-independent pathway. J Lipid Res 44:828–836

60. Sethi AA, Stonik JA, Thomas F, Demosky SJ, Amar M, Neufeld E, Brewer HB, Davidson WS, D'Souza W, Sviridov D, Remaley A (2008) Asymmetry in the lipid affinity of bihelical amphipathic peptides. A structural determinant for the specificity of ABCA1-dependent cholesterol efflux by peptides. J Biol Chem 283:32273–32282
61. Mendez A, Anantharamaiah GM, Segrest JP, Oram JF (1994) Synthetic amphipathic helical peptides that mimic apolipoprotein A-I in clearing cellular cholesterol. J Clin Invest 94:1698–1705
62. Barnaba C, Sahoo BR, Ravula T, Medina-Meza IG, Im SC, Anantharamaiah GM, Waskell L, Ramamoorthy A (2018) Cytochrome-P450-induced ordering of microsomal membranes modulates affinity for drugs. Angew Chem Int Ed Eng 57:3391–3395
63. Wool GD, Cabana VG, Lukens J, Shaw PX, Binder CJ, Witztum JL, Reardon CA, Getz GS (2011) 4F Peptide reduces nascent atherosclerosis and induces natural antibody production in apolipoprotein E-null mice. FASEB J 25:290–300
64. Bielicki JK, Zhang H, Cortez Y, Zheng Y, Narayanaswami V, Patel A, Johansson J, Azhar S (2010) A new HDL mimetic peptide that stimulates cellular cholesterol efflux with high efficiency greatly reduces atherosclerosis in mice. J Lipid Res 51:1496–1503
65. Fukushima D, Kupferberg JP, Yokoyama S, Kroon DJ, Kaiser ET, Kézdy FJ (1979) A synthetic amphiphilic helical docosapeptide with the surface properties of plasma apolipoprotein A-I. J Am Chem Soc 101:3703–3704
66. Yokohama S, Fukushima D, Kupferberg JP, Kézdy FJ, Kaiser ET (1980) The mechanism of activation of lecithin: cholesterol acyl transferase by apolipoprotein A-I and an amphiphilic peptide. J Biol Chem 255:7333–7339
67. Labuer C, Lins L, Vanloo B, Brasseur R, Rossenue M (1997) Design of a new class of amphipathic helical peptides for the plasma apolipoproteins that promote cellular cholesterol efflux but do not activate LCAT. Arterioscler Thromb Vasc Biol 17:580–588
68. Navab M, Reddy ST, Anantharamaiah GM, Imaizumi S, Hogh G, Hama S, Fogelman A (2011) Intestine may be a major site of action for the apoA-I mimetic peptide 4F whether administered subcutaneously or orally. J Lipid Res 52:1200–1210
69. Garber DW, Venkatachalapathi YV, Gupta KB, Ibdah J, Phillips MC, Hazelrig A, Segrest J, Anantharamaiah GM (1992) Turnover of synthetic class A amphipathic peptide analogues of exchangeable apolipoproteins in rats. Correlation with physical properties. Aterio Thromb 12:886–894
70. Bloedon LT, Dunbar R, Duffy D, Pinell-Salles-P, Norris R, DeGroot BJ, Movva R, Navab M, Fogelman AM, Rader DJ (2008) Safety, pharmacokinetics, and pharmacodynamics of oral apoA-I mimetic peptide D-4F in high-risk cardiovascular patients. J Lipid Res 49:1344–1352
71. Dunbar RL, Bloedon LT, Duffy D, Norris RB, Movva, Navab M, Fogelman AM, Rader DJ (2007) Daily oral administration of the apolipoprotein A-I mimetic peptide D-4F in patients with coronary heart disease or equivalent risk improves high-density lipoprotein anti-inflammatory function. J Am Coll Cardiol 49(Suppl A):1014–1123
72. Watson CE, Weissbach N, Kjems L, Ayalasomayajula S, Zhang Y, Chang I, Navab M, Hama S, Hough G, Reddy ST, Soffer D, Rader DJ, Fogelman AM, Schecter A (2011) Treatment of patients with cardiovascular disease with L-4F, an apoA1 mimetic, did not improve select biomarkers of HDL function. J Lipid Res 52:361–373
73. Harris JD, Evans V, Owen JS (2006) ApoE gene therapy to treat hyperlipidemia and atherosclerosis. Curr Opion Mol Ther 8:275–287
74. Clay MA, Anantharamaiah GM, Mistry MJ, Balasubramaniam A, Harmony JAK (1995) Localization of a domain in apolipoprotein E with both cytostatic and cytotoxic activity. Biochemistry 34:11142–11151
75. Nikoulin IR, Curtiss LK (1998) An apolipoprotein E synthetic peptide targets to lipoproteins in plasma and mediates both cellular lipoprotein interactions *in vitro* and acute clearance of cholesterol-rich lipoproteins *in vivo*. J Clin Invest 101:223–234
76. Datta G, Chaddha M, Garber DW, Chung BH, Tytler EM, Dashti N, Bradley WA, Gianturco SH, Anantharamaiah GM (2000) The receptor binding domain of apolipoprotein E, linked to a model class A amphipathic helix, enhances internalization and degradation of LDL by fibroblasts. Biochemistry 39:213–220
77. Garber DW, Handattu S, Aslan I, Datta G, Chaddha M, Anantharamaiah GM (2003) Effect of an arginine-rich amphipathic helical peptide on plasma cholesterol in dyslipidemic mice. Atherosclerosis 168:229–237
78. Datta G, Chaddha M, Handattu SP, Palgunachari MN, Nayyar G, Garber DW, Gupta H,

White CR, Anantharamaiah GM (2010) ApoE mimetic peptide reduces plasma lipid hydroperoxide content with a concomitant increase in HDL paraoxonase activity. Adv Exp Med Biol 660:1–4

79. Handattu SP, Monroe CE, Nayyar G, Palgunachari MN, Kadish I, van Groen T, Anantharamaiah GM, Garber DW (2013) *In vivo* and *in vitro* effects of an apolipoprotein E mimetic peptide on amyloid-beta pathology. J Alzheimers Dis 36:335–347
80. Anantharamaiah GM, Garber DW, Goldberg D, Morell E, Datta G, Palgunachari MN, Registrar TC, Appt SE, White CR (2018) Novel fatty acyl apoE mimetic peptides have increased potency to reduce plasma cholesterol in mice and macaques. J Lipid Res 59:2075–2083
81. Garber DW, Goldberg D, Anantharamaiah GM (2015) Apolipoprotein mimetic peptides: cholesterol-dependent and cholesterol-independent properties. In: Anantharamaiah GM, Goldberg D (eds) Apolipoprotein mimetics in the management of human disease. ADIS, Basel, pp 135–156
82. Handattu SP, Datta G, Epand RM, Epand RF, Palgunachari MN, Mishra VK, Monroe CE, Keenum TD, Chaddha M, Anantharamaiah GM, Garber DW (2010) Oral administration of L-mR18L, a single domain cationic amphipathic helical peptide, inhibits lesion formation in ApoE null mice. J Lipid Res 51:3491–3499
83. Nayyar G, Handattu SP, Monroe CE, Chaddha M, Datta G, Mishra VK, Keenum TD, Palgunachari MN, Garber DW, Anantharamaiah GM (2010) Two adjacent domains (141-150 and 151-160) of apoE covalently linked to a class A amphipathic helical peptide exhibit opposite atherogenic effects. Atherosclerosis 213:449–457
84. Gupta H, White CR, Handattu S, Garber DW, Datta G, Chaddha M, Dai L, Gianturco SH, Bradley WA, Anantharamaiah GM (2005) Apolipoprotein E mimetic peptide dramatically lowers plasma cholesterol and restores endothelial function in Watanabe heritable hyperlipidemic rabbits. Circulation 111:3112–3118
85. Handattu SP, Nayyar G, Garber DW, Palgunachari MN, Monroe CE, Keenum TD, Mishra VK, Datta G, Anantharamaiah GM (2013) Two apolipoprotein E mimetic peptides with similar cholesterol reducing properties exhibit differential atheroprotective effects in LDL-R null mice. Atherosclerosis 227:58–64
86. Sharifov OF, Nayyar G, Ternovoy VV, Mishra VK, Litovsky SH, Palgunachari MN, Garber DW, Anantharamaiah GM, Gupta H (2013) Cationic peptide mR18L with lipid lowering properties inhibits LPS-induced systemic and liver inflammation in rats. Biochem Biophys Res Commun 436:705–710
87. Vitek MP, Christensen DJ, Wilcock J, Davis WE, Van Nostrand Li FQ, Colton CA (2012) APOE-mimetic peptides reduce behavioral deficits, plaques and tangles in Alzheimer's disease transgenics. Neurodegener Dis 10:122–126
88. Vitek MP, Li F, Colton CA (2015) Apolipoprotein-E and mimetics as targets and therapeutics for Alzheimer's Disease. In: Anantharamaiah GM, Goldberg D (eds) Apolipoprotein mimetics in the management of human disease. Springer International Publishing, Basel, pp 157–182
89. Lappegård T, Abendstein Kjellmo C, Ljunggren S, Cederbrant K, Marcusson-Ståhl M, Mathisen M, Karlsson H, Hovland A (2018) Lipoprotein apheresis affects lipoprotein particle subclasses more efficiently compared to the PCSK9 inhibitor evolocumab, a pilot study. Transfus Apher Sci 57:91–96

Part II

In Vitro and Ex Vivo Model Systems for Atherosclerosis Research

Chapter 7

Isolation and Culturing of Primary Mouse and Human Macrophages

Alba de Juan and Begoña Lavin Plaza

Abstract

Macrophages are mature immune cells involved in the defense of the organism. Since their discovery, the main function attributed to macrophages has been phagocytosis. However, in recent years, several new functions such as angiogenesis, tissue remodeling, clearance of apoptotic cells, pro- and anti-inflammatory properties and tumor growth have been attributed to macrophages. To perform such varied functions, macrophages acquire specific phenotypes in response to external signals. The possibility of replicating these phenotypes in vitro represents a cutting-edge tool to understand potential macrophage functions in vivo. This chapter outlines protocols used to isolate and culture murine bone marrow-derived and human monocyte-derived macrophages. Furthermore, macrophage polarization processes into different phenotypes, with special relevance to atherosclerosis, are indicated.

Key words Bone marrow-derived macrophages, Monocyte-derived macrophages, Macrophage polarization, Atherosclerosis

1 Introduction

Macrophages are highly specialized cells of the innate immune system that derive from peripheral blood monocytes and mature once they infiltrate tissues [1, 2]. The first function described for macrophages was phagocytosis, one of the body's defense mechanism against pathogens [3]. Since their discovery, new roles and a wide range of different activities have been attributed to macrophages such as clearance of debris, pro- and anti-inflammatory properties, angiogenesis, tissue remodeling, tumor growth, and metastasis [4, 5]. Even today, highly specialized functions like their role in hematological malignancies [6] and the metabolic control in several tissues and organs [7] have been associated with macrophages which make them a very attractive therapeutic target for inflammatory diseases, including atherosclerosis and cancer. To participate in all these varied functions, macrophages specialize,

Dipak P. Ramji (ed.), *Atherosclerosis: Methods and Protocols*, Methods in Molecular Biology, vol. 2419,
https://doi.org/10.1007/978-1-0716-1924-7_7,
© The Author(s), under exclusive license to Springer Science+Business Media, LLC, part of Springer Nature 2022

depending on the stimuli found in the microenvironment, and acquire unique and specific phenotypes. In the context of atherosclerosis, macrophages are crucial components involved in the development and progression of the atheroma and are heavily involved in plaque rupture, leading to adverse cardiovascular event outcomes and poor patient prognosis [8–10]. Therefore, isolation and culture of macrophages with different ex vivo stimuli have been a very useful and widespread tool to investigate the phenotype and functions of different subtypes of macrophages. At the extremes of the broad macrophage phenotype spectrum, the so-called classical activated macrophages (CAMs or M1 macrophages) are developed in response to T-helper (Th)1 proinflammatory cytokines such as interleukin (IL)-2, IL-12, interferon (IFN)γ, tumor necrosis factor (TNF)α and β, while Th2 cytokines such as IL-4 and IL-13 as well as other anti-inflammatory cytokines like IL-10 and transforming growth factor (TGF)β activate macrophages toward an alternative activated macrophages (AAMs or M2 macrophages) phenotype [11]. In this chapter, we describe the most common in vitro protocols used to isolate and differentiate murine bone marrow-derived macrophages and human peripheral blood-derived macrophages into M1 macrophages and M2 macrophages. Although the mouse and human immune systems exhibit extensive similarities, discrepancies, mainly in the specific M1 and M2 phenotype markers [12] and the methodology to obtain macrophages, need to be taken into account when designing a new experiment. In addition, alternative methods such as macrophage isolation from different cell origins and alternative types of cell stimulation are provided.

2 Materials

2.1 Murine Bone Marrow-Derived Macrophages

1. Murine macrophage colony stimulating factor (M-CSF or CSF-1).
2. Murine IL-4.
3. Murine IFNγ.
4. Lipopolysaccharide (LPS).
5. High-glucose Dulbecco's modified Eagle's medium (DMEM) with stable L-Glutamine.
6. Roswell Park Memorial Institute Medium (RPMI)-1640 with L-glutamine.
7. Sterile phosphate buffered saline (PBS): 137 mM NaCl, 2.7 mM KCl, 10 mM Na_2HPO_4, and 1.8 mM KH_2PO_4, pH 7.4.
8. 10 mg/mL sterile-filtered penicillin–streptomycin (P/S).

9. 10 mg/mL sterile-filtered gentamycin in deionized water.
10. Fetal bovine serum (FBS).
11. Complete DMEM medium: high-glucose DMEM, 10% FBS, 5% P/S.
12. Complete RPMI medium: RPMI-1640 medium with L-glutamine, 10% FBS, 2% P/S.
13. Differentiation medium (two options): DMEM with stable glutamine, 20% FBS, 30% L929-M-CSF Conditioned Medium (LCM), 20 μg/mL gentamycin or DMEM with stable glutamine, 20% FBS, 10 μg/mL recombinant M-CSF, 20 μg/mL gentamycin.
14. Low ($\leq$10 EU/mL) endotoxin FBS (FBS-LE).
15. 0.45 μm vacuum filter unit.
16. Mice: mouse models of atherosclerosis.
17. Appropriate chemical for euthanasia of mice according to Institutional Animal Care and Use Committee.
18. Dissection board or equivalent.
19. Sterile dissection tools: scissors, scalpel, and forceps.
20. 25 G needles.
21. 5–10 mL syringes.
22. Sterile 1.5, 15, and 50 mL tubes.
23. Centrifuge/microcentrifuge.
24. Tissue culture T-75 cm^2 and T-175 cm^2 filter cap flasks.
25. Tissue culture dishes (100 $\times$ 20 mm or 150 $\times$ 20 mm).
26. Sterile tissue culture polystyrene pipettes (2, 10 mL).
27. 6-well plates for macrophage culture.
28. Humidified cell culture incubator with 5% CO_2 at 37 °C.
29. Commercially available Red Blood Cells Lysis Buffer (RBC lysis buffer). Alternatively, the following buffer can be used: 8.26 g ammonium chloride (NH_4Cl), 1 g potassium bicarbonate ($KHCO_3$), 0.037 g EDTA in 1 L ddH_2O.
30. 70% ethanol in distilled water.
31. Freezing medium: 90% FBS, 10% dimethyl sulfoxide (DMSO).
32. M1 Activation Medium: 10% FBS-LE, 20 μg/mL gentamycin, 20 ng/mL IFNγ, 100 ng/mL LPS.
33. M2 Activation Medium: 10% FBS-LE, 20 μg/mL gentamycin, 20 ng/mL IL-4.
34. Hemocytometer.
35. Sterile 200 and 500 μL tips.

36. 90 mm petri dish.
37. Ice.
38. Laminar flow hood.

2.2 Human Monocyte-Derived Macrophages

1. Murine M-CSF. Alternatively, human macrophages can be obtained by stimulation with granulocyte–macrophage colony stimulating factor (GM-CSF) (*see* **Note 1**).
2. Human IL-4.
3. Human IFNγ.
4. LPS.
5. RPMI-1640 medium with L-glutamine.
6. Sterile PBS.
7. 10 mg/mL sterile-filtered P/S.
8. FBS.
9. Human serum (HS).
10. PBS+: Sterile PBS, 0.5% human serum, 2 mM EDTA.
11. Complete RPMI medium: RPMI-1640 medium with L-glutamine, 10% FBS, 2% P/S.
12. Ficoll.
13. Human CD14+ Microbeads (130-050-201, Miltenyi).
14. Large Selection (LS) columns (130-042-401, Miltenyi).
15. 30 μm Pre-Separation Filters (130-041-407, Miltenyi).
16. 50 mL tubes and 50 mL tubes with filters (03-7100SI, DACOS).
17. 15 mL tubes.
18. Magnets MidiMACS.
19. Pipettes.
20. Fridge.
21. Centrifuge.

3 Methods

3.1 Isolation, Culture, and Polarization of Murine Bone Marrow-Derived Macrophages

1. Sacrifice mice using approved procedures of Institutional Animal Care and Use Committee (e.g., overdose of chemical anaesthetics (2–3 times the anaesthetic dose), an overdose of isoflurane, carbon dioxide (CO_2) exposure, cervical dislocation or barbiturate overdose). Confirm euthanasia using approved protocols such as cervical dislocation, decapitation, bilateral thoracotomy, vital tissue harvest or continued exposure to CO_2 for at least 15 min after a respiratory arrest (*see* **Note 2**).

2. Place the animals on a dissection board or equivalent and spray abdomen and hind-limbs with 70% ethanol to create a sterile surgical area and to avoid leftover fur that could contaminate the samples.
3. Perform a midline incision in the abdomen skin and peritoneum, exposing the guts that are removed from the animal, allowing for the dissection of the muscles attached to the pelvis and femurs.
4. Remove both hind limbs by cutting at the hip joint level. From each hind limb, one femur and one tibia should be collected (i.e., two femurs and two tibiae per mouse).
5. With the help of dissecting scissors, scalpel and tweezers, remove the skin and muscle of the hind limb to expose the bones. Cut at the level of the knee joint to separate femurs, tibiae and fibula and at the ankle joint, to separate the tibiae from the foot. Separate the fibula and discard from the tibia as no bone marrow is extracted from them (*see* **Note 3**).
6. Transfer bones (femurs and tibiae) from a single animal into a 15 mL tube containing 5 mL of PBS on ice. Perform all subsequent steps in a laminar flow hood.
7. For the isolation of bone marrow and in vitro culture, first add the two femurs and two tibiae to a standard 90 mm petri dish. Cut the epiphyses of all the bones to have access to the bone marrow. Two protocols can be performed to isolate the bone marrow as detailed below:
   (a) Centrifugation protocol: A 200 and 500 μL sterile tip and a 1.5 mL sterile tube are needed per bone. Cut the upper part of both tips with the help of a scalpel, insert the 200 μL tip into the 500 μL tip and introduce them in the 1.5 mL tube with the narrow end facing the bottom of the tube. With the help of forceps, place one bone inside the 200 μL tip and close the tube. Repeat this procedure with all bones. To obtain the bone marrow, centrifugate tubes at 310 × *g* for 3 min at room temperature in a microcentrifuge (*see* **Note 4**).
   (b) Flush protocol: A standard 90 mm petri dish, PBS, a 25 G needle and a 5 mL syringe are needed. Fill the syringe with PBS and insert the 25 G needle. Then, introduce the needle at one end of the bone and flush with PBS to allow the bone marrow to be expelled out from the bone into the Petri dish. Repeat this protocol with each of the four bones per mouse (*see* **Note 5**). Collect all the bone marrow into a 50 mL tube and centrifugate at 310 × *g* for 5 min at room temperature to pellet down the cells.

8. Resuspend the pellet from **step 7** with 500 μL of Red Blood Cell lysis buffer and keep on ice for 5 min. The bone marrow can be either used fresh or frozen and stored at −80 °C for future use. Use freezing medium if the bone marrow is frozen (*see* **Note 6**).
9. Prepare differentiation medium containing 500 mL of DMEM, 1 mL of 10 mg/mL gentamycin, and 100 mL of FBS. To stimulate macrophage differentiation, add 50 ng/mL murine M-CSF to the medium. Alternatively, 30% non-commercial L929-M-CSF Conditioned Medium (LCM) can be used (*see* **Note 7**).
10. Resuspend fresh or thawed frozen bone marrow in prewarmed (37 °C) differentiation medium and count cells.
11. Plate cell suspension in eight standard 100 × 20 mm dishes or four 150 × 20 mm dishes or eight 6-well plates or a combination of both as follows: 6–8 × 10^6 cells with 8 mL of differentiation medium in 100 × 20 plate or 12–15 × 10^6 cells with 20 mL of differentiation medium in 150 × 20 plate or 1.5–2 × 10^6 cells with 2 mL of differentiation medium in 6-well plate.
12. Culture cells for 6–7 days in differentiation medium using a humidified incubator at 37 °C with 5% CO_2. On Day 3, supplement the cells with an additional volume of differentiation medium. Wash cells with PBS at Day 5 and culture in fresh differentiation medium (*see* **Note 8**).
13. At Day 6–7, macrophages are fully differentiated as over 90% of the cultured cells contain the surface marker CD11b [13]. These cells are considered proliferative, nonactivated cells and are generally known as M0 macrophages. Cultured cells are now ready for macrophage polarization as **step 14**.
14. Remove the medium from M0 macrophages and wash them with PBS (*see* **Note 9**). Polarize M0 macrophages into M1 phenotype by incubation in M1 Activation Medium in a cell culture incubator. Alternatively, polarize M0 macrophages into M2 phenotype by incubation in M2 Activation Medium in a cell culture incubator (*see* **Note 10**).
15. Incubate M0 macrophages with the corresponding polarization mediums for 24 h or 48 h for RNA or protein analysis, respectively. Alternatively, cells can be incubated with the polarization medium overnight before further experimentation.
14. As an alternative to BMDMs, murine macrophages can be also isolated from the peritoneum of mice (*see* **Note 11**).

3.2 Isolation and Culture of Human Monocyte-Derived Macrophages

1. Isolate human peripheral blood mononuclear cells (PBMCs) from blood obtained from healthy donors, using the density gradient medium called Ficoll. Add 16 mL of Ficoll to 50 mL tubes with special filters and centrifuge for 5 min at 600 × *g* at room temperature to place the Ficoll separation medium below the filters (*see* **Note 12**).
2. Transfer the blood gently to the tubes with the Ficoll ready bellow the filters.
3. Centrifuge the tubes with the blood and the Ficoll for 15 min at 800 × *g* at room temperature without any break (*see* **Note 13**).
4. From the different phases obtained, collect the white ring with the cells of interest, usually in the middle, and transfer it to a new 50 mL tube.
5. Wash the cells 3 times with PBS, filling up the 50 mL tube followed by centrifugation at 4 °C for 5 min and 400 × *g*.
6. Discard the supernatants and resuspend the final pellet of the cells in 50 mL of PBS. Use a dilution of 1:10 for counting the cells using a hemocytometer.
7. Keep the cells in complete RPMI medium supplemented with 10% FBS and 2% P/S.
8. Monocytes are enriched from human PBMCs using a positive CD14+ selection with magnetic microbeads (*see* **Note 14**).
9. Use 100 μL of CD14+ microbeads in 1 mL of PBS supplemented with PBS+ for each 400 million of PBMCs. Incubate the cells at 4 °C (in the fridge and not on ice) for 15 min.
10. Place the LS columns on the magnets and wash them with 3 mL of cold PBS (*see* **Note 15**).
11. After the 15-min incubation (**step 9**), wash the cells with cold PBS and centrifuge them at 4 °C for 5 min at 400 × *g*.
12. Resuspend the cells in 1 mL of PBS+ and transfer them to the columns on the magnets (*see* **Note 16**).
13. Wash the columns 3 times with 3 mL of PBS+.
14. Transfer the columns to 15 mL tubes with no magnets and flush the cells with 4 mL PBS+ with the help of the plunger from the syringe included in the LS column.
15. Count the cells to calculate the suitable concentration (two million of CD14+ per mL).
16. Culture CD14+ cells for 5 days in RPMI supplemented with 10% FBS, 2% P/S and 100 ng/mL M-CSF.
17. After 5 days, almost every cell has differentiated into M0 macrophages and are ready for the polarization protocol (*see*

step 14 in Subheading 3.1). Remove cell culture containing M-CSF and wash the cells with PBS.

18. Culture M0 macrophages for 7 days in RPMI supplemented with 10% FBS, 2% P/S and 100 ng/mL LPS plus 20 ng/mL IFN-γ (for M1 polarization) or 20 ng/mL IL-4 (for M2 polarization).

4 Notes

1. GM-CSF is a cytokine secreted by macrophages, T cells, mast cells, natural killer cells, endothelial cells and fibroblasts which stimulates other cells. The effect of GM-CSF on monocytes includes the exit from the bloodstream and migration into the specific tissue, where they mature into macrophages and dendritic cells. Due to this promaturation effect, GM-CSF has also been used in vitro to obtain monocyte-derived macrophages or in combination with IL-4 to obtain monocyte-derived dendritic cells. Several groups have studied the differences of macrophages obtained using M-CSF and GM-CSF. While M-CSF favors the generation of macrophages with a resting/anti-inflammatory phenotype, GM-CSF has been shown to induce the expression of some proinflammatory genes. For this reason, monocyte-derived macrophages obtained with M-CSF are described in some studies as M0/M2-like macrophages while macrophages resulting after stimulation with GM-CSF are known as M1-like macrophages [14–16]. The choice of using M-CSF or GM-CSF depends on which type of in vivo environment the researcher wishes to mimic in vitro.
2. The three Rs (3Rs) are the guiding principles for more ethical use of animals in research. Replacement stands for methods that avoid, or replace, the use of animals in research. Reduction uses methods that enable researchers to obtain comparable levels of information from fewer animals or to obtain more information from the same number of animals. Refinement relates to methods that alleviate or minimize potential pain, suffering or distress, and enhance welfare of the animals used. The 3Rs have a broader scope than simply encouraging alternatives to animal testing, aiming to improve animal welfare and scientific quality where the use of animals cannot be avoided. In many countries, these 3Rs are now explicit in legislation governing animal use.
3. Further cleaning of femurs and tibiae is required to avoid potential contaminations from skin and muscle.
4. The bone becomes transparent once the full bone marrow has been expelled out and pelleted in the tube. The procedure

should be repeated if this is not achieved with the first centrifugation.

5. Similar to the previous protocol (**step 7**), the transparency of the bone will be an indicator of the correct isolation of the bone marrow.
6. No differences have been observed in macrophage differentiation and/or response to different stimuli when derived from frozen bone marrow [17].
7. Preparation of L929-M-CSF Conditioned Medium (LCM) consists of culturing the murine fibroblast cell line L929 and collecting the supernatant, which contains M-CSF secreted by the cells [17]. In a basic protocol, 5×10^5 M-CSF L929 cells are cultured in 10 mL of complete DMEM medium in 100 × 20 mm standard tissue culture dish till confluent. At this point, cells can be expanded in several T-75 cm flasks with 40 mL of complete DMEM media. Once confluent, collect conditioned media and replace it with fresh media. This process can be repeated up to 5 times every 48 h. After each medium collection, perform centrifugation of the medium at $1000 \times g$ for 5 min at 4 °C to pellet the cells. Then, transfer the medium to a new 50 mL tube and store at 4 °C. At the end of the medium collection step, filter all medium using a 0.45 μm filter attached to a vacuum unit under the laminar hood. Finally, store LCM medium in 50 mL aliquots at −20 °C until required. Validation of each LCM medium batch is required as L929 cells could potentially produce different amounts of M-CSF, as well as other molecules. An indicator of an appropriate LCM would be the correct cell attachment of cells to which it is added within a day in noncoated petri dishes.
8. In this step, it is important to check cell density and potential contaminations. Ideally, around the 90% of the plate should be covered by cells showing a rounded shape. The culture medium should not show any indication of contamination, which can potentially be evaluated by checking for bacteria in the medium under the magnifier and changes of the colour of the culture media as an indicator of changes in the pH, among others.
9. Removal of M-CSF from the medium minimizes potential interferences with the subsequent polarization process.
10. M1 and M2 phenotypes represent the extremes of the macrophage polarization process. However, intermediate phenotypes have also been discovered in vivo and associated with different pathological states. Additionally, and in the broad sense of the concept, macrophages can be "alternatively activated" by other stimuli and in fact, different macrophage phenotypes, and consequently associated functions, have been described over the last years. The classical M1 and alternative M2 activation of

macrophage phenotypes are thought to be at the extremes of the spectrum. Among the phenotypes of M2 macrophages, different subsets have been described: M2a (induced by IL-4 or IL-13), M2b (induced by immune complex, Toll-like receptor (TLR)), M2c (induced by glucocorticoids, IL-10, and TGF-β) and M2d (induced by TLR antagonists). These macrophage subtypes express different surface markers, secrete different cytokines and have different biological functions [15, 16, 18–21].

11. In summary, once mice have been euthanized, a small incision is made in the abdomen. After removing the abdominal skin to expose the peritoneum, inject 4–5 mL of PBS into the peritoneal cavity (using 5 mL syringe and a 25 G needle), avoiding puncturing the intestine or other organs. Gently massage the abdomen of the mice and try to recover as much PBS as possible with the same 5 mL syringe and a 25 G needle. Macrophages obtained with this method are considered steady-state resting (M0) macrophages. They can be centrifuged and resuspended in the required volume for culture. Macrophage yield can be increased by intraperitoneal injection of thioglycolate. The number of macrophages in the peritoneum is usually very low, being insufficient to perform some in vitro experiments and analysis. To increase the numbers of recruited macrophages, injection of sterile thioglycolate into the peritoneal cavity preceding the cell harvest can be performed. After thioglycolate injection, the yield of macrophages per mouse increases by tenfold. Although this is a wide-spread technique, some detractors have suggested that thioglycolate acts as an irritant that induces an inflammatory response leading to an increase in the recruitment of macrophages that might affect gene expression and activity [22]. Another point to take into consideration is the presence of B and T cells, in addition to macrophages, in the peritoneal cavity. Enrichment for macrophages or negative section for a similar kind of cell, for example monocytes, is therefore highly recommended.
12. It is important to keep this medium at room temperature since any changes of temperature can alter its density and affect the PBMCs isolation. Alternatively, normal 50 mL Falcon tubes can be used.
13. This step can take 5 min longer due to the lack of a break.
14. CD14+ monocytes represent about 80–95% of circulating monocytes. However, other populations have been characterized as representing a minor fraction of the blood monocytes and some protocols to obtain in vitro monocyte-derived macrophages do not include a monocyte subtype selection step. Flow cytometry analysis has allowed identification of

three different populations of human monocytes in peripheral blood, known as classical (CD14++, CD16−), intermediate (CD14+, CD16+) and nonclassical (CD14+, CD16++) monocytes. Classical monocytes comprise about 80–95% of circulating monocytes. These cells are highly phagocytic and are known to be important scavenger cells. Intermediate monocytes comprise about 2–8% of circulating monocytes. Their functions include the production of reactive oxygen species (ROS), antigen presentation, participation in the proliferation and stimulation of T cells, inflammatory responses, and angiogenesis. Nonclassical monocytes comprise about 2–11% of circulating monocytes. They are mobile cells and patrol the endothelium in search of injury [23].

15. LS columns have a syringe shape. It is necessary to separate the column from the plunge, place it on the magnets and use the plunge for the **step 14**.
16. When starting from a high quantity of cells, place the Pre-Separation Filters (30 μm) on the top of the columns to avoid cell aggregation.

Acknowledgments

The authors would like to thank Oscar M. Pello for providing advice on different aspects of this work.

References

1. Perdiguero EG, Geissmann F (2016) The development and maintenance of resident macrophages. Nat Immunol 17:2–8. https://doi.org/10.1038/ni.3341
2. Coillard A, Segura E (2019) *In vivo* differentiation of human monocytes. Front Immunol 10:1907. https://doi.org/10.3389/fimmu.2019.01907
3. Gordon S (2016) Phagocytosis: the legacy of Metchnikoff. Cell 166:1065–1068. https://doi.org/10.1016/j.cell.2016.08.017
4. Jakubzick CV, Randolph GJ, Henson PM (2017) Monocyte differentiation and antigen-presenting functions. Nat Rev Immunol 17:349–362. https://doi.org/10.1038/nri.2017.28
5. Guilliams M, Mildner A, Yona S (2018) Developmental and functional heterogeneity of monocytes. Immunity 49:595–613. https://doi.org/10.1016/j.immuni.2018.10.005
6. Petty AJ, Yang Y (2019) Tumor-associated macrophages in hematologic malignancies: new insights and targeted therapies. Cells 8(12):1526. https://doi.org/10.3390/cells8121526
7. Nicolás-Ávila JA, Lechuga-Vieco AV, Esteban-Martínez L et al (2020) A network of macrophages supports mitochondrial homeostasis in the heart. Cell 183(1):94–109.e23. https://doi.org/10.1016/j.cell.2020.08.031
8. Andrés V, Pello OM, Silvestre-Roig C (2012) Macrophage proliferation and apoptosis in atherosclerosis. Curr Opin Lipidol 23(5):429–438. https://doi.org/10.1097/MOL.0b013e328357a379
9. Pello OM, Silvestre C, De Pizzol M et al (2011) A glimpse on the phenomenon of macrophage polarization during atherosclerosis. Immunobiology 216(11):1172–1176. https://doi.org/10.1016/j.imbio.2011.05.010
10. Lavin B, Phinikaridou A, Anidia ME et al (2020) Sustained vascular inflammation accelerates atherosclerosis in remote arteries. Atheroscler Thromb Vasc Biol 40:2159–2170.

https://doi.org/10.1161/ATVBAHA.120.314387

11. Murray PJ, Allen JE, Biswas SK et al (2014) Macrophage activation and polarization: nomenclature and experimental guidelines. Immunity 41:14–20. https://doi.org/10.1016/j.immuni.2014.06.008
12. Jablonski KA, Amici SA, Webb LM (2015) Novel markers to delineate murine M1 and M2 macrophages. PLoS One 10(12): e0145342. https://doi.org/10.1371/journal.pone.0145342
13. Schmid MC, Khan SQ, Kaneda MM et al (2018) Integrin CD11b activation drives anti-tumor innate immunity. Nat Commun 9(1): 5379. https://doi.org/10.1038/s41467-018-07387-4
14. Sierra-Filardi E, Puig-Kröger A, Blanco FJ (2011) Activin A skews macrophage polarization by promoting a proinflammatory phenotype and inhibiting the acquisition of anti-inflammatory macrophage markers. Blood 117(19):5092–5101. https://doi.org/10.1182/blood-2010-09-306993
15. Yao Y, Xu XH, Jin L (2019) Macrophage polarization in physiological and pathological pregnancy. Front Immunol 10:792. https://doi.org/10.3389/fimmu.2019.00792
16. Palma A, Jarrah AS, Tieri P (2018) Gene regulatory network modeling of macrophage differentiation corroborates the continuum hypothesis of polarization states. Front Physiol 9:1659. https://doi.org/10.3389/fphys.2018.01659
17. Marim FM, Silveira TN, Lima DS et al (2010) A method for generation of bone marrow-derived macrophages from cryopreserved mouse bone marrow cells. PLoS One 5(12): e15263. https://doi.org/10.1371/journal.pone.0015263
18. Kadl A, Meher AK, Sharma PR et al (2010) Identification of a novel macrophage phenotype that develops in response to atherogenic phospholipids via Nrf2. Circ Res 107(6): 737–746. https://doi.org/10.1161/CIRCRESAHA.109.215715
19. Gleissner CA (2012) Macrophage phenotype modulation by CXCL4 in atherosclerosis. Front Physiol 3:1. https://doi.org/10.3389/fphys.2012.00001
20. Boyle JJ (2012) Heme and haemoglobin direct macrophage Mhem phenotype and counter foam cell formation in areas of intraplaque haemorrhage. Curr Opin Lipidol 23(5):453–461. https://doi.org/10.1097/MOL.0b013e328356b145
21. de Sousa JR, Da Costa Vasconcelos PF, Quaresma JAS (2019) Functional aspects, phenotypic heterogeneity and tissue immune response of macrophages in infectious diseases. Infect Drug Resist 12:2589–2611. https://doi.org/10.2147/IDR.S208576
22. Layoun A, Samba M, Santos MM (2015) Analysis upon toll-like receptors stimulation. J Vis Exp 98:52749. https://doi.org/10.3791/52749
23. Ziegler-Heitbrock L, Ancuta P, Crowe S et al (2010) Nomenclature of monocytes and dendritic cells in blood. Blood 116(16):e74–e80. https://doi.org/10.1182/blood-2010-02-258558

Chapter 8

Effective Transfection and Gene Silencing of Primary Murine Macrophages with Small Interfering RNA

Kim van Kuijk, Jan Nagenborg, and Judith C. Sluimer

Abstract

Transfection of murine primary macrophages to silence genes can be a challenging procedure because this cell type has developed mechanisms to evade cellular intrusion. The introduction of small interfering RNA (siRNA) encapsulated in liposomes to the cell to decrease gene expression is one of the methods that can be used to achieve gene silencing. There are different commercially available compounds to introduce siRNA into the cell, including Lipofectamine RNAiMAX and HiPerfect. The chapter will describe a method for gene silencing in mouse primary macrophages using liposome-based transfection of siRNA.

Key words Transfection, Macrophages, Primary cells, siRNA, RNA interference

1 Introduction

Macrophages are sensitive sensors of their environment to maintain the homeostatic state of various tissues in addition to being part of the innate immune system and fulfilling important immune functions in mouse and humans [1, 2]. As phagocytes, their main function is to engulf and digest foreign and potentially harmful particles, dead cells, and cell debris. Furthermore, they are capable of modulating their microenvironment via secretion of cytokines as a response to phagocytosis and activation. Macrophages maintain homeostatic conditions by either fueling or dampening inflammation [3, 4]. This is a delicate balance that is preserved in healthy conditions. A distortion of this balance, however, can result in increased tissue dysfunction, such as in atherosclerosis [5, 6]. Atherosclerosis is driven by a state of chronic inflammation due to macrophages' inability to resolve inflammation. This failed resolution results in an increase in macrophage content in the plaque, increased apoptosis of macrophages following extensive lipid uptake and an overall proinflammatory environment due to cytokine secretion together with the release of inflammatory particles

Dipak P. Ramji (ed.), *Atherosclerosis: Methods and Protocols*, Methods in Molecular Biology, vol. 2419,
https://doi.org/10.1007/978-1-0716-1924-7_8,
© The Author(s), under exclusive license to Springer Science+Business Media, LLC, part of Springer Nature 2022

from apoptotic and necrotic cells [7, 8]. Recent research has shown that particular phenotypes of macrophages are characterized by specific gene expression profiles and functions [9–11]. Altering gene expression of macrophages represents a promising way to modulate their phenotype and functions. The main function of macrophages as scavengers and consequently in effective degradation of intracellular foreign nucleic acids makes it hard to effectively silence genes in these cells [12].

A common approach to alter gene expression is gene silencing via small interfering RNA (siRNA). RNA interference is a natural defense mechanism for targeted gene silencing in eukaryotic cells. Delivering short double stranded RNA into the cell results in the specific silencing of genes highly homologous in their sequence [13]. In the past, several approaches for the delivery of foreign nucleic acids have been reported: physical disruption by electroporation, cationic polymers, and cationic lipids. Electroporation requires relatively expensive equipment. Also, the physical disruption of the membrane to introduce siRNA greatly affects the viability of the cells. Cationic polymers such as diethylaminoethyl (DEAE)-dextran form complexes with siRNA and binds to the membrane to facilitate their uptake via endocytosis. Although using cationic polymers is a simple method, the transfection efficiency of cells is relatively low compared to the efficiency of cationic lipids [14]. Cationic lipids such as Lipofectamine RNAiMAX or HiPerfect form complexes with siRNA similar to cationic polymers. The formed lipid vesicles fuse with the membrane and release the siRNA into the cytosol. This delivery approach represents a simple and highly effective transfection method combined with relatively low costs [14]. In this chapter, we address how to successfully transfect primary macrophages for efficient gene silencing and functional studies.

2 Materials

2.1 Production of L929 Cell Conditioned Medium

1. L929 cell line (NCTC clone 929, L cell, L-929, derivative of Strain L, ATCC® CCL-1™).
2. Cell culture medium: Roswell Park Memorial Institute (RPMI) 1640 with GlutaMAX™ supplemented with 25 mM HEPES, 10% heat-inactivated fetal calf serum (FCS; 56 °C for 30 min), 1% penicillin–streptomycin (P/S) (*see* **Note 1**).
3. T75 and T175 tissue culture flasks.
4. Sterile phosphate buffered saline (PBS).
5. Multistack culture chamber.
6. 5% CO_2 cell culture incubator.
7. Centrifuge.

8. Disposable vacuum filter system.
9. Water bath at 37 °C.

2.2 Isolation, Culturing, and Differentiation of Primary Macrophages

1. Mouse strain and transgene of choice (e.g., C57BL6/J mice).
2. Sterile Dulbecco's phosphate buffered saline (DPBS) with Calcium and Magnesium: 200 mg/L potassium chloride, 200 mg/L potassium phosphate monobasic, 8000 mg/L sodium chloride, 1150 mg/L sodium phosphate dibasic.
3. Differentiation medium: Cell culture medium supplemented with 15% L929 cell conditioned medium (*see* **Note 2**).
4. Trypsin (0.25% in sterile DPBS).
5. Macrophage detachment solution in DPBS: 40 mg/mL Lidocaine, 10 mM ethylenediaminetetraacetic acid (EDTA).
6. 10 mm^2 noncoated tissue culture dishes.
7. 24-well noncoated tissue culture plates.
8. 1 and 20 mL syringes.
9. 23G needles.
10. 70 μm cell strainers.
11. Sterile 50 mL tubes.
12. Sterile laminar flow hood.
13. Sterile pipettes and tips.
14. Scissors and forceps.
15. 70% ethanol.
16. Centrifuge at 4 °C.
17. Ice.

2.3 Transfection of Cells

1. siRNA for gene of interest and a scrambled siRNA (*see* **Note 3**). Fluorescently labeled siRNA can be included for monitoring transfection efficiency.
2. RNase-free water.
3. Lipofectamine transfection reagent (e.g., HiPerfect from Qiagen or RNAiMAX from ThermoFisher Scientific).
4. Opti-MEM (e.g., Thermofisher Scientific) (*see* **Note 4**).

3 Methods

3.1 Production of L929 Cell Conditioned Medium

1. Thaw L929 cells in water bath at 37 °C.
2. Resuspend L929 cells in cell culture medium and plate in T75 tissue culture flask at a density of 0.02×10^6 cells/cm^2.

3. Culture L929 cells to 80–90% confluency in T75 tissue culture flask.
4. Aspirate medium, wash with sterile PBS and incubate with trypsin (*see* Subheading 2.2) to detach the L929 cells.
5. Centrifuge at 350 × *g* and resuspend L929 cells by adding an equal volume of cell culture medium to the flask ensuring no clumping of the cells.
6. Expand L929 cells to obtain five, confluent T175 tissue culture flasks.
7. Centrifuge at 350 × *g*, resuspend cells in 2000 mL cell culture medium, and transfer to multistack culture chamber.
8. Incubate cells for 10 days and centrifuge at 350 × *g*.
9. Harvest the supernatant, sterilize through disposable vacuum filter system, and store at −80 °C until further use.

3.2 Isolation, Culturing and Differentiation of Primary Murine Bone Marrow–Derived Macrophages (BMDM) (See Note 5)

Primary macrophages are cultured in a cell culture incubator at 37 °C and 5% CO_2.

1. Clean mouse with 70% ethanol and remove skin around the hindlegs using scissors and forceps.
2. Excise the femur and tibia from the mice and remove the bones from the remaining muscle tissue using scissors and forceps (*see* **Note 6**). Keep the bones on ice from this step onward and work in a laminar flow hood to ensure a sterile environment.
3. Clean the femur and tibia first in 70% ethanol and subsequently in sterile PBS.
4. Cut the femur and tibia open on both sides.
5. Insert a 20 mL syringe into both bones using a 23G needle and flush both bones with 10 mL ice-cold sterile PBS through a 70 μm cell strainer into a sterile 50 mL tube (*see* **Note 7**).
6. Flush the remaining bone marrow through the 70 μm cell strainer using the plunger of a 1 mL syringe. This step will maximize yield.
7. Rinse the cell strainer with ice-cold PBS.
8. Centrifuge the bone marrow cells at 300 × *g* for 4 min at 4 °C (*see* **Note 8**).
9. Resuspend cells in differentiation medium. Plate the cells from one femur and tibia in a 10 mm^2 noncoated tissue culture dishe and place in a cell culture incubator (37 °C, 5% CO_2).
10. On day 4, add additional differentiation medium, that is 50% of the volume.
11. On day 6, replace the medium with fresh differentiation medium.

12. On day 7, detach cells from the tissue culture dishes using macrophage detachment solution in sterile DPBS (*see* **Note 9**).
13. After cell detachment from the plate, add an equal volume of sterile PBS to inactivate the lidocaine. Plates can be washed using sterile PBS to maximize cellular yield.
14. Centrifuge cells at 300 × *g* for 4 min at 4 °C and resuspend in differentiation medium (*see* **Note 8**).
15. Plate macrophages at a density of 0.1×10^6 cells/cm^2 in 24-well noncoated tissue culture plates (*see* **Note 10**).

3.3 Transfection of Cells

Opti-MEM should be used at room temperature while culture medium should be preheated in a 37 °C water bath. It is important to include good, relevant controls to evaluate morphological changes, expression of the target gene and/or inflammatory markers under investigation. These should include a scramble siRNA with transfection reagent, transfection reagent only and a negative control without siRNA or transfection reagent (*see* **Note 3**).

1. Warm Opti-MEM to room temperature (*see* **Note 4**).
2. Dilute the siRNA of interest and control siRNA to 50 nM in 47 μL of Opti-MEM per well of a 24-well tissue culture plate (*see* **Notes 11** and **12**).
3. Add 3 μL of HiPerfect to the diluted siRNA and vortex for 2–5 s.
4. Let mix of siRNA and HiPerfect stand at room temperature for 5–10 min.
5. Remove the cell culture medium and wash cells once with Opti-MEM (*see* **Note 4**).
6. Change medium to 150 μL of Opti-MEM (*see* **Note 4**).
7. Add 50 μL of the mix of siRNA and HiPerfect to cells and gently swirl the plate.
8. Incubate cells in cell culture incubator for 6 h.
9. Add 400 μL of cell culture medium without P/S (*see* **Note 13**).

3.4 Posttransfection

1. Transfection efficiency can be monitored using a fluorescently labeled siRNA (Fig. 1).
2. Collect the cells after the appropriate time of incubation depending on the downstream readout (*see* **Note 14**). These could include use of TRIzol for RNA analysis or protein lysis buffer in case of protein analysis (Fig. 2). If desired, functional assays can be performed after siRNA transfection such as proliferation, migration or inflammatory responses (*see* **Note 15**).

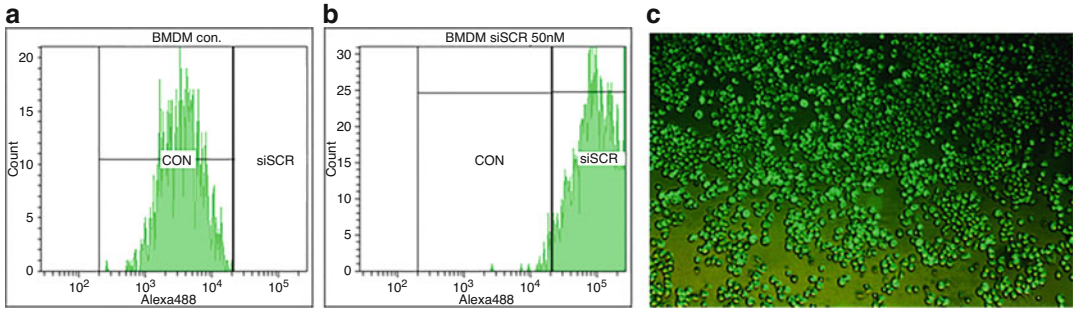

Fig. 1 Transfection efficiency of fluorescently labeled siSCR (Alexa Fluor 488, 50 nm). (**a**) Counts of A488-labeled BMDM 30 h posttransfection without and (**b**) with 50 nM of siRNA and 3 μL of HiPerfect measured by flow cytometry. (**c**) Image of the cells produced using brightfield microscopy (100×)

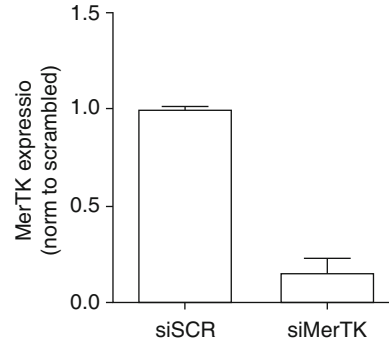

Fig. 2 Gene silencing following HiPerfect transfection of siRNA into BMDMs. Relative gene expression of the gene of interest (MerTK) compared to siSCR (scramble) in BMDM 30 h posttransfection with 50 nM of siRNA and 3 μL of HiPerfect

4 Notes

1. Growth factors in FCS can slightly affect cells, including macrophage behavior, and hence heat inactivation is required. In addition, using same FCS batches between experiments will reduce variation in readouts.
2. It is also possible to use commercially available M-CSF instead of L929 cell conditioned medium. It is recommended to treat the cells with 10 ng/mL M-CSF and replenish the medium with new M-CSF every 2 days.
3. siRNA against the gene of interest can be either purchased from commercial sources or designed using the following parameters: contiguous G and C nucleotides should be avoided; GC content should be between 35 and 55%; specificity against the gene of interest should be high; and off-target binding should be limited [15]. Generally, 2–3 siRNAs should be

designed, which should allow comparison of silencing efficiency as well as an independent confirmation of a phenotypic change.

4. Opti-MEM is especially recommended when performing transfection experiments with lipofectamine reagents as this allows the use of reduced serum concentration with a minimum of 50%. Alternatively, cell culture medium with reduced percentage of FCS may be tried (e.g., 2% or 5% FCS).
5. The transfection methods described in this chapter are also applicable to primary macrophages from other species, such as human peripheral blood-derived mononuclear cells.
6. When putting pressure on the spine with the scissors, movement of the tail can be used as an indicator for the excision point. It is important to cut the spine at a point where the tail is not moving anymore. At that point, the hip joint will stay unharmed and dislocation of the femur will occur under sterile conditions.
7. Cut off the minimal amount of bone necessary to flush femur and tibia. This is important as most progenitor cells reside in the head of the bone, normally located in the hip or knee joint.
8. Centrifugation should not be too harsh as this can influence macrophage behavior and therefore, inflammatory status.
9. Lidocaine detachment is needed as experience has shown that macrophages are very hard to detach from cell culture plates.
10. Cells should be plated 24 h before transfection to optimize cellular condition and prevent cellular stress responses as these can influence transfection efficiency.
11. Optimization includes testing the concentrations of siRNA (25, 50, and 100 nM) and lipofectamine reagent (1.5, 3 and 6 μL). In our experience, 50 nM siRNA works best for transfecting ~98% of primary macrophages with silencing efficiency between 60 and 90% (Figs. 1 and 2). Using higher concentrations of siRNA can induce cellular stress responses and thus transfection efficiency. RNAiMAX may be used instead of Lipofectamine at 1 μL and 25 nM siRNA for a 24-well plate of BMDM. Transfection efficiency and silencing are largely similar.
12. Volume is dependent on the well size (e.g., in the case of a 24-well plate, addition of 50 μL mix of siRNA and HiPerfect is recommended).
13. The presence of antibiotics in cell culture media could lead to cellular toxicity and lower the transfection efficiency. Therefore, it is recommended to use culture medium without antibiotics for transfection steps.

14. Time of collection can vary between 24 and 72 h depending on the expression levels of the gene of interest as well as half-life of the target protein.
15. In our experience, knockdown is sustained for at least 24 h after medium change.

References

1. Wynn TA, Chawla A, Pollard JW (2013) Macrophage biology in development, homeostasis and disease. Nature 96(7446):445–455
2. Mosser DM, Hamidzadeh K, Goncalves R (2020) Macrophages and the maintenance of homeostasis. Cell Mol Immunol 15:1–9
3. Watanabe S, Alexander M, Misharin AV, Budinger GRS (2019) The role of macrophages in the resolution of inflammation. J Clin Invest 192(7):2619–2628
4. Murray PJ, Wynn TA (2011) Protective and pathogenic functions of macrophage subsets. Nat Rev Immunol 11(11):723–737
5. Moore K, Sheedy F, Fisher E (2013) Macrophages in atherosclerosis: a dynamic balance. Nat Rev Immunol 13(10):709–721
6. Moore KJ, Tabas I (2011) Macrophages in the pathogenesis of atherosclerosis. Cell 145(3): 341–355
7. Lusis AJ (2000) Atherosclerosis. Nature 407: 233–241
8. Haansson GK, Robertson ANL, Söderberg-Nauclér C (2006) Inflammation and atherosclerosis. Annu Rev Pathol Mech Dis 1: 297–329
9. Murray PJ (2017) Macrophage polarization. Annu Rev Physiol 79:541–566
10. Gautier EL, Shay T, Miller J et al (2012) Gene expression profiles and transcriptional regulatory pathways underlying mouse tissue macrophage identity and diversity. Nat Immunol 13(11):1118–1128
11. Xue J, Schmidt SV, Sander J et al (2012) Transcriptome-based network analysis reveals a spectrum model of human macrophage activation. Immunity 40(2):274–288
12. Crowl JT, Gray EE, Pestal K et al (2017) Intracellular nucleic acid detection in autoimmunity. Annu Rev Immunol 35:313–336
13. Cerutti H, Mollano C (2006) On the origin and functions of RNA-mediated silencing: from protists to man. Curr Genet 50:81–99
14. Dokka S, Toledo D, Shi X et al (2000) High-efficiency gene transfection of macrophages by lipoplexes. Int J Pharm 206:97–104
15. Naito Y, Ui-Tei K (2012) siRNA design software for a target gene-specific RNA interference. Front Genet 3:102

Chapter 9

Monitoring Cellular Proliferation, Migration, and Apoptosis Associated with Atherosclerosis Plaques In Vitro

Kerry S. Wadey, Alexandros Somos, Stephen J. Cross, Lien M. Reolizo, Jason L. Johnson, and Sarah J. George

Abstract

Bromodeoxyuridine/5-bromo-2′-deoxyuridine (BrdU) is a nucleoside analog of thymidine and its incorporation into DNA during replication within S-phase of the cell cycle is used to quantify cell proliferation. Quantification of incorporated BrdU is considered the most direct measure of cell proliferation, and here we describe BrdU incorporation into cultured vascular smooth muscle cells (VSMCs) and endothelial cells in vitro. Incorporation of fluorescent-labeled ethynyldeoxyuridine/5-ethynyl-2′-deoxyuridine (EdU) is a novel alternative to BrdU assays and presents significant advantages. This method of detection of EdU based on a simple "click" chemical reaction, which covalently bonds EdU to a fluorescent dye is also outlined in this chapter with a protocol for quantitative analysis of EdU incorporation using a Fiji-based macro. We also describe how proliferation can be assessed by quantification of classical proliferative markers such as phopsho-Ser807/811 retinoblastoma (Rb), proliferating cell nuclear antigen (PCNA) and cyclin D1 by Western blotting. As these markers are involved in different aspects of the cell cycle regulation, examining their expression levels can not only reveal the relative population of proliferating cells but can also improve our understanding of the mechanism of action of a given treatment or intervention. The scratch wound assay is a simple and cost-effective technique to quantify cell migration. A protocol which involves creating a wound in a cell cultured monolayer and measuring the distance migrated by the cells after a predefined time period is also described. Gap creation can also be achieved via physical cell exclusion where cells are seeded in distinct reservoirs of a cell culture insert which reveal a gap upon removal. Cell migration may then be quantified by monitoring the rate of gap closure. The presence of cleaved caspase-3 is a marker of programmed cell death (apoptosis). To detect cleaved caspase-3 in vitro, immunocytochemistry and fluorescence can be performed as outlined in this chapter.

Key words Proliferation, DNA synthesis, BrdU, EdU, Migration, Apoptosis, Cleaved caspase-3, Immunocytochemistry, Western blotting, Smooth muscle cells, Endothelial cells

1 Introduction

During atherosclerotic plaque formation, medial vascular smooth muscle cells (VSMCs) dedifferentiate from a contractile phenotype to a synthetic, migratory, and proliferative phenotype. Growth

Dipak P. Ramji (ed.), *Atherosclerosis: Methods and Protocols*, Methods in Molecular Biology, vol. 2419,
https://doi.org/10.1007/978-1-0716-1924-7_9,
© The Author(s), under exclusive license to Springer Science+Business Media, LLC, part of Springer Nature 2022

factors secreted by endothelial cells, foam cell macrophages and degranulated platelets, such as platelet derived growth factor (PDGF), basic fibroblast growth factor (bFGF) and transforming growth factor β (TGF-β), stimulate replication of VSMC that have migrated into the tunica intima [1]. This aberrant VSMC proliferation results in intimal thickening which predisposes the artery to infiltration of lipids and inflammatory cells and thereby acts as a soil for atherosclerosis [2]. Additionally, VSMC migration and proliferation occurs later in the pathogenesis of atherosclerosis and leads to the formation of a fibrous cap, which accounts for much of the overall occlusive mass of an atheroma. Atypical endothelial cell proliferation has also been correlated with atherogenesis. Endothelial cell turnover rates are elevated at branch orifices (atherosclerosis-prone regions) where blood flow is disturbed and turbulent [3]. During coronary artery bypass graft surgery, harvesting and implantation of an undiseased vessel results in endothelial denudation [4]; here in particular, endothelial regrowth is highly important in the prevention of thrombus formation and subsequent long-term effects such as intimal hyperplasia and atherosclerosis [5]. Hence, robust assays for measuring VSMC and endothelial proliferation and migration are essential for furthering our understanding of disease progression in atherosclerosis as well as evaluating the potential of therapeutic interventions.

For decades, radiolabeled thymidine such as tritiated thymidine (^{3}H-TdR) was used in proliferation assays for detecting cells undergoing DNA replication in the S-phase of the cell cycle. However, due to the health risks associated with handling radioactive compounds and the time-consuming process of developing autoradiographs, contemporary studies commonly utilize the safe and more cost-effective thymidine analog bromodeoxyuridine/5-bromo-2-′-deoxyuridine (BrdU). Though monitoring tritiated thymidine or BrdU incorporation is the primary, gold-standard approach for assessing cellular proliferation, it is worth noting that this assay is an indicator of DNA synthesis which can transpire independently of cell division such as during gene duplication and DNA repair [6]. Furthermore, both thymidine analogs are known to be toxic [7–10], and a number of studies have reported that their incorporation into DNA has unpredictable effects on cell behavior and function [6]. Here, we have outlined a protocol for immunodetection of incorporated BrdU in cultured VSMCs and endothelial cells.

Ethynyldeoxyuridine/5-ethynyl-2′-deoxyuridine (EdU) is a thymidine analog where the methyl group in thymidine is replaced by a terminal alkyne group [11]. Detection of incorporated EdU entails a simple copper-catalyzed covalent reaction between the alkyne group of EdU and an azide with a fluorescent tag [12–15]. Due to the small size of the fluorescent azide probe, EdU units within double-stranded DNA are easily accessible and this

assay requires no more than standard detergent-based permeabilization of the cell and nuclear membranes. In contrast, antibody-based detection of BrdU requires a DNA hydrolysis or denaturation step to enable access of an anti-BrdU antibody to the BrdU units. This typically involves the use of concentrated acids or digestion with nucleases, which can disrupt DNA integrity (affecting nuclear counterstains such as DAPI), cell morphology and other antigen recognition sites (often rendering the assay unsuitable for dual immunocytochemistry). However, the EdU assay is fully compatible with nuclear counterstains and can me multiplexed with antibody-based detection of other antigens of interest. Furthermore, fluorescent labeling of EdU is safe and the entirety of the procedure can be completed in less than an hour.

Here, quantitative analysis of EdU labeling is performed using the open-source image analysis tool, Fiji [16, 17]. Automation of processing with Fiji is achieved using the built-in macro language. In the provided macro, nuclei are segmented from a fluorescent DAPI-stained image and optionally classified as being EdU positive or negative based on a separate EdU image. To obtain a total cell count, the DAPI image is first processed to remove out-of-focus light and high-frequency noise arising from the detector. The image is subsequently thresholded to produce a binary image (white nuclei, black background) and processed to remove small holes that arise in this binary image due to remaining noise. Adjacent nuclei, which have become merged during the binarization process, are separated by a pixel-wide line of background-labeled (black) pixels. Nuclei are identified as contiguous regions of foreground-labeled (white) pixels; however, only those with areas falling within an accepted size range are retained for further analysis. Where a separate EdU image is available, the mean intensity of the EdU signal coincident with each nucleus is measured and used for classification of nuclei as EdU positive or negative.

Retinoblastoma (Rb) protein (110 kDa) is a potent, negative regulator of cellular proliferation and operates by blocking the G1–S-phase transition. Rb exerts its antiproliferative action by binding to and altering the activity of transcription factors involved in cell cycle progression; for example, Rb complexes with members of the E2F transcription factor family impeding transactivation of downstream growth genes [18–20]. In the presence of a growth signal, cyclin D1 is up-regulated and forms an active complex with cyclin-dependent protein kinase 4 and 6 (CDK-4 and -6), which phosphorylates Rb at serine residues 807 and 811 [21–23]. Phosphorylation of $Ser^{807/811}$ permits subsequent phosphorylation of residues within Rb, alleviating its growth repressor function and facilitating transition of the cell cycle into S-phase [24, 25].

Proliferating cell nuclear antigen (PCNA) (36 kDa) is a non-histone auxiliary protein for DNA polymerase that is essential for DNA synthesis during the S-phase of the cell cycle. PCNA encircles

the DNA molecule and serves to anchor polymerases and other proteins involved in DNA metabolic processes [26, 27]. In response to a growth signal, expression levels of PCNA increase in G1 of the cell cycle, peak in S-phase, and decline in the G2/M phase. Though a widely used proliferative marker for diagnostic and research purposes, it should be noted that PCNA is also involved in, and elevated during, other cellular processes like chromatin remodeling, DNA repair, and sister-chromatin cohesion [28, 29].

Cyclin D1 (36 kDa) plays a pivotal role in cell cycle progression; it is highly responsive to extracellular proliferative signals and serves to link these cues to G1–S-phase transition [30]. Cyclin D1 is upregulated in response to a pro-growth extracellular signalling environment, and as mentioned, complexes with CDK-4 and -6 to form an active kinase for Rb [21–23]. Though cyclin-D1 neutralizing antibodies have been demonstrated to arrest cell cycle progression, knockout studies indicate that other cyclins can act as substitutes for cyclin D1 to promote cell replication. Regardless, cyclin D1 remains a well-favored indicator of proliferation.

Here, we describe a quick, reliable, and reproducible Western blotting protocol for detection and quantitation of proliferative markers phospho- $Ser^{807/811}$ Rb, PCNA and cyclin D1. It is important to note that the expression level of these markers is indicative of the proportion of replicating cells rather than the mean proliferative rate.

Migration of VSMCs and endothelial cells contributes to the pathogenesis of atherosclerosis and can be measured using the scratch wound assay [31–33]. Cell migration is affected by a variety of factors, including the underlying extracellular matrix, cell–cell interactions, soluble proteins, and mechanical forces [32, 34]. Furthermore, cells can migrate individually or as cellular sheets which maintain their intercellular junctions as they migrate [33]. The scratch wound assay is one of the simplest, cost effective and quantitative methods to study cell migration [34]. It involves the disruption of a confluent cellular monolayer by "wounding" [32–35]. Immediately after the monolayer is "wounded," images are taken and compared to those at the end of the experiment, which will allow for the total migration distance to be measured [31–35].

Conversely, the cell exclusion migration assay offers many benefits compared to the scratch assay. Firstly, scratching results in necrotic and apoptotic cell death, particularly in cells at the border of the gap; signals released by damaged cells may affect cell motility [36–38] and the rate of gap closure. Secondly, residues of extracellular matrix may remain in the gap and scratching can damage the culture surface. Finally, gap width may vary with the amount of pressure applied with the pipette tip. All these factors are likely to affect experimental outcome and reproducibility.

With physical cell exclusion assays, cells are seeded in a silicone, biocompatible culture insert which features reservoirs separated by a 500 μm thick wall and so cells only grow in designated areas; following cell attachment and recovery, the culture insert is removed to reveal a gap. This approach limits necrotic and apoptotic cell death, and creates a clean, precisely defined gap with no extracellular matrix residue or damage to the culture surface. Hence, one may study cell migration in a controlled manner to generate robust, reproducible results. Here, we describe a protocol for measuring vascular smooth muscle cell (VSMC) and endothelial cell migration using a simple physical cell exclusion assay and also outline a method for quantitative data analysis using the open-source Fiji image processing package.

Cleaved caspase-3 is a cysteine protease and an important mediator and effector of apoptosis [36–38]. The cleavage of caspase-3 is initiated by the binding of Fas Ligand to Fas which activates caspase-8, which can either directly cleave and activate caspase-3 or initiate the apoptosome (intrinsic) pathway [37]. Activation of the apoptosome pathway causes permeabilization of the mitochondrial outer membrane thereby releasing cytochrome *c*, which binds to Apaf-1 activating caspase-9 and subsequently cleaves caspase-3 [38]. The cleavage of caspase-3 is vital for efficient apoptosis to occur as it elicits the activation of caspases-2, 6, 8, and 10, the inhibition of reactive oxygen species (ROS) production, the condensation of chromatin, DNA fragmentation, cell blebbing and shrinkage [37–39]. Consequently, quantification of cleaved caspase-3 is a widely accepted assay for the estimation of apoptosis.

To detect cleaved caspase-3, cells must first be fixed to prevent the degradation of the cell structure, morphology and other essential cell components such as proteins [40]. Once fixed, the cell membranes must be permeabilized to facilitate the binding of the cleaved caspase-3 antibody [41]. Nonspecific binding of antibodies to other epitopes is prevented using preincubation with goat serum and dilution of antibodies in buffer supplemented with 1% bovine serum albumin [42]. Detection of bound anti-cleaved caspase-3 antibodies is achieved using biotinylated secondary antibodies and amplified by avidin-conjugated fluorophores [43]. Cleaved caspase-3 positive cells are counted to quantify the rate of apoptosis in each treatment group.

2 Materials

For all protocols described below, cells are cultured at 37 °C and 5% CO_2 in a humidified atmosphere. Any materials used in cell culture should be filtered and prepared in a sterile fume hood.

HPLC water with a sensitivity of 18 MΩ-cm at 25 °C should be used throughout, unless stated otherwise. All steps should be performed at room temperature, unless stated otherwise.

2.1 Proliferation: BrdU

2.1.1 General Cell Culture

1. VSMC growth media: Dulbecco's Modified Eagle Medium (DMEM) containing 1.0 g/L glucose, 100 μg/mL penicillin, 100 IU/mL streptomycin, 2 mM L-glutamine supplemented with 10% (v/v) fetal bovine serum (FBS).
2. Endothelial cell growth media: endothelial cell basal medium, 100 μg/mL penicillin, 100 IU/mL streptomycin, growth supplement (0.1 ng/mL recombinant human epidermal growth factor, 1 ng/mL recombinant human basic fibroblast growth factor, 90 μg/mL heparin, 1 μg/mL hydrocortisone, 4 μL/mL bovine hypothalamic extract, 0.02 mL/mL FBS).
3. Sterile, tissue culture grade phosphate buffered saline (PBS): 2.67 mM KCl, 1.47 mM KH_2PO_4, 137.9 mM NaCl, 8.06 mM $Na_2HPO_4{\cdot}7H_2O$, pH 7.0–7.3.
4. Trypsin–EDTA: 0.25% trypsin, 0.02% EDTA in PBS (*see* **Note 1**).
5. VSMC quiescence medium: serum-free DMEM containing 1.0 g/L glucose, 100 μg/mL penicillin, 100 IU/mL streptomycin, 2 mM L-glutamine (*see* **Note 2**).
6. Endothelial cell quiescence medium: 2% (v/v) FBS endothelial cell basal medium, 100 μg/mL penicillin, 100 IU/mL streptomycin (*see* **Notes 2** and **3**).
7. 75 and 150 cm^2 cell culture flasks.
8. 24-well tissue culture plates.
9. Cell scrapers.
10. Polypropylene tubes with a conical bottom.
11. Cell culture centrifuge.
12. Coverslipped Neubauer hemocytometer.

2.1.2 Cell Culture: BrdU Incorporation

1. VSMC growth media (*see* **Note 4**).
2. Endothelial cell growth media (*see* **Note 4**).
3. VSMC quiescence medium.
4. Endothelial cell quiescence medium.
5. Sterile 13 mm round glass coverslips.
6. Sterile curved forceps.
7. Human or bovine fibronectin.
8. 10 mM BrdU in DMSO. Store at −20 °C.

2.1.3 Immunocytochemistry for BrdU

1. 3% (w/v) paraformaldehyde (PFA) in PBS: Heat PBS until hot (but not boiling) and add to PFA. If mixing does not achieve dissolution of PFA, add one to two drops of concentrated NaOH and continue to mix. Aliquot and store at −20 °C (*see* **Note 5**).
2. 1% (v/v) Triton X-100 in PBS. Store at room temperature.
3. 3% (v/v) H_2O_2 in water. Store at 4 °C.
4. DNA denaturation solution: 125 U/mL benzonase nuclease in PBS supplemented with 1 mM $MgCl_2$ or 2 M HCl (in a fume hood, slowly add 35 mL of concentrated HCl (32% v/v, density = 1.16) to 165 mLof water in a glass laboratory bottle and mix). Always use fresh (*see* **Note 6** and Fig. 1d).
5. 1% (w/v) bovine serum albumin (BSA) in PBS.
6. Anti-BrdU IgG diluted in 20% serum blocking agent in 1% (w/v) BSA in PBS (*see* **Note 7**).
7. Biotinylated secondary antibody diluted in 1% (w/v) BSA in PBS (*see* **Note 8**).

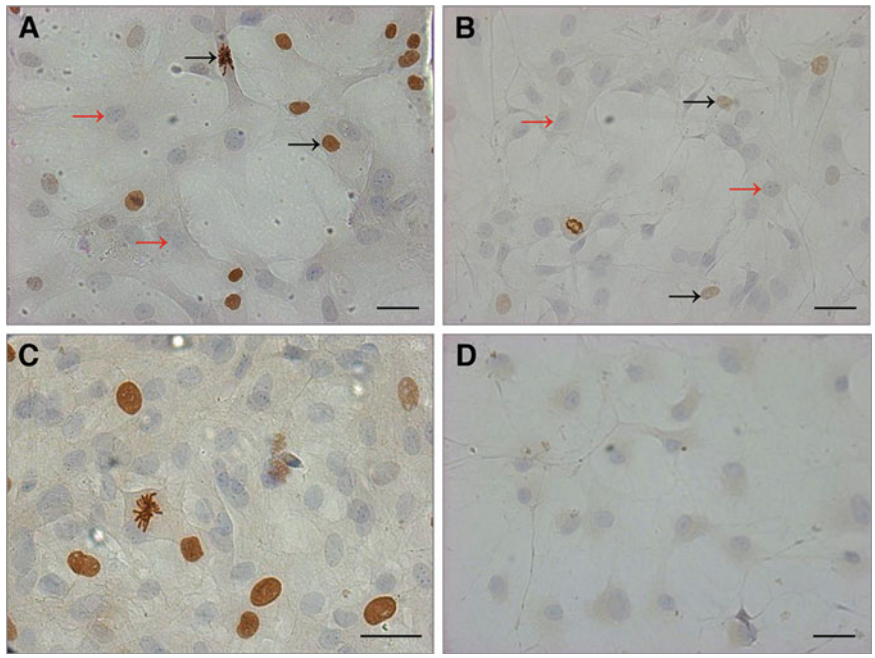

Fig. 1 Immunocytochemistry for incorporated BrdU in cultured primary rat aortic VSMCs. (**a**) BrdU-positive cells have distinct brown nuclei (black arrow) and BrdU-negative cells have grey/blue nuclei from staining with Mayer's hematoxylin (red arrow). (**b**) Example where colorimetric staining of BrdU is less distinct (black arrow) and more difficult to distinguish from BrdU-negative cells (red arrow). (**c**) Tight packing of cells at the middle of a well due to use of swirling motions to disperse cells during seeding. (**d**) Unsuccessful staining due to improper DNA denaturation; in this case, the HCl acid used was not fresh

8. Streptavidin–horseradish peroxidase (HRP) conjugate diluted in 1% (w/v) BSA in PBS.
9. (3,3′-diaminobenzidine) DAB peroxidase substrate (*see* **Note 9**).
10. Mayer's hematoxylin (*see* **Note 10**).
11. Tap water.

2.1.4 Imaging and Analysis

1. Needle.
2. Fine forceps.
3. Soft tissue.
4. Glass slides.
5. Aqueous mountant.
6. Light microscope with a camera mount.

2.2 Proliferation: EdU

2.2.1 Cell Culture: EdU Incorporation

VSMC and endothelial growth media are detailed in Subheadings 2.1.1 and 2.1.2. Replace 10 mM BrdU in DMSO with 10 μM EdU in DMSO (**item 8** of Subheading 2.1.2).

2.2.2 Fluorescent Labeling of EdU

1. Fixation: 3% (w/v) PFA in PBS (*see* **item 1** in Subheading 2.1.3).
2. 0.5% (v/v) Triton X-100 in PBS.
3. Kits for fluorescent labeling of incorporated EdU: Kits contain buffers, a copper catalyst solution, and a fluorescently labeled azide (*see* **Note 11**).
4. PBS.
5. 3% (w/v) BSA in PBS.

2.2.3 Imaging and Analysis

1. Needle.
2. Fine forceps.
3. Soft tissue.
4. Glass slides.
5. Liquid mountant formulated with DAPI or another fluorescent nuclear counterstain.
6. Fluorescence microscope with a camera mount.

2.2.4 Automated Data Analysis

1. Open-source Fiji image processing package (https://fiji.sc) (*see* **Note 12**).
2. Nuclei counting and EdU quantification macro for Fiji available at https://zenodo.org/record/4475547 (*see* Fig. 2).

```
minSize = 200;
maxSize = 10000;
measureEdU = true;
channelEdU = 2
thresholdEdU = 30;

setOption("BlackBackground", true);
setBatchMode("hide");

dapiRGBWin = getTitle();
print("Processing file \""+dapiRGBWin+"\"");

if (bitDepth() == 24) {
    run("Make Composite");
    run("Duplicate...", "duplicate channels=3");
    selectWindow(dapiRGBWin);
    close();
}

dapiWinOrig = getTitle();
run("Duplicate...", "duplicate");
dapiWin = getTitle();

if (measureEdU) {
    if (channelEdU == 1) {
        eduRGBWin = replace(dapiRGBWin, "b.", "r.");
    } else if (channelEdU == 2) {
        eduRGBWin = replace(dapiRGBWin, "b.", "g.");
    }
    selectWindow(eduRGBWin);
    if (bitDepth() == 24) {
        run("Make Composite");
        run("Duplicate...", "duplicate channels="+channelEdU);
        selectWindow(eduRGBWin);
        close();
    }
    eduWinOrig = getTitle();
    run("Duplicate...", "duplicate");
    eduWin = getTitle();
}

selectWindow(dapiWin);
run("Subtract Background...", "rolling=50");
run("Gaussian Blur...", "sigma=2");
run("Auto Threshold", "method=Otsu white");
run("Fill Holes");
run("Watershed");
if (measureEdU) {
    run("Set Measurements...", "mean redirect="+eduWin+" decimal=4");
} else {
    run("Set Measurements...", "redirect=None decimal=4");
}
```

```
run("Analyze Particles...", "size="+minSize+"-"+maxSize+" show=Nothing add display clear");
nNuclei = nResults();
print("Number of nuclei = "+nNuclei);

if (measureEdU) {
    nPos = 0;
    for (row=0;row<nNuclei;row++) {
        intensity = getResult("Mean", row);
        if (intensity > thresholdEdU) {
            nPos = nPos + 1;
        }
    }
    nNeg = nNuclei - nPos;
    print("Number of EdU+ nuclei = "+nPos);
    print("Number of EdU- nuclei = "+nNeg);
}

if (measureEdU) {
    run("Merge Channels...", "c1="+dapiWinOrig+" c3="+eduWinOrig+" create");
    for (row=0;row<nNuclei;row++) {
        roiManager("Select", row);
        intensity = getResult("Mean", row);
        if (intensity > thresholdEdU) {
            Overlay.addSelection("green");
        } else {
            Overlay.addSelection("white");
        }
    }
} else {
    selectWindow(dapiWinOrig);
    for (row=0;row<nNuclei;row++) {
        roiManager("Select", row);
        Overlay.addSelection("white");
    }
}
run("Flatten");

run("Select None");
selectWindow(dapiWin);
close();
if (measureEdU) {
    selectWindow(eduWin);
    close();
}
```

Fig. 2 Fiji macro for counting and classifying nuclei based on an optional EdU signal. Documentation has been removed from the displayed code. The full macro with comments is available from https:/zenodo.org/record/4475547

2.3 Proliferation: Western Blotting for Cell Cycle Markers

2.3.1 Protein Extraction

1. PBS.
2. Sodium dodecyl sulphate (SDS) protein lysis buffer: 1% (w/v) SDS, 50 mM Tris–HCl pH 8, 10% (v/v) glycerol. Aliquot the SDS protein lysis buffer and store at −20 °C. Once thawed, do not refreeze but keep at room temperature for up to a month (*see* **Notes 13** and **14**).
3. Inserts of 1 mL syringes.
4. 500 µL microcentrifuge tubes.
5. Benchtop microcentrifuge.
6. Ice.

2.3.2 Protein Assay

1. 96-well plate.
2. Protein assay kit for measuring protein concentration (*see* **Notes 14** and **15**).
3. 1 mg/mL and 100 µg/mL BSA in PBS.
4. Enzyme-linked immunosorbent assay (ELISA) plate reader.
5. Water.

2.3.3 1D Polyacrylamide Gel Electrophoresis

1. 2× Laemmli Sample buffer: 65.8 mM Tris–HCl pH 6.8, 26.3% (w/v) glycerol, 5% (v/v) β-mercaptoethanol, 2.1% (w/v) SDS, 0.01% bromophenol blue tracking dye (*see* **Notes 16** and **17**).
2. Dry block heater.
3. Protein ladder (*see* **Note 18**).
4. 0.5 mL microcentrifuge tubes.
5. Stain-free precast polyacrylamide protein gels with a 4–15% gradient (optimum separation range of 20–250 kDa) (*see* **Notes 19** and **20**).
6. Tris–glycine–SDS Running Buffer: 25 mM Tris, 192 mM glycine, 0.1% (w/v) SDS, pH 8.3.
7. Electrophoresis cell including a buffer tank, electrode assembly, lid with power cables, and a buffer dam (*see* **Note 20**).
8. PowerPac for power supply.

2.3.4 Stain-Free Total Protein Imaging

1. Cassette opening lever.
2. Stain-free polyacrylamide gel imaging system.
3. Imaging densitometer software (e.g., Image Lab Software available from Bio-Rad).

2.3.5 Protein Transfer

1. Prepackaged nitrocellulose or PVDF protein transfer packs (*see* **Note 20**).
2. Transfer System (*see* **Note 20**).
3. Tweezers or forceps.
4. Blot roller.

2.3.6 Immunodetection

1. Tris buffered saline supplemented with Tween 20 (TBST): 20 mM Tris, 137 mM NaCl, 0.1% (v/v) Tween 20, pH 7.6.
2. Blocking agent: 5% (w/v) BSA in TBST or 5% (w/v) fat-free milk powder in TBST.
3. 3% (w/v) BSA in TBST.
4. Primary antibody: anti-PCNA IgG, anti-phospho-Rb (Ser807/811) IgG, or anti-cyclin D1 IgG diluted in 3% (w/v) BSA in TBST.
5. HRP-labeled secondary antibody in 3% (w/v) BSA in TBST.
6. Polypropylene tubes.
7. Enhanced chemiluminescence Western blotting HRP substrate (*see* **Note 21**).
8. High-sensitivity chemiluminescence imaging system.
9. Forceps or tweezers.
10. 10 cm × 10 cm plastic dish.

11. Tube roller.
12. Rocking platform.

2.3.7 Densitometry

1. Imaging densitometer software (e.g., Image Lab Software available from Bio-Rad).

2.4 Migration: Scratch Wound Assay

1. VSMC growth media detailed in Subheading 2.1.1 supplemented with 2 mM hydroxyurea (*see* **Note 22**).
2. Endothelial cell growth media detailed in Subheading 2.1.1 supplemented with 2 mM hydroxyurea (*see* **Note 22**).
3. P200 pipette tips.
4. Inverted light miscroscope with a camera mount.
5. Open-source Fiji image processing package or preferred image processing software.

2.5 Migration: Cell Exclusion Assay

1. VSMC growth media detailed in Subheading 2.1.1 supplemented with 2 mM hydroxyurea (*see* **Note 22**).
2. Endothelial cell growth media detailed in Subheading 2.1.1 supplemented with 2 mM hydroxyurea (*see* **Note 22**).
3. Culture inserts with either 2, 3, or 4 reservoirs (*see* **Note 23**).
4. Sterile curved forceps.
5. Inverted light microscope with a camera mountant.
6. Open-source Fiji image processing package or preferred image processing software.

2.6 Apoptosis: Cleaved Caspase-3 Immunocytochemistry

2.6.1 Immunocytochemistry for Cleaved Caspase-3

1. 3% (w/v) PFA in PBS (*see* **item 1** in Subheading 2.1.3).
2. 0.2% (v/v) Triton X-100 in PBS.
3. 1% (w/v) BSA in PBS.
4. Blocking agent: 20% serum diluted in 1% (w/v) BSA in PBS.
5. Anti-active cleaved caspase-3 IgG diluted in 1% (w/v) BSA in PBS (*see* **Note 7**).
6. Biotinylated secondary antibody diluted in 1% (w/v) BSA in PBS (*see* **Note 8**).
7. Streptavidin–fluorophore conjugate diluted in 1% (w/v) BSA in PBS.
8. Liquid mountant formulated with DAPI or another fluorescent nuclear counterstain.
9. Rocking platform.
10. Curved forceps.
11. 13 mm round glass coverslips.
12. Aluminium foil.
13. Inverted fluorescence microscope with a camera mountant.

3 Methods

All cell culture techniques should be performed in a sterile fume hood using solutions warmed to 37 °C.

3.1 Cell Propagation from Frozen Stocks

1. Add 10 or 20 mL of VSMC or endothelial cell growth media to 75 or 150 cm^2 cell culture flasks, respectively, and equilibrate at 37 °C, 5% CO_2 in a humidified atmosphere.
2. Quickly thaw endothelial cells or VSMCs by running them under warm tap water.
3. Add cell suspension to 10 mL of VSMC or endothelial cell growth media in polypropylene tubes with a conical bottom (*see* **Notes 24** and **25**).
4. Centrifuge endothelial cells at 220 × *g* for 4 min and VSMC at 400 × *g* for 5 min to pellet the cells.
5. Discard supernatant and resuspend the cells in 1 mL of VSMC or endothelial cell growth media.
6. Add resuspended cells to cell culture flask containing VSMC or endothelial cell growth media.
7. Refresh the cutlure medium every 48–72 h until the cells become confluent.
8. Remove the media from the flask and wash once in PBS.
9. To detach the cells, add 5 or 10 mL of 1× Trypsin/EDTA to 75 or 150 cm^2 cell culture flasks, respectively (*see* **Note 26**).
10. Once the cells have rounded, quench the reaction using one volume of the appropriate growth media (*see* **Note 1**).
11. Scrape the bottom of the flask using a cell scraper, remove the flasks contents and add it to a suitably sized polypropylene tube with conical bottom.
12. Centrifuge endothelial cells at 220 × *g* for 4 min and VSMC at 400 × *g* for 5 min.
13. Discard the supernatant and add 2–5 mL of appropriate growth media. Pipet 10 μL onto a coverslipped Neubauer hemocytometer and calculate the number of cells/mL (*see* **Note 27**).

3.2 Proliferation: BrdU

3.2.1 Cell Culture

1. Insert sterile 13 mm round glass coverslips in a 24-well tissue culture plate using sterile curved forceps.
2. Seed cells to achieve a 70–80% confluency on coverslips in a 24-well tissue culture plate (*see* **Notes 28** and **29**). *Endothelial cells*: coat glass coverslips with either human or bovine fibronectin in accordance with manufacturer's instructions.

3. Allow the cells to recover overnight at 37 °C, 5% CO_2 in a humidified atmosphere.
4. Wash the cells thrice with PBS.
5. *VSMCs*: Add 500 µL of VSMC quiescence medium to the cells and incubate at 37 °C, 5% CO_2 in a humidified atmosphere for 72 h to achieve quiescence. *Endothelial cells*: Add 500 µL of endothelial cell quiescence medium to the cells and incubate at 37 °C, 5% CO_2 in a humidified atmosphere for 18 h to achieve quiescence.
6. Aspirate culture medium used for quiescence. *VSMCs*: Add 500 µL of VSMC growth culture medium supplemented with 10 µM BrdU in DMSO (*see* **Note 4**). *Endothelial cells*: Add 500 µL of endothelial cell growth medium supplemented with 10 µM BrdU in DMSO (*see* **Note 4**).
7. Incubate the cells at 37 °C, 5% CO_2 in a humidified atmosphere for a predetermined amount of time (*see* **Note 30**).

3.2.2 Immunocytochemistry for BrdU

1. Remove cell culture medium and wash cells twice with PBS (*see* **Note 31**).
2. Add 250 µL of 3% (w/v) PFA in PBS for 10 min.
3. Wash cells thrice with PBS.
4. Permeabilize the cells with three 5-min washes in 250 µL of 1% (v/v) Triton X-100 in PBS.
5. Wash the cells twice with PBS.
6. Add 250 µL of 3% (v/v) H_2O_2 for 5 min at 4 °C.
7. Wash the cells twice with PBS.
8. Either add 250 µL of 125 U/mL benzonase nuclease in PBS supplemented with 1 mM $MgCl_2$ and incubate for 2 h at 37 °C or add 250 µL of 2 M HCl and incubate for 30 min at 37 °C (*see* **Note 32**).
9. Wash the cells twice with PBS.
10. Add 250 µL of anti-BrdU IgG diluted in 20% serum in 1% BSA in PBS and incubate for 1.5 h at 37 °C or overnight at 4 °C.
11. Wash the cells four times with PBS.
12. Add 250 µL of biotinylated secondary IgG diluted in 1% BSA in PBS and incubate for 30 min.
13. Wash the cells four times with PBS.
14. Add 250 µL of streptavidin–HRP conjugate diluted in 1% BSA in PBS and incubate for 30 min.
15. Wash the cells four times with PBS.
16. Add 250 µL of DAB peroxidase substrate diluted in water and incubate for 5 min or as recommended by the manufacturer.

17. Wash the cells thrice with water.
18. Stain cell nuclei by adding 250 μL of filtered Mayer's hematoxylin diluted in water to cells and incubate for approximately 1 min.
19. Wash thrice in tap water.
20. Add 1 mL of tap water to cells and incubate for 30 min at room temperature to allow hematoxylin stain to develop.

3.2.3 Imaging and Analysis

1. Add a drop of aqueous mountant to a glass slide where the glass coverslip is to be placed.
2. Delicately lift the coverslip from the base of the well by pushing a pair of closed fine forceps underneath (*see* **Note 33**). Once lifted, rest the coverslip on a needle to prevent return to the base of the well.
3. Gently pick up the coverslip with the pair of fine forceps and remove some of the water by placing the edge of the coverslip against a clean tissue.
4. Place the coverslip upside-down on the drop of aqueous mountant (*see* **Note 34**).
5. Image the cells at an appropriate magnification such as 20× or 40× using a light microscope with a camera mountant. BrdU incorporation is identified as any brown nuclear staining and BrdU-negative cells are identified as those with grey-blue nuclei (*see* **Note 35** and Fig. 1). Approximately 400–500 cells should be counted per condition. The proliferative rate per condition is quantified by calculating the percentage of BrdU-positive cells.

3.3 Proliferation: EdU

3.3.1 Cell Culture

The method used for VSMC and endothelial cell seeding and culture is described under Subheadings 3.1 and 3.2.1 but the culture medium should be supplemented with 10 μM EdU instead of 10 μM BrdU.

3.3.2 Fluorescent Labeling of EdU

1. Remove cell culture medium and wash cells twice with PBS (*see* **Note 31**).
2. Add 250 μL of 3% (w/v) PFA in PBS for 10 min.
3. Wash cells thrice with PBS.
4. Permeabilize cells by adding 250 μL of 0.5% (v/v) Triton X-100 in PBS and incubate for 20 min.
5. During permeabilization of the cells, prepare master mix of reagents, or "reaction cocktail," containing buffers, copper catalyst solution, and a fluorescently labeled azide. These reagents are included in commercial Fluorescent Labeling Kits for EdU and should be prepared in accordance with

manufacturer's instructions. Use the "reaction cocktail" within 15 min of preparation for optimal results.

6. Remove the permeabilization buffer and wash cells twice with 3% (w/v) BSA in PBS.
7. Add 250 μL of the "reaction cocktail" and incubate for the indicated amount of time. Protect from light.
8. Wash the cells once with 3% (w/v) BSA in PBS
9. Add 1 mL of PBS to cells.

3.3.3 Imaging and Analysis

1. Add a drop of mountant formulated with DAPI to a glass slide where the glass coverslip is to be placed.
2. Mount coverslip on glass slide as described in **steps 2–4** of Subheading 3.2.3.
3. Image cells at an appropriate magnification such as 20× or 40× using a fluorescence microscope with a camera mountant. EdU-positive cells are identified as those with any fluorescent green nuclear staining. Approximately 400–500 cells should be counted per condition. The proliferative rate per condition is quantified by calculating the proportion of EdU-positive cells.

3.3.4 Automated Data Analysis

1. Within Fiji, open the nuclei counting macro (File > Open). The macro will appear in the Fiji scripting window (*see* **Note 36**).
2. Open pair of DAPI and EdU images (File > Open) and ensure DAPI window is the most recently selected (*see* **Notes 37** and **38**). If the analysis is to be run in the nuclei-counting mode alone (no EdU signal), only the DAPI image needs to be loaded.
3. Configure the analysis workflow by editing lines 14–18 of the macro. The "minSize" and "maxSize" parameters dictate the accepted range of nuclei cross-sectional areas (measured in px^2). If EdU signal is present, "measureEdU" must be set to "true." To use a red EdU signal, set "channelEdU" to "1," or to "2" for a green EdU signal. Nuclei with mean EdU intensity greater than "thresholdEdU" will be classed as EdU positive.
4. Start the macro by pressing "Run" within the script window (the images will disappear during processing). The macro has finished processing when the log and nuclei outlines image (*see* Fig. 3) is displayed. The log window records the DAPI image filename being processed, the total number of nuclei detected and, if using an EdU signal, the number of those nuclei classed as EdU positive or negative. The outlines image will show a white outline around all EdU negative nuclei and a green outline around all EdU positive nuclei.

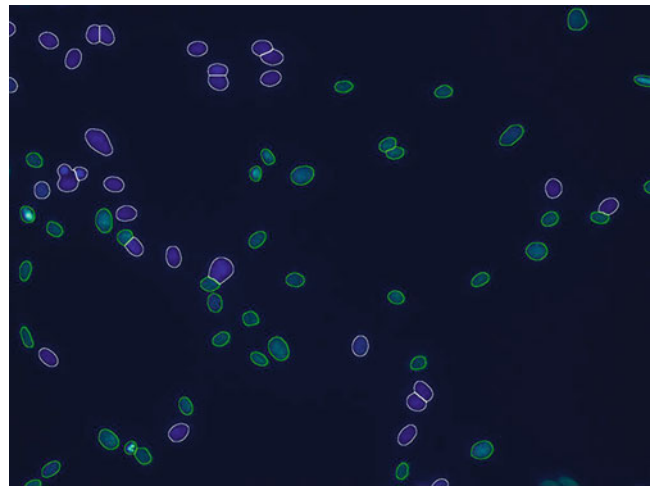

Fig. 3 Example image showing detected nuclei as outlines. Outline colors correspond to EdU classification, with EdU-positive nuclei outlined in green and EdU-negative nuclei outlined in white. Underlying image is a composite of raw DAPI (blue) and EdU (green) signals

3.4 Proliferation: Western Blotting for Cell Cycle Proteins

3.4.1 Cell Culture

1. The method for VSMC and endothelial cell culture and seeding is described in Subheading 3.1.
2. Seed VSMCs or endothelial cells in a 24-well tissue culture plate to achieve a 70–80% confluency (*see* **Note 28**).
3. Following seeding, the method for VSMC and endothelial cell culture is described in Subheading 3.2.1. Culture medium should not be supplemented with 10 μM BrdU or 10 μM EdU.

3.4.2 Protein Extraction

1. Remove cell culture medium and wash cells twice with PBS (*see* **Note 39**).
2. For a 24-well tissue culture plate, add 30 μL of desired protein lysis buffer to cells (60 μL of protein lysis buffer for a 12-well plate, 120 μL of protein lysis buffer for a 6-well plate).
3. Rub the culture surface with the insert of a 1 mL syringe to mechanically disrupt cells and transfer to 500 μL microcentrifuge tubes (*see* **Note 40**).
4. Centrifuge the samples at maximum speed in a microcentrifuge for 5 min to remove any debris (*see* **Note 41**).
5. Keep the samples on ice for determination of protein concentration or store at −80 °C.

3.4.3 Protein Assay

1. If cells were lysed in an SDS protein lysis buffer, warm samples to room temperature to prevent precipitation of SDS as this may interfere with the protein assay.

2. The protein concentration of each sample should be evaluated using a kit such as the Micro Bicinchoninic Acid Assay Kit (Thermo Scientific), following manufacturer's instructions.
3. Add 140 μL of water to wells of a 96-well plate.
4. For protein standards, add 0, 0.1, 0.25, 0.5, 1, 2.5, 5, and 10 μg of BSA in PBS to water. Analyze standards in duplicate.
5. For protein samples, add 2–5 μL of protein lysates to water. Analyze protein samples in duplicate.
6. Add 150 μL of Micro BCA reagent to each well and incubate at 37 °C for 45 min.
7. Read plates at 560 nm on an ELISA plate reader to determine optical density.
8. Create standard curve from protein standards to determine the protein concentration of the protein samples from their optical density.

3.4.4 1D Polyacrylamide Gel Electrophoresis

1. Once the volume of protein lysate for the desired amount of protein is calculated, transfer this volume to fresh 500 μL microcentrifuge tubes (*see* **Note 42**).
2. Add water to equalize volume and concentration.
3. Add one volume of 2× Laemmli sample buffer to protein lysates and mix by gently pipetting up and down (*see* **Note 43**).
4. Heat samples at 95 °C for 5 min on a dry block heater (*see* **Note 44**).
5. Set up the stain-free precast polyacrylamide protein gels, the buffer tank, the electrode assembly and the Tris–glycine–SDS Running Buffer in accordance with supplier's instructions.
6. Slowly and gently load 5–10 μL of a suitable protein ladder into one well of the polyacrylamide gel (*see* **Note 45**). Slowly load protein lysates into the wells of the polyacrylamide gel. Carry out electrophoresis at 300 V for approximately 15–20 min until the bromophenol blue tracking dye (component of Laemmli sample buffer) reaches the bottom of the gel.

3.4.5 Stain-Free Total Protein Imaging

1. Remove the stain-free polyacrylamide gel from the cassette using the cassette opening lever and carefully transfer to stain-free imaging system ensuring throughout that the gel does not tear (*see* Fig. 4c).
2. Pour a small amount of Tris–glycine–SDS Running Buffer over the gel to prevent drying out and move aside bubbles that will affect the imaging process.
3. On the stain-free polyacrylamide gel imaging system, induce fluorescence with a 1-min UV photoexcitation. The imaging software will generate an image of the total protein detected

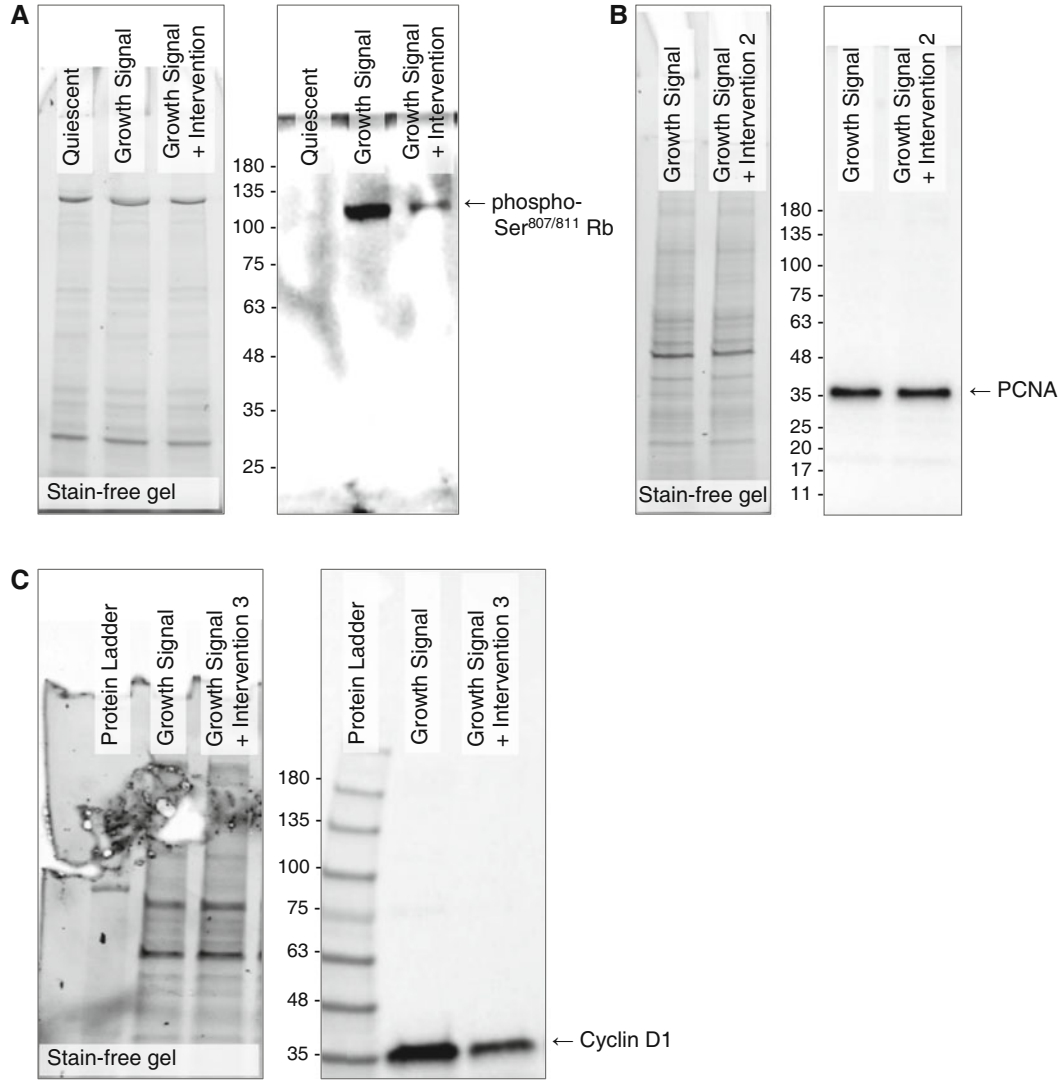

Fig. 4 Western blots for classical proliferation markers and stain-free imaging for total protein normalization. (**a**) Western blot for phospho-Ser807/811 Rb accompanied by image of stain-free gel. Example of Western blot with high background which will interfere with quantitation of phospho-Ser807/811 Rb protein expression levels using imaging densitometer software. (**b**) Western blot for PCNA accompanied by image of stain-free gel. (**c**) Western blot for cyclin D1 accompanied by image of stain-free gel. Example of stain-free gel with tearing which will interfere with quantitation of total protein using imaging densitometer software. Numbers indicate size of protein ladder markers in kDa

and if present, will also highlight overexposed bands (where the signal intensity is no longer proportional to the protein load). If some bands are overexposed, reduce the exposure time until all bands are within a linear dynamic range.

4. Use the imaging densitometer software for quantitation of total protein load in each lane.

3.4.6 Protein Transfer

Here, we describe a method for protein transfer using prewetted transfer packs that do not require any further treatment.

1. Using tweezers or forceps, transfer the bottom (anode) stack to the cassette; the stack should be placed flat and in the center of the anode electrode. This anode stack is layered with the transfer nitrocellulose or PVDF membrane.
2. Align the polyacrylamide gel on the nitrocellulose or PVDF membrane.
3. Place the top (cathode) stack on top of the polyacrylamide gel. Gently, use a blot roller to expel any trapped air bubbles (*see* **Note 46**).
4. Place the cassette lid with the cathode electrode on top and lock shut.
5. Insert cassette into the Transfer System and begin appropriate preprogrammed transfer protocol. Protein transfer will take 3–7 min depending on the type of transfer pack used.

3.4.7 Immunodetection

1. Remove the nitrocellulose or PVDF membrane from the transfer pack using clean forceps or tweezers (*see* **Note 47**).
2. In a plastic dish, block the membrane with 10–20 mL of 5% (w/v) fat-free milk powder or 5% (w/v) BSA in TBST for 30 min rocking gently.
3. Transfer the membrane to a polypropylene tube and incubate the membrane with a minimum of 3 mL of primary antibody diluted in 3% (w/v) BSA in TBST overnight at 4 °C on a roller.
4. Wash the membrane for 5, 10, and then 20 min in 10 mL of 3% (w/v) BSA in TBST (refreshing with each wash).
5. Incubate the membrane with a minimum of 3 mL of HRP-labeled secondary antibody diluted in 3% (w/v) BSA in TBST for 1 h at room temperature.
6. Wash the membrane for 5, 10 and then 20 min in 10 mL of 3% BSA in TBST (refreshing with each wash).
7. Remove the membrane from the polypropylene tube and transfer to a plastic dish filled with 20 mL of TBST.
8. Wash the membrane for a further 5 min by rocking (*see* **Note 48**).
9. Transfer the membrane to another plastic dish. Pipet 1–3 mL of a Western blotting HRP Substrate onto the membrane ensuring that the entire surface is covered (*see* **Note 49**). Incubation times should be indicated by manufacturers.
10. Visualize bands using a high-sensitivity chemiluminescence imaging system following manufacturer's instructions.

3.4.8 Densitometry

1. Determine band density using imaging densitometer software in accordance with the manufacturer's instructions. Normalize against total protein obtained from stain-free imaging.

3.5 Migration: Scratch Wound Assay

1. The method for VSMC and endothelial cell culture and seeding is described in Subheading 3.1.

3.5.1 Cell Seeding

2. Seed VSMCs or endothelial cells in a 24-well tissue culture plate to achieve full confluency (*see* **Note 28**).
3. Allow cells to recover overnight at 37 °C, 5% CO_2 in a humidified atmosphere.

3.5.2 Cell Treatment

1. Remove the culture medium and wash each well twice with 500 μL of PBS (*see* **Note 31**).
2. Prepare VSMC or endothelial growth media supplemented with 2 mM hydroxyurea.
3. Using a P200 pipette tip, make two parallel scratches in the middle of the well (*see* **Note 50** and Fig. 5).
4. Remove the culture medium from the wells and wash twice with 500 μL of PBS to remove cell debris.
5. Add 500 μL of VSMC or endothelial cell growth media supplemented with 2 mM hydroxyurea to each well.

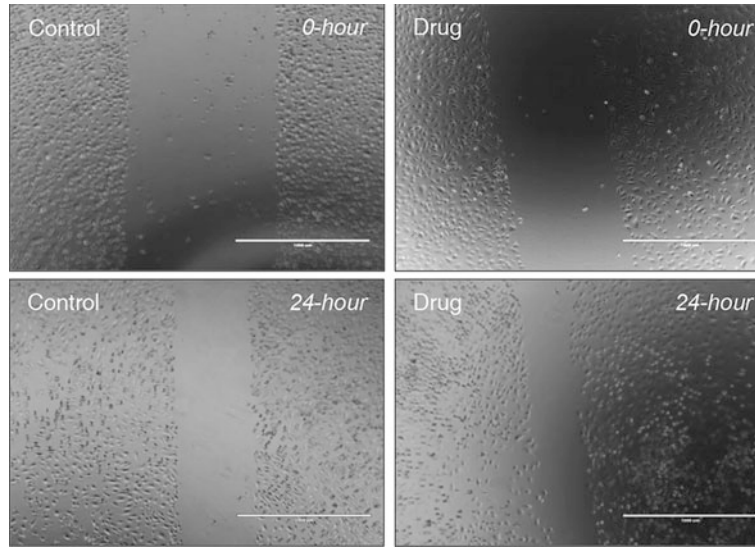

Fig. 5 A completed scratch wound migration assay in cultured human umbilical vein endothelial cells (HUVECs). A confluent monolayer of HUVECs were scratched with a pipette tip at 0-h. HUVECs were then either untreated (Control) or treated with a drug and migration into the created gap was visualized after 24 h. Migration can be observed in both groups with the treated group having a higher migratory rate than the control. Scale bars represent 1 mm

6. Take 4 images of each well (2 per scratch) at 4× resolution using an inverted light microscope with a camera mount for timepoint 0 h.
7. Allow wound healing to transpire for a predetermined amount of time (*see* **Note 51**) at 37 °C, 5% CO_2 in a humidified atmosphere.
8. Take 4 images of each well (2 per scratch) at 4× resolution for timepoint *x* hour.

3.5.3 Image Analysis

1. Open Fiji and drag the image into Fiji (*see* **Note 52**).
2. Select the "Straight Line Tool" and hold the shift button to drag a straight line along the scale bar. Click "Analyze" then "Measure" and record the pixel length (*see* **Note 53**).
3. Draw and measure a perpendicular line from one end of the wound to the other. Take five measurements per image.
4. Calculate the difference in wound size between timepoint 0 and *x* hour (*see* **Note 54**).

3.6 Migration: Cell Exclusion Assay

3.6.1 Cell Seeding

1. Use sterile curved forceps to transfer culture inserts to a tissue culture plate (*see* **Note 55**).
2. Gently push down the culture insert with the back of the curved forceps (*see* **Note 56**).
3. The method for VSMC and endothelial cell culture and seeding is described under Subheading 3.1.
4. Dilute the cell suspension in VSMC or endothelial cell growth medium such that the final concentration is 3×10^5 cells/mL.
5. For a culture insert with 2 reservoirs, pipet 70 μL of the cell suspension into each reservoir (*see* **Note 57**).
6. Incubate the cells overnight at 37 °C, 5% CO_2 in a humidified atmosphere to allow recovery.

3.6.2 Removal of Culture Insert

1. Once cells have reached confluency, gently remove the culture insert using sterile curved forceps by grabbing the corner of the structure and lifting away at an angle (*see* **Note 58**).
2. Wash the cells twice with PBS to remove culture medium and any floating cells or debris.
3. For VSMC, add 500 μL to 1 mL of VSMC growth medium supplemented with 2 mM hydroxyurea. For endothelial cells, add 500 μL to 1 mL of endothelial cell growth medium supplemented with 2 mM hydroxyurea.
4. Photograph the gap created on an inverted light microscope with a camera mountant for timepoint 0 h (*see* **Notes 59** and **60**) (*see* Fig. 6a).

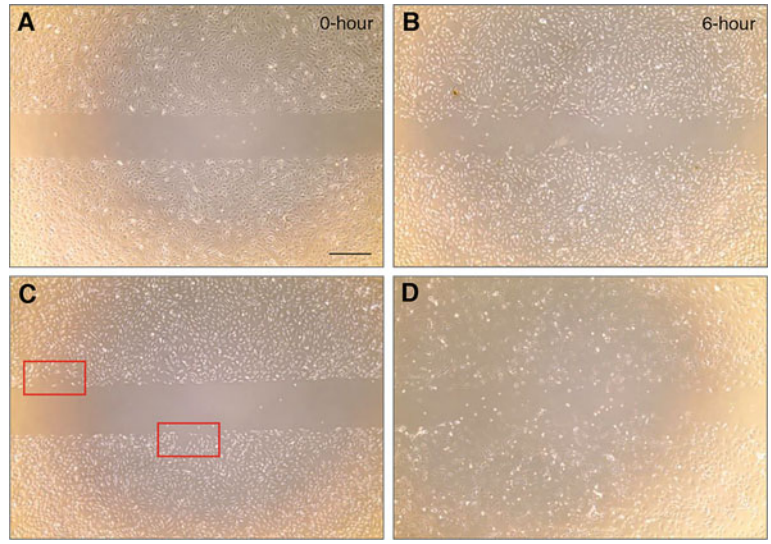

Fig. 6 Cell exclusion migration assay in cultured primary human umbilical vein endothelial cells. (**a**) Endothelial monolayer subsequent to removal of culture insert for gap creation. (**b**) Representative image of endothelial monolayer 6 h following removal of culture insert, where cells are cultured in 2% (v/v) FBS endothelial cell basal medium supplemented with 10 ng/mL recombinant human TNF-α and 2 mM hydroxyurea to inhibit proliferation. (**c**) Endothelial monolayer immediately following removal of culture insert for gap creation; regions at the gap border with poor cell coverage are highlighted. (**d**) Representative image of endothelial monolayer 18 h post-removal of culture insert; cells were treated with a pharmacological compound that induced apoptotic cell death

5. Incubate the cells at 37 °C, 5% CO_2 in a humidified atmosphere to allow cell migration and gap closure.
6. Photograph the closing gap on an inverted light microscope with a camera mountant for timepoint *x* hour (*see* **Notes 51** and **60**) (*see* Fig. 6b).

3.6.3 Imaging and Analysis

1. Within Fiji, open desired image for analysis (File > Open). Ensure the window for this image is the most recently selected.
2. Select the polygon selection tool in the Fiji tool bar and outline the border of the gap by drawing freehand or straight segmented lines (*see* Fig. 7a). Close the shape by clicking on the first point.
3. Retrieve measurements (Analyse > Measure, or simply *Windows:* Cntl + M or *Mac OS X*: Command + M). The area of the outlined shape will be displayed in a results window (*see* Fig. 7a). The area will be expressed as the number of pixels; units can be converted by using a microscope graticule.
4. Select the straight-line drawing tool in the Fiji tool bar and outline the length of the gap (*see* Fig. 7b).

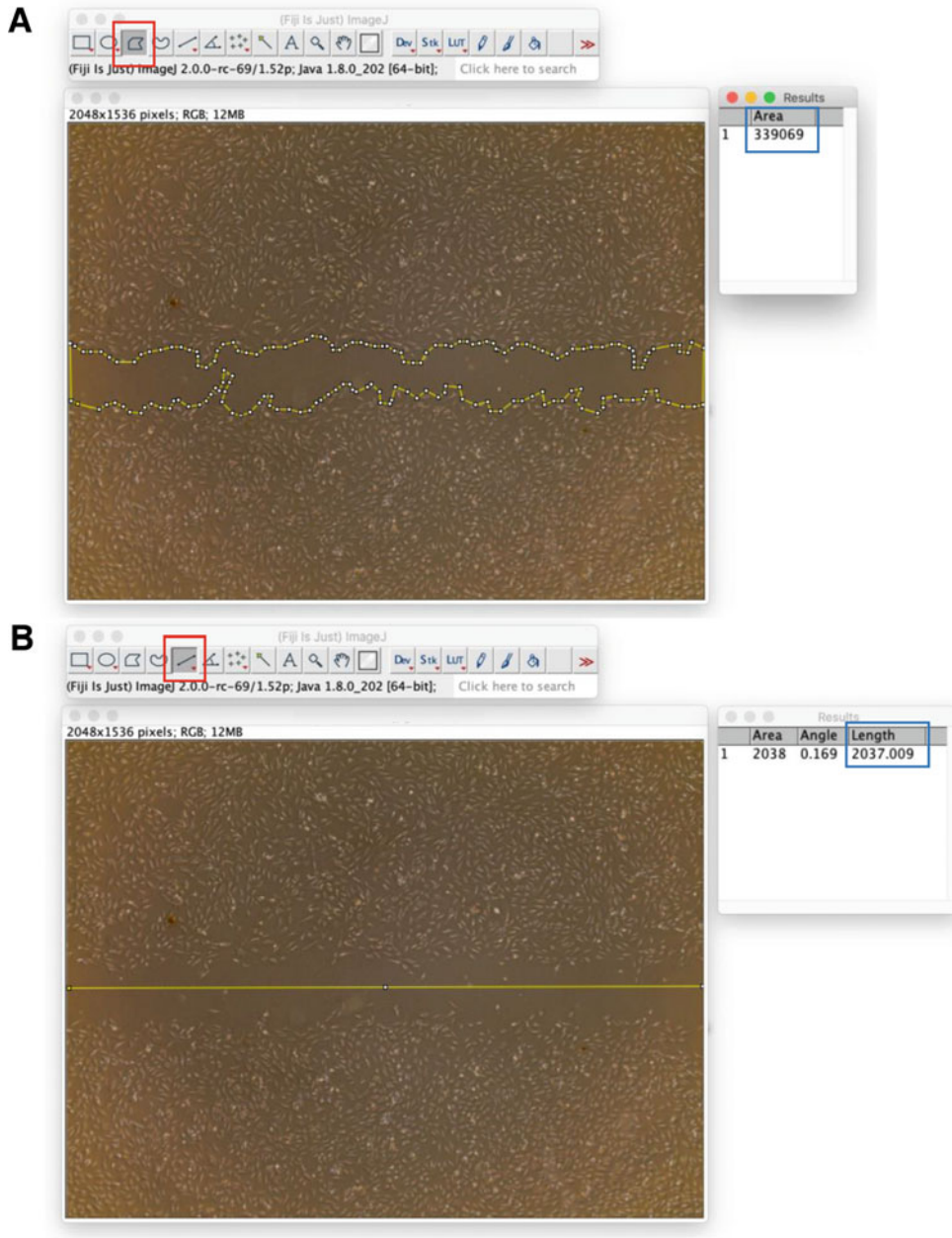

Fig. 7 Data analysis of cell exclusion migration assay using the Fiji image processing package. (**a**) Measurement of gap area using the polygon selection tool (indicated in red) for drawing straight segmented or freehand lines and shapes. Measurement Results window displays area of the region selected (indicated in blue); area is expressed as the number of pixels. (**b**) Measurement of length of gap using the straight-line drawing tool (indicated in red). Measurement Results window displays length outlined (indicated in blue); length is expressed as the number of pixels

5. Retrieve measurements (Analyse > Measure, or simply *Windows:* Cntl + M or *Mac OS X*: Command + M). The length of the gap will be displayed in a results window (*see* Fig. 7b). The length will be expressed as the number of pixels; units can be converted by using a microscope graticule.
6. The mean distance migrated can be calculated using the following formula, where x is the time allowed for cell migration:

$$\frac{\text{Area of gap (0 hour)}}{\text{Length of gap}} - \frac{\text{Area of gap } (x \text{ hour})}{\text{Length of gap}} = 2 \times \text{mean distance migrated}$$

3.7 Apoptosis: Cleaved Caspase-3 Immunofluorescence

3.7.1 Cell Seeding

1. The method for VSMC and endothelial cell culture and seeding is described in Subheading 3.1.
2. Seed VSMCs or endothelial cells in a 24-well tissue culture plate to achieve a 70–80% confluency (*see* **Note 28**).
3. Allow the cells to recover overnight at 37 °C, 5% CO_2 in a humidified atmosphere.

3.7.2 Cell Treatment

1. Remove the culture media and wash each well twice with 500 μL of PBS.
2. Prepare VSMC or endothelial cell growth media (*see* **Note 61**).
3. Remove PBS from the wells and add 500 μL of VSMC or endothelial growth media.
4. Incubate cells for 24 h at 37 °C, 5% CO_2 in a humidified atmosphere.

3.7.3 Cell Fixation

1. Remove culture medium from the wells.
2. Wash each well with 500 μL of PBS thrice (*see* **Note 31**).
3. Add 250 μL of 3% (w/v) PFA in PBS and incubate for 10 min.
4. Wash each well 3 times with 500 μL of PBS. If the primary antibody will not be added immediately, leave the last wash in the wells and store in at 4 °C.

3.7.4 Immunodetection

1. Remove PBS from the wells and add 500 μL of 0.2% (v/v) Triton in PBS for 5 min. Repeat this step twice more.
2. Remove the final wash of 0.2% (v/v) Triton in PBS and add 250 μL of 20% serum blocking reagent in PBS. Gently rock the plate for 30 min at room temperature.
3. Remove the 20% serum blocking reagent in PBS and wash the wells with 500 μL of PBS.
4. Remove the PBS wash and add 250 μL of anti-cleaved caspase-3 IgG diluted in 1% (w/v) BSA in PBS. Gently rock the plate overnight at 4 °C.

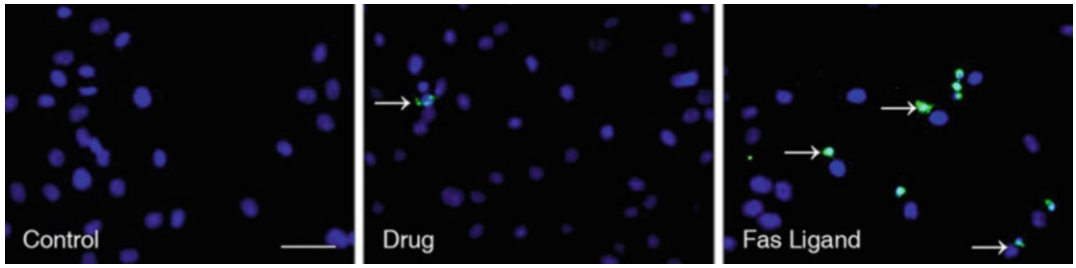

Fig. 8 Immunofluorescence for cleaved caspase-3 in cultured primary human saphenous vein vascular smooth muscle cells (VSMCs). VSMCs were either untreated (Control), treated with a drug, or as a positive control, apoptosis was induced with Fas Ligand. Representative images show no cleaved caspase-3-positive cells in the control group, while the drug group has one cleaved caspase-3-positive cell (white arrow). The Fas Ligand group has significantly higher levels of apoptotic cells (white arrows) indicating that the assay was successful. Scale bar represents 10 μm and applies to all panels

5. Wash thrice with 500 μL of PBS.
6. Remove the PBS and add 250 μL of biotinylated secondary antibody diluted in 1% (w/v) BSA in PBS. Gently rock the plate for 1 h at room temperature.
7. Wash thrice with 500 μL of PBS.
8. Remove the PBS and add 250 μL of streptavidin–fluorophore conjugate diluted in 1% (w/v) BSA in PBS. Gently rock for 1 h at room temperature (*see* **Note 62**).
9. Wash thrice with 500 μL of PBS.
10. Remove the PBS and add one drop of liquid mountant formulated with DAPI or another nuclear counterstain.
11. Using forceps, add a coverslip into each well. Cover the plate with aluminum foil and store at 4 °C until imaging (*see* **Note 34** and Fig. 8).

3.7.5 *Imaging Analysis*

1. Image cells using 40× magnification on an inverted fluorescence microscope with a camera mountant (*see* **Note 63**).
2. Cleaved caspase-3-positive cells are identified as those with any fluorescent green or red nuclear staining depending on the fluorophore used. Approximately 400–500 cells should be counted per condition.
3. The apoptotic rate per condition is quantified by calculating the proportion of cleaved caspase-3-positive cells.

4 Notes

1. This is equivalent to 1× trypsin/EDTA and should be diluted 1:10 from 10× trypsin/EDTA on the day of use and used fresh as stored 1× trypsin/EDTA loses its proteolytic activity due to

self-digestion. 10× trypsin/EDTA can be stored at 4 °C for 2 weeks. Do not exceed recommended time for trypsinization in protocols as this will result in excessive proteolytic cleavage of cell surface proteins, which may disrupt cell function.

2. Quiescence or serum starvation retards cell proliferation and allows for synchronization of cell cycle progression once a proliferative signal is introduced. Furthermore, when studying the action of specific proliferative agents, serum starvation prevents data from being confounded by components of the growth medium that cells are often seeded in (e.g., 10% (v/v) FBS culture medium or supplements).
3. Complete serum starvation will result in endothelial cell death; hence, in this protocol, we have recommended that endothelial cells are brought to quiscence in 2% (v/v) FBS endothelial cell basal medium for no longer than 18 h.
4. Though more costly, supplementing culture medium with growth factors, such as 20 ng/mL recombinant platelet-derived growth factor (PDGF) or 20 ng/mL recombinant basic fibroblast growth factor (bFGF), is thought to yield more physiologically relevant data than using 5–10% (v/v) FBS or supplements to stimulate cell proliferation. It is important that recombinant proteins are compatible with the species from which the cells are derived.
5. Powdered PFA should never be handled outside a fume hood as inhalation will irritate the nose and throat and can cause coughing, shortness of breath and lung damage. Once dissolved and cooled, the solution may be handled outside a fume hood. Do not microwave to defrost as PFA has a low flash point of 71 °C.
6. Never add water to concentrated acid, only concentrated acid to water.
7. It is important that the host species of the primary antibody is not the same species from which the serum blocking agent is derived.
8. Ideally, the host species of the secondary antibody should be the same species from which the serum blocking agent is derived.
9. Once the DAB peroxidase substrate is reconstituted in water in accordance with the manufacturer's instructions, it is essential that it is used within 15 min.
10. Before each use, Mayer's hematoxylin requires filtration to remove precipitates, and often needs diluting 1:2 to 1:4 in water to reduce strength.
11. We recommend Click-iT EdU Imaging Kit (Invitrogen) or BaseClick EdU Cell Proliferation Kit (Sigma-Aldrich).

12. The macro provided is compatible with both Fiji and ImageJ [44].
13. Regarding alternative protein lysis buffers that preserve the conformational and functional integrity of proteins, it is important that the buffer is supplemented with protease and phosphatase inhibitors. We recommend the SDS protein lysis buffer as it disrupts protein structure and function; hence, additional protease and phosphatase inhibitors are not required.
14. Though the bicinchoninic acid (BCA) protein assay is detergent-compatible, it has been noticed that protein lysis buffers with a high percentage of SDS (>2% (w/v)) interfere with this method of measuring protein concentration. Storing 1% (w/v) SDS protein lysis buffers for extended periods at room temperature also presents this issue of interference with the BCA protein assay, hence we recommend aliquoting and storing the buffer at −20 °C and storing for no longer than a month at room temperature.
15. It is important that the protein assay is compatible with the protein lysis buffer utilized and is sufficiently sensitive. We recommend the Micro Bicinchoninic Acid Assay Kit (Thermo Scientific).
16. Reducing agents like β-mercaptoethanol and dithiothreitol (DTT) are important for cleavage of disulphide bonds within the protein structure.
17. We recommend the Laemmli Sample Buffer (Bio-Rad) which ensures optimal band resolution for SDS-polyacrylamide gel electrophoresis performed using Tris/glycine/SDS running buffer.
18. The size range of the protein markers within a protein ladder should span the size of the protein of interest.
19. Due to an increasing number of errors arising from normalizing data with housekeeping proteins, journals are requiring authors to demonstrate that experimental conditions are not affecting the expression of the loading controls and are mandating the use of imaging techniques that yield linear signal ranges. Stain-free imaging technology meets these requirements and is a contemporary approach to measuring total protein for use as a loading control.

    Stain-free imaging technology requires use of a polyacrylamide gel containing a trihalo compound; this compound covalently modifies tryptophan residues in proteins generating a fluorescent signal which can be visualized by UV excitation at any stage during electrophoresis or Western blotting. As nitrocellulose and PVDF membranes produce autofluorescence, we recommend that visualization of total protein is undertaken

immediately following electrophoresis and prior to protein transfer.

20. We recommend the Mini-PROTEAN TGX Stain-free Protein Gels, the Mini-PROTEAN Tetra Vertical Electrophoresis Cell, the Trans-Blot Transfer Packs and Trans-Blot Turbo Transfer Starter System supplied by Bio-Rad for its high efficiency and high reproducibility.
21. We recommend the Immobilon Forte Western HRP Substrate (Merck Millipore) for its high sensitivity and signal enhancing properties.
22. Hydroxyurea inhibits cell cycle progression and therefore ensures that the wound healing or gap closure observed in scratch wound assays or cell exclusion assays, respectively, is exclusively the result of migration and not proliferation.
23. We recommend culture inserts supplied by Ibidi. Ibidi supply culture inserts in two formats: Option 1, dishes with culture inserts preattached to a polymer coverslip; Option 2, culture inserts for self-insertion (into a tissue culture plate). We have observed that Option 1 culture inserts are significantly more difficult to remove from the culture surface compared to Option 2. Removal of Option 1 culture inserts has resulted in partial and sometimes complete detachment of the cell monolayer. Hence, we recommend use of culture inserts for self-insertion.
24. Be sure to have warmed the culture media to 37 °C prior to commencing as this will improve cell viability.
25. Once the cells have thawed, it is important to remove the DMSO that the cells were originally stored in as quickly as possible as DMSO is toxic to defrosted cells.
26. Look under an inverted light microscope to see if the cells have become rounded. Cells should become rounded within 2–5 min of incubation with 1× Trypsin/EDTA. One rounded, firmly tap the side of the flask to dislodge the cells.
27. Methods for seeding cells for specific assays is described in subsequent sections.
28. In a 24-well tissue culture plate, we recommend a seeding density of 2×10^4 cells/well for human saphenous vein VSMCs, a seeding density of 4×10^4 cells/well for rat aortic VSMCs, and a seeding density of 4×10^4 cells/well for human umbilical vein–, saphenous vein–, and coronary artery–derived endothelial cells to achieve a 70–80% confluency. In a 24-well tissue culture plate, we recommend a seeding density of 3×10^4 cells/well for human saphenous vein VSMCs, a seeding density of 6×10^4 cells/well for rat aortic VSMCs, and a seeding density of 6×10^4 cells/well for human umbilical

vein–, saphenous vein–, and coronary artery–derived endothelial cells to achieve full confluency.

29. Following cell seeding, rock tissue culture plate from side-to-side and backward and forward to ensure even distribution of cells; swirling will cause a congregation of cells in the middle of the well (*see* Fig. 1c). This may cause proliferation rates to differ among the cell population due to the effects of cell–cell contacts on cell cycle progression.
30. A 24-h incubation period is often sufficient to induce enough cell proliferation to provide scope for inhibition of proliferation in intervention/treatment groups, as well as a window for further induction of proliferation in intervention/treatment groups.
31. Washing endothelial cells with PBS prior to fixation can cause cell rounding and detachment; therefore it is best to remove cell culture medium and then immediately add the fixing agent.
32. DNA denaturation enables access of the anti-BrdU antibody to the BrdU epitope within the DNA molecule. Nuclease-mediated DNA digestion (Option 1) and acid hydrolysis (Option 2) are both methods of DNA denaturation. Though the latter is a faster approach, it can destroy cell morphology and antigen recognition sites, hence may not be suitable for dual immunocytochemistry, and disrupts DNA integrity affecting nuclear counterstaining with fluorescent dyes like DAPI. Hence, in this protocol, we stain nuclei with Mayer's hematoxylin, which is compatible with both options, and describe a method of colorimetric, rather than fluorescent, labeling of BrdU.
33. It is helpful leave the tap water or PBS in the well when removing coverslips.
34. As some aqueous mountants dry quickly, only add to glass slides immediately before placing of the coverslip. The aqueous mountant will need curing before imaging in order to reach the best refractive index; curing times should be indicated in product datasheets. Use of an aqueous mountant can cause hematoxylin staining to fade over time. Therefore, it is important that cells are imaged and photographed within a week of staining.
35. With immunocytochemistry for BrdU colorimetric, staining will often produce a spectrum of light to deep brown nuclei (*see* Fig. 1b). This may be due to a mixed population of cells that have either just entered or are undergoing or have completed S-phase of the cell cycle. It can be difficult to distinguish light brown nuclei from BrdU-negative cells. It is important that a threshold is set for what one may consider a BrdU-

positive cell; keeping a reference image can be helpful to remain consistent while analyzing and counting cells.

36. Each step of the analysis workflow macro has been detailed via comments within the macro code (lines starting with "//") (*see* Fig. 2).
37. The most recently selected image window in Fiji is considered "active." The macro expects the active window to correspond to the blue (DAPI) image.
38. If using an EdU image, the final character of the DAPI image name must be "b" (e.g., "testb.tif") and the EdU image must have exactly the same name, but end in either "g" if green (e.g., "testg.tif") or "r" if red (e.g., "testr.tif").
39. Once the protein lysis buffer is added to the cells, it is important that it is not diluted by any remaining traces of PBS from the previous wash step. To remove the last remnants of PBS, it is helpful to switch from a 1 mL pipette to a 200 μL pipette with a finer tip, and to tilt the plate to pool the liquid.
40. The DNA content of protein lysates can result in a mucilaginous consistency, which can be resolved by either sonication or vigorously pipetting up and down to shear DNA. If DNA is not sheared, it will be difficult to accurately measure and pipet the protein lysates. Furthermore, when samples are later heated to 95 °C for protein denaturation, unsheared DNA will cause samples to solidify. If cells are lysed in an SDS protein lysis buffer, vigorous pipetting up and down to shear DNA will most often generate a foam. This will be removed by the subsequent centrifugation step; however, centrifugation may need to be extended to 15–20 min to completely remove the foam.
41. SDS precipitates at temperatures lower than 15 °C. Hence, if samples are kept on ice and not brought to room temperature, SDS will precipitate and be separated out from the sample buffer with any debris during centrifugation.
42. An equal amount of protein must be prepared for each sample, between 20 and 40 μg should be sufficient for immunodetection.
43. The volume of the protein lysate mixed with the sample buffer must not exceed the well capacity of the polyacrylamide gel.
44. Heating samples will cause condensation to appear on the lid of the microcentrifuge tubes; pulse centrifuge samples to pool this liquid.
45. A protein ladder should always be subjected to electrophoresis with protein lysates to approximate the size of detected proteins. Polyacrylamide gel electrophoresis separates proteins on the basis of size with smaller proteins migrating faster than

larger proteins. However, bands may not appear at the predicted size due to splice variants, post-translational modifications such as phosphorylation and glycosylation, relative charge of the amino acids, multimers of the protein, cleavage and degradation. Some proteins may also be resistant to denaturation and so many not be linearized, which can interfere with migration.

46. Refrain from moving the stack at this point as it may introduce air bubbles.
47. It is important to work quickly as the polyacrylamide gel can dry quickly and stick to the membrane.
48. We have observed that this step helps remove background signal.
49. It is important that the membrane is completely flat to prevent pooling in any one area.
50. The width of scratch can be changed by selecting a larger pipette; this can be helpful in the event that wound closure transpires quickly.
51. Imaging of gap closure at multiple time intervals allows for capture of changes in cell migratory rates if, for example, cells take time to respond to an intervention or stimulus, or the effects of an intervention or stimulus on cell motility are short-lived. Most often, it is sufficient to monitor cells over 24 h. If culture conditions or an intervention or treatment induce cell death, the rate of gap closure may not exclusively be a result of cell migration but also apoptotic cell death (*see* Fig. 6d).
52. Images can be enhanced in Fiji by changing the brightness and contrast. To do so, go to "Image," "Adjust," "Brightness/Contrast" and finish by clicking "Apply." Be sure to save the original file prior to saving the adjusted image. Also note, that any changes done to one image should be performed on all the same images. For example, if the DAPI needs to be brighter, then the same brightness should be applied to all DAPI images.
53. To convert the pixels to micrometers use the following equation.

$$\mu m = \frac{\text{Scale Bar Reference } (\mu m)}{\text{Scale Bar Measurement (Pixels)}}$$

54. To calculate distance travelled by the cells, subtract the final average wound size gap from the initial average wound size and divide it by 2. To convert the pixel distance to micrometers use the following equation:

$$\text{Migration Distance } (\mu\text{m}) = \text{Migration Distance (pixels)} \times \frac{\text{Scale Bar Reference } (\mu\text{m})}{\text{Scale Bar Measurement (Pixels)}}$$

55. It is helpful for subsequent imaging that all culture inserts are placed horizontally. Holding the culture insert in the middle while transferring to the culture surface ensures the silicone structure does not bend and change shape.
56. The bottom of the culture insert is coated with a sticky, biocompatible material that serves as a glue to keep the insert in place and prevent leakages, therefore it is important that it is placed the right way up. Culture inserts will not adhere to wet, uneven or unclean surfaces, or culture surfaces coated with extracellular matrix components such as fibronectin, collagen, or gelatin. Adherence to coated surfaces should be tested beforehand to ensure absence of any leakages.
57. As cells in a cell suspension settle over time to create a concentration gradient, gently pipet up and down to restore homogeneous cell dispersion. To avoid air bubbles that may create an unwanted gap in the cell monolayer, place the end of the pipette tip at the base of one the corners of the reservoirs and slowly dispense the cell suspension, then move to other corners until the full volume is dispensed. Be careful not to dislodge the culture insert.
58. Though culture inserts are only recommended for single-use, we have observed that they may be autoclaved and reused once. Further use affects the adhesive surface of the culture inserts.
59. Cell exclusion migration assays are designed to create highly defined cell gaps of a consistent size. However, removal of the culture inserts may reveal poor cell coverage at the border of the gap created or may sometimes cause partial detachment of cells at the border (*see* Fig. 6c). These irregularities in cell coverage produce inconsistencies in the size of the gap created; hence, it is important that measurements are still taken at time 0.
60. Ideally, the whole gap should be photographed in one view by using a 4× or 10× lens; this helps prevent overlap between serial images.
61. A positive control such as Fas Ligand can be added to ensure that the cleaved caspase 3 assay was successful.
62. Following addition of the streptavidin–fluorophore conjugate, for all remaining steps, cover the plate with aluminum foil to prevent photobleaching.
63. Imaging should be performed in a dark room to the prevent photobleaching.

Acknowledgments

Alexandros Somos is funded by a British Heart Foundation PhD studentship, FS/18/74/33976. Jason Johnson is funded by British Heart Foundation Senior Research Fellowship, FS/18/1/33234.

References

1. George SJ (2010) Pathogenesis of atherosclerosis. In: George SJ, Johnson J (eds) Atherosclerosis: molecular and cellular mechanisms. Wiley-VCH Verlag GmbH & Co, Weinheim, pp 3–20
2. Schwartz SM, deBlois D, O'Brien ERM (1995) The intima. Soil for atherosclerosis and restenosis. Circ Res 77(3):445–465
3. Obikane H, Abiko Y, Ueno H, Kusumi Y, Esumi M, Mitsumata M (2010) Effect of endothelial cell proliferation on atherogenesis: a role of p21(Sdi/Cip/Waf1) in monocyte adhesion to endothelial cells. Atherosclerosis 212 (1):116–122. https://doi.org/10.1016/j.atherosclerosis.2010.05.029
4. Thatte HS, Khuri SF (2001) The coronary artery bypass conduit: I. Intraoperative endothelial injury and its implication on graft patency. Ann Thorac Surg 72(6): S2245–S2252. https://doi.org/10.1016/s0003-4975(01)03272-6; discussion S2267–2270
5. Motwani JG, Topol EJ (1998) Aortocoronary saphenous vein graft disease: pathogenesis, predisposition, and prevention. Circulation 97 (9):916–931. https://doi.org/10.1161/01.cir.97.9.916
6. Duque A, Rakic P (2011) Different effects of bromodeoxyuridine and [3H]thymidine incorporation into DNA on cell proliferation, position, and fate. J Neurosci 31 (42):15205–15217. https://doi.org/10.1523/jneurosci.3092-11.2011
7. Ehmann UK, Williams JR, Nagle WA, Brown JA, Belli JA, Lett JT (1975) Perturbations in cell cycle progression from radioactive DNA precursors. Nature 258(5536):633–636. https://doi.org/10.1038/258633a0
8. Kolb B, Pedersen B, Ballermann M, Gibb R, Whishaw IQ (1999) Embryonic and postnatal injections of bromodeoxyuridine produce age-dependent morphological and behavioral abnormalities. J Neurosci 19(6):2337–2346. https://doi.org/10.1523/jneurosci.19-06-02337.1999
9. Sekerková G, Ilijic E, Mugnaini E (2004) Bromodeoxyuridine administered during neurogenesis of the projection neurons causes cerebellar defects in rat. J Comp Neurol 470 (3):221–239. https://doi.org/10.1002/cne.11016
10. Kuwagata M, Ogawa T, Nagata T, Shioda S (2007) The evaluation of early embryonic neurogenesis after exposure to the genotoxic agent 5-bromo-2′-deoxyuridine in mice. Neurotoxicology 28(4):780–789. https://doi.org/10.1016/j.neuro.2006.07.017
11. Salic A, Mitchison TJ (2008) A chemical method for fast and sensitive detection of DNA synthesis *in vivo*. Proc Natl Acad Sci U S A 105(7):2415–2420. https://doi.org/10.1073/pnas.0712168105
12. Breinbauer R, Köhn M (2003) Azide-alkyne coupling: a powerful reaction for bioconjugate chemistry. ChemBioChem 4(11):1147–1149. https://doi.org/10.1002/cbic.200300705
13. Wang Q, Chan TR, Hilgraf R, Fokin VV, Sharpless KB, Finn MG (2003) Bioconjugation by copper(I)-catalyzed azide-alkyne [3 + 2] cycloaddition. J Am Chem Soc 125 (11):3192–3193. https://doi.org/10.1021/ja021381e
14. Rostovtsev VV, Green LG, Fokin VV, Sharpless KB (2002) A stepwise huisgen cycloaddition process: copper(I)-catalyzed regioselective "ligation" of azides and terminal alkynes. Angew Chem Int Ed Engl 41 (14):2596–2599. https://doi.org/10.1002/1521-3773(20020715)41:14<2596::Aid-anie2596>3.0.Co;2-4
15. Kolb HC, Finn MG, Sharpless KB (2001) Click chemistry: diverse chemical function from a few good reactions. Angew Chem Int Ed Engl 40(11):2004–2021. https://doi.org/10.1002/1521-3773(20010601)40:11<2004::aid-anie2004>3.3.co;2-x
16. Rueden CT, Schindelin J, Hiner MC, DeZonia BE, Walter AE, Arena ET, Eliceiri KW (2017) ImageJ2: ImageJ for the next generation of scientific image data. BMC Bioinform 18 (1):529. https://doi.org/10.1186/s12859-017-1934-z

17. Schindelin J, Arganda-Carreras I, Frise E, Kaynig V, Longair M, Pietzsch T, Preibisch S, Rueden C, Saalfeld S, Schmid B, Tinevez JY, White DJ, Hartenstein V, Eliceiri K, Tomancak P, Cardona A (2012) Fiji: an open-source platform for biological-image analysis. Nat Methods 9(7):676–682. https://doi.org/10.1038/nmeth.2019
18. Brantley MA Jr, Harbour JW (2001) The molecular biology of retinoblastoma. Ocul Immunol Inflamm 9(1):1–8. https://doi.org/10.1076/ocii.9.1.1.3984
19. Dyson N (1998) The regulation of E2F by pRB-family proteins. Genes Dev 12 (15):2245–2262. https://doi.org/10.1101/gad.12.15.2245
20. Kaelin WG Jr (1999) Functions of the retinoblastoma protein. Bioessays 21(11):950–958. https://doi.org/10.1002/(sici)1521-1878(199911)21:11<950::Aid-bies7>3.0.Co;2-d
21. Sherr CJ (1994) G1 phase progression: cycling on cue. Cell 79(4):551–555. https://doi.org/10.1016/0092-8674(94)90540-1
22. Zarkowska T, Mittnacht S (1997) Differential phosphorylation of the retinoblastoma protein by G1/S cyclin-dependent kinases. J Biol Chem 272(19):12738–12746. https://doi.org/10.1074/jbc.272.19.12738
23. Harbour JW, Luo RX, Dei Santi A, Postigo AA, Dean DC (1999) Cdk phosphorylation triggers sequential intramolecular interactions that progressively block Rb functions as cells move through G1. Cell 98(6):859–869. https://doi.org/10.1016/s0092-8674(00)81519-6
24. Knudsen ES, Wang JY (1997) Dual mechanisms for the inhibition of E2F binding to RB by cyclin-dependent kinase-mediated RB phosphorylation. Mol Cell Biol 17 (10):5771–5783. https://doi.org/10.1128/mcb.17.10.5771
25. Knudsen ES, Wang JY (1996) Differential regulation of retinoblastoma protein function by specific Cdk phosphorylation sites. J Biol Chem 271(14):8313–8320. https://doi.org/10.1074/jbc.271.14.8313
26. Kong XP, Onrust R, O'Donnell M, Kuriyan J (1992) Three-dimensional structure of the beta subunit of *E. coli* DNA polymerase III holoenzyme: a sliding DNA clamp. Cell 69 (3):425–437. https://doi.org/10.1016/0092-8674(92)90445-i
27. Strzalka W, Ziemienowicz A (2011) Proliferating cell nuclear antigen (PCNA): a key factor in DNA replication and cell cycle regulation. Ann Bot 107(7):1127–1140. https://doi.org/10.1093/aob/mcq243
28. Mighell A (1995) PCNA and p53. Eur J Cancer B Oral Oncol 31b(6):403–404. https://doi.org/10.1016/0964-1955(95)00037-2
29. Maga G, Hubscher U (2003) Proliferating cell nuclear antigen (PCNA): a dancer with many partners. J Cell Sci 116(Pt 15):3051–3060. https://doi.org/10.1242/jcs.00653
30. Sherr CJ (1995) D-type cyclins. Trends Biochem Sci 20(5):187–190. https://doi.org/10.1016/s0968-0004(00)89005-2
31. Grada A, Otero-Vinas M, Prieto-Castrillo F, Obagi Z, Falanga V (2017) Research techniques made simple: analysis of collective cell migration using the wound healing assay. J Invest Dermatol 137(2):e11–e16. https://doi.org/10.1016/j.jid.2016.11.020
32. Cappiello F, Casciaro B, Mangoni ML (2018) A novel in vitro wound healing assay to evaluate cell migration. J Vis Exp (133):56825. https://doi.org/10.3791/56825
33. Jonkman JE, Cathcart JA, Xu F, Bartolini ME, Amon JE, Stevens KM, Colarusso P (2014) An introduction to the wound healing assay using live-cell microscopy. Cell Adhes Migr 8 (5):440–451. https://doi.org/10.4161/cam.36224
34. Rodriguez LG, Wu X, Guan JL (2005) Wound-healing assay. Methods Mol Biol 294:23–29. https://doi.org/10.1385/1-59259-860-9:023
35. Martinotti S, Ranzato E (2020) Scratch wound healing assay. Methods Mol Biol 2109:225–229. https://doi.org/10.1007/7651_2019_259
36. Shi Y (2004) Caspase activation, inhibition, and reactivation: a mechanistic view. Protein Sci 13(8):1979–1987. https://doi.org/10.1110/ps.04789804
37. Cullen SP, Martin SJ (2009) Caspase activation pathways: some recent progress. Cell Death Differ 16(7):935–938. https://doi.org/10.1038/cdd.2009.59
38. Brentnall M, Rodriguez-Menocal L, De Guevara RL, Cepero E, Boise LH (2013) Caspase-9, caspase-3 and caspase-7 have distinct roles during intrinsic apoptosis. BMC Cell Biol 14 (1):32. https://doi.org/10.1186/1471-2121-14-32
39. Porter AG, Jänicke RU (1999) Emerging roles of caspase-3 in apoptosis. Cell Death Differ 6 (2):99–104. https://doi.org/10.1038/sj.cdd.4400476
40. Kim S-O, Kim J, Okajima T, Cho N-J (2017) Mechanical properties of paraformaldehyde-treated individual cells investigated by atomic force microscopy and scanning ion conductance microscopy. Nano Convergence 4(1):5.

https://doi.org/10.1186/s40580-017-0099-9

41. Koley D, Bard AJ (2010) Triton X-100 concentration effects on membrane permeability of a single HeLa cell by scanning electrochemical microscopy (SECM). Proc Natl Acad Sci U S A 107(39):16783–16787. https://doi.org/10.1073/pnas.1011614107
42. Burry RW (2011) Controls for immunocytochemistry: an update. J Histochem Cytochem 59(1):6–12. https://doi.org/10.1369/jhc.2010.956920
43. Bratthauer GL (2010) The avidin–biotin complex (ABC) method and other avidin–biotin binding methods. In: Oliver C, Jamur MC (eds) Immunocytochemical methods and protocols. Humana Press, Totowa, pp 257–270. https://doi.org/10.1007/978-1-59,745-324-0_26
44. Schneider CA, Rasband WS, Eliceiri KW (2012) NIH Image to ImageJ: 25 years of image analysis. Nat Methods 9(7):671–675. https://doi.org/10.1038/nmeth.2089

Chapter 10

Monocyte Adhesion Assays for Detecting Endothelial Cell Activation in Vascular Inflammation and Atherosclerosis

Keman Xu, Fatma Saaoud, Stephanie Yu, Charles Drummer IV, Ying Shao, Yu Sun, Yifan Lu, Jianxin Sun, Jun Yu, Xiaohua Jiang, Hong Wang, and Xiaofeng Yang

Abstract

Monocyte adhesion assay, a fluorescence-based method, enables the detection and quantification of monocyte adhesion to endothelial cell (EC) monolayers in vitro and measures EC activation. We describe in this chapter a monocyte adhesion assay based on two published papers from our laboratory that can be effectively used in studying the mechanisms of both pro- and anti-inflammatory cytokines in EC activation. Endothelial cell monolayers are cultured and treated with desired drug, cytokines, or other stimuli and incubated with fluorescently labeled monocytes.

Key words Atherosclerosis, Endothelial cell activation, Inflammation, Monocytes, Monocyte adhesion assay, Adhesion molecules

1 Introduction

Cardiovascular diseases are the leading cause of morbidity and mortality worldwide. Atherosclerosis is one of the underlying causes of the development of cardiovascular diseases [1]. The activation and dysfunction of endothelial cells (ECs) are the earliest events and a central pathological process associated in the onset of atherosclerosis [2]. The innate immune system plays a critical role in disease development and accumulation of monocytes and macrophages is observed at the atherosclerotic lesion. Among the numerous stimuli, circulating proinflammatory cytokines bind to their receptors on the ECs, leading to the upregulation of leukocyte adhesion factors facilitating monocyte adhesion and extravasation to the subendothelial space. These monocytes differentiate into

Fatma Saaoud and Stephanie Yu shared second authorship.

Dipak P. Ramji (ed.), *Atherosclerosis: Methods and Protocols*, Methods in Molecular Biology, vol. 2419,
https://doi.org/10.1007/978-1-0716-1924-7_10,
© The Author(s), under exclusive license to Springer Science+Business Media, LLC, part of Springer Nature 2022

macrophages and take up oxidized low-density lipoproteins to form foam cells and fatty streaks, leading to more advanced atherosclerotic lesions [3, 4]. EC activation results in innate immune phenotypic changes of the endothelium in response to inflammatory mediators (Table 1) [2, 5–9]. EC activation is characterized by various vascular pathophysiological and immunological features, including upregulation of expression of EC adhesion molecules, such as intercellular adhesion molecule-1 (ICAM-1) and vascular cell adhesion molecule-1 (VCAM-1) [10], increased cytokine/chemokines secretion, activation of danger associated molecular patterns (DAMPs), upregulation of major histocompatibility complex-II and the activation of T-cell cosimulation receptors and coinhibition/immune checkpoint receptors (Table 2) [11]. Several experimental methods such as monocyte adhesion assay, Boyden chamber assay, Western blotting, real-time polymerase chain reaction (RT-PCR), flow cytometry, and RNA-sequencing have been used to examine EC activation (Table 3). We have focused here on endothelium adhesion assay, one of the most common functional EC activation assays used.

At the functional level, EC activation is assessed by quantifying the total number of monocytes that adhere to an EC layer. This experiment is performed by either a direct count or by indirect measurement of fluorescently labeled adherent monocytes. Monocyte adhesion assay is a powerful in vitro technique used to quantify the function of adhesion molecules in leukocyte–endothelial interactions. Initially, EC adhesion was quantified by manually counting leukocytes that adhered to the EC monolayer. Over time, quantification of radiolabeled leukocytes gradually superseded the manual counting. Recently, a fluorescence-based adhesion assay has emerged and replaced the radioactive isotope technique. The fluorescence-based technique allows for a more convenient, sensitive and flexible method for studying EC adhesion with fewer disposal requirements (Fig. 1a) [9, 12, 13]. The experimental principles of the adhesion assay include: (i) activation of EC monolayers with the desired drugs or cytokines; (ii) labeling of the nonstimulated monocytes with a cell-permeable fluorescent dye; (iii) incubation of the activated EC monolayer with the fluorescently labeled monocytes; (iv) washing off unlabeled cells; and (v) quantification of the fluorescently labeled cells associated with the EC by a fluorescence plate reader (Fig. 1b) [9, 14].

In this chapter, we describe a method that allows the enumeration of adhesive cells to an endothelial monolayer. Also, we demonstrate the flexibility in using such adhesion assay for assessing both activation and inhibition of EC activation.

Table 1
Different types of endothelial cell (EC) stimuli, their effects on ECs and disease models

Type	Stimulus	Effects	Related diseases
Mechanical stimuli	Shear stress	The mitochondrial electron transport chain transduces signaling, leading to the release of pronociceptive mediators and causes EC activation. Lower shear rates can promote leukocyte recruitment.	Atherosclerosis
Chemical stimuli	Histamine	Induces the rapid mobilization of P-selectin expressed on the endothelium and enhances leukocyte rolling.	Allergy, asthma
	Leukotrienes Platelet activating factor (PAF)	Increases the expression of CD11/CD18 and transforms leukocytes from reversible adhesion into firm adhesion.	Chronic inflammation
	Cytokines and chemokines	Increases the expression of adhesion molecules [intercellular adhesion molecule-1 (ICAM-1), vascular cell adhesion molecule-1 (VCAM-1)].	Inflammation
	Oxidative stress Lysophosphatidylcholine (LPC)	Produces reactive oxygen species (ROS) at an accelerated rate and increases leukocyte rolling, adhesion and migration.	Diabetes mellitus, metabolic syndrome
Pathological stimuli	Lipopolysaccharide (LPS)	Causes thrombosis-enhancing effects. LPS can induce neutrophils to make neutrophil extracellular traps (NETs).	Infections
Antiadhesive Anti-adhesive mediators	Nitric oxide (NO)	NO is an endogenous inhibitor of leukocyte adhesion.	Vasodilatation
	Adenosine	Adenosine A2 receptor inhibits neutrophilic superoxide production.	
	Prostacyclin (PGI2)	Inhibits platelet aggregation.	

2 Materials

2.1 Endothelial Cell Culture

1. Human aortic endothelial cells (HAECs).
2. M1999 media.
3. 20% fetal bovine serum (FBS): thaw FBS at room temperature (RT) or in a 37 °C water bath. Incubate in 56 °C water bath for 30 min post thaw. Cool on ice and store at −20 °C.

Table 2
Six major features of endothelial cell activation

Hallmark feature	Basic principle	Experiments	PMID
Upregulation of EC adhesion molecules	The adhesion of leukocytes to the vascular endothelium is a sign of EC activation. ICAM-1, VCAM-1, and PECAM-1 are immunoglobulin superfamily-like adhesion molecules expressed on the endothelium. These adhesion molecules cause leukocyte interaction with their respective receptors to mediate firm adhesion and extravasation.	Leukocyte endothelium adhesion assay	26085094
			26733204
		Photomicrograph	19858416
			27127201
		Flow cytometry	26733204
			25854700
Secretion of cytokines and chemokines	Cytokines and chemokines are secreted proteins that usually accompany growth, activation and differentiation functions. They regulate immune responses, including immune cell trafficking. Thus, their secretion plays an important role in studying the mechanisms of EC activation.	Cytokine array	25705917
			27992360
		Cytokine and chemokine blocking assay	26733204
		RT-PCR	26733204
Activation of DAMPs receptors	According to our previous data, ECs are identified as novel immune cells that perform specific innate immune functions, including in both DAMP and PAMP sensing. Increased pathogen concentrations can trigger an inflammatory response and lead to EC activation. Studying the concentration of inflammatory mediators, such as caspase-1, can indirectly show the activation of ECs.	Fluorochrome inhibitor of caspase (FLICA) kits	26037927
			25705917
		Western blots	25705917
Upregulation of MHC-II and cosignaling receptors	ECs can transdifferentiate into innate immune cells during inflammation and express MHC-II, DAMP receptors and T-cell costimulation/inhibition receptors on the cell surface.	RNA-sequencing	29769317
			31731100
		Database mining	30468648
Atherosclerosis	Atherosclerosis is one of the outcomes of EC activation. It can be used to analyze the severity of disease progression via quantification of atherosclerotic area/plaque percentage in the aortic sinus.	Histology and staining	12506016
			19858416
Immune-tolerogenic function	EC activation can induce suppressive immune regulatory T cells (T-regs). Consequently, T-regs upregulate the expression of immune checkpoint receptors and produce anti-inflammatory cytokines to prevent further downstream inflammatory processes.	Microarray database mining	30468648
			31731100

DAMPs danger associated molecular patterns, *EC* endothelial cells, *ICAM-1* intercellular adhesion molecule-1, *MHC-II* major histocompatibility class-II, *PAMP* pathogen-associated molecular pattern, *PECAM-1* platelet endothelial cell adhesion molecule-1, *RT-PCR* real time polymerase chain reaction, *T-regs* regulatory T cells, *VCAM-1* vascular cell adhesion molecule-1

Table 3
Methods for assessing endothelial cell activation *in* vitro

Technique	Description	PMID
Monocyte adhesion assay	Used to measure adhesiveness of blood monocytes into endothelial cell layer.	26733204, 26085094, 29371247, 27127201
Trans-well migration assay	Commonly used to study the migratory response of endothelial cells toward a chemoattractant.	29511499
Real-time polymerase chain reaction (RT-PCR)	Used to examine mRNA expression levels of adhesion molecules such as ICAM-1, VCAM-1, and E-selectin.	29371247
Western blotting	Used to examine protein levels of adhesion molecules such as ICAM-1, VCAM-1, and E-selectin.	29371247, 25705917
Flow cytometry analysis	Used to examine expression of adhesion molecules such as ICAM-1 and VCAM-1 as well as monocyte migration.	25705917, 26085094, 26733204
Cytokine array	Used to determine cytokine and chemokine expression in activated endothelial cells.	26085094, 25705917
RNA sequencing	Provides information on the expression levels of adhesion molecules and other endothelial cell activation genes.	29769317, 29371247
Microarray analysis	Used to examine the expression levels of adhesion molecules and cytokines/chemokines.	26733204, 27127201, 29371247
Endothelial cell biology PCR array	Used to examine expression of 84 endothelial cell-related genes.	27127201
Enzyme-linked immunosorbent assay (ELISA)	Used to determine protein levels of different cytokine/chemokines released from activated endothelial cells.	26085094
FAM-FLICA caspase-1 assay	Utilizes the fluorescent inhibitor probe FAM-YVAD-FMK to label active caspase-1 enzyme in living cells (the inflammatory sites of the endothelium).	25739025

ICAM-1 intercellular adhesion molecule-1, *VCAM* vascular cell adhesion molecule-1

4. 25 mg/mL Heparin: weigh 300 mg heparin in 15 mL tube. Add 12 mL of serum-free M199 media, mix well and filter through a 0.22 μm Nalgen filter. Store at 4 °C.
5. 10 mg Endothelial cell growth supplement (ECGS): add 10 mL of serum free M199 media into ECGS's vial containing 100 mg ECGS, mix well and filter through a 0.22 μm Nalgen filter. Store at −20 °C.
6. Penicillin/Streptomycin/Amphotericin-B (PSA): make 10 mL aliquots per tube and store at −20 °C.

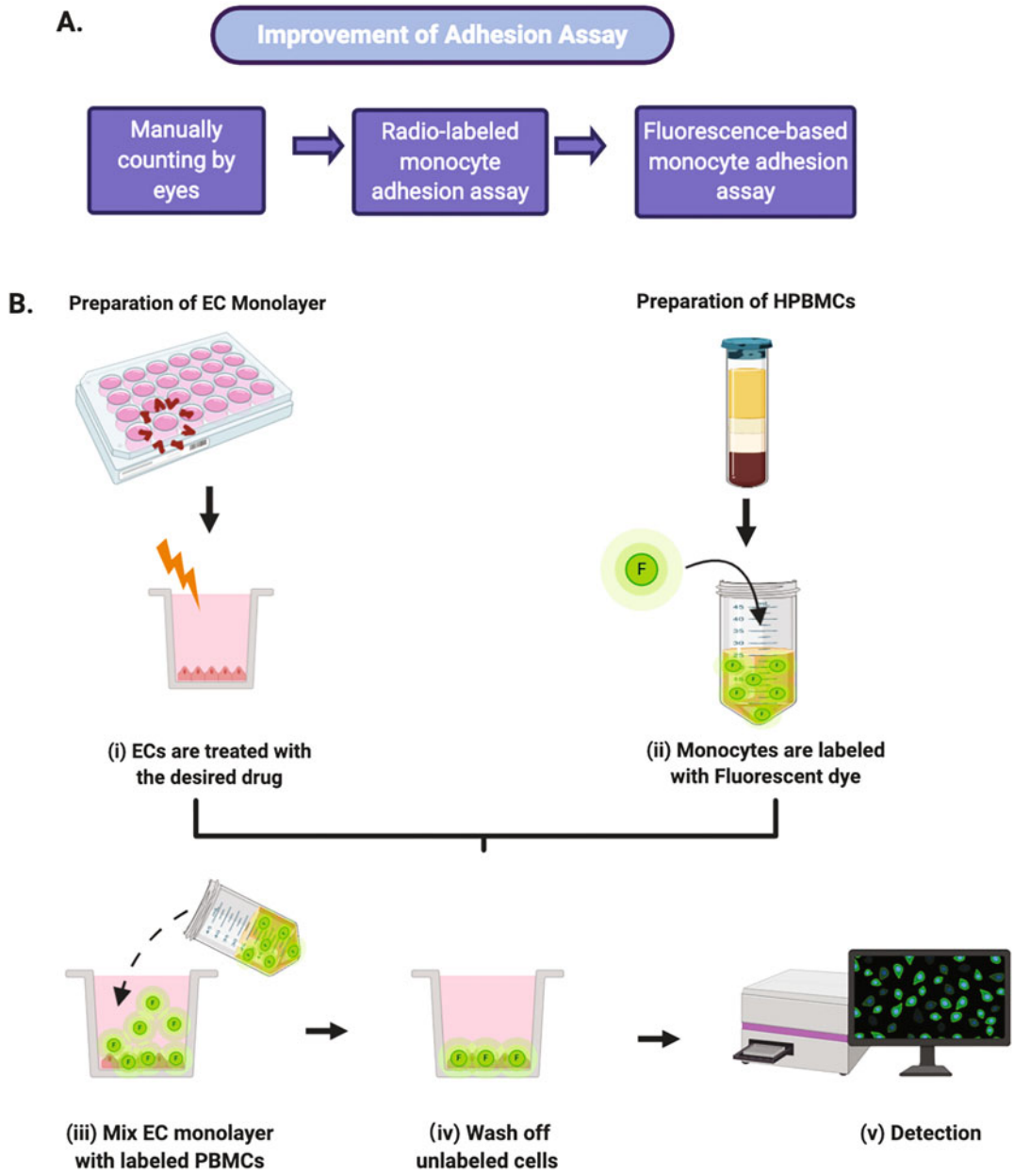

Fig. 1 Leukocyte adhesion assay experimental workflow. (**a**) A brief history of the development of adhesion assay. Currently, the fluorescence-based adhesion assay is the dominant tool used to study EC adhesion. (**b**) A schematic diagram of the fluorescence-based adhesion assay. The process includes EC monolayer and human peripheral blood mononuclear cells (HPBMCs) preparation and treatment, mixture of treated EC monolayer and labeled HPBMCs and detection and quantitation of fluorescence intensity

7. Endothelial cell growth media: In 500 mL of M199 media, add 100 mL of FBS (20%), 1 mL of 25 mg/mL heparin (50 μg/

mL), 3 mL of 10 mg/mL ECG (30 mg), and 5 mL of PSA (1%). Mix well and store at 4 °C.

8. 0.2% Gelatin: weight 1 g and dissolve in a 500 mL of ultrapure water (dH_2O). Autoclave and store at 4 °C.
9. 0.25% trypsin–ethylenediaminetetraacetic acid (EDTA) solution: 0.25% (w/v) trypsin, 0.2% (w/v) EDTA.4Na in 1 L of 1×HBSS. Store at −20 °C.
10. Hanks's Balanced Salt Solution (HBSS).
11. 0.2% gelatin-coated 75 cm^2 Corning cell culture flasks.
12. Sterile 50 mL centrifuge tubes.
13. Cell culture incubator (37 °C, 5% CO_2 atmosphere).
14. Centrifuge machine with swing-out bucket rotor.
15. Hemocytometer.
16. Falcon 24-well multiwell flat bottom TC-treated cell culture plate.
17. Adjustable volume micropipettes.
18. Micropipette tips.
19. Motorized Pipette Fillers.

2.2 Human Peripheral Blood Mononuclear Cell (PBMC) Isolation

1. Freshly collected heparinized human peripheral blood.
2. Ficoll Histopaque 1083 solution.
3. Sterile 1× phosphate-buffer saline (PBS).
4. Roswell Park Memorial Institute (I) 1640 media supplemented with 10% fetal calf serum (FCS).
5. 1 mL pipette.

2.3 Monocyte-Endothelial Cell Adhesion Assay

1. Calcein AM fluorescence dye.
2. Serum-free RPMI 1640 media.
3. Fluorescence microplate reader.

3 Methods

All solutions and equipment coming into contact with cells must be sterile. Proper sterile technique must be used accordingly.

3.1 Preparation of Endothelial Cell Monolayer

1. Culture HAECs (< passage 8) in 0.2% gelatin-coated 75 cm^2 Corning cell culture flasks in 20 mL of endothelial cell growth media and incubate the cells in a cell culture incubator at 37 °C with 5% CO_2 and 95% humidity.
2. Change media every other day until cells reach 90–100% confluency.

3. Remove culture media and wash cell twice with 10 mL of warm HBSS.
4. Completely aspirate HBSS and add 2 mL of 0.2% trypsin–EDTA solution. Ensure the trypsin solution fully covers the flask surface and return the cells to the cell culture incubator for 1 min.
5. Once the cells have fully detached, add 8 mL of M199 media to the flask to stop the trypsinization. Gently tilt the flask and carefully pipette up and down to ensure all HAECs are detached from the flask surface.
6. Transfer cells to a 50 mL tube and centrifuge at 400 × *g* for 5 min at 4 °C to pellet the cells.
7. Carefully aspirate off the supernatant. Flick the tip of the conical tube with your finger to loosen the cell pellet. Resuspend the cells in 5 mL of endothelial cell growth media, gently pipetting the cells to break up any clumps.
8. Count the cells with a hemocytometer and adjust the cell concentration to 50,000 cells/mL.
9. Seed 1 mL of the cell suspension in each well of a Falcon 24-well cell culture plate coated with 0.2% gelatin and incubate in a cell culture incubator at 37 °C, 5% CO_2 and 95% humidity.
10. Culture the cells for 48–72 h until the endothelial cells form a monolayer.
11. Treat the endothelial cell monolayer with the desired activator or inhibitor under investigation for 6–72 h.

3.2 Preparation of Human Peripheral Blood Mononuclear Cells (PBMC)

1. Add 20 mL of Histopaque 1083 solution into 50 mL centrifuge tubes (*see* **Note 1**) [15].
2. Add 25 mL of heparinized human peripheral blood onto Ficoll-Plaque in each tube. Layer the blood gently by allowing it to run down the side of the tube (*see* **Note 2**).
3. Centrifuge at 400 × *g* for 30 min at RT (*see* **Note 3**). After centrifugation, the human peripheral blood will be divided into five distinct layers (Fig. 2) [9, 13]. The red blood cells (RBCs) settle to the bottom of the tube and granulocytes (primarily neutrophils) serve as a "buffy coat" on top of the RBCs. Directly above the surface of the granulocytes is an intermediate phase of Ficoll, followed by the PBMC layer, and finally the plasma on the uppermost layer.
4. Without disturbing the PBMC layer, carefully aspirate off the plasma with plastic micropipette tips (leaving 2.5–5 mL of plasma above the PBMC layer).
5. Using a 1 mL pipette, carefully collect 10 mL of the PBMC layer (*see* **Note 4**).

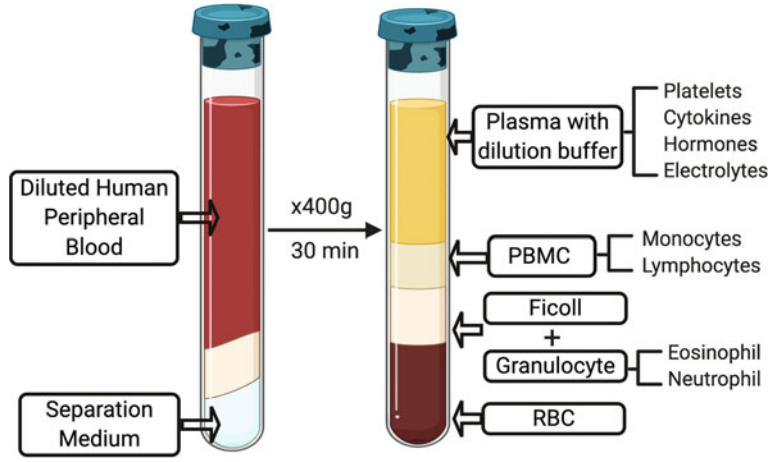

Fig. 2 Density gradient centrifugation of human peripheral blood mononuclear cells (PBMCs). After centrifugation, PBMCs can be divided into five layers. *RBC* red blood cells

6. Add 30 mL of PBS to these mononuclear cells and gently invert the tube several times to mix. Centrifuge the resuspended mononuclear cells at 250 × *g* for 10 min at room RT and carefully remove all the supernatant.
7. For platelet removal, resuspend the cell pellet in 0.5 mL of PBS. Then add another 15 mL of PBS and gently invert the tube several times to mix. Centrifuge at 350 × *g* for 5 min at RT and carefully remove the supernatant.
8. Resuspend the cell pellet in 1.5 mL of RPMI 1640 media supplemented with 10% FCS. Count the cells using a hemocytometer and adjust the cell concentration to 5×10^6 PBMCs/mL.

3.3 Monocyte-Endothelial Cell Adhesion Assay

1. Treat cultured HAECs in 24 well plates with desired drugs as Subheading 3.1, **step 11** (*see* **Note 5**). Treatment times will vary depending on the various drugs.
2. Prepare PBMCs during the last 40 min of treatment as Subheading 3.2.
3. Stain PBMCs with 2 μM of Calcein AM fluorescent dye in serum free RPMI 1640 media at 37 °C in cell culture incubator for 30 min (*see* **Note 6**).
4. Keep some PBMCs in the 37 °C cell culture incubator as a nonstaining control (*see* **Note 7**).
5. Wash the cells from **step 3** twice with 10 mL of PBS to remove any extra Calcein AM. For each wash, centrifuge cells at 250 × *g* for 10 min and carefully remove the supernatant.

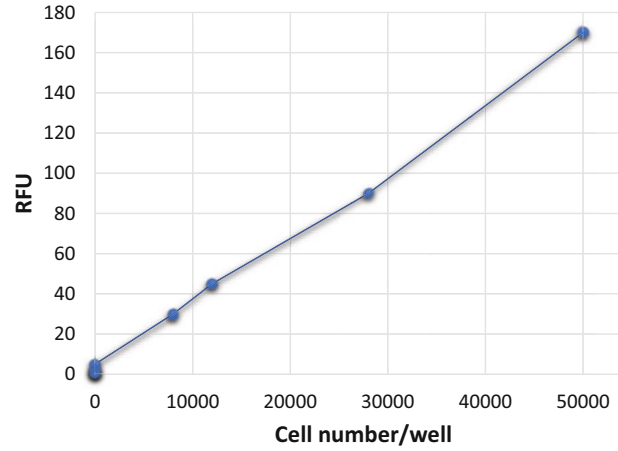

Fig. 3 Quantitation of fluorescently labeled PBMCs adhered to activated endothelial cells. Calcein AM fluorescently labeled monocytes were titrated in 1× PBS. Fluorescence was quantified using a fluorescence plate reader and represented as relative fluorescence unit (RFU)

6. Resuspend PBMCs in endothelial cell growth media and RPMI1640 media supplemented with 10% FCS (1:1) and adjust concentration to 1×10^6 cells/mL (*see* **Note 8**).
7. Remove M199 media from cultured HAECs from **step 1** and wash cells twice with PBS.
8. Add 1 mL (1×10^6) of labeled PBMCs to each well and incubate for 1 h in a cell culture incubator at 37 °C (*see* **Note 9**).
9. Carefully aspirate the media from each well (do not allow the cells to dry) and gently wash three times with PBS to remove unattached monocytes. Protect stained cells from light.
10. Add 1 mL of PBS to each well and read the fluorescence intensity of the labeled monocytes with a fluorescence microplate reader (*see* Fig. 3).

3.4 Example of Results

For better understanding, we have selected two published papers from our laboratory to demonstrate in detail how we implemented the monocyte adhesion assay. The fluorescence intensity was measured on a microplate fluorescence reader (FLx800, Bio-Tek, Winooski, VT) with a 494/517 nm filter set and 488 nm cutoff. The percentage of adherent monocytes to EC monolayer was represented as a percentage of the control group (Fig. 4) [13]. In the first paper, we investigated how the proinflammatory cytokine interleukin-17 (IL-17) promotes aortic EC activation [16]. The second paper [17] looks at how the anti-inflammatory cytokine interleukin-35 (IL-35) inhibits EC activation (Table 4). Interleukins (IL) have been identified as a group of cytokines that elicit a

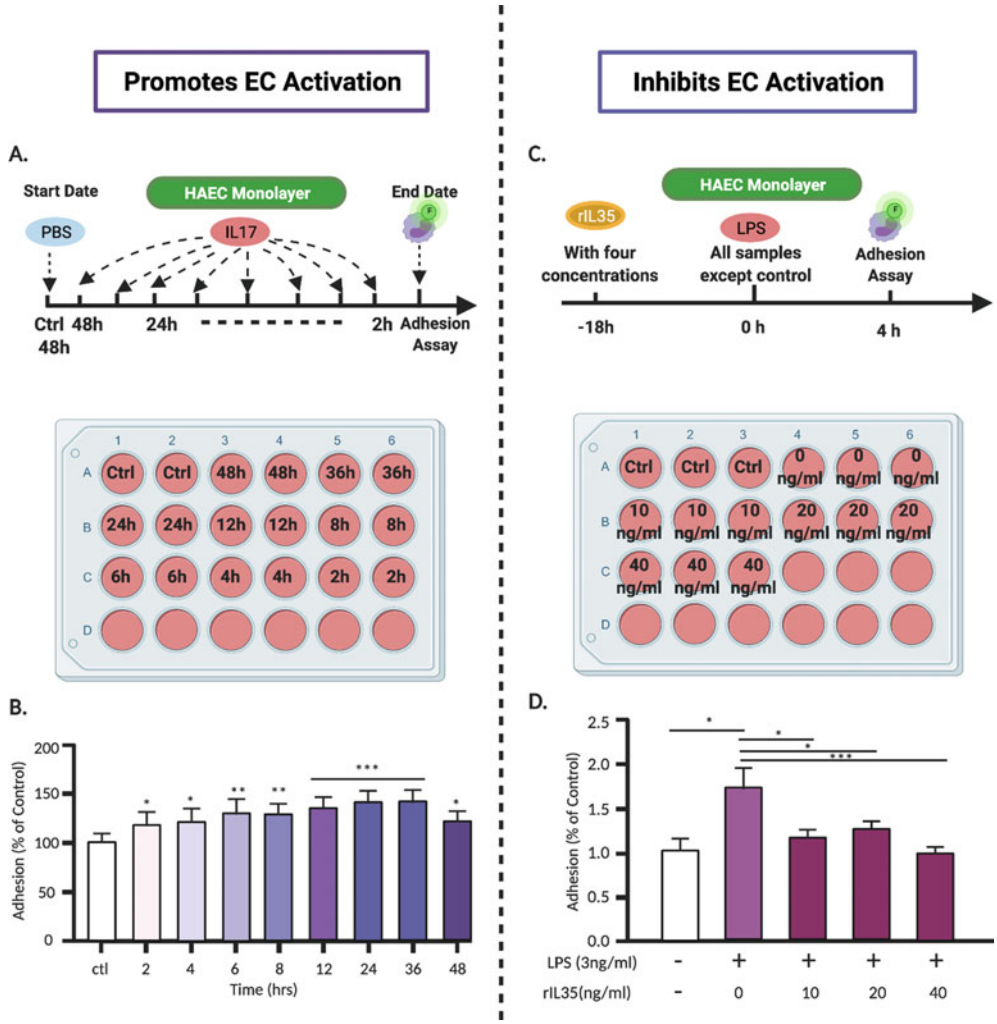

Fig. 4 Adhesion assay experimental design for evaluating the actions of pro- and anti-inflammatory stimuli. (**a**) HAECs were cultured in 24-well plates and then treated with human IL-17 for various time periods. (**b**) Monocytes adhesion to HAECs increases by IL-17A with time: 12-, 24-, and 36-h treatment periods demonstrate a significant increase in adhesion in a time dependent manner. (**c**) Four different concentrations (0, 10, 20 and 40 ng/mL) of rIL35 were added 18 h prior to HAEC treatment with LPS (3 ng/mL) in 24-well plates. (**d**) Fluorescence-labeled human PBMCs adhesion to HAECs stimulated by LPS + rIL35 or LPS only. The results showed that after LPS treatment, the adhesion of human PBMCs to HAECs was significantly increased. However, LPS plus as low as 10 ng/ml rIL35 could dramatically inhibited the adhesion of PBMCs to LPS-activated HAECs

wide range of responses in cells and tissues. They are involved in several immunomodulatory functions such as adhesion, migration, maturation and proliferation. Depending on their function, ILs can be characterized as either pro- or anti-inflammatory [18]. ILs are highly expressed in leukocytes and initiate a response through binding to high-affinity receptors located on the cell surface.

Table 4
Monocyte adhesion assay.

Treatment	IL-17A	LPS + IL-35
Cells	HAECs, PBMCs	HAECs, PBMCs
Experimental design (trait)	Time course	Dose response
Result	IL-17 significantly increased monocyte adhesion in a time dependent manner and promoted EC activation	IL-35 inhibited LPS-induced leukocyte adhesion to ECs in a dose dependent manner
EC status	Increases EC activation	Inhibits LPS-induced EC activation
PMID	26733204	26085094

EC endothelial cells, *HAECs* human aortic endothelial cells, *IL* interleukin, *LPS* lipopolysaccharide, *PBMCs* peripheral blood mononuclear cells

Therefore, ILs play a pivotal role in modulating leukocyte adhesion and EC activation. Since the specific function of a particular IL is dependent upon its interactions with receptors located on the target cells (ECs), monocyte-EC static adhesion assay is performed and are valuable in gaining insights into cytokine actions.

4 Notes

1. 40 mL of blood is sufficient for collecting 30×10^6 PBMCs for one plate.
2. The blood should not penetrate deep into the Ficoll-Plaque to avoid Ficoll toxicity to the cells. The first 5 mL of layering is the most sensitive and important.
3. Centrifugation of $400 \times g$ is optimal to obtain a clean buffy coat.
4. Do not collect more than 10 mL of cells as this will reduce yields.
5. In order to achieve the different experimental aims, HAECs are treated with various drugs. As examples, we outline two experimental strategies in studying both pro- and anti-inflammatory cytokines based on our published papers.
   (a) Study 1 [16]: To determine whether the proinflammatory cytokine IL-17 has the ability to activate ECs, HAEC monolayers were grown in 24-well plates and treated with IL-17 (100 ng/mL) at different time points (Fig. 4a) [9]. The adhesion assay was performed, and results showed that IL-17 increases the number of

monocytes adhering to HAECs in a time-dependent manner, therefore activating ECs (Fig. 4b) [9]

(b) Study 2 [17]: To determine whether the anti-inflammatory cytokine IL-35 has a potential therapeutic ability to reverse EC activation, HAECs were stimulated with lipopolysaccharides (LPS) to induce EC activation, then treated with IL-35 (0, 10, 20 and 40 ng/mL) for 18 h (Fig. 4c) [9]. The adhesion assay was performed, and the results demonstrated that IL-35 treatment decreased the number of monocyte adhesion to HAECs, therefore inhibiting EC activation (Fig. 4d).

6. Calcein AM should not affect the viability of ECs and fresh Calcein AM should be used each time.
7. At least one well of the 24-well plate is used as a nonstaining negative control (HAECs + PBMCs in PBS).
8. Each stimulation is performed in triplicate for statistical analysis and the experiments should be repeated at least three times.
9. 1×10^6 cells/mL of PBMCs in each well is sufficient for use in the adhesion assay.

Acknowledgment

This work was supported by NIH R01 grants to XY.

References

1. Roth GA, Johnson C, Abajobir A et al (2017) Global, regional, and national burden of cardiovascular diseases for 10 causes, 1990 to 2015. J Am Coll Cardiol 70(1):1–25. https://doi.org/10.1016/j.jacc.2017.04.052
2. Gimbrone MA Jr, Garcia-Cardena G (2016) Endothelial cell dysfunction and the pathobiology of atherosclerosis. Circ Res 118(4): 620–636. https://doi.org/10.1161/CIRCRESAHA.115.306301
3. Mestas J, Ley K (2008) Monocyte-endothelial cell interactions in the development of atherosclerosis. Trends Cardiovasc Med 18(6): 228–232. https://doi.org/10.1016/j.tcm.2008.11.004
4. Libby P, Pasterkamp G, Crea F, Jang IK (2019) Reassessing the mechanisms of acute coronary syndromes. Circ Res 124(1):150–160. https://doi.org/10.1161/circresaha.118.311098
5. Iruela-Arispe ML (2008) Endothelial cell activation. In: Angiogenesis. Springer, Boston. https://doi.org/10.1007/978-0-387-71518-6_3
6. Joseph EK, Green PG, Bogen O, Alvarez P, Levine JD (2013) Vascular endothelial cells mediate mechanical stimulation-induced enhancement of endothelin hyperalgesia via activation of P2X2/3 receptors on nociceptors. J Neurosci 33(7):2849–2859. https://doi.org/10.1523/JNEUROSCI.3229-12.2013
7. Branco A, Yoshikawa FSY, Pietrobon AJ, Sato MN (2018) Role of histamine in modulating the immune response and inflammation. Mediat Inflamm 2018:9524075. https://doi.org/10.1155/2018/9524075
8. Kelesidis T, Papakonstantinou V, Detopoulou P, Fragopoulou E, Chini M, Lazanas MC, Antonopoulou S (2015) The role of platelet-activating factor in chronic inflammation, immune activation, and comorbidities associated with HIV infection. AIDS Rev 17(4):191–201
9. Ray CJ, Abbas MR, Coney AM, Marshall JM (2002) Interactions of adenosine,

prostaglandins and nitric oxide in hypoxia-induced vasodilatation: in vivo and in vitro studies. J Physiol 544(Pt 1):195–209. https://doi.org/10.1113/jphysiol.2002.023440

10. Cybulsky MI, Gimbrone MA Jr (1991) Endothelial expression of a mononuclear leukocyte adhesion molecule during atherogenesis. Science 251(4995):788–791. https://doi.org/10.1126/science.1990440
11. Li X, Wang L, Fang P, Sun Y, Jiang X, Wang H, Yang XF (2018) Lysophospholipids induce innate immune transdifferentiation of endothelial cells, resulting in prolonged endothelial activation. J Biol Chem 293(28):11033–11045. https://doi.org/10.1074/jbc.RA118.002752
12. Lowe DJ, Raj K (2015) Quantitation of endothelial cell adhesiveness in vitro. J Vis Exp 100:e52924. https://doi.org/10.3791/52924
13. All figures were created with Biorender.com https://biorender.com/
14. Cell BIOLABS I (2020) Leukocyte endothelium adhesion assay
15. Fuss IJ (2009) Isolation of whole mononuclear cells from peripheral blood and cord blood. Curr Protoc Immunol Chapter 7:Unit7.1. https://doi.org/10.1002/0471142735.im0701s85
16. Mai J, Nanayakkara G, Lopez-Pastrana J, Li X, Li YF, Wang X, Song A, Virtue A, Shao Y, Shan H, Liu F, Autieri MV, Kunapuli SP, Iwakura Y, Jiang X, Wang H, Yang XF (2016) Interleukin-17A promotes aortic endothelial cell activation via transcriptionally and post-translationally activating p38 mitogen-activated protein kinase (MAPK) pathway. J Biol Chem 291(10):4939–4954. https://doi.org/10.1074/jbc.M115.690081
17. Sha X, Meng S, Li X, Xi H, Maddaloni M, Pascual DW, Shan H, Jiang X, Wang H, Yang XF (2015) Interleukin-35 inhibits endothelial cell activation by suppressing MAPK-AP-1 pathway. J Biol Chem 290(31):19307–19318. https://doi.org/10.1074/jbc.M115.663286
18. Brocker C, Thompson D, Matsumoto A, Nebert DW, Vasiliou V (2010) Evolutionary divergence and functions of the human interleukin (IL) gene family. Hum Genomics 5(1):30–55. https://doi.org/10.1186/1479-7364-5-1-30

Chapter 11

Chick Embryo Ex Vivo Aortic Sprouting Assays for Cardiovascular Research

Selvaraj Vimalraj and Anuradha Dhanasekaran

Abstract

Angiogenesis is the formation of new blood vesicles and is controlled by a dynamic cascade of molecular and cellular activities. The whole procedure can be replicated in vitro under chemically specified conditions by cultivating chick aortic explants in biomatrices. In this technique, angiogenesis is powered by endogenous molecules that the aorta releases to promote its outgrowth. In an ordered series of morphogenetic events, sprouting endothelial cells are strongly associated with macrophages, fibroblasts, and pericytes, recapitulating all the phases of the angiogenic process. The structural, morphologic, and molecular properties of the angiogenic process can be studied and the effectiveness of pro/antiangiogenic drugs can also be evaluated using this aortic culture. We describe in this chapter the basic procedure currently used in our laboratory to measure the angiogenic properties for cardiovascular research.

Key words Chick embryo, Aorta rings, Angiogenesis, Sprouting, Cardiovascular diseases

1 Introduction

The angiogenic mechanisms in atherosclerosis and other cardiovascular diseases are poorly understood and have been of substantial recent interest for basic research and as potential treatment for ischemic coronary diseases and improving atheroprotective elements of the endothelium. Some evidence suggests that neovascularization potentially contributes to atherosclerotic injuries and is a key factor in plaque destabilization. For patients with ischemic heart or vascular disease, therapy targeted at angiogenic factors has been suggested as an indirect route for biological treatment [1]. Angiogenic mechanisms are regularly studied in the laboratory for gaining mechanistic insights and delineating targets for clinical evaluation. To that end, a few in vitro models have been created to investigate the angiogenic cycle and assess the effectiveness of potential pro/antiangiogenic drugs [2]. Among the angiogenic assays, the ex vivo aortic ring assay has been demonstrated to be

Dipak P. Ramji (ed.), *Atherosclerosis: Methods and Protocols*, Methods in Molecular Biology, vol. 2419,
https://doi.org/10.1007/978-1-0716-1924-7_11,
© The Author(s), under exclusive license to Springer Science+Business Media, LLC, part of Springer Nature 2022

especially solid and reproducible. The chick aortic ring assay has many similarities to the rodent aortic ring assay with some distinct advantages. For example, the chick aortic ring assay overcomes the utilization of large laboratory animals, is quick with duration of 1–3 days, and can be completed in serum free medium. Aortic rings are obtained from day 9 to 11 chick eggs and sliced into rings similar to those for the rodent aorta. Once the rings are cultured on Matrigel, a considerable outgrowth of the cells occurs in 48 h with obvious development of vessel-like morphological structures. If the aortic ring is turned prior to explanations, the optimal time for detecting endothelial cell outgrowth can be reduced to 24 h.

The aortic rings' angiogenic reaction is a self-restricted cycle controlled at numerous levels [3]. In the development, differentiation, and stabilization of vascular tubes, paracrine and juxtacrine signaling between endothelial cells, fibroblasts, macrophages, and pericytes play a crucial role. The model of the ex vivo aortic ring incorporates the benefits of both in vivo and in vitro studies. In a given environment, neovessel growth occurs and the cultivation system can be easily applied to various test conditions. Repeated passages in culture do not change the endothelium of the aorta, which behaves like endothelial cells in vivo.

Microvessels are formed from an adequately cap polarized layer of endothelial cells and pericytes. The interstitial space between growing out of microvessels contains fibroblasts. There are no circling leukocytes so there is no bloodstream, but resident macrophages and dendritic cells relocate out of the aortic adventitia and efficiently engage in the angiogenic process [4]. The ex vivo aortic ring test has become very well-known due to its reliability and reproducibility and is currently used in numerous angiogenic assays for cardiovascular research. Although this technique is generally simple and easy to implement, it can nevertheless pose several challenges. These include significant death, increased risks of contamination, and more stringent incubation management [5]. We define here important conventions required to effectively plan and properly manipulate chick aortic ring cultures. This chapter should be useful for new researchers in the field and those that are using other model systems on the potential benefits of the use of chick embryos.

2 Materials

1. Fertilized brown leghorn chicken egg (*Gallus gallus domesticus)* (*see* **Notes 1–3**).
2. Egg incubator.
3. Buddy Mk2 Digital egg monitor (Avitronics).
4. Digital scale.

5. Caliper.
6. Scalpel (blade no. 11).
7. Petri dishes.
8. Forceps.
9. Glass slide.
10. Coverslips.
11. Inverted microscope.
12. Paraffin.
13. Tissue paper.
14. Sterile cabinet or hood.
15. 24-well plate.
16. Cell culture incubator.
17. Suitable imaging software: Angioquant, Image J.
18. Matrigel™ basement matrix (BD Biosciences).
19. 70%, 95%, and 100% ethanol.
20. Acidified ethanol: 95% ethanol in concentrated HCl.
21. 1× phosphate buffered saline (PBS): Add 1.44 g of Na_2HPO_4, 0.24 g of KH_2PO_4, 8 g of NaCl, and 0.2 g of KCl to 800 mL of distilled water. Adjust the pH to 7.4 and make up to a final volume of 1 L using distilled water.
22. 10% neutral buffered formalin: Add 10 mL of formalin to 90 mL of distilled water and then add 0.9 g of NaCl and 1.2 g of Na_2HPO_4. Adjust the pH to 7.0.
23. Xylene.
24. Hematoxylin staining solution: Dissolve 0.64 g of hematoxylin in 64 mL of distilled water using gentle heat. Then, add 6 g of ammonium alum, 20 mL of ethanol, and 16 mL of glycerol to make up a final volume of 100 mL.
25. Eosin staining solution: Dissolve 0.1 g of Eosin Y (C.I. 45,380) in 100 mL of 70% ethanol and then add 2–3 drops of glacial acetic acid.
26. Dulbecco's Modified Eagle's Medium (DMEM): With 3.7 g/L $NaHCO_3$ (w/o: glucose, w/o: L-glutamine, w/o: sodium pyruvate, w/o: HEPES).
27. Fetal bovine serum (FBS).
28. 100× penicillin–streptomycin.

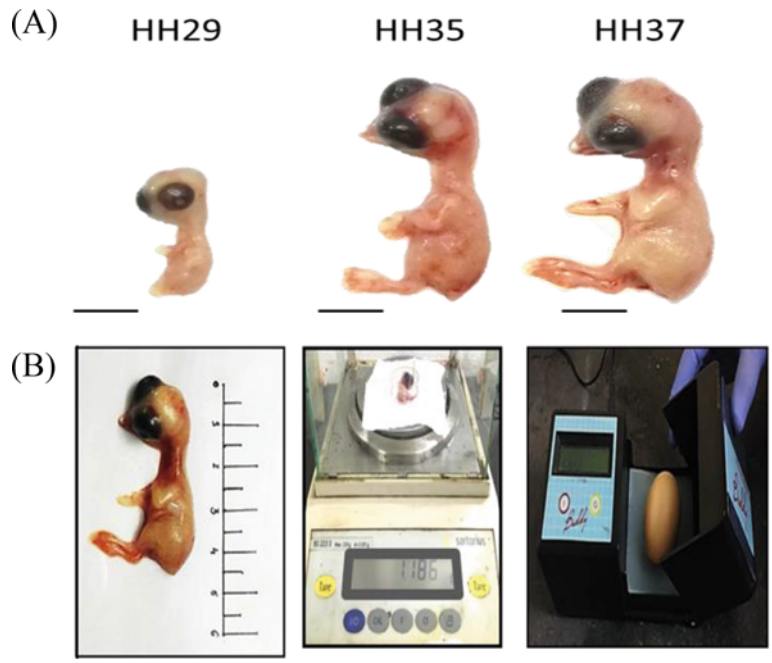

Fig. 1 Analysis of physical deformities of the chick embryo**.** Chick embryos staged at HH29, HH35, and HH37 were analysed. The embryos were evaluated for standard range of crown-rump length, heart rate and weight associated with healthy chick embryos. (**a**) Stages HH29, HH35 and HH37 embryos without any physical deformities. The scale bar is equal to 1 cm. (**b**) The physical attributes were measured using methodology described in this chapter. (Image obtained with permission [3])

3 Methods

3.1 Prenatal Assessment of Fertilized Brown Leghorn Chick Embryo (Gallus gallus domesticus)

1. Clean the eggs thoroughly with tissue paper and sterilize them with 70% ethanol.
2. Maintain the eggs in a humidified incubator at 37 °C with 60% relative humidity (*see* **Notes 4** and **5**).
3. Select eggs at stage HH29 (day 6), HH35 (day 9) and HH37 (day 11) and ensure that no notable deformities are present in the embryos (Fig. 1a) (*see* **Note 6**).
4. In order to check the embryos for any deformities, measure the crown-rump length, heart rate and weight: (a) measure the length from the vertex to the tip of the coccyx using a caliper according to Mobarak and Al-Asmari [6] (Fig. 1b); (b) measure the weight of the embryo using digital scale (wet condition) at HH29, HH35 and HH37 stages as shown in Fig. 1b [7]; and (c) determine the heart rate using a digital egg monitor, Buddy Mk2 as shown in Fig. 1b [8] (*see* **Note 7**).

3.2 Chick Aorta Dissection and Histological Analysis

1. Cut the aortic arches (systemic and pulmonary) from the embryo staged HH29, HH35 and HH37 (Fig. 2a, b) in petri dishes using forceps and scalpel. Clean them with 1× PBS (*see* **Notes 8–11**).
2. Fix the dissected arches for 24 h in 10% neutral buffered formalin [9].
3. Dehydrate the samples with ethanol sequentially (3 times for 5 min in 95% ethanol and 3 times for 5 min in 100% ethanol) followed by 3 times for 15 min in xylene.
4. Fix the aorta in paraffin and section it (~5 μm thickness) using glass slides and a microtome.
5. To deparaffinize, rehydrate in reverse order of dehydration step (i.e., xylene, 3 times for 5 min each; 100% ethanol, 3 times for 3 min each, 95% ethanol, 2 times for 3 min; 70% ethanol, 1 time for 3 min) followed by water for 5 min and stain with hematoxylin staining solution for 3 min.
6. De-stain the section with acidified ethanol and stain with eosin staining solution for 3 min followed by dehydration step as described in **step 3**.
7. Mount the slides of stained aortic arches and dry overnight at room temperature before imaging in an inverted microscope (*see* Fig. 2c).

3.3 Chick Aortic Ring Assay

1. Dissect the aortic arches and wash it with 1× PBS (*see* **Notes 8–12**).
2. Under sterile conditions, slice the arches into 4–5 numbers of smaller rings per vessel having no more than 1 mm of thickness (*see* **Notes 5** and **13**).
3. Coat the Matrigel™ on coverslips kept in 24-well plates and place the sliced aortic rings on prepared coverslips (*see* **Note 12**).
4. Culture the aortic ring with DMEM medium containing 10% FBS and 1% Pen-Strep at 37 °C with 5% CO_2 [10] (*see* **Note 14**).
5. Image the sprouting of endothelial cells from the aortic ring at different time points using an inverted microscope (*see* **Notes 15** and **16**) (*see* Fig. 3).
6. Analyze the image using Angioquant software [11] and ImageJ software [12].
7. Count endothelial tubes and tip cells under a microscope using requisite guidelines [5] (*see* **Note 17**).

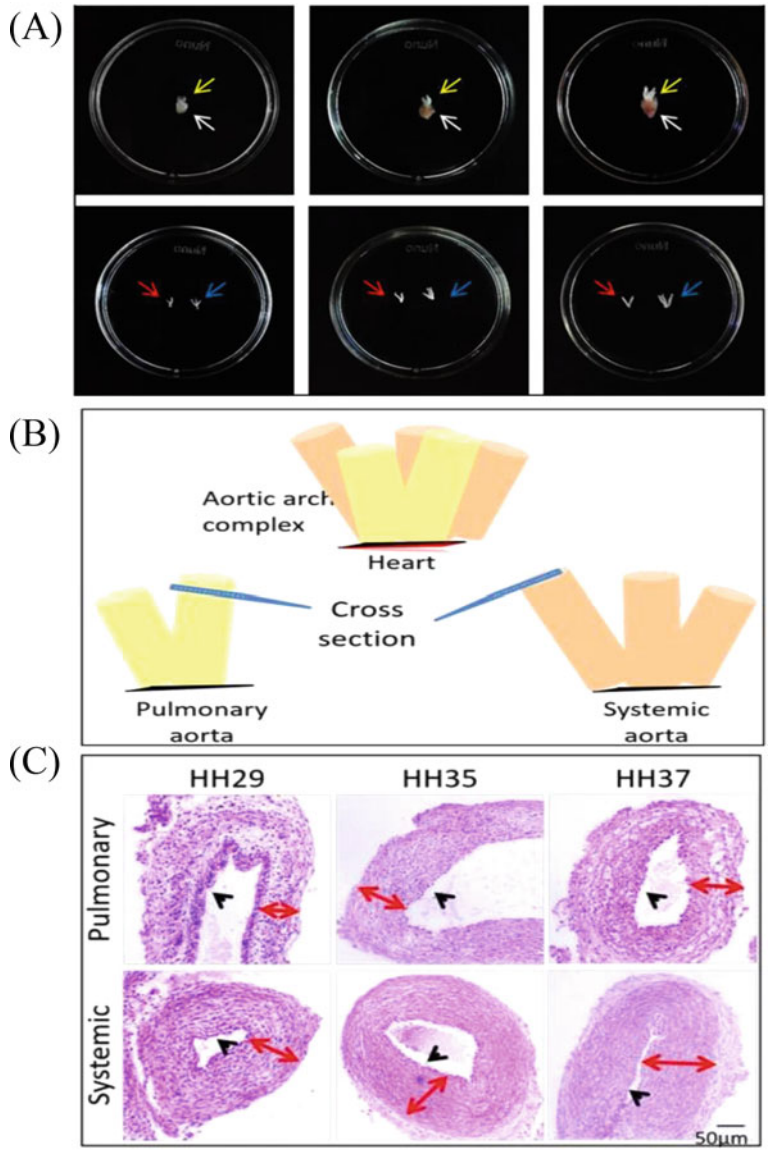

Fig. 2 Culturing and imaging of aorta. (**a**) The embryo stages at HH29, HH35, and HH37 heart–aorta complexes (pulmonary-white arrow shows heart and yellow arrow shows aorta) and aortic arches (systemic-blue arrow shows systemic aorta and the red arrow shows pulmonary aorta) respectively. (**b**) Schematic view of the aortic arch complex. (**c**) Pulmonary aorta and systemic aorta histology images. (Images were obtained with permission [3])

3.4 Sprouting of Endothelial Cells: Zonal Segmentation and Generation Study

1. Culture chick aortic rings up to 72 h to divide sprouting of endothelial cells into three different zones (I, II, and III) as shown in Fig. 4.

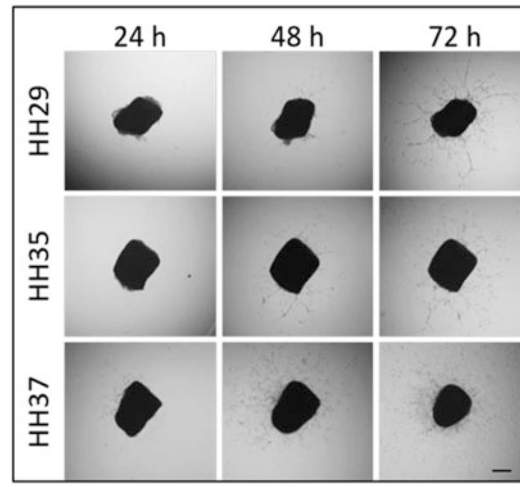

Fig. 3 Chick aorta ring assay allows study of endothelial tip cells and spouting. Images were taken at 4× magnification and the scale bar equals to 200 μm. (Image obtained with permission [3])

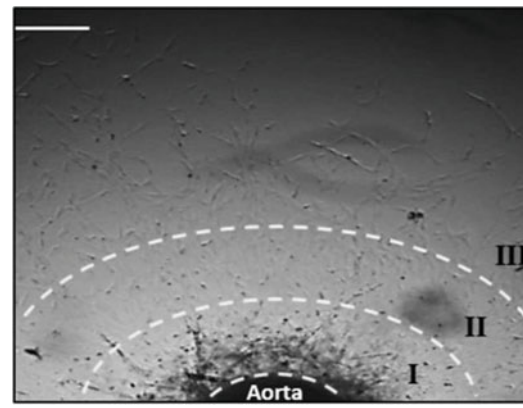

Fig. 4 Endothelial sprouting cells generation. The image of chick aorta sprouting zonal segmentation. 4× magnifications with scale bar equal to 200 μm. (Image obtained with permission [3])

2. Allocate endothelial cells spouting from the aorta ring into three generations, I, II, and III after 24-, 48-, and 72-h culture, respectively.
3. Generation I: Sprouting at 24 h of culture. The radial migration of endothelial cells involves six linear cells originating from the surface of the aorta.
4. Generation II: Additional sprouting attained at 48 h. Following six cells of generation I, the rest of the cells are noted as generation II.
5. Generation III: Additional sprouting attained at 72 h. After generation II, the rest of the cells are defined as generation III.

4 Notes

1. A major strength of the chick embryo aortic sprouting assay is that it overcomes the various limitations associated with animal studies such as acceptance of the procedure, expenses, need for specialized facilities, and the need for veterinary supervision.
2. Since the biological differences between the chick and mammalian blood vessels seem to be negligible, the case for using models of mammalian organ culture is comparatively low. It should, however, be noted that embryonic vasculature requires actively proliferating populations of cells, while adult vessels are essentially quiescent or inactive. Although this could be a significant disadvantage for some studies, there are many advantages for others, especially for angiogenic research on cardiovascular diseases.
3. Candling is a technique used in embryology to observe the development and growth of an embryo within an egg. The original sources of light used were candles and hence the name. The technique employs a bright light source behind the egg to reveal its contents through the shell. Avoid nonfertile eggs.
4. Potential causes of poor development include unsuitable chemicals, temperature or pH. If the incubation temperature decreases below 35 °C, vascular outgrowths may be impaired. Thus, requisite temperature and humidity must be set on the egg incubator before transferring eggs into it.
5. Keep the eggs' blunt end face to the upper side [9].
6. Chick embryos are staged according to Hamburger and Hamilton (HH) stage [13].
7. Buddy digital egg monitor is a noninvasive method to measure the embryos' heart rate which involves measurement of the infrared light-absorbed by blood present in the embryo.
8. Maintaining pH at 7.0 throughout the experiment and minimizing the exposure time to higher pH during aortic ring dissection is essential.
9. Avoid physical disruption to the aorta at any stage of the operation in order not to strain or collapse the aorta or the aortic rings.
10. In case more than one aorta ring is being used for the assay, complete processing of one before going on to the next one is recommended.
11. During dissection of the aorta under the dissection microscope, it is not appropriate to hold petri dishes on ice. To ensure the quality of the aorta and its cellular elements, regular

restoration of the ice-cold fluid is required. No adverse effects on angiogenic activity were observed when the total operation time was completed within 4 h.

12. During the dissection process, the aortic ring should be kept moist with PBS. Be gentle during the move from the dissection area to the incubator or microscope point. Over the duration of a study, caution must be taken not to disturb the Matrigel™ basement matrix while changing the medium or carrying out treatments.
13. 1 mm is standardized to be the optimum size of the aortic rings. Less in size leads to difficulty in handling and less in the degree of outgrowth. Increased size would likely result in a lower yield per aorta, even though they have adequate outgrowth.
14. Penicillin–streptomycin is an antibiotic which is used for the prevention of cell culture contamination. FBS provides the adequate nutrient supply to the DMEM medium.
15. The sprouting rate of older embryos is less than that of young embryos. For each experiment, it is necessary to keep a control group.
16. Sprouting from aortic rings will be healthy if proper measures are taken and the angiogenic activity will be greatly reliable.
17. The total number of stable aortic cultures at the growth reaches more than 50 microvessels at days 6–10. The model should be rejected if consistently low new vessel growth is observed below 10 microvessels.

Acknowledgments

This work was supported by Department of Science and Technology, INSPIRE Faculty Program, Government of India for the research grant to S. Vimalraj (grant no. DST/INSPIRE/04/2017/002913).

References

1. Camaré C, Pucelle M, Nègre A et al (2017) Angiogenesis in the atherosclerotic plaque. Redox Biol 12:18–34
2. Vimalraj S, Saravanan S, Raghunandhakumar S et al (2020) Melatonin regulates tumor angiogenesis via miR-424-5p/VEGFA signaling pathway in osteosarcoma. Life Sci 256:118011
3. Katakia YT, Duddu S, Nithya S et al (2020) *Ex vivo* model for studying endothelial tip cells: revisiting the classical aortic-ring assay. Microvasc Res 128:103939
4. Rameshrad M, Babaei H, Azarmi Y et al (2016) Rat aorta as a pharmacological tool for in vitro and in vivo studies. Life Sci 145:190–204
5. Nowak-Sliwinska P, Alitalo K, Allen E et al (2018) Consensus guidelines for the use and interpretation of angiogenesis assays. Angiogenesis 21(3):425–532
6. Mobarak YM, Al-Asmari MA (2011) Endosulfan impacts on the developing chick embryos: morphological, morphometric and skeletal changes. Int J Zool Res 7:107–127

7. Wolanski NJ, Renema RA, Robinson FE et al (2006) Relationship between chick conformation and quality measures with early growth traits in males of eight selected pure or commercial broiler breeder strains. Poult Sci 85: 1490–1497
8. Lierz M, Gooss O, Hafez HM (2006) Noninvasive heart rate measurement using a digital egg monitor in chicken and turkey embryos. J Avian Med Surg 20:141–146
9. Kumar P, Kumar HA, Sundaresan L et al (2018) Thalidomide remodels developing heart in chick embryo: discovery of a thalidomide mediated hematoma in heart muscle. Naunyn Schmiedeberg's Arch Pharmacol 391(10):1093–1105
10. Kumar P, Kasiviswanathan D, Sundaresan L et al (2015) Harvesting clues from genome wide transcriptome analysis for exploring thalidomide mediated anomalies in eye development of chick embryo: nitric oxide rectifies the thalidomide mediated anomalies by swinging back the system to normal transcriptome pattern. Biochimie 121:253–267
11. Niemistö A, Dunmire V, Yli-Harja O, Wei Zhang A, Shmulevich I (2005) Robust quantification of i*n vitro* angiogenesis through image analysis. IEEE Trans Med Imaging 24: 549–553
12. Braunbeck T, Kais B, Lammer E et al (2014) The fish embryo test (FET): origin, applications, and future. Environ Sci Pollut Res 22: 16247–16261
13. Hamburger V, Hamilton HL (1951) A series of normal stages in the development of the chick embryo. Dev Dyn 195(4):231–272

Chapter 12

Purification and Analysis of Circulating Lipid Particles

Barnaby W. R. Roper, Basmah Al-Sayejh, Ahmed Al-Aufi, Gary A. Cuthbert, Katie Lacey, Shervanthi Homer-Vanniasinkam, Michael A. Harrison, Darren C. Tomlinson, Ramzi Ajjan, and Sreenivasan Ponnambalam

Abstract

Lipid particles found in circulating extracellular fluids such as blood or lymph are essential for cellular homeostasis, metabolism and survival. Such particles provide essential lipids and fats which enable cells to synthesize new membranes and regulate different biochemical pathways. Imbalance in lipid particle metabolism can cause pathological states such as atherosclerosis. Here, elevated low-density lipoprotein (LDL) accumulation leads to fat-filled lesions or plaques in arterial walls. In this chapter, we provide a detailed set of protocols for the rapid and safe purification of lipid particles from human blood using high-speed ultracentrifugation. We provide a detailed set of assays for further analysis of the biochemical and cellular properties of these lipid particles. By combining these assays, we can better understand the complex roles of different lipid particles in normal physiology and disease pathology.

Key words Lipid particles, LDL, VLDL, HDL, Gradient purification, SDS-PAGE, Human umbilical vein endothelial cells (HUVECs), Human embryonic kidney 293T (HEK293T) cells

1 Introduction

Lipid particles are used by many biological organisms as a source of fuel, nutrients and building blocks. In higher eukaryotes, different types of lipid particles are found in extracellular fluids such as lymph and blood. Many lipid particles are synthesized de novo but are dependent on the ingestion of dietary lipids and triglycerides via the intestine. This can give rise to a variety of lipid particles released into the circulation. Transport of such lipid particles via circulatory systems enables delivery of these building blocks to cells, tissues and organs for metabolism into different molecules, and to provide energy. The different lipid particles have distinct functional properties: they share features such as a unilamellar lipid monolayer around a hydrophobic core, with overlapping constituents such as

Dipak P. Ramji (ed.), *Atherosclerosis: Methods and Protocols*, Methods in Molecular Biology, vol. 2419,
https://doi.org/10.1007/978-1-0716-1924-7_12,
© The Author(s), under exclusive license to Springer Science+Business Media, LLC, part of Springer Nature 2022

lipoproteins, lipids, and fatty acids. Generally, each class of lipid particle is recognized by one or more specific membrane-bound receptors which facilitate internalization and processing by cells and tissues.

The largest class of lipid particle is the chylomicron (CM), which is irregular in shape and ~100–600 nm in diameter. Chylomicron biogenesis occurs in the endoplasmic reticulum of small intestine cells termed enterocytes [1]. These chylomicrons are transported through the enterocyte secretory pathway into the lymph. The chylomicron can undergo lipolysis to generate smaller lipid particles in vivo, while its remnants can be endocytosed via non–receptor-mediated and receptor-mediated mechanisms for uptake and processing by different cells and tissues. One potential receptor for chylomicron remnants is the low-density lipoprotein receptor-related protein 1 (LRP1) [2].

The liver is a major site for the processing, metabolism and synthesis of different lipoproteins and lipid particles. Very low-density lipoprotein (VLDL), low-density lipoprotein (LDL), intermediate density lipoprotein (IDL) and high-density lipoprotein (HDL) are different single lipid monolayer particles with hydrophobic cores and distinct functional properties. These lipid or lipoprotein particles can have common molecular components, especially lipoproteins, triglycerides, cholesterol, and cholesteryl esters. However, the amount and functional significance of such components are unique to each class of lipid particle. VLDL, IDL, and LDL are classed as proatherogenic factors where elevated levels of these particles in circulatory fluids are indicative of, or associated with, increased cholesterol levels and the risk of pathological conditions such as heart attacks, strokes and peripheral arterial disease [3]. LDL metabolism is a well-established process in which LDL particles are recognized by the LDL receptor (LDL-R), a type I membrane glycoprotein widely expressed on many mammalian cells and tissues. Interestingly, LDL-R can bind both LDL and VLDL but enables each class of lipid particle to be internalized and trafficked through different pathways [4]. A VLDL receptor (VLDL-R) which bears significant homology to LDL-R, facilitates recognition and internalization of VLDL particles, which are ~30–80 nm diameter [5]. Targeting VLDL uptake and metabolism decreases risk of arterial disease in vivo [6]. VLDL synthesis occurs within the liver; the removal of triglycerides from VLDL by lipoprotein lipase results in both IDL (~25–35 nm diameter) and LDL (~22–28 nm diameter) species, which are smaller and denser lipid particles with a higher concentration of cholesteryl esters [7]. IDL has an intermediate density between VLDL and LDL. The *Apolipoprotein E* (*ApoE*) gene encodes at least 3 protein isoforms, ApoE2, ApoE3, and ApoE4. Each ApoE isoform is associated with different lipid particle populations. Genetic polymorphisms

within the *ApoE* locus are linked to Alzheimer's Disease and hypercholesterolemia [8].

High-density lipoproteins (HDLs) are the smallest class of particles at ~5–15 nm diameter. HDL has the highest protein–lipid ratio, thus explaining why HDL is the densest of the five different classes of lipid particles. In contrast to other types of lipid particles, HDL is often referred to as "good cholesterol" where higher HDL levels correlate with decreased risk of vascular disease and other pathological conditions. Interestingly, HDL recognition is facilitated by novel membrane proteins termed Class B scavenger receptors (SR-B1, CD36). The exact role of HDL is open to much current debate: one hypothesis is that HDL functions as a cholesterol sink and subsequent HDL delivery to the liver enables cholesterol removal, mixing with bile salts and excretion through the gut [9]. The separation and purification of these different lipid particles for biochemical, cellular and physiological studies in vitro and in vivo is thus of much interest, and importance, in understanding lipid metabolism with implications for understanding different disease states and designing specific therapeutic strategies. Here, we provide a rapid and effective protocol for the purification and analysis of different lipid particles from human blood using biochemical and cellular assays.

2 Materials

2.1 Blood Taking and Plasma Purification

1. Butterfly needles for venipuncture.
2. Blood collection tubes containing sodium heparin anticoagulant (*see* **Note 1**).
3. Alcohol swabs.
4. Cotton wool.
5. Adhesive plaster.
6. Tourniquet.
7. 50 mL sterile conical screw cap tubes.
8. Low-speed refrigerated centrifuge with swing-out rotor.
9. Class 1 hood for blood handling.
10. Disposable sterile plastic 10 mL pipettes and pipette controller.
11. Digital balance.
12. Dialysis tubing.
13. Phosphate buffered saline (PBS): 1.37 mM NaCl, 27 mM KCl, 100 mM Na_2HPO_4, 18 mM KH_2PO_4 for dialysis.
14. Retort stand and boss.

2.2 Ultracentrifugation

1. Sealable ~5 mL ultracentrifuge tubes capable of withstanding 543,000 × *g*.
2. HEPES buffered saline (HBS): 0.85% (w/v) sodium chloride, 10 mM HEPES, pH 7.4.
3. OptiPrep™ Density Gradient Medium (Sigma-Aldrich).
4. Narrow barreled glass Pasteur pipettes and pipette controller.
5. Benchtop ultracentrifuge capable of 543,000 × *g*.
6. Fixed angle ultracentrifuge rotor capable of 543,000 × *g*.
7. BCA protein assay kit.

2.3 Agarose Gel Electrophoresis

1. Electrophoresis grade agarose powder.
2. 0.5× TBE (Tris–borate–EDTA) buffer: 80 mM boric acid, 90 mM Tris–HCl, 3 mM EDTA, pH 8.3.
3. Horizontal agarose gel electrophoresis gel rig.
4. Power supply.
5. 1.5 mL microcentrifuge tubes.
6. Microwave.
7. 6× Agarose Gel Loading Dye: 15% Ficoll®-400, 50 mM EDTA, 19.8 mM Tris–HCl, 0.48% (w/v) SDS, 0.25% (w/v) bromophenol blue, pH 8.0.
8. Ethanol.
9. Acetic acid.
10. Sudan Black B Lipid Stain: Dissolve 0.5 g of Sudan Black in a 37 °C solution of 60% (v/v) ethanol. Stir for 2–5 h to ensure maximum dye saturation and then filter using a funnel lined with filter paper to remove precipitates. Treat 100 mL of Sudan black solution with 0.2 mL of 25% (w/v) sodium hydroxide as a preservative for long-term storage at room temperature, protect from light by storage in a dark bottle and wrap aluminum foil around the bottle.
11. Rocker/shaker.
12. Sealable plastic box.
13. Airtight dark container.
14. Digital PC-based gel documentation system capable of transmitted light imaging and storing 16-bit images as .tif files.

2.4 SDS-PAGE

1. 10% (w/v) Ammonium persulfate (APS) solution.
2. *N,N,N′,N′*-tetraethylmethylenediamine (TEMED).
3. 30% acrylamide–bisacrylamide solution (37.5:1 ratio).

4. 5× SDS PAGE sample buffer: 250 mM Tris pH 6.8, 10% (w/v) SDS, 50% (v/v) glycerol, 0.25% (w/v) bromophenol blue, 10% (v/v) β-mercaptoethanol.
5. 1× SDS-PAGE running buffer: 25 mM Tris, 192 mM glycine, 0.1% (w/v) SDS.
6. 20 × 10 cm vertical gel electrophoresis system containing loading rig, glass plates and buffer tank.
7. SDS-PAGE prestained polypeptide markers ranging from 245 to 10 kDa.
8. 20% SDS-PAGE resolving gel: 6.7 mL 30% (v/v) acrylamide, 1.25 mL 3 M Tris–HCl pH 8.8, 1.75 mL water, 100 μL 10% (w/v) SDS, 200 μL 10% (w/v) APS, 8 μL of TEMED for 10 mL of resolving gel (sufficient for one gradient gel). Add APS and TEMED when the gel needs to be poured.
9. 6% SDS PAGE resolving gel: 2.0 mL 30% (v/v) acrylamide, 1.25 mL 3 M Tris–HCl pH 8.8, 6.45 mL water, 100 μL 10% (w/v) SDS, 200 μL 10% (w/v) APS, 8 μL of TEMED for 10 mL of resolving gel (sufficient for one gradient gel). Add APS and TEMED when the gel needs to be poured.
10. 5% SDS PAGE stacking gel: 1.67 mL 30% (v/v) acrylamide, 1.25 mL 1 M Tris–HCl pH 6.8, 7.0 mL water, 100 μL 10% (w/v) SDS, 100 μL 10% (w/v) APS, 20 μL of TEMED for 10 mL of stacking gel (sufficient for one gradient gel). Add APS and TEMED when the gel needs to be poured.
11. Pen.
12. 50 mL sterile screw cap tubes.
13. Distilled water.
14. Sterile plastic 25 mL pipettes.
15. Propanol.
16. Filter paper.
17. Heating block set at 95 °C.
18. Coomassie blue protein staining solution: Dissolve 2.5 g of Brilliant Blue R in a solution of 450 mL water, 450 mL methanol, 100 mL acetic acid for 1 L of stain. Stir for 1–2 days to ensure maximum dye saturation and then filter using a funnel lined with filter paper (*see* **Note 2**).
19. Coomassie destaining solution: 10% methanol, 10% glacial acetic acid.
20. Digital PC-based gel documentation system capable of transmitted light imaging and storing 16-bit images as .tif files.

2.5 Protein and Cholesterol Assay

1. HDL and LDL/VLDL Quantitation assay Kit (Sigma-Aldrich): Includes cholesterol assay buffer, 2× LDL/VLDL

precipitation buffer, cholesterol probe in DMSO, enzyme mix, cholesterol esterase, 2 μg/ μL cholesterol standard (*see* **Note 3**).

2. 96-well plastic plates.
3. Multichannel pipette.
4. Phosphate-buffered saline (PBS): 1.37 mM NaCl, 27 mM KCl, 100 mM Na_2HPO_4, 18 mM KH_2PO_4. Autoclave at 121 °C for 20 min on standard sterilization cycle.
5. Microcentrifuge tubes.
6. Microcentrifuge.
7. Incubator at 37 °C.
8. Variable wavelength absorbance plate reader.

2.6 Lipid Particle Labeling with Fluorescent Dil

1. 3 mg/mL stock of $DiIC_{18}(5)$-DS (1,1′-Dioctadecyl-3,3,3′,3′-Tetramethylindodicarbocyanine-5,5′-Disulfonic acid; Dil) or $DiIC_{18}(5)$ (1,1′-Dioctadecyl-3,3,3′,3′-Tetramethylindodicarbocyanine, 4-Chlorobenzenesulfonate salt; DiD) (*see* **Note 4**).
2. Dimethyl sulfoxide (DMSO).
3. 1.5 mL microcentrifuge tubes.
4. Aluminum foil.
5. Incubator at 37 °C.
6. Dialysis tubing set up for dialysis.
7. PBS.

2.7 Cell Culture and Cell Lysis

1. DiL-labeled lipoproteins from Subheading 2.6.
2. Complete Dulbecco's modified Eagle medium (DMEM) with 25 mM glucose supplemented with 10% (v/v) fetal bovine serum, 1% (v/v) of 100× MEM nonessential amino acids solution, 1% (v/v) of 200 mM L-glutamine, and 1% (v/v) of 10,000 U/mL penicillin–streptomycin.
3. Serum-free medium such as Opti-MEM (ThermoFisher).
4. Endothelial Cell Growth Medium (ECGM) supplemented with 0.4% (v/v) endothelial cell growth supplement, 0.1 ng/mL recombinant epidermal growth factor (EGF), 1 ng/mL recombinant basic fibroblast growth factor (bFGF), 1 μg/mL hydrocortisone, and 90 μg/mL heparin (PromoCell).
5. MCDB131 medium (no glutamine) supplemented with 0.2% (w/v) BSA.
6. Primary human umbilical vein endothelial cells (HUVECs).
7. HEK293T cell line.
8. Cell culture incubator.
9. Laminar flow hood.

10. 0.1% (w/v) sterile filtered pig skin gelatin.
11. 0.01% (w/v) poly-L-lysine solution.
12. Trypsin-EDTA solution (e.g., 1 mg/mL porcine trypsin in PBS, pH 7.4, 2 mM EDTA, filter-sterilized through a 0.22 μm filter).
13. T75 flasks for cell maintenance.
14. 100% ethanol.
15. PBS.
16. 24 well plates to house coverslips.
17. 13 mm #1.5 round glass coverslips.
18. Glass microscopy slides.
19. 3% (w/v) paraformaldehyde (PFA).
20. 4′,6-diamidino-2-phenylindole (DAPI).
21. Fine metal tweezers.
22. Antifade medium for mounting glass coverslips for long-term storage.
23. Clear nail varnish.

2.8 Confocal Microscopy

1. Variable wavelength confocal microscope capable of multichannel fluorescence imaging.
2. Microscope software for visualization of images.

3 Methods

3.1 Blood Collection

1. Collect blood from human volunteers under institutional local ethical approval using butterfly needles for venipuncture based on the size of the volunteer's vein.
2. Constrict the blood flow above the vein in the arm using a tourniquet. Wipe the area around the vein using a sterile disposable alcohol swab. Insert the butterfly needle carefully into a vein in the arm and collect ~20 mL of human blood into a blood collection tube containing sodium heparin (*see* **Note 1**). Remove the tourniquet during blood taking.
3. Wipe the arm with cotton wool after taking blood and place an adhesive plaster over the punctured vein.

3.2 Lipid Particle Purification

1. Immediately centrifuge blood at 1500 × *g* for 10 min at 4 °C in a centrifuge with a swing out rotor. This step will separate blood into a lower dark red layer (erythrocytes and platelets) from a fuzzy white interface (buffy coat layer of lymphocytes) and the top straw or yellow colored layer (plasma).

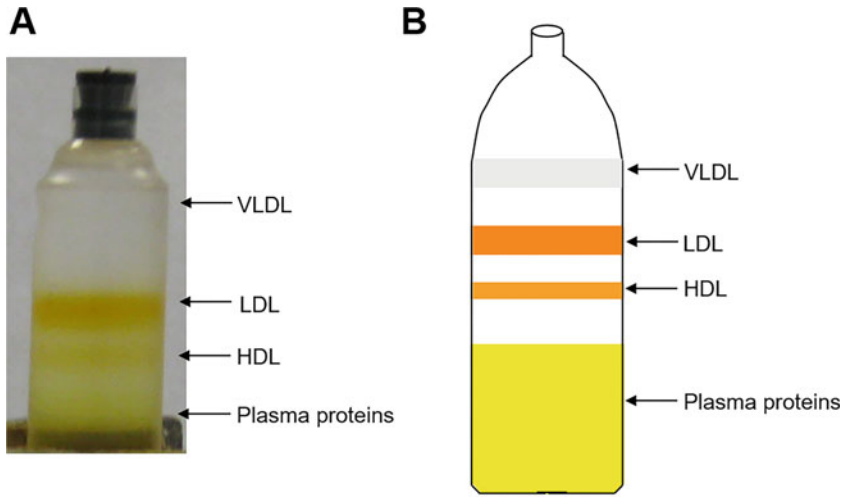

Fig. 1 Fractionation of plasma lipoproteins using an iodixanol gradient and ultracentrifugation. (**a**) Blood plasma mixed with iodixanol was subjected to ultracentrifugation. This causes lipoproteins to separate according to their relative density. VLDL forms an almost indistinct grey band near the top of the tube. LDL appears as a large orange band below this, a third of the way down the tube. HDL forms an orange-yellow band between LDL and the yellow plasma proteins at the base of the tube. 250 μL fractions were taken from the top of the tube. (**b**) Schematic representation of lipid particle populations

2. Carefully transfer the clear yellow layer (blood plasma) to a sterile 50 mL tube in a Class I hood.
3. Recentrifuge the plasma again at 1500 × *g* for 10 min at 4 °C to remove any remaining red and white blood cells.
4. Remove the plasma and mix with iodixanol (OptiPrep™) in a 4:1 ratio using disposable sterile 10 mL plastic pipettes. This will give a 12% (v/v) iodixanol concentration in the final gradient.
5. Carefully load ~5 mL sealable ultracentrifuge tubes with 1 mL of HBS.
6. Carefully layer the plasma–OptiPrep solution from **step 4** under the HBS in the ultracentrifuge tubes using a narrow-barreled glass Pasteur pipette and pipette controller until the tubes are at their rated capacity.
7. Seal tubes and balance to 2 decimal places using a digital balance. Place into a fixed angle ultracentrifuge rotor.
8. Place the rotor in the ultracentrifuge.
9. Centrifuge the plasma–OptiPrep mixture at 543,000 × *g* for 3 h at 16 °C.
10. Remove the ultracentrifuge tubes from the rotor and clamp the tube on a retort stand (*see* Fig. 1).
11. Collect 250 μL fraction volumes from the top of the gradient for subsequent analysis (*see* **Note 5**).

12. Dialyze lipid fractions overnight against 1000 volumes of PBS at 4 °C.
13. Determine the protein content of lipid particle (e.g., by BCA assay).

3.3 Lipid Particle Electrophoretic Analysis

3.3.1 Agarose Gel Electrophoresis

1. Melt a suspension of 0.5% (w/v) agarose in 0.5× TBE buffer in the microwave and cool to 55–60 °C.
2. Pour the melted agarose solution into a horizontal gel electrophoresis rig and allow to set with plastic comb in place (*see* **Note 6**).
3. Carefully remove the plastic comb and place the gel within the electrophoresis tank in 0.5× TBE buffer.
4. Mix 3 μL of each 250 μL centrifugation fraction with 6× gel loading dye at a ratio of 5:1.
5. Load samples onto the 0.5% agarose gel and carry out electrophoresis at 80 V for 60 min.
6. Carefully remove the gel and place in a sealable plastic box. Immerse the gel in a fixation solution of ethanol-acetic acid (75% ethanol, 5% acetic acid) and gently rock at room temperature for 15 min. Discard fixation solution.
7. Incubate the agarose gel with the Sudan Black solution and allow to gently agitate at room temperature for 30–180 min with frequent monitoring until saturated.
8. Discard the Sudan Black solution and rinse the gel twice briefly in 50% (v/v) ethanol.
9. Leave the gel to de-stain in 50% (v/v) ethanol overnight at 4 °C in an air-tight dark container until lipid bands are distinct.
10. Digitally analyze the gel using a gel documentation system capable of transmitted light imaging and collect images as .tif files (*see* Fig. 2a and **Note 7**).

3.3.2 Protein Analysis of Lipid ParticlesLipid particles Using Gradient SDS-PAGE

1. Assemble the polyacrylamide gel rig as per the manufacturer's instructions. With a pen, mark the outer glass plate up to where the resolving gel will be added (roughly 1 cm below where the comb will be inserted).
2. In two separate 50 mL sterile screw cap tubes, prepare 6% and 20% polyacrylamide gel mixtures omitting APS and TEMED until immediately prior to pouring the gel.
3. Using a 25 mL serological pipette, take up 8 mL of the 6% solution followed by 8 mL of the 20% solution (*see* **Note 8**).
4. Take up one bubble of air into the serological pipette which will mix the two gel solutions forming a gradient.
5. Pipette the solution into the gel rig between the two glass plates, moving along the length of the gel casing.

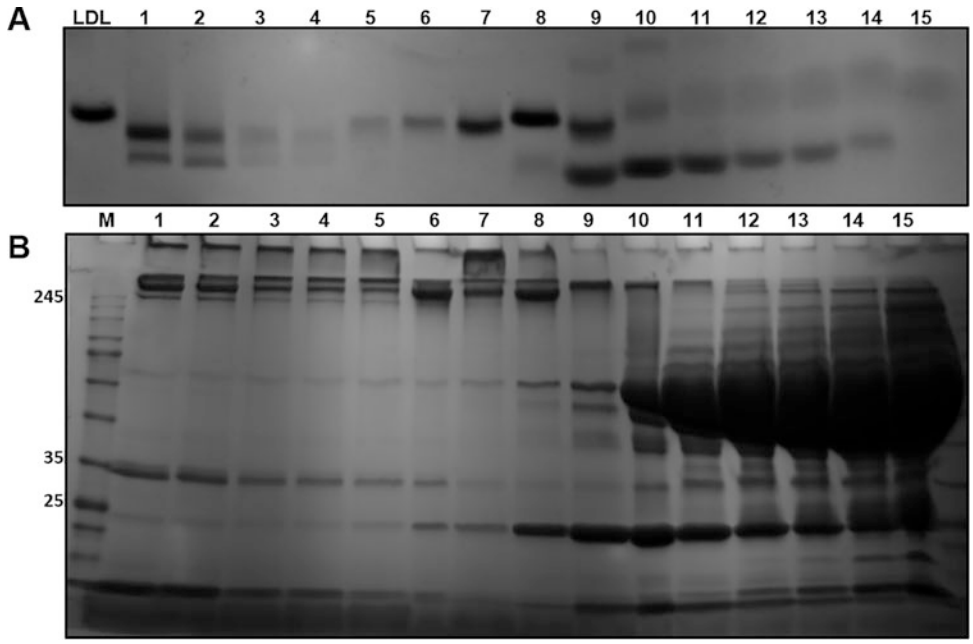

Fig. 2 Gel electrophoresis analysis of fractionated lipid particles. (**a**) Agarose gel electrophoresis. Samples (3 μL) of each 250 μL fraction (#1–15) were analyzed on 0.5% (w/v) agarose gels and stained with Sudan black. As a reference, purified LDL collected by centrifuge tube needle puncture was analyzed in the first lane (LDL). As the smallest and densest lipoprotein particle, HDL migrates the furthest. LDL shows the slowest mobility as although it is smaller than VLDL, it contains far fewer apolipoproteins so has an overall lower negative charge (*see* **Note 7**). In the later fractions (#10 onward), high levels of serum proteins affect HDL migration properties. (**b**) SDS-PAGE analysis of samples (20 μg) of each 250 μL fraction (#1–15) analyzed on 6–20% gradient gels and stained with Coomassie. ApoB-48 (MW ~241 kDa) is indicative of chylomicrons (CM) and ApoB-100 (MW ~512 kDa; indicative of VLDL and LDL) are difficult to detect by conventional SDS-PAGE. ApoA1 (MW ~28 kDa) is indicative of HDL and initially appears in fraction #6, becoming more abundant in fraction #8 onward. ApoA1 migrates at an apparent MW ~24 kDa

6. Carefully add a layer of propanol to sit above the gel mixture in a visibly separate layer. Allow the gel to set for 20–30 min. Gently tilt to ensure the gel is visibly solid below the still liquid propanol.
7. Pour off the propanol and rinse with distilled water three times. Use filter paper to remove any residual water, without touching the gel itself.
8. Make 10 mL of 5% stacking gel and pipette on top of the set resolving gel until flush with the top of the gel plates. Immediately insert the well comb, ensuring not to trap any bubbles in the wells. Allow to set for 30 min.
9. Place the gel rig in the electrophoresis running tank and fill the internal reservoir with 1× SDS PAGE running buffer.

10. Prepare lipoprotein fraction samples by combing 20 μg of each centrifugation fraction with 5× SDS sample buffer in a 4:1 ratio (*see* **Note 9**).
11. Incubate protein samples for 10 min at 95 °C to denature proteins.
12. Pipette prestained molecular weight markers into the first well followed by fraction samples in order.
13. Begin electrophoresis at 120 V at room temperature until the SDS sample buffer dye bands have migrated off the gel after approximately 1.5 h.
14. Dismantle the gel rig and remove the polyacrylamide gel from between the glass plates.
15. Incubate the gel with Coomassie protein stain for 4 h to overnight with gentle agitation.
16. Briefly wash the gel with distilled water 3× to remove excess stain.
17. Incubate the gel in a Coomassie destaining solution for 3–6 h, changing the solution upon saturation, until bands become visibly distinct (*see* Fig. 2b).

3.4 Cholesterol Assay of Lipid Particle Fractions

We here present a generic protocol for determining the cholesterol content of serum samples using a commercial cholesterol assay kit. This protocol provides an overview of the stages involved; however, the specific details of the manufacturer's protocol should be adhered to (*see* **Note 3**).

1. Select an assay kit for measuring blood serum cholesterol levels, in this case assaying the centrifugation fractions in place of whole serum.
2. Prepare the kit-provided cholesterol standards by diluting 20 μL of the cholesterol standard solution with 140 μL of the cholesterol assay buffer to generate a 0.25 μg/μL solution.
3. In duplicate add 0, 4, 8, 12, 16 and 20 μL of this solution to a 96-well plastic plate.
4. To separate HDL from LDL and VLDL in the centrifugation fractions, mix 100 μL of each fraction (50 μL per duplicate) with 100 μL of 2× precipitation buffer in a microcentrifuge tube.
5. Incubate for 10 min at room temperature.
6. Centrifuge at 2000 × *g* for 10 min.
7. Carefully pipette the clear supernatant containing the HDL fraction into a separate microcentrifuge tube leaving the precipitated LDL/VLDL fraction.

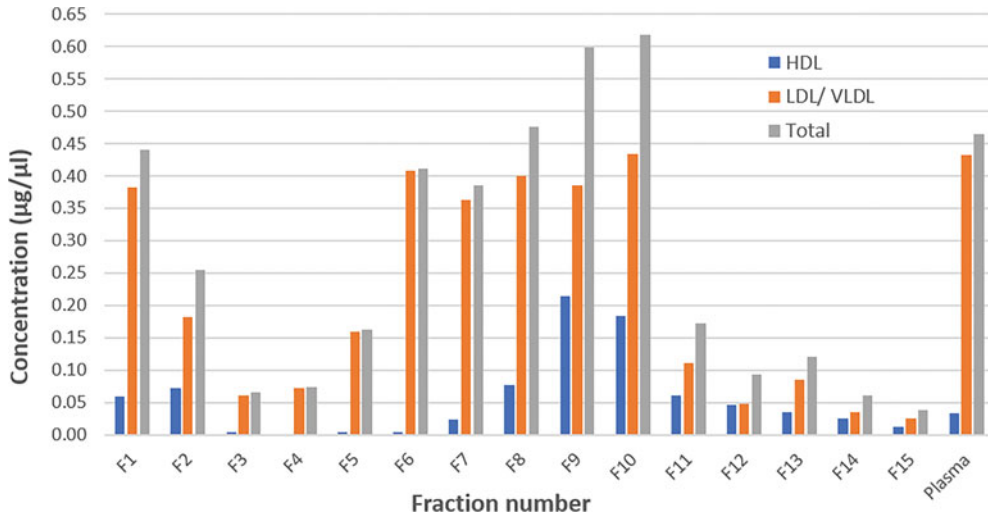

Fig. 3 Cholesterol quantification in plasma fractions. HDL and LDL/VLDL profiling using a cholesterol assay. Fifty microliters of each lipid fraction was first separated into HDL and LDL/VLDL fractions followed by enzymatic determination of cholesterol concentration. VLDL signal is apparent in fractions #1 and #2. LDL signal appears in fractions #6–10. HDL signal appears most strongly in fractions #8–10. If HDL and LDL/VLDL are imperfectly separated during the VLDL/LDL precipitation of this assay, then they may be reported as the other population during the cholesterol quantification stage

8. Centrifuge at 2000 × *g* for 10 min again and remove any residual HDL containing supernatant (*see* **Note 10**).
9. Resuspend the LDL/VLDL precipitate in 200 µL of PBS.
10. In duplicate, add 50 µL of the HDL supernatant or resuspended LDL/VLDL precipitate to the 96-well plate for each fraction (*see* **Note 11**).
11. Assemble the kit provided assay reaction mix as instructed per well: 44 µL cholesterol assay buffer, 2 µL cholesterol probe, 2 µL cholesterol enzyme mix and 2 µL cholesterol esterase.
12. Using a multichannel pipette add 50 µL of the reaction mix to each well containing either cholesterol standard or fraction sample and mix well by pipetting.
13. Incubate the plate for 60 min at 37 °C protected from light.
14. Measure the colorimetric absorbance at 570 nm using a 96-well plate reader to determine the presence of cholesterol in each fraction. This will generate absorbance values for the cholesterol standards as well as HDL and VLDL/LDL populations for each fraction.
15. Calculate the mean absorbance by averaging the values received from the duplicated wells for each condition.

16. From all averaged results, subtract the value received from the zero-cholesterol standards condition to adjust for the baseline.
17. Using the averaged absorbance readings from the kit-provided cholesterol standards, construct a standard curve of absorbance (y) versus known μg quantity of cholesterol (x) as defined by the kit.
18. Generate a line of best fit for the standard curve and calculate the straight-line equation for the correlation of cholesterol mass and resultant signal in the form $y = mx + c$
19. Use the standard curve calculated m and c values alongside the experimentally derived absorbance value y to calculate the mass of cholesterol in a given fraction: $x = (y - c)/m$
20. Divide the value received by the μL quantity of fraction sample that was added to wells initially (50 μL) and multiply by any dilution factor in the assay (2× dilution factor here) to give a concentration in μg/μL.
21. Plot fraction number (x) against the cholesterol concentration (y) for LDL/VLDL, HDL and the sum of the two as total cholesterol (*see* Fig. 3).

3.5 Lipid Particle Labelling with Fluorescent DiI Derivatives

1. From gel analyses for lipid and protein content (*see* **Note 12**), select fractions corresponding to the lipid particles and lipoproteins of interest.
2. Aliquot 50–100 μL of each fraction into a 1.5 mL microcentrifuge tube.
3. Using a 3 mg/mL stock of DiI derivative (in DMSO) add 300 μg DiI derivative per 1 mg of lipoprotein particles and mix by gentle pipetting.
4. Protect the solution from light by wrapping in aluminum foil and incubate for 16–20 h (overnight) at 37 °C.
5. Dialyze the lipoprotein particles against >1000 volumes of PBS for 24 h at 37 °C, changing the buffer at least once, to remove unincorporated DiI derivative and DMSO (*see* **Note 13**).
6. Recover fluorescent lipid particles after dialysis and store in 1.5 mL microcentrifuge tubes at 4 °C protected from light.

3.6 HUVEC and HEK293T Cell Culture and Stimulation of DiI-Labeled Lipoprotein Uptake

All steps are carried out in a laminar flow hood working at Biosafety Level 1. All media are prewarmed to 37 °C prior to use.

1. Sterilize 13 mm diameter round glass coverslips by dipping in 100% ethanol and allowing to air dry in a well of a 24 well plate.
2. Coat coverslips with 500 μL of cell adhesion stratum, as appropriate for each cell type, and incubate for 1 h at room temperature. For HUVECs, use sterile filtered 0.1% (w/v) pig skin

gelatin in PBS. For HEK293T cells, use 0.01% (w/v) poly-L-lysine.

3. Aspirate the solution and wash coverslips three times with PBS. Allow coverslips and plates to air dry for 1 h.
4. Using standard protocols, split HUVECs (*see* **Note 14**) [10] and HEK293T cells (*see* **Note 15**) [11] at 40% confluence onto the coverslips and incubate overnight in complete growth medium to allow cells to adhere to the coverslips.
5. The following day, replace medium with starvation medium and incubate for 3 h. HUVECs should be starved in MCDB131, 0.2% (w/v) BSA. HEK293T cells should be starved in serum-free medium.
6. Aspirate starvation medium and replace with fresh starvation medium supplemented with 10–50 μg/mL DiI-labeled lipid particles and place in a humidified tissue culture incubator at 37 °C for 5 min (*see* **Note 16**).
7. Aspirate the medium, wash once with 1 mL of ice-cold PBS and replace with prewarmed complete medium. Place in a humidified cell culture incubator at 37 °C for 55 min.
8. Aspirate medium and wash cells three times with 1 mL of ice-cold PBS.
9. Add 0.5 mL of 3% (w/v) paraformaldehyde (PFA) to each well and incubate for 15 min at 37 °C.
10. Aspirate fixative and wash cells 3 times with 1 mL of PBS (*see* **Note 17**).
11. Incubate the coverslips in their 24-well plate with 1 μg/mL 4′,6-diamidino-2-phenylindole (DAPI) in PBS for 2 h at room temperature protected from light.
12. Aspirate medium and wash three times with PBS.
13. On a single glass microscopy slide, dispense a drop (~25 μL) of mounting medium.
14. Using a pair of fine tweezers, carefully remove coverslips from the 24-well plate and invert with cells "facing down" onto the drop of mounting medium. Leave to dry overnight protected from light.
15. The following day, seal the edges of the coverslip using clear nail varnish (*see* **Note 18**).

3.7 Confocal Microscopy

1. Collect images with the confocal microscope using the Plan-Apochromat 63×/1.40 oil objective lens (*see* Fig. 4).
2. Excite detection of nuclear DNA staining using DAPI with a 405 nm laser and emission at 435 nm (filter range 0–585 nm). Excite the fluorescent DiI derivative with a 555 nm laser line

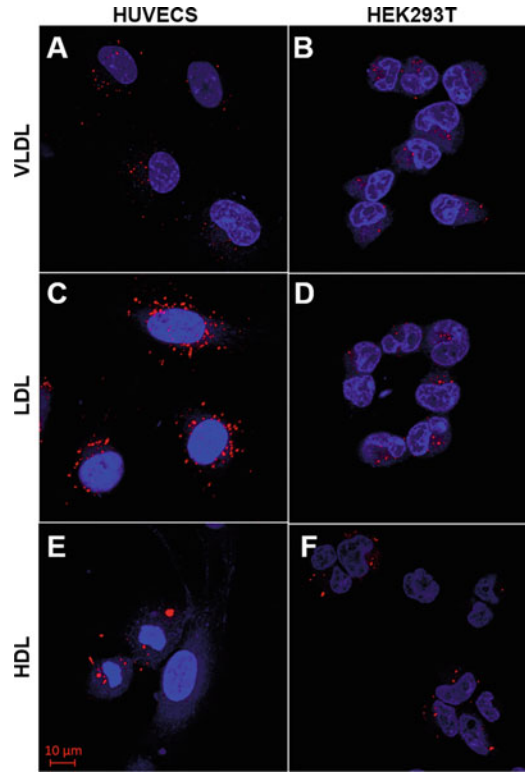

Fig. 4 Confocal microscopy on fluorescent labelled lipid particle uptake in primary and immortalised human cells. Primary human endothelial cells (**a**, **c**, **e**) or immortalised HEK293T (**b**, **d**, **f**) cells were serum starved and then incubated with 10 μg/mL fluorescent labeled lipid particles for 5 min before chase for 55 min (*see* Subheading 3.6). The only exception being that cell incubation with 50 μg/mL labeled HDL was necessary to detect signal for HEK293T cells. VLDL and LDL show a punctate pattern (red) surrounding the DAPI stained nucleus (blue) indicative of clustering in late endosomes. This patten appears irregular when cells were treated with fluorescent labeled HDL. Scale bar, 10 μm

and detect emission at 585 nm (filter range 560–1000 nm). Frame-scan channels to reduce the risk of signal overlap.

3. Visualize lipid particle uptake by the appearance of a punctate pattern of red "dots" where lipid particles have been endocytosed and delivered to specific intracellular compartments such as endosomes and lysosomes (*see* Fig. 4). There are also some differences between the staining patterns, especially that for HDL (*see* **Note 19**).

4 Notes

1. Vacutainer tubes precoated with anticoagulant (sodium heparin, EDTA, sodium citrate, etc.) can be selected for blood collection, dependent on their interaction with downstream experiments. Sodium heparin is the suggested anticoagulant for use in this work due to its compatibility with the HDL and LDL/VLDL Quantitation Kit (Sigma-Aldrich) that we routinely use. If not performing this step, then other anticoagulants could be used. Alternatively, provided that blood is mixed immediately after taking the sample, solutions of liquid anticoagulant can be used. Commonly, we mix 18 mL of blood with 2 mL of 3.8% sodium citrate (9:1 ratio) preadded to a 50 mL screw cap tube.
2. There are several commercially available Coomassie stains which claim shorter staining times, reduced background staining and do not require a destaining step which could be pursued at the operator's discretion. Here we present a generic method using an in-house stain for widely applicable use. It should however be noted that Fig. 2b was generated using a commercial Coomassie stain.
3. There are many commercially available cholesterol assay kits designed for blood plasma analyses that can be selected according to the specific requirements of the operator. Many of these assays employ the approach of providing the user with cholesterol standards to generate a concentration curve of absorbance/fluorescence readings from which to determine the cholesterol concentration of the experimental samples. Here, an HDL and LDL/VLDL quantitation kit was selected for its ability to separate HDL from VLDL/LDL prior to cholesterol quantification as another method of delineating lipoprotein particle species. This assay kit precipitates both LDL and VLDL, separating them from HDL before a generic cholesterol determination step. There is little danger of mistaking LDL and VLDL cholesterol as they are spatially separated after ultracentrifugation with little or no overlap. If using a different assay kit, then follow the manufacturer's protocols.
4. DiI and DiD can be used interchangeably with similar spectral properties and fluorescence properties in hydrophobic environments such as lipid particles.
5. A P200 pipette is best used for this purpose as the smaller pipette tip aperture is at lower risk of disturbing the boundary between layers. In some cases, as for the clearly defined orange LDL band, it is apparent that the LDL fraction often exceeds 250 μL. In this case, at the operator's discretion, more than 250 μL can be collected within a fraction. This needs to be

done carefully as there is potential of overlapping LDL and HDL species due to their close proximity within the gradient (*see* Fig. 1). It is not necessary to collect all the fractions toward the bottom of the ultracentrifuge tube as the lower third of the gradient contains largely plasma proteins.

6. Do not make the agarose gel unnecessarily thick as this may impede the Sudan Black lipid stain from penetrating effectively into the gel and reduce lipid particle detection.
7. Lipoprotein particles differ in electrophoretic mobility dependent on their size and electrical charge. Chylomicrons are the largest class of lipoproteins and will not migrate out of the gel wells (*see* Fig. 2a). LDL appears closest to the origin, followed by the larger VLDL particle. This is because in addition to apolipoprotein B-100 which they both carry, VLDL also contains apolipoproteins A5, C1, C2, C3, and E which increase the negative charge of VLDL and therefore electrophoretic mobility. The band for HDL appears furthest from the origin. In the later HDL fractions, the mobility of HDL appears to decrease. This is likely to be attributable to an increasing presence of human serum albumin binding to HDL and increasing the apparent size of particles.
8. These volumes assume the use of the suggested 20 × 10 cm gel system. The exact volume to occupy the resolving gel portion of a particular gel rig should be worked out on a case-by-case basis. Regardless, an equal volume of 6% and 20% polyacrylamide solutions should be used.
9. Some lipid particle fractions will have very low protein concentration and it may not be possible to add 20 μg of protein due to SDS-PAGE well volume restriction. In this case, add as much volume of each fraction as possible. It is possible to concentrate the fractions but given that they contain low concentrations of protein, they likely do not contain the lipoproteins of interest so this may be an inefficient use of time.
10. The VLDL/ LDL particles form a diffuse white to yellow precipitate above the soluble HDL fraction and separating the two can be difficult. Repeated centrifugation during the separation stage may be necessary. As the HDL and LDL/ VLDL fractions are subsequently assayed for cholesterol content by the same protocol, any unsuccessfully separated material persisting in the wrong separated aliquot will be reported by the assay as the wrong type of cholesterol. If the HDL fraction remains cloudy despite repeated centrifugation, dilute the sample 1:1 in PBS and repeat the treatment with 2× precipitation buffer. Doing this will increase the dilution factor of the assay to 4×, which needs to be taken into account when

determining the cholesterol concentration in **step 20** of Subheading 3.4.

11. Commonly, these assay kits provide cholesterol standards for the operator to generate a standard curve from which to interpret their results. Some fractions may require dilution with cholesterol assay buffer to receive signals which fit within this standard curve. This must be determined on a per fraction basis.
12. Analysis of different lipoprotein particle fractions derived from human blood with subsequent biochemical analysis will enable the operator to identify specific lipid particle fractions of interest. After agarose electrophoresis and SDS-PAGE (*see* Fig. 2), we identified fraction #2 as enriched for VLDL, #8 for LDL and #10 for HDL. It must be kept in mind that overlap of LDL and HDL populations (Fig. 1) is unavoidable without further centrifugation or gel filtration steps.
13. Some DiI derivative may remain in the lipid particle fraction as aggregates following dialysis. If so, centrifuge at 16,000 × *g* for 10 min to sediment unincorporated fluorescent dye aggregates before use.
14. Endothelial cells (HUVECs) are grown in complete supplemented ECGM unless otherwise stated. For maintenance, fresh medium should be provided every 2–3 days. HUVECs should be passaged upon reaching ~90% confluence (every ~6 days) and split 1:3 into flasks coated with 0.1% (w/v) pig skin gelatin. To split cells, first wash 2× with prewarmed 37 °C sterile filtered PBS and aspirate. Add 1 mL of trypsin solution and incubate for 2–5 min until the cells come away from the plastic. Quench the trypsin by adding 9 mL of supplemented ECGM and split cells 1:3 for cell maintenance or otherwise dependent on experimental parameters.
15. Immortalized cells (HEK293T) are grown in complete supplemented DMEM unless otherwise stated. HEK293T cells should be passaged upon reaching ~80% confluence (every ~5 days) and seeded at 25% confluence. It is not necessary to precoat plastic but if seeding onto glass then this should be coated with 0.01% (w/v) poly-L-lysine. To split cells, first wash 2× with prewarmed 37 °C sterile filtered PBS and aspirate. Add 1 mL of trypsin solution and incubate for ~3 min, until cells come away from the plastic. Quench the trypsin by adding 9 mL of supplemented DMEM and seed cells at 25% for cell maintenance or otherwise dependent on experimental parameters.
16. It may be necessary to optimize the concentration of each DiI-labeled lipid particle used depending on cell type and other experimental conditions. In this study 10 μg/mL of

DiI-labeled lipid particle usually produced the most optimal results; however, HEK293T cells required 50 μg/mL DiI-labeled HDL.

17. The operator may want to use an antibody to simultaneously label their cells for an intracellular marker or reference. If so, cells should be incubated with 0.5% (w/v) BSA in PBS for 1 h to reduce nonspecific binding, prior to primary and secondary antibody incubations following the manufacturer's instructions.
18. Sealing with nail varnish prevents the mounting medium from drying up and causing air bubbles to form between the coverslip and the glass slide.
19. The labeled LDL and VLDL staining patterns are relatively similar showing a pattern of punctate dots radiating outward from the nuclear periphery into the cell cytoplasm (*see* Fig. 4). Of note, the staining pattern for HDL is more irregular and less rounded in appearance (*see* Fig. 4).

Acknowledgments

This work was supported by a PhD studentship from the British Heart Foundation (B.W.R.R.), a PhD studentship from Heart Research UK (K.L.) and a PhD studentship from the Kingdom of Saudi Arabia Ministry of Education (B.A-S.)

References

1. Xiao C, Stahel P, Lewis GF (2019) Regulation of hylomicron secretion: focus on post-assembly mechanisms. Cell Mol Gastroenterol Hepatol 7(3):487–501. https://doi.org/10.1016/j.jcmgh.2018.10.015
2. Actis Dato V, Chiabrando GA (2018) The role of low-density lipoprotein receptor-related protein 1 in lipid metabolism, glucose homeostasis and inflammation. Int J Mol Sci 19(6): 1780. https://doi.org/10.3390/ijms19061780
3. Lee Y, Siddiqui WJ (2021) Cholesterol levels. In: StatPearls [Internet]. StatPearls Publishing, Treasure Island. Accessed 1 March 2021
4. Jeon H, Blacklow SC (2005) Structure and physiologic function of the low-density lipoprotein receptor. Annu Rev Biochem 74: 535–562. https://doi.org/10.1146/annurev.biochem.74.082803.133354
5. Dlugosz P, Nimpf J (2018) The Reelin receptors apolipoprotein E receptor 2 (ApoER2) and VLDL receptor. Int J Mol Sci 19(10): 3090. https://doi.org/10.3390/ijms19103090
6. Perman JC, Bostrom P, Lindbom M, Lidberg U, StAhlman M, Hagg D, Lindskog H, Scharin Tang M, Omerovic E, Mattsson Hulten L, Jeppsson A, Petursson P, Herlitz J, Olivecrona G, Strickland DK, Ekroos K, Olofsson SO, Boren J (2011) The VLDL receptor promotes lipotoxicity and increases mortality in mice following an acute myocardial infarction. J Clin Invest 121(7): 2625–2640. https://doi.org/10.1172/JCI43068
7. Chappell DA, Medh JD (1998) Receptor-mediated mechanisms of lipoprotein remnant catabolism. Prog Lipid Res 37(6):393–422. https://doi.org/10.1016/s0163-7827(98)00017-4
8. Phillips MC (2014) Apolipoprotein E isoforms and lipoprotein metabolism. IUBMB Life 66(9):616–623. https://doi.org/10.1002/iub.1314

9. Asztalos BF, Niisuke K, Horvath KV (2019) High-density lipoprotein: our elusive friend. Curr Opin Lipidol 30(4):314–319. https://doi.org/10.1097/MOL.0000000000000612
10. Howell GJ, Herbert SP, Smith JM, Mittar S, Ewan LC, Mohammed M, Hunter AR, Simpson N, Turner AJ, Zachary I, Walker JH, Ponnambalam S (2004) Endothelial cell confluence regulates Weibel-Palade body formation. Mol Membr Biol 21(6):413–421. https://doi.org/10.1080/09687860400011571
11. Jopling HM, Howell GJ, Gamper N, Ponnambalam S (2011) The VEGFR2 receptor tyrosine kinase undergoes constitutive endosome-to-plasma membrane recycling. Biochem Biophys Res Commun 410(2):170–176. https://doi.org/10.1016/j.bbrc.2011.04.093

Chapter 13

Preparation of LDL, Oxidation, Methods of Detection, and Applications in Atherosclerosis Research

Chandrakala Aluganti Narasimhulu and Sampath Parthasarathy

Sampath Parthasarathy is deceased at the time of publication. This chapter is dedicated to his memory.

Abstract

The concept of lipid peroxidation has been known for a long time. It is now well established that LDL plays a major role in atherosclerosis. Oxidized low-density lipoprotein (Ox-LDL) has been studied for over 35 years. Numerous pro- and anti-atherogenic properties have been attributed to Ox-LDL. Component composition of Ox-LDL is complex due to the influence of various factors, including the source, method of preparation, storage and use. Hence, it is very difficult to clearly define and characterize Ox-LDL. It contains unoxidized and oxidized fatty acid derivatives both in the ester and free forms, their decomposition products, cholesterol and its oxidized products, proteins with oxidized amino acids and cross-links, polypeptides with varying extents of covalent modification with lipid oxidation products and many others. The measurement of lipid oxidation has been a great boon, not only to the understanding of the process but also in providing numerous serendipitous discoveries and methodologies. In this chapter, we outline the methodologies for the preparation and testing of various lipoproteins for oxidation studies.

Key words LDL, HDL, Oxidation, Myeloperoxidase, Macrophages, Reverse cholesterol transport

1 Introduction

The concept of lipid peroxidation has been known for a long time [1–4]. Food chemists know that the double bonds of polyunsaturated fatty acids (PUFA) readily undergo oxidation and render the molecule rancid or putrid. Numerous reviews have addressed the mechanisms of peroxidation or rancidity, as it is commonly known, of polyunsaturated lipids [1, 2, 4]. The smell and odor coming from rancid fat depend on the extent of oxidation, the type of fatty acids, and the nature of products derived from the decomposition of the peroxidized fat. While no specific pathology was attributed to the dietary consumption or body's generation of rancid fat, the scientists who studied the ageing process named the fluorescent

Dipak P. Ramji (ed.), *Atherosclerosis: Methods and Protocols*, Methods in Molecular Biology, vol. 2419,
https://doi.org/10.1007/978-1-0716-1924-7_13,
© The Author(s), under exclusive license to Springer Science+Business Media, LLC, part of Springer Nature 2022

pigments that accumulated in tissues of older animals as ceroids or lipofuscins, which contained products from peroxidized lipids [5] and their degradation products [2, 6, 7]. They were usually considered end products of death and destruction, not products that led to death and destruction, or of rebuilding and resurrection. The chemists who studied the peroxidation process, on the other hand, knew of oxygen radicals and their abilities to cause damage to biological molecules. They studied oxidative damage to DNA and to specific nucleotides, to PUFA and to specific amino acids and proteins [8–12]. It was not until the 80s that a potential link between oxidative damage and a specific pathological process was suggested.

It is now well established that LDL plays a major role in atherosclerosis [13, 14]. The concept that the atherogenicity of LDL could be mediated through its oxidation, or endothelial cell modification, as it was originally called [15], originated over 35 years ago [15–17]. A simple observation that in vitro incubation of macrophages with oxidized LDL, and not with native LDL, resulted in cellular cholesterol ester accumulation [18] led to the proposal of the concept. The nidus came from the observations that acetyl LDL [19] and malondialdehyde LDL (MDA-LDL) [20, 21], both of which represented a change in net charge on the LDL particle, and that peroxidation of PUFA generated malondialdehyde (MDA). Since then, many different types of modification of LDL have been described (Fig. 1). Reactive oxygen species, oxidases and lipid oxygenases, peroxidases, sphingomyelinase (SMase), elastase, and many other processes have been identified to contribute to the formation of subendothelial modified lipoproteins [22–28]. In addition, altered LDL particles that are desialylated [29, 30] or charge modified have been isolated from plasma [31, 32].

The oxidation of LDL by cupric ions was the most thoroughly studied "pathway" [33]. Even within the context of this, the oxidation of LDL is a complex process involving both the lipid and protein components of LDL. They not only undergo independent oxidative changes but also form complex adducts [34–38]. Many other pathways for the oxidation of LDL have been described [35–38]. They could be enzymatic or nonenzymatic, which lead to oxidative changes in amino acids as well as proteolysis and cross-links of apolipoprotein B (apoB) occur, that result in extensive alteration in the protein composition and structure [35]. In addition, the peroxidized lipids (POLs) decompose generating both free and core aldehydes and ketones that covalently modify ε-amino groups of lysine residues of the protein moiety [36]. These moieties eventually generate Schiff's bases, thus modifying charges on the amino acids, which results in both intra- and intermolecular cross-links between proteolyzed apoB. Many amino acids of apoB (e.g., His, Cys, Tyr, Met, and Lys) may actually participate in the oxidation of LDL [37, 38]. The long polymer

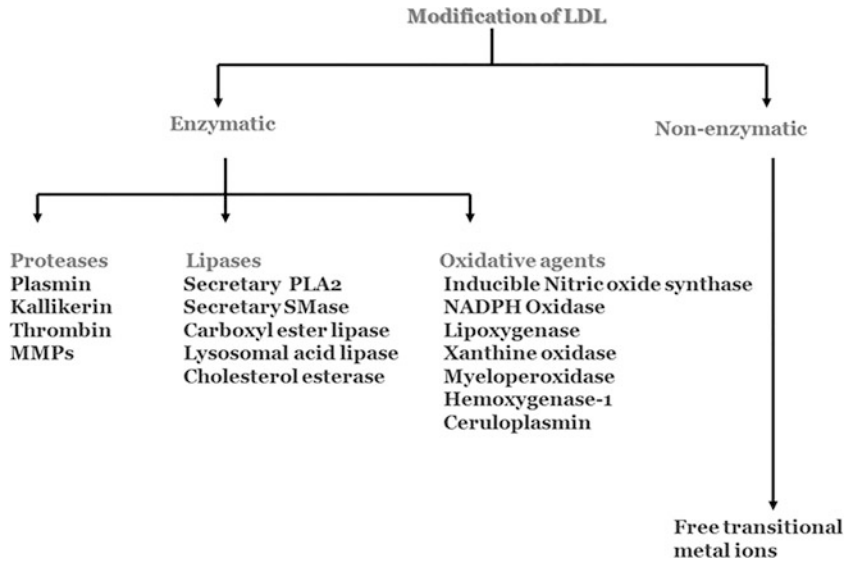

Fig. 1 Different enzymatic/nonenzymatic agents involved in modification of LDL. *MMPs* matrix metalloproteinases, *PLA_2* phospholipase A_2, *SMase* sphingomyelinase

apoB also undergoes oxidative cleavage [35] at many unknown sites, and such a complex mixture of damaged lipids, proteins and the formation new chemical identities drastically modify the lipoprotein. However, these changes occur over time and represent sequential events. There is no way of defining intermediate particles, although minimally oxidized or minimally modified LDL might represent one of the earliest oxidative changes.

The Ox-LDL is avidly scavenged and degraded by macrophages. Oxidative modification is not unique to LDL, like other lipoproteins such as very low-density lipoprotein (VLDL), beta very low-density lipoprotein (β-VLDL) and even high-density lipoprotein (HDL) have been suggested to undergo similar oxidative changes [39–50] with accompanying changes in their pro-atherosclerotic behavior [51–55]. However, other oxidized lipoproteins have not been studied to the extent Ox-LDL was studied.

Ox-LDL could be defined as a particle derived from circulating LDL that may have peroxides or their degradation products generated within the LDL molecule or elsewhere in the body associated with the particle [34] (Fig. 2). This would include even minor modifications such as minimally oxidized LDL that may have minimal lipid peroxides or their degradation products but no changes in apoprotein.

Many different mechanisms have been suggested for the oxidation of LDL, depending on the purpose (Table 1) [56–70]. Studies aimed at fundamental mechanism(s) of generating an atherogenic Ox-LDL species focused on cellular systems. Studies that were

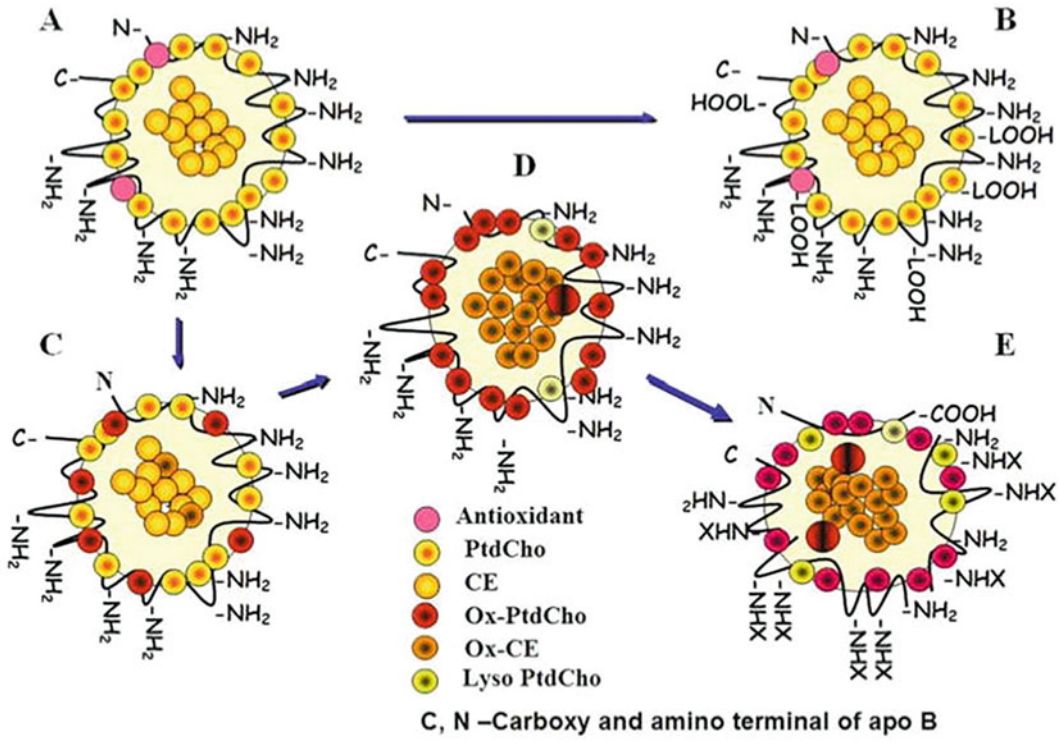

Fig. 2 Forms of oxidized low-density lipoprotein. (**a**) Unoxidized native LDL with amino groups of lysine residues of apoB and representative lipids. (**b**) Lipid peroxides generated elsewhere associated with such LDL. (**c**) LDL lipids might get oxidized resulting in the generation of cholesterol ester and phospholipid peroxides. (**d**) Such LDL might undergo extensive oxidation leading to protein changes. (**e**) Extensive protein changes and lipid decomposition might hallmark the end stages of oxidation

Table 1
Suggested mechanisms for the oxidation of LDL

	Mechanism	References
1	Lipoxygenase reaction	[56, 57]
2	Copper and ceruloplasmin-mediated oxidation	[58, 59]
3	Iron-mediated oxidation	[60, 61]
4	Peroxidase-mediated oxidation including myeloperoxidase and heme	[62–64]
5	Peroxynitrite mediated oxidation	[59, 65]
6	Thiol-dependent oxidation	[66, 67]
7	Xanthine oxidase, NADPH oxidase, and other superoxide generators	[58]
8	AAPH or other means of radical generation including cytochromes	[59, 65]
9	Heme and cytochromes	[68, 69]
10	Lysosomal oxidation	[70]

focused on changes that occurred during oxidation used chemical models of oxidation. Studies that investigated the effects of Ox-LDL chose methods that produced the desired effects.

Not all the oxidation mechanisms are comparable or lead to similar products even under in vitro conditions. For example, peroxidase-mediated oxidations require co-oxidants such as H_2O_2 or lipid peroxides or even cosubstrates. Contrary to expectations, such oxidations were actually "fueled" by "antioxidants." For example, the myeloperoxidase (MPO) catalyzed oxidations were propelled by the presence of free tyrosine, estradiol or even vitamin E [25, 71, 72]. This could be construed as evidence for an intermediate prooxidant role for antioxidants. Similarly, many thiols actually enhance the oxidation of LDL depending on the peroxide or redox metal content of LDL [73].

Some of the oxidants damage the proteins more readily than others. For example, treatment of LDL with 2,2′-azobis(2-amidinopropane) dihydrochloride (AAPH), a radical generator or peroxynitrite, resulted in more protein oxidation than lipid peroxidation [74–77]. Similarly, peroxidase-catalyzed oxidation generated very little aldehyde products as compared to metal-catalyzed oxidations [78–80]. Lipoxygenase reactions, which are exclusively intracellular, might require additional reactions or transfers before or after the reactions occur [81, 82]. To our knowledge, no one has characterized Ox-LDL isolated from animals or humans to the extent that details of mechanistic insights could be derived.

The detection of Ox-LDL, at least in vitro, has been quite easy. The presence of very small amounts of MDA has always been used as a yard stick for minimally or terminally oxidized LDL [83–86], although numerous publications concluded a short-term oxidation always resulted in a "mildly" oxidized LDL as opposed to long-term oxidations [87–90]. Yet enzymatic (lipoxygenase, peroxidase) reactions and treatment with peroxynitrite that generated lower amounts of MDA, were always considered fully oxidized LDL due the ability of macrophages to engulf such LDL. The studies by Witztum and coworkers [91, 92] resulted in the identification of many antigenic epitopes in Ox-LDL and have led to the development of monoclonal antibodies. Commercial use of these and other antibodies have identified pathologies [93–108], in which circulating levels of Ox-LDL could become elevated [100, 102, 109]. Many others have reported the generation of antibodies (e.g., antibodies to peroxide modified proteins) [110, 111], peroxidized phosphatidylethanolamine [110] and others that cross-reacted with materials in the atherosclerotic arteries.

The measurement of lipid oxidation has been a great boon, not only to the understanding the process but also in providing numerous serendipitous discoveries and methodologies. The formation of conjugated dienes during lipid peroxidation was successfully exploited to generate the "lag time" concept by Esterbauer and

associates [112] that is still used as a yard stick for measuring the oxidizability of LDL. Similarly, the discovery of isoprostanes by Roberts, Morre and others [113, 114] also created tremendous excitement and opportunity to look for such LDL in vivo [83].

In this chapter, we will outline methodologies for the preparation and testing of various lipoproteins for oxidation studies. Several points need to be kept in mind, which include (a) lipoprotein content, composition, presence or absence of anti- and prooxidant materials could differ amongst species; (b) lipoproteins are not homogeneous particles. There could be subfractions and contaminations by other proteins, depending on the methodology. Extensive purification steps, while assuring the quality of the isolated lipoprotein, could influence the susceptibility to oxidation; (c) such purification steps could also remove components that promote or inhibit oxidation; (d) the in vitro addition of antioxidants, metal chelators and even high levels of salts could influence oxidation, as there is no yardstick for the effective removal of these added contaminants; (e) we lose the ability of determining the influences of plasma proteins, solutes and other lipoproteins on the oxidation of another lipoprotein; (f) protecting the plasma or lipoproteins during isolation is no guarantee that the method achieved its goals. Evidence indicates that even in sealed tubes, prolonged centrifugation could "bleach" the lipoproteins pointing to oxidation. Dissolved oxygen, gas permeability in the synthetic centrifugation tubes and even release of peroxides internally could make a difference; (g) even traces of hemolysis during blood drawing could generate iron or hemoglobin or other proteins which could influence oxidation; (h) greatest problem that we have seen is on the concentrations of lipoproteins used in the preparation of various types of Ox-LDL. A few micrograms of LDL per milli liter get more readily oxidized than a milligram of LDL in the same volume. As the concentration of LDL is increased its "oxidizability" decreases due to self-quenching. Different modes of oxidation are affected differently. Methodological problems also arise as you raise the quantity of lipoproteins; and (i) to date, no one has separated an oxidized fraction of Ox-LDL from a mixture of oxidized and unoxidized preparations. In other words, you cannot partially oxidize an LDL and isolate the affected and unaffected lipoproteins. If you size-fractionate by gel electrophoresis, you see one particle and not two distinct populations. Adding EDTA or antioxidants after a partial oxidation could lead to misleading results, as these agents do not affect the decomposition of preexisting peroxides. However, there have been numerous claims of isolation of Ox-LDL from plasma [93, 115–121]; however, most rely on preisolation of "LDL" fraction not from the whole plasma.

2 Materials

2.1 Collection of Plasma and Isolation of Human LDL

1. Butterfly needles for collecting blood.
2. 10 mL vacutainer tubes (EDTA).
3. Tourniquet.
4. Alcohol wipes.
5. Ice.
6. Centrifuge tubes.
7. Cold centrifuge.

2.2 Isolation of LDL

1. Plasma.
2. Ice.
3. Table-top ultracentrifuge.
4. Potassium bromide (KBr).
5. Glass Pasteur pipette.
6. Rubber bulb.
7. Centrifuge tube stand and sealer.
8. 0.15 M sodium chloride (NaCl) solution.
9. 5 mL centrifuge tubes.
10. Rotor.
11. 15 mL centrifuge tubes.
12. Balance, weigh boats and spatula.

2.3 LDL Dialysis, Storing of LDL and Determination of Protein Concentration

1. LDL sample from Subheading 2.2.
2. Sterile Phosphate Buffer Saline (PBS): 137 mM NaCl, 2.7 mM KCl, 8 mM Na_2HPO_4, 2 mM KH_2PO_4.
3. 0.3 mM EDTA.
4. Dialysis tubing (MWCO 12 kDa).
5. Magnetic plate.
6. Stirrer bar.
7. Clamps for dialysis bag.
8. Ethanol.
9. Rubber bulb.
10. Pasteur pipette.
11. Glass beaker.
12. 0.4 μm sterilization filters.
13. 15 mL centrifuge tubes.
14. Aluminum foil.

15. Fridge or freezers.
16. Protein assay kit.
17. 96-well plates.
18. Plate reader.

2.4 Preparation of Copper-Oxidized LDL or HDL

1. UV spectrophotometer.
2. Cuvettes.
3. LDL from Subheading 2.2.
4. HDL.
5. PBS.
6. 5 μM copper sulfate solution.
7. Incubator or water bath at 30 °C.
8. Micro pipettes.
9. Pipette tips.

2.5 Preparation of Myeloperoxidase (MPO)-oxidized LDL or HDL

1. UV spectrophotometer.
2. Cuvettes.
3. LDL from Subheading 2.2.
4. HDL.
5. PBS.
6. 0.2 U myeloperoxidase (MPO)/mL
7. 100 μM Hydrogen peroxide (H_2O_2).
8. 100 μM tyrosine.
9. Incubator or water bath at 30 °C.
10. Micro pipettes.
11. Pipette tips.

2.6 Preparation of Acetyl LDL

1. 0.5 g/mL saturated sodium acetate solution.
2. LDL from Subheading 2.2.
3. 100% Acetic anhydride.
4. 0.3 mM EDTA.
5. Micro pipettes.
6. Pipette tips.
7. Beaker.
8. Ice.
9. Test tubes.
10. Stirrer bar.
11. Magnetic plate.
12. Dialysis membrane.

13. Protein determination kit.
14. 0.2 μm syringe filter.

2.7 Electrophoretic Mobility of Lipoproteins on Agarose Gels

1. Agarose.
2. Balance.
3. 50× TAE buffer: Weigh 242 g Tris-base and dissolve in 750 mL of ddH_2O. Add 57.1 mL of 100% glacial acetic acid followed by 100 mL of 0.5 M EDTA. Adjust the pH 8.0 and make final volume to 1 L.
4. 1× TAE buffer: Dilute 20 mL of 50× TAE buffer into 980 mL of ddH_2O.
5. 50 μg/mL Nile Red in acetone.
6. 50% ethanol.
7. Transverse Electrophoresis kit.
8. Gel casting tray.
9. Gel combs.
10. Voltage source.
11. UV-light source.
12. Microwave.
13. Conical flask.
14. Micro pipettes.

2.8 Mouse Peritoneal Macrophage Isolation

1. 8–10 weeks old mice.
2. Anesthesia chamber.
3. 1–2% Isoflurane.
4. 70% ethanol or isopropanol.
5. Alcohol wipes.
6. Ice-cold saline.
7. 5 mL syringes.
8. 25G needles.
9. Scissors.
10. Forceps.
11. 15 mL centrifuge tubes.
12. Glass Pasteur pipettes.
13. Centrifuge.
14. Complete Roswell Park Memorial Institute (RPMI) 1640 medium: RPMI 1640 medium supplemented with 10% fetal bovine serum, 2 mM L-glutamine, 1% penicillin-streptomycin antibiotic solution.
15. Water bath.

16. Biological safety cabinet.
17. Pipettes.
18. Trypan blue solution.
19. Cell culture plates (6-well, 12-well, chamber slides of 4 or 8-wells).
20. Cell culture incubator.
21. Styrofoam block and pins for mounting the mouse.
22. Aluminum foil.

2.9 THP-1 Cell Culture

1. THP1 monocytes (ATCC TIB-202).
2. Complete RPMI 1640 medium.
3. T-75 tissue culture flasks.
4. Water bath.
5. 70% ethanol.
6. Centrifuge tubes.
7. Biological safety cabinet.
8. Cell culture incubator.
9. 50 ng/mL phorbol-12-myristate-13-acetate (PMA).
10. 20 ng/mL interleukin-4 (IL-4).
11. 100 ng/mL lipopolysaccharide (LPS).

2.10 Foam Cell Preparation

1. Peritoneal macrophages or other macrophage sources from Subheadings 2.8 to 2.9.
2. Modified forms of LDL from Subheadings 2.4–2.6.
3. Cell culture incubator.

2.11 Staining of Foam Cells

2.11.1 Oil Red O Staining for Cultured Cells

1. Oil Red O Stock: Add 0.35 g of Oil Red O to 100 mL of isopropanol. Stir overnight, filter through 0.2 μm filter and store at room temperature (RT).
2. Oil Red O Working Solution: Mix 6 mL of Oil Red O stock solution with 4 mL of ddH_2O and filter the solution using 0.2 μm filter after 20 min and store at room temperature (RT).
3. 10% formalin in PBS.
4. 100% and 60% isopropanol.
5. PBS.
6. Micropipettes and tips.
7. ddH_2O.
8. Pipette.
9. Rocker/shaker.
10. Microscope.

2.11.2 Nile Red Staining

1. 1 mg/mL Nile Red stock in DMSO.
2. 1 μg/mL Nile Red working solution: Prepare this by diluting the Nile Red stock in phenol-free, serum-free RPMI 1640 cell culture medium prior to staining.
3. 100% DMSO.
4. PBS.
5. Micropipettes and tips.
6. Fluorescence microscope.

2.12 Macrophage Cholesterol Determination

1. 96-well plate.
2. Protein assay kit.
3. Amplex Red Cholesterol Assay kit (Invitrogen) or equivalent containing 1× reaction buffer and protease inhibitors.
4. 2 mg/mL cholesterol for standard curve.
5. Water bath or incubator.
6. Fluorescence plate reader.
7. Micropipettes and tips.

2.13 Reverse Cholesterol Transport Assay

1. Foam cells.
2. HDL or ox-HDL.
3. 96-well plate.
4. Fluorescence plate reader.
5. Fluorescence microscope.
6. Micropipettes and tips.
7. Oil red O stain from Subheading 2.11.1.
8. Sterile PBS.
9. 5 mM cholesterol and 2 mM [22-(*N*-(7-nitrobenz-2-oxa-1,3-diazol-4-yl)amino)-23,24-bisnor-5-cholen-3β-Ol] (NBD)-cholesterol in chloroform.
10. 20 mM lysophosphatidyl choline (Lyso-PtdCho) stock solution in chloroform: methanol (1:1 ratio).
11. Complete RPMI 1640 medium.
12. Test tubes.
13. Cell culture incubator.
14. Nitrogen.
15. Vortex.
16. 0.22 μm filter.

2.14 SDS-PAGE Gel Electrophoresis

1. Polyacrylamide gel (PAGE) electrophoresis system: gel preparation stand, gel tank, glass plates, combs, lids with electrodes, power supply unit.
2. 30% acrylamide solution.
3. 10% sodium dodecyl sulfate (SDS).
4. 10% ammonium persulfate (APS).
5. Micropipettes.
6. Resolving gel buffer: 1.5 M Tris–HCl, pH 8.8. Add 100 mL water to a 1 L graduated cylinder or a glass beaker. Weigh 181.7 g Tris–HCl and transfer to the cylinder. Add water to a volume of 900 mL. Mix and adjust pH with HCl. Make up to 1 L with water and store at 4 °C.
7. Stacking gel buffer: 0.5 M Tris–HCl, pH 6.8. Weigh 60.6 g Tris and prepare a 1 L solution as in the previous step (**step 5**). Store at 4 °C.
8. 10× Running Buffer, pH 8.3: Add 30.3 g Tris base, 144.4 g glycine and 10 g SDS to 800 mL ddH_2O. Make final volume to 1 L with ddH_2O.
9. 1× Running Buffer.
10. *N*,*N*,*N*′,*N*′-Tetramethyl-ethylenediamine (TEMED), Store at 4 °C.
11. Pipette tips.
12. Prestained molecular size markers.
13. G-250 Coomassie blue stain.
14. Gel imager.

3 Methods

3.1 Collection of Plasma

1. Collect blood by venipuncture from consenting donors after an overnight fast, usually about 12 h (*see* **Note 1**).
2. Tie the tourniquet to the upper arm, identify the venous blood vessel and gently insert the butterfly needle.
3. Once you observe the blood coming out, insert the collector into EDTA vacutainer tube and gently collect the blood through the walls of the tube. Typically, collect 100 mL of blood into 10–12 of 10 mL EDTA vacutainer tubes. Mix blood with EDTA several times and place on ice.
4. Centrifuge the tubes at 2350 × *g* for 20 min at 4 °C (*see* **Note 1**).
5. Collect the plasma without any air bubbles and store at −80 °C until use.

3.2 Isolation of LDL

1. Place fresh plasma on ice. If the plasma is frozen then thaw the plasma to room temperature and place on ice.
2. Weigh ~989 mg of solid KBr for every 2 mL of plasma. Add the required amount of KBr to the tube containing the plasma.
3. Dissolve the KBr by gently inverting the tube without forming air bubbles (*see* **Note 2**).
4. Place the centrifuge tubes in the tube stand.
5. Aliquot 2.5 mL of Plasma-KBr in each centrifuge tube.
6. Overlay 2.5 mL of 0.15 M NaCl solution on the top of the KBr-Plasma very gently without disturbing the lower layer using a glass Pasteur pipette and rubber bulb.
7. Seal the tubes using the sealer and centrifuge 280,000 × *g* for 2 h at 4 °C.
8. Identify the yellow/orange color band in the upper middle of the tube.
9. Gently remove the upper part (clear solution) of LDL band and then collect the LDL into 15 mL centrifuge tube. Pool all the LDL fractions from the eight tubes if the source is same.
10. Add ~653 mg of KBr for 2 mL of LDL and gently mix until KBr dissolves in the LDL fraction.
11. Aliquot 2 or 2.5 mL into the centrifuge tubes and overlay the 0.15 M NaCl solution using glass Pasteur pipette and rubber bulb.
12. Recentrifuge at 112,000 × *g* for 1 h at 4 °C.
13. Collect the clear yellow orange LDL band and keep for dialysis for purification of the LDL. Collect dense band only [25, 122, 123] (*see* **Note 3**).

3.3 LDL Dialysis, Storage, and Protein Concentration

1. Wash the dialysis membrane as suggested by the manufacturer.
2. Rinse the dialysis membrane with ethanol and then with sterile PBS two times.
3. Remove all the buffer droplets from the dialysis bag and clamp the dialysis bag on one side (*see* **Note 4**).
4. Gently place the LDL in the dialysis bag without air bubbles using glass Pasteur pipette.
5. Close the other end also without air bubbles with a clamp and make sure that there is no leakage.
6. Choose the glass beaker depending on the LDL volume for dialysis (e.g., 500 mL beaker for 1 mL of LDL sample).
7. Fill the beaker with sterile PBS and add 0.3 mM EDTA.

8. Place the dialysis bag with the LDL sample in the buffer and keep the whole set up on a magnetic plate with a stirrer bar overnight at 4 °C.
9. Transfer the LDL into a tube and filter-sterilize by passing through 0.4 μm filter.
10. Store the isolated LDL at 4 °C and use within 1 or 2 weeks (*see* **Note 5**).
11. Determine the concentration of protein in the isolated LDL using any commercially available kit (*see* **Note 6**).

3.4 Preparation of Copper-Oxidized LDL/HDL

1. Add 5 μM of copper sulfate solution to 100 μg of LDL/HDL in 1 mL of PBS at 37 °C (*see* **Note 7**).
2. Measure the formation of conjugated dienes at an optical density of 234 nm for 16–18 h using UV-spectrophotometer (*see* Figs. 3 and 4).
3. Different forms of Ox-LDL can be collected depending on different extents of oxidation. Usually excess EDTA is added to "arrest" further oxidation. The three different forms of oxidized LDL that are routinely used are (a) mm-LDL—samples collected at the end of the initial lag phase, which are considered as mildly oxidized LDL (MO-LDL); (b) FO-LDL—samples collected at the end of the propagation phase, which are considered as fully oxidized LDL (FO-LDL); and (c) Ox-Mod-LDL—samples collected at the end of 16–18 h, which are considered as oxidatively modified LDL (Ox-Mod-LDL) (*see* **Note 7**).

3.5 Preparation of Myeloperoxidase (MPO)-Oxidized LDL/HDL

1. Add 0.2 U of MPO and 100 μM of H_2O_2 to 100 μg of LDL in 1 mL of PBS at 37 °C either in the presence or the absence of 100 μM tyrosine (*see* **Notes 8–10**).
2. Measure the formation of conjugated dienes at an optical density of 234 nm for 16–18 h using UV spectrophotometer (*see* Figs. 5 and 6).

3.6 Preparation of Acetyl LDL

1. Prepare saturated sodium acetate solution in a tube (*see* **Note 11**).
2. Mix equal volumes (1:1 ratio) of LDL and sodium acetate solution in a clean test tube.
3. Place a stirrer bar and keep the tube in a beaker filled with ice on a magnetic plate.
4. Allow the stirrer bar to gently agitate without forming air bubbles.
5. Add 2 μL of ice-cold 100% acetic anhydride every 5 min until 30 min.

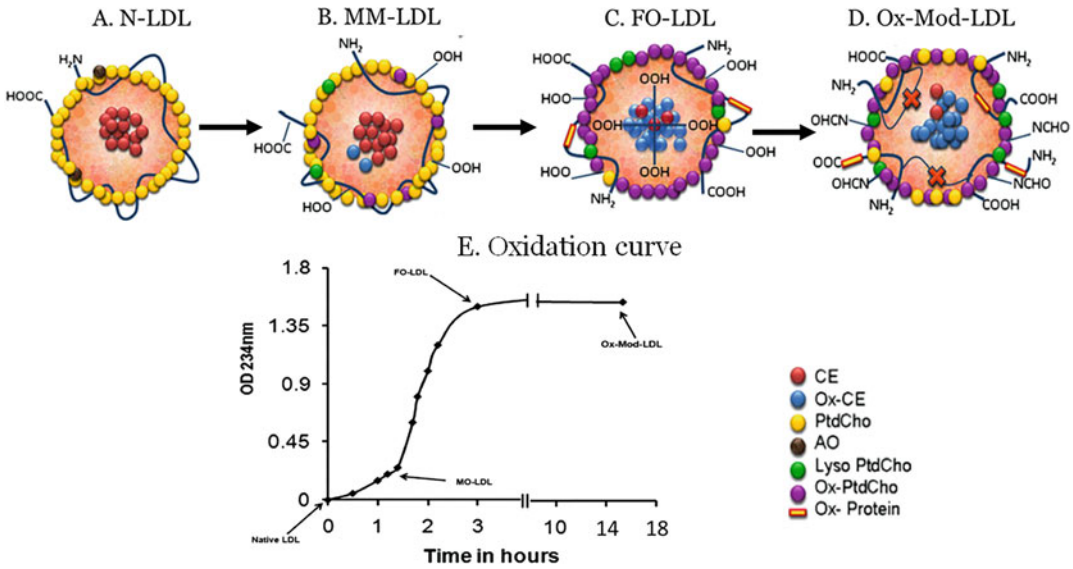

Fig. 3 Different forms of oxidized low-density lipoprotein. (**a**) Unoxidized native LDL with amino groups of lysine residues of apo B and representative lipids. (**b**) MM-LDL: LDL lipids might get mildly oxidized resulting in limited generation of cholesterol ester and phospholipid peroxides. (**c**) FO-LDL: Such LDL might undergo extensive oxidation leading to protein changes as well as the generation of large amounts of lipid peroxides. (**d**) Ox-Mod-LDL: Extensive protein change and lipid decomposition and protein modification by products of lipid peroxidation represent the end stages of oxidation; (**e**) Oxidation curve

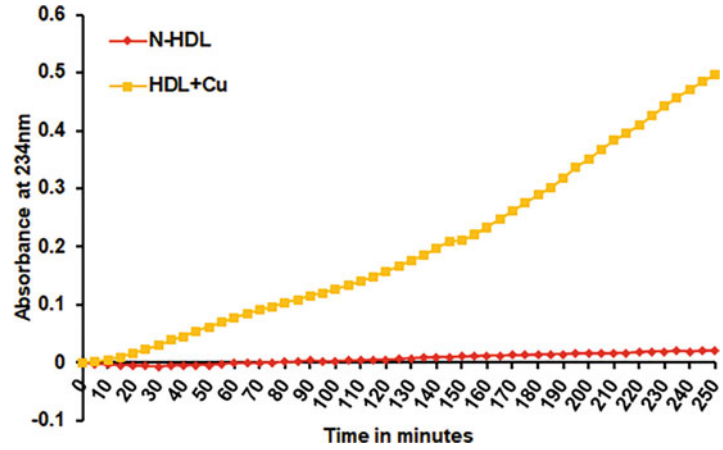

Fig. 4 Copper (Cu)-oxidized high-density lipoprotein. Copper (Cu)-oxidized HDL oxidation curve

6. Leave the sample on the magnetic plate in ice for almost 1 h until visible turbidity appears.
7. Remove the sample and dialyze overnight against PBS with 0.3 mM EDTA.
8. Filter-sterilize the sample using 0.2 μm syringe filter.

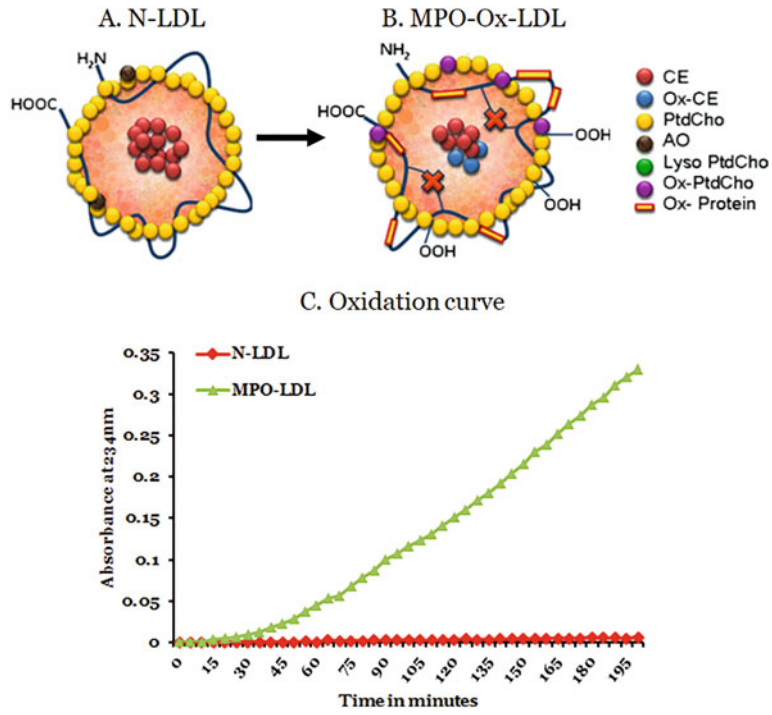

Fig. 5 MPO-oxidized low-density lipoprotein. (**a**) Unoxidized native LDL with amino groups of lysine residues of apoB and representative lipids. (**b**) MPO-oxidized LDL with more protein (amino acid) oxidation and less lipid peroxidation. (**c**) Oxidation curve

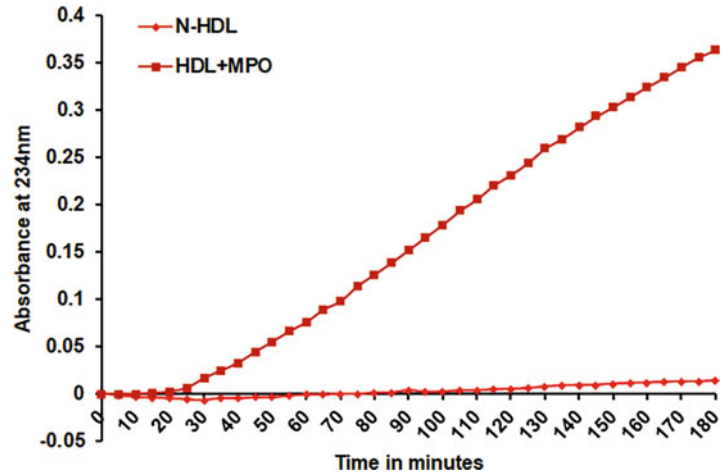

Fig. 6 MPO-oxidized high-density lipoprotein. MPO-oxidized HDL oxidation curve

9. Estimate the protein concentration of the sample using any commercially available kit and store at 4 °C.

3.7 Electrophoretic Mobility of Lipoproteins on Agarose Gel

1. Measure 0.5 g of agarose using a balance.
2. Mix weighed agarose with 100 mL of 1× TAE buffer in a microwavable flask.
3. Microwave for 1–3 min until the agarose is completely dissolved (*see* **Notes 12** and **13**).
4. Allow the agarose solution to cool down for 5 min so that it is comfortable to keep hand on the flask.
5. Pour the agarose into a gel tray with the well comb and allow to solidify at room temperature for 1 h.
6. Once the gel solidified, place the agarose gel into the gel tank.
7. Fill the tank with 1× TAE until the gel is covered or immersed.
8. Carefully load 20 μL of native LDL and different forms of oxidized LDL samples into the wells of the gel.
9. Perform electrophoresis at 50 V for 1 h.
10. Turn the power off, disconnect the electrodes from the power source and then carefully remove the gel from the gel tank.
11. Gently place the gel in a staining solution of Nile Red for 1 h.
12. Destain the gel with 50% ethanol for 1 h.
13. Record the images using UV light source to visualize the LDL and modified LDL forms (i.e., mildly modified LDL [mm-LDL], fully oxidized LDL [FO-LDL], and completely oxidized LDL [Ox-LDL]) (*see* Figs. 7 and 8).

3.8 Mouse Peritoneal Macrophage Isolation for Foam Cell Formation

All procedures must be approved by the Institutional Animal Care and Use Committee following the relevant guidelines and regulations. The whole procedure should be performed under sterile conditions (*see* **Note 14**). All instruments used in the procedure should be autoclaved and bead-sterilized prior to use.

1. Euthanize mice using isoflurane for 5–10 min in an anesthesia chamber.
2. Spray 70% ethanol on the mice and place the mouse facing ventral side up on Styrofoam block wrapped with aluminum foil.
3. Using scissors and forceps to make a small incision on the outer skin of the peritoneum to expose the inner skin lining of the peritoneal cavity.
4. Wipe the peritoneal cavity with alcohol wipes.
5. Fill the syringe with 3 mL of ice-cold saline, lift the skin with forceps and inject gently without air bubbles and without puncturing the peritoneal organs.
6. Shake the animal gently for 3 min or gently massage the peritoneal cavity to dislodge the attached cells into saline.

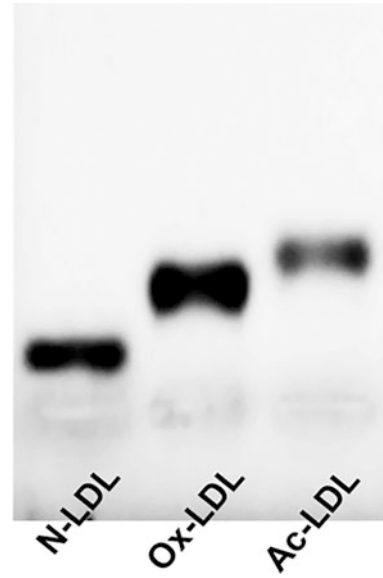

Fig. 7 Electrophoretic mobility. Mobility of different modified forms of Ox-LDL during agarose gel electrophoresis

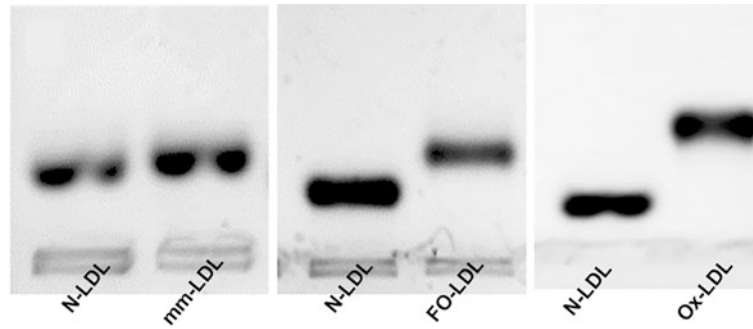

Fig. 8 Electrophoretic mobility. Mobility of different extents of modified forms of Ox-LDL during agarose gel electrophoresis

7. Collect the peritoneal cells either with syringe and 25G needle or make small incision with scissors, lift the skin with forceps and collect the cells into 15 mL centrifuge tube with a sterilized glass Pasteur pipette (*see* **Note 15**).
8. Centrifuge the cells at 850 × *g* for 5 min.
9. Aspirate the supernatant and suspend the cell pellet in 1 mL of complete RPMI-1640 medium (prewarmed to room temperature).
10. Aliquot the 2×10^5 cells/mL in 6-well/12-well culture plates with 2 or 1 mL complete RPMI-1640 medium or chamber slides with 10,000 cells/mL depending on the experiment planned.

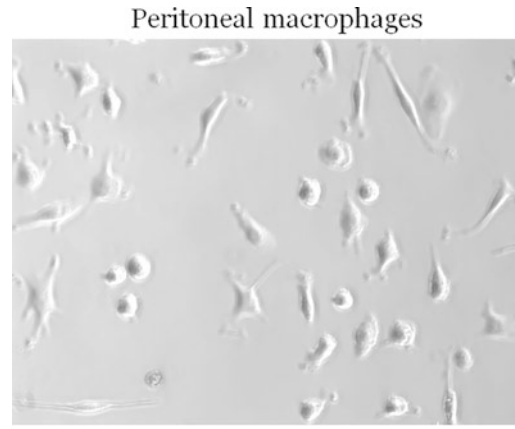

Fig. 9 Peritoneal macrophages

11. Culture the cells overnight at 37 °C in a 5% CO_2 incubator. The cultured peritoneal macrophages will appear as shown in Fig. 9. Use the peritoneal macrophages for the planned experiments [122, 124–126].

3.9 Cell Culture

3.9.1 THP-1 Cell Culture

1. Thaw the vial of THP-1 monocytes at 37 °C in a water bath.
2. Take the vial out from the water bath once the contents have thawed, spray with 70% of ethanol to decontaminate, wipe, and place the vial in biological safety cabinet.
3. Transfer the vial contents into a centrifuge tube containing minimum of 2 mL of complete RPMI 1640 medium and centrifuge at 850 × *g* for 5 min.
4. Aspirate the supernatant and resuspend the cell pellet in 1 mL of complete RPMI 1640 medium.
5. Transfer the whole content into a T-75 flask. Place the flask in an upright position in an incubator with 5% CO_2 at 37 °C (*see* **Note 16**).
6. After 2–3 days, observe the cell density, count the cells to maintain the cell density for subculture and to plate for experimental purposes [127, 128]. Monocytes are shown in Fig. 10a (*see* **Note 16**).

3.9.2 Differentiation of Monocytes into Macrophages [127]

1. To obtain monocyte-derived macrophages (MDMs), differentiate THP-1 cells with 50 ng/mL of PMA for 72 h in complete RPMI 1640 medium. Macrophages are depicted in Fig. 10b.
2. For subsequent polarization of macrophages, wash differentiated and adherent cells twice with complete RPMI 1640 medium to remove any nonadhered cells and replace with fresh media containing either 50 ng/mL of PMA, 100 ng/mL of LPS plus 50 ng/mL PMA, or 20 ng/mL of IL-4 plus

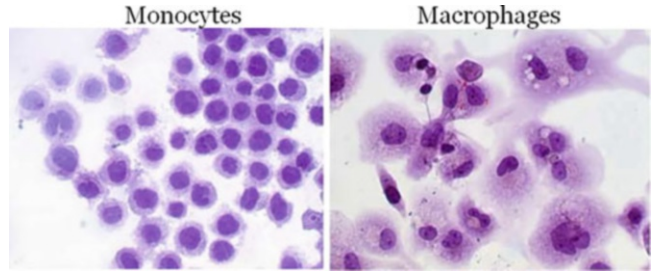

Fig. 10 Monocytes and monocyte derived macrophages (MDMs)

50 ng/mL of PMA for a further 24 h to generate PMA controls (MΦ-PMA), M1-like macrophages (MΦ-LPS/IFNγ), and M2-like macrophages (MΦ-IL-4), respectively (*see* **Note 17**).

3.10 Preparation of Foam Cells

1. Incubate peritoneal macrophages or MDM overnight with modified forms of LDL for 24 h at 37 °C in a cell culture incubator (*see* **Note 18**).

3.11 Staining of Foam Cells

3.11.1 Oil Red O Staining for Cultured Cells [122, 129]

1. Take the cells out of the cell culture incubator following formation of foam cells with different treatments with modified lipoproteins and remove the medium.
2. Rinse the cells with ~2 mL of PBS and remove PBS completely.
3. Add enough volume (~2 mL) of 10% formalin in PBS to cover the cells and incubate for 10 min at RT.
4. Discard the formalin in PBS and then add fresh formalin in PBS followed by further incubation for at least 1 h.
5. Gently remove the formalin with a pipette and wash the cells twice with 2 mL of ddH_2O.
6. Wash the cells with ~2 mL of 60% isopropanol to cover the surface of cells for 5 min at RT.
7. Allow the cells to dry completely at RT.
8. Add 1 mL of Oil Red O working solution and incubate at RT for 30–60 min on a rocker/shaker (*see* **Note 19**).
9. Remove the Oil Red O solution and add ddH_2O. Wash the cells 4 times with ddH_2O.
10. Acquire images using bright field microscope for analysis. Images will appear as shown in Fig. 11.
11. Keep the cells in PBS and/or store the stained cells at 4 °C.

3.11.2 Nile Red staining

1. Take the cells out of the cell culture incubator following formation of foam cells with different treatments with modified lipoproteins and remove the medium.
2. Rinse the cells with ~2 mL of PBS and remove 1× PBS completely.

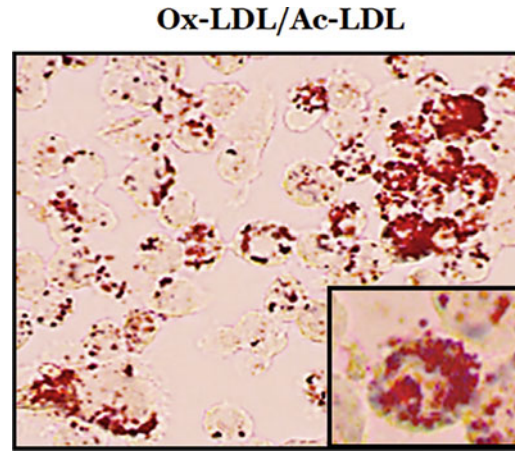

Fig. 11 Ox-LDL/Ac-LDL uptake by RAW264.7 cells—Oil Red O staining. RAW264.7 macrophages were treated with Ox-LDL/Ac-LDL for 24 h under serum free conditions. The cells were then stained with Oil Red O and observed under a microscope

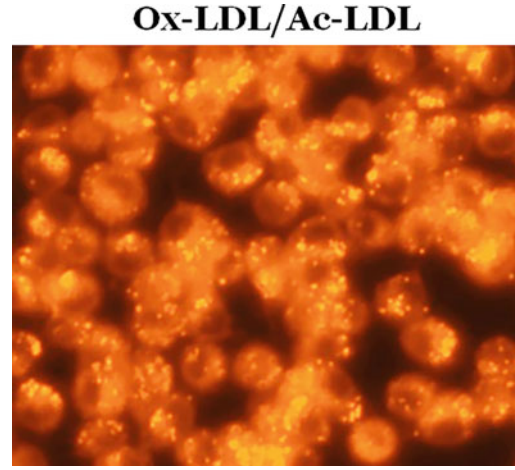

Fig. 12 Ox-LDL/Ac-LDL uptake by RAW264.7 cells—Nile Red staining. RAW264.7 macrophages were treated with Ox-LDL/Ac-LDL for 24 h under serum free conditions. The cells were then stained with Nile Red and observed under a microscope

3. Add enough volume (~1 mL) of Nile Red working solution to cover the cells and incubate for 10–15 min at RT.
4. Remove the staining solution and wash the cells 2 times with 1× PBS.
5. Acquire images under green excitation light using the fluorescence microscope for analysis (*see* Fig. 12).
6. Keep cells in PBS and/or store the stained cells at 4 °C.

3.12 Macrophage Cholesterol Determination

1. Lyse the cells in 1× reaction buffer supplemented with protease inhibitor cocktail present in the Amplex Red Cholesterol Assay kit.
2. Use an aliquot of sample for determining protein concentration using the Protein assay kit.
3. Heat the remaining cell lysate at 60 °C for 30 min to inactivate enzymes that could interfere and compete with the assay.
4. Prepare standards for cholesterol standard curve: Dilute an amount of 2 mg/mL (5.17 mM) cholesterol into 1× reaction buffer to produce cholesterol concentrations of 0–8 μg/mL (0–20 μM). Use 1× reaction buffer without cholesterol as a negative control.
5. Use 50 μL of the standards and samples in triplicate in 96-well plate. Add 50 μL of Amplex Red reagent to each well and incubate for 30 min at 37 °C.
6. Measure the fluorescence using a fluorescence microplate reader with an excitation range of 530–560 nm and emission detection at approximately 590 nm.
7. This assay allows both total cholesterol and cholesterol esters to be quantified by including cholesterol esterase into the reaction (*see* **Note 20**).
8. Normalize the cholesterol content with the amount of total cellular protein [130].

3.13 Reverse Cholesterol Transport Assay

1. For a typical reaction, mix 3 μmol of cholesterol (600 μL from the stock), 10 nmol of NBD-cholesterol (5 μL from the stock) and 3 μmol of lyso-PtdCho (150 μL from the stock) together in a test tube followed by drying under nitrogen.
2. Add 1 mL of sterile PBS to the dried content and vigorously vortex the mixture for 1–2 min.
3. Filter the aqueous solution through 0.22 μm filter and make sure the entire procedure is performed under dark conditions.
4. Incubate macrophages overnight with 120 μM concentration of cholesterol/lyso-PtdCho mixed micelles in a cell culture incubator.
5. Wash twice with PBS and add complete RPMI-1640 medium (*see* **Note 21**).
6. Incubate the cells with 0–200 μg/mL of native HDL or 25 and 50 μg/mL of ox-HDL (MPO or Cu-mediated oxidation as Subheadings 3.4 and 3.5) for 4 h (*see* **Note 22**).
7. Collect the medium and measure fluorescence intensity.
8. After removal of the medium, wash the cells with PBS and visualize the images using fluorescence microscope (Fig. 13).

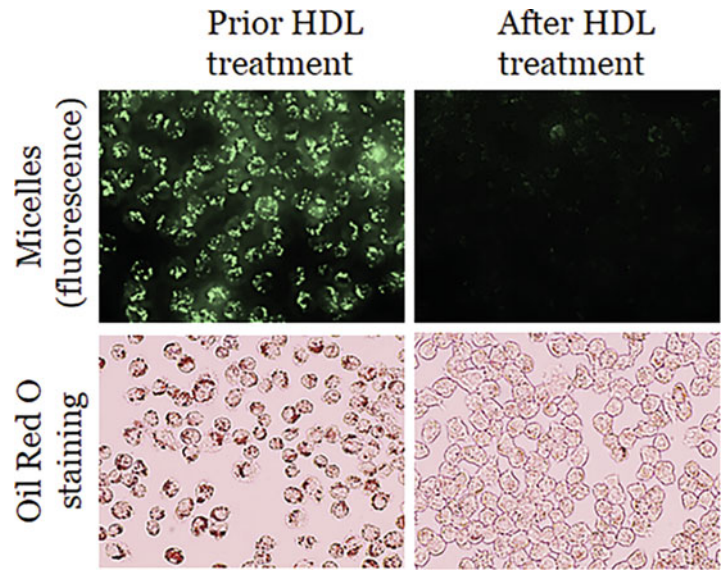

Fig. 13 Cholesterol efflux from foam cells in the presence of HDL. Foam cells were formed using RAW 264.7 macrophages with cholesterol (unlabeled and NBD-cholesterol)/lyso-PtdCho mixed micelles. Foam cells were incubated with 0 and 200 μg/mL of HDL for 4 h. Fluorescence images and Oil Red O staining show reduction in cholesterol ester droplet accumulations in cells after incubation with HDL

3.14 SDS-PAGE Gel Electrophoresis

1. Prepare the gels using 30% acrylamide solution and the buffers depending on the percentage of the gels required (*see* **Note 23**).
2. Set up the gel in the electrophoresis equipment.
3. Load 5 μL of prestained molecular size markers together with 20 μL of sample containing 25–50 μg of protein.
4. Perform electrophoresis in 1× running buffer first at 100 V for 5 min and then at 150–180 V for about 1–2 h until the blue track dye reaches the bottom of the gel.
5. Gently remove the gels from the plates and wash with water.
6. Stain with G-250 Coomassie blue stain and observe the bands (Fig. 14). Record the images using gel imager.

4 Notes

1. Blood collection for oxidation studies are usually carried out in anticoagulant containing tubes. Although lipoproteins could be isolated from serum for other purposes, clotted blood could release iron, hemoglobin and other components that have prooxidant activities. It is assumed that the EDTA or citrate

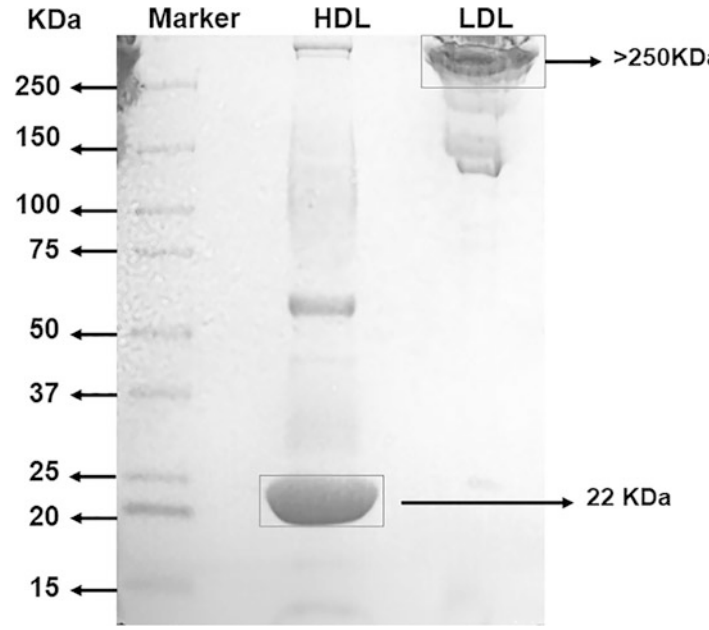

Fig. 14 SDS-PAGE for LDL and HDL

that are usually used as anticoagulants (not heparin) might also prevent any metal catalyzed artifactual oxidation. In most cases, human venous blood is used [25]. Gently collect the blood through the walls of the vacutainer tube to avoid air bubbles and immediate oxidation. Make sure to maintain slow acceleration/deceleration in a fixed angle rotor to remove any remaining cells or debris. If plasma is from multiple donors then pool to minimize the interindividual variation and store as 32 mL aliquots at −80 °C for a maximum of 6 months.

2. Do not vortex as this can cause aggregation of LDL.
3. Caution: Collect LDL under dim light. Make sure to avoid collecting too much non-LDL solution as this would dilute the LDL preparation. To check the purity, one single band of LDL should appear on agarose gel as shown in Fig. 15.
4. Make sure to get rid of all the buffer droplets from the dialysis bag to avoid air oxidation of LDL in the dialysis bag.
5. Immediately after LDL isolation and collection, wrap the tube containing the lipoprotein with aluminum foil to avoid light oxidation before storing. The higher the concentration of the LDL, as produced using the method described here, the better is its storage. Usually, in our laboratory a concentration of 5 mg of LDL protein per mL or more is preferred. LDL concentration is usually expressed as mg protein/mL. If buying commercial LDL or Ox-LDL, make sure that the concentration is depicted in mg protein/mL and not in mg/mL cholesterol.

Fig. 15 Electrophoretic mobility assay. LDL mobility on agarose gel electrophoresis

If it is the later, you may have to determine protein concentration or assume that approximately 1 mg protein is 2.5 mg cholesterol equivalent.

6. Care should be taken to avoid introduction of air bubbles in the wells to avoid interference with the measurement of protein concentration.
7. Make sure to isolate and prepare LDL/HDL under sterile conditions and maintain this during the preparation of oxidized LDL/HDL to avoid any contamination in further experiments. The degree of oxidation of LDL/HDL can be assessed by the determination of peroxide content using leucomethylene blue (LMB) assay and thiobarbituric acid reactive substances (TBARS) assay. Further, oxidation of LDL can also be confirmed using electrophoretic mobility assay [122–124].
8. Make sure to use freshly prepared H_2O_2 to avoid peroxide decomposition.
9. Add the enzyme last after the preparation of the mixture to avoid reaction with other components.
10. The degree of LDL oxidation can be assessed by determination of peroxide content using LMB and TBARS assays [25, 122, 123]. Further, oxidation can also be confirmed using electrophoretic mobility assay [25, 122, 123, 131]. The formation of dityrosine (fluorescent adducts) could also be followed [132, 133].

11. Care should be taken in the preparation of saturated sodium acetate solution to not form more precipitate in order to avoid super saturation. Further, acetylation can also be confirmed using electrophoretic mobility assay (*see* Fig. 7) [122, 129].
12. Please take care not to overboil the agarose solution as some of the buffer will evaporate and thereby alter the final percentage of agarose in the gel. Swirl the flask in between once or twice to avoid over boiling.
13. Care should be taken while microwaving the gel solution to avoid hand burns.
14. Make sure to sterilize all the equipment used to avoid contamination. Make sure not to disrupt any organs during dissection to avoid contamination of peritoneal macrophages with other cells in the blood.
15. Discard the sample if any visible blood contamination is found in the peritoneal lavage during the procedure. Count the cells using trypan blue for the viability.
16. Check the cell viability using trypan blue solution while counting the cells. Care should be taken to ensure that the THP-1 cells are not overconfluent and do not exceed passage number 12. The responses will be compromised in both cases.
17. M1 MΦ (LPS 100 ng/mL)—confirm with markers of iNOS, TNF-α, and IL-6. M2 MΦ (IL-4 20 ng/mL)—confirm with markers of IL-10 and mannose receptor-c type 1(MRC).
18. Please make sure to have the macrophage confluency around 60–70% prior to incubation with modified LDL as this will provide enough room for uptake (i.e., cells become larger) and to avoid overcrowding and detachment from the cell surface.
19. Please do not incubate the foam cells in Oil Red O for longer periods than suggested in order to avoid crystal formation.
20. Care should be taken to avoid introduction of air bubbles in the wells to avoid the interference with measurement.
21. Make sure that the fluorescence micelles are prepared under dark conditions to avoid fluorescence quenching. In addition, to confirm the fluorescence intensity within the cells, prepare cell lysates and measure fluorescence using fluorescence plate reader or stain the cells with Oil Red O/Nile Red to observe remaining CE accumulation [129, 134].
22. Use the HDL immediately after preparation or store appropriately to avoid loss in functionality.
23. Care should be taken in each step (e.g., preparation of buffers, gel, loading of samples, electrophoresis of the gel) to avoid changes in pH, temperature and introduction of air bubbles, which will all affect the protein separation. Furthermore, please

ensure to load equal quantity of the protein in the wells. In addition to agarose gels, SDS-PAGE electrophoresis can also be used for further confirmation of the purity of LDL and HDL prior to cell culture treatments, which is optional but preferable.

References

1. Johnson DR, Decker EA (2015) The role of oxygen in lipid oxidation reactions: a review. Annu Rev Food Sci Technol 6:171–190. https://doi.org/10.1146/annurev-food-022814-015532
2. Ayala A, Muñoz MF, Argüelles S (2014) Lipid peroxidation: production, metabolism, and signaling mechanisms of malondialdehyde and 4-hydroxy-2-nonenal. Oxidative Med Cell Longev 2014:360438. https://doi.org/10.1155/2014/360438
3. Ito J, Komuro M, Parida IS, Shimizu N, Kato S, Meguro Y, Ogura Y, Kuwahara S, Miyazawa T, Nakagawa K (2019) Evaluation of lipid oxidation mechanisms in beverages and cosmetics via analysis of lipid hydroperoxide isomers. Sci Rep 9(1):7387. https://doi.org/10.1038/s41598-019-43645-1
4. Domínguez R, Pateiro M, Gagaoua M, Barba FJ, Zhang W, Lorenzo JM (2019) A comprehensive review on lipid oxidation in meat and meat products. Antioxidants (Basel) 8(10):429. https://doi.org/10.3390/antiox8100429
5. Moreno-García A, Kun A, Calero O, Medina M, Calero M (2018) An overview of the role of lipofuscin in age-related neurodegeneration. Front Neurosci 12:464. https://doi.org/10.3389/fnins.2018.00464
6. Gaschler MM, Stockwell BR (2017) Lipid peroxidation in cell death. Biochem Biophys Res Commun 482(3):419–425. https://doi.org/10.1016/j.bbrc.2016.10.086
7. Raghavamenon A, Garelnabi M, Babu S, Aldrich A, Litvinov D, Parthasarathy S (2009) Alpha-tocopherol is ineffective in preventing the decomposition of preformed lipid peroxides and may promote the accumulation of toxic aldehydes: a potential explanation for the failure of antioxidants to affect human atherosclerosis. Antioxid Redox Signal 11(6):1237–1248. https://doi.org/10.1089/ars.2008.2248
8. Phaniendra A, Jestadi DB, Periyasamy L (2015) Free radicals: properties, sources, targets, and their implication in various diseases. Indian J Clin Biochem 30(1):11–26. https://doi.org/10.1007/s12291-014-0446-0
9. Therond P (2006) Oxidative stress and damages to biomolecules (lipids, proteins, DNA). Ann Pharm Fr 64(6):383–389. https://doi.org/10.1016/s0003-4509(06)75333-0
10. Goto S, Radak Z (2013) Implications of oxidative damage to proteins and DNA in aging and its intervention by caloric restriction and exercise. J Sport Health Sci 2:75–80. https://doi.org/10.1016/j.jshs.2013.03.004
11. Yang L, Mih N, Anand A, Park JH, Tan J, Yurkovich JT, Monk JM, Lloyd CJ, Sandberg TE, Seo SW, Kim D, Sastry AV, Phaneuf P, Gao Y, Broddrick JT, Chen K, Heckmann D, Szubin R, Hefner Y, Feist AM, Palsson BO (2019) Cellular responses to reactive oxygen species are predicted from molecular mechanisms. Proc Natl Acad Sci U S A 116(28):14368–14373. https://doi.org/10.1073/pnas.1905039116
12. Sharma P, Jha AB, Dubey RS, Pessarakli M (2012) Reactive oxygen species, oxidative damage, and antioxidative defense mechanism in plants under stressful conditions. J Bot 2012:217037. https://doi.org/10.1155/2012/217037
13. Linton MF, Yancey PG, Davies SS, Jerome WG, Linton EF, Song WL, Doran AC, Vickers KC (2000) The role of lipids and lipoproteins in atherosclerosis. In: Feingold KR, Anawalt B, Boyce A et al (eds) Endotext. MDText.com, Inc. Copyright © 2000–2020. MDText.com, Inc., South Dartmouth
14. Borén J, Chapman MJ, Krauss RM, Packard CJ, Bentzon JF, Binder CJ, Daemen MJ, Demer LL, Hegele RA, Nicholls SJ, Nordestgaard BG, Watts GF, Bruckert E, Fazio S, Ference BA, Graham I, Horton JD, Landmesser U, Laufs U, Masana L, Pasterkamp G, Raal FJ, Ray KK, Schunkert H, Taskinen M-R, van de Sluis B, Wiklund O, Tokgozoglu L, Catapano AL, Ginsberg HN (2020) Low-density lipoproteins cause atherosclerotic cardiovascular disease: pathophysiological, genetic, and therapeutic insights: a consensus statement from the European Atherosclerosis Society Consensus Panel. Eur Heart J 41(24):

2313–2330. https://doi.org/10.1093/eurheartj/ehz962

15. Steinbrecher UP, Parthasarathy S, Leake DS, Witztum JL, Steinberg D (1984) Modification of low density lipoprotein by endothelial cells involves lipid peroxidation and degradation of low density lipoprotein phospholipids. Proc Natl Acad Sci U S A 81(12):3883–3887. https://doi.org/10.1073/pnas.81.12.3883
16. Quinn MT, Parthasarathy S, Fong LG, Steinberg D (1987) Oxidatively modified low density lipoproteins: a potential role in recruitment and retention of monocyte/macrophages during atherogenesis. Proc Natl Acad Sci U S A 84(9):2995–2998. https://doi.org/10.1073/pnas.84.9.2995
17. Steinberg D (2005) Thematic review series: the pathogenesis of atherosclerosis: an interpretive history of the cholesterol controversy, part III: mechanistically defining the role of hyperlipidemia. J Lipid Res 46(10): 2037–2051. https://doi.org/10.1194/jlr.R500010-JLR200
18. Parthasarathy S, Quinn MT, Steinberg D (1988) Is oxidized low density lipoprotein involved in the recruitment and retention of monocyte/macrophages in the artery wall during the initiation of atherosclerosis? Basic Life Sci 49:375–380. https://doi.org/10.1007/978-1-4684-5568-7_58
19. Goldstein JL, Ho YK, Basu SK, Brown MS (1979) Binding site on macrophages that mediates uptake and degradation of acetylated low density lipoprotein, producing massive cholesterol deposition. Proc Natl Acad Sci U S A 76(1):333–337. https://doi.org/10.1073/pnas.76.1.333
20. Brown MS, Basu SK, Falck JR, Ho YK, Goldstein JL (1980) The scavenger cell pathway for lipoprotein degradation: specificity of the binding site that mediates the uptake of negatively-charged LDL by macrophages. J Supramol Struct 13(1):67–81. https://doi.org/10.1002/jss.400130107
21. Fogelman AM, Shechter I, Seager J, Hokom M, Child JS, Edwards PA (1980) Malondialdehyde alteration of low density lipoproteins leads to cholesteryl ester accumulation in human monocyte-macrophages. Proc Natl Acad Sci U S A 77(4):2214–2218. https://doi.org/10.1073/pnas.77.4.2214
22. Funk CD, Cyrus T (2001) 12/15-lipoxygenase, oxidative modification of LDL and atherogenesis. Trends Cardiovasc Med 11(3–4):116–124. https://doi.org/10.1016/s1050-1738(01)00096-2
23. Griendling KK, Sorescu D, Ushio-Fukai M (2000) NAD(P)H oxidase: role in cardiovascular biology and disease. Circ Res 86(5):494–501. https://doi.org/10.1161/01.res.86.5.494
24. Lu T, Parthasarathy S, Hao H, Luo M, Ahmed S, Zhu J, Luo S, Kuppusamy P, Sen CK, Verfaillie CM, Tian J, Liu Z (2010) Reactive oxygen species mediate oxidized low-density lipoprotein-induced inhibition of oct-4 expression and endothelial differentiation of bone marrow stem cells. Antioxid Redox Signal 13(12):1845–1856. https://doi.org/10.1089/ars.2010.3156
25. Santanam N, Parthasarathy S (1995) Paradoxical actions of antioxidants in the oxidation of low density lipoprotein by peroxidases. J Clin Invest 95(6):2594–2600. https://doi.org/10.1172/jci117961
26. Delporte C, Boudjeltia KZ, Noyon C, Furtmüller PG, Nuyens V, Slomianny MC, Madhoun P, Desmet JM, Raynal P, Dufour D, Koyani CN, Reyé F, Rousseau A, Vanhaeverbeek M, Ducobu J, Michalski JC, Nève J, Vanhamme L, Obinger C, Malle E, Van Antwerpen P (2014) Impact of myeloperoxidase-LDL interactions on enzyme activity and subsequent posttranslational oxidative modifications of apoB-100. J Lipid Res 55(4):747–757. https://doi.org/10.1194/jlr.M047449
27. Deevska GM, Sunkara M, Morris AJ, Nikolova-Karakashian MN (2012) Characterization of secretory sphingomyelinase activity, lipoprotein sphingolipid content and LDL aggregation in ldlr−/− mice fed on a high-fat diet. Biosci Rep 32(5):479–490. https://doi.org/10.1042/bsr20120036
28. Polacek D, Byrne RE, Scanu AM (1988) Modification of low density lipoproteins by polymorphonuclear cell elastase leads to enhanced uptake by human monocyte-derived macrophages via the low density lipoprotein receptor pathway. J Lipid Res 29(6): 797–808
29. Summerhill VI, Grechko AV, Yet SF, Sobenin IA, Orekhov AN (2019) The atherogenic role of circulating modified lipids in atherosclerosis. Int J Mol Sci 20(14):3561. https://doi.org/10.3390/ijms20143561
30. Orekhov AN, Ivanova EA, Melnichenko AA, Sobenin IA (2017) Circulating desialylated low density lipoprotein. Cor Vasa 59(2): e149–e156. https://doi.org/10.1016/j.crvasa.2016.10.003
31. Puig N, Montolio L, Camps-Renom P, Navarra L, Jiménez-Altayó F, Jiménez-Xarrié E, Sánchez-Quesada JL, Benitez S (2020) Electronegative LDL promotes inflammation and triglyceride accumulation

in macrophages. Cell 9(3):583. https://doi.org/10.3390/cells9030583

32. Ivanova EA, Bobryshev YV, Orekhov AN (2015) LDL electronegativity index: a potential novel index for predicting cardiovascular disease. Vasc Health Risk Manag 11:525–532. https://doi.org/10.2147/vhrm.S74697
33. Wagner P, Heinecke JW (1997) Copper ions promote peroxidation of low density lipoprotein lipid by binding to histidine residues of apolipoprotein B100, but they are reduced at other sites on LDL. Arterioscler Thromb Vasc Biol 17(11):3338–3346. https://doi.org/10.1161/01.ATV.17.11.3338
34. Parthasarathy S, Raghavamenon A, Garelnabi MO, Santanam N (2010) Oxidized low-density lipoprotein. Methods Mol Biol 610:403–417. https://doi.org/10.1007/978-1-60327-029-8_24
35. Fong LG, Parthasarathy S, Witztum JL, Steinberg D (1987) Nonenzymatic oxidative cleavage of peptide bonds in apoprotein B-100. J Lipid Res 28(12):1466–1477
36. Fruebis J, Parthasarathy S, Steinberg D (1992) Evidence for a concerted reaction between lipid hydroperoxides and polypeptides. Proc Natl Acad Sci U S A 89(22):10588–10592. https://doi.org/10.1073/pnas.89.22.10588
37. Van Antwerpen P, Legssyer I, Zouaoui Boudjeltia K, Babar S, Moreau P, Moguilevsky N, Vanhaeverbeek M, Ducobu J, Nève J (2006) Captopril inhibits the oxidative modification of apolipoprotein B-100 caused by myeloperoxydase in a comparative in vitro assay of angiotensin converting enzyme inhibitors. Eur J Pharmacol 537(1):31–36. https://doi.org/10.1016/j.ejphar.2006.03.022
38. Gießauf A, van Wickern B, Simat T, Steinhart H, Esterbauer H (1996) Formation of N-formylkynurenine suggests the involvement of apolipoprotein B-100 centered tryptophan radicals in the initiation of LDL lipid peroxidation. FEBS Lett 389(2):136–140. https://doi.org/10.1016/0014-5793(96)00546-7
39. Parthasarathy S, Quinn MT, Schwenke DC, Carew TE, Steinberg D (1989) Oxidative modification of beta-very low density lipoprotein. Potential role in monocyte recruitment and foam cell formation. Arteriosclerosis 9(3):398–404. https://doi.org/10.1161/01.atv.9.3.398
40. Bowry VW, Stanley KK, Stocker R (1992) High density lipoprotein is the major carrier of lipid hydroperoxides in human blood plasma from fasting donors. Proc Natl Acad Sci U S A 89(21):10316–10320. https://doi.org/10.1073/pnas.89.21.10316
41. Rijke YBd, Hessels EM, Berkel TJv (1992) Recognition sites on rat liver cells for oxidatively modified beta-very low density lipoproteins. Arterioscl Thromb 12(1):41–49. https://doi.org/10.1161/01.ATV.12.1.41
42. Bradamante S, Barenghi L, Giudici GA, Vergani C (1992) Free radicals promote modifications in plasma high-density lipoprotein: nuclear magnetic resonance analysis. Free Radic Biol Med 12(3):193–203. https://doi.org/10.1016/0891-5849(92)90027-E
43. Bonnefont-Rousselot D, Khalil A, Delattre J, Jore D, Gardès-Albert M (1997) Oxidation of human high-density lipoproteins by .OH and .OH/O(.-)2 free radicals. Radiat Res 147(6):721–728
44. Greilberger J, Jürgens G (1998) Oxidation of high-density lipoprotein HDL3 leads to exposure of apo-AI and apo-AII epitopes and to formation of aldehyde protein adducts, and influences binding of oxidized low-density lipoprotein to type I and type III collagen in vitro1. Biochem J 331(Pt 1):185–191. https://doi.org/10.1042/bj3310185
45. Bergt C, Oram JF, Heinecke JW (2003) Oxidized HDL. Arterioscler Thromb Vasc Biol 23(9):1488–1490. https://doi.org/10.1161/01.ATV.0000090570.99836.9C
46. Asztalos BF (2004) High-density lipoprotein metabolism and progression of atherosclerosis: new insights from the HDL atherosclerosis treatment study. Curr Opin Cardiol 19(4):385–391. https://doi.org/10.1097/01.hco.0000126979.41946.7e
47. Navab M, Ananthramaiah GM, Reddy ST, Van Lenten BJ, Ansell BJ, Fonarow GC, Vahabzadeh K, Hama S, Hough G, Kamranpour N, Berliner JA, Lusis AJ, Fogelman AM (2004) The oxidation hypothesis of atherogenesis: the role of oxidized phospholipids and HDL. J Lipid Res 45(6):993–1007. https://doi.org/10.1194/jlr.R400001-JLR200
48. Stojanović N, Krilov D, Herak JN (2006) Slow oxidation of high density lipoproteins as studied by EPR spectroscopy. Free Radic Res 40(2):135–140. https://doi.org/10.1080/10715760500456789
49. Malle E, Marsche G, Panzenboeck U, Sattler W (2006) Myeloperoxidase-mediated oxidation of high-density lipoproteins: fingerprints of newly recognized potential proatherogenic lipoproteins. Arch Biochem Biophys 445(2):245–255. https://doi.org/10.1016/j.abb.2005.08.008

50. Ferretti G, Bacchetti T, Nègre-Salvayre A, Salvayre R, Dousset N, Curatola G (2006) Structural modifications of HDL and functional consequences. Atherosclerosis 184(1): 1–7. https://doi.org/10.1016/j.atherosclerosis.2005.08.008
51. Kervinen K, Hörkkö S, Beltz WF, Antero Kesaniemi Y (1995) Modification of VLDL apoprotein B by acetaldehyde alters apoprotein B metabolism. Alcohol 12(3):189–194. https://doi.org/10.1016/0741-8329(94)00081-N
52. Nagano Y, Arai H, Kita T (1991) High density lipoprotein loses its effect to stimulate efflux of cholesterol from foam cells after oxidative modification. Proc Natl Acad Sci U S A 88(15):6457–6461. https://doi.org/10.1073/pnas.88.15.6457
53. Ghiselli G, Giorgini L, Gelati M, Musanti R (1992) Oxidatively modified HDLs are potent inhibitors of cholesterol biosynthesis in human skin fibroblasts. Arterioscler Thromb 12(8):929–935. https://doi.org/10.1161/01.ATV.12.8.929
54. Van Lenten BJ, Wagner AC, Nayak DP, Hama S, Navab M, Fogelman AM (2001) High-density lipoprotein loses its anti-inflammatory properties during acute influenza a infection. Circulation 103(18): 2283–2288. https://doi.org/10.1161/01.cir.103.18.2283
55. Jaouad L, Milochevitch C, Khalil A (2003) PON1 paraoxonase activity is reduced during HDL oxidation and is an indicator of HDL antioxidant capacity. Free Radic Res 37(1): 77–83. https://doi.org/10.1080/1071576021000036614
56. Shen J, Herderick E, Cornhill JF, Zsigmond E, Kim HS, Kühn H, Guevara NV, Chan L (1996) Macrophage-mediated 15-lipoxygenase expression protects against atherosclerosis development. J Clin Invest 98(10):2201–2208. https://doi.org/10.1172/jci119029
57. Harats D, Shaish A, George J, Mulkins M, Kurihara H, Levkovitz H, Sigal E (2000) Overexpression of 15-lipoxygenase in vascular endothelium accelerates early atherosclerosis in LDL receptor-deficient mice. Arterioscler Thromb Vasc Biol 20(9):2100–2105. https://doi.org/10.1161/01.ATV.20.9.2100
58. Tribble DL, Gong EL, Leeuwenburgh C, Heinecke JW, Carlson EL, Verstuyft JG, Epstein CJ (1997) Fatty streak formation in fat-fed mice expressing human copper-zinc superoxide dismutase. Arterioscl Thromb Vasc Biol 17(9):1734–1740. https://doi.org/10.1161/01.ATV.17.9.1734
59. Patel RP, Diczfalusy U, Dzeletovic S, Wilson MT, Darley-Usmar VM (1996) Formation of oxysterols during oxidation of low density lipoprotein by peroxynitrite, myoglobin, and copper. J Lipid Res 37(11):2361–2371
60. Lamb DJ, Leake DS (1994) Iron released from transferrin at acidic pH can catalyse the oxidation of low density lipoprotein. FEBS Lett 352(1):15–18. https://doi.org/10.1016/0014-5793(94)00903-1
61. Lamb DJ, Hider RC, Leake DS (1993) Hydroxypyridinones and desferrioxamine inhibit macrophage-mediated LDL oxidation by iron but not by copper. Biochem Soc Trans 21(3):234S–234S. https://doi.org/10.1042/bst021234s
62. Brennan ML, Anderson MM, Shih DM, Qu XD, Wang X, Mehta AC, Lim LL, Shi W, Hazen SL, Jacob JS, Crowley JR, Heinecke JW, Lusis AJ (2001) Increased atherosclerosis in myeloperoxidase-deficient mice. J Clin Invest 107(4):419–430. https://doi.org/10.1172/jci8797
63. McMillen TS, Heinecke JW, LeBoeuf RC (2005) Expression of human myeloperoxidase by macrophages promotes atherosclerosis in mice. Circulation 111(21):2798–2804. https://doi.org/10.1161/CIRCULATIONAHA.104.516278
64. Gieseg S, Duggan S, Gebicki JM (2000) Peroxidation of proteins before lipids in U937 cells exposed to peroxyl radicals. Biochem J 350(Pt 1):215–218
65. Parthasarathy S (1987) Oxidation of low-density lipoprotein by thiol compounds leads to its recognition by the acetyl LDL receptor. Biochim Biophys Acta 917(2): 337–340. https://doi.org/10.1016/0005-2760(87)90139-1
66. Sparrow CP, Olszewski J (1993) Cellular oxidation of low density lipoprotein is caused by thiol production in media containing transition metal ions. J Lipid Res 34(7):1219–1228
67. Frei B, Forte TM, Ames BN, Cross CE (1991) Gas phase oxidants of cigarette smoke induce lipid peroxidation and changes in lipoprotein properties in human blood plasma. Protective effects of ascorbic acid. Biochem J 277(Pt 1):133–138. https://doi.org/10.1042/bj2770133
68. Bhatnagar A (2004) Cardiovascular pathophysiology of environmental pollutants. Am J Physiol-Heart Circ Physiol 286(2): H479–H485. https://doi.org/10.1152/ajpheart.00817.2003

69. Bouloumie A, Marumo T, Lafontan M, Busse R (1999) Leptin induces oxidative stress in human endothelial cells. FASEB J 13(10): 1231–1238
70. Santanam N, Shern-Brewer R, McClatchey R, Castellano PZ, Murphy AA, Voelkel S, Parthasarathy S (1998) Estradiol as an antioxidant: incompatible with its physiological concentrations and function. J Lipid Res 39(11): 2111–2118
71. Yamamoto K, Niki E (1988) Interaction of α-tocopherol with iron: antioxidant and prooxidant effects of α-tocopherol in the oxidation of lipids in aqueous dispersions in the presence of iron. Biochim Biophys Acta 958(1):19–23. https://doi.org/10.1016/0005-2760(88)90241-X
72. Bowry VW, Ingold KU, Stocker R (1992) Vitamin E in human low-density lipoprotein. When and how this antioxidant becomes a pro-oxidant. Biochem J 288(Pt 2):341–344. https://doi.org/10.1042/bj2880341
73. Santanam N, Parthasarathy S (1995) Cellular cysteine generation does not contribute to the initiation of LDL oxidation. J Lipid Res 36(10):2203–2211
74. Graham A, Hogg N, Kalyanaraman B, O'Leary V, Darley-Usmar V, Moncada S (1993) Peroxynitrite modification of low-density lipoprotein leads to recognition by the macrophage scavenger receptor. FEBS Lett 330(2):181–185. https://doi.org/10.1016/0014-5793(93)80269-Z
75. Noguchi N, Gotoh N, Niki E (1994) Effects of ebselen and probucol on oxidative modifications of lipid and protein of low density lipoprotein induced by free radicals. Biochim Biophys Acta 1213(2):176–182. https://doi.org/10.1016/0005-2760(94)90024-8
76. Kim JG, Sabbagh F, Santanam N, Wilcox JN, Medford RM, Parthasarathy S (1997) Generation of a polyclonal antibody against lipid peroxide-modified proteins. Free Radic Biol Med 23(2):251–259. https://doi.org/10.1016/s0891-5849(96)00615-6
77. Dinis TCP, Santos CL, Almeida LM (2002) The apoprotein is the preferential target for peroxynitrite-induced LDL damage protection by dietary phenolic acids. Free Radic Res 36(5):531–543. https://doi.org/10.1080/10715760290025915
78. Heinecke JW (1997) Pathways for oxidation of low density lipoprotein by myeloperoxidase: tyrosyl radical, reactive aldehydes, hypochlorous acid and molecular chlorine. Biofactors 6(2):145–155. https://doi.org/10.1002/biof.5520060208
79. Cornicelli JA, Trivedi BK (1999) 15-lipoxygenase and its inhibition: a novel therapeutic target for vascular disease. Curr Pharm Des 5(1):11–20
80. Kühn H, Römisch I, Belkner J (2005) The role of lipoxygenase-isoforms in atherogenesis. Mol Nutr Food Res 49(11):1014–1029. https://doi.org/10.1002/mnfr.200500131
81. Benz DJ, Mol M, Ezaki M, Mori-Ito N, Zelán I, Miyanohara A, Friedmann T, Parthasarathy S, Steinberg D, Witztum JL (1995) Enhanced levels of lipoperoxides in low density lipoprotein incubated with murine fibroblast expressing high levels of human 15-lipoxygenase. J Biol Chem 270(10):5191–5197. https://doi.org/10.1074/jbc.270.10.5191
82. Qian SY, Yue GH, Tomer KB, Mason RP (2003) Identification of all classes of spin-trapped carbon-centered radicals in soybean lipoxygenase-dependent lipid peroxidations of omega-6 polyunsaturated fatty acids via LC/ESR, LC/MS, and tandem MS. Free Radic Biol Med 34(8):1017–1028. https://doi.org/10.1016/s0891-5849(03)00031-5
83. Palinski W, Rosenfeld ME, Ylä-Herttuala S, Gurtner GC, Socher SS, Butler SW, Parthasarathy S, Carew TE, Steinberg D, Witztum JL (1989) Low density lipoprotein undergoes oxidative modification in vivo. Proc Natl Acad Sci U S A 86(4):1372–1376. https://doi.org/10.1073/pnas.86.4.1372
84. Aviram M (1990) Malondialdehyde affects the physico-chemical and biological characteristics of oxidized low density lipoprotein. Atherosclerosis 84(2):141–143. https://doi.org/10.1016/0021-9150(90)90084-V
85. Lecomte E, Artur Y, Chancerelle Y, Herbeth B, Galteau MM, Jeandel C, Siest G (1993) Malondialdehyde adducts to, and fragmentation of, apolipoprotein B from human plasma. Clin Chim Acta 218(1): 39–46. https://doi.org/10.1016/0009-8981(93)90220-x
86. Requena JR, Fu MX, Ahmed MU, Jenkins AJ, Lyons TJ, Baynes JW, Thorpe SR (1997) Quantification of malondialdehyde and 4-hydroxynonenal adducts to lysine residues in native and oxidized human low-density lipoprotein. Biochem J 322(Pt 1):317–325. https://doi.org/10.1042/bj3220317
87. Lyons TJ, Li W, Wells-Knecht MC, Jokl R (1994) Toxicity of mildly modified low-density lipoproteins to cultured retinal capillary endothelial cells and pericytes. Diabetes 43(9):1090–1095. https://doi.org/10.2337/diab.43.9.1090

88. Scaccini C, Jialal I (1994) LDL modification by activated polymorphonuclear leukocytes: a cellular model of mild oxidative stress. Free Radic Biol Med 16(1):49–55. https://doi.org/10.1016/0891-5849(94)90242-9
89. Sigari F, Lee C, Witztum JL, Reaven PD (1997) Fibroblasts that overexpress 15-lipoxygenase generate bioactive and minimally modified LDL. Arterioscler Thromb Vasc Biol 17(12):3639–3645. https://doi.org/10.1161/01.ATV.17.12.3639
90. Kennedy S, Fournet-Bourguignon MP, Breugnot C, Castedo-Delrieu M, Lesage L, Reure H, Briant C, Leonce S, Vilaine JP, Vanhoutte PM (2003) Cells derived from regenerated endothelium of the porcine coronary artery contain more oxidized forms of apolipoprotein-B-100 without a modification in the uptake of oxidized LDL. J Vasc Res 40(4):389–398. https://doi.org/10.1159/000072817
91. Salonen JT, Ylä-Herttuala S, Yamamoto R, Butler S, Korpela H, Salonen R, Nyyssönen K, Palinski W, Witztum JL (1992) Autoantibody against oxidised LDL and progression of carotid atherosclerosis. Lancet (London, England) 339(8798): 883–887. https://doi.org/10.1016/0140-6736(92)90926-t
92. Palinski W, Hörkkö S, Miller E, Steinbrecher UP, Powell HC, Curtiss LK, Witztum JL (1996) Cloning of monoclonal autoantibodies to epitopes of oxidized lipoproteins from apolipoprotein E-deficient mice. demonstration of epitopes of oxidized low density lipoprotein in human plasma. J Clin Invest 98(3):800–814. https://doi.org/10.1172/jci118853
93. Barros MRAC, Bertolami MC, Abdalla DSP, Ferreira WP (2006) Identification of mildly oxidized low-density lipoprotein (electronegative LDL) and its auto-antibodies IgG in children and adolescents hypercholesterolemic offsprings. Atherosclerosis 184(1): 103–107. https://doi.org/10.1016/j.atherosclerosis.2004.11.027
94. Salmon S, Maziere C, Theron L, Beucler I, Ayrault-Jarrier M, Goldstein S, Polonovski J (1987) Immunological detection of low-density lipoproteins modified by malondialdehyde in vitro or in vivo. Biochim Biophys Acta 920(3):215–220. https://doi.org/10.1016/0005-2760(87)90097-X
95. Parums DV, Brown DL, Mitchinson MJ (1990) Serum antibodies to oxidized low-density lipoprotein and ceroid in chronic periaortitis. Arch Pathol Lab Med 114(4): 383–387
96. Virella G, Virella I, Leman RB, Pryor MB, Lopes-Virella MF (1993) Anti-oxidized low--density lipoprotein antibodies in patients with coronary heart disease and normal healthy volunteers. Int J Clin Lab Res 23(1): 95–101. https://doi.org/10.1007/BF02592290
97. Holvoet P, Perez G, Zhao Z, Brouwers E, Bernar H, Collen D (1995) Malondialdehyde-modified low density lipoproteins in patients with atherosclerotic disease. J Clin Invest 95(6):2611–2619. https://doi.org/10.1172/jci117963
98. Festa A, Kopp HP, Schernthaner G, Menzel EJ (1998) Autoantibodies to oxidised low density lipoproteins in IDDM are inversely related to metabolic control and microvascular complications. Diabetologia 41(3): 350–356. https://doi.org/10.1007/s001250050914
99. Lehtimäki T, Lehtinen S, Solakivi T, Nikkilä M, Jaakkola O, Jokela H, Ylä-Herttuala S, Luoma JS, Koivula T, Nikkari T (1999) Autoantibodies against oxidized low density lipoprotein in patients with angiographically verified coronary artery disease. Arterioscler Thromb Vasc Biol 19(1):23–27. https://doi.org/10.1161/01.ATV.19.1.23
100. Frostegård J, Wu R, Lemne C, Thulin T, Witztum JL, de Faire U (2003) Circulating oxidized low-density lipoprotein is increased in hypertension. Clin Sci (Lond) 105(5): 615–620. https://doi.org/10.1042/cs20030152
101. Herrick AL, Illingworth KJ, Hollis S, Gomez-Zumaquero JM, Tinahones FJ (2001) Antibodies against oxidized low-density lipoproteins in systemic sclerosis. Rheumatology 40(4):401–405. https://doi.org/10.1093/rheumatology/40.4.401
102. Tanaga K, Bujo H, Inoue M, Mikami K, Kotani K, Takahashi K, Kanno T, Saito Y (2002) Increased circulating malondialdehyde-modified LDL levels in patients with coronary artery diseases and their association with peak sizes of LDL particles. Arterioscler Thromb Vasc Biol 22(4): 662–666. https://doi.org/10.1161/01.atv.0000012351.63938.84
103. Meraviglia MV, Maggi E, Bellomo G, Cursi M, Fanelli G, Minicucci F (2002) Autoantibodies against oxidatively modified lipoproteins and progression of carotid restenosis after carotid endarterectomy. Stroke 33(4): 1139–1141. https://doi.org/10.1161/01.STR.0000014420.15948.2E
104. Hsu RM, Devaraj S, Jialal I (2002) Autoantibodies to oxidized low-density lipoprotein in

patients with type 2 diabetes mellitus. Clin Chim Acta 317(1):145–150. https://doi.org/10.1016/S0009-8981(01)00767-7

105. Tsimikas S, Bergmark C, Beyer RW, Patel R, Pattison J, Miller E, Juliano J, Witztum JL (2003) Temporal increases in plasma markers of oxidized low-density lipoprotein strongly reflect the presence of acute coronary syndromes. J Am Coll Cardiol 41(3):360–370. https://doi.org/10.1016/s0735-1097(02)02769-9
106. Wang J, Qiang H, Zhang C, Liu X, Chen D, Wang S (2003) Detection of IgG-bound lipoprotein(a) immune complexes in patients with coronary heart disease. Clin Chim Acta 327(1):115–122. https://doi.org/10.1016/S0009-8981(02)00342-X
107. Koskenmies S, Vaarala O, Widen E, Kere J, Palosuo T, Julkunen H (2004) The association of antibodies to cardiolipin, beta 2-glycoprotein I, prothrombin, and oxidized low-density lipoprotein with thrombosis in 292 patients with familial and sporadic systemic lupus erythematosus. Scand J Rheumatol 33(4):246–252. https://doi.org/10.1080/03009740410005386
108. Luoma JS, Kareinen A, Närvänen O, Viitanen L, Laakso M, Ylä-Herttuala S (2005) Autoantibodies against oxidized LDL are associated with severe chest pain attacks in patients with coronary heart disease. Free Radic Biol Med 39(12):1660–1665. https://doi.org/10.1016/j.freeradbiomed.2005.08.007
109. Yamaguchi Y, Yoshikawa N, Kagota S, Nakamura K, Haginaka J, Kunitomo M (2006) Elevated circulating levels of markers of oxidative-nitrative stress and inflammation in a genetic rat model of metabolic syndrome. Nitric Oxide 15(4):380–386. https://doi.org/10.1016/j.niox.2006.04.264
110. Kim JG, Taylor WR, Parthasarathy S (1999) Demonstration of the presence of lipid peroxide-modified proteins in human atherosclerotic lesions using a novel lipid peroxide-modified anti-peptide antibody. Atherosclerosis 143(2):335–340. https://doi.org/10.1016/S0021-9150(98)00320-7
111. Wall SB, Oh JY, Diers AR, Landar A (2012) Oxidative modification of proteins: an emerging mechanism of cell signaling. Front Physiol 3:369. https://doi.org/10.3389/fphys.2012.00369
112. Esterbauer H, Striegl G, Puhl H, Rotheneder M (1989) Continuous monitoring of in vitro oxidation of human low density lipoprotein. Free Radic Res Commun 6(1):67–75. https://doi.org/10.3109/10715768909073429
113. Moore K, Roberts LJ 2nd (1998) Measurement of lipid peroxidation. Free Radic Res 28(6):659–671. https://doi.org/10.3109/10715769809065821
114. Moore KP, Darley-Usmar V, Morrow J, Roberts LJ (1995) Formation of F_2-isoprostanes during oxidation of human low-density lipoprotein and plasma by peroxynitrite. Circ Res 77(2):335–341. https://doi.org/10.1161/01.RES.77.2.335
115. Gugliucci Creriche A, Stahl AJ (1993) Glycation and oxidation of human low density lipoproteins reduces heparin binding and modifies charge. Scand J Clin Lab Invest 53(2):125–132. https://doi.org/10.3109/00365519309088399
116. Sánchez-Quesada JL, Pérez A, Caixàs A, Ordónmez-Llanos J, Carreras G, Payés A, González-Sastre F, de Leiva A (1996) Electronegative low density lipoprotein subform is increased in patients with short-duration IDDM and is closely related to glycaemic control. Diabetologia 39(12):1469–1476. https://doi.org/10.1007/s001250050600
117. Demuth K, Myara I, Chappey B, Vedie B, Pech-Amsellem MA, Haberland ME, Moatti N (1996) A cytotoxic electronegative LDL subfraction is present in human plasma. Arterioscler Thromb Vasc Biol 16(6):773–783. https://doi.org/10.1161/01.atv.16.6.773
118. Dai L, Zhang Z, Winyard PG, Gaffney K, Jones H, Blake DR, Morris CJ (1997) A modified form of low-density lipoprotein with increased electronegative charge is present in rheumatoid arthritis synovial fluid. Free Radic Biol Med 22(4):705–710. https://doi.org/10.1016/s0891-5849(96)00389-9
119. Moro E, Zambon C, Pianetti S, Cazzolato G, Pais M, Bittolo Bon G (1998) Electronegative low density lipoprotein subform (LDL-) is increased in type 2 (non-insulin-dependent) microalbuminuric diabetic patients and is closely associated with LDL susceptibility to oxidation. Acta Diabetol 35(3):161–164. https://doi.org/10.1007/s005920050123
120. Sánchez-Quesada JL, Camacho M, Antón R, Benítez S, Vila L, Ordóñez-Llanos J (2003) Electronegative LDL of FH subjects: chemical characterization and induction of chemokine release from human endothelial cells. Atherosclerosis 166(2):261–270. https://doi.org/10.1016/s0021-9150(02)00374-x
121. Parasassi T, Bittolo-Bon G, Brunelli R, Cazzolato G, Krasnowska EK, Mei G, Sevanian A, Ursini F (2001) Loss of apoB-100 secondary structure and conformation in hydroperoxide rich, electronegative LDL(−).

Free Radic Biol Med 31(1):82–89. https://doi.org/10.1016/s0891-5849(01)00555-x

122. Aluganti Narasimhulu C, Selvarajan K, Brown M, Parthasarathy S (2014) Cationic peptides neutralize ox-LDL, prevent its uptake by macrophages, and attenuate inflammatory response. Atherosclerosis 236(1): 133–141. https://doi.org/10.1016/j.atherosclerosis.2014.06.020
123. Chandrakala AN, Sukul D, Selvarajan K, Sai-Sudhakar C, Sun B, Parthasarathy S (2012) Induction of brain natriuretic peptide and monocyte chemotactic protein-1 gene expression by oxidized low-density lipoprotein: relevance to ischemic heart failure. Am J Physiol Cell Physiol 302(1):C165–C177. https://doi.org/10.1152/ajpcell.00116.2011
124. Selvarajan K, Narasimhulu CA, Bapputty R, Parthasarathy S (2015) Anti-inflammatory and antioxidant activities of the nonlipid (aqueous) components of sesame oil: potential use in atherosclerosis. J Med Food 18(4): 393–402. https://doi.org/10.1089/jmf.2014.0139
125. Selvarajan K, Moldovan L, Chandrakala AN, Litvinov D, Parthasarathy S (2011) Peritoneal macrophages are distinct from monocytes and adherent macrophages. Atherosclerosis 219(2):475–483. https://doi.org/10.1016/j.atherosclerosis.2011.09.014
126. Aluganti Narasimhulu C, Burge KY, Doomra M, Riad A, Parthasarathy S (2018) Primary prevention of atherosclerosis by pretreatment of low-density lipoprotein receptor knockout mice with sesame oil and its aqueous components. Sci Rep 8(1):12270. https://doi.org/10.1038/s41598-018-29849-x
127. Deme P, Aluganti Narasimhulu C, Parthasarathy S (2019) Evaluation of anti-inflammatory properties of herbal aqueous extracts and their chemical characterization. J Med Food 22(8):861–873. https://doi.org/10.1089/jmf.2019.0009
128. Barrett R, Narasimhulu CA, Parthasarathy S (2018) Adrenergic hormones induce extrapituitary prolactin gene expression in leukocytes-potential implications in obesity. Sci Rep 8(1):1936. https://doi.org/10.1038/s41598-018-20378-1
129. Sengupta B, Narasimhulu CA, Parthasarathy S (2013) Novel technique for generating macrophage foam cells for in vitro reverse cholesterol transport studies. J Lipid Res 54(12):3358–3372. https://doi.org/10.1194/jlr.M041327
130. Fernandez-Ruiz I, Puchalska P, Narasimhulu CA, Sengupta B, Parthasarathy S (2016) Differential lipid metabolism in monocytes and macrophages: influence of cholesterol loading. J Lipid Res 57(4):574–586. https://doi.org/10.1194/jlr.M062752
131. Narasimhulu CA, Vardhan S (2015) Therapeutic potential of ocimum tenuiflorum as MPO inhibitor with implications for atherosclerosis prevention. J Med Food 18(5): 507–515. https://doi.org/10.1089/jmf.2014.0125
132. Tien M (1999) Myeloperoxidase-catalyzed oxidation of tyrosine. Arch Biochem Biophys 367(1):61–66. https://doi.org/10.1006/abbi.1999.1226
133. Vlasova II, Sokolov AV, Arnhold J (2012) The free amino acid tyrosine enhances the chlorinating activity of human myeloperoxidase. J Inorg Biochem 106(1):76–83. https://doi.org/10.1016/j.jinorgbio.2011.09.018
134. Aluganti Narasimhulu C, Litvinov D, Sengupta B, Jones D, Sai-Sudhakar C, Firstenberg M, Sun B, Parthasarathy S (2016) Increased presence of oxidized low-density lipoprotein in the left ventricular blood of subjects with cardiovascular disease. Physiol Rep 4(6):e12726. https://doi.org/10.14814/phy2.12726

Chapter 14

Monitoring Modified Lipoprotein Uptake and Macropinocytosis Associated with Macrophage Foam Cell Formation

Alaa Alahmadi and Dipak P. Ramji

Abstract

Macrophage foam cell formation plays a crucial role in the initiation and progression of atherosclerosis. Macrophages uptake native and modified low density lipoprotein (LDL) through either receptor-dependent or receptor-independent mechanisms to transform into lipid laden foam cells. Foam cells are involved in the formation of fatty streak that is seen during the early stages of atherosclerosis development and therefore represents a promising therapeutic target. Normal or modified lipoproteins labeled with fluorescent dyes such as 1,1′-dioctadecyl-3-3-3′,3′-tetramethylindocarbocyanine perchlorate (Dil) are often used to monitor their internalization during foam cell formation. In addition, the fluorescent dye Lucifer Yellow (LY) is widely used as a marker for macropinocytosis activity. In this chapter, we describe established methods for monitoring modified lipoprotein uptake and macropinocytosis during macrophage foam cell formation.

Key words Foam cells, LDL, 1′-Dioctadecyl-3-3-3′,3′-tetramethylindocarbocyanine perchlorate dye (Dil), Lucifer Yellow, Macropinocytosis

1 Introduction

Deregulated cholesterol homeostasis in macrophages plays an important role in the initiation of atherosclerotic lesions. The imbalance of cholesterol influx and cholesterol efflux leads to excessive intracellular cholesterol accumulation in macrophages and therefore their transformation into foam cells [1]. In addition to macrophages, endothelial cells (ECs) and, particularly, vascular smooth muscle cells (VSMCs) can transform into foam cells [2]. These foam cells contribute to all stages of atherosclerosis. In the early stages, they initiate disease progression while in late stage, they release matrix-metalloproteinase enzymes (MMPs) that promote plaque rupture [2, 3]. Apoptosis and necrosis of foam cells leads to the formation of a lipid-rich necrotic core that

Dipak P. Ramji (ed.), *Atherosclerosis: Methods and Protocols*, Methods in Molecular Biology, vol. 2419,
https://doi.org/10.1007/978-1-0716-1924-7_14,
© The Author(s), under exclusive license to Springer Science+Business Media, LLC, part of Springer Nature 2022

subsequently activates the inflammasome pathway and causes a state of chronic inflammation that is associated with atherosclerosis [4].

In vitro assays using cultured macrophages and smooth muscle cells are often used to monitor cholesterol uptake either by receptor-mediated endocytosis or non–receptor-mediated endocytosis such as macropinocytosis. Such assays typically follow the uptake of a fluorescent tag, such as 1,1′-dioctadecyl-3-3-3′,3′-tetramethylindocarbocyanine perchlorate (Dil)-labeled oxidized LDL (Dil-oxLDL) and Lucifer Yellow (LY) [5–9].

1.1 OxLDL Uptake

Dil is a fluorescent lipophilic stain that has the ability to diffuse into the LDL particles, in particular the hydrophobic part, without affecting the binding capability of LDL to its apolipoprotein B or cognate cell surface receptors [10, 11]. Dil-oxLDL molecules are recognized by scavenger receptors (SRs), such as SR-A and cluster of differentiation 36 (CD36), that are expressed at high levels on the surface of macrophages and smooth muscle cells (SMCs) (Fig. 1). As a result of uncontrolled oxLDL internalization via such SRs, macrophages and SMCs transform into foam cells [1, 6, 12]. The labeling of oxLDL with Dil aids the visualization and quantification of internalized oxLDL [6]. In addition to oxLDL, other forms of modified LDL and other lipoproteins are extensively used in atherosclerosis research to monitor cholesterol uptake such as Dil-HDL, Dil-LDL, and Dil-acetylated LDL (Dil-acLDL).

1.2 Macropinocytosis

In addition to scavenger receptors, macrophages uptake a significant amount of LDL (native and modified) by receptor-independent processes, such as macropinocytosis (Fig. 1), which also contributes to foam cell formation [13]. Macropinocytosis is an actin-dependent fluid phase process in which the plasma membrane of cells ruffles and engulfs lipids and other solutes in the surrounding environment in fluid-filled intracellular vacuoles called macropinosomes. The fluorescent and nonfluorescent fluid-phase tracers such as LY, Dil-LDL, cholesterol crystal, and horseradish peroxidase (HRP) are often used in research to monitor macropinocytosis [7, 13–16]. Inhibitors, such as actin polymerization inhibitor cytochalasin D, and those against the phosphoinositide 3-kinase (PI3K) pathways are often used to distinguish macropinocytosis from other forms of uptake [17, 18]. LY is most extensively employed because of the ability of monitoring cells that have taken up the dye in real time [19]. The macropinosomes can efficiently engulf and internalize LY from the surrounding environment. LY is not toxic to the cells and it is not affected by changes in pH. Moreover, it does not adsorb to macrophage surface but accumulates inside with its concentration reflecting that in the surrounding medium [20]. Consequently, measuring the

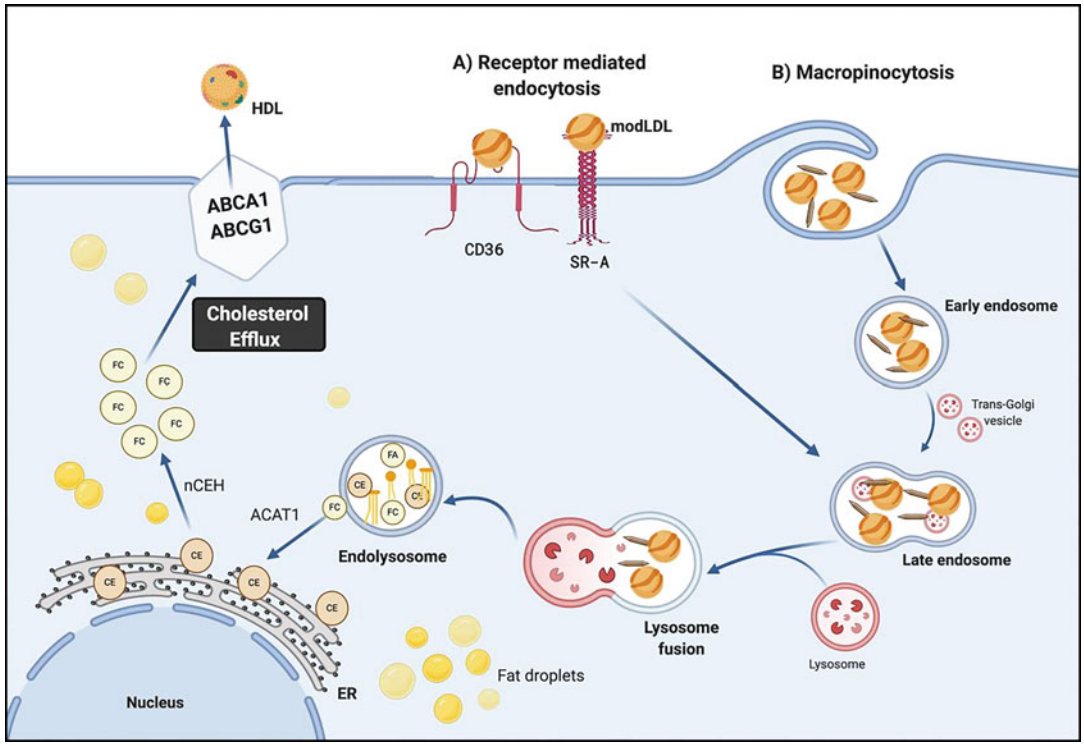

Fig. 1 An overview of processes involved in modified lipoprotein uptake by macrophages. In receptor-mediated endocytosis A), macrophages uptake modified LDL (modLDL), such as oxidized LDL, by their scavenger receptors SR-A and CD36. In addition, macrophages engulf large amount of modified LDL, unmodified LDL, and cholesterol crystals by non–receptor-mediated endocytosis processes such as macropinocytosis B). During this process, actin-mediated protrusions of the plasma membrane ruffles fold back and form cup-shaped ruffles. This leads to the internalization of the surrounding contents in fluid-filled intracellular vacuoles (macropinosomes). Early endosome (macropinosomes) then maturates to late endosome through its fusions with *trans*-Golgi vesicles. Late endosome then fuses with lysosome and lysosome–endosome hybrid is formed. Due to high acidity and presence of lysosomal acid lipase (LAL) in the lysosomes, the cholesterol ester (CE) part in LDL is digested into free fatty acids (FA) and free cholesterol (FC). Finally, the FAs are transported to the mitochondria where they are oxidized to generate energy for the cell and FC is moved to the endoplasmic reticulum (ER) where it is esterified to CE by acyl coenzyme A: cholesterol acyltransferase (ACAT1/ACAT2). The CE is then either stored as lipid droplet or digested to FC by neutral cholesteryl ester hydrolases (nCEH) to FC for efflux from macrophage through ATP-binding cassette transporters. *CE* cholesterol ester, *FA* fatty acid, *nCEH* neutral cholesteryl ester hydrolases, *ACAT1* acyl coenzyme A: cholesterol acyltransferase, *ABCA1 and ABCG1* ATP-binding cassette (ABC) transporters A1 and G1. (Image created with BioRender.com)

fluorescent signals of LY in cells can be used as an indicator for the level of macropinocytosis [21–23].

Together, oxLDL uptake by scavenger receptors and macropinocytosis are important pathways during foam cell formation and their inhibition is a promising therapeutic target for atherosclerosis.

2 Materials

Autoclave glassware for 20–30 min at 121 °C (975 kPa). Prepare and store all reagents at room temperature, unless stated otherwise.

2.1 General Reagents and Equipment for oxLDL Uptake and Macropinocytosis Assays

1. Cultured model cells (e.g., human THP-1 macrophages, mouse RAW264.7 cell line, human monocyte-derived macrophages [HMDM], mouse peritoneal macrophages, bone marrow-derived macrophages [BMDM], vascular smooth muscle cells [VSMCs]) (*see* **Note 1**).
2. Cell culture incubator.
3. Hemocytometer.
4. 12-well clear and flat-bottom cell culture plates.
5. Phosphate buffered saline (PBS): 137 mM NaCl, 2.7 mM KCl, 8 mM Na_2HPO_4, 2 mM KH_2PO_4, pH 7.4.
6. 0.2% (w/v) fatty acid–free bovine serum albumin (BSA) medium: 1 g BSA, 500 mL RPMI-1640 Medium with L-glutamine and sodium bicarbonate (*see* **Note 2**).
7. 2% Paraformaldehyde (PFA) solution: 2 g paraformaldehyde (PFA), 2 M sodium hydroxide, 50 mL PBS (*see* **Note 3**).
8. 0.05% (w/v) trypsin–EDTA or cell scrapers for cell detachment (*see* **Note 4**).
9. Roswell Park Memorial Institute Medium (RPMI)-1640 with L-glutamine supplemented with 10% (v/v) HI-FCS (56 °C, 30 min).
10. Microcentrifuge.
11. BD FACSCanto™ flow cytometry system or BD LSRFortessa™ cell analyzer or suitable flow cytometer.
12. 5 mL round bottom polystyrene tubes.
13. 1.5 mL safe lock microcentrifuge tubes.

2.2 Reagents for oxLDL Uptake Assay

1. Dil-oxLDL working solution: 5 μg/mL Dil-oxLDL, 0.2% (w/v) fatty acid–free BSA medium (*see* **Note 5**).

2.3 Reagents for Macropinocytosis

1. 100 μg/mL LY in 0.2% (w/v) fatty acid–free BSA medium (*see* **Notes 6–8**).

3 Methods

Conduct all procedures at room temperature and under sterile conditions, unless specified otherwise (*see* **Note 9**).

3.1 OxLDL Uptake Assay

1. Count the number of cells (e.g., THP-1 macrophages, HMDM, BMDM) using a hemocytometer and seed them in a 12-well clear and flat-bottom cell culture plate in 0.2% (w/v) fatty acid–free BSA medium (*see* **Note 1**).
2. Add 1000 μL of Dil-oxLDL working solution to the desired wells. Add 1000 μL of 0.2% (w/v) fatty acid–free BSA media to a control well for determination of background values (*see* **Note 10**).
3. Incubate the treated cells for 24 h or as required at 37 °C in a cell culture incubator with 5% (v/v) CO_2 (*see* **Note 11**).
4. Aspirate the media and carefully wash the cells with 1000 μL of PBS.
5. Detach the cells from the plate by incubating them with 1 mL of 0.05% trypsin–EDTA for 10 min at 37 °C and then deactivating the trypsin enzyme by adding 2 mL of RPMI-1640 medium with L-glutamine, supplemented with 10% (v/v) HI-FCS (*see* **Note 12**).
6. Mix well and then collect the cell suspension in 1.5 mL microcentrifuge tube.
7. Pellet the cells by centrifugation using the microcentrifuge at 9000 × *g* for 5 min.
8. Resuspend the pellet in 500 μL of 2% PFA solution.
9. Quantify Dil-oxLDL uptake by using flow cytometer according to the instructions of the model used. Count at least 10,000 events for each sample (*see* Fig. 2).

3.2 Lucifer Yellow–Based Macropinocytosis Assay

1. Count the cells (e.g., THP-1 macrophages, HMDM, BMDM) and plate them at a desired density (2.5×10^5 cells/cm^2 is typically used) in a 12-well clear and flat-bottom cell culture plate in 0.2% (w/v) fatty acid–free BSA medium (*see* **Note 1**).
2. Add 1000 μL of 100 μg/mL LY in 0.2% (w/v) fatty acid–free BSA medium to the desired wells. Add 1000 μL of 0.2% (w/v) fatty acid–free BSA media to a control well for determination of background values (*see* **Note 10**).
3. Incubate the plate for 24 h or as required at 37 °C in a cell culture incubator with 5% (v/v) CO_2 (*see* **Note 11**).
4. Remove the overlying media and wash cells with 1000 μL of PBS.
5. Detach the cells from the plate by incubating them with 1 mL of 0.05% trypsin–EDTA for 10 min at 37 °C and then deactivating the trypsin enzyme by adding 2 mL of RPMI-1640 medium with L-glutamine, supplemented with 10% (v/v) HI-FCS (*see* **Note 12**).

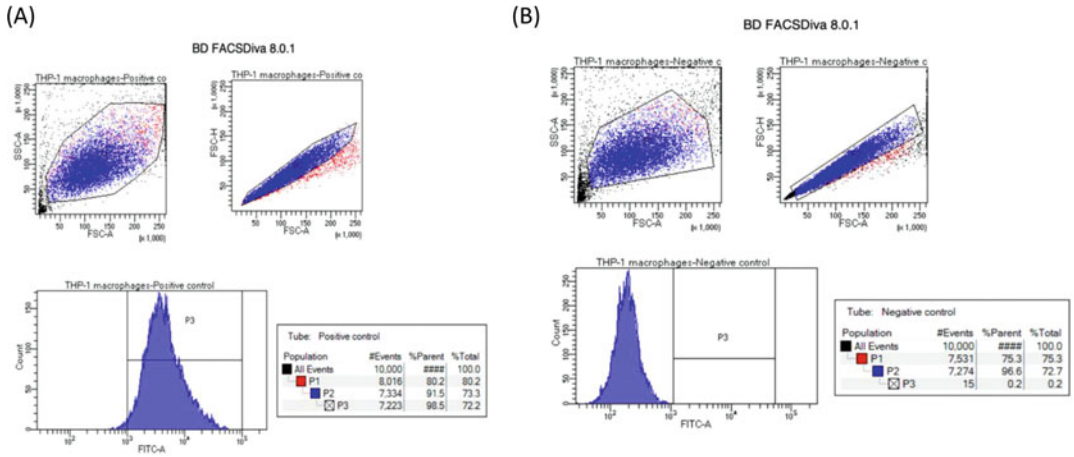

Fig. 2 Example of sequential gating strategy for experimental negative and positive controls. The figure shows an example for FACS gating strategy for macropinocytosis assay. Panel **(A)** represents macrophages that were treated with LY for 24 h (positive staining control) while panel **(B)** represents macrophages that were not treated with LY (negative control). The first plot (Dot plot) in the figures (**A**, **B**) shows cells that have passed through the laser. Macrophages are then gated, and debris are excluded with the help of forward scatter (FSC-A) and side scatter (SSC-A). The FSC-A allows determination of the cell size while SSC-A reflects cell granularity (P1). From the first plot (P1), single cells are gated in order to exclude doublets (P2). From the single cell dot plot (P2), a histogram plot is chosen to evaluate the amount of labeled reagent that has been internalized by macrophages (P3), in this case FITC fluorochrome (LY-FITC). A positive control (**A**) shown on the left has a high count of events/cells expressing at high fluorescence intensity, while the negative control (**B**) shown on the right has no cells expressing any fluorescence

6. Mix vigorously and then transfer the suspension to 1.5 mL microcentrifuge tube.
7. Centrifuge the suspension using a microcentrifuge at 9000 × *g* for 5 min.
8. Resuspend the resulting pellet in 500 μL of 2% (w/v) PFA.
9. Quantify LY uptake by using flow cytometer according to the instructions of the model used. Count at least 10,000 events for each sample (*see* Fig. 2).

4 Notes

1. Various cell types can be used, such as THP-1 macrophages (2.5×10^5 cells/cm^2), BMDM (3.75×10^5 cells/cm^2), HMDM (3.75×10^5 cells/cm^2), mouse macrophage cell lines such as RAW264.7 (2.5×10^5 cells/cm^2) and J774A.1 (2.5×10^5 cells/cm^2) and VSMCs (2.4×10^4 cells/cm^2).
2. Store solution at 4 °C and warm it at 37 °C before use. During all the steps in these two assays, you have to use serum–free media (0.2% (w/v) fatty acid–free BSA media is frequently

used) due to the ability of serum to stimulate cholesterol efflux which subsequently affects the assay accuracy.

3. Store solution at 4 °C and it is better to use this cold.
4. You can purchase 0.05% trypsin–EDTA from commercial sources or use a cell scrapper to detach the cells from the tissue culture plate.
5. You can purchase DiI-OxLDL from commercial suppliers or prepare it using published protocols [24, 25].
6. Lucifer Yellow CH dilithium salt comes as a powder and should be dissolved in dH_2O first before diluting in 0.2% (w/v) fatty acid–free BSA media for use in the assay.
7. You can also use other macropinocytosis tracers such as DiI-LDL (10–50 μg/mL) and horseradish peroxidase (HRP) (1 mg/mL). These concentrations are commonly employed in the literature.
8. Inhibitors such as LY294002 (100 μM), wortmannin (250 nM), amiloride (0.5 mM), and cytochalasin D (2.5, 5, and 10 μM) [16, 17, 26] are frequently used in the literature to determine uptake by macropinocytosis compared to other processes.
9. Do at least three independent experiments for statistical analysis and each experiment should be performed in duplicate or triplicate.
10. When investigating the actions of specific agents on these processes, you can add the desired compounds at the time of adding Dil/LY or before (e.g., 24 h; pretreatment). In addition, you can add inhibitors just 1 h before adding your agent.
11. Incubation for 24 h is the most common used in the literature. However, 4, 6, 12, and 36 h have also been used [24, 27–29].
12. Cell scrapers can also be used to detach the cells instead of trypsin-EDTA by adding 1 mL of PBS and scraping the cells.

Acknowledgments

We thank the British Heart Foundation for financial support (grants PG/16/25/32097 and FS/17/75/33257). AA received PhD studentship from the Kingdom of Saudi Arabia (Jeddah University).

References

1. McLaren JE, Michael DR, Ashlin TG, Ramji DP (2011) Cytokines, macrophage lipid metabolism and foam cells: implications for cardiovascular disease therapy. Prog Lipid Res 50(4):331–347. https://doi.org/10.1016/j.plipres.2011.04.002

2. Chistiakov DA, Melnichenko AA, Myasoedova VA, Grechko AV, Orekhov AN (2017) Mechanisms of foam cell formation in atherosclerosis. J Mol Med 95(11):1153–1165. https://doi.org/10.1007/s00109-017-1575-8
3. Chu EM, Tai DC, Beer JL, Hill JS (2013) Macrophage heterogeneity and cholesterol homeostasis: classically-activated macrophages are associated with reduced cholesterol accumulation following treatment with oxidized LDL. Biochim Biophys Acta 1831(2): 378–386. https://doi.org/10.1016/j.bbalip.2012.10.009
4. Shah PK (2019) Inflammation, infection and atherosclerosis. Trends Cardiovasc Med 29(8): 468–472. https://doi.org/10.1016/j.tcm.2019.01.004
5. Ooi BK, Ahemad N, Yap WH (2019) A reliable and reproducible assay for determining the effect of natural product on macrophages lipid uptake and cholesterol efflux: a case study of maslinic acid. Prog Drug Discov Biomed Sci 2(1):a0000031
6. Xia F, Li R, Wang C, Yang S, Tian L, Dong H, Pei C, He S, Jiang P, Cheng H (2013) IRGM1 regulates oxidized LDL uptake by macrophage via actin-dependent receptor internalization during atherosclerosis. Sci Rep 3(1):1–6
7. Michael DR, Davies TS, Laubertová L, Gallagher H, Ramji DP (2015) The phosphoinositide 3-kinase signaling pathway is involved in the control of modified low-density lipoprotein uptake by human macrophages. Lipids 50(3):253–260
8. Ding L, Zhang L, Kim M, Byzova T, Podrez E (2017) Akt3 kinase suppresses pinocytosis of low-density lipoprotein by macrophages via a novel WNK/SGK1/Cdc42 protein pathway. J Biol Chem 292(22):9283–9293
9. Fan J, Liu L, Liu Q, Cui Y, Yao B, Zhang M, Gao Y, Fu Y, Dai H, Pan J (2019) CKIP-1 limits foam cell formation and inhibits atherosclerosis by promoting degradation of Oct-1 by REGγ. Nat Commun 10(1):1–14
10. Raniolo S, Vindigni G, Biocca S (2016) Cholesterol level regulates lectin-like oxidized low-density lipoprotein receptor-1 function. Biomed Spectrosc Imaging 5(s1):S87–S99
11. Gu L, Wang Y, Xu Y, Tian Q, Lei G, Zhao C, Gao Z, Pan Q, Zhao W, Nong L (2017) Lunasin functionally enhances LDL uptake via inhibiting PCSK9 and enhancing LDLR expression in vitro and in vivo. Oncotarget 8(46):80826
12. Chistiakov DA, Bobryshev YV, Orekhov AN (2016) Macrophage-mediated cholesterol handling in atherosclerosis. J Cell Mol Med 20(1):17–28
13. Kruth HS (2011) Receptor-independent fluid-phase pinocytosis mechanisms for induction of foam cell formation with native LDL particles. Cur Opin Lipidol 22(5):386
14. Bederska M, Borucki W, Znojek E (2012) Movement of fluorescent dyes Lucifer yellow (LYCH) and carboxyfluorescein (CF) in Medicago truncatula Gaertn roots and root nodules. Symbiosis 58(1):183–190
15. Kruth HS (2013) Fluid-phase pinocytosis of LDL by macrophages: a novel target to reduce macrophage cholesterol accumulation in atherosclerotic lesions. Curr Pharm Des 19(33): 5865–5872
16. Anzinger J, Chang J, Xu Q, Buono C, Li Y, Leyva F, Park B-C, Greene L, Kruth H (2010) Native low-density lipoprotein uptake by macrophage colony-stimulating factor-differentiated human macrophages is mediated by macropinocytosis and micropinocytosis. Arterioscler Thromb Vasc Biol 30(10):2022–2031
17. Michael DR, Ashlin TG, Davies CS, Gallagher H, Stoneman TW, Buckley ML, Ramji DP (2013) Differential regulation of macropinocytosis in macrophages by cytokines: implications for foam cell formation and atherosclerosis. Cytokine 64(1):357–361
18. Barthwal MK, Anzinger JJ, Xu Q, Bohnacker T, Wymann MP, Kruth HS (2013) Fluid-phase pinocytosis of native low density lipoprotein promotes murine M-CSF differentiated macrophage foam cell formation. PLoS One 8(3):e58054
19. Hanani M (2012) Lucifer yellow—an angel rather than the devil. J Cell Mol Med 16(1): 22–31
20. Swanson J, Silverstein SC (1988) Pinocytic flow through macrophages. In: Pernis B, Silverstein SC, Vogel H (eds) Processing and presentation of antigens. Academic, San Diego, pp 15–27
21. Colin M, Delporte C, Janky RS, Lechon A-S, Renard G, Van Antwerpen P, Maltese WA, Mathieu V (2019) Dysregulation of macropinocytosis processes in glioblastomas may be exploited to increase intracellular anti-cancer drug levels: the example of temozolomide. Cancers 11(3):411
22. Gong X, Sun R, Gao Z, Han W, Liu Y, Zhao L, Jing L, Yao X, Sun X (2018) Tubeimoside 1 acts as a chemotherapeutic synergist via stimulating macropinocytosis. Front Pharmacol 9:1044
23. Basrai MA, Naider F, Becker JM (1990) Internalization of lucifer yellow in Candida albicans

by fluid phase endocytosis. Microbiology 136(6):1059–1065

24. Xu S, Huang Y, Xie Y, Lan T, Le K, Chen J, Chen S, Gao S, Xu X, Shen X (2010) Evaluation of foam cell formation in cultured macrophages: an improved method with oil red O staining and DiI-oxLDL uptake. Cytotechnology 62(5):473–481
25. Cheng X, Zhang D-L, Li X-B, Ye J-T, Shi L, Huang Z-S, Gu L-Q, An L-K (2014) Syntheses of diacyltanshinol derivatives and their suppressive effects on macrophage foam cell formation by reducing oxidized LDL uptake. Bioorg Chem 52:24–30
26. Collins RF, Touret N, Kuwata H, Tandon NN, Grinstein S, Trimble WS (2009) Uptake of oxidized low density lipoprotein by CD36 occurs by an actin-dependent pathway distinct from macropinocytosis. J Biol Chem 284(44): 30288–30297
27. Lara-Guzmán OJ, Gil-Izquierdo Á, Medina S, Osorio E, Álvarez-Quintero R, Zuluaga N, Oger C, Galano J-M, Durand T, Muñoz-Durango K (2018) Oxidized LDL triggers changes in oxidative stress and inflammatory biomarkers in human macrophages. Redox Biol 15: 1–11
28. Yang H, Chen S, Tang Y, Dai Y (2011) Interleukin-10 down-regulates oxLDL induced expression of scavenger receptor a and Bak-1 in macrophages derived from THP-1 cells. Arch Biochem Biophys 512(1): 30–37
29. Gu H-F, Li H-Z, Tang Y-L, Tang X-Q, Zheng X-L, Liao D-F (2016) Nicotinate-curcumin impedes foam cell formation from THP-1 cells through restoring autophagy flux. PLoS One 11(4):e0154820

Chapter 15

A Fluorescence-Based In Vitro Method to Assess Cholesterol Efflux

Sara Fernández-Castillejo, Anna Pedret, Úrsula Catalán Santos, and Rosa Solà

Abstract

Cholesterol efflux (ChE) capacity is associated with the incidence of cardiovascular events and has been proposed as an emerging cardiovascular risk factor. ChE has been traditionally assessed by in vitro radioactive methods but these are not appropriate when assessing a large number of samples. Therefore, alternative, reproducible nonradioactive methods have been developed. This chapter describes a robust nonradioactive method using a fluorescent tracer to assess ChE in vitro.

The measurement of ChE in vitro requires three main components: a cholesterol-loaded donor cell, a cholesterol tracer, and a cholesterol acceptor. This method involves labeling of murine macrophage J774A.1 cells using the fluorescent sterol dipyrromethene boron difluoride (BODIPY)-cholesterol. The cholesterol acceptors from humans or animals include lipid-free apolipoprotein (ApoA)-1, high-density lipoprotein (HDL), HDL_2 and HDL_3 subfractions, serum, plasma or ApoB-depleted serum or plasma. While lipid-free ApoA-1 mediates ChE via only ATP-binding cassette (ABC)A1 transporter, the remaining acceptors mediate ChE via ABCA1, ABCG1 and scavenger receptor class B type 1 (SRB1) transporters. The reproducibility of this BODIPY-ChE assay is excellent as the intra-assay coefficients of variation (CVs) were <10% (30 replicates on the same day) and the interassay CVs were <14% (10 experiments performed on different days, with 3 replicates each). The fluorescent method therefore represents a reproducible, safe and useful tool to evaluate ChE as an emerging cardiovascular risk factor.

Key words Cholesterol efflux, Reverse cholesterol transport, Fluorescent, Nonradioactive, Macrophages, Atherosclerosis, BODIPY

1 Introduction

Emerging cardiovascular risk factors include high-density lipoprotein (HDL) functionality, in particular its capacity to uptake the excess cholesterol from peripheral tissues and deliver it to the liver where it is further excreted into the bile, a process known as reverse cholesterol transport (RCT). In the first step of RCT, HDL acts as an acceptor of cellular cholesterol effluxed from lipid-loaded cells of the peripheral tissues, a process that is known as cholesterol efflux

Dipak P. Ramji (ed.), *Atherosclerosis: Methods and Protocols*, Methods in Molecular Biology, vol. 2419,
https://doi.org/10.1007/978-1-0716-1924-7_15,
© The Author(s), under exclusive license to Springer Science+Business Media, LLC, part of Springer Nature 2022

(ChE) capacity [1–3]. The ChE process involves cholesterol localized on the cell membrane, which in turn, may be derived from intracellular sites such as the late endosomal/lysosomal compartment and the Golgi apparatus. Given that the removal of cholesterol from lipid-laden macrophages leads to a reduction in both plaque lipid content and inflammation, this flux of cholesterol out of the vascular intima ultimately protects arteries from forming a lipid-rich necrotic core plaque [4]. An inverse association between ChE from macrophages and coronary artery disease (CAD) has been shown by both carotid intima-media thickness and angiographic measurements, independently of the HDL cholesterol levels, in 203 healthy volunteers and 793 patients with CAD [5, 6]. Moreover, ChE is also inversely correlated with type 2 diabetes and with the incident of coronary heart disease events, independently of age, sex, diabetes, hypertension, smoking, alcohol use, waist–hip ratio, body mass index, low-density lipoprotein (LDL) cholesterol levels, triglycerides, and HDL cholesterol or apolipoprotein (Apo)A-I concentrations in 1745 patients with incident coronary heart disease and 1749 healthy participants from the prospective European Prospective Investigation into Cancer and Nutrition (EPIC) Norfolk study [7].

Several in vitro models have been devised to assess ChE, though there is no gold standard for that, and protocols vary considerably. However, the measurement of ChE in in vitro methods always requires three main components: a cholesterol-loaded donor cell, a cholesterol tracer or probe and a cholesterol acceptor [8, 9].

Regarding the cholesterol-loaded donor cell, macrophages such as the human macrophage cell line THP-1 and the murine macrophage cell lines J774A.1 and RAW264.7, are the most relevant cell types for studying atherosclerosis given the central role of macrophage foam cells in disorders of lipid accumulation [9, 10]. Efflux pathways in these cells, particularly those involving ATP-binding cassette transporter (ABC) subfamily A member 1 (ABCA1) and subfamily G member 1 (ABCG1), are efficiently upregulated by exposer of the cells to cyclic adenosine monophosphate (cAMP) or to Liver X receptor (LXR) agonists such as T0901317 [11]. ChE assays are also performed using different cell lines that do not express the ABC transporters such as baby-hamster kidney cells (BHK) or human epithelial HeLa cells, which are stably transfected with mifepristone-inducible human ABCA1 cDNA [6, 9, 12–14]. Studies in humans and animals suggest that ABCA1-mediated ChE is an important mode of efflux by which the severity of atherosclerosis is modulated. Therefore, it is plausible that monitoring of ABCA1-mediated efflux rather than ABCG1 provides a proper method for assessing the mode of efflux of greatest relevance to evaluating the severity of atherosclerosis and its clinical consequences [15].

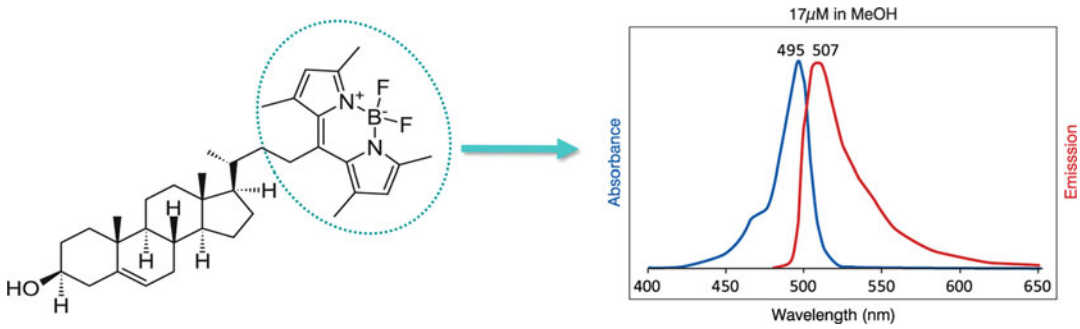

Fig. 1 BODIPY-cholesterol structure and spectroscopic data in methanol. BODIPY-cholesterol is a fluorescent cholesterol probe in which carbon 24 of the cholesterol molecule is linked directly to a boron dipyrromethene difluoride (BODIPY) moiety, depicted with a discontinued circle in this figure. The use of this fluorescent probe can be useful to study ChE avoiding the usage of radioactivity. (Source: Adapted from Avanti Polar Lipids, Inc.)

When it comes to cholesterol tracer or probe, ChE has been traditionally assessed so far by labeling cells with radioactive cholesterol tracers such as tritiated cholesterol ([^{3}H]-cholesterol). This radioactive approach for measuring ChE has provided large amounts of data on both the efficiency of various extracellular acceptors and different pathways [4, 9]. However, despite the low energy of tritium's radiation and the relatively long half-life of this radiotracer, the use of [^{3}H]-cholesterol does not lend to the high-throughput assessment of ChE capacity of a large number of samples such as in the case of clinical trials [11]. For this reason, the development of a safe alternative and reproducible method to assess ChE that avoids the use of radiotracers is of paramount importance. In this sense, Sankaranarayanan et al. (2011) developed a cellular model to assess ChE that avoids the use of radioactivity [11]. This model uses murine J774A.1 macrophages labeled with boron dipyrromethene difluoride (BODIPY) cholesterol (BODIPY-Ch), a fluorescent cholesterol probe in which carbon 24 of the cholesterol molecule is linked directly to a BODIPY moiety (Fig. 1). Sankaranarayanan et al. (2011) demonstrated that BODIPY-Ch undergoes efflux to HDL at an almost identical rate as [^{3}H]-Cholesterol [11]. Moreover, ChE capacity assessed using this fluorescent and nonradioactive in vitro method is inversely associated with the incidence of cardiovascular events in a population-based cohort of 2924 adults of the Dallas Heart Study after a median follow-up period of 9.4 years [15].

Concerning the cholesterol acceptors, several specimens have been used in in vitro methods assessing ChE. These include total serum or plasma, ApoB-depleted serum or plasma, isolated total HDLs, HDL_2 and HDL_3 subfractions, and lipid-free ApoA1. de la Llera et al. (1994) identified that most of the ChE stimulated by human serum was attributable to the non–ApoB lipoprotein-

containing fraction and that this ChE could be measured simply and reliably using total plasma without ApoB (plasma from which ApoB had been precipitated) [16]. The use of ApoB-depleted plasma eliminates the role of LDL and VLDL in assessing ChE, making the assessment more specific for HDL-mediated ChE than assessments using total serum or plasma. Although it is cheap and fast to obtain this specimen, possible cholesterol acceptors other than HDL subfractions, such as albumin, are also present, and they may interfere in HDL-mediated ChE [10, 13, 17]. The use of isolated HDL by ultracentrifugation also has its limitations. For instance, ultracentrifugation methods limit HDL density to 1.21 g/mL and do not accurately represent the contribution of pre-β HDL, which is found in the density range 1.21–1.25 g/mL [17, 18]. While lipid-free ApoA-1 mediates ChE only via ABCA1 transporter, the remaining acceptors mediate ChE via ABCA1, ABCG1 and scavenger receptor class B type 1 (SRB1) transporters [6]. No data are available to suggest that the use of a particular acceptor might be more physiologically relevant or better than another for assessing cellular ChE-mediated by HDL.

Several protocols exist describing methods to assess RCT in vivo [9] and radioactive models to assess ChE in vitro [9, 19]. However, to date no detailed protocol describing a fluorescent method to assess ChE in vitro is available. In this context, this chapter comprehensively describes methodological details of an in vitro fluorescent-based method to assess ChE, which is a safe, efficient and reproducible alternative to the traditional radioactive models. To that purpose, the model developed by Sankaranarayanan et al. (2011) has been taken as a reference protocol [11], and some methodological modifications that enhance reproducibility have been added.

2 Materials

2.1 Growth Period

1. *Mus musculus* monocytic J774A.1 cell line (DSMZ-ACC170).
2. 48-well cell culture plates.
3. Cell culture incubator.
4. Complete culture medium: Low-glucose Dulbecco's Modified Eagle Medium (LG-DMEM), 10% heat-inactivated fetal bovine serum (hiFBS; 56 °C for 1 h), 100 U/mL penicillin and 100 mg/mL streptomycin.
5. Phase-contrast inverted microscope.

2.2 Labeling Period

1. Ultrasound shaker water bath.
2. Fluorescent TopFluor-Cholesterol probe (BODIPY-ch): This TopFluor-Cholesterol fluorescent probe is a cholesterol analog in which C24 of the cholesterol molecule is linked directly to a dipyrromethene boron difluoride (BODIPY) moiety. The detailed structure of this BODIPY-Ch molecule and its spectroscopic data are depicted in Fig. 1 (*see* **Note 1**).
3. Labeling medium: The labeling medium consists of LG-DMEM containing the Acyl-CoA:cholesterol acyltransferase inhibitor Sandoz 58-035 (iACAT; 5 μM) and cholesterol, where the BODIPY-Ch accounts for 20% (0.025 mM) and unlabeled cholesterol for the remaining 80% (0.1 mM) of total cholesterol (0.125 mM), both complexed with methyl-β-cyclodextrin (CD; 10 mM) at a molar ratio of 1:80 (total cholesterol:CD). This labeling medium is usually prepared concentrated (2×; undiluted labeling medium) and diluted afterward (1:2) as a laboratory routine (final labeling medium) as follows. First, undiluted labeling medium is prepared in LG-DMEM containing BODIPY-Ch and unlabeled cholesterol, both complexed with CD. Second, this undiluted labeling medium containing BODIPY-Ch, unlabeled cholesterol and CD is further diluted 1:2 in LG-DMEM containing iACAT to obtain the final labeling medium. Therefore, the concentrations specified in the preparation of the undiluted labeling medium protocol are twice the final concentration of the labeling medium (*see* **Note 2**).
4. Undiluted labeling medium: LG-DMEM, 0.25 mM total cholesterol (0.05 mM BODIPY-Ch and 0.2 mM unlabeled cholesterol), 20 mM methyl-β-cyclodextrin (CD). Calculate the volume of undiluted labeling medium needed for the experiment, according to the total samples that will be assessed, adding some extra volume in excess due to any losses during pipetting or the filtration process. For a single 48-well plate, it is recommended to prepare 10 mL of undiluted labeling medium (*see* **Note 2**). Clean the round-bottom glass tube that will be used to prepare the labeling medium with chloroform and allow it to dry at room temperature. Using filter tips, add BODIPY-Ch to the round-bottom glass tube to get a concentration of 0.05 mM and unlabeled cholesterol to get a concentration of 0.2 mM of undiluted labeling medium in the volume previously calculated (i.e., 10 mL) (*see* **Notes 3** and **4**). Cover the tube with aluminum foil to avoid light interaction and dry under N_2. Prepare LG-DMEM containing 20 mM of CD in a polypropylene tube and add it to the round-bottom glass tube, which contains both forms of dried cholesterols (*see* **Notes 5–8**). Close tight the tube and seal it with parafilm. Sonicate the medium in an ultrasound bath for at least

30 min at 37 °C to allow both BODIPY-Ch and unlabeled cholesterol to complex with CD (*see* **Notes 9–11**). When the sonication is over, place the glass tube, containing the undiluted labeling medium, in a shaking water bath for 3 h at 37 °C protected from light. Keep the undiluted labeling medium at 4 °C until use (*see* **Notes 12** and **13**).

5. Final labeling medium: LG-DMEM, 0.125 mM total cholesterol (0.025 mM BODIPY-Ch and 0.1 mM unlabeled cholesterol), 10 mM CD, 5 μM Sandoz 58-035 (ACAT inhibitor; iACAT). The day when the cells are labeled, the undiluted labeling media must be further sonicated in the ultrasound bath (30 min, 37 °C). After the sonication process, filter the undiluted labeled media through a sterile filter using a 0.22 μm pore size in a laminar airflow cabinet (*see* **Notes 14** and **15**). To monitor the fluorescence of the labeling media during its whole preparation process, it is recommended to save an aliquot of undiluted labeling before and after its filtration and kept at 4 °C until its reading at the end of the experiment. About 350–400 μL/aliquot will be enough to monitor fluorescence in triplicate. Measure the approximate volume of the undiluted labeling media once filtered and add an equal volume of LG-DMEM (*see* **Notes 2** and **16**). Pipette iACAT at a final concentration of 5 μM to get the final labeling medium used to label the cells (*see* **Note 17**).

2.3 Equilibration Period

1. Equilibration medium: LG-DMEM, 0.2% of fatty acid-free bovine serum albumin (FAF-BSA), 5 μM iACAT, 3 μM T0901317.

2.4 Acceptors Period

1. LG-DMEM supplemented with 5 μM iACAT.

2.5 Determination of Cholesterol Content in the Media and Cells

1. 96-well black plates.
2. Shaker.
3. Microfuge tubes.
4. Parafilm.
5. Microcentrifuge.
6. Fluorescence reader with $\lambda_{ex} = 495$ and $\lambda_{em} = 507$ (or similar) fluorescence filters.
7. Extraction buffer: 1% (w/v) cholic acid, methanol.

3 Methods

The experimental procedure to measure ChE using the TopFluor-Cholesterol fluorescent probe comprises several steps. To facilitate the experimenter with the fluorescent in vitro method to assess

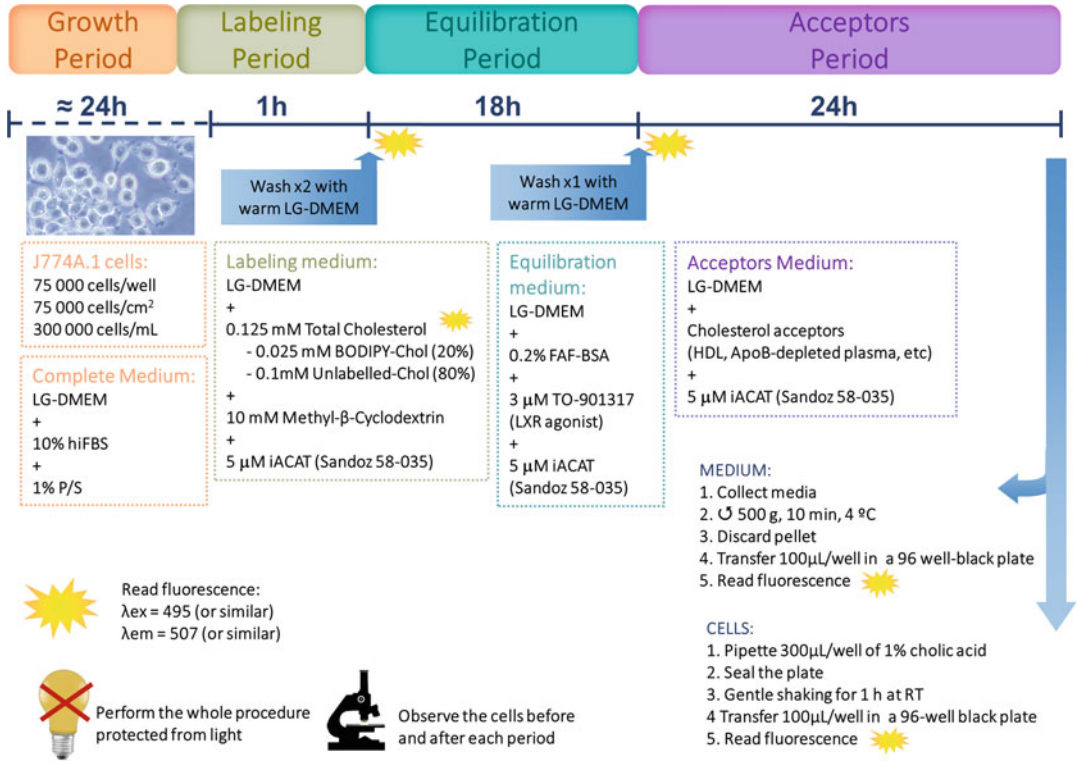

Fig. 2 Scheme of the proposed in vitro fluorescent model to assess cholesterol efflux. *LD-DMEM* Low-glucose Dulbecco's Modified Eagle Medium, *hiFBS* heat-inactivated fetal bovine serum, *P/S* penicillin and streptomycin, *BODIPY* dipyrromethene boron difluoride, *iACAT* acyl-CoA:cholesterol acyltransferase inhibitor, *FAF-BSA* fatty acid-free bovine serum albumin, *LXR* liver X receptor, *HDL* high-density lipoprotein, *Apo* apolipoprotein, *RT* room temperature

ChE, a schematic representation of the whole procedure is detailed in Fig. 2.

A schedule of the ChE procedure is also depicted in Table 1. The time points proposed in Table 1 are given merely as a guideline, but it is suggested to follow the proposed schedule. As an example, the labeling media can be prepared the same day that the cells are labeled (day 2) but since the preparation of the labeling medium is time-consuming and this media is stable for at least 48 h when stored correctly at 4 °C, it is recommended to prepare this medium the previous day of its use for labeling cells (day 1). On day 1, it is recommended to start preparing this labeling media, to thaw cells and to allow them to grow for 24 h (Growth Period). On day 2, the labeling media is completely prepared and used to label cells for 1 h (Labeling Period). Afterward, cells are equilibrated for 18 h (Equilibration Period). On day 3, it is necessary to prepare for the procedures required in the Acceptors Period (additional 24 h). Finally, on day 4, media and cell lysates are processed, and fluorescence intensity is measured in these samples.

Table 1
Proposed schedule for undertaking the cholesterol efflux procedure

Day 1	Day 2	Day 3	Day 4
8:00	**12:00**	**8:30**	**10:00**
Start preparing labeling medium	Finish preparing labeling medium	Prepare the conditions for the acceptors period	Process media and cell samples as specified in the protocol
Store at 4 °C			Read the fluorescence intensity in the media and cells samples
	13:30	**9:00**	
14:00	*LABELING PERIOD:*	*ACCEPTORS* PERIOD	
GROWTH PERIOD:	Incubate cells in labeling medium	Wash cells with warm LG-DMEM twice	
Prepare complete medium	Prepare the conditions for the equilibration period	Incubate cells with the acceptors	
Thaw cells and incubate for 24 h			
	14:30 *EQUILIBRATION* PERIOD: Wash cells with warm LG-DMEM once Incubate cells with the equilibration conditions		

On day 1, it is recommended to start preparing the labeling media, to thaw cells and to allow them to grow for 24 h (Growth Period). On day 2, the labeling media is completely prepared and used to label the cells for 1 h (Labeling Period). Afterward, the cells are equilibrated for 18 h (Equilibration Period). On day 3, it is necessary to prepare the conditions required in the Acceptors Period (additional 24 h). Finally, on day 4, media and cell lysates are processed, and fluorescence intensity is measured in these samples. Although the time points proposed are given merely as a guideline, it is suggested to follow the proposed schedule. As an example, the labeling media can be prepared the same day that the cells are labeled (day 2) but since the preparation of the labeling medium is time-consuming and this media is stable for at least 48 h when stored correctly at 4 °C, it is recommended to prepare this medium the previous day of its use for labeling cells (day 1). *LG-DMEM* low-glucose Dulbecco's Modified Eagle Medium

3.1 Growth Period: Cells Thaw, Growth and Seeding

Different murine monocytic-macrophage cell lines (such as J774A.1 and RAW264.7), human monocytic cell lines (such as THP-1), ABCA1-transfected nonmonocytic cell lines (such as BHK and human epithelial HeLa cells) and primary mouse macrophages isolated from the peritoneal cavity are usually employed to assess the capacity of several cholesterol acceptors to promote ChE from lipid-laden cells. In the experimental procedures detailed in the present protocol, the *Mus musculus* monocytic-macrophage J774A.1 cell line (DSMZ-ACC170) is used since it typically

shows more consistency in the results obtained and, in addition, efflux pathways (especially the expression of ABCA1 but also ABCG1) are easily upregulated by exposure of these cells to LXR agonists such as T0901317 [11]. Moreover, and more importantly, ChE assessed in this murine J774A.1 cell line is inversely associated with the incidence of cardiovascular events in a population-based cohort [15].

The growth period procedure should be undertaken as follows:

1. Thaw and seed the murine J774A.1 macrophage cells at a density of 75,000 cells/cm^2 in 48-well culture cell plates, adding 250 μL of cell suspension at a density of 300,000 cells/mL (*see* **Notes 18** and **19**).
2. Allow cells to grow routinely for 24 h in complete culture medium in a humidified cell incubator containing 5% CO_2 and 95% O_2 at 37 ° C (*see* **Note 20**).
3. After 24 h of culture, semiconfluent J774A.1 cells (ideally 50–70% confluence) should display a typical monolayer and semiquiescent phenotype of macrophage cells under a phase-contrast inverted microscope (*see* **Note 21**).

3.2 Labeling Period: Labeling Cells with Fluorescent Cholesterol

1. Take the cells that have been growing for 24 h in complete medium in the 48-well plate and observe them under a phase-contrast inverted microscope to ensure their correct morphology (*see* **Note 22**).
2. To monitor the lack of fluorescence of the growing medium (complete medium in contact with cells for 24 h), it is recommended to save an aliquot of this growing medium. About 350–400 μL will be enough to monitor fluorescence in triplicate.
3. Discard the complete media of the remaining wells.
4. It is important to set up a "blank condition" (run in triplicate) of nonlabeled cells. To this purpose, incubate 3 wells with LG-DMEM (0.25 mL/well) instead of labeling medium.
5. Incubate the remaining wells with warm (37 °C) final labeling medium for 1 h (0.25 mL/well) in a humidified cell culture incubator containing 5% CO_2 and 95% O_2 at 37 ° C (*see* **Note 23**).

3.3 Equilibration Period: Cholesterol Equilibration and Cell Conditioning

1. Observe the J774A.1 cells under the microscope to ensure their correct morphology.
2. Save an aliquot of LG-DMEM media for the blank condition, and an additional one of the media in labeled-cells condition to monitor fluorescence at the end of the ChE experiment.
3. Discard the media of the remaining wells.

4. Gently wash all cells twice with warm (37 °C) LG-DMEM (*see* **Note 24**).
5. Equilibrate all wells, including those of the blank condition, by adding 0.25 mL/well of equilibration medium containing LG-DMEM supplemented with fatty acid-free bovine serum albumin (FAF-BSA; 0.2%), iACAT (5 μM) and the nonsteroidal LXR agonist T0901317 (3 μM) for 18 h in a humidified cell incubator containing 5% CO_2 and 95% O_2 at 37 ° C (*see* **Notes 25** and **26**).

3.4 Acceptors Period: Promotion of ChE

1. Observe the J774A.1 cells under the microscope to ensure their correct morphology.
2. Save an aliquot of the media after the equilibration period of both the blank condition and any of the labeled cells condition to monitor fluorescence at the end of the experiment.
3. Discard the media of the remaining wells.
4. Gently wash all cells once with warm (37 °C) LG-DMEM (*see* **Note 27**).
5. Add 0.25 mL/well of LG-DMEM supplemented with iACAT (5 μM).
6. It is necessary to set up a "background ChE" condition (analyzed in triplicate) to monitor the passive and nonspecific ChE. Incubate these cells with no extracellular acceptor.
7. It is highly recommended to set up an "inter-plate control" condition (analyzed in triplicate) adding a control acceptor that must be used in all set of experiments in the same project. The specimen used should be the same as the tested samples specimen (i.e., isolated HDL, ApoB-depleted samples, etc.). The interplate control will allow you to ensure proper reproducibility of all the set of experiments performed.
8. Add accurately the corresponding acceptor to the remaining wells in triplicate (*see* **Notes 28** and **29**).
9. Incubate J774A.1 cells for 24 h in a humidified cell incubator containing 5% CO_2 and 95% O_2 at 37 ° C (*see* **Note 30**).

3.5 Determination of Cholesterol Content in the Media and Cells

1. At the end of the incubation of the cells, observe them under a microscope to ensure their correct morphology (*see* **Notes 31** and **32**).
2. Collect the media from each well in microfuge tubes, and centrifuge at 500 × *g* at 4 °C for 10 min to discard detached cells and cellular debris. Discard the pellet and transfer the cell-free media to new microfuge tubes (*see* **Note 33**).
3. Extract cellular lipids by adding 300 μL/well of extraction buffer to the cells, seal the plate with parafilm to avoid the methanol evaporation and incubate with gentle shaking for 1 h at room temperature protected from light (*see* **Notes 34** and **35**).

4. Transfer 100 μL per well of the cell-free media or the cellular lipid solvent fractions to a 96-well black plate (two replicates for each culture well).
5. Record the fluorescence intensity in a fluorescence reader at λ excitation = 495 nm and λ emission = 507 nm or similar. Investigators should set the technical parameters according to their specific fluorescence reader (*see* **Note 36**).

3.6 Calculation of Acceptors-Mediated ChE

1. Calculate Raw ChE according to the following formula

$$\%\text{of raw ChE} = [\text{media fluorescence}/(\text{media fluorescence} + \text{cells fluorescence})] \times 100,$$

   in which fluorescence values are expressed in relative fluorescent units (RFU) (*see* **Note 37**).
2. Subtract background ChE (cells incubated with no extracellular acceptors) from raw ChE to obtain the "acceptors-mediated ChE" values and calculate the mean of the duplicate wells corresponding to the same sample. *See* **Notes 38** and **39** for expected results and reproducibility of the method.

3.7 Monitoring Fluorescence of the Labeling Media and the Experimental Conditions

1. To monitor the fluorescence of the labeling media during its whole preparation process, transfer 100 μL per well (in duplicate) of the aliquots saved in each step of the labeling media preparation to a 96-well black plate: undiluted labeling media before and after its filtration, and final labeling media.
2. To monitor the lack or the presence of fluorescence in the media obtained throughout the experimental procedure, transfer 100 μL per well (in triplicate) of the aliquots saved after each period to a 96-well black plate: cellular growth period, labeling period and equilibration period (from both the blank and the labeled-cells conditions).
3. Record the fluorescence intensity in a fluorescence reader at λ excitation = 495 nm and λ emission =507 nm or similar, as detailed above.

4 Notes

1. Since BODIPY-Ch is light sensitive, it is recommended to perform the whole experimental procedure in dim light. We use BODIPY-ch from Avanti Polar Lipids.
2. The proposed volumes of undiluted labeling medium preparation for a single 48-well plate are 62.5 μL of 8 mM BODIPY-ch, 8 μL of 250 mM unlabeled cholesterol, 2 mL of 100 mM CD and 8 mL of LG-DMEM. The final concentration of these reagents in the undiluted labeling medium are 0.05 mM of

BODIPY-ch, 0.2 mM of undiluted cholesterol and 20 mM of CD, all diluted in LG-DMEM. The proposed volumes of final labeling medium preparation for a single 48-well plate are 8 mL of LG-DMEM and 8 μL of 10 mM iACAT. The final concentration of these reagents in the labeling medium is 0.025 mM of BODIPY-ch, 0.1 mM of undiluted cholesterol, 10 mM of CD and 5 μM of iACAT.

3. Notice that the concentrations of BODIPY-Ch and unlabeled cholesterol added to prepare the undiluted labeling medium (0.05 and 0.2 mM, respectively) are twice the final concentrations in the final labeling medium (0.025 and 0.1 mM, respectively), as the medium prepared will be further diluted 1:2 as described below (*see* **Note 4**) to get the final labeling medium.
4. Stock solutions of BODIPY-Ch and unlabeled cholesterol should be prepared in chloroform (i.e., 8 and 250 mM, respectively), aliquoted (i.e., 100 μL/aliquot), dried under N_2 and stored at −20 or − 80 °C. The day these stock solutions are needed, resuspend the aliquot in the volume selected to aliquot (100 μL in this example) just before pipetting in the round-bottom glass tube. This procedure avoids any potential pipetting errors as chloroform may evaporate when stored at −20 or −80 °C.
5. For a single 48-well plate, it is recommended to prepare about 10 mL of this LG-DMEM containing 20 mM CD.
6. Notice that the concentrations of CD specified (20 mM) is twice the final concentration in the final labeling medium (10 mM), as the medium prepared will be further diluted 1:2 to get the final labeling medium. Despite this, the molar ratio between total cholesterol and CD remains the same as in the final labeling medium, which is 1:80 (total cholesterol–CD).
7. Prepare the stock solution of CD at 100 mM in ultrapure water in a polypropylene tube and allow to stir for at least 30 min at room temperature to ensure effective dissolution. This solution may be stored for several months at 4 °C. It is crucial not to freeze this solution.
8. Although the mean molecular weight of CD is 1320 g/mol, it can vary between lots due to variation in the methyl content of the product. It is highly recommended to prepare the stock solution using the specific molecular weight indicated by the supplier.
9. Should the dry residue of cholesterol remain adhered to the glass tube after these 30 min, sonicate for an additional 15–30 min at 37 °C.
10. During the whole sonication process, it is important to control the temperature and to avoid reaching 38 °C or more. Should

this happen, it is recommended to add some ice to the ultrasound bath to cool down the water to 36–37 °C. It is also important to degasify the water for 1 min before the use of the water sonicator bath to increase the sonication efficiency.

11. Alternative sonicators to the ultrasound bath can be used such as probe-type sonicators. However, the ultrasound bath is recommended as it avoids the direct contact of the media with the device.
12. The labeling media can be prepared the same day that the cells are labeled. However, since the preparation of the labeling medium is time-consuming and this media is stable for at least 48 h when stored correctly at 4 °C, it is recommended to prepare this medium the previous day of its use for labeling cells (see the schedule proposal in Table 1).
13. When stored at 4 °C, some precipitates may appear in the media because of incomplete complex formation of total cholesterol with CD due to incorrect cholesterol–CD ratio used and because of incorrect temperature used during the preparation of the labeling media. Should this be the case, discard the solution, review the calculations and prepare a new undiluted labeling media if needed.
14. From this point on, perform the procedure in a laminar airflow cabinet to maintain the necessary asepsis during the whole process, unless otherwise stated.
15. Some volume of the undiluted labeling media may be lost in the filter.
16. Although the recommended volume of undiluted labeling media for a single 48-well plate is 10 mL, this volume will be reduced to around 8.5–9 mL due to the filtration process and for the aliquots detailed above to monitor fluorescence.
17. iACAT is added at this stage to prevent the formation of esterified cholesterol pools by the ACAT enzyme. Since the movement of cholesterol through the cellular membrane is in the free rather than in the esterified form, any cholesterol esterification that may occur in the absence of iACAT may affect the efflux of labeled cholesterol.
18. Alternatively, thawed J774A.1 macrophage cells can be seeded and expanded at 1–2 $\times$ 10^6 cells/75 cm^2 (100,000 cells/mL) and kept for days until use in a humidified cell incubator containing 5% CO_2 and 95% O_2 at 37 °C. In this case, the culture medium must be refreshed every 2 days and it is recommended to monitor the cell growth thoroughly because too great density may cause cell detachment. Split 1:3 to 1:4 with a cell scraper when cells reach 90% confluence. Before the ChE experimental procedure, preconfluent cells must be

scraped, counted, and seeded at 75,000 cells/cm^2 in 48-well culture cell plates.

19. The whole ChE assessment procedure has been set up to be performed in 48-well plates with 0.5 mL/well to have enough volume to measure the fluorescence of each well in triplicate at the end of the experiment.
20. Inactivate the FBS by incubating it at 56 °C for 1 h in a water bath.
21. It is recommended to undertake all set of experiments of a particular project in the same thaw or cell passage to achieve maximum consistency of results and to avoid alterations in morphology, response to stimuli, growth rates and changes in protein expression.
22. At this point, semiconfluent J774A.1 cells should display a typical monolayer and semiquiescent phenotype of macrophage cells under a phase-contrast inverted microscope.
23. Incubation of cells with labeling media for 1 h is enough to monitor ChE. Longer periods of incubation may be detrimental for the cells due to the high concentration of cholesterol in the media.
24. Since cholesterol is added to J774A.1 cells in excess, it is crucial to wash cells at least twice with warm (37 °C) LG-DMEM to completely remove the cholesterol that may have not been taken up by cells. It is recommended to wash cells with warm (37 °C) LG-DMEM rather than sterile PBS because sometimes PBS compromises the confluency of the cells.
25. This equilibration period of 18 h allows for the equilibration of the pools of intracellular cholesterol to optimize the further ChE process. While the presence of iACAT prevents the formation of esterified cholesterol, the presence of T0901317 up-regulates the protein expression of ABCA1 (mainly) and ABCG1 transporters [9].
26. In some cases, the equilibration period can be performed in the absence of T0901317 or any alternative LXR agonist so that the effects of a determined bioactive compound on LXR activation can be studied.
27. It is crucial to wash cells with warm (37 °C) LG-DMEM. One wash is enough, more washes (2 and 3) have been previously tested but do not improve the results. It is recommended to wash cells with warm (37 °C) LG-DMEM rather than sterile PBS because sometimes PBS compromises the confluency of cells.
28. Add no acceptors to the blank condition.

29. Different cholesterol acceptors and their more common concentrations tested include lipid-free ApoA1 (0–50 μg/mL), dialyzed total HDL or HDL_2 or HDL_3 subfractions (25–100 μg of total protein/mL), serum or plasma (1–5%) or ApoB-depleted serum or plasma (1–5%). While lipid-free ApoA-1 mediates ChE via only ABCA1 transporter, the remaining acceptors mediate ChE via ABCA1, ABCG1 and SRB1 transporters.
30. Alternatively, the incubation period of labeled cells with the corresponding acceptors may vary from 4 to 24 h. However, the longer this incubation period, the greater the ChE rate obtained.
31. At this time point, cells may show 100% confluency, especially in those wells incubated with plasma, sera, or ApoB-depleted sera or plasma. However, no minimum percentage of confluency is needed to assure effectiveness of the experimental procedure.
32. From this point on, the experimental procedure does not need to be performed in the laminar airflow cabinet.
33. The media can also be filtered through a 0.45 μm pose size filter as an alternative to centrifugation to discard detached cells and cellular debris.
34. Alternatively, cellular lipids can be extracted with NaOH (0.2 M) or hexane-isopropanol (3:2, v:v).
35. Even sealing the plate for the 1 h-incubation, the extraction buffer solution may evaporate a little. In general, when incubating 300 μL for 1 h, the final volume obtained is around 250 μL.
36. Despite BODIPY excitation and emission maxima are 495 and 507 nm respectively, similar wavelength can be used according to the laboratory's resources. Please check the excitation and emission spectra of BODIPY depicted in Fig. 1.
37. In some in vitro models assessing ChE, the fluorescence of the cellular fraction is monitored in only one well, which is used to calculate ChE of all the experimental wells. However, some differences in cell number and thus fluorescence of this cellular fraction may turn up in the different experimental wells. As a consequence, the coefficients of variation (CV) are greater in the cell fraction than in the media fraction yielding, therefore, higher global CV to the model [11] (*see* Subheading 3.1). However, it is technically more accurate to record the fluorescence of the cellular fraction in each well and calculate the percentage of ChE using the media fraction and its corresponding cellular fraction.

Table 2
Expected ChE values according to the specimen used as acceptor, its concentration, and its human or animal origin

Specimen	Humans		Mice	
	Acceptor concentration	% ChE range	Acceptor concentration	% ChE range
HDL	100 μg/mL[a]	30–40	50 μg/m[b]	30–35
ApoB-depleted sera	3%	35–45	3%	20–40
Sera	No data	No data	1%	30–40

It is recommended to calculate the HDL concentration according to ApoA1 + ApoA2 levels in this specimen. Calculating HDL concentration according to total protein may impair the ChE experimental procedure since HDL specimens may contain other proteins such as albumin and this, in turn, may underestimate the HDL cholesterol efflux capacity. However, the determination of ApoA1 and ApoA2 in some specimens may be complicated due to the low available HDL volume

HDL high-density lipoprotein, *Apo* apolipoprotein, *ChE* cholesterol efflux

[a]This concentration refers to 100 μg of ApoA1 + ApoA2 protein/mL

[b]This concentration refers to 50 μg of total protein/mL

38. Expected results: The expected fluorescence values obtained during the preparation of the labeling medium depend on the fluorescence reader settings employed. However, a good approach is to calculate the percentage of fluorescence loss during labeling medium preparation. In this sense, the fluorescence loss is around 10% in the labeling media filtering and around 65% in the labeling media dilution. The expected percentages of acceptors-mediated ChE depend on several factors such as the specimen used as acceptor and its concentration (*see* **Note 29**) as detailed in Table 2. However, the values obtained using this fluorescent model range between 20 and 45% using standard acceptors such as total HDL (50–100 μg/mL), ApoB-depleted sera (3%) or sera (1%). These percentages of ChE obtained with the fluorescent model (using BODIPY-Ch) happen to be greater than those obtained with the traditional radioactive model (using [^{3}H]-cholesterol) [11, 15, 20] and similar to those obtained with cholesterol analogs bearing BODIPY [21], as previously published [11]. Moreover, the passive or nonspecific ChE obtained in cells incubated with no extracellular acceptor ranges between 4 and 12% in this fluorescent model.
39. Reproducibility of the model: The CV of the medium and cellular fractions is <4% and <15%, respectively, obtained with 30 replicates measured on the same day. The intra-assay CV of the model is <10% obtained in 30 replicates measured on the same day. The inter-assay CV is <14%, obtained in 10 experiments performed on different days, with three replicates each. These CV values are similar to those observed in the reference article [11].

Acknowledgments

This work was funded by the AppleCOR Project, which was made possible with the support of the Ministerio de Economía, Indústria y Competitividad, the Agencia Estatal de Investigación, and the European Regional Development Fund. The NFOC-Salut group is a consolidated research group of the Generalitat de Catalunya, Spain (reference no. 2017 SGR 522). The role of the funders was limited to an economic contribution through a competitive call. The funders had no role in the conception, design, performance, or approval of the work.

References

1. Karathanasis SK, Freeman LA, Gordon SM, Remaley AT (2017) The changing face of HDL and the best way to measure it. Clin Chem 63:196–210. https://doi.org/10.1373/clinchem.2016.257725
2. Lüscher TF, Landmesser U, Von Eckardstein A, Fogelman AM (2014) High-density lipoprotein: vascular protective effects, dysfunction, and potential as therapeutic target. Circ Res 114:171–182. https://doi.org/10.1161/CIRCRESAHA.114.300935
3. Rye K-A, Bursill CA, Lambert G et al (2009) The metabolism and anti-atherogenic properties of HDL. J Lipid Res 50(Suppl): S195–S200. https://doi.org/10.1194/jlr.R800034-JLR200
4. Favari E, Chroni A, Tietge UJFF et al (2015) Cholesterol efflux and reverse cholesterol transport. Handb Exp Pharmacol 224: 181–206. https://doi.org/10.1007/978-3-319-09665-0
5. Khera AV, Cuchel M, de la Llera-Moya M et al (2011) Cholesterol efflux capacity, high-density lipoprotein function, and atherosclerosis. N Engl J Med 364:127–135. https://doi.org/10.1056/NEJMoa1001689
6. Anastasius M, Kockx M, Jessup W et al (2016) Cholesterol efflux capacity: an introduction for clinicians. Am Heart J 180:1–10. https://doi.org/10.1016/j.ahj.2016.07.005
7. Saleheen D, Scott R, Javad S et al (2015) Association of HDL cholesterol efflux capacity with incident coronary heart disease events: a prospective case-control study. Lancet Diabetes Endocrinol 3:507–513. https://doi.org/10.1016/S2213-8587(15)00126-6
8. Litvinov D, Savushkin E, Garaeva E, Dergunov A (2016) Cholesterol efflux and reverse cholesterol transport: experimental approaches. Curr Med Chem 23:3883–3908. https://doi.org/10.2174/0929867323666160809093009
9. Escolà-Gil JC, Lee-Rueckert M, Santos D et al (2015) Quantification of in vitro macrophage cholesterol efflux and in vivo macrophage-specific reverse cholesterol transport. Methods Mol Biol 1339:211–233. https://doi.org/10.1007/978-1-4939-2929-0
10. Rohatgi A (2015) High-density lipoprotein function measurement in human studies: focus on cholesterol efflux capacity. Prog Cardiovasc Dis 58:32–40. https://doi.org/10.1016/j.pcad.2015.05.004
11. Sankaranarayanan S, Kellner-Weibel G, de la Llera-Moya M et al (2011) A sensitive assay for ABCA1-mediated cholesterol efflux using BODIPY-cholesterol. J Lipid Res 52: 2332–2340. https://doi.org/10.1194/jlr.D018051
12. Adorni MP, Zimetti F, Billheimer JT et al (2007) The roles of different pathways in the release of cholesterol from macrophages. J Lipid Res 48:2453–2462. https://doi.org/10.1194/jlr.M700274-JLR200
13. Sankaranarayanan S, Oram JF, Asztalos BF et al (2009) Effects of acceptor composition and mechanism of ABCG1-mediated cellular free cholesterol efflux. J Lipid Res 50:275–284. https://doi.org/10.1194/jlr.M800362-JLR200
14. Zhang J, Cai S, Peterson BR et al (2011) Development of a cell-based, high-throughput screening assay for cholesterol efflux using a fluorescent mimic of cholesterol. Assay Drug Dev Technol 9:136–146. https://doi.org/10.1089/adt.2010.0288
15. Rohatgi A, Khera A, Berry JD et al (2014) HDL cholesterol efflux capacity and incident cardiovascular events. N Engl J Med 371:

2383–2393. https://doi.org/10.1038/jid.2014.371

16. de la Llera MM, Atger V, Paul JL et al (1994) A cell culture system for screening human serum for ability to promote cellular cholesterol efflux. Relations between serum components and efflux, esterification, and transfer. Arterioscler Thromb 14:1056–1065. https://doi.org/10.1161/01.ATV.14.7.1056
17. Rosenson RS, Brewer HB, Ansell BJ et al (2016) Dysfunctional HDL and atherosclerotic cardiovascular disease. Nat Rev Cardiol 13:48–60. https://doi.org/10.1038/nrcardio.2015.124
18. Miyazaki O, Ogihara J, Fukamachi I, Kasumi T (2014) Evidence for the presence of lipid-free monomolecular apolipoprotein A-1 in plasma. J Lipid Res 55:214–225. https://doi.org/10.1194/jlr.M041038
19. Hafiane A, Genest J (2015) HDL-mediated cellular cholesterol efflux assay method. Ann Clin Lab Sci 45:659–668
20. Hölttä-Vuori M, Uronen RL, Repakova J et al (2008) BODIPY-cholesterol: a new tool to visualize sterol trafficking in living cells and organisms. Traffic 9:1839–1849. https://doi.org/10.1111/j.1600-0854.2008.00801.x
21. Liu Z, Thacker SG, Fernandez-Castillejo S et al (2014) Synthesis of cholesterol analogues bearing BODIPY fluorophores by Suzuki or Liebeskind-Srogl cross-coupling and evaluation of their potential for visualization of cholesterol pools. Chembiochem 15:2087–2096. https://doi.org/10.1002/cbic.201402042

Chapter 16

Monitoring the Anisotropy and Fluidity of the HDL Monolayer as Surrogates of HDL Functionality

Sara Fernández-Castillejo, Anna Pedret Figuerola, Úrsula Catalán Santos, Claude Motta, and Rosa Solà

Abstract

The fluidity of the biological lipid layers modulates processes involved in cardiovascular disease. High-density lipoprotein (HDL) monolayer fluidity is considered as a surrogate of HDL functionality. In particular, the more fluid the HDL monolayer is, the greater the cholesterol efflux (ChE) is observed. Fluidity depends on cholesterol and on the saturation and length of the fatty acids present in lipid layers. Specifically, low cholesterol and short-chain and/or low-saturated fatty acids content in the lipid layers increases fluidity. Lipid peroxidation is also involved in regulating the monolayers' fluidity. HDL oxidation decreases its fluidity and ChE capacity. Accordingly, the presence of antioxidants in biological membranes and in HDL increases fluidity. The fluidity is assessed in polarization studies that measures the steady-state anisotropy (r) using fluorescent probes (such as 1,6-diphenyl-1,3,5-hexatriene; DPH) that mimic the molecular movements of the sample analyzed. Since r refers to the rigidity and fluidity refers to the viscosity of lipid layers, the fluidity index is the inverse value of r (i.e., $1/r$). This chapter describes a method for measuring HDL monolayer fluidity and r. The reproducibility of this method was excellent as the intra-assay coefficients of variation (CV) were <2.5 (20 replicates on the same day) and the interassay CV were <5% (60 replicates measured on 3 different days; 20 replicates/day). The method therefore represents a reproducible and useful tool to evaluate HDL functionality as an emerging cardiovascular risk factor.

Key words 1,6-Diphenyl-1,3,5-hexatriene (DPH), Anisotropy, Fluidity, HDL, Lipid layer

1 Introduction

The fluidity of biological lipid layers is a physical characteristic that refers to its viscosity [1, 2]. Fluidity modulates several biological processes involved in cardiovascular disease, for instance, cholesterol efflux (ChE) from lipid-laden cells carried out by high-density lipoprotein (HDL) [3–6].

Fluidity is determined by the composition of the lipid layers [5, 7–9]. In particular, the cholesterol present in the lipid layers forms complexes with phospholipids, creating structures of low fluidity known as lipid rafts. Moreover, fluidity also depends on

Dipak P. Ramji (ed.), *Atherosclerosis: Methods and Protocols*, Methods in Molecular Biology, vol. 2419,
https://doi.org/10.1007/978-1-0716-1924-7_16,
© The Author(s), under exclusive license to Springer Science+Business Media, LLC, part of Springer Nature 2022

the saturation and length of the fatty acids present in the lipid layers. On the one hand, the single bond present in saturated fatty acids is rigid as opposed to the double bond. On the other hand, the long chains of fatty acids can form strong intermolecular interactions, restricting fluidity. Therefore, low cholesterol and low long-chain and/or low-saturated fatty acids content increases the fluidity of lipid layers [8, 10].

The importance of fluidity in cardiovascular disease lays in the fact that HDL fluidity reflects the functional behavior of HDL to such an extent that an increased fluidity has been considered as an intermediate marker of enhanced HDL functionality [3, 5, 9]. Moreover, we have previously reported that HDL fluidity, among others, is a major determinant for ChE [6, 11]. In particular, the more fluid the HDL monolayer is, the greater the ChE rate from lipid-laden macrophages to HDL is observed [6, 9, 12, 13]. Furthermore, when it comes to cells membrane fluidity, our group has reported that this inversely correlates with HDL ChE capacity [5].

Lipid peroxidation decreases monolayers' fluidity. Girona et al. observed that HDL oxidation results in decreased HDL monolayer fluidity, decreased macrophages' membrane fluidity and decreased ChE from these cells [5]. Moreover, some authors have described that the presence of antioxidants in biological membranes [14] and in the HDL monolayer [13, 15] also increases fluidity. In this sense, our group has reported that virgin olive oil intake increases HDL antioxidant content, HDL monolayer fluidity and ChE in healthy volunteers in a crossover trial [13].

The assessment of the fluidity of lipid layers is determined through studies that employ polarized light from which the steady-state anisotropy (r) values are obtained [16, 17]. While r refers to the rigidity of the lipid layers, the fluidity refers to the viscosity of such lipid layers. Therefore, the fluidity index is the inverse value of the r ($1/r$) [1, 18, 19]. When a polarized light beam impacts the lipid layer, the excited molecules present in this layer are displaced from their original orientation modifying the polarization plane of the light beam [1, 18]. This depolarization phenomenon can be monitored by using fluorescent probes linked to lipid layers because once they are excited with a particular wavelength, they inform about the molecular movements present in the sample analyzed [1] (Fig. 1).

The fluorescent probe employed to monitor fluidity of lipid layers is 1,6-Diphenyl-1,3,5-hexatriene (DPH) [16, 20], a polyene hydrocarbon with a stable all-*trans* configuration of an elongated rectangular shape. DPH meets the four criteria for being a good molecular probe: high intensity; short half-time life; being a structural analog of the studied molecule; and high specificity. First, DPH is highly fluorescent at $\lambda_{ex}/\lambda_{em}$ of 360/460 nm, and only in lipid-rich medium. Second, DPH has a half-time of only

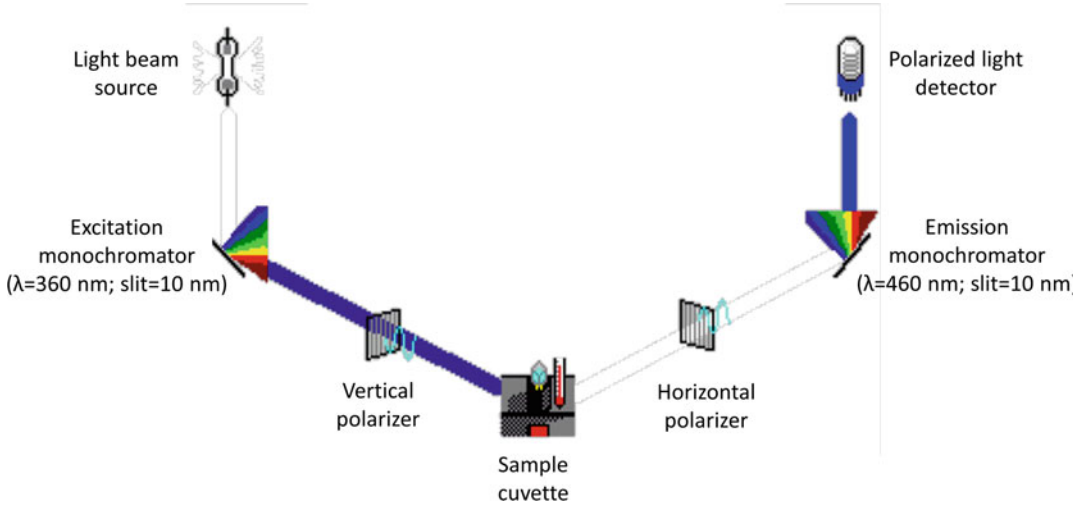

Fig. 1 Schematic diagram of the spectrofluorometer principle

7×10^{-9} s. Third, DPH is a structural analog of the fatty acids that links to the fatty acids of the lipid layers without interfering with their movement. Finally, DPH is highly specific to fatty acids because it does not interact with other molecules. All these characteristics make DPH the most efficient and the most widely used fluorescent probe to monitor lipid layers anisotropy [1, 2].

To date, no specific and detailed article describing the protocol used to measure fluidity of lipid layers is available. In this context, this chapter comprehensively describes a method for measuring HDL monolayer fluidity and *r*, which could be extended to other biological lipid layers.

2 Materials

1. 0.01 M phosphate-buffered saline (PBS) solution: 1 L ultrapure water, 1 package (≈10 g) of PBS powder. This solution must be stored at 4 °C.
2. 2.15 mM (0.5 mg/mL) DPH Stock solution: 5 mg tetrahydrofuran, 10 mL DPH. This stock solution is stable for more than 6 months when stored at −20 °C protected from light [2] (*see* **Note 1**).
3. 1 μM DPH working solution: 12 mL PBS solution, 6 μL DPH stock solution. This working solution must be freshly prepared every day. DPH must be added while vortexing vigorously to avoid aggregate formation that may embed in the lipidic layer. Protect this solution from light.

4. Sample solution: 3 mL of DPH working solution, 25 μL of the sample to be analyzed. Protect this solution from light (*see* **Note 2**).
5. Round-bottom glass tubes.
6. Round-bottom polypropylene tubes.
7. Shaker.
8. Optic glass or quartz cuvettes.
9. LS50-B spectrofluorometer.

3 Methods

1. Prepare the DPH stock solution in a round-bottom glass tube (*see* **Note 3**).
2. Prepare the DPH working solution in a round-bottom polypropylene tube (*see* **Note 4**).
3. Turn on the spectrofluorometer and set the following parameters (see Fig. 1).
   (a) $\lambda_{ex} = 360$ nm,
   (b) $\lambda_{em} = 460$ nm,
   (c) Slit = 10 nm in both wavelengths.
   (d) Integration time = 1 s.
   (e) Stirrer: off.
4. Pipette 2 mL of the DPH working solution into an optic glass or quartz cuvette (*see* **Note 5**).
5. Calculate the grating correction factor (GF) of this DPH working solution and verify that it is correct. Keep this value to measure the fluorescence intensity of the samples (*see* **Notes 6–9**).
6. Pipette 3 mL of the DPH working solution in a new round-bottom polypropylene tube and add 25 μL of the sample to the tube (*see* **Note 10**).
7. Incubate the sample solution shaking for 30 min at room temperature protected from light.
8. Pipette the sample solution into an optic glass or quartz cuvette (*see* **Note 5**).
9. Read the r of the sample using the GF previously recorded with the DPH working solution (*see* **Notes 11** and **12**).
10. Calculate the fluidity of the sample using the following formula (see **Notes 13** and **14**):

$$\text{Fluidity} = 1/r$$

4 Notes

1. Since DPH is a fluorescent probe, all the solutions that contain DPH must be protected from light with an aluminum foil.
2. HDL samples can be fresh or frozen. No differences in r values have been observed between the two types of samples (Table 1).
3. DPH stock solution is stable for more than 6 months if stored properly (−20 ° C protected from light) [2].
4. DPH working solution must be freshly prepared every day. DPH must be added while vortexing vigorously to avoid aggregate formation that may embed in the lipidic layer.
5. After use, cuvettes must be cleaned carefully with ultrapure water without detergent and allowed to dry completely.
6. The GF can also be measured in a cuvette containing the sample solution. The GF should not change.
7. The GF value depends on the spectrofluorometer employed [2]. In the PerkinElmer LS50-B spectrofluorometer, the reference values for GR are 1.24–1.34 Arbitrary Units (AU).
8. Most of the spectrofluorometers automatically calculate GF. If not, GF can be manually calculated using the following formula:

$$\mathrm{GF} = I_{\mathrm{HV}}/I_{\mathrm{HH}},$$

where I_{HV} stands for the fluorescence emission intensity measured when the excitation polarizer is horizontal and the emission polarizer is vertical to the polarization axis of the polarizer plane, and I_{HH} stands for the fluorescence emission intensity measured when both the excitation and the emission polarizers are horizontal to the polarization axis of the polarizer plane [2].

Table 1
Anisotropy values obtained in the PerkinElmer LS50B spectrofluorometer in frozen and fresh HDL samples

	Frozen HDL($n = 18$)	Fresh HDL($n = 14$)
Mean (AU)	0.203	0.204
SD	0.010	0.010
CV (%)	4.700	4.870

Data were obtained in HDL measured on different days. *CV* coefficient of variation, *HDL* high-density lipoprotein, *SD* standard deviation

9. If the GF value is incorrect, check the I_{HV} and the I_{HH} and manually calculate it. Should the error persist, prepare the working solution again.
10. Should you be short of the sample volume required, less volume can be employed provided that the emission slit in the spectrofluorometer is increased. For every increment of 10 nm of the emission slit, the signal is amplified 4 times.
11. Most of the spectrofluorometers automatically calculate the *r* value. If not, *r* can be manually calculated using the following formula.

$$r = [I_{VV} - (\mathrm{GF}\tilde{n}I_{HV})]/[I_{VV} + (2\mathrm{GF}\tilde{n}I_{HV})],$$

where I_{VV} stands for the fluorescence emission intensity measured when both the excitation and the emission polarizers are vertical to the polarization axis of the polarizer plane, and I_{HV} stands for the fluorescence emission intensity measured when both the excitation polarizer is horizontal and the emission polarizer is vertical to the polarization axis of the polarizer plane [2].

12. If the *r* values are incorrect, check the I_{HV} and the I_{HH} and manually calculate these values. Should the error persist, prepare the working and the sample solutions again.
13. Expected results: GF values depend on the spectrofluorometer employed. In the PerkinElmer LS50-B spectrofluorometer, the GF expected values range 1.24–1.34 AU. *r* values also depend on the spectrofluorometer employed. In the PerkinElmer LS50-B spectrofluorometer, the r values of the HDL monolayer range 0.190–0.210 AU. Other authors have reported similar HDL *r* values obtained with other spectrofluorometers; 0.206–0.279 AU [4, 5, 8, 9]. If the GF or the *r* values are incorrect, check the I_{VV}, I_{HV} and I_{HH} and manually calculate these values. Should the error persist, prepare the working solution again.
14. Reproducibility of the measurement: The intra-assay coefficient of variation (CV) of the GF measured in the DPH working solution is <3% obtained in 20 replicates measured on the same day. The interassay CV of the GF measured in the DPH working solution is <2.5% obtained in 60 replicates measured on 3 different days (20 replicates/day) (Table 2). The intra-assay CV of the *r* measured in HDL samples is <2.5% obtained in 20 replicates measured on the same day. The interassay CV of the *r* measured in HDL samples is <5%, obtained in 60 replicates measured on 3 different days (20 replicates/day) (Table 2).

Table 2
Reproducibility (CV; %) of the GF and the *r* of HDL in the PerkinElmer LS50-B spectrofluorometer

	CV (%)	
	Intra-assay[a]	Interassay[b]
GF	<3	<2.5
HDL	<2.5	<5

[a]The intra-assay CV values were obtained in 20 replicates measured on the same day
[b]The interassay CV values were obtained in 60 replicates measured on 3 different days (20 replicates/day). *CV* coefficient of variation, *GF* grating correction factor, *HDL* high-density lipoprotein

Acknowledgments

The VOHF project (AGL2009-13517-457 C03-01) and the AppleCOR Project (AGL2016-76943-C2) were made possible with the support of the Ministerio de Economía, Indústria y Competitividad, the Agencia Estatal de Investigación, and the European Regional Development Fund. The NFOC-Salut group is a consolidated research group of the Generalitat de Catalunya, Spain (reference no. 2017 SGR 522). The role of the funders was limited to an economic contribution through a competitive call. The funders had no role in the conception, design, performance or approval of the work.

References

1. Shinitzky M, Barenholz Y (1978) Fluidity parameters of lipid regions determined by fluorescence polarization. BBA Rev Biomembr 515: 367–394
2. Litman BJ, Barenholz Y (1982) Fluorescent probe: diphenylhexatriene. Methods Enzymol 81:678–685
3. Bonnefont-Rousselot D, Motta C, Khalil A et al (1995) Physicochemical changes in human high-density lipoproteins (HDL) oxidized by gamma radiolysis-generated oxyradicals. Effect on their cholesterol effluxing capacity. Biochim Biophys Acta 1255:23–30
4. Solà R, La Ville AE, Richard JL et al (1997) Oleic acid rich diet protects against the oxidative modification of high density lipoprotein. Free Radic Biol Med 22:1037–1045. https://doi.org/10.1016/S0891-5849(96)00490-X
5. Girona J, LaVille AE, Solà R et al (2003) HDL derived from the different phases of conjugated diene formation reduces membrane fluidity and contributes to a decrease in free cholesterol efflux from human THP-1 macrophages. Biochim Biophys Acta Mol Cell Biol Lipids 1633: 143–148. https://doi.org/10.1016/S1388-1981(03)00108-2
6. Fernández-Castillejo S, Rubió L, Hernáez Á et al (2017) Determinants of HDL cholesterol efflux capacity after virgin olive oil ingestion: interrelationships with fluidity of HDL monolayer. Mol Nutr Food Res 61(12):1–21. https://doi.org/10.1002/mnfr.201700445
7. Ferretti G, Bacchetti T, Nègre-Salvayre A et al (2006) Structural modifications of HDL and functional consequences. Atherosclerosis 184: 1–7. https://doi.org/10.1016/j.atherosclerosis.2005.08.008
8. Solà R, Baudet MF, Motta C et al (1990) Effects of dietary fats on the fluidity of human high-density lipoprotein: influence of the overall composition and phospholipid fatty acids. Biochim Biophys Acta 1043:43–51. https://doi.org/10.1016/0005-2760(90)90108-A

9. Solà R, Motta C, Maille M et al (1993) Dietary monounsaturated fatty acids enhance cholesterol efflux from human fibroblasts. Atheroscler Thromb 13:958–966
10. Davidson W, Gillotte K, Lund-Katz S et al (1995) Effect of HDL phospholipid acyl chain composition on the efflux of cellular free cholesterol. J Biol Chem 270:5882–5890
11. Pedret A, Fernández-Castillejo S, Valls R-M et al (2018) Cardiovascular benefits of phenol-enriched virgin olive oils: new insights from the virgin olive oil and HDL functionality (VOHF) study. Mol Nutr Food Res 62(16): e1800456. https://doi.org/10.1002/mnfr.201800456
12. Helal O, Berrougui H, Loued S, Khalil A (2013) Extra-virgin olive oil consumption improves the capacity of HDL to mediate cholesterol efflux and increases ABCA1 and ABCG1 expression in human macrophages. Br J Nutr 109:1844–1855. https://doi.org/10.1017/S0007114512003856
13. Hernáez Á, Fernández-Castillejo S, Farràs M et al (2014) Olive oil polyphenols enhance high-density lipoprotein function in humans: a randomized controlled trial. Arterioscler Thromb Vasc Biol 34:2115–2119. https://doi.org/10.1161/ATVBAHA.114.303374
14. Suwalsky M, Orellana P, Avello M et al (2006) Human erythrocytes are affected in vitro by extracts of Ugni molinae leaves. Food Chem Toxicol 44:1393–1398. https://doi.org/10.1016/j.fct.2006.03.003
15. Farràs M, Fernández-Castillejo S, Rubió L et al (2018) Phenol-enriched olive oils improve HDL antioxidant content in hypercholesterolemic subjects. A randomised, double-blind, cross-over, controlled trial. J Nutr Biochem 51:99–104. https://doi.org/10.1016/j.jnutbio.2017.09.010
16. Dumas D, Muller S, Gouin F et al (1997) Membrane fluidity and oxygen diffusion in cholesterol-enriched erythrocyte membrane. Arch Biochem Biophys 341:34–39. https://doi.org/10.1006/abbi.1997.9936
17. Dachet C, Motta C, Neufcour D, Jacotot B (1990) Fluidity changes and chemical composition of lipoproteins in type IIa hyperlipoproteinemia. Biochim Biophys Acta 1046:64–72. https://doi.org/10.1016/0005-2760(90)90095-F
18. Lentz BR, Moore BM, Barrow DA (1979) Light-scattering effects in the measurement of membrane microviscosity with diphenylhexatriene. Biophys J 25:489–494. https://doi.org/10.1016/S0006-3495(79)85318-7
19. Jähnig F (1979) Structural order of lipids and proteins in membranes: evaluation of fluorescence anisotropy data. Proc Natl Acad Sci U S A 76:6361–6365. https://doi.org/10.1073/pnas.76.12.6361
20. Dachet C, Motta C, Neufcour D, Jacotot B (1990) Fluidity changes and chemical composition of lipoproteins in type IIa hyperlipoproteinemia. Biochim Biophys Acta 1046:64–72. https://doi.org/10.1016/0005-2760(90)90095-F

Chapter 17

Assessment of Ex Vivo Antioxidative Potential of Murine HDL in Atherosclerosis

Andrea Rivas-Urbina, Noemi Rotllan, David Santos, Josep Julve, Joan Carles Escolà-Gil, and Jose Luis Sanchez-Quesada

Abstract

This chapter provides details on a simple and reproducible method used to determine the capacity of murine HDL to prevent the oxidation of LDL. The principle of the method is based on the rearrangement of double bonds of polyunsaturated fatty acids that occurs during the oxidation of human LDL, which generates a sigmoidal curve. The shape and length of the curve is modified in the presence of HDL, and such modifications are easily quantifiable by measuring the absorbance of conjugated dienes at 234 nm. The general technique described herein may be applied to evaluate the effect of HDL obtained from different experimental murine models of atherosclerosis.

Key words Antioxidant, Oxidation, HDL, LDL, Conjugated diene

1 Introduction

Although reverse cholesterol transport (RCT) is considered the main atheroprotective function of high-density lipoproteins (HDL) [1], these lipoproteins also exert other beneficial actions against the development of cardiovascular disease. A major anti-atherogenic mechanism of HDL depends on its capacity to inhibit the oxidative modification of LDL, thereby precluding the inflammatory, apoptotic and proliferative actions of oxidized LDL, as well as its capacity to promote foam cell formation. HDL protects both lipid and protein moieties of LDL from oxidation, inhibiting the accumulation of primary and secondary peroxidation products that are responsible for inflammation [2].

Chemical and physical properties of HDL such as lipid and protein composition, size and density determine its efficiency in the inhibition of LDL oxidation [3–5]. Regarding the lipid moiety, the capacity of HDL to decrease LDL oxidation correlates with sphingosine-1-phosphate levels [6]. Also, the content of free

Dipak P. Ramji (ed.), *Atherosclerosis: Methods and Protocols*, Methods in Molecular Biology, vol. 2419,
https://doi.org/10.1007/978-1-0716-1924-7_17,
© The Author(s), under exclusive license to Springer Science+Business Media, LLC, part of Springer Nature 2022

cholesterol and triglyceride alters the oxidation kinetics of lipoproteins by altering the fluidity of the HDL surface [7]. Additionally, several proteins transported by HDL have been related to its antioxidant properties, such as apolipoprotein A-I (apoA-I) [8, 9], apoA-II [10], apoA-IV [11], apoE [12], apoM [13], apoD, apoF, apoJ, apoL-1, and serum amyloid A [14]. Similar to these proteins, HDL-associated hydrolases can also contribute to the antioxidative activity of HDL, such as paraoxonase (PON) 1, platelet-activating factor acetylhydrolase (PAF-AH), and lecithin-cholesterol acyltransferase (LCAT) [15–17]. The quantification of these molecules gives a partial appraisal of the antioxidant properties of HDL, but direct measurement of the antioxidant capacity of the whole HDL particle is advisable.

Although numerous methods have been used to determine the antioxidant capacity of HDL, they are usually complex and cumbersome. Indeed, most methods cannot be applied to large number of samples from clinical studies. Here, we describe a reproducible method to measure the capacity of HDL to inhibit the oxidative modification of LDL. The rationale of the method is based on the formation of conjugated diene (CD), a product of lipid peroxidation with an absorbance maximum at 234 nm [18]. This product is formed during the oxidation of lipoproteins due to the remodeling of double bonds in polyunsaturated fatty acids that are part of phospholipids, triglycerides, and esterified cholesterol. In the case of LDL, the continuous monitoring at 234 nm of the oxidation process induced by an oxidant stimulus (i.e., copper sulfate) generates a sigmoidal curve, which allows the study of the LDL susceptibility to oxidation. The pro- or antioxidant effects of different molecules can be assessed analyzing their effect on the main parameters of the oxidation kinetics of LDL together the lag phase time or the maximal velocity of propagation. This method is a modification of a previous report developed specifically to measure the antioxidant capacity of HDL in humans [19]. The method compares the susceptibility to oxidation of an LDL control in the absence or the presence of HDL and constitutes a quantitative and reproducible approach. A schematic diagram of the method steps is depicted in Fig. 1.

2 Materials

1. Phosphate-buffered saline (PBS): 137 mM NaCl, 2.7 mM KCl, 6.5 mM $Na_2HPO_4 \bullet 2H_2O$, 1.5 M KH_2PO_4, pH 7.4.
2. Density solution at 1.006 g/mL: 200 mM NaCl, 1 mM EDTA, 2 μM butylated hydroxytoluene (BHT) (*see* **Notes 1** and **2**).

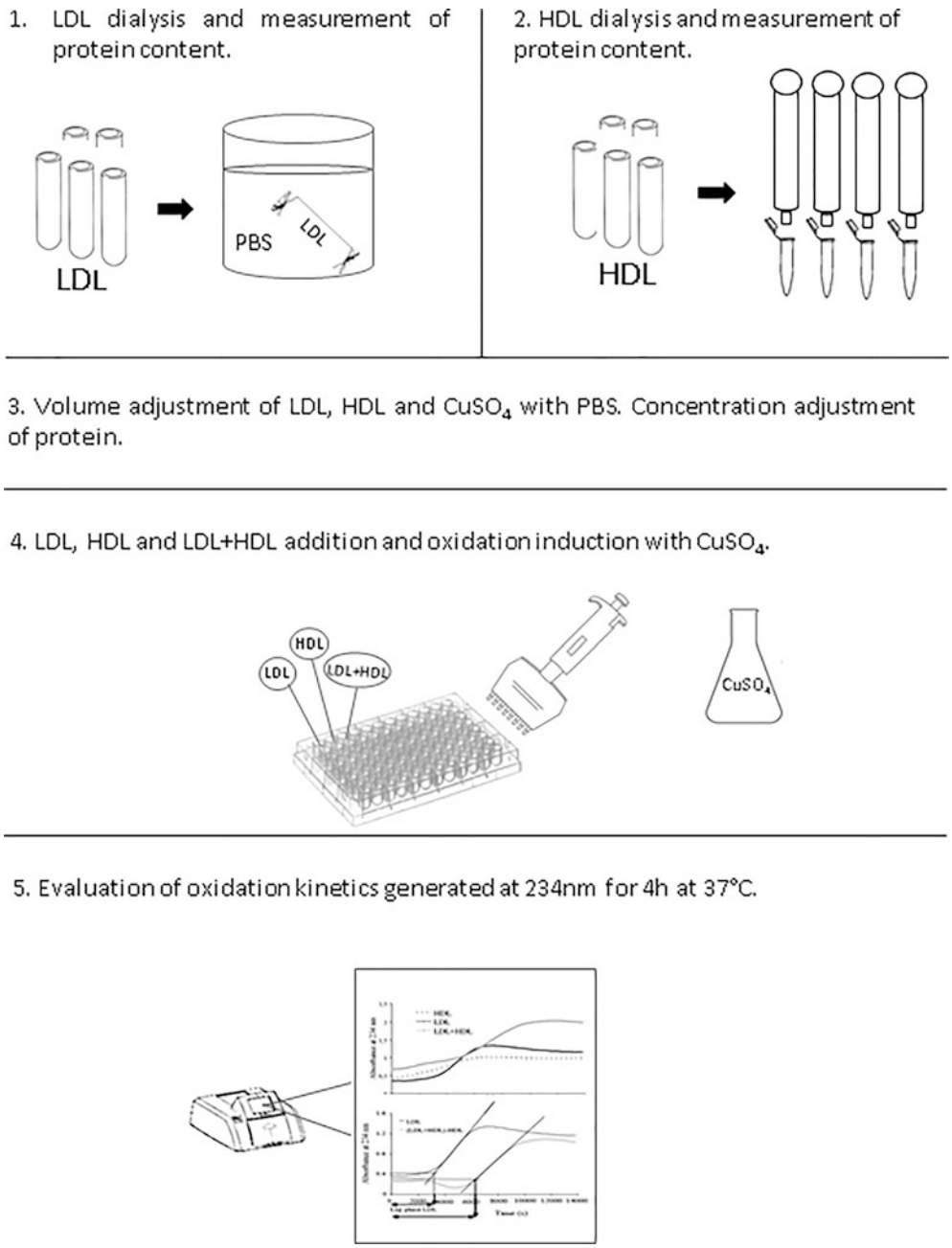

Fig. 1 Steps of the HDL antioxidant capacity method. Steps 1 and 2: Isolated LDL and HDL are dialyzed against PBS buffer to remove salt, EDTA and impurities from samples. Step 3: Adjustment of LDL and HDL concentrations (final volume = 200 μL per well, including $CuSO_4$). Step 4: LDL, HDL, and LDL+HDL are added into individual wells in a plate for UV detection (all samples should be performed in duplicate). It is important to adjust the final volume of lipoproteins and $CuSO_4$ in each well to 200 μL with PBS. Oxidation starts with 5 μM $CuSO_4$ in each well. Step 5: The oxidation kinetics is continuously monitored at a wavelength of 234 nm for 4 h at 37 °C by using a multidetection microplate reader

3. Density solutions at 1.019 g/mL, 1.063 g/mL, 1.210 g/mL, and 1.340 g/mL. The density of each solution is reached by adding the appropriate amount of solid potassium bromide (KBr) to the solution at 1.006 g/mL (*see* **Note 1**).
4. Dialysis membrane tubing 3.5 K MWCO.
5. 50% sucrose solution.
6. Thick wall polycarbonate ultracentrifugation tubes (25 × 89 mm, maximum volume 20 mL) for isolating human LDL.
7. Thick wall polycarbonate ultracentrifugation tubes (13 × 64 mm, maximum volume 2.6 mL) for isolating mouse HDL.
8. P2 gel filtration desalting columns (e.g., CentriPure P2 Zetadex).
9. Protein Assay Kit (e.g., Pierce BCA Protein Assay Kit).
10. 96-microwell plates for UV detection.
11. 10 mL pipettes.
12. Preparative fixed-angle rotor.
13. High-speed ultracentrifuge.
14. 100 μM $CuSO_4$.
15. UV microplate reader with kinetics function and capacity to evaluate sigmoid curves.

3 Methods

3.1 Human LDL Isolation

1. Obtain pool of plasma from normolipemic subjects for purification of LDL by sequential ultracentrifugation using a preparative fixed-angle rotor [20] (*see* **Note 1**).
2. Adjust the plasma to a density of 1.019 g/mL by adding solid KBr according to the equation from Radding and Steinberg [21]:

$$\text{gr KBr} = [\text{volume} \times (\text{initial density} - \text{final density})]/[1 - (0.312 \times \text{final density})],$$

3. Add a maximum of 15 mL of plasma adjusted to 1.019 g/mL to each thick wall polycarbonate ultracentrifugation tubes (25 × 89 mm) and overlay with 5 mL of a solution of the same density (*see* **Notes 1** and **2**). Use the number of tubes required according to the rotor used.
4. Ultracentrifuge the tubes at 100,000 × *g* for 18 h at 4 °C.

5. Discard the upper layer, consisting of VLDL and IDL (approximately 3–4 mL), by aspiration.
6. Collect the infranatant that contains LDL, HDL and the remaining plasma proteins by aspirating from the bottom of the tube with a 10 mL pipette.
7. Adjust the volume of the collected infranatant to the original volume of plasma (15 mL per tube) with a density solution of 1.019 g/mL and then add solid KBr to obtain a density of 1.063 g/mL according to the equation of Radding and Steinberg [21].
8. Ultracentrifuge the tubes at 100,000 × *g* for 18 h at 4 °C.
9. Collect the upper layer that contains pure LDL (approximately 3–4 mL per tube) by aspiration.
10. Extensively dialyze the LDL against PBS in a dialysis membrane tubing. Use at least a volume of 2 L of PBS per mL of LDL to achieve a concentration of EDTA below 0.5 μM.
11. Measure the protein content in PBS-dialyzed LDL by any commercial method available (e.g., Pierce BCA Protein Assay Kit) and prepare 0.8 mL aliquots at 1.2 g protein/L.
12. Add 200 μL of the 50% sucrose solution to each LDL aliquots to obtain 1 mL of LDL at a concentration of 1 g/L and 10% sucrose (*see* **Note 3**). Freeze these aliquots at −80 °C for future assays.

3.2 Murine HDL Isolation

HDL (density range 1.063–1.210 g/mL) is isolated from individual mice by sequential ultracentrifugation using an analytical fixed-angle rotor (*see* **Note 4**).

1. Adjust mouse plasma (typically 0.4 mL) to a density of 1.063 g/mL by adding 205 μL of 1.340 g/mL density solution and 0.6 mL of 1.006 g/mL density solution.
2. Mix gently and overlay with 1.1 mL of density solution at 1.063 g/mL in thick wall polycarbonate ultracentrifuge tubes (13 × 64 mm).
3. Ultracentrifuge the tubes at 100,000 × *g* for 18 h at 4 °C.
4. Discard the floating VLDL+LDL layer and collect 1 mL of the infranatant, containing HDL and the remaining plasma proteins, by aspirating from the bottom.
5. Adjust this infranatant to density of 1.210 g/mL by adding 1.11 mL of density solution at 1.340 g/mL and 0.4 mL of density solution at 1.210 g/mL.
6. Centrifuge the tubes again at 100,000 × *g* for 18 h at 4 °C to allow HDL to float.

7. Collect 200 μL of HDL and store at 4 °C until the oxidation assay is performed (ideally less than 3 days).

3.3 Oxidation Assay

1. Equilibrate P2 gel filtration desalting columns with PBS.
2. Apply 150 μL of HDL into the column.
3. Add 180 μL of PBS once the HDL has entered the column.
4. Elute with 200 μL of PBS to collect HDL (*see* **Note 5**).
5. Measure the protein content of the HDL obtained using a commercially available protein assay kit (e.g., Pierce BCA Protein Assay Kit) (*see* **Note 6**).
6. Calculate the volume of LDL and HDL required to add 20 μg of each lipoprotein in the well of 96-microwell plates (final concentration of 0.1 g protein/L of each lipoprotein).
7. In independent wells of 96-microwell plates, separately add LDL, HDL and the mixture LDL+HDL followed by the calculated volume of PBS to achieve a volume of 190 μL in each well. All measurements should be performed in duplicate.
8. Induce oxidation by adding 10 μL of the 100 μM $CuSO_4$ stock solution to each well (final concentration of 5 μM $CuSO_4$ in the well, *see* **Note 7**).
9. Follow the oxidation kinetics by continuously monitoring the formation of conjugated dienes at a wavelength of 234 nm for 4 h at 37 °C using a UV-microplate reader (*see* **Note 8**).
10. From the characteristic sigmoidal curves of LDL, HDL, and HDL+LDL obtained after the oxidation process (*see* Fig. 2), calculate the lag phase time from the intersection point between the maximal slope of the curve and initial absorbance (Fig. 2, *see* **Note 9**).
11. Subtract the kinetics of HDL alone from the kinetics of HDL +LDL to obtain the curve (HDL+LDL)-HDL and hence evaluate the effect of HDL (Fig. 2, *see* **Note 10**).
12. As the lag phase time of the (HDL+LDL)-HDL curve is longer than that of LDL alone results are expressed as the increment of lag phase time versus LDL alone.

4 Notes

1. LDL (density range 1.019–1.063 g/mL) can be isolated from a pool of plasma obtained from normolipemic subjects by sequential ultracentrifugation using a preparative fixed-angle rotor Subheading 3.1) [20]. The plasma is adjusted to the appropriate density by adding solid KBr, according to the equation from Radding and Steinberg [21].

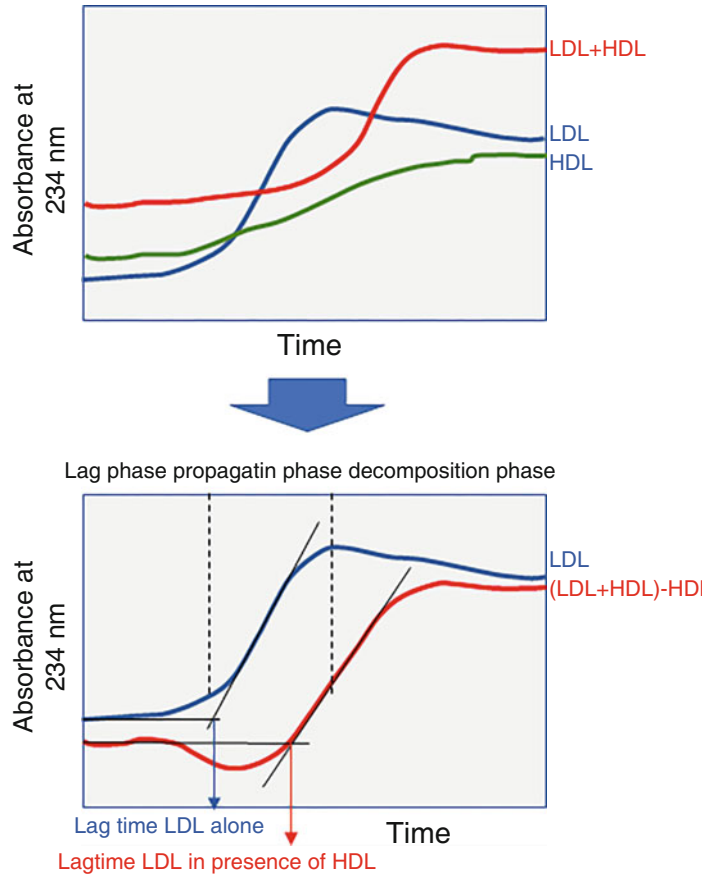

Fig. 2 Representative curves obtained after monitoring oxidation kinetics and lag phase time calculation. Upper panel: Murine HDL (green line), human LDL (blue line), and LDL+HDL (red line). LDL and HDL (at 0.1 g/L of protein) were oxidized in presence of 5 μM $CuSO_4$. Lower panel: HDL curve is subtracted from the (LDL +HDL) curve to obtain and the curve corresponding to (LDL+HDL)-HDL. Lag phase time is calculated as shown in the figure from the intersection point between the basal absorbance and the maximal curve slope of the propagation phase

$$\text{gr KBr} = [\text{volume} \times (\text{initial density} - \text{final density})]/[1 - (0.312 \times \text{final density})],$$

This equation is also used to prepare different density solutions. Alternatively, LDL can be obtained from different commercial sources.

2. To avoid lipoperoxidation during isolation of lipoproteins, all solutions must contain 1 mM EDTA and 2 μM BHT, and ultracentrifugation should be performed at 4 °C using rotors stored in a cold room.

3. Freezing of LDL in the presence of 10% sucrose is essential to maintain the physicochemical properties of LDL after freezing [22].
4. Solutions of density needed for HDL isolation are prepared by adding different amounts of solid KBr to a density solution at 1.006 g/mL containing 200 mM NaCl, 1 mM EDTA and 2 μM BHT. The amount of KBr is calculated according to the equation from Radding and Steinberg [21], as described in **Note 1**.
5. The volumes used for this step are critical to avoid the presence of EDTA, which would interfere with the oxidative process. Never elute the HDL fraction with a volume larger than 200 μL, although smaller volumes can be used. Although P2 columns are recommended for mice studies due to the small volume of HDL usually obtained, PD-10 desalting columns are the choice for studies with human HDL (see Ref. [19] for more details).
6. As an alternative to protein quantification, the HDL concentration can be adjusted by other components such as cholesterol or phospholipid. Since the composition of murine HDL is highly variable depending on the genetic background and dietary regimens, it is strongly encouraged using the phospholipid moiety instead of the protein because this component is less variable during the metabolism of HDL in the blood. In this case, the final concentration of phospholipids in both LDL and HDL should be brought to 1 mM. The main drawback of using phospholipids as an adjustment parameter is that most laboratories usually do not have available rapid methods for phospholipid quantification.
7. The addition of $CuSO_4$ must be done with multichannel high-precision pipette, as fast as possible.
8. The time of the kinetics can vary depending on the mouse model used and the experimental conditions. In some models, the oxidation reaction of the mixture LDL+HDL can be longer than 4 h.
9. Most of available software provides automatic calculation of the lag phase time from oxidation kinetics. Alternative to lag phase time, the maximum rate of the oxidation kinetics can also be used to estimate the lipoproteins susceptibility to oxidation. This approach is especially useful for HDL in some mouse models in which the oxidation curve appears as a smoothed sigmoidal shape.
10. Lipids in HDL are also oxidized in response to $CuSO_4$ and generate their own conjugated dienes, which superimpose to the conjugated dienes formed in LDL. To overcome this problem, the kinetics of HDL alone must be subtracted

from LDL+HDL to obtain an estimation of the effect of HDL on the oxidation of LDL.

Acknowledgments

This work was partly funded by the Instituto de Salud Carlos III and FEDER "Una manera de hacer Europa" grants FIS 16-00471 (to J.L.S-Q.), FIS 17-00232 (to J. J.) and FIS 19-00136 (to J. C. E.-G.), PFIS contract FI17/00031 (to A. R.-U.) and Miguel Servet Type 2 contract (CPII18/00004 to J. J.); Ministerio de Ciencia, Innovación y Universidades, grants PID2019-104367RB-100 (to N. R.) and Subprograma Ramón y Cajal (RUC-20172879 to N. R.) and Red de Investigación "Enfermedades Metabólicas y Cáncer" (RED2018-102799-T to J. J.); and Fundació La Marató de TV3 2016 (303/C/2016, 201602.31 to J. J.). All authors are members of the Quality Research Group 2017-SGR-1149 from Generalitat de Catalunya. A. R.-U., N. R., J. J., J. L. S.-Q., and J. C. E.-G. are members of the Group of Vascular Biology from the Spanish Atherosclerosis Society. CIBER de Diabetes y Enfermedades Metabólicas Asociadas is an Instituto de Salud Carlos III Project.

References

1. He Y, Kothari V, Bornfeldt KE (2018) High-density lipoprotein function in cardiovascular disease and diabetes mellitus. Arterioscler Thromb Vasc Biol 38(2):e10–e16. https://doi.org/10.1161/ATVBAHA.117.310222
2. Navab M, Ananthramaiah GM, Reddy ST, Van Lenten BJ, Ansell BJ, Fonarow GC, Vahabzadeh K, Hama S, Hough G, Kamranpour N, Berliner JA, Lusis AJ, Fogelman AM (2004) The oxidation hypothesis of atherogenesis: the role of oxidized phospholipids and HDL. J Lipid Res 45(6):993–1007
3. Sakuma N, Yoshikawa M, Hibino T, Ohte N, Kamiya T, Kunimatsu M, Kimura G, Inoue M (2002) HDL3 exerts a more powerful antiperoxidative and protective effect against peroxidative modification of LDL than HDL2 does. J Nutr Sci Vitaminol (Tokyo) 48(4):278–282
4. Kontush A, Chantepie S, Chapman MJ (2003) Small, dense HDL particles exert potent protection of atherogenic LDL against oxidative stress. Arterioscler Thromb Vasc Biol 23(10):1881–1888
5. Zerrad-Saadi A, Therond P, Chantepie S, Couturier M, Rye KA, Chapman MJ, Kontush A (2009) HDL3-mediated inactivation of LDL-associated phospholipid hydroperoxides is determined by the redox status of apolipoprotein A-I and HDL particle surface lipid rigidity: relevance to inflammation and atherogenesis. Arterioscler Thromb Vasc Biol 29(12):2169–2175. https://doi.org/10.1161/ATVBAHA.109.194555
6. Kontush A, Therond P, Zerrad A, Couturier M, Negre-Salvayre A, de Souza JA, Chantepie S, Chapman MJ (2007) Preferential sphingosine-1-phosphate enrichment and sphingomyelin depletion are key features of small dense HDL3 particles: relevance to antiapoptotic and antioxidative activities. Arterioscler Thromb Vasc Biol 27(8):1843–1849
7. Fernandez-Castillejo S, Rubio L, Hernaez A, Catalan U, Pedret A, Valls RM, Mosele JI, Covas MI, Remaley AT, Castaner O, Motilva MJ, Sola R (2017) Determinants of HDL cholesterol efflux capacity after virgin olive oil ingestion: interrelationships with fluidity of HDL monolayer. Mol Nutr Food Res 61(12). https://doi.org/10.1002/mnfr.201700445
8. Garner B, Witting PK, Waldeck AR, Christison JK, Raftery M, Stocker R (1998) Oxidation of high density lipoproteins. I Formation of methionine sulfoxide in apolipoproteins AI and AII is an early event that accompanies

lipid peroxidation and can be enhanced by alpha-tocopherol. J Biol Chem 273(11): 6080–6087

9. Panzenbock U, Stocker R (2005) Formation of methionine sulfoxide-containing specific forms of oxidized high-density lipoproteins. Biochim Biophys Acta 1703(2):171–1e81. S1570-9639(04)00310-3 [pii]. https://doi.org/10.1016/j.bbapap.2004.11.003
10. Boisfer E, Stengel D, Pastier D, Laplaud PM, Dousset N, Ninio E, Kalopissis AD (2002) Antioxidant properties of HDL in transgenic mice overexpressing human apolipoprotein A-II. J Lipid Res 43(5):732–741
11. Ostos MA, Conconi M, Vergnes L, Baroukh N, Ribalta J, Girona J, Caillaud JM, Ochoa A, Zakin MM (2001) Antioxidative and antiatherosclerotic effects of human apolipoprotein A-IV in apolipoprotein E-deficient mice. Arterioscler Thromb Vasc Biol 21(6):1023–1028
12. Gaidukov L, Viji RI, Yacobson S, Rosenblat M, Aviram M, Tawfik DS (2010) ApoE induces serum paraoxonase PON1 activity and stability similar to ApoA-I. Biochemistry 49(3): 532–538. https://doi.org/10.1021/bi9013227
13. Elsoe S, Ahnstrom J, Christoffersen C, Hoofnagle AN, Plomgaard P, Heinecke JW, Binder CJ, Bjorkbacka H, Dahlback B, Nielsen LB (2012) Apolipoprotein M binds oxidized phospholipids and increases the antioxidant effect of HDL. Atherosclerosis 221(1):91–97. https://doi.org/10.1016/j.atherosclerosis.2011.11.031
14. Davidson WS, Silva RA, Chantepie S, Lagor WR, Chapman MJ, Kontush A (2009) Proteomic analysis of defined HDL subpopulations reveals particle-specific protein clusters: relevance to antioxidative function. Arterioscler Thromb Vasc Biol 29(6):870–876
15. Mackness M, Durrington P, Mackness B (2004) Paraoxonase 1 activity, concentration and genotype in cardiovascular disease. Curr Opin Lipidol 15(4):399–404
16. Kontush A, Chapman MJ (2006) Antiatherogenic small, dense HDL—guardian angel of the arterial wall? Nat Clin Pract Cardiovasc Med 3(3):144–153
17. Kontush A, Chapman MJ (2006) Functionally defective high-density lipoprotein: a new therapeutic target at the crossroads of dyslipidemia, inflammation, and atherosclerosis. Pharmacol Rev 58(3):342–374
18. Esterbauer H, Striegl G, Puhl H, Rotheneder M (1989) Continuous monitoring of in vitro oxidation of human low density lipoprotein. Free Radic Res Commun 6(1):67–75
19. de Juan-Franco E, Perez A, Ribas V, Sanchez-Hernandez JA, Blanco-Vaca F, Ordonez-Llanos J, Sanchez-Quesada JL (2009) Standardization of a method to evaluate the antioxidant capacity of high-density lipoproteins. Int J Biomed Sci 5(4):402–410
20. Havel RJ, Eder HA, Bragdon JH (1955) The distribution and chemical composition of ultracentrifugally separated lipoproteins in human serum. J Clin Invest 34:1345–1353
21. Radding CM, Steinberg D (1960) Studies on the synthesis and secretion of serum lipoproteins by rat liver slices. J Clin Invest 39: 1560–1569
22. Rumsey SC, Galeano NF, Arad Y, Deckelbaum RJ (1992) Cryopreservation with sucrose maintains normal physical and biological properties of human plasma low density lipoproteins. J Lipid Res 33:1551–1561

Chapter 18

Dual-Fluorescence In Vitro Efferocytosis Assay

Arif Yurdagul Jr

Abstract

The clearance of dead cells by macrophages, termed "efferocytosis," drives the resolution of inflammation, restricts necrosis, and restores homeostasis. Defects in efferocytosis contribute to many diseases, particularly atherosclerosis. Multiple methods to test efferocytosis by macrophages in vitro exist, but each has distinct disadvantages. This chapter describes an improved method to test apoptotic cell binding and internalization by bone marrow–derived macrophages that takes advantage of the high-affinity between streptavidin and biotin.

Key words Macrophages, Efferocytosis, Apoptotic cell (AC) binding, AC internalization, Streptavidin, Biotin

1 Introduction

Efferocytosis involves apoptotic cell (AC) binding and its subsequent internalization by macrophages [1]. Methods to accurately quantify these events in vitro have proven challenging, as simple fluorescent labeling of ACs is insufficient to distinguish between firmly adherent vs. internalized apoptotic cells and relying on pH-sensitive fluorescent probes only reveals information on phagolysosomal acidification [2]. This chapter describes an assay that accurately quantifies efferocytosis (i.e., AC internalization) by bone marrow–derived macrophages using a streptavidin/biotin-chase procedure [2]. ACs are labeled with a long-lasting, membrane-intercalating fluorescent dye (PKH67) [3] and then incubated with the cell impermeant Sulfo-NHS-Biotin, which binds primary amines of proteins only on the cell surface of apoptotic cells. These fluorescently labeled and biotinylated ACs are then added to macrophages and over time these ACs become internalized. Unbound ACs are washed away and macrophages are fixed in formaldehyde. Subsequently, fluorescent streptavidin (of a different wavelength from that used for ACs) is incubated with macrophages. The ACs that were not internalized by macrophages

Dipak P. Ramji (ed.), *Atherosclerosis: Methods and Protocols*, Methods in Molecular Biology, vol. 2419,
https://doi.org/10.1007/978-1-0716-1924-7_18,
© The Author(s), under exclusive license to Springer Science+Business Media, LLC, part of Springer Nature 2022

stain for fluorescent streptavidin (i.e., dual fluorescence), whereas those ACs that were internalized by macrophages are not available to bind to streptavidin and therefore remain unlabeled (i.e., ACs stained for the membrane-intercalating fluorescent dye are negative for fluorescent streptavidin). This dual-fluorescence assay allows for the simultaneous detection of adherent and internalized apoptotic cells. Importantly, this protocol is amenable for use with different sources of ACs, such as zymosan-elicited apoptotic polymorphonuclear leukocytes (PMNs) or dexamethasone-induced apoptotic thymocytes, and various types of macrophages (i.e., Kupffer cells, microglial cells, alveolar macrophages, adipose tissue macrophages, etc.).

2 Materials

Prepare and store all reagents as indicated. Diligently follow all waste disposal regulations when disposing of waste materials. Sodium azide is not added to purchased reagents.

2.1 Culturing of L929 Cells for L929-Conditioned Media (L9CM)

1. NCTC clone 929 (L cell, L-929, derivative of Strain L; ATCC® CCL-1™).
2. Dulbecco's Modified Eagle's Medium (DMEM) (high glucose): 4500 mg/L glucose, 584 mg/L L-glutamine, 110 mg/L sodium pyruvate.
3. Cell culture media: DMEM (high glucose), 10% (v/v) heat-inactivated fetal bovine serum (FBS), 1× penicillin–streptomycin.
4. 0.025% trypsin.
5. 10 cm^2 tissue culture plates.

2.2 Culturing of the Jurkat T Cell Line

1. Jurkat T, Clone E6–1 (ATCC® TIB-152™).
2. Cell culture media: DMEM, 10% (v/v) heat-inactivated FBS, 1× penicillin–streptomycin.
3. 10 cm^2 petri dishes.

2.3 Bone Marrow-Derived Macrophage (BMDM) Isolation and Culture

1. BMDM cell culture media: DMEM (high glucose), 10% (v/v) heat-inactivated FBS, 20% (v/v) L9CM. 1× penicillin–streptomycin. L9CM is prepared as described in Subheading 3.1.
2. Syringes and 23G needles.
3. 70% ethanol.
4. Dressing forceps.
5. Iris scissors.
6. 40 μm cell strainers.

7. 15 mL and 50 mL polypropylene conical tubes.
8. 10 cm^2 petri dishes.
9. Centrifuge.

2.4 Apoptotic Cell Preparation, Fluorescence Labeling, and Biotinylation

1. EZ-Link Sulfo-NHS-Biotin (ThermoFisher Scientific).
2. PKH67 fluorescent staining kit (Sigma-Aldrich). This kit contains Diluent C described in Subheading 3.4.
3. EL Series Ultraviolet Hand Lamp attached to a lampstand (UVP).
4. 60 mm^2 petri dishes.
5. 15 mL polypropylene conical tubes.
6. Centrifuge.
7. 1× phosphate buffered saline (PBS), pH 8.0.
8. 1% bovine serum albumin (BSA) or 1% FBS.

2.5 Efferocytosis Assay

1. 4% formaldehyde.
2. PBS, pH 8.0.
3. Streptavidin-Cy3.
4. Epifluorescence microscope.

3 Methods

3.1 Culturing of L929 Cells for L929-Conditioned Media (L9CM)

1. Split confluent L929 cells in cell culture media at a ratio of 1:10 into tissue culture plates. Culture for 2 days.
2. Aspirate media and feed cells with fresh cell culture media. Culture for 2 days.
3. Collect media from L929 cells, which is now ready for differentiating bone marrow cells isolated from mice into macrophages.
4. Replace media on L929 cells after collection and culture over the next 2 days. Repeat **steps 1–3** for collecting more L9CM (*see* **Note 1**).

3.2 Culturing of the Jurkat T Cell Line

1. Split cells every 3–4 days at a 1:3 ratio into petri dishes with cell culture media when they are between 1.5–2 × 10^6 cells/mL.

3.3 BMDM Isolation and Culture

1. Fill syringe with cell culture media and attach a 23G needle to the syringe.
2. Euthanize a mouse according to your Institutional Animal Care and Use Committee protocol, then spray the mouse with 70% ethanol.

3. Use dressing forceps and iris scissors to trim the femurs and tibias, remove the skin and muscle, and place the cleaned femurs and tibias in a conical tube.
4. In a sterile environment, such as a cell culture hood, cut the ends of the femurs and tibias to expose the medullary cavity.
5. Place the 23G needle, mentioned in **step 1**, in one end of the medullary cavity and flush the bone with cell culture media to collect bone marrow in a petri dish.
6. Pipette the bone marrow repeatedly to disaggregate into cells, then filter this bone marrow suspension through a 40 μm cell strainer.
7. Centrifuge the bone marrow cells at 600 × *g* for 5 min.
8. Resuspend the bone marrow cells in 48 mL of BMDM cell culture media and place them into four 10 cm^2 petri dishes (*see* **Note 2**).
9. Replace BMDM cell culture media 5 days after plating and use between days 7–10 (when they are fully differentiated) (*see* **Note 3** for recommendations on replating).

3.4 Apoptotic Cell Preparation, Fluorescence Labeling, and Biotinylation

1. Centrifuge Jurkat T cells at 600 × *g* for 5 min and resuspend the pellet in 1× PBS. Centrifuge once more.
2. Using the PKH67 fluorescence staining kit, prepare a 2× Cell Suspension solution by adding 1 mL of Diluent C (provided in kit) to the cell pellet and gently pipette up and down (*see* **Note 4**).
3. Prepare a 2× Dye Solution by adding 4 μL of the PKH67 to 1 mL of Diluent C (provided in kit) in a polypropylene tube and mix vigorously.
4. Add the Jurkat cell suspension (1.5–2 × 10^6 cells/mL) to the 1 mL of 2× Dye Solution and pipette up and down continuously for 2–3 min (*see* **Note 5**).
5. Add 2 mL of 1% BSA or FBS for 1 min to remove excess dye and terminate the staining procedure.
6. Centrifuge the fluorescently labeled Jurkat cells at 600 × *g* for 5 min and resuspend the cell pellet in 1× PBS and transfer to a 60 mm^2 petri dish.
7. Remove the dish lid and place the cells 4–5 in. from the UVP and expose the fluorescently labeled Jurkat cells to UV light for 15 min in a cell culture hood with the hood UV light on (*see* **Note 6**).
8. Place the dish lid back onto the plate and incubate the cells at 37 °C for at least 2 h (*see* **Note 7**).
9. Centrifuge apoptotic Jurkat T cells (ACs) at 600 × *g* for 5 min.

10. Resuspend ACs at a concentration of 25×10^6 cell/mL in 1× PBS containing 1 mM EZ-Link Sulfo-NHS-Biotin for 30 min.
11. Add cell culture media to ACs and centrifuge at 600 × *g* for 5 min. Repeat this **step 2** additional times to remove unbound biotin and resuspend fluorescent and biotinylated ACs in serum-free DMEM (complete culture media without FBS).

3.5 Efferocytosis Assay

1. Add the fluorescent and biotinylated ACs to BMDMs at a 3:1 (AC–macrophage) ratio for 45 min.
2. Remove unbound ACs by rinsing with serum-free DMEM twice, then fix BMDMs with 4% formaldehyde for 10 min followed by three rinses with 1× PBS.
3. Incubate macrophages with Cy3-labeled streptavidin (1:1000 dilution in 1× PBS) for 30 min followed by three rinses with 1× PBS.
4. Capture images on an epifluorescence microscope and quantify the following: (1) total macrophages/image; (2) all $PKH67^+$ macrophages/image; (3) $PKH67^+$ $Cy3^-$ macrophages/image; and (4) $PKH67^+$ $Cy3^+$ macrophages/image.
5. Internalized ACs are quantified as: ($PKH67^+$ $Cy3^-$ macrophages)/($PKH67^+$ $Cy3^-$ macrophages + $PKH67^+$ $Cy3^+$ macrophages); and uninternalized ACs are quantified as: ($PKH67^+$ $Cy3^+$ macrophages) / ($PKH67^+$ $Cy3^-$ macrophages + $PKH67^+$ $Cy3^+$ macrophages). The sum of internalized and uninternalized ACs yields the percent of ACs either adherent to or internalized by macrophages.
6. Figure 1 shows an example of this procedure using cytochalasin D, a fungal toxin that disrupts actin filaments and inhibits actin polymerization. The results show a predicted lowering of AC interactions with macrophages (~55% decrease) and a more substantial reduction in AC internalization (~85% decrease).

4 Notes

1. This regimen of day 1—splitting, day 3—feeding, and day 5—collection must be followed as changing these days may lead to alterations in the concentration of M-CSF1 (the factor produced by L929 cells that differentiates bone marrow cells into macrophages) and causes the production of metabolic byproducts that lead to inconsistent macrophage differentiation. Alternatively, M-CSF1 from commercial sources can be used (typical concentration of 25 to 50 ng/mL).

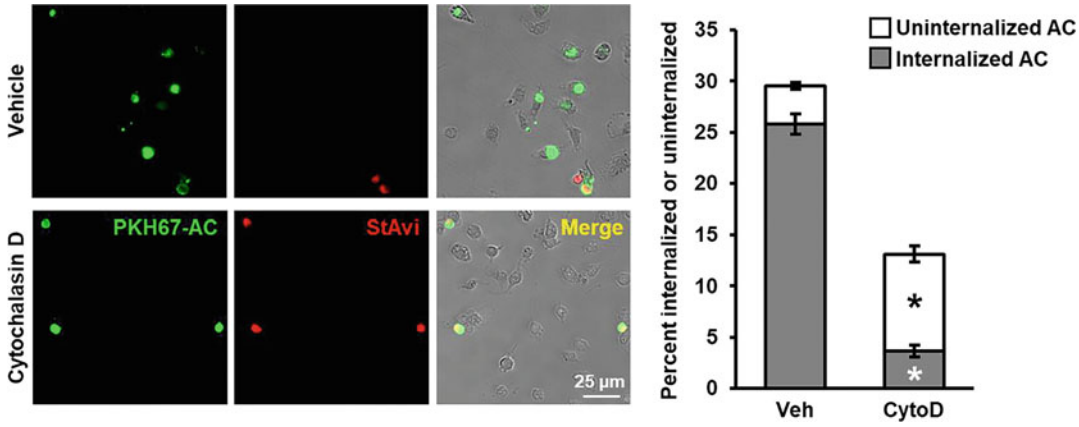

Fig. 1 Dual fluorescence efferocytosis assay. Macrophages were either treated with Cytochalasin D (5 μM for 30 min) or vehicle treated. Fluorescently labeled and biotinylated ACs were then incubated with macrophages at a 3:1 (AC–macrophage) ratio for 45 min. Unbound ACs were rinsed and macrophages were fixed with 4% formaldehyde. After rinsing, macrophages were incubated with Streptavidin-Cy3. Following rinsing, images were captured on an epifluorescence microscope and quantified ($n = 4$ biological replicates). Asterisk indicates statistical significance compared to the respective group for vehicle-treated macrophages

2. Isolating bone marrow from femurs and tibias from both legs of one mouse yields enough cells for four confluent 10 cm^2 petri dishes by the time macrophages are fully differentiated.
3. Cell scrapers or Ca^{2+} and Mg^{2+}-free PBS containing EDTA is used to detach BMDMs from petri dishes for replating purposes.
4. Leaving cells in Diluent C for an extended period results in cell death.
5. A cell concentration greater than 1×10^7 cell/mL will result in heterogeneous staining.
6. UV wavelength used is 254 nm.
7. Monitor cells for morphological features of apoptosis every 30 min. This method consistently yields at least 85% apoptosis as assessed by Annexin V staining.

Acknowledgments

This work was supported by an NIH grant, R00 HL145131.

References

1. Yurdagul A Jr, Doran AC, Cai B, Fredman G, Tabas IA (2017) Mechanisms and consequences of defective efferocytosis in atherosclerosis. Front Cardiovasc Med 4:86. https://doi.org/10.3389/fcvm.2017.00086
2. Wang Y, Subramanian M, Yurdagul A Jr, Barbosa-Lorenzi VC, Cai B, de Juan-Sanz J, Ryan TA, Nomura M, Maxfield FR, Tabas I (2017) Mitochondrial fission promotes the continued clearance of apoptotic cells by

macrophages. Cell 171(2):331–345e322. https://doi.org/10.1016/j.cell.2017.08.041

3. Esmann L, Idel C, Sarkar A, Hellberg L, Behnen M, Moller S, van Zandbergen G, Klinger M, Kohl J, Bussmeyer U, Solbach W, Laskay T (2010) Phagocytosis of apoptotic cells by neutrophil granulocytes: diminished proinflammatory neutrophil functions in the presence of apoptotic cells. J Immunol 184(1):391–400. https://doi.org/10.4049/jimmunol.0900564

Chapter 19

Investigation of Mitochondrial Bioenergetic Profile and Dysfunction in Atherosclerosis

Yee-Hung Chan and Dipak P. Ramji

Abstract

Mitochondrial function and activity are key indicators of overall cell health and mitochondrial dysfunction is closely associated with disruptions in normal cellular function. Altered mitochondrial function and cellular metabolism has been implicated in processes involved in ageing and associated pathologies. In atherosclerosis, compromised mitochondrial respiration can promote plaque instability and other processes that encourage pathogenesis and dysfunction. For example, increasing respiration promotes vascular smooth muscle cell (VSMC) proliferation and attenuates macrophage and VSMC apoptosis. Use of Agilent Seahorse technology to study mitochondrial bioenergetics has largely replaced previous outdated methods which provided limited insight into mitochondrial function and were associated with various issues. This chapter describes the use of Seahorse Agilent technology (Mito Stress Test) to study key parameters of mitochondrial respiration on cultured cells relevant to atherosclerosis.

Key words Mitochondrial respiration, Cellular metabolism, Mito Stress Test, Agilent Seahorse technology, XFe96 Analyzer

1 Introduction

Mitochondria are the major source of ATP production in the cell with central roles in various other processes, including the maintenance of ionic homeostasis, enabling muscular function and facilitating extracellular communication. Mitochondrial function is vital for energy-consuming cellular repair pathways activated in response to increased deposits of proteins damaged by reactive oxygen/nitrogen species (ROS/RNS). The mitochondria is also a major source of ROS generation [1]; elevated ROS production, along with dampened antioxidant activities can lead to oxidative stress. Mitochondrial damage can compromise cellular function; mitochondrial dysfunction has been implicated in, and is associated with, various pathologies. Mitochondrial DNA (mtDNA) is particularly prone to damage by ROS due to its close proximity to the site of ROS generation as well as lack of protective histones [2]. In

Dipak P. Ramji (ed.), *Atherosclerosis: Methods and Protocols*, Methods in Molecular Biology, vol. 2419,
https://doi.org/10.1007/978-1-0716-1924-7_19,
© The Author(s), under exclusive license to Springer Science+Business Media, LLC, part of Springer Nature 2022

atherosclerosis, endogenous mtDNA damage has been correlated with significantly decreased mitochondrial respiration; increasing respiration can promote vascular smooth muscle cell (VSMC) proliferation and attenuate VSMC/macrophage apoptosis [3]. Therefore, monitoring changes in metabolism by studying mitochondrial bioenergetics can provide valuable insights into cellular function/dysfunction [4].

Evaluation of mitochondrial function in cultured cells was previously carried out by measurement of either oxygen consumption of isolated mitochondria or activity of specific enzymes [4]. Whilst these approaches can provide an insight to mitochondrial function, the physiological perspective is lacking [5, 6] due to the very fact that the organelle is studied in isolation, rather than in its natural environment within the cell. Clark electrodes provided a way of quantifying oxygen consumption in cultured cells by removing them from their growth substrate and suspending in a stirred, buffered solution [7]. However, this leads to several issues; in this detached state, many cells undergo anoikis and experience nonlaminar shear (induced by stirring of the oxygen electrode), leading to elevated ROS production and mitochondrial damage, and oxidative stress respectively [8–10]. The effects of ROS and RNS on mitochondrial function in cells are hence difficult to detect using this experimental approach [4]. Additionally, the kinetic information provided is limited to a single component of cellular bioenergetics, and constant oxygen consumption results in decreasing oxygen pressure experienced by the cells or isolated mitochondria, reducing reliability of data by introducing potential artifacts. Alternatives include the extremely sensitive, luminescent ATP assays which measure total energy metabolism. However, cells will adjust their metabolism to maintain a specific ATP budget, and so changes in ATP levels are typically only detected during pathology. Other options include colorimetric based assays, 3-(4,5-dimethylthiazole-2-yl)-2,5-diphenyltetrazolium bromide (MTT)/2,3-bis (2-methoxy-4-nitro-5-sulfophenyl)-5-[(phenylamino) carbonyl]-2H-tetrazolium hydroxide (XTT) and Alamar Blue assays, which are less sensitive than ATP assays, and may be less accurate due to cell toxicity. Furthermore, both luminescent ATP, MTT/XTT, and Alamar Blue assays are destructive and unable to provide kinetic information, and so only provide limited insight into mitochondrial function and bioenergetics.

Agilent Technologies have developed a way to monitor oxygen consumption rate (OCR) from live cells in real time, allowing assessment of mitochondrial function within the context of the cell. Cells are cultured in an appropriate microplate which is placed into an Agilent Seahorse Extracellular Flux (XF) Analyzer machine. The machine uses a collection of sensors to monitor extracellular fluxes of oxygen consumption and acid release. The Mito Stress Test assay has been abundantly used to study mitochondrial

respiration [11–15]. This assay involves continuous measurement of OCR during sequential stimulation by various inhibitor drug compounds that target specific components of the electron transport chain, resulting in measurable changes in OCR. The sensor cartridges used in the assay contain integrated injection ports which add modulators of respiration (i.e., inhibitor compounds) into the cell membrane. Oligomycin inhibits ATP synthase of complex V, carbonyl cyanide 4-(trifluoromethoxy)phenylhydrazone (FCCP) uncouples oxygen consumption from ATP production, and rotenone and antimycin A inhibits complex I and complex III respectively, completely shutting down mitochondrial respiration. FCCP stimulation mimics a physiological increase in "energy demand" by collapsing the proton gradient and disrupting mitochondrial membrane potential, resulting in uninhibited electron flow through the electron transport chain and maximal oxygen consumption by complex IV. From these changes in OCR, measurement of multiple parameters is possible; basal respiration, ATP production, proton leak, maximal respiration, spare respiratory capacity, and nonmitochondrial respiration (*see* Fig. 1 and Table 1). This method provides real time kinetic information of multiple parameters and hence a much more comprehensive view of cellular bioenergetics as opposed to the endpoint assays mentioned previously. Additionally, the label-free and nondestructive nature of this approach enables ATP or other viability and proliferation assays to be carried out post analysis, which generates further information and enables data normalization. Therefore, Seahorse analysis is a high-throughput method for studying parameters of mitochondrial bioenergetics; glycolysis can also be studied using a different assay kit (e.g., glycolytic rate assay). This chapter describes the use of the Mito Stress Test to monitor changes in cellular metabolism by studying mitochondrial respiration.

2 Materials

1. Cell culture model system.
2. CO_2 incubator set to 37 °C, 5% CO_2, 95% humidity.
3. Non-CO_2 incubator set to 37 °C.
4. Water bath set to 37 °C.
5. Calibrated pH meter.
6. Seahorse XF96 Extracellular Flux Analyzer.
7. Class II laminar flow cabinet.
8. Appropriate cell culture medium, for example, RPMI-1640 supplemented with 10% (v/v) heat-inactivated fetal bovine serum (FBS) and 100 U/mL penicillin and 100 μg/mL streptomycin (pen-strep), if using THP-1 cells (*see* **Note 1**).

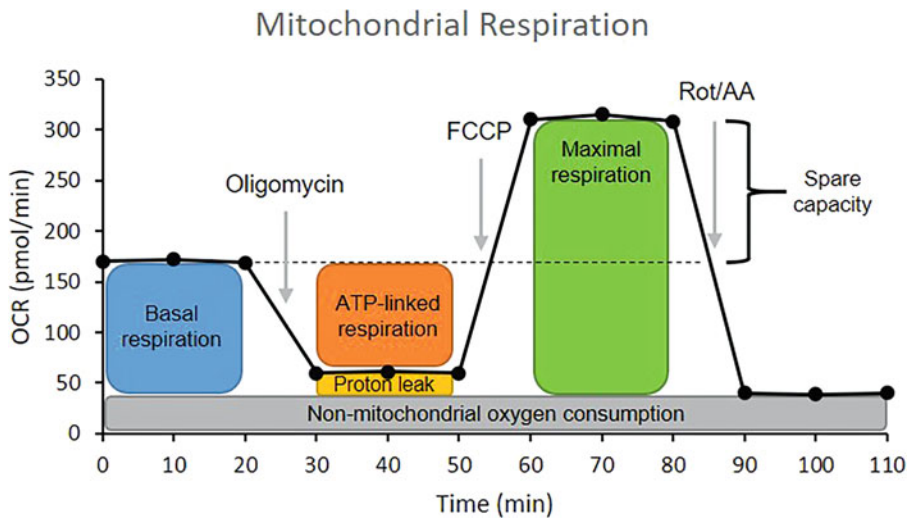

Fig. 1 Parameters of mitochondrial function measured as part of the Mito Stress Test Assay. Sequential stimulations of cells using mitochondrial inhibitor drugs induce changes in oxygen consumption rate (OCR), enabling measurement of multiple parameters. *FCCP* carbonyl cyanide 4-(trifluoromethoxy)phenylhydrazone, *rot/AA* rotenone/antimycin A

Table 1
Measured parameters in the Mito Stress Test Assay

Parameter	Explanation
Basal respiration	Oxygen consumption used to meet the normal cellular ATP demand and resulting from mitochondrial proton leak
ATP production	Reduction in OCR stimulated by oligomycin represents the fraction of basal respiration used to fuel ATP production
Maximal respiration	Point of maximal operation of the respiratory chain that causes rapid oxidation of substrates to meet the metabolic challenge
Spare respiratory capacity	Ability of the cell to respond to an increased energy demand; an indicator of cell fitness/flexibility
Nonmitochondrial respiration	Respiration that occurs independently of the mitochondria

Descriptions of parameters measured as part of the Mito Stress Test assay from Seahorse, Agilent Technologies. *OCR* oxygen consumption rate

9. Sterile 1× phosphate buffered saline (PBS): 155 mM NaCl, 1 mM Na_2HPO_4, 3 mM KH_2PO_4-$7H_2O$, pH 7.4.
10. Cell counter/hemocytometer.
11. Inverted brightfield microscope.
12. Sterile 15- and 50-mL tubes.
13. XF96 cell culture microplate (Seahorse, Agilent Technologies).

14. XF96 sensor cartridge with utility plate (Seahorse, Agilent Technologies).
15. XF Calibrant solution (Seahorse, Agilent Technologies).
16. XF DMEM Base Medium or XF RPMI Medium.
17. Sodium pyruvate.
18. Glucose.
19. L-glutamine.
20. 1 M sodium hydroxide (NaOH) solution.
21. Assay medium: XF Dulbecco's Modified Eagle's Medium (DMEM) Base Medium or XF RPMI (without phenol red), 10 mM sodium pyruvate, 10 mM glucose, 2 mM L-glutamine, adjust to pH 7.3 using 1 M NaOH solution.
22. Seahorse XF Cell Mito Stress Test Kit: oligomycin, carbonyl cyanide 4-(trifluoromethoxy)phenylhydrazone (FCCP), rotenone, and antimycin A (inhibitor drug compounds to be prepared as described in Subheading 3.4).

3 Method

All procedures should be performed under sterile conditions in a Class II cabinet and at room temperature, unless otherwise specified. The following volumes and quantities given are for one 96-well plate of Seahorse analysis (*see* Fig. 2 for a summary of the experimental strategy).

3.1 Cell Preparation (Prior to the Assay)

1. Seed cells at a previously optimized density in the XF96 cell culture microplate (*see* **Notes 2–7**).
2. Do not seed cells into background correction wells of XF96 cell culture microplate—A1, A12, H1, and H12; add only medium in these wells.
3. Remove medium from cells (*see* **Note 8**) and wash the cells with PBS (*see* **Note 9**).
4. Add treatment(s) to cells as necessary and incubate for the desired time in a CO_2 incubator set to 37 °C, 5% CO_2, 95% humidity (*see* **Note 10**).
5. Prepare assay medium (*see* **Notes 11–15**).
6. Prewarm 10 mL of assay medium to 37 °C in a water bath.
7. Remove any treatment or culture medium from the cells via aspiration (*see* **Note 8**) and wash once with 180 μL of assay medium.
8. Add 180 μL of assay medium to all wells.

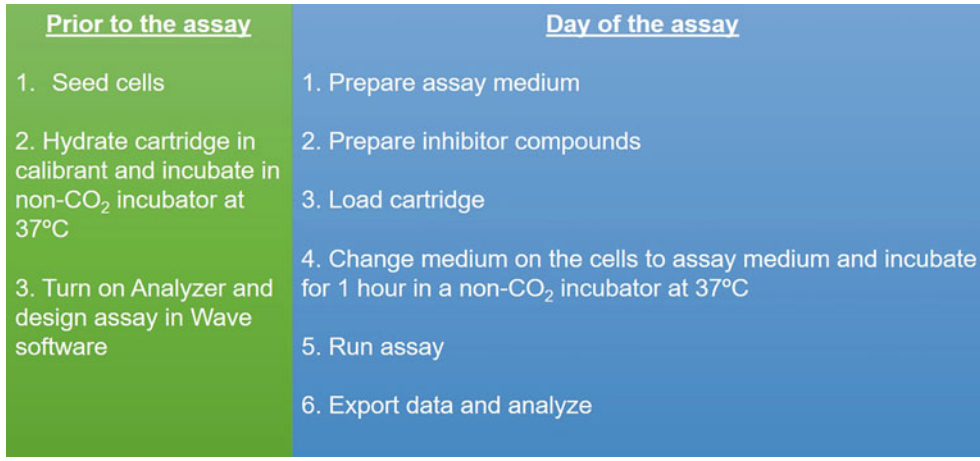

Fig. 2 Summary of the experimental approach of the Mito Stress Test assay. Cells are seeded in advance of the assay; the cartridge must be hydrated on the day prior to performing the assay. Preparation of assay medium and inhibitor drugs should be done fresh and just before running the assay

3.2 Assay Preparation (The Day Before the Assay)

1. Prewarm the XF Calibrant solution to 37 °C in the water bath.
2. Hydrate XF96 sensor cartridge with XF Calibrant solution a minimum of 12 h prior to the assay in a non-CO_2 incubator set to 37 °C (*see* **Note 16**).
3. Switch on Seahorse XFe96 Analyzer machine and open the analyzer software, Wave 2.6, and leave until day of the assay (*see* **Note 17**).

3.3 Setting Up the Software (The Day of the Assay)

1. Set-up an experimental protocol in the Wave software in advance and save the assay template (*see* **Notes 18** and **19**).
2. Check cells under the microscope for any abnormalities (*see* **Note 20**).
3. Incubate cells for 45 min to 1 h in non-CO_2 incubator set to 37 °C.
4. During this incubation time, prepare stock solutions of mitochondrial inhibitor drug compounds as described in the following section.

3.4 Preparation of Drug Compounds

1. Remove inhibitor compounds from the freezer and allow to come to room temperature for 10 min.
2. Add the following volumes of assay medium to the compounds to prepare stock solutions of the inhibitors; 630 μL to oligomycin, 720 μL to FCCP, and 540 μL to rotenone and antimycin A, to obtain 100 μM stocks of oligomycin and FCCP, and 50 μM stocks of rotenone and antimycin A.
3. Gently pipette up and down ~10 times to solubilize the compounds.

Table 2
Example preparation of Mito Stress Test drug compounds

Compound	Stock concentration (μM)	Volume of stock (μL)	Volume of assay medium (μL)	Final volume (μL)	Final concentration (μM)
Oligomycin	100	240	2760	3000	8
FCCP	100	480	2520	3000	16
Rot/AA	50 each	240 of both	1920	2400	5 of each

Note that the final concentrations prepared here are 10× the final concentrations in the wells experienced by the cells. *FCCP* carbonyl cyanide 4-(trifluoromethoxy)phenylhydrazone, *Rot/AA* rotenone/antimycin A

4. Prepare 2–3 mL of each compound for use in the assay (*see* Table 2 for an example) (*see* **Notes 21–23**).
5. Load XF96 sensor cartridge placed in hydrated utility plate with stock solutions of compounds prepared in previous step by adding 25 μL of oligomycin, FCCP and rotenone/antimycin A (rot/AA) mixture to ports A, B and C respectively (*see* **Notes 24–26**).

3.5 Assay

1. For a minimum of 15 min immediately prior to starting the assay, incubate the loaded cartridge in the non-CO_2 incubator set to 37 °C.
2. Follow on-screen prompts and instructions when ready.
3. Calibrate XFe96 Analyzer by loading XF96 sensor cartridge and utility plate into the instrument tray on the right-hand side.
4. After calibration is complete, replace utility plate with preincubated cell culture microplate.
5. Begin assay as prompted by the on-screen instructions (*see* **Note 27**).

4 Notes

1. Heat inactivate FBS by heating at 56 °C for 1 h.
2. An appropriate cell seeding density should be optimized for each cell type depending on cell size and proliferation rate; basal respiration OCR values should fall approximately between 150 and 250 pmol/min. Values above this threshold suggest that a lower cell number/density should be used.
3. Seed cells in a maximum final volume of 200 μL per well.
4. It is important that cells form an evenly distributed monolayer within the microplate wells as clusters/clumps can result in

impaired cell adhesion and subsequent inaccurate rate measurements. A confluency of 70–90% is recommended.

5. As a guideline; for monocytes/macrophages seed 1.5–2.0 $\times$ 10^5 cells/well; and for endothelial cells seed 1.0 $\times$ 10^5 cells/well. For smooth muscle cells, seed at a lower density as these cells are of much larger size in comparison, for example, 2.5–5.0 $\times$ 10^4 cells/well.
6. To differentiate THP-1 monocytes into macrophages, incubate cells with 0.16 μM phorbol 12-myristate 13-acetate (PMA; diluted in supplemented RPMI-1640 medium) overnight (for up to 24 h) before proceeding.
7. It is also possible to coat the wells of the microplate with matrix, such as Matrigel, if required to achieve maximum cell adherence and viability.
8. Remove liquid from the wells by manually pipetting or by using a vacuum aspirator, being careful not to touch the bottom of the wells (i.e., the cells). Leave approximately 20 μL of liquid in the wells to prevent drying out the cells.
9. For washing, add the same volume of PBS per well as that used to seed the cells in **step 1**.
10. Examples of treatments include addition of a therapeutic agent or even a stimulatory/detrimental substance, for example, a proinflammatory cytokine or another inflammation-inducing agent to determine their effect on cellular respiration.
11. Prepare fresh for each assay.
12. Prepare assay medium by adding the supplements included in the assay kit to the XF DMEM Base Medium or XF RPMI medium. It is recommended to start with 1 mM pyruvate, 2 mM L-glutamine, and 10 mM glucose. When the recommended supplement concentrations are used, pH adjustment is not needed.
13. Add the defined volumes of XF supplements to the XF DMEM Base Medium or XF RPMI medium to achieve the desired final concentrations.
14. Medium composition can also be adjusted depending on cell type/desired study conditions, which may be necessary to maintain the viability of certain cell types, for example, increasing the final concentration of L-glutamine.
15. An alternative to commercially available XF Assay Medium can be prepared as follows: Dissolve DMEM Base (8.3 g/L) in 500 μL dH_2O. Dissolve 1.85 g NaCl in 500 mL of dH_2O. Combine both solutions and remove 20 mL from the mixture. To the remaining 980 mL, add 10 mL of 200 mM L-glutamine, 1.1 g of sodium pyruvate, and 15 mg of phenol red. Add 1.8 g

of glucose (giving a final concentration of 10 mM). Prewarm assay medium before pH adjustment.

16. Add 200 μL of the prewarmed XF calibrant solution per well.
17. Leave the analyzer machine on with software open for a minimum of 5 h beforehand to ensure that the temperature is stable at 37 °C by the assay start time.
18. In the software, fill in as much information as possible. Assign the appropriate labels to all wells being used (e.g., "vehicle control") as these will be taken into account in the data report generated after the assay is complete to avoid any confusion.
19. The default instrument protocol does not require modifications and is recommended, although it is possible to alter the number of measurements before/after an injection, or the length of time each measurement is performed. This will affect how the data is acquired during the assay.
20. Cell morphology, health, purity and seeding uniformity should be checked by inspecting under a microscope to ensure cells are healthy, free of contamination and evenly distributed amongst the wells before conducting the assay.
21. Final working concentrations of compounds should be optimized for different cell types/cell lines but tend to fall within the range of 0.5–2.0 μM for oligomycin and 0.125–2.0 μM for FCCP. For most cell types, it is recommended to use 1.5 μM for oligomycin and 0.5 μM for Rot/AA. Note that too much FCCP can diminish responses in OCR, so a titration experiment to find the optimal final concentration is especially important for FCCP.
22. Stock compounds can also be purchased separately and can be prepared as the following as an alternative: Dissolve oligomycin A in dimethyl sulfoxide (DMSO) to make a stock solution of 1 mM; dissolve FCCP in DMSO to make a stock solution of 2 mM; dissolve rotenone in DMSO to make a stock solution of 10 mM; dissolve antimycin A in ethanol to make a stock solution of 10 mM. Inhibitor drugs are stable at −20 °C for up to 1 month; aliquot and avoid repeated freeze–thaw cycles. Handle agents with caution and in accordance with recommended safety precautions as these are acutely toxic.
23. Concentrations loaded into the ports need to be 10× the desired final concentrations in the well.
24. To modify the assay, add test compound into port A and oligomycin, FCCP, and rot/AA into ports B, C, and D, respectively, to inject the test compound prior to injection of the first inhibitor compound, oligomycin. For the negative controls, assay medium should be used in place of the test compound.

25. There are two approaches to loading the injection ports of the sensor cartridge: constant loading volume/variable compound concentration and variable loading volume/constant compound concentration. The first approach is described in this chapter where the same volume of each compound is loaded in each injection port, and each compound is prepared at differing concentrations.
26. The variable loading volume/constant compound approach entails preparing the compound working solutions at a constant concentration and loading a different volume for each compound into the injection port; loading 20, 22, and 25 μL into ports A (oligomycin), B (FCCP), and C (rot/AA), respectively.
27. Data are typically expressed as pmol O_2/min/mkg of protein for standardization and to account for different cell densities among the wells. Data may also be presented as percentage change from baseline/control for comparison. Therefore, it is typical to measure changes in protein concentration after assaying; this can be done using a Bradford assay or an enzyme linked immunosorbent assay (ELISA). Cell viability could also be measured by assaying cell supernatants for lactase dehydrogenase or staining cells with crystal violet solution for example. This is important as changes in proliferation and viability may have occurred between the start and the end of the assay/experiment.

Acknowledgments

We thank the British Heart Foundation for financial support (grants PG/16/25/32097 and FS/17/75/33257).

References

1. Murphy MP (2009) How mitochondria produce reactive oxygen species. Biochem J 417: 1–13
2. Trifunovic A, Wredenberg A, Falkenberg M et al (2004) Premature ageing in mice expressing defective mitochondrial DNA polymerase. Nature 429:417–423
3. Yu EPK, Reinhold J, Yu H et al (2017) Mitochondrial respiration is reduced in atherosclerosis, promoting necrotic core formation and reducing relative fibrous cap thickness. Arterioscler Thromb Vasc Biol 37(12):2322–2332
4. Dranka BP, Benavides GA, Diers AR et al (2011) Assessing bioenergetic function in response to oxidative stress by metabolic profiling. Free Radic Biol Med 51:1621–1635
5. Brand MD, Nicholls DG (2011) Assessing mitochondrial dysfunction in cells. Biochem J 435:297–312
6. Will Y, Hynes J, Ogurtsov VI et al (2006) Analysis of mitochondrial function using phosphorescent oxygen-sensitive probes. Nat Protoc 1:2563–2572
7. Clark LC Jr, Wolf R, Granger D et al (1953) Continuous recording of blood oxygen tensions by polarography. J Appl Physiol 6: 189–193
8. Hwang J, Saha A, Boo YC et al (2003) Oscillatory shear stress stimulates endothelial

production of O_2- from p47phox-dependent NAD(P)H oxidases, leading to monocyte adhesion. J Biol Chem 278:47291–47298

9. De Keulenaer GW, Chappell DC, Ishizaka N et al (1998) Oscillatory and steady laminar shear stress differentially affect human endothelial redox state: role of a superoxide-producing NADH oxidase. Circ Res 82: 1094–1101
10. Li AE, Ito H, Rovira II et al (1999) A role for reactive oxygen species in endothelial cell anoikis. Circ Res 85:304–310
11. Patel M, Yarlagadda V, Adedoyin O et al (2018) Oxalate induces mitochondrial dysfunction and disrupts redox homeostasis in a human monocyte derived cell line. Redox Biol 15:207–215
12. Czajka A, Malik AN (2016) Hyperglycemia induced damage to mitochondrial respiration in renal mesangial and tubular cells: implications for diabetic nephropathy. Redox Biol 10: 100–107
13. McCrimmon A, Domondon M, Sultanova RF et al (2020) Comprehensive assessment of mitochondrial respiratory function in freshly isolated nephron segments. Am J Physiol Renal Physiol 318:F1237–F1245
14. Chacko BK, Kramer PA, Ravi S et al (2014) The bioenergetic health index: a new concept in mitochondrial translational research. Clin Sci 127:367–373
15. Chacko BK, Kramer PA, Ravi S et al (2013) Methods for defining distinct bioenergetic profiles in platelets, lymphocytes, monocytes and neutrophils, and the oxidative burst from human blood. Lab Invest 93:690–700

Chapter 20

Probing Inflammasome Activation in Atherosclerosis

Yee-Hung Chan and Dipak P. Ramji

Abstract

Atherosclerosis is driven by chronic inflammation in all stages of the disease. Inflammation is fueled by elevated levels of pro-inflammatory cytokines. Interleukins (IL) are cytokines of particular importance in atherosclerosis, due to their key involvement in various pro-atherogenic processes, including infiltration of immune cells to the lesion, stimulation of the production of other pro-inflammatory mediators by other sources, and generation of lipid laden foam cells, all of which contribute to plaque development and progression. Various stimuli that are abundant in atherosclerotic plaques, including oxidized low-density lipoprotein, cholesterol crystals and reactive oxygen species can trigger inflammasome activation. Importantly, activation of the nucleotide oligomerization domain leucine-rich repeat and pyrin domain containing protein 3 (NLRP3) inflammasome activates the caspase-1 protease and results in the generation and release of potent pro-inflammatory cytokines, IL-1β and IL-18. Both cytokines are influential in driving chronic inflammation and atherogenesis. This chapter describes the use of enzyme-linked immunosorbent assay (ELISA) and Western blot to quantify these cytokines in cell supernatant and lysate respectively, after stimulating inflammasome activation in cultured cells.

Key words NLRP3, IL-1β, IL-18, ELISA, Western blot, immunoblotting, cholesterol crystal, lipopolysaccharide

1 Introduction

Atherosclerosis is driven by chronic inflammation that ensues from cholesterol deposition within the arterial wall. Inflammation underlies all stages of the disease, from early atherogenesis through to the onset of clinical manifestations (e.g., myocardial infarction and cerebrovascular accident) [1]. Persistent, nonresolving inflammation results from an imbalance of anti- and pro-inflammatory cytokines in favor of the latter. Interleukins (IL) are a key class of cytokines that are critically involved in the differentiation, polarization, and function of innate and adaptive lymphocytes [2]. IL-1β and IL-18 (part of the IL-1 cytokine family) are two potent pro-inflammatory cytokines, secreted in response to various stimuli and "danger" signals commonly present in atherosclerotic plaques, that

Dipak P. Ramji (ed.), *Atherosclerosis: Methods and Protocols*, Methods in Molecular Biology, vol. 2419,
https://doi.org/10.1007/978-1-0716-1924-7_20,
© The Author(s), under exclusive license to Springer Science+Business Media, LLC, part of Springer Nature 2022

enhance disease severity by promoting processes that facilitate plaque progression and even rupture. Example signals include oxidized low-density lipoprotein (oxLDL), foam cell death and crystalline cholesterol, which can induce activation of the nucleotide oligomerization domain (NOD) leucine-rich repeat and pyrin domain containing protein 3 (NLRP3) inflammasome. Inflammasome assembly and action requires "danger" signals, which activate pattern recognition receptors (e.g., scavenger receptors, toll-like receptors and NOD-like receptors (NLRs)) in macrophages and other immune cells [3, 4]. Specifically, two signals are required for inflammasome activation; a priming signal (e.g., lipopolysaccharide (LPS)), followed by an activation signal (e.g., cholesterol crystals) [5]. The apoptosis-associated speck-like (ASC) protein is an adaptor protein than connects NLR proteins to caspase-1 [6]. Subsequent activation of the caspase-1 protease by the NLRP3 inflammasome, lysosomal destabilization and reactive oxygen species (ROS) release results in cleavage and secretion of mature IL-1β and IL-18 [7]. This inflammasome is hence a major driver of the IL-1 family-mediated proinflammatory signaling, receiving much attention in the context of atherosclerosis. Therefore, detection and measurement of these cytokines in cell supernatant has been widely used in combination with Western blot analysis (also called "immunoblotting") of inflammasome activation markers in cell lysates. This methodological approach hence forms the focus of this chapter.

1.1 Enzyme-Linked Immunosorbent Assay (ELISA)

The enzyme-linked immunosorbent assay (ELISA) is a microplate-based assay technique that enables detection and quantification of soluble compounds (e.g., peptides, proteins, glycoproteins, and hormones). The assay uses a highly specific antibody-to-antigen interaction to enable quantitative measurement. The most used ELISA format is the "sandwich" assay, which indirectly immobilizes and detects the presence of the target macromolecule (*see* Fig. 1). The microplate is first coated with a capture antibody (raised against the antigen of interest); the target antigen contained within the sample is then immobilized and complexed with an enzyme-conjugated detection antibody, which binds to the immobilized antigen. The enzyme used is typically horseradish peroxidase (HRP) or alkaline phosphatase (ALP), and acts to catalyze a reaction that converts the added substrate (usually tetramethylbenzidine (TMB) or 2,2′-azino-bis(3-ethylbenzothiazoline-6-sulfonic acid (ABTS)) into a colored and measurable product. The analyte is ultimately bound between two antibodies (the capture antibody and the detection antibody), hence termed "sandwich" format, each detecting a different epitope of the target antigen, yielding higher sensitivity and specificity compared to other ELISA formats. Production of a standard curve using an antigen of known concentration (i.e., the standard) enables determination of the antigen

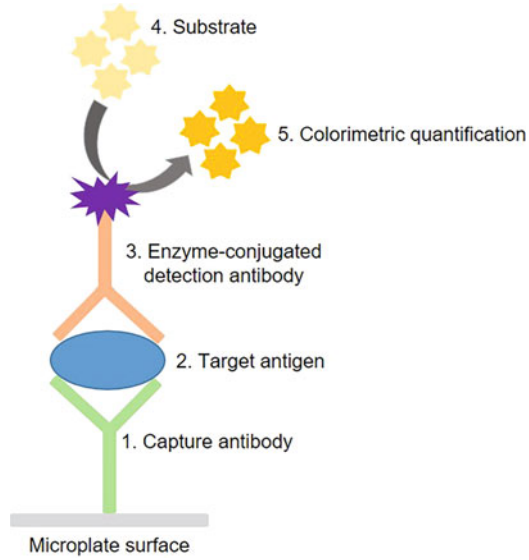

Fig. 1 Diagrammatic illustration of the steps in a sandwich ELISA format. The microplate is coated with capture antibody (raised against the antigen of interest); antigens present in the sample will then bind to the capture antibody. A detection antibody that is conjugated to an enzyme then binds to the target antigen. A substrate is then added to the plate; the enzyme converts the substrate into a colored product which can then be measured using a plate reader

concentration within the samples using the measured optical density (OD) value obtained by the plate reader [8–10].

1.2 Western Blotting

Western blotting enables the detection of an individual protein from a complex mixture of proteins extracted from a range of sample types, including cells and tissues (*see* Fig. 2). Proteins within the sample are first denatured and then separated according to size (molecular weight), typically achieved via sodium dodecyl sulfate–polyacrylamide gel electrophoresis (SDS-PAGE). The proteins are then transferred to a solid support (onto a blotting membrane), and the target protein is identified using appropriate antibodies. The membrane is incubated with a primary antibody that recognizes and binds to a specific target protein, followed by a secondary antibody, which recognizes and binds to the primary antibody. Similar to that used in ELISAs, the secondary antibody may be conjugated to a reporter enzyme (e.g., HRP or ALP) that generates color or light, enabling detection and visualization. The secondary antibody may be visualized via various methods, including staining, immunofluorescence, and even radioactivity. Similar to the principle of the ELISA discussed above, this method enables indirect detection of a specific target protein. Western blotting hence allows

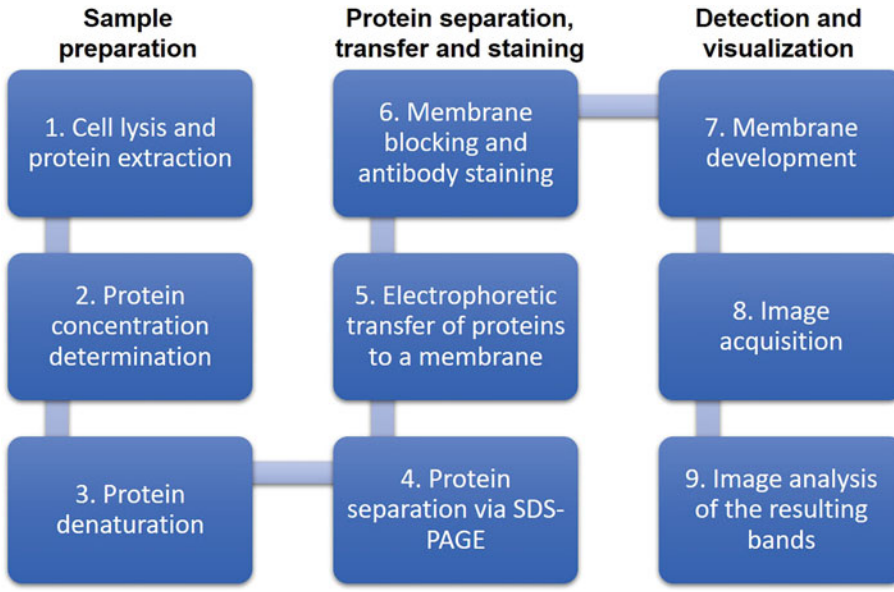

Fig. 2 Summary of key processes involved in performing a Western blot. Abbreviations: SDS-PAGE, sodium dodecyl sulfate–polyacrylamide gel electrophoresis

evaluation of the size of a protein of interest, as well as quantification of protein expression.

Together, these methods enable detection of inflammasome activation via measurement of IL-1β and IL-18 secreted by cells, achieved by ELISA of their supernatant, and confirmed by Western blot analysis of NLRP3-associated proteins.

2 Materials

2.1 Cell Culture

1. Cultured cells (e.g., macrophages, peripheral blood mononuclear cells (PBMCs)) (*see* **Note 1**).
2. 12-well sterile cell culture microplate.
3. Appropriate culture medium: e.g., RPMI-1640 supplemented with 10% (v/v) heat-inactivated fetal bovine serum (FBS), 100 U/mL penicillin and 100 μg/mL streptomycin (pen-strep) if using THP-1 macrophages or human monocyte-derived macrophages (HMDMs).
4. Sterile 1× phosphate buffered saline (PBS): 155 mM NaCl, 1 mM Na_2HPO_4, 3 mM KH_2PO_4-$7H_2O$, pH 7.4.
5. Bovine serum albumin (BSA; Fraction V, sterile filtered).
6. Culture medium containing 0.2% (w/v) BSA in place of FBS (BSA medium) (*see* **Note 2**).
7. Lipopolysaccharide (LPS) and cholesterol crystals (*see* **Note 3**).

8. Cell counter/hemocytometer.
9. Centrifuge and microfuge.
10. Sterile microfuge tubes.
11. Water bath set to 37 °C.
12. Incubator set to 37 °C, 5% CO_2, 95% humidity.
13. Class II laminar flow cabinet.
14. Inverted brightfield microscope.

2.2 ELISA

The following materials and subsequent protocol described are specifically for the DuoSet IL-1β ELISA from R&D Systems, a readily available and commonly used sandwich ELISA kit. The same principle and methods can also be applied to the DuoSet IL-18 ELISA kit from the same company. Other ELISA kits from other companies may still be used to measure the concentration of these cytokines released by the cells.

1. Human IL-1β DuoSet ELISA: Contains human IL-1β Standard, human IL-1β capture antibody, human IL-1β detection antibody, and streptavidin-HRP.
2. DuoSet ELISA Ancillary Reagent kit: Contains clear microplates (*see* **Note 4**), ELISA plate sealers (adhesive strips), color reagent A (1× H_2O_2), color reagent B (1× tetramethylbenzidine (TMB) (*see* **Note 5**), stop solution (1×; 2 M H_2SO_4), reagent diluent (RD; 10× concentrate; 1% (w/v) BSA in PBS, pH 7.2–7.4, 0.2 μm filtered), wash buffer (25× concentrate; 0.05% (v/v) Tween® 20 in PBS, pH 7.2–7.4) (*see* **Notes 6** and **7**).
3. 1× wash buffer (working concentration): Dilute 25× wash buffer 1:25 with dH_2O (*see* **Note 6**).
4. 1× RD (working concentration, also used as blocking buffer): Dilute 10× RD 1:10 with PBS (*see* **Note 6**).
5. Sterile 1× PBS: 137 mM NaCl, 2.7 mM KCl, 8.1 mM Na_2HPO_4, 1.5 mM KH_2PO_4, pH 7.2–7.4, 0.2 μm filtered (*see* **Note 8**).
6. Clean paper towels.
7. Multichannel pipettes and sterile reagent reservoirs.
8. Squirt bottle/manifold dispenser/auto-washer.
9. Vortex mixer.
10. Microplate reader (spectrophotometer).

2.3 Western Blotting

1. Radioimmunoprecipitation assay (RIPA) buffer (cell lysis buffer—ice-cold): 150 mM NaCl, 1% Triton™ X-100, 0.5% sodium deoxycholate, 0.1% sodium dodecyl sulphate (SDS),

50 mM Tris–HCl, pH 8.0, protease inhibitor cocktail (*see* **Note 9**).

2. Ice-cold, sterile 1× phosphate buffered saline (PBS): 155 mM NaCl, 1 mM Na_2HPO_4, 3 mM KH_2PO_4 $7H_2O$, pH 7.4.
3. 2× Laemmli buffer (loading buffer): 4% (w/v) SDS, 10% (v/v) 2-mercaptoethanol, 20% (v/v) glycerol, 0.004% (w/v) bromophenol blue, 0.125 M Tris-HCl, pH 6.8.
4. 1× Running buffer (tris–glycine–SDS): 25 mM Tris base, 190 mM glycine, 0.1% (w/v) SDS, pH 8.3.
5. Transfer buffer (for semidry apparatuses): 48 mM Tris, 39 mM glycine, 20% (v/v) methanol, 0.04% (w/v) SDS (*see* **Note 10**).
6. 1× Tris-buffer saline with Tween 20® (polysorbate 20) (TBST): 100 mL of 10× tris-buffered saline (TBS; 24 g Tris and 88 g NaCl in 900 mL of water; adjust final volume to 1 L and pH to 7.6) and 1 mL of Tween 20 detergent in 900 mL of water.
7. Blocking buffer: 3% (v/v) nonfat milk in 1× TBST or 5% (w/v) BSA dissolved in 1× TBST buffer. Mix well and filter (*see* **Note 11**).
8. Precast 4–20% (w/v) Polyacrylamide protein gel (a discontinuous, precast gel, with a stacking gel component and a resolving/separating gel component) (*see* **Note 12**).
9. Nitrocellulose or polyvinylidene fluoride (PVDF) membrane, 0.45 μm (*see* **Note 13**).
10. dH_2O.
11. 100% methanol (if using PVDF membrane).
12. Filter paper.
13. Ice.
14. Cell scrapers.
15. Precooled microfuge tubes.
16. Molecular weight protein ladder.
17. Microfuge.
18. Protein quantification assay (e.g., Coomassie or Bradford reagent assay kit).
19. Dry block heater.
20. Blotting and Vertical Electrophoresis System including transfer apparatus.
21. PowerPac for power supply.
22. Rocking platform (rocker)/orbital shaker or equivalent.
23. Tweezers or forceps.

24. 10 cm × 10 cm plastic dishes (or equivalent for membrane incubations).
25. Primary antibody (anti-NLRP3/ASC/caspase-1) and associated HRP-labelled secondary antibody, including against a housekeeping protein as a loading control (e.g., β-actin).
26. Transparent plastic wrap.
27. High sensitivity chemiluminescence imaging system (or another appropriate imaging system compatible for the antibody used).

3 Methods

3.1 Cell Priming and Stimulation

Conduct all procedures in this section using aseptic technique under sterile conditions (i.e., using sterile equipment in a Class II cabinet).

1. Seed cells at an appropriate density in compatible culture medium prewarmed to 37 °C (e.g., for macrophages, seed 5×10^5 in 1 mL/well) in a 12-well plate (*see* **Note 14**).
2. Place the plate back in the incubator for a minimum of 1 h undisturbed, to allow adherence of the cells to the wells.
3. Remove the culture medium from the wells via aspiration, taking care not to disturb the adhered cells.
4. Wash cells by adding 1 mL/well of PBS and then removing this via aspiration.
5. Prime cells by incubating with 100 ng/mL LPS in BSA medium for a minimum of 3–6 h and typically up to 24 h at 37 °C (*see* **Notes 15–17**).
6. Wash the cells as described in **step 4**.
7. Stimulate cells by incubating with 0.5 mg/mL cholesterol crystals in BSA medium for 6–24 h at 37 °C (*see* **Note 18**).
8. Collect cell supernatants via aspiration using a pipette and transfer to separate microfuge tubes.
9. Centrifuge at 9000 × *g* for 10 min at room temperature to pellet any contaminating crystals.
10. Transfer the supernatant into new microfuge tubes and prepare various dilutions of the supernatants using BSA medium: undiluted, 1:2, 1:5, 1:10, 1:100, 1:1000, and so on (*see* **Note 19**).
11. Store at −20 °C (short-term) or −80 °C (long-term) for future use or proceed with the ELISA.

3.2 ELISA

3.2.1 Day Prior to Assay

1. Prepare diluted capture antibody. Using the kit for the first time, reconstitute the contents (240 μg) in 550 μL of PBS, giving a stock concentration of 480 μg/mL. Dilute the stock with PBS to give final concentration of 4 μg/mL (e.g., for 96 wells, add 80 μL of stock to 9520 μL of PBS) (*see* **Note 20**).
2. Add 100 μL of the diluted capture antibody to all wells of the microplate (provided in the ELISA kit) to be used with a multichannel pipette and a sterile reagent reservoir.
3. Seal the plate using the transparent adherent plastic provided in the kit.
4. Incubate the plate overnight at room temperature until the next day.

3.2.2 ELISA

1. Remove the capture antibody from the wells via aspiration or decanting.
2. Wash wells 3× with wash buffer; fill each well with ~400 μL of wash buffer using a squirt bottle, manifold dispenser or autowasher. After the last wash, blot plate against clean paper towels by tapping firmly for several times (*see* **Notes 21** and **22**).
3. Perform blocking by adding 300 μL of blocking buffer (1× RD) to the wells.
4. Incubate for 1 h at room temperature.
5. Prepare the 7-point standard; dilute 3.7 μL of stock (of the provided standard) with 996.3 μL of 1× RD and mix well by vortexing briefly. Prepare twofold serial dilutions as shown in Fig. 3.
6. Remove blocking buffer from wells via aspiration or decanting.
7. Wash wells 3× with wash buffer; fill each well with ~400 μL of wash buffer using a squirt bottle, manifold dispenser or autowasher. After the last wash, blot plate against clean paper towels by tapping firmly for several times (*see* **Note 22**).
8. Add 100 μL of samples and standards to the wells and seal the plate (*see* **Note 23**).
9. Incubate for 2 h at room temperature.
10. Empty the contents of the wells via aspiration or decanting.
11. Wash wells as described in **step 7**.
12. Prepare working solution of detection antibody: If using for the first time, reconstitute the 12 μg in 1 mL of 10× RD, giving a stock concentration of 12 μg/mL. Dilute with 1× RD to give a final concentration of 200 ng/mL (e.g., for 96 wells, add 160 μL of stock to 9440 μL of 1× RD) (*see* **Note 20**).
13. Add 100 μL of diluted detection antibody to each of the wells.

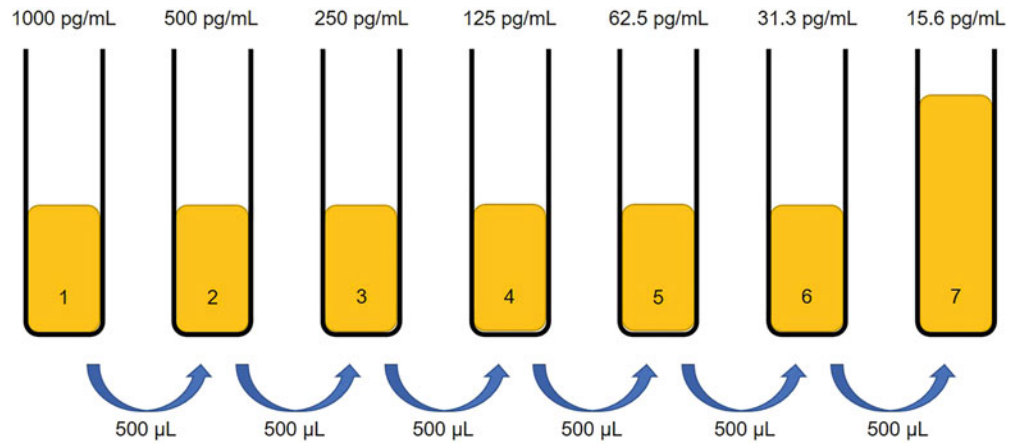

Fig. 3 Preparation of a 7-point standard using serial dilution. Prepare 7 microfuge tubes in a rack and label 1–7. In tube 1, prepare the high standard by diluting 3.7 µL of stock (of the provided standard) with 996.3 µL of 1× RD and mix well by vortexing briefly. In tubes 2–7, add 500 µL of 1× RD. Transfer 500 µL of the contents of tube 1 into tube 2 and vortex tube 2 briefly to mix well. Transfer 500 µL of the contents of tube 2 into tube 3 and vortex tube 3 briefly to mix well etc., until tube 7 has been prepared, as shown. Note that all other tubes will have a final volume of 500 µL whereas tube 7 will have a final volume of 1000 µL. The resulting final concentrations for each tube are shown at the top and are now ready to be assayed along with the samples

14. Incubate for 2 h at room temperature.
15. Remove the detection antibody from wells via aspiration or decanting.
16. Wash wells as described in **step 7**.
17. Prepare working solution of streptavidin-HRP: Dilute 1:40 for final working concentration (e.g., for 96 wells, add 240 µL of the stock to 9360 µL of 1× RD) (*see* **Notes 20** and **24**).
18. Add 100 µL of working solution streptavidin HRP to wells.
19. Cover with foil and incubate for 20 min at room temperature.
20. Remove streptavidin HRP from wells via aspiration or decanting.
21. Wash wells as described in **step 7**.
22. Prepare working substrate solution: Combine equal volumes of Color Reagent A and Color Reagent B (e.g., for 96 wells, add 4.8 mL of Color Reagent A to 4.8 mL of Color Reagent B) (*see* **Note 20**).
23. Add 100 µL of working substrate solution to the wells.
24. Cover with foil and incubate for 20 min at room temperature (*see* **Note 25**).
25. Add 50 µL of stop solution to each well.
26. Tap the plate gently to mix well.

27. Measure absorbance (OD) at 450 nm in a spectrophotometer (plate reader).
28. Using the absorbance readings, plot a standard curve: increasing concentration on the x-axis and increasing OD on the y-axis.
29. Calculate the antigen concentration of the samples (*see* **Note 26**).

3.3 Western Blotting

All steps for protein extraction from cells or tissue (fresh or frozen) must be carried out at 2–8 °C.

3.3.1 Cell Lysis and Protein Extraction

1. After removing cell supernatants for ELISA, place the cell culture plate containing the remaining cells on ice and discard any residual culture medium via aspiration with a pipette.
2. Wash cells by adding 1 mL of ice-cold PBS per well.
3. Remove the PBS from wells via aspiration.
4. Add sufficient volume of ice-cold cell lysis buffer to the cells; the volume depends on the cell number/size of the cell culture vessel used (e.g., ~60 μL of buffer per well for 12-well plate) (*see* **Note 27**).
5. Scrape adherent cells off the culture plate surface using a cold plastic cell scraper.
6. Gently transfer the cell suspension into a precooled microfuge tube (*see* **Note 28**).
7. Maintain constant agitation (e.g., by placing on an orbital shaker) for 30 min at 4 °C (*see* **Note 29**).
8. Centrifuge tubes at 4 °C for 20 min at 16,000 × *g*.
9. Gently remove the tubes from the centrifuge and place on ice.
10. Aspirate the supernatant and transfer to a fresh tube kept on ice.
11. Discard the pellet and proceed with the supernatant (keep on ice) or store at −80 °C for future use.

3.3.2 Sample Preparation for SDS-PAGE

1. Remove a small volume of lysate to perform a protein quantification assay to determine the protein concentration for each cell lysate (*see* **Notes 30** and **31**).
2. Determine an appropriate concentration that can be obtained from all samples (e.g., 50 μg). Transfer this volume of lysates to new microfuge tubes to standardize the protein concentration amongst all the samples (*see* **Note 32**).
3. Add dH_2O to the tubes to equalize the final volume.
4. Add an equal volume of 2× Laemmli buffer to each sample and mix by pipetting up and down a few times (*see* **Note 33**).

5. To reduce and denature the samples, heat at 95–100 °C for 5 min on a dry block heater (*see* **Note 34**).
6. Centrifuge the samples at 16,000 × *g* for 5 min.

3.3.3 Loading and Electrophoresis of the Gel for SDS-PAGE

1. Assemble the rack/gel rig according to the manufacturer's instructions.
2. Pour adequate 1× running buffer into the electroporator to cover the gel completely and place the gel inside.
3. Load equal quantities of protein into the wells of the gel along with a molecular weight marker (the volume loaded into the lanes depend on their size; refer to the manufacturer's guidance) (*see* **Note 35**). As a guideline, load 20–30 μg of total protein from cell lysate, or 10–100 ng of purified protein.
4. Connect to a power supply and perform electrophoresis at 80–100 V (for stacking gel) for approximately 1 h. Once the samples enter the resolving gel, increase the voltage to 100–150 V until the bromophenol blue dye front reaches the end of the gel (*see* **Notes 36** and **37**).

3.3.4 Transferring the Protein from the Gel to the Membrane

After protein separation, the transfer of the proteins from the gel to a solid support, that is, a flexible membrane (nitrocellulose or PVDF) enables easier handling and can be achieved using electricity ("electroblotting"). This can be done using wet (tank) or semidry apparatuses (both of which require transfer buffer and a transfer unit), whereby an electric field oriented perpendicular to the gel surface induces protein movement from the gel to the membrane.

For a PVDF membrane, the following equilibration steps are required.

1. Cut the PVDF membrane to an appropriate size according to the size of the prepared gel.
2. Fill a plastic dish with methanol and submerge the membrane for 1–2 min.
3. Remove the methanol.
4. Submerge the membrane in cold transfer buffer and incubate for 5 min. For a nitrocellulose membrane, only this step is required for equilibration; do not incubate in methanol.
5. Cut 6 filter paper sheets to the same area measurements as that of the prepared gel.
6. For semidry apparatuses, wet the sponges and filter papers in 1× transfer buffer.
7. Prepare the "sandwich" stack as illustrated in Fig. 4, ensuring no air bubbles are present between the gel and the membrane (*see* **Notes 38** and **39**).

Fig. 4 Example of a prepared stack ("sandwich") for electrophoretic protein transfer. The membrane is placed between the gel surface and the positive electrode in a sandwich; the perpendicularly oriented electric field causes the proteins to move out of the gel and onto the membrane. The sponges and filter papers at each end offer protection to the gel and blotting membrane

8. Transport the prepared stack to the transfer apparatus (blotter unit) placed on ice to maintain 4 °C.
9. If using wet (tank) blotting, add sufficient volume of 1× transfer buffer to the apparatus to completely cover the stack (the sandwich is placed between positive and negative electrodes and submerged in 1× transfer buffer to which an electrical field is applied).
10. Turn on the power source and set an appropriate voltage (~120 V) to begin electrophoretic protein transfer for approximately 90 min (*see* **Note 40**).
11. Dismantle the gel rig and remove the polyacrylamide gel from between the glass plates (*see* **Note 41**).

3.3.5 Antibody Staining

1. Handle the membrane carefully using tweezers or forceps, as necessary.
2. Block the membrane by submerging the membrane in blocking buffer in a plastic dish and incubate for a minimum of 1 h (or overnight) at room temperature (or 4 °C) (*see* **Note 42**).
3. Remove the blocking buffer and wash the membrane by submerging in 1% TBST in a plastic dish and incubating for 1 min at room temperature.
4. Submerge the membrane in primary antibody diluted in blocking buffer according to the manufacturer's recommendations in a plastic dish and incubate for a minimum of 2 h at 4 °C with agitation (*see* **Notes 43–45**).
5. Remove the primary antibody solution.
6. Wash the membrane 3× by submerging in 1× TBST in a plastic dish and incubating for 5 min each (*see* **Note 46**).
7. Submerge the membrane in secondary antibody diluted in blocking buffer according to the manufacturer's

recommendations in a plastic dish and incubate for 1–2 h at room temperature with agitation (*see* **Notes 44** and **45**).

8. Wash the membrane 3× by submerging in 1× TBST in a plastic dish and incubating for 5 min each (*see* **Note 46**).
9. Remove any remaining residual buffer and cover the membrane in transparent plastic wrap.
10. Acquire image of the membrane using darkroom development techniques for chemiluminescence, or normal image scanning methods for colorimetric detection (*see* **Notes 47–52**).

4 Notes

1. Inflammasome activation may be measured in myeloid and lymphoid cells so these cell types may also be used.
2. FBS contained within the culture medium may interfere with the ELISA and so must be substituted for BSA prior to extracting the cell supernatant for assay.
3. To obtain cholesterol crystals from cholesterol powder, dissolve this in 95% (v/v) ethanol at a concentration of 12.5 g/L and then heat to 60 °C. Filter the solution through a Whatman paper to remove any remaining powder/undissolved cholesterol and leave the solution at room temperature overnight to allow crystallization. Collect the formed crystals and autoclave to sterilize. Grind the crystals using a Dounce homogenizer (or equivalent) to obtain crystals of equal size and store at −20 °C until use.
4. Special absorbent plates ensure the adherence of the antibody/antigen to the surface. Alternatively, NUNC immune plates may be used.
5. May cause skin, eye and respiratory irritation. Avoid contact and inhalation.
6. Store at 4 °C until use.
7. Avoid microbial contamination of reagents and buffers by using sterile consumables and carrying out procedures under sterile conditions where possible whilst minimizing exposure of buffers to air etc.
8. Use of PBS made from tablets may result in interference in the assay.
9. This buffer is suitable for whole cell extracts, membrane-bound proteins, and nuclear proteins. Note that protein-protein interactions will be disrupted but the ionic detergents will bring proteins into solution more readily. It is also possible to use NP-40 buffer: 150 mM NaCl, 1% (v/v) NP-40 or Triton

X-100, 50 mM Tris, pH 8.0, which is suitable for cytoplasmic and membrane-bound proteins, and whole cell extracts.

10. The low ionic strength and low conductivity of this transfer buffer is optimal for tank (wet) blotting and some semidry apparatuses. Protein transfer can be done in wet or semidry conditions. Wet conditions may be beneficial to avoid the gel drying out and is preferred for larger proteins. Note that the transfer buffer composition is different for wet tank blotting; 25 mM Tris base, 190 mM glycine, 20% (v/v) methanol, pH 8.3 (for proteins larger than 80 kDa, include 0.1% (w/v) SDS). However, as the semidry approach entails wetting the filter paper, gel and membrane in transfer buffer, advantages include conservation of buffer volumes, production of less heat, and reduced band distortion (yielding better quality bands).
11. Choice of blocking buffer depends on the protein to be detected and antibody used. For example, BSA blocking solution is preferable for phosphorylated protein detection, as milk contains casein (a phosphoprotein and biotin) and may cause interference. Although usually preferred, nonfat milk may not be compatible with all antibodies. Always follow the manufacturer's guidance for the antibody being used.
12. The percentage polyacrylamide gel used is dependent on the size of the protein. Stain-free, precast polyacrylamide protein gels with a 4–15% gradient (optimum separation range of 20–250 kDa) may also be used. Using commercially available precast gels may be more convenient to manually preparing gels from scratch. Always check the manufacturer's recommended buffer compositions to be used with the polyacrylamide gel.
13. PVDF membranes possess higher protein binding capacity and may offer better protein retention, strength (mechanical support) and chemical compatibility compared to nitrocellulose. However, PVDF may also result in increased background and so thorough and careful washing is very important.
14. The cell density used should be adjusted according to the size of the culture vessel being used and hence may require optimization.
15. The indicated LPS concentration should be used as a guide as it is possible to use other concentrations according to published studies (e.g., 50 pg/mL [11]; 10 [12], 50 [13], and 100 [14] ng/mL; 1 μg/mL [15]) and hence incubation time needs to be adjusted according to the concentration used. Priming leads to activation of the nuclear factor-κB transcription factor together with upregulation of inflammasome components and pro-IL-

1β via the stimulation of pattern recognition receptors such as membrane Toll-like receptors (see [5] for review).

16. In some circumstances, priming with LPS etc. may not be required as in the case of PMA-differentiated THP-1 macrophages, as the PMA itself may act as a priming signal (and IL-1β can be detected from these cells without stimulation). Additionally, older THP-1s may spontaneously differentiate and produce cytokines that encourage this differentiation; this may hence result in no changes between the negative and positive control.
17. The presence of contaminants (e.g., mycobacteria) may elevate the baseline and also lead to similar results between the negative and the positive control.
18. The incubation time may require optimization but generally falls between 6 and 24 h based on published studies using 0.5 mg/mL of cholesterol crystals [15, 16]. Other agents may also be used to stimulate NLRP3 inflammasome activation (see [5, 17–19] for reviews) (e.g., 0.5 mg/mL calcium phosphate crystals or monosodium urate crystals [20] (250 μg/mL of the latter has also been used [21]); 3 mM [22] or 5 mM ATP [14]; 5 μM nigericin [14]).
19. This is vital when performing the assay for the first time in order to determine the optimal dilution factor for the samples and to ensure that the samples fall within the detection range/range of the standard curve.
20. Prepare fresh for each assay.
21. Complete removal of the solution at each step is essential for good assay performance.
22. Thorough and consistent washing is imperative for assay performance. Wash buffer should be dispensed with sufficient force and removed completely from the wells via aspiration or decanting. After the last wash, remove any remaining wash buffer by inverting the plate and blotting against clean paper towels forcefully multiple times.
23. Samples and standards should be assayed in duplicate as a minimum. A blank must also be included (1× RD) to enable background subtraction.
24. Light sensitive; carry out all incubations at room temperature but protected from light from this point onward.
25. As H_2O_2 contained within the substrate solution is the substrate for HRP, a blue color change is induced.
26. The antigen concentration can be calculated using the OD value at 450 nm and the formula of the standard curve (using

antigens of a known concentration). Any dilution factors used also need to be accounted for via multiplication.

27. Refer to the manufacturer's instructions for the lysis buffer being used. Generally, use 1 mL per 10^7 cells/100 mm dish/150 cm^2 flask; 0.5 mL per 5×10^6 cells/60 mm dish/75 cm^2 flask. Lysis buffer contains detergents, along with protease and phosphatase inhibitors, which solubilize the proteins within the sample. Both the low temperature and presence of protease inhibitors inhibit protein degradation.
28. Alternatively, cells may be treated with trypsin-EDTA solution and washed with PBS to detach them from the plate prior to resuspension in lysis buffer in a microcentrifuge tube.
29. Mechanical agitation is necessary to achieve protein extraction from a tissue sample (e.g., homogenization or sonication).
30. It is important to incorporate a positive control (a known source of protein e.g., purified protein or a control lysate) to confirm staining specificity.
31. The protein concentration in the samples may be quantified using the Bradford assay or Coomassie protein assay reagent, combined with a spectrophotometer at 595 nm. Determination of protein concentration is via comparison with provided standards of known concentration (like that used in the ELISA). If the resulting protein yield is low, try repeating the protocol using a lysis buffer that contains a higher concentration of protease inhibitor cocktail to help increase protein concentration.
32. It is possible to use the formula; concentration = mass/volume, to standardize the protein concentration in each well after protein extraction. Protein concentration standardization is imperative for consistent and robust comparison of samples.
33. The proteins contained within the sample are diluted with Laemmli (loading) buffer containing glycerol, which facilitates the sinking of the samples into the wells of the gel. The presence of a tracking dye, such as bromophenol blue, in the loading buffer enables visualization and monitoring of the separation process.
34. The Laemmli buffer contains β-mercaptoethanol, which disrupts disulfide bridges to enable complete denaturation. Additionally, the SDS present in this buffer provides a great amount of negative charge to the protein, giving an overall negative charge throughout, enabling protein separation according to size. Unless the antibody datasheet indicates that nonreducing and nondenaturing conditions be used, it is typically recommended to reduce and denature the samples. Therefore, after heating in the Laemmli buffer, the proteins will move toward

the positive electrode when a voltage is applied due to the negative charge, enabling electrophoresis of proteins.

35. The SDS-PAGE gel has a stacking gel component and resolving gel component. The higher stacking gel is slightly acidic with a lower acrylamide concentration, creating a porous gel. This results in poor protein separation but enables the formation of thin and defined bands. The resolving (separating) gel is basic, containing a higher polyacrylamide content, reducing the size of the pores of the gel. The proteins thus separate according to their size more efficiently in this gel, as the smaller proteins move much more easily and rapidly in comparison to larger proteins.
36. The exact running time and voltage may require optimization; depending on the size of the gel used, 30 min to an hour may be sufficient. Too high a voltage may lead to overheating and distortion of the bands so the voltage used should be optimized. It is advised to follow the manufacturer's instructions. A reducing gel should be used unless nonreducing conditions are recommended as per the antibody datasheet.
37. When connecting the power source to the tank using the cables, always connect red to red and black to black.
38. Patchy and uneven spotting on the blot is usually attributed to improper transfer. Air bubbles trapped between the gel and the membrane may lead to background signals. An example of a method to remove air bubbles is by rolling using a 10 mL plastic pipette (or another appropriate tool) over the membrane attached to the gel.
39. The close contact of the gel and the membrane helps to ensure the production of a clear image, and the placement of the membrane between the gel and positive electrode enables the migration of the negatively charged proteins from the gel to the membrane.
40. The time and voltage for protein transfer may require optimization. It is recommended to follow the accompanying manufacturer's instructions to begin with.
41. The membrane may be reversibly stained to check for successful/complete transfer of the proteins before proceeding with antibody staining (e.g., using Ponceau S staining).
42. Blocking the membrane prevents antibodies from binding nonspecifically and reduces background. This prevents false-positive results. Blocking time should be optimized based on the protein/antibody being used; refer to the manufacturer's instructions.
43. The antibody is typically diluted in wash buffer, such as PBS or TBST (e.g., 5% (w/v) BSA in TBST solution). Refer to the

manufacturer's instructions/datasheet for the recommended composition of blocking buffer and final concentration of the antibody needed. The blot may simultaneously or subsequently be probed with an antibody against a housekeeping protein (e.g., β-actin or glyceraldehyde 3-phosphate dehydrogenase (GAPDH)) as a/the loading control (i.e., to check for the presence of equal amount of protein).

44. Incubation for 2 h is usually recommended although some antibodies may require overnight incubation. Refer to the manufacturer's instructions/datasheet for the antibody in use.
45. It is important to maintain agitation for the entirety of the incubation time (e.g., using a shaker/with rocking motion) for all antibody incubations to facilitate even binding of the antibody throughout the membrane.
46. Consistent and thorough washing (especially after antibody incubations) is vital to minimize background and remove any unbound antibody. However, be careful not to wash the membrane for an excessive duration as this can result in a reduced signal.
47. Refer to the manufacturer's recommendations for optimal signal development, detection, and visualization.
48. The proteins may be detected using colorimetry, chemiluminescence or fluorescence techniques.
49. Weak signals may be attributed to low antibody or antigen concentration; increasing the exposure time may produce clearer bands. Nonfat milk may mask the antigen leading to a weak signal; use BSA instead or reduce the concentration of milk in the buffer.
50. Atypical bands can occur due to protease degradation and modification of the proteins, which generates bands at unexpected positions. If the protein band appears to be a higher position than expected, reheat the sample to denature the proteins further. Blurry bands may be caused by using too high of a voltage or the presence of air bubbles during transfer, and negative (white) bands on the film are caused by excess protein or antibody.
51. The use of buffers that are too old may also be a contributing factor to high background, along with having too high of an antibody concentration, causing over/excess binding to PVDF membranes. Exposure times may also need optimization as over/excess exposure may produce high background.
52. The data produced by Western blot is often considered semi-quantitative; it enables comparison of protein levels between samples but cannot be utilized as an absolute measure of quantity.

Acknowledgments

We thank the British Heart Foundation for financial support (grants PG/16/25/32097 and FS/17/75/33257).

References

1. Chan Y-H, Ramji DP (2020) A perspective on targeting inflammation and cytokine actions in atherosclerosis. Future Med Chem 12(7): 613–626
2. Garlanda C, Dinarello CA, Mantovani A et al (2013) The interleukin-1 family: back to the future. Immunity 39:1003–1018
3. Prochnicki T, Mangan MS, Latz E (2016) Recent insights into the molecular mechanisms of the NLRP3 inflammasome activation. F1000Res 5:1469
4. Grebe A, Hoss F, Latz E (2018) NLRP3 inflammasome and the IL-1 pathway in atherosclerosis. Circ Res 122:1722–1740
5. Silvis MJM, Demkes EJ, Fiolet ATL et al (2021) Immunomodulation of the NLRP3 inflammasome in atherosclerosis, coronary artery disease, and acute myocardial infarction. J Cardiovasc Transl 14:23–34
6. Wen H, Ting JP-Y, O'Neill LAJ (2012) A role for the NLRP3 inflammasome in metabolic diseases-did Warburg miss inflammation? Nat Immunol 13(4):352–357
7. Tschopp J, Schroder K (2010) NLRP3 inflammasome activation: the convergence of multiple signalling pathways on ROS production? Nat Rev Immunol 10(3):210–215
8. Shah K, Maghsoudlou P (2016) Enzyme-linked immunosorbent assay (ELISA): the basics. Br J Hosp Med (Lond) 77(7): C98–C101
9. Konstantinou GN (2017) Enzyme-linked immunosorbent assay (ELISA). Methods Mol Biol 1592:79–94
10. Engvall E (2010) The ELISA, enzyme-linked immunosorbent assay. Clin Chem 56(2): 319–320
11. Duewell P, Kono H, Rayner KJ et al (2010) NLRP3 inflammasomes are required for atherogenesis and activated by cholesterol crystals. Nature 464:1357–1361
12. Bruchard M, Rebe C, Derangere V et al (2015) The receptor NLRP3 is a transcriptional regulatory of T_H2 differentiation. Nat Immunol 16:859–870
13. Arbore G, West EE, Spolski R et al (2016) T helper 1 immunity requires complement-driven NLRP3 inflammasome activity in $CD4^+$ T cells. Science 352(6292):aad1210
14. Bambouskova M, Potuckova L, Paulenda T et al (2021) Itaconate confers tolerance to late NLRP3 inflammasome activation. Cell Rep 34(10):108756
15. Rajamaki K, Lappalainen J, Oorni K et al (2010) Cholesterol crystals activate the NLRP3 inflammasome in human macrophages: a novel link between cholesterol metabolism and inflammation. PLoS One 5(7):e11765
16. Varghese GP, Folkersen L, Strawbridge RJ et al (2016) NLRP3 inflammasome expression and activation in human atherosclerosis. J Am Heart Assoc 5(5):e003031
17. Jin Y, Fu J (2019) Novel insights into the NLRP3 inflammasome in atherosclerosis. J Am Heart Assoc 8(12):e012219
18. Karasawa T, Takahashi M (2017) The crystal-induced activation of NLRP3 inflammasomes in atherosclerosis. Inflamm Regen 37:18
19. Baldrighi M, Mallat Z, Li X (2017) NLRP3 inflammasome pathways in atherosclerosis. Atherosclerosis 267:127–138
20. Pazar B, Ea H-K, Narayan S et al (2011) Basic calcium phosphate crystals induce monocyte/macrophage IL-1β secretion through the NLRP3 inflammasome *in vitro*. J Immunol 186(4):2495–2502
21. Conforti-Andreoni C, Spreafico R, Qian HL et al (2011) Uric acid-driven Th17 differentiation requires inflammasome-derived IL-1 and IL-18. J Immunol 187:5842–5850
22. Samstad EO, Niyonzima N, Nymo S et al (2015) Cholesterol crystals induce complement-dependent inflammasome activation and cytokine release. J Immunol 192(6): 2837–2845

Chapter 21

Investigation of Platelet Aggregation in Atherosclerosis

Ronan Lordan, Alexandros Tsoupras, and Ioannis Zabetakis

This chapter is dedicated to Prof. Constantinos A. Demopoulos, Emeritus Professor at the University of Athens, Greece, our valued teacher, colleague, and friend.

Abstract

Platelet activation and aggregation is implicated in all stages of inflammation-related atherosclerosis from the initial steps of endothelial dysfunction and plaque formation, to plaque rupture and atherothrombotic events, such as acute coronary syndrome, myocardial infarction, and ischemic incidences. Platelet aggregometry assays are the mainstream for evaluating and monitoring platelet reactivity in such conditions and for the investigation of prophylactic and therapeutic approaches. The most established methodology is light transmittance aggregometry (LTA). Here we describe the appropriate preparation of platelet suspensions from human blood and the methodology of LTA-based assays that is used for basic and clinical research for monitoring and evaluating the activities of several thrombotic mediators, as well as determining the dose efficacy and safety of several pharmaceutical and nutraceutical compounds intended for therapeutic and prophylactic interventions for atherosclerosis.

Key words Atherosclerosis, Inflammation, Thrombosis, Platelet aggregation, Light transmission aggregometry, Platelet-activating factor, Thrombin, ADP, Collagen, Antiplatelet

1 Introduction

Human platelets are critically involved in normal hemostasis, vessel constriction, repair and host defense, as well as in pathological bleeding and thrombosis [1, 2]. Primary hemostasis consists of the interaction between platelets and the vessel wall. At the site of damage of a vessel wall, platelets are rapidly engaged in a sequential functional response, including platelet activation, adhesion, spreading, shape change, aggregation, exposure of a procoagulant surface, and clot formation. The rapid progression of these different capacities causes the activated platelets to form a hemostatic plug that occludes the site of injury to prevent blood loss. An increased risk of bleeding could be present when platelet count is reduced and/or one of their functions is defective. Conversely, when platelets are

Dipak P. Ramji (ed.), *Atherosclerosis: Methods and Protocols*, Methods in Molecular Biology, vol. 2419,
https://doi.org/10.1007/978-1-0716-1924-7_21,
© The Author(s), under exclusive license to Springer Science+Business Media, LLC, part of Springer Nature 2022

improperly over-activated and act in concert with other cells, such as leukocytes, endothelial or smooth muscle cells, they play a crucial part in the onset and progression of several inflammation-related disorders [1–5].

Inflammation and thrombosis are key processes of the hemostatic and immune systems for healing and homeostasis. However, these processes can be left unresolved and continuously triggered by several risk factors. These include a person's age, genetics, diet, poor lifestyle, and pre-existing conditions such as periodontitis and various infections. These risk factors can contribute to the development of atherosclerosis and cardiovascular diseases (CVD) [3, 6].

More specifically, inflammation-related systemic activation of platelets is closely associated to their interaction with activated endothelial cells and leukocytes in the inflamed endothelium of microvessels and the artery wall, which leads to the activation and migration of monocytes into the subendothelium followed by subsequent differentiation into macrophages. The inflammatory microenvironment favors the continuous transformation of macrophages to foam cells via uptake of oxidized low-density lipoprotein (oxLDL) within the subendothelium, and thus the formation of atherosclerotic plaques occurs. As such plaques continue to develop and become unstable, diffused platelets adhere and aggregate within atherosclerotic lesions, forming occluding arterial thrombi that may result in thromboembolic events as a result of plaque rupture. These include stroke and myocardial infarction, which are two of the major causes of morbidity and mortality in the Western world [1, 6–8].

The potent inflammatory and thrombotic mediators, platelet-activating factor (PAF), and thrombin are implicated in such pro-atherosclerotic processes. PAF is a pro-inflammatory phospholipid implicated in the activation of several cells, including leukocytes and endothelial cells. PAF facilitates the interactions of these cells with platelets in an autocrine, paracrine, and juxtacrine manner [1, 2, 9]. Collagen and ADP are other well-established platelet agonists that affect platelet reactivity, for which specific antiplatelet therapies exist against their signaling pathways associated with platelet aggregation and clot formation [10].

The various effects of these platelet agonists were initially considered to occur via different pathways, whereby each agonist binds to a specific membrane G protein-coupled receptor. However, it is now known that the intracellular signaling induced by these platelet agonists is interconnected, thus platelet activation and aggregation seems to be more complex than what was initially thought [1, 3].

Antiplatelet compounds of dietary or pharmacological origin beneficially reduce platelet-related inflammation and platelet reactivity, which can contribute to atherosclerosis [2, 11–15]. The study of compounds that beneficially affect platelet reactivity induced by such inflammatory and thrombotic mediators is of great importance for the design of future therapies against

atherosclerotic diseases. Reliable platelet aggregation tests are required to assess such a wide range of platelet functions, platelet aggregatory agonists, and antiplatelet compounds. Light transmission aggregometry (LTA), firstly developed by Born [16] and O'Brien [17] in the 1960s, is considered the gold standard for testing platelet function and evaluating and monitoring platelet defects. Indeed, these assays have also been adapted to study the effects of various platelet agonists and antiplatelet compounds on platelet reactivity.

LTA detects and quantifies the changes of the transmission of light through a platelet suspension, namely platelet-rich plasma (PRP), washed platelets or gel-filtered platelets, when the platelets are activated and aggregated. Thus, in the presence of a platelet agonist, such as PAF and PAF-like lipid molecules, thrombin, arachidonic acid (AA), ADP or collagen, dose-dependent platelet aggregation occurs, which can be monitored by the synchronous increase of the light transmittance, measured against the stable light transmittance of a blank control of platelet-poor plasma (PPP) [18] (Fig. 1).

In addition, LTA-based assays facilitate the study of the dose efficacy and safety of bioactive compounds affecting platelet reactivity as part of in vitro and ex vivo measurements. Several examples of these applications have been published previously for determining the antiplatelet effects of various natural and pharmacological compounds [19–24]. Such applications are of great importance for the design of future prophylactic interventions and therapeutic strategies for platelet-related activities in atherosclerosis [2].

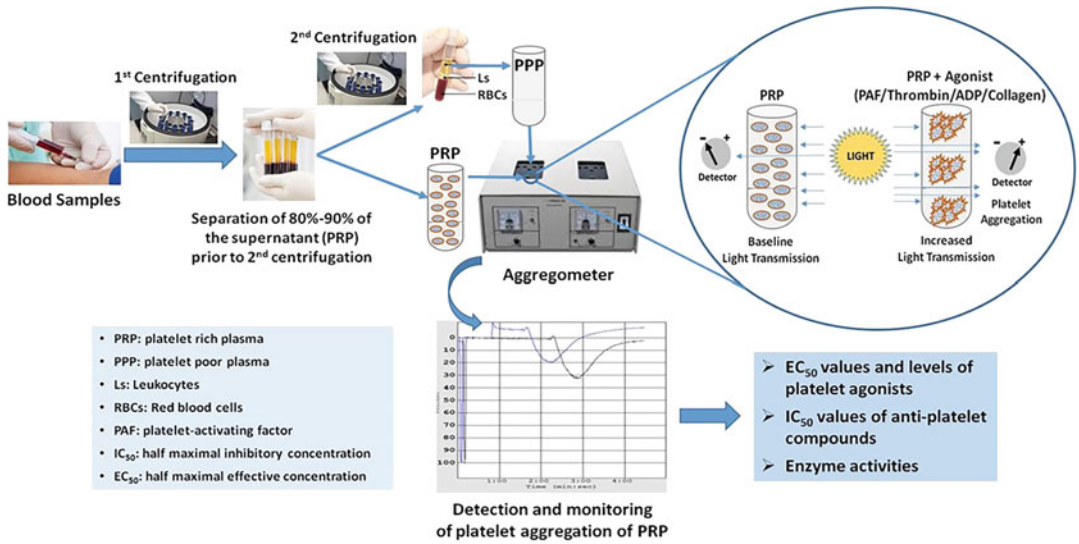

Fig. 1 Overview of light transmittance aggregometry (LTA). LTA detects and quantifies the changes of the transmission of light through a platelet suspension sample, such as platelet-rich plasma (PRP), washed platelets, or gel-filtered platelets, when platelets are activated and aggregated. (Reproduced from [18])

However, in Europe, regulations are set in place by the European Food Safety Authority (EFSA) before a health claim can be made in relation to the antiplatelet properties of a compound, molecule, or mixture. EFSA has outlined several guidelines that must be met before issuing a health claim for food bioactives, supplements, or nutraceuticals. EFSA's guidance is provided through "the scientific requirements for health claims related to antioxidants, oxidative damage, and cardiovascular health" [25]. Within this document, there is a specific section on antiplatelet compounds, "Claims on reduced platelet aggregation" that must be adhered to before labeling a product with antiplatelet properties. Since states of platelet hyperactivity and hypercoagulability are more commonly observed in subjects with cardiovascular risk factors, EFSA's health claim mentions that reduction of platelet aggregation in subjects with platelet activation during sustained exposure to the food/constituent (e.g., 4 weeks) would be considered a beneficial physiological effect worthy of a health claim. Antiplatelet molecules of dietary or natural origin that demonstrates these properties can be granted a health claim by EFSA. LTA-based assays are one of the accepted methodologies allowed to determine these effects. However, to date, only one such product has been granted a health claim by EFSA. Fruitflow®, a water-soluble, tomato-based nutraceutical has demonstratable antiplatelet and antihypertensive effects in humans [26, 27]. Fruitflow® can claim that their product "helps maintain normal platelet aggregation, which contributes to healthy blood flow." Indeed, a 3 g dose of Fruitflow® recently demonstrated antiplatelet effects that were approximately one-third the effect of 75 mg of aspirin in a double-blinded randomized clinical trial of 47 healthy subjects [27]. Provexis, the company responsible for producing this product has had to work particularly hard to attain their health claim. However, now that they have managed to create a product and trail blaze in this particular field of research, it is likely that more products will manage this achievement over the next few years.

LTA assays are time-consuming, costly, technically challenging and are affected by many preanalytical and analytical variables. Thus, they must be carefully controlled and performed using specific instrumentation (e.g., aggregometer) and monitored by laboratories with expert personnel [28]. Thus, this chapter will outline the appropriate methodology for the preparation of human PRP and PPP and the analytical procedures of LTA-based assays that are required to assess human platelet aggregation induced by various platelet agonists implicated in atherosclerosis. In particular, we will outline the use of PAF, thrombin, collagen, and ADP. This methodology also describes the assessment and dose efficacy and safety of antiplatelet compounds affecting platelet reactivity using human PRP in vitro and ex vivo. This is important for acquisition of platelet-related CVD health claims for bioactive

compounds, as well as for preclinical evaluation of the health benefits or side effects of these antiplatelet compounds on platelet function and cardiovascular health before the use of these compounds in *in vivo* and clinical research.

The methods and protocols described in this chapter can be applied as a tool for research in a basic and clinical setting by clinical researchers, biochemists, pharmacologists, and food and nutrition scientists who wish to assess platelet function and the effects of antiplatelet bioactive compounds in relation to atherosclerosis.

2 Materials

A platelet aggregometer is required to perform the methods described herein. We recommend the Chrono-log-490 two-channel turbidimetric platelet aggregometer coupled to the accompanying AGGRO/LINK software package (Chrono-log, Havertown, PA, USA; Abingdon on Thames, UK). Cuvettes and disposable magnetic stirrers can also be obtained from Chrono-log.

2.1 Preparation of Platelet-Rich Plasma (PRP) and Platelet-Poor Plasma (PPP)

1. Blood collection systems: Those described here are obtained specifically from Sarstedt Ltd. (Wexford, Ireland) and include 20 G safety needle or similar wide bore needles and sodium citrate anticoagulant S-monovettes (0.106 mol/L in a 1:10 ratio of sodium citrate to blood).
2. Standard polypropylene tubes.
3. Standard polypropylene Pasteur pipettes.
4. Centrifuge with no brake settings enabled.
5. Spectrophotometer.
6. Plastic cuvettes.

2.2 Platelet Agonist Preparation

1. ADP: Gently tap the vial containing 2.5 mg of ADP to get the contents to the bottom. Reconstitute with 5 mL of irrigation grade physiological saline (0.9%). Allow to sit for 10 min with occasional inversion. Aliquot for long-term storage at −80 °C. Thaw and dilute ADP to the desired working concentrations immediately before experimentation (*see* **Note 1**).
2. Collagen: Invert or swirl 1 mg/mL collagen stock before every use. Prepare aliquots of 20 μL and store at −80 °C. Thaw and dilute collagen to the desired working concentrations immediately before experimentation (*see* **Note 2**).
3. PAF: Dilute crystalline PAF in an appropriate amount of a solution of chloroform/methanol (1:1 v/v) of analytical grade, so that the stock concentration is 10^{-4} M. Aliquot for storage at −20 °C. When ready for use, evaporate the PAF aliquot under a stream of nitrogen gas and re-dissolve in bovine

serum albumin in 0.9% saline (2.5 mg BSA/mL). Dilute PAF to the desired working concentrations immediately before experimentation (*see* **Note 3**).

4. Thrombin: Dissolve stable active thrombin or thrombin receptor activator peptide 6 (TRAP-6) in saline to formulate a stock concentration of 0.1 U/μL (*see* **Note 4**). Aliquot for storage at −80 °C. Thaw and dilute thrombin or TRAP-6 to desired working concentrations immediately before experimentation (*see* **Note 5**).
5. Dissolve bovine serum albumin in 0.9% physiological saline at a concentration of 2.5 mg BSA/mL.

3 Methods

3.1 Preparation of Platelet-Rich Plasma (PRP) and Platelet-Poor Plasma (PPP)

Blood withdrawal, preparation, and processing of human blood to obtain PRP can be performed as previously described [18] and as outlined in detail below:

1. Blood is collected from the median cubital vein or cephalic vein of healthy volunteers (*see* **Notes 6** and **7**) via venepuncture using a 20 G safety needle (*see* **Notes 8** and **9**). Blood is drawn into a sodium citrate anticoagulant S-monovette using the aspiration method (0.106 mol/L in a 1:10 ratio of sodium citrate to blood) (*see* **Notes 10** and **11**). The monovette should be gently inverted three times to ensure effective mixing of the anticoagulant with the blood (*see* **Note 12**).
2. The collected blood samples are then centrifuged at 194 × *g* for 18 min at 24 °C with no brake applied to prevent platelet activation. The supernatant PRP is then gently transferred to polypropylene tubes using a polypropylene Pasteur pipette and the PRP is stored at 24 °C until use (Fig. 1, first centrifugation; *see* **Note 13**).
3. The PPP is obtained by further centrifuging the remainder of the PRP collection monovette at 1465 × *g* for 20 min at 24 °C, again with no brake applied. The transparent supernatant of this centrifugation is collected and referred to as the PPP (Fig. 1, second centrifugation).
4. PRP can be adjusted to 500,000 platelets/μL if required by the addition of a respective volume of PPP according to the absorbance of the PRP measured (*see* **Note 14**). The absorbance is measured using a spectrophotometer set at 530 nm and the PPP is used as a blank for this measurement. 1 mL of PPP and PRP are placed in plastic cuvettes and the absorbance is measured. An absorbance of 0.8 is equivalent to 500,000 platelets/μL.

5. All procedures should take place at 24 °C and should be carried out with minimal handling of the samples. To ensure platelet viability, all experiments should be conducted within 2.5 h of the initial blood draw for optimum performance.

3.2 Basic Aggregometry Protocol

This protocol will guide you through the LTA-based basic aggregometry testing in an aggregometer. However, consult the manufacturer's guidelines associated with your particular model of aggregometer and adjust this method accordingly. The basic aggregometry protocol in human PRP can be performed as previously described and outlined in detail below [18]:

1. Draw and process blood samples as described in Subheading 3.1.
2. Prior to testing, add 500 μL of PPP to a glass aggregometer cuvette without a stirrer and place it in its specific well in the aggregometer.
3. Pipette 250/500 μL (volume depends on the use of a spacer or not) of PRP into another glass aggregometer cuvette and place it in its specific sample chamber set at 37 °C (*see* **Notes 15–18**). Add a small disposable stirrer to the cuvette, which spins at 1200 rpm (*see* **Note 19**) and allow the cuvette to prewarm for 2–3 min before testing. This allows the assay to mimic the *in vivo* conditions of blood flow.
4. Then, automatically calibrate (zero) the PRP against the PPP (follow the manufacturer's instructions). In doing so, the instrument is set to 100% transmission and then 0% transmission in order to gauge the possible parameters. When complete, wait for 30 s to establish a stable baseline, prior to the addition of any agonists.
5. Baseline light transmission is measured when PRP suspensions are placed in an aggregometer cuvette in the absence of an agonist. Increased light transmission is detected when platelets start to aggregate in the presence of an agonist in the aggregometer cuvette (Fig. 2a). According to the detection of these changes of the light transmission, specific aggregation curves are acquired. A characteristic example of an aggregation curve of a maximum-irreversible platelet aggregation is shown in Fig. $2B_1$, while a characteristic example of an aggregation curve of a maximum-reversible platelet aggregation is also shown in Fig. $2B_2$.
6. The latent aggregation curve (Fig. $2B_2$) of maximum-reversible platelet aggregation of PRP induced by an agonist (PAF, thrombin, collagen, or ADP) is determined as the 100% aggregation of platelets. This aggregation curve is necessary to determine for each PRP sample in order to carry out some of

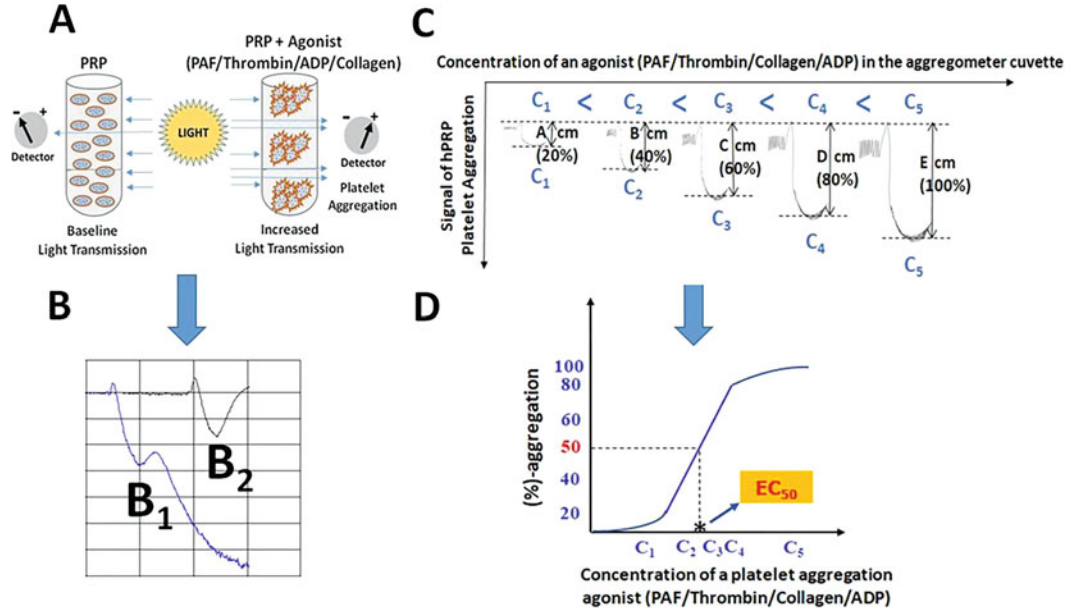

Fig. 2 Application of LTA assay for evaluating and monitoring the effect of platelet agonists (i.e., PAF, thrombin, collagen, or ADP) on platelet aggregation in PRP. (**a**): Detection of increased light transmission during platelet aggregation in response to the addition of an agonist; (**b**) Characteristic examples of an aggregation curve of a maximum-irreversible platelet aggregation [B1: Trace 1 (blue)] and of an aggregation curve of a maximum-reversible platelet aggregation (100% aggregation) [B2: trace 2 (black)]; (**c**) An example of the concentration-dependent addition of agonists that can induce reversible platelet aggregation; i.e., the higher the concentration of the agonist (C5 > C4 > C3 > C2 > C1), the higher the platelet aggregation curve (E > D > C > B > A); (**d**) The linear relationship between the concentrations of an agonist within a specific range that induces platelet aggregation within the 20%–80% of the maximum-reversible platelet aggregation of hPRP. From this linear curve, the concentration of the agonist needed to induce 50% of platelet aggregation can be calculated, which is known as the EC_{50} value. The lower the EC_{50} value for an agonist, the higher the potency of its platelet aggregation effect. (Reproduced from [18]. *LTA* light transmission aggregometry, *PAF* platelet-activating factor, *hPRP* human platelet-rich plasma)

the applications of LTA, including the evaluation of the effects of platelet agonists and antiplatelet compounds on platelet reactivity.

3.3 Application of LTA for the Evaluation of Platelet Reactivity of PRP Induced by Inflammatory and Thrombotic Mediators and Platelet Agonists (EC_{50} Values)

The application of LTA for evaluating platelet reactivity of human PRP induced by platelet agonists can be achieved as previously described [18].

1. Blood collection and processing is carried out as previously described in Subheading 3.1, followed by the basic aggregometry protocol of the LTA-based assay in an aggregometer (Subheading 3.1).
2. PRP suspensions are prepared in aggregometer cuvettes, and the aggregation curve of maximum-reversible platelet aggregation of PRP induced by a platelet agonist (i.e., PAF, thrombin,

collagen, or ADP) is determined and characterized as the 100% aggregation of platelets (Fig. 2B_1).

3. Several concentrations of the platelet agonist (ADP = 2 to 10 μM; Collagen = 1 to 5 μg/mL; PAF = 2.6×10^{-8} to 2.6×10^{-5} mol/L; Thrombin = 0.01 mU/μL to 1 mU/μL) are added to the aggregometer cuvette, which can induce reversible platelet aggregation in a dose-dependent manner (Fig. 2c). The higher the concentration of the platelet agonist, the higher the platelet aggregation curve detected by the aggregometer (Fig. 2c).
4. A linear relationship exists between the concentrations of a platelet agonist within a specific range (see **step 3** above). When ready for use, dilute the stock solutions in appropriate amounts of saline to obtain working solutions that will be in the range of 0.01 mU/μL to 1 mU/μL when added to PRP using volumes between 1 μL and 8 μL of the working solution. Calculate the concentrations in advance depending on the planned volume of PRP being used during experimentation (*see* **Notes 1–5**) that induces platelet aggregation within the 20%–80% of the maximum-reversible platelet aggregation of PRP. From this linear curve, the concentration of the agonist required to induce 50% of platelet aggregation of PRP can be calculated, which is termed the EC_{50} value (half maximal effective concentration) of the specific platelet agonist for platelet aggregation (Fig. 2d). It should be noted that the lower the EC_{50} value for an agonist, the higher the potency of its platelet aggregation effect.

3.4 LTA for the Evaluation of the Inhibitory Effects (IC_{50} Values) of an Antiplatelet Agent Against Platelet Aggregation of PRP

The application of LTA for evaluating the inhibitory effects of an antiplatelet agent either of natural, dietary, or pharmacological origin against platelet aggregation can be achieved as previously described [18, 29–32].

1. Blood collection and processing should be conducted as previously described (Subheading 2.1), followed by the basic aggregometry protocol (Subheading 3.1) and the LTA assay (Subheading 3.2).
2. The aggregation curve of the maximum-reversible platelet aggregation of PRP (100% aggregation of platelets) induced by a specific concentration of an agonist (ADP = 2 to 10 μM; Collagen = 1 to 5 μg/mL; PAF = 2.6×10^{-8} to 2.6×10^{-5} mol/L; Thrombin = 0.01 mU/μL to 1 mU/μL) in the absence of any antiplatelet agent is determined as the 0% inhibition (baseline).
3. Platelet suspensions of PRP are then incubated with the addition of various concentrations of the antiplatelet compound to be studied for 2 min with stirring, prior to the addition of any agonist.

4. By the addition of the same concentration of the agonist that was used for the baseline aggregation curve (100% of aggregation—0% of inhibition) to the preincubated PRP cuvettes containing antiplatelet agent PRP suspensions, a reduction of the platelet aggregation curve is observed (inhibitory effect) in relation to the baseline aggregation curve in a concentration-dependent manner.
5. The higher the concentration of the antiplatelet agent in the aggregometer cuvette, the lower the platelet aggregation curve recorded by the aggregometer detector of the LTA assay, indicating the inhibitory effect of the antiplatelet agent on platelet aggregation as a percentage of inhibition in relation to the baseline aggregation curve (0% inhibition—100% aggregation).
6. A linear relationship exists between the concentrations of the antiplatelet agent within a specific range that inhibits platelet aggregation within the 20%–80% of the maximum-reversible platelet aggregation of PRP. From this linear curve, the concentration of the agonist needed to achieve 50% inhibition of platelet aggregation can be calculated, which is known as the IC_{50} value of the inhibitory effect of the specific antiplatelet agent against platelet aggregation. The IC_{50} values reflect the inhibitory strength of each antiplatelet agent, since the lower the IC_{50} value for an antiplatelet agent, the higher its inhibitory effect against platelet aggregation induced by an agonist such as PAF or thrombin (*see* **Notes 20–24**).

4 Notes

1. ADP is usually transported as a lyophilized preparation (e.g., Chrono-log, Havertown, PA, USA; Labmedics LLP, Abingdon on Thames, UK). Solution can be aliquoted for storage at −80 °C for up to a year. When ready for use, thaw and dilute the stock solution in saline to obtain working solutions between 2 and 10 μM when volumes between 1 and 8 μL of the working solution are added to PRP. Calculate the concentrations in advance depending on the planned volume of PRP being used during experimentation.
2. Collagen is usually purchased as a stock solution in a concentration of 1 mg/mL (e.g., Chrono-log, Havertown, PA, USA; Labmedics LLP, Abingdon on Thames, UK), in which 1 mg of native collagen fibrils (type I) (obtained from equine tendons in this case) are suspended in 1 mL of isotonic glucose solution of pH 2.7. Aliquots of 20 μL of stock solution can be stored at −80 °C for up to a year. When ready for use, thaw and dilute in appropriate amounts of saline to obtain working solutions of

collagen, so that the final concentration when added to PRP in the cuvette will be in the range of 1–5 μg/mL when volumes between 1 and 8 μL of the working solution are added. Calculate the concentrations in advance depending on the planned volume of PRP being used during experimentation.

3. Standard PAF in crystalline form can be purchased from Sigma Aldrich (Wicklow, Ireland). When placing at −20 °C, make sure to note the volume of solution in the aliquots as chloroform:methanol (1:1 v/v) evaporates over time. If you wish to keep PAF for long-term storage, leave it in its crystalline form and store it at −20 °C under a nitrogen atmosphere. Serially dilute the solutions of PAF dissolved in BSA-saline so that the final concentration in the aggregometer cuvette will range from 2.6×10^{-8} to 2.6×10^{-5} mol/L when volumes between 1 and 8 μL of the working solution are added (*see* **Note 3**). Calculate the concentrations in advance depending on the planned volume of PRP being used during experimentation. Normal aggregation in PRP is usually observed with PAF of $1–5 \times 10^{-8}$ mol/L.
4. Lyophilized standard active thrombin from human plasma or the more stable TRAP-6 can be purchased from Sigma Aldrich (Wicklow, Ireland). In experiments with PRP, it is recommended to use TRAP-6 or active gamma thrombin (-γ-thrombin), which have been shown to activate in vitro the thrombin receptor and cause platelet aggregation in a concentration-dependent manner, without this activation being affected by the presence of plasma fibrinogen in the PRP. In contrast, platelet aggregation induced by simple active thrombin may be affected by the presence of fibrinogen in the plasma and the subsequent formation of permanent clots.
5. When ready for use, dilute the stock solutions in appropriate amounts of saline to obtain working solutions that will be in the range of 0.01 mU/μL to 1 mU/μL when added to PRP using volumes between 1 and 8 μL of the working solution. Calculate the concentrations in advance depending on the planned volume of PRP being used during experimentation (*see* **Note 4**).
6. For PRP isolation and platelet aggregometry tests, volunteers need to donate fasting blood samples (for at least 8 h), since postprandial changes in plasma levels of glucose and insulin usually affect platelet reactivity. Furthermore, lipids in PRP can interfere with LTA. Thus, it is recommended that all blood sampling be conducted in the morning hours after overnight sleep fasting.
7. Many pharmaceutical compounds and various reagents are known to interfere with platelet function. Ensure that the

potential donors have not used the following drugs 2 weeks prior to blood draw: antihistamines, antibiotics, aspirin, anesthetics, dextran, PAF-inhibitors such as rupatadine or herbal medicines, non-steroidal anti-inflammatory medications (aspirin, clopidogrel, cilostazol, ibuprofen, ticlopidine, ticagrelor, prasugrel—or any other vascular or cardiovascular related medications). Some foods and beverages such as coffee, tea, garlic, and wine can also impact platelet function. Ensure that volunteers have been fasting for a minimum of 8 h prior to testing.

8. Ensure to use a wide bore needle for blood withdrawal if the one recommended in this protocol is not available to prevent unnecessary platelet aggregation and hemolysis that can result in nucleotide release by platelets that can cause desensitization of platelets, particularly to agonists like ADP.
9. Venepuncture should be clean without the requirement of probing for a vein, to avoid platelet activation and hemolysis. Follow your local standard operating protocols for venepuncture.
10. Other blood collection systems are just as acceptable. However, it is advised to use a closed blood collection system to minimize the potential health risks to the phlebotomist, particularly in clinical samples. The BD Vacutainer® Blood Collection apparatus is another recommended system.
11. Ensure that the monovettes or similar collection tubes are in date before use.
12. It is recommended that platelets are handled and stored in polypropylene, polyethylene, polycarbonate, or siliconized glass labware. In addition, stored platelets should always be sealed with a cap to ensure that the pH of the PRP remains stable. Note that un-siliconized glass containers, vigorous movement of containers or pipettes can cause platelet activation. Deviation of these recommendations may lead to a loss of platelet function or premature platelet activation.
13. Blood and intact platelets should preferentially be handled at room temperature (approximately 24 °C). Note that platelets at 4 °C can activate and suffer loss of function.
14. The number of platelets in the PRP for platelet aggregometry tests is adjusted to 500,000/μL, if needed, only in in vitro experiments. In ex vivo experiments, this adjustment in the PRP is not required but a patient or volunteers platelet count should be taken into consideration when drawing conclusions from experiments.
15. All vials of working solutions of ADP, collagen, and thrombin need to be kept in ice (2–8 °C) during an experiment and can be used continuously for 8 h. PAF does not require ice.

16. The aggregometer should be turned on at least 20 min prior to testing to allow the temperature of the sample well (chamber) to reach a temperature of 37 °C.
17. Use pipette tips with a wide orifice to prevent damage or activation of the platelets. Also, avoid unnecessary pumping or vigorous pipetting techniques to prevent activation of the platelets or bubble formation.
18. The Chrono-log cuvettes can be fitted with a spacer. This is a small rubber object placed underneath the cuvette to raise the height of the cuvette. Ordinarily, 500 μL of PRP would be required to test in the Chrono-log aggregometer. However, spacers allow for a lower volume of PRP to be used (e.g., 250 μL).
19. Some aggregometer models use stirrers set at 1000 rpm as opposed to 1200 rpm. This is satisfactory. This setting is usually adjustable and depends widely on the pre-set within the model of the aggregometer used.
20. It is important to wear gloves when handling clinical material for personal protection. However, gloves also cause smudges or fingerprints occurring on the cuvette that may affect the light transmittance. Inspect and clean all cuvettes before use with a lint-free disposable tissue such as a Kimwipe.
21. LTA can be applied to evaluate the inhibitory effects (IC_{50} values) of an antiplatelet agent against platelet aggregation of PRP induced by PAF, thrombin, collagen, or ADP. These types of experiments provide information on the pathways that this antiplatelet compound can affect or inhibit (e.g., the PAF/PAF-receptor pathway or the thrombin/PAR-1 pathway, or a combination of both, etc.), and at which concentration these effects are induced [2, 18, 24]. These in vitro results are crucial for determining further research in cells and cell-related responses in vitro, ex vivo, in vivo and in clinical research.
22. Suitable controls should be used before carrying out in vitro studies by using a known antagonist of platelet activation via specific agonists. For instance, if testing with PAF, pharmacological inhibitors such as aspirin, rupatadine, or CV-3988 may be used, or inhibitors of natural origin such as Ginkgolide B and bioactive lipids like 1-hexadecyl-2-docosahexaenoyl-*sn*-glycero-3-phosphocholine.
23. Ensure that all compounds assessed are dissolved in the same solvent when making comparisons between compounds and carry out appropriate solvent controls. Some solvents occasionally used for hard to dissolve or non-water-soluble compounds, such as metal complexes, can cause platelet reactivity. For instance, high concentrations or amounts of DMSO can cause platelet activation, whereas lower concentrations or

amounts do not cause platelet reactivity. Ethanol can be used as a solvent for samples, but it must be diluted with water to the point that the final solution does not contain more than 1-part ethanol in 5 parts water in the sample solution to be assessed in the aggregometer. At these levels of ethanol, platelets remain intact. It is also recommended to have a relative blank estimation.

24. We suggest using PRP in the range of 500,000 platelets/μL. Problems can occur with setting optical baseline measurements if the platelet count is below 50,000 platelets/μL. Certainly using PRP above at least 100,000 platelets/μL is encouraged.

Acknowledgments

We would like to express our thanks to Prof. Sean Arkins (University of Limerick), Dr. Constantina Nasopoulou (University of the Aegean), and Dr. Eleni Sioriki (Ghent University) for their support in establishing our assay.

Author Contributions

All authors contributed equally to this work.

References

1. Stoke KY, Granger DN (2012) Platelets: a critical link between inflammation and microvascular dysfunction. J Physiol 590:1023–1034. https://doi.org/10.1113/jphysiol.2011.225417
2. Lordan R, Tsoupras A, Zabetakis I (2020) Platelet activation and prothrombotic mediators at the nexus of inflammation and atherosclerosis: potential role of antiplatelet agents. Blood Rev 21:100694. https://doi.org/10.1016/j.blre.2020.100694
3. Zabetakis I, Lordan R, Tsoupras A (eds) (2019) The impact of nutrition and statins on cardiovascular diseases. Elsevier, London
4. van der Meijden PEJ, Heemskerk JWM (2019) Platelet biology and functions: new concepts and clinical perspectives. Nat Rev Cardiol 16:166–179. https://doi.org/10.1038/s41569-018-0110-0
5. Paniccia R, Priora R, Alessandrello Liotta A et al (2018) Platelet function tests: a comparative review. Vasc Health Risk Manag 11:133–148. https://doi.org/10.2147/VHRM.S44469
6. Tsoupras A, Lordan R, Zabetakis I (2018) Inflammation, not cholesterol, is a cause of chronic disease. Nutrients 10:604. https://doi.org/10.3390/nu10050604
7. Badimon L, Vilahur G (2014) Thrombosis formation on atherosclerotic lesions and plaque rupture. J Intern Med 276:618–632. https://doi.org/10.1111/joim.12296
8. Kaplan ZS, Jackson SP (2011) The role of platelets in atherothrombosis. Hematol Am Soc Educ Program Book 2011(2011):51–61. https://doi.org/10.1182/asheducation-2011.1.51
9. Kaplan RC, Frishman WH (2001) Systemic inflammation as a cardiovascular disease risk factor and as a potential target for drug therapy. Heart Dis 3:326–332. https://doi.org/10.1097/00132580-200109000-00009
10. Li Z, Delaney MK, O'Brien KA et al (2010) Signaling during platelet adhesion and activation. Arterioscler Thromb Vasc Biol 30:2341–2349. https://doi.org/10.1161/ATVBAHA.110.207522

11. Tsoupras A, Lordan R, Zabetakis I (2019) Inflammation and cardiovascular diseases. In: Zabetakis I, Lordan R, Tsoupras A (eds) The impact of nutrition and statins on cardiovascular diseases. Elsevier, London
12. Olas B (2018) Dietary supplements with antiplatelet activity: a solution for everyone? Adv Nutr 9:51–57. https://doi.org/10.1093/advances/nmx014
13. Olas B (2020) Biochemistry of blood platelet activation and the beneficial role of plant oils in cardiovascular diseases. In: Makowski GS (ed) Advances in clinical chemistry. Elsevier, Cambridge, MA
14. Choleva M, Boulougouri V, Panara A et al (2019) Evaluation of anti-platelet activity of grape pomace extracts. Food Funct 10: 8069–8080. https://doi.org/10.1039/C9FO02138H
15. Ngo T, Kim K, Bian Y et al (2019) Cyclocurcumin from curcuma longa selectively inhibits shear stress-induced platelet aggregation. J Funct Foods 61:103462. https://doi.org/10.1016/j.jff.2019.103462
16. Born GVR (1962) Aggregation of blood platelets by adenosine diphosphate and its reversal. Nature 194:927–929. https://doi.org/10.1038/194927b0
17. O'Brien JR (1961) The adhesiveness of native platelets and its prevention. J Clin Pathol 14: 140–149. https://doi.org/10.1136/jcp.14.2.140
18. Tsoupras A, Zabetakis I, Lordan R (2019) Platelet aggregometry assay for evaluating the effects of platelet agonists and antiplatelet compounds on platelet function *in vitro*. MethodsX 6:63–70. https://doi.org/10.1016/j.mex.2018.12.012
19. Koukouraki P, Tsoupras A, Sotiroudis G et al (2020) Antithrombotic properties of spirulina extracts against platelet-activating factor and thrombin. Food Biosci 37:100686. https://doi.org/10.1016/j.fbio.2020.100686
20. Lordan R, Walsh AM, Crispie F et al (2019) The effect of ovine milk fermentation on the antithrombotic properties of polar lipids. J Funct Foods 54:289–300. https://doi.org/10.1016/j.jff.2019.01.029
21. Tsoupras AB, Papakonstantinou V, Stamatakis GM et al (2015) Biochemical evaluation of ruthenium-based complexes towards PAF (platelet activating factor) and thrombin. Potent anti-inflammatory agents. Sci Lett J 4: 208
22. Sioriki E, Lordan R, Nahra F et al (2018) In vitro anti-atherogenic properties of N-heterocyclic carbene aurate(I) compounds. ChemMedChem 13:2484–2487. https://doi.org/10.1002/cmdc.201800601
23. Tsoupras A, Lordan R, Harrington J et al (2020) The effects of oxidation on the antithrombotic properties of tea lipids against PAF, thrombin, collagen, and ADP. Foods 9:385. https://doi.org/10.3390/foods9040385
24. Tsoupras A, O'Keeffe E, Lordan R et al (2019) Bioprospecting for antithrombotic polar lipids from salmon, herring, and boarfish by-products. Foods 8:416. https://doi.org/10.3390/foods8090416
25. EFSA Panel on Dietetic Products & Allergies (2011) Guidance on the scientific requirements for health claims related to antioxidants, oxidative damage and cardiovascular health. EFSA J 9:e05136. https://doi.org/10.2903/j.efsa.2018.5136
26. O'Kennedy N, Raederstorff D, Duttaroy AK (2017) Fruitflow®: the first European food safety authority-approved natural cardioprotective functional ingredient. Eur J Nutr 56:461–482. https://doi.org/10.1007/s00394-016-1265-2
27. Uddin M, Biswas D, Ghosh A et al (2018) Consumption of fruitflow® lowers blood pressure in pre-hypertensive males: a randomised, placebo controlled, double blind, cross-over study. Int J Food Sci Nutr 69:494–502. https://doi.org/10.1080/09637486.2017.1376621
28. Cattaneo M, Cerletti C, Harrison P et al (2013) Recommendations for the standardization of light transmission aggregometry: a consensus of the working party from the platelet physiology sub-committee of ssc/isth. J Thromb Haemost 11:1183–1189. https://doi.org/10.1111/jth.12231
29. Tsoupras A, Lordan R, Shiels K et al (2019) In vitro antithrombotic properties of salmon (*Salmo salar*) phospholipids in a novel food-grade extract. Mar Drugs 17:62. https://doi.org/10.3390/md17010062
30. Tsoupras A, Lordan R, Demuru M et al (2018) Structural elucidation of Irish organic farmed salmon (*Salmo salar*) polar lipids with antithrombotic activities. Mar Drugs 16:176. https://doi.org/10.3390/md16060176
31. Lordan R, Vidal NP, Huong Pham T et al (2020) Yoghurt fermentation alters the composition and antiplatelet properties of milk polar lipids. Food Chem 332:127384. https://doi.org/10.1016/j.foodchem.2020.127384f
32. Lordan R, O'Keeffe E, Dowling D et al (2019) The *in vitro* antithrombotic properties of ale, lager, and stout beers. Food Biosci 28:83–88. https://doi.org/10.1016/j.fbio.2019.01.012

Chapter 22

Extracellular Vesicles in Atherosclerosis Research

Jessica O. Williams, Cass Whelan, Jamie Nash, and Philip E. James

Abstract

The methodologies described in this chapter inform on how to incorporate extracellular vesicles (EV) in model systems to investigate their role in the initiation and progression of the atherosclerotic plaque. The section will cover application of EV in coagulation and thrombus formation, monocytic migration, and adhesion to endothelial monolayers. These methodologies can be used with EV isolated from any cell type and under any conditions.

Key words Atherosclerosis, Extracellular vesicles, Monocyte migration, Static adhesion, Thrombus formation

1 Introduction

Extracellular vesicles (EV) are submicron, phospholipid membrane-bound particles. The term EV is an umbrella term encompassing a number of small vesicle populations, including exosomes, oncosomes, microvesicles, and apoptotic bodies [1]. EV are largely representative of their parent cell and often express traceable markers, carry DNA, RNA, lipids, and proteins and play a crucial role in normal intracellular communication [2]. This traceability and possession of key cell contents undoubtedly makes them an interesting target for mechanistic studies of disease progression and potential therapeutics.

EV are produced by most cell types and are found ubiquitously within bodily fluids, including blood, urine, and sweat. Often a drastic increase of cellular EV production is seen in disease. The ability of key cells implicated in atherosclerosis, including but not limited to, monocytes, macrophages, endothelial cells, and adipocytes, to produce EV is integral to their importance in atherosclerotic plaque formation. It is of course implicit that more than one type of EV is involved in the process of atherosclerosis, starting from pathological and inflammatory stimuli all the way through to

Dipak P. Ramji (ed.), *Atherosclerosis: Methods and Protocols*, Methods in Molecular Biology, vol. 2419,
https://doi.org/10.1007/978-1-0716-1924-7_22,
© The Author(s), under exclusive license to Springer Science+Business Media, LLC, part of Springer Nature 2022

plaque rupture. Therefore, applying EV isolated from many cell types cultured under a variety of conditions in in vitro models, it should be possible to mimic the inflammatory milieu and determine the relative EV production and roles. The combination of these isolated EV populations and target cells in co-culture models allows a clearer mechanistic understanding of the diseased environment.

EV are present within developing and advanced atherosclerotic plaques and have been implicated in all stages of the plaque development process [3]. This is coupled with EV being identified as a biomarker for cardiovascular disease [4]. It is therefore likely that your research may question what role EV play mechanistically in atherosclerosis and how this can be measured in vitro, to provide quantitative and reliable results. An easy way to begin to answer this question is by isolating EV specific to your question and applying them to established in vitro methodologies.

One challenge of working with EV is often their isolation. Our methodology for EV isolation has been thoroughly documented in our publications [5–7] and is beyond detailed inclusion here. This is used as a standard for all EV experiments within our laboratory. Indeed, it is important to note that these standards, as expected of all peer-reviewed publications, are in line with the International Society of Extracellular Vesicle (ISEV) guidelines [8] that are constantly being updated in line with new findings in this field.

The methodology in this chapter will inform on how to apply isolated EV populations to in vitro assays model systems commonly used in atherosclerosis research. These include turbidity and lysis, monocyte migration, thrombus formation, and leucocyte adhesion to endothelial cells.

Turbidimetric analysis has been extensively used as a quantitative high-throughput technique to monitor clot formation and stability, and can be applied to freshly isolated or frozen plasma samples. This assay is a combination assay that covers both clot formation (turbidity) and clot breakdown (fibrinolysis).

Monocytic migration assays are common place in atherosclerotic research. Migration of monocytes in response to inflammatory or other pathological stimuli is key to the formation of an atherosclerotic plaque. If you are particularly interested in determining the migration path (chemotaxis) of individual target cells, then applying a Boyden chamber type setup is advised. However, if your focus is to quantify the overall extent of migration across a fixed path length, the method we describe in this chapter is simple and robust.

The thrombus formation methodology described in this chapter is a new technique that has been developed in our laboratory. It is based on well-documented incorporation of fluorescent fibrinogen spiked into a native fibrinogen sample in order to visualize the formation of fibrin polymers. We have applied this to study blood clot formation and the association with EV in real time.

The binding of leukocytes to endothelial cells is a critical step in the formation of atherosclerotic plaque. This method allows leukocyte binding to be quantified and thus allows the impact of adding EV from a variety of cell types, or produced under a number of inflammatory conditions, to be determined.

2 Materials

2.1 Turbidity and Lysis Assay: EV and Coagulation

1. Flat bottom 96-well plate.
2. Universal container.
3. 100 U/mL Thrombin *(see* **Note 1**).
4. 100 μg/mL tissue plasminogen activator (tPA) (*see* **Note 2**).
5. 1 M $CaCl_2$ (*see* **Note 3**).
6. Human fresh frozen plasma (FFP): Collected normally for transfusion into sodium citrate tube, centrifuged at 800 × *g* for 20 min at room temperature with no brake to remove platelets before being transferred into 1.5 mL aliquots stored in 1.5 mL microcentrifuge tubes at −80 °C.
7. Permeation Buffer: Weigh 12.12 g of Tris and 11.68 g of NaCl and transfer to a container of 1.8 L of deionized water. Mix and adjust pH with HCl to 7.4. Make up to 2 L with deionized water and store at room temperature.
8. Ice.
9. Stop watch.
10. Water bath at 37 °C.
11. Plate shaker.
12. Vortex mixer.
13. 1.5 mL microcentrifuge tubes.
14. 8-channel pipette.
15. Plate reader for determining absorption at 340 nm.

2.2 EV and Monocyte Migration

1. Human THP-1 monocytic cell line (5×10^5 cells/well). Recommended use between passages 5 and 15.
2. Complete Roswell Park Memorial Institute (RPMI) Medium with L-glutamine and sodium bicarbonate, 10% fetal bovine serum, 1% penicillin/streptavidin.
3. Cell culture incubator.
4. Water bath at 37 °C.
5. Falcon® or similar cell culture inserts (*see* **Note 4**).
6. Falcon® or matched similar companion 12-well plates (*see* **Note 5**).

7. 20 ng/mL monocyte chemoattractant protein-1 (MCP-1).
8. 1× Phosphate Buffered Saline (PBS): 137 mM NaCl, 2.7 mM KCl, 10 mM Na_2HPO_4, and 1.8 mM KH_2PO_4.
9. Cell counter.

2.3 EV and Thrombus Formation

1. 100 U/mL thrombin, human plasma.
2. 1 M $CaCl_2$.
3. 1× Hanks Balanced Salt Solution (HBSS) (without $CaCl_2$ and $MgCl_2$).
4. Fibrinogen from human plasma, Alexa Fluor™ 488 Conjugate.
5. Human fresh frozen plasma (FFP): Collected normally for transfusion into sodium citrate tube, centrifuged at 800 × *g* for 20 min at room temperature with no brake to remove platelets before being transferred into 1.5 mL aliquots stored in 1.5 mL microcentrifuge tubes at −80 °C.
6. Water bath at 37 °C.
7. 1.5 mL microcentrifuge tubes.
8. Ice.
9. Stop Watch.
10. Cell slide.
11. Cover slip.
12. Immersion oil.
13. Fluorescent microscope with a 488 nm laser.
14. Lens cleaning paper.

2.4 EV and Leukocyte Adhesion to Endothelial Cells

1. 96-well flat bottom tissue culture plate.
2. 0.1 μg/mL tumor necrosis factor (TNF)-α.
3. CellTrace™ Calcein Red-Orange.
4. Krebs-BSA: 140 mM NaCl, 3.6 mM KCl, 0.5 mM NaH_2PO_4, 0.2 mM $MgSO_4$, 1.5 mM $CaCl_2$, 1% Bovine Serum Albumin.
5. Human umbilical cord endothelial cells (HUVEC) or endothelial cell line (e.g., we have successfully utilized the HECV cell line) (*see* **Note 6**).
6. Media 199 supplemented with 35 μg/mL gentamycin, 2.5 μg/mL amphotericin B, 10% fetal bovine serum, 1 ng/mL human endothelial growth factor, 1 μg/mL hydrocortisone.
7. Serum-Free Media (SFM): Media 199 supplemented with 35 μg/mL gentamycin, 2.5 μg/mL amphotericin B, 1 ng/mL human endothelial growth factor, 1 μg/mL hydrocortisone.

8. Human THP-1 monocytic cell line (1×10^6 cells/well). Recommended use between passages 5 and 15. Alternatively, leukocytes can be used.
9. Cell culture incubator.
10. Centrifuge.
11. Fluorescent Microscope with Axovision Software.
12. Image J software.

3 Methods

3.1 Turbidity and Lysis Assay: EV and Coagulation

1. Take FFP and thaw in a 37 °C water bath.
2. Pipette 6876 μL of Permeation Buffer and 270 μL of 1 M $CaCl_2$ into a universal container labeled "activation mix" and place on ice.
3. Pipette 5500 μL of Permeation Buffer into a universal container labeled "lysis mix" and place on ice.
4. Add 80 μL of Permeation Buffer to a 1.5 mL microcentrifuge tube labeled "diluted thrombin" and place on ice.
5. Add 760 μL of permeation buffer to a 1.5 mL microcentrifuge tube labeled "diluted tPA" and place on ice.
6. Vortex FFP and centrifuge at $850 \times g$ for 30 s at room temperature.
7. Pipette 25 μL of FFP into each well of a 96-well plate.
8. Add 65 μL of Permeation Buffer to each well (*see* **Note 7**).
9. Add the desired EV Concentration (recommended 1×10^{10} particles/mL).
10. Place the 96-well plate on a plate shaker set at the lowest speed.
11. Take aliquots of thrombin and tissue plasminogen activator from −20 °C and add 20 μL of thrombin to the 1.5 mL microcentrifuge tube labeled "diluted thrombin."
12. Add 54 μL of the "diluted thrombin" to the universal container labeled "Activation Mix." Vortex and place on ice.
13. Add 40 μL of tPA to the microcentrifuge tube labeled "diluted tPA."
14. Add 500 μL of "diluted tPA" to the universal container labeled "lysis mix." Vortex and place on ice.
15. Set up a plate reader at 37 °C to measure absorbance in wells every 12 s for 1 to 4 h at 340 nm (*see* **Notes 8** and **9**).
16. Add 30 μL of lysis mix to each well of the first column of the plate using an 8-channel pipette. Repeat for subsequent columns in intervals of 10 s.

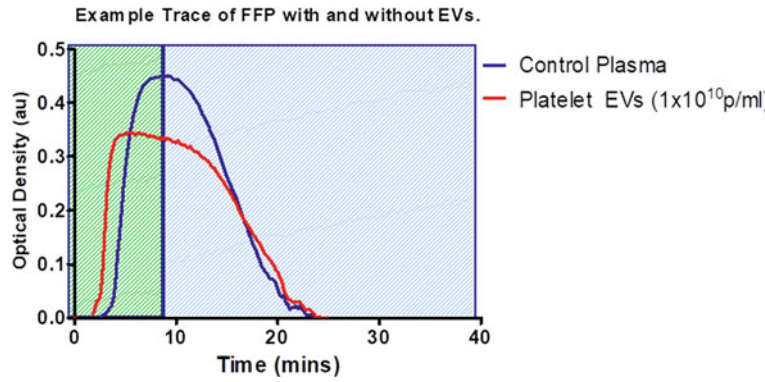

Fig. 1 An example trace result for the coagulation and lysis of fresh frozen plasma (FFP) with extracellular vesicles (EV). An example trace of fresh frozen plasma without EVs (blue) and with the addition of platelet derived EVs (red) at a final concentration of 1×10^{10} particles/mL. The green area represents the formation of the clot. The blue area represents the lysis of the formed clot, relative to the control. The graph demonstrates clot formation and lysis is complete within 1 h

17. At 2 min, add 30 μL of the activation mix to the first column of the plate using an 8-channel pipette. Repeat for subsequent columns in intervals of 10 s (*see* **Note 10**).
18. Keep the stopwatch running until the plate reader measures the first well. This time is the delay from starting the assay to reading the first well. An example trace over 1 h is shown in Fig. 1 (*see* **Note 11**).

3.2 EV and Monocyte Migration

1. Add 1 mL of complete RPMI to the bottom (basolateral) of each well of a 12-well plate (Fig. 2).
2. Add 20 ng/mL of MCP-1 to each basolateral well (excluding controls, *see* **Note 12**).
3. Insert a cell culture insert into every well of the 12-well plate.
4. Seed 1×10^6 THP-1 monocytes/mL in the top (apical) compartment of each cell culture insert (*see* **Note 13**).
5. Add the desired concentration of EV to the top of the cell culture insert (EV concentration is recommended between 1×10^9 and 1×10^{10} particles/mL).
6. Incubate at 37 °C for 3 h.
7. Remove cell suspension that remains in the apical portion of the cell culture insert, being careful not to touch the membrane with the pipette tip.
8. Lift the insert and use 500 μL of 1× PBS to wash the underside of the membrane into the basolateral well. This will move all the migrated cells into the well.

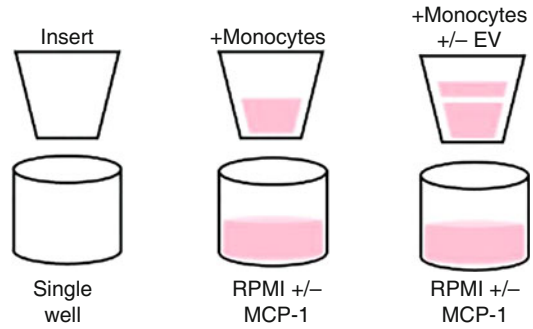

Fig. 2 Example diagram of monocytic migration assay. Representation of a single well housing a single cell culture insert. Image depicts the addition of monocytes, Roswell Park Memorial Institute (RPMI) medium, monocyte chemoattractant protein-1 (MCP-1), and extracellular vesicles (EV)

9. Discard the cell culture insert.
10. Cell count the media portion of the basolateral well (*see* **Note 14**).
11. Compare the data from wells incubated in the absence or the presence of MCP-1 to determine if migration has occurred. If there is a significant difference between these two parameters, then the number of migrated cells in the presence of MCP-1 should be set as an arbitrary value of 1.
12. Monocyte migration in the absence or the presence of EV should then be expressed as a fold-change in comparison to the proportion of cells that have moved from the apical to basolateral compartments in response to MCP-1 control without EV.

3.3 EV and Thrombus Formation

1. Remove FFP from freezer storage and thaw in a 37 °C water bath.
2. Pipette 85 μL of FFP and 5 μL of fluorescently conjugated fibrinogen to a 1.5 mL microcentrifuge tube and label "plasma mix" (*see* **Note 15**).
3. Add the desired EV concentration (recommended 1×10^9 particles in 100 μL) to the "plasma mix" (*see* **Note 16**).
4. In a separate 1.5 mL microcentrifuge tube, create an "activation mix" composed of 1 M $CaCl_2$, 100 U/mL thrombin and HBSS that when added to the "plasma mix" does not exceed the total volume of 100 μL and consists of 20 mM of $CaCl_2$ and 0.5 U/mL of thrombin.
5. Once the "activation mix" is added to the "plasma mix," start the stop watch immediately.

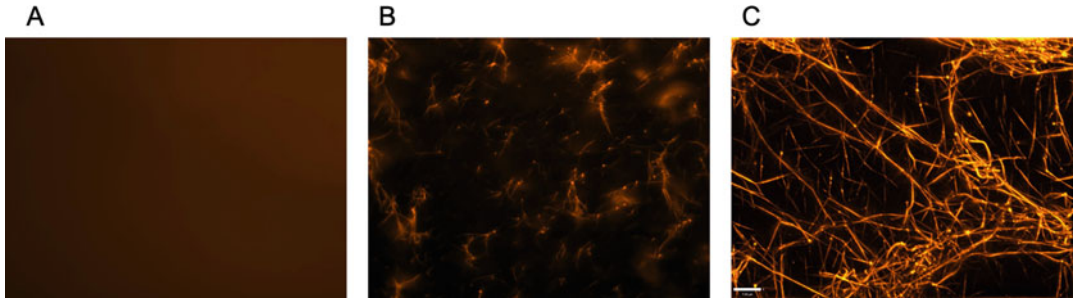

Fig. 3 Progression of thrombus formation over 15 min. Capture of activated clot formation from (**a**) 0 min, to clot beginning to form at 5 min (**b**) and the clot fully formed after 15 min (**c**) visualized using a 488 nm laser and a 100× magnified microscope

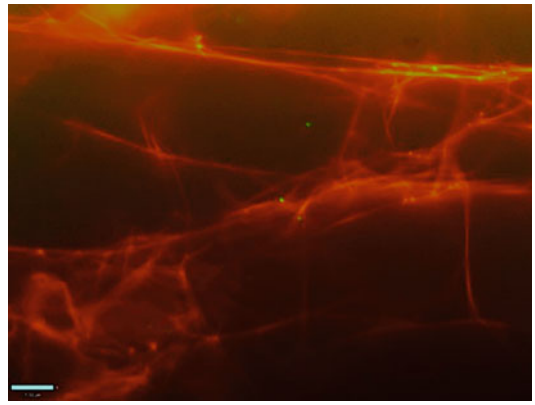

Fig. 4 Visualization of extracellular vesicles (EV) in thrombus formation. Combined image overlay of activated clot (orange) and endothelial extracellular vesicles (green) captured after 15 min using a 488 nm laser at 100× magnification

6. Transfer 20 μL of the combined "activation and plasma mix" to a cell slide and place a coverslip over the top of the sample (*see* **Note 17**).
7. While waiting, set up the fluorescent microscope up to the point where it is ready to be used.
8. After 15 min, add a drop of immersion oil to the cell slide and capture 3 still images from each respective slide (Figs. 3 and 4). Take the mean from these 3 images to create an *n* of 1 (*see* **Notes 18** and **19**).
9. Post image capture, clean the microscope with the lens cleaning paper to remove any residue of immersion oil.

3.4 EV and Leukocyte Adhesion to Endothelial Cells

1. Plate 5×10^5 HUVECs/100 μL onto a 96-well plate.
2. Once 90% confluent, remove M199 media and add 100 μL of EV at the desired concentration (recommended EV concentration is between 1×10^9 and 1×10^{10} particles/mL) in SFM.
3. Incubate for up to 6 h at 37 °C, 5% CO_2, in a cell culture incubator.
4. Add 1 μL of CellTraceTM Calcein Red-Orange to the leukocytes (e.g., THP-1 monocytes) with the desired concentration (approximately 1 μL/1 mL of the leukocyte sample (leukocytes at 1 × 108 cells/mL)) and incubate for 10 min in the dark (*see* **Note 20**).
5. Centrifuge the leukocytes for 2 min at 250 × *g*.
6. Discard the supernatant and resuspend the leukocyte pellet in 1 mL of Krebs-BSA.
7. Dilute this further to 10 mL using SFM.
8. Remove EV from HUVECs by washing with SFM.
9. Add labeled leukocytes to HUVECs and incubate for 1 h at 37 °C (*see* **Note 21**).
10. Wash the HUVECs three times with Krebs-BSA. On the final wash, do not remove buffer.
11. Visualize leukocyte adhesion using fluorescent microscopy (Fig. 5).
12. Use Axovision software to take 5 high-resolution images per well.
13. Analyze leukocyte adhesion by using Image J to determine the proportion of the leukocyte coverage in the field of view and express this as a percentage of the total field of view.

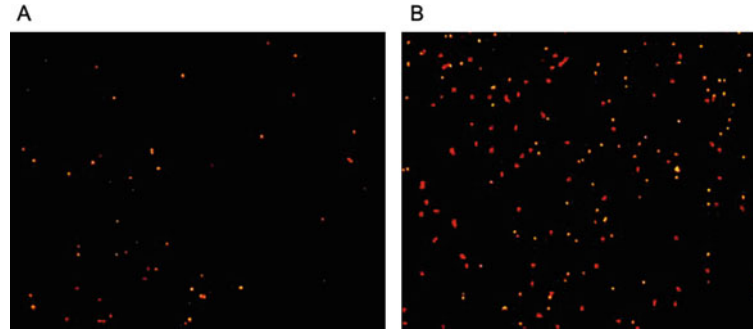

Fig. 5 Capture of fluorescent leucocyte adhesion to an endothelial cell monolayer. Fluorescently labeled leukocytes that have adhered to an endothelial cell layer with the (**a**) addition of normoxic (21% oxygen) derived extracellular vesicles (EV) and (**b**) addition of hypoxic (1% oxygen) derived EV

4 Notes

1. Thrombin final working concentration is 0.03 U/mL.
2. tPA final working concentration is 83.2 ng/mL.
3. $CaCl_2$ final working concentration is 7.5 mM.
4. A 8 μm pore size should be required for cellular inserts used for monocytic migration assays.
5. It should be ensured that the 12-well plates used are specifically produced to house the inserts described in **Note 4**. These specific companion plates must be used in order to house the cell culture insert correctly.
6. Human primary cells can be used immediately following reaching confluency. Human endothelial cell lines, including HECV are recommended to be used before passage 15.
7. The assay volume is 150 μL. When adding EVs, this must be taken into account, for example, 10 μL of EVs in the assay would require 55 μL of permeation buffer.
8. The readings need to be taken every 12 s; therefore, this limits the maximum amount of samples that can be analyzed to approximately 30 samples.
9. Wells should be read in columns, not rows.
10. This assay should include controls where activation and lysis mix are not included.
11. This assay should be carried out at room temperature, unless otherwise stated.
12. This experiment requires a number of controls. Firstly, a negative control should be used. This is a set of wells with no MCP-1 in the basolateral compartment. Expect little to no migration of monocytes in this control as there is no stimuli to induce monocytic migration. Secondly, a positive control should be included. This is a set of wells with no treatments, therefore only RPMI complete medium should be used in the apical compartment of insert, the basolateral compartment should contain MCP-1. Vehicle controls should be included for all treatments (e.g., if EV are diluted in filtered phosphate buffered saline, use the same volume of filtered phosphate buffered saline without EV as a vehicle control).
13. The monocytes should be in a maximum volume of 500 μL.
14. Multiple repeats of each condition should be carried out. If migrated cell numbers are small, wells of the same treatment can be combined for counting.

15. This assay is performed at room temperature and away from the light. A small lamp may be used to illuminate the room to aid user.
16. A control with no EVs should be included. A EV only control should also be included. This control should have no $CaCl_2$ or thrombin.
17. Slides should be ready to be visualized immediately after the 15 min incubation with the "activation mix."
18. Contents can be analyzed using an image analysis software (e.g., Image J and/or Adobe Photoshop).
19. Endothelial cells labeled with CFSE cell tracker were cultured to produce the fluorescently labeled EV used in this assay.
20. This method can be adapted for adipocyte adhesion by replacing the leukocyte steps with 3T3-L1 adipocytes.
21. This experiment should include a number of controls, TNF-α (0.1 μg/mL) should be used as a positive control for adhesion and added for 1 h with no EV. The negative control should consist of SFM only with no EV.

References

1. Van Neil G, D'Angelo G, Raposo G (2018) Shedding light on the cell biology of extracellular vesicles. Nat Rev Mol Cell Biol 19:213–228
2. Gaceb A, Martinez MC, Andriantsitohaina R (2014) Extracellular vesicles: new players in cardiovascular diseases. Int J Biochem Cell Biol 50: 24–28
3. Charla IE, Mercer J, Maffia P, Nicklin SA (2020) Extracellular vesicle signalling in atherosclerosis. Cell Signal 75:109751
4. Nozaki T, Sugiyama S, Koga H et al (2009) Significance of a multiple biomarkers stratergy including endothelial dysfunction to improve risk stratification for cardiovascular events in patients at high risk for coronary artery disease. J Am Coll Cardiol 54(7):601–608
5. Willis GR, Connolly K, Ladell K, Davies TS, Guschina IA, Ramji D, Miners K, Price DA, Clayton A, James PE, Rees DA (2014) Young women with polycystic ovary syndrome have raised levels of circulating annexin V-positive platelet microparticles. Hum Reprod 29(12): 2756–2763
6. Connoly KD, Willis GR, Datta DBN, Eklins EA, Ladell K, Price DA, Guschina IA, Rees DA, James PE (2014) Lipoprotein-apheresis reduces circulating microparticles in individuals with familial hypercholesterolemia. J Lipid Res 55: 2064–2072
7. Burnely-Hall N, Willis G, Davis J, Rees DA, James PE (2017) Nitrite-derived nitric oxide reduces hypoxia-inducible factor 1α-mediated extracellular vesicle production by endothelial cells. Nitric Oxide 28(63):1–12
8. Lötvall J, Hill AF, Hochberg F et al (2014) Minimal experimental requirements for definition of extracellular vesicles and their functions: a position statement from the International Society for Extracellular Vesicles. J Extracell Vesicles 3. https://doi.org/10.3402/jev.v3.26913

Chapter 23

The Use of Wire Myography to Investigate Vascular Tone and Function

Kayleigh Griffiths and Melanie Madhani

Abstract

Wire myography enables the investigation of vascular tone and function of small vessels. The vessel of interest is harvested from the experimental model of choice, and then mounted as ring preparations onto a four-channel wire myograph. This technique enables ex vivo measurements of isometric response of vessels to different pharmacological agents. Here we describe in detail how to dissect, mount, and normalize vessels for the wire myography technique. We will also provide examples of how to construct concentration-response curves to a contractile and vasodilatory pharmacological agent.

Key words Wire myograph, Vascular tone, Isolated arteries, Endothelial function, Vascular reactivity

1 Introduction

Wire myography is an ex vivo technique used to measure vascular reactivity and functional responses in vessels with internal diameters ranging from 60 μm to 10 mm. The myography technique was developed in 1976 by Mulvany and Halpern, who carried out experiments to study contractile responses of isolated small resistance arteries [1, 2]. This versatile technique is used in many fields of research, including pharmacology and vascular physiology. The advantage of this technique includes the ability to use different vessel types, including small and large arteries, veins, and lymph vessels from a variety of species and transgenic models [3–8]. Many different pathophysiological disease states such as hypertension, atherosclerosis, diabetes, aging, ischemic heart disease, and heart failure can also be examined [9–15].

Traditionally, vessels are dissected from the model of choice and placed immediately into a petri dish containing an ice-cold Krebs–Henseleit buffer (KHB) solution to maintain tissue viability. Using forceps and dissecting scissors, the vessel is cleaned very carefully from adhering connective tissues and cut into ring segments

Dipak P. Ramji (ed.), *Atherosclerosis: Methods and Protocols*, Methods in Molecular Biology, vol. 2419,
https://doi.org/10.1007/978-1-0716-1924-7_23,
© The Author(s), under exclusive license to Springer Science+Business Media, LLC, part of Springer Nature 2022

(~1–2 mm length). The vessels are then mounted on a four-channel wire myograph system (e.g., Danish MyoTechnologies model 620 M) as ring preparations by threading them onto two stainless steel or tungsten wires and securing the wires on two supports. This allows assessment of four vessels simultaneously. Each vessel is kept in a chamber containing KHB solution at 37 °C, gassed with 95% O_2/5% CO_2, and is viable for several hours.

Prior to starting an experiment, it is essential to standardize the baseline experimental conditions for vessel function measurement so that reproducible and reliable results can be obtained from sample to sample. Normalization involves pre-stretching an intact vessel to an internal circumference that the vessel would have when relaxed under a transmural pressure of 100 mmHg (for example, this will mimic the physiological state of the vessel in respect to the pressure and circumference) [16]. The normalization procedure is performed by using a normalization module software (e.g., ADInstruments Normalization Module or DMT Normalization Module). Briefly, the vessel is stretched in a stepwise manner and the force recorded. Stretch is initially recorded by manually turning the micrometer screw, and the user reading the value on the dial of the myograph system, which they then input into the normalization software program. Following this, the force is automatically calculated which will then generate a curve and the internal circumference 100 value (IC_{100}). Further details about the principle of normalization have been discussed in detail by several groups [2, 17]. In our laboratory, we use the ADInstruments DMT Normalization Module, and therefore we will describe this protocol.

It is essential to test the endothelial integrity of the vessel prior to commencing the assessment of the pharmacological agent of interest. As such, assessment of endothelial function is made possible with the use of acetylcholine. Pharmacological agents are added cumulatively directly to the chamber to enable a concentration-response curve to be constructed, and vessel tension is monitored throughout. In this chapter, we demonstrate the methods in how to set up a vessel on to the myograph and generate concentration-response curves to the thromboxane mimetic 9,11-dideoxy-11α,9-α-epoxymethano-prostaglandin $F_{2\alpha}$ (U46619), which is used to stimulate vasoconstriction, followed by acetylcholine to induce vasorelaxation. For the purpose of this guide, we will primarily describe the methods for mouse mesenteric resistance vessels in the main text, with notes for guidance on the use of larger diameter vessels such as the mouse conduit vessel (thoracic aorta).

2 Materials

Prepare all solutions using ultrapure water (deionized water of 18.2 MΩ-cm) and analytical grade reagents.

1. Multi-wire myograph system (e.g., Danish MyoTechnologies (DMT) model 620 M).
2. Computer with installed software (e.g., LabChart ADInstruments).
3. Power system (e.g., Powerlab ADInstruments).
4. Krebs–Henseleit Buffer (KHB): 119 mM NaCl, 4.7 mM KCl, 1.18 mM KH_2PO_4, 25.1 mM $NaHCO_3$, 1.19 mM $MgSO_4$, 11 mM Glucose, 2.5 mM $CaCl_2$ (*see* **Note 1**).
5. Carbogen gas mixture (95% O_2 /5% CO_2) and tubing to connect to the myograph system.
6. A sintered glass gassing stick and tubing to gas the KHB solution with the 95% O_2/5% CO_2 mixture.
7. Dissecting microscope with light fixture.
8. Dissecting tools: scissors (e.g., Weiss strabismus scissors, straight with rounded tips), dissection petri dish (*see* **Note 2**), dissecting pins, high quality forceps (e.g., watchmaker 3 steel), spring dissection scissors (e.g., Mcpherson-Vannas scissors, 8 cm long), small screw driver (usually supplied with the DMT myograph system).
9. Container of ice or other method for ensuring that KHB remains cold.
10. 500 mL glass beaker.
11. Water bath or other heating system set at 37 °C.
12. Graticule eye piece for the microscope to measure vessel length.
13. 25 μm diameter Tungsten wire (e.g., ADInstruments, DMT100128) for small resistance vessels (*see* **Note 3** for conduit vessel advice), cut to approximately 2.2 cm in length.
14. 4.8 M Potassium chloride (KCl) stock solution, kept at room temperature.
15. 1 μM, 10 μM, 100 μM, 1 mM, and 10 mM stock solutions of acetylcholine dissolved in KHB and kept on ice. Prepare fresh on the day of experiment.
16. 1 μM, 10 μM, 100 μM, 1 mM, and 10 mM stock solutions of 9,11-dideoxy-11α,9α-epoxymethano-prostaglandin $F_{2\alpha}$ (U46619) dissolved in KHB and kept on ice (*see* **Note 4** for conduit vessel advice).
17. 8% acetic acid solution, kept at room temperature, for cleaning the myograph chambers at the end of the experiment.

3 Methods

3.1 Dissection of Small Mesenteric Resistance Vessels

1. Fill a glass beaker with KHB (~250 mL), keep on ice and gas with 95% O_2/5% CO_2. This will be used when cleaning and dissecting the fat from the vessel, and during mounting.
2. Anesthetize the animal according to the Animals (Scientific Procedures) Act of 1986 and European Commission guidelines and local ethics protocol. Perform a midline laparotomy to expose the mesenteric bed.
3. Using scissors (e.g., Weiss strabismus scissors straight with rounded tips), carefully remove the intestine together with its feeding vasculature and the superior mesenteric artery. Be careful not to stretch or damage the vasculature during this procedure.
4. Transfer the excised section immediately into the dissecting petri dish and cover with cold KHB. Pin down the mesentery on the connective tissue to avoid damaging the vessels, continue to pin the rest of the mesentery to enable the fanning out (Fig. 1a) and take care to avoid overstretching the vessels.
5. Under the microscope, first identify the arteries and the order of branch to use (for example first or second order) (*see* **Note 5** and Fig. 1b).
6. Next, carefully clean the artery by dissecting the fat and connective tissue away from the vessels using the spring dissection scissors and forceps (*see* **Note 6**), again avoid contact with the arteries. Once the vein is identified, this can be cut away to aid visibility for artery dissection.
7. When most of the arteries are clean of connective tissue and fat, cut 4 vessel segments of an appropriate length of 1–2 mm (*see* **Note 7**).
8. Try to eliminate any blood clots within the vessel if present (*see* **Note 8**).

3.2 Mounting the Mesenteric Resistance Vessels

Prior to beginning the experiment, each bath should be washed out several times with distilled water followed by cold KHB. The myograph should be calibrated using the manufacturer's guidelines. It is then possible to save the calibrated settings to use for future experiments.

1. Switch on the computer and wire myograph system.
2. Switch on the heater in the wire myograph system and set to 37 °C.
3. Open the LabChart software and save the experimental file with an appropriate name.

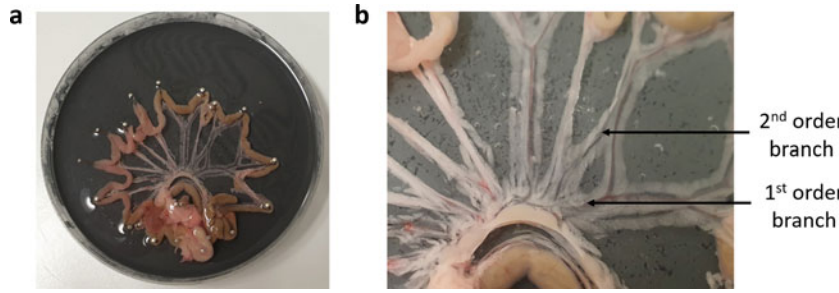

Fig. 1 Mouse mesentery. (**a**) Mouse mesentery fanned out and pinned using connective tissue prior to vessel dissection, (**b**) Mouse mesentery with arrows to indicate first and second order vessels

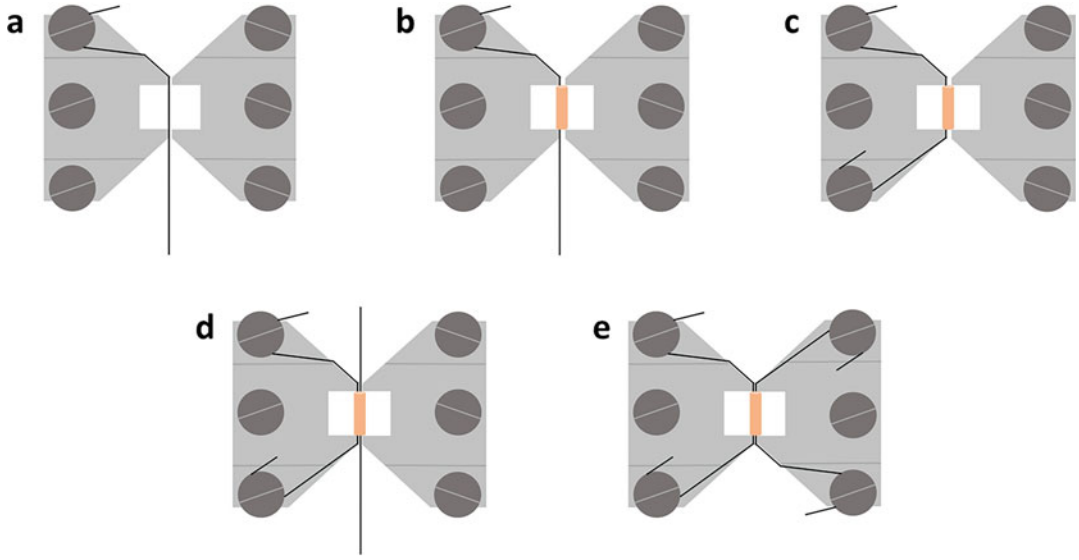

Fig. 2 Mounting vessel and wire. Diagram to demonstrate how to mount the vessels and wire the jaws step by step (**a**–**e**). The orange rectangle represents the artery

4. Add KHB to a 500 mL glass beaker and place it in the 37 °C water bath. Place a sintered glass gassing stick into the KHB to continuously gas with 95% O_2/5% CO_2. This KHB will be used to wash and re-fill each chamber.
5. Cut a single piece of 25 μm tungsten wire approximately 2.2 cm long (*see* **Note 3** for conduit vessel advice).
6. Place the wire on the left-hand jaw and center between both jaws, move the jaws together until the wire is clamped (*see* **Note 9**).
7. Wrap the top end of the wire around the screw clockwise and tighten the screw (Fig. 2a).
8. Fill the myograph chamber of the 620 M with 5 mL of cold, freshly gassed (95% O_2/5% CO_2) KHB (*see* **Note 10**).

9. Transfer a single vessel into the chamber.
10. Using forceps, feed the vessel onto the end of the wire and thread until the vessel is in the middle of both jaws. Try to do this in one smooth motion as this helps to prevent damage of the vessel (*see* **Note 11** and Fig. 2b).
11. Take the free end of the wire with the forceps and gently pull the wire along the jaw and wrap clockwise around the screw. Tighten the screw with the screwdriver (Fig. 2c).
12. Cut a second piece of wire (25 μm tungsten), approximately 2.2 cm long (*see* **Note 3** for conduit vessel advice).
13. Gently feed the second wire through the lumen of the mounted vessel (*see* **Note 12**), and clamp the wire between the two jaws (Fig. 2d).
14. Use forceps to secure the end of the wire in a clockwise direction and tighten the screw. Take the free end of the wire and wind clockwise around the remaining jaw and tighten the screw (Fig. 2e).
15. Move the jaws slightly apart so that the wires are not touching each other but are not stretching the vessel.
16. Measure the vessel length using a previously calibrated eyepiece graticule in the dissecting microscope. Position the beginning of the ruler at one end of the vessel and record the measurement (referred to as α1 endpoint). Measure the length of vessel in ocular divisions and make a note of the measurement at the other end of the vessel segment (referred to as the α2 endpoint). These values will be used during the normalization procedure in Subheading 3.3.
17. Place the myograph unit with the mounted vessel onto the myograph interface and plug the transducer cables into the back of the interface. Open the gas supply to the myograph and ensure that the vessel is gassed with 95%O_2/5%CO_2 at all times (*see* **Note 13**).
18. Replace the KHB in the chamber with 5 mL of 37 °C, freshly gassed (95%O_2/5%CO_2) KHB.
19. Use the menu on the myograph to zero the channel.
20. Cover the channel with the chamber cover and allow the vessel to equilibrate for 45 min.
21. Repeat **steps 5–20** for the remaining vessels.

3.3 Equilibration and Normalization

After an equilibration period of 45 min at a resting tension, the vessels are normalized to enable comparison of vessel function [2]. During this period, regular KHB change prior to the assessment of vascular reactivity is pertinent.

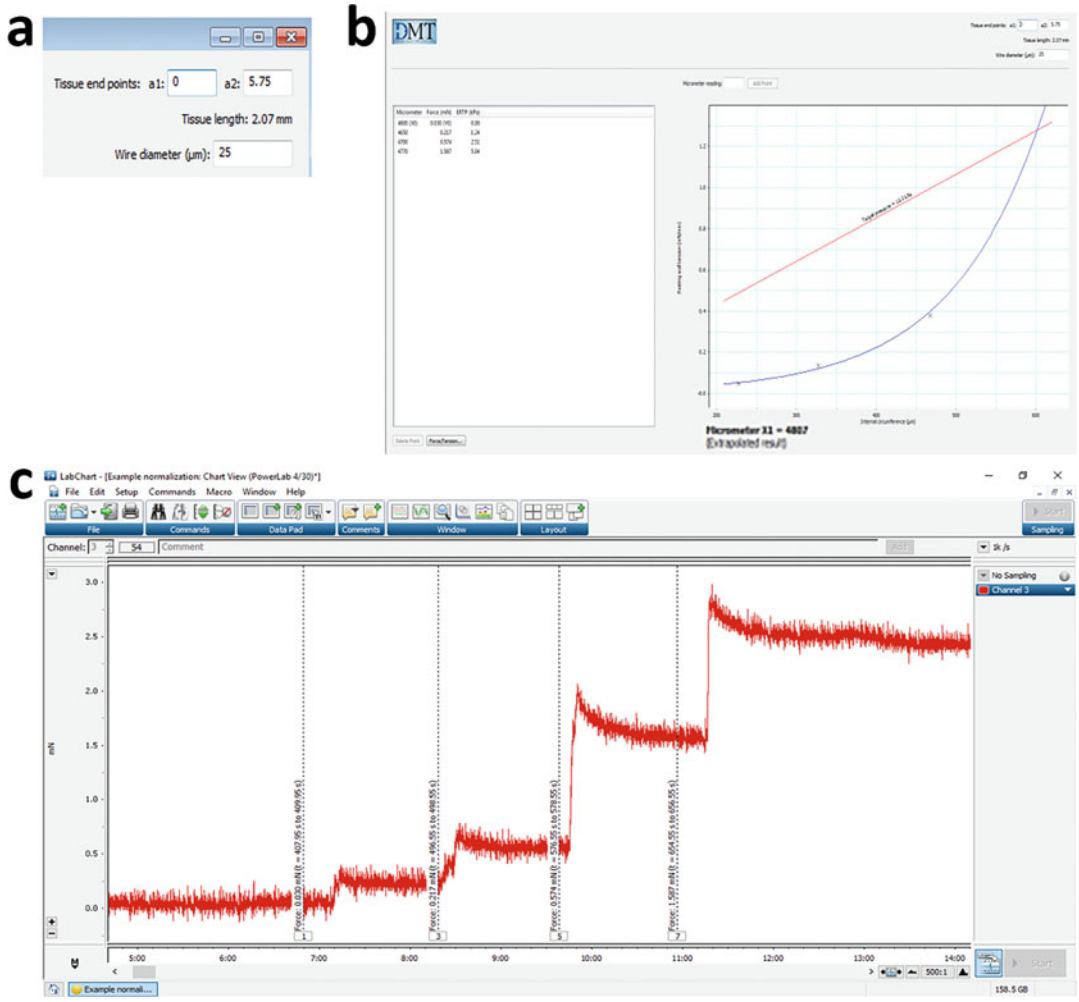

Fig. 3 Example of a normalization trace generated by LabChart. (**a**) Example of tissue endpoints and calculated vessel length. (**b**) Trace for one channel showing force generated over time in a stepwise manner during normalization. (**c**) The corresponding force and micrometer readings, as well as the calculated resting wall tension and internal circumference data. Once the artery has reached a tension corresponding to a pressure of 100 mmHg, a micrometer X1 value is generated. This value is used to manually set the distension of the artery. Software used is LabChart 7, ADInstruments

1. Add 5 mL of 37 °C, freshly gassed ($95\%O_2/5\%CO_2$) KHB to the bath.
2. Press start on the LabChart trace.
3. Zero each chamber before beginning normalization.
4. Click the DMT tab, select the channel of choice, and fill in the boxes with the appropriate tissue end points and wire diameter (Fig. 3a). This will enable the automatic calculation of the vessel length from the eyepiece calibration (mm/div) value found in the DMT normalization settings window.

Tissue end point α1: the graticule reading for the far end of the vessel segment.

Tissue end point α2: the graticule reading for the near end of the vessel segment.

Wire diameter μm: 25 (*see* **Note 3** for conduit vessel instructions).

5. Take an initial reading from the micropositioner, ensure that the wires are slightly apart, but not stretching or putting any force onto the vessel before taking this reading. This is known as X_0. Record this value in the "micrometer reading" box on LabChart and press add point. The programme will show a 60 s countdown when it is recording the force measurement (Y_0).
6. After 60 s, when the box for the micrometer reading becomes available, slowly stretch the vessel by turning the micropositioner and moving the jaws apart until a small increase in force is visible on the LabChart trace.
7. Take another reading from the micropositioner, record on the LabChart file, and add point. Repeat **steps 6** and **7** in a stepwise fashion (Fig. 3b), until an exponential curve is generated in which the LabChart window will display a "micrometer X1" value (Fig. 3c). This X1 value will be the optimal passive tension. Use this value to adjust the micromillimeter scale.
8. Replace the KHB in each chamber with 5 mL of 37 °C, freshly gassed ($95\%O_2/5\%CO_2$) KHB and allow the vessels to continue equilibrating for another 20 min.

3.4 Assessing if the Vessel Is Viable

Before beginning any experimental procedures, it is important to assess the vessel viability and this is done by contracting the vessel using a potassium chloride (KCl) solution.

1. Add final concentration of 4.8 mM of KCl to the myograph chamber (*see* **Note 14**).
2. Allow a few minutes for the vessel to contract and plateau (*see* **Note 15** and Fig. 4).
3. To wash the vessel, replace the KHB in each chamber 3 times with 5 mL of 37 °C, freshly gassed ($95\%O_2/5\%CO_2$) KHB.
4. Leave the vessel to equilibrate for 30 min. During this time the tension should return to basal tension; if this does not occur, carry out an extra KHB wash.
5. If a vessel does not contract to KCl, then it should be excluded from the experiment.

3.5 Calculating the EC_{50} for Mesenteric Vessels in Response to U46619

When assessing relaxation of small mesenteric resistance vessels, it is first important to contract the vessel to 50% of its maximum (EC_{50}) (*see* **Note 16** for conduit information).

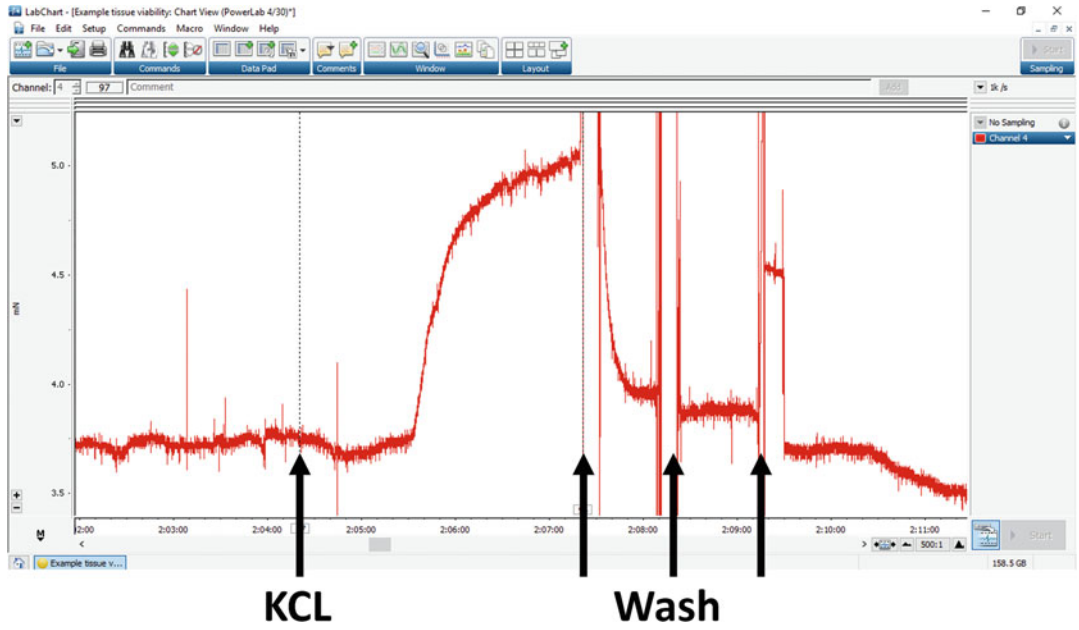

Fig. 4 An example trace of the potassium chloride (KCl) contraction used to assess vessel viability. 4.8 mM KCl (final concentration) is added to the bath to generate an increase in force (contraction). Once the curve has plateaued, the chamber is washed out 3 times with 5 mL of 37 °C, freshly gassed (95%O_2/5%CO_2) KHB and the vessel allowed to stabilize. The vertical dotted line indicates the time point at which the KCl is added to the bath and the bath is washed

1. Start with the lowest concentration of U46619 (1 μM) and add to the bath to give a final concentration of 1 nM (*see* **Note 14**). Wait a few minutes to observe if the vessel has contracted, then gradually add cumulative concentrations to the bath to give a final bath concentration of 1 μM (*see* **Note 17** and Fig. 5).
2. Following the addition of the final concentration of U46619, allow the curve to plateau. Once it has plateaued, immediately wash the vessel by replacing the KHB in each chamber with 5 mL of 37 °C, freshly gassed (95%O_2/5%CO_2) KHB 3–4 times.
3. Allow the vessel to stabilize for 30 min and return to baseline tone.

3.6 Assessment of Endothelial Integrity

This method relies on the relaxation function of the endothelium. The procedure is performed to ensure that the endothelium is not damaged during the dissection or mounting procedure (*see* **Note 18**).

1. Begin by contracting the vessel using U46619, starting with the lowest concentration (1 μM) to give a final bath concentration of 1 nM (*see* **Note 14**). Wait a few minutes to observe if the vessel has contracted.

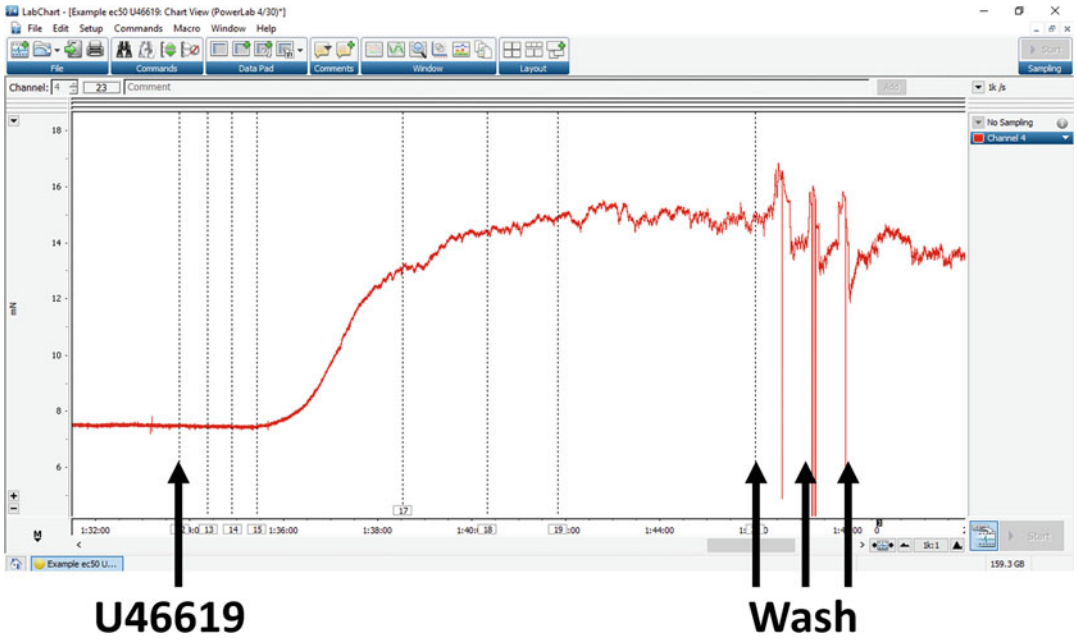

Fig. 5 An example of a U46619 concentration-response curve used to generate the EC_{50} value. Concentrations are added in a cumulative manner starting with the lowest concentration of U46619 (final bath concentration of 1 nM). Each contraction is allowed to plateau before the next concentration is added. After the final concentration (e.g., final bath concentration 1 μM) is added, the chamber is washed out 3 times with 5 mL of 37 °C, freshly gassed (95%O_2/5%CO_2) KHB and the vessel is allowed to equilibrate. The EC_{50} is calculated by determining the concentration that causes 50% of the maximum contraction

2. Monitor the vessel tension carefully while gradually adding cumulative concentrations of U46619 to the bath until the vessel reaches the EC_{50} value of the maximum contraction.
3. When the contraction reaches a stable plateau, add 10 mM acetylcholine (final concentration 10 μM) to the bath to relax the vessel (Fig. 6).
4. Once the vessel relaxation has plateaued, wash the vessel, by replacing the KHB in each chamber with 5 mL of 37 °C, freshly gassed (95%O_2/5%CO_2) KHB 3 times and allow 30 min for the vessel to return to the basal tone.
5. Calculate the percentage relaxation induced by acetylcholine in relation to the contraction induced by U46619. If a 50–100% relaxation with acetylcholine is observed, then the vessel can be used for the next stage of the experiment. If the relaxation to acetylcholine is <50%, then this indicates poor endothelial integrity and therefore this vessel should be discarded.

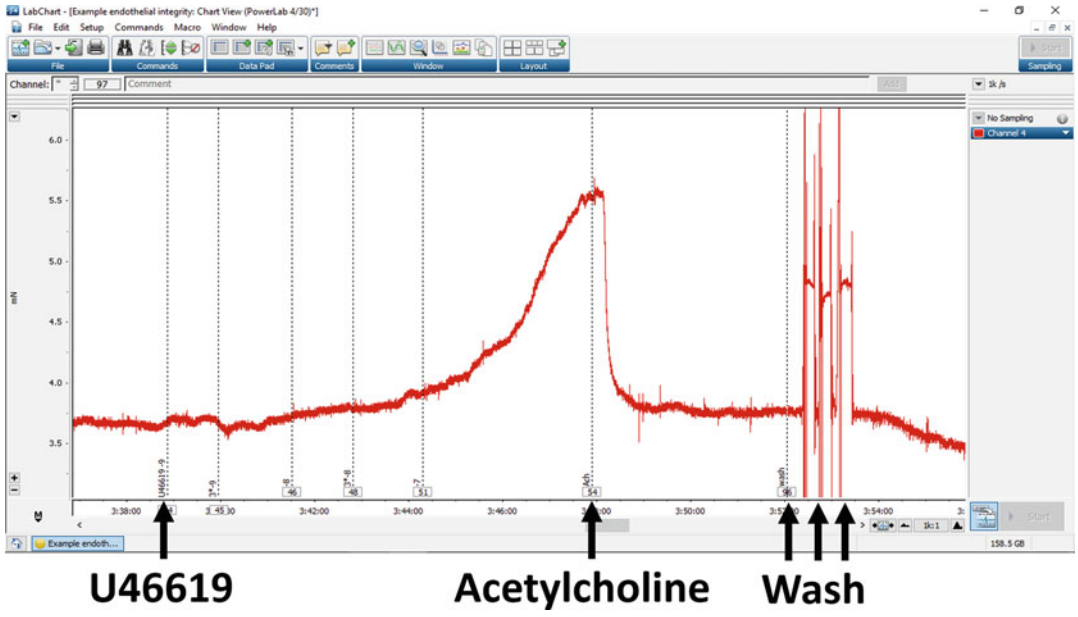

Fig. 6 An example of an acetylcholine relaxation response to determine endothelial integrity. The vessel is pre-contracted with U46619 until the tension equates to the EC_{50} value. As soon as the contraction begins to plateau, acetylcholine (final bath concentration of 1 μM) is added to the bath. This initiates a relaxation of the endothelium if intact. The chamber is washed out with 5 mL of 37 °C, freshly gassed (95%O_2/5%CO_2) KHB 3 times

3.7 Concentration-Response Curve to Acetylcholine to Assess vasodilatory Response

1. Pre-constrict the vessel using the EC_{50} concentration of U46619 as in Subheading 3.6, **steps 1** and **2**.
2. Once the contraction has started to plateau, add the lowest concentration of acetylcholine (1 μM) to the bath, to give a final concentration of 1 nM to the bath and wait a few minutes to allow for relaxation.
3. Add the next concentration of acetylcholine. Allow time for the vessel to relax and plateau before continuing to add increasing concentrations to create a cumulative concentration-response curve, until the final bath concentration is 30 μM (Fig. 7).
4. When the final concentration has been added and the relaxation has plateaued, wash the vessel by replacing the KHB in each chamber 3 times with 5 mL of 37 °C, freshly gassed (95% O_2/5%CO_2) KHB and allow the vessel to stabilize for 30 min before continuing with additional protocols.

3.8 Cleaning Procedure for Myograph Chamber Following Experiments

After the end of each experiment, the myograph chamber should be cleaned to prevent buildup of salts and other pharmacological agents (*see* **Note 19**).

1. Fill the bath with the 8% acetic acid solution and leave for a few minutes.
2. Remove the 8% acetic acid solution from the bath.
3. Wash the bath several times with distilled water.

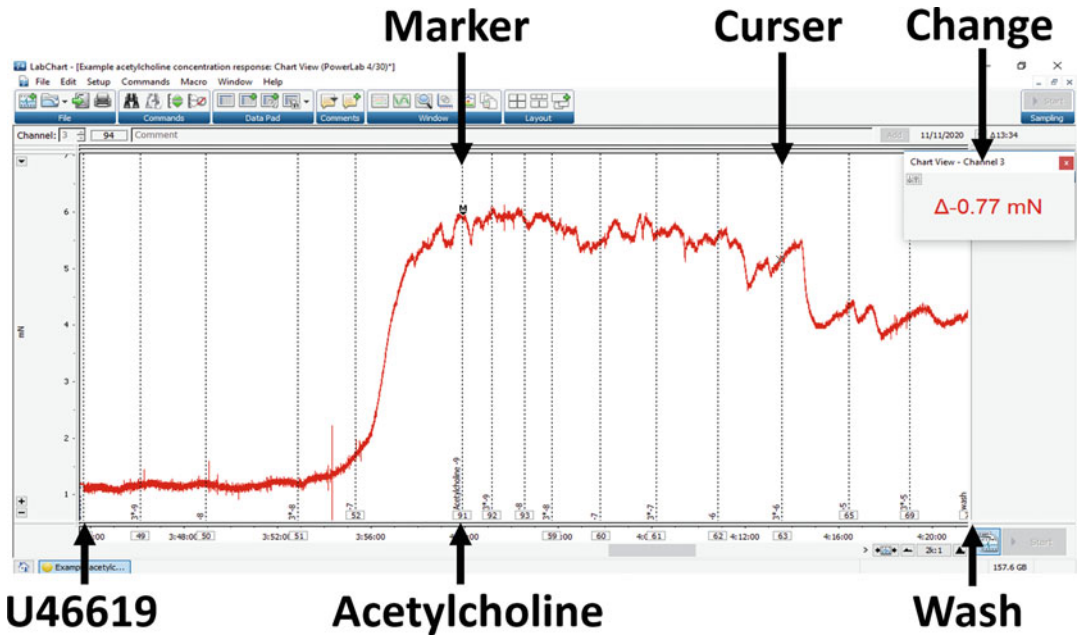

Fig. 7 An example of a concentration-response curve for acetylcholine-induced relaxation. The vessel is pre-contracted with U46619 until the tension equates to the EC_{50} value. Concentrations of acetylcholine are added in a cumulative manner (minimum to maximum concentration) until a final bath concentration of 30 μM is reached. The chamber is washed out with 5 mL of 37 °C, freshly gassed (95%O_2/5%CO_2) KHB 3 times. To determine the change in vessel relaxation in relation to contraction, the marker "M" is placed where the contraction plateaus (indicated by the first arrow on top). The curser (indicated by the second arrow on top) is then placed on the concentration of interest. Change in vessel tension (mN) is provided by LabChart (indicated by the third arrow on top)

3.9 Data Analysis

Data analysis can be completed manually in "chart view" and is used to calculate the change from baseline.

1. Take the marker ("M") from the bottom left corner of the screen and place at the desired point of the recording; for example, where the contractile curve has plateaued following the addition of U46619 (Fig. 7).
2. Move the mouse cursor to the desired point on the recording; for example, the maximum effect initiated by the relaxing agent at the concentration of interest. The LabChart programme then displays the value of the difference between the two points in mN (Fig. 7).
3. Following this, when analyzing concentration-response curves, the vessel responses to agonists, for example acetylcholine, are often expressed as a percentage relaxation response to the vasoconstrictor, in this case to U46619.

4 Notes

1. When preparing the KHB solution, mix all salts apart from the $CaCl_2$ until dissolved. Thereafter, gas (95% O_2/5% CO_2) the solution for 10–15 min and then add the $CaCl_2$ (this is done to prevent precipitation occurring). KHB should be made up several hours prior to or the day before the experiment and stored at 4 °C to allow time for the KHB to become ice-cold. During a standard one-day experiment, approximately 1 L of KHB is used.
2. The dissecting petri dish contains approximately 5 mm thick layer of Sylgard or silicone gel to hold dissecting pins.
3. When using larger diameter arteries (e.g., mouse conduit vessel) stainless steel wire of 40 μm diameter (ADInstruments, DMT 400447) should be used and cut to 2.2 cm long.
4. Aliquots of 10 mM stock solutions of U46619 can be made in advance and stored at −20 °C until required. When using larger diameter arteries (e.g., mouse conduit vessel), a 10 mM stock solution of phenylephrine should be made instead of U46619. Phenylephrine should be prepared fresh on the day of the experiment and kept on ice.
5. Arteries can be identified by their shape; at branching sites they have a distinct "V" shape versus veins that are "U" shaped. Arteries are also more robust, whereas veins are flaccid.
6. Dissection of a blood vessel is best done under a dissecting microscope. It is important to dissect as much of the fat and connective tissue as possible as this can affect vascular responses. To dissect, cut along the length of the artery, rather than horizontally. It is also important that the vessel is not overstretched as this can cause damage and ultimately affect the outcome of experiments. While dissecting the vessel, ensure that the KHB is cold at all times and always replace the KHB with fresh gassed (95% O_2/5% CO_2) KHB, as the buffer pH will change while dissecting the blood vessel.
7. A tip includes using the end of the small screwdriver as a guide to provide the approximate vessel length of 2 mm. If the vessel is too long and exceeds the length of the jaws, it can affect the contraction and relaxation during experiments.
8. It is important to remove clots within the vessel as these can cause damage to the endothelium. To minimize the chance of clot formation, the artery should be extracted immediately after the mouse has been sacrificed. If a clot forms in the vessel, it can be removed by careful shaking of the vessel in the KHB solution.

9. Be careful when moving the jaws, as they are very sensitive. Do not force the jaws together. It is important that the wire remains straight during mounting as it is easier to guide the vessel on and prevents damage to the vessel.
10. Keeping the KHB ice-cold helps the lumen of the vessel to remain open and therefore aids when mounting the vessel onto the wire.
11. If the vessel lumen is closed, try to very gently push the vessel onto the end of the wire as this may open the lumen. Alternatively, use forceps to gently squeeze the end of the vessel.
12. It is important that the two wires remain parallel and don't twist as this will affect the normalization procedure. In the case that the two wires become twisted, remove the second wire and thread again.
13. Ensure that the bubbling is not too vigorous as this can affect the force reading.
14. When using LabChart, it is possible to add comments to the trace indicating when a pharmacological agent has been added or when washing the chambers. This is done by typing into the comments box and pressing "return." A comment can be added to all channels at the same time, as indicated by the "*" or one specific channel. It is essential to add comments to the LabChart trace especially when conducting concentration-response curves as this will help with the analysis.
15. In some cases, the vessel does not contract on the first application of KCl. If this happens, washout the chamber with 5 mL of 37 °C, freshly gassed ($95\%O_2/5\%CO_2$) KHB 3 times and leave the vessel for 10 min before repeating **steps 1–3**. If the vessel has not contracted after two additions of KCl, then it is not viable.
16. Phenylephrine is used instead of U46619 for vessels such as mouse conduit (thoracic aorta). Additionally for vessels such as conduit, the EC_{80} will be calculated. The type of vasoconstrictor used is often dependent on the vessel being studied. For example, phenylephrine is often used in thoracic aortas as it specifically binds to α1 adrenoreceptors and therefore avoids activation with other receptors. On the other hand, U46619 is a thromboxane A2 agonist and can be used in the study of mesenteric resistance vessels.
17. It is important to wait until the contraction is stable before adding the next concentration. At the lowest concentrations, there may be no sign of contraction. Therefore, wait for 2–3 min before adding the next concentration.

18. Some studies may require the removal of the endothelium; for example, when assessing the effect of a lack of the endothelium. The endothelium is removed either mechanically or chemically. In this instance, acetylcholine-induced relaxation is absent.
19. Refer to the manufacturer's guidelines for more detailed information on how to clean the myograph.

Acknowledgments

This work was supported by the British Heart Foundation PG/19/87/34792.

References

1. Mulvany MJ, Halpern W (1976) Mechanical properties of vascular smooth muscle cells in situ. Nature 260:617–619
2. Mulvany MJ, Halpern W (1977) Contractile properties of small arterial resistance vessels in spontaneously hypertensive and normotensive rats. Circ Res 41:19–26. https://doi.org/10.1161/01.RES.41.1.19
3. Gonzaléz-Candia A, Candia AA, Figueroa EG et al (2020) Melatonin long-lasting beneficial effects on pulmonary vascular reactivity and redox balance in chronic hypoxic ovine neonates. J Pineal Res 68:e12613
4. Feelisch M, Akaike T, Griffiths K et al (2020) Long-lasting blood pressure lowering effects of nitrite are NO-independent and mediated by hydrogen peroxide, persulfides, and oxidation of protein kinase G1α redox signalling. Cardiovasc Res 116:51–62. https://doi.org/10.1093/cvr/cvz202
5. Khammy MM, Angus JA, Wright CE (2016) Vascular reactivity of rabbit isolated renal and femoral resistance arteries in renal wrap hypertension. Eur J Pharmacol 773:32–41. https://doi.org/10.1016/j.ejphar.2016.01.004
6. Dautov RF, Stafford I, Liu S et al (2014) Hypoxic potentiation of nitrite effects in human vessels and platelets. Nitric Oxide 40:36–44. https://doi.org/10.1016/j.niox.2014.05.005
7. Lee S, Roizes S, von der Weid PY (2014) Distinct roles of L- and T-type voltage-dependent Ca2+ channels in regulation of lymphatic vessel contractile activity. J Physiol 592:5409–5427. https://doi.org/10.1113/jphysiol.2014.280347
8. Metz AK, Luke CE, Dowling A, Henke PK (2020) Acute experimental venous thrombosis impairs venous relaxation but not contraction. J Vasc Surg 71:1006–1012.e1. https://doi.org/10.1016/j.jvs.2019.03.064
9. Ford TJ, Rocchiccioli P, Good R et al (2018) Systemic microvascular dysfunction in microvascular and vasospastic angina. Eur Heart J 39:4086–4097. https://doi.org/10.1093/eurheartj/ehy529
10. Renshall L, Arnold N, West L et al (2018) Selective improvement of pulmonary arterial hypertension with a dual ETA/ETB receptors antagonist in the apolipoprotein E−/− model of PAH and atherosclerosis. Pulm Circ 8:2045893217752328. https://doi.org/10.1177/2045893217752328
11. Small HY, McNeilly S, Mary S et al (2019) Resistin mediates sex-dependent effects of perivascular adipose tissue on vascular function in the Shrsp. Sci Rep 9:1–9. https://doi.org/10.1038/s41598-019-43326-z
12. Hubert F, Belacel-Ouari M, Manoury B et al (2014) Alteration of vascular reactivity in heart failure: role of phosphodiesterases 3 and 4. Br J Pharmacol 171:5361–5375. https://doi.org/10.1111/bph.12853
13. Leo CH, Hart JL, Woodman OL (2011) Impairment of both nitric oxide-mediated and EDHF-type relaxation in small mesenteric arteries from rats with streptozotocin-induced diabetes. Br J Pharmacol 162:365–377. https://doi.org/10.1111/j.1476-5381.2010.01023.x
14. Nicholson CJ, Sweeney M, Robson SC, Taggart MJ (2017) Estrogenic vascular effects are diminished by chronological aging. Sci Rep 7:1–13. https://doi.org/10.1038/s41598-017-12153-5
15. Arif S, Borgognone A, Lin EL-S et al (2015) Role of aldehyde dehydrogenase in hypoxic vasodilator effects of nitrite in rats and humans.

Br J Pharmacol 172:3341–3352. https://doi.org/10.1111/bph.13122

16. Mulvany MJ (2004) Procedures for investigating of small vessels using small vessel myograph. DMT Danish Myo Technology, Ann Arbor, MI
17. Slezák P, Waczulíková I, Bališ P, Púzserová A (2010) Accurate normalization factor for wire myography of rat femoral artery. Physiol Res 59:1033–1036

Part III

In Vivo Model Systems for Atherosclerosis Research

Chapter 24

Pig and Mouse Models of Hyperlipidemia and Atherosclerosis

Godfrey S. Getz and Catherine A. Reardon

Abstract

Atherosclerosis is a chronic inflammatory disorder that is the underlying cause of most cardiovascular disease. Resident cells of the artery wall and cells of the immune system participate in atherogenesis. This process is influenced by plasma lipoproteins, genetics, and the hemodynamics of the blood flow in the artery. A variety of animal models have been used to study the pathophysiology and mechanisms that contribute to atherosclerotic lesion formation. No model is ideal as each has its own advantages and limitations with respect to manipulation of the atherogenic process and modeling human atherosclerosis and lipoprotein profile. In this chapter we will discuss pig and mouse models of experimental atherosclerosis. The similarity of pig lipoprotein metabolism and the pathophysiology of the lesions in these animals with that of humans is a major advantage. While a few genetically engineered pig models have been generated, the ease of genetic manipulation in mice and the relatively short time frame for the development of atherosclerosis has made them the most extensively used model. Newer approaches to induce hypercholesterolemia in mice have been developed that do not require germline modifications. These approaches will facilitate studies on atherogenic mechanisms.

Key words Pig, Mouse, Lipoproteins, Atherosclerosis, Coronary arteries, Diet, apoE deficiency, LDL deficiency, PCSK9, Antisense oligonucleotides

1 Introduction

The term "animal model" refers to "a pathological or physiological condition that occurs in such an animal and is similar to one occurring in humans" (*Merriam Webster Dictionary*). So in this chapter we will contrast our animal models of atherosclerosis to the process as observed in human subjects. Atherosclerosis is a focal inflammatory process in large and medium sized arteries. There are several risk factors for the development of atherosclerosis that include hyperlipidemia, hypertension, smoking, obesity, and diabetes, some of which will be examined in the models we will discuss. Most of these are predominantly environmentally determined, although there are some examples of single gene abnormalities

Dipak P. Ramji (ed.), *Atherosclerosis: Methods and Protocols*, Methods in Molecular Biology, vol. 2419,
https://doi.org/10.1007/978-1-0716-1924-7_24,
© The Author(s), under exclusive license to Springer Science+Business Media, LLC, part of Springer Nature 2022

that strongly influence the presence (or absence) of atherosclerosis. Among these are familial hypercholesterolemia resulting from a mutation of the gene encoding the low density lipoprotein receptor (LDLR), familial dyslipidemia associated with the homozygosity for the *APOE2* allele, gain or loss of function of proprotein convertase subtilisin/kexin 9 (PCSK9) and *LPA*, the gene that encodes the size variants of apo(a). Each of these mutations primarily affects plasma lipoprotein homeostasis.

Essentially, spontaneous atherosclerosis, as opposed to that attributable to the genetic mutations, occurs only in humans in post-industrial societies. Experimental animals do not develop atherosclerosis unless manipulated either nutritionally or genetically or both. The animal species that have been employed for atherosclerosis research are nonhuman primates, dogs, rabbits, pigs, hamsters, rats and mice, as well as birds such as chickens and pigeons. We have previously reviewed several of these experimental models [1]. Given the contents of this collection and other reviews, we will focus on pigs and mice in this chapter. Pigs are chosen because their lipoproteins and lesion development and distribution are similar to the pathophysiology of humans, while mice are chosen because they are easily managed experimentally and genetically. In addition, mouse animal husbandry is relatively inexpensive, and they have a relatively short life span so experiments can be completed in a reasonable time frame. For these reasons, the mouse is by far the most widely used animal model for atherosclerosis research.

The clinical consequences of atherosclerotic cardiovascular disease (CVD) are myocardial infarction (coronary artery atherosclerosis), stroke (carotid artery atherosclerosis), peripheral artery disease (femoral artery atherosclerosis), and aortic aneurysm (aortic atherosclerosis). Briefly, the atherosclerotic lesion begins with the influx of apoB-containing lipoproteins into the arterial intima in atherosclerosis susceptible regions, where they are retained by binding to proteoglycans and become oxidized. The susceptible regions in the artery wall are the result of hemodynamically determined flow disturbance, usually at branch points and arterial bends. The modified lipoproteins activate the overlying endothelium to induce the expression of adhesion molecules that promote the migration of blood monocytes into the intima. There the monocytes differentiate into macrophages expressing scavenger receptors that are responsible for the uptake of the modified lipoproteins to form the prototypic foam cells of the developing atherosclerotic plaque. Lipoproteins, even unmodified lipoproteins, may also be taken up by macropinocytosis. The foam cell macrophages secrete cytokines and chemokines that interact with the surrounding cells to promote further evolution of the plaque. Smooth muscle cells from the media migrate into the intima, where they may proliferate and take up lipids themselves to become foam cells that are not easily distinguished from the monocyte-derived foam cells. The

smooth muscle cells also synthesize collagen and additional matrix components, while the proliferating cells fashion the fibrous cap that overlies and stabilizes the plaque. The complex inflammatory environment results in the attraction of other immune cells, such as dendritic cells, T cells, B cells, and mast cells. Cholesterol homeostasis becomes dysfunctional in foam cells and the accumulation of free cholesterol induces apoptosis, with the apoptotic cells removed by neighboring macrophages called efferocytes. If not efficiently cleared, the apoptotic cells may progress to necrosis, ultimately forming the necrotic core, which together with proteases secreted by lesional macrophages may destabilize the plaque. The unstable plaque may ultimately rupture and elicit thrombosis, to produce the clinical sequelae of mature atheroma.

As hyperlipidemia is a significant driver of atherogenesis, it is appropriate to provide a brief summary of the human plasma lipoprotein network. Dietary fat includes triglyceride, cholesterol and its esters and phospholipid as well as fat soluble vitamins. These are hydrolyzed to simpler components by lipases, esterases, or phospholipases prior to being absorbed by enterocytes in the small intestine. The absorption of cholesterol is facilitated by Niemann–Pick type C1 like protein (NPC1L1), the target of the drug ezetimibe to limit cholesterol absorption which is often used in combination with a statin to treat hyperlipidemia. After absorption, the lipids are re-esterified and the triglycerides and cholesteryl esters are packaged into large apoB48-containing triglyceride-rich chylomicron particles. The lipidation of apoB48 is catalyzed by the microsomal triglyceride transfer protein (MTTP). Chylomicrons, as their name suggests, passage to the lacteals, lymph ducts, and ultimately into the blood stream. In the capillaries, their triglycerides are lipolyzed by lipoprotein lipase (LPL) made in parenchymal cells (muscle and adipocytes) with the help of the chaperone GPIHBP1 (GPI anchored, heparin binding protein 1). The liberated fatty acids provide either fuel for oxidation or are stored as cytoplasmic droplets depending on the tissue. The resultant cholesteryl ester-rich chylomicron remnants acquire apoE from the plasma and are removed by the liver by one of three receptors: LDL receptor like protein 1 (LRP-1), LDLR, or heparin sulfate proteoglycans (HSPG). The liver synthesizes fatty acids from carbohydrate, and these are incorporated into the hepatic triglyceride-rich very low density lipoprotein (VLDL) particles, which are smaller than chylomicrons. ApoB100 and apoE are the core proteins of VLDL. Secreted VLDL is also lipolyzed, liberating its fatty acids to generate intermediate density lipoprotein (IDL) that can be further metabolized to LDL. VLDL also contains apoproteins C-I, C-II, and C-III. ApoC-II is an activator of LPL, while apo C-III is an inhibitor of the lipase. The hepatocyte LDL receptor is responsible for the clearance of LDL from the plasma while the receptor on peripheral tissue cells mediates the uptake of LDL into cells that

require cholesterol. Hepatic cholesterol homeostasis is controlled by local cholesterol synthesis, uptake from LDL and chylomicron remnants and excretion in the bile either as free cholesterol or bile acids. Cholesterol synthesis and expression of the LDL receptor is regulated by the well-studied active cholesterol pool, localized mostly in the endoplasmic reticulum. High density lipoprotein (HDL) is also an important carrier of cholesterol in the blood by the process of reverse cholesterol transport from tissues, including atheromas. HDL has two core proteins, apoA-I and apoA-II, both of which are made in the liver and the intestine. The proteome of HDL is very heterogeneous, including additional proteins such as apoA-IV, apoA-V, apoE, and apoCs and many minor protein species. Human HDL is heterogeneous in size, with two major subspecies HDL_3 and HDL_2. Many of the non-apoB apoproteins can exchange between HDL and VLDL. Triglycerides and cholesteryl ester in the core can also exchange between HDL and apoB-containing lipoproteins catalyzed by cholesteryl ester transfer protein (CETP). There are three isoforms of apoE, apoE2, apoE3 and apoE4, which are determined by individual alleles. ApoE3 is the most prevalent isoform. As indicated above, apoB may exist as either apoB100 or apoB48. ApoB48 is generated by the editing of the mRNA for apoB100 to introduce a termination codon in the middle of the mRNA through a C to U base modification. ApoB100 is a powerful ligand for the LDL receptor, while apoB48 is not. In humans, the apoB mRNA editing occurs only in the intestine.

2 Hyperlipidemia and Atherosclerosis in the Pig

2.1 Pig Lipoproteins

A major reason for the choice of the pig as an atherosclerotic experimental model is its similarity in cardiovascular physiology and anatomy to humans. So unless otherwise noted, it is taken for granted that what applies to humans also applies here. The major plasma lipoproteins in pigs are LDL and HDL. Unlike the human pattern, pig HDL is more homogeneous in size and density [2, 3]. But similar to human HDL, the lipidome and proteome are very complex, containing about 250 lipid species and more than 500 protein spots by mass spectrometry [4]. Similar to humans, apoA-II is present as a dimer [5]. Cholesteryl ester can move unidirectionally from HDL to LDL despite the lack of CETP in this species [6]. The pig does not contain allelic variants of apoE. However, similar to humans, apoB100 is only expressed in the liver and the editing of the apoB mRNA in enterocytes is almost as efficient in the pig (82%) as in humans (90%) [6].

Hypercholesterolemia in pigs has been induced by dietary intervention or resulting from naturally occurring variants or induced genetic modifications. Feeding a high cholesterol (1.5%)

high fat (15% lard) diet to miniature pigs leads to the appearance of two new lipoproteins in addition to increased levels of LDL. This includes cholesteryl ester-rich β-VLDL, containing apoE, and a large cholesterol-rich HDL (HDLc) containing apoE as its major protein [7]. Two LDL subspecies, LDL_1 and LDL_2, are present in the plasma of chow fed Yorkshire minipigs. The responsiveness to dietary cholesterol (0% to 2.5% cholesterol) in the presence of 15% fat in Yorkshire minipigs was studied by Pownall and colleagues [8]. Plasma cholesterol levels and LDL subspecies did not differ between 0% and 1% dietary cholesterol. But as dietary cholesterol increased beyond 1.0%, plasma cholesterol levels rose and the LDL increased in size and decreased in density with a progressive reduction in its triglyceride content.

Genetic hyperlipidemia has been examined in pigs with naturally occurring allelic variants of apoB100 and the LDL receptor. As a result of isolated breeding of pigs around the world, there are many porcine strains. A variety of immunologically distinct allotypic epitopes on apoB have been identified. Genetic studies by Rapacz and colleagues indicate that the apoB proteins contain a unique distinctive epitope encoded by allelic variants (designated *Lpb*) of the *Apob* gene [9]. Some of these variants are functionally significant. Alloimmunization experiments have identified rarer allotypic variants in other apoproteins associated with LDL as well [9]. The LDL from pigs heterozygous for *Lpb2* and *Lpb3* allelic variants have been physically separated into Lpb2 and Lpb3 containing particles, taking advantage of the immunochemical distinctions of the apoB proteins [10]. Allotypes Lpb9, Lpb10, and Lpb101 are confined to miniature pigs [11]. Among the *Lpb* alleles, *Lpb5* is associated with spontaneous hypercholesterolemia due to increased LDL levels and advanced atherosclerosis and has received the most attention as a model of familial hypercholesterolemia [9]. Lpb5 pigs also have two other allotypic lipoprotein antigens (Lpr and Lpu). Pigs with the *Lpb5* allele are phenotypically heterogeneous, with some demonstrating moderate hypercholesterolemia (designated Lpb5.2 pigs) and others with severe hypercholesterolemia (designated Lpb5.1 pigs). The LDL in both subtypes have decreased affinity for the LDL receptor. The apoB of *Lpb5* carrier pigs contains 13 amino acid polymorphisms compared to phenotypically normal apoB [12]. The most important of these polymorphisms are at Asp3164 and Ala3447, which together are thought to influence the microenvironment of a lysine residue important for interaction with the LDL receptor. However, the LDL in Lpb5.1 pigs is more buoyant than the LDL found in Lpb5.2 and normal lipidemic pigs [13]. The LDL from Lpb5 pigs and normal lipidemic pigs were fractionated by ultracentrifugation into 5 fractions [14]. Fractions 2 ($d = 1.021$–1.028 g/mL) and 3 ($d = 1.032$–1.043 g/mL) were enriched in cholesterol and this was influenced by the *Lpu* allelic variant of an unidentified apoprotein. Compared to normal

lipidemic animals, pigs heterozygotes for the *Lpb5/Lpu1* haplotype had 6.6-fold more cholesterol in fraction 2 and homozygotes had 12.7-fold more cholesterol. In fraction 3, the heterozygous and homozygous pigs have 4.6- and 6.9-fold more cholesterol, respectively. The cholesterol content of the other 3 fractions were similar to normal lipidemic pigs.

As the buoyant LDL mass in Lpb5 pigs was not due to increased conversion from the precursor VLDL [13], the fractional catabolic rate (FCR) of normal LDL and the cholesterol enriched LDL from Lpb5 pigs was examined [15]. When injected into control pigs, the FCR of LDL from Lpb5 pigs was ~30% lower than normal LDL, consistent with its lower affinity for the LDL receptor. When injected into Lpb5 pigs, the FCR of both LDLs were similar but the FCR for both LDLs were lower than that observed in control pigs. This suggests that LDL metabolism in the Lpb5 pigs is complex, involving not only differences in the LDL but also in the ability to clear LDL. Indeed a mutation in the LDL receptor was discovered in these pigs involving a substitution of arginine at position 84 by a cysteine [16]. Thus, these pigs carry mutations in their apoB and their LDL receptor. Based on selective breeding to segregate the two genes, it appears that the mutation in the LDL receptor plays a larger role in the genesis of the hypercholesterolemia in this strain of pigs. The larger LDL found in pigs homozygous for LDLR R84C mutation is enriched in sphingosine-1-phosphate, ceramide, and sphingomyelin [17].

Although the familial hypercholesterolemia was associated with the *Lpb5* allotype, other allotypes may also be associated with hypercholesterolemia. This was demonstrated by the study of a three family sibship of hypercholesterolemia [18]. There was considerable variability within each family, so parameters were examined in those with high (mean 316 mg/dL), intermediate (mean 159 mg/dL), and normal (mean 105 mg/dL) cholesterol levels. LDL cholesterol, apoB, apoE, and apoC-III levels followed a similar gradient.

Atherosclerotic pig models have also been generated by genetic manipulations of the genes for apoE and the LDL receptor. These genetic models will be discussed in more detail in the next section.

2.2 Pig Models of Atherosclerosis

2.2.1 Diet-Induced Atherosclerosis

Since the morphology of porcine atherosclerotic lesions is similar to that of human lesions, they are a useful model. Their morphology and development includes the formation of complex lesions with necrotic cores, neovascularization, calcification and thin fibrous caps and similar distribution of atherosclerotic plaques in the vascular tree, including in the coronary arteries, a clinically important site in humans. The focal development of lesions has been evaluated based on the high permeability of lesion-prone areas of the aortic arch to Evans blue dye in Yorkshire-Landrace pigs fed 1.5% cholesterol and 19.5% lard [19]. Blue stained areas indicating increased

permeability manifest even before lesions are detectable either grossly or microscopically. By 2–6 weeks of atherogenic diets, there is increased adhesion of blood monocytes to the endothelium in the blue areas compared to less permeable white areas of the aorta of the hyperlipidemic pigs and blue areas of the aortas of normolipidemic pigs. ApoB is immunochemically detectable in the extracellular areas of the blue stained areas but not white areas or blue areas of the aortas of normolipidemic pigs [20]. By 12 weeks of diets, the monocytes are mostly within the intima [19]. The intima in the blue areas is thickened with edema and contains collagen and elastin. The endothelial cells overlaying the blue areas are short and cuboidal and relatively rich in endoplasmic reticulum and lysosomes in contrast to the flattened, elongated traditional profile characteristic of normal endothelium [21]. Longer-term feeding of this pig model has shown that more advanced lesions are present in the infrarenal abdominal aorta, the aortic arch, the carotid arteries, and the proximal portion of the coronary arteries, though the presence can be variable. By 6 months of feeding, the advanced coronary lesions exhibit extracellular lipid pools, lipid-rich necrotic cores, a thin fibrous cap, macrophages, and calcification. Also in the coronary artery lesions, there are signs of inflammation. The differential permeability demonstrated in the aortic arch with Evans blue, which is almost certainly the response to hemodynamic forces, offers an excellent opportunity to define the genetic control of early atherogenesis taking advantage of state-of-the-art modern methodologies, such as single cell RNA sequencing.

Diabetes is one of the most prevalent risk factors in the aggravation of atherogenic vascular disease. This increased risk has been demonstrated in the Yorkshire pig model by streptozotocin-mediated induction of type 1 diabetes at the time of high fat diet initiation [22]. Though diabetes did not change the plasma cholesterol levels, plasma triglyceride levels were increased. By 12 weeks of diet, the aortic area stained by Sudan IV (neutral lipids) was twice as extensive in the diabetic animals and the aorta contained twice as much cholesterol as non-diabetic animals. Coronary lesions occurred predominantly in the first 2–3 mm of the artery and by 20 weeks of diet, coronary artery stenosis was much more extensive in the diabetic vessels.

This same diabetic pig model was used to correlate coronary lesions with hemodynamics [23]. In areas of persistent endothelial low shear stress, as determined by angiography, intravascular ultrasound (IVUS), and computational hemodynamics, eccentric thin capped plaques were observed. These lesions had decreased smooth muscle cells which underwent phenotypic modulation towards myofibroblasts, decreased procollagen type I mRNA and collagen content along with increased mRNA and protein levels of several metalloproteinases. The role of wall shear stress was also examined

in a carotid collar model using Rapacz pigs with the LDLR R84C mutation that were "downsized" by crossing with minipigs [24]. Lesions only developed in the post-stenotic region accompanied by both low shear stress and oscillating flow. With respect to mechanisms of early atherogenesis, Gerrity used electron microscopy to show the migration of monocytes into the intima and transformation to foam cells [25]. As LDL enters the intima, it is oxidized by the cells of the intima and this facilitates its uptake by scavenger receptors on the lesion macrophages. The proportion of LDL in the lesion that was oxidized was assessed in minipigs fed a diet highly enriched in cholesterol for 6, 14, and 24 weeks [26]. Without any further increase of plasma LDL after 6 weeks of diet, LDL continues to accumulate in the intima. By 24 weeks of diet, essentially all of the LDL in the intima of the left anterior descending coronary artery was oxidized, as quantitatively measured immunochemically, and was associated with monocyte/macrophages. As the lesion progresses, the artery undergoes compensatory enlargement as has been described by Glagov and colleagues in human coronary arteries [27].

The Wilensky group examined lesions in hypercholesterolemic type 1 diabetic pigs after 1, 3, 6, and 9 months of diet [28]. Unfortunately, cholate was included in the diet to enhance the hypercholesterolemia. There were no lesions at 1 month. By 3 months more than half of the coronary arteries and 90% of the thoracic artery had developed lesions in contrast to only 20% of the carotid arteries. By 6 months and beyond, all of the coronary arteries and thoracic artery samples had lesions. By 9 months, the most complex advanced lesions were seen in the coronary arteries. The expression of 59 genes known to be differentially expressed in stable and unstable human atherosclerotic plaques or known to influence atherogenesis were examined in the vascular sites. The expression of genes involved in cholesterol metabolism, insulin response, and inflammation increased significantly after 3 months of diet and were upregulated in the coronary artery more than in the carotid and thoracic aortas [28]. This study is a valuable contribution in that it examines three vascular sites at four different times so that the pattern of progression and gene expression can be dynamically evaluated. It is, however, limited in that the same arterial samples are not assessed for histology and gene expression. For example, one coronary artery was assessed histologically and the other major coronary artery was employed for gene expression analysis. Also, the whole artery was used for gene analysis so that this does not reflect differences in lesion and non-lesion areas. With further application of state-of-the-art methodology, much can be learned with this model.

The above studies demonstrated that type I diabetes augmented atherosclerosis in hypercholesterolemic pigs. The metabolic syndrome is a complex syndrome in which obesity, impaired

glucose tolerance, insulin resistance, and hypertension co-exist with atherosclerosis. Ossabaw minipigs are susceptible to the development of metabolic syndrome. Atherosclerosis in male Yucatan minipigs and Ossabaw minipigs have been compared [29]. The features of the metabolic syndrome were observed in the Ossabaw pigs, but not the Yucatan pigs fed an atherogenic diet containing 2% cholesterol, 19.5% fat and sodium cholate. The male Ossabaw minipigs also displayed coronary microcirculatory dysfunction. The coronary atherosclerosis was more diffuse in the Ossabaw minipigs extending over much of the coronary vessels, while in the Yucatan minipigs, the lesions were mostly confined to the proximal portion of the left anterior descending artery. The inclusion of cholate in the diet is a potential confounding factor, but in another study a similar outcome was obtained in female Ossabaw pigs fed an atherogenic diet without cholate [30]. The Ossabaw pigs fed the same cholate-containing diet for 4 months had diffuse compensatory expanded coronary arteries (the Glagov phenomenon) [31].

Most of the above description relates to Yorkshire pigs. Yet other strains of pigs have also been used in diet-induced atherosclerosis studies. In one study, Gottingen minipigs have been compared to domestic Swedish Landrace swine [32]. Abdominal aortic atherosclerosis was observed in both strains after 18 months of a lipid-rich diet, but macroscopic lesions were only observed in the coronary arteries of the Gottingen minipigs despite comparable plasma cholesterol levels. The coronary arteries showed pronounced proliferative lesions. Other minipig strains used for atherosclerosis experiments include Yucatan pigs, Ossabaw pigs, and Bama pigs. The Yucatan pigs and Ossabaw miniature pigs are relatively atherosclerosis sensitive strains among the studied subspecies, while the Landrace pigs are relatively resistant. The differences among strains of pigs studied alongside of one another implies an importance of the genetic background in which atherosclerosis develops.

Among the modulators of atherosclerosis is gender. Most reports have been with male pigs. Jacobsson et al. compared male and female Gottingen minipigs [33]. LDL levels were initially higher in females than males but equalized with the progression of the experiment. Abdominal aortic lesions were similar in both sexes, but the coronary arteries had higher cholesterol content in females than males.

2.2.2 Natural and Genetically Engineered Mutant Pigs

Up to this point, we have mainly described dietary induction of hypercholesterolemia and atherosclerosis, with or without diabetes induction. But there are pig models with natural genetic mutations and that have been genetically engineered that also develop atherosclerosis, some of which have been reviewed by Hamamdzic and Wilensky [34]. The Rapacz familial hypercholesterolemia model with the *Lpb5* allele and *Ldlr* R84C mutation is one of the first genetic models of atherosclerosis to be studied [35]. The lesions

grow relatively slowly in low fat chow diet fed pigs. Lesions were observed in the coronary arteries and the peripheral iliac and femoral arteries by 12 months of age. At this time point, the coronary lesions were composed mostly of macrophage-derived foam cells, while the peripheral arteries were more fibrous. By 2 years stenotic coronary artery lesions were found characterized by necrotic cores, granular calcium deposits, cholesterol clefts, and neovascularization. The peripheral arteries were smooth muscle-rich and fibrous. By 3 years, the coronary arteries were more complex with fibrous caps and more extensive vascularization and possible signs of rupture. The complexity of these lesions was correlated with the extent and duration of hypercholesterolemia. However, this model requires an extended time course for lesion development, making it an expensive experimental model. The model has been now been downsized by crossing into the Gottingen minipig.

Our understanding of the regulation of the LDL receptor has advanced in the last 10–15 years with discovery of PCSK9, an autocatalytic protease that is secreted into the plasma primarily from the liver [36]. PCSK9 binds to the LDL receptor targeting the receptor to the lysosome for degradation rather than recycling back to the cell surface. The reduced density of the receptor on the cell surface results in an attenuation of the clearance of plasma LDL. Gain of function (GOF) and loss of function (LOF) variants of the protein have been identified [37]. A major GOF variant involves the substitution of aspartic acid 374 by tyrosine in human PCSK9's catalytic domain leading to enhanced LDLR degradation and increased plasma LDL levels. Capitalizing on this property, Al Mashhadi et al. [38] employed Sleeping Beauty transposons and somatic cell nuclear transfer to generate transgenic Yucatan minipigs expressing PCSK9-D374Y under the control of liver-specific promoter to generate hypercholesterolemic pigs. To induce a more significant hypercholesterolemia, male transgenic pigs were fed a 20% lard diet supplemented with 2% cholesterol for up to 1 year. Atherosclerosis was increased in the left anterior descending coronary artery, the aorta, and the iliofemoral arteries compared to nontransgenic pigs [38, 39]. In this study, the most advanced lesion of each vascular site was examined histologically. In the coronary artery, the lesion was extensive, contained necrotic cores, intraplaque vascularization and hemorrhage as well as calcification. These were very human-like lesions. This model lends itself to *in vivo* imaging and significant tissue sampling for biochemistry and gene expression analysis, a significant advantage over mouse models of atherosclerosis.

Another approach to the reduction of liver expression of the LDL receptor is to knock out the receptor gene using an adeno-associated virus (AAV) containing a neomycin resistant gene insert with an upstream termination codon into exon 4 followed by

somatic cell nuclear transfer [40]. This truncation reproduces one of the human LDLR mutations. Homozygous *Ldlr−/−* Yucatan minipigs had six to eightfold higher levels of plasma LDL compared to wild-type pigs on standard chow or a high fat diet. No lesions were noted in 7-month-old wild-type pigs on standard chow but early lesions were observed in the abdominal aorta and the right coronary artery, left anterior descending coronary artery and circumflex artery of chow fed *Ldlr−/−* pigs. Both heterozygous and homozygous receptor deficient Yucatan minipigs were fed a high fat (40%), high cholesterol (1%) diet for 3 or 6 months. Although small lesions were found with this diet in control and heterozygote pigs, much more extensive lesions were present in the three vascular sites in the *Ldlr−/−* pigs.

An AAV-mediated strategy was used to delete the third exon of the *APOE* gene (coding for the LDLR binding domain) followed by somatic cell nuclear transfer achieved the development of *APOE* deficient Yucatan minipigs [41]. These animals accumulated apoB48-containing remnants in their plasma, which was accentuated by the feeding of a high fat (20% lard), high cholesterol (2%) diet initiated at 8 weeks of age. Coronary arteries and the thoracic aorta in pigs on the high fat diet exhibited flattened xanthoma type lesions. More progressive fibroatheromatous lesions are seen in the abdominal aorta and the iliofemoral arteries. *APOE* deficiency was created in Bama minipigs using clustered regularly interspaced short palindromic repeats (CRISPR)/CRISPR associated protein 9 (cas9) technology and somatic cell nuclear transfer [42]. Three classes of mutants were obtained—a 4 bp or 5 bp deletion which created frame shift mutants expressing no apoE ($APOE^{-/-}$) and a 39 bp in-frame deletion which expressed low levels of apoE lacking 13 amino acids within the LDL receptor binding domain ($APOE^{m/m}$). Male pigs were studied on chow diet or were fed a 30% fat, 1.5% cholesterol diet for 6 months. The $APOE^{-/-}$ pigs had elevated HDL and LDL cholesterol especially on the high fat diet. Coronary arteries exhibited extensive sudanophilic lesions while the aortas had fibroatheromatous lesions. Clearly with the difference in lipoprotein profiles between $APOE^{-/-}$ pigs and $LDLR^{-/-}$ pigs, there is a difference in the distribution and progression of atherosclerosis.

2.2.3 Atherosclerosis Regression

The characterization of experimental atherosclerosis has two major goals: the understanding of the mechanism and pathogenesis of the disease evolution and the exploration of the ability to reverse these changes. A few studies of regression of dietarily induced atherosclerosis have been reported in pigs. Hypercholesterolemia was induced with 15% beef tallow and 1.5% cholesterol in Gottingen minipigs. After 6 months of diet, the animals were switched to a standard chow diet for a further 9 months [43]. The blood cholesterol levels rapidly returned to baseline levels of ~70 mg/dL from

over 1000 mg/dL. The fatty streak lesions in the thoracic aorta regressed, while the fibrous plaques in the abdominal aorta were resistant to regression. In another study, the influence of fish oil or its constituent polyunsaturated fatty acids on regression of lesions in several arteries of Yucatan minipigs was examined [44]. In this case, the diet induction period was 8 months and was followed by a 4-month regression period with standard diet with and without the supplementation with fish oil or an oil mixture with similar polyunsaturated:saturated fat ratio but different ratios of n-3 and n-6 fatty acids as the fish oil. Plasma cholesterol returned to baseline by 2 months in all regression diets. There was substantial reduction of fatty streak lesions in the ascending aorta, the thoracic aorta, and the carotid arteries, but not in the abdominal aorta. These changes were not influenced by the ratio of n-3 and n-6 fatty acids in the diet. For the coronary arteries, there was a tendency to exhibit a reduction in the area of sudanophilia with the addition of the fish oil (high in n-3 fatty acids) to the regression diet but the changes in this relatively brief regression duration did not achieve statistical significance.

Summarizing this section of this chapter, the minipig is an attractive model for the study of experimental atherosclerosis, especially with the emergence of new molecular approaches to the genetic modulation of the pigs without requiring extensive and expensive genetic crosses. The similarity of the pathophysiology of the lesions in these animals with that of humans, including developing lesions in the coronary arteries, is a major advantage of this model. The development of atherosclerotic cardiovascular disease in humans is a multifactorial, multifocal vascular disease that evolves over a lifetime that is coterminal with the lifetime of the investigator. So it is not feasible to exactly simulate the time scale of the disease development. It is necessary to accelerate the evolution of the pathology by inducing hypercholesterolemia, either dietarily or genetically. This is of course the major limitation of these models of the human disease.

3 Hyperlipidemia and Atherosclerosis in the Mouse

3.1 Mouse Lipoproteins

The lipoproteins of mice differ in a number of respects from those of humans. The predominant lipoprotein in humans is LDL, but in mice HDL is the predominant lipoprotein with low LDL levels. A number of antiatherogenic properties of HDL and its major apoprotein apoA-I have been identified [45]. Mice have a monodisperse HDL profile, whereas humans have two major HDL subfractions designated HDL_2 and HDL_3. This human HDL heterogeneity may be functionally significant in that one of the HDL subspecies may be more efficient in carrying cholesterol from the periphery to the liver for disposal as either free cholesterol or bile

acid. Transgenic expression of human apoA-I confers a human-like HDL polydispersity in mice, indicating that the human HDL heterogeneity is largely determined by the detailed amino acid sequence of apoA-I [46]. ApoA-I is made up of ten amphipathic α-helices of 22 or 11 amino acids in length. Most of these are interrupted by a proline residue. In mouse apoA-I, unlike the human protein, helices seven and eight are not interrupted by a proline residue and this seems to contribute to the difference in size distribution of the HDL [47]. Based on the regular amphipathic helix structure of apoA-I, mimetic amphipathic helices containing 18 amino acids have been synthesized [48]. These mimetic peptides exhibit many of the functional anti-inflammatory and anti-oxidative functional properties of intact apoA-I. Polymorphisms in apoA-I or apoA-II, the second most abundant protein in HDL, are found in inbred strains of mice. As an example of such polymorphisms, C57BL/6 and FVB apoA-I differ by two amino acids located in an important lipid binding helix (helix 10). Glu225 in C57BL/6 is a Lys in FVB apoA-I and Val226 is an Ala. These are the only two polymorphisms found among 40 different strains of mice. We have compared the HDL of C57BL/6 and FVB strains in some detail [49]. The FVB HDL is larger than the C57BL/6 HDL and has twice as much apoA-II and more phospholipid. In apoA-II, there are three polymorphic sites in mice: Asp20 in C57BL/6 apoA-II is Glu in FVB, Met26 is a Val, and Ala38 is a Val. The FVB apoA-I is more tightly associated with HDL than is the C57BL/6 apoA-I.

The proteome of HDL is extremely complex carrying as it does of the order of 80–100 different proteins, many of them in low abundance [50, 51]. One of the more abundant minor proteins on HDL is apoE. ApoE is also found on chylomicron remnants and VLDL, where it serves as a major ligand mediating their clearance from the plasma by LDLR and LRP1. In humans, the three major allelic variants of apoE differ from one another at residues 112 and 158. ApoE2 has a Cys at both these sites, apoE3 has a Cys at residue 112 and Arg at residue 158 and apoE4 has Arg at both sites. No allelic variants of mouse apoE exist. Like human apoE4, mouse apo E has arginine residues at both positions. The amino acids at positions 112 and 158 do not directly interact with the LDL receptor though they do affect the conformation of the protein around the receptor binding domain [52]. Such receptor interaction is different among isoforms. In apoE3, Arg158 forms a salt bridge with Asp154, freeing Arg150 to interact with the receptor. On the other hand, in apoE2, Cys158 cannot form a salt bridge so Asp154 forms a salt bridge with Arg150 thus impairing its interaction with the receptor. The isoforms also differ in their association with lipoproteins, with apoE3 preferentially found on HDL while apoE4 is preferentially associated with VLDL.

In humans, cholesteryl ester transfer protein catalyzes the exchange of cholesteryl esters and triglycerides among the plasma

lipoproteins. However, mice lack this transferase, so that there is normally little catalytic exchange of core lipids.

The apoB mRNA editing mechanism to generate apoB48 exists only in the intestine, not the liver in humans. Thus, apoB48 is an excellent marker for lipoproteins of intestinal origin, namely chylomicrons and their remnants. However in the mouse, apoB editing also occurs in the liver. The knockout of a major component of the editing complex, apobec-1, results in an inability to produce apoB48 [53].

3.2 Mouse Models of Atherosclerosis

In recent decades, most experimental atherosclerosis studies have been focused on the mouse. However, the wild-type mouse is not hyperlipidemic under standard chow conditions and does not develop atherosclerotic lesions. Early studies on murine atherosclerosis used a diet containing 1.25% cholesterol and 0.5% cholic acid to induce atherosclerosis in a variety of inbred strains of mice [54]. These studies indicated that there is a wide range of atherosclerosis susceptibility among the strains with the C57BL/6 strain being among the most susceptible. Lesions induced with this strategy are relatively modest, consisting mostly of foam cell-rich lesions at the apex of the aortic root.

3.2.1 Genetically Engineered Mouse Models of Atherosclerosis

In order to take advantage of the relative ease of genetically manipulating mice to study potential mechanisms of experimental atherosclerosis, it is necessary to dramatically increase the level of apoB-containing lipoproteins. These studies were enormously enhanced by the generation of *Apoe* deficient and *Ldlr* deficient mice. "A golden age for experimental atherosclerosis dawned when Nobuyo Maeda and Jan Breslow knocked out the *Apoe* gene in mice" [55] in 1992. Shortly after the reports from Plump et al. [56] and Zhang et al. [57] on apoE deficiency, the *Ldlr−/−* murine mouse model was reported by Ishibashi et al. [58]. These two models are the most widely used atherosclerosis models, but they differ in a number of respects including their dietary requirements for the development of atherosclerosis. However, it should be noted that the manipulations of genes or therapeutic treatment in the two models do not necessarily have the same effect on atherogenesis [59].

While some models develop atherosclerosis while being maintained on chow, many models require feeding of a high fat, high cholesterol diet. For the study of atherosclerosis in mice, three main diets have been used: 15% fat, 1.0–1.5% cholesterol, and 0.5% cholic acid (the so-called Paigen diet) [60]; the Western type diet (WTD) containing 21% fat and 0.2%–1.25% cholesterol [61]; and a semi-synthetic diet with varying levels of cholesterol [62]. The WTD is often associated with some level of insulin resistance. To counter this, a modified diet consisting of 4.4% fat and 1% cholesterol has been advocated [63].

In the *Apoe−/−* model, atherosclerosis will develop spontaneously while being fed a normal chow diet though it is greatly accentuated by the feeding of a high fat, cholesterol-rich diet, the so-called WTD. Since apoE is an important ligand mediating the clearance of chylomicron remnants, there is an accumulation of cholesterol-rich apoB48-containing chylomicron remnants in chow fed *Apoe−/−* mice, which is further increased by feeding the WTD. On the other hand, the *Ldlr−/−* model is a murine model of human familial hypercholesterolemia and accumulates LDL on chow diet. However, *Ldlr−/−* mice require the feeding of the WTD in order to elicit sufficient hypercholesterolemia to accelerate atherosclerotic lesion development. With this diet, triglyceride-rich VLDLs accumulate along with the LDL.

Other mouse models of atherosclerosis have also been developed. As mentioned above, the mouse is almost unique among species in expressing both apoB100 and apoB48 in the liver. The removal of the ability to produce apoB48 in the liver and intestine of mice by deletion of the *Apobec1* gene results in the exclusive production of apoB100-containing lipoproteins. When these animals were crossed with $Ldlr^{-/-}$ mice, a model was obtained that develops severe atherosclerosis on a chow diet [64]. ApoB100 only mice ($Apob^{100/100}$) were also generated by mutating the edited codon in the mouse *Apob* gene [65]. In order to distinguish the potential atherogenicity of larger remnant sized lipoproteins and smaller LDL sized lipoproteins, Young and colleagues generated $Apoe^{-/-}$ $apoB^{100/100}$ animals and $Ldlr^{-/-}$ $apoB^{100/100}$ animals [66]. Female animals of these two strains fed standard chow had similar plasma cholesterol levels, but in the $Ldlr^{-/-}$ $apoB^{100/100}$ animals, the mean lipoprotein particle size was 24 nm while in the $Apoe^{-/-}$ $apoB^{100/100}$ animals the mean particle size was 63 nm. Atherosclerosis in the whole aorta was greater for the $Ldlr^{-/-}$ $apoB^{100/100}$ animals indicating that the apoB-containing LDL particles are more atherogenic than larger particles. It is likely that the smaller particles, although containing less cholesterol per particle, more readily permeate the endothelium of the artery than the larger particles to drive atherogenesis. Once in the subendothelial space, the lipoprotein sphingomyelin is digested by sphingomyelinase derived from endothelial cells or macrophages, resulting in the lipoprotein aggregation and binding to matrix heparan sulfate proteoglycan. ApoB100 in the LDL binds to these proteoglycans via residues 3359–3369, residues that are not present in apoB48 [67]. ApoB48 associates with the proteoglycan via residues 84–94 that are likely masked in apoB100 [68]. Transgenic mice expressing APOE3* Leiden variant of human apoE, a natural mutant of apoE with low affinity for the LDLR and associated with type III dyslipidemia, also develop atherosclerosis when fed a WTD and has been used by several groups [69].

Each of these models has been employed to assess the impact of relevant modifier genes on the process of atherosclerosis. Many of these studies have been summarized in two valuable reviews [70, 71]. The studies often involve knocking out an individual gene, either globally in the animal or in specific cell types by the addition of loxP sites in the gene and breeding to a transgenic mouse expressing Cre recombinase under the control of a tissue specific promoter. If the expression of Cre is under the control of drug inducible promoter, then the elimination of conditional gene expression can be time dependent.

With respect to the gene selected, the genetic effect is large and there is an implicit selection bias in the genes chosen for manipulation. However in free living human populations, aside from single gene defects such as in familial hypercholesterolemia, the frequency of atherosclerotic associated cardiovascular disease is usually the result of small variations in multiple genes interacting with elements of the environment [72]. Multiple genome wide association studies (GWAS) have described gene associations with various phenotypes relevant to atherosclerotic heart disease. The mouse analog of this is found in the mouse hybrid diversity panel which incorporates the genome of 100 inbred strains of mice. To identify genes impacting atherosclerosis, each of these strains is crossed into the apoE3* Leiden/CETP transgenic background. This background was chosen because both genes behave as dominant genes. The inbred strains differ in their susceptibility to atherosclerosis. Therefore, like the GWAS, these represent the natural variants of relevant genes. Overall, the genes associated with cardiovascular disease and coronary atherosclerosis in mice are highly concordant with human genes associated with similar phenotypes.

Atherosclerosis is a multifocal pathology. In mice, lesions first appear at the aortic root and the lesser curvature of the aortic arch followed by lesions at the branches of the arch, such as the innominate artery and the carotid and subclavian arteries [73]. As the animal ages, lesions develop at the branches of the abdominal aorta and the common iliac arteries. The sites of lesion development is a function of blood flow disturbance, developing first where the blood flow is most disturbed. The pattern is very similar for *Apoe*$^{-/-}$ and *Ldlr*$^{-/-}$ mice. A notable limitation of most murine models is that coronary lesions are not prominent features. However, this pattern does not apply uniformly across strains of differing atherosclerosis susceptibility. 129S6/SvEvTac (129S6) mice are more resistant to the development of aortic root atherosclerosis than C57BL/6 when fed the Paigen cholate containing diet [54]. Consistent with this, the aortic root lesions in *Apoe*$^{-/-}$ mice on 129S6 genetic background are much smaller than that in *Apoe*$^{-/-}$ mice in the C57BL/6 background. But interestingly the aortic arch lesions exhibited the reverse pattern [74]. An intercross

between these two strains revealed quantitative trait locus (QTLs) that associate with the angle of the curvature of the arch of the aorta and the extent of lesion development at this site. This difference in the angle of curvature of the arch may have changed the hemodynamic environment to accelerate lesion growth in the 129S6 strain. A related study was performed with *Apoe*$^{-/-}$ mice in the DBA/2J genetic background, an atherosensitive strain and 129S6 *Apoe*$^{-/-}$ mice. The DBA/2J *Apoe*$^{-/-}$ mice had ten times as much lesion at the aortic root as the 129S6 *Apoe*$^{-/-}$ mice but the lesions at the aortic arch were similar in size [75]. It is also not unusual for a genetic perturbation or therapeutic treatment to have different effects on atherosclerosis at different arterial sites. An example of discordance between aortic root atherosclerosis and the innominate artery lesions was observed with fractalkine deficiency in the *Ldlr*$^{-/-}$ background. In this case, fractalkine deficiency reduced innominate artery lesions without affecting the aortic root lesions [76].

There are many approaches to the assessment of atherosclerosis. It may be assessed by in vivo imaging, by *en face* gross measurements of lipid staining across the whole vessel or by cross-sectional histological analysis. It is clear from the above discussions that for comparable assessment of lesions, they have to be analyzed at specific physical locations, preferably multiple specific locations, at specific times after the initiation of the atherogenic regime and with high regard to the precision of the genetic background. Although the histological analysis of the aortic root is by far the most common method for lesion measurement, it has to be borne in mind that this is not necessarily fully reflective of lesion development at all regions of the vasculature. There are three aortic sinuses at the aortic root and generally these are not distinguished from one another. However, the individual sinuses do not necessarily develop lesions at the same rate. The sinus associated with the left coronary artery (LC) usually contributes to the largest proportion of the root lesion with much smaller lesions in the sinus associated with the right coronary artery (RC) and the sinus not associated with either coronary artery (NC). To ascertain that this pattern is constant, we generally mount our hearts so that we can distinguish each of these sinuses under the microscope. Several genetic manipulations have been shown to have greater impact on one sinus than the others. For example, in *Ldlr*$^{-/-}$ mice lacking the vitamin D receptor, the NC sinus is much larger than it is in the controls [77]. This is also seen in *Ldlr*$^{-/-}$ animals lacking lymphotoxin β in T cells (unpublished observations).

3.2.2 Immune Cells in Atherosclerotic Models

The atherosclerotic plaque is a chronic inflammatory lesion made up of activated endothelial cells, smooth muscle cells, macrophages, and other cells of the immune system. The critical contribution of each of these cell lineages has been addressed with particular

targeting. Macrophages are derived initially from blood monocytes, which in turn originate from bone marrow precursors. This was established by the transplantation of bone marrow from CD45.2 *Apoe*$^{-/-}$ mice with the CD45.2 allelic variant into lethally irradiated CD45.1 *Apoe*$^{-/-}$ recipients with the CD45.1 allelic variant, thus allowing differentiation of bone marrow-derived cells from recipient cells. This study demonstrated that essentially all of the macrophage cells in the aorta were derived from the bone marrow [78]. The development of monocytes in the bone marrow is dependent on macrophage colony stimulating factor (MCSF). MCSF in the periphery regulates survival and function of macrophages. *Apoe*$^{-/-}$ mice lacking MCSF have reduced blood monocytes and 80% reduction in aortic root atherosclerosis [79]. Hypercholesterolemia induces monocytosis in mice [80]. Inhibition of the chemokine and chemokine receptors CCL2, CX3CR1, and CCR5 in *Apoe*$^{-/-}$ mice attenuate the hypercholesterolemia-induced monocytosis [81]. The level of the Ly6C^{hi} inflammatory monocyte subset and the Ly6C^{lo} reparative monocytes were reduced by 50% and 40%, respectively. Atherosclerosis is very largely eliminated in these mice. The normal aorta has signs of inflammation in the regions that are prone to develop lesions like the lesser curvature of the aortic arch. In contrast to the greater curvature and the descending thoracic aorta, the intima of the lesser curvature exhibits an accumulation of macrophages and dendritic cells [82]. This is found only in the aorta of the strains of mice that are susceptible to atherosclerosis. On the other hand, the adventitial leukocytes are present in similar numbers regardless of strain susceptibility. The numbers in the intima are dependent on the vascular cell adhesion molecule (VCAM) expression.

Lymphocytes are the second most abundant cells derived from the blood found in the atherosclerotic plaque and the majority of these lymphocytes are T cell subtypes [83]. Depending upon the setting, quite robust atherosclerotic lesions develop in the absence of these cells. When recombination activating genes (*Rag1* or *Rag2*) are absent, mature T or B cells do not develop. In the absence of these cells in *Apoe*$^{-/-}$*Rag2*$^{-/-}$ mice fed chow, plasma lipids and aortic root atherosclerosis are lower than in *Apoe*$^{-/-}$ mice [84, 85], while the innominate artery lesions were not impacted [84]. When fed the WTD diet, adaptive immune deficiency had little impact on aortic root lesions [85] and this was also the case for immune deficient *Ldlr*$^{-/-}$ mice [86]. Among the T cell subsets [83], T-helper (Th)1 cells, producing interferon (IFN)γ, are mainly responsible for the inflammatory activity, in part by stimulating the lesional macrophages. Th2 cells, producing interleukin (IL)-4 and IL-5, have controversial effects on atherosclerosis. Th17 cells have been shown to be either proatherogenic or atheroprotective. On the other hand, regulatory T (Treg) cells (FoxP3+) are mostly

suppressive of atherosclerosis. It is worth noting that the density of T cells is highly dynamic during the progression of atherogenesis. This is particularly seen in the *Apoe*$^{-/-}$ model, in which the decline in T cells as the lesion evolves is more profound than it is in the *Ldlr*$^{-/-}$ model [87]. Thus, it is possible that the role of T cells varies as a function of the evolution of the atherogenic plaque. The T cells may originate from either the blood or the adventitia or both. When labeled T cells are injected into *Rag1*$^{-/-}$ mice, they appear first in the adventitia of the normal mouse and ultimately appear in the intima [88]. Selectin and chemokine networks are involved in the migration of T cells into atherosclerotic lesions. Some of these chemokine networks are the same as for monocyte migration. This is established with the knockout of these molecules [89]. Interaction of T cells with antigen presenting cells is facilitated by a series of costimulatory molecules and coinhibitory molecules. A number of these costimulatory/coinhibitory molecules have been shown to be proatherogenic in mouse models [90]. In the former category is lymphotoxin which exists in two forms: a homotrimer (lymphotoxin α3) which interacts with TNFα receptor; and a heterotrimer consisting of two lymphotoxin β subunits and one lymphotoxin α subunit which interacts with lymphotoxin β receptor (LTβR). In the absence of the homotrimer in the *Ldlr*$^{-/-}$ model, lesions, especially early lesions, are attenuated in the aortic root (Reardon et al. Unpublished). There is not a great deal of information on the role of LTβR on atherosclerosis.

A minor subset of T cells implicated in the atherosclerosis are the invariant natural killer (iNKT) cells. These cells represent a bridge between the innate and adaptive immune systems. They respond to glycolipid or phospholipid antigens presented by a major histocompatibility complex (MHC) type I-like antigen presenting molecule CD1d. The glycolipid antigens may be of endogenous or microbial origin. The prototypic antigen derived from marine algae is alpha galactosyl ceramide (αGalCer) that is frequently used to stimulate iNKT cells. Treatment of mice with this antigen enhances atherosclerosis. The invariant T cell receptor on iNKT cells is composed of a Vα14Jα18 α-chain with a limited set of β-chains. The proatherogenic action of these cells is determined from experiments with αGalCer treatment and *Cd1d*$^{-/-}$ or *Ja18*$^{-/-}$ mice in both the *Apoe*$^{-/-}$ and the *Ldlr*$^{-/-}$ backgrounds or by the adoptive transfer of iNKT cells into immunodeficient recipients [91]. The proatherogenic action of NKT cells is mediated by the release of proinflammatory cytokines and the release of two cytotoxic molecules, perforin and granzyme, which may promote necrotic core formation.

The interrogation of the function of genes of the resident cells of the vessel wall, namely endothelial cells and smooth muscle cells, can be accomplished by the selective knockout of genes in these cell

type using for example Tie2 Cre and SM22α Cre, respectively. Such selective knockout animals can then be crossed into either *Apoe*$^{-/-}$ or *Ldlr*$^{-/-}$ animals in order to assess the effects of the selected endothelial cells (EC) or smooth muscle cells (SMC) genes on atherosclerosis.

3.2.3 Human apoE Isoforms Expressed in the Mouse

As mentioned above, mice and humans differ in their apoE isoforms. Mice have a single apoE, while humans have three isoforms, apoE2, apoE3 and apoE4, that have different effects on lipoprotein metabolism and atherosclerosis. Maeda and colleagues have created mouse models in which the human apoE isoforms replace the mouse apoE gene [92]. The *APOE2* gene replacement mouse has a phenotype similar to human type III dyslipidemia and spontaneously develops atherosclerosis. The replacement of murine *Apoe* with human *APOE4* results in a complex phenotype characterized by the accumulation of apoE poor remnants and increased atherosclerosis compared to the *APOE3* replacement mice when the mice express high levels of human LDL receptor. The *APOE4* replacement phenotype is thought to be attributable to the increased affinity of apoE4 for the LDL receptor, so that remnants attach to the surface of the hepatocytes with little uptake into the hepatocytes [93]. When fed a high cholesterol diet containing cholate, all of the gene replacement mice develop more atherosclerosis than do wild-type C57BL/6 mice [94, 95]. Both human apoE4 and mouse apoE have an arginine at position 112. The presence of Arg112 in human apoE4 allows for Arg61 to interact with Glu255 forming an interaction between the N- and C-terminal domains that contributes to its higher lipid binding affinity [52, 96]. Since mouse apoE contains a threonine at position 61, the replacement of threonine with an arginine at this position 61 is said to "humanize" the protein. In the course of the construction of a mouse model with this Thr61-Arg61 replacement, Raffai and Weisgraber introduced a neomycin cassette in intron three of the *Apoe* gene [97]. This reduced the expression of mouse apoE to 5% of normal levels in the so-called hypomorphic apoE mouse. This level can be reduced further to 2% by crossing the hypomorphic mouse with the *Apoe*$^{-/-}$ mouse. The hypomorphic apoE mouse exhibits a normal lipoprotein profile when fed a chow diet but it is susceptible to diet-induced hypercholesterolemia. This suggests that this level of expression of apoE is close to the threshold of the amount of apoE necessary to maintain normal lipoprotein metabolism. Cre-mediated excision of the neomycin cassette normalizes the level of apoE expression and the lipoprotein phenotype.

3.2.4 ApoE Expression in Hepatocytes and Other Cells

ApoE is primarily produced by hepatocytes but is also widely expressed in other cells, including various endocrine cells, astrocytes, macrophages, and adipocytes [98]. The

hypercholesterolemia and atherosclerosis phenotype of *Apoe*$^{-/-}$ mice can be reversed by transplanting them with wild-type bone marrow (restoring expression of apoE in the monocyte/macrophages) [99, 100]. This reversal of the atherogenic phenotype occurs despite the fact that plasma apoE levels are only 1–2% that found in the wild-type mouse. The contribution of macrophage-derived apoE on the hyperlipidemia and atherosclerosis needs to be kept in mind when performing bone marrow transplantation studies in this mouse model. This same phenotype can be achieved by infecting *Apoe*$^{-/-}$ animals with recombinant viral vectors expressing apoE [101]. In this case, apoE is expressed in hepatocytes. Transgenic animals expressing apoE in the adrenal glands at modest levels, when crossed with *Apoe*$^{-/-}$ animals can also rescue the atherogenic phenotype [102]. However, transplantation of visceral adipose tissue into *Apoe*$^{-/-}$ mice is not able to duplicate these rescue experiments despite the fact that the level of apoE in the plasma is about the same as is found with bone marrow transplantation [103]. It is not clear how adipocyte-derived apoE differs from bone marrow-derived apoE, although the level of apoE glycosylation may play a role. Even though apoE is expressed in many cells of the body, apoE expression in macrophages has an important role in atherogenesis even in the face of normal apoE production in the liver. Thus, the transplantation of *Apoe* deficient bone marrow into wild-type recipients results in some atherosclerosis in the aortic root [104].

ApoE is a multifunctional protein. It functions as a transport protein, it facilitates the clearance of lipoprotein remnants, and it facilitates cholesterol efflux and reverse cholesterol transport [98]. One of consequences of hypercholesterolemia is that monocytosis is induced which contributes to the density of macrophages in the lesion [80]. Cholesterol homeostasis in the hemopoietic stem cells is critical for regulating the proliferation of these cells. Thus, stem cells that are deficient in the major cholesterol transporters ATP-binding cassette transporter (ABC)A1 and ABCG1 proliferate to a greater extent than do wild-type stem cells [105]. A profound monocytosis results when bone marrow from *Abca1*$^{-/-}$*;Abcg1*$^{-/-}$ animals is transplanted into *Ldlr*$^{-/-}$ recipients. Cell surface apoE (cell autonomous apoE) is important for the completion of this cholesterol homeostatic regulation [106, 107].

3.2.5 Additional Ldlr Deficient Models

Most of the atherosclerosis studies in mice with elevated LDL levels have been done with mice with global deficiency of the *Ldlr* gene (Ldlr−/− mice). But the development of new genetic technologies has provided alternative approaches to the elimination of LDLR function. Currently the most widely used strategy is the hepatic expression of PCSK9 GOF mutants either in the germline or by infection with recombinant AAV [108–110]. By diverting the LDL

receptor to the lysosomes for degradation, this limits the amount that recycles to the cell surface leading to decreased clearance of LDL from the blood. This function is markedly accentuated in the GOF mutants. The most frequently employed GOF mutant is D374Y (human) or D377Y (mouse) in which aspartic acid is replaced by tyrosine. The injection of this GOF mutant into mice reduces LDLR on the cell surface by about 80%. We mentioned above that inbred strains of mice exhibit different susceptibility to atherosclerosis. Even though the injection of the GOF function mutant virus induces hypercholesterolemia in most strains, their differential atherosusceptibility is not altered by PCSK9-mediated induction of atherosclerosis [109]. A great advantage of the viral induction of LDLR deficiency is that it avoids the much more cumbersome and time consuming effort of crossing a naturally occurring or genetically engineered mutant mouse with either *Ldlr−/−* mice or *Pcsk9* D374Y transgenic mice. For example, the diabetic Akita mouse model injected with AAV-PCSK9 D374Y shows that diabetes aggravated lesions formation compared to similarly treated wild-type mice [110]. It is important to note that PCSK9 may also have local effects, influencing the function of the LDLR in the context of the atherosclerotic plaque itself. There are important other methods for the postnatal reduction of the LDLR, such as AAV mediated delivery of Cas9 and guide RNA to the *Ldlr* gene (AAV-CRISPR) to liver cells [111]. In this study, AAV-PCSK9 D374Y injection was compared to AAV-CRISPR injection. In male mice fed the western type diet for 20 weeks atherosclerosis (*en face* analysis) ranked in the order $Ldlr^{-/-}$, AAV–CRISPR > AAV-Pcsk9 D374Y. The interaction of gender and the AAV-mediated PCSK9 expression is quite complex [111, 112]. Given this complexity, cross gender comparisons should be avoided in assessing effects on lipid homeostasis and atherosclerosis. An additional approach to induce significant reduction of LDL receptor expression in the liver is to inject an antisense oligonucleotide (ASO) to the *Ldlr* mRNA [113]. This approach also produces the expected phenotype of elevated plasma LDL cholesterol levels and atherosclerosis.

3.2.6 Coronary Artery Atherosclerosis

Most of the models described so far do not develop significant coronary artery lesions, although small lesions may be found at the origins of these arteries. However, more complex lesions may be found in the coronary arteries in mice with greater interference of cholesterol homeostasis. Mice lacking both *Apoe* and the *Ldlr* and fed a WTD develop obstructive proximal atherosclerosis, myocardial infarction, and early mortality [114]. This can be markedly attenuated by blocking the endothelin type A receptor. Macrophage urokinase plasminogen activator transgenesis coupled with *Apoe* deficiency also produces stenosis of the proximal coronaries

[115]. The most frequently used model of obstructive coronary arteries was described by Krieger and colleagues [116]. They showed that *Srb1*$^{-/-}$ *Apoe* $^{-/-}$ double knockout mice exhibited spontaneous coronary stenosis, myocardial infarction, and premature mortality (mean age 6 weeks). This phenotype was substantially attenuated by the early administration of the antioxidant probucol, although the timing of the administration of probucol modulates the onset of the fatal phenotype [117]. *Srb1*$^{-/-}$ /hypomorphic apoE(Arg61) and *Srb1*$^{-/-}$*Ldlr*$^{-/-}$ mice exhibit a similar phenotype but only when fed a WTD [118, 119]. Extensive coronary artery atherosclerosis was also observed with *Pdzk1*$^{-/-}$*Srb1*$^{-/-}$ mice fed the Paigen diet [120]. PDZ domain-containing protein 1 (PDZK1) is an adaptor protein that binds scavenger receptor (SR)-BI and mediates its expression and localization. In order to investigate the effect of diabetes on coronary atherosclerosis, hyperglycemia was induced in *Srb1*$^{-/-}$ hypomorphic apoE mice by streptozotocin injection [121]. Hyperglycemia in the animals maintained on chow surprisingly reduced aortic root lesions but in the WTD fed animals, the presence of diabetes augmented atherosclerosis in both the aortic root and the coronary arteries.

3.2.7 The Intestinal Microbiome

It is not uncommon to find discrepancies in the reported results of genetic or therapeutic treatments on murine atherosclerosis by different investigators. One possible explanation for these discrepancies is the impact of the intestinal microbiome represented in different vivariums. This is especially a problem with mice who are coprophagic. There are several strategies that could be used to suggest the involvement of the microbiome as a relevant regulator of the atherosclerosis phenotype. One could employ germ-free mice, a useful but difficult strategy. There is also the issue that the immune system in germ-free mice is different from specific pathogen free or conventional housed mice. A simpler approach, though less specific, is the oral administration of poorly absorbed broad spectrum antibiotics to eliminate the microbiome. Animals could also be caged individually so that they cannot share microbiomes.

The gut microbiome can release products such as lipopolysaccharide or related toxins or relevant atherogenic metabolites generated during their metabolism of foodstuff such as antigens, short chain fatty acids, and secondary bile acids. Among the microbial transformations that has been shown to influence atherogenesis is that of dietary choline and L-carnitine into trimethylamine (TMA) by the TMA lyase present in certain commensal bacteria [122]. TMA is oxidized in the liver to TMA N-oxide (TMAO) by flavin-containing monooxygenases (FMO). This was identified by Hazen and colleagues using an unbiased mass spectrometry approach as blood metabolites that predicted increased risk for CVD [123]. This report had a major impact on the field. The role

of choline enrichment of the diet was further studied in *Apoe*$^{-/-}$ mice finding that this augmented atherosclerosis in both male and female mice. This effect could be attenuated by administration of the choline analog 3,3,-dimethyl-1-butanol, an inhibitor of TMA lyase [124]. However, the effects of enrichment of the diet with choline on atherosclerosis is not a universal finding [125]. In this study feeding male mice had no impact on atherosclerosis. The possible reconciliation of these apparently contrasting findings may be related to the timing of the addition of choline to the diet and the age-dependent regulation of FMO expression in the mice of each gender [126].

3.2.8 Regression of Atherosclerosis

Many of the patients who consult their physicians about cardiovascular disease have already advanced atherosclerosis. Most murine atherosclerosis studies have involved germline mutations of the gene of interest, which makes it difficult to reverse the atherogenic impact on developed lesions. However, a number of approaches have been devised to examine lesion regression in mouse models, all of which are dependent on rapidly reducing hyperlipidemia. Many of these have been developed by Fisher and colleagues. Microsomal triglyceride transfer protein (MTTP) is a protein essential for the lipidation of apoB and the formation of apoB-containing lipoproteins. In one approach, *Ldlr*$^{-/-}$ mice were fed a WTD to establish lesions and then switched to a chow diet with an inhibitor of MTTP to reduce the level of apoB-containing lipoproteins. Compared to lesions at the time of diet switching, the aortic root lesions after 2 weeks of chow diet/MTTP inhibitor treatment were characterized by a reduction in inflammatory macrophages and an increase in reparative (M2) macrophages, characteristics of regressing lesions [127]. This approach also promotes regression in the AAV-PCSK9 model of atherosclerosis [128]. The Reversa mouse is another model that can be used to examine atherosclerosis regression. These mice are *Ldlr*$^{-/-}$ *Apob*$^{100/B100}$, *Mttp*$^{fl/fl}$ Mx-1Cre$^{+/+}$ [129]. Established lesions are obtained by feeding WTD and the reduction of plasma lipids is induced by switching to a chow diet and induction of Cre recombinase with polyI:polyC to knockout the MTTP gene. Although the lesion size did not change markedly after 2 weeks, lipid content and CD68^{+} cell density were markedly reduced in the lesions along with increased collagen content [130]. CD68^{+} cells isolated by laser capture microdissection had increased expression of C-C chemokine receptor type 7 (CCR7) and decreased expression of inflammatory genes. The Fisher laboratory also developed an aortic transplant model to study regression. When the aortic arch with well-established lesions from donor *Apoe*$^{-/-}$ mice was transplanted into the abdominal aorta of wild-type mice, lesion size was reduced by 40% and CD68^{+} foam cell content by 75% [131]. The reduction of CD68^{+} cells is likely due to

migration to lymph nodes [132] mediated by the upregulation of CCR7 in macrophages. *Lxr*, *Abca1*, and *Srb1* gene expression were also increased, suggesting increased efflux of macrophage cholesterol. A number of antiatherogenic functions have been ascribed to HDL. This transplant model was used to demonstrate that HDL has a role in lesion regression. The transplantation of the aortic arch from $Apoe^{-/-}$ mice into recipient mice with varying levels of HDL ($Apoa1^{-/-}$, wild type and human *Apoa1* transgenic) revealed that migration of $CD68^{+}$ cells was licensed by HDL [133]. The plasticity of macrophages is indicated by the transformation of M1 macrophages to M2 reparative macrophages in the presence of HDL. A recent paper used three models of regression—the aortic transplant model, the genetic switching off of MTTP expression and the administration of an antisense to apoB100- to demonstrate that Tregs are necessary for lesion regression and the proresolving and tissue reparative functions of lesion macrophages [134]. A final regression model takes advantage of antisense technology. Hypercholesterolemia was induced in wild-type mice using an antisense to *Ldlr* mRNA. Once lesions were established, the hypercholesterolemia was reversed by treatment with a sense version of the oligonucleotide to restore hepatic LDLR expression. This led to a substantial reduction in the macrophage content in the aortic root lesions after 3 weeks [113].

4 Conclusion

It is clear from the above descriptions that the models for atherogenesis initiation, progression, and regression have been advanced by modern genetic technologies. The next major advance of the field will come from the examination of the modulation of the multiple genes that each make lesser contribution than those described in this chapter, which currently mostly focuses on genes whose elimination creates major effects on the described processes. Such advances will be more akin to what is encountered in human populations and patients.

References

1. Getz GS, Reardon CA (2012) Animal models of atherosclerosis. Arterioscler Thromb Vasc Biol 32(5):1104–1115. https://doi.org/10.1161/atvbaha.111.237693
2. Janado M, Martin WG, Cook WH (1966) Separation and properties of pig-serum lipoproteins. Can J Biochem 44(8):1201–1209. https://doi.org/10.1139/o66-137
3. Terpstra AHM, Sanchez-Muniz FJ, West CE, Woodward CJH (1982) The density profile and cholesterol concentration of serum lipoproteins in domestic and laboratory animals. Comp Biochem Physiol B Comp Biochem 71(4):669–673. https://doi.org/10.1016/0305-0491(82)90479-5
4. Padró T, Cubedo J, Camino S, Béjar MT, Ben-Aicha S, Mendieta G, Escolà-Gil JC, Escate R, Gutiérrez M, Casani L, Badimon L, Vilahur G (2017) Detrimental effect of hypercholesterolemia on high-

density lipoprotein particle remodeling in pigs. J Am Coll Cardiol 70(2):165–178. https://doi.org/10.1016/j.jacc.2017.05.018

5. Puppione DL, Whitelegge JP, Yam LM, Schumaker VN (2005) Mass spectral analysis of pig (Sus scrofa) apo HDL: identification of pig apoA-II, a dimeric apolipoprotein. Comp Biochem Physiol B Biochem Mol Biol 141(1):89–94. https://doi.org/10.1016/j.cbpc.2005.01.014
6. Terpstra AH, Stucchi AF, Foxall TL, Shwaery GT, Vespa DB, Nicolosi RJ (1993) Unidirectional transfer in vivo of high-density lipoprotein cholesteryl esters to lower-density lipoproteins in the pig, an animal species without plasma cholesteryl ester transfer activity. Metabolism 42(12):1524–1530. https://doi.org/10.1016/0026-0495(93)90146-f
7. Mahley RW, Weisgraber KH, Innerarity T, Brewer HB Jr, Assmann G (1975) Swine lipoproteins and atherosclerosis. Changes in the plasma lipoproteins and apoproteins induced by cholesterol feeding. Biochemistry 14(13):2817–2823. https://doi.org/10.1021/bi00684a005
8. Pownall HJ, Jackson RL, Roth RI, Gotto AM, Patsch JR, Kummerow FA (1980) Influence of an atherogenic diet on the structure of swine low density lipoproteins. J Lipid Res 21(8):1108–1115
9. Rapacz J, Hasler-Rapacz J, Taylor KM, Checovich WJ, Attie AD (1986) Lipoprotein mutations in pigs are associated with elevated plasma cholesterol and atherosclerosis. Science 234(4783):1573–1577. https://doi.org/10.1126/science.3787263
10. Rapacz J Jr, Hasler-Rapacz J, Rapacz J, McConathy WJ (1989) Separation of swine plasma LDL from Lpb2/3 heterozygotes into two apoB allelic haplotypes, Lpb2 and Lpb3, with apoB epitope specific antibodies. J Lipid Res 30(2):199–206
11. Rapacz J, Hasler-Rapacz JO, Hu ZL, Rapacz JM, Vögeli P, Hojný J, Janik A (1994) Identification of new apolipoprotein B epitopes and haplotypes and their distribution in swine populations. Anim Genet 25(Suppl 1):51–57. https://doi.org/10.1111/j.1365-2052.1994.tb00403.x
12. Twisk J, Gillian-Daniel DL, Tebon A, Wang L, Barrett PH, Attie AD (2000) The role of the LDL receptor in apolipoprotein B secretion. J Clin Invest 105(4):521–532. https://doi.org/10.1172/jci8623
13. Cooper ST, Aiello RJ, Checovich WJ, Attie AD (1992) Low density lipoprotein heterogeneity in spontaneously hypercholesterolemic pigs. Mol Cell Biochem 113(2):133–140. https://doi.org/10.1007/bf00231533
14. Lee DM, Mok T, Hasler-Rapacz J, Rapacz J (1990) Concentrations and compositions of plasma lipoprotein subfractions of Lpb5-Lpu1 homozygous and heterozygous swine with hypercholesterolemia. J Lipid Res 31(5):839–847
15. Checovich WJ, Fitch WL, Krauss RM, Smith MP, Rapacz J, Smith CL, Attie AD (1988) Defective catabolism and abnormal composition of low-density lipoproteins from mutant pigs with hypercholesterolemia. Biochemistry 27(6):1934–1941. https://doi.org/10.1021/bi00406a020
16. Grunwald KA, Schueler K, Uelmen PJ, Lipton BA, Kaiser M, Buhman K, Attie AD (1999) Identification of a novel Arg-->Cys mutation in the LDL receptor that contributes to spontaneous hypercholesterolemia in pigs. J Lipid Res 40(3):475–485
17. Hoogendoorn A, den Hoedt S, Hartman EMJ, Krabbendam-Peters I, Te Lintel HM, van der Zee L, van Gaalen K, Witberg KT, Dorst K, Ligthart JMR, Drouet L, Van der Heiden K, van Lennep JR, van der Steen AFW, Duncker DJ, Mulder MT, Wentzel JJ (2019) Variation in coronary atherosclerosis severity related to a distinct LDL (low-density lipoprotein) profile: findings from a familial hypercholesterolemia pig model. Arterioscler Thromb Vasc Biol 39(11):2338–2352. https://doi.org/10.1161/atvbaha.119.313246
18. Hasler-Rapacz J, Prescott MF, Von Linden-Reed J, Rapacz JM Jr, Hu Z, Rapacz J (1995) Elevated concentrations of plasma lipids and apolipoproteins B, C-III, and E are associated with the progression of coronary artery disease in familial hypercholesterolemic swine. Arterioscler Thromb Vasc Biol 15(5):583–592. https://doi.org/10.1161/01.atv.15.5.583
19. Gerrity RG, Naito HK, Richardson M, Schwartz CJ (1979) Dietary induced atherogenesis in swine. Morphology of the intima in prelesion stages. Am J Pathol 95(3):775–792
20. Feldman DL, Hoff HF, Gerrity RG (1984) Immunohistochemical localization of apoprotein B in aortas from hyperlipemic swine. Preferential accumulation in lesion-prone areas. Arch Pathol Lab Med 108(10):817–822
21. Gerrity RG, Richardson M, Somer JB, Bell FP, Schwartz CJ (1977) Endothelial cell morphology in areas of in vivo Evans blue uptake in the aorta of young pigs. II Ultrastructure of the intima in areas of differing permeability to proteins. Am J Pathol 89(2):313–334

22. Gerrity RG, Natarajan R, Nadler JL, Kimsey T (2001) Diabetes-induced accelerated atherosclerosis in swine. Diabetes 50(7): 1654–1665. https://doi.org/10.2337/diabetes.50.7.1654
23. Koskinas KC, Sukhova GK, Baker AB, Papafaklis MI, Chatzizisis YS, Coskun AU, Quillard T, Jonas M, Maynard C, Antoniadis AP, Shi GP, Libby P, Edelman ER, Feldman CL, Stone PH (2013) Thin-capped atheromata with reduced collagen content in pigs develop in coronary arterial regions exposed to persistently low endothelial shear stress. Arterioscler Thromb Vasc Biol 33(7): 1494–1504. https://doi.org/10.1161/atvbaha.112.300827
24. Thim T, Hagensen MK, Hørlyck A, Kim WY, Niemann AK, Thrysøe SA, Drouet L, Paaske WP, Bøtker HE, Falk E (2012) Wall shear stress and local plaque development in stenosed carotid arteries of hypercholesterolemic minipigs. J Cardiovasc Dis Res 3(2):76–83. https://doi.org/10.4103/0975-3583.95358
25. Gerrity RG (1981) The role of the monocyte in atherogenesis: I. Transition of blood-borne monocytes into foam cells in fatty lesions. Am J Pathol 103(2):181–190
26. Holvoet P, Theilmeier G, Shivalkar B, Flameng W, Collen D (1998) LDL hypercholesterolemia is associated with accumulation of oxidized LDL, atherosclerotic plaque growth, and compensatory vessel enlargement in coronary arteries of miniature pigs. Arterioscler Thromb Vasc Biol 18(3): 415–422. https://doi.org/10.1161/01.ATV.18.3.415
27. Glagov S, Weisenberg E, Zarins CK, Stankunavicius R, Kolettis GJ (1987) Compensatory enlargement of human atherosclerotic coronary arteries. N Engl J Med 316(22):1371–1375. https://doi.org/10.1056/nejm198705283162204
28. Mohler ER 3rd, Sarov-Blat L, Shi Y, Hamamdzic D, Zalewski A, Macphee C, Llano R, Pelchovitz D, Mainigi SK, Osman H, Hallman T, Steplewski K, Gertz Z, Lu MM, Wilensky RL (2008) Site-specific atherogenic gene expression correlates with subsequent variable lesion development in coronary and peripheral vasculature. Arterioscler Thromb Vasc Biol 28(5): 850–855. https://doi.org/10.1161/atvbaha.107.154534
29. Neeb ZP, Edwards JM, Alloosh M, Long X, Mokelke EA, Sturek M (2010) Metabolic syndrome and coronary artery disease in Ossabaw compared with Yucatan swine. Comp Med 60(4):300–315
30. Dyson MC, Alloosh M, Vuchetich JP, Mokelke EA, Sturek M (2006) Components of metabolic syndrome and coronary artery disease in female Ossabaw swine fed excess atherogenic diet. Comp Med 56(1):35–45
31. Choy JS, Luo T, Huo Y, Wischgoll T, Schultz K, Teague SD, Sturek M, Kassab GS (2015) Compensatory enlargement of ossabaw miniature swine coronary arteries in diffuse atherosclerosis. Int J Cardiol Heart Vasc 6:4–11. https://doi.org/10.1016/j.ijcha.2014.11.003
32. Jacobsson L (1986) Comparison of experimental hypercholesterolemia and atherosclerosis in Göttingen mini-pigs and Swedish domestic swine. Atherosclerosis 59(2): 205–213. https://doi.org/10.1016/0021-9150(86)90049-3
33. Jacobsson L (1989) Comparison of experimental hypercholesterolemia and atherosclerosis in male and female mini-pigs of the Göttingen strain. Artery 16(2):105–117
34. Hamamdzic D, Wilensky RL (2013) Porcine models of accelerated coronary atherosclerosis: role of diabetes mellitus and hypercholesterolemia. J Diabetes Res 2013:761415. https://doi.org/10.1155/2013/761415
35. Prescott MF, McBride CH, Hasler-Rapacz J, Von Linden J, Rapacz J (1991) Development of complex atherosclerotic lesions in pigs with inherited hyper-LDL cholesterolemia bearing mutant alleles for apolipoprotein B. Am J Pathol 139(1):139–147
36. Schulz R, Schlüter KD, Laufs U (2015) Molecular and cellular function of the proprotein convertase subtilisin/kexin type 9 (PCSK9). Basic Res Cardiol 110(2):4. https://doi.org/10.1007/s00395-015-0463-z
37. Davignon J, Dubuc G, Seidah NG (2010) The influence of PCSK9 polymorphisms on serum low-density lipoprotein cholesterol and risk of atherosclerosis. Curr Atheroscler Rep 12(5):308–315. https://doi.org/10.1007/s11883-010-0123-6
38. Al-Mashhadi RH, Sørensen CB, Kragh PM, Christoffersen C, Mortensen MB, Tolbod LP, Thim T, Du Y, Li J, Liu Y, Moldt B, Schmidt M, Vajta G, Larsen T, Purup S, Bolund L, Nielsen LB, Callesen H, Falk E, Mikkelsen JG, Bentzon JF (2013) Familial hypercholesterolemia and atherosclerosis in cloned minipigs created by DNA transposition of a human PCSK9 gain-of-function mutant. Sci Transl Med 5(166):166ra161.

https://doi.org/10.1126/scitranslmed.3004853

39. Shim J, Al-Mashhadi RH, Sørensen CB, Bentzon JF (2016) Large animal models of atherosclerosis–new tools for persistent problems in cardiovascular medicine. J Pathol 238(2): 257–266. https://doi.org/10.1002/path.4646
40. Davis BT, Wang XJ, Rohret JA, Struzynski JT, Merricks EP, Bellinger DA, Rohret FA, Nichols TC, Rogers CS (2014) Targeted disruption of LDLR causes hypercholesterolemia and atherosclerosis in Yucatan miniature pigs. PLoS One 9(4):e93457. https://doi.org/10.1371/journal.pone.0093457
41. Shim J, Poulsen CB, Hagensen MK, Larsen T, Heegaard PMH, Christoffersen C, Bolund L, Schmidt M, Liu Y, Li J, Li R, Callesen H, Bentzon JF, Sørensen CB (2017) Apolipoprotein E deficiency increases remnant lipoproteins and accelerates progressive atherosclerosis, but not xanthoma formation, in gene-modified minipigs. JACC Basic Transl Sci 2(5):591–600. https://doi.org/10.1016/j.jacbts.2017.06.004
42. Fang B, Ren X, Wang Y, Li Z, Zhao L, Zhang M, Li C, Zhang Z, Chen L, Li X, Liu J, Xiong Q, Zhang L, Jin Y, Liu X, Li L, Wei H, Yang H, Li R, Dai Y (2018) Apolipoprotein E deficiency accelerates atherosclerosis development in miniature pigs. Dis Model Mech 11(10). https://doi.org/10.1242/dmm.036632
43. Kobari Y, Koto M, Tanigawa M (1991) Regression of diet-induced atherosclerosis in Göttingen miniature swine. Lab Anim 25(2): 110–116. https://doi.org/10.1258/002367791781082478
44. Barbeau ML, Klemp KF, Guyton JR, Rogers KA (1997) Dietary fish oil. Influence on lesion regression in the porcine model of atherosclerosis. Arterioscler Thromb Vasc Biol 17(4):688–694. https://doi.org/10.1161/01.atv.17.4.688
45. Rosenson RS, Brewer HB Jr, Ansell BJ, Barter P, Chapman MJ, Heinecke JW, Kontush A, Tall AR, Webb NR (2016) Dysfunctional HDL and atherosclerotic cardiovascular disease. Nat Rev Cardiol 13(1): 48–60. https://doi.org/10.1038/nrcardio.2015.124
46. Schultz JR, Verstuyft JG, Gong EL, Nichols AV, Rubin EM (1993) Protein composition determines the anti-atherogenic properties of HDL in transgenic mice. Nature 365(6448): 762–764. https://doi.org/10.1038/365762a0
47. Reschly EJ, Sorci-Thomas MG, Davidson WS, Meredith SC, Reardon CA, Getz GS (2002) Apolipoprotein A-I alpha -helices 7 and 8 modulate high density lipoprotein subclass distribution. J Biol Chem 277(12): 9645–9654. https://doi.org/10.1074/jbc.M107883200
48. Getz GS, Reardon CA (2011) Apolipoprotein A-I and A-I mimetic peptides: a role in atherosclerosis. J Inflamm Res 4:83–92. https://doi.org/10.2147/jir.S12983
49. Sontag TJ, Carnemolla R, Vaisar T, Reardon CA, Getz GS (2012) Naturally occurring variant of mouse apolipoprotein A-I alters the lipid and HDL association properties of the protein. J Lipid Res 53(5):951–963. https://doi.org/10.1194/jlr.M021154
50. Vaisar T, Pennathur S, Green PS, Gharib SA, Hoofnagle AN, Cheung MC, Byun J, Vuletic S, Kassim S, Singh P, Chea H, Knopp RH, Brunzell J, Geary R, Chait A, Zhao XQ, Elkon K, Marcovina S, Ridker P, Oram JF, Heinecke JW (2007) Shotgun proteomics implicates protease inhibition and complement activation in the antiinflammatory properties of HDL. J Clin Invest 117(3):746–756. https://doi.org/10.1172/jci26206
51. Pamir N, Pan C, Plubell DL, Hutchins PM, Tang C, Wimberger J, Irwin A, Vallim TQA, Heinecke JW, Lusis AJ (2019) Genetic control of the mouse HDL proteome defines HDL traits, function, and heterogeneity. J Lipid Res 60(3):594–608. https://doi.org/10.1194/jlr.M090555
52. Mahley RW, Weisgraber KH, Huang Y (2009) Apolipoprotein E: structure determines function, from atherosclerosis to Alzheimer's disease to AIDS. J Lipid Res 50 Suppl(Suppl): S183–S188. https://doi.org/10.1194/jlr.R800069-JLR200
53. Davidson NO, Shelness GS (2000) Apolipoprotein B: mRNA editing, lipoprotein assembly, and presecretory degradation. Annu Rev Nutr 20:169–193. https://doi.org/10.1146/annurev.nutr.20.1.169
54. Paigen B, Ishida BY, Verstuyft J, Winters RB, Albee D (1990) Atherosclerosis susceptibility differences among progenitors of recombinant inbred strains of mice. Arteriosclerosis 10(2):316–323. https://doi.org/10.1161/01.atv.10.2.316
55. Hansson GK (2014) A journey in science: medical scientist in translation. Mol Med 20(1):381–389. https://doi.org/10.2119/molmed.2014.00092
56. Plump AS, Smith JD, Hayek T, Aalto-Setälä K, Walsh A, Verstuyft JG, Rubin EM, Breslow JL (1992) Severe

hypercholesterolemia and atherosclerosis in apolipoprotein E-deficient mice created by homologous recombination in ES cells. Cell 71(2):343–353. https://doi.org/10.1016/0092-8674(92)90362-g

57. Zhang SH, Reddick RL, Piedrahita JA, Maeda N (1992) Spontaneous hypercholesterolemia and arterial lesions in mice lacking apolipoprotein E. Science 258(5081):468–471. https://doi.org/10.1126/science.1411543
58. Ishibashi S, Brown MS, Goldstein JL, Gerard RD, Hammer RE, Herz J (1993) Hypercholesterolemia in low density lipoprotein receptor knockout mice and its reversal by adenovirus-mediated gene delivery. J Clin Invest 92(2):883–893. https://doi.org/10.1172/jci116663
59. Getz GS, Reardon CA (2016) Do the Apoe−/− and Ldlr−/− mice yield the same insight on atherogenesis? Arterioscler Thromb Vasc Biol 36(9):1734–1741. https://doi.org/10.1161/atvbaha.116.306874
60. Paigen B, Morrow A, Holmes PA, Mitchell D, Williams RA (1987) Quantitative assessment of atherosclerotic lesions in mice. Atherosclerosis 68(3):231–240. https://doi.org/10.1016/0021-9150(87)90202-4
61. Curtiss LK, Black AS, Bonnet DJ, Tobias PS (2012) Atherosclerosis induced by endogenous and exogenous toll-like receptor (TLR) 1 or TLR6 agonists. J Lipid Res 53(10):2126–2132. https://doi.org/10.1194/jlr.M028431
62. Teupser D, Persky AD, Breslow JL (2003) Induction of atherosclerosis by low-fat, semisynthetic diets in LDL receptor-deficient C57BL/6J and FVB/NJ mice: comparison of lesions of the aortic root, brachiocephalic artery, and whole aorta (en face measurement). Arterioscler Thromb Vasc Biol 23(10):1907–1913. https://doi.org/10.1161/01.Atv.0000090126.34881.B1
63. Hartvigsen K, Binder CJ, Hansen LF, Rafia A, Juliano J, Hörkkö S, Steinberg D, Palinski W, Witztum JL, Li AC (2007) A diet-induced hypercholesterolemic murine model to study atherogenesis without obesity and metabolic syndrome. Arterioscler Thromb Vasc Biol 27(4):878–885. https://doi.org/10.1161/01.Atv.0000258790.35810.02
64. Powell-Braxton L, Véniant M, Latvala RD, Hirano KI, Won WB, Ross J, Dybdal N, Zlot CH, Young SG, Davidson NO (1998) A mouse model of human familial hypercholesterolemia: markedly elevated low density lipoprotein cholesterol levels and severe atherosclerosis on a low-fat chow diet. Nat Med 4(8):934–938. https://doi.org/10.1038/nm0898-934
65. Véniant MM, Sullivan MA, Kim SK, Ambroziak P, Chu A, Wison MD, Hellerstein MK, Rudel LL, Walzem RL, Young SG (2000) Defining the atherogenicity of large and small lipoproteins containing apolipoprotein B100. J Clin Invest 106(12):1501–1510. https://doi.org/10.1172/jci10695
66. Véniant MM, Withycombe S, Young SG (2001) Lipoprotein size and atherosclerosis susceptibility in Apoe(−/−) and Ldlr(−/−) mice. Arterioscler Thromb Vasc Biol 21(10):1567–1570. https://doi.org/10.1161/hq1001.097780
67. Borén J, Olin K, Lee I, Chait A, Wight TN, Innerarity TL (1998) Identification of the principal proteoglycan-binding site in LDL. A single-point mutation in apo-B100 severely affects proteoglycan interaction without affecting LDL receptor binding. J Clin Invest 101(12):2658–2664. https://doi.org/10.1172/jci2265
68. Flood C, Gustafsson M, Richardson PE, Harvey SC, Segrest JP, Borén J (2002) Identification of the proteoglycan binding site in apolipoprotein B48. J Biol Chem 277(35):32228–32233. https://doi.org/10.1074/jbc.M204053200
69. van Vlijmen BJ, van den Maagdenberg AM, Gijbels MJ, van der Boom H, HogenEsch H, Frants RR, Hofker MH, Havekes LM (1994) Diet-induced hyperlipoproteinemia and atherosclerosis in apolipoprotein E3-Leiden transgenic mice. J Clin Invest 93(4):1403–1410. https://doi.org/10.1172/jci117117
70. Hopkins PN (2013) Molecular biology of atherosclerosis. Physiol Rev 93(3):1317–1542. https://doi.org/10.1152/physrev.00004.2012
71. Stylianou IM, Bauer RC, Reilly MP, Rader DJ (2012) Genetic basis of atherosclerosis: insights from mice and humans. Circ Res 110(2):337–355. https://doi.org/10.1161/circresaha.110.230854
72. von Scheidt M, Zhao Y, Kurt Z, Pan C, Zeng L, Yang X, Schunkert H, Lusis AJ (2017) Applications and limitations of mouse models for understanding human atherosclerosis. Cell Metab 25(2):248–261. https://doi.org/10.1016/j.cmet.2016.11.001
73. Nakashima Y, Plump AS, Raines EW, Breslow JL, Ross R (1994) ApoE-deficient mice develop lesions of all phases of atherosclerosis throughout the arterial tree. Arterioscler

Thromb 14(1):133–140. https://doi.org/10.1161/01.atv.14.1.133

74. Tomita H, Zhilicheva S, Kim S, Maeda N (2010) Aortic arch curvature and atherosclerosis have overlapping quantitative trait loci in a cross between 129S6/SvEvTac and C57BL/6J apolipoprotein E-null mice. Circ Res 106(6):1052–1060. https://doi.org/10.1161/circresaha.109.207175
75. Kayashima Y, Makhanova NA, Matsuki K, Tomita H, Bennett BJ, Maeda N (2015) Identification of aortic arch-specific quantitative trait loci for atherosclerosis by an intercross of DBA/2J and 129S6 apolipoprotein E-deficient mice. PLoS One 10(2):e0117478. https://doi.org/10.1371/journal.pone.0117478
76. Teupser D, Pavlides S, Tan M, Gutierrez-Ramos JC, Kolbeck R, Breslow JL (2004) Major reduction of atherosclerosis in fractalkine (CX3CL1)-deficient mice is at the brachiocephalic artery, not the aortic root. Proc Natl Acad Sci U S A 101(51):17795–17800. https://doi.org/10.1073/pnas.0408096101
77. Szeto FL, Reardon CA, Yoon D, Wang Y, Wong KE, Chen Y, Kong J, Liu SQ, Thadhani R, Getz GS, Li YC (2012) Vitamin D receptor signaling inhibits atherosclerosis in mice. Mol Endocrinol 26(7):1091–1101. https://doi.org/10.1210/me.2011-1329
78. Lessner SM, Prado HL, Waller EK, Galis ZS (2002) Atherosclerotic lesions grow through recruitment and proliferation of circulating monocytes in a murine model. Am J Pathol 160(6):2145–2155. https://doi.org/10.1016/s0002-9440(10)61163-7
79. de Villiers WJ, Smith JD, Miyata M, Dansky HM, Darley E, Gordon S (1998) Macrophage phenotype in mice deficient in both macrophage-colony-stimulating factor (op) and apolipoprotein E. Arterioscler Thromb Vasc Biol 18(4):631–640. https://doi.org/10.1161/01.atv.18.4.631
80. Swirski FK, Libby P, Aikawa E, Alcaide P, Luscinskas FW, Weissleder R, Pittet MJ (2007) Ly-6Chi monocytes dominate hypercholesterolemia-associated monocytosis and give rise to macrophages in atheromata. J Clin Invest 117(1):195–205. https://doi.org/10.1172/jci29950
81. Combadière C, Potteaux S, Rodero M, Simon T, Pezard A, Esposito B, Merval R, Proudfoot A, Tedgui A, Mallat Z (2008) Combined inhibition of CCL2, CX3CR1, and CCR5 abrogates Ly6C(hi) and Ly6C(lo) monocytosis and almost abolishes atherosclerosis in hypercholesterolemic mice. Circulation 117(13):1649–1657. https://doi.org/10.1161/circulationaha.107.745091
82. Jongstra-Bilen J, Haidari M, Zhu SN, Chen M, Guha D, Cybulsky MI (2006) Low-grade chronic inflammation in regions of the normal mouse arterial intima predisposed to atherosclerosis. J Exp Med 203(9):2073–2083. https://doi.org/10.1084/jem.20060245
83. Getz GS, Reardon CA (2018) T Cellsin atherosclerosis in Ldlr−/− and Apoe−/− mice. J Immunol Sci 2(3):69–76. https://doi.org/10.29245/2578-3009/2018/3.1144
84. Reardon CA, Blachowicz L, White T, Cabana V, Wang Y, Lukens J, Bluestone J, Getz GS (2001) Effect of immune deficiency on lipoproteins and atherosclerosis in male apolipoprotein E-deficient mice. Arterioscler Thromb Vasc Biol 21(6):1011–1016. https://doi.org/10.1161/01.atv.21.6.1011
85. Dansky HM, Charlton SA, Harper MM, Smith JD (1997) T and B lymphocytes play a minor role in atherosclerotic plaque formation in the apolipoprotein E-deficient mouse. Proc Natl Acad Sci U S A 94(9):4642–4646. https://doi.org/10.1073/pnas.94.9.4642
86. Daugherty A, Puré E, Delfel-Butteiger D, Chen S, Leferovich J, Roselaar SE, Rader DJ (1997) The effects of total lymphocyte deficiency on the extent of atherosclerosis in apolipoprotein E−/− mice. J Clin Invest 100(6):1575–1580. https://doi.org/10.1172/jci119681
87. Roselaar SE, Kakkanathu PX, Daugherty A (1996) Lymphocyte populations in atherosclerotic lesions of apoE −/− and LDL receptor −/− mice. Decreasing density with disease progression. Arterioscler Thromb Vasc Biol 16(8):1013–1018. https://doi.org/10.1161/01.atv.16.8.1013
88. Galkina E, Kadl A, Sanders J, Varughese D, Sarembock IJ, Ley K (2006) Lymphocyte recruitment into the aortic wall before and during development of atherosclerosis is partially L-selectin dependent. J Exp Med 203(5):1273–1282. https://doi.org/10.1084/jem.20052205
89. Gencer S, Evans BR, van der Vorst EPC, Döring Y, Weber C (2021) Inflammatory chemokines in atherosclerosis. Cells 10(2):226. https://doi.org/10.3390/cells10020226
90. Ley K, Gerdes N, Winkels H (2017) ATVB distinguished scientist award: how costimulatory and coinhibitory pathways shape atherosclerosis. Arterioscler Thromb Vasc Biol 37(5):764–777. https://doi.org/10.1161/atvbaha.117.308611

91. Getz GS, Reardon CA (2017) Natural killer T cells in atherosclerosis. Nat Rev Cardiol 14(5):304–314. https://doi.org/10.1038/nrcardio.2017.2
92. Pendse AA, Arbones-Mainar JM, Johnson LA, Altenburg MK, Maeda N (2009) Apolipoprotein E knock-out and knock-in mice: atherosclerosis, metabolic syndrome, and beyond. J Lipid Res 50 Suppl(Suppl): S178–S182. https://doi.org/10.1194/jlr.R800070-JLR200
93. Altenburg M, Arbones-Mainar J, Johnson L, Wilder J, Maeda N (2008) Human LDL receptor enhances sequestration of ApoE4 and VLDL remnants on the surface of hepatocytes but not their internalization in mice. Arterioscler Thromb Vasc Biol 28(6): 1104–1110. https://doi.org/10.1161/atvbaha.108.164863
94. Sullivan PM, Mezdour H, Quarfordt SH, Maeda N (1998) Type III hyperlipoproteinemia and spontaneous atherosclerosis in mice resulting from gene replacement of mouse Apoe with human Apoe*2. J Clin Invest 102(1):130–135. https://doi.org/10.1172/jci2673
95. Knouff C, Hinsdale ME, Mezdour H, Altenburg MK, Watanabe M, Quarfordt SH, Sullivan PM, Maeda N (1999) Apo E structure determines VLDL clearance and atherosclerosis risk in mice. J Clin Invest 103(11): 1579–1586. https://doi.org/10.1172/jci6172
96. Li H, Dhanasekaran P, Alexander ET, Rader DJ, Phillips MC, Lund-Katz S (2013) Molecular mechanisms responsible for the differential effects of apoE3 and apoE4 on plasma lipoprotein-cholesterol levels. Arterioscler Thromb Vasc Biol 33(4):687–693. https://doi.org/10.1161/atvbaha.112.301193
97. Raffai RL, Weisgraber KH (2002) Hypomorphic apolipoprotein E mice: a new model of conditional gene repair to examine apolipoprotein E-mediated metabolism. J Biol Chem 277(13):11064–11068. https://doi.org/10.1074/jbc.M111222200
98. Getz GS, Reardon CA (2009) Apoprotein E as a lipid transport and signaling protein in the blood, liver, and artery wall. J Lipid Res 50 Suppl(Suppl):S156–S161. https://doi.org/10.1194/jlr.R800058-JLR200
99. Linton MF, Atkinson JB, Fazio S (1995) Prevention of atherosclerosis in apolipoprotein E-deficient mice by bone marrow transplantation. Science 267(5200):1034–1037. https://doi.org/10.1126/science.7863332
100. Boisvert WA, Spangenberg J, Curtiss LK (1995) Treatment of severe hypercholesterolemia in apolipoprotein E-deficient mice by bone marrow transplantation. J Clin Invest 96(2):1118–1124. https://doi.org/10.1172/jci118098
101. Kashyap VS, Santamarina-Fojo S, Brown DR, Parrott CL, Applebaum-Bowden D, Meyn S, Talley G, Paigen B, Maeda N, Brewer HB Jr (1995) Apolipoprotein E deficiency in mice: gene replacement and prevention of atherosclerosis using adenovirus vectors. J Clin Invest 96(3):1612–1620. https://doi.org/10.1172/jci118200
102. Thorngate FE, Rudel LL, Walzem RL, Williams DL (2000) Low levels of extrahepatic nonmacrophage ApoE inhibit atherosclerosis without correcting hypercholesterolemia in ApoE-deficient mice. Arterioscler Thromb Vasc Biol 20(8):1939–1945. https://doi.org/10.1161/01.atv.20.8.1939
103. Huang ZH, Reardon CA, Subbaiah PV, Getz GS, Mazzone T (2013) ApoE derived from adipose tissue does not suppress atherosclerosis or correct hyperlipidemia in apoE knockout mice. J Lipid Res 54(1):202–213. https://doi.org/10.1194/jlr.M031906
104. Fazio S, Babaev VR, Murray AB, Hasty AH, Carter KJ, Gleaves LA, Atkinson JB, Linton MF (1997) Increased atherosclerosis in mice reconstituted with apolipoprotein E null macrophages. Proc Natl Acad Sci U S A 94(9):4647–4652. https://doi.org/10.1073/pnas.94.9.4647
105. Tall AR, Yvan-Charvet L, Westerterp M, Murphy AJ (2012) Cholesterol efflux: a novel regulator of myelopoiesis and atherogenesis. Arterioscler Thromb Vasc Biol 32(11): 2547–2552. https://doi.org/10.1161/atvbaha.112.300134
106. Tall AR, Yvan-Charvet L (2015) Cholesterol, inflammation and innate immunity. Nat Rev Immunol 15(2):104–116. https://doi.org/10.1038/nri3793
107. Yvan-Charvet L, Pagler T, Gautier EL, Avagyan S, Siry RL, Han S, Welch CL, Wang N, Randolph GJ, Snoeck HW, Tall AR (2010) ATP-binding cassette transporters and HDL suppress hematopoietic stem cell proliferation. Science 328(5986): 1689–1693. https://doi.org/10.1126/science.1189731
108. Herbert B, Patel D, Waddington SN, Eden ER, McAleenan A, Sun XM, Soutar AK (2010) Increased secretion of lipoproteins in transgenic mice expressing human D374Y PCSK9 under physiological genetic control. Arterioscler Thromb Vasc Biol 30(7): 1333–1339. https://doi.org/10.1161/atvbaha.110.204040

109. Roche-Molina M, Sanz-Rosa D, Cruz FM, García-Prieto J, López S, Abia R, Muriana FJ, Fuster V, Ibáñez B, Bernal JA (2015) Induction of sustained hypercholesterolemia by single adeno-associated virus-mediated gene transfer of mutant hPCSK9. Arterioscler Thromb Vasc Biol 35(1):50–59. https://doi.org/10.1161/atvbaha.114.303617

110. Bjørklund MM, Hollensen AK, Hagensen MK, Dagnaes-Hansen F, Christoffersen C, Mikkelsen JG, Bentzon JF (2014) Induction of atherosclerosis in mice and hamsters without germline genetic engineering. Circ Res 114(11):1684–1689. https://doi.org/10.1161/circresaha.114.302937

111. Jarrett KE, Lee C, De Giorgi M, Hurley A, Gillard BK, Doerfler AM, Li A, Pownall HJ, Bao G, Lagor WR (2018) Somatic editing of Ldlr with adeno-associated viral-CRISPR is an efficient tool for atherosclerosis research. Arterioscler Thromb Vasc Biol 38(9):1997–2006. https://doi.org/10.1161/atvbaha.118.311221

112. Vozenilek AE, Blackburn CMR, Schilke RM, Chandran S, Castore R, Klein RL, Woolard MD (2018) AAV8-mediated overexpression of mPCSK9 in liver differs between male and female mice. Atherosclerosis 278:66–72. https://doi.org/10.1016/j.atherosclerosis.2018.09.005

113. Basu D, Hu Y, Huggins LA, Mullick AE, Graham MJ, Wietecha T, Barnhart S, Mogul A, Pfeiffer K, Zirlik A, Fisher EA, Bornfeldt KE, Willecke F, Goldberg IJ (2018) Novel reversible model of atherosclerosis and regression using oligonucleotide regulation of the LDL receptor. Circ Res 122(4):560–567. https://doi.org/10.1161/circresaha.117.311361

114. Caligiuri G, Levy B, Pernow J, Thorén P, Hansson GK (1999) Myocardial infarction mediated by endothelin receptor signaling in hypercholesterolemic mice. Proc Natl Acad Sci U S A 96(12):6920–6924. https://doi.org/10.1073/pnas.96.12.6920

115. Cozen AE, Moriwaki H, Kremen M, DeYoung MB, Dichek HL, Slezicki KI, Young SG, Véniant M, Dichek DA (2004) Macrophage-targeted overexpression of urokinase causes accelerated atherosclerosis, coronary artery occlusions, and premature death. Circulation 109(17):2129–2135. https://doi.org/10.1161/01.Cir.0000127369.24127.03

116. Braun A, Trigatti BL, Post MJ, Sato K, Simons M, Edelberg JM, Rosenberg RD, Schrenzel M, Krieger M (2002) Loss of SR-BI expression leads to the early onset of occlusive atherosclerotic coronary artery disease, spontaneous myocardial infarctions, severe cardiac dysfunction, and premature death in apolipoprotein E-deficient mice. Circ Res 90(3):270–276. https://doi.org/10.1161/hh0302.104462

117. Braun A, Zhang S, Miettinen HE, Ebrahim S, Holm TM, Vasile E, Post MJ, Yoerger DM, Picard MH, Krieger JL, Andrews NC, Simons M, Krieger M (2003) Probucol prevents early coronary heart disease and death in the high-density lipoprotein receptor SR-BI/apolipoprotein E double knockout mouse. Proc Natl Acad Sci U S A 100(12):7283–7288. https://doi.org/10.1073/pnas.1237725100

118. Wang G, Kim RY, Imhof I, Honbo N, Luk FS, Li K, Kumar N, Zhu BQ, Eberlé D, Ching D, Karliner JS, Raffai RL (2014) The immunosuppressant FTY720 prolongs survival in a mouse model of diet-induced coronary atherosclerosis and myocardial infarction. J Cardiovasc Pharmacol 63(2):132–143. https://doi.org/10.1097/fjc.0000000000000031

119. Fuller M, Dadoo O, Serkis V, Abutouk D, MacDonald M, Dhingani N, Macri J, Igdoura SA, Trigatti BL (2014) The effects of diet on occlusive coronary artery atherosclerosis and myocardial infarction in scavenger receptor class B, type 1/low-density lipoprotein receptor double knockout mice. Arterioscler Thromb Vasc Biol 34(11):2394–2403. https://doi.org/10.1161/atvbaha.114.304200

120. Yesilaltay A, Daniels K, Pal R, Krieger M, Kocher O (2009) Loss of PDZK1 causes coronary artery occlusion and myocardial infarction in Paigen diet-fed apolipoprotein E deficient mice. PLoS One 4(12):e8103. https://doi.org/10.1371/journal.pone.0008103

121. Gonzalez L, MacDonald ME, Deng YD, Trigatti BL (2018) Hyperglycemia aggravates diet-induced coronary artery disease and myocardial infarction in SR-B1-knockout/ApoE-hypomorphic mice. Front Physiol 9:1398. https://doi.org/10.3389/fphys.2018.01398

122. Tang WHW, Li DY, Hazen SL (2019) Dietary metabolism, the gut microbiome, and heart failure. Nat Rev Cardiol 16(3):137–154. https://doi.org/10.1038/s41569-018-0108-7

123. Wang Z, Klipfell E, Bennett BJ, Koeth R, Levison BS, Dugar B, Feldstein AE, Britt EB, Fu X, Chung YM, Wu Y, Schauer P, Smith JD, Allayee H, Tang WH, DiDonato

JA, Lusis AJ, Hazen SL (2011) Gut flora metabolism of phosphatidylcholine promotes cardiovascular disease. Nature 472(7341): 57–63. https://doi.org/10.1038/nature09922

124. Wang Z, Roberts AB, Buffa JA, Levison BS, Zhu W, Org E, Gu X, Huang Y, Zamanian-Daryoush M, Culley MK, DiDonato AJ, Fu X, Hazen JE, Krajcik D, DiDonato JA, Lusis AJ, Hazen SL (2015) Non-lethal inhibition of gut microbial trimethylamine production for the treatment of atherosclerosis. Cell 163(7):1585–1595. https://doi.org/10.1016/j.cell.2015.11.055
125. Lindskog Jonsson A, Caesar R, Akrami R, Reinhardt C, Fåk Hållenius F, Borén J, Bäckhed F (2018) Impact of gut microbiota and diet on the development of atherosclerosis in Apoe(−/−) mice. Arterioscler Thromb Vasc Biol 38(10):2318–2326. https://doi.org/10.1161/atvbaha.118.311233
126. Getz GS, Reardon CA (2018) Diet, microbes, and murine atherosclerosis. Arterioscler Thromb Vasc Biol 38(10):2269–2271. https://doi.org/10.1161/atvbaha.118.311513
127. Hewing B, Parathath S, Mai CK, Fiel MI, Guo L, Fisher EA (2013) Rapid regression of atherosclerosis with MTP inhibitor treatment. Atherosclerosis 227(1):125–129. https://doi.org/10.1016/j.atherosclerosis.2012.12.026
128. Peled M, Nishi H, Weinstock A, Barrett TJ, Zhou F, Quezada A, Fisher EA (2017) A wild-type mouse-based model for the regression of inflammation in atherosclerosis. PLoS One 12(3):e0173975. https://doi.org/10.1371/journal.pone.0173975
129. Lieu HD, Withycombe SK, Walker Q, Rong JX, Walzem RL, Wong JS, Hamilton RL, Fisher EA, Young SG (2003) Eliminating atherogenesis in mice by switching off hepatic lipoprotein secretion. Circulation 107(9): 1315–1321. https://doi.org/10.1161/01.cir.0000054781.50889.0c
130. Feig JE, Parathath S, Rong JX, Mick SL, Vengrenyuk Y, Grauer L, Young SG, Fisher EA (2011) Reversal of hyperlipidemia with a genetic switch favorably affects the content and inflammatory state of macrophages in atherosclerotic plaques. Circulation 123(9): 989–998. https://doi.org/10.1161/circulationaha.110.984146
131. Trogan E, Feig JE, Dogan S, Rothblat GH, Angeli V, Tacke F, Randolph GJ, Fisher EA (2006) Gene expression changes in foam cells and the role of chemokine receptor CCR7 during atherosclerosis regression in ApoE-deficient mice. Proc Natl Acad Sci U S A 103(10):3781–3786. https://doi.org/10.1073/pnas.0511043103
132. Llodrá J, Angeli V, Liu J, Trogan E, Fisher EA, Randolph GJ (2004) Emigration of monocyte-derived cells from atherosclerotic lesions characterizes regressive, but not progressive, plaques. Proc Natl Acad Sci U S A 101(32):11779–11784. https://doi.org/10.1073/pnas.0403259101
133. Feig JE, Rong JX, Shamir R, Sanson M, Vengrenyuk Y, Liu J, Rayner K, Moore K, Garabedian M, Fisher EA (2011) HDL promotes rapid atherosclerosis regression in mice and alters inflammatory properties of plaque monocyte-derived cells. Proc Natl Acad Sci U S A 108(17):7166–7171. https://doi.org/10.1073/pnas.1016086108
134. Sharma M, Schlegel MP, Afonso MS, Brown EJ, Rahman K, Weinstock A, Sansbury BE, Corr EM, van Solingen C, Koelwyn GJ, Shanley LC, Beckett L, Peled D, Lafaille JJ, Spite M, Loke P, Fisher EA, Moore KJ (2020) Regulatory T cells license macrophage pro-resolving functions during atherosclerosis regression. Circ Res 127(3):335–353. https://doi.org/10.1161/circresaha.119.316461

Chapter 25

Use of Rabbit Models to Study Atherosclerosis

Jianglin Fan, Manabu Niimi, Yajie Chen, Ritsuko Suzuki, and Enqi Liu

Abstract

Rabbits are a useful animal model for examining human hyperlipidemia and atherosclerosis because they have unique features of lipoprotein metabolism that are similar to those in humans. Feeding rabbits a cholesterol-rich diet is a simple means to induce experimental atherosclerosis. Indeed, cholesterol-fed rabbits were first applied to address the relationship between dietary cholesterol and atherosclerosis more than 100 years ago. However, the methods for investigating atherosclerosis using cholesterol-fed rabbits have not been well formulated. In this chapter, we attempt to provide readers with the essential methods to use cholesterol-fed rabbits in the examination of atherosclerosis from cholesterol diet preparation to lesion analysis. These protocols are compiled for both experienced and young researchers who intend to use rabbits for the investigation of lipoprotein metabolism and atherosclerosis.

Key words Rabbits, Atherosclerosis, Hypercholesterolemia, Animal models, Plaques

1 Introduction

Rabbits (*Oryctolagus cuniculus*) are often used as an experimental animal model for the study of atherosclerosis [1]. As herbivores, rabbits are sensitive to a cholesterol diet and rapidly develop hypercholesterolemia and atherosclerosis [2, 3]. The first experiment using cholesterol-fed rabbits was performed 100 years ago [4] and this model is still playing an important role in cardiovascular research [1, 5, 6]. Although numerous laboratories are using this model for different research purposes, a comprehensive protocol for cholesterol-fed rabbit experiments is lacking. Paucity of such a comprehensive protocol not only hampers the proper use of this model for cardiovascular research, but also results in many questions regarding the reproducibility of results reported by different laboratories. In this chapter, we describe the entire protocol for cholesterol-fed rabbit experiments. The protocol consists of 7 parts: (1) how to prepare a cholesterol diet and how to feed rabbits; (2) how to collect blood and separate plasma; (3) how to measure plasma lipids and lipoproteins; (4) how to perform rabbit

Dipak P. Ramji (ed.), *Atherosclerosis: Methods and Protocols*, Methods in Molecular Biology, vol. 2419,
https://doi.org/10.1007/978-1-0716-1924-7_25,
© The Author(s), under exclusive license to Springer Science+Business Media, LLC, part of Springer Nature 2022

autopsy and collect aortas; (5) how to stain aortas using Sudan IV staining and analyze aortic gross lesions; (6) how to dissect aortas for histological analysis; and (7) how to quantify the microscopic lesions and cellular components. As some researchers may be beginners in using rabbits, the protocol will be described in plain words with pictures and sketches. At the end of each part, we have included notes based on our experience. This protocol is also applicable to other transgenic and knock-out rabbit experiments [6]. There are three important points for researchers to consider when performing cholesterol-fed rabbit experiments regardless of research purposes. First, what kind of a cholesterol diet will be used and how long you will feed rabbits must be decided. Second, you need to know the methods to monitor rabbit plasma lipids and lipoproteins after cholesterol diet feeding. Third, a plan regarding how to make a pathological analysis of atherosclerosis is required.

2 Materials

2.1 Preparation of a Cholesterol Diet

Usually, cholesterol diets can be purchased from rabbit feed companies, but such diets (e.g., 0.3% cholesterol and 3% soybean oil by weight) can be made in the laboratory (Fig. 1) because commercially customized diets are usually expensive and will take around a month after ordering.

1. Normal regular diet.
2. Cholesterol.
3. Soybean oil.
4. 300 mL beaker.
5. Stirrer bar.
6. Thermometer.

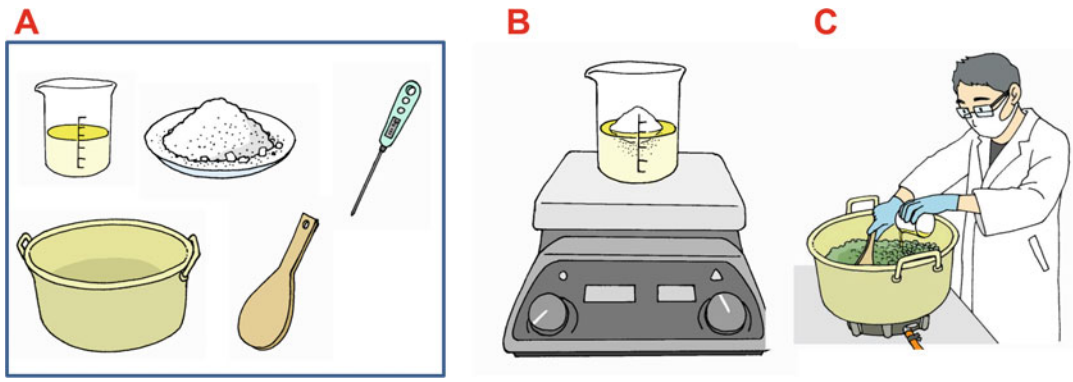

Fig. 1 Protocol for making a cholesterol-rich diet. (**a**) Materials; (**b**) preparation of oil and cholesterol mixture; and (**c**) making a diet

7. Magnetic heating stirrer.
8. Aluminum pot.
9. Ladle.
10. Gas stove.
11. Fume hood (recommended).

2.2 Collection of Blood

1. 0.5 M EDTA solution, pH 8.0.
2. 1.5 mL microtubes.
3. 20 or 22-G needles.
4. Alcohol cotton swabs.
5. Ice box.
6. Rabbit restrainers.
7. Clippers.

2.3 Preparation and Analysis of Plasma Lipids and Lipoproteins

1. 96-well plates.
2. 20 μL and 200 μL micropipettes.
3. Enzymatic assay kits for determining total cholesterol, triglycerides, and HDL-C.
4. Centrifuge.
5. Microplate reader.
6. 1% agarose gel for electrophoresis.
7. Fat Red 7B staining solution.

2.4 Rabbit Autopsy and Separation of Aortas

1. Surgical instruments for rabbit autopsy: Ophthalmological scissors, surgical scissors, forceps, hemostats, two plastic or metal trays with a cover, a cork board, pins and sinkers.
2. 6.5% pentobarbital sodium solution.
3. Electric shaver.
4. PBS: 137 mM NaCl, 2.7 mM KCl, 10 mM Na_2HPO_4, and 1.8 mM KH_2PO_4.
5. 10% neutral buffered formalin.

2.5 Sudan IV Staining and Aortic Gross Lesion Analysis

1. 70% ethanol.
2. 10% Sudan IV dissolved in 70% ethanol: Add 10 g of Sudan IV on the magnetic heating stirrer at 60 °C overnight and filter through 5 μm filter paper.
3. Plastic or aluminum trays with a cover.
4. Shaker.
5. Running water.
6. Digital camera.

7. Film table.
8. Ruler.
9. 10% neutral buffered formalin.
10. Computer with appropriate image analysis software.

2.6 Dissecting the Aorta for Sections

1. Blades.
2. Paraffin.
3. Tissue processing cassettes.
4. Microtome.

2.7 Histological and Immunohistochemical Staining

1. Paraffin sections.
2. Hematoxylin and Eosin (HE) stain.
3. Elastica Van Gieson's (EVG) stain.
4. 100% Xylene.
5. Gradient ethanol solutions: 100%, 99.5%, 90%.
6. 0.3% H_2O_2 in methanol.
7. 0.1 M citric acid solution: Dissolve 9.2 g citric acid in 1 L of ddH_2O. Store at room temperature.
8. 0.1 M trisodium citrate dehydrate solution: Dissolve 9.41 g of trisodium citrate in 1 L of ddH_2O. Store at room temperature.
9. Citric acid buffer: Add 9.5 mL of 0.1 M citric acid solution to 40.5 mL of 0.1 M trisodium citrate dehydrate solution. Make final volume to 100 mL with ddH_20.
10. Primary Antibody: RAM-11 anti-macrophage monoclonal antibody (1×300).
11. Primary antibody: HHF35 anti-muscle-actin monoclonal antibody (1:400).
12. Secondary antibody: Peroxidase-labeled goat anti-mouse IgG.
13. 3-amino-9-ethylcarbazole (AEC).
14. PBS: 137 mM NaCl, 2.7 mM KCl, 10 mM Na_2HPO_4, and 1.8 mM KH_2PO_4.
15. Distilled water.
16. Water-soluble mounting medium.
17. Glass slides and coverslips.

2.8 Quantification of Microscopic Lesion Area and Macrophage/ Smooth Muscle Cells

1. HE-stained slides.
2. EVG-stained slides.
3. Immunohistochemical slides stained with antibodies against macrophages and smooth muscle cells.

4. Light microscope equipped with a digital camera.
5. Computer with image analysis software.

3 Methods

3.1 Preparation of a Cholesterol Diet

The method described here is for making 5 kg of cholesterol diet, which can be scaled up or down as required (*see* **Notes 1–4**).

1. Pour 150 mL of soybean oil into a 300 mL beaker with a stirrer bar and heat it on a magnetic heating stirrer. Put a thermometer in the beaker to monitor the temperature of the oil.
2. Measure 15 g of cholesterol powder and place it into the oil while the temperature is around 100–150 °C (Fig. 1b). Cholesterol will dissolve in the oil in approximately 5 min.
3. At the same time, place 5 kg of regular normal regular diet into an aluminum pot on a gas stove to heat in a fume hood. Mix with a ladle until the temperature is approximately 45 °C (you can touch by hand).
4. Keep blending the feed in the pot with a ladle while pouring the hot oil and cholesterol mixture on to the feed to evenly coat it (Fig. 1c).
5. Store the feed in a refrigerator at 4 °C after it has cooled.
6. For feeding rabbits with a cholesterol diet, please *see* **Notes 1–4**.

3.2 Collection of Blood

1. Monitor plasma lipid levels weekly after feeding a cholesterol-rich diet. For this purpose, rabbits need to be fasted overnight (approximately 16 h). For example, you can remove the food holder from the cages at 5 p.m. and collect blood at 9 a.m. the next day (*see* **Note 5**).
2. Take rabbits out from the cages and fix in a restrainer (Fig. 2a, b) (*see* **Note 6**).
3. Collect blood from the auricular intermediate artery (Fig. 2c). Remove fur and stimulate the artery to dilate by tapping before sterilizing with alcohol cotton swabs (Fig. 2d).
4. Grab the ear with the left hand and insert a 22G needle (with needle bevel facing up) from the distal end of the artery and approximately 1–2 cm deep (Fig. 2e, f). Blood will almost automatically come out from the needle adaptor.
5. Collect the blood in a microtube with 0.5 M EDTA (*see* **Note 7**).
6. Invert the tubes 2–3 times gently and place them on ice.

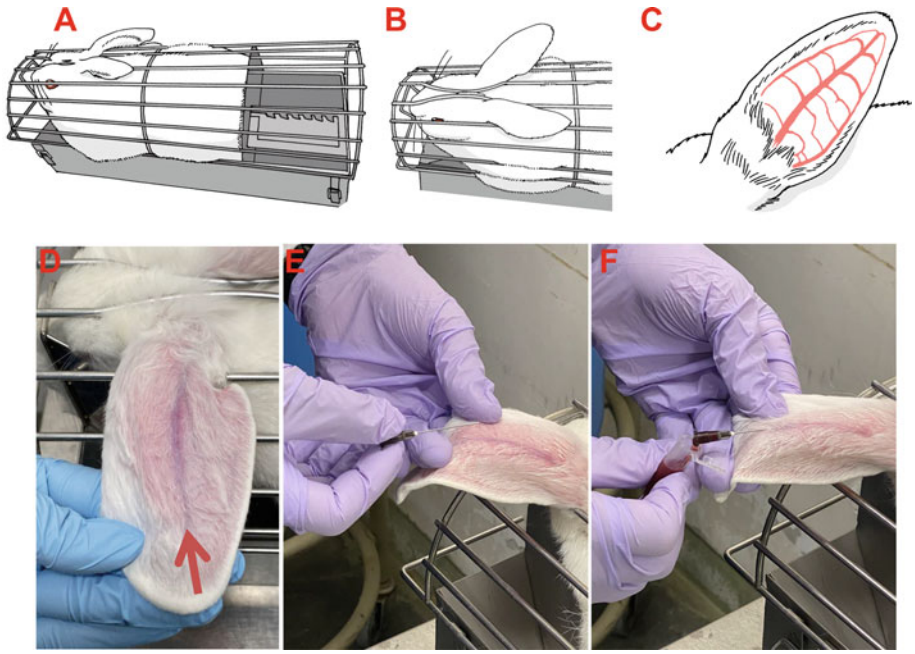

Fig. 2 Schematic illustration of collecting blood from rabbit ear artery. A rabbit is put into a restrainer (**a**) and ear is pulled out (**b**). Auricular arteries are shown (**c**). The arrow indicates the auricular intermediate artery (**d**). With the left hand grabbing the ear, use your index finger and middle finger at the back and thumb on the top to fix the ear as shown in (**e**). Insert a needle (with needle bevel facing up) along the artery. Blood will almost automatically come out from the needle adaptor (**f**)

7. Stop any bleeding by pressing the artery with the left thumb and index finger for a few seconds after removing the needle. A clipper can also be used if bleeding cannot be stopped.

3.3 Preparation of Plasma and Analysis of Lipids and Lipoproteins

1. Centrifuge the microtubes containing the blood at 1500 × *g* for 20 min at 4 °C.
2. Collect the plasma into a new tube.
3. Measure plasma levels of total cholesterol, triglycerides, HDL-cholesterol, and phospholipids using colorimetric enzymatic kits following the manufacturer's instruction (*see* **Notes 8–10**).
4. Apply 8 μL of plasma sample and calibration standards in the kit on a 96-well microplate.
5. Add 240 μL of assay reagent in the kit and mix by pipetting.
6. Incubate at 37 °C for 10 min.
7. Measure optical density with a microplate reader and calculate lipid concentrations.

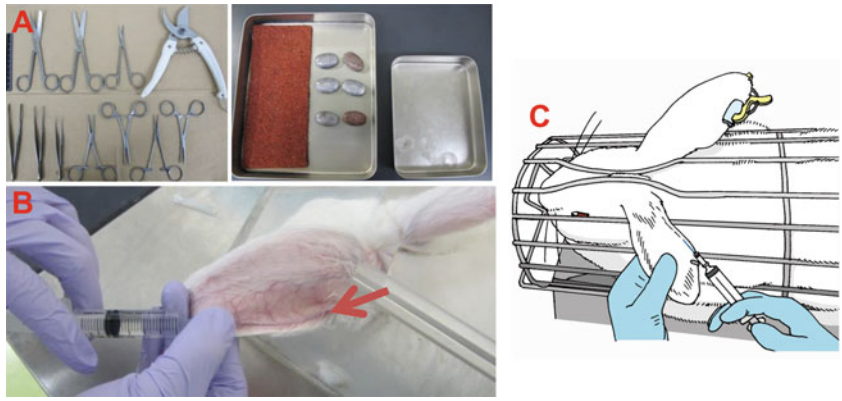

Fig. 3 Materials required for rabbit autopsy and euthanasia methods. Surgical instruments for autopsy (left) and trays and sinkers (right) (**a**), and the method of injection of pentobarbital sodium solution through an ear vein (**b**, **c**) for euthanasia. The arrow indicates the vein

8. Plasma lipoproteins can be easily analyzed by 1% agarose gel electrophoresis followed by neutral lipid staining with Fat red 7B (*see* **Notes 11–13**).

3.4 Rabbit Autopsy and Collection of Aortas

1. Euthanize rabbits by injecting overdoses of pentobarbital sodium solution (100 mg/kg body weight) through an ear vein (Fig. 3b, c) (*see* **Note 14–16**).
2. Place the rabbits in a supine position (Fig. 4a).
3. Shave thoracic and abdominal fur with an electric shaver. Remove all skin and expose the muscle layer (Fig. 4b).
4. Cut open the abdominal cavity using a pair of scissors to expose all internal organs (Fig. 4c).
5. Remove all internal organs, including the liver, stomach, small and large intestines (Fig. 4d) (*see* **Note 17**).
6. Open the thoracic cavity by cutting the diaphragm and bilateral ribs, remove adipose/connective tissue on the heart and expose the aortic arch and bilateral carotid arteries (Fig. 4e).
7. Remove the trachea and lungs (Fig. 4f). At this step, you can see the heart and aorta with three branches originating from the aortic arch, including the brachiocephalic artery, left carotid artery and left subclavian artery, in the thoracic cavity and abdominal aorta with the celiac artery, superior mesenteric artery and bilateral renal arteries in the abdominal cavity. The entire aorta with all branches and iliac arteries can be observed (Figs. 4g and 5).
8. Remove the heart from the aorta (Fig. 6a).
9. Carefully harvest the aorta by cutting the bilateral carotid arteries, subclavian arteries, intercostal arteries, and lumbar arteries along the backbone (Fig. 6b) (*see* **Note 18**).

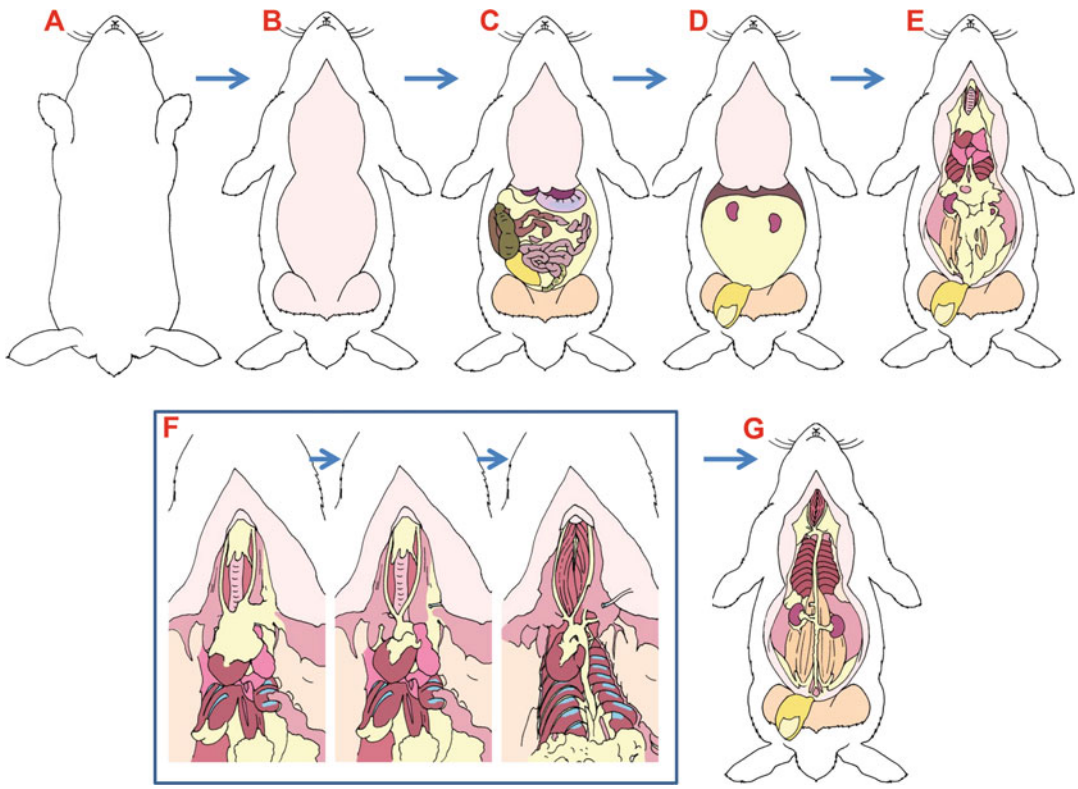

Fig. 4 Procedures of rabbit autopsy. Place rabbits on the table in the supine position (**a**) and remove the skin (**b**). Open the abdominal cavity (**c**) and remove all internal organs (**d**). Open the thoracic cavity and expose the heart and lungs (**e**). Separate all adipose and connective tissue from the aorta and heart to visualize the heart, aortic arch, common carotid arteries (**f**), abdominal aorta with renal arteries and kidneys (**g**)

10. Place the aorta into a tray filled with PBS (cool on ice) (Fig. 6c, d) and carefully trim the peri-aortic adipose and connective tissue using ophthalmological scissors (Fig. 7a).
11. Place the aorta on a cork board to visualize the entire aortic tree (Fig. 7b).
12. Cut the aorta open longitudinally using a pair of ophthalmological scissors (Fig. 8a–e) starting from the aortic arch to the iliac arteries.
13. Fix the aorta on the cork board with the surface up using stainless steel pins (Fig. 9a).
14. Sink the aorta on a cork board in 10% buffered formalin (Fig. 9b). As the cork board will float, put an iron or lead weight or fishing sinker to make it sink completely (Fig. 9b).
15. Fix the aorta for 24 h or longer until Sudan IV staining.

3.5 Staining Aortas with Sudan IV Stain

1. Remove aortas from the formalin solution and rinse in running water for 1 h to remove formalin odor.

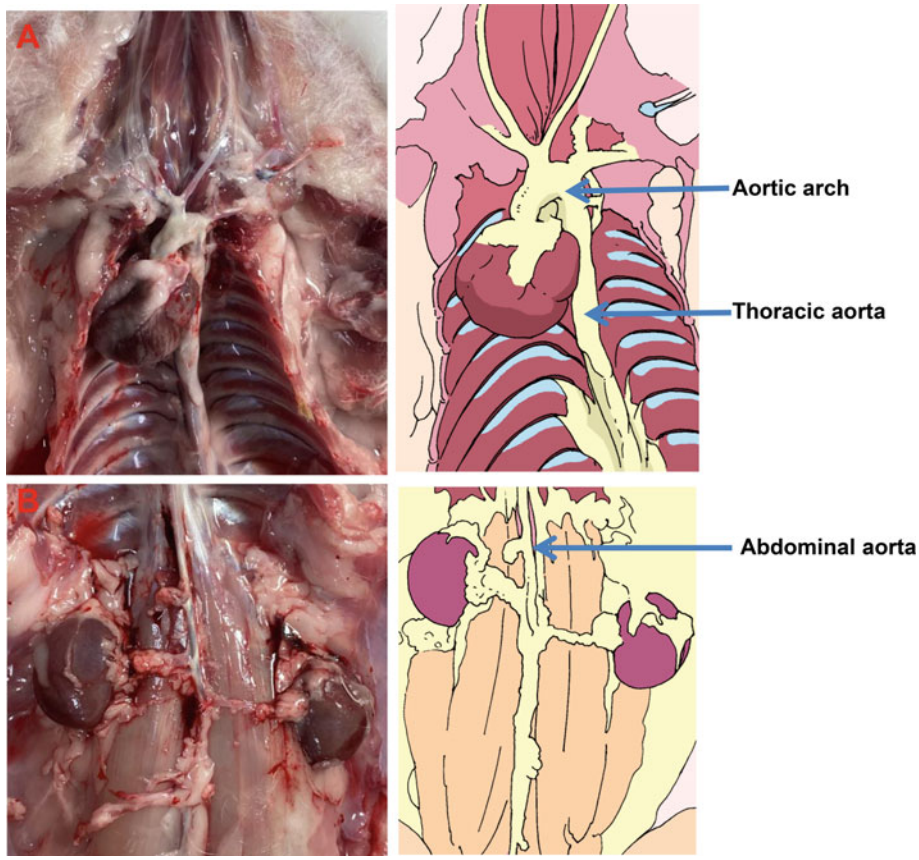

Fig. 5 Separation of aortas after removing other organs. Expose heart along with thoracic aorta (**a**) and abdominal aorta with kidneys (**b**)

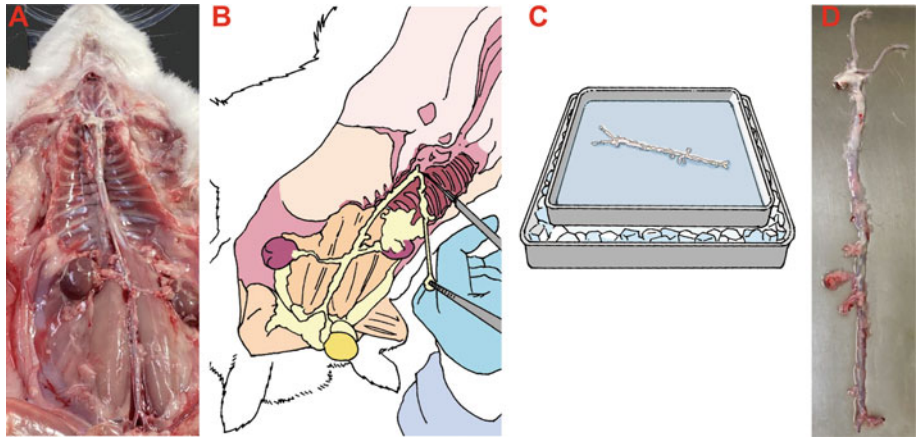

Fig. 6 Collecting the rabbit aorta from the body. The aortic tree is clearly seen *in situ* before removing (**a**), removed from the body (**b**) and put into a tray with PBS on the ice (**c**). Isolated aorta surface contains adipose and connective tissue before trimming (**d**)

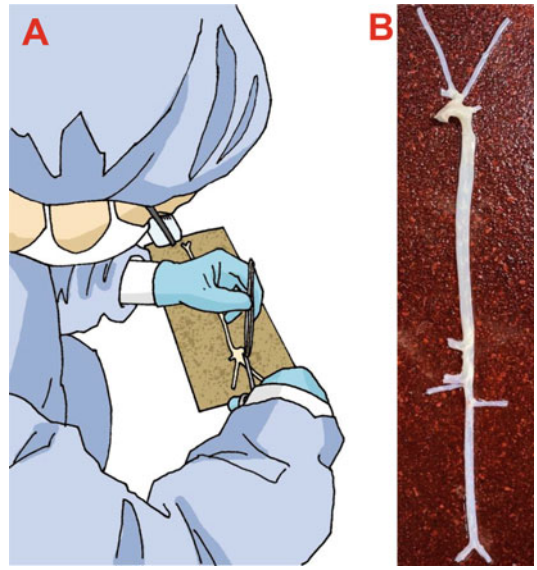

Fig. 7 Trimming the aorta on a cork board. Remove all adipose and connective tissue using a pair of ophthalmological scissors and tweezers (**a**). Isolated aorta after trimming (**b**)

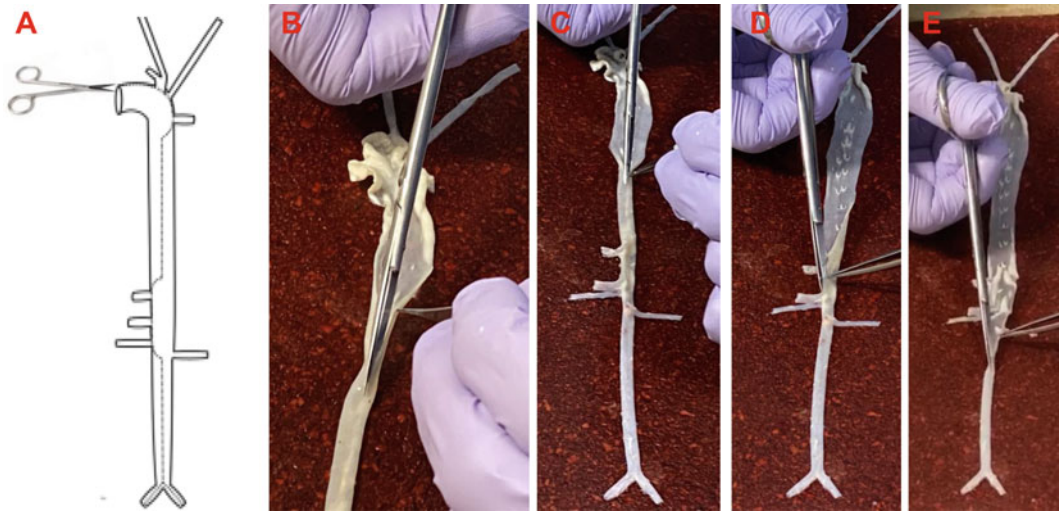

Fig. 8 Exposure of the aortic surface. Cut the aorta open longitudinally using a pair of ophthalmological scissors from the aortic arch to abdominal aorta (**a–e**)

2. Soak the aortas in 70% ethanol for 30 min and then in Sudan IV solution overnight (Fig. 9c, d) (*see* **Notes 19–21**).
3. Rinse the aortas in 70% ethanol for 3 min and then in fresh 70% ethanol to destain the background for 30 min (Fig. 9e) (*see* **Note 22**).

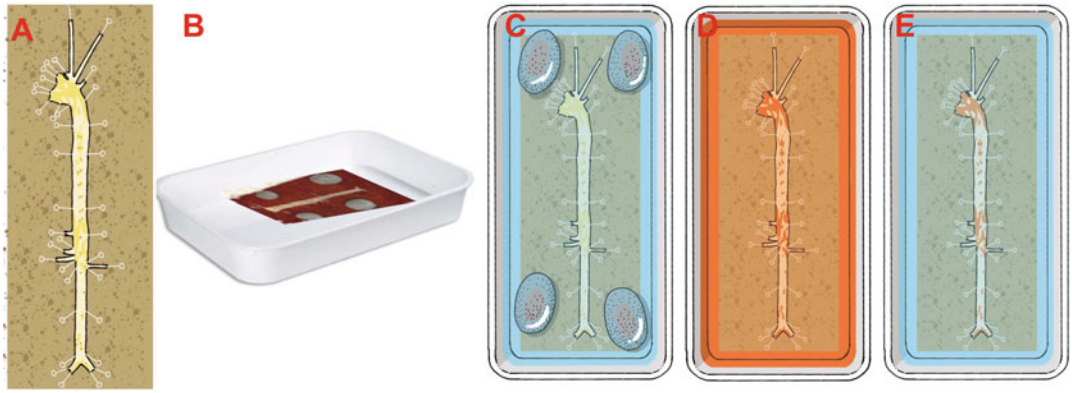

Fig. 9 Fixation and Sudan IV staining. Fix the aorta on the cork board with stainless pins (**a**) and then place it in formalin solution with weights on the cork board (**b**). Aorta is washed and then stained with Sudan IV and destained with ethanol (**c**–**e**)

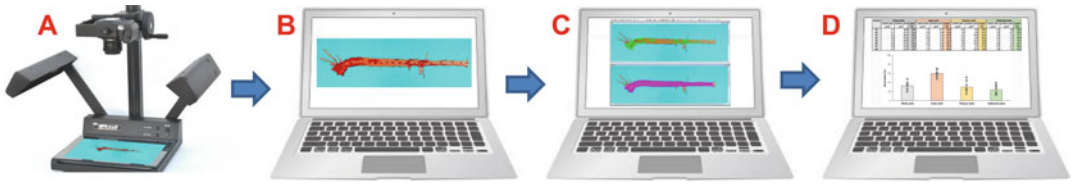

Fig. 10 Photographing the aorta and analyzing the gross lesions using an image analysis system. (**a**) Photographing aorta using a digital camera; (**b**) importing the images into the computer; (**c**) tracing the outline of each aorta and lesions; and (**d**) quantification of the lesion area

4. Rinse the aortas with running water for 10 min before photographing or store in 10% neutral buffered formalin if you cannot proceed to the next step.
5. Place the aorta on the filming table, take a photo with a digital camera and then put it back to the formalin solution (Fig. 10a). Place a ruler beside the aorta to indicate the actual size in the pictures.
6. Import each image of the aorta into a computer using the WinRoof image analysis software or other image analysis software (Fig. 10b) (*see* **Note 23**).
7. Trace the outline of each aorta manually and first calibrate the sudanophilic area (red in color) with a green color threshold. All sudanophilic area is identified by green color extraction and calculation is conducted automatically (Fig. 10c). Calculate the gross lesions and express as the percentage of Sudan IV staining area relative to the regional aortic area. Transform the data into Excel files and analyze using statistical software (Fig. 10d).
8. To quantify the distribution of atherosclerotic lesions, divide the aorta arbitrarily into three parts to calculate each part lesion area separately: (1) the aortic arch is defined from the aortic

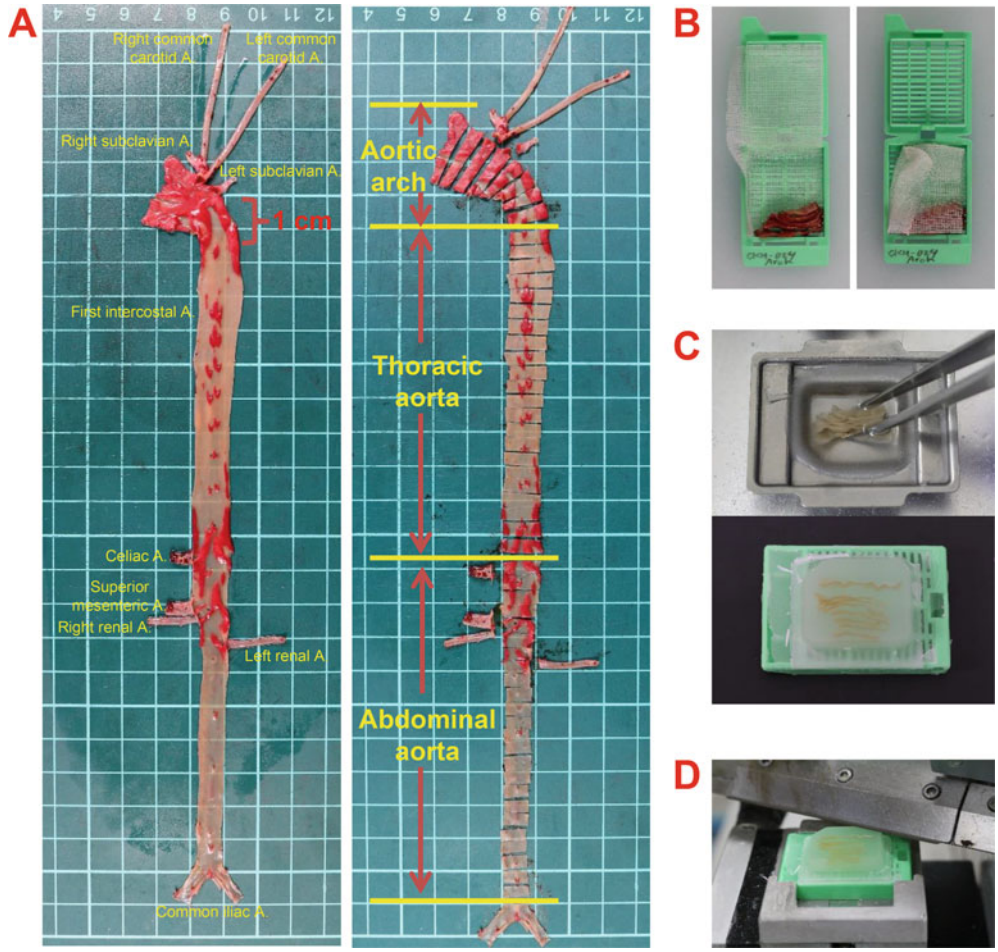

Fig. 11 Representative aortic tree after Sudan IV staining. Red areas on the surface of the aorta are Sudan IV-stained lesions (**a**, left). Aortic trees are divided into three parts and cut into segments as shown (**a**, right): 8 segments for arch, approximately 20 segments for thoracic aorta, and approximately 25 for abdominal aorta. They are loaded in cassettes (**b**, left) covered by a gauze to keep them in orientation and order (**b**, right). These segments are embedded in paraffin (**c**) and then ready for sectioning using a microtome (**d**)

root to the thoracic aorta approximately 1 cm from the left subclavian artery; (2) the thoracic aorta is up to the orifice of the celiac artery; and (3) the abdominal aorta is extended to the branches of the iliac arteries (Fig. 11a left) (*see* **Note 24**).

3.6 Dissection of the Aorta and Preparation of Paraffin Sections

1. Dissect each part of the aorta into 3–4-mm thick segments (approximately 8 for aortic arch, 20 for thoracic, and 25 for abdominal aortas) using a blade as shown in Fig. 11a right.
2. Place these segments sequentially into tissue processing cassettes and cover with gauze to maintain good orientation and order (Fig. 11b) (*see* **Note 25**).

3. Embed cassettes in paraffin using the tissue processor (Fig. 11c).
4. Section the paraffin-embedded aorta blocks using a microtome (Fig. 11d). Usually, 3 μm-thick sections are required (*see* **Note 26**).

3.7 Histological and Immunohistochemical Staining

Serial paraffin sections are routinely stained with HE and EVG stain. This can be performed at a pathological laboratory or core facility (*see* **Notes 27** and **28**). Additional serial sections can be stocked for immunohistochemical (IH) staining using antibodies (Abs) against macrophages, smooth muscle cells, and other inflammatory factors (*see* **Note 29**).

1. For IH staining, deparaffinize paraffin sections (prepared as above) are deparaffinized in 100% xylene (3 × 7 min each) and gradient ethanol solution (2× in 100% ethanol for 1 min each; 99.5% ethanol for 1 min and 90% ethanol for 1 min).
2. Treat sections with 0.3% H_2O_2 solution for 30 min and then wash in PBS (3 × 5 min each).
3. Incubate sections with the first Ab either 2 h at room temperature or overnight at 4 °C.
4. Wash with PBS (3 × 5 min each) and then incubate with the secondary Ab for 1 h at room temperature.
5. Wash in PBS (3 × 5 min each) and add AEC on the slides for colorization.
6. Wash in distilled water and then running water.
7. Counterstain the nucleus with hematoxylin stain for 3 seconds and quickly wash in running water.
8. Put a coverslip using water-soluble aqueous mounting medium.
9. Representative micrographs of HE and EVG staining and IH staining for macrophages and smooth muscle cells are shown in Fig. 12a.

3.8 Quantitation of Microscopic Lesions and Cellular Components

Before quantifying the microscopic lesions and cellular components, you need to make an observation of all HE-stained slides first. By observing HE-stained slides, you can know whether lesions are present either locally or diffusely, the components of the lesions such as macrophage or foam cells-rich or smooth muscle cell-rich, whether the lesions are those of early-stage or advanced lesions. This information is very important to know beforehand.

1. Image all EVG-stained specimens and IH-stained specimens under a light microscope with a digital camera.
2. Import all images into the computer using the appropriate software (e.g., WinRoof) and measure intimal lesion area

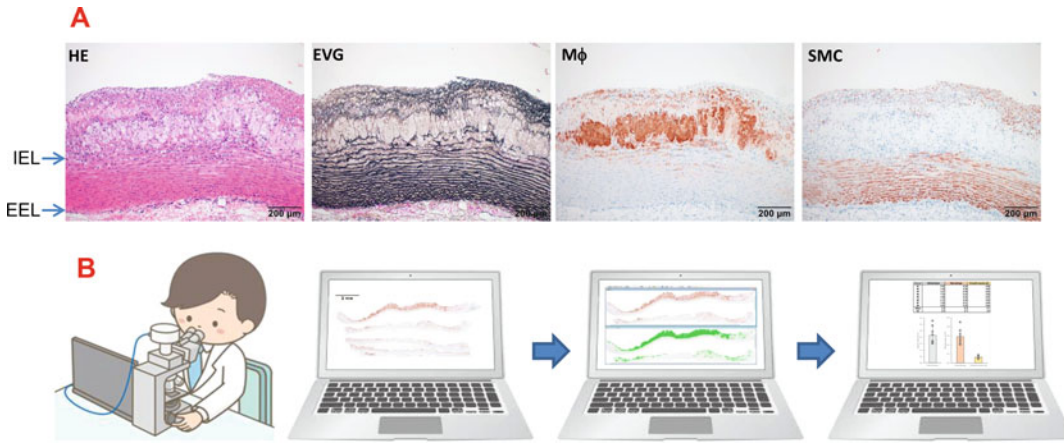

Fig. 12 Representative micrographs of aortic lesions and quantification of microscopic lesions. Paraffin sections were stained with HE, EVG or immunohistochemically stained with antibodies against macrophages and smooth muscle cells (**a**). *IEL* internal elastic lamina, *EEL* external elastic lamina. Quantification of microscopic lesion area and macrophage/smooth muscle cell area using an image analysis system (**b**): importing the images into the computer; tracing the outline of lesion area or staining area; and quantification of the lesion area and staining area

defined by the internal elastic lamina using EVG-stained specimens (Fig. 12b). The microscopic lesion area is expressed as the mean value (mm^2) of each segment on the slide (*see* **Note 30**).

3. Perform quantification of lesional macrophages and smooth muscle cells using each IH-stained specimens. The amount of macrophages and smooth muscle cells in the intimal lesions can be either expressed as positive % or actual value (mm^2) (*see* **Notes 31** and **32**). Also *see* **Notes 33–37** for additional important considerations.

4 Notes

1. As the absorption of dietary cholesterol requires fat, you must add oil into the diet. Otherwise, rabbits will use their internal fat, which makes them lean or sick. In addition, using soybean oil, which consists of unsaturated fatty acids, can prevent the levels of plasma cholesterol from becoming too high. Other vegetable oils, such as peanut oil or corn oil, can be used because they are all unsaturated fatty acids. Animal fat (saturated fatty acids) like tallow and lard is not recommended.
2. We recommend using a 0.3–0.5% cholesterol diet for most experiments. Rabbits cannot tolerate a 1–2% cholesterol diet for a month as they develop severe liver dysfunction. If plasma cholesterol levels are too high (>2000 mg/dL), rabbits become sick and have massive accumulation of lipids in the

liver, spleen, and other organs, which is often criticized as "unphysiological."

3. Adult rabbits at 4 months or older can consume approximately ~150 g a day. You can either feed ab libitum or restricted (100–150 g/day/adult rabbit).
4. Records of food consumed along with body weight may need to be taken daily.
5. Fasting rabbits can minimize the variations in plasma triglycerides. However, if you want to measure postprandial plasma lipids, fasting is not necessary.
6. Blood collection requires you to fix rabbits in a restrainer. If restrainers are not available in your laboratory, you can wrap a rabbit in a cloth or unused lab gown.
7. Both plasma and serum can be used for the analysis of lipids and lipoproteins. If using plasma, we recommend using EDTA, as in the protocol, but you need to determine whether other assays are required in the future before choosing anticoagulants. Some assays may need specific anticoagulants such as heparin to measure lipase activity. A protease inhibitor in addition to anticoagulants may be needed such as aprotinin for the measurement of plasma insulin and lipoproteins.
8. Plasma lipids should be measured weekly, especially for the first 4 weeks, because you need to determine whether plasma levels of cholesterol are elevated in each animal. Non-responder rabbits can be excluded from the experiments if their plasma cholesterol levels do not increase after cholesterol diet feeding. Fresh plasma can be stored in a refrigerator for several days. If you cannot measure plasma lipids right way, store the plasma in a freezer.
9. To measure plasma lipids, there are no differences between fresh and frozen plasma. However, you must use fresh samples for the analysis of lipoproteins (stored at 4 °C within 3 days). Plasma lipids can be either measured using colorimetric enzymatic kits as described here or using auto-analyzers.
10. Depending on your research purposes, plasma can be also used for other analyses such as free fatty acids, glucose, insulin, and other plasma markers.
11. Plasma lipoproteins can be measured at 8 and 16 weeks when the plasma levels of cholesterol are stable.
12. For the analysis of lipoproteins, you can use either ultracentrifugation or fast-protein liquid chromatography (FPLC). FPLC is much easier and quicker than ultracentrifugation, but the latter provides more information in terms of lipoproteins with different densities. For the measurement of apolipoproteins, they can be fractionated using 4–20% SDS-polyacrylamide gel

electrophoresis followed by Western blotting with cocktail antibodies of anti-apolipoprotein (apo)AI, apoB, apoE, and CI-III [7]. Please refer to a recent report for these assays in details [8].

13. The major lipoproteins increased in cholesterol-fed rabbits are intestinally and hepatically derived remnant lipoproteins called β-very low density lipoproteins (VLDLs), whereas LDLs are slightly increased. Therefore, measuring LDL-cholesterol levels is not necessary.
14. Use the protocol of your institution to euthanize rabbits.
15. It is not necessary to perfuse the animals if you do not intend to perform electron microscopic observations or in situ hybridization.
16. Usually, it will take approximately 30 min to autopsy one rabbit.
17. If you need other organs such as liver and kidneys for your experiment, you can collect them according to your purposes.
18. If aortic samples are required for other analyses, such as Western blotting and polymerase chain reaction, cut the aorta before placing into formalin solution. In such cases, take a photo to record the original and removed aorta area for latter calculation.
19. Sudan IV solution should be prepared in advance and should be stocked in a shading container or covered by shading paper.
20. Sudan IV solution can be re-used 2–3 times, but you must filter it before use.
21. It is recommended that all staining procedures be performed on a shaker.
22. The entire procedure from aorta collection to Sudan IV staining is shown in Fig. 13.
23. Many types of imaging software, such as NIH image, can be used.
24. Unlike humans, the rabbit aortic arch anatomy does not have clear ascending and descending aorta parts. For the convenience of analysis, we define the aortic arch arbitrarily starting from the aortic root to the thoracic aorta approximately 1 cm from the left subclavian artery for adult rabbits. Another way to define the aortic arch endpoint is the middle point between the first intercostal artery orifices and the left subclavian artery (Fig. 12a).
25. The orientation of all segments in cassettes is important for cutting sections. If orientation is bad, the following sections are difficult for observation and analysis.

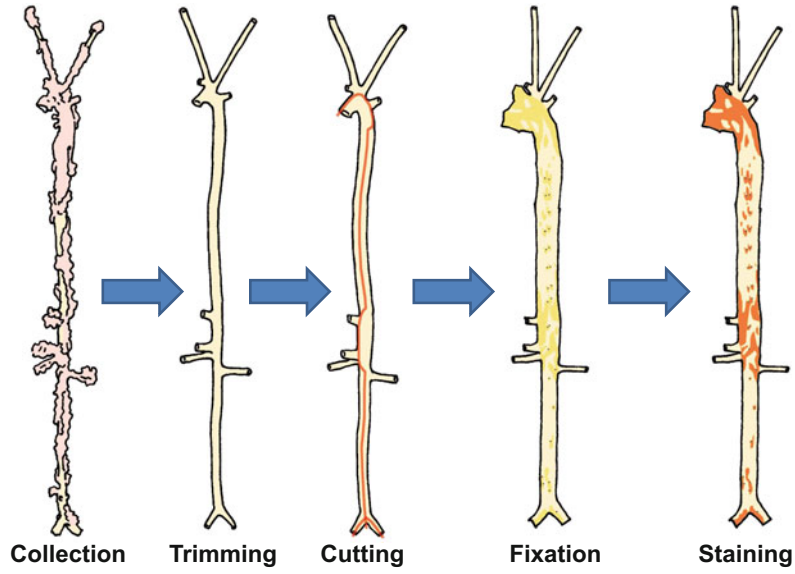

Fig. 13 The whole steps from aorta collection to Sudan IV staining. After the aorta is collected, it will be trimmed and cut open before fixation and staining with Sudan IV

26. Cutting paraffin-embedded sections using a microtome is not difficult after training. Therefore, if there is no a pathological facility, you can do it yourself.
27. HE staining is essential for histological evaluation of the lesions, whereas EVG staining is used for quantification of the microscopic lesion size because the internal elastic lamina can be visualized for measuring intimal lesions. Histological changes in the aorta are first evaluated using HE-stained specimens to determine whether lesions are present, and if they are, what features they have such as cellular/extracellular features and plaque stability features.
28. Other staining such as Masson's trichrome for staining collagen can be used according to your research purposes.
29. You can also perform immunohistochemical staining using other antibodies along with quantitative analysis as for macrophages and smooth muscle cells.
30. If the lesions are extensively involved in the media, you need to measure them separately.
31. We usually select the aortic arch for the quantification of microscopic lesions and macrophages/smooth muscle cells because in cholesterol-fed rabbits, the aortic arch lesions are the most consistently present compared with other aortic parts. If the lesions are extensively present in all parts of aortas, all of them should be analyzed accordingly.

32. The complete results of lesion analysis should contain the following data: (1) gross (or *en face*) lesion size of the total aorta, along with the aortic arch, thoracic and abdominal aortas; (2) microscopic lesions size of the aortic arch; and (3) % of macrophages and smooth muscle cells of the aortic arch.
33. Unlike mice, laboratory rabbits are generally outbred. Thus, commercial rabbits from different breeders may exhibit variations in responses to a cholesterol diet and their plasma lipid levels can vary. Such variations in plasma lipid levels will affect the lesions and interfere with the interpretation of experiments. To avoid or minimize such variations, commercial rabbits can be prescreened by feeding them a cholesterol diet for a short term (1 week) in advance and those with similar plasma lipid levels can be selected for experiments. For each group, 10 or more rabbits are needed.
34. The age of rabbits should be considered because young rabbits are more susceptible to aortic atherosclerosis than old rabbits even though they have similar plasma cholesterol levels [9]. We usually use 4–6-month-old rabbits for cholesterol feeding experiments.
35. Male and female rabbits are different in terms of response to a cholesterol diet and atherosclerosis. In our experience, female rabbits develop higher hypercholesterolemia and greater aortic lesions than their counterpart male rabbits. In general, male rabbits are recommended for experiments because estrogen may influence the results.
36. Early-stage lesions of atherosclerosis can be observed after 6–8 weeks of cholesterol diet feeding. For most experiments, we recommend feeding for 16 weeks to generate fatty streaks. If complicated lesions are required, rabbits can be fed for a longer time, such as 28 weeks or longer [10, 11], depending on your experiment purposes.
37. The methods for analysis of rabbit coronary atherosclerosis have been described in detail in the previous papers [1, 12].

Acknowledgments

We thank Mrs. Kato, Y. for her technical assistance in making pathological specimens. This work was supported in part by JSPS KAKENHI (JP17K08783 and JP15H04718), the National Natural Science Foundation of China (No. 81941001 and 81770457), Innovation team programme supported by Guangdong Province (2020KCXTD038), and the JSPS-CAS Bilateral Joint Research Program (JPJSBP 120187204).

References

1. Fan J, Kitajima S, Watanabe T, Xu J, Zhang J, Liu E, Chen YE (2015) Rabbit models for the study of human atherosclerosis: from pathophysiological mechanisms to translational medicine. Pharmacol Ther 146:104–119. https://doi.org/10.1016/j.pharmthera.2014.09.009
2. Fan J, Watanabe T (2000) Cholesterol-fed and transgenic rabbit models for the study of atherosclerosis. J Atheroscler Thromb 7(1):26–32
3. Fan J, Chen Y, Yan H, Niimi M, Wang Y, Liang J (2018) Principles and applications of rabbit models for atherosclerosis research. J Atheroscler Thromb 25(3):213–220. https://doi.org/10.5551/jat.RV17018
4. Steinberg D (2004) Thematic review series: the pathogenesis of atherosclerosis. An interpretive history of the cholesterol controversy: part I. J Lipid Res 45(9):1583–1593. https://doi.org/10.1194/jlr.R400003-JLR200
5. Niimi M, Chen J, Yan H, Wang Y, Koike T, Fan J (2020) Hyperlipidemic rabbit models for anti-atherosclerotic drug development. Appl Sci 10(23):8681. https://doi.org/10.3390/app10238681
6. Matsuhisa F, Kitajima S, Nishijima K, Akiyoshi T, Morimoto M, Fan JL (2020) Transgenic rabbit models: now and the future. Appl Sci 10(21):7416. https://doi.org/10.3390/App10217416
7. Wang C, Nishijima K, Kitajima S, Niimi M, Yan H, Chen Y, Ning B, Matsuhisa F, Liu E, Zhang J, Chen YE, Fan J (2017) Increased hepatic expression of endothelial lipase inhibits cholesterol diet-induced hypercholesterolemia and atherosclerosis in transgenic rabbits. Arterioscler Thromb Vasc Biol 37(7):1282–1289. https://doi.org/10.1161/ATVBAHA.117.309139
8. Niimi M, Yan H, Chen Y, Wang Y, Fan J (2020) Isolation and analysis of plasma lipoproteins by ultracentrifugation. J Vis Exp: e61790. https://doi.org/10.3791/61790(2020)
9. Keyamura Y, Nagano C, Kohashi M, Niimi M, Nozako M, Koyama T, Itabe H, Yoshikawa T (2015) Dietary cholesterol atherogenic changes in juvenile rabbits. Biol Pharm Bull 38(5):785–788. https://doi.org/10.1248/bpb.b14-00775
10. Chen Y, Waqar AB, Nishijima K, Ning B, Kitajima S, Matsuhisa F, Chen L, Liu E, Koike T, Yu Y, Zhang J, Chen YE, Sun H, Liang J, Fan J (2020) Macrophage-derived MMP-9 enhances the progression of atherosclerotic lesions and vascular calcification in transgenic rabbits. J Cell Mol Med 24(7):4261–4274. https://doi.org/10.1111/jcmm.15087
11. Liang J, Liu E, Yu Y, Kitajima S, Koike T, Jin Y, Morimoto M, Hatakeyama K, Asada Y, Watanabe T, Sasaguri Y, Watanabe S, Fan J (2006) Macrophage metalloelastase accelerates the progression of atherosclerosis in transgenic rabbits. Circulation 113(16):1993–2001. https://doi.org/10.1161/CIRCULATIONAHA.105.596031
12. Li S, Wang YN, Niimi M, Ning B, Chen Y, Kang D, Wang Z, Yu Q, Waqar AB, Liu E, Zhang J, Shiomi M, Chen YE, Fan J (2016) Angiotensin II destabilizes coronary plaques in Watanabe heritable hyperlipidemic rabbits. Arterioscler Thromb Vasc Biol 36(5):810–816. https://doi.org/10.1161/ATVBAHA.115.306871

Chapter 26

Genetically Engineered Hamster Models of Dyslipidemia and Atherosclerosis

Xunde Xian, Yuhui Wang, and George Liu

Abstract

Animal models of human diseases play an extremely important role in biomedical research. Among them, mice are widely used animal models for translational research, especially because of ease of generation of genetically engineered mice. However, because of the great differences in biology between mice and humans, translation of findings to humans remains a major issue. Therefore, the exploration of models with biological and metabolic characteristics closer to those of humans has never stopped.

Although pig and nonhuman primates are biologically similar to humans, their genetic engineering is technically difficult, the cost of breeding is high, and the experimental time is long. As a result, the application of these species as model animals, especially genetically engineered model animals, in biomedical research is greatly limited.

In terms of lipid metabolism and cardiovascular diseases, hamsters have several characteristics different from rats and mice, but similar to those in humans. The hamster is therefore an ideal animal model for studying lipid metabolism and cardiovascular disease because of its small size and short reproduction period. However, the phenomenon of zygote division, which was unexpectedly blocked during the manipulation of hamster embryos for some unknown reasons, had plagued researchers for decades and no genetically engineered hamsters have therefore been generated as animal models of human diseases for a long time. After solving the problem of *in vitro* development of hamster zygotes, we successfully prepared enhanced green fluorescent protein (eGFP) transgenic hamsters by microinjection of lentiviral vectors into the zona pellucida space of zygotes. On this basis, we started the development of cardiovascular disease models using the hamster embryo culture system combined with the novel genome editing technique of clustered regularly interspaced short palindromic repeats (CRISPR)/CRISPR associated protein 9 (Cas9). In this chapter, we will introduce some of the genetically engineered hamster models with dyslipidemia and the corresponding characteristics of these models. We hope that the genetically engineered hamster models can be further recognized and complement other genetically engineered animal models such as mice, rats, and rabbits. This will lead to new avenues and pathways for the study of lipid metabolism and its related diseases.

Key words Hamster models, Atherosclerosis, Dyslipidemia, Transgenic, Genetically engineered

Dipak P. Ramji (ed.), *Atherosclerosis: Methods and Protocols*, Methods in Molecular Biology, vol. 2419,
https://doi.org/10.1007/978-1-0716-1924-7_26,
© The Author(s), under exclusive license to Springer Science+Business Media, LLC, part of Springer Nature 2022

1 History of Hamster Use in Lipid Metabolism Disorders and Atherosclerosis Studies

Hamster (Syrian golden hamster) is a rodent laboratory animal that is widely used in different research areas, including cancer [1], reproductive medicine [2], virology [3], cardiovascular diseases, and diabetes. Compared with rabbits and minipigs, hamsters have obvious advantages in terms of glucose and lipid metabolism and cardiovascular diseases. For example, they have a small size (adult weight of 150 g), a short reproductive cycle (gestation time of 17 days) and are easy to feed and manipulate. When compared with the commonly used model animals, rats and mice, hamsters possess the characteristics of lipid metabolism and metabolic cardiovascular disease that are very similar to those of humans (*see* Table 1) [4]. This made hamster as one of the main experimental animals used to study metabolic cardiovascular diseases such as dyslipidemia without gene modification technology.

As early as the 1950s, studies of atherosclerosis (AS) in hamsters had been initiated [5]; feeding hamster with milk and egg yolk diets resulted in obvious vascular responses and extensive thrombosis. Studies on lipid metabolism and atherosclerosis were consistently reported in hamster models for the following decades [6–8]. In 1987 [9], the processes and characteristics of atherosclerosis in male Syrian golden hamsters induced by high fat were extensively reviewed by Nistor and co-workers. When these hamsters were fed a high-fat diet containing 3% cholesterol and 15% butter for 4 weeks, their plasma total cholesterol increased significantly and reached 17-fold after 10 months. Low density lipoprotein (LDL) cholesterol was also increased by four-fold after 4 weeks and 13-fold after 10 months. Mononuclear cells had adhered to the surface of endothelial cells and lipid deposition was observed in the aortic arch and thoracic aorta at 4 weeks, as well as a small amount of smooth muscle cell infiltration in the intima. Furthermore, lipid deposition also began in smooth muscle cells (SMCs) of the intima-media after 6 months of high-fat feeding, suggesting that AS lesions had characteristics similar to those observed in humans with cholesterol crystals, calcium deposits, and necrotic nuclei. Subsequent studies have confirmed that dietary cholesterol intake does increase hepatic production of very low density lipoprotein (VLDL) and LDL cholesterol in hamsters [10]. However, there was no effect on high density lipoprotein (HDL) transport to the liver [11]. In another study around that time, Schaefer's team from the United States also induced atherosclerosis with a high-fat diet in hamsters with the F1B strain and found that lovastatin reduced non-high-density lipoprotein cholesterol [12].

While LDL receptor and ApoE knockout mice were widely used in dyslipidemic and atherosclerotic studies in the 1990s after gene knockout technology [13], hamsters were still widely used in

Table 1
Differences in lipid metabolism and atherosclerosis among several species

	Mice	Hamsters	Minipigs	Humans
Major lipoproteins	HDL	HDL/LDL	LDL/HDL	LDL
CETP	No	Yes	No	Yes
ApoB editing	Intestine/liver	Intestine	Intestine	Intestine
ApoB48	CM/VLDL	CM	CM	CM
Liver LDL-R	High	Low	Low	Low
Extrahepatic	50%	85%	?	90%
Cholesterol synthesis				
High-fat diet	Insensitive	Sensitive	Moderate	Sensitive
Atherosclerosis	Resistance	Susceptible	Susceptible	Susceptible
CAD	Difficult	?	?	Major lesion
Stroke	Difficult	?	?	Major lesion
Genetic background	Inbreed	Close Colony	Non-inbreeder	
Breeding/husbandry	Easy	Easy	Difficult	
Genetic models	Numerous	Few	Few	

the study of dyslipidemia based on the similar characteristics of lipid metabolism in hamsters and humans. Since 2000, the Adeli's team in Canada has investigated lipid metabolism using hamster models [14]. Early on, the team used a fructose-fed hamster model to study changes in lipid metabolism and its regulatory mechanisms, targeting insulin resistance in hamsters [14–16]. They found that the characteristics of insulin resistance in hamsters facilitated the alteration of lipid metabolism and contributed to the study of lipid metabolism; fructose-fed hamsters had overproduction of VLDL and those fed fructose for 2 weeks had marked hyperinsulinemia and hypertriglyceridemia [14]. In addition, it was found that statins could improve insulin resistance in hamsters [17]. Over the past two decades, the team has made important contributions to the study of apolipoprotein (Apo)B metabolism and its role using the hamster model [18–21]. They found that glucagon-like peptides (GLP-1 and GLP-2) could regulate intestinal and hepatic lipid metabolism [22–27].

The increasing use of hamsters has gradually revealed more advantages. Cholesteryl ester transfer protein (CETP) is an important protein in reverse cholesterol transport (RCT), and hamsters have high levels of CETP activity similar to humans [28]. CETP mediates the constant exchange of lipid components between HDL particles and other lipoproteins or cell membranes while increasing cholesterol efflux from peripheral tissues to the liver. Therefore, the

hamster was found to be a better animal model to study RCT than a mouse model that do not express CETP [29].

Previous studies have shown that the hamster model has many advantages: (1) 49% of total plasma cholesterol is distributed on HDL and 48% is distributed on LDL [30]; (2) higher activity of CETP [28]; (3) editing of ApoB in the small intestine, leading to ApoB48 present in small intestine-derived chylomicrons (CM) but not in liver-derived VLDL [31]; (4) low density lipoprotein receptor (LDLR) activity in hamster liver [32]; (5) extrahepatic cholesterol synthesis in hamsters accounts for 85% of the total, which is relatively close to 90% in humans, whereas in mice, this accounts for only 50% [33]; (6) hamsters are susceptible to hypercholesterolemia, hypertriglyceridemia, and atherosclerosis induced by dietary interventions and also develop coronary atherosclerosis [34]; and (7) insulin resistance and type 2 diabetes can also be induced by high-sugar diet [35]. Taken together, these advantages demonstrate that the hamster model can play a crucial role in the study of lipid metabolism disorders and atherosclerosis.

However, it is noteworthy that wild-type hamsters have poor reproducibility and consistency in aortic lesions caused by diet-derived fat and cannot ideally be used for the study of diet-induced atherosclerosis [36]. This indicates that genetically modified animals would be a better model for mimicking human diseases and studying monogenic correlations of diseases, which can be analyzed for genetic function at each stage of ontogeny. Though researchers have used hamsters as an experimental animal in biomedical research, the lack of genetic engineering technology limited its further application as an animal model of disease.

Previous research in our laboratory was based on genetically engineered mice [37] and rabbits [38]. In order to make full use of the advantages of hamster, the construction of a genetically engineered hamster model for dyslipidemia was carried out, such as low density lipoprotein receptor (LDLR) [39], lecithin cholesterol acyl transferase (LCAT) [40], ApoC2 [41], ApoC3 [42], and adenosine triphosphate-binding cassette transporter A1 (ABCA1) [43] (*see* Fig. 1). Other genetically engineered hamster models are still under study and we hope that these hamster models will complement the currently used genetically engineered mouse, rat and rabbit models, and contribute to our deeper understanding of lipid metabolism and related diseases.

2 Transgenic Hamsters

Though hamsters are small rodents with characteristics similar to humans in lipid and glucose metabolism that mice and rats do not possess, the rapid development of transgenic and knockout mice over the past 20–30 years has gradually replaced hamster

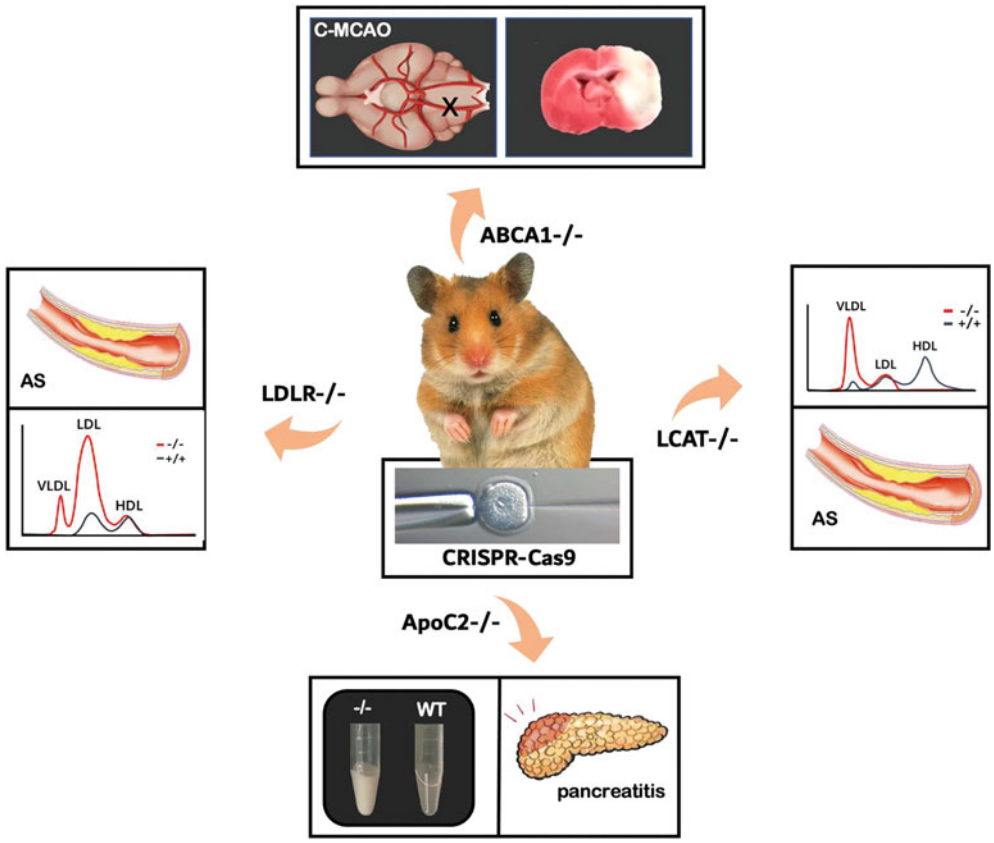

Fig. 1 Gene targeted hamster models of dyslipidemia and atherosclerosis by CRISPR/Cas-9. Dyslipidemic hamster models of hypercholesterolemia, hypertriglyceridemia, and hypo-alpha-lipoproteinemia have been created via CRISPR-Cas 9 technology. AS: atherosclerosis; C-MCAO: contra-lateral middle cerebral artery occlusion; VLDL: very low density lipoprotein; LDL: low density lipoprotein; HDL: high density lipoprotein

dominance by mouse models. The traditional transgenic technique is aimed to establish a transgenic animal model that can be passed on to the offspring by injecting a linearized expression plasmid carrying exogenous DNA into the male pronucleus of the zygote. Unfortunately, successful establishment of transgenic hamsters were not reported for a long time due to the blockage of two-cell development of hamster zygotes in *in vitro* culture. By optimizing the culture conditions of hamster zygotes, multicellular hamster embryos were obtained in our laboratory. On this basis, Gao et al. obtained a male founder capable of stably expressing enhanced green fluorescent protein (eGFP) in multiple organs by microinjecting a lentivirus transferring the gene of eGFP into the perivitelline space and confirmed by *in vivo* imaging that eGFP was also expressed in the testis. The colony of eGFP transgenic hamsters was generated for the first time after mating this line with wild-type female hamsters [44]. However, due to the inefficient

incorporation of exogenous genes into the genome by this method and other unsolved problems, no transgenic hamster model with hereditary lipid metabolism disorder has been reported yet.

Unlike genetical transgenic hamsters, Bentzon's research team produced a somatic transgenic model of proprotein convertase subtilisin/kexin type 9 (PCSK9) by administering animals with liver-targeted adeno-associated virus (AAV) carrying genes for gain-of-function mutants of PCSK9 [45]. Hamsters with gain-of-function mutants of the PCSK9 gene exhibit familial hypercholesterolemia similar to human disease, mainly by increasing degradation of LDLR in the liver, thereby leading to a reduction in LDL clearance from the plasma resulting in elevated LDL-C levels, eventually accelerating the development of atherosclerotic plaques [46]. It should be noted that as both PCSK9 and LDLR are conserved genes in a variety of species with little difference, PCSK9 transgene can be used as a general method to construct animal models of hypercholesterolemia and AS [46–48]. Moreover, this AAV-mediated somatic cell transgene approach cannot only be used in high-throughput experiments, but also has a greater prospect for animal species or strains that cannot be manipulated by germline gene editing.

The method of AAV-mediated somatic transgene for the preparation of dyslipidemic hamster model has its limitations, mainly because the individual size of hamsters is relatively large and the amount of AAV vector required is relatively high and hence the cost of preparing AAV vectors will also be higher if a large number of animals are required for the experimental design. In addition, most of the human disorders of lipid metabolism are caused by loss-of-function mutations in genes involved in the regulation of lipid metabolism. There are not many genes found to cause dyslipidemia due to overexpression. Cases like gain-of-function mutations in PCSK9 are relatively rare. Genes such as ApoC3 and angiopoietin-like proteins (ANGPTL) 3/4 are known to cause hypertriglyceridemia in mice via transgenes [49] but it is difficult to find patients with hypertriglyceridemia with similar causes observed in transgenic mice, implying that the application of this technique is limited at present.

3 Gene Knockout Hamsters

Since the twenty-first century, genetic engineering has developed rapidly, and more and more gene editing techniques have been applied to scientific research and even in medical applications. Gene editing techniques mainly include homologous recombination, insertional mutagenesis, RNA interference, and artificial endonuclease methods that have been widely used in recent years. Compared with the traditional homologous recombination of

embryonic stem cells, the artificial endonuclease method is simpler to operate and has a shorter production cycle and a significantly higher targeting efficiency. Therefore, it has become a major technology in the field of gene editing.

Artificial endonuclease includes the first-generation zinc finger endonuclease (ZFN) [50], a second-generation transcription activator-like effector nuclease (TALEN) [51], and third generation clustered regularly interspaced short palindromic repeats (CRISPR)/CRISPR-associated (Cas) 9 (CRISPR/Cas System) [52]. The principle of these methods is to cleave DNA duplexes to form breaks at specific target genes by the action of endonuclease, then to form the insertion or deletion of bases by non-homologous recombination, resulting in frame shift mutations and premature stop codons, leading to the loss of gene function. Among them, CRISPR/Cas9 system has been widely used in human cells, as well as in zebrafish, mouse, rat, rabbit, pig, and monkey since it was first used for gene editing in 2012.

Based on the successful construction of eGFP transgenic hamsters in our group, CRISPR/CAS9 technology was applied to study the regulators of lipid metabolism. Recently, several knockout hamsters, including LDLR, Apoc2, Apoc3, ABCA1, and LCAT, were constructed successively. A series of genetically engineered hamster models therefore provides a new platform for biomedical translational research.

At the same time, Wang's group from the University of Utah used CRISPR/Cas9 system to study the gene targeting of immunomodulatory factors in hamsters, and successfully constructed signal transducers and activators of transcription (STAT)2, procadherin 1 (PCDH1), recombination-activating gene (RAG)1, RAG2, potassium voltage-gated channel subfamily Q member 1 (KCNQ1), interleukin-2 receptor subunit gamma (IL-2RG), and other genetically deficient hamsters, and a series of studies on infection and immune-related fields have been conducted [44, 53–56]. In the face of Coronavirus disease (COVID)-19 currently sweeping the world, the team also successfully used STAT2 and IL-2RG-deficient hamsters to demonstrate their susceptibility to severe acute respiratory syndrome coronavirus 2 (SARS-COV-2) [56, 57], thus providing powerful animal models to combat the epidemic situation of new corona virus.

However, although genetically engineered hamsters are gaining increasing attention worldwide, some limitations of the CRISPR/Cas9 system and hamsters themselves in the current genetically engineered hamster technology exist: (1) the target gene sequence recognized by CRISPR/Cas9 technology using single guide RNA (sgRNA) is 20 bp in size and the theoretical off-target probability is relatively high, so large-scale screening for off-target is required after hamster models have been prepared; (2) at present, the genetically engineered hamsters produced by

CRISPR/Cas9 technology are all systemic knockout models and the establishment of conditional knockout hamsters still depends on homologous recombination technology; and (3) compared with mice, hamster zygotes are still more difficult to manipulate, the knockout efficiency is low, and the preparation cycle of genetically engineered hamsters is still relatively long. However, with the development of new gene editing technology, these problems will be overcome eventually in the near future.

3.1 LDLR Knockout Hamsters

Familial hypercholesterolemia (FH) is an autosomal dominant disorder caused mainly by partial or complete loss of LDLR function due to a defect in the LDLR gene. Patients present with abnormal increases in plasma LDL-C levels and apolipoprotein B-containing lipoproteins, and early-onset coronary heart disease [58–60]. Statistically, the incidence of heterozygous familial hypercholesterolemia (HeFH) is 1/200 to 1/500, whereas the incidence of homozygous familial cholesterolemia (HoFH) is 1/160,000 to 1/1,000,000 [61]. Among them, the risk of coronary heart disease is more than 2 times that of the normal population in HeFH and more than 5 times in HoFH. Therefore, the prevention, early intervention and treatment of FH are essential.

Recently, $LDLR^{-/-}$ mice [62], $LDLR^{-/-}$rats [63], Watanabe Hereditary Hyperlipidemia (WHHL) Rabbits [64], and $Apobec1^{-/-}$ mice [65] are commonly used disease model animals to study the pathogenesis of FH. Mice and rats naturally lack CETP and the major plasma lipoprotein is HDL [66] while rabbits are naturally deficient in liver lipase as well as ApoAII [67]. These differences in lipid metabolism from humans limit the use of these animal models. Therefore, we successfully constructed LDLR-deficient hamsters as an animal model to study FH using CRISPR-Cas9 technique. Our data demonstrated that plasma LDL-C was significantly increased in LDLR knockout hamsters and homozygous hamsters had levels close to human Ho-FH. Additionally, plasma LDL-C was also higher in heterozygous hamsters with LDLR deficiency than in wild-type hamsters and the increase was more pronounced after feeding a high-fat diet, suggesting that LDLR-deficient hamsters should have a dominant disease similar to human FH [68]. In order to fully understand the altered pattern of plasma lipids and differences in atherosclerotic lesions in three commonly used rodents, including mice, rats, and hamsters with LDLR deficiency, we performed a systematic comparative study of these three LDLR-deficient animal models.

When fed a normal diet, plasma total cholesterol (TC) levels in $LDLR^{-/-}$ hamsters were similar to those in HoFH patients, whereas TC levels were only slightly increased in $LDLR^{-/-}$ mice and rats, similar to plasma TC levels in HeFH patients. However, TG levels were also significantly increased in $LDLR^{-/-}$hamsters, whereas plasma triglyceride (TG) was unchanged in $LDLR^{-/-}$ rats

and mice. We analyzed the distribution of cholesterol plasma lipoproteins by fast protein liquid chromatography (FPLC) and found that LDL-C was predominant in both HoFH patients and $LDLR^{-/-}$ hamsters; however, LDL-C was only slightly increased in $LDLR^{-/-}$ mice and rats. It is well known that high-fat diet is an important means to induce hyperlipidemia and atherosclerosis in experimental animal models. In order to compare the changes of plasma lipids induced by high-fat diet in the 3 rodents, we fed a high-fat, high-cholesterol diet of 0.5% cholesterol and 15% lard to wild type (WT), $LDLR^{+/-}$, $LDLR^{-/-}$ mice, rats, and hamsters for 12 weeks. Both $LDLR^{+/-}$ and $LDLR^{-/-}$ hamsters developed severe hypercholesterolemia with plasma TC levels of 2081 ± 161.6 mg/dL and 4997 ± 233.5 mg/dL, respectively. On the other hand, plasma cholesterol levels were lower in $LDLR^{-/-}$ rats and mice than in $LDLR^{+/-}$ hamsters. However, plasma cholesterol in heterozygous rats and mice was not significantly different from WT, indicating that rats and mice with only one copy of the LDLR gene were resistant to hypercholesterolemia induced by high-fat/high-cholesterol diet. Of note, plasma cholesterol levels were higher in WT hamsters than in WT mice and rats. Similarly, plasma TG levels were higher in WT hamsters compared to WT mice and rats, and $LDLR^{-/-}$ hamsters exhibited severe hypertriglyceridemia while TG was moderately elevated in $LDLR^{-/-}$mice and rats. It is concluded that hamsters are rodents sensitive to hypercholesterolemia and hypertriglyceridemia induced by a special diet [69].

Analysis of aortic atherosclerotic lesions in three genotypes of mice, rats, and hamsters after 12 weeks of feeding a high-fat diet showed that neither WT nor $LDLR^{+/-}$ mice and rats had lesions, and $LDLR^{-/-}$ rats had fewer lesions (4.4%) than $LDLR^{-/-}$mice (21%). Aortas from WT, $LDLR^{+/-}$, and $LDLR^{-/-}$hamsters developed atherosclerotic lesions that were copy number dependent on the LDLR gene. Unlike $LDLR^{-/-}$mice with predominant aortic root lesions, $LDLR^{-/-}$hamsters exhibited predominant aortic arch and abdominal aortic atherosclerotic lesions, similar to those in FH patients [69]. We further analyzed atherosclerotic plaques in three high-fat diet fed rodents and found no obvious lesions in WT, $LDLR^{+/-}$ mice and rats. However, WT, $LDLR^{+/-}$ $LDLR^{-/-}$ hamster showed atherosclerotic plaques depending on the LDLR gene copy number. Furthermore, coronary atherosclerosis is a major feature of FH. Pathological analysis of the three rodents fed a high-fat diet revealed that $LDLR^{-/-}$ rats did not show coronary atherosclerotic lesions, whereas $LDLR^{-/-}$ mice had coronary atherosclerotic lesions, in which fewer coronary arteries with $<50\%$ occlusion area were smaller than $LDLR^{+/-}$ hamsters. In $LDLR^{-/-}$ hamsters, 82% of the coronary arteries had varying degrees of atherosclerotic damage, with 8% of coronary artery occlusion over 50%. This comparative study suggests that LDLR-deficient

hamsters are more susceptible to coronary atherosclerosis induced by a high-fat diet [68–70].

3.1.1 The Application Value of Heterozygous LDLR Knockout Hamsters in Drug Development

Because LDLR is a major gene regulating plasma cholesterol, other factors involved in cholesterol, such as PCSK9, hydroxy methyl glutaryl coenzyme A (HMG CoA) reductase, and inducible degrader of the LDLR (IDOL), regulate plasma LDL levels mainly by affecting LDLR [71]. Therefore, animal models with LDLR deficiency are not suitable for the screening and development of cholesterol-lowering drugs. Commonly used laboratory animals such as mice and rats are insensitive to a high-fat diet. Because LDLR knockout is recessive in mice and rats, plasma cholesterol levels in LDLR heterozygotes are not much different from WT. Even feeding a high-fat diet does not induce hypercholesterolemia in these rodents. Therefore, $LDLR^{+/-}$ mice and rats are neither used as animal models for the study of hypercholesterolemia and atherosclerosis, nor are they suitable for the study of lipid-lowering drugs. Although wild-type hamsters have long been used in lipid-lowering drug studies, atherosclerotic lesions induced by high-fat diets are mild and the effects of potential drugs are not readily observed. Whereas the LDLR gene mutant hamsters are dominantly inherited, heterozygous animals can develop overt hyperlipidemia and atherosclerotic lesions by means of a high-fat diet, which is similar to those in FH patients [69].

Next, we determined that hypercholesterolemia and severity of atherosclerotic lesions in hamsters can be modulated by cholesterol content in a high-fat diet, resulting in a human-like FH animal model with varying degrees of lesions in the whole aorta and aortic root, and whether coronary artery lesions can be observed in $LDLR^{+/-}$hamsters after high-fat diet feeding [70]. The results demonstrated that $LDLR^{+/-}$ hamsters with one copy of the LDLR gene display a hyperlipidemic phenotype and can be used directly for the study of atherosclerotic cardiovascular disease by replicating patients with heterozygous FH in the clinic and will be an ideal platform for the screening of novel drugs that target the LDLR pathway.

Currently, the $LDLR^{+/-}$ hamster model has been used for the evaluation of multiple drugs. PCSK9 is a liver protease that internalizes LDLR for degradation by lysosomes [72]. Individuals with PCSK9 nonsense mutations have been reported to have reduced plasma LDL-C levels and coronary heart disease events [73, 74]. PCSK9 antibodies are currently approved for the treatment of primary hypercholesterolemia by lowering plasma LDL-C. In collaboration with Novo Nordisk, we applied PCSK9 monoclonal antibody, Evolocumab, and the cholesterol absorption inhibitor ezetimibe to $LDLR^{+/-}$ hamsters fed a high-fat diet. Both PCSK9 monoclonal antibody and ezetimibe were found to reduce LDL-C, TC, TG, and atherosclerotic lesion formation in $LDLR^{+/-}$

hamsters [39]. In addition, studies have shown that elderly patients with FeFH are more likely to develop dementia than control populations [75]. Dementia is associated with damage to the blood–brain barrier [76]. However, high cholesterol and high LDL in plasma are two risk factors for blood–brain barrier injury [77]. The study of cognitive impairment in aged $LDLR^{+/-}$ hamsters showed that Chinese medicine YangXue QingNao pill and silybin capsule could increase cerebral blood flow and improve learning and memory deficits in aged $LDLR^{+/-}$ hamsters [78]. The results further confirm that $LDLR^{+/-}$ hamster is a useful rodent model for evaluating drug candidates affecting the LDLR pathway.

3.2 LCAT Knockout Hamsters

LCAT is mainly synthesized and secreted by the liver and is the only cholesterol esterase in the plasma [79]. It has two different catalytic activities, one is phospholipase A2 activity, which releases fatty acids from the sn-2 position of phosphatidylcholine and other phospholipids, and the other is transesterification activity, which transfers fatty acids to hydroxyl group of cholesterol. LCAT promotes HDL maturation by converting cholesterol and phosphatidylcholine into cholesteryl esters and lysolecithin and plays an indispensable role in maintaining HDL stability and RCT [80]. The major characteristics of LCAT mutant population [81] are very low HDL-C levels, elevated free cholesterol and TG levels. It includes two types: fish-eye disease (FED) with partial deficiency of LCAT activity and familial LCAT deficiency (FLD) with complete loss of LCAT activity. Corneal turbidity is the main manifestation in FED patients while anemia and renal dysfunction are the main manifestations in FLD patients. LCAT has been proposed to have alpha and beta activities acting on LDL and HDL, respectively, which have different effects on atherosclerosis [82]. However, there is no direct experimental evidence to date.

Recently, we successfully created LCAT-deficient hamsters using CRISPR/Cas9 gene editing techniques. Compared to wild-type hamsters, LCAT-deficient hamsters had slightly increased plasma TC levels and decreased HDL-C levels and HDL-C/TC ratios by 95%, while non-HDL-C as well as free cholesterol levels were threefold higher than WT on a regular chow diet. In addition, TG levels reached 1000 mg/dL. The circulating levels of phosphatidylcholine and phosphatidylethanolamine were significantly increased, whereas cholesteryl ester was significantly decreased and lysolecithin slightly reduced. FPLC analysis showed that VLDL/CM were significantly elevated, whereas HDL disappeared. ApoB100 and ApoB48 were significantly increased in LCAT-deficient hamsters [40]. In the following study, Guo et al. investigated the effects of age and sex on plasma lipid levels in LCAT-deficient hamsters. LCAT-deficient hamsters over 16 months of age had lower TC levels than WT, but lipoprotein profiles were not

significantly different between young and old LCAT-deficient hamsters. Circulating free cholesterol levels were increased 2- and six-fold over WT and plasma TG 3- to six-fold in male and female LCAT-deficient hamsters, respectively, accompanied by complete loss of ApoAI and HDL [83].

It has been reported that the RCT, anti-inflammatory and antioxidant effects of HDL are the possible functions of its anti-atherosclerotic effects. Low levels of HDL are often associated with hypertriglyceridemia, such as in diabetes mellitus, in which atherosclerosis is exacerbated by multiple factors. Although defective LCAT function leads to reduced HDL, and theoretically interfering with RCT should exacerbate atherosclerosis, clinical findings are conflicting, even showing that low HDL is not associated with worsening atherosclerosis [84]. We postulate that there is also another important lipid transport process in human plasma to modulate LCAT-mediated lipid metabolism, which is dependent on CETP to transport cholesteryl esters from mature HDL to LDL and VLDL, in the exchange of triglycerides from them to HDL. Thus, CETP is potentially considered to be a pro-atherogenic factor. HDL is a predominant lipoprotein in mice that have no endogenous CETP expression, leading to an anti-atherogenic property. Contradictory atherosclerotic findings in LCAT-deficient models in mice with LDLR or ApoE-deficient background, in which primary lipoprotein profiles modulated by dietary interventions, but not LCAT itself, are the key contributor to atherosclerosis [85, 86]. In addition, studies of LCAT overexpression in rabbits and squirrel monkeys showed that it prevented atherosclerosis in the former and showed anti-atherosclerotic lipoprotein profile in the latter. Thus, hamster as a rodent with CETP would be an ideal model to test if LCAT deficiency would be pro-atherogenic. Indeed, LCAT-deficient hamsters fed a high-fat diet containing 0.5% cholesterol for 12 weeks revealed a marked increase in lesions in the aorta and aortic root, so LCAT has a protective effect on atherosclerosis [40]. We further found that LCAT-deficient male hamsters over 16 months on chow diet developed spontaneous atherosclerotic lesions even though their plasma TC levels was lower than WT hamsters at same age and no atherosclerotic lesions were found in WT or young LCAT-deficient hamsters. Oxidative stress is thought to play an important role in the process of spontaneous atherosclerosis in these aged LCAT deficient hamsters. The above studies demonstrate that LCAT exerts atherosclerotic protective effect in hamster model and the mechanism of LCAT anti-atherosclerosis can be further studied using this model.

3.3 ABCA1 Knockout Hamsters

Numerous studies have identified elevated LDL-C as an important risk factor for atherosclerotic CVD [87] while decreased HDL-C is also an important risk factor for CVD. ABCA1 is one of the most

important lipid transporters affecting plasma HDL-C levels [88], which plays a crucial role in cholesterol metabolism.

ABCA1 uses ATP as an energy source to promote the efflux of intracellular free cholesterol and phospholipids and binds to apoAI, which is lipid-deficient on the cell surface to form nascent HDL. Since ABCA1 plays an important role in the initial steps of RCT and HDL production, it is referred to as the RCT gatekeeper [89]. This ABCA1-mediated process is important for reducing both foam cell formation and vessel wall inflammatory response to lipid accumulation [90]. ABCA1-mediated increase in cholesterol efflux by 50% and plasma HDL-C levels by 30% have been shown to be associated with reduced coronary artery disease (CAD) by 35–50% [91]. In addition, ABCA1 may also be involved in the inflammatory response [91, 92]. Li et al. found reduced ABCA1 transcript levels in subjects are inversely correlated with plasma high sensitivity C-reactive protein (hs-CRP) levels. In addition, *in vitro* experiments have shown that ABCA1 can act as an anti-inflammatory receptor to inhibit the expression of inflammatory factors such as interleukin (IL)-1β, IL-6, and tumor necrosis factor-α (TNF-α) [93]. In addition, ABCA1-mediated efflux of cellular cholesterol prevents the accumulation of excess cholesterol in membranes, a process in which HDL particles perform various functions to prevent diseases such as atherosclerosis, diabetes, and Alzheimer's disease. Patients with Tangier's disease (TD) caused by ABCA1 gene mutations not only exhibit an almost complete absence of HDL in plasma, blockage of intracellular cholesterol accumulation and phospholipid efflux, but also apoptosis and inflammation. These patients are prone to spontaneous atherosclerosis and have significant renal damage and granulomas at the extremities. However, ABCA1$^{-/-}$ mice with severely reduced HDL were not hypertriglyceridemic and had no spontaneous atherosclerosis and no significant renal damage or granulomas. Even when crossed with ApoE- or LDLR-deficient mice, atherosclerotic lesions were not aggravated by ABCA1 deficiency due to their marked reduction in plasma cholesterol. A more pronounced atherosclerotic lesion occurs only when macrophage ABCA1 is specifically deleted without a difference in plasma cholesterol compared to controls [94]. Unlike conditional knockout mice, such inherited tissue-specific gene mutations do not occur in humans.

Based on the similarities of lipid metabolism between hamsters and humans, a low HDL-C hamster model with ABCA1 knockout was constructed by CRISPR/Cas technique. ABCA1$^{-/-}$ hamsters were relatively consistent in terms of dyslipidemia to patients with ABCA1 loss-of-function mutations: (1) plasma TC did not change much; (2) free cholesterol concentrations increased threefold; (3) plasma TG levels increased approximately 2- to sixfold; (4) ApoA1 as well as HDL-C were barely detectable; (5) plasma

lipoprotein profiling showed a significant increase in VLDL fractions; and (6) there was a decrease in CETP activity [43].

Importantly, ABCA1$^{-/-}$ hamsters also had significantly shorter lifespan, with only about half a year (wild-type hamsters typically live for 2–3 years) and significantly reduced body weight. Compared with WT hamsters, hematology, blood viscosity, and coagulation levels were significantly changed in ABCA1$^{-/-}$ hamsters, including significantly increased white blood cells, decreased lymphocyte proportion, increased platelet number, volume and decreased platelet distribution width.

Nordestgaard et al. found that promoting the ABCA1 gene-mediated lipid efflux process is also an important factor in preventing Alzheimer's disease [95]. Through Y-maze (used in spatial working memory of rodents reflecting the recognition and memory ability) and novelty cognition experiments, we found that ABCA1$^{-/-}$ hamsters had impaired cognition and memory compared with WT hamsters, suggesting that ABCA1 loss also had a detrimental effect on brain function. At the same time, the levels of inflammatory factors in the brain and kidneys of ABCA1$^{-/-}$ hamsters were significantly higher than those in normal hamsters, such as IL-6, TNF-α, cluster of differentiation 36 (CD36), and other markers were upregulated, indicating that ABCA1 deletion also caused inflammatory responses in some tissues of the body.

Although there were no obvious abnormalities in morphology by hematoxylin and eosin (HE) staining in the brain of ABCA1$^{-/-}$ hamsters, the disappearance of cytoplasmic Nissl bodies, disorganization of cells, and swelling and rounding of neurons were observed in Nissl staining, accompanied by the formation of large vesicles. Hypertrophy of glomeruli and atrophy of some glomeruli were observed in renal glomeruli.

At 5 months of age, ABCA1$^{-/-}$ hamsters developed atherosclerotic plaques in the aortic roots in these animals to some extent. Due to ABCA1 deficiency, ApoAI is unable to accept the efflux of cholesterol to produce HDL, thereby leading to decreased HDL in blood and RCT dysfunction, and a large amount of TC accumulated in the liver, spleen, bone marrow, skin, and other tissues, eventually causing atherosclerosis (our unpublished research).

These results suggest that the phenotypes of ABCA1 knockout hamsters are relatively consistent with clinical patients with ABCA1 loss-of-function mutations in terms of lipid metabolism disorders, and the study of extremely low HDL-related diseases in ABCA1 knockout hamsters may better provide experimental evidence for clinical practice.

3.4 ApoC2 Knockout Hamsters

Hypertriglyceridemia (HTG) is a multifactorial disease divided into hereditary and non-hereditary disorders and has been proved to be an independent risk factor for cardiovascular disease. It is characterized by impaired synthesis or degradation of TG resulting in a large

accumulation of TG in plasma. Familial chylomicronemia (FCS), caused mainly by loss-of-function LPL mutations, is a rare genetic disorder with a prevalence of approximately one per million [96, 97]. LPL is responsible for hydrolysis of TG-rich lipoproteins, including CM and VLDL [98]. ApoC2 serves as a major activator of LPL catalytic activity and thus plays a crucial role in the LPL-mediated hydrolysis of TG [99]. Currently, there are more than 30 different case reports of ApoC2 mutations worldwide [97]. Numerous clinical data have shown that human plasma TG levels above 1000 mg/dL (11.3 mmol/L) are at risk of acute pancreatitis, whereas plasma TG is usually as high as 10,000 mg/dL in patients with ApoC2 mutations. As expected, severe hypertriglyceridemia is highly prone to recurrent acute pancreatitis that are life-threatening [100, 101]. Therefore, such patients need repeated hemodialysis if necessary, which seriously affects the quality of life.

In view of the important role of ApoC2 in triglyceride metabolism, the establishment of an ApoC2-deficient animal model can further investigate the function of ApoC2 and provide a powerful platform for drug screening. ApoC2 knockout mouse models have not been reported for unknown reasons although gene targeting techniques have been widely applied since the 1990s. In 2016, Remaley's team from NIH established ApoC2 mutant mice using zinc finger nuclease technology [102]. This mouse model expresses an immature ApoC2 protein that cannot be efficiently cleaved and accumulates in large amounts in HDL, resulting in the inability of plasma TG carried on CM and VLDL to be efficiently hydrolyzed. Although ApoC2 mutant mice showed moderately elevated plasma TG (around 600 mg/dL), their plasma TG levels remained much lower than in human ApoC2-deficient patients. In addition, loss-of-function mutations in human ApoC2 usually result in a decrease or even loss of plasma ApoC2 content, whereas ApoC2 concentration is significantly increased in ApoC2 mutant mice, which is not consistent with clinical findings. In another study, Liu et al. used the TALEN technique to target the ApoC2 gene in zebrafish and successfully constructed a zebrafish model with ApoC2 deficiency [103], showing a reduction in LPL activity and then chylomicronemia, a phenotype similar to that observed in ApoC2-deficient patients. However, zebrafish is not a mammal. As an animal model of ApoC2-deficient human disease, there are some limitations in applied research, such as atherosclerosis, and even the route of administration is significantly different from that of humans.

To mimic human FCS caused by ApoC2 deficiency, we constructed an ApoC2 knockout hamster model for the first time using the CRISPR/Cas9 system [41]. ApoC2 knockout hamsters display pink blood vessels during lactation, milky plasma with extremely high TG levels (20,000 mg/dL), and markedly elevated cholesterol (1700 mg/dL), all die within 9 days after birth. Further study

discovered that neonatal hamsters in the dying phase had significantly lower blood glucose levels, but repeated glucose injections were not effective in rescuing their deaths. Morphological analysis revealed marked changes in the liver, kidney, and pancreas. It was speculated that ApoC2 KO neonatal hamsters may die from severe hypertriglyceridemia-induced hypoglycemia and multiple organ damage.

In our study, the neonatal ApoC2 KO hamsters can survive to adulthood after weaning by continuous intravenous injection of WT hamster serum. This adult hamster still presents with ApoC2 deficiency, severe hypertriglyceridemia (HTG) but there are no obvious morphological changes in the liver, kidney, and pancreas, indicating that the ApoC2 gene-deficient hamster model closely resembles the phenotype of patients with ApoC2 deficiency in human familial chylomicronemia.

Accumulating studies have shown that hamsters are commonly used animal models for experimental gene therapy using AAV as a vector. Xiao et al. ameliorated muscular dystrophy by intramuscular injection of AAV-delta-SG cDNA to Bio14.6 hamsters (congenital muscular dystrophy) [104]. Injection of AAV-MG53 into delta-Sarcoglycan-deficient hamsters has also been shown to rescue amyotrophy and heart failure [105]. To evaluate the efficacy and safety of gene therapy by AAV for hypertriglyceridemia in ApoC2-deficient hamsters, we administered AAV-hApoC2 via orbital or jugular veins to neonatal and adult ApoC2 knockout hamsters, respectively, which resulted in a liver specific expression of human ApoC2 to prevent neonatal death and effectively ameliorated severe hypertriglyceridemia in a long-term manner due to ApoC2 deficiency [106]. These novel findings provide a new insight into the potential treatment for clinical patients with severe hypertriglyceridemia caused by ApoC2 deficiency.

3.5 ApoC3 Knockout Hamsters

Unlike ApoC2, ApoC3 inhibits LPL-mediated hydrolysis of TG on triglyceride-rich lipoprotein (TRL) [107, 108] by affecting the function of other apolipoproteins (ApoE and ApoB) [109–112] and the clearance of lipoprotein remnants via the receptor pathway to disrupt lipid homeostasis. Population studies have reported that genetic variants of loss-of-function ApoC3 are inversely associated with plasma TG and coronary heart disease, suggesting that ApoC3 is a potential therapeutic target for cardiovascular disease. Therefore, after long-term experimental studies, monoclonal antibodies and antisense nucleic acids against ApoC3 have also been developed at the clinical trial stage [113–118]. However, although ApoC3 transgenic mice develop severe HTG and show aggravated atherosclerotic lesions after crossing with atherosclerosis-susceptible LDLR knockout mice, LDLR-ApoC3 double knockout mice show only improvements in plasma lipid profiles such as TG and cholesterol reductions, but no beneficial effect on atherosclerosis

when compared with LDLR knockout control mice. On this basis, we constructed the ApoC3 knockout hamster model using CRISPR-Cas9 technology [42]. Plasma TG was markedly reduced in ApoC3-deficient hamsters, a phenotype consistent with human and mouse. Although ApoC3-deficient individuals had relatively low plasma LDL levels, ApoC3 knockout hamsters had no significant changes in HDL and LDL compared with WT hamsters under regular chow diet condition, which is different from population studies. We hypothesized that this difference was due to dietary lipid intake. Human daily diets always contain more lipids, and the content of exogenous cholesterol is relatively high; however, the common rodent diet has less fat and cholesterol. When ApoC3 knockout hamsters were fed a high-fat diet, their VLDL and LDL levels were decreased and HDL levels were increased, showing an anti-atherogenic lipoprotein profile phenotype. Quantitative analysis of aortic lesions demonstrated that although atherosclerotic lesions at aortic root were not significantly different from WT controls, lesions in thoracic and abdominal aorta sites were significantly reduced. Meanwhile, ApoC3$^{-/-}$ hamsters had reduced levels of malondialdehyde (MDA) in plasma, suggesting a reduction in lipid peroxidation and inflammatory factors in vivo. In addition, ApoC3 itself can increase vascular cell adhesion molecule (VCAM)-1 and intercellular adhesion molecule-1 (ICAM-1) expression and promote monocyte adhesion [119], and increase smooth muscle cell proliferation and reactive oxygen species (ROS) production [120]. Thus, after excluding differences in lipid profiles between mice and humans and the complexity of the LDLR knockout background, our study demonstrates that targeting ApoC3 as an inhibitory target not only ameliorates dyslipidemia but also benefits in the treatment of later cardiovascular disease.

4 Limitations of Hamsters as Animal Models of Dyslipidemia and Atherosclerosis

Although hamsters have many advantages as a rodent model similar to human lipid metabolism, the following limitations remain.

1. Standardized experimental methods need to be systemically established. Compared with the wide application of rodent species such as mice and rats, the application range of hamsters is relatively small and the standard experimental methods need to be established and optimized. These include, for example, blood sample collection, including orbital vein, femoral vein, abdominal aorta, cardiac puncture, and anesthesia. The tail of hamster is short and common caudal vein injection in rodents is not applicable so intravenous administration should be considered, such as external jugular vein, sublingual vein, axillary vein, orbital venous plexus, and dorsal penile vein. In our

laboratory, the route of administration through the external jugular vein is intuitive. Although techniques are more complex, the reliability of intravenous administration can be ensured. Other experimental methods and techniques, such as the preparation of primary cells such as hepatocytes, cardiomyocytes and nerve cells, and the preparation of different tissues for morphological observation or omics studies, need to be optimized to establish a relatively unified, reliable, and easy-to-compare method.

2. Lack of dedicated equipment and tools. Because the existing experimental equipment and reagents are designed for mice and there is no hamster-specific equipment, it is inconvenient for the corresponding experimenter. For example, a common sphygmomanometer used for rat tail cannot be applied for hamsters. Small animal limb sphygmomanometers have corresponding cuffs for both mouse and rat (corresponding to body weights of 30 and 300 g, respectively) but adult hamsters weighing 120–150 g require special customization. The probes of B-ultrasonography are also designed for mouse and rat but not hamster. In addition, various commercially available antibodies against different mouse antigens are available but few recognize hamster-specific antigens. Therefore, we usually have to select polyclonal antibodies that recognize human and mouse antigens for screening and use cross-reactivity to detect them for hamster accordingly.
3. Lack of inbred strains. At present, most WT hamsters belong to the close colony and do not breed in inbred strains, resulting in relatively large intra-group sample differences, and it is difficult to draw a clear conclusion when the sample size is small in specific experiments. Therefore, the sample size required for the experiment is large, which makes the experiment more difficult. However, considering the diversity of the human population, this characteristic of hamsters is highly similar to that of the population, making hamsters an advantage in translational studies of human diseases. The conclusions drawn with hamsters as laboratory animals may be closer to human disease when the sample size is appropriately increased.

Despite these limitations, hamster as an experimental model will gain more attention in the field of lipid disorders and cardiovascular disease due to its similarity to humans in terms of lipid metabolism and the success of more genetically engineered models. With the development of technology, the popularization and standardization of experimental methods and the development of new experimental equipment and tools, and the generation of corresponding inbred strains, the application prospect of

genetically engineered hamster models in the field of lipid metabolism and cardiovascular diseases will be promising.

Acknowledgements

We thank Yitong Xu, Pingping Lai, Haozhe Shi, Jiaobao Guo, Gonglie Chen, and Lili Wei for excellent editorial assistance.

References

1. Mishima T, Tajima Y, Kuroki T, Kosaka T, Adachi T, Kitasato A, Tsuneoka N, Kitajima T, Kanematsu T (2009) Chemopreventative effect of an inducible nitric oxide synthase inhibitor, ONO-1714, on inflammation-associated biliary carcinogenesis in hamsters. Carcinogenesis 30(10): 1763–1767. https://doi.org/10.1093/carcin/bgp194
2. Ancel C, Bentsen AH, Sébert ME, Tena-Sempere M, Mikkelsen JD, Simonneaux V (2012) Stimulatory effect of RFRP-3 on the gonadotrophic axis in the male Syrian hamster: the exception proves the rule. Endocrinology 153(3):1352–1363. https://doi.org/10.1210/en.2011-1622
3. Rohwer RG (1984) Virus like sensitivity of the scrapie agent to heat inactivation. Science 223(4636):600–602. https://doi.org/10.1126/science.6420887
4. Zadelaar S, Kleemann R, Verschuren L, de Vries-Van der Weij J, van der Hoorn J, Princen HM, Kooistra T (2007) Mouse models for atherosclerosis and pharmaceutical modifiers. Arterioscler Thromb Vasc Biol 27(8): 1706–1721. https://doi.org/10.1161/atvbaha.107.142570
5. Altschul R (1950) Experimental cholesterol arteriosclerosis. II. Changes produced in golden hamsters and in guinea pigs. Am Heart J 40(3):401–409. https://doi.org/10.1016/0002-8703(50)90323-1
6. Coyne MJ, Bonorris GG, Chung A, Cove H, Schoenfield LJ (1977) Dietary cholesterol affects chenodeoxycholic acid action on biliary lipids. Gastroenterology 72(5 Pt 1): 927–931
7. Filip DA, Nistor A, Bulla A, Radu A, Lupu F, Simionescu M (1987) Cellular events in the development of valvular atherosclerotic lesions induced by experimental hypercholesterolemia. Atherosclerosis 67(2–3):199–214. https://doi.org/10.1016/0021-9150(87)90280-2
8. Cincotta AH, Meier AH (1984) Circadian rhythms of lipogenic and hypoglycaemic responses to insulin in the golden hamster (Mesocricetus auratus). J Endocrinol 103(2): 141–146. https://doi.org/10.1677/joe.0.1030141
9. Nistor A, Bulla A, Filip DA, Radu A (1987) The hyperlipidemic hamster as a model of experimental atherosclerosis. Atherosclerosis 68(1–2):159–173. https://doi.org/10.1016/0021-9150(87)90106-7
10. Chen J, Song W, Redinger RN (1996) Effects of dietary cholesterol on hepatic production of lipids and lipoproteins in isolated hamster liver. Hepatology 24(2):424–434. https://doi.org/10.1002/hep.510240222
11. Woollett LA, Kearney DM, Spady DK (1997) Diet modification alters plasma HDL cholesterol concentrations but not the transport of HDL cholesteryl esters to the liver in the hamster. J Lipid Res 38(11):2289–2302
12. Otto J, Ordovas JM, Smith D, van Dongen D, Nicolosi RJ, Schaefer EJ (1995) Lovastatin inhibits diet induced atherosclerosis in F1B golden Syrian hamsters. Atherosclerosis 114(1):19–28. https://doi.org/10.1016/0021-9150(94)05457-t
13. Kuhlencordt PJ, Gyurko R, Han F, Scherrer-Crosbie M, Aretz TH, Hajjar R, Picard MH, Huang PL (2001) Accelerated atherosclerosis, aortic aneurysm formation, and ischemic heart disease in apolipoprotein E/endothelial nitric oxide synthase double-knockout mice. Circulation 104(4):448–454. https://doi.org/10.1161/hc2901.091399
14. Taghibiglou C, Carpentier A, Van Iderstine SC, Chen B, Rudy D, Aiton A, Lewis GF, Adeli K (2000) Mechanisms of hepatic very low density lipoprotein overproduction in insulin resistance. Evidence for enhanced lipoprotein assembly, reduced intracellular ApoB degradation, and increased microsomal triglyceride transfer protein in a fructose-fed hamster model. J Biol Chem 275(12):

8416–8425. https://doi.org/10.1074/jbc.275.12.8416

15. Taghibiglou C, Rudy D, Van Iderstine SC, Aiton A, Cavallo D, Cheung R, Adeli K (2000) Intracellular mechanisms regulating apoB-containing lipoprotein assembly and secretion in primary hamster hepatocytes. J Lipid Res 41(4):499–513
16. Adeli K, Taghibiglou C, Van Iderstine SC, Lewis GF (2001) Mechanisms of hepatic very low-density lipoprotein overproduction in insulin resistance. Trends Cardiovasc Med 11(5):170–176. https://doi.org/10.1016/s1050-1738(01)00084-6
17. Mangaloglu L, Cheung RC, Van Iderstine SC, Taghibiglou C, Pontrelli L, Adeli K (2002) Treatment with atorvastatin ameliorates hepatic very-low-density lipoprotein overproduction in an animal model of insulin resistance, the fructose-fed Syrian golden hamster: evidence that reduced hypertriglyceridemia is accompanied by improved hepatic insulin sensitivity. Metabolism 51(4):409–418. https://doi.org/10.1053/meta.2002.30954
18. Au CS, Wagner A, Chong T, Qiu W, Sparks JD, Adeli K (2004) Insulin regulates hepatic apolipoprotein B production independent of the mass or activity of Akt1/PKBalpha. Metabolism 53(2):228–235. https://doi.org/10.1016/j.metabol.2003.09.011
19. Qiu W, Kohen-Avramoglu R, Mhapsekar S, Tsai J, Austin RC, Adeli K (2005) Glucosamine-induced endoplasmic reticulum stress promotes ApoB100 degradation: evidence for Grp78-mediated targeting to proteasomal degradation. Arterioscler Thromb Vasc Biol 25(3):571–577. https://doi.org/10.1161/01.Atv.0000154142.61859.94
20. Su Q, Tsai J, Xu E, Qiu W, Bereczki E, Santha M, Adeli K (2009) Apolipoprotein B100 acts as a molecular link between lipid-induced endoplasmic reticulum stress and hepatic insulin resistance. Hepatology 50(1):77–84. https://doi.org/10.1002/hep.22960
21. Qiu W, Zhang J, Dekker MJ, Wang H, Huang J, Brumell JH, Adeli K (2011) Hepatic autophagy mediates endoplasmic reticulum stress-induced degradation of misfolded apolipoprotein B. Hepatology 53(5):1515–1525. https://doi.org/10.1002/hep.24269
22. Hsieh J, Longuet C, Baker CL, Qin B, Federico LM, Drucker DJ, Adeli K (2010) The glucagon-like peptide 1 receptor is essential for postprandial lipoprotein synthesis and secretion in hamsters and mice. Diabetologia 53(3):552–561. https://doi.org/10.1007/s00125-009-1611-5
23. Hsieh J, Longuet C, Maida A, Bahrami J, Xu E, Baker CL, Brubaker PL, Drucker DJ, Adeli K (2009) Glucagon-like peptide-2 increases intestinal lipid absorption and chylomicron production via CD36. Gastroenterology 137(3):997–1005, 1005.e1001-1004. https://doi.org/10.1053/j.gastro.2009.05.051
24. Hein GJ, Baker C, Hsieh J, Farr S, Adeli K (2013) GLP-1 and GLP-2 as yin and yang of intestinal lipoprotein production: evidence for predominance of GLP-2-stimulated postprandial lipemia in normal and insulin-resistant states. Diabetes 62(2):373–381. https://doi.org/10.2337/db12-0202
25. Taher J, Baker CL, Cuizon C, Masoudpour H, Zhang R, Farr S, Naples M, Bourdon C, Pausova Z, Adeli K (2014) GLP-1 receptor agonism ameliorates hepatic VLDL overproduction and de novo lipogenesis in insulin resistance. Mol Metab 3(9):823–833. https://doi.org/10.1016/j.molmet.2014.09.005
26. Hsieh J, Trajcevski KE, Farr SL, Baker CL, Lake EJ, Taher J, Iqbal J, Hussain MM, Adeli K (2015) Glucagon-like peptide 2 (GLP-2) stimulates postprandial chylomicron production and postabsorptive release of intestinal triglyceride storage pools via induction of nitric oxide signaling in male hamsters and mice. Endocrinology 156(10):3538–3547. https://doi.org/10.1210/en.2015-1110
27. Farr S, Baker C, Naples M, Taher J, Iqbal J, Hussain M, Adeli K (2015) Central nervous system regulation of intestinal lipoprotein metabolism by glucagon-like peptide-1 via a brain-gut axis. Arterioscler Thromb Vasc Biol 35(5):1092–1100. https://doi.org/10.1161/atvbaha.114.304873
28. Castro-Perez J, Briand F, Gagen K, Wang SP, Chen Y, McLaren DG, Shah V, Vreeken RJ, Hankemeier T, Sulpice T, Roddy TP, Hubbard BK, Johns DG (2011) Anacetrapib promotes reverse cholesterol transport and bulk cholesterol excretion in Syrian golden hamsters. J Lipid Res 52(11):1965–1973. https://doi.org/10.1194/jlr.M016410
29. Briand F (2010) The use of dyslipidemic hamsters to evaluate drug-induced alterations in reverse cholesterol transport. Curr Opin Investig Drugs 11(3):289–297
30. Fernandez ML, Wilson TA, Conde K, Vergara-Jimenez M, Nicolosi RJ (1999) Hamsters and guinea pigs differ in their plasma lipoprotein cholesterol distribution

when fed diets varying in animal protein, soluble fiber, or cholesterol content. J Nutr 129(7):1323–1332. https://doi.org/10.1093/jn/129.7.1323

31. Liu GL, Fan LM, Redinger RN (1991) The association of hepatic apoprotein and lipid metabolism in hamsters and rats. Comp Biochem Physiol A Comp Physiol 99(1–2): 223–228. https://doi.org/10.1016/0300-9629(91)90263-c
32. Spady DK, Dietschy JM (1985) Dietary saturated triacylglycerols suppress hepatic low density lipoprotein receptor activity in the hamster. Proc Natl Acad Sci U S A 82(13):4526–4530. https://doi.org/10.1073/pnas.82.13.4526
33. Dietschy JM, Turley SD, Spady DK (1993) Role of liver in the maintenance of cholesterol and low density lipoprotein homeostasis in different animal species, including humans. J Lipid Res 34(10):1637–1659
34. Sima A, Bulla A, Simionescu N (1990) Experimental obstructive coronary atherosclerosis in the hyperlipidemic hamster. J Submicrosc Cytol Pathol 22(1):1–16
35. Dekker MJ, Baker C, Naples M, Samsoondar J, Zhang R, Qiu W, Sacco J, Adeli K (2013) Inhibition of sphingolipid synthesis improves dyslipidemia in the diet-induced hamster model of insulin resistance: evidence for the role of sphingosine and sphinganine in hepatic VLDL-apoB100 overproduction. Atherosclerosis 228(1):98–109. https://doi.org/10.1016/j.atherosclerosis.2013.01.041
36. Dillard A, Matthan NR, Lichtenstein AH (2010) Use of hamster as a model to study diet-induced atherosclerosis. Nutr Metab (Lond) 7:89. https://doi.org/10.1186/1743-7075-7-89
37. Cui X, Wang Y, Meng L, Fei W, Deng J, Xu G, Peng X, Ju S, Zhang L, Liu G, Zhao L, Yang H (2012) Overexpression of a short human seipin/BSCL2 isoform in mouse adipose tissue results in mild lipodystrophy. Am J Physiol Endocrinol Metab 302(6):E705–E713. https://doi.org/10.1152/ajpendo.00237.2011
38. Ding Y, Wang Y, Zhu H, Fan J, Yu L, Liu G, Liu E (2011) Hypertriglyceridemia and delayed clearance of fat load in transgenic rabbits expressing human apolipoprotein CIII. Transgenic Res 20(4):867–875. https://doi.org/10.1007/s11248-010-9467-5
39. Wu Y, Xu MJ, Cao Z, Yang C, Wang J, Wang B, Liu J, Wang Y, Xian X, Zhang F, Liu G, Chen X (2019) Heterozygous Ldlr-deficient mamster as a model to evaluate the efficacy of PCSK9 antibody in hyperlipidemia and atherosclerosis. Int J Mol Sci 20(23): 5936. https://doi.org/10.3390/ijms20235936
40. Dong Z, Shi H, Zhao M, Zhang X, Huang W, Wang Y, Zheng L, Xian X, Liu G (2018) Loss of LCAT activity in the golden Syrian hamster elicits pro-atherogenic dyslipidemia and enhanced atherosclerosis. Metabolism 83: 245–255. https://doi.org/10.1016/j.metabol.2018.03.003
41. Gao M, Yang C, Wang X, Guo M, Yang L, Gao S, Zhang X, Ruan G, Li X, Tian W, Lu G, Dong X, Ma S, Li W, Wang Y, Zhu H, He J, Yang H, Liu G, Xian X (2020) ApoC2 deficiency elicits severe hypertriglyceridemia and spontaneous atherosclerosis: a rodent model rescued from neonatal death. Metabolism 109:154296. https://doi.org/10.1016/j.metabol.2020.154296
42. Guo M, Xu Y, Dong Z, Zhou Z, Cong N, Gao M, Huang W, Wang Y, Liu G, Xian X (2020) Inactivation of ApoC3 by CRISPR/Cas9 protects against atherosclerosis in hamsters. Circ Res 127(11):1456–1458. https://doi.org/10.1161/circresaha.120.317686
43. Wei L, Shi H, Lin X, Zhang X, Wang Y, Liu G, Xian X (2019) Impact of cholesterol on ischemic stroke in different human-like hamster models: a new animal model for ischemic stroke study. Cell 8(9):1028. https://doi.org/10.3390/cells8091028
44. Gao M, Zhang B, Liu J, Guo X, Li H, Wang T, Zhang Z, Liao J, Cong N, Wang Y, Yu L, Zhao D, Liu G (2014) Generation of transgenic golden Syrian hamsters. Cell Res 24(3):380–382. https://doi.org/10.1038/cr.2014.2
45. Bjørklund MM, Hollensen AK, Hagensen MK, Dagnaes-Hansen F, Christoffersen C, Mikkelsen JG, Bentzon JF (2014) Induction of atherosclerosis in mice and hamsters without germline genetic engineering. Circ Res 114(11):1684–1689. https://doi.org/10.1161/circresaha.114.302937
46. Herbert B, Patel D, Waddington SN, Eden ER, McAleenan A, Sun XM, Soutar AK (2010) Increased secretion of lipoproteins in transgenic mice expressing human D374Y PCSK9 under physiological genetic control. Arterioscler Thromb Vasc Biol 30(7): 1333–1339. https://doi.org/10.1161/atvbaha.110.204040
47. Seidah NG, Abifadel M, Prost S, Boileau C, Prat A (2017) The proprotein convertases in hypercholesterolemia and cardiovascular diseases: emphasis on proprotein convertase

subtilisin/kexin 9. Pharmacol Rev 69(1): 33–52. https://doi.org/10.1124/pr.116.012989

48. Abifadel M, Varret M, Rabès JP, Allard D, Ouguerram K, Devillers M, Cruaud C, Benjannet S, Wickham L, Erlich D, Derré A, Villéger L, Farnier M, Beucler I, Bruckert E, Chambaz J, Chanu B, Lecerf JM, Luc G, Moulin P, Weissenbach J, Prat A, Krempf M, Junien C, Seidah NG, Boileau C (2003) Mutations in PCSK9 cause autosomal dominant hypercholesterolemia. Nat Genet 34(2): 154–156. https://doi.org/10.1038/ng1161
49. Roche-Molina M, Sanz-Rosa D, Cruz FM, García-Prieto J, López S, Abia R, Muriana FJ, Fuster V, Ibáñez B, Bernal JA (2015) Induction of sustained hypercholesterolemia by single adeno-associated virus-mediated gene transfer of mutant hPCSK9. Arterioscler Thromb Vasc Biol 35(1):50–59. https://doi.org/10.1161/atvbaha.114.303617
50. Carbery ID, Ji D, Harrington A, Brown V, Weinstein EJ, Liaw L, Cui X (2010) Targeted genome modification in mice using zinc-finger nucleases. Genetics 186(2):451–459. https://doi.org/10.1534/genetics.110.117002
51. Carlson DF, Tan W, Lillico SG, Stverakova D, Proudfoot C, Christian M, Voytas DF, Long CR, Whitelaw CB, Fahrenkrug SC (2012) Efficient TALEN-mediated gene knockout in livestock. Proc Natl Acad Sci U S A 109(43): 17382–17387. https://doi.org/10.1073/pnas.1211446109
52. Wang H, Yang H, Shivalila CS, Dawlaty MM, Cheng AW, Zhang F, Jaenisch R (2013) One-step generation of mice carrying mutations in multiple genes by CRISPR/Cas-mediated genome engineering. Cell 153(4): 910–918. https://doi.org/10.1016/j.cell.2013.04.025
53. Fan Z, Li W, Lee SR, Meng Q, Shi B, Bunch TD, White KL, Kong IK, Wang Z (2014) Efficient gene targeting in golden Syrian hamsters by the CRISPR/Cas9 system. PLoS One 9(10):e109755. https://doi.org/10.1371/journal.pone.0109755
54. Jangra RK, Herbert AS, Li R, Jae LT, Kleinfelter LM, Slough MM, Barker SL, Guardado-Calvo P, Román-Sosa G, Dieterle ME, Kuehne AI, Muena NA, Wirchnianski AS, Nyakatura EK, Fels JM, Ng M, Mittler E, Pan J, Bharrhan S, Wec AZ, Lai JR, Sidhu SS, Tischler ND, Rey FA, Moffat J, Brummelkamp TR, Wang Z, Dye JM, Chandran K (2018) Protocadherin-1 is essential for cell entry by New World hantaviruses. Nature 563(7732):559–563. https://doi.org/10.1038/s41586-018-0702-1
55. Miao J, Ying B, Li R, Tollefson AE, Spencer JF, Wold WSM, Song SH, Kong IK, Toth K, Wang Y, Wang Z (2018) Characterization of an N-terminal non-core domain of RAG1 gene disrupted Syrian hamster model generated by CRISPR Cas9. Viruses 10(5):243. https://doi.org/10.3390/v10050243
56. Li R, Miao J, Tabaran AF, O'Sullivan MG, Anderson KJ, Scott PM, Wang Z, Cormier RT (2018) A novel cancer syndrome caused by KCNQ1-deficiency in the golden Syrian hamster. J Carcinog 17:6. https://doi.org/10.4103/jcar.JCar_5_18
57. Brocato RL, Principe LM, Kim RK, Zeng X, Williams JA, Liu Y, Li R, Smith JM, Golden JW, Gangemi D, Youssef S, Wang Z, Glanville J, Hooper JW (2020) Disruption of adaptive immunity enhances disease in SARS-CoV-2-infected Syrian hamsters. J Virol 94(22):e01683-20. https://doi.org/10.1128/jvi.01683-20
58. Defesche JC, Gidding SS, Harada-Shiba M, Hegele RA, Santos RD, Wierzbicki AS (2017) Familial hypercholesterolaemia. Nat Rev Dis Primers 3:17093. https://doi.org/10.1038/nrdp.2017.93
59. Benn M, Watts GF, Tybjaerg-Hansen A, Nordestgaard BG (2012) Familial hypercholesterolemia in the Danish general population: prevalence, coronary artery disease, and cholesterol-lowering medication. J Clin Endocrinol Metab 97(11):3956–3964. https://doi.org/10.1210/jc.2012-1563
60. Gidding SS, Champagne MA, de Ferranti SD, Defesche J, Ito MK, Knowles JW, McCrindle B, Raal F, Rader D, Santos RD, Lopes-Virella M, Watts GF, Wierzbicki AS (2015) The agenda for familial hypercholesterolemia: a scientific statement from the American Heart Association. Circulation 132(22):2167–2192. https://doi.org/10.1161/cir.0000000000000297
61. Singh S, Bittner V (2015) Familial hypercholesterolemia--epidemiology, diagnosis, and screening. Curr Atheroscler Rep 17(2):482. https://doi.org/10.1007/s11883-014-0482-5
62. Powell-Braxton L, Véniant M, Latvala RD, Hirano KI, Won WB, Ross J, Dybdal N, Zlot CH, Young SG, Davidson NO (1998) A mouse model of human familial hypercholesterolemia: markedly elevated low density lipoprotein cholesterol levels and severe atherosclerosis on a low-fat chow diet. Nat

Med 4(8):934–938. https://doi.org/10.1038/nm0898-934

63. Sithu SD, Malovichko MV, Riggs KA, Wickramasinghe NS, Winner MG, Agarwal A, Hamed-Berair RE, Kalani A, Riggs DW, Bhatnagar A, Srivastava S (2017) Atherogenesis and metabolic dysregulation in LDL receptor-knockout rats. JCI Insight 2(9): e86442. https://doi.org/10.1172/jci.insight.86442
64. Shiomi M (2020) The history of the WHHL rabbit, an animal model of familial hypercholesterolemia (II) - contribution to the development and validation of the therapeutics for hypercholesterolemia and atherosclerosis. J Atheroscler Thromb 27(2):119–131. https://doi.org/10.5551/jat.RV17038-2
65. Kassim SH, Li H, Vandenberghe LH, Hinderer C, Bell P, Marchadier D, Wilson A, Cromley D, Redon V, Yu H, Wilson JM, Rader DJ (2010) Gene therapy in a humanized mouse model of familial hypercholesterolemia leads to marked regression of atherosclerosis. PLoS One 5(10):e13424. https://doi.org/10.1371/journal.pone.0013424
66. Russell JC, Proctor SD (2006) Small animal models of cardiovascular disease: tools for the study of the roles of metabolic syndrome, dyslipidemia, and atherosclerosis. Cardiovasc Pathol 15(6):318–330. https://doi.org/10.1016/j.carpath.2006.09.001
67. Rizzo M, Taylor JM, Barbagallo CM, Berneis K, Blanche PJ, Krauss RM (2004) Effects on lipoprotein subclasses of combined expression of human hepatic lipase and human apoB in transgenic rabbits. Arterioscler Thromb Vasc Biol 24(1):141–146. https://doi.org/10.1161/01.ATV.0000107027.73816.ce
68. Guo X, Gao M, Wang Y, Lin X, Yang L, Cong N, An X, Wang F, Qu K, Yu L, Wang Y, Wang J, Zhu H, Xian X, Liu G (2018) LDL receptor gene-ablated hamsters: a rodent model of familial hypercholesterolemia with dominant inheritance and diet-induced coronary atherosclerosis. EBioMedicine 27:214–224. https://doi.org/10.1016/j.ebiom.2017.12.013
69. He K, Wang J, Shi H, Yu Q, Zhang X, Guo M, Sun H, Lin X, Wu Y, Wang L, Wang Y, Xian X, Liu G (2019) An interspecies study of lipid profiles and atherosclerosis in familial hypercholesterolemia animal models with low-density lipoprotein receptor deficiency. Am J Transl Res 11(5):3116–3127
70. Wang J, He K, Yang C, Lin X, Zhang X, Wang Y, Liu G, Xian X (2019) Dietary cholesterol is highly associated with severity of hyperlipidemia and atherosclerotic lesions in heterozygous LDLR-deficient hamsters. Int J Mol Sci 20(14):3515. https://doi.org/10.3390/ijms20143515
71. Luo J, Yang H, Song BL (2020) Mechanisms and regulation of cholesterol homeostasis. Nat Rev Mol Cell Biol 21(4):225–245. https://doi.org/10.1038/s41580-019-0190-7
72. Horton JD, Cohen JC, Hobbs HH (2007) Molecular biology of PCSK9: its role in LDL metabolism. Trends Biochem Sci 32(2): 71–77. https://doi.org/10.1016/j.tibs.2006.12.008
73. Cohen J, Pertsemlidis A, Kotowski IK, Graham R, Garcia CK, Hobbs HH (2005) Low LDL cholesterol in individuals of African descent resulting from frequent nonsense mutations in PCSK9. Nat Genet 37(2): 161–165. https://doi.org/10.1038/ng1509
74. Cohen JC, Boerwinkle E, Mosley TH Jr, Hobbs HH (2006) Sequence variations in PCSK9, low LDL, and protection against coronary heart disease. N Engl J Med 354(12): 1264–1272. https://doi.org/10.1056/NEJMoa054013
75. Hyttinen L, TuulioHenriksson A, Vuorio AF, Kuosmanen N, Härkänen T, Koskinen S, Strandberg TE (2010) Long-term statin therapy is associated with better episodic memory in aged familial hypercholesterolemia patients in comparison with population controls. J Alzheimers Dis 21(2):611–617. https://doi.org/10.3233/jad-2010-091381
76. van de Haar HJ, Burgmans S, Hofman PA, Verhey FR, Jansen JF, Backes WH (2015) Blood-brain barrier impairment in dementia: current and future in vivo assessments. Neurosci Biobehav Rev 49:71–81. https://doi.org/10.1016/j.neubiorev.2014.11.022
77. Schreurs MP, Cipolla MJ (2014) Cerebrovascular dysfunction and blood-brain barrier permeability induced by oxidized LDL are prevented by apocynin and magnesium sulfate in female rats. J Cardiovasc Pharmacol 63(1): 33–39. https://doi.org/10.1097/fjc.0000000000000021
78. Gu YY, Huang P, Li Q, Liu YY, Liu G, Wang YH, Yi M, Yan L, Wei XH, Yang L, Hu BH, Zhao XR, Chang X, Sun K, Pan CS, Cui YC, Chen QF, Wang CS, Fan JY, Ma ZZ, Han JY (2018) YangXue QingNao Wan and Silibinin capsules, the two chinese medicines, attenuate cognitive impairment in aged LDLR (+/−) golden Syrian hamsters involving protection of blood brain barrier. Front Physiol 9:658.

https://doi.org/10.3389/fphys.2018.00658

79. Kunnen S, Van Eck M (2012) Lecithin:cholesterol acyltransferase: old friend or foe in atherosclerosis? J Lipid Res 53(9): 1783–1799. https://doi.org/10.1194/jlr.R024513
80. Asztalos BF, Schaefer EJ, Horvath KV, Yamashita S, Miller M, Franceschini G, Calabresi L (2007) Role of LCAT in HDL remodeling: investigation of LCAT deficiency states. J Lipid Res 48(3):592–599. https://doi.org/10.1194/jlr.M600403-JLR200
81. Pavanello C, Calabresi L (2020) Genetic, biochemical, and clinical features of LCAT deficiency: update for 2020. Curr Opin Lipidol 31(4):232–237. https://doi.org/10.1097/mol.0000000000000697
82. Oldoni F, Baldassarre D, Castelnuovo S, Ossoli A, Amato M, van Capelleveen J, Hovingh GK, De Groot E, Bochem A, Simonelli S, Barbieri S, Veglia F, Franceschini G, Kuivenhoven JA, Holleboom AG, Calabresi L (2018) Complete and partial lecithin:cholesterol acyltransferase deficiency is differentially associated with atherosclerosis. Circulation 138(10):1000–1007. https://doi.org/10.1161/circulationaha.118.034706
83. Guo M, Liu Z, Xu Y, Ma P, Huang W, Gao M, Wang Y, Liu G, Xian X (2020) Spontaneous atherosclerosis in aged LCAT-deficient hamsters with enhanced oxidative stress-brief report. Arterioscler Thromb Vasc Biol 40(12):2829–2836. https://doi.org/10.1161/atvbaha.120.315265
84. Rousset X, Shamburek R, Vaisman B, Amar M, Remaley AT (2011) Lecithin cholesterol acyltransferase: an anti- or pro-atherogenic factor? Curr Atheroscler Rep 13(3):249–256. https://doi.org/10.1007/s11883-011-0171-6
85. Furbee JW Jr, Sawyer JK, Parks JS (2002) Lecithin:cholesterol acyltransferase deficiency increases atherosclerosis in the low density lipoprotein receptor and apolipoprotein E knockout mice. J Biol Chem 277(5): 3511–3519. https://doi.org/10.1074/jbc.M109883200
86. Ng DS, Maguire GF, Wylie J, Ravandi A, Xuan W, Ahmed Z, Eskandarian M, Kuksis A, Connelly PW (2002) Oxidative stress is markedly elevated in lecithin:cholesterol acyltransferase-deficient mice and is paradoxically reversed in the apolipoprotein E knockout background in association with a reduction in atherosclerosis. J Biol Chem 277(14):11715–11720. https://doi.org/10.1074/jbc.M112320200
87. Baigent C, Keech A, Kearney PM, Blackwell L, Buck G, Pollicino C, Kirby A, Sourjina T, Peto R, Collins R, Simes R (2005) Efficacy and safety of cholesterol-lowering treatment: prospective meta-analysis of data from 90,056 participants in 14 randomised trials of statins. Lancet 366(9493): 1267–1278. https://doi.org/10.1016/s0140-6736(05)67394-1
88. Lake NJ, Taylor RL, Trahair H, Harikrishnan KN, Curran JE, Almeida M, Kulkarni H, Mukhamedova N, Hoang A, Low H, Murphy AJ, Johnson MP, Dyer TD, Mahaney MC, Göring HHH, Moses EK, Sviridov D, Blangero J, Jowett JBM, Bozaoglu K (2017) TRAK2, a novel regulator of ABCA1 expression, cholesterol efflux and HDL biogenesis. Eur Heart J 38(48):3579–3587. https://doi.org/10.1093/eurheartj/ehx315
89. Oram JF, Lawn RM (2001) ABCA1. The gatekeeper for eliminating excess tissue cholesterol. J Lipid Res 42(8):1173–1179
90. Nagappa M, Taly AB, Mahadevan A, Pooja M, Bindu PS, Chickabasaviah YT, Gayathri N, Sinha S (2016) Tangier's disease: An uncommon cause of facial weakness and non-length dependent demyelinating neuropathy. Ann Indian Acad Neurol 19(1):137–139. https://doi.org/10.4103/0972-2327.175436
91. Singaraja RR, Brunham LR, Visscher H, Kastelein JJ, Hayden MR (2003) Efflux and atherosclerosis: the clinical and biochemical impact of variations in the ABCA1 gene. Arterioscler Thromb Vasc Biol 23(8): 1322–1332. https://doi.org/10.1161/01.Atv.0000078520.89539.77
92. Li C, Guo R, Lou J, Zhou H (2012) The transcription levels of ABCA1, ABCG1 and SR-BI are negatively associated with plasma CRP in Chinese populations with various risk factors for atherosclerosis. Inflammation 35(5):1641–1648. https://doi.org/10.1007/s10753-012-9479-9
93. Tang C, Liu Y, Kessler PS, Vaughan AM, Oram JF (2009) The macrophage cholesterol exporter ABCA1 functions as an anti-inflammatory receptor. J Biol Chem 284(47):32336–32343. https://doi.org/10.1074/jbc.M109.047472
94. van Eck M, Bos IS, Kaminski WE, Orsó E, Rothe G, Twisk J, Böttcher A, Van Amersfoort ES, Christiansen-Weber TA, Fung-Leung WP, Van Berkel TJ, Schmitz G (2002) Leukocyte ABCA1 controls susceptibility to atherosclerosis and macrophage

recruitment into tissues. Proc Natl Acad Sci U S A 99(9):6298–6303. https://doi.org/10.1073/pnas.092327399

95. Nordestgaard LT, Tybjærg-Hansen A, Nordestgaard BG, Frikke-Schmidt R (2015) Loss-of-function mutation in ABCA1 and risk of Alzheimer's disease and cerebrovascular disease. Alzheimers Dement 11(12): 1430–1438. https://doi.org/10.1016/j.jalz.2015.04.006
96. Do R, Willer CJ, Schmidt EM, Sengupta S, Gao C, Peloso GM, Gustafsson S, Kanoni S, Ganna A, Chen J, Buchkovich ML, Mora S, Beckmann JS, Bragg-Gresham JL, Chang HY, Demirkan A, Den Hertog HM, Donnelly LA, Ehret GB, Esko T, Feitosa MF, Ferreira T, Fischer K, Fontanillas P, Fraser RM, Freitag DF, Gurdasani D, Heikkilä K, Hyppönen E, Isaacs A, Jackson AU, Johansson A, Johnson T, Kaakinen M, Kettunen J, Kleber ME, Li X, Luan J, Lyytikäinen LP, Magnusson PK, Mangino M, Mihailov E, Montasser ME, Müller-Nurasyid M, Nolte IM, O'Connell JR, Palmer CD, Perola M, Petersen AK, Sanna S, Saxena R, Service SK, Shah S, Shungin D, Sidore C, Song C, Strawbridge RJ, Surakka I, Tanaka T, Teslovich TM, Thorleifsson G, Van den Herik EG, Voight BF, Volcik KA, Waite LL, Wong A, Wu Y, Zhang W, Absher D, Asiki G, Barroso I, Been LF, Bolton JL, Bonnycastle LL, Brambilla P, Burnett MS, Cesana G, Dimitriou M, Doney AS, Döring A, Elliott P, Epstein SE, Eyjolfsson GI, Gigante B, Goodarzi MO, Grallert H, Gravito ML, Groves CJ, Hallmans G, Hartikainen AL, Hayward C, Hernandez D, Hicks AA, Holm H, Hung YJ, Illig T, Jones MR, Kaleebu P, Kastelein JJ, Khaw KT, Kim E, Klopp N, Komulainen P, Kumari M, Langenberg C, Lehtimäki T, Lin SY, Lindström J, Loos RJ, Mach F, McArdle WL, Meisinger C, Mitchell BD, Müller G, Nagaraja R, Narisu N, Nieminen TV, Nsubuga RN, Olafsson I, Ong KK, Palotie A, Papamarkou T, Pomilla C, Pouta A, Rader DJ, Reilly MP, Ridker PM, Rivadeneira F, Rudan I, Ruokonen A, Samani N, Scharnagl H, Seeley J, Silander K, Stančáková A, Stirrups K, Swift AJ, Tiret L, Uitterlinden AG, van Pelt LJ, Vedantam S, Wainwright N, Wijmenga C, Wild SH, Willemsen G, Wilsgaard T, Wilson JF, Young EH, Zhao JH, Adair LS, Arveiler D, Assimes TL, Bandinelli S, Bennett F, Bochud M, Boehm BO, Boomsma DI, Borecki IB, Bornstein SR, Bovet P, Burnier M, Campbell H, Chakravarti A, Chambers JC, Chen YD, Collins FS, Cooper RS, Danesh J, Dedoussis G, de Faire U, Feranil AB, Ferrières J, Ferrucci L, Freimer NB, Gieger C, Groop LC, Gudnason V, Gyllensten U, Hamsten A, Harris TB, Hingorani A, Hirschhorn JN, Hofman A, Hovingh GK, Hsiung CA, Humphries SE, Hunt SC, Hveem K, Iribarren C, Järvelin MR, Jula A, Kähönen M, Kaprio J, Kesäniemi A, Kivimaki M, Kooner JS, Koudstaal PJ, Krauss RM, Kuh D, Kuusisto J, Kyvik KO, Laakso M, Lakka TA, Lind L, Lindgren CM, Martin NG, März W, McCarthy MI, McKenzie CA, Meneton P, Metspalu A, Moilanen L, Morris AD, Munroe PB, Njølstad I, Pedersen NL, Power C, Pramstaller PP, Price JF, Psaty BM, Quertermous T, Rauramaa R, Saleheen D, Salomaa V, Sanghera DK, Saramies J, Schwarz PE, Sheu WH, Shuldiner AR, Siegbahn A, Spector TD, Stefansson K, Strachan DP, Tayo BO, Tremoli E, Tuomilehto J, Uusitupa M, van Duijn CM, Vollenweider P, Wallentin L, Wareham NJ, Whitfield JB, Wolffenbuttel BH, Altshuler D, Ordovas JM, Boerwinkle E, Palmer CN, Thorsteinsdottir U, Chasman DI, Rotter JI, Franks PW, Ripatti S, Cupples LA, Sandhu MS, Rich SS, Boehnke M, Deloukas P, Mohlke KL, Ingelsson E, Abecasis GR, Daly MJ, Neale BM, Kathiresan S (2013) Common variants associated with plasma triglycerides and risk for coronary artery disease. Nat Genet 45(11):1345–1352. https://doi.org/10.1038/ng.2795
97. Wolska A, Dunbar RL, Freeman LA, Ueda M, Amar MJ, Sviridov DO, Remaley AT (2017) Apolipoprotein C-II: new findings related to genetics, biochemistry, and role in triglyceride metabolism. Atherosclerosis 267:49–60. https://doi.org/10.1016/j.atherosclerosis.2017.10.025
98. Merkel M, Eckel RH, Goldberg IJ (2002) Lipoprotein lipase: genetics, lipid uptake, and regulation. J Lipid Res 43(12): 1997–2006. https://doi.org/10.1194/jlr.r200015-jlr200
99. Wang H, Eckel RH (2009) Lipoprotein lipase: from gene to obesity. Am J Physiol Endocrinol Metab 297(2):E271–E288. https://doi.org/10.1152/ajpendo.90920.2008
100. Ueda M, Dunbar RL, Wolska A, Sikora TU, Escobar MDR, Seliktar N, deGoma E, DerOhannessian S, Morrell L, McIntyre AD, Burke F, Sviridov D, Amar M, Shamburek RD, Freeman L, Hegele RA, Remaley AT, Rader DJ (2017) A novel APOC2 missense mutation causing apolipoprotein C-II deficiency with severe triglyceridemia and pancreatitis. J Clin Endocrinol Metab 102(5):

1454–1457. https://doi.org/10.1210/jc.2016-3903

101. Ewald N, Hardt PD, Kloer HU (2009) Severe hypertriglyceridemia and pancreatitis: presentation and management. Curr Opin Lipidol 20(6):497–504. https://doi.org/10.1097/MOL.0b013e3283319a1d
102. Sakurai T, Sakurai A, Vaisman BL, Amar MJ, Liu C, Gordon SM, Drake SK, Pryor M, Sampson ML, Yang L, Freeman LA, Remaley AT (2016) Creation of apolipoprotein C-II (ApoC-II) mutant mice and correction of their hypertriglyceridemia with an ApoC-II mimetic peptide. J Pharmacol Exp Ther 356(2):341–353. https://doi.org/10.1124/jpet.115.229740
103. Liu C, Gates KP, Fang L, Amar MJ, Schneider DA, Geng H, Huang W, Kim J, Pattison J, Zhang J, Witztum JL, Remaley AT, Dong PD, Miller YI (2015) Apoc2 loss-of-function zebrafish mutant as a genetic model of hyperlipidemia. Dis Model Mech 8(8):989–998. https://doi.org/10.1242/dmm.019836
104. Xiao X, Li J, Tsao YP, Dressman D, Hoffman EP, Watchko JF (2000) Full functional rescue of a complete muscle (TA) in dystrophic hamsters by adeno-associated virus vector-directed gene therapy. J Virol 74(3):1436–1442. https://doi.org/10.1128/jvi.74.3.1436-1442.2000
105. He B, Tang RH, Weisleder N, Xiao B, Yuan Z, Cai C, Zhu H, Lin P, Qiao C, Li J, Mayer C, Li J, Ma J, Xiao X (2012) Enhancing muscle membrane repair by gene delivery of MG53 ameliorates muscular dystrophy and heart failure in δ-Sarcoglycan-deficient hamsters. Mol Ther 20(4):727–735. https://doi.org/10.1038/mt.2012.5
106. Yang C, Tian W, Ma S, Guo M, Lin X, Gao F, Dong X, Gao M, Wang Y, Liu G, Xian X (2020) AAV-mediated ApoC2 gene therapy: reversal of severe hypertriglyceridemia and rescue of neonatal death in ApoC2-deficient hamsters. Mol Ther Methods Clin Dev 18:692–701. https://doi.org/10.1016/j.omtm.2020.07.011
107. Brown WV, Baginsky ML (1972) Inhibition of lipoprotein lipase by an apoprotein of human very low density lipoprotein. Biochem Biophys Res Commun 46(2):375–382. https://doi.org/10.1016/s0006-291x(72)80149-9
108. Ramms B, Patel S, Nora C, Pessentheiner AR, Chang MW, Green CR, Golden GJ, Secrest P, Krauss RM, Metallo CM, Benner C, Alexander VJ, Witztum JL, Tsimikas S, Esko JD, Gordts P (2019) ApoC-III ASO promotes tissue LPL activity in the absence of apoE-mediated TRL clearance. J Lipid Res 60(8):1379–1395. https://doi.org/10.1194/jlr.M093740
109. Mann CJ, Khallou J, Chevreuil O, Troussard AA, Guermani LM, Launay K, Delplanque B, Yen FT, Bihain BE (1995) Mechanism of activation and functional significance of the lipolysis-stimulated receptor. Evidence for a role as chylomicron remnant receptor. Biochemistry 34(33):10421–10431. https://doi.org/10.1021/bi00033a014
110. Agnani G, Bard JM, Candelier L, Delattre S, Fruchart JC, Clavey V (1991) Interaction of LpB, LpB:E, LpB:C-III, and LpB:C-III:E lipoproteins with the low density lipoprotein receptor of HeLa cells. Arterioscler Thromb 11(4):1021–1029. https://doi.org/10.1161/01.atv.11.4.1021
111. Crosby J, Peloso GM, Auer PL, Crosslin DR, Stitziel NO, Lange LA, Lu Y, Tang ZZ, Zhang H, Hindy G, Masca N, Stirrups K, Kanoni S, Do R, Jun G, Hu Y, Kang HM, Xue C, Goel A, Farrall M, Duga S, Merlini PA, Asselta R, Girelli D, Olivieri O, Martinelli N, Yin W, Reilly D, Speliotes E, Fox CS, Hveem K, Holmen OL, Nikpay M, Farlow DN, Assimes TL, Franceschini N, Robinson J, North KE, Martin LW, DePristo M, Gupta N, Escher SA, Jansson JH, Van Zuydam N, Palmer CN, Wareham N, Koch W, Meitinger T, Peters A, Lieb W, Erbel R, Konig IR, Kruppa J, Degenhardt F, Gottesman O, Bottinger EP, O'Donnell CJ, Psaty BM, Ballantyne CM, Abecasis G, Ordovas JM, Melander O, Watkins H, Orho-Melander M, Ardissino D, Loos RJ, McPherson R, Willer CJ, Erdmann J, Hall AS, Samani NJ, Deloukas P, Schunkert H, Wilson JG, Kooperberg C, Rich SS, Tracy RP, Lin DY, Altshuler D, Gabriel S, Nickerson DA, Jarvik GP, Cupples LA, Reiner AP, Boerwinkle E, Kathiresan S (2014) Loss-of-function mutations in APOC3, triglycerides, and coronary disease. N Engl J Med 371(1):22–31. https://doi.org/10.1056/NEJMoa1307095
112. Clavey V, Lestavel-Delattre S, Copin C, Bard JM, Fruchart JC (1995) Modulation of lipoprotein B binding to the LDL receptor by exogenous lipids and apolipoproteins CI, CII, CIII, and E. Arterioscler Thromb Vasc Biol 15(7):963–971. https://doi.org/10.1161/01.atv.15.7.963
113. Crawford DC, Dumitrescu L, Goodloe R, Brown-Gentry K, Boston J, McClellan B Jr, Sutcliffe C, Wiseman R, Baker P, Pericak-Vance MA, Scott WK, Allen M, Mayo P,

Schnetz-Boutaud N, Dilks HH, Haines JL, Pollin TI (2014) Rare variant APOC3 R19X is associated with cardio-protective profiles in a diverse population-based survey as part of the epidemiologic architecture for genes linked to environment study. Circ Cardiovasc Genet 7(6):848–853. https://doi.org/10.1161/circgenetics.113.000369

114. Jørgensen AB, Frikke-Schmidt R, Nordestgaard BG, Tybjærg-Hansen A (2014) Loss-of-function mutations in APOC3 and risk of ischemic vascular disease. N Engl J Med 371(1):32–41. https://doi.org/10.1056/NEJMoa1308027
115. Saleheen D, Natarajan P, Armean IM, Zhao W, Rasheed A, Khetarpal SA, Won HH, Karczewski KJ, O'Donnell-Luria AH, Samocha KE, Weisburd B, Gupta N, Zaidi M, Samuel M, Imran A, Abbas S, Majeed F, Ishaq M, Akhtar S, Trindade K, Mucksavage M, Qamar N, Zaman KS, Yaqoob Z, Saghir T, Rizvi SNH, Memon A, Hayyat Mallick N, Ishaq M, Rasheed SZ, Memon FU, Mahmood K, Ahmed N, Do R, Krauss RM, MacArthur DG, Gabriel S, Lander ES, Daly MJ, Frossard P, Danesh J, Rader DJ, Kathiresan S (2017) Human knockouts and phenotypic analysis in a cohort with a high rate of consanguinity. Nature 544(7649):235–239. https://doi.org/10.1038/nature22034
116. Wulff AB, Nordestgaard BG, Tybjærg-Hansen A (2018) APOC3 loss-of-function mutations, remnant cholesterol, low-density lipoprotein cholesterol, and cardiovascular risk: mediation- and meta-analyses of 137 895 individuals. Arterioscler Thromb Vasc Biol 38(3):660–668. https://doi.org/10.1161/atvbaha.117.310473
117. Maeda N, Li H, Lee D, Oliver P, Quarfordt SH, Osada J (1994) Targeted disruption of the apolipoprotein C-III gene in mice results in hypotriglyceridemia and protection from postprandial hypertriglyceridemia. J Biol Chem 269(38):23610–23616
118. Pollin TI, Damcott CM, Shen H, Ott SH, Shelton J, Horenstein RB, Post W, McLenithan JC, Bielak LF, Peyser PA, Mitchell BD, Miller M, O'Connell JR, Shuldiner AR (2008) A null mutation in human APOC3 confers a favorable plasma lipid profile and apparent cardioprotection. Science 322(5908):1702–1705. https://doi.org/10.1126/science.1161524
119. Kawakami A, Aikawa M, Alcaide P, Luscinskas FW, Libby P, Sacks FM (2006) Apolipoprotein CIII induces expression of vascular cell adhesion molecule-1 in vascular endothelial cells and increases adhesion of monocytic cells. Circulation 114(7):681–687. https://doi.org/10.1161/circulationaha.106.622514
120. Li H, Han Y, Qi R, Wang Y, Zhang X, Yu M, Tang Y, Wang M, Shu YN, Huang W, Liu X, Rodrigues B, Han M, Liu G (2015) Aggravated restenosis and atherogenesis in ApoCIII transgenic mice but lack of protection in ApoCIII knockouts: the effect of authentic triglyceride-rich lipoproteins with and without ApoCIII. Cardiovasc Res 107(4):579–589. https://doi.org/10.1093/cvr/cvv192

Chapter 27

Atherosclerosis Induced by Adeno-Associated Virus Encoding Gain-of-Function PCSK9

Martin Mæng Bjørklund, Juan A. Bernal, and Jacob F. Bentzon

Abstract

Induction of atherosclerosis in mice with one or more genetic alterations (e.g., conditional deletion of a gene of interest) has traditionally required crossbreeding with *Apoe* or *Ldlr* deficient mice to achieve sufficient hypercholesterolemia. However, this procedure is time consuming and generates a surplus of mice with genotypes that are irrelevant for experiments. Several alternative methods exist that obviate the need to work in mice with germline-encoded hypercholesterolemia. In this chapter, we detail an efficient and increasingly used method to induce hypercholesterolemia in mice through adeno-associated virus-mediated transfer of the proprotein convertase subtilisin/kexin type 9 (*PCSK9)* gene.

Key words Atherosclerosis, Hypercholesterolemia, Adeno-associated virus, PCSK9, Animal models, Non-germline, Viral gene transfer

1 Introduction

Since their development in the 1990s, mouse lines with homozygous germline deletion of the *Apoe* or *Ldlr* gene [1–3] have been the preferred mouse models to study atherosclerosis [4]. Where researchers have aimed to study the function of a particular gene in atherosclerosis, this has generally been achieved by crossing mice lacking or overexpressing that gene with the *Apoe* or *Ldlr* line. This is manageable for single genes of interests, but for experiments utilizing more complicated genetic tools or naturally occurring variants, extensive and time-consuming breeding is required. Examples include the use of Cre/loxP or Dre/rox tools to knock out or overexpress genes in specific cell types and/or time points [5], high-throughput gene targeting and mapping of atherosclerosis-modulating gene variants in complex strain crosses [6].

Effective and more flexible methods that allow researchers to induce hypercholesterolemia in any mouse strain without crossing

Dipak P. Ramji (ed.), *Atherosclerosis: Methods and Protocols*, Methods in Molecular Biology, vol. 2419,
https://doi.org/10.1007/978-1-0716-1924-7_27,
© The Author(s), under exclusive license to Springer Science+Business Media, LLC, part of Springer Nature 2022

with *Apoe* or *Ldlr* deficient mice have recently emerged and have become increasingly prevalent [7, 8]. In this chapter, we detail a non-germline method to initiate hypercholesterolemia and induce atherosclerosis in mice. The method is based on a single tail vein injection of a recombinant adeno-associated virus (rAAV) encoding a gain-of-function mutant form of the human or murine *PCSK9* gene that causes degradation of hepatic low-density lipoprotein (LDL) receptors and, together with high-fat diet feeding, raises plasma LDL to atherogenic levels. We provide an overview of the steps involved in the production and quantification of the rAAV vector as well as the preparation of animals and intravenous rAAV injection. Most users will want to solicit the help of a core facility for rAAV production, but the protocol is included here for those that do not have that possibility. Throughout the chapter, we highlight critical elements and pitfalls in the procedure.

Overexpression of PCSK9 is a rational tool to induce hypercholesterolemia and atherosclerosis in experiments where the mechanisms under investigation and the additional experimental procedures are not themselves expected to influence the efficiency of the rAAV-*PCSK9*^{DY} technique. High levels of plasma PCSK9 may have direct, non-hypercholesterolemia-mediated effects on atherogenesis [9], as is also the case for global *Apoe* and *Ldlr* deletion [10], but these will be similar across groups and should not bias conclusions. Other non-germline methods for atherosclerosis induction exist, including the use of rAAV-*IDOL* overexpression [11], AAV-*CRISPR-Cas9* knockout of the *Ldlr* gene [12], and antisense oligonucleotides targeting LDLR mRNA [13].

Different serotypes of the rAAV capsids are available and tissue tropism differs between the serotypes [14]. In the present context, we have used serotype 8 and 9 which both transduce murine hepatocytes and, in combination with a liver-specific promoter, drive efficient and long-term expression of the *PCSK9* gene.

As for other means of inducing atherosclerosis, the genetic background of the mouse is an important factor with C57BL/6 being highly atherosclerosis-prone and other strains, such as FVB/N and 129S2 less so [8].

2 Materials

2.1 *rAAV*-PCSK9^{DY} Production

2.1.1 Plasmid Transfection

1. *pAAV-PCSK9*^{DY} shuttle plasmids from Bjørklund et al. [7] containing gain-of-function mutants of mouse or human PCSK9 under a liver-specific HCR/hAAT promoter flanked by AAV2 inverted terminal repeats (ITRs) (Addgene plasmid #58376 or #58379; www.addgene.org) (*see* **Note 1**).

2. Rep/Cap plasmid encoding the AAV2 replicase and capsid proteins of serotype 8 or 9 (e.g., Addgene plasmid #112864 or #112865; www.addgene.org).
3. Helper plasmid carrying adenovirus-derived genes (e.g., *pAd-DeltaF6*, Addgene plasmid #112867; www.addgene.org).
4. Competent bacteria suitable for cloning unstable inserts (e.g., Stbl4).
5. Bacteria culture medium: LB medium.
6. Bacterial culture incubator.
7. A 2000 mL baffled shake flask.
8. *AhdI*, *XmaI*, and *BglI* restriction enzymes.
9. Distilled water.
10. 10× restriction enzyme buffer for *Ahd*I and *Xma*I: 200 mM Tris-acetate, 100 mM Magnesium acetate, 500 mM Potassium acetate, 1 mg/mL bovine serum albumin (BSA), pH 7.9.
11. 10× restriction enzyme buffer for *Bgl*I: 1 M NaCl, 500 mM Tris–HCl, 100 mM $MgCl_2$, 1 mg/mL BSA, pH 7.9.
12. Equipment for agarose gel electrophoresis.
13. HEK293T cells (ATCC® CRL-3216™).
14. Cell culture medium with either 10% or 2% fetal bovine serum (FBS): DMEM with 4.5 g/L glucose, 4 mM L-glutamine, 1 mM sodium pyruvate, supplemented with 10% or 2% FBS and without antibiotics.
15. Cell culture medium for Polyethylenimine (PEI) transfection: DMEM with 2 mM L-glutamine, supplemented with 10% FBS and without antibiotics.
16. Sterile phosphate-buffered saline (PBS): 1.54 mM KH_2PO_4, 155.17 mM NaCl, 2.71 mM Na_2HPO_4, pH 7.4.
17. 0.025% trypsin.
18. T-175 cm^2 flask and 1720 cm^2 hyperflask cell culture vessels.
19. 150 mm cell culture petri dishes.
20. 1 μg/μL PEI, Linear, MW 25000, Transfection Grade.
21. 0.22 μm sterile syringe filter.
22. 12 M Hydrochloric acid.
23. Vortex mixer.
24. Cell culture incubator.
25. Water bath.

2.1.2 Harvest of the Cell Lysate

1. 50 mL sterile conical polypropylene centrifuge tubes.
2. Lysis buffer: 2 mM $MgCl_2$, 150 mM NaCl, 50 mM Tris–HCl, pH 8.

3. 1 M $MgCl_2$.
4. Centrifuge.
5. Benzonase Nuclease (≥250 U/μL).
6. Dry ice.
7. Vortex mixer.
8. Water bath.

2.1.3 Purification in an Iodixanol Gradient

1. 60% iodixanol solution (OptiPrep™ density gradient medium).
2. 5× OptiPrep™ dilution buffer (ODB): 5× PBS, 5 mM filter sterilized $MgCl_2$, 12.5 mM KCl.
3. Iodixanol Gradient Layer Solutions (*see* Table 1).
4. Ultracentrifuge capable of centrifuging at 340,000 × *g*.
5. 37.4 mL OptiSeal polypropylene ultracentrifuge tubes.
6. 5 mL syringes.
7. 18G needles.
8. Stand with clamp.
9. Glass Pasteur pipette.

2.1.4 *rAAV*-PCSK9^{DY} Particle Concentration and Suspension

1. Millipore Amicon Ultra-15 centrifugal filter unit.
2. 0.001% Pluronic® F-68 in PBS: Add 5 μL of 100× Pluronic F-68 to 49.95 mL of PBS.
3. Primers targeting the HCR region of the *PCSK9*^{DY} construct (*see* Table 2).
4. PCR master mix containing a DNA-binding dye (e.g., SYBR green), a hot start polymerase, recommended buffer and dNTPs.
5. Centrifuge.
6. Quantitative PCR machine.

2.2 Tail Vein Injection of the rAAV-PCSK9^{DY} Solution

Most of the materials needed for the tail vein injection can be prepared in advance. The following will be required in addition to the rAAV-*PCSK9*^{DY} stock solution.

1. Mice.
2. A mouse restrainer.
3. Heating cabinet to keep mice at 28–30 °C or a container with warm (30–35 °C) water to dilate tail veins.
4. Wet ice to keep the rAAV solution cold.
5. Paper towel.
6. Permanent marker.

Table 1
Iodixanol Gradient Layer Solutions

Layer (%)	OptiPrep 60% (mL)	5 M NaCl (mL)	5× dilution buffer (ODB) (mL)	dH_2O (mL)	Phenol red (μL)	Volume (mL)
15	45	36	36	63	–	180
25	100	–	48	92	600	240
40	136	–	40	24	–	200
60	200	–	–	–	500	200

Table 2
Primers used for titration

Target gene	Primer sequence (5′ – 3′)	Annealing temperature (°C)	Product size (bp)
HCR promoter forward	CATCCTCCAGCAGCTGTTTG TG	64.1	221
HCR promoter reverse	CTCCTCTCCACCGAAA TTCCAAG	63.8	

Fig. 1 A tail cuff to induce stasis of blood in the tail veins. Made by inserting a loop of ligature into a 1 mL syringe. When the plunger is moved, the cuff is tightened or loosened accordingly

7. Sterile PBS.
8. 70% ethanol diluted in H_2O.
9. Cotton swabs.
10. Water bath.
11. Tail cuff: made by inserting a loop of ligature into a 1 mL syringe (Fig. 1).
12. A 1 mL syringe connected to a polyethylene tube (inner diameter 0.38 mm and outer diameter 1.09 mm) via a 27 G needle. Two needles, each one split in two parts using a needle holder, are used at each end of the polyethylene tube (Fig. 2).

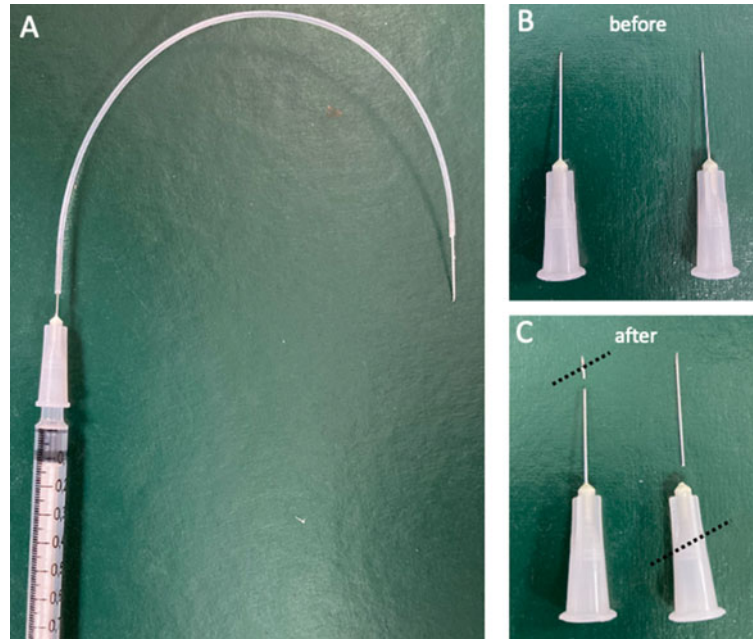

Fig. 2 (**a**) Finished assembly of a practical injection device for tail vein injections. It consists of a 1 mL syringe, parts of two 27 G needles and a connecting plastic tube. (**b**) Two intact 27 G needles. (**c**) The two needles each carefully split into two pieces by using a needle holder to break the needle apart. The bottom part of the left needle is connected to the syringe, while the upper part of the right needle is used at the tip of the connecting plastic tube

3 Methods

3.1 rAAV-PCSK9^{DY} Production (See Note 2)

3.1.1 Plasmid Transfection

1. Culture bacteria carrying the pAAV-*PCSK9^{DY}* vector at 32 °C overnight in LB medium. A 400 mL culture in a 2000 mL baffled shake flask will yield approximately 800 μg of plasmid (*see* **Note 3**).
2. Test ITRs integrity by digesting *pAAV-PCSK9^{DY}* plasmids with *AhdI*, *BglI,* or *XmaI* restriction enzymes (*see* **Note 4**).
3. Prepare the PEI solution for transfection: Dissolve PEI powder in H_2O that has been preheated to 80 °C and cooled down to room temperature. Once stabilized, neutralize to pH 7.0 with 12 M hydrochloric acid, filter sterilize the solution through a 0.22 μm filter, aliquot and store at −20 °C (*see* **Note 5**).
4. Culture HEK293T cells on 150 mm cell culture dishes in cell culture medium with 2% FBS to 90–95% confluency.
5. The day before transfection, wash HEK293T cells from 5 confluent 150 mm cell culture dishes with PBS and trypsinize with 0.025% trypsin.

6. Neutralize trypsin with cell culture medium containing 10% FBS and plate the cells in 2 hyperflasks with cell culture medium containing 10% FBS (*see* **Note 6**).
7. Prepare the PEI transfection mixture in a T-175 cm^2 flask by adding 140 mL of prewarmed cell culture medium for PEI transfection, 360 μg Rep/Cap plasmid, 960 μg helper plasmid, 360 μg shuttle *pAAV-PCSK9$^{D\Upsilon}$* plasmid, and 5.8 mL linear PEI (1 μg/μL). Vortex the mixture for 15 s and incubate at room temperature for 15 min.
8. Remove the medium from the hyperflasks and carefully add half of the PEI transfection mixture to each hyperflask.
9. Add prewarmed cell culture medium supplemented with 2% FBS.
10. Incubate the cells at 37 °C for 3 days.

3.1.2 Harvest of the Cell Lysate

1. Collect the cells and medium by shaking/tapping the hyperflasks and transfer everything into 50 mL polypropylene centrifuge tubes. Wash the hyperflasks twice with approximately 100 mL of PBS and transfer it to the tubes as well.
2. Centrifuge the cells at 2900 × *g* for 5 min at room temperature. Discard the supernatant.
3. Lift the cells in each tube with 5 mL of PBS and combine them into a single 50 mL polypropylene centrifuge tube, centrifuge at 2900 × *g* for 5 min and discard the supernatant.
4. Resuspend the final pellet in 10 mL of cell lysis buffer.
5. Freeze the crude lysate using dry ice and thaw in a 37 °C water bath to lyse the cells at least 3 times. Vortex the lysate after each cycle.
6. To remove DNA from the lysate, add $MgCl_2$ to a final concentration of 1 mM, and add Benzonase Nuclease to a final concentration of 25 U/mL. Mix by vortexing.
7. Incubate at 37 °C in a water bath for 30 min.
8. Centrifuge at 3500 × *g* for 10 min at room temperature. Collect and transfer the supernatant into 50 mL polypropylene centrifuge tubes. Discard the pellet.
9. Continue with the purification step described in Subheading 3.1.3 or store the lysate at −80 °C until ready to continue.

3.1.3 Purification in an Iodixanol Gradient

1. To prepare the iodixanol gradient, place the tip of a glass Pasteur pipette at the bottom of the OptiSeal polypropylene ultracentrifuge tubes and consecutively place the following solutions at the tube bottom (each solution will underlie the previous) (Fig. 3): 8 mL of 15% iodixanol; 6 mL of 25%

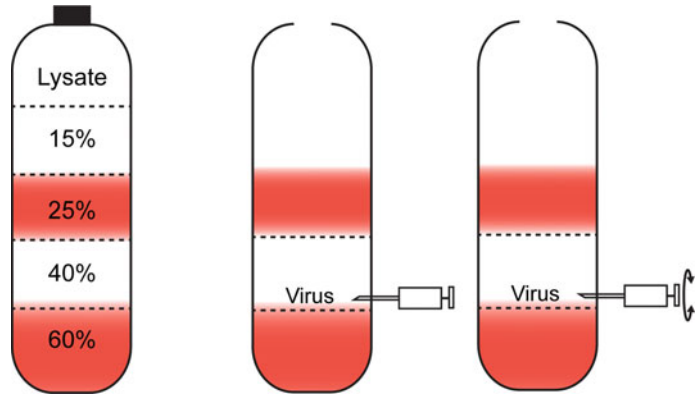

Fig. 3 (**a**) The iodixanol gradient loaded with lysate and ready for ultracentrifugation. (**b** and **c**) Extraction of the rAAV-*PCSK9*^{DY}-containing solution after ultracentrifugation. Insertion of the needle with the bevel facing upwards just above the 60% iodixanol layer. The last part of the layer is extracted with the bevel faced downwards to prevent contamination with the 25% layer that contains cellular debris

iodixanol; 5 mL of 40% iodixanol; and 5 mL of 60% iodixanol. Take care to avoid bubbles.

2. Once the iodixanol gradient is prepared, load 5–6 mL of viral lysate over the gradient tube using a Pasteur pipette taking care not to disturb the gradient (hold the pipette tip towards the tube wall). Top off the tube with cell lysis buffer avoiding air bubbles.
3. Cap the tube with the black plug and cover with the spacer. Place the tube into the ultracentrifuge. Centrifuge at 340,000 × *g* for 3 h at 16 °C.
4. The rAAV-*PCSK9*^{DY} viral solution should sit between the 40% and 60% iodixanol layers (Fig. 3). To harvest the virus particles from the gradient, hold the tube in the clamp placed on a stand so the tube is at eye level and remove the cap of the tube. Use a 5 mL syringe attached to a 18G needle to pierce into the centrifuge tube just above the 60% layer with the needle bevel pointing upwards, facing the 40% layer, and aspirate the interface. Collect approximately 3 mL of the gradient and then rotate the needle 180°, so that the bevel now faces the 60% layer. Collect an additional 2 mL of the 40–60% interface.
5. You may store the virus at −80 °C or continue with the concentration step described in Subheading 3.1.4.

*3.1.4 rAAV-*PCSK9^{DY} *Concentration and Titration*

1. Pre-wet the Millipore Amicon centrifugal filter unit with 0.001% Pluronic® F-68 in PBS.
2. Place the viral solution into the filter unit.

3. Centrifuge at 3000 × *g* for approximately 25 min at 4 °C.
4. Discard the flow through and add more PBS with 0.001% Pluronic® F-68 to the top of the filter. Centrifuge again as in **step 3**. Repeat until the retention solution becomes clear.
5. Resuspend the virus particles in 1020 μL of PBS with 0.001% Pluronic® F-68 and divide them in 5 aliquots of 200 μL and 1 aliquot containing the rest (roughly 20 μL) that will be used for titration by quantitative PCR. Store the rAAV-*PCSK9*^{DY} stock solution at −80 °C (*see* **Note 7**).
6. To determine the titer of the rAAV-*PCSK9*^{DY} vector solution (in viral genomes per mL), perform quantitative PCR using the primer sequences targeting the HCR promotor of the *PCSK9*^{DY} construct shown in Table 2 (*see* **Note 8**).

3.2 Tail Vein injection of the rAAV-PCSK9^{DY} Solution (See Notes 9 and 10)

Approval of the project by the local Institutional Animal Care and Use Committee is required before the initiation of the study.

1. Keep the mice in a warm environment (28–30 °C) up to 30 min before injection or soak the tail briefly in warm (30–35 °C) water to dilate tail veins.
2. Gently secure the mouse in the mouse restrainer, if not already done during the water-based tail vein dilation procedure.
3. Place the tail cuff around the proximal part of the tail and tighten it. Note the course of the dilated veins on both sides of the tail (*see* **Note 11**).
4. Turn the tail to one side in order to have the vein pointing upwards. Wipe the tail with a cotton swab soaked in 70% ethanol to increase vein visibility, and with the bevel of the needle facing upward gently insert the needle parallel to the skin surface into the vein (*see* **Note 12**).
5. Once inside the vein and with visible blood in the plastic tube connecting the needle and the syringe, loosen the tail cuff and slowly inject the rAAV-*PCSK9*^{DY} solution (*see* **Note 13**).
6. Inject a total volume of 100 μL rAAV-*PCSK9*^{DY} solution containing the desired amount of virus particles (we recommend $1.0x10^{11}$ virus particles per mouse for serotype 8 and 5.0×10^{10} virus particles per mouse for serotype 9).
7. After injection, carefully remove the needle and press for 10 s at the injection site with the tip of two fingers (with gloves) using a piece of paper towel in between (*see* **Note 14**).
8. Move the mouse to a cage and initiate a high-fat, cholesterol-rich diet to induce sustained hypercholesterolemia (*see* **Notes 15** and **16)** and atherosclerosis (*see* **Note 17**).

4 Notes

1. In our hands, both the mouse and human rAAV-*PCSK9*$^{D\Upsilon}$ versions work well. For routine work, we recommend using the mouse version to exclude the theoretical possibility of immune responses. For studies where it is important to monitor the amount of endogenously produced PCSK9, the human version can be used and plasma levels of vector-produced and endogenous PCSK9 can be determined using ELISA kits specific for mouse and human PCSK9.
2. Working with rAAV vectors should be done according to local biosafety guidelines [15]. Of note, when rAAV constructs in which the transgene does not encode a potentially tumorigenic gene product or a toxin molecule and, furthermore, is produced in the absence of a helper virus and followed by vector purification, it can be handled in a Biosafety Level 1 (BSL-1) facility. Otherwise, it should be handled as Biosafety Level 2 (BSL-2) biohazardous material. rAAV vectors should be administered to animals inside a biosafety cabinet and with the use of recommended personal protective equipment. Be aware to persistently follow all waste disposal regulations when disposing waste materials.
3. To improve plasmid stability, we recommend culturing the bacteria overnight at 32 °C. To avoid the loss of unstable ITRs sequences in the shuttle pAAV-*PCSK9*$^{D\Upsilon}$ vectors, we advise to maintain plasmids in bacteria designed for cloning unstable repeats found in viral expression vectors (e.g., Stbl4). Mutations in *rec*A or *rec*B and in *rec*J genes are essential to reduce homologous recombination, and bacteria should also be restriction negative (*mcr*B, *mrr*) to enhance genomic cloning capacity.
4. To test ITRs integrity by digesting *pAAV-PCSK9*$^{D\Upsilon}$ plasmids with *AhdI*, *BglI,* or *XmaI* restriction enzymes, use the following protocol:
   (a) Dilute up to 1 μg DNA shuttle vector to 21.5 μL with distilled water.
   (b) Add 2.5 μL of 10× restriction enzyme buffer for *Ahd*I and *Xma*I, or 10× restriction enzyme buffer for *Bgl*I, respectively.
   (c) Add 10 U per reaction (1 μL) of restriction enzyme for a final 25 μL volume.
   (d) Incubate for 1 h at 37 °C.
   (e) Analyze by agarose gel electrophoresis.

5. We recommend testing PEI transfection efficiency each time you prepare a new batch.
6. The protocol is given for one rAAV preparation, but it is recommended to make at least two virus particle preparations (or multiples of that) at the same time for the purpose of keeping rotor balance in the centrifugation steps. In that case, the steps in the protocol should be multiplied accordingly.
7. Under these storage conditions (−80 °C), the rAAV-*PCSK9*$^{D\Upsilon}$ vector is stable for at least 2 years.
8. For absolute quantification of viral genomes, construct a standard curve with known copy numbers (10^5–10^8) of the *pAAV-PCSK9*$^{D\Upsilon}$ plasmid. Use a double-stranded DNA-binding dye like SYBR Green or similar, and a master mix containing a polymerase complexed with an antibody to allow a hot start reaction. Prepare the reaction for each sample in a final 20 μL volume with 200 nM of each primer, 10 μL of 2x SYBR Green master mix, and 1 μL of different dilutions of *pAAV-PCSK9*$^{D\Upsilon}$ preparation. Perform the reaction on the quantitative PCR machine using the following thermal settings: Hot start 95 °C for 10 min and then 40 cycles consisting of 95 °C for 15 s, 60 °C for 30 s, and 72 °C for 30 s. We routinely obtain above $1.0{\cdot}10^{13}$ viral genomes per preparation.
9. Alternative administration routes for rAAV-*PCSK9*$^{D\Upsilon}$ are possible, including intraperitoneal [17] and femoral injection [8].
10. For experiments using tamoxifen-inducible recombinases, the timing of rAAV-*PCSK9*$^{D\Upsilon}$ injections after tamoxifen injections is important. We have experienced lower efficiency of the rAAV technique when it is performed shortly after tamoxifen injections. To avoid this, we recommend waiting 2 weeks after the last tamoxifen administration before injecting the rAAV-*PCSK9*$^{D\Upsilon}$ vector.
11. The accessible tail veins of mice are the lateral veins located on each side of the tail, while the artery is located on the ventral side.
12. This injection procedure requires a bit of practice because the vein is quite delicate. Therefore, we recommend initial training of the procedure using saline. If a missed injection occurs, make a new attempt on the contralateral vein. It is also possible to try another injection site more proximal to the first attempted, but be aware that the vein may be collapsed and difficult to locate and puncture. If injection is altogether unsuccessful, the mouse can be returned to its cage and a new attempt can be made 1–2 days later.

13. You should feel no resistance in the plunger while injecting. In case you do, the needle tip might be located outside the vein or there is a blockage somewhere in the injection device.
14. Venous bleeding stops quickly after removal of the tail cuff and the needle. This time point is also useful for marking the tail of the mouse using a permanent marker (e.g., to mark "injected" or "missed injection").
15. Many different high-fat, cholesterol-rich diets are available and choosing one can be complicated. The final choice depends on the research question and whether supplements (e.g., cholate, sodium chloride, etc.) are desired for the animal model. Plasma total cholesterol increases rapidly and elevated levels can be detected within 3 days after the rAAV-*PCSK9*^{DY} injection.
16. Total cholesterol can be determined using an enzymatic cholesterol reagent such as the CHOD-PAP method combined with spectrophotometric analysis [16].
17. In our hands, wild-type C57BL/6 mice develop advanced atherosclerotic lesions in the aortic root within 12–16 weeks after rAAV-*PCSK9*^{DY} injection, and elevated plasma cholesterol levels can last for more than 1 year [8].

Acknowledgments

This work was supported by grants from The Lundbeck Foundation (R230-2016-3644 to MMB), the Novo Nordisk Foundation (NNF17OC00306889 to JFB), and the Ministerio de Ciencia, Innovación y Universidades (MCIU) (BFU2016-75144-R to JAB). The CNIC is supported by the Instituto de Salud Carlos III (ISCIII), the Ministerio de Ciencia e Innovación (MCIN) and the Pro CNIC Foundation, and is a Severo Ochoa Center of Excellence (SEV-2015-0505).

References

1. Zhang SH, Reddick RL, Piedrahita JA et al (1992) Spontaneous hypercholesterolemia and arterial lesions in mice lacking apolipoprotein E. Science 258(5081):468–471. https://doi.org/10.1126/science.1411543
2. Plump AS, Smith JD, Hayek T et al (1992) Severe hypercholesterolemia and atherosclerosis in apolipoprotein E-deficient mice created by homologous recombination in ES cells. Cell 71(2):343–353. https://doi.org/10.1016/0092-8674(92)90362-G
3. Ishibashi S, Brown MS, Goldstein JL et al (1993) Hypercholesterolemia in low density lipoprotein receptor knockout mice and its reversal by adenovirus-mediated gene delivery. J Clin Invest 92(2):883–893. https://doi.org/10.1172/JCI116663
4. Daugherty A, Tall AR, Daemen MJAP et al (2017) Recommendation on design, execution, and reporting of animal atherosclerosis studies: a scientific statement from the American Heart Association. Circ Res 121(6):e53–e79. https://doi.org/10.1161/RES.0000000000000169
5. Alencar GF, Owsiany KM, Karnewar S et al (2020) Stem cell pluripotency genes Klf4 and Oct4 regulate complex SMC phenotypic changes critical in late-stage atherosclerotic

lesion pathogenesis. Circulation 142(21): 2045–2059. https://doi.org/10.1161/CIRCULATIONAHA.120.046672

6. Lusis AJ, Seldin MM, Allayee H et al (2016) The hybrid mouse diversity panel: a resource for systems genetics analyses of metabolic and cardiovascular traits. J Lipid Res 57(6): 925–942. https://doi.org/10.1194/jlr.R066944
7. Bjørklund MM, Hollensen AK, Hagensen MK et al (2014) Induction of atherosclerosis in mice and hamsters without germline genetic engineering. Circ Res 114(11):1684–1689. https://doi.org/10.1161/CIRCRESAHA.114.302937
8. Roche-Molina M, Sanz-Rosa D, Cruz FM et al (2015) Induction of sustained hypercholesterolemia by single adeno-associated virus-mediated gene transfer of mutant hPCSK9. Arterioscler Thromb Vasc Biol 35(1):50–59. https://doi.org/10.1161/ATVBAHA.114.303617
9. Giunzioni I, Tavori H, Covarrubias R et al (2016) Local effects of human PCSK9 on the atherosclerotic lesion. J Pathol 238(1):52–62. https://doi.org/10.1002/path.4630
10. Getz GS, Reardon CA (2016) Do the Apoe−/− and Ldlr−/− mice yield the same insight on atherogenesis? Arterioscler Thromb Vasc Biol 36(9):1734–1741. https://doi.org/10.1161/ATVBAHA.116.306874
11. Bornfeldt KE, Kramer F, Batorsky A et al (2018) A novel type 2 diabetes mouse model of combined diabetic kidney disease and atherosclerosis. Am J Pathol 188(2):343–352. https://doi.org/10.1016/j.ajpath.2017.10.012
12. Jarrett KE, Lee C, De Giorgi M et al (2018) Somatic editing of *Ldlr* with adeno-associated viral-CRISPR is an efficient tool for atherosclerosis research. Arterioscler Thromb Vasc Biol 38(9):1997–2006. https://doi.org/10.1161/ATVBAHA.118.311221
13. Basu D, Hu Y, Huggins LA et al (2018) Novel reversible model of atherosclerosis and regression using oligonucleotide regulation of the LDL receptor. Circ Res 122(4):560–567. https://doi.org/10.1161/CIRCRESAHA.117.311361
14. Wu Z, Asokan A, Samulski RJ (2006) Adeno-associated virus serotypes: vector toolkit for human gene therapy. Mol Ther 14(3): 316–327. https://doi.org/10.1016/j.ymthe.2006.05.009
15. Collins DE, Reuter JD, Rush HG et al (2017) Viral vector biosafety in laboratory animal research. Comp Med 67(3):215–221. https://doi.org/10.1002/cphc.201700089
16. Allain CC, Poon LS, Chan CSG et al (1974) Enzymatic determination of total serum cholesterol. Clin Chem 20(4):470–475. https://doi.org/10.1093/CLINCHEM/20.4.470
17. Lu H, Howatt DA, Balakrishnan A et al (2016) Hypercholesterolemia induced by a PCSK9 gain-of-function mutation augments angiotensin II-induced abdominal aortic aneurysms in C57BL/6 mice-brief report. Arterioscler Thromb Vasc Biol 36(9):1753–1757. https://doi.org/10.1161/ATVBAHA.116.307613

Chapter 28

Monitoring Leukocyte Migration During Atherosclerosis In Vivo

Keiichiro Matoba

Abstract

Transendothelial leukocyte migration is an early event in the progression of vascular inflammation, the underlying molecular mechanism of atherosclerosis. Inflammatory mediators such as adhesion molecules and chemokines are essential in this process. Leukocyte migration into the vascular wall can be monitored by the detection of CD11b-positive immune cells in animal models of atherosclerosis. This chapter will describe an immunohistochemical technique used to evaluate leukocyte migration in vivo.

Key words Leukocyte migration, CD11b integrin, Immunohistochemistry, Paraffin-embedded tissue, Aorta

1 Introduction

Atherosclerosis is the leading cause of cardiovascular disease and a worldwide public health problem. Given the epidemic of cardiovascular disease, unraveling the mechanisms regulating atherogenic signaling is of considerable interest. To this end, the analysis of leukocyte migration is critically important. The adhesion and migration of leukocytes occur at the initial step during atherosclerotic plaque formation [1]. These processes are mediated by adhesion molecules and chemokines. The CD11b integrin, also known as Mac-1, supports the firm adhesion of circulating leukocytes to intercellular adhesion molecule 1 (ICAM-1)-expressing endothelium [2]. Migrated leukocytes are visualized through the immunostaining of CD11b in serial sections of specimens from the aorta [3, 4]. Aortic tissues are harvested, fixed to maintain architecture and antigenicity, and then sectioned. Staining with a CD11b antibody can produce informative images. This method can be adapted to other tissue types and research fields, including arthritis, multiple sclerosis, and tumor growth.

Dipak P. Ramji (ed.), *Atherosclerosis: Methods and Protocols*, Methods in Molecular Biology, vol. 2419,
https://doi.org/10.1007/978-1-0716-1924-7_28,
© The Author(s), under exclusive license to Springer Science+Business Media, LLC, part of Springer Nature 2022

2 Materials

Prepare and store all reagents at room temperature unless otherwise indicated. Follow the lab safety regulations when disposing of waste materials.

2.1 Fixation and Sectioning

1. 10 mM Phosphate-buffered saline, pH 7.4 (PBS).
2. 10% neutral buffered formalin.
3. Paraffin.
4. Microtome and blade.
5. Positively charged microscope slides.
6. Xylene.
7. Graded alcohols of different concentrations: 100% ethanol, 90% ethanol, and 70% ethanol.
8. Autoclave.
9. Water bath at 40 °C.
10. Oven at 60 °C.
11. Distilled water.
12. 10 mM sodium citrate buffer, pH 6.0.

2.2 Immunostaining

1. Blocking reagent: 10% normal serum with 1% bovine serum albumin (BSA) in PBS (*see* **Note 1**). Store at 4 °C.
2. CD11b primary antibody: 1 μg/ml diluted in PBS with 1%BSA (*see* **Note 2**). Store at 4 °C.
3. Secondary antibody: Fluorophore-conjugated secondary antibody diluted in PBS with 1%BSA (*see* **Note 3**). Store at 4 °C.
4. Mounting medium with 4′,6-diamidino-2-phenylindole (DAPI).
5. Humidified chamber.
6. Tissue paper.
7. Fluorescence microscope with filter set.

3 Methods

Carry out all procedures at room temperature unless otherwise indicated. All steps involving fluorophore-conjugated secondary antibodies should be performed in the dark to avoid photobleaching.

3.1 Formalin Fixation, Sectioning of Paraffin-Embedded Aorta, and Deparaffinization

1. Harvest aorta after transcardiac perfusion with PBS.
2. Fix the freshly dissected aorta in 10% neutral buffered formalin for 24–48 h.
3. Place paraffin in a mold and cool briefly to immobilize the tissue.
4. Cut 4 μm-thick tissue sections using a microtome and then float them in a 40 °C water bath containing distilled water.
5. Transfer the sections onto positively charged microscope slides (*see* **Note 4**). Allow the slides to dry overnight.
6. Place the slides in a 60 °C oven for 15 min.
7. Deparaffinize the slides in xylene using three changes for 5 min each (*see* **Note 5**).
8. Treat slides by gradually reducing the ethanol concentration from 100% to 90% and then to 70%. Wash in 100% ethanol twice for 15 min each time, 90% ethanol twice for 15 min each time, and then 70% ethanol twice for 15 min each time (*see* **Note 6**).
9. Rinse the slides with running tap water to remove the ethanol.
10. Place slides in an autoclave and cover with 10 mM sodium citrate buffer at pH 6.0. Heat at 121 °C (2 atm) for 10 min (*see* **Note 7**). Allow slides to cool at room temperature for approximately 20 min.
11. Wash in distilled water three times for 2 min each.
12. Aspirate excess liquid from the slides.

3.2 CD11b Immunostaining

1. Incubate slides with blocking reagent for 60 min in a humidified chamber to inhibit non-specific binding of the primary antibody.
2. Remove blocking reagent and wash the slides with three changes of PBS for 5 min each time. Wipe around the sections with tissue paper.
3. Add enough CD11b primary antibody solution to cover the samples, except for the negative control, which should be incubated without the primary antibody. Incubate overnight at 4 °C in a humidified chamber (*see* **Note 8**).
4. Remove the primary antibody solution and wash the slides with three changes of PBS for 5 min each.
5. Add enough fluorophore-conjugated secondary antibody to cover the slides, including the negative control (*see* **Note 9**).
6. Incubate at room temperature for 60 min in a dark chamber.
7. Wash with three changes of PBS for 5 min each. Aspirate as much liquid as possible from the slides without drying them.
8. Immediately, mount the coverslip with mounting medium.

9. View on a fluorescence microscope with appropriate filters. Store slides in a dark location at room temperature or 4 °C.
10. Signal intensity can be quantified using the ImageJ software program.

4 Notes

1. The secondary antibody cross-reacts with endogenous immunoglobulins in the tissue. In order to minimize this, the blocking serum should ideally be derived from the same species as that in which the secondary antibody is raised.
2. The optimal concentration of primary antibody should be titrated. We recommend starting at 1 μg/ml.
3. It is recommended that the concentration of the secondary antibody be titrated for optimal performance for each study. Follow the antibody-specific protocol on the secondary antibody datasheet.
4. The use of charged slides helps the sections adhere to the slide.
5. In order to perform antibody staining, paraffin should be removed from the specimens. Three changes of xylene is usually sufficient for the removal of paraffin. Fresh xylene must be used to avoid high background staining caused by inadequate deparaffinization.
6. Do not allow slides to dry at any time during this procedure to avoid inconsistent staining.
7. Certain antibodies work best only when tissues are heated in sodium citrate buffer that acts as antigen retriever. Antigen retrieval improves the accessibility of the tissue for antibody staining. Read the primary antibody datasheet for recommendations. The optimal incubation time may vary for each animal type.
8. Avoid the drying out of tissues by using sufficient volumes of solutions. Keep slides lying flat so that the antibody solutions do not drain off. Increased signal intensity can clearly be seen with overnight incubation in comparison to shorter incubation. Some additional optimization will be required in order to obtain an ideal signal with shorter incubation. Adjust dilutions and incubation time appropriately based on the results obtained.
9. Chromogenic staining with or without counterstaining can also be performed if desired.

Acknowledgments

This work was supported by JSPS KAKENHI (20K08645), Suzuken Memorial Foundation, Takeda Science Foundation, MSD Life Science Foundation, and Japan Diabetes Foundation to K.M.

References

1. Takeda Y, Matoba K, Kawanami D et al (2019) ROCK2 regulates monocyte migration and cell to cell adhesion in vascular endothelial cells. Int J Mol Sci 20:1331
2. Takeda Y, Matoba K, Sekiguchi K et al (2020) Endothelial dysfunction in diabetes. Biomedicines 8:182
3. Lu Y, Zhang L, Liao X et al (2013) Kruppel-like factor 15 is critical for vascular inflammation. J Clin Invest 123:4232–4241
4. Mencarelli A, Renga B, Distrutti E et al (2009) Antiatherosclerotic effect of farnesoid X receptor. Am J Physiol Heart Circ Physiol 296: 272–281

Chapter 29

Evaluation of Plaque Burden and Lipid Content in Atherosclerotic Plaques

Yee-Hung Chan, Alaa Alahmadi, Reem Alotibi, and Dipak P. Ramji

Abstract

Atherosclerosis is a chronic inflammatory disease characterized by the formation of lipid-rich, fibrous plaques within the arterial wall of medium and large arteries. Plaques prone to rupture are typically rich in lipids and pro-inflammatory markers. Cells within the plaque can take up lipids via different mechanisms leading to the formation and accumulation of lipid-rich foam cells, a key hallmark of the disease. Evaluation of plaque burden and lipid content is hence important to determine disease progression and severity. This chapter describes the most commonly used staining methods that enable visualization and analysis of mouse atherosclerotic plaques. These methods include *en face* preparation of mouse aorta, and staining sections of arteries using hematoxylin and eosin, Oil Red O, and Masson's Trichrome.

Key words Staining, *En face*, Hematoxylin and eosin, Oil Red O, Masson's Trichrome

1 Introduction

Atherosclerosis is characterized by the formation of lipid-rich, fibrous plaques (fibroatheromas) within the arterial wall. Lipid retention and accumulation within the arterial intima results in the infiltration of immune cells to the lesion. Vascular smooth muscle cells (VSMCs) also invade (from the tunica media layer into the intima) and proliferate, synthesizing extracellular matrix (ECM) proteins such as collagen and elastin, forming a fibrous cap that encapsulates and stabilizes the atherosclerotic plaque [1]. Plaques rich in lipid content and pro-inflammatory macrophages have a thin, inflamed and unstable fibrous cap and are particularly prone to rupture [2]. Plaque rupture results in lumen-occlusive thrombosis, leading to the onset of cardiovascular events, such as myocardial infarction and cerebrovascular accident [3–5].

Analysis of plaque burden is achieved by measurement of multiple parameters, including plaque size, lipid content, distribution, and stability. This requires exploiting different staining methods

Dipak P. Ramji (ed.), *Atherosclerosis: Methods and Protocols*, Methods in Molecular Biology, vol. 2419,
https://doi.org/10.1007/978-1-0716-1924-7_29,
© The Author(s), under exclusive license to Springer Science+Business Media, LLC, part of Springer Nature 2022

that enable visualization of the different key components. Mouse models are commonly used in atherosclerosis research to study the effect of various therapeutic agents and strategies on atherosclerosis before progression onto clinical studies. Common anatomical sites assessed for atherosclerotic plaque in mice include the aortic root (at the three valve cusps), the descending aorta, and the brachiocephalic/innominate artery. Analysis of aortic root and brachiocephalic plaques are typically carried out after transverse sectioning of the appropriate tissue into thin sections (microns in thickness) captured onto slides followed by staining. However, as the sections are typically 5–10 μm thick, as is necessary for contrast imaging, only a small fraction of the tissue is observed in two dimensions [6]. Therefore, *en face* preparations are also used to visualize the whole aorta from the heart to the common iliac arteries, allowing analysis of plaque distribution and quantification [6]. This approach enables quantification of lesions and their distribution, providing a more global and accurate view of the extent of atherosclerosis.

1.1 Hematoxylin and Eosin (H&E)

The hematoxylin and eosin (H&E) stain is a principal and popular stain in histology [7, 8]. This popularity comes from its simplicity and ability to provide a very clear image of tissue structure. The combination of H and E allows distinguishing between different tissue organelles, where all the basophilic organelles (such as nuclei, rough endoplasmic reticulum, and ribosomes) are stained a deep purple to blue color, and eosinophilic organelles (such as cytoplasm, smooth endoplasmic reticulum, and cell membrane) are stained pink [8]. Hematoxylin is a natural dye that is colorless until oxidized by atmospheric oxygen to hematein when combined with a mordant, such as iron, chromium, or aluminum. This binding leads to the formation of a positively charged dye–mordant complex that is reddish brown in color [9]. During staining, the positively charged metal ion in the hematein has affinity to the negatively charged phosphate groups in DNA [10]. On the other hand, eosin, eosin Y (eosin yellowish) in particular, is an artificial dye derived from highly fluorescent fluorescein [8, 11]. Due to its acidity (negative charge nature), it binds to positively charged elements in stained tissue, such as cytoplasm and ECM [8]. Application of eosin generates three shades of pink which helps to distinguish between different tissues, cells, or organelles; for example, dark reddish orange indicates red blood cells, pale pink signifies collagen and bright pink illustrates/signifies smooth muscle cells [10].

1.2 Oil Red O

Oil Red O (ORO) solution is a red diazo dye that is strongly solubilized in hydrophobic and natural fat [10]. ORO only stains neutral lipids and hydrophobic components of cells (e.g., triglycerides, cholesterol esters, and diacylglycerols) without staining the

amphiphilic lipids in cell membranes (such as phospholipids and sphingolipids) [12]. Although a key limitation is that only neutral lipids are stained, ORO is extensively used in research for assessing the presence of lipid droplets in samples due to its high selectivity and numerous other advantages, as it is harmless, low-cost and timesaving because staining can be carried out within a couple of hours. Moreover, it can be used with different sample types, whether the tissue is fresh, frozen, or formalin fixed [12]. However, it is important to note that paraffin-embedded tissue samples cannot be used for ORO staining [10, 13].

1.3 Masson's Trichrome

There are many different stains commercially available for staining collagen fibers in atherosclerosis research, but the most commonly used stain is Masson's Trichrome. This stain is suitable for a range of tissues, including epithelial, cardiac, and muscle tissues, whether using formalin-fixed, paraffin-embedded sections or frozen sections. Three dyes are used to selectively stain muscle, collagen fibers, fibrin, and erythrocytes; collagen fibers are stained blue, nuclei stained black, and background is stained red. The porousness of the tissue determines the size of the dye molecule that colors it. Generally, the less porous tissues are colored by the smallest dye molecule; whenever a dye of large molecular size is able to penetrate, it will do so at the expense of the smaller molecule. Others suggest that tissue is stained first with the acid dye, Biebrich Scarlet, which binds with the acidophilic tissue components. Phospho acids then cause the less permeable components to retain the red color while this red color is removed from the collagen, which simultaneously binds with the aniline blue. Together, these different staining methods enable measurements of the vessel, lumen and plaque sizes, aortic plaque distribution, and analysis of plaque lipid and collagen content [14, 15].

2 Materials

2.1 Mouse Dissection

1. CO_2 in a chamber.
2. 70% (v/v) ethanol.
3. Chlorhexidine surgical scrub.
4. Surgical board.
5. Straight forceps with serrated tips.
6. Straight fine forceps.
7. Straight blunt scissors.
8. Straight sharp fine scissors.
9. 26G needles.
10. Gravity perfusion system (~120 cm pressure).
11. Saline solution containing 40 U/mL heparin.

12. Ornithine carbamoyltransferase (OCT).
13. Cryomolds (15 × 15 × 5 mm).
14. Dry ice (*see* **Note 1**).
15. Paper towels.
16. Plastic dish.

2.2 En Face *Staining*

1. 1× Phosphate-buffered saline (PBS): 137 mM NaCl, 10 mM Na_2HPO_4, 2.7 mM KCl, 1.8 mM KH_2PO_4, pH 7.4.
2. 4% (w/v) Paraformaldehyde (PFA) solution: 4 g of PFA, 2 M sodium hydroxide (NaOH), 50 mL PBS (*see* **Note 2**).
3. Sudan IV: 1 g Sudan IV powder dissolved in 100 mL of 70% (v/v) ethanol and 100 mL of acetone (*see* **Note 3**).
4. 0.5% (w/v) Oil Red O (ORO) solution in propylene glycol (*see* **Note 3**).
5. Blunt end minutien insect pins.
6. Dark surface (e.g., black wax).
7. Digital camera.
8. Measuring ruler (*see* **Note 4**).
9. Iris scissors.
10. Fine scissors.
11. Surgical forceps.
12. Dissecting microscope.

2.3 *Sectioning*

1. Cryostat.
2. Poly-L-lysine coated microscope slides or Superfrost Plus slides (75 × 25 × 1 mm).
3. Chuck (*see* **Note 5**).
4. Slide holder box.
5. OCT.
6. Stainless steel microtome blades (e.g., Type S 35).
7. Pencil.
8. Microscope.
9. Small, fine paintbrush.

2.4 *General Staining*

1. Glass coplin staining jars.
2. Distilled water.
3. Tap water.
4. Graded ethyl alcohol (ethanol): 70%, 95%, and 100% (v/v).
5. Absolute xylene (*see* **Note 6**).
6. Glass coverslips (1.0–1.5 thickness).

7. Plastic disposable Pasteur pipettes.
8. Clear (colorless) nail varnish or equivalent.
9. Brightfield (light) microscope.
10. Fiji (ImageJ) software.

2.5 H&E Staining

1. Harris-modified hematoxylin solution (*see* **Note 3**) (e.g., 7 g/L concentration from Sigma) or another regressive, general purpose, ready-to-use hematoxylin solution.
2. 0.5% (w/v) Eosin Y solution (aqueous) for microscopy.
3. DPX mountant for histology.
4. Class II laminar-flow cabinet (fume hood).

2.6 ORO Staining

1. 4% (w/v) Paraformaldehyde: 4 g paraformaldehyde (PFA), 2 M sodium hydroxide (NaOH), 50 mL 1× PBS, pH 7.2–7.4 (*see* **Note 3**).
2. Water bath set to 65 °C.
3. Harris-modified hematoxylin solution.
4. 0.5% Oil Red O (ORO) solution in propylene glycol (*see* **Note 3**).
5. Absolute 1,2-propanediol (propylene glycol).
6. 85% (v/v) propylene glycol in distilled water.
7. Aqueous mounting medium (e.g., Fluoromount G).

2.7 Masson's Trichrome Staining

1. Saturated picric acid: 1.3% (w/v) in water.
2. 37–40% Formaldehyde.
3. Glacial acetic acid.
4. Hematoxylin powder.
5. 29% (v/v) Ferric chloride solution in water.
6. Concentrated hydrochloric acid (HCl).
7. 1% (w/v) aqueous Biebrich scarlet.
8. 1% aqueous acid fuchsin in 95% ethanol.
9. 5% (w/v) Phosphomolybdic acid.
10. 5% (w/v) Phosphotungstic acid.
11. Aniline blue powder.
12. Resinous mounting medium.
13. Bouin's fixative solution: 75 mL of saturated picric acid, 25 mL of formaldehyde (37–40%), 5 mL of glacial acetic acid. Mix well. Solution is stable for 2 years (*see* **Note 7**).
14. Weigert's Iron Hematoxylin working solution: Stock solution A: 1 g of hematoxylin in 100 mL of 95% (v/v) ethanol. Mix well, solution is stable for 1 year (*see* **Note 6**). Stock solution B: 4 mL of ferric chloride solution, 95 mL of distilled

water, and 1 mL of concentrated hydrochloric acid. Mix well, solution is stable for 1 year (*see* **Note 8**). Mix equal parts of stock solution A and B. Solution is stable for 3 months.

15. Biebrich Scarlet-Acid Fuchsin solution: 90 mL of Biebrich scarlet, 10 mL of acid fuchsin (1%), 1 mL of glacial acetic acid. Mix well (*see* **Note 9**).
16. Phosphotungstic-phosphotungstic acid solution: 25 mL of phosphomolybdic acid (5%), 25 mL of phosphotungstic acid (5%). Mix well (*see* **Note 9**).
17. Aniline blue solution: 2.5 g of aniline blue powder, 2 mL of glacial acetic acid, 100 mL of distilled water. Mix well. Solution is stable for 6 months (*see* **Note 9**).
18. 1% (v/v) acetic acid solution: 1 mL of glacial acetic acid, 99 mL of distilled water. Mix well. Solution is stable for 1 year (*see* **Note 9**).
19. Water bath or incubator at 56 °C.

3 Methods

3.1 Mouse Dissection

All animal procedures should be performed with the approval of the Institutional Animal Care and carried out using protocols and guidelines of Institute and Government taking 3Rs into account.

1. Sterilize surgical tools and dissection area with 70% ethanol and chlorhexidine surgical scrub, finishing with 70% ethanol.
2. Euthanize the mouse via increasing levels of CO_2 in a chamber (inhalation overdose) (*see* **Note 10**).
3. Place the mouse in supine position on a surgical board covered with a sufficient layer of paper towels to soak up any fluids that leak.
4. Bind upper and lower limbs outwardly to the board using 26G syringe needles.
5. Sterilize the external surface of the mouse using a small amount of 70% ethanol.
6. Pinch skin using forceps and make a midline incision using scissors to expose the abdominal cavity.
7. Dissect up into the thoracic cavity, going through the diaphragm.
8. Bisect the thoracic cavity, cutting the ribs laterally to the sternum to expose the thymus, heart, and lungs.
9. Remove the lungs and esophagus for full access to the heart.

10. Create a small nick in the vena cava or right atrium, or cut one of the femoral arteries, to enable draining of the blood (*see* **Note 11**).
11. Insert a 26G needle attached to a gravity perfusion setup (120 cm water pressure) into the apex of the left ventricle and perfuse the circulatory system with saline solution containing 40 U/mL heparin (*see* **Notes 12** and **13**).
12. Continue perfusion until the saline solution that is flowing out from the cut becomes clear.
13. Soak up any residual fluid in the dissection area using paper towels.
14. Cut open the peritoneal cavity using sharp fine scissors and forceps to expose the abdominal organs and extend the incision length to the suprapubic area of the mouse.
15. Remove the intestines, liver, kidney, stomach, spleen, and any other obstructing tissues for better visualization of the entire descending aorta.
16. Lift the heart at the apex with forceps and cut the left and right carotid arteries and the left subclavian artery near the descending aorta/spine.

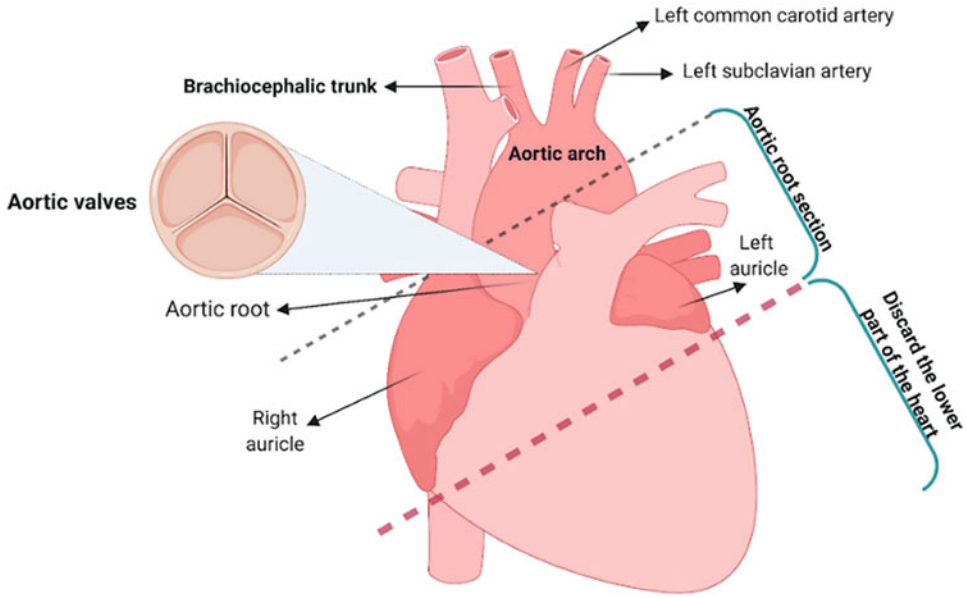

Fig. 1 Scheme for guiding aorta and aortic root sectioning. Cut away approximately 60% of the heart as indicated by the red dotted line. Mount the apical (top) part of the heart in a cryomold with OCT and flash freeze to enable cryosectioning and detailed morphometric analyses of atherosclerotic lesions in the aortic root at the three valve cusps. Diagram created using biorender.com

17. Dissect out the heart and transfer to a clean plastic dish.
18. Cut away the lower ~60% of the ventricular mass (*see* Fig. 1).
19. Embed the upper cardiac portion in OCT with the aortic arch positioned upwards in a cryomold and immediately snap freeze in dry ice. Store at −80 °C until sectioning.

3.2 En Face Preparation and Staining of the Aorta

1. Remove the entire length of the aorta from the heart to the iliac bifurcation carefully using surgical forceps and iris scissors (*see* **Note 14**).
2. Store the dissected aorta in 4% PFA for 24–48 h for fixation.
3. Carefully clean the aorta by removing the perivascular adipose and adventitial tissue using fine scissors under a dissecting microscope (*see* **Notes 15** and **16**).
4. Reveal the intimal surface by making a longitudinal cut using the fine scissors in the coronal plane through the inner curvature and down the anterior aspect of the aorta.
5. Make another cut through the greater curvature of the aortic arch to the subclavian branch, including the brachiocephalic artery.
6. Using the blunt end of minutien insect pins, pin the tissue onto a dark surface (e.g., black wax) to enable clear visualization of the aortic architecture (*see* **Notes 17** and **18**).
7. Place a drop of PBS onto the aorta to prevent drying.
8. If required, stain neutral lipids via incubation with Sudan IV for 10–15 min at room temperature or alternatively, with 0.5% ORO solution for 2–4 h at 25 °C (lipids are stained an orange-red color to enable better plaque visualization) (*see* **Note 19**).
9. Capture images of the pinned aorta with a measuring ruler for scale using a digital camera (*see* **Notes 20** and **21**).

3.3 Sectioning Using a Cryostat

1. In the cryostat set to −20 °C, remove the frozen heart in OCT from the cryomold and mount onto a chuck, with the top of the heart exposed, by freezing with sufficient OCT for sample adhesion.
2. Add more OCT if necessary, to cover the entirety of the sample (*see* **Note 22**).
3. Secure the sectioning blade into the blade holder.
4. Adjust the distance between the chuck holder and the blade holder.
5. Adjust the temperature of the cryostat for best sectioning performance, usually between −16 and −20 °C (*see* **Notes 23** and **24**).

6. Label slides using a pencil (*see* **Note 25**).
7. Cut the sample at 30 μm, checking periodically under a microscope to monitor descent of the aortic root to identify the origin of the valve leaflets.
8. Take sequential sections, 8–10 μm thickness, of the aortic root, from the origin of the aortic valves to the ascending aorta and capture onto the slides (*see* **Notes 26–29**).
9. Allow slides to air dry at room temperature for 1 h (*see* **Note 30**).
10. Store slides in a slide holder box at −80 °C until use.

3.4 H&E Staining

Ensure all glassware is cleaned and wiped dry before conducting all staining methods. All steps should be carried out at room temperature unless otherwise specified.

1. Remove slides containing unfixed sections from the freezer and thaw to room temperature.
2. Rinse slides two to three times in tap water.
3. Fill glass coplin staining jars with Harris-modified hematoxylin solution and incubate slides for 5 min (*see* **Note 31**).
4. Rinse in running tap water until the water becomes clear to remove the excess hematoxylin (*see* **Note 32**).
5. Dip the slides in a coplin jar filled with 95% ethyl alcohol.
6. Stain with eosin solution for 10 min.
7. Dehydrate samples by immersing slides in 95% ethyl alcohol for 5 min.
8. Transfer the slides to a coplin jar containing 100% ethyl alcohol for 5 min (repeat this step twice).
9. Transfer the slides to a coplin jar containing absolute xylene for 5 min (repeat this step twice using fresh xylene each time) (*see* **Note 33**).
10. Mount with DPX mountant for histology by adding 1 drop for each section using a plastic disposable Pasteur pipette.
11. Place coverslip on top and gently apply pressure onto the coverslip until the DPX reaches the edges of the coverslip and no air bubbles remain.
12. Seal with clear nail varnish.
13. Allow slides to dry at room temperature for a few hours.
14. Visualize using a brightfield microscope using an appropriate magnification (*see* **Note 34**).

3.5 ORO Staining

1. Preheat ORO solution to 65 °C for 1 h prior to use (*see* **Note 35**).

2. Remove frozen slides from the freezer to thaw at room temperature for 10 min.
3. Fix sections by immersing in ice-cold 4% PFA in a coplin staining jar for 5 min.
4. Rinse the slides in a coplin jar containing distilled water for 5 min (repeat twice).
5. Fill a glass coplin staining jar with Harris-modified hematoxylin solution and incubate the slides for 3–5 min.
6. Wash off excess hematoxylin stain by running under tap water until the water clears (*see* **Note 32**).
7. Rinse the slides in a coplin jar containing fresh distilled water for 5 min.
8. Incubate slides in absolute propylene glycol in another coplin staining jar for 5 min.
9. Stain section with ORO for 30 min at 65 °C.
10. Transfer slides to 85% propylene glycol for 5 min.
11. Rinse slides in distilled water for 5 min and repeat this step again.
12. Add 1 drop of aqueous mountant to each section using a plastic disposable Pasteur pipette.
13. Place coverslip on top and gently apply pressure onto the coverslip until the mountant reaches the edges of the coverslip and no air bubbles remain.
14. Seal the edges of the coverslip with clear nail polish.
15. Allow slides to dry at room temperature for a few hours.
16. Capture images of the sections using a light microscope (*see* **Note 36**).

3.6 Masson's Trichrome Staining

1. For formalin-fixed, paraffin-embedded sections, deparaffinize sections (by placing slides in a 55 °C oven for 10–30 min to melt the paraffin and passing the slides through 2 changes of xylene for 5 min each) and rehydrate by passing through 100%, 95%, and 70% ethyl alcohol for 5 min each.
2. Wash in distilled water.
3. For formalin-fixed tissue, incubate in Bouin's fixative solution for 1 h at 56 °C to re-fix the sections and improve staining quality (*see* **Note 37**).
4. Rinse in tap water for 5–10 min to remove the yellow color (picric acid).
5. Fill a coplin staining jar with Weigert's iron hematoxylin working solution and incubate the slides in the solution for 10 min.

6. Rinse in running warm tap water (approximately 25 °C) for 5–10 min.
7. Rinse in distilled water.
8. Fill a coplin staining jar with Biebrich scarlet-acid solution and incubate the slides for 10–15 min (*see* **Note 38**).
9. Wash in distilled water.
10. Fill a coplin staining jar with phosphomolybdic phosphotungstic acid solution and incubate the slides for 10–15 min or until the red color disappears.
11. Transfer slides directly (without rinsing) to another coplin jar containing aniline blue solution and stain the slides for 5–10 min.
12. Rinse briefly in distilled water.
13. Incubate slides in 1% acetic acid solution in another coplin jar for 2–5 min.
14. Wash in distilled water.
15. Dehydrate quickly by passing slides through 95% ethyl alcohol and 100% ethyl alcohol (to wipe off Biebrich scarlet-acid fuchsin staining) in separate coplin jars, and clear in xylene, all 2–5 min each.
16. Mount with resinous mounting medium.
17. Place coverslip on top and seal the edges of the coverslip with clear nail polish.
18. Allow slides to dry at room temperature for a few hours.
19. Capture images of sections using a light microscope.

3.7 Image Analysis Using ImageJ

1. Download and open Fiji (ImageJ) software.
2. Open image to be analyzed (*see* **Note 39**).
3. Draw outlines around the vessel, lumen and all visible plaques, as accurately as possible using the "Oval" (or another appropriate) selection brush tool.
4. Save these templates separately as ROI files (use "Ctrl" + "T" shortcut to bring up the ROI Manager window) (*see* **Note 40**).
5. To set the scale bar, draw a straight line (select straight tool from ImageJ tool bar) to create a line along the length of the scale bar as accurately as possible and then measure it using "Ctrl" + "M" shortcut.
6. Next choose "Analyze"- > "Set Scale." The length of the line is automatically entered in pixels as "Distance in Pixels."
7. Enter the length of the scale bar in "Known Distance" as it is shown in your image.
8. Change "Unit of Length" as appropriate (e.g., "mm," "um") and click "OK." The software will automatically then change the image size to mm size (*see* **Note 41**).

9. Measure the templates (i.e., drawings of the vessel, lumen, and plaque) by selecting these from the ROI manager and using the "Ctrl" + "M" shortcut. This will give measurements of the vessel, lumen, and plaque to be used for subsequent analysis.
10. To quantify areas of positive staining, click- > "Color"-- > "Dichromacy"- > "Deuteranope"- > "OK"; a greyscale version of the image will appear alongside the original.
11. Convert the image to 8-bit format; click "Image"- > "Type"-- > "8-bit" (*see* **Note 42**).
12. Adjust the threshold range of the image until only the areas of positive staining are selected (by comparing with the original image); click "Image"- > "Adjust"- > "Threshold" and adjust the sliders/settings (*see* **Notes 43–45**).
13. Apply this threshold to the image (*see* **Note 46**).
14. Ensure the plaque drawing is still applied (can be done from the ROI Manager) to the image (*see* **Note 47**).
15. Click "Analyze"- > "Analyze Particles" and ensure "Summarize" is ticked before clicking "OK."
16. The results window containing the "%Area" value represents the percentage of lipid staining in the plaque.

4 Notes

1. Dry ice is sufficient for snap freezing samples in OCT but liquid nitrogen can also be used.
2. Store the prepared PFA solution at 4 °C and keep ice cold during use.
3. Protect from light, store in a darkened bottle/cover the bottle with foil.
4. This is for scale, optional.
5. This is used to mount the frozen sample for sectioning; the size is custom to the cryostat.
6. Flammable, avoid contact and inhalation.
7. Carcinogenic and irritant, handle with care.
8. Corrosive, avoid contact and inhalation.
9. Avoid contact and inhalation.
10. Other methods of sacrifice (Schedule 1) include exposing the mouse to a supratherapeutic dose of an anesthetic. A method should be used that does not damage organs of interest and required for analysis (e.g., aorta, brachiocephalic artery, and heart). Death should be confirmed via a secondary method (e.g., ensuring lack of pulse or response to painful or aversive stimuli).

11. Mouse vessels are small in size and hence fragile, so added care should be taken during handling, surgical extraction, preparation for staining and microscopy, to prevent damage.
12. The arterial endothelium is particularly fragile; any excessive mechanical force will cause damage to endothelial cells. If the vessel is perfused with too much force, endothelial cells may break or detach from the vessel wall, and so perfusion using a hand-operated syringe should be avoided.
13. It is recommended to use a perfusion pressure slightly below the measured arterial pressure of the mouse.
14. *In situ* endothelial cells can also become damaged if the vessel is stretched during preparation, especially during harvesting of the vessel or when removing surrounding adipose tissue attached to the adventitia.
15. Leaving the freshly dissected aorta in saline for a few hours can facilitate cleaning.
16. Atherosclerotic lesions can be easily displaced during processing, particularly for mouse arterial tissues extracted after bone marrow transplantation. Lesions are especially prone to dislodgement during tissue handling (e.g., when removing the adventitia and cutting it open to reveal the underlying intimal surface).
17. Atherosclerotic lesions tend to be the largest in size on the inner curvature and at the branches of the brachiocephalic and left carotid arteries.
18. It is possible to conduct *en face* preparations even after experimental manipulation, such as a partial ligation of the carotid artery.
19. Large atherosclerotic plaques can be seen without staining.
20. The aorta can also be stained with ORO and visualized using a stereo microscope.
21. After *en face* preparation of the aorta, imaging and staining must be done within 3 days.
22. Ensure that the entire sample is completely covered by OCT as excess OCT can just be trimmed off using the Cryostat, rather than risk trimming away the sample prematurely.
23. The temperature of the cryostat may need to be adjusted and optimized for the sample depending on the tissue type but generally ranges from −16 °C to −20 °C.
24. Curling of the freshly cut sections suggests the temperature is too low while the section will adhere to the blade if the temperature is too high—adjust accordingly.

25. Labeling of the slides should be done using a pencil to prevent wash off during staining procedures, as is possible with permanent marker.
26. It may be useful to use a paintbrush to guide the sections as they are cut.
27. Appearance of the valve leaflets can be used as a reference point to increase consistency between samples.
28. Alternatively, sections can be oriented relative to the disappearance of the aortic valve cusps to represent lesion area throughout the root.
29. There is considerable regional difference in size of lesions in the aortic root, and so it is recommended to perform measurement of lesion size throughout the aortic root.
30. Sections should be allowed to dry at room temperature for at least 30 min; 1 h is recommended.
31. Solutions can be reused up to 10 times, after which they should be replaced with fresh solutions.
32. Do not subject slides directly to the water stream.
33. This step should be carried out in a fume hood.
34. Weak hematoxylin staining can be due to inadequate staining time or having too thin a section.
35. ORO solution may form precipitates when exposed to air; filter these from the solution before use by passing through a filter. Avoid exposing ORO solution to air where possible during the staining process.
36. Staining with ORO may vary between batches. This is as the efficacy of the ORO solution may be affected by exposure to light, repeated heating and/or repeated use. Improve staining quality consistency by using fresh ORO solution where possible or only re-using ORO solution for up to a maximum of 3–5 times.
37. Fixing with Bouin's solution is optional although preferred, as it improves staining quality.
38. Solution can be reused a few times although fresh solutions may yield better quality staining.
39. Analysis should be carried out in a blinded fashion where possible to minimize any bias/unconscious bias.
40. Saving the template as an "ROI" file avoids the need for repeated drawings and improves consistency should there be a need to repeat analysis in the future.
41. It is possible to convert measurements from pixels to μm^2 or mm^2 by carrying out a scale conversion manually, or by using the software.

42. Threshold adjustment can only be performed on black and white images so 8-bit conversion is required if the image is in color (i.e., RBG format).
43. Note that this method is subjective and affected by how the staining is perceived by the user. Analysis should hence be done in a blinded manner where possible to reduce any potential unconscious bias.
44. Staining may vary between batches. Adjustment of the threshold settings may be required between batches, but these settings should be consistent and uniform for images of the same batch.
45. Parameters used by imaging software to acquire measurements should be defined in detail; thresholds applied to quantify and detect areas of positive staining should be standardized and consistent per batch of slides.
46. There are other ways to analyze images with multicolor staining (i.e., ORO and Masson's Trichrome staining). For ORO-stained images, choose "Image" from ImageJ bar- > color- > color deconvolution, new window will bring up: choose the "FastRed FastBlue DAB" vector and click "OK." (Note that various vectors are available in ImageJ and the most appropriate one should be selected based on the staining method). ImageJ then creates 3 different versions of your image, separating the colors. Close the top two images using the "X" button and keep the one that looks reddish/pinkish (i.e., the image that picks up the red staining the best). Use this image to adjust the threshold by clicking on "Image"- > Adjust- > Threshold. Use the default threshold ImageJ comes up with (no need to adjust the sliders or threshold manually) and click "apply." After that, apply the drawing of plaque to the image again. Click on "Analyze" - > analyze particles. This will bring up a window, make sure "summarize" is ticked and click "OK." A results summary window appears; the "%Area" value correlates to % positive staining of plaque provided that the plaque template is applied to the image.
47. The software will analyze the entire image if no templates are applied to the image or no areas of interest are highlighted.

Acknowledgements

We thank the British Heart Foundation for financial support (grants PG/16/25/32097 and FS/17/75/33257). AA and RA received PhD studentships from the Kingdom of Saudi Arabia (Jeddah University).

References

1. Sitia S, Tomasoni L, Atzeni F et al (2010) From endothelial dysfunction to atherosclerosis. Biochim Biophys Acta 1852(7):1498–1510
2. Bergheanu SC, Bodde MC, Jukema JW (2017) Pathophysiology and treatment of atherosclerosis: current view and future perspective on lipoprotein modification treatment. Neth Heart J 25(4):231–242
3. Virani SS, Alonso A, Aparicio HJ et al (2021) Heart disease and stroke statistics - 2021 update. Circulation 143(8):e254–e743
4. Chan Y-H, Ramji DP (2020) A perspective on targeting inflammation and cytokine actions in atherosclerosis. Future Med Chem 12(7): 613–626
5. Moss JWE, Ramji DP (2016) Cytokines: roles in atherosclerosis disease progression and potential therapeutic targets. Future Med Chem 8(11):1317–1330
6. Ko KA, Fujiwara K, Krishnan S et al (2017) *En face* preparation of mouse blood vessels. J Vis Exp 2017(123):55460
7. Fischer AH, Jacobson KA, Rose J et al (2008) Hematoxylin and eosin staining of tissue and cell sections. Cold Spring Harb Protoc 2008(2):prot4986
8. Chan JK (2014) The wonderful colors of the hematoxylin-eosin stain in diagnostic surgical pathology. Int J Surg Pathol 22(1):12–32
9. Titford M (2005) The long history of hematoxylin. Biotech Histochem 80(2):73–78
10. Andres-Manzano MJ, Andres V, Dorado B (2015) Oil red O and hematoxylin and eosin staining for quantification of atherosclerosis burden in mouse aorta and aortic root. Methods Mol Biol 1339:85–99
11. Robertson TA, Bunel F, Roberts MS (2013) Fluorescein derivatives in intravital fluorescence imaging. Cell 2(3):591–606
12. Mehlem A, Hagberg CE, Muhl L et al (2013) Imaging of neutral lipids by oil red O for analyzing the metabolic status in health and disease. Nat Protoc 8(6):1149–1154
13. Kraus NA, Ehebauer F, Zapp B et al (2016) Quantitative assessment of adipocyte differentiation in cell culture. Adipocytes 5(4): 351–358
14. Onyije F, Ngokere A, Ligha A et al (2017) Computer-assisted image analysis in the diagnosis of gynaecological lesions: a quantitative and comparative investigation of haematoxylin-eosin with special dyes on tissue. J Cancer Res Pract 4(1):5–13
15. Saleh S, Hanna G, El-Nabi SH et al (2020) Dapagliflozin, a sodium glucose cotransporter 2 inhibitors, protects cardiovascular function in type-2 diabetic murine model. J Genet 99:46

Chapter 30

Monitoring Cellularity and Expression of Key Markers in Atherosclerotic Plaques

Yee-Hung Chan, Reem Alotibi, Alaa Alahmadi, and Dipak P. Ramji

Abstract

Atherosclerotic plaques are highly diverse and heterogeneous structures, even within the same individual, and can vary depending on its anatomical location within the vascular bed. Early in the disease and throughout its progression, immune cells infiltrate the lesion, contributing to the plaque phenotype via different mechanisms. Detailed characterization of constituent cell populations within plaques is hence required for more accurate assessment of disease severity and inflammatory burden. A wide range of fluorophore-conjugated antibodies targeted to key cell types implicated in all stages of the disease are commercially available, enabling visualization of the dynamic cellular landscape present within lesions. This chapter describes the use of immunofluorescence staining of atherosclerotic plaque sections to study plaque cellularity and expression of key markers.

Key words Immunofluorescence, Antibodies, Macrophages, T cells, Smooth muscle cells

1 Introduction

Atherosclerotic plaques typically consist of a lipid core encapsulated by a fibrous cap (made of connective tissue and extracellular matrix (ECM) proteins) with numerous immune cells, predominantly pro-inflammatory M1 macrophages and T lymphocytes [1, 2]. The phenotype of atherosclerotic plaques can provide valuable information regarding disease progression and severity. For example, stable plaques tend to contain a smaller atheromatous core less rich in lipids and encapsulated by a thick fibrous cap coinciding with the presence of alpha smooth muscle actin $(\alpha SMA)^+$ smooth muscle cells (SMCs) and abundant ECM macromolecules (e.g., collagens, elastins, and proteoglycans) [3]. Over time, evolution of the atherosclerotic plaque is facilitated by persisting, non-resolving inflammation, increasing cell death and promoting the growth of the necrotic core [4]. Eventual degradation of the fibrous cap is facilitated via enhanced expression and activity of

Dipak P. Ramji (ed.), *Atherosclerosis: Methods and Protocols*, Methods in Molecular Biology, vol. 2419,
https://doi.org/10.1007/978-1-0716-1924-7_30,
© The Author(s), under exclusive license to Springer Science+Business Media, LLC, part of Springer Nature 2022

matrix metalloproteinase (MMP) enzymes, such as MMP-2 and MMP-9 [5]. Plaques that are vulnerable to rupture are typically surrounded by a thin, unstable and inflamed fibrous cap (<60 μm) abundant in monocytes/macrophages and T cells [6]. Inflammatory processes and activated immune cells can negatively affect the fibrous cap by impeding SMC interstitial collagen synthesis, promoting collagenase activity, inhibiting SMC proliferation and enhancing cell death [7]. This results in degradation of key structural components, compromised stability, and the eventual breakdown of the fibrous cap [8]. Therefore, detailed characterization of plaque cellularity and main components using key markers allow the delineation of plaque burden and inflammation. This is necessary when evaluating the efficacy of potential anti-atherogenic agents in attenuating atherogenesis and promoting plaque stability, as well as providing more information regarding plaque status beyond lipid content and size.

Immunofluorescence (IF) staining has been abundantly used in research, including atherosclerosis research, as this technique enables visualization of numerous components in any given tissue or cell type. This method uses antibodies targeted to specific markers (i.e., epitopes) expressed by specific tissues/cell types. Examples of markers that can be used to detect key cell types implicated in atherosclerosis are shown in Table 1. However, it is also possible to stain for the different cell types using non-fluorescent antibodies, such as horseradish peroxidase (HRP) or alkaline phosphate conjugated secondary antibodies. These enzymes catalyze a color-producing reaction to enable visualization via substrates such as 3,3′-diaminobenzidine (DAB) and other chromogens. In IF, antibodies are conjugated to a fluorophore (rather than an enzyme) which can be visualized using a fluorescence microscope, as the fluorescent label emits upon photoexcitation. Fluorescent detection has various advantages over chromogenic detection, including easier multiplexing and better target co-localization while the staining protocol is simpler, involving less steps. There are two different types of IF assays: direct (primary) and indirect (secondary). Although the direct method is more rapid, as the fluorophore-conjugated primary antibody reacts directly with the target epitope, the indirect method is more commonly used for its high sensitivity, possibility for signal amplification and ability to even detect several targets in the same sample. The indirect IF method involves the use of a primary antibody that binds to the target epitope, and a secondary antibody tagged with a fluorophore that recognizes and binds to the primary antibody (*see* Fig. 1). IF staining using the indirect approach [9] to detect the presence of key cell types within atherosclerotic plaques will be described in this chapter.

Table 1
Example of markers used to identify key cell types in atherosclerotic plaques

Cell type	Marker(s)
Monocytes	Ly6C, CD115, CCR2
Macrophages	CD11b, MOMA-2, MAC-1/2/3, F4/80
M1 macrophages	CD68, CD80, CD64, CD16, CD32, iNOS
M2 macrophages	CD163, CD206
T cells	CD3
Cytotoxic T cells	CD8, CD45, CD54
Helper T cells	CD4, CD191, CCR6
Smooth muscle cells	αSMA, SMC myosin heavy chain (MYH11), myocardin, smoothelin, SM22α/transgelin (TAGLN)
B cells	B220/CD45R, CD138

Abbreviations: *Ly6C* lymphocyte antigen 6 complex, *CD* cluster of differentiation, *CCR* C-C chemokine receptor type, *M1* classically activated, pro-inflammatory, *M2* alternatively activated, *MOMA* monocyte and macrophage marker, *MAC-1/2/3* macrophage-1/2/3 antigen, *F4/80* the murine homologue of epidermal growth factor-like module-containing mucin-like hormone receptor-like 1 (EMR1), *iNOS* inducible nitric oxide synthase, *αSMA* alpha smooth muscle actin, *SMC* smooth muscle cell

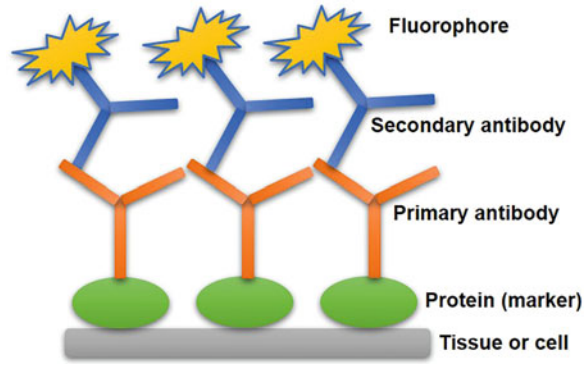

Fig. 1 Diagrammatic representation of the mechanism behind indirect immunofluorescence staining. A primary antibody recognizes and binds to a target epitope on the cell or tissue; a secondary antibody tagged with a fluorophore recognizes and binds to the primary antibody. This enables visualization of the fluorophore using a fluorescent microscope

2 Materials

1. Glass coplin staining jars.
2. Slides containing frozen, unfixed sections (8–10 μm thickness) (*see* **Note 1**).

3. 1× phosphate buffered saline (PBS): 137 mM NaCl, 10 mM Na_2HPO_4, 2 mM KH_2PO_4, 2.7 mM KCl, pH 7.2–7.4.
4. 99% glacial acetone (*see* **Note 2**).
5. PAP pen or another wax hydrophobic barrier pen.
6. Bovine serum albumin (Fraction V; BSA) (*see* **Note 3**).
7. Primary and secondary antibodies (including isotype controls) targeted to markers of cells/components of interest (refer to Table 2 for specific examples).
8. Slide staining tray(s), black with black lid.
9. Distilled water.
10. 70% (v/v) and 100% ethyl alcohol (ethanol).
11. Sudan black powder.
12. Sudan black solution: 0.3% (w/v) Sudan black powder dissolved in 70% (v/v) ethanol (diluted with distilled water) (*see* **Note 4**).
13. Blocking buffer: 5% (v/v) animal serum in PBS containing 1% (w/v) BSA (*see* **Notes 5** and **6**).
14. Antibody dilution buffer: 1% (w/v) bovine serum albumin (BSA, fraction V) in PBS (*see* **Note 6**).
15. Mounting medium (e.g., Fluoroshield™ with DAPI or Vectashield).
16. Slide holder box.
17. Fridge or equivalent for incubation at 4 °C.
18. Glass coverslips (1.0–1.5 mm thickness).
19. Clear (colorless) nail varnish.
20. ImageJ image analysis software or equivalent.
21. Epifluorescence microscope.

3 Method

3.1 Staining

1. Remove slides from the freezer and allow to thaw at room temperature for approximately 10 min.
2. Place slides in a coplin jar filled with glacial acetone and incubate slides for 10 min to fix the sections (*see* **Note 7**).
3. Wash slides twice with PBS for 5 min in separate coplin jars to remove residual acetone (*see* **Notes 8** and **9**).
4. Draw a few circles around each individual section on the slide carefully and accurately using the PAP pen (*see* **Note 10**).
5. Transfer slides to the slide staining tray and carry out staining from this step onwards.

Table 2
Example of antibody concentrations used to stain for CD3$^+$ T cells, αSMA$^+$ smooth muscle cells, and MOMA-2$^+$ macrophages

Primary antibody	Isotype control	Secondary antibody
Rabbit anti-CD3 epsilon (ab187281)	Rabbit IgG (ab171870)	Goat anti-rabbit IgG H&L AF488 (ab150077)
Stock: 0.2 mg/mL	Stock: 1 mg/mL	Stock: 2 mg/mL
Dilution 1:100	Dilution 1:500	Dilution 1:500
Working conc: 0.002 mg/mL	Working conc: 0.002 mg/mL	Working conc: 0.004 mg/mL
Rabbit anti-mouse αSMA (ab5694)		Donkey anti-rabbit IgG AF488 (ab150073)
Stock: 0.2 mg/mL		Stock: 2 mg/mL
Dilution 1:100		Dilution 1:500
Working conc: 0.002 mg/mL		Working conc: 0.004 mg/mL
Rat anti-mouse MOMA-2 (ab33451)	Rat IgG2b (ab18541)	Goat anti-rat IgG AF488 (ab150157)
Stock: 0.5 mg/mL	Stock: 0.5 mg/mL	Stock: 2 mg/mL
Dilution 1:100	Dilution 1:100	Dilution 1:500
Working conc: 0.005 mg/mL	Working conc: 0.005 mg/mL	Working conc: 0.004 mg/mL

All antibodies are available from Abcam with accompanying catalog numbers included in brackets beginning with "ab." Abbreviations: *CD* cluster of differentiation, *IgG* immunoglobulin G, *H&L* heavy and light chains, *AF* Alexa Fluor, *αSMA* alpha smooth muscle actin, *MOMA-2* monocyte and macrophage marker

Table 3
Filters required to visualize most commonly used fluorophores on a fluorescence microscope

Fluorophore	Filter	Color
Alexa Fluor (AF)488	Fluorescein isothiocyanate (FITC)	Green
Alexa Fluor (AF)594	Tetramethylrhodamine isothiocyanate (TRITC)	Red
DAPI	DAPI	Blue

Microscope filters required to visualize the three most used fluorophores are stated, along with the color they appear as. Abbreviations: *DAPI* 4′,6-diamidino-2-phenylindole

6. Add 50–100 μL of blocking buffer to each section and incubate at room temperature for 30 min (*see* **Notes 11–13**).
7. Remove blocking buffer from the sections by tapping (*see* **Note 9**).
8. Add 50–100 μL of primary antibody or isotype control (diluted in antibody dilution buffer) to the appropriate sections (*see*

Notes 14 and **15**). *See* Table 2 for example antibody concentrations.

9. Incubate overnight at 4 °C.
10. Remove primary antibody/isotype control from the sections by tapping the edge of the slide (*see* **Note 9**).
11. Wash sections twice with ~100 μL of PBS for 5 min each (*see* **Note 16**).
12. Add 50–100 μL of appropriate secondary antibody (diluted in antibody dilution buffer) to the sections and incubate for 1 h at room temperature with appropriate secondary antibody (*see* **Notes 14** and **17**).
13. Remove the secondary antibody by tapping the edge of the slide (*see* **Note 9**).
14. Add 50–100 μL of Sudan black solution to the sections and incubate for 20 min (*see* **Notes 12** and **18**).
15. Remove the Sudan black solution by tapping the edge of the slide (*see* **Note 9**).
16. Add one drop of mounting medium to each section.
17. Place a coverslip on top of the sections and seal using a small volume of clear nail varnish brushed over the edges.
18. Keep slides protected from light and at 4 °C and capture images using a fluorescence microscope as soon as possible (*see* **Note 19**).
19. Capture images of slides using a fluorescence microscope with appropriate filters for visualization (*see* Table 3) (*see* **Notes 20–23**).
20. Carry out image analysis using ImageJ software by threshold adjustment to quantify areas of fluorescence (i.e., positive staining) within plaques as described in Subheading 3.2.

3.2 Image Analysis

1. Download and open Fiji (ImageJ) software.
2. Open image to be analyzed.
3. Draw an outline around all plaques present within the vessel using the "Oval" (or another appropriate) selection brush tool (*see* **Note 24**).
4. Save this template as a Report Object Instance (ROI) file (use the "Ctrl" + "T" shortcut to bring up the ROI Manager window) (*see* **Note 25**).
5. To quantify areas of positive staining, click- > "Color"-- > "Dichromacy"- > "Deuteranope"- > "OK"; a grayscale version of the image will appear alongside the original (*see* **Note 26**).

6. Convert the image to 8-bit format; click "Image"- > "Type"-- > "8-bit" (*see* **Note 27**).
7. Adjust the threshold range of the image until only the areas of positive staining are selected by comparing with the original image; click "Image"- > "Adjust"- > "Threshold" and adjust the sliders/settings (*see* **Note 28**).
8. Apply this threshold to the image (*see* **Note 29**).
9. Ensure the plaque drawing is still applied (can be done from the ROI Manager) to the image (*see* **Note 30**).
10. Click "Analyze"- > "Analyze Particles" and ensure "Summarize" is ticked before clicking "OK."
11. The results window containing the "%Area" value represents the percentage of positive staining in the plaque.

4 Notes

1. Use sections that have not been fixed by any means; this protocol is suitable for snap-frozen sections. Sections that have been previously fixed (e.g., formalin-fixed, paraffin embedded) will require antigen retrieval prior to staining, to restore epitope-antibody reactivity as fixing masks the epitopes present on the tissue, which need to be recovered for successful staining.
2. Store the acetone at −20 °C as it will not freeze at this temperature.
3. Keep sterile to prevent any unwanted growth in the serum.
4. The prepared solution should be protected from light.
5. Type of serum used should match the species that the secondary antibody is raised in.
6. Aliquot buffer in single-use volumes and store at −20 °C until use.
7. Ensure all sections are fully submerged in the ice-cold acetone.
8. Slides should be washed thoroughly with PBS to remove any residual acetone.
9. Remove solutions from slides by gently tapping the long edge of the slide multiple times onto the slide holding strips of the staining tray.
10. The PAP pen creates a hydrophobic barrier surrounding the sections, preventing reagent run-off and cross-contamination between different antibodies. This allows use of different antibodies on different sections on the same slide as well as smaller reagent volumes. Be careful not to touch the section itself with the pen.

11. From this step onwards, protect slides from light during the staining process using the black staining tray with black lid to incubate the slides. Only remove the lid when treating the slides and replace the lid for all incubations/during all other times.
12. The exact volume required depends on the size of the sections but generally fall within the range of 50–100 μL per section; the actual volume is not important but should enable complete submersion of the entire section. Once an appropriate volume is selected, use the same volume for subsequent incubation steps with the various solutions.
13. The blocking buffer prevents antibodies from binding to non-target epitopes as antibodies compete with the protein in the buffer for target epitopes, thereby reducing non-specific binding.
14. The dilution factor is antibody-dependent and optimization may be required depending on the sample (*see* Table 2 for example dilution factors required for certain antibodies used for staining of aortic root sections). Dilute all antibodies to the desired concentration using the antibody dilution buffer. Mix well by vortexing briefly and keep on ice protected from light until use. Prepare fresh dilutions of the antibodies per use/for each use.
15. The primary antibody and isotype controls used should have the same or very similar final concentrations.
16. Important to wash thoroughly with PBS to remove all traces of the primary antibody.
17. The secondary antibody should be derived from a different species to that of the sample. The secondary antibody must be against the host species of the primary antibody, to avoid cross-reacting of the secondary antibody with endogenous immunoglobulins in the tissue sample.
18. This helps to prevent autofluorescence.
19. Images of the sections should be captured immediately after staining due to gradual loss of fluorescence over time. Therefore, the time between staining completion and image capture should be consistent and maintained throughout.
20. The isotype control should not show any fluorescence/positive staining. If this is not the case, this suggests non-specific binding of the antibodies (i.e., high background staining).
21. Optimal brightness, intensity, and contrast settings should be determined and used subsequently to capture images of all sections stained as part of the same batch for consistent analysis. These optimal settings should be used subsequently to

capture images of all sections within the same batch for consistency of image analysis.

22. A magnification allowing visualization of the entire cross section of the artery (e.g., aortic root) should be used. A higher magnification can also be used to visualize specific regions of interest at a higher resolution if required.
23. If the image is stained with more than one fluorochrome, it is possible to create an image containing all stains overlaying each other, provided each antibody is conjugated to different fluorochromes that can be visualized on different filters of the same microscope. In this case, fluorophores should be selected to minimize spectral overlap according to their excitation and emission wavelengths (information provided by the manufacturer).
24. It may be necessary to increase the brightness/contrast settings temporarily on the image, to see the structures better as fluorescence images may appear dark. Reset the settings if they were adjusted before proceeding.
25. This avoids the needs for repeated drawings should further analysis be required and improves consistency.
26. The original image will be useful when adjusting the threshold to select areas of positive staining, as this relies on the perception of/interpretation by the researcher. Where possible, it is important for image analysis to be carried out by at least two independent researchers in a blinded fashion to minimize any bias/unconscious bias.
27. Threshold adjustment requires the image to be in 8-bit format.
28. The threshold settings applied should be consistent and used for all stained images as part of the same batch.
29. The software should then highlight the positively stained areas.
30. If needed, reselect the template from the ROI window.

Acknowledgements

We thank the British Heart Foundation for financial support (grants PG/16/25/32097 and FS/17/75/33257). AA and RA received PhD studentships from the Kingdom of Saudi Arabia (Jeddah University).

References

1. Nielsen SH, Jonasson L, Kalogeropoulos K et al (2020) Exploring the role of extracellular matrix proteins to develop biomarkers of plaque vulnerability and outcome. J Intern Med 287(5):493–513

2. Chan Y-H, Ramji DP (2020) A perspective on targeting inflammation and cytokine actions in atherosclerosis. Future Med Chem 12(7): 613–626
3. Adiguzel E, Ahmad PJ, Franco C et al (2009) Collagens in the progression and complications of atherosclerosis. Vasc Med 14:73–89
4. Moss JWE, Ramji DP (2016) Cytokines: roles in atherosclerosis disease progression and potential therapeutic targets. Future Med Chem 8(11): 1317–1330
5. Wagsater D, Zhu C, Bjorkegren J et al (2011) MMP-2 and MMP-9 are prominent matrix metalloproteinases during atherosclerosis development in the Ldlr−/−Apob100/100 mouse. Int J Mol Med 28:247–253
6. Bergheanu SC, Bodde MC, Jukema JW (2017) Pathophysiology and treatment of atherosclerosis: current view and future perspective on lipoprotein modification treatment. Neth Heart J 25(4):231–242
7. Libby P, Buring JE, Badimon L et al (2019) Atherosclerosis. Nat Rev Dis Primers 5(56): 1–18
8. Moss JWE, Williams JO, Ramji DP (2018) Nutraceuticals as therapeutic agents for atherosclerosis. Biochim Biophys Acta Mol Basis Dis 1864:1562–1572
9. Im K, Mareninov S, Diaz MFP et al (2019) An introduction to performing immunofluorescence staining. Methods Mol Biol 1897: 299–311

Chapter 31

Monitoring Cellular Proliferation and Apoptosis in Atherosclerosis Plaques and Intimal Thickenings

Kerry S. Wadey, Jason L. Johnson, and Sarah J. George

Abstract

Immunohistochemistry for specific proteins characteristic of proliferative or apoptotic cells allows for monitoring of these cell behaviors in biological tissues samples, including atherosclerotic plaques and intimal thickenings. Proliferating cell nuclear antigen (PCNA) and Ki-67 are widely used markers of cell proliferation and cleaved caspase-3 is a well-established marker of apoptosis that can be detected in tissue samples using immunohistochemistry. This technique enables quantification of the abundance of these proteins and provides information on the distribution of these biomarkers in tissues. By combining with immunohistochemistry for specific cell type markers, it is also possible to determine which cell types are proliferating or undergoing apoptosis. Here, we detail protocols for immunohistochemistry of PCNA, Ki-67, and cleaved caspase-3 for evaluation of cellular proliferation and apoptosis in atherosclerotic plaques in vivo. In addition, we outline methods for the quantification and localization of cell proliferation using bromodeoxyuridine/5-bromo-2′-deoxyuridine (BrdU) and ethynyldeoxyuridine/5-ethynyl-2′-deoxyuridine(EdU) labeled tissue samples collected from animals exposed to BrdU or EdU.

Key words Proliferation, Apoptosis, Immunohistochemistry, EdU, BrdU, PCNA, Ki-67, Cleaved caspase-3

1 Introduction

BrdU (bromodeoxyuridine/5-bromo-2′-deoxyuridine) and EdU (ethynyldeoxyuridine/5-ethynyl-2′-deoxyuridine) are nucleoside analogs of thymidine that are incorporated into the DNA molecule during DNA synthesis allowing for identification of cells that have entered or undergone S-phase of the cell cycle. Though quantification of BrdU or EdU incorporation is considered one of the most direct and robust measures of cell proliferation, in *in vivo* studies, it requires for animals to be administered the thymidine analogs often via feeding or intraperitoneal injection. Hence BrdU- and EdU-labeling are not useful approaches for assessing proliferation in animals that have not received this treatment and when analyzing human tissue samples. Furthermore, thymidine analogs are

Dipak P. Ramji (ed.), *Atherosclerosis: Methods and Protocols*, Methods in Molecular Biology, vol. 2419,
https://doi.org/10.1007/978-1-0716-1924-7_31,
© The Author(s), under exclusive license to Springer Science+Business Media, LLC, part of Springer Nature 2022

reportedly toxic [1–4] and studies have observed that they have unpredictable effects on cell behavior and function [5].

Here, we describe a protocol for fluorescent and colorimetric labeling of incorporated BrdU in paraffin-embedded tissue sections, including preparation of samples for immunohistochemistry, DNA hydrolysis to allow access of the anti-BrdU antibody to the BrdU units, and immunodetection. We also outline a quick, high-throughput method for detection of incorporated EdU in tissue sections, which entails a simple copper-catalyzed covalent reaction between the alkyne group of EdU [6] and an azide with a fluorescent tag [7–10]. Additionally, due to its small size, EdU units within double-stranded DNA are easily accessible, and a DNA hydrolysis step is not required. Hence, EdU-labeling presents significant advantages over performing immunohistochemistry for BrdU.

For *in vivo* studies where animals may not have been administered a thymidine analog, and in human tissue samples, we detail a protocol for immunodetection of common proliferation markers proliferating cell nuclear antigen (PCNA) and Ki-67, which are used for both diagnostic and research purposes to evaluate the number of replicating cells. PCNA encircles the DNA molecule and anchors polymerases and other proteins involved in DNA metabolic processes [11, 12] such as DNA synthesis, chromatin remodeling, DNA repair, and sister-chromatin cohesion [13, 14]. Expression levels of PCNA peak in S-phase of the cell cycle; PCNA is not expressed in G_0. The function of the nuclear protein Ki-67 remains unclear; however, it is preferentially expressed in late G_1, S, G_2, and M phases of the cell cycle and is absent in G_0 [15]. As Ki-67 is only expressed in non-quiescent cycling cells, it has become a widely used marker of cell proliferation, particularly in cancer research and pathology [15].

We also describe a method for detection of apoptotic cells by immunohistochemistry for active cleaved caspase-3, the main but not exclusive executioner of apoptosis [16, 17]. In the apoptosome pathway, cytosolic release of cytochrome c from the mitochondria triggers activation of cleaved caspase-3, which in turn catalyzes the cleavage of other key apoptotic proteins involved in nuclear condensation, DNA fragmentation, cell shrinkage, and membrane blebbing [18].

2 Materials

1. HPLC water with a sensitivity of 18 MΩ-cm at 25 °C.
2. Phosphate buffered saline (PBS): 137 mM NaCl, 2.7 mM KCl, 10 mM Na_2HPO_4, KH_2PO_4, pH 7.4.

3. Paraffin-embedded tissue sections dried onto adhesion optimized glass slides designed to minimize tissue loss during staining.
4. Fume hood.
5. Microwave oven.
6. Microwaveable plastic histology staining dish with a lid.
7. Glass histology staining dishes.
8. Glass coplin jars.
9. Slide racks.
10. Humidified chamber for glass slide incubations at different temperatures (e.g., 4 °C, 37 °C).
11. Wax pen.
12. Soft tissue.

2.1 Immunohistochemistry for Markers of Proliferation and Apoptosis, and BrdU

1. 100% Xylene/xylene substitute (*see* **Note 1**).
2. 100% industrial methylated spirit (IMS).
3. 70% (v/v) IMS: Dilute 100% IMS in water and mix.

2.1.1 Deparaffinization and Rehydration

2.1.2 Antigen Retrieval

1. 10 mM citrate buffer, pH 6.0: Dissolve 1.92 g of citric acid in just under 1 L of water by continually stirring with a magnetic stirrer. Once dissolved, bring to pH 6.0 by adding concentrated NaOH dropwise. Make volume up to 1 L. Store at room temperature.
2. Cold running tap water.

2.1.3 Quenching Endogenous Peroxidase Activity (for Colorimetric Detection Only)

1. 3% (v/v) H_2O_2 in water. Store at 4 °C.

2.1.4 DNA Denaturation (for BrdU and EdU Detection Only)

1. 125 U/mL benzonase nuclease in PBS supplemented with 1 mM $MgCl_2$. Always make up fresh.

2.1.5 Protein Blocking

1. 20% (v/v) serum diluted in 1% (w/v) BSA in PBS or commercial blocking reagent for immunohistochemistry.

2.1.6 Immunodetection

1. Anti-BrdU IgG diluted in 1% (w/v) bovine serum albumin (BSA) in PBS.
2. Anti-Ki-67 IgG diluted in 1% (w/v) BSA in PBS.

3. Anti-PCNA IgG diluted in 1% (w/v) BSA in PBS.
4. Anti-cleaved caspase-3 diluted in 1% (w/v) BSA in PBS.
5. Non-immune IgG control diluted in 1% (w/v) BSA in PBS.
6. Biotinylated secondary antibody diluted in 1% (w/v) BSA in PBS (*see* **Note 2**).
7. Streptavidin-horseradish peroxidase (HRP) conjugate diluted in 1% (w/v) BSA in PBS.
8. 3,3′-Diaminobenzidine (DAB) peroxidase substrate.
9. Mayer's hematoxylin (*see* **Note 3**).
10. Streptavidin-fluorophore conjugate diluted in 1% (w/v) BSA in PBS.

2.1.7 Mounting

1. Distyrene, a plasticizer, and xylene (DPX) mountant.
2. Liquid mountant formulated with 4′,6-diamidino-2-phenylindole (DAPI) or another fluorescent nuclear counterstain.
3. Glass coverslips.

2.1.8 Imaging and Analysis

1. Light microscope with a camera mount.
2. Fluorescence microscope with a camera mount.

2.2 Fluorescent Labeling of EdU in Tissue Sections

2.2.1 Deparaffinization and Rehydration

1. 100% Xylene/xylene substitute (*see* **Note 1**).
2. 100% industrial methylated spirit (IMS).
3. 70% (v/v) IMS: Dilute 100% IMS in water and mix.

2.2.2 Antigen Retrieval

1. 10 mM citrate buffer, pH 6.0: Dissolve 1.92 g of citric acid in just under 1 L of water by continually stirring with a magnetic stirrer. Once dissolved, bring to pH 6.0 by adding concentrated NaOH dropwise. Make volume up to 1 L. Store at room temperature.
2. Cold running tap water.

2.2.3 Detection of EdU

1. Commercial Fluorescent Labeling Kits for EdU: kits contain buffers, a copper catalyst solution, and a fluorescently labeled azide (biotinylated azides are also commercially available).
2. 3% (w/v) bovine serum albumin (BSA) in PBS.

2.2.4 Mounting, Imaging, and Analysis

1. Liquid mountant formulated with DAPI or another fluorescent nuclear counterstain.
2. Glass coverslips.
3. Fluorescence microscope with a camera mount.

3 Methods

3.1 Immunohistochemistry for Markers of Proliferation and Apoptosis, and BrdU

3.1.1 Deparaffinization and Rehydration

1. Place paraffin-embedded tissue sections dried onto adhesion optimized glass slides in a slide rack.
2. Deparaffinize tissue sections by placing the slides and slide rack in a glass histology staining dish of 100% Xylene/xylene substitute and incubate for 5 min (*see* **Note 4**). Ensure that slides are completely immersed and shake to dispel any air bubbles.
3. Repeat twice by transferring slides to fresh dishes of 100% Xylene/Xylene substitute. When transferring slides between dishes in subsequent steps, shake the slide rack to fully drain any liquid so that the previous dish's liquids are not transferred to the next one.
4. Transfer slides to a glass dish of 100% IMS to remove Xylene/Xylene substitute and incubate for 5 min (*see* **Note 4**). Ensure that slides are completely immersed and shake to dispel any air bubbles.
5. Repeat once by transferring slides to a fresh dish of 100% IMS.
6. To begin rehydration, transfer slides to a fresh dish of 70% IMS and incubate for 5 min.
7. To fully rehydrate tissue sections, transfer slides to a dish of water and incubate for 5 min. Ensure that tissue sections are not left to dry at any point.

3.1.2 Antigen Retrieval

1. Fill any remaining slots on the slide rack with blank slides (*see* **Note 5**).
2. Transfer slides and the slide rack to a microwaveable plastic histology staining dish with a lid. Fill the dish with 10 mM citrate buffer so that the liquid level is approximately half a centimeter above the top of the slides. Loosely place the lid on the dish to prevent buildup of pressure.
3. Microwave tissue sections for a total of 10 min on the highest heat setting (*see* **Note 6**).
4. Allow the slides to cool for 30 min at room temperature (*see* **Note 7**).
5. Transfer the slides to cold running tap water for 5 min (*see* **Note 8**).
6. Wash the slides twice with PBS in glass coplin jars.

3.1.3 Quenching Endogenous Peroxidase Activity

This step is only required for colorimetric staining (*see* **Note 9**).

1. Transfer slides to a fresh coplin jar containing 3% (v/v) H_2O_2 in water and incubate for 5 min at 4 °C.
2. Wash slides twice with PBS in glass coplin jars.

3.1.4 DNA Denaturation

This step is only required for immunohistochemistry for BrdU (*see* **Note 10**).

1. Draw around sections with a wax pen (*see* **Note 11**). Dry the area around the tissue section with a dry soft tissue so any remaining PBS does not dilute the benzonase nuclease solution; be careful not to touch or damage the tissue section.
2. Add 50 μL of 125 U/mL benzonase nuclease in PBS supplemented with 1 mM $MgCl_2$ to tissue sections (*see* **Note 12**).
3. Place the slides in a humidified chamber for 2 h at 37 °C.
4. Wash the slides twice with PBS in glass coplin jars.

3.1.5 Protein Blocking

1. Draw around sections with a wax pen if not done previously (*see* **Note 11**). Dry the area around the tissue sections with a dry soft tissue so any remaining PBS does not dilute the blocking reagent; be careful not to touch or damage the tissue section.
2. Add 50 μL of 20% (v/v) blocking sera (*see* **Note 13**) diluted in 1% (w/v) BSA in PBS or commercial protein blocking reagent to tissue sections (*see* **Notes 12** and **14**).
3. Place the slides in a humidified chamber. Where serum is used as a blocking agent, incubate for 30 min at room temperature. Commercial protein blocking reagents should be used in accordance with the manufacturer's instructions.

3.1.6 Immunodetection

1. Remove blocking agent with a dry soft tissue.
2. Add 50 μL of anti-BrdU IgG, anti-Ki-67 IgG, anti-PCNA IgG, or anti-cleaved caspase-3 IgG diluted in 1% (w/v) BSA in PBS to tissue sections (*see* **Note 12**).
3. Add 50 μL of the non-immune IgG control diluted in 1% (w/v) BSA in PBS to a second tissue section (*see* **Notes 12** and **15**).
4. Incubate overnight at 4 °C in a humidified chamber.
5. Wash slides four times with PBS in glass coplin jars.
6. Dry the area around the tissue sections with a dry soft tissue so any remaining PBS does not dilute the secondary antibody.
7. Add 50 μL of the biotinylated secondary antibody diluted in 1% (w/v) BSA in PBS to tissue sections and incubate for 45 min at room temperature in a humidified chamber (*see* **Note 12**).
8. Wash slides four times with PBS in glass coplin jars.

9. Dry the area around the tissue sections with a dry soft tissue so any remaining PBS does not dilute the streptavidin with a HRP or fluorescent tag.
10. Add 50 μL of streptavidin-HRP (for colorimetric staining) or streptavidin-fluorophore (for fluorescence staining) diluted in 1% (w/v) BSA in PBS to tissue sections and incubate for 45 min at room temperature in a humidified chamber (*see* **Notes 12** and **16**).
11. Wash slides four times with PBS in glass coplin jars.
12. For colorimetric staining, dry the area around the tissue sections with a dry soft tissue.
13. Add 50 μL of DAB peroxidase substrate diluted in water to tissue sections (*see* **Notes 12**, **17**, and **18**) and incubate for 5 min or as recommended by the manufacturer.
14. Wash slides twice in water in glass coplin jars.
15. Stain cell nuclei by adding 50 μL of filtered Mayer's hematoxylin diluted in water to tissue sections and incubate for approximately 1 min (*see* **Note 12**).
16. Wash slides three times in tap water in glass coplin jars.
17. Leave slides in tap water for 30 min at room temperature to allow for hematoxylin stain to develop.

3.1.7 Mounting

For colorimetric staining:

1. Dehydrate tissue sections by placing slides in a slide rack and performing 3-min incubations in 70% IMS, 2× 100% IMS and then 2× Xylene/Xylene substitute (*see* **Note 19**); this is the reverse process of deparaffinization and rehydration.
2. Pipette DPX mountant onto coverslips, then place slides upside down against coverslips, press gently and lift. Air bubbles can be removed by gently pressing down on the area (*see* **Note 20**).

For fluorescence staining:

1. Add 1–3 drops of mountant formulated with DAPI or another fluorescent nuclear counterstain to each tissue section depending on the size.
2. Place a coverslip on top and gently press down. Air bubbles can be removed by gently pressing down on the area (*see* **Note 20**).

3.1.8 Imaging and Analysis

1. For colorimetric staining, identify BrdU-, Ki-67-, PCNA- and cleaved caspase-3-positive cells as those with brown nuclei and negative cells as those with gray/blue nuclei (*see* Fig. 1 and **Note 21**).
2. For fluorescent staining, identify BrdU-, Ki-67-, PCNA- and cleaved caspase-3-positive cells as those with fluorescent nuclei;

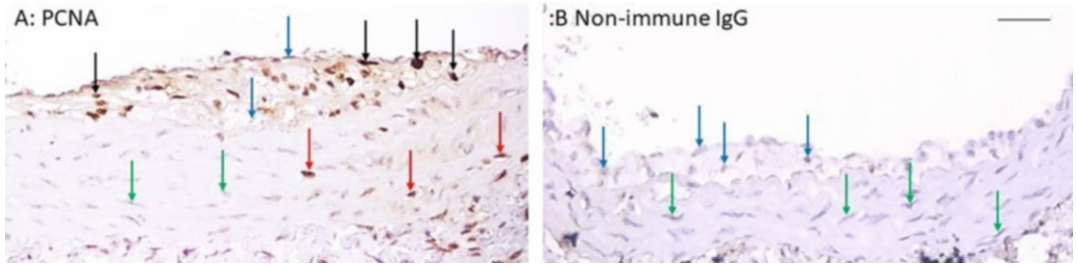

Fig. 1 Immunohistochemistry for PCNA in mouse brachiocephalic artery atherosclerotic plaques. Mouse brachiocephalic artery atherosclerotic plaques were subjected to immunohistochemistry for PCNA to identify proliferative cells. (**a**) Representative image of section incubated with anti-PCNA antibody, which shows nuclei stained with hematoxylin (blue) and PCNA positive cells (brown). (**b**) Representative image section incubated with non-immune IgG control as a negative control. The red arrows indicate some of the PCNA positive medial cells and the green arrows indicate some of the PCNA negative medial cell. The black arrows indicate some of the PCNA positive intimal cells and the blue arrows indicate some of the PCNA negative intimal cells. Scale bar represents 25 μm and applies to both panels

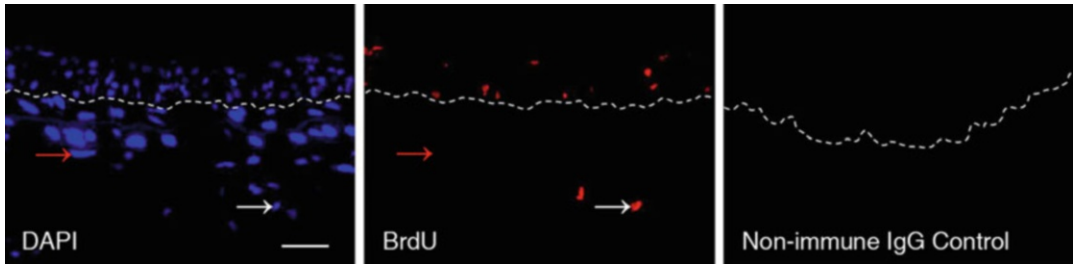

Fig. 2 Immunofluorescence (IF) for BrdU in rat carotid arteries injured via balloon angioplasty to induce vascular remodeling and neointima formation in vivo. Rat carotid arteries were retrieved 10 days following balloon injury; rats were administered BrdU in the last 24 h prior to sacrifice to identify proliferative cells. Representative images show nuclei stained with DAPI (blue) and BrdU-labeled cells (red). The red arrows indicate a negative cell and the white arrow a BrdU-positive cell. Non-immune IgG control was used as a negative control. The dashed line indicates the intimal:medial boundary. Scale bar represents 20 μm and applies to all panels

all nuclei will be stained fluorescent blue with DAPI (*see* Figs. 2 and 3 and **Note 21**).

3. As it is important to determine subcellular localization of staining, image tissue sections with a ×40 or ×60 lens. Approximately 200–400 cells should be counted per condition.
4. Determine the rate of proliferation or apoptotic cell turnover by calculating the percentage of positive cells.

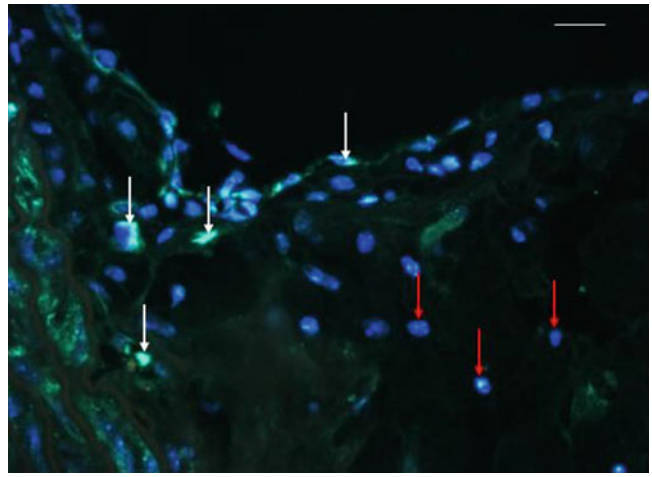

Fig. 3 A mouse brachiocephalic artery atherosclerotic plaque subjected to immunofluorescence (IF) with anti-cleaved caspase-3 antibody. Representative image showing nuclei stained with DAPI (blue) and cleaved caspase-3 positive cells (blue). The red arrows indicate some negative cells, and the green arrows indicate some cleaved caspase-3 positive cells. Scale bar represents 25 μm

3.2 Fluorescent Labeling of EdU in Tissue Sections

3.2.1 Deparaffinization and Rehydration

1. Deparaffinize tissue sections as in **steps 1–3** in Subheading 3.1.1.
2. Remove Xylene/Xylene substitute and rehydrate tissue sections as in **steps 4–7** in Subheading 3.1.1.

3.2.2 Antigen Retrieval

1. Perform antigen retrieval as in Subheading 3.1.2.

3.2.3 Detection of EdU

1. Prepare "reaction cocktail" containing buffers, copper catalyst solution, and a fluorescently labeled azide. These reagents are included in commercial Fluorescent Labeling Kits for EdU and should be prepared in accordance with manufacturer's instructions. Use the "reaction cocktail" within 15 min of preparation for optimal results.
2. Wash slides twice with 3% (w/v) BSA in PBS in glass coplin jars.
3. Dry the area around the tissue sections with a dry soft tissue so any remaining liquid does not dilute the "reaction cocktail." Be careful not to touch or damage the tissue section.
4. Add 50 μL of "reaction cocktail" to tissue sections and incubate for 30 min at room temperature in a humidified chamber (*see* **Note 12**).
5. Wash slides three times with 3% (w/v) BSA in PBS in glass coplin jars.

3.2.4 Mounting, Imaging, and Analysis

1. Add 1–3 drops of liquid mountant formulated with DAPI or another fluorescent nuclear counterstain to each tissue section depending on size.
2. Place a coverslip on top and gently press down (*see* **Note 20**).
3. Identify EdU-positive cells as those with fluorescent nuclei (*see* **Note 21**); all nuclei will be stained fluorescent blue with DAPI. As it is important to determine subcellular localization of staining, view tissue sections with a ×40 or ×60 lens on a fluorescent microscope with a camera mountant. Count approximately 200–400 cells per condition. Determine the rate of proliferation by calculating the percentage of EdU-positive cells.

4 Notes

1. Breathing Xylene vapors in even small amounts can cause headaches, dizziness, drowsiness, and nausea, with complications becoming more serious with higher levels of exposure. It is hence important that deparaffinization of tissue sections is performed in a fume hood. Xylene can also irritate and burn skin so gloves must be worn throughout. Xylene substitutes are recommended as a non-toxic replacement.
2. The secondary antibody must be raised against the host species of the primary antibody.
3. Mayer's hematoxylin requires filtration to remove precipitates and often needs diluting 1:2 to 1:4 in water to reduce strength.
4. Due to shedding of paraffin wax and transfer of Xylene/Xylene substitute to IMS, dishes of xylene/xylene substitute and IMS will become progressively dirtier with continued use. Hence, xylene and ethanol should be discarded once the liquids become cloudy or change color. Diligently follow waste disposal regulations when discarding xylene/xylene substitute and ethanol. It is best that dishes of the liquids are covered with a lid between uses. Longer incubation times may be required for deparaffinization and rehydration if the xylene/xylene substitute and ethanol used are not fresh.
5. Filling any remaining slots on the slide rack with blank slides will help prevent formation of large air bubbles during the heating process that can often damage tissue sections or lift tissue sections from surface of the slides.
6. Due to splattering from boiling, after 5 min, the liquid levels will need to be topped up with 10 mM citrate buffer. It is important that the slides are always immersed in citrate buffer; if tissue sections dry out, this will affect the staining outcome. In some cases, liquid levels may need to be topped up with

10 mM citrate buffer more than once; hence, it is important that the microwaving process is observed (at a distance) to ensure that the slides never dry out.

7. Slowly cooling slides assists the antigen retrieval process so this step should not be accelerated.
8. The flow of tap water should not be too high as this may damage tissue sections or cause tissue sections to lift from the surface of the slides.
9. DAB is oxidized by hydrogen peroxide in a reaction that is catalyzed by HRP (conjugated to a secondary antibody or streptavidin) to produce a brown precipitate. Endogenous peroxidases can also catalyze oxidation of DAB by hydrogen peroxide generating false positive staining, hence the activity of endogenous peroxidases should be quenched with hydrogen peroxide.
10. DNA denaturation is required in order to enable access of the anti-BrdU antibody to the BrdU epitope within the DNA molecule. Nuclease-mediated DNA digestion and acid hydrolysis are both methods of DNA denaturation; however, acid hydrolysis can damage tissue integrity and disrupts DNA integrity affecting nuclear counterstaining with dyes like DAPI and Mayer's hematoxylin. Hence, for immunohistochemistry for BrdU, we recommend DNA denaturation by nuclease-mediated DNA digestion.
11. Wax pens should be stored at room temperature. At warmer temperatures, such as on a warm day, the wax may melt and when used to delineate tissue sections, the melted wax can spill out of the pen onto the slide and even over the tissue section. Hence, at warmer temperatures, we recommend that wax pens are tested on blank slides and cooled in a fridge for 5 min if the test demonstrates that the wax inside the pen has melted.
12. Increase the volume for larger tissue sections; a sufficient volume should be added to cover the tissue section without having to spread the solution thinly. Be careful to not damage the tissue with the pipette tip.
13. The host species of the blocking serum should match the species the secondary antibody is raised in. With dual immunohistochemistry, if secondary antibodies are raised in distinct species, it may be important to use blocking sera from both species.
14. Blocking with sera or other commercial protein blocking reagents markedly reduces non-specific binding of antibodies to tissue.
15. To account for any non-specific interactions of the primary antibody with the tissue sample, for each condition, a second

tissue section should be treated with a non-immune IgG control. The non-immune IgG control must be diluted to the same concentration of the primary antibody, and match the species and isotype (for example, IgG_1, IgG_{2A}, IgG_{2B}, and IgM) of the primary antibody.

16. Following addition of the streptavidin-fluorophore, protect slides from light for all remaining steps to prevent photobleaching.
17. Once the fast DAB peroxidase substrate is reconstituted in water (in accordance with manufacturer's instructions), it is essential that it is used within 15 min.
18. Once immunodetection is completed, a second antigen may be probed for (dual immunohistochemistry). If a biotin/avidin amplification step is required for the second antigen, a biotin/avidin block should be used where kits are available commercially.
19. As the first dish of xylene/xylene substitute used during deparaffinization will contain the most wax, this should ideally not be used for dehydration of stained tissue sections.
20. Mountants will need curing before imaging in order to reach the optimal refractive index; curing times should be indicated in product datasheets. Protect slides from light if necessary.
21. Immunostaining will often produce a spectrum of cells with light to deep brown nuclei (colorimetric staining) or low to high fluorescence intensity. This may be due to a mixed population of cells that are at different stages in the cell cycle. It can be difficult to distinguish faintly stained nuclei from negative cells. It is important that a threshold is set for what one may consider a positive cell; keeping a reference image can be helpful to remain consistent while analyzing and counting cells.

Acknowledgments

Jason Johnson is funded by British Heart Foundation Senior Research Fellowship, FS/18/1/33234.

References

1. Ehmann UK, Williams JR, Nagle WA, Brown JA, Belli JA, Lett JT (1975) Perturbations in cell cycle progression from radioactive DNA precursors. Nature 258(5536):633–636. https://doi.org/10.1038/258633a0
2. Kolb B, Pedersen B, Ballermann M, Gibb R, Whishaw IQ (1999) Embryonic and postnatal injections of bromodeoxyuridine produce age-dependent morphological and behavioral abnormalities. J Neurosci 19(6):2337–2346. https://doi.org/10.1523/jneurosci.19-06-02337.1999
3. Sekerková G, Ilijic E, Mugnaini E (2004) Bromodeoxyuridine administered during neurogenesis of the projection neurons causes cerebellar defects in rat. J Comp Neurol 470

(3):221–239. https://doi.org/10.1002/cne.11016

4. Kuwagata M, Ogawa T, Nagata T, Shioda S (2007) The evaluation of early embryonic neurogenesis after exposure to the genotoxic agent 5-bromo-2′-deoxyuridine in mice. Neurotoxicology 28(4):780–789. https://doi.org/10.1016/j.neuro.2006.07.017
5. Duque A, Rakic P (2011) Different effects of bromodeoxyuridine and [3H]thymidine incorporation into DNA on cell proliferation, position, and fate. J Neurosci 31 (42):15205–15217. https://doi.org/10.1523/jneurosci.3092-11.2011
6. Salic A, Mitchison TJ (2008) A chemical method for fast and sensitive detection of DNA synthesis in vivo. Proc Natl Acad Sci U S A 105(7):2415–2420. https://doi.org/10.1073/pnas.0712168105
7. Breinbauer R, Köhn M (2003) Azide-alkyne coupling: a powerful reaction for bioconjugate chemistry. Chembiochem 4(11):1147–1149. https://doi.org/10.1002/cbic.200300705
8. Wang Q, Chan TR, Hilgraf R, Fokin VV, Sharpless KB, Finn MG (2003) Bioconjugation by copper(I)-catalyzed azide-alkyne [3 + 2] cycloaddition. J Am Chem Soc 125 (11):3192–3193. https://doi.org/10.1021/ja021381e
9. Rostovtsev VV, Green LG, Fokin VV, Sharpless KB (2002) A stepwise huisgen cycloaddition process: copper(I)-catalyzed regioselective "ligation" of azides and terminal alkynes. Angew Chem Int Ed Engl 41 (14):2596–2599. https://doi.org/10.1002/1521-3773(20020715)41:14<2596::Aid-anie2596>3.0.Co;2-4
10. Kolb HC, Finn MG, Sharpless KB (2001) Click chemistry: diverse chemical function from a few good reactions. Angew Chem Int Ed Engl 40(11):2004–2021. https://doi.org/10.1002/1521-3773(20010601)40:11<2004::aid-anie2004>3.3.co;2-x
11. Kong XP, Onrust R, O'Donnell M, Kuriyan J (1992) Three-dimensional structure of the beta subunit of *E. coli* DNA polymerase III holoenzyme: a sliding DNA clamp. Cell 69 (3):425–437. https://doi.org/10.1016/0092-8674(92)90445-i
12. Strzalka W, Ziemienowicz A (2011) Proliferating cell nuclear antigen (PCNA): a key factor in DNA replication and cell cycle regulation. Ann Bot 107(7):1127–1140. https://doi.org/10.1093/aob/mcq243
13. Mighell A (1995) PCNA and p53. Eur J Cancer B Oral Oncol 31b(6):403–404. https://doi.org/10.1016/0964-1955(95)00037-2
14. Maga G, Hubscher U (2003) Proliferating cell nuclear antigen (PCNA): a dancer with many partners. J Cell Sci 116(Pt 15):3051–3060. https://doi.org/10.1242/jcs.00653
15. Bologna-Molina R, Mosqueda-Taylor A, Molina-Frechero N, Mori-Estevez AD, Sánchez-Acuña G (2013) Comparison of the value of PCNA and Ki-67 as markers of cell proliferation in ameloblastic tumors. Med Oral Patol Oral Cir Bucal 18(2):e174–e179. https://doi.org/10.4317/medoral.18573
16. Bressenot A, Marchal S, Bezdetnaya L, Garrier J, Guillemin F, Plénat F (2009) Assessment of apoptosis by immunohistochemistry to active caspase-3, active caspase-7, or cleaved PARP in monolayer cells and spheroid and subcutaneous xenografts of human carcinoma. J Histochem Cytochem 57(4):289–300. https://doi.org/10.1369/jhc.2008.952044
17. Gown AM, Willingham MC (2002) Improved detection of apoptotic cells in archival paraffin sections: immunohistochemistry using antibodies to cleaved caspase 3. J Histochem Cytochem 50(4):449–454. https://doi.org/10.1177/002215540205000401
18. Jin Z, El-Deiry WS (2005) Overview of cell death signaling pathways. Cancer Biol Ther 4 (2):139–163. https://doi.org/10.4161/cbt.4.2.1508

Chapter 32

Investigation of Atherosclerotic Plaque Vulnerability

Sarah J. George and Jason L. Johnson

Abstract

Histochemical and immunohistochemical approaches permit the detection and evaluation of proteins and cell types within murine brachiocephalic artery atherosclerotic plaques, that can be subsequently analyzed to provide inferences on atherosclerotic plaque vulnerability. Here we describe the specific histochemical techniques deployed to examine the expression of elastin, fibrillar collagens, and neutral lipids, alongside immunohistochemistry protocols for the identification of macrophages (CD68) and vascular smooth muscle cells (α-smooth muscle actin). We will also describe how analyses derived from these methods can be combined to determine evidence of previous plaque rupture and susceptibility to rupture.

Key words Histochemistry, Immunohistochemistry, Mouse models of atherosclerosis, Image analysis

1 Introduction

The techniques of histochemistry and immunohistochemistry are appropriate for the localization and quantification of proteins and cell-specific markers within histological sections of atherosclerotic plaques. However, assessment of specific proteins or individual cell types cannot identify atherosclerotic plaques susceptible to rupture or those that have previously ruptured. Instead, a combination of approaches is required. Seminal studies from cardiovascular pathologists established that the main histological features of disrupted human coronary artery plaques include thinning of the fibrous cap through loss of vascular smooth muscle cells alongside depletion of structural collagens that provide most of the tensile strength [1, 2]. Conversely, the marked accumulation of lipid-laden macrophages (foam cells) and accompanying expansion of the lipid-rich necrotic core (through ongoing death of foam cell macrophages) are observed within ruptured plaques [1, 2]. Furthermore, a large proportion of plaque ruptures in humans do not advance to occlusive thrombosis, and it is proposed such plaques undergo a healing

Dipak P. Ramji (ed.), *Atherosclerosis: Methods and Protocols*, Methods in Molecular Biology, vol. 2419,
https://doi.org/10.1007/978-1-0716-1924-7_32,
© The Author(s), under exclusive license to Springer Science+Business Media, LLC, part of Springer Nature 2022

process, contributing to plaque growth [3]. Correspondingly, the presence of distinct layers of collagen, elastin, and vascular smooth muscle cells within plaques, alongside the layering of multiple lipid-rich/necrotic cores, have been observed in coronary plaques, and therefore their presence is considered to serve as a surrogate marker of previous plaque disruption [3].

Based upon the differential plaque characteristics observed between ruptured and non-ruptured plaques, the reasoning has been applied that such features differ between human coronary plaques deemed prone to rupture (vulnerable or unstable) and those viewed as less likely to rupture (stable) [2]. Indeed, results from clinical trials utilizing statin treatment of patients with unstable coronary disease revealed less clinical events associated with plaque rupture, inferring key determinants within vulnerable plaques had been modulated to stabilize the plaques [4]. Associated imaging studies have validated a beneficial increase in plaque components such as fibrous cap thickness (dependent upon collagen and smooth muscle cell content), alongside reduced plaque lipid content and foam cell macrophage accumulation with statin treatment [5]. As such, clinically advantageous interventions are also manifested within human plaques, rendering them more stable and less liable to rupture. Furthermore, proof-of-principle studies in mouse atherosclerosis models have also shown that statins beneficially change plaque composition, implying transition to a stable plaque phenotype [6]. In addition, statin therapy lowered the incidence of buried fibrous layers, a surrogate marker of healed previous plaque rupture [6]. In addition to statin treatment, the inhibition of individual or broad-spectrum metalloproteinase activity favorably modifies plaque characteristics, including composition and presence of buried fibrous layers [7, 8].

Here we describe the associated methods for investigating plaque composition in histological tissues sections, including Picro-sirius Red (PSR) as a well-characterized histochemical stain for the assessment and quantification of collagen content, Elastin van Gieson (EVG) for the detection of elastin fibers, and Oil Red O to evaluate the presence of neutral lipids. We also outline the immunohistochemical protocols for the assessment of macrophage (CD68) and vascular smooth muscle cell (α-smooth muscle actin) content within atherosclerotic plaques. Finally, we provide the procedures for utilizing the abovementioned methods to determine the presence of buried fibrous layers and indices of plaque vulnerability.

2 Materials

2.1 Chemicals

2.1.1 Picro-Sirius Red (PSR) Staining

1. Xylene substitute.
2. 100% ethanol (industrial methylated spirits: IMS).
3. 70% ethanol (IMS).
4. Running tap water.
5. Distilled water.
6. 0.1% (w/v) Picro-sirius red solution.
7. 0.01 M hydrochloric acid.
8. Distyrene, plasticizer and xylene (DPX) mountant.

2.1.2 Elastin Van Gieson (EVG) Staining

1. Xylene substitute.
2. 100% ethanol (industrial methylated spirits: IMS).
3. Running tap water.
4. 0.5% (w/v) potassium permanganate.
5. Distilled water.
6. 1% oxalic acid.
7. 70% (v/v) ethanol (IMS).
8. 50% (v/v) Miller's elastin stain.
9. Van Gieson stain.
10. Distyrene, plasticizer and xylene (DPX) mountant.

2.1.3 Oil Red O (ORO) Staining

1. Phosphate buffered saline (PBS): 137 mM NaCl, 2.7 mM KCl, 10 mM Na_2HPO_4, 1.8 mM KH_2PO_4, pH 7.4.
2. 10% (v/v) formalin in PBS.
3. Distilled water.
4. 60% (v/v) isopropanol.
5. 99% (v/v) isopropanol.
6. 1% (w/v) dextrin.
7. Oil Red O powder.
8. Oil Red O stock solution: 2% (w/v) Oil Red O (saturated) in 99% (v/v) isopropanol.
9. Oil Red O working solution: 60% (v/v) Oil Red O stock solution and 40% (v/v) dextrin solution (1%), mixed well, left to stand for 1 h and then filtered.
10. Mayer's hematoxylin (*see* **Note 1**).
11. Tap water.
12. Aqueous mountant.

2.1.4 Immunohistochemistry for Macrophages and Vascular Smooth Muscle Cells

1. Xylene substitute.
2. 100% ethanol (industrial methylated spirits: IMS).
3. 70% ethanol (IMS).
4. Running tap water.
5. Distilled water.
6. PBS.
7. 10 mM citrate buffer, pH 6.0: Dissolve 1.92 g of citric acid in just under 1 L of distilled water by continually stirring with a magnetic stirrer. Once dissolved, bring to pH 6.0 by adding concentrated NaOH dropwise. Make volume up to 1 L. Store at room temperature.
8. 3% (v/v) H_2O_2 in water, or commercial endogenous peroxidase blocking reagent for immunohistochemistry.
9. 20% (v/v) serum diluted in PBS, or commercial blocking reagent for immunohistochemistry (*see* **Note 2**).
10. Anti-CD68 IgG antibody.
11. Anti-α-smooth muscle actin IgG antibody.
12. 1% (w/v) bovine serum albumin (BSA) in PBS.
13. Biotinylated secondary antibody diluted in 1% (w/v) BSA in PBS (*see* **Note 3**).
14. Streptavidin-horseradish peroxidase (HRP) diluted in 1% (w/v) BSA in PBS.
15. 3,3′-Diaminobenzidine (DAB) peroxidase substrate.
16. Mayer's hematoxylin (*see* **Note 1**).
17. Distyrene, plasticizer and xylene (DPX) mountant.

2.2 Equipment

2.2.1 PSR Staining

1. Microscope slide autostainer machine for automated histochemical staining, or for manual staining, glass coplin jars or glass/plastic staining troughs and slide racks.
2. Incubator at 60 °C.
3. Drying oven.
4. Glass coverslips (50 mm long).
5. Brightfield microscope.
6. Image analysis software.
7. Disposal plastic Pasteur pipettes.

2.2.2 EVG Staining

1. Microscope slide autostainer machine for automated histochemical staining, or for manual staining, glass coplin jars or glass/plastic staining troughs and slide racks.
2. Incubator at 60 °C.
3. Glass coverslips (50 mm long).

4. Brightfield microscope.
5. Image analysis software.
6. Disposal plastic Pasteur pipettes.

2.2.3 ORO Staining

1. Glass coplin jars or glass/plastic staining troughs and slide racks.
2. Glass coverslips (50 mm long).
3. Brightfield microscope.
4. Image analysis software.
5. Disposal plastic Pasteur pipettes.

2.2.4 Immunohistochemistry

1. Microwave oven.
2. Plastic microwavable staining dish with lid.
3. Glass coplin jars.
4. Glass/plastic staining troughs.
5. Plastic slide racks.
6. Humidifying chamber for microscope slide incubations.
7. Incubator at 60 °C.
8. Wax hydrophobic barrier pen for encircling tissue sections.
9. Soft tissue paper.
10. Glass coverslips (50 mm long).
11. Brightfield microscope.
12. Image analysis software.

3 Methods

3.1 Picro-Sirius Red Histochemistry for Fibrillar Collagens

1. Picro-sirius Red staining can be achieved manually or through the use of an automated slide staining machine (*see* **Note 4**).
2. Place the slides at 60 °C for 30 min (*see* **Note 5**).
3. Dewax the slides by placing in xylene substitute for 3 × 3 min (*see* **Note 6**).
4. Place the slides in 100% ethanol (industrial methylated spirits: IMS) for 2 × 3 min (*see* **Note 7**).
5. Place the slides in 70% ethanol (IMS) for 5 min (*see* **Note 8**).
6. Immerse the slides in tap water for 5 min.
7. Immerse the slides in distilled water 2 × 3 min.
8. Incubate the slides in 0.1% (w/v) Picro-sirius Red solution for 90 min.
9. Place the slides in 0.01 M hydrochloric acid for 2 × 15 s (*see* **Note 9**).

10. Immerse the slides in distilled water for 2 × 2 min.
11. Place the slides in a drying oven at 37 °C for 90 min (*see* **Note 10**).
12. Place the slides in 100% (v/v) ethanol (IMS) for 5 min.
13. Place the slides in xylene substitute for 3 × 5 min.
14. Pipette DPX mountant on to a glass coverslip using a plastic disposable Pasteur pipette.
15. Invert the glass slide onto the glass coverslip and gently push down onto the slide until DPX has reached the edges of the coverslip and there are no bubbles within the DPX.
16. Cure overnight at room temperature.
17. View under a brightfield microscope at ×10 magnification (*see* **Note 11**).
18. Measure the relative amount of collagen (which appears as red under a brightfield microscope) using suitable computerized image analysis software (such as ImageJ) and express as an average percentage of the atherosclerotic plaque cross-sectional area (*see* **Note 12**).

3.2 Elastin Van Gieson Histochemistry for Elastin

1. EVG staining can be achieved manually or through the use of an automated slide staining machine (*see* **Note 4)**.
2. Place the slides at 60 °C for 30 min (*see* **Note 5**).
3. Dewax the slides by placing in xylene substitute for 3 × 3 min (*see* **Note 6**).
4. Place the slides in 100% ethanol (industrial methylated spirits: IMS) for 2 × 3 min (*see* **Note 7**).
5. Place the slides in 70% ethanol (IMS) for 5 min (*see* **Note 8**).
6. Immerse the slides in tap water for 5 min.
7. Incubate the slides in 0.5% (w/v) potassium permanganate for 10 min.
8. Immerse the slides in distilled water for 3 min.
9. Incubate the slides in 1% oxalic acid for 5 min.
10. Immerse the slides in distilled water for 3 min.
11. Place the slides in 70% (v/v) ethanol (IMS) for 2 min.
12. Incubate the slides in 50% (v/v) Miller's elastin stain for 60 min.
13. Place the slides in 70% (v/v) ethanol (IMS) for 2 min.
14. Place the slides under running tap water for 3 min.
15. Incubate the slides in Van Gieson stain for 20 s.
16. Place the slides in 100% (v/v) ethanol (IMS) for 2 × 5 min.
17. Place the slides in xylene substitute for 2 × 5 min.

18. Pipette the DPX mountant on to a glass coverslip using a plastic disposable Pasteur pipette.
19. Invert the glass slide onto the glass coverslip and gently push down onto the slide until DPX has reached the edges of the coverslip and there are no bubbles in the DPX.
20. Cure overnight at room temperature.
21. View under a brightfield microscope at ×10 magnification.
22. Measure the relative elastin content (which appears as black under a brightfield microscope) using suitable computerized image analysis software (such as ImageJ) and express as an average percentage of the atherosclerotic plaque cross-sectional area.

3.3 Oil Red O Histochemistry for Neutral Lipids

1. Allow freshly prepared or previously cryo-preserved frozen sections to air dry for 30 min.
2. Immerse the slides in 10% (v/v) formalin in PBS for 10 min to fix the tissue sections (*see* **Note 13**).
3. Immerse the slides in distilled water for 2 × 3 min.
4. Briefly immerse the slides in 60% (v/v) isopropanol for 20 s.
5. Incubate the slides in Oil Red O working solution for 15 min.
6. Briefly immerse the slides in 60% (v/v) isopropanol for 20 s.
7. Immerse the slides in distilled water for 2 × 3 min.
8. Stain the cell nuclei by adding 50 μL (or a greater volume if necessary) of filtered Mayer's hematoxylin diluted in water to tissue sections and incubate for 1 min.
9. Wash the slides in tap water for 2 × 30 s.
10. Leave the slides in tap water for 5 min at room temperature to allow for the hematoxylin stain to develop.
11. Pipette an aqueous mountant on to a glass coverslip using a plastic disposable Pasteur pipette (*see* **Note 14**).
12. Invert glass slide onto the glass coverslip and gently push down onto the slide until the mountant has reached the edges of the coverslip and there are no bubbles within the mountant.
13. Cure for 1 h at room temperature.
14. View under a brightfield microscope at ×10 magnification.
15. Measure the relative amount of lipid (which appears as red under a brightfield microscope) using suitable computerized image analysis software (such as ImageJ) and express as an average percentage of the atherosclerotic plaque cross-sectional area (*see* **Note 15**).

3.4 Immunohistochemistry for Macrophages and Vascular Smooth Muscle Cells

1. Place glass microscope slides containing paraffin-embedded tissue sections in a microwavable slide rack.
2. Place the slides at 60 °C for 30 min (*see* **Note 5**).
3. Dewax the slides by placing in xylene substitute for 3 × 3 min (*see* **Note 6**).
4. Place the slides in 100% ethanol (industrial methylated spirits: IMS) for 2 × 3 min in order to remove the xylene substitute (*see* **Note 7**).
5. Place the slides in 70% ethanol (IMS) for 5 min (*see* **Note 8**).
6. Immerse the slides in tap water for 5 min to rehydrate the tissue sections.
7. Fill any remaining slots within the slide rack with blank microscope slides (*see* **Note 16**).
8. Transfer the slide rack containing the slides to a microwaveable container with a lid.
9. Add 10 mM citrate buffer to the container ensuring that the slides are covered by approximately half a centimeter of buffer.
10. Loosely place the lid on the container to prevent the buildup of pressure.
11. Microwave tissue sections for 2 × 5 min on the highest heat setting (*see* **Note 17**).
12. Allow the slides to cool for 30 min at room temperature (*see* **Note 18**).
13. Immerse the slides in cold running tap water for 5 min (*see* **Note 19**).
14. Wash the slides twice with PBS in glass coplin jars.
15. Transfer the slides to a fresh coplin jar containing 3% (v/v) H_2O_2 in distilled water and incubate for 5 min at 4 °C (*see* **Note 20**).
16. Wash the slides twice with PBS in glass coplin jars.
17. Draw around the tissue sections on glass slide with a wax hydrophobic barrier pen (*see* **Note 21**).
18. Re-immerse the slides in PBS to ensure that they do not dry out.
19. Add 50 μL of 20% (v/v) blocking serum diluted in 1% (w/v) BSA in PBS or commercial protein blocking reagent to the tissue sections (*see* **Note 22**).
20. Place the slides in a humidifying chamber where serum is used as a blocking agent and incubate for 30 min at room temperature. Commercial protein blocking reagents should be used in accordance with the manufacturer's instructions.

21. Tap the glass slide gently on its side to remove the serum/blocking reagent. Remove any excess with a dry soft tissue.
22. For the identification of macrophages, add 50 μL (or a greater volume if necessary) of anti-CD68 IgG diluted in 1% (w/v) BSA in PBS to tissue sections.
23. For the identification of vascular smooth muscle cells, add 50 μL (or a greater volume if necessary) of anti-α-smooth muscle actin diluted in 1% (w/v) BSA in PBS to tissue sections.
24. Add 50 μL (or a greater volume if necessary) of a non-immune IgG control diluted in 1% (w/v) BSA in PBS to a serial tissue section (*see* **Note 23**).
25. Incubate overnight at 4 °C in a humidifying chamber.
26. Wash the slides four times with PBS in glass coplin jars.
27. Add 50 μL (or a greater volume if necessary) of a species-relevant biotinylated secondary antibody diluted in 1% (w/v) BSA in PBS to tissue sections and incubate for 30 min at room temperature in a humidifying chamber.
28. Wash the slides four times with PBS in glass coplin jars.
29. Add 50 μL (or a greater volume if necessary) of streptavidin-HRP diluted in 1% (w/v) BSA in PBS to tissue sections and incubate for 30 min at room temperature in a humidifying chamber.
30. Wash the slides four times with PBS in glass coplin jars.
31. Add 50 μL (or a greater volume if necessary) of DAB peroxidase substrate diluted in distilled water to tissue sections (*see* **Notes 24** and **25**) and incubate for 10 min or as recommended by the manufacturer.
32. Wash the slides three times in distilled water in glass coplin jars.
33. Stain cell nuclei by adding 50 μL (or a greater volume if necessary) of filtered Mayer's hematoxylin diluted in water to tissue sections and incubate for 1 min.
34. Wash the slides three times in tap water in glass coplin jars.
35. Leave the slides in running cold tap water for 5 min at room temperature to allow for hematoxylin stain to develop.
36. Dehydrate tissue sections by placing the slides in a slide rack and performing 5-min incubations in 70% ethanol (IMS), 2× in 100% ethanol (IMS) and then 3× xylene substitute (*see* **Note 26**). This is the reverse process of deparaffinization and rehydration.
37. Pipette DPX mountant onto coverslips.
38. Place the slides upside down against coverslips, press gently and lift.

39. Remove air bubbles by gently pressing down on the area.
40. Cure the mountant overnight before imaging in order to reach the optimal refractive index.
41. View under a brightfield microscope at ×10 magnification.
42. Measure the staining using suitable computerized image analysis software (such as ImageJ) and express as an average percentage of the atherosclerotic plaque cross-sectional area.

3.5 Identification of Buried Fibrous Layers

1. Inspect α-smooth muscle actin immunolabeled plaque sections for the presence of buried fibrous layers, identified as α-smooth muscle cell-rich layers (*see* Fig. 1Ai, Aii).
2. Inspect EVG-stained serial section to confirm the identified buried fibrous layer is also invested with elastin (*see* Fig. 1Bi, Bii).
3. Inspect PSR-stained serial section to confirm the identified buried fibrous layer is also invested with collagen (*see* Fig. 1Ci, Cii).
4. Determine and count the number of buried fibrous layers per plaque and present as discontinuous data (incidence of buried fibrous layers) analyzed by the Mann–Whitney test, or as contingency data (presence or absence of a buried fibrous layer) analyzed by Fisher exact test for 2-group comparisons (*see* **Note 27**).

3.6 Assessment of Plaque Vulnerability

1. Quantify the percentage of atherosclerotic plaque area occupied by macrophages (CD68 immuno-positive cells), (*see* **Note 28**).
2. Quantify the percentage of atherosclerotic plaque area occupied by vascular smooth muscle cells (α-SM actin immuno-positive cells), (*see* **Note 28**).
3. Quantify the percentage of atherosclerotic plaque area occupied by collagen, from PSR-stained serial section.
4. Quantify the percentage of atherosclerotic plaque area occupied by lipid, from Oil Red O-stained serial frozen sections, or EVG-stained paraffin-wax sections (*see* **Note 15**).
5. Calculate the vulnerability index by dividing the percentage of plaque area occupied by macrophages and lipid, by that of vascular smooth muscle cells and collagen. A score significantly >1 implies increased vulnerability, conversely significantly <1 suggests heightened stability (*see* **Note 29**).

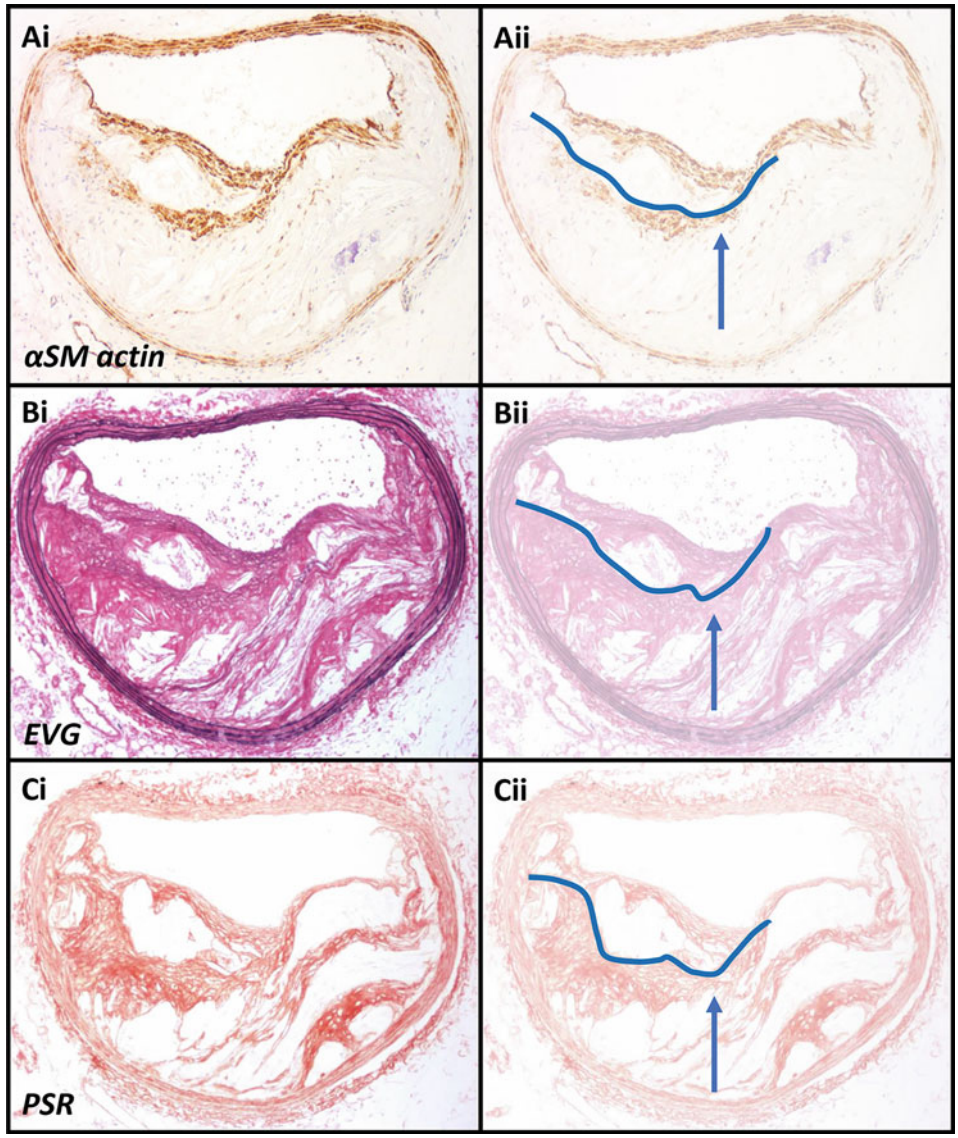

Fig. 1 Identification of buried fibrous layers within mouse atherosclerotic plaques. Serial sections from an apolipoprotein E-deficient mouse brachiocephalic atherosclerotic plaque for the identification of buried fibrous layers. (**A**) Plaque section immunolabeled for vascular smooth muscle cells (α-SM actin), (**B**) plaque section stained for elastin (EVG), and (**C**) plaque section stained for collagen (PSR). The presence of buried fibrous layers can be observed in non-modified images (Ai, Bi, and Ci), and corresponding faded images with blue lines and arrows indicating presence of the most recent buried fibrous layer (Aii, Bii, and Cii). EVG = elastin van Gieson, PSR = Picro-sirius Red; αSM actin = alpha smooth muscle actin

4 Notes

1. Mayer's hematoxylin requires filtration to remove precipitates and often needs diluting 1:2 to 1:4 in water to reduce strength.

2. Serum should match the species the secondary antibody is raised in, and aliquoted and stored at −20 °C. Commercial blocking reagents should be prepared and stored in accordance with manufacturer's instructions.
3. The secondary antibody must be complementary to the species the primary antibody is raised in. Working concentrations and storage instructions are typically indicated in product data-sheets from supplier.
4. If an automatic slide stainer is not available, then the sections can be stained manually.
5. Heating slides at 60 °C for 30 min melts the paraffin-wax and enables maximal adherence of tissue sections to the slides and prevents sections from lifting or falling off the slide during histochemical staining or immunohistochemistry procedures.
6. Ensure that the slides are completely immersed and shake slide rack gently to dispel any air bubbles to ensure complete paraffin-wax removal.
7. When transferring slides between different or graduated solvents, shake the slide rack to fully drain any liquid so that the previous pot's liquids are not transferred to the next one.
8. Ensure that the tissue sections are not left to dry at any point until a coverslip had been applied.
9. This step is required to remove excess Picro-sirius red staining to non-collagenous tissue structures. However, prolonged incubation in 0.01 M hydrochloric acid will result in the removal of collagen-specific staining.
10. Picro-sirius red in solution is partially miscible in ethanol, therefore it is necessary to dry slides in order to remove excess water before transferring the slides into ethanol.
11. Picro-sirius red staining of collagen can also be assessed under polarized light.
12. Qualitative analysis of fiber thickness/age can be assessed by delineating the green and red fibers indicated under polarized light, as fiber color variation transits from green to red proportional to the increase of fiber thickness/age. The relative amount of each fiber color is expressed as a percentage of the total amount of collagen in the area of interest.
13. If immunohistochemistry is also to be undertaken on the same slide, sections should instead be fixed in ice-cold acetone for 10 min, and then allowed to air dry for a further 10 min.
14. Oil Red O stain is partially miscible in solvents; therefore, it is necessary to mount/coverslip slides with an aqueous mountant to avoid the stain leaching from the section.

15. If frozen sections are not available, EVG-stained plaque sections can also be utilized to estimate plaque lipid content [6]. In brief, color images of delipidated paraffin sections can be digitally processed into monochrome with image analysis software, to render tissue as black and delipidated areas as white. The total white area within the plaque is then expressed as a percentage of the total plaque area to provide the fractional lipid content. This method has been supported through assessment against Oil Red O-stained sections, which demonstrated that this is a valid method for estimating plaque lipid content [6].
16. Filling the slide rack with blank microscope slides will help prevent the formation of large air bubbles during the heating process, which can often damage tissue sections or detach tissue sections from the surface of slides.
17. Due to the escape of buffer during boiling, after 5 min the buffer levels will need to be replenished with distilled water to ensure the slide remained covered. It is important that the slides are always immersed in citrate buffer as the drying out of tissue sections will affect the specificity of subsequent immune-labeling.
18. This cooling step should not be omitted or shortened to ensure efficient antigen retrieval.
19. The flow of tap water should be gentle in order to prevent the damage or potential loss of tissue sections from the slides.
20. This step is essential when using colorimetric staining where DAB is oxidized by hydrogen peroxide through catalysis with HRP (conjugated to a secondary antibody or streptavidin) to produce a brown precipitate. As endogenous peroxidase activity can also catalyze oxidation of DAB by hydrogen peroxide, generating false positive staining, the activity of endogenous peroxidase activity should always be quenched.
21. The use of a wax hydrophobic barrier pen provides a barrier around the tissue section ensuring that the liquid remains in contact with the section and avoids leaking of solution or drying out of the section. This also permits the use of smaller reagent volumes.
22. Blocking with serum or other commercial protein blocking reagents markedly reduces non-specific binding of antibodies to tissue sections.
23. To account for any non-specific interactions of the primary antibody with the tissue sample, for each condition, a serial tissue section should be incubated with a non-immune IgG control. The non-immune IgG control must be diluted to the same concentration of the primary antibody and match the

species and isotype (for example, IgG1, IgG2A, IgG2B, and IgM) as that of the primary antibody.

24. Once the DAB peroxidase substrate is reconstituted in distilled water (in accordance with manufacturer's instructions), it is essential that it is used within 15 min.
25. The brown DAB precipitate is insoluble in water, alcohol, and xylene substitute, thereby allowing for flexibility with subsequent treatments and choice of mountant.
26. Do not use xylene substitute initially deployed during deparaffinization as this will contain abundant dissolved wax and should therefore not be used for dehydration of stained tissue sections.
27. Layered structures are observed within advanced mouse atherosclerotic plaques which are rich in elastin and collagen and are populated by α-smooth muscle actin-positive cells, regarded as smooth muscle cells [9] (*see* Fig. 1). These characteristics are highly suggestive of remnants of previous fibrous caps that have ruptured and have been integrated into plaques during their progression. When similar "buried" structures are observed in human plaques, they are interpreted as indicative of previous, clinically silent, healed plaque rupture [3, 10]. Numerous lines of evidence endorse a comparable interpretation in mice [9]: buried fibrous layers are only seen at sites where plaque ruptures occur; they are associated with fibrin deposition; and they can be modulated independently of changes in plaque size [6]. This suggests that buried fibrous layers either represent sites of previous plaque rupture in mice, or occur in parallel with plaque rupture, and are therefore useful indicators of previous plaque instability, and have therefore previously been used quantitatively [6–8, 11–13].
28. Cell-lineage and single-cell next-generation sequencing experiments in mouse models of atherosclerosis have highlighted potential limitations in using CD68 and α-SM actin as macrophage and VSMC markers, respectively [14, 15].
29. The division of plaque macrophage and lipid content by that of VSMCs and collagen yields a vulnerability index, with a higher number implying a deleterious shift in cellular and extracellular components, as described previously [13, 16, 17].

Acknowledgments

Jason Johnson is funded by British Heart Foundation Senior Research Fellowship, FS/18/1/33234.

References

1. Davies MJ (2000) The pathophysiology of acute coronary syndromes. Heart 83(3): 361–366
2. Falk E, Nakano M, Bentzon JF, Finn AV, Virmani R (2013) Update on acute coronary syndromes: the pathologists' view. Eur Heart J 34(10):719–728
3. Burke AP, Kolodgie FD, Farb A, Weber DK, Malcom GT, Smialek J et al (2001) Healed plaque ruptures and sudden coronary death - Evidence that subclinical rupture has a role in plaque progression. Circulation 103(7): 934–940
4. Davies MJ (2001) Going from immutable to mutable atherosclerotic plaques. Am J Cardiol 88(4A):2F–9F
5. Falk E (1992) Why do plaques rupture? Circulation 86(6 Suppl):III30–III42
6. Johnson J, Carson K, Williams H, Karanam S, Newby A, Angelini G et al (2005) Plaque rupture after short periods of fat-feeding in the apolipoprotein E knockout mouse: model characterisation, and effects of pravastatin treatment. Circulation 111:1422–1430
7. Johnson JL, Baker AH, Oka K, Chan L, Newby AC, Jackson CL et al (2006) Suppression of atherosclerotic plaque progression and instability by tissue inhibitor of metalloproteinase-2: involvement of macrophage migration and apoptosis. Circulation 113(20):2435–2444
8. Johnson JL, Devel L, Czarny B, George SJ, Jackson CL, Rogakos V et al (2011) A selective matrix metalloproteinase-12 inhibitor retards atherosclerotic plaque development in apolipoprotein E-knockout mice. Arterioscler Thromb Vasc Biol 31(3):528–535
9. Jackson CL, Bennett MR, Biessen EA, Johnson JL, Krams R (2007) Assessment of unstable atherosclerosis in mice. Arterioscler Thromb Vasc Biol 27(4):714–720
10. Mann J, Davies MJ (1999) Mechanisms of progression in native coronary artery disease: role of healed plaque disruption. Heart 82: 265–268
11. Johnson JL, George SJ, Newby AC, Jackson CL (2005) Divergent effects of matrix metalloproteinases -3, -7, -9 and -12 on atherosclerotic plaque stability in mouse brachiocephalic arteries. Proc Natl Acad Sci U S A 102(43): 15575–15580
12. Johnson JL, Fritsche-Danielson R, Behrendt M, Westin-Eriksson A, Wennbo H, Herslof M et al (2006) Effect of broad-spectrum matrix metalloproteinase inhibition on atherosclerotic plaque stability. Cardiovasc Res 71(3):586–595
13. Di Gregoli K, George SJ, Newby AC, Johnson JL (2016) Differential effects of tissue inhibitor of metalloproteinase (TIMP)-1 and TIMP-2 on atherosclerosis and monocyte/macrophage invasion. Cardiovasc Res 109(2): 318–330
14. Feil S, Fehrenbacher B, Lukowski R, Essmann F, Schulze-Osthoff K, Schaller M et al (2014) Transdifferentiation of vascular smooth muscle cells to macrophage-like cells during atherogenesis. Circ Res 115(7): 662–667
15. Shankman LS, Gomez D, Cherepanova OA, Salmon M, Alencar GF, Haskins RM et al (2015) KLF4-dependent phenotypic modulation of smooth muscle cells has a key role in atherosclerotic plaque pathogenesis. Nat Med 21(6):628–637
16. Di Gregoli K, Mohamad Anuar NN, Bianco R, White SJ, Newby AC, George SJ et al (2017) MicroRNA-181b controls atherosclerosis and aneurysms through regulation of TIMP-3 and elastin. Circ Res 120(1):49–65
17. Di Gregoli K, Somerville M, Bianco R, Thomas AC, Frankow A, Newby AC et al (2020) Galectin-3 identifies a subset of macrophages with a potential beneficial role in atherosclerosis. Arterioscler Thromb Vasc Biol 40(6): 1491–1509

Chapter 33

Use of Mouse Carotid Artery Ligation Model of Intimal Thickening to Probe Vascular Smooth Muscle Cell Remodeling and Function in Atherosclerosis

Helen Williams, Bethan A. Brown, Jason L. Johnson, and Sarah J. George

Abstract

The thickening of the intima is a critical underlying component of atherosclerosis. Consequently, robust and reproducible animal models of intimal thickening are essential for a greater understanding of the mechanisms underlying the process of intimal thickening and to evaluate new approaches for the reduction of intimal thickening and thereby atherosclerosis. The ligation of the carotid artery in the mouse causes the thickening of the intimal layer of the artery. This model is relatively simple and is reproducible and therefore is a preferred and well-established model of intimal thickening. Here, we detail a protocol for carotid artery ligation in the mouse and methods for histological examination and quantification of intimal thickening.

Key words Mouse, Carotid artery, Intimal thickening, Proliferation, Migration

1 Introduction

Pathological intimal thickening occurs early in the pathogenesis of atherosclerosis and is the "soil" for the development of advanced plaques [1]. Consequently, an animal model of intimal thickening provides a platform to investigate the underlying mechanisms responsible for the altered cellular behavior that leads to thickening of the intima and test novel therapeutic approaches to retard intimal thickening. We routinely use the mouse carotid artery ligation model to induce intimal thickening *in vivo* [2–5]. Using the carotid artery ligation model, it is possible to evaluate intima size, as well as smooth muscle cell content, endothelial coverage, proliferation, migration, and apoptosis.

To perform a ligation, the left carotid artery is exposed and tied with a tight knot of suture thread to cause 100% occlusion of the artery (*see* Fig. 1). The ligation of the carotid artery causes blood stasis, turbulence, platelet activation, micro-thrombosis, inflammation, smooth muscle cell migration and proliferation and therefore

Dipak P. Ramji (ed.), *Atherosclerosis: Methods and Protocols*, Methods in Molecular Biology, vol. 2419,
https://doi.org/10.1007/978-1-0716-1924-7_33,
© The Author(s), under exclusive license to Springer Science+Business Media, LLC, part of Springer Nature 2022

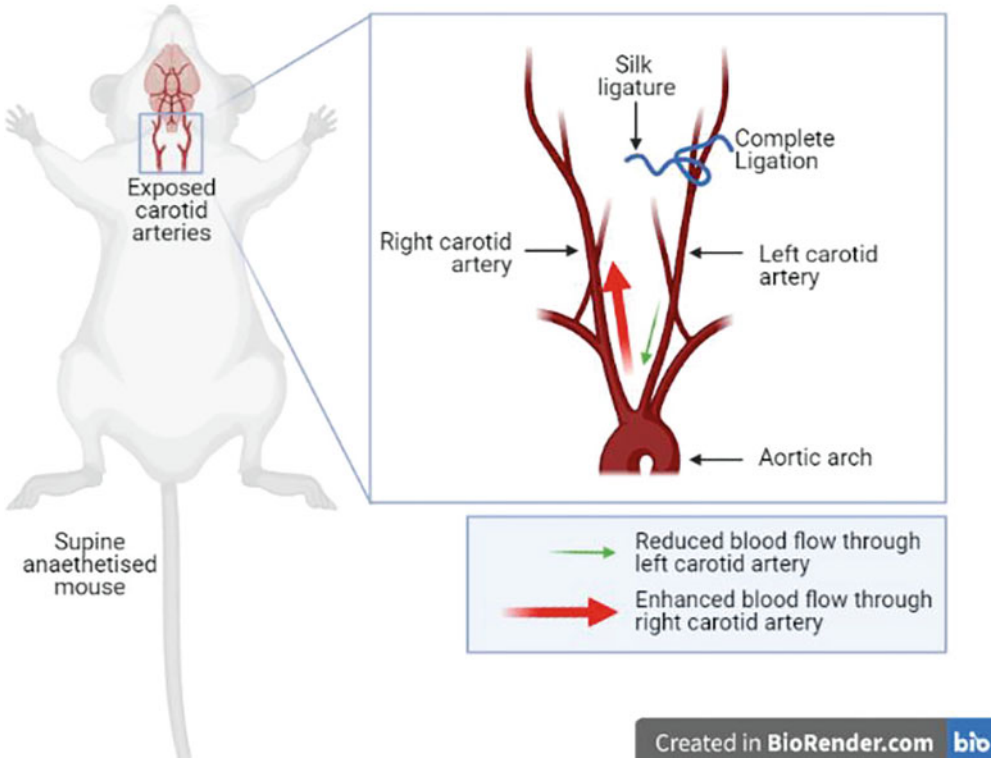

Fig. 1 Schematic diagram of the mouse left carotid artery ligation model. The schematic diagram illustrates the exposed carotid arteries of an anaesthetized mouse placed in the supine position. The left carotid artery is ligated with a silk ligature, resulting in reduced blood flow through the left carotid artery and enhanced blood flow through the right carotid artery and subsequent thickening of the intima. Created with BioRender.com

intimal thickening (*see* Fig. 2). The right carotid artery will experience increased blood flow as a compensatory mechanism, so it can be used to monitor effects of altered blood flow on arterial remodeling due to enhanced shear stress. Due to these changes the right carotid is not suitable as an internal control, instead sham operated animals should be used.

Advantages of the carotid artery ligation model include that it is a small animal model utilizing one of the least sentient mammals. The small size of the mouse makes this model relatively cheap in terms of purchasing, housing, and feeding the animals and the amount of drug used for the studies. The entire mouse genome is documented, and many genetically modified mice are available. Chimeric mice can be created, or transgenic mice can be used to assess the role of specific genes using knockouts and knock-ins; and reporter mice can be utilized to assess the role of particular signaling pathways.

This model can be performed in mice of different ages and males and females and therefore it can be utilized to study the effect of aging [6] and gender. Moreover, cardiovascular risk factors can

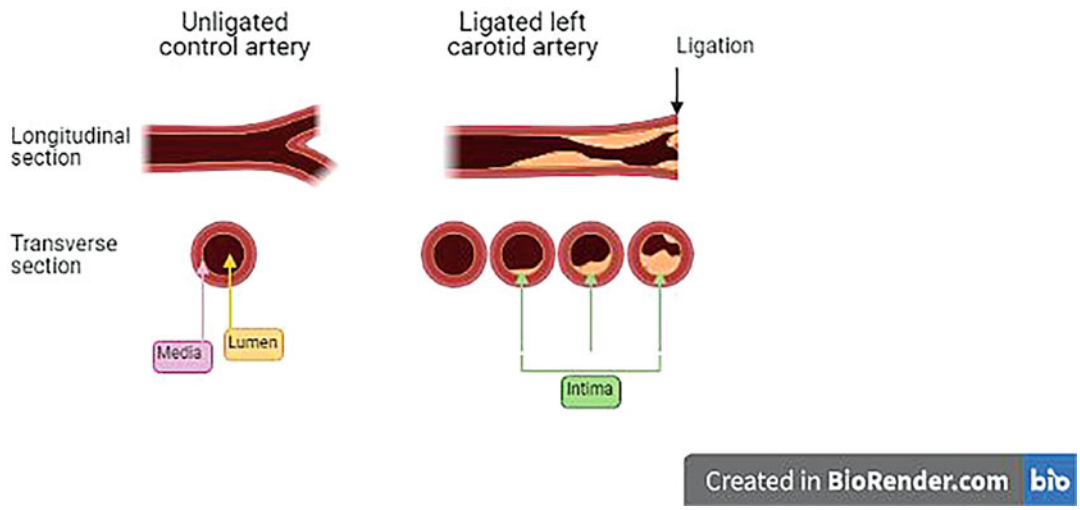

Fig. 2 Schematic representation of the mouse carotid artery before and after ligation. The schematic diagram illustrates the unligated mouse left carotid artery in longitudinal and transverse section. The control artery is composed of a medial layer and an open lumen. The left carotid artery is ligated proximal to the bifurcation (right-hand side) which induces the thickening of the intimal layer which encroaches the lumen. The intima can be observed both in the longitudinal and transverse sections. Created with BioRender.com

be incorporated into the model; for example, genetically modified mice are useful models of atherosclerosis (e.g., Apolipoprotein E knockout mice), which can be used to super-impose atherosclerosis [7], or mice can be rendered diabetic using streptozotocin [8].

The model utilizes a relatively simple surgery, requires only one intervention and can incorporate gene or drug delivery. Importantly, one can evaluate the proliferation and migration rates in the neointima produced, as well as measuring intimal size and composition together with gene/protein expression.

The disadvantages of this model include that is a non-spontaneous model, which requires artificial surgery to induce. Additionally, it is only a model of intimal thickening not a model of vein graft failure or in-stent restenosis and therefore researchers should be cautious in terms of extrapolating to the human disease scenarios. A predominating factor is the formation of a thrombus that initiates lesion formation, which may not always be the case in humans. Additionally, the carotid artery is small and therefore each carotid artery cannot be divided into segments for different types of analysis (i.e., formalin-fixed paraffin sections, isopentane-frozen sections, and mRNA or protein extractions). Finally, the effects seen in mouse models do not always translate into humans due to genetic and phenotypic variations.

2 Materials

2.1 Surgical Procedure

2.1.1 Materials

1. 3% Isoflurane.
2. 100% Oxygen cylinder or concentrator machine.
3. 7.5% (w/w) Povidone-Iodine Surgical Scrub.
4. 0.3 mg/mL Buprenorphine (Vetergesic).
5. 400 mg/mL Pentobarbital sodium solution (Euthatal).
6. 50 mg/mL bromodeoxyuridine (BrdU).

2.1.2 Equipment (See Fig. 3)

Asterisks indicate equipment that should be sterilized by autoclaving prior to use.

1. Isoflurane anesthetic machine.
2. Perspex anesthesia chamber.

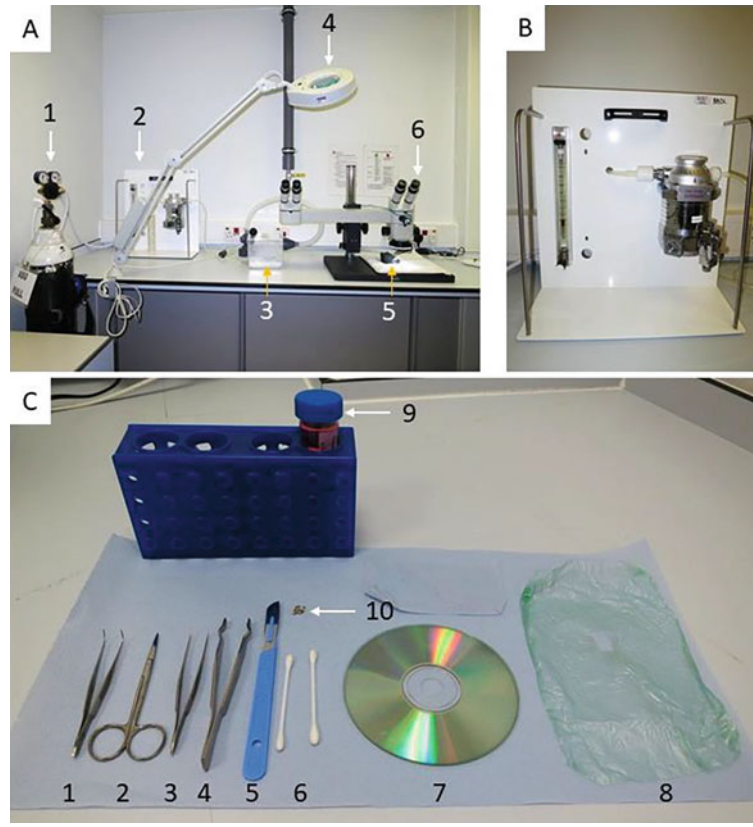

Fig. 3 Surgical equipment required for carotid artery ligation. (**a**) 1: Oxygen cylinder, 2: isoflurane anesthetic machine, 3: box for induction of anesthesia, 4: light, 5: tube for maintenance, and 6: binocular dissection microscope. (**b**) Isoflurane anesthetic machine. (**c**) 1: curved forceps, 2: scissors, 3: fine curved forceps, 4: skin staple clamp, 5: scapel, 6: cotton buds, 7: compact disc, 8: drape with rectangular hole, 9: iodine, and 10: skin wound clips

3. Dissection microscope.
4. Light.
5. Hair clippers.
6. Heated mat.
7. Warmed mouse cage.
8. Wound closure clips and clamp*.
9. Two pairs of blunt, curved forceps*.
10. Blunt-ended (blunt/blunt) dissection scissors*.
11. Scalpel*.
12. Cotton buds*.
13. Transparent over-drape*.
14. Silk suture 5-0*.
15. Compact disc*.
16. Surgical clothing: gown, gloves, scrubs, mask, hair-net, and plastic overshoes (*see* **Note 1**).
17. Alzet mini-osmotic pumps (*see* **Note 2**).

2.2 Sample Preservation, Processing, and Analysis

2.2.1 Materials

1. Phosphate buffered saline (PBS): 137 mM NaCl, 2.7 mM KCl, 10 mM Na_2HPO_4, 1.8 mM KH_2PO_4, pH 7.4.
2. Formalin/PBS: 10% (v/v) formalin in PBS.
3. 1.5% (w/v) agar in 1% (v/v) formalin in PBS.
4. Paraffin wax.
5. Distyrene, plasticizer and xylene (DPX).

Formalin-Fixed Samples (*See* **Note 3**)

Isopentane-Frozen Samples (*See* **Note 4**)

1. Isopentane.
2. Optimum cutting temperature compound.

Liquid Nitrogen Frozen Samples (*See* **Note 5**)

1. mRNA extraction kit.
2. 5% sodium dodecyl sulfate (SDS) lysis buffer: 5% (w/v) SDS, 50 mM Tris–HCl pH 6.8, 10% (v/v) glycerol.

Elastic Van Gieson (EVG) Staining

1. Xylene substitute.
2. 100% ethanol (industrial methylated spirits: IMS).
3. Running tap water.
4. 0.5% (w/v) potassium permanganate.
5. Distilled water.
6. 1% oxalic acid.
7. 70% (v/v) ethanol (IMS).
8. 50% (v/v) Millers elastin stain.
9. Van Gieson stain.

Immunodetection of BrdU Incorporation

1. Xylene substitute.
2. 100% ethanol (IMS).
3. 70% ethanol (IMS).
4. 10 mM citrate buffer, pH 6.0: Dissolve 1.92 g of citric acid in just under 1 L of water by continually stirring with a magnetic stirrer. Once dissolved, bring to pH 6.0 by adding concentrated NaOH dropwise. Make volume up to 1 L. Store at room temperature.
5. Running tap water.
6. PBS.
7. 3% (v/v) H_2O_2 in water (for colorimetric detection protocol).
8. 10 mM HCl (*see* **Note 6**) or 125 U/mL benzonase nuclease in PBS supplemented with 1 mM $MgCl_2$ (colorimetric and fluorescent detection protocols, respectively).
9. 20% (v/v) serum diluted in PBS or commercial blocking reagent for immunohistochemistry (*see* **Note 7**).
10. Anti-BrdU IgG.
11. 1% (w/v) bovine serum albumin (BSA) in PBS.
12. Biotinylated secondary antibody diluted in 1% (w/v) BSA in PBS (*see* **Note 8**).
13. Streptavidin-horseradish peroxidase (HRP) diluted in 1% (w/v) BSA in PBS.
14. 3,3′-Diaminobenzidine (DAB) peroxidase substrate.
15. Mayer's hematoxylin (*see* **Note 9**).
16. Streptavidin with a fluorophore tag diluted in 1% (w/v) BSA in PBS (*see* **Note 10**).
17. DPX mountant.
18. Liquid mountant formulated with 4′,6-diamidino-2-phenylindole (DAPI: or another fluorescent nuclear counterstain).

2.2.2 Equipment

Formalin-Fixed Samples

1. Syringes.
2. Rack for syringes.
3. Hot plate.
4. 500 mL glass beaker.
5. Histology cassettes.
6. 500 mL plastic beaker.
7. Refrigerator (4 °C).
8. Tissue processor machine.
9. Wax embedding center.
10. Wax embedding molds.

11. Microtome.
12. Microtome blades.
13. Cold plate.
14. Tissue floating water bath.
15. Glass slides (basic and super-adherent) (*see* **Note 11**).
16. Racks for glass slides with lid.
17. Forceps.
18. Scissors.
19. 1.5 mL screw cap tubes.

Isopentane-Frozen Samples

1. Glass slides (basic and super-adherent) (*see* **Note 11**).
2. Racks for glass slides with lid.
3. 1.5 mL cryovials.
4. 50 mL beaker.
5. 30 cm long pair of forceps.
6. Vacuum flask containing liquid nitrogen.
7. −80 °C freezer.
8. Cryostat.
9. Cryostat chuck mounts.
10. Fine forceps.
11. Soft toothbrush or fine paint brush.
12. Aluminum foil.

Liquid Nitrogen Frozen Samples

1. 1.5 mL cryovials.
2. 30 cm long pair of forceps.
3. Vacuum flask containing liquid nitrogen.
4. −80 °C freezer.
5. Fine scissors.
6. Fine forceps.
7. 1.5 mL RNAse-free microcentrifuge tube for mRNA extraction.
8. 1.5 mL microcentrifuge tube for protein extraction.
9. Wet ice.
10. Polystyrene ice container.
11. Fine scissors.
12. Vortex.
13. Microcentrifuge.

EVG Staining

1. Slide autostainer machine for automated staining or for manual staining glass coplin jars or glass staining troughs and slide racks.
2. Glass coverslips (50 mm long).
3. Brightfield microscope.
4. Disposal plastic Pasteur pipette.

Immunodetection of Incorporated BrdU

1. Microwave oven.
2. Plastic microwavable staining dish with lid.
3. Glass coplin jars.
4. Refrigerator (4 °C).
5. Glass square staining troughs.
6. Slide racks.
7. Humidified chamber for glass slide incubations.
8. Wax hydrophobic barrier pen for marking slides.
9. Soft paper tissue.
10. Glass coverslips (50 mm long).
11. Brightfield microscope.
12. Fluorescence microscope.

3 Methods

3.1 Surgical Procedure

3.1.1 Carotid Artery Ligation

The procedure is for carotid artery ligation on the left common carotid artery of male and female adult mice approximately 2 months old to investigate intimal thickening *in vivo* (*see* **Note 12**). The procedure must follow appropriate animal research guidelines (*see* **Note 13**).

1. Anesthetize mice by inhalation of 3% Isoflurane in 100% oxygen at 1 L/min (*see* Fig. 3).
2. Remove hair (*see* **Note 14**) from the surgical area using hair clippers (*see* **Note 15**).
3. Position the nose into the anesthetic tube and tape the mouse to a sterile surface (e.g., using autoclaved compact discs) on top of the clean heated mat positioned under the dissecting microscope.
4. Clean the skin area with iodine surgical scrub using a cotton bud.
5. Cover the mouse with a sterile transparent over-drape with a small hole through which the surgery is conducted.
6. Using a scalpel, make a 1 cm wound to open the neck (*see* Fig. 4a).

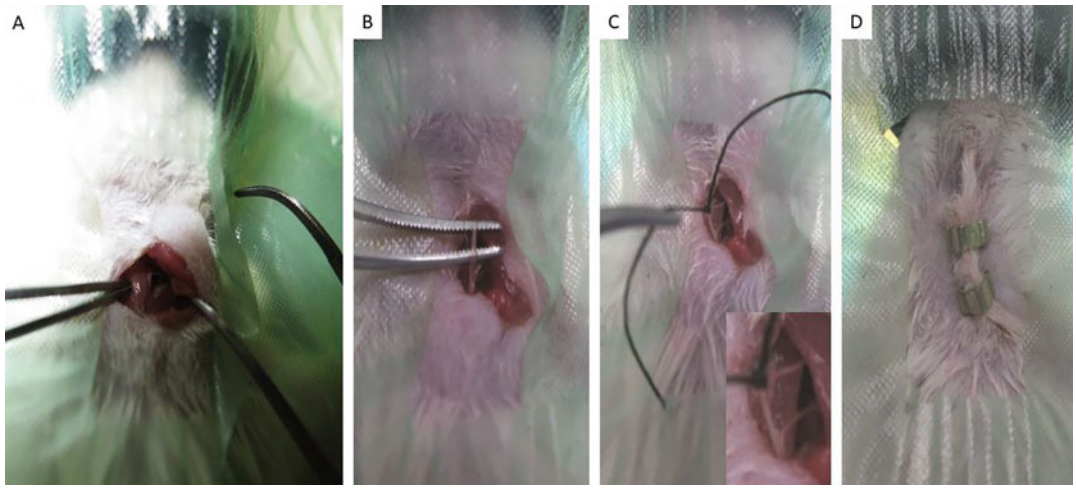

Fig. 4 Surgical procedure. (**a**) After removing a small area of fur in the neck area with hair clippers, the skin is cleaned with iodine using cotton buds. The drape with a rectanular hole is placed over the neck area. A small incision is made in the skin and the left carotid artery is then isolated from surrounding tissue and the nerve which runs alongside the artery by blunt dissection. (**b**) The curved forceps are placed under the left carotid artery. (**c**) The 5-0 silk suture is threaded under the left carotid artery and then tied to ligate the artery proximal to the bifurcation. Insert shows higher magnification of the ligated artery. Excess suture is removed by cutting with scissors. (**d**) The wound is closed with wound clips. It is then essential to apply appropriate postoperative pain relief (Vetergesic) before recovery

7. Expose the left carotid artery using blunt-ended dissection scissors.
8. Isolate the left carotid artery from the surrounding tissue and the nerve which runs alongside. Place the curved forceps underneath the isolated left carotid artery (*see* Fig. 4b and **Note 16**).
9. Thread the 5-0 silk suture beneath the left carotid artery. Tie the left carotid artery using 5-0 silk suture just proximal to the carotid bifurcation (*see* Fig. 4c).
10. Remove excess suture with scissors (*see* **Note 17**) and close the wound with clips (*see* Fig. 4d).
11. For experimental designs that require the use of an osmotic pump (Alzet) to deliver compounds such as BrdU during the study period, implant these subcutaneously in the neck area at this stage (*see* **Notes 18** and **19**).
12. For experimental designs that require the local delivery of pharmaceuticals/compounds or gene therapy this is given at this stage either applied to the adventitia of the carotid artery directly or in pluronic gel (*see* **Notes 20** and **21**).
13. Administer appropriate postoperative pain relief such as 1.5 μg of buprenorphine hydrochloride (Vetergesic) (50 mg/kg for a 30 g mouse) for analgesia.
14. Allow the mouse to recover in a warmed cage until it can walk before returning to a clean cage in the mouse room.

3.1.2 Termination of Animal and Collection of Arterial Samples

1. Remove the ligated artery at various timepoints after ligation between 3 and 28 days to examine intimal thickening.
2. Carry out terminal anesthesia of the mouse with 20 mg of pentobarbital sodium (Euthatal).
3. Dissect the ligated left carotid artery and the contralateral right carotid artery.
4. Remove fat/debris under a dissecting microscope using blunt-ended dissection scissors.

3.2 Preservation of Samples

3.2.1 Formalin-Fixation of Samples

1. Add 500 μL of 10% (v/v) formalin in PBS to labeled 1.5 mL screw cap tubes.
2. Place dissected artery (*see* Fig. 5) in 500 μL of 10% (v/v) formalin in PBS for 24 h fixation.
3. Transfer the fixed arteries into screw cap tubes containing 1.5 mL of PBS.
4. Store fixed tissue at 4 °C until histological processing.

3.2.2 Isopentane-Frozen Samples

1. Place 5 mL of isopentane into a 50 mL plastic beaker.
2. Hold beaker using a 30 cm long pair of forceps.
3. Immerse the bottom of the beaker in liquid nitrogen until small crystals form.
4. Remove beaker from liquid nitrogen.
5. Drop artery into isopentane.
6. After 5 s remove frozen artery and place in labeled 1.5 mL cryovial.
7. Place cryovial in liquid nitrogen until moving to storage in −80 °C freezer.

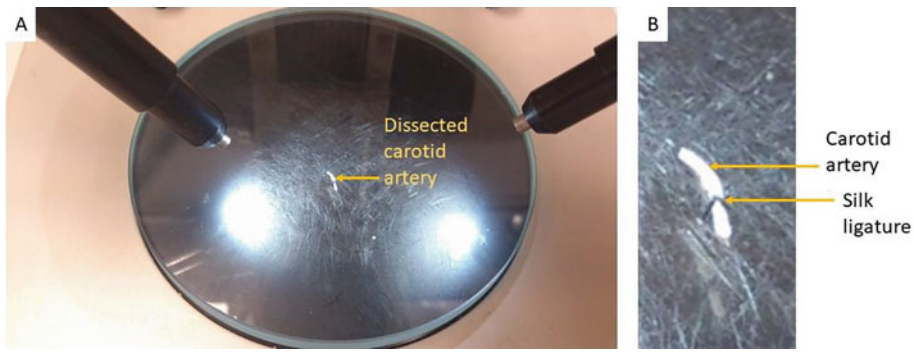

Fig. 5 Dissected carotid artery. (**a**) After termination of the mouse, the ligated carotid artery is cut 1 cm proximal to the ligation and at the bifurcation distally to the ligation. The explanted artery is fixed in 10% formalin in PBS for 24 h. (**b**) Higher power image of the removed left carotid artery

3.2.3 Frozen Samples

1. Remove ligature from carotid artery using scissors and forceps.
2. Place artery in labeled 1.5 mL cryovial.
3. Place cryovial in liquid nitrogen.
4. After 1 min remove cryovial from liquid nitrogen.
5. Store cryovial in −80 °C freezer.

3.3 Processing of Arterial Samples

3.3.1 Formalin-Fixed Samples

1. Use a mixture of 1.5% (w/v) agar and 1% (v/v) formalin in PBS to stabilize the vessel for embedding in the correct orientation (*see* Fig. 6a).
2. Warm 1.5% (w/v) agar and 1% (v/v) formalin in PBS solution in a water bath until it melts (*see* Fig. 6b).
3. Using syringe bases, make pellets of agar approximately 5 mm deep (*see* Fig. 6c).
4. Either lay the vessel flat on the base of the bottom of the cavity for longitudinal sections (*see* Fig. 6d) or stand up for transverse sections.
5. Remove the knot if this prevents the carotid artery from lying flat.

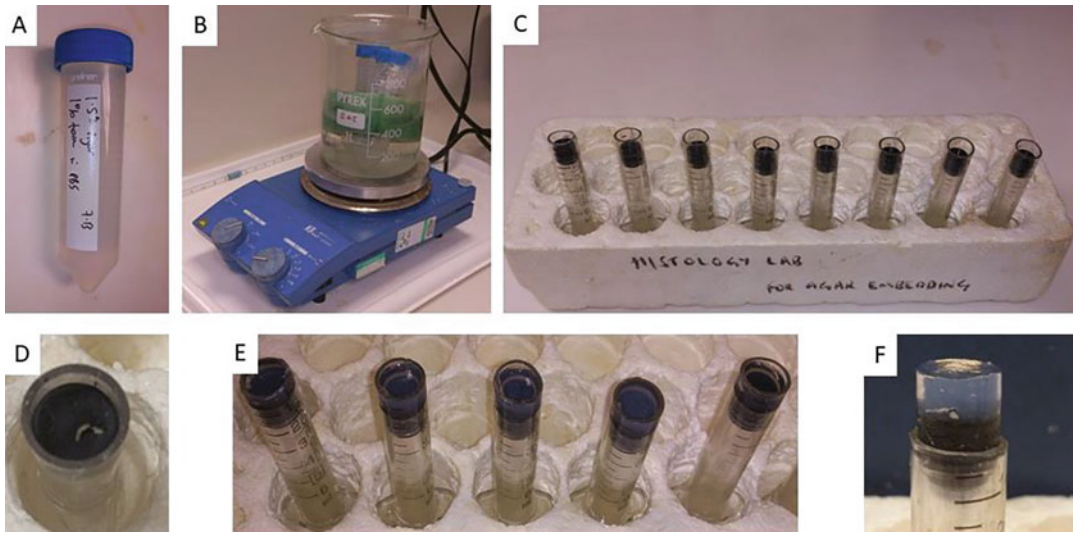

Fig. 6 Agar embedding of carotid artery. (**a**) 1.5% (w/v) agar in 1% (v/v) formalin in PBS is used to stabilize the vessel for embedding in the longitudinal orientation. (**b**) 1.5% (w/v) agar in 1% (v/v) formalin in PBS is warmed in a water bath to melt and enable pipetting into mold. (**c**) Syringe bases are used to make pellets of agar approximately 5 mm deep. (**d**) The vessel is either laid flat on the base of the bottom of the syringe cavity for longitundinal sections as shown here or can be embedded in a vertical position for transverse sections. The knot can be removed if this prevents it from lying flat or hampers vertical positioning. (**e**) The agar is left to set for 5 min until it appears translucent. (**f**) The set pellet is removed and placed in a histology processing cassette

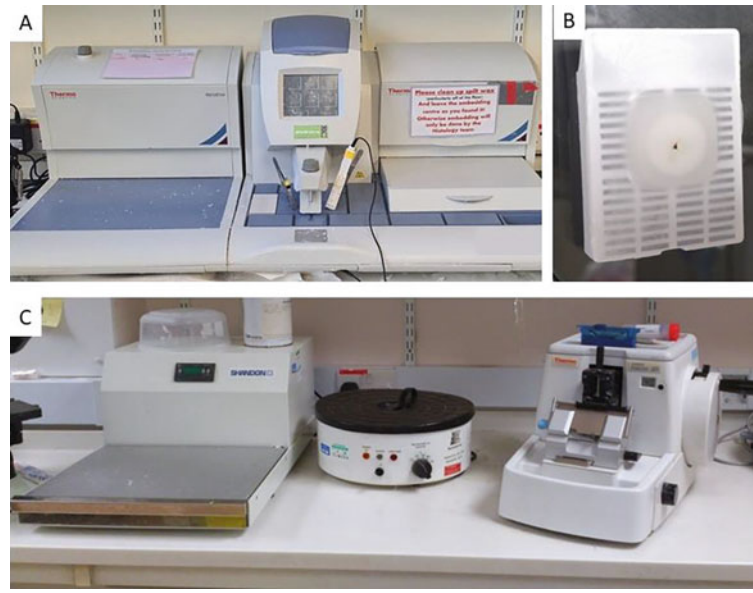

Fig. 7 Paraffin wax embedding and cutting. (**a**) The agar pellets within cassettes are processed overnight in a tissue processing machine. The processed agar pellets are then embedded in paraffin wax using the embedding center such as the one shown here. (**b**) An agar pellet embedded in paraffin wax using a histology cassette. (**c**) The histology cassette is placed in paraffin wax block side down on the cold plate (left) to cool the blocks and make cutting easier. The block is mounted on the microtome (right) for cutting sections. The cut sections (3 mm) are floated on a water bath (middle) for easy mounting on glass slides for subsequent analysis

6. Leave the agar to set for 5 min until it appears translucent (*see* Fig. 6e).
7. Carefully remove the set agar plugs containing the blood vessels by pushing the syringe plunger (*see* Fig. 6f) and then place them into histological cassettes before completely submerging in a 500 mL beaker containing 250 mL of PBS and storing in the fridge until processing.
8. Process the cassettes overnight in a tissue processing machine (*see* **Note 22**).
9. Embed the agar pellets in paraffin wax using the embedding center (*see* Fig. 7a).
10. Attach the paraffin wax embedded agar pellets to the histology cassettes (*see* Fig. 7b) so they can be mounted on the microtome and sections can be cut. The ligated vessel is now on the exposed surface of the block, embedded in the agar pellet within the wax (*see* Fig. 7b).
11. Place the block on the cold plate (*see* Fig. 7c) to cool the blocks to −12 °C for at least 30 min to facilitate cutting.

12. Mount the block on the microtome (*see* Fig. 7c) for cutting sections.
13. Cut sections (3 μm) and float on a tissue floating water bath (*see* Fig. 7c) for easy mounting onto glass slides for histological staining or super-adherent slides for immunohistochemistry or immunofluorescence protocols.
14. When using longitudinal sections, cut 4× adjacent 3 μm sections for EVG staining (*see* Subheading 3.4.1).
15. When using transverse sections, cut 4× 3 μm sections at 150 μm intervals. This is achieved by retaining the first section for staining and then cutting and storing 50 × 3 μm sections on glass slides and then retaining the next section. Repeat this process twice more to retain a total of 4 sections which are 150 μm apart (*see* **Note 23**). Stain these sections with EVG using protocol in Subheading 3.4.1.
16. Place slides into slide rack.
17. Dry slides overnight in 37 °C oven.

3.3.2 Isopentane-Frozen Samples

1. Remove frozen arteries from −80 °C freezer and place in vacuum flask containing liquid nitrogen.
2. Chill a clean cryostat mounting chuck by placing on the cooling area (−20 to −15 °C) within the cryostat (*see* **Note 24**).
3. Remove one sample at a time from liquid nitrogen using 30 cm long forceps.
4. Remove the precooled chuck from the cryostat.
5. Cover the surface of the chuck with OCT.
6. Once the OCT exhibits a semisolid consistency, place the sample on the chuck perpendicular to the chuck and with the ligated end uppermost.
7. Rapidly add more OCT over the tissue, covering the artery entirely.
8. Place chuck quickly back into the cryostat.
9. Once the OCT has solidified, place the chuck in the cutting position.
10. Cut 5–8 μm sections.
11. Mount sections on glass slides by pressing slide onto section.
12. Place glass slides containing sections in slide rack stored within the cryostat.
13. Once all sections are cut, place lid on slide rack, cover in aluminum foil, and store in −80 °C freezer until histological staining or immunohistochemistry or immunofluorescence.

3.3.3 Liquid Nitrogen Frozen Samples

Remove frozen arteries from −80 °C freezer and place in vacuum flask containing liquid nitrogen.

Protein Extraction

1. Add 250 μL of SDS lysis buffer to labeled screw cap tubes.
2. Using forceps remove frozen sample from the cryovial and place in tube containing SDS lysis buffer.
3. Using fine scissors cut sample into small pieces approximately $1mm^3$.
4. Vortex sample for 5 min.
5. Place sample on ice for 30 min.
6. Centrifuge sample for 5 min at 13,000 × *g* and 4 °C for 5 min in microcentrifuge.
7. Using pipette remove supernatant and place in 0.5 mL microcentrifuge tubes.
8. Freeze supernatant samples in −80 °C freezer until analysis by protein assay, Western blotting, or ELISA.

mRNA Extraction

1. Using forceps, remove frozen sample from cryovial and place in RNAse-free microcentrifuge tube.
2. Follow manufacturers' instructions of mRNA extraction kit.
3. Freeze extracted mRNA in −80 °C freezer until analysis.

3.4 Histological Analysis

*3.4.1 Elastin Van Gieson Staining (*See ***Note 25****)*

1. EVG staining can be achieved manually or using an automatic slide staining machine (*see* **Note 26**).
2. Place slides at 60 °C for 30 min (*see* **Note 27**).
3. Dewax slides by placing in xylene substitute for 2× 3 min (*see* **Note 28**).
4. Place slides in 100% ethanol (industrial methylated spirits: IMS) for 2× 3 min (*see* **Note 29**).
5. Place slides in 70% ethanol (IMS) (*see* **Note 30**).
6. Immerse slides in tap water for 5 min.
7. Incubate slides in 0.5% (w/v) potassium permanganate for 10 min.
8. Immerse slides in distilled water for 3 min.
9. Incubate slides in 1% oxalic acid for 5 min.
10. Immerse slides in distilled water for 3 min.
11. Place slides in 70% (v/v) ethanol (IMS) for 2 min.
12. Incubate slides in 50% (v/v) Miller's elastin stain for 60 min.
13. Place slides in 70% (v/v) ethanol (IMS) for 2 min.
14. Place slides under running tap water for 3 min.
15. Incubate slides in Van Gieson stain for 20 s.

16. Place slides in 100% (v/v) ethanol (IMS) for 2× 5 min.
17. Place slides in xylene substitute for 2× 5 min.
18. Pipette DPX mounting medium on to a glass coverslip using plastic disposal Pasteur pipette.
19. Invert glass slide onto the glass coverslip and gently push down slide until DPX has reached the edges of the coverslip and there are no bubbles in the DPX.
20. Cure overnight at room temperature.
21. View on a light microscope at ×10 magnification.
22. Measure EVG stained vessel parameters using ImageJ software (*see* Fig. 8a–h). For longitudinal sections, trace the intima area in whole sections (*see* Fig. 8c). If the section is incomplete and the site of ligation and an open distal end of the artery is not apparent (*see* Fig. 8b), then cut further sections as described in

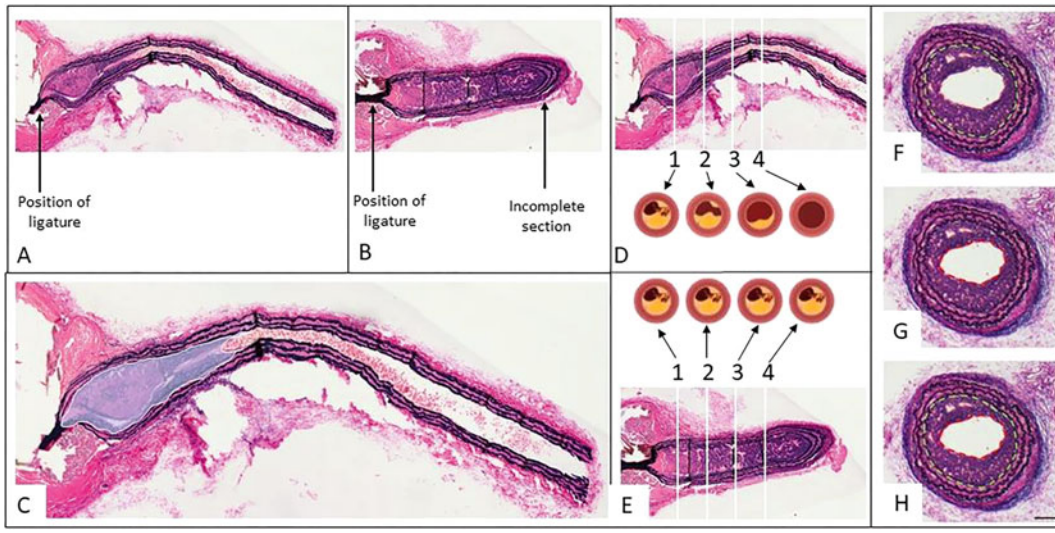

Fig. 8 Elastic van Gieson (EVG) stained carotid arteries and analysis. EVG stained ligated left carotid arteries to measure intimal thickening [9]. (**a**) Ligated left carotid artery with position of ligature indicated. Intimal thickening is present at proximal end (left) and no intimal thickening is observed at distal end (right). (**b**) Ligated left carotid artery with position of ligature indicated. Intimal thickening is present at proximal end (left). However, section is not complete as distal end is not open (right). (**c**) To measure the intima, the intimal area is traced. (**d**, **e**) Ligated artery and schematic representation of intima at 150, 300, 450, and 600 mm. Illustrating the potential pitfall of measuring intimal thickening just at the proximal end (1 and 2) using transverse sections and the consequent need to measure at multiple defined points (1–4) or with longitudinal sections to gain accurate evaluation of the size of the intima. (**f**–**h**) To measure intimal area in ligated left carotid arteries using transverse sections, two initial measurements are required. (**f**) The internal elastic lamina (IEL, green) is outlined and the area within is calculated. (**g**) The lumen edge of the intima (red) is outlined and the area within is calculated. (**h**) The area of the lumen (red) is subtracted from the area of the IEL (green) to give the intimal area for that artery. The scale bar represents 150 μM and refers to (**f**–**h**)

Subheading 3.3.1 **steps 13–15** and perform EVG stain as described in Subheading 3.4.1 **steps 1–19**, until this is achieved (*see* **Note 31**). For transverse sections, trace the intima and media areas (*see* Fig. 8f–h and **Note 32**).

*3.4.2 Immunodetection of BrdU Incorporation (See **Notes 33** and **34**)*

Deparaffinization and Rehydration

1. Place slides containing paraffin-embedded tissue sections in a slide rack.
2. Place slides at 60 °C for 30 min (*see* **Note 27**).
3. Incubate the slides into a glass square staining trough containing xylene substitute for 5 min (*see* **Note 28**).
4. Repeat twice by transferring slides to fresh troughs of xylene substitute (*see* **Note 29**).
5. Transfer slides to a glass square staining trough containing 100% IMS to remove xylene substitute and incubate for 5 min (*see* **Note 28**).
6. Repeat once by transferring slides to a fresh trough of 100% IMS.
7. To begin rehydration, transfer slides to a fresh trough of 70% IMS and incubate for 5 min.
8. To fully rehydrate tissue sections, transfer slides to a trough of water and incubate for 5 min.

Antigen Retrieval and Quenching of Endogenous Peroxidase

1. Fill any remaining slots on the slide rack with blank slides (*see* **Note 35**).
2. Transfer slides and the slide rack to a microwaveable pot with a lid.
3. Fill the pot with 10 mM citrate buffer so that the liquid level is approximately half a centimeter above the top of the slides.
4. Loosely place the lid on the pot to prevent buildup of pressure.
5. Microwave tissue sections for 2× 5 min on the highest heat setting (*see* **Note 36**).
6. Allow the slides to cool for 30 min at room temperature (*see* **Note 37**).
7. Transfer slides to cold running tap water for 5 min (*see* **Note 38**).
8. Wash slides twice with PBS in glass coplin jars.
9. Transfer slides to a fresh coplin jar containing 3% (v/v) H_2O_2 in water and incubate for 5 min at 4 °C (*see* **Note 39**).
10. Wash slides twice with PBS in glass coplin jars.

DNA Denaturation (*See* **Note 40**)

1. Place slides in glass coplin jars containing 10 mM HCl.
2. Incubate for 10 min at room temperature.
3. Wash slides twice with PBS in glass coplin jars.

Immunohistochemistry (Colorimetric) Immunofluorescence

1. Firstly, draw around sections on glass slide with a wax hydrophobic barrier pen (*see* **Note 41**).
2. Dry the area around the tissue section with a dry soft tissue (*see* **Note 42**).
3. Add 50 μL of 125 U/mL benzonase nuclease in PBS supplemented with 1 mM $MgCl_2$ to tissue sections (*see* **Note 43**).
4. Place the slides in a humidified chamber for 2 h at 37 °C.
5. Wash the slides twice with PBS in glass coplin jars.

Protein Blocking

1. Draw around sections on glass slide with a wax hydrophobic barrier pen (*see* **Note 41**).
2. Dry the area around the tissue sections with a dry soft tissue of any remaining PBS (*see* **Note 42**).
3. Add 50 μL of 20% (v/v) blocking sera diluted in 1% (w/v) BSA in PBS or commercial protein blocking reagent to tissue sections (*see* **Note 44**).
4. Place slides in a humified chamber where serum is used as a blocking agent and incubate for 30 min at room temperature. Commercial protein blocking reagents should be used in accordance with the manufacturer's instructions.

Immunodetection

1. Tap glass slide gently on its slide to knock off blocking reagent. Remove any excess with a dry soft tissue.
2. Add 50 μL (or a greater volume if necessary) of anti-BrdU IgG diluted in 1% (w/v) BSA in PBS to tissue sections.
3. Add 50 μL (or a greater volume if necessary) of the non-immune IgG control diluted in 1% (w/v) BSA in PBS to a second tissue section (*see* **Note 45**).
4. Incubate overnight at 4 °C in a humidified chamber.
5. Wash slides four times with PBS in glass coplin jars.
6. Dry the area around the tissue sections with a dry soft tissue so any remaining PBS does not dilute the secondary antibody.
7. Add 50 μL (or a greater volume if necessary) of the biotinylated secondary antibody diluted in 1% (w/v) BSA in PBS to tissue sections and incubate for 45 min at room temperature in a humidified chamber.
8. Wash slides four times with PBS in glass coplin jars.

9. Dry the area around the tissue sections with a dry soft tissue so any remaining PBS does not dilute the streptavidin with a HRP or fluorescent tag.
10. Add 50 μL (or a greater volume if necessary) of streptavidin-HRP (for colorimetric staining) or streptavidin-fluorophore (for fluorescence staining) diluted in 1% (w/v) BSA in PBS to tissue sections and incubate for 45 min at room temperature in a humidified chamber (*see* **Note 46**).
11. Wash slides four times with PBS in glass coplin jars.
12. For colorimetric staining, dry the area around the tissue sections with a dry soft tissue (*see* **Note 42**).
13. Add 50 μL (or a greater volume if necessary) of DAB peroxidase substrate diluted in water to tissue sections (*see* **Notes 47** and **48**) and incubate for 5 min or as recommended by the manufacturer.
14. Wash slides twice in water in glass coplin jars.
15. Stain cell nuclei by adding 50 μL (or a greater volume if necessary) of filtered Mayer's hematoxylin diluted in water to tissue sections and incubate for approximately 1 min.
16. Wash slides three times in tap water in glass coplin jars.
17. Leave slides in tap water for 30 min at room temperature to allow for hematoxylin stain to develop.

Mounting

1. *For colorimetric detection*: Dehydrate tissue sections by placing slides in a slide rack and performing 3-min incubations in 70% IMS, 2× 100% IMS and then 2× Xylene substitute (*see* **Note 49**). This is the reverse process of deparaffinization and rehydration. Pipette DPX mountant onto coverslips.
2. *For fluorescence detection*: Add 1–3 drops of mountant formulated with DAPI onto coverslips.
3. Place slides upside down against coverslips, press gently and lift.
4. Remove air bubbles by gently pressing down on the area.
5. The mountant will need curing overnight before imaging in order to reach the optimal refractive index.

Imaging and Analysis

1. For colorimetric detection, identify BrdU-positive cells as those with brown nuclei and negative cells as those with gray/blue nuclei.
2. For fluorescent detection, identify BrdU-positive cells as those with fluorescent nuclei; all nuclei will be stained fluorescent blue with DAPI.

3. As it is important to determine subcellular localization of staining, image tissue sections with a ×40 or ×60 lens. Approximately 200–400 cells should be counted per condition.
4. Determine the rate of proliferation by calculating the percentage of BrdU-positive cells.
5. Migration can be estimated by counting the number of BrdU-negative cells.

4 Notes

1. Surgical clothing includes sterile gown, sterile gloves, surgical scrubs, face mask, hair-net, and plastic overshoes.
2. Alzet mini-osmotic pumps utilize an osmotic pressure difference between a compartment within the pump, called the salt sleeve, and the tissue environment in which the pump is implanted to deliver its contents. The high osmolality of the salt sleeve causes water to flux into the pump through a semipermeable membrane which forms the outer surface of the pump. As the water enters the salt sleeve, it compresses the flexible reservoir, displacing the test solution from the pump at a controlled, predetermined rate. The compressed reservoir cannot be refilled, and therefore the pumps are designed for single use only.

   The rate of delivery by the pump is controlled by the water permeability of the pump's outer membrane. Thus, the delivery profile of the pump is independent of the drug formulation dispensed. Drugs of various molecular configurations, including ionized drugs and macromolecules, can be dispensed continuously in a variety of compatible vehicles at controlled rates. The molecular weight of a compound, or its physical and chemical properties, has no bearing on its rate of delivery by the pumps. The volume delivery rate of pumps is fixed at manufacture. Osmotic pumps are available with a variety of delivery rates between 0.11 and 10 μL/h and delivery durations between 1 day and 6 weeks. While the volume delivery rate of the pump is fixed, different dosing rates can be achieved by varying the concentration of agent in the solution or suspension used to fill the pump reservoir.

   In this carotid artery ligation model, an osmotic pump can be used to deliver Bromodeoxyuridine/5-bromo-2-′-deoxyuridine (BrdU) continuously, which avoids the need for multiple injections. This enables the quantification of cell proliferation by subsequent immunohistochemistry or immunofluorescence for BrdU. Migration rates can also be estimated by quantifying the number of BrdU-negative cells in the intima.

3. Formalin-fixed, paraffin wax embedded samples can be used for quantification of proliferation, estimation of migration, measurement of intimal area and assessing protein expression by immunohistochemistry or immunofluorescence.
4. Isopentane-frozen samples can be used for immunohistochemistry or immunofluorescence protocols that do not work with formalin-fixed, paraffin wax embedded samples.
5. Snap-frozen samples can be used for mRNA and protein extraction and subsequent analysis by quantitative PCR and Western blotting or ELISAs, respectively.
6. 10 mM HCl must be made from concentrated HCl freshly on the day of use.
7. Sera should match the species the secondary antibody is raised in, and aliquoted and stored at −20 °C. Commercial blocking reagents should be prepared and stored in accordance with manufacturer's instructions.
8. The secondary antibody must be complementary to the species the primary antibody is raised in. Working concentrations and storage instructions are typically indicated in product datasheets from the supplier.
9. Mayer's hematoxylin requires filtration to remove precipitates, and often needs diluting 1:2 to 1:4 in water to reduce strength.
10. Working concentrations and storage instructions are typically indicated in product datasheets.
11. Histological stains such as EVG staining can be performed on sections adhered to conventional glass slides. For immunohistochemistry of immunofluorescence, it is important to adhere tissues to coated slides which provide enhanced adhesion of the section ("super-adherent").
12. It is possible to perform the procedure in mice of other ages to investigate the effect of aging; for example, mice of 18–20 months old can be utilized as aged/elderly mice [6].
13. All procedures should be conducted in accordance with the appropriate Government and Institutional Guidelines for animal research. All studies must be planned and carried out in accordance with the 3Rs of Replacement, Reduction, and Refinement (e.g., nc3rs.org.uk) and with the ARRIVE guidelines (e.g., arriveguidelines.org).
14. It is important to remove all hair in the neck area where the incision will occur.
15. It is important to remove the mouse hair in a separate laboratory area to where the surgery will take place and to clean up any hair thoroughly in order to keep the surgical area clean.

16. It is preferable to have a pair of forceps with a tight curve to facilitate this step where the forceps are placed under the carotid artery.
17. If a drug or virus needs to be applied topically to the ligated artery, then this is done at this step prior to the closing of the wound.
18. If an Alzet mini-osmotic pump is to be used, then an area of skin on the back of the neck should also be shaved prior to surgery. A 1 cm incision in the skin is made with a scalpel, the pump inserted subcutaneously, and the wound clipped as per the main carotid artery ligation surgery.
19. When using Alzet pumps, always refer to the inserted batch information for actual delivery rates for the batch. The filling information is provided with the pumps. Also note that pumps need to be "primed" in saline at 37 °C prior to insertion, so will need to be filled 1 or 2 days before surgery.
20. Pharmaceuticals/compounds or gene therapy can be delivered to the adventitia of the carotid artery either directly or in pluronic gel [5]. Pluronic gel is a liquid when cold (placed on ice or stored in the fridge) and forms a solid gel at body temperature, thus keeping the pharmaceuticals/compounds or gene therapy in close contact with the vessel.
21. 40% (w/v) pluronic gel can be diluted to a maximum of 1:1 with solutions containing pharmacologicals/compounds or gene therapy.
22. Using a tissue processor machine, the fixed artery samples are dehydrated and cleared to the state where they are completely infiltrated and embedded with paraffin wax in preparation for cutting thin sections on a microtome.
23. Samples must be cut through cautiously and it is preferable that every section is saved to enable the best one to be analyzed. It is possible to look at an unstained section under the microscope to determine the optimum section.
24. The chuck should be clean. A toothbrush or paint brush can be used to remove OCT and/or tissue fragments. Ice crystals can be removed by dipping the chuck in methanol.
25. To determine the intimal area of left carotid arteries, and the total vessel area, lumen area, medial area and medial thickness of right carotid arteries, Elastin van Gieson (EVG) staining is performed.
26. If an automatic slide stainer is not available, then the sections can be stained with EVG manually.
27. Heating slides at 60 °C for 30 min melts the paraffin wax and enables maximal adherence to the slides and prevents sections

from lifting or falling off the slide during the staining procedure or immunohistochemistry and immunofluorescence procedures.

28. Ensure that the slides are completely immersed and shake slide rack gently to dispel any air bubbles.
29. When transferring slides between subsequent steps in this procedure, shake the slide rack to fully drain any liquid so that the previous pot's liquids are not transferred to the next one.
30. Ensure that tissue sections are not left to dry at any point during **steps 2–15** of Subheading 3.4.1.
31. If the transverse section was taken at 150 or 300 μm, one would conclude that there was no difference in the size of the intima between the ligated carotid arteries (*see* Fig. 8d, e). However, if taken at 450 or 600 μm, one would conclude that intimal thickening was different between the samples. Consequently, we consider that it is more appropriate to measure the entire lesion area in longitudinal sections to avoid any bias due to the location of the transverse section.
32. The longitudinal sections are more technically demanding and there is a risk of losing the sample if not experienced in this approach and therefore in this case, we would recommend that multiple (preferably 4) transverse sections at 150 μm intervals are analyzed to avoid the bias of using one location.
33. Proliferation and migration can be assessed using BrdU incorporation. Moreover, smooth muscle cell content can be assessed by immunohistochemistry or immunofluorescence for α-smooth muscle actin [3–6].
34. Sections must not be permitted to dry out in this procedure from **step 4** in Subheading "Deparaffinization and Rehydration" until mounting of slide in **step 3** of Subheading "Mounting".
35. Filling the slide rack with blank slides will help prevent formation of large air bubbles during the heating process that can often damage tissue sections or lift tissue sections from surface of slides.
36. Due to splattering from boiling, after 5 min the liquid levels will need to be topped up with distilled water. It is important that the slides are always immersed in citrate buffer; if tissue sections dry out, this will affect the staining outcome.
37. This cooling step in the antigen retrieval process should not be omitted or shortened.
38. The flow of tap water should not be too high as this may damage tissue sections or cause tissue sections to lift from the surface of the slides.

39. This step is only required for colorimetric staining (not fluorimetric) where DAB is oxidized by hydrogen peroxide in a reaction that is catalyzed by HRP (conjugated to a secondary antibody or streptavidin) to produce a brown precipitate. Endogenous peroxidases can also catalyze oxidation of DAB by hydrogen peroxide generating false positive staining, hence the activity of endogenous peroxidases should be quenched.
40. This step is specifically required for immunohistochemistry for BrdU in order to enable access of the anti-BrdU antibody to the BrdU epitope within the DNA molecule. Acid hydrolysis can damage tissue integrity and disrupt DNA integrity affecting nuclear counterstaining with fluorescent dyes like DAPI. If immunofluorescence detection is utilized, it is advisable to avoid the acid hydrolysis procedure and use nuclease-mediated DNA digestion instead using benzonase.
41. The use of the wax hydrophobic barrier pen provides a barrier around the tissue section ensuring the liquid remains in contact with the section and avoids leaking of solution or drying out of the section.
42. Ensure slide is dry so any remaining PBS does not dilute the added solution. However, be careful not to touch or damage the tissue section.
43. Increase the volume for larger tissue sections; a sufficient volume should be added to cover the tissue section without having to spread the solution thinly. Be careful to not damage the tissue with the pipette tip.
44. Blocking with sera or other commercial protein blocking reagents markedly reduces non-specific binding of antibodies to tissue.
45. To account for any non-specific interactions of the primary antibody with the tissue sample, for each condition, a second tissue section should be treated with a non-immune IgG control. The non-immune IgG control must be diluted to the same concentration of the primary antibody, and match the species and isotype (for example, IgG1, IgG2A, IgG2B, and IgM) of the primary antibody.
46. *For fluorescence staining*: Protect from light.
47. Once the fast DAB peroxidase substrate is reconstituted in water (in accordance with manufacturer's instructions), it is essential that it is used within 15 min.
48. The brown DAB precipitate is insoluble in water, alcohol, and xylene substitute allowing for flexibility with subsequent treatments and choice of mountants.

49. As the first pot of xylene substitute used during deparaffinization will contain the most wax, this should not be used for dehydration of stained tissue sections.

Acknowledgments

Helen Williams is funded by British Heart Foundation project grant, PG/17/66/33216.
Bethan Brown was funded by British Heart Foundation PhD studentship, FS/13/68/30489.
Jason Johnson is funded by British Heart Foundation Senior Research Fellowship, FS/18/1/33234.

References

1. Schwartz SM, deBlois D, O'Brien ERM (1995) The intima. Soil for atherosclerosis and restenosis. Circ Res 77(3):445–465
2. Tsaousi A, Williams H, Lyon C, Taylor V, Swain A, Johnson J, George S (2011) Wnt4/β-catenin signalling induces VSMC proliferation and is associated with intimal thickening. Circ Res 108:427–436
3. Johnson JL, Dwivedi A, Somerville M, George SJ, Newby AC (2011) Matrix metalloproteinase (MMP)-3 activates MMP-9 mediated vascular smooth muscle cell migration and neointima formation in mice. Arterioscler Thromb Vasc Biol 31(9):e35–e44. https://doi.org/10.1161/atvbaha.111.225623
4. Williams H, Mill CA, Monk BA, Hulin-Curtis S, Johnson JL, George SJ (2016) Wnt2 and WISP-1/CCN4 induce intimal thickening via promotion of smooth muscle cell migration. Arterioscler Thromb Vasc Biol 36(7):1417–1424. https://doi.org/10.1161/atvbaha.116.307626
5. Hulin-Curtis S, Williams H, Wadey KS, Sala-Newby GB, George SJ (2017) Targeting Wnt/β-catenin activated cells with dominant-negative N-cadherin to reduce neointima formation. Mol Ther Methods Clin Dev 5:191–199. https://doi.org/10.1016/j.omtm.2017.04.009
6. Brown BA, Williams H, Bond AR, Angelini GD, Johnson JL, George SJ (2018) Carotid artery ligation induced intimal thickening and proliferation is unaffected by ageing. J Cell Commun Signal 12(3):529–537. https://doi.org/10.1007/s12079-017-0431-5
7. Chang Z, Huangfu C, Grainger AT, Zhang J, Guo Q, Shi W (2017) Accelerated atherogenesis in completely ligated common carotid artery of apolipoprotein E-deficient mice. Oncotarget 8(66):110289–110299
8. Edwards MS, Fuselier PA (1983) Enhanced susceptibility of mice with streptozotocin-induced diabetes to type II group B streptococcal infection. Infect Immun 39(2):580–585. https://doi.org/10.1128/iai.39.2.580-585.1983
9. Johnson JL, Baker AH, Oka K, Chan L, Newby AC, Jackson CL, George SJ (2006) Suppression of atherosclerotic plaque progression and instability by tissue inhibitor of metalloproteinase-2: involvement of macrophage migration and apoptosis. Circulation 113:2435–2444

Chapter 34

Assessing Efferocytosis in Atherosclerotic Lesions In Situ.

Arif Yurdagul Jr

Abstract

Whereas most atherosclerotic lesions are relatively benign, some plaques with large necrotic cores and thin fibrous caps are vulnerable to rupture, which results in many cardiovascular events and sudden death. Defects in the clearance of apoptotic cells, termed "efferocytosis," is the leading cause of necrotic core expansion. This chapter describes a method that identifies macrophage-associated terminal deoxynucleotidyl transferase (TUNEL)-positive events (i.e., efferocytosis events) and TUNEL events free from association with macrophages (i.e., uncleared apoptotic events) in atherosclerotic lesions. This assay has been critical to the understanding of how clinically dangerous atherosclerotic plaques form and will remain a crucial assay that reveals new insights into how macrophages carry out efferocytosis and how this process becomes defective as atherosclerosis advances.

Key words Atherosclerosis, Apoptosis, Necrotic Core, TUNEL, Efferocytosis, Macrophages

1 Introduction

The macrophage population in many organs and tissues is relatively low compared to other non-immune cells [1]. Despite this, apoptotic cells (AC) are rarely found in tissues where cell turnover is known to be high, indicating that (a) macrophages rapidly mobilize to areas of cell death and (b) macrophages successively execute multiple rounds of AC internalization (termed "continual efferocytosis"). Clearance of apoptotic cells maintains homeostasis and normal tissue function, whereas impairments in efferocytosis cause non-resolving inflammatory diseases, such as atherosclerosis [2–5]. Early in lesion development, macrophages carry out efferocytosis efficiently and attenuate inflammation. However, plaque macrophages undergo cellular and molecular reprogramming that result in defective efferocytosis, which leads to the secretion of inflammatory cytokines and secondary necrosis-factors that cause necrotic core expansion and advanced atherosclerosis [6]. Expansion of the necrotic core is a major cause of plaque rupture and cardiovascular events.

Dipak P. Ramji (ed.), *Atherosclerosis: Methods and Protocols*, Methods in Molecular Biology, vol. 2419,
https://doi.org/10.1007/978-1-0716-1924-7_34,
© The Author(s), under exclusive license to Springer Science+Business Media, LLC, part of Springer Nature 2022

Successful clearance of apoptotic cells involves several stages: (a) apoptotic cells secrete "find-me" signals such as the nucleotides ATP and UTP and the chemokine C-X3-C motif chemokine ligand 1 (CX3CL1) [7]; (b) macrophages engage phosphatidylserine on apoptotic cells using various bridging molecules and AC-binding receptors, such as growth arrest-specific 6 (Gas6) and c-mer proto-oncogene tyrosine kinase (MerTK), respectively [8]; and (c) macrophages subsequently internalize the bound apoptotic cell through cytoskeletal rearrangements, primarily driven by temporally coordinated Ras-related C3 botulinum toxin substrate 1 (Rac1)/Ras homolog family member A (RhoA) activation mechanisms; and (d) macrophages then fuse their lysosomes to the developing phagosome to form the phagolysosome. The formation of the phagolysosome is driven by a Rubicon-dependent process termed "LC3-associated phagocytosis" (LAP) and functions to breakdown and degrade the apoptotic cell [9]. The inability of macrophages to carry out any of these steps in efferocytosis worsens atherosclerosis. While the role of defective efferocytosis in the advancement of atherosclerosis is known to be detrimental, the cellular and molecular mechanisms causing impairments in efferocytosis remain an active and exciting area of research that may have a significant translational impact. This is underscored by the positive results from the Canakinumab Anti-inflammatory Thrombosis Outcomes Study (CANTOS) and Colchicine Cardiovascular Outcomes Trial (COLCOT) trials that recently demonstrated lowering inflammation reduces cardiovascular events [10]. This chapter describes a method that allows for the detection of efferocytosis events by macrophages in atherosclerotic plaques.

2 Materials

Prepare and store all reagents as indicated. Diligently follow all waste disposal regulations when disposing of waste materials. Sodium azide is not added to purchased reagents.

2.1 Rehydration of Paraffin-Embedded Tissue Sections on Glass Sides

1. Xylene.
2. 100% Ethanol.
3. 95% Ethanol.
4. 70% Ethanol
5. 50% Ethanol.
6. Distilled H_2O.
7. Plastic staining rack stand.
8. Plastic staining jars.

2.2 Antigen Retrieval

1. Pressure cooker.
2. Antigen retrieval solution: 10 mM citrate, pH 6.0.
3. 1× Phosphate Buffered Saline (PBS).

2.3 TUNEL Reaction and Anti-Mac2 Immunostaining

1. TUNEL kit (fluorescein) (e.g., Sigma-Aldrich). This kit contains Enzyme Solution and Label Solution mentioned in Subheading 3.3.
2. TBST: 1× Tris-buffered saline, 0.1% Tween-20.
3. Blocking solution: 1× PBS, 2% bovine serum albumin. Strain through a 0.22 μm filter.
4. Pap pen.
5. Rat anti-Mac2 antibody (e.g., Cedarlane, clone M3/38).
6. Goat anti-Rat IgG secondary antibody, Alexa Fluor 546.
7. DAPI-containing mounting media.
8. PBS.
9. Parafilm.
10. Incubator or equivalent at 37 °C and 4 °C.
11. Coverslips.
12. Humidifying chamber.
13. Fluorescence microscope.

3 Methods

3.1 Rehydration of Tissue Sections on Glass Sides

1. Place glass slides that contain tissue sections in a plastic staining rack stand and carefully dip into a plastic staining jar with Xylene 30 times. Place the plastic staining rack stand in a new plastic staining jar containing fresh xylene and repeat the dip procedure (*see* **Note 1**).
2. Move the staining rack containing the glass slides into 100% ethanol and carefully dip 30 times. Place the plastic staining rack stand in a new plastic staining jar containing fresh 100% ethanol and repeat the dip procedure.
3. Move the glass slides into 95% ethanol and carefully dip 30 times. Place the plastic staining rack stand in a new plastic staining jar containing fresh 95% ethanol and repeat the dip procedure.
4. Move the glass slides into 70% ethanol and carefully dip 30 times. Place the plastic staining rack stand in a new plastic staining jar containing fresh 70% ethanol and repeat the dip procedure.
5. Move the glass slides into 50% ethanol and carefully dip 30 times. Place the plastic staining rack stand in a new plastic

staining jar containing fresh 50% ethanol and repeat the dip procedure.

6. Move the glass slides into distilled water and carefully dip 30 times. Place the plastic staining rack stand in a new plastic staining jar containing fresh distilled water and repeat the dip procedure. Leave in distilled water until the next step.

3.2 Antigen Retrieval

1. Place slides in antigen retrieval solution (*see* **Note 2**) and move into a pressure cooker. Pressure cook on high for 5 min.
2. Open steam release carefully and move slides out of the pressure cooker (*see* **Note 3**). Let the slides incubate in antigen retrieval solution for another 30 min.
3. Rinse the slides three times in 1× PBS for 5 min each time (dip ten times carefully upon placing the slides in 1× PBS). Keep slides in PBS until the next step.

3.3 TUNEL Reaction and Immunostaining with an Anti-Mac2 Antibody

1. Add 50 μL of the Enzyme Solution (provided in kit) to 450 μL of the Label Solution (provided in kit) and mix well. This results in a total of 500 μL of a TUNEL reaction mixture.
2. Dry the area around the tissue sections and place the slides in a humidifying chamber (*see* **Note 4**).
3. Add 50 μL of the TUNEL reaction mixture on the tissue and lay a piece of parafilm over the TUNEL reaction mixture to distribute the mixture evenly over the tissue.
4. Incubate the slides at 37 °C for 50 min (*see* **Note 5**).
5. Rinse the slides three times in 1× PBS for 5 min each time (dip ten times carefully upon placing the slides in 1× PBS).
6. Dry the area around the tissue sections and use a pap pen to draw a circle around the tissue. This creates a hydrophobic ring that is suitable to contain liquids on the specimen.
7. Add the blocking solution to the tissue sections for 1 h at room temperature.
8. Remove the blocking solution and add the Rat anti-Mac2 antibody (diluted in 1× TBST at a 1:10,000 ratio) and incubate at 4 °C for 12–16 h.
9. Remove the primary antibody and rinse tissue sections in 1× TBST three times for 5 min each time (dip ten times carefully upon placing the slides in 1× TBST).
10. Dry area surrounding the tissue sections and add the fluorescently labeled anti-rat secondary antibody (diluted in blocking solution at a 1:200 ratio) and incubate for 2–3 h at room temperature.

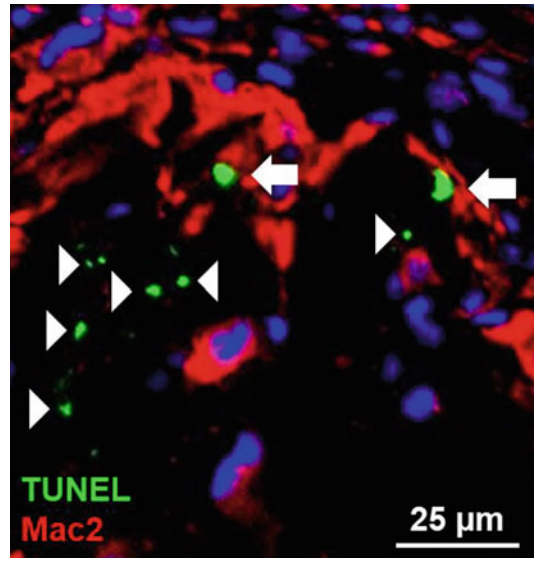

Fig. 1 A Representative Image of an Atherosclerotic Plaque after Performing the *In Situ* Efferocytosis Assay. LDL receptor knockout mice were fed a high-fat Western diet for 16 weeks. Mice were then sacrificed and the hearts were collected, fixed and embedded in paraffin. Five-micron thick cross sections were affixed onto glass slides and the protocol described herein was carried out. Efferocytosis events ($TUNEL^+$ cells colocalizing with or juxtaposed to $Mac2^+$ macrophages) are identified with arrows. Uncleared apoptotic cells are identified with arrowheads

11. Remove the secondary antibody solution and rinse tissue sections in 1× PBS three times for 5 min each time (dip ten times carefully upon placing the slides in 1× PBS).
12. Dry the area around the tissue section and carefully add DAPI-containing mounting media to the tissue section, then mount a coverslip onto the tissue section and set for at least 6 h (or until the coverslip is no longer mobile on the slide) (Fig. 1).
13. Capture images on a fluorescence microscope.
14. Quantify the number of free (apoptotic cells are considered "free" when not surrounded by or not in contact with $Mac2^+$ macrophages) versus Mac2-associated $TUNEL^+$ cells ($TUNEL^+$ cells that are either colocalizing or juxtaposed to $Mac2^+$ macrophages).
15. Plot data as a ratio of Mac2-associated: free $TUNEL^+$ events to represent efferocytosis efficiency.

4 Notes

1. Frozen sections may also be used for this protocol. However, as methods of fixation and recovery of antigens can vary, the procedures leading up to Subheading 3.3 must be experimentally optimized by the user.
2. Other antigen retrieval buffers are compatible with TUNEL reactions and anti-Mac2 immunostaining, such as Proteinase K treatment.
3. The steam is extremely hot so wear eye protection.
4. Make sure that the tissue specimens themselves do not dry out as this can impact TUNEL reactions and immunostaining.
5. The TUNEL reaction should be carried out between 45 and 60 min. However, as shorter time points may not result in observable staining and extended times can rapidly cause false-positive events, the specific time required for the TUNEL reaction must be experimentally optimized by the user.

Acknowledgments

This work was supported by an NIH grant, R00 HL145131.

References

1. Yurdagul A Jr, Doran AC, Cai B, Fredman G, Tabas IA (2017) Mechanisms and consequences of defective efferocytosis in atherosclerosis. Front Cardiovasc Med 4:86. https://doi.org/10.3389/fcvm.2017.00086
2. Back M, Yurdagul A Jr, Tabas I, Oorni K, Kovanen PT (2019) Inflammation and its resolution in atherosclerosis: mediators and therapeutic opportunities. Nat Rev Cardiol 16(7):389–406. https://doi.org/10.1038/s41569-019-0169-2
3. Doran AC, Yurdagul A Jr, Tabas I (2020) Efferocytosis in health and disease. Nat Rev Immunol 20(4):254–267. https://doi.org/10.1038/s41577-019-0240-6
4. Wang Y, Subramanian M, Yurdagul A Jr, Barbosa-Lorenzi VC, Cai B, de Juan-Sanz J, Ryan TA, Nomura M, Maxfield FR, Tabas I (2017) Mitochondrial fission promotes the continued clearance of apoptotic cells by macrophages. Cell 171(2):331–345. https://doi.org/10.1016/j.cell.2017.08.041
5. Yurdagul A Jr, Subramanian M, Wang X, Crown SB, Ilkayeva OR, Darville L, Kolluru GK, Rymond CC, Gerlach BD, Zheng Z, Kuriakose G, Kevil CG, Koomen JM, Cleveland JL, Muoio DM, Tabas I (2020) Macrophage metabolism of apoptotic cell-derived arginine promotes continual efferocytosis and resolution of injury. Cell Metab 31(3):518–533. https://doi.org/10.1016/j.cmet.2020.01.001
6. Kasikara C, Doran AC, Cai B, Tabas I (2018) The role of non-resolving inflammation in atherosclerosis. J Clin Invest 128(7):2713–2723. https://doi.org/10.1172/JCI97950
7. Elliott MR, Chekeni FB, Trampont PC, Lazarowski ER, Kadl A, Walk SF, Park D, Woodson RI, Ostankovich M, Sharma P, Lysiak JJ, Harden TK, Leitinger N, Ravichandran KS (2009) Nucleotides released by apoptotic cells act as a find-me signal to promote phagocytic clearance. Nature 461(7261):282–286. https://doi.org/10.1038/nature08296
8. Scott RS, McMahon EJ, Pop SM, Reap EA, Caricchio R, Cohen PL, Earp HS, Matsushima GK (2001) Phagocytosis and clearance of apoptotic cells is mediated by MER. Nature

411(6834):207–211. https://doi.org/10.1038/35075603

9. Martinez J, Malireddi RK, Lu Q, Cunha LD, Pelletier S, Gingras S, Orchard R, Guan JL, Tan H, Peng J, Kanneganti TD, Virgin HW, Green DR (2015) Molecular characterization of LC3-associated phagocytosis reveals distinct roles for Rubicon, NOX2 and autophagy proteins. Nat Cell Biol 17(7):893–906. https://doi.org/10.1038/ncb3192
10. Ridker PM (2020) From CANTOS to CIRT to COLCOT to clinic: will all atherosclerosis patients soon be treated with combination lipid-lowering and inflammation-inhibiting agents? Circulation 141(10):787–789. https://doi.org/10.1161/CIRCULATIONAHA.119.045256

Chapter 35

Monitoring Atheroprotective Macrophage Cholesterol Efflux In Vivo

Andrea Rivas-Urbina, Noemi Rotllan, David Santos, Josep Julve, Jose Luis Sanchez-Quesada, and Joan Carles Escolà-Gil

Abstract

This chapter provides details on the methodologies currently used to monitor macrophage cholesterol efflux in vivo in mice. The general principles and techniques described herein can be applied to evaluate the effect of different experimental pathophysiological conditions or the efficacy of different therapeutic strategies on the modulation of in vivo cholesterol efflux to plasma acceptors and the rate of reverse transport of unesterified cholesterol from macrophages to feces in mice.

Key words Cholesterol, Cholesterol efflux, HDL, Macrophage, Method, Reverse cholesterol transport

1 Introduction

High-density lipoproteins (HDLs) show a broad range of atheroprotective functions [1]. The HDL-mediated promotion of macrophage-specific reverse cholesterol transport (RCT) in vivo is one of the main cardioprotective actions attributed to HDL.

RCT is defined as the main multistep physiological route of unesterified cholesterol and bile acid elimination from the body to the liver and intestine, and ultimately into feces [2]. The promotion of unesterified cholesterol efflux from cholesterol-loaded macrophages located in the artery wall, which is the first step of the RCT pathway, is considered one of the major mechanisms responsible for HDL-mediated atheroprotection [3]. However, the main obstacle in quantification of in vivo cholesterol efflux is the inability to specifically estimate the cholesterol derived from macrophage foam cells. To overcome this quantitative problem, an assay was developed to measure the in vivo transfer of the minute amount of cholesterol derived from macrophage foam cells to plasma, liver, and feces by prior labeling of [^{3}H]-cholesterol in foam cell

Dipak P. Ramji (ed.), *Atherosclerosis: Methods and Protocols*, Methods in Molecular Biology, vol. 2419,
https://doi.org/10.1007/978-1-0716-1924-7_35,
© The Author(s), under exclusive license to Springer Science+Business Media, LLC, part of Springer Nature 2022

macrophages *ex vivo* and subsequent injection of the cholesterol-labeled macrophages into the peritoneal cavity of recipient mice [4]. Here, we describe a standard method in which, after injection into mice of radiolabeled macrophages, the appearance of [^{3}H]-tracer is determined in serum at different time points, and also in the liver at 48 h after the injection [5]. Most importantly, the delivery of fecal [^{3}H]-tracer can be also measured over 48 h. Additionally, this approach further allows the determination of the relative distribution of fecal radioactivity into neutral sterols and bile acids (*see* Fig. 1 for a detailed description of the methodological steps). With this procedure, the net flux of cholesterol mass from the macrophages is not determined, but rather the unidirectional efflux of the radiolabeled cholesterol from the macrophages to plasma and feces. It should be noted that the radiolabeled macrophages are injected into the peritoneal cavity, which is used as a surrogate of the intimal space, thus the amount of the cholesterol acceptors or their ability to remove cholesterol from macrophages in the peritoneum may differ from those in the arterial intima.

2 Materials

2.1 Preparation of Acetylated LDL (ac-LDL)

1. Human LDL. This can be purchased or obtained from a pool of plasma from normolipidemic subjects by sequential ultracentrifugation, using a preparative fixed-angle rotor, at a density range of 1.019–1.063 g/mL. Dialyze at 4 °C against 10 mM of Tris–HCl, 1 mM of EDTA, pH 7.4 (*see* **Note 1**).
2. Saturated sodium acetate: Add sodium acetate trihydrate to 50 mL of distilled water and mix by stirring until saturation is reached (solubility of sodium acetate is 1 g for 0.8 mL of water).
3. Acetic anhydride, 97% purity (e.g., Acetic Anhydride, Reagent, ACS, 97%, Spectrum™ from Fisher Scientific).
4. Ice-water bath.
5. Stirrer.
6. Dialysis membrane tubing 3.5 K MWCO.
7. Dialysis buffer: 10 mM of Tris–HCl, 1 mM of EDTA, pH 7.4.
8. Roswell Park Memorial Institute medium (RPMI) 1640 supplemented with 2 mM of glutamine.
9. PD-10 desalting column.
10. Sterile filter with 0.2 μm diameter pore.

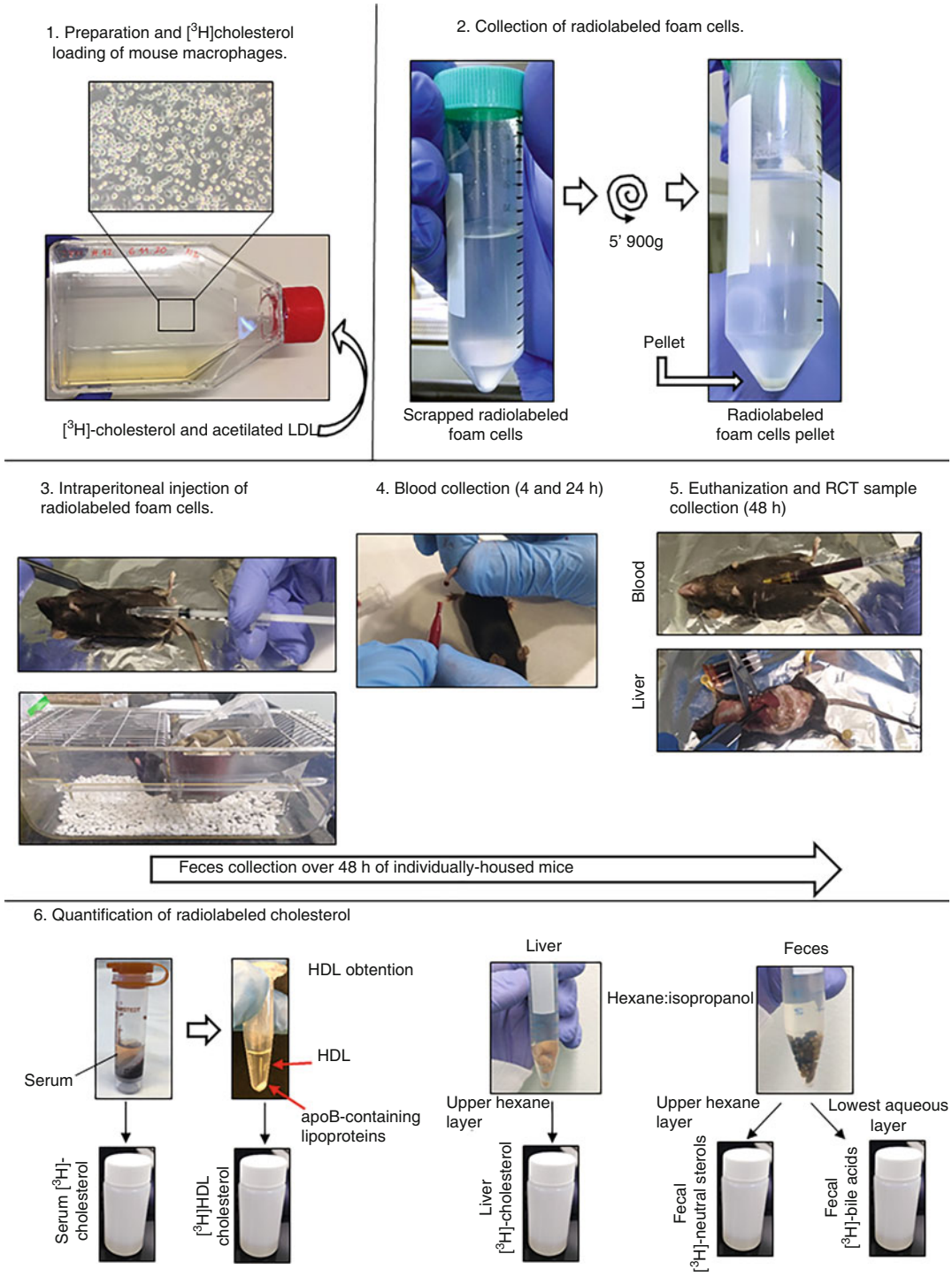

Fig. 1 Steps of the method for quantification of macrophage cholesterol efflux and the overall transport to feces in vivo. This method follows the fate of [^{3}H]-cholesterol from mouse macrophages injected into the peritoneal cavity of the mouse. (1) Mouse macrophages are loaded with ac-LDL and [^{3}H]-cholesterol to become foam cells. (2) Radiolabeled foam cells are gently detached from the plastic surface of 75 cm^2 flasks and resuspended in sterile PBS. (3) The radiolabeled mouse macrophages are then injected intraperitoneally into the mouse, and each mouse is placed in a cage for 48 h for feces collection. (4) Blood is collected at 4 and

2.2 Cell Culture

1. Mouse J774A.1 (ATCC® TIB-67™) macrophages.
2. Macrophage growth medium: RPMI 1640 medium supplemented with 2 mM glutamine, 10% heat-inactivated FCS (56 °C for 1 h), 100 U/mL penicillin, 100 μg/mL streptomycin.
3. 75 cm^2 cell culture flasks.
4. Cell culture incubator.
5. Sterile phosphate-buffered saline (PBS): 137 mM NaCl, 2.7 mM KCl, 6.5 mM $Na_2HPO_4{\cdot}2H_2O$, 1.5 M KH_2PO_4, pH 7.4.
6. Cell scrapers.
7. 15 mL polypropylene tubes.
8. Cell counting chamber.

2.3 Macrophage Radiolabeling and Injection

1. 40–60 Ci/mmol [1α,2α(*n*)-^{3}H]-cholesterol.
2. RPMI 1640 medium supplemented with 2 mM glutamine, 10% Lipoprotein-depleted serum (LPDS), 100 U/mL penicillin, 100 μg/mL streptomycin. LPDS can be isolated by sequential ultracentrifugation of plasma at a density ≥ 1.21 g/mL followed by dialysis at 4 °C against 10 mM of Tris–HCl, 1 mM of EDTA, pH 7.4. To inactivate the LPDS, place it in a 56 °C water bath for 1 h.
3. Sterile filters with a 0.2 μm pore size.
4. Nitrogen gas/stream.
5. Absolute ethanol (>99.9%).
6. PBS.
7. Serum-free RPMI 1640 medium: RPMI 1640 medium supplemented with 2 mM glutamine, 0.2% bovine serum albumin (BSA; essentially fatty acid-free), 100 U/mL penicillin, 100 μg/mL streptomycin.
8. 2 mL plastic Pasteur pipettes.
9. 50 mL polypropylene tubes.
10. 20 mL Scintillation vials.
11. Scintillation rack.

Fig. 1 (continued) 24 h and [^{3}H]-radioactivity measured in serum and HDL after precipitating apoB-containing lipoproteins. (5) After 48 h, the mouse is euthanized, the blood is collected by cardiac puncture and the liver removed. (6) [^{3}H]-radioactivity is measured in serum and HDL after precipitating apoB-containing lipoproteins. Lipids from the liver and feces are extracted with hexane:isopropanol and partitioned against Na_2SO_4. Liver [^{3}H]-radioactivity is determined in the upper layer, which contains the [^{3}H]-cholesterol. In the feces extract, the amount of [^{3}H]-radioactivity is determined in the upper layer (neutral sterols) and the lowest layer (bile acids)

12. Scintillation fluid.
13. 0.4% (w/v) trypan blue solution.
14. 1 mL syringes with 26–29G needles.
15. Isoflurane.
16. Commercial serum collecting tubes.
17. Scalpel blade.
18. The tissue adhesive Histoacryl®.
19. Liquid scintillation detector/counter.
20. Cell culture incubator.
21. Vortex mixture.
22. Microcentrifuge tubes.
23. Centrifuge.
24. Microcentrifuge.
25. Fume Hood.

2.4 Quantification of Macrophage Cholesterol Efflux

1. Isoflurane.
2. 1 mL syringe with 26 G needle.
3. Commercial serum collecting tubes.
4. Dissecting board.
5. Sterile scissors and forceps.
6. Saline.
7. Phosphotungstate precipitation reagent: 0.44 mM phosphotungstic acid, 20 mM $MgCl_2$ (*see* **Note 2**).
8. 15 mL polypropylene or glass tubes resistant to hexane.
9. Solvent for lipid extraction: hexane:isopropanol (3:2, v:v).
10. Tube rotator.
11. 0.47 M Na_2SO_4 in double-distilled water.
12. 5 mL glass tubes.
13. Nitrogen gas/stream.
14. Chloroform.
15. Thin layer chromatography (TLC) plates, size 6 × 20 cm.
16. Cholesterol reference standard: 10 mg/mL of cholesterol, 10 mg/mL of cholesterol stearate dissolved in chloroform.
17. TLC running solvent: hexane:diethyl ether:ethyl acetate (50:50:1.5; v:v:v).
18. TLC glass tanks.
19. Iodine crystals.
20. Fume hood.

21. Vortex mixer.
22. Microcentrifuge tubes.
23. Microcentrifuge.

3 Methods

3.1 Acetylation of LDL

1. Adjust human LDL to 2 mg/mL of apoB-100 or total protein content and add an equivalent volume of saturated sodium acetate (*see* **Note 1**).
2. Add 1 μL of acetic anhydride and gently shake the mixture in an ice-water bath for 30 min.
3. Add another 1 μL of acetic anhydride and stir the mixture for 30 min.
4. Dialyze the mixture at 4 °C against dialysis buffer.
5. Before using the mixture to radiolabel mouse macrophages, incorporate the acetylated LDL (ac-LDL) into RPMI 1640 medium supplemented with 2 mM glutamine using a PD-10 desalting column and elute by gravity. For this, equilibrate a PD-10 desalting column first with 25 mL of RPMI 1640 medium supplemented with 2 mM glutamine and add 2.5 mL of ac-LDL. Elute with 3.5 mL of RPMI 1640 medium supplemented with 2 mM glutamine and collect by gravity the ac-LDL-containing eluate into a separate tube.
6. Filter the suspension through a sterile filter with 0.2 μm diameter pore to avoid aggregated ac-LDL. Ensure that the ac-LDL suspension contains approximately 0.7–1 mg/mL of apoB-100 or total protein.

3.2 Cell Culture

1. Seed and expand adherent mouse J774A.1 cells in 75 cm^2 cell culture flasks in macrophage growth medium and keep in a humidified cell culture incubator (5% CO_2) at 37 °C until use.
2. Change the macrophage growth medium every 2 days; pour the macrophage growth medium from the flasks and wash the cells with 10 mL of warm PBS. Following this step, add fresh, warm macrophage growth medium and keep in a humidified cell culture incubator (5% CO_2) at 37 °C.
3. Maintain the cells until they are about 90% confluent (*see* **Note 3**).
4. Wash the cells with warm PBS and replace the macrophage growth medium.
5. Scrape the cells gently from the plastic surface with a cell scraper.

6. Place the cell suspension in a polypropylene tube. Count the cells in a counting chamber and place them in new flasks, adding five million cells per flask (*see* **Note 4**).
7. Add macrophage growth medium to bring the volume up to 10 mL. Grow the cells for 5 days, changing the media every second day (*see* **Note 5**).

3.3 Macrophage Radiolabeling and Injection

1. Add ac-LDL to RPMI 1640 medium supplemented with 2 mM glutamine, 10% LPDS, 100 U/mL penicillin, 100 μg/mL streptomycin to produce a final concentration of 0.05 mg/mL. Filter the media through a sterile filter with a 0.2 μm diameter pore size.
2. Evaporate the [^{3}H]-cholesterol solution under nitrogen gas in a fume hood. After evaporation, reconstitute the [^{3}H]-cholesterol in absolute ethanol (e.g., dissolve 50 μCi of [^{3}H]-cholesterol in 25 μL of absolute ethanol where 50 μCi of [^{3}H]-cholesterol is the amount needed to radiolabel the cells of one flask). Add 5 μCi/mL of [^{3}H]-cholesterol to the RPMI 1640 medium containing the ac-LDL, 10% LPDS, 100 U/mL penicillin, 100 μg/mL streptomycin.
3. Wash the flasks with warm PBS twice.
4. Pour out the PBS and add 10 mL of RPMI 1640 medium supplemented with 2 mM glutamine, 10% LPDS, 100 U/mL penicillin, 100 μg/mL streptomycin, 1 mg of ac-LDL, and 50 μCi of [^{3}H]cholesterol to each flask.
5. Incubate the mixture in a humidified cell culture incubator (5% CO_2) at 37 °C for 48 h.
6. Pour out the radiolabeled media, wash with warm PBS, and add 10 mL of serum-free RPMI 1640 medium. Equilibrate the cells for 4 h in a humidified cell culture incubator (5% CO_2) at 37 °C.
7. Pour out the medium from the flasks and wash the cells with 10 mL of PBS.
8. Add 10 mL of PBS to each flask and keep in a cell culture incubator for 10 min.
9. Detach the cells from the plastic surface with a plastic Pasteur pipette. Gently wash the plastic surface with a brushing motion. Use the fluid in the flask to flush them.
10. Put the PBS containing the cells into one polypropylene tube (pool the cells of all flasks in one 50 mL polypropylene tube).
11. Sediment the cells at 1000 × *g* at 4 °C for 10 min.
12. Pour out the supernatant and resuspend the cell pellet with the required amount of PBS (the injection dose for each mouse usually comprises one million cells in 500 μL of PBS).

13. Aliquot the cell suspension into scintillation vials, with 500 μL in each.
14. Retain an extra volume to measure the amount of radioactivity and the viability of the injected cells.
15. To measure the amount of radioactivity, add 100 μL of cell suspension to one scintillation vial (in duplicate). Add 4 mL of liquid scintillation fluid to each vial. Cap the vials and vortex for 30 s. Keep the vials at room temperature (RT) and place them in the scintillation rack. After 30 min, measure the [^{3}H]-radioactivity in a scintillation counter using a 10 min reading program. The total injected dose in 500 μL should be approximately between 1 and 2 millions of cpm (*see* **Note 6**).
16. Mix 30 μL of cell suspension and add 30 μL of 0.4% (w/v) trypan blue. Count the viable (white, clear, and round) and dead (blue and misshapen) cells in a counting chamber (*see* **Note 7**).
17. Load radiolabeled macrophages into 1 mL syringe with a 26–29G needle.
18. Anesthetize each mouse with isoflurane. Inject 500 μL of radiolabeled cells into the peritoneal cavity of each mouse (*see* **Note 8**).
19. Place each mouse individually in a cage with some paper-based bedding material for 48 h. Water and food should be provided *ad libitum*.
20. Collect a small amount of blood from the tail vein at 4 and 24 h in ready-made commercial serum collecting tubes (*see* **Note 9**).
21. Centrifuge the blood at 10,000 × *g* for 10 min at room temperature (RT). Remove the serum and divide it in two parts: i) Take 25 μL to measure the serum radioactivity and ii) Take 25 μL and mix well with 50 μL of phosphotungstate precipitation reagent in a 1.5 mL tube. Leave for 10 min at RT and centrifuge at 10,000 × *g* for 2 min at RT. Separate the supernatant, which contains the HDL, from the precipitate. Add 4 mL of scintillation fluid to the scintillation vials that contain serum and HDL supernatant, respectively, and measure the radioactivity as described in **step 15**.

3.4 Sample Collection and Quantification of Macrophage Cholesterol Efflux and Overall Transport to Feces In Vivo

1. At 48 h, euthanize the mice by an overdose of isoflurane.
2. Perform a one-time cardiac puncture with a 26G needle of a 1 mL syringe and collect the maximum volume of blood from each mouse (*see* **Note 10**).
3. Collect the blood in ready-made commercial serum collecting tubes, and centrifuge at 10,000 × *g* for 10 min at RT.

4. Pin the mice onto a dissection board with their abdomens up. Open the abdominal cavity using a cut along the median axis of the muscular wall. Remove the whole liver and mince into several pieces (without gallbladder, *see* **Note 11**).
5. Wash liver samples in containers with saline.
6. Separate and collect feces from bedding material on the cage floor.
7. Divide the serum in two parts: (1) Take 25 μL to measure serum radioactivity and (2) Take 25 μL and mix with 50 μL of phosphotungstate precipitation reagent and separate the supernatant containing HDL from the precipitate. In both cases, add 4 mL of scintillation fluid and count radioactivity as described in Subheading 3.3, **step 15**.
8. Take the whole liver and feces samples and place each sample into a 15 mL tube (glass or polypropylene tubes resistant to hexane).
9. In all tubes (those containing livers and feces), add 10 mL of solvent for lipid extraction (hexane:isopropanol) and rotate samples on a tube rotator overnight at 4 °C.
10. Transfer the fluid carefully to a new tube, taking care to prevent the entry of solid particles (*see* **Note 12**).
11. Add 3 mL of 0.47 M Na_2SO_4 to separate the hexane and isopropanol into two layers.
12. Rotate samples for 10–15 min.
13. Centrifuge at 1000 × *g* at 4 °C for 10 min.
14. In the case of liver tubes, the upper layer contains approximately 6 mL of lipid mixture.
15. Transfer 4 ml of the upper layer, containing the lipids, into a scintillation vial to measure [^{3}H]-radioactivity.
16. Put 2 mL into a 5 mL glass tube for TLC analyses (continue to **step 22**).
17. In the case of feces, transfer all the content of the upper layer (neutral sterols) and the lower layer (bile acids) into two separate scintillation vials.
18. Dry the vials containing the upper layer (mainly hexane) for 48–72 h in a fume hood. Use a nitrogen stream to aid rapid drying.
19. Retain the lowest aqueous layer in their scintillation vials until the radioactivity is measured.
20. Add 4 mL of scintillation fluid to each vial, cap the vials, vortex vigorously to resuspend lipid extracts and store the samples for 30 min. Vortex again, place the scintillation vials in a scintillation rack and measure the [^{3}H]-radioactivity for 10 min.

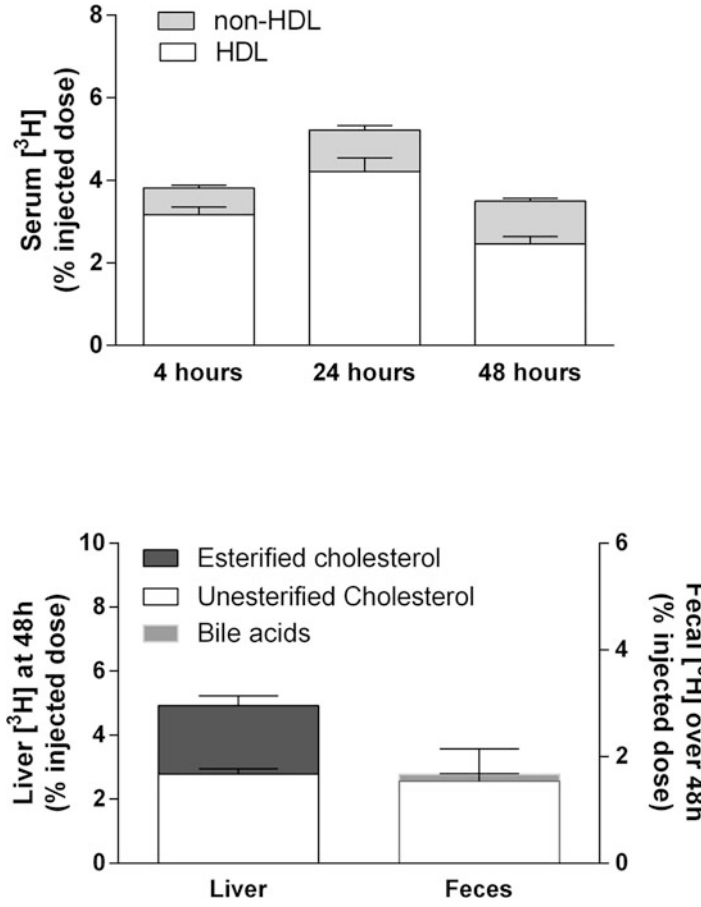

Fig. 2 Representative example of quantification of macrophage-derived cholesterol in serum, liver, and feces in vivo. Upper panel: A representative example of the % of [^{3}H]-radioactivity measured in serum and HDL (at 4, 24, and 48 h) of mice fed a Western-type diet (TD88137, Envigo) for 4 weeks is shown. Lower panel: A representative example of the % of [^{3}H]-radioactivity measured in liver and feces of mice fed a Western-type diet for 4 weeks is shown

21. Liver and fecal [^{3}H]-radioactivity are expressed as the % of the injected dose in the liver or feces of each mouse. In the case of serum, the calculation is expressed as the % of injected dose per mL of serum (*see* Fig. 2 for an example).
22. Dry the glass tube containing 2 mL of the whole liver lipid extract (*see* **step 16**) for 24 h in a fume hood. Use a nitrogen stream to aid rapid drying (*see* **Note 13**).
23. Resuspend the liver lipid extract in 20 μL of chloroform and apply the sample onto a TLC plate on the line near the bottom (*see* **Note 14**).

24. Apply cholesterol reference standard containing the unlabeled cholesterol and cholesterol esters onto one lane of each TLC plate (*see* **Note 15**).
25. To run the TLC, prepare TLC running solvent. Pour 200 mL into a TLC glass tank. Cap the tank and let the solvent vapors saturate the tank chamber.
26. Add approximately 50 g of iodine crystals to another tank and cap the tank to form iodine vapor.
27. Put the TLC plates into the glass tank containing the running solvent against the wall. Run the solvent front until it is 3 cm away from the top line (approximately 45 min).
28. Remove the TLC plates from the tank and dry them in a fume hood. Place the TLC plates in the iodine tank until the spots are clearly stained (yellow and brown).
29. With a tip of a pipette, carefully scratch off the silica gel containing the stained cholesterol bands (*see* **Note 16**). Transfer the powder of each band to a scintillation vial, add 4 mL of scintillation liquid and count radioactivity as described in Subheading 3.3, **step 15**.
30. The amount of liver [^{3}H]-cholesterol as esterified and unesterified form can thus be measured.

4 Notes

1. Human LDL is used to produce acetylated LDL as described in Subheading 3.1. Alternatively, acetylated LDL can be purchased from commercial sources.
2. Reagent for precipitating apoB-containing lipoproteins.
3. Monitor the cell growth because too great density may cause cell detachment.
4. It should be noted that one flask of cells provides enough macrophages to inject into three mice.
5. The cells should be grown until they reach 80% confluence.
6. These steps are carried out to determine the amount of cells and radioactivity injected into mice. These results are used to normalize results from other experiments.
7. The percentage of viable cells should be greater than 70%.
8. Narcosis of mice should be checked to avoid excess cardiac and respiratory suppression.
9. The cut should be made 0.5 cm from the tip of the tail using a scalpel blade and 150 μL of blood should be obtained per sample. The blood flow can be stopped by applying one drop of histoacryl.

10. The needle should be inserted 0.5 cm from the center of the thorax towards the animal's chin, holding the syringe 25–30° away from the chest. The plunger should be pulled back gently to obtain the maximum amount of blood available (usually 1 mL).
11. To remove the liver, the falciform and coronary ligaments that keep the organ intimately connected with the diaphragm should be cut. The liver can then be removed, together with the inferior vena cava and the liver vessels. The weight of the whole liver is approximately 1–1.5 g.
12. Care should be taken not to lose any of the semifluid mass of the chymus by accidental pouring.
13. The following steps in the Methods describe a TLC method that can be used to separate [^{3}H]-cholesterol from [^{3}H]-cholesterol ester, thereby enabling measurement of the distribution of hepatic [^{3}H]-cholesterol.
14. For each sample, 10 μL should be loaded and allowed to evaporate before applying more of the sample.
15. Unesterified cholesterol band is located near the start position, whereas cholesteryl esters band is close to the front of the running solvent.
16. Outline the bands with a pencil. Note that the bands rapidly disappear when the plate is removed from the tank.

Acknowledgments

This work was partly funded by the Instituto de Salud Carlos III and FEDER "Una manera de hacer Europa" grants FIS 16-00471 (to J.L.S-Q.), FIS 17-00232 (to J. J.) and FIS 19-00136 (to J.C.E-G), PFIS contract FI17/00031 (to A.R-U) and Miguel Servet Type 2 contract (CPII18/00004 to J.J.); Ministerio de Ciencia, Innovación y Universidades, grants PID2019-104367RB-100 (to N.R) and Subprograma Ramón y Cajal (RUC-20172879 to N.R.) and Red de Investigación "Enfermedades Metabólicas y Cáncer" (RED2018-102799-T to J.J); Fundació La Marató de TV3 2016 (303/C/2016, 201602.31 to J.J.). All authors are members of the Quality Research Group 2017-SGR-1149 from Generalitat de Catalunya. A.R-U, N.R, J.J, J.L.S.-Q, and J.C.E-G are members of the Group of Vascular Biology from the Spanish Atherosclerosis Society. CIBER de Diabetes y Enfermedades Metabólicas Asociadas is an Instituto de Salud Carlos III Project.

References

1. He Y, Kothari V, Bornfeldt KE (2018) High-density lipoprotein function in cardiovascular disease and diabetes mellitus. Arterioscler Thromb Vasc Biol 38:e10–e16
2. Lee-Rueckert M, Escola-Gil JC, Kovanen PT (2016) HDL functionality in reverse cholesterol transport--challenges in translating data emerging from mouse models to human disease. Biochim Biophys Acta 1861:566–583
3. Ouimet M, Barrett TJ, Fisher EA (2019) HDL and reverse cholesterol transport. Circ Res 124: 1505–1518
4. Zhang Y, Zanotti I, Reilly MP, Glick JM, Rothblat GH, Rader DJ (2003) Overexpression of apolipoprotein A-I promotes reverse transport of cholesterol from macrophages to feces in vivo. Circulation 108:661–663
5. Cedo L, Metso J, Santos D, Garcia-Leon A, Plana N, Sabate-Soler S et al (2020) LDL receptor regulates the reverse transport of macrophage-derived unesterified cholesterol via concerted action of the HDL-LDL axis: insight from mouse models. Circ Res 127:778–792

Chapter 36

Flow Cytometry Analysis of Hematopoietic Stem/Progenitor Cells and Mature Blood Cell Subsets in Atherosclerosis

Alhomidi Almotiri, Ali Abdelfattah, and Neil P. Rodrigues

Abstract

Advancing age causes physiologic decline in tissue function. In the hematopoietic system this manifests as a progressive reduction in blood or immune cell function and clonal hematopoiesis, where a mutated hematopoietic stem cell can dominate blood cell production and confer an increased propensity for myeloid malignancy. In the aging cardiovascular system, atherosclerosis causes an inflammatory cell- driven accumulation of lipid-derived plaques in major arteries which constrains blood flow and can lead to myocardial infarction and stroke. Clonal hematopoiesis in the elderly has recently been associated with a substantially increased risk of atherosclerosis-related cardiovascular disease. However, the direct association between deregulated hematopoiesis in clonal hematopoiesis and atherosclerosis is poorly defined. Herein, we describe a flow cytometry method to prospectively analyze the crucial hematopoietic stem/progenitor, inflammatory and lymphoid cell participants in atherosclerosis. This analysis can be applied to decipher the complex relationship between hematopoietic cell types involved in clonal hematopoiesis and atherosclerosis in mouse models.

Key words Hematopoietic stem cell, Atherosclerosis, Inflammatory cell, Flow cytometry, FACS

1 Introduction

Aging increases the risk of onset of both cardiovascular disease and cancer [1]. Atherosclerosis is a cardiovascular condition in which cholesterol accumulates as plaques in medium and large arteries, and, through inflammatory-mediated mechanisms, plaque rupture leads to blood clots that often cause heart attacks and strokes in older patients [2]. Why atherosclerosis occurs during aging is multi-factorial [2]. One recently identified contributing factor is the identification of clonal hematopoiesis in the elderly—where pre-leukemia mutations arise in hematopoietic stem cells (HSCs) that are transmitted to their blood cell progeny, which also harbor those mutations [3]. Clonal hematopoiesis in the elderly is also associated with an overall relative increased risk of developing myeloid malignancy [4].

Dipak P. Ramji (ed.), *Atherosclerosis: Methods and Protocols*, Methods in Molecular Biology, vol. 2419,
https://doi.org/10.1007/978-1-0716-1924-7_36,
© The Author(s), under exclusive license to Springer Science+Business Media, LLC, part of Springer Nature 2022

Loss of function mutations (and therefore deficiency) in Tet methylcytosine dioxygenase 2 (Tet2), an essential epigenetic regulator of HSCs and hematopoietic function that allows demethylation of cytosine [5], have been implicated as a central driver of atherosclerosis through clonal hematopoiesis [4]. How does Tet2 deficiency regulate atherosclerosis through clonal hematopoiesis? In atherosclerosis, activation of the arterial endothelium results in the accumulation of modified forms of low-density lipoprotein (LDL) in the arterial intima that initiates a localized inflammatory response [6]. Monocytes are subsequently recruited to the site of inflammation in response to numerous chemotactic factors and migrate into the arterial wall where they differentiate into macrophages and take up large amounts of modified LDL to transform into lipid-laden foam cells [7]. The sustained recruitment of immune cells then results in an accumulation of foam cells and the development of atherosclerotic plaques [8]. Tet2 deficiency appears to be critical in regulating monocyte/macrophage functionality, which is crucial to exacerbating recruitment of immune cells in this context and which also allows for the elaboration of pro-inflammatory cytokines including interleukin (IL)-1β and IL-6 [4, 9]. Other studies have confirmed this role for Tet2 and further identified that another epigenetic regulator involved in clonal hematopoiesis, DNA [cytosine-5]-methyltransferase 3a (Dnmt3a), is a causal participant in cardiovascular disease through a distinct pro-inflammatory signature [10]. Thus, an inflammatory response appears to promote the development of atherosclerosis in association with perturbed hematopoietic cell function in clonal hematopoiesis. This pro-inflammatory environment may additionally influence leukemia development from clonal hematopoiesis. In support of this hypothesis, multiple studies have shown that a high-fat diet (HFD) causing obesity induces inflammatory cytokine IL-6 expression as part of an accelerated development of leukemia [11, 12]. In addition, a HFD and associated obesity drives the development of another hematologic malignancy, multiple myeloma [13].

However, the precise role of a HFD in promoting acute myeloid leukemia (AML), a poor prognosis myeloid cell cancer that predominantly impacts the elderly, and the association between atherosclerosis, deregulated HSC/hematopoietic cell function in clonal hematopoiesis and AML development is poorly defined. We and others have shown that atherosclerosis prone apolipoprotein E (ApoE) or LDL receptor (LDLR) knockout mice fed a HFD develop atherosclerosis and display expanded HSC enriched populations in the bone marrow as well as myeloid cell compartments in the peripheral blood [14, 15]. However, considerable heterogeneity exists within the HSC and progenitor (HSPCs) populations and in mature blood cells [16]. Resolving this heterogeneity will aid the understanding of the roles of specific hematopoietic cell subsets in

atherosclerosis and their roles in clonal hematopoiesis and the development of AML leading from this. Fluorescence-activated cell sorting (FACS) technology allows for the facile identification of highly pure, prospective isolation of hematopoietic cell subsets involved in atherosclerosis. Here, we describe a FACS-based method to isolate mouse HSPC subsets and mature blood cells, including those with specific inflammatory function, from bone marrow, spleen, and peripheral blood.

2 Materials

2.1 Cell Harvesting and Processing

2.1.1 Bone Marrow (BM) and Spleen

1. C57/BL6 mice (*see* **Note 1**).
2. Dissection tools: scissors and forceps.
3. 70% ethanol.
4. Pestle and mortar for BM crushing (*see* **Note 2**).
5. 70 μm cell strainer.
6. 50 mL and 15 mL centrifuge tubes.
7. Phosphate-buffered saline (PBS) 1×, pH 7.4 supplemented with 2% heat-inactivated fetal bovine serum (FBS): To prepare 1000 mL of 1× PBS, dissolve 8 g NaCl (137 mM), 200 mg KCl (2.7 mM), 1.44 g Na_2HPO_4 (10 mM), 245 mg KH_2PO_4 (1.8 mM) in 1000 mL distilled water and adjust pH to 7.4.
8. Syringe plunger with rubber seal (*see* **Note 3**).
9. A refrigerated centrifuge with tube volumes ranging from 1.5 to 5 mL.
10. 1.5 mL microcentrifuge tubes.
11. Clean tissues.
12. 10 cm^2 plates.
13. Automated or manual cell counters.

2.1.2 Peripheral Blood (PB)

1. Scalpel blades.
2. Ethylenediaminetetraacetic acid (EDTA) treated tubes.
3. Ammonium chloride (NH_4Cl) solution: 0.8% NH_4Cl, 0.1 mM EDTA in water, buffered with $KHCO_3$ to achieve a final pH of 7.2–7.6.
4. 1.5 mL microcentrifuge tubes.
5. Centrifuge with a capacity of at least 1.5 mL tubes.

2.2 Cell Staining

2.2.1 General Requirements for Staining

1. Information about the antibodies described in this protocol are presented in Table 1. The stock concentration of fluorochrome-conjugated C-KIT-APC, SCA-1-APC-Cy7, CD150-PE-Cy7, CD16/32-PE-Cy7, CD127-BV650, CD135-PE, Ter119-APC-Cy7, CD71-PE, GR1-PE-Cy7, MAC1-APC, CD42d-PerCP, CD4-PerCP, CD8-BV650, Ly6G-PE-Cy7, SA-PerCP, and CD115-APC-Cy7 antibodies is 0.2 mg/mL while for B220-FITC, CD48-FITC, CD34-FITC, CD41-FITC, Ly6C-FITC, and purified anti-CD16/32 is 0.5 mg/mL. The stock concentration of the biotinylated antibodies CD3, CD4, CD8a, B220, MAC1, GR1, and Ter119 is 0.5 mg/mL (*see* **Note 4**).

Table 1
Information about the antibodies described in this protocol

	Antigen	Clone	Fluorochrome	Dilution	Manufacturer
Hematopoietic stem cell and primitive and committed progenitors	Pool of lineage$^+$ markers: CD3, CD4, CD8a, B220, MAC1, GR1, Ter119	CD3: 17A2 The others are shown below individually	Biotin	CD3 and CD8:1/40, B220 and GR1:1/20, CD4:1/80, MAC1:1/10, Ter119:1/5	Biolegend, eBiosciences
	SCA-1	D7	APC-Cy7	1/25	Biolegend
	C-KIT	2B8	APC,	1/100	Biolegend
	CD150	TC15-12F12.2	PE-Cy7	1/100	Biolegend
	CD48	HM48-1	FITC	1/50	Biolegend
	CD135 (Flt3)	A2F10	PE	1/50	Biolegend
	CD34	RAM34	FITC	1/25	Ebiosciences
	CD16/32	93	PE-Cy7	1/25	Biolegend
	CD127 (IL-7rα)	A7R34	BV650	1/100	Biolegend
Lymphoid cell panel	CD4	GK1.5	PerCP	1/1000	Biolegend
	CD8a	53–6.7	BV650	1/1000	Biolegend
	B220/CD45R	RA3-6B2	FITC, APC	1/1000	Biolegend
Myeloid and inflammatory cell panel	CD11b (MAC1)	M1/70	APC	1/1000	Biolegend
	GR1	RB6-8C5	FITC, PE-Cy7	1/1000	Biolegend
	Ter119	TER-119	APC-Cy7	1/1000	Biolegend
	CD71	RI7217	PE	1/1000	Biolegend
	CD41	MWReg30	FITC	1/1000	Biolegend
	CD42d	1C2	PerCP	1/1000	Biolegend
	Ly6G	1A8	PE-Cy7	1/1000	Biolegend
	Ly6C	HK1.4	FITC	1/1000	Biolegend
	CD115	AFS98	APC-Cy7	1/1000	Biolegend
	Fc block	93	NA	1/50	Biolegend
	Streptavidin	NA	PerCP	1/100	Biolegend, ebiosciences

2. PBS supplemented with 2% FBS for all staining procedures.
3. Fluorescence minus one (FMO) control (*see* **Note 5**).
4. Single stains (*see* **Note 6**).
5. Unstained control sample.

2.2.2 Hematopoietic Stem Cells, Primitive Progenitors, and Committed Progenitors from BM

1. Lineage biotinylated cocktail: For 1 mL of lineage cocktail, add biotin conjugated CD4 (12.5 μL), CD3e (25 μL), CD8a (25 μL), Gr1 (50 μL), Mac-1 (100 μL), B220 (50 μL), and Ter119 (200 μL) to 537.5 μL of PBS 2% FBS.
2. Fc receptors blocking antibody (purified anti-CD16/32) for 1 sample: 1 μL blocking antibody, 49 μL PBS 2% FBS.
3. Streptavidin (SA) conjugated with PerCP (SA-PerCP) for 1 sample: 1 μL SA-PerCP, 99 μL PBS 2% FBS (*see* **Note 7**).
4. Staining mix of hematopoietic stem cells and primitive progenitors for one sample: 1 μL C-KIT-APC, 4 μL SCA-1-APC-Cy7, 1 μL CD150-PE-Cy7, 2 μL CD48-FITC, 10 μL lineage biotinylated cocktail, 32 μL PBS 2% FBS.
5. Staining mix of committed progenitors for one sample: 1 μL C-KIT-APC, 4 μL SCA-1-APCCy7, 4 μL CD16/32-PE-Cy7, 4 μL CD34-FITC, 1 μL CD127-BV650, 2 μL CD135-PE, 10 μL lineage biotinylated cocktail, 74 μL PBS 2% FBS.
6. Incubator/device for incubation at 4 °C.
7. Ice.

2.2.3 Mature Hematopoietic Cells in BM, PB, and Spleen

1. The staining mix of myeloid, lymphoid, and inflammatory cell panels is prepared at 1/1000 dilution at final volume of 50 μL for each sample (*see* **Note 8**). Myeloid cell staining mix includes Ter119-APC-Cy7 and CD71-PE (erythroid lineage), GR1-PE-Cy7 and MAC1-APC (granulocytic and monocytic lineage), CD41-FITC and CD42d-PerCP (mature megakaryocytes); lymphoid cell staining mix includes CD4-PerCP and CD8-BV650 (T cells) and B220-FITC (B cells); and inflammatory cell staining mix includes MAC1-APC and Ly6G-PE-Cy7 (granulocytes), Ly6C-FITC and CD115-APC-Cy7 (monocytes and macrophages (inflammatory cells)).

2.3 Cell Analysis and Characterization Using Flow Cytometry

1. Flow cytometer equipped with four lasers: blue, red, violet and yellow/green (e.g., BD LSRFortessa™ (BD Biosciences)). Set the detector voltages as follows: FSC, 350/10 nm; SSC, 350/10 nm; FITC, 530/30 nm; APC, 670/30 nm; PE, 585/15 nm; PerCP-Cy5.5, 710/50; APC-Cy7, 780/60 nm; PE-Cy7, 780/60 nm; PB, 450/50 nm; and BV650, 670/30 nm.
2. Polystyrene FACS tubes.

3. 5 mg/mL stock solution of 4′,6-diamidino-2-phenylindole (DAPI).
4. 30 μm cell strainer.

3 Methods

3.1 Sample Harvesting and Processing

In the protocol described in this chapter, PB, BM, and spleen from C57/BL6 mice are required. First, obtain the PB while the mouse is alive and when the mice are sacrificed, extract the BM and spleen. After obtaining cell suspensions from BM, PB, and spleen, always store at 4 °C (*see* **Note 9**).

3.1.1 PB

1. Using a scalpel blade, nick the surface of the tail vein and collect at least 50 μL of PB in EDTA-treated tubes (*see* **Note 10**).
2. Gently invert the tube to mix the blood with EDTA to prevent clotting.
3. Into three 1.5 mL microcentrifuge tubes (for myeloid, lymphoid, and inflammatory panels), add 12 μL of blood to each tube and then add 600 μL of NH_4Cl solution to each tube. For unstained control, aliquot 6 μL of blood from one of the control samples and add 300 μL of NH_4Cl solution.
4. Mix and incubate for 6 min at room temperature (RT). Then, gently shake the bottom of the tube to disturb the cells and incubate for a further 6 min.
5. Centrifuge for 10 min at 300 × *g* at RT. Discard the supernatant carefully and stain the cells as described in Subheading 3.2.3.

3.1.2 BM and Spleen

1. After obtaining the blood, sacrifice the mice by cervical dislocation. Spray the mice with 70% ethanol.
2. Remove the spleen and put it in cold PBS 2% FBS. Then, remove the femurs and tibias and thoroughly clean the bone surrounding muscles using clean tissues and put them in cold PBS 2% FBS (*see* **Note 11**).
3. Using pestle and mortar, thoroughly crush the bones in 10 mL of PBS 2% FBS and filter through 70 μm cell strainer into a 50 mL centrifuge tube. Repeat this step twice to end up with cell suspension of 30 mL. Keep the cells on ice. For processing the spleen, put the mesh of a 70 μm cell strainer in 10 cm^2 plate and add 2 mL of PBS 2% FBS. Mince the spleen on the mesh using the rubber seal of a syringe until it completely dissociates.
4. Remove the mesh containing the remaining tissue fragments of the minced spleen. Collect the cells from the plate in a 15 mL

tube and add PBS 2% FBS to the plate to collect the remaining cells, transfer to the tube and make 7 mL cell suspension.

5. Count BM and spleen cells using automated or manual cell counters.
6. Aliquot ten million cells for stem cells and primitive progenitors staining and eight million cells for committed progenitors staining. For mature cell staining, from BM and spleen, aliquot 200,000 cells from cell suspension to each myeloid, lymphoid, or inflammatory cell panel.
7. Prepare the FMO controls by aliquoting 50 μL from BM cells (this may correspond to about 200,000 cells) to each 1.5 mL microcentrifuge tube. In this protocol, we have 7 fluorochromes so 7 tubes containing 50 μL of cells should be prepared (*see* **Note 12**).
8. Prepare control unstained samples by aliquoting 50 μL from the BM cells to a single 1.5 mL microcentrifuge tube.
9. Prepare single stain controls by aliquoting 50 μL from the BM cells (this may correspond to about 200,000 cells) to each 1.5 mL microcentrifuge tube. In this protocol we have 7 fluorochromes so 7 tubes containing 50 μL of cells should be prepared (*see* **Note 13**).

3.2 Cell Staining

3.2.1 Hematopoietic Stem Cells and Primitive Progenitors from the BM

1. Centrifuge the sample containing ten million cells at 500 × *g* for 5 min at 4 °C. Discard the supernatant.
2. Resuspend the pellet in 50 μL of Fc block antibody (anti CD16/CD32) for 5 min at 4 °C.
3. Add 50 μL of staining mix to the sample to make a final volume of 100 μL and incubate for 30 min at 4 °C or on ice in the dark.
4. Wash the cells with 1 mL of PBS 2% FBS, centrifuge at 500× *g* for 5 min at 4 °C, and discard the supernatant.
5. Resuspend the pellet in 100 μL of SA-PerCP and incubate for 20 min at 4 °C in the dark.
6. Wash the cells with 1 mL of PBS 2% FBS, centrifuge at 500 × *g* for 5 min at 4 °C, discard the supernatant, and resuspend in 700 μL of PBS 2% FBS.
7. Filter the cells using 30 μm cell strainer into a FACS tube and keep them on ice until acquisition on flow cytometer (*see* **Note 14**).

3.2.2 Committed Hematopoietic Progenitors from the BM

1. Centrifuge the sample containing eight million cells at 500 × *g* for 5 min at 4 °C. Discard the supernatant.
2. Resuspend the pellet in 100 μL of staining mix and incubate for 30 min at 4 °C or on ice in dark.

3. Wash the cells with 1 mL of PBS 2% FBS, centrifuge at 500 × *g* for 5 min at 4 °C, and discard the supernatant.
4. Resuspend the pellet in 100 μL of SA-PerCP and incubate for 20 min at 4 °C in the dark.
5. Wash the cells with 1 mL of PBS 2% FBS, centrifuge at 500 × *g* for 5 min at 4 °C, discard the supernatant, and resuspend in 600 μL of PBS 2% FBS.
6. Filter the cells using 30 μm cell strainer into a FACS tube and keep them on ice until acquisition on flow cytometer.

3.2.3 Hematopoietic Mature Cells in BM, PB, and Spleen

1. Add 50 μL of the staining mix of myeloid, lymphoid, and inflammatory cell panel to the corresponding tube of the myeloid, lymphoid, and inflammatory panel for BM, spleen, and PB.
2. Incubate for 30 min at 4 °C in dark.
3. Wash the cells with 1 mL of PBS 2% FBS, centrifuge at 500 × *g* for 5 min at 4 °C, and discard the supernatant.
4. Resuspend the cells in 200 μL of PBS 2% FBS, transfer them to FACS tubes, and keep them on ice at 4 °C until acquisition on flow cytometer.

3.2.4 Control Samples

1. Add 200 μL of PBS 2% FBS to the unstained control sample without adding any staining antibody.
2. For single stain controls, add 0.2 μL from the corresponding fluorochrome to the corresponding tube (that contains 50 μL from **Step 9** in Subheading 3.1.2) and incubate for 30 min at 4 °C in the dark.
3. For FMO controls, add 0.2 μL from each antibody to the corresponding tube (that contains 50 μL from **Step 7** in Subheading 3.1.2) and incubate for 30 min at 4 °C in the dark (*see* **Note 15**).
4. Wash the cells from single stain and FMO controls with 1 mL of PBS 2% FBS, centrifuge at 500 × *g* for 5 min at 4 °C, and discard the supernatant.
5. Resuspend the cells in 200 μL of PBS 2% FBS and keep them on ice at 4 °C until acquisition on flow cytometer.

3.3 Flow Cytometry Analysis

1. Before analyzing the samples on the BD LSRFortessa™, add DAPI at a final concentration of 0.5–1 μg/mL to the samples and mix. This is to exclude $DAPI^+$ dead cells when analyzing the samples.
2. Set up the plots, gates, and voltages for stem cell and progenitor sample experiments (Fig. 1). Use unstained and FMO controls to help with setting the gates (*see* **Note 16**).

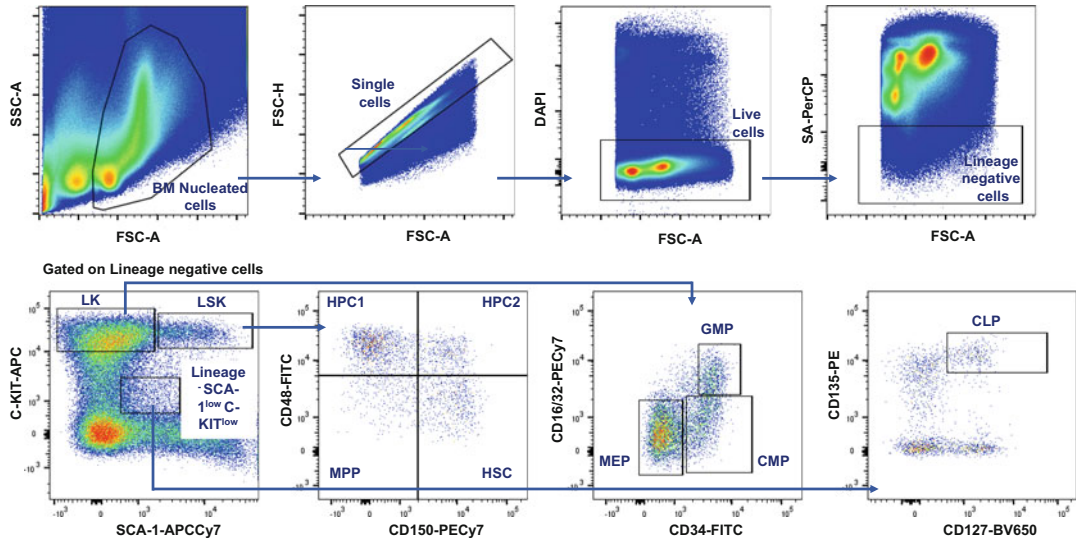

Fig. 1 Gating strategy for BM hematopoietic stem/progenitor cells (HSPCs) and committed progenitors. Flow cytometry plots and gating strategy of the analysis of BM hematopoietic stem/progenitor cells (HSC, MPP, HPC1, HPC2) and myeloid committed progenitors (CMP, GMP, MEP), and the lymphoid committed progenitor (CLP) from young adult C57/BL6 mice. Cells are gated using SSC-A vs. FSC-A to exclude debris. Then, the cells are gated using FSC-A vs. FSC-H to exclude doublets and clumps. Next, the cells are gated from $DAPI^-$ gate to exclude dead cells. Lineage negative cells are then gated from live cells. Using SCA-1 and C-KIT markers, lineage negative cells are divided into LSK (Lineage negative, SCA-1^+, C-KIT^+), LK (Lineage negative, SCA-1^-, C-KIT^+), and $Lineage^-$ SCA-1^{low} C-KIT^{low}. HSPCs are gated from LSK population using CD150 and CD48. Myeloid committed progenitors are gated from LK population using CD34 and CD16/32. CLP is gated from $Lineage^-$ SCA-1^{low} C-KIT^{low} population as $CD127^+$ and $CD135^+$. Hematopoietic stem cells (HSC): LSK $CD150^+$ $CD48^-$, Multi-potent progenitors (MPP): LSK $CD150^-$ $CD48^-$, Hematopoietic progenitor cell I (HPC-1): LSK $CD150^-$ $CD48^+$, and Hematopoietic progenitor cell II (HPC-2): LSK $CD150^+$ $CD48^+$, Common myeloid progenitors (CMP): LK $CD34^+$ $CD16/32^-$, Granulocyte-macrophage progenitors (GMP): LK $CD34^+$ $CD16/32^+$, megakaryocytic-erythroid progenitors (MEP): LK $CD34^-$ $CD16/32^-$, Common lymphoid progenitors (CLP): $Lineage^-$ SCA-1^{low} C-KIT^{low} $CD127^+$ $CD135^+$

3. Compensate the spectral overlap between the fluorochromes using the single stain controls and make sure you apply the compensation to all the samples within the experiment (*see* **Note 17**).
4. Analyze the samples at low speed and not more than an acquisition rate of 4000 cells/s (*see* **Note 18**). From the FSC-A vs. SSC-A gate, acquire at least 2,500,000 cells for stem cell and primitive progenitor sample [this is to analyze hematopoietic stem cells (HSC), multi-potent progenitor (MPP), hematopoietic progenitor cells (HPC)1 and HPC2.] and 1,500,000 cells for the committed progenitor samples [this is to analyze common myeloid progenitor (CMP), granulocyte-monocyte progenitor (GMP), megakaryocyte-erythrocyte progenitor (MEP), and common lymphoid progenitor (CLP)] (*see* **Note 19**).

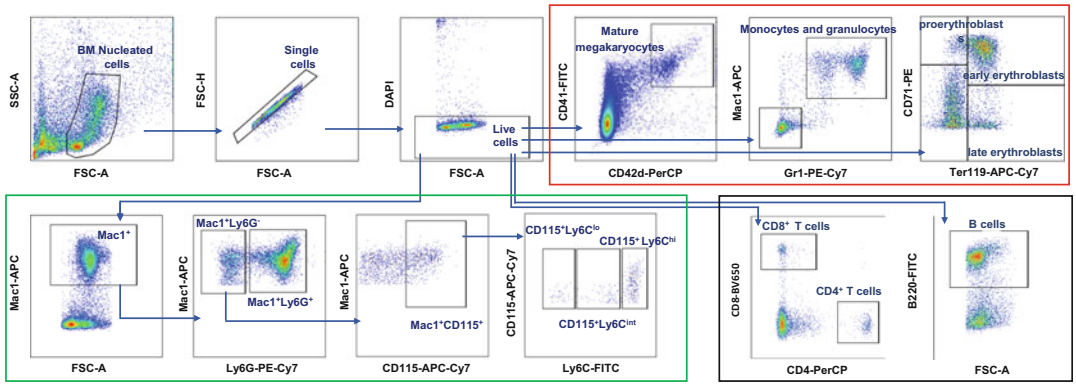

Fig. 2 Gating strategy for mature myeloid, inflammatory myeloid, and lymphoid cells. Flow cytometry plots and gating strategy of the analysis of BM mature cells isolated from C57/BL6 mice. Cells are gated using SSC-A vs. FSC-A to exclude debris. Then, the cells are gated using FSC-A vs. FSC-H to exclude doublets and clumps. Next, the cells are gated from $DAPI^-$ gate to exclude dead cells. The red box represents the gating strategy of myeloid cells including mature megakaryocytes ($CD41^+$ $CD42d^+$), monocytes and granulocytes ($Mac1^+$ $Gr1^+$), proerythroblasts ($CD71^+$ $Ter119^{-/low}$), early erythroblasts ($CD71^+$ $Ter119^+$), and late erythroblasts ($CD71^-$ $Ter119^+$). The green box represents the gating strategy of inflammatory cells which can be analyzed from $Mac1^+$ $Ly6G^-$ $CD115^+$ myeloid cell population into three main populations according to Ly6C expression: phagocytic and pro-inflammatory macrophages ($Mac1^+$ $Ly6G^-$ $CD115^+$ $Ly6C^{high}$), pro-inflammatory macrophages ($Mac1^+$ $Ly6G^-$ $CD115^+$ $Ly6C^{intermediate}$), and anti-inflammatory macrophages ($Mac1^+$ $Ly6G^-$ $CD115^+$ $Ly6C^{low}$). The black box represents the gating strategy of lymphoid cells including $CD4^+$ T cells, $CD8^+$ T cells, and $B220^+$ B cells

5. Make a separate experiment template on the machine for the mature cells and set up the plots and gates (Fig. 2) as well as the compensation using the controls as described in **Steps 2** and **3** in this section.
6. Run the mature cell samples by acquiring 30,000 cells from the live cell gate.
7. After running all the samples and making sure the compensation has been done correctly, data can be exported and fully analyzed in an external software such as FlowJo.

4 Notes

1. This protocol was optimized using young adult mice in the C57/BL6 background, aged between 8 and 12 weeks old. According to our experience, it can be applied to aged C57/BL6 mice as well.
2. Another way of obtaining BM cells is by flushing out the bone using PBS containing 2% FBS using 10 mL syringes with 25G needles.
3. This is used for spleen mincing and processing.

4. Antibodies should be titrated before use in experiments.
5. The FMO control tube contains all the fluorochromes used in the panel except the one that is being tested. It is important to have FMO controls to aid identification of the negative populations from the true positive population when using multicolor flow cytometry panels.
6. For each antibody stain in the panel, there should be a single stain tube for compensation purposes.
7. Addition of streptavidin as a secondary antibody is to detect biotinylated antibodies.
8. An example to clarify, if you have ten samples, you need to have a final volume of 500 μL of PBS 2% FBS (10 samples × 50 μL = 500 μL) and add 0.5 μL from each antibody to the 500 μL PBS 2% FBS (500/1000 = 0.5 μL).
9. Storing cells at 4 °C maintains cell viability more than storing them at RT [17].
10. Because some blood sticks to the wall of the tube and it is difficult to collect, it is better to collect more than 50 μL given that the blood will be divided into three samples for myeloid, lymphoid, and inflammatory staining panels and 12 μL will be required for each panel as well as for the unstained, single stain, and FMO controls.
11. In case acquisition and analysis of BM cells cannot take place on the same day, do not crush the bones and keep them in PBS 2% FBS as this will improve viability for up to 16 h [17].
12. In this protocol, FMO samples are taken from the BM cells. However, when doing only PB analysis without extracting the BM, at least 6 μL for each tube of FMO will be needed, so obtain more PB but, for ethical reasons, do not extract more than 10% of the total blood volume of a mouse.
13. If the number of cells is limiting and needed for analysis, flow cytometry compensation beads can be used for single stain controls.
14. After staining the cells, samples should preferably be analyzed in the same day or maximum within 24 h as the viability and signal intensity will be affected if they are left longer [17, 18].
15. For FMO tubes, use the same fluorochrome-conjugated antibody that was used in the actual sample (e.g., if C-KIT-APC was used in the panel, use in the FMO panel the same C-KIT-APC, not other APC-conjugated antibodies).
16. The BD LSRFortessa™ by default will show many fluorochromes in the setting page of the experiment, so it is important to remove the fluorochromes that are not used in your panel. Set the voltages as recommended. Run and record the

actual sample for several seconds to check the cells are in the plots and to make sure there is no "off plot" cells. The experiment is not yet compensated but this should be done to make sure that your voltages are not extremely low nor extremely high which will make the cells go off-scale.

17. It is essential to know that some fluorochromes have broad emission spectra which will spill over into other channels. BD Biosciences and other websites provide useful details about this issue in order to enable proper compensation that will negate this impact. Failure of compensation or to compensate properly will mean data analysis is compromised.
18. Running the sample at high acquisition rate will result in a reduction of single cells and will affect the accuracy of analysis and will increase the doublets (i.e., cells sticking together). Adhere to the specified acquisition rate and check the single cell percentage on the screen so that it is no less than 95%.
19. Acquiring the number of cells as specified in the protocol is important to ensure collecting enough cells for the analysis of rare cell populations, such as HSC.

References

1. Koene RJ, Prizment AE, Blaes A et al (2016) Shared risk factors in cardiovascular disease and cancer. Circulation 133(11):1104–1114. https://doi.org/10.1161/circulationaha.115.020406
2. Ramji DP (2019) Polyunsaturated fatty acids and atherosclerosis: insights from pre-clinical studies. Eur J Lipid Sci Technol 121(1): 1800029. https://doi.org/10.1002/ejlt.201800029
3. Jaiswal S, Ebert BL (2019) Clonal hematopoiesis in human aging and disease. Science 366(6465):eaan4673. https://doi.org/10.1126/science.aan4673
4. Jaiswal S, Natarajan P, Silver AJ et al (2017) Clonal hematopoiesis and risk of atherosclerotic cardiovascular disease. N Engl J Med 377(2):111–121. https://doi.org/10.1056/NEJMoa1701719
5. Moran-Crusio K, Reavie L, Shih A et al (2011) Tet2 loss leads to increased hematopoietic stem cell self-renewal and myeloid transformation. Cancer Cell 20(1):11–24. https://doi.org/10.1016/j.ccr.2011.06.001
6. McLaren JE, Michael DR, Ashlin TG et al (2011) Cytokines, macrophage lipid metabolism and foam cells: implications for cardiovascular disease therapy. Prog Lipid Res 50(4): 331–347. https://doi.org/10.1016/j.plipres.2011.04.002
7. Javadifar A, Rastgoo S, Banach M et al (2021) Foam cells as therapeutic targets in atherosclerosis with a focus on the regulatory roles of non-coding RNAs. Int J Mol Sci 22(5): 2529–2529. https://doi.org/10.3390/ijms22052529
8. Wolf D, Ley K (2019) Immunity and inflammation in atherosclerosis. Circ Res 124(2): 315–327. https://doi.org/10.1161/circresaha.118.313591
9. Fuster JJ, MacLauchlan S, Zuriaga MA et al (2017) Clonal hematopoiesis associated with TET2 deficiency accelerates atherosclerosis development in mice. Science 355(6327): 842–847. https://doi.org/10.1126/science.aag1381
10. Sano S, Oshima K, Wang Y et al (2018) CRISPR-mediated gene editing to assess the roles of tet2 and Dnmt3a in clonal hematopoiesis and cardiovascular disease. Circ Res 123(3):335–341. https://doi.org/10.1161/circresaha.118.313225
11. Yan F, Shen N, Pang JX et al (2017) Fatty acid-binding protein FABP4 mechanistically links obesity with aggressive AML by enhancing aberrant DNA methylation in AML cells. Leukemia 31(6):1434–1442. https://doi.org/10.1038/leu.2016.349
12. Yun JP, Behan JW, Heisterkamp N et al (2010) Diet-induced obesity accelerates acute

lymphoblastic leukemia progression in two murine models. Cancer Prev Res (Phila) 3(10):1259–1264. https://doi.org/10.1158/1940-6207.Capr-10-0087

13. Lwin ST, Olechnowicz SW, Fowler JA et al (2015) Diet-induced obesity promotes a myeloma-like condition *in vivo*. Leukemia 29(2):507–510. https://doi.org/10.1038/leu.2014.295
14. Murphy AJ, Akhtari M, Tolani S et al (2011) ApoE regulates hematopoietic stem cell proliferation, monocytosis, and monocyte accumulation in atherosclerotic lesions in mice. J Clin Invest 121(10):4138–4149. https://doi.org/10.1172/jci57559
15. Feng Y, Schouteden S, Geenens R et al (2012) Hematopoietic stem/progenitor cell proliferation and differentiation is differentially regulated by high-density and low-density lipoproteins in mice. PLoS One 7(11):e47286. https://doi.org/10.1371/journal.pone.0047286
16. Haas S, Trumpp A, Milsom MD (2018) Causes and consequences of hematopoietic stem cell heterogeneity. Cell Stem Cell 22(5):627–638. https://doi.org/10.1016/j.stem.2018.04.003
17. Papazian AE, Kfoury YS, Scadden DT (2017) Shipping mouse bone marrow: keep it in the bone. Exp Hematol 49:68–72. https://doi.org/10.1016/j.exphem.2016.12.008
18. Cossarizza A, Chang HD, Radbruch A et al (2017) Guidelines for the use of flow cytometry and cell sorting in immunological studies. Eur J Immunol 47(10):1584–1797. https://doi.org/10.1002/eji.201646632

Chapter 37

Whole Mount Preparation of Mouse Aorta for Confocal Microscopy Studies of the Intima

Ana Barettino, Ignacio Benedicto, and Vicente Andrés

Abstract

Confocal imaging of the mouse aorta is a powerful, indispensable technique for the study of cardiovascular pathology *ex vivo*. Whole mount *en face* preparations allow visualization of wide areas of the luminal vessel surface, thus enabling a thorough analysis of multiple cellular and structural features of the endothelial cell-rich intimal layer. This method is a suitable tool for the study of endothelial cell dysfunction and leukocyte infiltration, both of which contribute to the onset of pathological vascular conditions such as atherosclerosis. This chapter provides a complete guide on how to perfuse-fix mouse aorta, dissect the vessel, immunostain target proteins, and carry out *en face* confocal image acquisition and analysis.

Key words Whole mount immunofluorescence, *En face* immunofluorescence, Endothelial dysfunction, Atherosclerosis, Aorta

1 Introduction

Cardiovascular disease (CVD) is the leading cause of mortality worldwide, accounting for an estimated 17.9 million deaths each year [1]. The main underlying cause of CVD is atherosclerosis, which manifests clinically as coronary heart disease, cerebrovascular disease, peripheral arterial disease, and other pathologies. Atherosclerosis is characterized by the accumulation of lipid-rich deposits (atheroma plaques) within the inner part of the vessel wall. These deposits initiate and sustain a chronic inflammatory pathological process that affects the structure and function of large arteries [2]. Atheroma plaque buildup takes place beneath luminal endothelial cells (ECs), which form the interface between blood and the vessel wall. ECs are not mere structural blood vessel components, but also play key roles in the regulation of many physiological functions crucial for the correct performance of the vessel, including hemostasis, vascular tone, barrier function, and the inflammatory response [3]. Because increasing evidence suggests that one of

Dipak P. Ramji (ed.), *Atherosclerosis: Methods and Protocols*, Methods in Molecular Biology, vol. 2419,
https://doi.org/10.1007/978-1-0716-1924-7_37,
© The Author(s), under exclusive license to Springer Science+Business Media, LLC, part of Springer Nature 2022

the initial steps in the development of atherosclerosis is EC dysfunction [4, 5], studying its nature and regulatory mechanisms is fundamental to understanding vascular pathology and ultimately developing new therapeutic approaches.

In whole mount *en face* aorta preparations, the vessel is opened longitudinally and mounted lumen-side up, exposing the complete endothelial monolayer. This method is an essential complement to the analysis of transverse sections of the vessel (aortic rings), especially when studying alterations to luminal ECs. Studying the endothelial phenotype with aortic rings has certain constraints which can be overcome by carrying out whole mount *en face* analysis. An aortic ring consists of just 8–10 μm section of the whole aorta and contains very few ECs. In contrast, whole mount *en face* imaging permits the examination of millimeter-wide areas of the vessel lining, making it much easier to detect subtle alterations and changes restricted to discrete areas, such as atherosclerosis-associated intima lesions. Moreover, these preparations allow the study of hundreds of ECs per image, so that the acquired images are likely to be more representative and higher statistical power can be achieved. Another advantage of whole mount *en face* preparations is that they enable visualization of whole cells and not just sections through them. This not only facilitates more accurate quantitative image analysis, but is also essential for the study of multiple EC features that cannot be analyzed in vessel cross-sections, such as cell shape and morphology, cell alignment within the monolayer, intercellular junctions (e.g., tight junctions, adherens junctions), subcellular localization of organelles and/or proteins, and interactions between ECs and the extracellular matrix (ECM). Importantly, visualization of whole cells also enables 3D spatial reconstruction.

Wild-type and genetically modified mice are widely used as experimental models for the study of aortic diseases. Here, we describe affordable, rapid and easy-to-follow protocols for confocal microscopy analysis of *en face* mouse aorta preparations. Briefly, transcardial perfusion fixation replaces blood with a fixative solution to quickly preserve the tissue. This fluid replacement is done at a controlled, uniform flow speed that prevents EC detachment. The aorta is then dissected out from the mouse, cleaned from perivascular fat, opened longitudinally, pinned to a surface lumen-side up and fixed overnight. A piece of the tissue with the endothelium fully exposed is then immunostained, mounted and imaged using confocal microscopy techniques. We also provide a guide to the quantitative image analysis of some basic features and pathological alterations of the intimal layer.

2 Materials

1. Fume hood.
2. Sterile phosphate-buffered saline (PBS): 1.54 mM KH_2PO_4, 155.17 mM NaCl, 2.70 mM Na_2HPO_4, pH 7.4. Autoclave or filter to sterilize.
3. Fixation solution: 4% paraformaldehyde (PFA) in PBS. For a total volume of 500 mL, heat 400 mL PBS in a fume hood to approximately 60 °C on a hot plate with a magnetic stirrer. Then, add 20 g paraformaldehyde followed by 1 M NaOH dropwise until the powder is dissolved. Add PBS to a final volume of 500 mL, leave to cool to room temperature, filter and then adjust pH to 7.4. Use fresh or store frozen at −20 °C (*see* **Note 1**).
4. Gravity perfusion system: Infusion bottle/dropper (or empty and clean 500 mL saline infusion bottle), 25G butterfly cannula/winged infusion set, gravity infusion set with 150 cm extension tube.
5. Waste beaker.
6. 1 mL syringe.
7. Mouse model system.
8. Mouse anesthetic (ketamine/xylazine cocktail): 225 mg/kg ketamine, 15 mg/kg xylazine. For a 10 mL vial, mix 8 mL saline with 1.5 mL of 100 mg/mL ketamine and 0.5 mL of 20 mg/mL xylazine. Use fresh or store at 4 °C in the dark for up to 1 month.
9. 25G needles.
10. Standard balance scale.
11. Cork board.
12. Paper towels.
13. Plastic tray.
14. 70% ethanol in distilled water.
15. Dissection tools: Straight serrated-tip forceps, straight blunt scissors (to cut mouse skin and open the ribcage), straight or curved serrated-tip fine forceps, straight sharp fine scissors (to remove the aorta), microdissecting spring scissors, straight fine-tipped forceps, and 0.1 mm steel minutien pins (to remove adventitial fat, open the aorta longitudinally, pin it flat and manipulate the tissue).
16. Scalpel blade.
17. Timer.

18. Stereomicroscope and cold light source with double gooseneck.
19. Syringe needle or tape.
20. Waste bin.
21. 2 mL microfuge tubes.
22. Regular plastic dishes.
23. Dissecting dish.
24. Sylgard-coated plastic dish: Mix and apply Sylgard 184 (e.g., Sigma-Aldrich) to the bottom of a regular plastic dish to create an even smooth surface.
25. Plastic Pasteur pipette.
26. Blocking and permeabilization buffer: 5% (w/v) BSA, 0.3% Triton X100 in PBS.
27. Normal goat serum (NGS).
28. Primary antibodies: Armenian hamster anti-CD31 (MAB1398Z, Merck, 1:100), rabbit anti-GLG1 (ab103439, Abcam, 1:100), Alexa Fluor 647-conjugated rabbit anti-ERG (ab196149, Abcam, 1:100), biotin-conjugated mouse anti-CD45.2 (553771, BD Biosciences, 1:200).
29. Fluorochromes and fluorochrome-conjugated secondary antibodies and streptavidin: Hoechst 33342 (B2261, Sigma, 1:1000), goat anti-Armenian hamster IgG H&L Alexa Fluor 488 (ab173003, Abcam, 1:400), goat anti-rabbit IgG H&L Alexa Fluor 647 (A21245, ThermoFisher, 1:400), streptavidin Cyanine Cy3 (016-160-084, Jackson ImmunoResearch, 1:200).
30. Washing buffer: 0.05% Tween 20 in PBS.
31. 4 °C cold room.
32. Aluminum foil (or dark box).
33. Rocker 2D shaker.
34. Microscope slides.
35. 24 × 24 mm glass cover slides.
36. 85% glycerol in water.
37. Slide storage boxes.
38. Confocal microscope and software for image capture.
39. Glycerol immersion objectives: LD LCI Plan-Apochromat 25×/0.8 Imm Korr DIC M27, I LCI Plan-Neofluar 63×/1.3 Imm Korr DIC M27.
40. Computer.
41. Software for image analysis and quantification.
42. Software for three-dimensional reconstruction.

3 Methods

3.1 Perfusion Fixation of Mouse Aorta

1. Prepare the perfusion device using a dropper for gravity perfusion. Load the dropper with freshly prepared fixation solution at room temperature (*see* **Note 1**). Insert a gravity infusion set with the key closed and fit a cannula at the end (*see* Fig. 1a). Hang the dropper 1.5 m above the surface of the dissection table (*see* Fig. 1b). Place the cannula needle over the waste beaker and then slowly open the flow key so that the fluid begins to run. Make sure the drip chamber is half filled. Then, let the fluid flow freely through the line and the cannula to get rid of any air bubbles. Once the line has no bubbles, close the flow on the roller clamp (*see* **Note 2**).
2. Weigh the mouse on a balance scale. Inject intraperitoneally with the required amount of mouse anesthetic (225 mg/kg ketamine and 15 mg/kg xylazine). Check that the mouse is deeply anesthetized by testing the plantar/palmar reflex. The mouse must be unresponsive before you continue with the procedure.
3. Keep clean dissection tools at hand.
4. Immobilize the mouse body before dissection. On a cork board covered with paper towels, pin down the mouse face up by the fore and hind limbs (e.g., with syringe needles or tape). Place the mouse and board in a tray to prevent liquid from spilling.

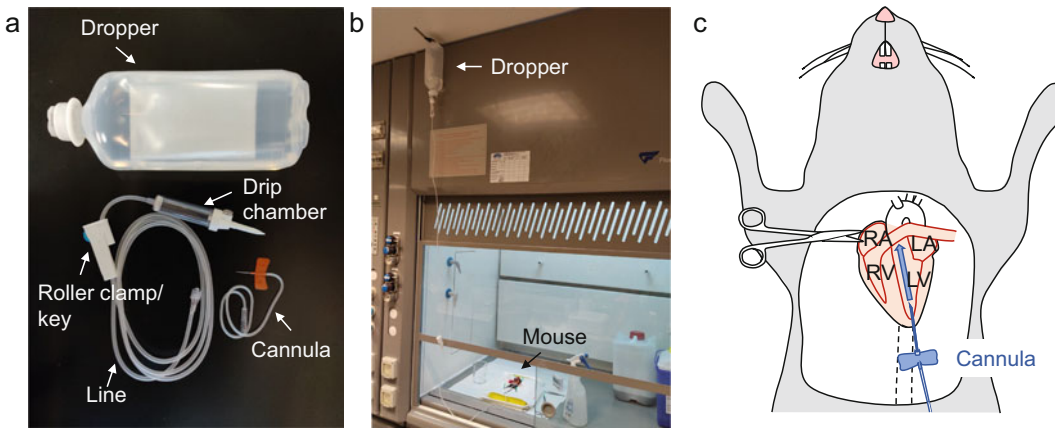

Fig. 1 Perfusion fixation of mouse aorta. (**a**) Perfusion set consisting of a dropper containing the fixation solution, an infusion set with a roller clamp to control flow speed and a 25G cannula. (**b**) Representative image of a perfusion setup. The infusion set is placed ~1.5 m above the dissection table, which is located in a fume hood. (**c**) Schematic representation of intracardial perfusion fixation of a mouse. The perfusion cannula is inserted into the left ventricle. Fixation solution flows towards the aorta (arrow). The right atrium is cut to allow fluid drainage

5. Spray 70% ethanol over the mouse abdomen. Make sure the following steps are performed as quick as possible in order to complete perfusion fixation before the heart stops beating.
6. Using blunt scissors and forceps, cut the mouse skin from the base of the abdomen to the top of the thorax without breaking any of the vessels that irrigate the tissues.
7. Open the abdomen below the ribcage.
8. Lift the sternum with forceps and cut the diaphragm carefully. The heart must remain intact.
9. Open the ribcage on both sides to expose the heart.
10. Place the cannula needle in the waste beaker and open the flow key to achieve an approximate flow rate of 1.5 drops/s.
11. Gently hold the heart with forceps and introduce the cannula needle in the bottom part (apex) of the left ventricle, pointing towards the aorta (*see* Fig. 1c). Insert to the minimum depth needed to fully penetrate the ventricle wall. Pushing the needle in too far can perforate the inner wall of the heart or the aortic root and compromise perfusion. Make sure the needle is securely inserted into the heart and does not detach during perfusion, holding it manually during the process if necessary.
12. Rapidly cut the right atrium with straight sharp fine scissors and check that fluid is draining correctly *(see* **Note 3**).
13. Perfuse the animal for 5 min (*see* **Note 4**). Monitor the perfusion process; organs should lighten, tissue becomes stiffer, and there may be spontaneous movement of the tail ("formalin dance").
14. Extract the needle from the heart and place it in the waste bin. Close the flow on the roller clamp (*see* **Note 5**).

3.2 Dissection of the Mouse Aorta and Heart

1. Gently dry the thoracic cavity with paper towels.
2. Gain better access to the aorta by removing the esophagus and lungs. Other organs can also be removed if necessary.
3. To extract the thoracic aorta and aortic arch, cut the aorta at the level of the diaphragm, grip the segment of the diaphragm that is attached to the end of the thoracic aorta, and cut the connective tissue between the aorta and the thoracic cavity muscle wall without stretching the vessel. Cut carefully using fine scissors and forceps until the aortic arch area is exposed. The abdominal aorta can be extracted and processed as well if desired (*see* **Note 6**).
4. Cut the left and right carotid arteries and the left subclavian artery with fine scissors.
5. Dissect out the heart and aorta together and place them in a regular plastic dish containing ice cold PBS (*see* Fig. 2a).

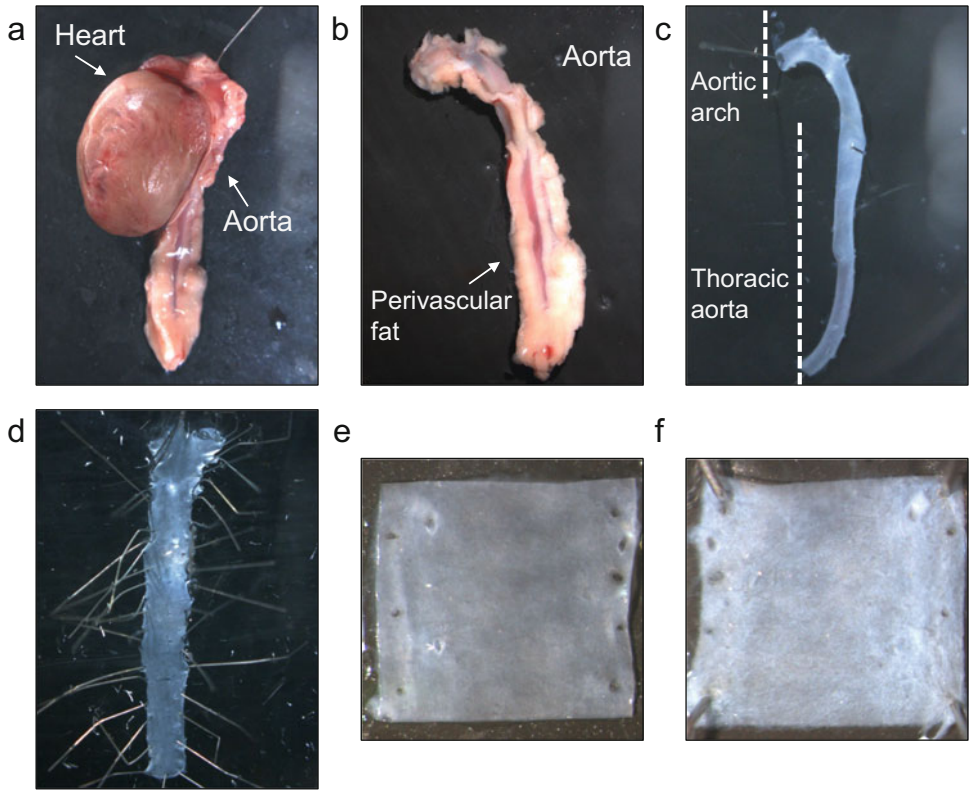

Fig. 2 Step-by-step aorta processing for confocal studies of the intima layer. (**a**) Example of a freshly dissected mouse aorta bound to the heart through the aortic root. (**b**) Intact dissected aorta with attached perivascular fat surrounding the vessel. (**c**) Aortic arch and thoracic aorta after removal of perivascular fat. (**d**) Aorta opened longitudinally from the outer curvature and pinned lumen-side up with minutien pins. (**e**) Luminal side of a piece of opened aorta showing the endothelium layer. (**f**) External side of a piece of opened aorta showing adventitial layer

6. Under a stereomicroscope, separate the aorta from the heart by cutting at the point where the artery emerges (*see* Fig. 2b) (*see* **Note** 7).
7. Place the aorta in a clean dissecting dish (*see* **Note 8**), always maintaining it wet with PBS.
8. Under a stereomicroscope, clean the aorta by removing all adventitial fat with straight fine-tipped forceps and microdissection spring scissors, avoiding excessive manipulation of the tissue (*see* Fig. 2c).
9. Cut the branches of the brachiocephalic trunk, left carotid and left subclavian arteries around 2 mm from where they emerge.
10. Cut all small bifurcations along the vessel, as close as possible to the base.

3.3 Aorta Processing

1. Open the aorta longitudinally and introduce the tips of a pair of microdissecting spring scissors into the arterial lumen. Start by cutting the outer curvature of the aortic arch from the ascending arch to the left subclavian artery (*see* **Note 9**). Continue cutting along the length of the thoracic aorta along the outer curvature.
2. Transfer the aorta to a plastic dish coated with Sylgard 184.
3. Pin the aorta flat and lumen-side up with steel minutien pins separated by about 1 mm from each other and placed as close to the edge as possible (*see* Fig. 2d). The aorta must be pinned with tension but without breaking the tissue. This step is crucial to flatten the intimal layer as much as possible.
4. Cover the sample with fixation solution and incubate overnight at 4 °C.

3.4 Immunofluorescence Staining

1. Discard the fixation solution into an appropriate waste container. Gently wash three times with ice cold PBS, making sure that the sample remains pinned to the plate. Keep the sample in fresh PBS during **steps 2** and **3**.
2. Cut the aorta transversally into 4 mm pieces (*see* **Note 10**) with a scalpel blade (*see* **Note 11**).
3. Remove the pins, carefully pick up each piece of aorta by a corner with fine tweezers and transfer to a 2 mL microfuge tube (*see* **Note 12**) containing sterile PBS (*see* **Note 13**).
4. Carefully remove PBS with a Pasteur pipette (*see* **Note 14**). Avoid touching the sample.
5. Incubate samples in 25 μL of primary antibody mix at an appropriate dilution in blocking and permeabilization buffer containing 5% NGS (*see* **Note 15**). Make sure that the sample is completely covered with liquid and moves freely when the tube is tapped. Incubate overnight at 4 °C with gentle agitation (in the dark if using fluorescently labeled primary antibodies). For a negative control, use a piece of aorta for each condition incubated in blocking and permeabilization buffer containing 5% NGS but without primary antibodies.
6. Wash the sample by filling the tubes with washing buffer and placing them horizontally with gentle agitation for 2 h at room temperature. Change the washing buffer every 15 min.
7. Remove washing buffer and add 25 μL of fluorochrome-conjugated secondary antibody mix at the appropriate dilution in blocking and permeabilization buffer containing 2% NGS. Incubate for 2 h at room temperature with gentle agitation in the dark.
8. Wash the sample as in **step 6**.

9. To mount the sample, transfer it to a labeled microscope slide using fine-tipped tweezers. If necessary, add a drop of PBS to make sure the sample does not dry out.
10. Using a stereomicroscope, identify the aortic lumen (*see* Fig. 2e) and adventitia (*see* Fig. 2f). The luminal side has an organized wave pattern, whereas the external side is a whitish filamentous layer (*see* **Note 16**). Observing the exits of the small bifurcations can help to identify the two sides.
11. Place the aorta flat, lumen-side up, and remove excess liquid with a paper towel. Avoid touching the sample as this would dry it out through capillary action.
12. Add a glycerol drop to the middle of a glass coverslip and quickly and firmly lay it on top of the sample (*see* **Note 17**). Gently press the coverslip against the sample, which should be fully covered with glycerol and without any folds (*see* **Note 18**).
13. Store samples at 4 °C in the dark in slide storage boxes until confocal imaging.

3.5 Confocal Imaging of the Aortic Intima Layer

1. Place the microscope slide on the confocal microscope stage. Use a 25× objective and a DAPI (4′,6-diamidino-2-phenylindole) epifluorescence filter to find the tissue. Change to the appropriate objective for each specific analysis. A 25× objective should be enough for general visualization of the intima layer (e.g., cell morphology, polarization, ECM proteins, leukocyte recruitment). At least a 63× objective must be used for detailed imaging (e.g., intercellular junctions, integrin activation). Adjust the focus to visualize the intima layer (e.g., locating EC nuclei, which are organized as a single layer of rounded nuclei).
2. Locate a representative area of the sample. Depending on the study, regions with or without bifurcations can be chosen (*see* **Note 19**). Acquire confocal sections every 1–1.5 μm from the luminal side until you reach the first layer of smooth muscle cells (identified by the elongated morphology of their nuclei). Additional sections can be taken to image the entire thickness of the vessel (*see* **Note 20**). Maintain room temperature constant to avoid loss of focus. Laser parameters should be adjusted according to the staining performance (*see* **Note 21**). Offset should not exceed −10 and gain should be adjusted for each particular staining. A resolution of 1024 × 1024 pixels is recommended. With these settings, the acquisition of a 4-laser image with 16 z-stacks should take around 10 min.
3. For every piece of aorta, acquire images from at least three different fields. Avoid the sample edges. Sequential images of the intima layer will be obtained as a stack. Image analysis software can be used to represent the maximal intensity

projection, which can be used to analyze the obtained results. If desired, additional software can be used to create three-dimensional reconstructions of the sample.

3.6 Image Analysis of the Aortic Intima Layer

Whole mount *en face* preparations of mouse aorta can be used to study multiple parameters and alterations of the intima layer. These include luminal EC morphology, intercellular junctions, cell polarization, interaction of ECs with the ECM, and leukocyte extravasation into the subendothelial space. Here, we show some examples of different analyses that can be performed using this method. We quantify images with ImageJ software; however, other image analysis tools can be used instead. To obtain accurate results, we recommend analysis of as many cells as possible from at least three fields per sample.

1. EC morphology (*see* Fig. 3): Pathological conditions can induce changes in EC shape. Exposing ECs to atheroprotective laminar flow or atheroprone oscillatory flow has been shown to result in markedly different cell morphologies [6, 7]. Study of EC morphology and shape requires the use of antibodies targeting at least one plasma membrane protein that delineates the EC contour (e.g., CD31). Create a maximal intensity projection and draw a region of interest (ROI) with the free-hand selection tool around the cell perimeters. Avoid cells that are incomplete or located at wavy regions of the sample since their morphology in the maximal intensity projection can be estimated wrongly. For each cell, determine the area, shape descriptors (e.g., circularity, aspect ratio, roundness, solidity), and ferret diameter.
2. EC polarization (*see* Fig. 3a): ECs respond to hemodynamic forces to maintain vascular homeostasis [8, 9]. The Golgi apparatus (GA) in ECs from large blood vessels has been reported to be positioned against the flow direction [10, 11] and defects in its polarization could indicate pathological processes. Generate the maximal intensity projection for an EC marker (e.g., CD31), a nuclear dye (e.g., Hoechst 33342), and a GA stain (e.g., GLG1, GM130). Draw vector lines with the arrow tool from the center of mass of the EC nucleus to the center of mass of the GA in the same cell. Measure the angle between this vector and blood flow direction (*see* **Note 22**), which will be defined as 0°. Data can be represented using rose diagrams. Calculate the percentage of correctly polarized endothelial cells containing a GA positioned 180° (±45°) against flow direction.
3. Leukocyte extravasation into the aorta intima layer (*see* Fig. 3b): Leukocytes are major participants in vascular disease onset, progression, and severity [12]. Atherosclerosis is

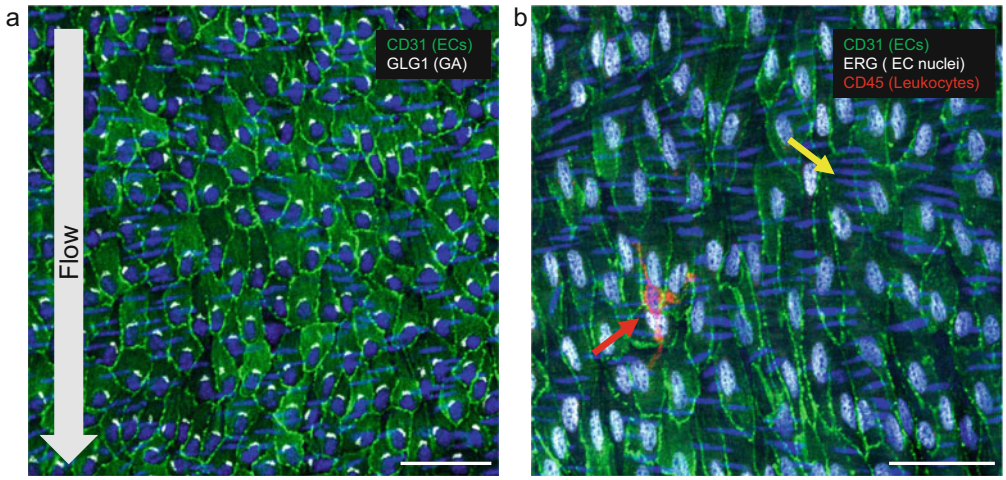

Fig. 3 Confocal microscopy images of C57BL/6J mouse aorta intima layer. (**a**) Representative immunofluorescence image showing staining of the endothelial cell (EC) marker CD31 (MAB1398Z, Merck, 1:100) in green, the Golgi apparatus (GA) marker GLG1 (ab103439, Abcam, 1:100) in white, and Hoechst 33342 (B2261, Sigma, 1:1000) labeling cell nuclei in blue. Note that the GA in most ECs is positioned upstream of the nuclei, polarized opposite to the blood flow direction (arrow). (**b**) Representative confocal image showing CD31 in green, the EC nucleus marker ERG (ab196149, Abcam, 1:100) in white, the leukocyte marker CD45.2 (553771, BD Biosciences, 1:200) in red, and Hoechst 33342 in blue. The image shows an infiltrated leukocyte in the intima layer (red arrow). Note that smooth muscle cells can be recognized by the peculiar, elongated morphology of their ERG-negative nuclei (yellow arrow), perpendicular to blood flow. Scale bar, 50 μm

characterized by chronic inflammation and leukocyte recruitment into the subendothelial space [13], which contributes to atheroma plaque formation. Leukocyte infiltration does not take place homogeneously across the entire aorta, but rather at specific sites where atheroma plaques tend to develop, such as the inner curvature of the aortic arch and arterial bifurcations. Whole mount *en face* preparations offer the opportunity to examine wide areas of the intima in a single image, thus being a very useful technique for these studies. Samples can be stained with antibodies targeting a leukocyte marker (e.g., CD45), together with an EC marker (e.g., CD31) and a nuclear dye. Examine the subendothelial space (beneath luminal $CD31^+$ ECs), count $CD45^+$ cells, and express the result as the number of cells per area (*see* **Note 23**). Check all the z-stacks carefully since $CD45^+$ cells can be found at different depths within the intima.

4 Notes

1. Paraformaldehyde is toxic by skin contact and inhalation; it should be handled in a fume hood with gloves and safety glasses throughout the procedure.

2. Other perfusion systems can be used for this method. If available, solutions can be perfused using perfusion pumps (e.g., syringe pumps or peristaltic pumps), setting the pumping rate at 4 mL/min.
3. If liquid is coming out of the mouse's nose, the needle should be repositioned as this indicates that the liquid is flowing through the pulmonary circulation and not through the aorta.
4. Although a 5-min perfusion step is enough for whole mount *en face* immunofluorescence assays, longer perfusion is needed (approximately 20 min) if additional tissues are collected for further studies.
5. Closure of the flow key causes abrupt exit of liquid and must be done carefully once the needle is withdrawn from the animal.
6. The abdominal aorta can also be extracted and processed with this protocol. However, note that perivascular fat in this segment is denser and the frequency of bifurcations is higher, which may complicate the cleaning process.
7. Since the tissue is soaked in paraformaldehyde, an FFP3 mask, gloves, and safety glasses must be worn while working at the stereomicroscope.
8. Stick a piece of black tape on the dissecting dish to increase contrast and allow better visualization of the aorta.
9. For atherosclerosis studies, we recommend cutting of the aortic arch along the outer curvature to leave the inner curvature intact. The inner curvature is a known atheroprone site and therefore a region of interest.
10. Each segment can be stained with a different antibody mix, allowing the study of multiple features in the same animal. To obtain representative results from the whole length of the vessel, several aorta segments per individual should be stained with the same antibody mix and analyzed. Larger portions can be used to cover a wider area if required for the desired analysis; however, it may be more difficult to keep larger pieces flat when mounting, possibly resulting in a wavy sample that makes imaging more challenging.
11. To keep track of aorta orientation, cut a corner of the piece as a reference. It may be necessary to know blood flow direction for certain studies (*see* **Note 22**).
12. 2 mL microfuge tubes have wider bottoms and samples suffer less friction against the walls than in 1.5 mL tubes.
13. At this point, samples can be stored at 4 °C for some time. However, we recommend that the following steps be performed as soon as possible to avoid the potential loss of sample integrity over time.

14. Coupling the Pasteur pipette to a 200 μL pipette tip allows more precise removal of the liquid.
15. Primary antibody concentration should be optimized by the researcher.
16. Fibers tend to attach to the adventitia layer and should be removed to avoid interference with confocal microscope imaging.
17. To mount samples, glycerol must be applied to the coverslip first. If glycerol is applied directly to the tissue, there is a greater risk that the sample will float and fold when mounted.
18. If the sample is mounted incorrectly (e.g., upside down, folded, etc.) carefully lift the coverslip with fine-tipped tweezers and repeat **steps 10–11**.
19. Depending on the research interest, areas of the sample with or without bifurcations can be chosen. Bifurcations are areas of turbulent flow and might not be representative of other regions.
20. A stack of sections of the whole vessel can be obtained, allowing visualization of the intima, media, and adventitial layers of the aorta. However, *en face* immunofluorescence is not the preferred technique for the study of the media due to the modest penetration of antibodies. Nevertheless, this technique enables nuclear staining of smooth muscle cells (e.g., using Hoechst 33342) to quantify their abundance in the media. In addition, elastin autofluorescence (*see* **Note 21**) enables the visualization of elastin layers to assess their integrity and linearity.
21. Elastin layers in the media have strong autofluorescence in the 420–510 nm emission range [14]. We strongly recommend labeling proteins of interest with fluorochromes with emission peaks outside this range or the use of dyes with very high emission efficiency to achieve a good signal-to-noise ratio with low levels of laser excitation.
22. Quantification of GA polarization requires spatial information about the direction of blood flow. This can be tracked by cutting a corner of the sample to record the orientation.
23. Because leukocytes can aggregate, accurate quantification requires counting not the number of $CD45^+$ areas, but of the number of nuclei within each of them. Moreover, leukocytes can have cellular protrusions and must not be counted as multiple cells and caution should be taken to avoid interpreting the kidney-like shape of a leukocyte nucleus as two nuclei from different cells.

Acknowledgments

We thank Simon Bartlett for English editing. Work in Dr. Andrés' laboratory is supported by the Spanish Ministerio de Ciencia e Innovación (MCIN)/Agencia Estatal de Investigación (AEI)/10.13039/501100011033 (grants PID2019-108489RB-I00 and EIN2020-112278) and the Instituto de Salud Carlos III (ISCIII) (AC17/00067, and CB16/11/00405) with cofunding from the European Regional Development Fund (ERDF/FEDER, "A way to make Europe"), and the Progeria Research Foundation. A.B. is supported by the MCIN/10.13039/501100011033 and Fondo Europeo Social ("El FSE invierte en tu futuro") (pre-doctoral contract BES-2017-079705), and I.B. by the Comunidad Autónoma de Madrid (grant 2017-T1/BMD-5247). The CNIC is supported by the MCIN, the ISCIII, the Pro CNIC Foundation, and is a Severo Ochoa Center of Excellence (grant CEX2020-001041-S funded by MICIN/AEI/10.13039/501100011033).

References

1. World Health Organization (2017) Cardiovascular diseases. http://www.who.int. Accessed 10 Dec 2020
2. Bentzon JF, Otsuka F, Virmani R, Falk E (2014) Mechanisms of plaque formation and rupture. Circ Res 114(12):1852–1866
3. Davignon J, Ganz P (2004) Role of endothelial dysfunction in atherosclerosis. Circulation 109(23 suppl 1):27–32
4. Bonetti PO, Lerman LO, Lerman A (2003) Endothelial dysfunction: a marker of atherosclerotic risk. Arterioscler Thromb Vasc Biol 23(2):168–175
5. Sitia S, Tomasoni L, Atzeni F, Ambrosio G, Cordiano C, Catapano A et al (2010) From endothelial dysfunction to atherosclerosis. Autoimmun Rev 9(12):830–834. https://doi.org/10.1016/j.autrev.2010.07.016
6. Kraiss LW (2005) Distinct endothelial phenotypes evoked by arterial waveforms derived from atherosclerosis-susceptible and -resistant regions of human vasculature. Perspect Vasc Surg Endovasc Ther 17(3):268–269
7. McCue S, Dajnowiec D, Xu F, Zhang M, Jackson MR, Langille BL (2006) Shear stress regulates forward and reverse planar cell polarity of vascular endothelium in vivo and in vitro. Circ Res 98(7):939–946
8. Davies PF (2009) Hemodynamic shear stress and the endothelium in cardiovascular pathophysiology. Nat Clin Pract Cardiovasc Med 6(1):16–26
9. Baeyens N, Bandyopadhyay C, Coon BG, Yun S, Schwartz MA (2016) Endothelial fluid shear stress sensing in vascular health and disease. J Clin Invest 126(3):821–828
10. Franco CA, Jones ML, Bernabeu MO, Vion AC, Barbacena P, Fan J et al (2016) Non-canonical wnt signalling modulates the endothelial shear stress flow sensor in vascular remodelling. elife 5:1–22
11. Kwon HB, Wang S, Helker CSM, Rasouli SJ, Maischein HM, Offermanns S et al (2016) In vivo modulation of endothelial polarization by Apelin receptor signalling. Nat Commun 7:1–12
12. Schnoor M, Alcaide P, Voisin MB, Van Buul JD (2015) Crossing the vascular wall: common and unique mechanisms exploited by different leukocyte subsets during extravasation. Mediat Inflamm 2015:2015
13. Swirski FK, Nahrendorf M (2013) Leukocyte behavior in atherosclerosis, myocardial infarction and heart failure. Science 339(6116):161–166
14. Croce AC, Bottiroli G (2014) Autofluorescence spectroscopy and imaging: a tool for biomedical research and diagnosis. Eur J Histochem 58(4):320–337

Chapter 38

Isolation of Mouse Aortic RNA for Transcriptomics

Rosa M. Nevado, Magda R. Hamczyk, and Vicente Andrés

Abstract

Aging is associated with alterations in the arterial wall that promote vascular disease development and its clinical manifestations, including myocardial infarction, stroke, and arterial dissection. The arterial wall is comprised of three layers, intima, media and adventitia, each with distinct cellular composition and function, which can therefore contribute differently to vascular disease initiation and progression. Hence, studying transcriptomic alterations, either in the entire arterial wall or separately in the three arterial layers, can aid in disentangling the etiopathology of vascular disease and thus pave the way for innovative treatments. This chapter describes protocols for total RNA extraction from complete mouse aorta and separately from intima, media, and adventitia layers for subsequent transcriptomic analysis.

Key words Adventitia, Aorta, Vascular disease, Intima, Media, RNA extraction, Transcriptomics

1 Introduction

Arteries carry the oxygenated blood from the left ventricle of the heart to the rest of the body. The aorta is the largest artery in the body and can be divided into four parts: ascending aorta, aortic arch, descending thoracic aorta and abdominal aorta. The aortic vessel wall is formed by three concentric layers, intima, media and adventitia, which differ in their cellular composition and function. The intima is the innermost layer and normally consists of a monolayer of endothelial cells (ECs) that line the vascular lumen. ECs respond to numerous mechanical and chemical stimuli by secreting a plethora of regulatory molecules, including growth factors, vasoactive molecules and regulators of blood clotting [1, 2]. Moreover, ECs can regulate lipid transport into the vessel wall and leukocyte recruitment and extravasation [3, 4]. In pathological conditions, the intima can expand to form a neointimal lesion (intimal hyperplasia or atheroma plaque) containing non-ECs and non-cellular components.

Dipak P. Ramji (ed.), *Atherosclerosis: Methods and Protocols*, Methods in Molecular Biology, vol. 2419,
https://doi.org/10.1007/978-1-0716-1924-7_38,
© The Author(s), under exclusive license to Springer Science+Business Media, LLC, part of Springer Nature 2022

The media is the middle layer that is predominantly responsible for the biomechanical properties of the artery. It is comprised of several layers of vascular smooth muscle cells (VSMCs) separated by elastin-rich extracellular matrix [5]. VSMCs present a quiescent and contractile phenotype in the healthy artery wall; however, certain stimuli, such as inflammation or mechanical injury, can induce a phenotypic switch in VSMCs that leads to increased proliferation, migration, and secretion of extracellular matrix and inflammatory factors, thus contributing to atherosclerotic plaque growth [6].

The adventitia is the outermost arterial layer and exhibits the highest level of cellular heterogeneity as it contains fibroblasts, immune cells, progenitor cells, microvessels, and adrenergic nerves embedded in a connective tissue matrix [7]. Adventitia not only provides structural support to the artery, as initially thought, but also regulates vascular function and contributes to pathological conditions [8].

Cellular crosstalk between intima, media, and adventitia is essential for blood vessel wall homeostasis and aberrant communication and interaction between these three layers promotes vascular disease, including atherosclerosis, calcification, and aneurysm formation [9–11]. Vascular disease is unequivocally associated with aging and is one of the major causes of deaths worldwide [12]. Progressive pathological changes in the arteries lead to most life-threatening manifestations of cardiovascular disease, such as stroke and myocardial infarction. Understanding the function of each arterial layer in health and disease is therefore crucial for identifying molecular pathways and gene targets for vascular disease prevention and treatment.

Transcriptomics technologies, such as microarrays and RNA-sequencing (RNA-seq), are very powerful tools to study the presence and quantity of multiple RNA molecules in a tissue, including mRNA, microRNA, long non-coding RNA, and circular RNA. While microarrays enable analysis of a set of predetermined sequences, RNA-seq detects all sequences in a high-throughput manner using less starting RNA material than microarrays [13]. RNA-seq is typically used to compare gene expression profiles between different conditions, time points, or tissues/cell types; however, it has broader applications including identification of splicing alterations, disease-associated single nucleotide polymorphisms, and gene fusions. This chapter describes protocols to isolate high-quality total RNA from the entire mouse aorta and separately from intima, media, and adventitia for subsequent transcriptomic studies (Fig. 1).

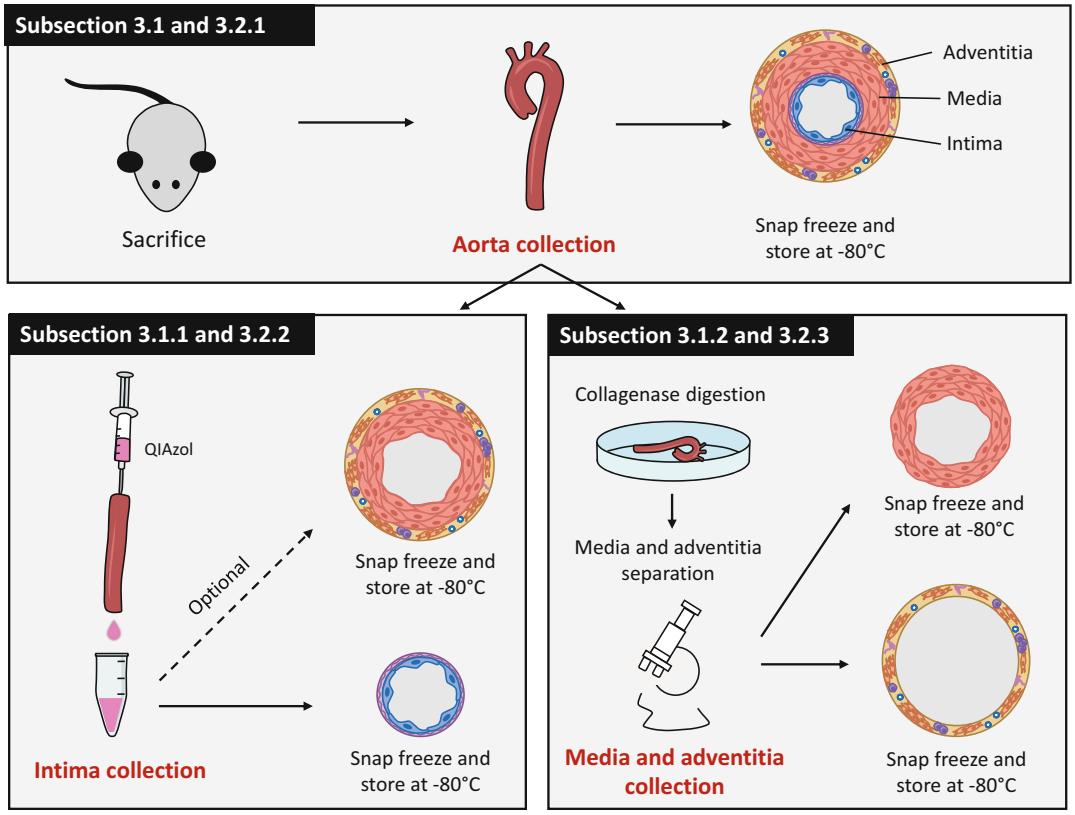

Fig. 1 Protocol overview for total RNA isolation from the entire mouse aorta and from intima, media, and adventitia separately. Subheadings 3.1 and 3.2.1: Sacrifice the mouse, collect the aorta, and remove perivascular fat tissue. Snap-freeze the entire aorta and store at −80 °C for RNA extraction or continue with Subheading 3.1.1 to isolate intima or with Subheading 3.1.2 to isolate media and adventitia. Subheadings 3.1.1 and 3.2.2: After aorta collection, remove the aortic arch, insert a needle with a syringe filled with QIAzol into the aortic lumen, and flush 200 μL of QIAzol to lyse the intima. Snap-freeze the intima lysed in QIAzol and store at −80 °C until RNA extraction (optionally, snap-freeze the remaining media with adventitia layers and store at −80 °C). Subheadings 3.1.2 and 3.2.3: After aorta collection, digest the aorta with type 2 collagenase solution and separate the media from the adventitia under a stereomicroscope. Snap-freeze the media and adventitia separately and store at −80 °C until RNA extraction

2 Materials

2.1 Mouse Aorta Dissection and Collection of Intima, Media, and Adventitia

1. Personal protective equipment (disposable gloves, face mask, sanitary cap, and surgical clothing).
2. Mice.
3. CO_2 euthanasia chamber.
4. Disposable paper towels.
5. Small animal surgical board (alternatively, expanded polystyrene or cork board).

6. Adhesive tape, needles, or pins (depending on the type of surgical board used).
7. 70% ethanol in distilled water.
8. Sterile phosphate buffered saline (PBS): 1.54 mM KH_2PO_4, 155.17 mM NaCl, 2.70 mM Na_2HPO_4, pH 7.4.
9. Forceps (three types): straight serrated tips forceps, straight or curved serrated tips fine forceps, and straight fine tips forceps.
10. Scissors (two types): straight blunt scissors and straight sharp fine scissors.
11. 10 mL syringes.
12. Regular plastic dishes.
13. Disposable plastic tubes suitable for disruption procedure (e.g., screw-cap or safe-lock 2 mL microcentrifuge tubes).
14. Permanent marker.
15. Stereomicroscope.
16. Liquid nitrogen (preferably) or dry ice (alternatively, RNAlater reagent can be used for RNA stabilization at room temperature).
17. Container for liquid nitrogen or dry ice.
18. Deep freezer (−80 °C).
19. Needles (25G or 23G depending on the aortic lumen diameter) (Subheading 3.1.1).
20. 1 mL syringes (Subheading 3.1.1).
21. RNase-free disposable 1.5 or 2 mL microcentrifuge tubes (Subheading 3.1.1).
22. Monophasic solution of phenol and guanidine thiocyanate (e.g., QIAzol, TRIzol; *see* **Note 1**) (Subheading 3.1.1).
23. Fume hood (Subheading 3.1.1).
24. Collagenase type 2 (Subheading 3.1.2).
25. 0.22 μm sterile syringe filter (Subheading 3.1.2).
26. 15 mL sterile plastic tubes (Subheading 3.1.2).
27. 35 mm plastic culture plates (Subheading 3.1.2).
28. CO_2 incubator (set to 37 °C and 5% CO_2) (Subheading 3.1.2).

2.2 RNA Extraction

1. Personal protective equipment (lab coat, disposable gloves, and safety glasses).
2. Specific lab area only for RNA work (not essential but highly recommended).
3. Fume hood.

4. RNase decontamination solution (e.g., RNaseZap, RNase AWAY or RNase Erase).
5. Autoclaved micropipettes (exclusively dedicated to RNA manipulation).
6. RNase-free disposable micropipette tips with filter.
7. RNase-free disposable 1.5 or 2 mL microcentrifuge tubes.
8. Autoclaved racks for 1.5 or 2 mL microcentifuge tubes.
9. High-speed refrigerated microcentrifuge (with rotor for 2 mL tubes).
10. Tissue disruptor/homogenizer (e.g., TissueLyser, Qiagen; *see* **Note 2**) (except for Subheading 3.2.2).
11. 5 mm stainless steel beads (Qiagen) (except for Subheading 3.2.2).
12. TissueLyser single-bead dispenser for 5 mm beads (Qiagen) (except for Subheading 3.2.2).
13. Vortex mixer.
14. Total RNA extraction kit (e.g., miRNeasy Micro Kit from Qiagen; the kit includes QIAzol lysis reagent, RNeasy MinElute spin columns, 1.5 mL and 2 mL collection tubes, RNase-free RWT and RPE buffers, and RNase-free water, *see* **Note 3**).
15. RNase-free DNase set (Qiagen; the set includes RNase-free DNase I, RNase-free buffer RDD, and RNase-free water).
16. Water treated with 0.05% diethyl pyrocarbonate (DEPC) or RNase-free water.
17. 96–100% ethanol.
18. 80% ethanol (prepared by diluting 96–100% ethanol with RNase-free water).
19. Chloroform (without isoamyl alcohol).
20. Liquid nitrogen (preferably) or dry ice.
21. Container for liquid nitrogen or dry ice.
22. Ice.
23. Fridge (2–8 °C) for storing RNeasy MinElute spin columns and RNase-Free DNase set.
24. Permanent marker.
25. NanoDrop spectrophotometer (e.g., Wilmington, USA).
26. 2100 Bioanalyzer (e.g., Agilent, USA).
27. Bioanalyzer RNA 6000 nano or pico kit (e.g., Agilent, USA).

3 Method

3.1 Mouse Aorta Dissection

1. Prepare clean dissection tools and all other materials necessary to sacrifice the mice and to extract the aorta, such as loading a 10 mL syringe with PBS and fitting a 25G needle and labeling 2 mL microcentrifuge tube(s) using a permanent marker (*see* **Note 4**).
2. Place the mouse in a CO_2 chamber for euthanasia.
3. Confirm mouse death by the determination of the cessation of respiratory movements and unresponsiveness to plantar reflex stimulation.
4. Place the mouse in the supine position on a surgical board.
5. Extend the fore and hind limbs outwards and secure using tape, needles, or pins to immobilize the body and facilitate dissection.
6. Disinfect and wet the fur by spraying 70% ethanol over the mouse abdomen (*see* **Note 5**). Wipe off the excess of ethanol using a paper towel.
7. Using forceps, grab and lift the skin at the base of the abdomen. Using blunt scissors, cut the skin towards the lower limbs and then towards the thorax.
8. Remove abdominal skin and the skin covering the ribcage.
9. Hold the sternum with forceps and cut the diaphragm using fine scissors. Be sure not to incise the heart.
10. Open the ribcage bilaterally and remove its anterior portion to expose the heart, thymus, and lungs.
11. Remove the lungs and esophagus to facilitate access to the aorta.
12. Move the intestine to one side and cut the abdominal aorta just below the renal arteries. Insert a syringe with a needle into the left ventricle and wash out blood inside the aorta by injecting approximately 5 mL of PBS (*see* **Note 6**). Absorb excess fluid with paper towels to ensure good view within the thoracic cavity.
13. Using forceps and fine scissors, grip the diaphragm fragment that is attached to the end of the thoracic aorta and carefully cut the connective tissue between the aorta and the dorsal surface of the thoracic cavity (*see* **Note 7**). If necessary, release the heart from the anterior chest wall using blunt dissection.
14. Place the aorta with the heart on a plastic dish containing clean PBS.
15. Under a stereomicroscope, separate the aorta from the heart using fine scissors.

16. Still under stereomicroscope carefully remove fat tissue surrounding the aorta using straight fine tips forceps.
17. Wash aorta with clean PBS.
18. Depending on the type of sample to be used for RNA extraction (entire aorta, intima, media, or adventitia) continue as follows (Fig. 1). For RNA extraction from entire aorta: (1) place the aorta in a 2 mL plastic tube compatible with the tissue disruptor/homogenizer to be used for RNA extraction; (2) snap-freeze the aorta in liquid nitrogen (preferably) or dry ice; and (3) store samples at −80 °C until RNA extraction (then continue as indicated in Subheading 3.2.1). For RNA extraction from the intima continue as indicated in Subheadings 3.1.1 and 3.2.2. For RNA extraction from media and/or adventitia, continue as indicated in Subheadings 3.1.2 and 3.2.3. *See* Fig. 2a for guidelines regarding the amount of starting material in different scenarios.

3.1.1 Intima Collection

1. Still under stereomicroscope cut and remove aortic arch to obtain the straight part of the aorta (descending thoracic aorta, *see* **Note 8**).
2. Using a 1 mL syringe with a needle, wash gently the thoracic aorta lumen with clean PBS to ensure complete blood removal.
3. Under stereomicroscope, carefully insert in one end of the thoracic aorta a clean 23G or 25G needle (the one that best fits the aortic lumen diameter).

   Steps from **4** to **5** should be performed in a fume hood (*see* **Note 1**).
4. Using forceps hold the aorta with the needle in a vertical position and insert a 1 mL syringe filled with QIAzol. Place a collection tube below and pass 200 μL of QIAzol through the aortic lumen to lyse the intima (*see* Fig. 1 and **Note 9**).
5. Snap-freeze in liquid nitrogen (preferably) or dry ice the intima sample lysed in QIAzol.
6. Store samples at −80 °C until RNA extraction.
7. The remaining media and adventitia layers can be washed in PBS, snap-frozen and stored at −80 °C for further studies (*see* Fig. 1 and **Note 10**).

3.1.2 Media and Adventitia Collection

1. Prepare collagenase solution. Weight 10 mg of type 2 collagenase (for one aorta), place it in a 15 mL sterile plastic tube and dissolve in 5 mL of sterile PBS to obtain a 2 mg/mL solution (*see* **Note 11**).
2. Filter the collagenase solution through a sterile 0.22 μm syringe filter and collect the filtered solution in a clean 15 mL plastic tube.

3. Put the aorta in a 35 mm plastic culture plate containing 5 mL of the collagenase solution. Incubate for 10 min at 37 °C in 5% CO_2 incubator without agitation (*see* **Note 12**).
4. Transfer the aorta to a clean plastic culture plate containing fresh PBS.
5. Under stereomicroscope, use two straight fine tips forceps to separate the media and adventitia. The adventitia should be rolled off the medial aorta in a manner similar to removing a sock from a foot (*see* **Note 13**).
6. Wash the media and the adventitia with clean PBS.
7. Place each aortic layer in a 2 mL plastic tube compatible with the tissue disruptor/homogenizer to be used for RNA extraction.
8. Snap-freeze media and adventitia samples in liquid nitrogen (preferably) or dry ice.
9. Store samples at −80 °C until RNA extraction (*see* **Note 14**).

3.2 RNA Isolation

3.2.1 RNA Isolation from Whole Mouse Aorta

1. Precool TissueLyser adapter.
2. Clean all the materials (e.g., racks, pipettes) and working surfaces with RNase decontamination solution. Use RNase-free pipette tips with filter (*see* **Note 15**).

   Steps 3, **4**, **6**, 7, and **10** should be performed in a fume hood (*see* **Note 1**).
3. Place aorta samples on ice and immediately add 700 μL of QIAzol reagent to each tube (*see* **Note 16** and Fig. 2a).
4. Add one 5 mm stainless steel bead to each tube using a single-bead dispenser (*see* **Note 17**).
5. Introduce samples in a TissueLyser (*see* **Note 2**) and perform several rounds of tissue disruption (2 min at 50 Hz each) until achieving complete tissue homogenization. To avoid overheating, place the samples and the TissueLyser adapter on ice for 1–2 min between each disruption cycle.
6. Transfer each homogenate (without stainless steel bead) to a new 1.5 mL tube. To ensure complete dissociation of nucleoprotein complex, incubate the samples at room temperature for 5 min.
7. Add 140 μL of chloroform to each tube and shake vigorously using a vortex mixer until a uniform pink suspension is obtained (approximately 30 s of mixing).
8. Leave at room temperature for 2–3 min.
9. Centrifuge at 12,000 × *g* at 4 °C for 15 min.

10. Transfer the upper aqueous phase (containing the RNA) to a new tube and discard the remaining interphase and the lower organic phase (*see* **Note 18**).
11. Add to each sample, 1.5 volumes of 100% ethanol and mix properly by pipetting up and down several times.
12. Transfer up to 700 μL of each sample (together with any precipitate that may have formed) into a labeled RNeasy MinElute spin column placed in a 2 mL collection tube and close the lid gently.
13. Centrifuge at $\geq$8000 $\times$ *g* for 15 s at room temperature.
14. Carefully remove the RNeasy MinElute spin column from each collection tube and discard the flow-through (*see* **Note 19**).
15. Repeat **steps 12–14** using the remaining sample volume.
16. Add 350 μL of RWT buffer to each RNeasy MinElute spin column.
17. Centrifuge for 15 s at $\geq$8000 $\times$ *g* and discard the flow-through.
18. Prepare DNase I working solution by mixing 70 μL of RDD buffer and 10 μL of DNase I stock solution (*see* **Note 20**). Multiply the volumes by the number of samples to be treated with DNase I (add one extra volume for each 10 samples). Gently invert the tube to mix all reagents (*see* **Note 21**).
19. Add 80 μL of DNase I working solution onto each RNeasy MinElute spin column membrane (*see* **Note 22**).
20. Incubate for 15 min at a room temperature.
21. Pipette 350 μL of buffer RWT into each RNeasy MinElute spin column.
22. Centrifuge for 15 s at $\geq$8000 $\times$ *g* and discard the flow-through.
23. Pipette 500 μL of RPE buffer onto each RNeasy MinElute spin column and close the lid gently.
24. Centrifuge for 15 s at $\geq$8000 $\times$ *g* and discard the flow-through.
25. Pipette 500 μL of 80% ethanol onto each RNeasy MinElute spin column and close the lid gently.
26. Centrifuge for 2 min at $\geq$8000 $\times$ *g* and discard the collection tube together with the flow-through.
27. Transfer each RNeasy MinElute spin column into a new 2 mL collection tube.
28. Open the lid of each spin column and centrifuge for 5 min at maximum speed to dry the membrane (*see* **Note 23**). Discard the collection tube together with the flow-through.

29. Place each RNeasy MinElute spin column in a new labeled 1.5 mL collection tube. Add 16–18 μL of RNase-free water directly to the center of the spin column membrane and close the lid gently (*see* **Note 24**).
30. Elute RNA by centrifuging at maximum speed for 1 min.
31. Place the tubes containing RNA eluate on ice.
32. Assess RNA concentration and purity using a NanoDrop spectrophotometer (*see* **Note 25**).
33. Assess RNA quantity and quality in a 2100 Bioanalyzer using RNA 6000 nano or pico kit (*see* **Notes 26** and **27**).
34. Continue with downstream preparation or store the samples at −80 °C for further use.

3.2.2 RNA Isolation from Intima

1. Clean all the materials (e.g., racks, pipettes) and working surfaces with RNase decontamination solution. Use RNase-free pipette tips with filter (*see* **Note 15**).
2. Thaw intima samples lysed in QIAzol.

   Steps 3, **7**, and **10** should be performed in a fume hood (*see* **Note 1**).
3. Pool intima samples as indicated in Fig. 2. Each sample of intimal RNA should be prepared from a pool of at least 8–10 aortas (Fig. 2a). For example, to prepare a pool originating from 9 mice (Fig. 2b): (1) prepare 3 microcentrifuge tubes; (2) pool intima samples from 3 animals in each one of the tubes; and (3) add 100 μL of QIAzol reagent to each tube to reach a final volume of 700 μL.
4. Shake vigorously for 45 s.
5. Leave for 5 min at room temperature.
6. Follow **steps 7–34** as indicated in Subheading 3.2.1. In **step 12**, it is necessary to add all volume corresponding to the same intima pool to the same spin column, hence repeat **steps 12–15** as many times as needed.

3.2.3 RNA Isolation from Media and Adventitia

1. Precool TissueLyser adapter.
2. Clean all the materials (e.g., racks, pipettes) and working surfaces with RNase decontamination solution. Use RNase-free pipette tips with filter (*see* **Note 15**).

   Steps 3, **4**, **6**, **7**, and **10** should be performed in a fume hood (*see* **Note 1**).
3. Place pooled media or adventitia samples on ice and immediately add 700 μL of QIAzol reagent to each tube (*see* **Note 28**). Each sample of medial or adventitial RNA should be prepared from a pool of at least 3–5 aortas (*see* **Note 29** and Fig. 2a).

   Follow **steps 4–34** in Subheading 3.2.1.

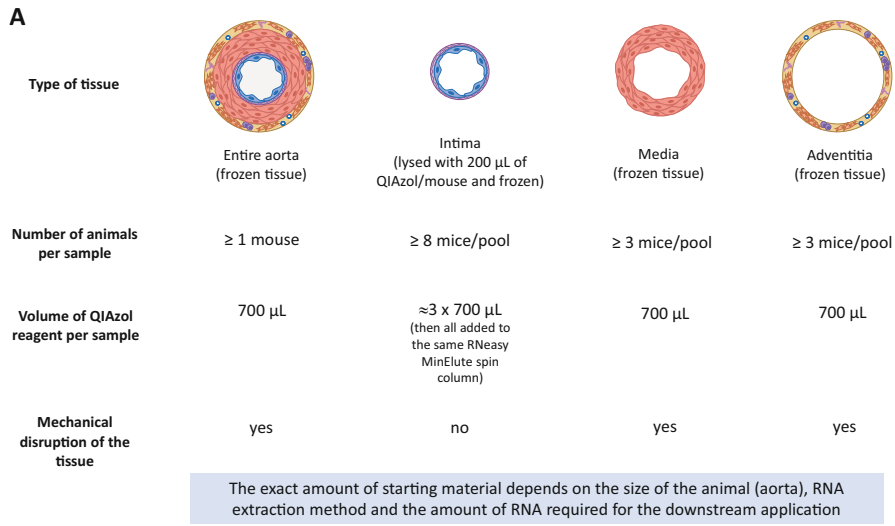

Fig. 2 Technical details of tissue collection and disruption for total RNA isolation from the entire aorta and from intima, media, and adventitia separately. (**a**) RNA can be isolated either from entire aorta or from intima, media, and adventitia layers separately. Figure indicates for each sample type, the recommended amount of starting material (number of animals per pool), the volume of QIAzol reagent, and the need for mechanical tissue disruption. (**b**) To prepare a pooled intima sample originating from 9 mice, prepare 3 tubes and in each one of the tubes join intima samples from 3 animals (200 µL of intima lysed in QIAzol), and add 100 µL of QIAzol to each tube to reach a final volume of 700 µL. Then continue with **steps 7–34** in Subheading 3.2.2. Remember to add all samples to the same RNeasy MinElute spin column in **step 12**

4 Notes

1. QIAzol lysis reagent contains toxic and corrosive agents (phenol and guanidine thiocyanate), hence all steps involving this reagent should be performed in a fume hood using personal protective equipment.
2. TissueLyser disrupts and homogenates the tissue by high-speed shaking of a sample in 2 mL microcentrifuge tube containing a stainless steel bead. Use TissueLyser LT for simultaneous processing of up to 12 samples and TissueLyser II for high-throughput disruption and homogenization of up to 48 samples. Other tissue disruption methods can be used (e.g., Polytron immersion disperser equipped with disposable sterile aggregates) as long as the risk of cross-contamination and RNA degradation is minimalized.
3. The miRNeasy kit uses phenol/guanidine-mediated sample lysis and silica membrane-based purification of total RNA, including microRNAs. The miRNeasy Micro kit is adequate for RNA isolation from small amounts of tissue (up to 5 mg).

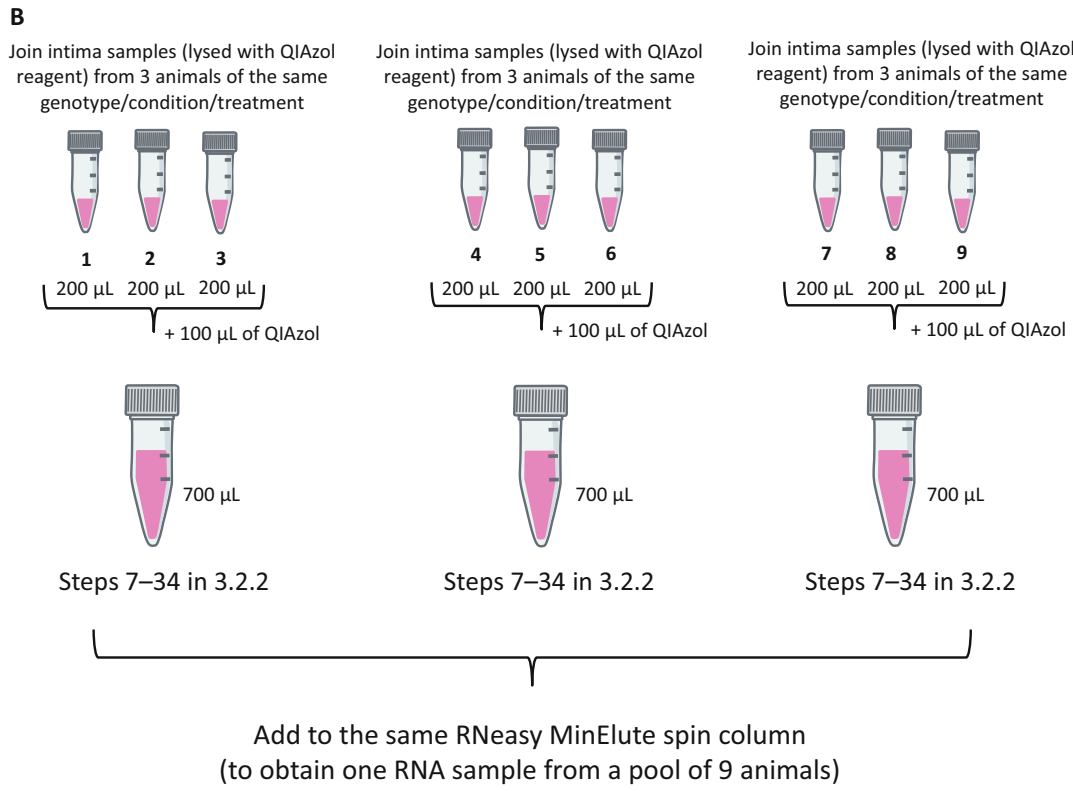

Fig. 2 (continued)

To extract RNA from tissue samples from up to 50 mg, use miRNeasy Mini Kit. Depending on the downstream application, other commercial kits can be used for RNA isolation, such as RNeasy (Qiagen) or Direct-zol RNA kits (Zymo Research). Although higher RNA yield can be obtained with traditional TRIzol method (based on [14]), we discourage using it as this gives lower RNA purity compared to commercial kits.

4. To avoid RNA degradation work as quickly as possible, prepare all the materials beforehand.
5. Avoid any contact of tissue samples with the mouse fur as it contains RNases.
6. If other organs need to be collected, instead of cutting abdominal aorta, cut the right atrium and inject into the left ventricle approximately 10 mL of PBS to remove blood from all organs.
7. Perform this step in a precise and meticulous manner. It is important not to stretch the aorta to avoid any cell damage, especially to the endothelium.

8. Aortic arch contains three major branches through which QIAzol reagent would leak out. Hence, for practical reasons, we recommend using descending thoracic aorta only to ensure linear flow of lysis reagent and to avoid possible intima sample loss and contamination.
9. Pass the QIAzol reagent through the aortic lumen in a slow and constant manner to avoid QIAzol overflow, which may result in adventitia degradation and intima sample contamination. It typically takes a few seconds to flush 200 μL of QIAzol through the aortic lumen.
10. To ensure that the intima lysis was complete, cut a 1–2 mm of aortic ring before and after passing QIAzol reagent though the aortic lumen and fix both pieces in 4% formaldehyde. Stain aortic tissue samples with a common nuclear dye (e.g., DAPI, Hoechst) and an endothelial cell-specific marker [e.g., platelet/endothelial cell adhesion molecule-1 (PECAM1) or ETS-related genes transcription factor (ERG)] for whole mount immunofluorescence. Acquire florescent images using a confocal microscope. Nuclei and endothelial cell markers should be absent in the luminal part of the aorta in samples treated with QIAzol. In contrast, aortic tissue collected prior to QIAzol lysis should present nuclei and endothelial cell marker expression in the luminal surface.
11. For optimal performance, always use freshly prepared collagenase solution. To avoid delays in aorta processing, which may result in RNA degradation, prepare collagenase solution just before mouse euthanasia. Total volume of collagenase solution to be prepared depends on the number of aortas to be processed.
12. The digestion with collagenase makes the removal of the adventitia easier. Furthermore, most endothelium is lost during this step. Alternatively, you may skip **steps 1–3** and separate the media from the adventitia mechanically without enzymatic digestion. However, this alternative protocol is more difficult and requires more expertise. Furthermore, to ensure that the endothelium is removed completely, collapse the aorta and rub it back and forth with caution.
13. This step should be performed as quickly as possible to avoid RNA degradation. It is crucial to practice adventitia and media separation before performing actual experiments.
14. Aortic media and adventitia samples can be collected and stored in individual tubes and pooled before RNA extraction. This would be a preferred option in case you need to regenotype animals, pool samples obtained on different dates or pool

them based on certain criteria that cannot be known before sample collection. Otherwise, samples can be pooled directly after isolation. To do so, open a tube already containing a media or an adventitia sample, add the next sample to be pooled together and snap-freeze immediately. Repeat this process until completing the pool. Process aortas one by one unless you have enough expertise or staff to process the samples in batches.

15. The RNA isolation procedure should be carried out as quickly as possible to avoid RNA degradation.
16. If high amount of RNA is needed, use more than one aorta per sample. If a sample weight exceeds 50 mg, extract RNA with miRNeasy Mini kit.
17. Use clean and sterile stainless steel beads and avoid touching them. In case you do not have a bead dispenser, use a sterile 1000 μL pipette tip with filter for dispensing of grinding beads into individual tubes.
18. The sample separates into three phases: a lower pink phase (organic phase containing protein), a white interphase (containing DNA), and an upper colorless phase (aqueous phase containing RNA). Aqueous phase (approximately 350 μL) must be collected with caution as the interphase and organic phase material can be aspirated accidentally into the pipette tip, contaminating the RNA sample with DNA, protein, and phenol. The organic phase containing phenol and chloroform should be discarded following adequate biosecurity procedures.
19. To avoid carryover of ethanol, ensure that the RNeasy MinElute spin column does not contact the flow-through.
20. To prepare DNase I stock solution, inject RNase-free water into the vial with lyophilized enzyme using an RNase-free needle and syringe. Dissolve the DNase I by inverting the vial and remove the reconstituted enzyme using the syringe and needle. Aliquot and store at 2–8 °C for short-term use (for long-term storage, keep the aliquots at −20 °C).
21. Do not vortex the reconstituted DNase I as this will denature the enzyme and decrease its activity.
22. It is crucial to pipette the DNase I solution directly on the spin column membrane to ensure complete DNA digestion.
23. Since ethanol may interfere with downstream applications, it is essential to dry the spin column membrane. Given that this centrifugation step is carried out at maximum speed with open spin column lids, place the spin columns in the centrifuge with

at least one empty place/slot between them to avoid damaging the lids.

24. Elution volume should be no less than 14 μL and depends on the amount of starting material (16–18 μL is typically adequate for one aorta). If using higher amounts of starting material (e.g., pooled aortic samples), you may need to increase the elution volume. Bear in mind that the dead volume of the spin column is 2 μL.
25. RNA purity is assessed by calculating the ratio of absorbance at 260 nm and 280 nm. "Pure" RNA should have a 260/280 ratio of approximately 2.0. Abnormal 260/280 ratios typically indicate protein or phenol contamination due to carryover during the aqueous phase collection.
26. Bioanalyzer provides an objective measurement of RNA quality with RNA Integrity Number (RIN). Bioanalyzer system has various advantages over traditional agarose gel electrophoresis, including very low RNA sample volume required (1 μL), high sensitivity (as low as 5 ng and 50 pg of total RNA for 6000 nano and pico kits, respectively). For transcriptomic studies use samples of RIN $\geq$7, yet the closer the value to 10, the better.
27. In case of limited access/no access to Bioanalyzer equipment, assess RNA integrity by traditional agarose electrophoresis. It is important to prevent RNase contamination and sample degradation when size fractionating RNA samples on a gel. Hence, clean all the equipment (buffer chamber, tray, comb) with RNase decontamination solution, use fresh electrophoresis buffer and RNase-free pipette tips with filter. In brief, prepare a 1.1–1.2% agarose gel in Tris/Borate/EDTA (TBE) or Tris/Acetate/EDTA (TAE) buffer and place it in an electrophoresis tank filled with TBE or TAE buffer, respectively. Add a nucleic acid intercalating agent (e.g., ethidium bromide, GelRed, GelGreen) to both the gel and the electrophoresis buffer. Heat an aliquot of each RNA sample at 70 °C for 1 min and place it on ice. Add loading buffer to RNA samples and load 100–500 ng RNA per lane. Use electrophoresis voltage up to 10 V/cm and stop electrophoresis when the dye line is approximately 80% of the way down the gel. Take a picture using a gel documentation system. Agarose gel electrophoresis of RNA samples is cheap and easy to perform, yet does not always provide reliable results. RNA integrity is assessed by measuring the ratio of 28S and 18S rRNA bands, which should be approximately 2:1 (range 1.5–2.5:1). Moreover, no excessive smearing should be observed between the rRNA bands and below the 18S rRNA band.

28. If the samples were collected in individual tubes, add a QIAzol drop to each sample to be pooled and transfer it using clean straight fine tips forceps to a tube containing 700 μL of QIAzol reagent.
29. If high amount of RNA is needed, use more media or adventitia samples per pool. If a pooled sample weight exceeds 50 mg, use miRNeasy Mini kit for RNA extraction.

Acknowledgments

We thank Pilar Gonzalo for optimizing intima collection protocol. Work in Dr. Andrés' laboratory is supported by the Spanish Ministerio de Ciencia e Innovación (MCIN)/Agencia Estatal de Investigación (AEI)/10.13039/501100011033 (grant PID2019-108489RB-I00) and the Instituto de Salud Carlos III (ISCIII) (AC16/00091, AC17/00067, and CB16/11/00405) with cofunding from the European Regional Development Fund (ERDF/FEDER, "Una manera de hacer Europa"), and the Progeria Research Foundation. R.M.N. is supported by the Ministerio de Educación, Cultura y Deporte (pre-doctoral contract FPU16/05027). M.R.H. is supported by the MCIN (post-doctoral contract IJC2019-040798-I). The CNIC is supported by the MCIN, the ISCIII, and the Pro CNIC Foundation, and is a Severo Ochoa Center of Excellence (grant CEX2020-001041-S funded by MICIN/AEI/10.13039/501100011033).

References

1. Kerr P, Tam R, Plane F (2011) Endothelium. In: Fitridge R, Thompson M (eds) Mechanisms of vascular disease: a reference book for vascular specialists. Barr Smith Press, Adelaide
2. Gimbrone MA Jr, García-Cardeña G (2016) Endothelial cell dysfunction and the pathobiology of atherosclerosis. Circ Res 118:620–636
3. Khaddaj Mallat R, Mathew John C, Kendrick DJ et al (2017) The vascular endothelium: a regulator of arterial tone and interface for the immune system. Crit Rev Clin Lab Sci 54: 458–470
4. Pi X, Xie L, Patterson C (2018) Emerging roles of vascular endothelium in metabolic homeostasis. Circ Res 123:477–494
5. Lacolley P, Regnault V, Segers P et al (2017) Vascular smooth muscle cells and arterial stiffening: relevance in development, aging, and disease. Physiol Rev 97:1555–1617
6. Basatemur GL, Jørgensen HF, Clarke MCH et al (2019) Vascular smooth muscle cells in atherosclerosis. Nat Rev Cardiol 16:727–744
7. Majesky MW (2015) Adventitia and perivascular cells. Arterioscler Thromb Vasc Biol 35: e31–e35
8. Tinajero MG, Gotlieb AI (2020) Recent developments in vascular adventitial pathobiology: the dynamic adventitia as a complex regulator of vascular disease. Am J Pathol 190:520–534
9. Li M, Qian M, Kyler K et al (2018) Endothelial–vascular smooth muscle cells interactions in atherosclerosis. Front Cardiovasc Med 5:1–8

10. Wang D, Wang Z, Zhang L et al (2017) Roles of cells from the arterial vessel wall in atherosclerosis. Mediat Inflamm 2017:1–9
11. Shimokawa H, Satoh K (2014) Vascular function. Arterioscler Thromb Vasc Biol 34: 2359–2362
12. Hamczyk MR, Nevado RM, Barettino A et al (2020) Biological versus chronological aging. J Am Coll Cardiol 75:919–930
13. Lowe R, Shirley N, Bleackley M et al (2017) Transcriptomics technologies. PLoS Comput Biol 13:e1005457
14. Chomczynski P, Sacchi N (1987) Single-step method of RNA isolation by acid guanidinium thiocyanate–phenol–chloroform extraction. Anal Biochem 162:156–159

Chapter 39

Redox Proteomics Analysis of Atherosclerotic Aortas: Application of the "OxICAT" Method

Manousos Makridakis and Antonia Vlahou

Abstract

Atherosclerosis development and progression have been linked to vascular reactive oxygen species (ROS). Plaque formation and especially instability, frequently resulting in acute coronary syndromes, have been linked to cell apoptosis and senescence, but also mainly to increased cellular oxidative stress. ROS are characterized by their high chemical reactivity and a resulting short half-life. This high reactivity usually involves reversible and/or irreversible protein modifications and specifically the covalent oxidative modification of cysteine residues. The latter can be used for the identification of protein-chemical footprints, leading to indirect monitoring of ROS. Proteomics and especially liquid chromatography tandem mass spectrometry (LC-MS/MS) approaches have emerged as a powerful tool to identify such protein modifications in biological samples (e.g., body fluids, tissues, cells). Application of a well-established quantitative thiol trapping technique termed OxICAT enables the detection and quantification of oxidative thiol modifications of thousands of proteins in a single experiment. In this chapter, a step-by-step guide for the redox proteomics analysis of atherosclerotic aortas, by utilizing the OxICAT method, as optimized by our group is provided.

Key words Redox proteomics, OxICAT, Reactive oxygen species, Cysteine oxidation, Oxidative modifications

1 Introduction

1.1 Tissue Homogenization

Vascular diseases (such as atherosclerosis, blood clots, stroke, aneurysm, and coronary and carotid artery disease) have been linked to endothelial dysfunction and increased production of reactive oxygen species (ROS). NADPH oxidases (Nox) are mainly responsible for the production of ROS and subsequent oxidative stress [1]. The latter (oxidative stress) is one of the main mechanisms participating in the inflammatory process associated with lipid deposition in the arterial wall, a hallmark of atherosclerosis [2, 3]. Atherogenesis is the injury result of vascular endothelial cells that is triggered by ROS, generated from the tissues [4]. In addition, atherosclerotic plaque formation and instability, associated with cardiovascular

Dipak P. Ramji (ed.), *Atherosclerosis: Methods and Protocols*, Methods in Molecular Biology, vol. 2419,
https://doi.org/10.1007/978-1-0716-1924-7_39,
© The Author(s), under exclusive license to Springer Science+Business Media, LLC, part of Springer Nature 2022

diseases, are in part caused by injury of vascular endothelial cells and/or apoptosis and cell senescence within the lesion, but also mainly due to oxidative stress and the subsequent production of ROS [5].

Homogenization of vascular tissue is quite challenging mainly due to its elasticity (high collagen concentration) and limited amounts available. Tissue homogenization is important in sample preparation. There are many different homogenization methods (e.g., Teflon potter, liquid nitrogen with pestle and mortar, sonication) to select from, but bead based homogenizers are more efficient, reproducible, easy to use and allow for the simultaneous processing of many samples (up to 24) at the same time and under the exact same conditions. Optimum results can be obtained utilizing a variety of different beads (e.g., stainless steel) and/or various size (e.g., 0.9–2 mm diameter). Beads can infiltrate the tissue sample contributing to a successful subsequent protein extraction.

1.2 Preventing Artificial Oxidation

Redox proteomics usually investigates reversible and/or irreversible protein modifications, focusing mainly on the covalent oxidative modifications of cysteine. As mentioned above, ROS play a key role in vascular diseases, which, in combination with the fact that proteins are prone to oxidation in many different ways under oxidative stress, makes the identification and quantification of ROS-modified amino acid residues very important for better understanding of disease mechanisms and determination of putative protein biomarkers [6]. Protein thiol modifications on cysteine residues, more specifically, have been found to confer significant impact on the protein function hence consisting a frequent target of analysis [6].

Thiols are characterized by high reactivity. As such, artificial (ex vivo) oxidation of protein thiols can occur during sample preparation. This may involve oxidation by molecular oxygen, a reaction which is catalyzed by trace metal ion contaminants in reagent solutions. Common metal ions have different effectiveness to catalyze thiol oxidation ($Cu^{2+} > Fe^{3+} > Ni^{2+} \gg Co^{2+}$). Oxidation reactions are usually affected by pH and temperature, with lower values of these two parameters leading to slower oxidation rates. For obvious reasons, the majority of redox proteomics protocols recommend buffer degasification (to eliminate oxygen) and inclusion of metal chelating agents such as EDTA (for scavenging metal ions) in the lysis buffer [6]. In addition, acidification or alkylation of the sample contributes to the elimination or at least significant reduction of artificial oxidation reactions during sample preparation. The OxICAT is a thiol trapping method that prevents artificial oxidation by the means of alkylation (through Iodoacetamide), while at the same time it enables for the relative quantification of oxidative thiol modifications in thousands of proteins in a single

experiment. The main advantage of the alkylating reagents (Iodoacetamide) compared to acidification (trichloroacetic acid (TCA)) for blocking of free thiols is the irreversible nature of the alkylation reaction. In contrast to alkylation, acidification is a reversible method for blocking of free thiols, and thus can lead to undesired oxidation upon increase of the pH level [6].

1.3 OxICAT

The OxICAT method relies on the application of the Isotope Coded Affinity Tag (ICAT) technology and can be used to identify and quantify the oxidative thiol modifications in proteins [7]. Commercially available ICAT reagents include three essential groups (Fig. 1): a thiol-reactive group (e.g., iodoacetamide), an isotope-coded light or heavy linker and a biotin tag to facilitate peptide enrichment [6]. The method is based on the fact that only free thiols are susceptible to direct labeling by the ICAT reagent, and thus, under oxidative stress conditions, a decrease in labeling is expected due to Cys thiol oxidation. One main advantage of the OxICAT method is that it can label both free and reversibly oxidized thiols in the same sample, hence allowing their simultaneous study. In the first step, irreversible labeling of free thiols with one of the ICAT probes (light or heavy) is performed. Then, reduction of all reversible oxidized thiols is conducted by using a thiol reducing agent (such as tris(2-carboxyethyl)phosphine (TCEP)), followed by their labeling with the second ICAT probe (Fig. 2). With the OxICAT method therefore, both free and reversibly oxidized Cys residues can be detected and quantified. The application of the OxICAT methodology in the investigation of cysteine oxidation in atherosclerotic aortas is hence described here in detail.

1.4 LC-MS/MS Analysis and Data Processing

Many efforts have been undertaken to elucidate the molecular mechanisms associated with cardiovascular disease [8]. Proteomic techniques (and especially LC-MS/MS based) are considered extremely powerful tools that can be utilized to obtain valuable information with regards to the molecular mechanisms of the disease [8]. Hypersensitive mass spectrometry systems utilizing hybrid mass analyzers technology combine both high mass resolution and accuracy, while at the same time are capable to producing large amounts of data [9]. What is even more interesting is the fact that present instrumentation in combination with sensitive labeling techniques (such as ICAT: isotope coded affinity tag) [10] can provide sufficient and reliable information not only for the abundance of protein molecules but for their post translational modifications, including oxidation [7]. Adaptations of the classical protein labeling techniques such as ICAT (isotope coded affinity tag), ITRAQ (isobaric tags for relative and absolute quantitation) and SILAC (stable isotope labeling by amino acids in cell culture) have been used for the study of residue oxidation [6]. Sophisticated algorithms and software have been developed for the analysis of

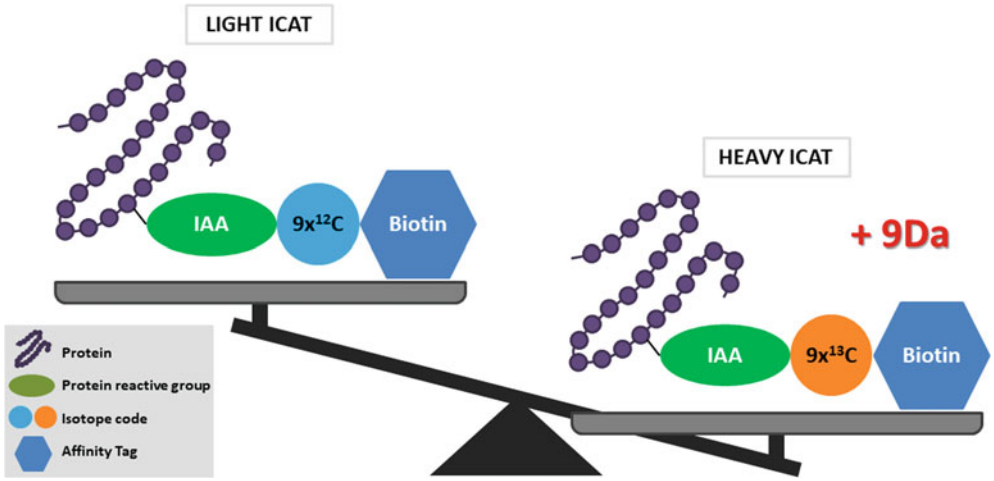

Fig. 1 Schematic overview of the ICAT chemistry. Heavy and light ICAT reagents consist of three different groups: (1) The protein reactive group (usually iodoacetamide, IAA) that covalently links the ICAT reagent to the protein by alkylation of free cysteines. (2) The isotope-coded tag which uniquely distinguishes labeled proteins (the heavy reagent tag includes nine heavy isotopes, whereas the light reagent tag contains no heavy isotopes). The tags share the shame physicochemical properties but differ in mass. This mass difference (9 Da) allows a mass-spectrometric comparison of peptides labeled with heavy and light reagents. (3) The affinity tag (biotin) that enables the selection and concentration of the cysteine-containing peptides, facilitating their enrichment in the sample

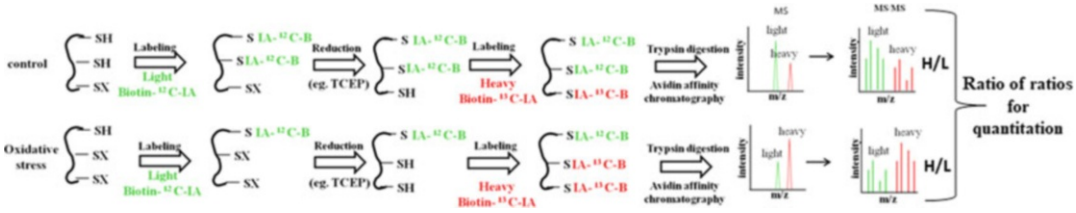

Fig. 2 Experimental workflow of the OxICAT method. Light ICAT label is highlighted in green and forms covalent bonds to free thiols (SH) of the cysteine residues. Heavy ICAT label is highlighted in red and forms covalent bonds to reversible oxidized cysteines (SX). At the end of the experimental procedure, the initially free cysteine thiols and the reversible oxidized cysteines per sample are identified and quantified

the raw data files produced by the advanced mass spectrometry platforms. The latest proteomics software packages are designed for large scale mass-spectrometric data sets analysis. They specifically aim at high-resolution MS data following the technological advancements in the mass spectrometry systems. Several labeling techniques (such as ICAT, ITRAQ, SILAC) as well as label free quantification are supported, covering a broad spectrum of the proteomics methodologies applied [11]. The same packages include tools for the statistical analysis of the obtained data,

although this is also often performed by specialized program languages (R, Python).

2 Materials

It is highly recommended to prepare all the solutions with ultrapure water (18 MΩ-cm at 25 °C) and analytical grade reagents (≥99% purity, HPLC grade reagents). Prepare and keep all buffers at room temperature, unless specified otherwise. Please use the appropriate precautions, as stated in the material safety data sheet, when handling the chemical reagents and solvents described in this section.

1. Homogenization (Redox) buffer: 8 M Urea, 2% (w/v) CHAPS, 50 mM Tris–HCl pH 6.8, 1 mM EDTA, pH 7.0 (*see* **Notes 1–4**). Store in aliquots at −20 °C until use.
2. 3.6% (v/v) protease inhibitors (*see* **Note 2**).
3. Denaturing Alkylation Buffer (DAB): 6 M Urea, 0.5% SDS, 10 mM EDTA, 200 mM Tris–HCl, pH 8.5. (*see* **Notes 4–6**). Store in aliquots at −20 °C until use.
4. Buffer degasification apparatus.
5. Iodoacetamide.
6. Bead based homogenizer.
7. Stainless steel homogenization beads (0.9–2.0 mm diameter).
8. Bradford Reagent solution.
9. Spectrophotometer (Ultraviolet-visible) for defining protein concentration.
10. ICAT kit. The kit contains: light ICAT reagent, heavy ICAT reagent, reduction buffer: 50 mM TCEP (*see* **Note 7**), denaturation buffer: 0.1% (w/v) SDS, 50 mM Tris–HCl pH 8.5, 0.125 μg/μL trypsin proteomics grade stock solution, ICAT cartridge–cation exchange, cation exchange buffer–load: 10 mM potassium dihydrogen phosphate (KH_2PO_4), 25% acetonitrile, pH 3.0, cation exchange buffer–elute: 10 mM KH_2PO_4, 25% acetonitrile, 350 mM KCl, pH 3.0, cation exchange buffer–clean: 10 mM KH_2PO_4, 25% acetonitrile, 1 M KCl, pH 3.0, cation exchange buffer–storage: 10 mM KH_2PO_4, 25% acetonitrile, pH 3.0, 0.1% NaN_3, ICAT cartridge–avidin, 1× PBS: 10 mM sodium dihydrogen phosphate (NaH_2PO_4), 150 mM NaCl, affinity buffer–load: 2× PBS, pH 7.2, affinity buffer–wash 1: 1× PBS, pH 7.2, affinity buffer–wash 2: 50 mM ammonium bicarbonate (NH_4HCO_3), 20% methanol, pH 8.3, affinity buffer–elute: 30% acetonitrile, 0.4% TFA (Trifluoroacetic acid), affinity

buffer–storage: 2× PBS, pH 7.2, cleaving reagent A (*see* **Note 8**), cleaving reagent B (*see* **Notes 9** and **10**).

11. Zeba spin desalting columns.
12. 0.5, 1.5, and 2 mL Eppendorf tubes and 1.5 mL safe lock Eppendorf tubes.
13. 15 and 50 mL Falcon tubes.
14. Vortex.
15. pH indicator strips.
16. Centrifuge.
17. Humidified container.
18. Centrifugal vacuum concentrator.
19. Dionex Ultimate 3000 RSLC (Rapid Separation Liquid Chromatography) nanoflow system.
20. Hybrid mass analyzer: Orbitrap Velos FTMS (Fourier transform mass spectrometer).
21. Trap column C18 (reversed phase), 0.075 mm (diameter), 2 cm (length), 3 μm (particle size), 100 Å (pore size).
22. Analytical column C18 (reversed phase), 0.075 mm (diameter), 50 cm (length), 2 μm (particle size), 100 Å (pore size).
23. Mobile phase A: 0.1% formic acid, pH 3.5.
24. Mobile phase B: 0.1% formic, 80% acetonitrile.
25. Orbitrap Velos FTMS (Fourier-transform mass spectrometry) or equivalent mass spectrometer.
26. Commercially available software packages for MS data analysis (e.g., Proteome Discoverer: Thermo Scientific or open access software such as MaxQuant).
27. Open access R program for statistical analysis.

3 Methods

The general experimental workflow is shown in Fig. 2.

3.1 Tissue Homogenization

1. Homogenize tissue in a bead-based homogenizer following the addition of Homogenization (Redox) buffer in the tissue sample (usually 100–200 μL buffer on 10–50 mg tissue net weight). Use stainless steel homogenization beads (0.9–2.0 mm diameter) (*see* **Note 11**).
2. After homogenization, centrifuge the samples at 14,000 x *g* for 10 min at room temperature (*see* **Note 12**). Transfer the supernatant into a clean tube and add protease inhibitors.

3. Determine protein concentration with a colorimetric assay (e.g., Bradford or Lowry). At this point, samples are quite stable and can be stored at −80 °C until use.

3.2 Preventing Artificial (Ex Vivo) Oxidation and Induce Thiol Trapping

1. Degasify buffer to eliminate oxygen.
2. Dissolve the ICAT reagent in 20 μL of acetonitrile, mix it with the sample and perform the labeling reaction for 2 h at 37 °C in the dark. Besides labeling, alkylation is also performed through the iodoacetamide which is included in the ICAT reagent (*see* **Note 13**).

3.3 OxICAT

3.3.1 Labeling with Cleavable ICAT Reagents

1. Begin the labeling process with at least 200 μg of protein in the sample (*see* **Note 14**).
2. Dissolve the light ICAT reagent in 20 μL of acetonitrile, mix it with the sample and perform the labeling reaction for 2 h at 37 °C in the dark (*see* **Notes 15–17**).
3. Desalt the sample, remove the excess probe and perform buffer exchange (in DAB buffer) using Zeba spin columns (*see* **Note 18**).
4. Saturate the column with DAB buffer with three times addition of 300 μL of DAB buffer to the column followed by centrifugation at 1500 × *g* for 1 min, each time.
5. Apply the sample to the column and elute via centrifugation at 1500 × *g* for 2 min in ~80 μL of DAB buffer.
6. Reduce the samples with 1.25 mM TCEP by adding 2 μL of the 50 mM stock solution to the 80 μL of sample that has been eluted in DAB buffer for 30 min at 37 °C (*see* **Note 19**).
7. Continue the labeling process (*see* **Note 20**) by adding the heavy ICAT reagent (dissolved in 20 μL acetonitrile) followed by incubation for 2 h at 37 °C in the dark (*see* **Note 21**).
8. Remove excess heavy probe and carry out sample cleaning and desalting using the Zeba spin columns, as described in **steps 3–5** except that buffer exchange is now performed in denaturation buffer and the sample is now eluted using ~80 μL of this buffer (*see* **Note 22**).

3.3.2 Trypsin Digestion

1. Add 20 μL of acetonitrile to the eluate (sample) to obtain a final volume of 100 μL.
2. Add 100 μL of the 0.125 μg/μL trypsin stock solution, resulting in a trypsin–protein ratio: 12.5 μg /200 μg = 1/16; *see* **Note 23**), to the sample and incubate for 12–16 h in a humidified container in the dark at room temperature (RT).

3.3.3 Cation Exchange for Cleaning Up the Peptides

1. Assemble the cation-exchange cartridge (*see* **Note 24**).
2. Dilute the sample mixture by adding 4 mL of the Cation Exchange Buffer–Load and vortex to mix. Check the pH using pH indicator strips. If the pH is not between 2.5 and 3.3, adjust by adding more Cation Exchange Buffer–Load (*see* **Note 25**).
3. Condition the cartridge by injecting 2 mL of the Cation Exchange Buffer–Load (*see* **Note 25**). Divert to waste and discard the flow through.
4. Slowly inject (~1 drop/s) the diluted sample mixture onto the cation-exchange cartridge and collect the flow-through into a clean tube (15 mL Falcon tube).
5. Inject 1 mL of the Cation Exchange Buffer–Load to wash the TCEP, SDS and excess ICAT reagents from the cartridge. Collect the flow-through into the same tube used in **step 4** (*see* **Note 26**).
6. Elute the peptides by slowly injecting (~1 drop/s) 500 μL of the Cation Exchange Buffer–Elute (*see* **Note 27**). Capture the eluate in a clean 1.5 mL tube. Collect the eluted peptides as a single fraction.
7. After eluting the peptides, clean and store the cartridge as follows: Wash the trypsin from the cation-exchange cartridge by injecting 1 mL of the Cation Exchange Buffer–Clean. Divert to waste and discard flow through (*see* **Note 28**). Inject 2 mL of the Cation Exchange Buffer–Storage (*see* **Note 29**). Remove the cartridge and seal the ends of the cartridge with the two end caps. Keep a record of the number of times that cartridge has been used (*see* **Note 24**). Store the cartridge at 2–8 °C.

3.3.4 Avidin Affinity Chromatography for Peptide Purification

1. Assemble the avidin cartridge (*see* **Note 30**).
2. Inject 2 mL of the Affinity Buffer–Elute. Divert to waste and discard flow through (*see* **Note 31**).
3. Inject 2 mL of the Affinity Buffer–Load. Divert to waste and discard flow-through (*see* **Note 32**).
4. Neutralize the cation-exchange fraction by adding 500 μL of the Affinity Buffer–Load (*see* **Note 32**). Check the pH using pH indicator strips. If the pH is not 7, adjust by adding more Affinity Buffer–Load. Mix by vortex and centrifuge at 1000 × *g* for 1 min (RT) to bring all solution to the bottom of the tube.
5. Slowly inject (~1 drop/5 s) the neutralized fraction from **step 4** onto the avidin cartridge and collect the flow-through (*see* **Note 33**).

6. Inject 500 μL of Affinity Buffer–Load (*see* **Note 32**) onto the cartridge and continue to collect the flow-through (*see* **Note 34**).
7. Reduce the salt concentration by injecting 1 mL of Affinity Buffer–Wash 1. Divert the output to waste (*see* **Note 35**).
8. Remove the nonspecifically bound peptides by injecting 1 mL of Affinity Buffer–Wash 2 (*see* **Note 36**). Collect the first 500 μL in a clean 1.5 mL tube (Wash fraction). Divert the remaining 500 μL to waste and discard flow through.
9. Inject 1 mL of ultrapure water, divert to waste and discard flow-through.
10. To elute the labeled peptides, use 800 μL of the Affinity Buffer–Elute (*see* **Note 31**). Slowly inject (~1 drop/5 s) 50 μL of the Affinity Buffer–Elute and discard the eluate. Inject the remaining 750 μL of Affinity Buffer–Elute and collect the eluate in a clean 1.5 mL tube.
11. After finishing with the peptide elution, clean the cartridge by injecting 2 mL of the Affinity Buffer–Elute, divert to waste and discard flow-through (*see* **Note 31**).
12. Continue by injecting 2 mL of Affinity Buffer–Storage *(see* **Note 37**), divert to waste and discard flow through.
13. Remove the cartridge and seal the ends of the cartridge with the two end caps. Keep a record of the number of times the cartridge has been used. Store the cartridge at 2–8 °C.
14. Evaporate the affinity-eluted fraction to dryness in a centrifugal vacuum concentrator.

3.3.5 Biotin Cleavage

1. Prepare the final cleaving reagent in a clean 1.5 mL tube by combining Cleaving Reagent A and Cleaving Reagent B in a 95:5 ratio. Approximately 90 μL of final cleaving reagent per sample is needed.
2. Mix the freshly prepared cleaving reagent with the dried peptide sample.
3. Incubate the sample with the cleaving reagent for 2 h at 37 °C (*see* **Note 38**).
4. Centrifuge at 1000 × *g* for 1 min (RT) to bring all the solution to the bottom of the tube.
5. Evaporate the sample to dryness in a centrifugal vacuum concentrator.

3.4 LC-MS/MS Analysis and Data Processing

1. Resuspend the sample in 12 μL of mobile phase A and load 6 μL onto a Dionex Ultimate 3000 RSLC (Rapid Separation Liquid Chromatography) nanoflow system or equivalent. Load

onto a Dionex 0.1 × 20 mm 5 μm C18 nano trap column at a flow rate of 5 μL/min in 0.1% formic acid and 2% acetonitrile.

2. Subsequently, apply the samples onto an Acclaim PepMap C18 nano column 75 μm × 50 cm (Dionex, Sunnyvale, CA, USA), 2 μm 100 Å at a flow rate of 0.3 μL/min.
3. Maintain the trap and nanoflow column at 35 °C.
4. Elute the samples with a gradient of solvent A: 0.1% formic acid versus solvent B: 80% acetonitrile, 0.1% formic acid starting at 2% B for 10 min, rising to 33% B at 90 min, then to 80% B at 95 min, isocratic 80% B until 105 min and then reducing at 2% B at 120 min.
5. Wash and reequilibrate the column with blank (mobile phase A) prior to injection of the next sample.
6. Ionize the eluent using a Proxeon nanospray ESI source operating in positive ion mode into an Orbitrap Velos FTMS (Fourier-transform mass spectrometry) or equivalent mass spectrometer. Adjust the ionization voltage at 2.6 kV and the capillary temperature at 275 °C.
7. Operate the mass-spectrometer in MS/MS mode scanning from 380 to 1600 amu (atomic mass unit).
8. Set the resolution of ions in MS^1 at 60,000 and 7500 for HCD (Higher-energy Collisional Dissociation) MS^2.
9. Select the top 20 multiple charged ions from each scan for MS/MS analysis using HCD at 40% collision energy.
10. Use the following AGC settings: 1,000,000 for full scan in the FTMS and 200,000 for MS^n.
11. Enable dynamic exclusion with a repeat count of 1, exclusion duration of 30 s (*see* **Note 39**).
12. Upload tandem mass spectra from LC-MS/MS (Liquid Chromatography coupled with tandem mass spectrometry) analysis of the OxICAT samples to a mass spectrometry proteomic data processing software package (such as Proteome Discoverer, MaxQuant and others).
13. Perform the peptide and protein identification with the SEQUEST search engine utilizing the SwissProt reviewed protein database. Apply the following search parameters: (1) precursor mass tolerance: 10 ppm and fragment mass tolerance: 0.05 Da; (2) full tryptic digestion; (3) max missed cleavage sites: 2; (4) dynamic modifications: oxidation of methionine, deamidation of asparagine and glutamate, acetylation (any N terminus), ICAT-C, ICAT-C:13C(9); (5) event detector mass precision: 2 ppm; (6) precursor mass: 600–6000 Da; (7) collision energy: 0–100 eV; and (8) target FDR (strict): 0.01;

(9) target FDR (relaxed): 0.05; (10) FDR validation based on: *q*-Value.

14. Further process the obtained results by applying the following filters: (1) high and medium confidence peptides (FDR <5%); and (2) peptide rank = 1.
15. Subsequently, perform label-based quantification at the peptide level based on the ICAT reporter ion intensities detected by the Reporter Ions Quantifier Node in Proteome Discoverer. Calculate the abundance for each distinct peptide as the mean of reported ions from all matching spectra.
16. Group spectra based on sequence and, in the case of modifications, consider the peptides as distinct when modifications are different.
17. Represent the reporter ion intensities for each individual peptide as a ratio of heavy and light labeled peptides. Only peptides for which both heavy and light reporter ion labeled peptides can be detected and quantified should be considered for further analyses.
18. Discard cysteine residues where only light or heavy reporter ions were detected.
19. Calculate the mean heavy-to-light (H/L) ratio for each labeled peptide. Consider only cysteine residues that were labeled with both light and heavy ICAT labels in at least three biological replicates.
20. Determine the fold change of the oxidation status of a peptide in a specific comparison by calculating the ratio of the respective H/L ratios among samples of different groups.
21. Consider labeled peptides with a statistically significant ($P < 0.05$) fold change ≥ 1.2 or ≤ 0.8 to show a significant change in their oxidation status [12].

4 Notes

1. This redox buffer is very efficient in tissue solubilization and protein extraction due to its high concentration of urea (chaotropic agent) in combination with a zwitterionic detergent such as CHAPS.
2. Redox buffer is prepared by addition of all the components at room temperature and stored in aliquots at −20 °C. Protease inhibitors should be added fresh upon tissue lysis.
3. Reducing agents (such as DTE, TCEP), although helpful in the homogenization process, must be avoided in the redox buffer. In the first step of the OxICAT method, the ICAT probe (light or heavy) must irreversibly label only the initial (in vivo) free

(reduced) thiols. By including a reducing agent in the redox buffer, besides the free thiols, the reversible oxidized thiols will be reduced and thus labeled with the ICAT probe.

4. EDTA scavenges trace metal ion contaminants in reagents solutions which are able to catalyze oxidation by molecular oxygen.
5. Similar to the redox buffer, DAB does not contain any reducing agent. The solubilized sample with redox buffer is mixed with DAB buffer until a final volume of 100 μL before the ICAT labeling process. DAB has similar composition with the redox buffer to retain the proteins in solution and offers the slightly alkaline pH required for the ICAT labeling process.
6. When iodoacetamide is present in limiting quantities in a slightly alkaline pH, cysteine modification will be the exclusive reaction. Excess iodoacetamide or nonbuffered iodoacetamide reagent can also alkylate amines (lysine, N-termini), thioethers (methionine), imidazoles (histidine), and carboxylates (aspartate, glutamate).
7. Reduction must be performed with TCEP, which besides being a strong reductant is also compatible with the ICAT probes. Other reducing agents (e.g., mercaptoethanol and DTE) should be avoided because they can react with the ICAT reagents, competing with protein derivatization.
8. Contains concentrated TFA and should be stored at RT.
9. Contains a scavenger that reduces side reactions during the cleaving reaction and should be stored at −20 °C.
10. ICAT reagents are required for the labeling process. ICAT cartridge–cation exchange, cation exchange buffer–load, cation exchange buffer–elute, cation exchange buffer–clean and cation exchange buffer–storage are required for cleaning up the peptides using cation exchange. ICAT cartridge–avidin, affinity buffer–load, affinity buffer–wash 1, affinity buffer–wash 2, affinity buffer–elute and affinity buffer–storage are required for the purification of the biotinylated peptides. Cleaving reagent A and cleaving reagent B are required for the cleavage of the ICAT reagent labeled peptides.
11. Bead-based homogenization relies on collision of the beads with the tissue. Commercially available beads are manufactured from various materials (e.g., stainless steel, zirconium oxide, glass) and can be selected depending on the tissue sample. Glass beads perform better with soft tissues, zirconium oxide is recommended for intermediate types of tissue and stainless steel is used for samples considered more difficult to homogenize. The homogenizers can analyze simultaneously up to 24 samples with very good reproducibility results obtained in

our hands. Air cool or refrigerator system is used to protect the samples from overheating. Contamination is eliminated by utilizing disposable beads that are used only once and discarded afterward. Selection of the appropriate beads depends on the tissue type. Stainless steel beads have a wide range of applications and are suitable for almost any kind of tissue: soft (brain tissue) and hard type of tissues (vessels, bladder). Specific type of tubes (such as safe-lock Eppendorf tubes) should be used with the bead-based homogenizers to ensure that the caps will remain sealed during the vigorous shaking and vortexing performed in the bead homogenizer. It is also recommended that the final sample volume following the addition of beads and homogenization buffer should not exceed the 1/3 of the volume capacity of the tube.

12. Centrifugation should be performed at RT. This is due to the fact that certain components of the redox buffer (Urea) tend to precipitate at low temperature (e.g., 4 °C).
13. Iodoacetamide irreversible blocks the free thiols.
14. OxICAT is a double-labeling method in the same sample that specifically labels peptides with cysteine residues. The cysteine-containing peptides are enriched after labeling through avidin affinity chromatography. Frequency of cysteine residue accounts for 2–3% in proteins; thus, a sufficient starting amount (at least 200 μg) should be used to obtain enough cysteine-containing peptides labeled with the ICAT probes for the quantification process.
15. Iodoacetamide is unstable and light-sensitive. Solutions should be prepared immediately before use and alkylation should be performed in the dark. If iodoacetamide is present in limiting quantities and in a slightly alkaline pH, cysteine modification will be the exclusive reaction. Excess iodoacetamide or non-buffered iodoacetamide reagent can also alkylate amines (lysine, N-termini), thioethers (methionine), imidazoles (histidine), and carboxylates (aspartate, glutamate).
16. Iodoacetamide is a sulfhydryl-reactive alkylating reagent routinely used in proteomics to block reduced cysteine residues for protein characterization and peptide mapping. Alkylation with iodoacetamide results in the covalent addition of a carbamidomethyl group (57.07 Da) which prevents the formation of disulfide bonds. Reducing agents added after alkylation may react with excess iodoacetamide.
17. Light ICAT reagent irreversibly labels the in vivo reduced thiol group of cysteines: R-SH → R-SICAT light.
18. Removal of excess light/heavy ICAT labels and simultaneous sample desalting can be performed with the Zeba spin columns. These are 7 K MWCO, 0.5 mL polypropylene devices

containing a proprietary high-performance size-exclusion chromatography resin that regularly provides efficient protein desalting and recovery in a centrifuge format. The low-binding resin maximizes protein recovery. Alternatively, the desalting and cleaning of the sample can be performed with a precipitation step, for example, TCA (trichloroacetic acid)-NLS (*N*-lauroylsarcosine sodium salt solution) precipitation, acetone precipitation. However, the precipitation step may increase the variability among samples compared with the desalting columns and is more laborious and time consuming.

19. Reversible oxidized thiols such as S-NO, S-S, and S-OH are expected to be reduced at this step.
20. OxICAT is a variation of the ICAT method to investigate the redox status of the cysteine free thiols. In ICAT, different samples are labeled with the light and heavy probe and then mixed before trypsinization. However, in the OxICAT approach (which is a double-labeling method), the same sample is labeled sequentially with light (followed by TCEP reduction) and heavy ICAT reagents to identify the oxidation status of specific cysteine residues.
21. This process is expected to label the reversible oxidized thiols which were reduced in the previous step.
22. DAB buffer consists of a combination of high urea concentration (6 M) along with a strong detergent such as SDS (0.5%) that is likely to deactivate trypsin during the trypsinization process, resulting in significantly lower number of tryptic peptides. However, denaturation buffer contains a considerably lower concentration of SDS (0.1%) which is sufficient to keep the proteins in solution, while at the same time is unlikely to affect the trypsinization process.
23. Trypsinization is an enzymatic reaction. Trypsin-to-protein ratio is an important aspect for the stoichiometry of the reaction. If the ratio is too low, tryptic digestion slows down, producing lower number of tryptic peptides. If the ratio is too high, trypsin autocleavage effects can contaminate the sample. Usually, a ratio of 1:10 up to 1:100 is considered optimum depending on the initial protein amount.
24. Mark the inlet and outlet ends of the cartridge (or mark with a directional arrow) for future use. Use the same flow direction in all runs to prevent particles that may accumulate at the cartridge inlet from clogging the outlet tubing. The cation-exchange cartridge can be used up to 50 times.
25. Cation-exchange buffer-load is a phosphate buffer with acetonitrile that adjusts the pH and lowers the salt concentration.

26. Keep the flow-through until you confirm that loading on the cation-exchange cartridge is successful. If loading fails, you can repeat loading using the flow-through after troubleshooting the cause of the loading failure.
27. Cation-exchange buffer-elute is a phosphate buffer with acetonitrile and salt that raises the salt concentration to elute the peptides.
28. Cation-exchange buffer-clean is a phosphate buffer with acetonitrile and high salt concentration that cleans the cation-exchange cartridge after peptide elution.
29. Cation exchange buffer-storage is a phosphate buffer with acetonitrile and sodium azide that maintains the proper pH and prevents growth of microorganisms.
30. Mark the inlet and outlet ends of the cartridge (or mark with a directional arrow) for future use. Use the same flow direction in all runs to prevent particles that may accumulate at the cartridge inlet from clogging the outlet tubing. The avidin cartridge has a maximum recommended load of 8–10 nmol for a nominal 1-kDa peptide. The avidin cartridge can be cleaned, activated and reused for up to 50 cation-exchange fractions.
31. Affinity buffer-elute conditions the affinity cartridge and elutes ICAT reagent-labeled peptides. Injecting the Elute buffer before loading the sample is required to free up low-affinity binding sites on the avidin cartridge.
32. Affinity buffer-load is a phosphate buffer that adjusts the pH to approximately 7.2.
33. Flow-Through contains unlabeled peptides. If needed, MS/MS analysis can be performed on this fraction to increase the protein coverage of the sample. However, this analysis does not provide ICAT reagent-labeled peptide quantification information.
34. Keep the flow through until you confirm that loading on the avidin cartridge is successful. If loading fails, you can repeat loading using the flow through after troubleshooting the cause of the loading failure.
35. Affinity buffer-wash 1 is a phosphate buffer that decreases the salt concentration.
36. Affinity buffer-wash 2 is a bicarbonate solution with methanol that decreases the salt concentration and reduces nonspecifically bound peptides.
37. Affinity buffer-storage is a phosphate buffer with sodium azide that maintains the proper pH and prevents growth of microorganisms.

38. Cleaving reagent A cleaves the biotin from the labeled peptide while cleaving reagent B contains a scavenger that reduces side reactions during the cleaving reaction.
39. The specific LC-MS/MS instrumentation and settings are indicative. The analysis can be performed with any type of instrumentation, adjusting the appropriate settings.

Acknowledgments

This project has received funding from the Hellenic Foundation for Research and Innovation (HFRI) and the General Secretariat for Research and Innovation (GSRI), under grant agreement No 695 (MolProt-CKD).

References

1. Douglas G, Bendall JK, Crabtree MJ, Tatham AL, Carter EE, Hale AB, Channon KM (2012) Endothelial-specific Nox2 overexpression increases vascular superoxide and macrophage recruitment in ApoE(−)/(−) mice. Cardiovasc Res 94(1):20–29. https://doi.org/10.1093/cvr/cvs026
2. Abd Alla J, El Faramawy Y, Quitterer U (2013) Microarray gene expression profiling reveals antioxidant-like effects of angiotensin II inhibition in atherosclerosis. Front Physiol 4:148. https://doi.org/10.3389/fphys.2013.00148
3. Nomura J, Busso N, Ives A, Matsui C, Tsujimoto S, Shirakura T, Tamura M, Kobayashi T, So A, Yamanaka Y (2014) Xanthine oxidase inhibition by febuxostat attenuates experimental atherosclerosis in mice. Sci Rep 4:4554. https://doi.org/10.1038/srep04554
4. Sano E, Tashiro S, Tadakuma H, Takei T, Ueda T, Tsumoto K (2012) Type 1 IFN inhibits the growth factor deprived apoptosis of cultured human aortic endothelial cells and protects the cells from chemically induced oxidative cytotoxicity. J Cell Biochem 113(12):3823–3834. https://doi.org/10.1002/jcb.24259
5. Xu S, Chamseddine AH, Carrell S, Miller FJ Jr (2014) Nox4 NADPH oxidase contributes to smooth muscle cell phenotypes associated with unstable atherosclerotic plaques. Redox Biol 2:642–650. https://doi.org/10.1016/j.redox.2014.04.004
6. Mermelekas G, Makridakis M, Koeck T, Vlahou A (2013) Redox proteomics: from residue modifications to putative biomarker identification by gel- and LC-MS-based approaches. Expert Rev Proteomics 10(6):537–549. https://doi.org/10.1586/14789450.2013.855611
7. Leichert LI, Gehrke F, Gudiseva HV, Blackwell T, Ilbert M, Walker AK, Strahler JR, Andrews PC, Jakob U (2008) Quantifying changes in the thiol redox proteome upon oxidative stress in vivo. Proc Natl Acad Sci U S A 105(24):8197–8202. https://doi.org/10.1073/pnas.0707723105
8. Mokou M, Lygirou V, Vlahou A, Mischak H (2017) Proteomics in cardiovascular disease: recent progress and clinical implication and implementation. Expert Rev Proteomics 14(2):117–136. https://doi.org/10.1080/14789450.2017.1274653
9. Aebersold R, Mann M (2003) Mass spectrometry-based proteomics. Nature 422(6928):198–207. https://doi.org/10.1038/nature01511
10. Gygi SP, Rist B, Gerber SA, Turecek F, Gelb MH, Aebersold R (1999) Quantitative analysis of complex protein mixtures using isotope-coded affinity tags. Nat Biotechnol 17(10):994–999. https://doi.org/10.1038/13690
11. Tyanova S, Temu T, Cox J (2016) The MaxQuant computational platform for mass spectrometry-based shotgun proteomics. Nat Protoc 11(12):2301–2319. https://doi.org/10.1038/nprot.2016.136
12. Muller A, Eller J, Albrecht F, Prochnow P, Kuhlmann K, Bandow JE, Slusarenko AJ, Leichert LI (2016) Allicin induces thiol stress in bacteria through S-Allylmercapto modification of protein cysteines. J Biol Chem 291(22):11477–11490. https://doi.org/10.1074/jbc.M115.702308

Chapter 40

Intravital Microscopy in Atherosclerosis Research

Georg Wissmeyer, Mohamad B. Kassab, Yoichiro Kawamura, Aaron D. Aguirre, and Farouc A. Jaffer

Abstract

Atherosclerosis is a lipid-driven inflammatory disorder that narrows the arterial lumen and can induce life-threatening complications from coronary artery disease, cerebrovascular disease, and peripheral artery disease. On a mechanistic level, the development of novel cellular-resolution intravital microscopy imaging approaches has recently enabled in vivo studies of underlying biological processes governing disease onset and progress. In particular, multiphoton microscopy has emerged as a promising intravital imaging tool utilizing two-photon–excited fluorescence and second-harmonic generation that provides subcellular resolution and increased imaging depths beyond confocal and epifluorescence microscopy. In this chapter, we describe the state-of-the-art multiphoton microscopy applied to the study of murine atherosclerosis.

Key words Atherosclerosis, Inflammation, Intravital imaging, Intravital microscopy, Molecular imaging, Multiphoton microscopy, Gated microscopy

1 Introduction

Atherosclerosis is a chronic inflammatory disease underlying coronary artery disease (CAD) and myocardial infarction, sudden cardiac death, ischemic stroke and peripheral artery disease, and is the leading cause of disability and death worldwide. At present, assessment of pathobiological mechanisms driving atherosclerosis mainly relies on classical histopathology and ex vivo studies. However, the pathogenesis of atherosclerosis involves in vivo dynamic events driven by cells and molecules that occur over timeframes faster than overall disease progression. Intravital imaging technologies, such as multiphoton microscopy (MPM), allow to study disease onset and progression in vivo and in real-time, and can therefore help to better understand the underlying biomolecular processes. For example, one of the key goals in atherosclerosis research is to better understand the role of trafficking and resident leukocyte classes in atheroma progression and myocardial infarction healing

Dipak P. Ramji (ed.), *Atherosclerosis: Methods and Protocols*, Methods in Molecular Biology, vol. 2419,
https://doi.org/10.1007/978-1-0716-1924-7_40,
© The Author(s), under exclusive license to Springer Science+Business Media, LLC, part of Springer Nature 2022

[1, 2]. In this chapter, we detail the ability to perform in vivo MPM in larger arterial vascular disease in murine subjects.

Intravital molecular microscopy (IVM) technologies based on fluorescence contrast are a key pillar of modern biological research, and cellular and subcellular resolution approaches such as confocal microscopy (CFM), have enabled the molecular assessment of atherosclerosis in mice in vivo [3–5]. Advances in laser technology have led to the development of MPM, where longer excitation wavelengths allow for increased imaging depths of up to 300 μm, compared to around 80 μm in conventional CFM. Moreover, the physical principles of MPM minimize photobleaching and out-of-focus absorption, thus vastly decreasing photodamage to the biological specimen [6, 7]. Sophisticated MPM systems allow for simultaneous multichannel multimodality image acquisition (e.g., via two-photon–excited fluorescence (2PEF)) of various fluorescent dyes/proteins and of nonlinear optical microscopy techniques (i.e., second-harmonic generation (SHG) and third-harmonic generation (THG)) [8]. These capabilities are particularly attractive for comprehensive imaging of associated biomolecular processes in atherosclerosis, where cell types of interest may be individually labeled and imaged via dedicated channels acquired separately from channels dedicated to imaging surrounding tissue substructure, such as collagen via SHG and THG contrast [9]. With asset costs and complexity of MPM systems steadily decreasing, multimodal IVM is set to become accessible to a fast-growing biological research community and will lead to a significant improvement to the study of atherosclerosis.

A commonly used animal model for atherosclerosis research is the Apolipoprotein E knockout ($ApoE^{-/-}$) mouse in combination with a Western-type diet (high fat and cholesterol content). As of today, no mouse model can fully recapitulate every pathophysiological aspect of human atherosclerosis. However, a variety of transgenic mouse models have been established in the past decades allowing, for example, to investigate lipid metabolism in early phase atherosclerosis or to study plaque vulnerability in advanced atherosclerosis [10, 11]. However in common mouse models, atherosclerotic plaques develop in vessels such as the brachiocephalic or carotid arteries [12] that are not suitable for conventional intravital microscopy, either because of the need for highly invasive surgery and/or due to artifacts induced by cardiac and respiratory motion. This is of particular relevance for MPM, where both in-plane and through-plane motion can affect image quality [13–15]. In the case of the carotid artery, mechanical stabilization of the artery relative to the microscopy setup (e.g., via spatially fixated coverslips) allows for real-time IVM microscopy. However, any kind of mechanical- or pressure-based fixation may alter native physiology (e.g., by altering flow and leukocyte recruitment) and may therefore not be physiologically relevant. A promising approach for

motion-compensated IVM leverages gating technologies (i.e., via cardiorespiratory synchronization with the IVM image acquisition) [16]. However, gated imaging requires sophisticated hardware and software, and off-the-shelf IVM systems for gated acquisition are not commercially available yet.

In this chapter, we detail a method for performing intravital MPM on a large-caliber vascular disease model that reflects the current possibilities of IVM microscopy. The described method is fully transferable to gated MPM of murine carotid atherosclerosis but is introduced based on established protocols and commercially available hardware, utilizing a thrombosis model, to demonstrate leukocyte trafficking, as relevant to atherosclerosis pathobiology [17].

2 Materials

The selection of microscope settings (i.e., excitation wavelengths and emission filters) as well as the selection of endogenous and/or exogenous fluorescence labels/agents depends on the specific molecular and/or cellular target(s) to be investigated in the study (*see* **Note 1**). Exogenous fluorophore solutions should be prepared right before procedure and remain protected from light.

2.1 Multiphoton Microscope

1. Sophisticated multiphoton microscopy (MPM) suites for high-speed 2D and 3D multimodal image acquisition are provided by multiple manufacturers with similar specifications and one commercially available MPM system is the FVMPE-RS (Olympus, Japan). The microscope employs two tunable broad bandwidth lasers for excitation wavelengths ranging from 680 to 1300 nm and a set of four corresponding photo multiplier tubes (PMTs) for simultaneous 4-channel imaging. A broad excitation bandwidth and respective optical dichroic/filter system allows for SHG and THG as well as for simultaneous imaging of dye- and protein-based fluorophores (*see* **Note 2**).
2. Scanning is performed with a set of galvanometer and resonant scanning mirrors in combination with a piezo-driven z-stage for the objective.
3. A water immersion objective dedicated for multiphoton excitation, such as the XLPLN25XWMP2 (Olympus, Japan), is applied with a magnification of 25×, a working distance of 2 mm and a numerical aperture (NA) of 1.05 (*see* **Note 3**).
4. The MPM may only be equipped with a bright-field eyepiece for sample alignment. However, a digital camera for acquiring bright-field microscopy images, particularly for serial studies, is useful.

5. 3D adjustment of the specimen (i.e., the mouse model) can be performed with XYZ stages implemented into the microscope and/or with a set of additionally mounted stages (*see* **Note 4**).
6. Sophisticated analysis of 2D images and 3D image stacks can be performed with ImageJ image processing software (v. 1.53f, freeware, NIH https://imagej.nih.gov/ij/download.html) (*see* **Note 5**).

2.2 Exogeneous Fluorophores

1. Dilution of imaging agents: Depending on manufacturer specifications, phosphate buffered saline (1× PBS) or 0.9% (normal) saline solutions are used.
2. Blood microcirculation and negative cell contrast: Fluorescein isothiocyanate (FITC)-dextran (MW 2,000,000). Excitation/Emission 490/520 nm. Solution prepared at a dosage of 25–50 mg/kg.
3. Leukocyte and platelet labeling [18]: Rhodamine 6G. Excitation/Emission 528/552 nm. Solution prepared at a dosage of 2.5 mg/kg.
4. More specific and comprehensive cell labeling can be achieved with genetically encoded fluorescent tags (e.g., green fluorescence protein (GFP)) or antibody-based labeling, including for neutrophils (e.g., a phycoerythrin-conjugated antibody to Ly6G, clone 1A8) and for cell nuclei (e.g., 4′,6-diamidino-2-phenylindol).

2.3 Murine Model

1. Mouse model: In our experiment C57BL/6J male mice, aged between 13 and 17 weeks were used. However, any mouse type (C57BL/6J, ApoE$^{-/-}$, LDLr$^{-/-}$, etc.) could be employed.
2. Surgical setup: Standard rodent animal surgical equipment for vascular dissection, nylon suture for ligation (7–0, 0.5 metric, black monofilament), stereomicroscope.
3. Inhalational anesthesia: 1–2% isoflurane. When the MPM does not allow incorporation of an inhalational anesthesia setup, use intraperitoneal Ketamine/xylazine injection at a dosage of 80/12 mg/kg.
4. Homeothermic monitoring system: Closed loop body temperature control system for mouse model with heating pad sized according to the microscopy setup.
5. Retro-orbital injection: A 27-gauge needle with a 1 mL syringe attached.

2.4 Epifluorescence Microscope

1. A commercially available epifluorescence microscope (EFM) is the Nikon Eclipse 90i (Nikon Imaging, Japan). It allows for real-time microscopy (image and video acquisition) in samples ranging from thin tissue to small animals. Illumination

wavelengths are selected via a range of filter sets (e.g., allowing for excitation in the FITC channel at 475/35 nm).

2. The selected lower-magnification EFM allows for fluorescence and bright-field imaging to provide a rapid roadmap for fluorescence signals, which is particularly useful for facilitating MPM studies, as it provides a "big picture" view of labeled vascular pathology, and allows one to focus on specific regions for high-resolution, high-magnification MPM studies.
3. Software for image acquisition and analysis is provided by the manufacturer (Nikon, i-Series control software) (*see* **Note 5**).

3 Methods

As a prelude to murine atherosclerosis studies employing anticipated commercially available gating software in the future, a murine deep venous thrombosis (DVT) model is established in the femoral/saphenous vein and induced by combined ligation (flow restriction) and light irradiation [19]. This model generates rapid platelet and leukocyte trafficking in a model relevant to human stasis DVT, as well as atherothrombosis. Intravital MPM is then performed with two-photon excitation fluorescence (2PEF) in the selected channels for functional imaging as well as in the SHG channel for monitoring vessel morphology via collagen. Labeled platelets and leukocytes accumulate at the freshly induced thrombus which is observable (e.g., as negative contrast following FITC dextran injection). In contrast to CFM, MPM offers prolonged imaging without photobleaching at greater imaging depths while providing 2D and 3D image acquisition at high frame rates. The step-by-step methods are explained in the following sections.

3.1 Mouse Preparation

1. Obtain institutional animal committee approval for planned experiments and follow animal handling protocols that apply at your laboratory.
2. Induce inhalational anesthesia (1–2% isoflurane) if applicable or induce anesthesia with Ketamine/xylazine injection (IP, 80/12 mg/kg). Inject maintenance doses when necessary and in conjunction with laboratory protocol (e.g., every 30–45 min; *see* **Note 6**).
3. Immobilize and fixate mouse in dorsal position on a mobile platform (*see* **Note 4**). Supply external heating to 37 °C as necessary.
4. Applying the surgical setup, make a surgical incision longitudinally from the mid-inguinal ligament to the knee. Excise the exposed body of adipose tissue and connective tissue to permit vessel exposure of femoral/saphenous vein and artery.

5. Separate the femoral vein carefully from the concomitant femoral artery and nerve proximal of the venous bifurcation, and ligate with a nylon suture to induce complete vessel occlusion, resulting in marked decrease in blood flow at the saphenous vein [19] (*see* **Note 7**).
6. Intraorbital injection is employed by gently applying pressure onto the left periorbital area and exposing the left eye. A 27-gauge needle with a 1 mL syringe is attached into the orbital venous sinus with the needle facing forward at a 45° angle. Inject desired molecular, cellular and angiographic imaging agents as detailed next and permit circulation for 10 min prior to imaging.
7. To visualize the blood lumen of target arteries and veins, inject the exogenous fluorophore FITC-dextran via intravenous or retro-orbital injection, and permit circulation for 10 min prior to imaging.
8. To visualize circulating and trafficking leukocytes and platelets, coinject the exogenous fluorophore Rhodamine 6G in the same manner as FITC-dextran.
9. Transfer mouse to the MPM suite while keeping the femoral artery surgically exposed but moist and light-protected.

3.2 Thrombus Model

1. On the EFM microscope, choose a relatively high NA objective lens with increased irradiance for thrombus formation (e.g., Nikon Plan Fluor, 10×, NA 0.3). Choose objective lens for larger region-of-interest (ROI) when (bright-light) imaging (Nikon Plan Fluor, 4×, NA 0.13).
2. Localize and determine a suitable ROI of the saphenous vein (area with minimal branching) using bright-light microscopy at the lowest reasonable intensity setting to avoid photobleaching. Centralize the field of view (FOV) in the ROI and match the axial position of the focal plane around 100 μm below the vessel dome along the *Z* axis. Record this FOV position in advance for MPM imaging.
3. Apply fluorescence imaging in the FITC-channel (Excitation 475/35 nm) over the ROI as long as necessary to induce thrombus formation via light irradiation. Adjust light intensity directly or by ND filter settings to around 2.5 mW (*see* **Note 8**).
4. Observe thrombus induction and formation in the EFM image feed and halt irradiation once thrombus reaches desired extent and/or volume (Fig. 1) [20].
5. Transfer mouse to the MPM suite and keep the vein surgically exposed as well as moist and light-protected.

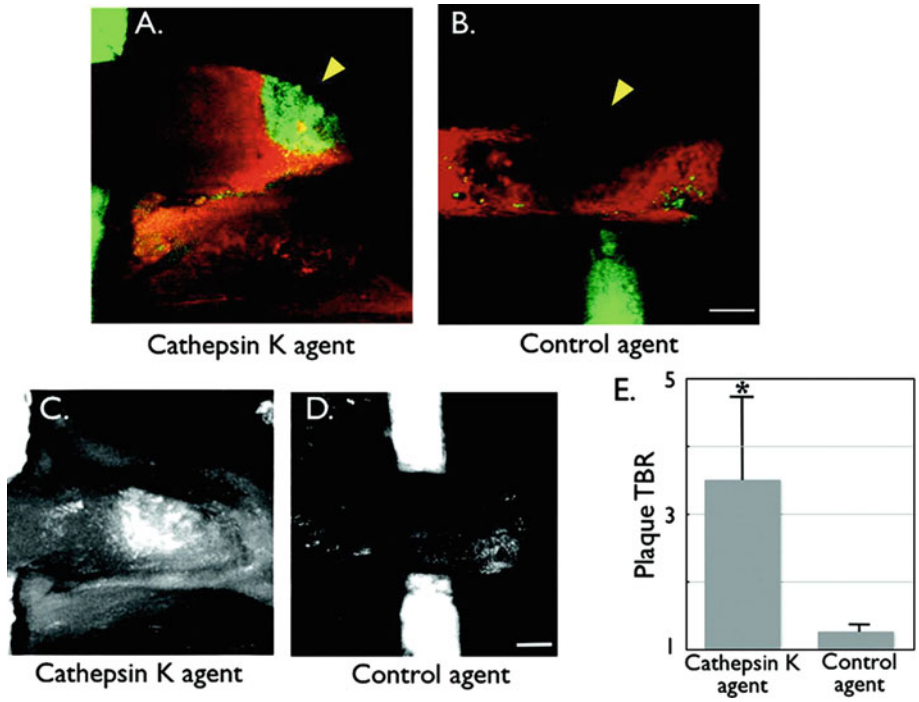

Fig. 1 In vivo imaging of Cathepsin K (CatK) activity in carotid atherosclerotic plaques of ApoE$^{-/-}$ mice. Atheroma were surgically exposed and then underwent laser scanning intravital fluorescence microscopy 24 h after injection of the CatK or control K imaging agent (5 nmol). Multiwavelength imaging allowed detection of the CatK signal and a spectrally resolved intravascular agent injected just before imaging. A cylindrical Cy5.5 dye-filled phantom (green) was placed under the carotid artery to facilitate localization. (**a**) Fusion in vivo image of a carotid vessel (5× magnification; 13 × 13-μm in-plane resolution; 10-μm slice thickness) demonstrating focal CatK signal (green) in an atherosclerotic lesion (arrowhead). The lesion was confirmed to be within the vascular space as defined by the intravascular agent (red). (**b**) Fusion image of a carotid plaque (arrowhead) in the control group demonstrating minimal NIRF signal in the CatK channel. The plaque appears as a signal void or filling defect within the vascular space. (**c**, **d**) Projection images of the carotid plaques after injection of the CatK imaging agent (**c**) or control agent (**d**), demonstrating greater plaque TBRs (**e**) in the CatK vs. control group (*$P < 0.05$). Projection images processed and windowed identically. Scale bar, 250 μm. (Reproduced from ref. 20 with permission from Wolters Kluwer Health, Inc.)

3.3 Multiphoton Microscopy

1. Place the surgically exposed animal into the MPM setup and situate the equipment for fixation, body heating, and anesthesia. Position and orient the animal to match the capabilities of the MPM system (*see* **Note 9**). Apply optical matching medium onto the ROI and couple the water immersion objective (*see* **Note 10**).
2. Localize the ROI determined on the EFM with bright-light microscopy or by direct observation via the eyepieces. Conduct a first 2PEF scan in the FITC channel to match the FOV with the desired ROI (i.e., the proximal edge of thrombus formation). Adjust the focal plane axially (i.e., to 100 μm below the vessel dome; anterior topmost surface).

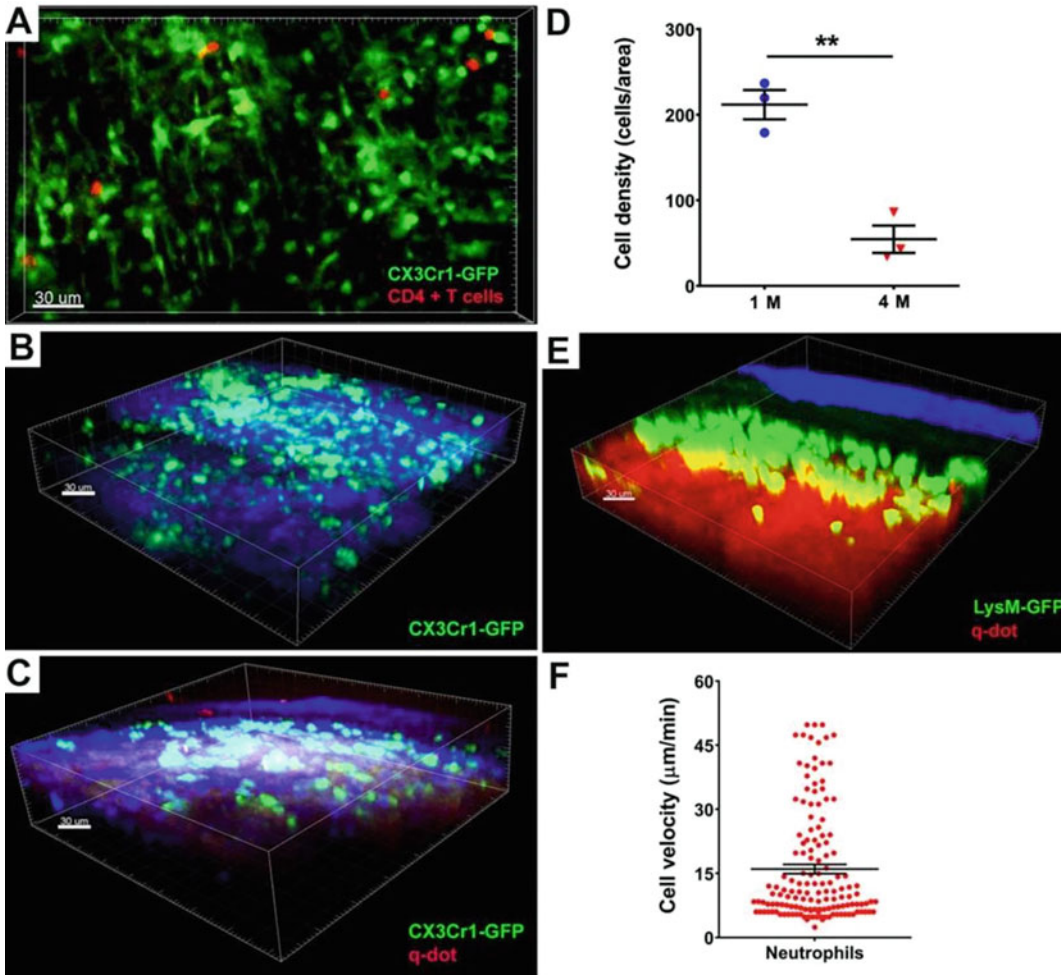

Fig. 2 Intravital two-photon imaging and PET-based scanning reveal immune cell behavior in aortic arch grafts. (**a**) Representative picture showing monocytes/macrophages (green) and CD4+ T cells (red) in CBA aortic arch grafts 1 week after transplantation into B6 CX3CR1 GFP/+ mice ($n = 3$) (GFP, green fluorescent protein). Male → male strain combination is depicted in this figure. Monocytes/macrophages (green) in male B6 ApoE$^{-/-}$ aortic arch grafts (**b**) 1 month ($n = 3$) and (**c**) 4 months ($n = 3$) after transplantation into male B6 CX3CR1 GFP/+ mice. (**d**) Reduction of density of CX3CR1 GFP+ cells within regressing plaques (212 ± 17 cells/area (220 × 240 μm^2) at 1 month (blue) vs. 54 ± 16 cells/area at 4 months (red), $n = 3$, $^{**}p < 0.01$). (**e**) Representative image of male B6 ApoE$^{-/-}$ aortic arch grafts transplanted into male B6 LysM-GFP mice 1 day after engraftment ($n = 3$). Collagen appears blue due to second harmonic generation. Blood vessels are labeled red after injection of quantum dots. Scale bars, 30 μm. (**f**) Velocity of LysM-GFP cells in male B6 ApoE$^{-/-}$ aortic arch grafts 24 h after engraftment (mean velocity is 16.02 μm/min ± 1.08); analyzed cells pooled from 3 independent experiments. (Reproduced from ref. 21 with permission from Wolters Kluwer Health, Inc.)

3. Select target fluorescence channels by adjusting the wavelength (s) of the excitation laser(s) and the respective PMT channel. Select filters or filter sets according to the targeted fluorescence and SHG/THG channels (*see* **Note 11**). Utilizing live image

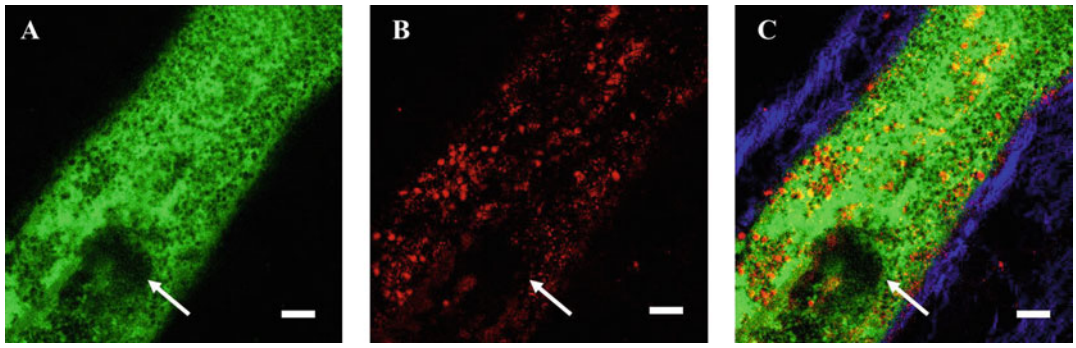

Fig. 3 Proximal edge of an acute stasis deep vein thrombosis (DVT) formed in the murine saphenous vein following fluorescein isothiocyanate (FITC) injection and FITC-based light illumination for 60 s. (**a**) FITC-dextran (green) image of vessel lumen and thrombus (white arrow) and leukocytes appearing as negative-contrast. (**b**) Leukocytes and platelets visualized by Rhodamine 6G (red) injected after FITC-light thrombus induction. (**c**) Merged FITC-dextran, Rhodamine 6G and SHG (blue) signals, with SHG visualizing primarily type I collagen in the vessel wall. Scale bar, 50 μm

read-out, fine-tune acquisition settings for each channel (i.e., laser intensity, sensitivity, gain and offset) (*see* **Note 12**).

4. Adjust the scan size of the ROI and the scan speed for image acquisition. Slower scan speeds usually increase SNR while minimized scan areas and fast scan speeds are favorable for live imaging of leukocyte dynamics.
5. Acquire 2D data (i.e., images of stacks with multiple channels simultaneously, in single shot or continuous mode) (Fig. 2). Fine-tune image settings as needed to compensate for varying contrast inherent to the sample or caused by photobleaching.
6. For 3D image acquisition, use 2D scans to find the upper and lower boundaries of the focal planes accessible. Adjust the focal plane axially to match the vessel dome to determine the upper boundary as primary reference point. Determine the lower boundary as the axial plane where signal strength and resolution are yet undistorted. Set boundaries for scanning Z series accordingly and choose step size depending on whether high acquisition speed or high definition data is desired.
7. Acquire 3D data by performing a Z series scan. Adjust spatial scan dimensions to improve acquisition performance and record relevant 3D data [21] (Fig. 3).
8. The study of atherosclerosis or thrombosis induced in larger arteries (e.g., in the carotid artery) for 2D and 3D image acquisition may be impeded by tissue movement (i.e., by cardiac and respiratory movement). If available, apply cardiorespiratory synchronization with prospective gating to overcome this limitation [16] (*see* **Note 13**).

3.4 MPM Image Analysis

1. The Olympus MPM software comes with potent tools for image analysis and data management. For image analysis independent of the MPM platform, ImageJ has been established as freely accessible standard software.
2. Export or transfer data to a format accessible by ImageJ or use a Plugin provided by the manufacturer to convert the format (*see* **Note 5**). Similar to TIFF images, the Olympus OIR image format stores data as hyperstack. Sort the data depending on the study at hand (e.g., by merging data acquired in multiple specific channels or by excluding a specific channel from the data set).
3. Use ImageJ functionality (z-Project) or plugins (3D Viewer, Volume Viewer) to create 3D visualizations of the loaded stack.
4. Use ImageJ ROI tool to measure the signal intensity at a specific point or the average signal intensity in a specific area as well as in a region without or with little apparent signal (background). Use these data to determine the respective SNR in each channel or the overall SNR for a given Z stack.

3.5 Correlative Fluorescence Microscopy

1. Perform correlative fluorescence microscopy of fresh-frozen cryocut sections (*see* **Note 14**) of the thrombus model to corroborate MPM data (e.g., the localization of fluorophores to specific cells and regions) as this step is critical for result interpretation. Moreover, it allows deeper assessment of areas below the depth-sensing capability of MPM (i.e., depths >80–100 μm).
2. Perfuse the femoral/saphenous vein after sacrifice by gently injecting 20 mL of cold PBS from the left ventricle. Then excise the femoral/saphenous vessels with their surrounding tissue and directly embed as fresh-frozen tissue into optimal cutting temperature compound and suspend to −80 °C.
3. Cryocut serial 5–10 μm sections of fresh-frozen excised sample and transfer to a dedicated confocal fluorescence microscope or EFM (*see* **Note 14**).
4. Acquire fluorescence images in the respective channels used during MPM and/or in endogenous and exogenous channels of histology labels (*see* **Note 15**).
5. Correlate histopathology to confirm specificity of functional and morphological data obtained by MPM.

4 Notes

1. Prior to planning the studies, it is important to observe that the selection of fluorophores for 2PEF matches the laser excitation in MPM/2PEF. The upper wavelength cut-off of around

1300 nm (depending on the system and/or manufacturer) commonly comes hand-in-hand with decreasing laser power at higher wavelengths. While theoretically enabling the use of fluorophores with excitation wavelengths of up to 650 nm, the utilization of fluorophores for 2PEF above around 600 nm should be carefully matched to the spectral distribution of laser power at hand. Alternatively, excitation wavelengths in the high visible range and the NIR may be utilized for single photon absorption fluorescence for such fluorophores if the MPM/ the optical system layout allows for it.

2. In contrast to CFM and epifluorescence microscopes, commercial MPM setups may require guidance/service through the manufacturer when refitting respective dichroic/filter elements/sets to avoid damage (e.g., to the PMTs).
3. A lower magnification objective (e.g., 10×) may be applied to achieve longer working distances, albeit at lower photon collection rate and reduced SNR. Objectives with longer working distances may be selected to help acquire images in a given ROI of a specimen that would otherwise be spatially inaccessible (e.g., when laterally masked by the abdomen in a mouse model). For imaging thin specimen prepared with cover glass as well as deep tissue ROIs in intravital studies on the same setup, an objective with correction ring should be selected (e.g., for correcting 0–0.23 mm of cover glass).
4. The MPM system might not come equipped with an XYZ stage suitable for intravital imaging (e.g., in terms of axis movement). Here, a set of (additional) manual XY(Z) stages fixated atop the XYZ platform inherent to the MPM system may allow for reproducible sample orientation, serial studies and movement between spatially separated ROIs. Such a removable platform may also be used for the permanent installation of equipment necessary for animal handling (i.e., mouse fixation), animal heater system and tubing for isoflurane anesthesia.
5. Most manufacturers provide software for the conversion of image file types. Olympus provides a plugin for ImageJ to load vsi/oir/omp2info file formats accessible (e.g., at https://imagej.net/OlympusImageJPlugin). Nikon provides a plugin for ImageJ to load nk2 file formats accessible e.g., at https://imagej.nih.gov/ij/plugins/nd2-reader.html.
6. In case isoflurane gas anesthesia is utilized, be aware of increased image artifacts caused by arterial pulsation due to the vasodilatory actions of isoflurane.
7. For survival studies and to keep the target thrombus or atheroma physiologically preserved, minimal amounts of PBS or deionized (DI) water need to be applied to the tissue throughout the procedure.

8. Depending on the mouse model, the EFM light source, the duration of EFM illumination and other variables, the duration for thrombus induction will vary and can take up to several minutes. For example, an irradiation of 6 mW/mm^2 will cause thrombus induction at around 3–4 min. Record irradiation duration and power to find the optimal ratio between illumination power setting and irradiation duration in an iterative process and adjust settings according to your system parameters.
9. MPM systems commonly exhibit "slow" and "fast" axis modes, giving the possibility to select between high definition (galvo) and high speed (resonant) scanning, respectively. This may affect acquisition speed of individual ROIs and it is important to orientate the animal accordingly prior to imaging and to, for example, match the "fast" axis with the lateral orientation of the target vessel.
10. Deionized (DI) water may evaporate quickly and needs to be reapplied periodically for prolonged imaging. An alternative optical matching medium to DI water is lubricant eye gel (GenTeal, Alcon, Switzerland). Another alternative to DI water is isotonic saline solution or PBS, as water can cause tissue swelling due to osmotic shifts.
11. Depending on how sophisticated the applied MPM is, wavelength and filter selection can be performed indirectly by a dye selector embedded in the control software.
12. Unnecessary photobleaching can be avoided by fine-tuning channel parameters in a region adjacent to the ROI (i.e., at the distal end of the thrombus). When fine-tuning, avoid sensor-saturation and adjust laser and PMT settings to maximize dynamic range. Save acquisition settings for subsequent imaging of similar models.
13. Minor vessel motions may be minimized by using a mechanical stabilizer, such as a fixated cover glass. For imaging major arteries or when imaging at ROIs inflicted by respiratory movement, gating triggered by mechanical ventilation and cardiac pacing can be considered. Note that nonsurgical models of atherosclerotic plaques visualizing the behavior of leukocytes in atherosclerotic branches in murine carotid artery have been reported. Here, combined cardiac triggering and image post-processing was applied to correct for motion artifacts [22, 23].
14. Fresh-frozen cryocut sectioning: After sacrifice, DVT and control sections of the vessels are harvested, thoroughly washed in PBS, and frozen in an optimal cutting temperature compound on dry ice. The frozen tissue is then cut into 5–10 μm thick sections using an embedded cryocutting microscopy system. Sections are placed on microscopy slides and assessed by

fluorescence microscopy, or air-dried and processed for histological and immunohistochemistry staining.

15. Histology labels are, for example, hematoxylin and eosin (H&E stain) for general morphology and the Carstair's method for staining collagen as well as visualizing vessel wall morphology.

Acknowledgments

The authors are grateful to Emily Cronin-Furman, PhD, for helpful discussions on multiphoton microscopy. The work presented in this chapter was funded, in part, by grants NIH R01 HL150538 and R01 HL137913 to F.A.J..

References

1. Mulder WJM, Jaffer FA, Fayad ZA, Nahrendorf M (2014) Imaging and nanomedicine in inflammatory atherosclerosis. Sci Transl Med 6:1–12. https://doi.org/10.1126/scitranslmed.3005101
2. Badimon L, Vilahur G (2014) Thrombosis formation on atherosclerotic lesions and plaque rupture. J Intern Med 276:618–632. https://doi.org/10.1111/joim.12296
3. Brown EB, Campbell RB, Tsuzuki Y, Xu L, Carmeliet P, Fukumura D, Jain RK (2001) *In vivo* measurement of gene expression, angiogenesis and physiological function in tumors using multiphoton laser scanning microscopy. Nat Med 7:864–868
4. Jaffer FA (2011) Intravital fluorescence microscopic molecular imaging of atherosclerosis. Methods Mol Biol 680:131–140. https://doi.org/10.1007/978-1-60761-901-7_9
5. Choi M, Kwok SJJ, Yun SH (2015) *In vivo* fluorescence microscopy: lessons from observing cell behavior in their native environment. Physiology 30:40–49. https://doi.org/10.1152/physiol.00019.2014
6. Taqueti VR, Jaffer FA (2013) High-resolution molecular imaging via intravital microscopy: illuminating vascular biology *in vivo*. Integr Biol (United Kingdom) 5:278–290. https://doi.org/10.1039/c2ib20194a
7. Ntziachristos V (2010) Going deeper than microscopy: the optical imaging frontier in biology. Nat Methods 7:603–614. https://doi.org/10.1038/nmeth.1483
8. Zipfel WR, Williams RM, Webb WW (2003) Nonlinear magic: multiphoton microscopy in the biosciences. Nat Biotechnol 21: 1369–1377. https://doi.org/10.1038/nbt899
9. Megens RTA, Reitsma S, Schiffers PHM, Hilgers RHP, De Mey JGR, Slaaf DW, oude Egbrink MGA, van Zandvoort MAMJ (2007) Two-photon microscopy of vital murine elastic and muscular arteries: combined structural and functional imaging with subcellular resolution. J Vasc Res 44:87–98. https://doi.org/10.1159/000098259
10. Oppi S, Lüscher TF, Stein S (2019) Mouse models for atherosclerosis research—which is my line? Front Cardiovasc Med 6:1–8. https://doi.org/10.3389/fcvm.2019.00046
11. Breslow JL (1996) Mouse models of atherosclerosis. Science (80-) 272:685–688. https://doi.org/10.1126/science.272.5262.685
12. Emini Veseli B, Perrotta P, De Meyer GRA, Roth L, Van der Donckt C, Martinet W, De Meyer GRY (2017) Animal models of atherosclerosis. Eur J Pharmacol 816:3–13. https://doi.org/10.1016/j.ejphar.2017.05.010
13. Maresca D, Jansen K, Renaud G, den Dekker W, van Soest G, Li X, Zhou Q, Cannata J, Shung KK, van der Steen AFW (2012) Intravascular ultrasound chirp imaging. Appl Phys Lett 100(043703):10–13. https://doi.org/10.1063/1.3679375
14. Rademakers T, Douma K, Hackeng TM, Post MJ, Sluimer JC, Daemen MJAP, Biessen EAL, Heeneman S, van Zandvoort MAMJ (2013) Plaque-associated vasa vasorum in aged apolipoprotein E-deficient mice exhibit proatherogenic functional features *in vivo*. Arterioscler Thromb Vasc Biol 33:249–256. https://doi.org/10.1161/ATVBAHA.112.300087

15. Megens RTA, Bianchini M, Schmitt MMN, Weber C (2015) Optical imaging innovations for atherosclerosis research: multiphoton microscopy and optical nanoscopy. Arterioscler Thromb Vasc Biol 35:1339–1346. https://doi.org/10.1161/ATVBAHA.115.304875
16. Vinegoni C, Aguirre AD, Lee S, Weissleder R (2015) Imaging the beating heart in the mouse using intravital microscopy techniques. Nat Protoc 10:1802–1819. https://doi.org/10.1038/nprot.2015.119
17. Haka AS, Potteaux S, Fraser H, Randolph GJ, Maxfield FR (2012) Quantitative analysis of monocyte subpopulations in murine atherosclerotic plaques by multiphoton microscopy. PLoS One 7:e44823. https://doi.org/10.1371/journal.pone.0044823
18. Herr N, Mauler M, Bode C, Duerschmied D (2015) Intravital microscopy of leukocyte-endothelial and platelet-leukocyte interactions in mesenterial veins in mice. J Vis Exp 2015: 1–6. https://doi.org/10.3791/53077
19. Okano M, Hara T, Nishimori M, Irino Y, Satomi-Kobayashi S, Shinohara M, Toh R, Jaffer FA, Ishida T, Hirata K (2020) *In vivo* imaging of venous thrombus and pulmonary embolism using novel murine venous thromboembolism model. JACC Basic to Transl Sci 5:344–356. https://doi.org/10.1016/j.jacbts.2020.01.010
20. Jaffer FA, Kim DE, Quinti L, Tung C-H, Aikawa E, Pande AN, Kohler RH, Shi GP, Libby P, Weissleder R (2007) Optical visualization of cathepsin K activity in atherosclerosis with a novel, protease-activatable fluorescence sensor. Circulation 115:2292–2298. https://doi.org/10.1161/CIRCULATIONAHA.106.660340
21. Li W, Luehmann HP, Hsiao H-M, Tanaka S, Higashikubo R, Gauthier JM, Sultan D, Lavine KJ, Brody SL, Gelman AE, Gropler RJ, Liu Y, Kreisel D (2018) Visualization of monocytic cells in regressing atherosclerotic plaques by intravital 2-photon and positron emission tomography–based imaging—brief report. Arterioscler Thromb Vasc Biol 38: 1030–1036. https://doi.org/10.1161/ATVBAHA.117.310517
22. McArdle S, Chodaczek G, Ray N, Ley K (2015) Intravital live cell triggered imaging system reveals monocyte patrolling and macrophage migration in atherosclerotic arteries. J Biomed Opt 20:1. https://doi.org/10.1117/1.JBO.20.2.026005
23. Chèvre R, González-Granado JM, Megens RTA, Sreeramkumar V, Silvestre-Roig C, Molina-Sanchez P, Weber C, Soehnlein O, Hidalgo A, Andres V (2014) High-resolution imaging of intravascular atherogenic inflammation in live mice. Circ Res 114:770–779. https://doi.org/10.1161/CIRCRESAHA.114.302590

Chapter 41

Localization of Long Noncoding RNA in Formalin-Fixed, Paraffin-Embedded Vascular Tissue Using In Situ Hybridization

Jessica P. Scanlon, Andrew H. Baker, and Judith C. Sluimer

Abstract

In situ hybridization (ISH) is a technique for the detection of the location of RNA within a tissue of interest. This process uses oligonucleotides with complementary sequences to bind to the target RNA, and colorimetric detection to allow for the visualization of this binding. The process of ISH means that the specific location of the RNA in question can be detected, including in which cell types it is present, and the intracellular location. In the case of long noncoding RNA (lncRNA), which do not lead to the production of proteins, ISH is essential for tissue localization. Moreover, RNA abundance is often lower than for protein-coding genes, thus necessitating enhanced detection through double-digoxigenin (DIG) labeling of the probes. Here, we describe the theory and practicalities of performing ISH for lncRNA, with particular reference to vascular tissues.

Key words Long noncoding RNA, In situ hybridization, Vascular, Localization

1 Introduction

In situ hybridization (ISH) is a technique that allows for the detection of the location of RNA within a tissue of interest. ISH is a similar process to immunohistochemistry (IHC), which detects the presence and location of proteins within a tissue sample, but with ISH detecting RNA instead of protein. This makes ISH a useful tool for analyzing gene expression within the context of the tissue itself. ISH can be performed on fixed cells or tissue samples, each of which come with their own optimizations. In this chapter, we will discuss ISH in the setting of vascular tissues, although this protocol can be utilized across all tissue samples.

ISH is an invaluable tool particularly for noncoding RNAs, where the RNA itself carries out its actions, and is not translated into protein, and the traditional approaches such as IHC cannot be utilized. ISH has therefore been optimized for noncoding RNA

Dipak P. Ramji (ed.), *Atherosclerosis: Methods and Protocols*, Methods in Molecular Biology, vol. 2419,
https://doi.org/10.1007/978-1-0716-1924-7_41,
© The Author(s), under exclusive license to Springer Science+Business Media, LLC, part of Springer Nature 2022

approaches [1]. While historically noncoding RNAs were considered "junk" RNA, there is now an increasing body of evidence of functional importance for a range of noncoding RNAs (such as microRNAs, lncRNA, PIWI-interacting RNAs, small nucleolar RNAs), which are often highly tissue and cell type specific, and have roles in human diseases [2]. LncRNA have been described more recently than the more well-studied miRNAs. LncRNAs are greater than 200 nucleotides in length, can form secondary structures and can impact gene regulation through a variety of functions (e.g., sponges, guides, decoys). Interestingly, noncoding RNAs are increasingly being identified as having roles in vascular disease [3, 4], including atherosclerosis [5, 6] and myocardial infarction [7–9]. These emerging roles means that techniques to detect their location within tissues, be this spatially or in specific cell types, are increasing in utility.

ISH was first established as a technique in 1969 [10, 11], utilizing complementary oligonucleotides (probes) radiolabeled with stable isotopes (such as ^{35}S, ^{125}I, ^{32}P). Since then, this technique has been refined and optimized, and has been adapted for the use of non–radioactively labeled probes, such as biotinylated, tyramide, and digoxigenin (DIG) probes. As DIG is only found in plants, using this method ensures there will be no background cross reactivity with animal or human tissues. DIG-labeled probes also have the benefit of allowing for histological analysis of the tissue at the same time, which is not possible when fluorescence detection systems are used [12]. Additionally, low RNA abundance of lncRNA requires double-DIG labelling of probes to amplify the signal above the detection threshold. In this chapter, we will outline the protocol for double-DIG-labeled RNA probes. This process involves the DIG probes being recognized by an anti-DIG-alkaline phosphatase (AP) conjugate, and for the AP to be reduced into a purple precipitate via nitro blue tetrazolium/5-bromo-4-chloro-3-indolyl phosphate (NBT/BCIP) (*see* Fig. 1).

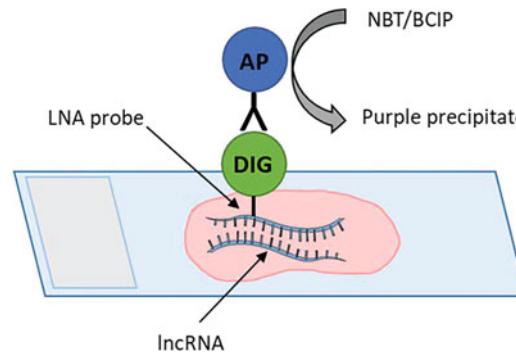

Fig. 1 Schematic diagram of in situ hybridization using double-DIG-labeled LNA probe. *NBT/BCIP* nitro blue tetrazolium/5-bromo-4-chloro-3-indolyl phosphate

A key component of ISH is the generation of a Locked Nucleic Acid (LNA) probe with a sequence that is complimentary to the RNA target. This will allow the complimentary sequences to bind wherever the target is found in situ within the tissue, and this location detected. The design of the LNA probe is of great importance, and can be carried out through commercial companies, which will take into account key parameters in the RNA of interest (length of target sequence, guanine and cytosine content, secondary structure) and design an efficient and specific probe accordingly. The tissues in question need to be formalin-fixed, paraffin-embedded (FFPE) sectioned on a microtome that are subsequently mounted onto slides. This allows preservation of the cellular architecture of the tissue in question, and visualization of the presence of your protein or RNA of interest within this context.

Due to the importance of the surrounding cellular context that ISH provides, ISH is often coupled with IHC, so that RNA localization to specific tissue and cell types can be identified. This marker analysis can be performed on serial sections, or on the same tissue sections following ISH. The latter allows for a more precise analysis of the presence or absence of colocalization of the ISH RNA target and IHC protein target, as shown in the case of the lncRNA PELATON in atherosclerotic tissue [6].

2 Materials

All steps prior to and including probe hybridization (*see* **step 3.3**) need to be carried out under RNase-free conditions (*see* **Note 1**). To do so, use diethyl pyrocarbonate (DEPC)-treated deionized water for all reagents, and wipe down all surfaces and plasticware with RNaseZAP prior to use. Use analytical grade reagents. Prepare and store all reagents at room temperature (unless indicated otherwise). Follow all waste disposal regulations when disposing of waste materials.

2.1 Equipment

1. Fume hood.
2. Light microscope.
3. Slides and coverslips.
4. Slide racks and containers.
5. Slide chamber.
6. Forceps.
7. Hybridization oven, incubator, or hot plate.

2.2 Reagents

1. Formalin-fixed, paraffin-embedded sections on coated glass slides.
2. RNaseZAP.

3. DEPC-treated water: In a fume hood, add 1 ml DEPC to 1 L of H_2O. Leave overnight in fume hood, then autoclave before use.
4. Xylene.
5. Ethanol solutions: 100% ethanol, 96% ethanol, and 70% ethanol, all made up using DEPC-treated water.
6. Hydrophobic barrier pen.
7. Phosphate buffered saline (PBS): 0.01 M phosphate buffer, 0.0027 M potassium chloride, 0.137 M sodium chloride, pH 7.4 in DEPC-treated water.
8. 1× PBS-Tween (PBS-T): Add 1 mL of Tween to 1 L of 1× PBS and mix well.
9. Proteinase K: Dilute as required (*see* **Note 2**) in DEPC PBS.
10. 1× Hybridization buffer: Using 2× Qiagen hybridization buffer stock, dilute 1:1 in DEPC-treated water.
11. Double-digoxigenin (DIG)-labeled locked nucleic acid (LNA) Probe: Reconstitute probe as detailed on the manufacturer's sheet. Dilute to desired concentration (*see* **Note 3**) in 1× Hybridization buffer.
12. Rubber cement (e.g., Marabu Fixogum).
13. 5× Saline-sodium citrate buffer (SSC): 0.15 M sodium chloride, 0.015 M sodium citrate (typically prepared by diluting 20× SSC buffer in DEPC-treated water).
14. Maleic acid buffer: 100 mM maleic acid and 150 mM NaCl, pH 7.5.
15. 1× Blocking buffer: 10× blocking buffer (DIG wash and block buffer kit), dilute in Maleic acid buffer. Alternative blocking reagent: Tris-buffered saline (8g/L NaCl, 0,605g/L Tris, adjust pH with HCL to 7.4–7.6)with 1% BSA, 10% sheep serum.
16. Anti-DIG-AP: Anti-DIG antigen binding fragments (Fab) fragments conjugated to alkaline phosphatase (AP). Dilute to 1:500 in 1× blocking buffer.
17. AP Detection reagent: Dissolve 1 nitro blue tetrazolium/5-bromo-4-chloro-3-indolyl phosphate (NBT/BCIP) AP Detection tablet into 10 mL water, producing concentrations of 0.4 mg/mL NBT, 0.19 mg/mL BCIP, 100 mM Tris buffer pH 9.5, and 50 mM $MgSO_4$. Add 1 drop of 125 nM levamisole to every 10 mL of reagent. Keep away from light prior to use (*see* **Note 4**).
18. Nuclear counter stain: nuclear fast red or equivalent.
19. Mounting media: Pertex or similar xylene-based mounting media.

3 Methods

All steps prior to and including probe hybridization need to be carried out under RNase-free conditions (*see* **Note 1**), meaning that all surfaces and plasticware should be wiped down with RNaseZAP prior to use. Set either a hot plate or incubator to 37 °C and another incubator to the hybridization temperature (*see* **Note 5**), before starting the protocol. To ensure tissue integrity is maintained, it is essential to treat the tissues gently throughout (*see* **Note 6**).

3.1 Slide Preparation

1. The slides with tissue mounted sections should be placed in a slide rack and submersed fully in Xylene for 5 min in a fume hood to dewax the paraffin surrounding the tissue.
2. The slides are then incubated in ethanol solutions with descending concentration for 5 min each to rehydrate the sections, starting with 100% ethanol, followed by 96%, and then 70% ethanol.
3. Wash the sections in RNase-free water (i.e., DEPC-treated water) followed by another wash in PBS for 5 min.
4. Use a hydrophobic barrier pen to draw around the tissue section on the slide (*see* **Note 7**).

3.2 Antigen Retrieval

1. Pipette proteinase K onto each tissue section (approx. 30–100 μL dependent on the size of tissue, *see* **Note 8**) and place slides individually on a hot plate or in a humidified slide chamber in an incubator at 37 °C for 1–10 min (*see* **Note 2** for variations on concentration and length of incubation).
2. Remove the slides from the incubator and wash in RNase-free water.
3. Wash the slides in PBS, twice, each for 2 min.

3.3 Probe Hybridization

1. Prepare the double-DIG-labeled LNA Probe and an appropriate negative control probe (*see* **Note 9**) at desired concentration (*see* **Note 3**) in 1× hybridization buffer.
2. To each section, add 30 μL of double-DIG-labeled RNA Probe or control probe, then gently place a coverslip over the tissue section.
3. Seal the coverslip using rubber cement. The rubber cement can be drawn up into a needle and carefully pipetted around the edge of the coverslip to prevent evaporation of the probe (*see* **Note 10**).
4. Place slides in a slide tray/chamber and place in an incubator to hybridize (*see* **Note 5** for temperature and duration).

3.4 Stringency Washes

1. Prewarm the SSC to the hybridization temperature (*see* **Note 11** for SSC concentration).
2. Take the slides out of the incubator, confirm tissues have not dried out during hybridization and carefully remove the rubber cement using forceps without moving the coverslip on the slide surface.
3. Place the slides in the prewarmed SSC and allow the coverslips to float off (*see* **Note 6**).
4. Wash three times in prewarmed SSC for 5 min at hybridization temperature.
5. Take the slides out of the incubator and wash in SSC at room temperature for 5 min, followed by a 5 min wash in 1× PBS.

3.5 Detection

1. Incubate slides with blocking buffer in a humidified slide chamber for 60 min to block unspecific binding.
2. Incubate samples with anti-DIG-AP in a humidified slide chamber (*see* **Note 12** for timings).
3. Wash slides 3 times in 1× PBS-T for 5 min.
4. Add NBT/BCIP AP detection reagent to each section. In this step, the reagents must be protected from light. Check reaction at several timepoints from 30 min to 5 h and stop when reaction has occurred (*see* **Note 13**).
5. To stop the detection reaction, place the slides in H_2O for 5 min.

3.6 Counterstain and Fixation

1. Incubate with a nuclear fast red counterstain for 5 min (*see* **Note 14**).
2. Wash with H_2O to stop the reaction.
3. Dehydrate the slides through ethanol solutions with ascending concentration (70%, 80%, 95%, 100%) for 20 s each (*see* **Note 15**).
4. Place slides in xylene for 2 min. This acts as a clearing agent to remove any traces of alcohols remaining.
5. To mount slides, place one drop of mounting media onto the tissue and place a coverslip on top (*see* **Note 16**).
6. Leave to dry and cure for approximately 24 h prior to visualization on a brightfield microscope to allow for final colors to develop.

4 Notes

1. RNase-free conditions are required until the RNA probe has been hybridized to its target. RNases break down the bonds between nucleotides, and lead to the degradation of RNA. As we need to detect a specific RNA sequence, we need this to be protected, until after the detection has occurred. After this step, the location of the probe is fixed, and therefore RNA degradation will not affect downstream steps in the protocol. To get rid of potential RNases, water is treated with DEPC, and RNaseZAP is used for surfaces.
2. The concentration of proteinase K, as well as the length of incubation can be varied to optimize this process. Proteinase K is utilized to denature the proteins in the tissue sections, unmasking antigens and RNA, which would otherwise go undetected. However, this must be achieved without over digesting, which would lead to tissue degradation and loss of tissue morphology. The nature of the tissue in question is key to this process meaning that optimization is often required for different tissue types, as well as for different fixations. Typically, a starting concentration of 1 μg/mL and testing incubation times between 1 and 10 min at 37 °C is suggested.
3. LNA probes are preferred over traditional DNA or RNA oligonucleotide probes due to superior thermal stability upon hybridization, and hence specificity and sensitivity for detection of very short sequences. The concentration of LNA probe used needs to be optimized for each probe and tissue type. It is recommended to test a range of concentrations to ensure correct localization is detected, but in the absence of unspecific background staining. A suggested starting range is 20–100 nM of probe. An optimal concentration will have no background staining, be present in expected cell types and cellular structures, but will not be detected at high intensity in all cells and structures (overstaining) so that differential expression can be seen. Expected expression patterns may be derived from RNA expression profiles from cell lysates and/or publications. A Ubiquitin C probe may be used as a positive control during first optimization on new tissue types, while a negative control often used is a scramble probe.
4. The NBT/BCIP AP detection reagent is used to detect the presence of AP, which has been added via the anti-DIG-AP antibody. BCIP is the substrate for AP, which is subsequently dephosphorylated, and then oxidized by NBT to produce a blue/purple precipitate, which is further reduced to deepen the produced colour to dark blue/purple. Levamisole is added to quench the endogenous alkaline phosphatase activity, and thus

prevent nonspecific background signals. NBT/BCIP is one of the most sensitive colorimetric substrates and hence should not be replaced with a different substrate, when working with low-abundance lncRNA.

5. The length of time and temperature to be used for probe hybridization can vary and should be optimized for each probe used. Probe time can be varied from 1 to 4 h, or overnight dependent on target abundance and the kinetics of the probe and target. Therefore, incubation time can be tested for optimal results. The hybridization temperature for an LNA probe is approximately 30 °C below its melting temperature. This typically means a 50–60 °C hybridization temperature. Aim for similar numbers when custom designing a probe. Generally, 50 °C is low stringency and 60 °C is high stringency. The temperature in this step causes the probe and target to denature. Lower temperature is less stringent and will allow probe binding to sequences similar to the target RNA and will therefore produce nonspecific binding and results.
6. Tissue sections, especially vascular tissues, are fragile and must be treated gently so that tissue integrity is not lost. When washing, washes must be poured into the dish surrounding the slides, never directly onto the slides, as this may cause the tissues to come away from the slide. When removing coverslips posthybridization (*see* **step 3.4**), the coverslips must be left to float off, otherwise partial tissue sections may come away with the coverslip. Prolonged digestion of the tissue with proteinase K (*see* **Note 2**), will weaken the tissue, making it more likely to disintegrate/fall off the slide. When the tissue sections have wrinkled or folded, nonspecific staining will occur (*see* Fig. 2),

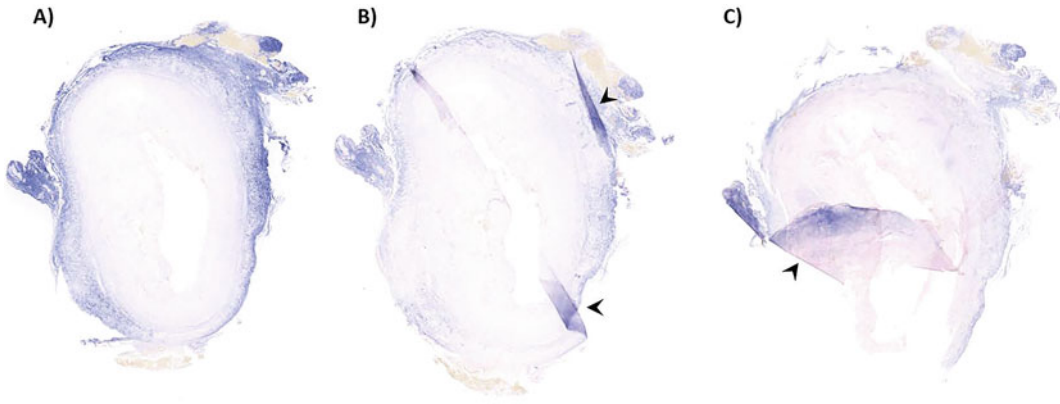

Fig. 2 Tissue integrity in vein graft sections. (**a**) Intact tissue section, (**b**) slight tissue folding, and (**c**) large section of tissue folding. lncRNA stain in purple, nuclear red counterstain. Arrowheads to show areas of tissue folding

meaning that not only will morphology be impaired, but that results will not be accurate.

7. After the tissue sections have been rehydrated, it is essential that they are kept covered with liquid and not allowed to dry out. If the tissue sections dry out, this can lead to protein denaturation, which may affect detection by antibodies and cause nonspecific background staining, as well as reducing the quality of tissue morphology. The use of the hydrophobic barrier PAP pen to draw around the tissue section provides a heat stable and water-repellent barrier, which ensures reagents are localized to the tissue section, aiding retention of liquid surrounding the tissue.
8. Throughout the protocol, the tissue section must be kept hydrated. Dependent on the tissue size, the amount of each reagent needed to cover the tissue section and area enclosed within the wax pen circle will alter, from around 30 to 100 μL. It is best to test this out and keep to the same volume throughout the experiment.
9. A negative control probe is required in addition to the probe against your RNA of interest, to ensure that the staining visualized by your target RNA probe is due to the probe used, and not background or nonspecific binding. Scramble probes are routinely used, which have a sequence which should not identify or bind to any RNA sequences present in your tissue. Tissues hybridized with scramble probe should be clear of purple precipitate, showing only the nuclear counterstain, in contrast to the tissue hybridized with the target probe, which will have both purple precipitate and nuclear counterstain present (*see* Fig. 3).
10. The coverslip must be entirely sealed after probe is added. If not sealed correctly, the high hybridization temperatures will cause liquid to be lost due to evaporation, which will alter the probe concentration and cause tissue drying out, ultimately

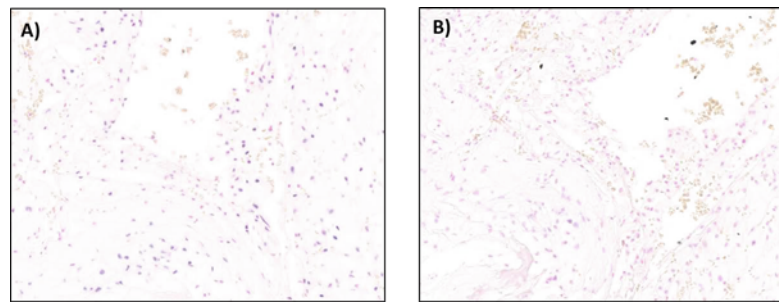

Fig. 3 LncRNA probe versus scramble control in vein graft sections. Tissue sections stained with (**a**) LncRNA probe and (**b**) scramble probe. lncRNA/scramble probe in purple, nuclear red counterstain

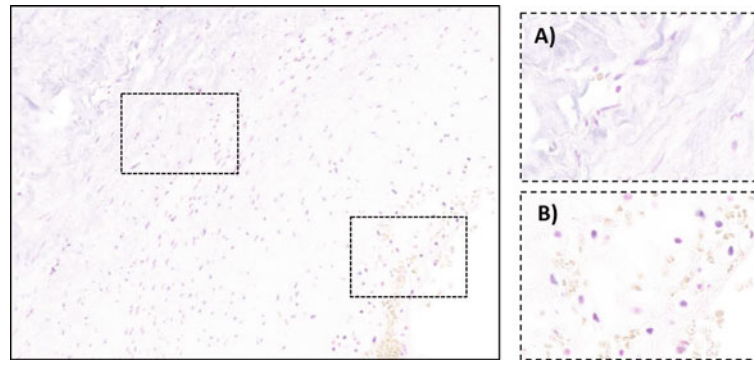

Fig. 4 Specific versus background staining in vein graft sections. LncRNA stain in purple, nuclear red counterstain. Zoomed in images show areas of (**a**) background and (**b**) specific staining

resulting in false-positive staining (*see* **Note 2**). Bubbles must also be avoided when placing the coverslip upon the tissue and probe, as this will result in unstained tissue.

11. The stringency and therefore specificity of binding is determined by both the hybridization steps (*see* **Note 9**) and posthybridization washes. The posthybridization washes are responsible for washing away the nonspecifically bound probe (*see* Fig. 4). The number of base pair matches that are required for the bound probe to remain dictates the stringency. This can be affected by the salt content and temperature of the washes, with increased temperature and reduced salt content both increasing the stringency of the probe. Here, a balance must be maintained between sufficient stringency to remove nonspecific hybridization, but not washing away appropriately bound probe. A good starting point is washing using the hybridization temperature followed by room temperature washes. Furthermore, 5× SSC can be used for all washes, but this can be reduced to 2.5× or less in subsequent washes, to increase the stringency if background probe remains, either at hybridization temperature, or room temperature, dependent on the level of background seen.
12. Incubation with anti-DIG-AP can be performed for a minimum of 30 min at room temperature, but up to overnight at 4 °C. This is often used when probe hybridization was performed for an hour, not overnight, to allow for one overnight stage.
13. The length of time for detection can vary greatly depending on factors such as the probe and tissue type. Visually check from 30 min, every 30 min. NBT/BCIP precipitate is generally slow

to appear but will increase in intensity up to approximately 6 h. You must be careful not to overstain as this will give background staining. To ensure no background staining is present, check the control sections at the same time as those with the target RNA probe and stop all sections if any colour is detected on these, as this will be purely background/nonspecific staining. Background/nonspecific staining can often be seen as a "wash" of purple across the tissue, rather than cellular localization of precipitate as expected with a target RNA probe.

14. A nuclear counterstain is recommended to ensure that cells can be clearly detected. This also means you can determine the difference between nuclear or cytoplasmic staining of your RNA of interest. For the described ISH protocol, a nuclear red counterstain is recommended, as the red stain will contrast the purple ISH stain, unlike hematoxylin, which should not be used, as the two stains are similar in colour, and thus hard to differentiate. A methyl green nuclear stain may be used.
15. NBT/BCIP dissolves slightly in ethanol so you may lose some of the precipitate. Hence use short washes in ethanol.
16. When mounting slides, ensure that no air bubbles are present between the tissue and coverslip, as this will impede the visualization of the tissue. If air bubbles are trapped under the coverslip, gentle pressure can be applied onto the coverslip to move the bubbles aside.

References

1. Jørgensen S, Baker A, Møller S, Nielsen BS (2010) Robust one-day in situ hybridization protocol for detection of microRNAs in paraffin samples using LNA probes. Methods 52(4): 375–381. https://doi.org/10.1016/j.ymeth.2010.07.002
2. Esteller M (2011) Non-coding RNAs in human disease. Nat Rev Genet 12(12): 861–874. https://doi.org/10.1038/nrg3074
3. Hung J, Miscianinov V, Sluimer JC, Newby DE, Baker AH (2018) Targeting non-coding RNA in vascular biology and disease. Front Physiol 9:1655. https://doi.org/10.3389/fphys.2018.01655
4. Uchida S, Dimmeler S (2015) Long noncoding RNAs in cardiovascular diseases. Circ Res 116(4):737–750. https://doi.org/10.1161/circresaha.116.302521
5. Holdt LM, Beutner F, Scholz M, Gielen S, Gäbel G, Bergert H, Schuler G, Thiery J, Teupser D (2010) ANRIL expression is associated with atherosclerosis risk at chromosome 9p21. Arterioscler Thromb Vasc Biol 30(3): 620–627. https://doi.org/10.1161/atvbaha.109.196832
6. Hung J, Scanlon JP, Mahmoud AD, Rodor J, Ballantyne M, Fontaine MAC, Temmerman L, Kaczynski J, Connor KL, Bhushan R, Biessen EAL, Newby DE, Sluimer JC, Baker AH (2020) Novel plaque enriched long noncoding RNA in atherosclerotic macrophage regulation (PELATON). Arterioscler Thromb Vasc Biol 40(3):697–713. https://doi.org/10.1161/atvbaha.119.313430
7. Ishii N, Ozaki K, Sato H, Mizuno H, Susumu S, Takahashi A, Miyamoto Y, Ikegawa S, Kamatani N, Hori M, Satoshi S, Nakamura Y, Tanaka T (2006) Identification of a novel non-coding RNA, MIAT, that confers risk of myocardial infarction. J Hum Genet 51(12):1087–1099. https://doi.org/10.1007/s10038-006-0070-9
8. Zangrando J, Zhang L, Vausort M, Maskali F, Marie PY, Wagner DR, Devaux Y (2014) Identification of candidate long non-coding RNAs in response to myocardial infarction. BMC

Genomics 15(1):460. https://doi.org/10.1186/1471-2164-15-460

9. Vausort M, Wagner DR, Devaux Y (2014) Long noncoding RNAs in patients with acute myocardial infarction. Circ Res 115(7):668–677. https://doi.org/10.1161/circresaha.115.303836
10. Pardue ML, Gall JG (1969) Molecular hybridization of radioactive DNA to the DNA of cytological preparations. Proc Natl Acad Sci U S A 64(2):600–604. https://doi.org/10.1073/pnas.64.2.600
11. Gall JG (2016) The origin of in situ hybridization—a personal history. Methods 98:4–9. https://doi.org/10.1016/j.ymeth.2015.11.026
12. Tanner M, Gancberg D, Di Leo A, Larsimont D, Rouas G, Piccart MJ, Isola J (2000) Chromogenic in situ hybridization: a practical alternative for fluorescence in situ hybridization to detect HER-2/neu oncogene amplification in archival breast cancer samples. Am J Pathol 157(5):1467–1472. https://doi.org/10.1016/s0002-9440(10)64785-2

Part IV

Emerging Techniques in Atherosclerosis Research

Chapter 42

In Vivo Gene Editing in Lipid and Atherosclerosis Research

Marco De Giorgi, Kelsey E. Jarrett, Thomas Q. de Aguiar Vallim, and William R. Lagor

Abstract

The low-density lipoprotein receptor (*Ldlr*) and apolipoprotein E (*Apoe*) germline knockout (KO) models have provided fundamental insights in lipid and atherosclerosis research for decades. However, testing new candidate genes in these models requires extensive breeding, which is highly time and resource consuming. In this chapter, we provide methods for rapidly modeling hypercholesterolemia and atherosclerosis as well as testing new genes in adult mice through somatic gene editing. Adeno-associated viral (AAV) vectors are exploited to deliver the Clustered Regularly Interspaced Short Palindromic Repeats (CRISPR)/Cas9 genome editing system (AAV-CRISPR) to the liver. This tool enables rapid and efficient editing of lipid- and atherosclerosis-related genes in the liver.

Key words CRISPR/Cas9, AAV, Gene editing, Ldlr, Hypercholesterolemia, Atherosclerosis, Lipid, Mouse model

1 Introduction

The low-density lipoprotein receptor (*Ldlr*) and apolipoprotein E (*Apoe*) germline knockout (KO) models are the most used mouse models of atherosclerosis and have provided fundamental insights into pathogenic factors and mechanisms contributing to this disease [1]. *Ldlr* encodes the primary liver receptor for apolipoprotein B (apoB)-containing lipoproteins and mutations in the human *LDLR* gene have been associated with familial hypercholesterolemia [2, 3]. *Apoe* encodes a lipoprotein ligand for lipoprotein receptors such as Ldlr and Ldlr-related proteins (Lrp), thereby promoting the hepatic uptake of lipoproteins from the circulation [4]. As a consequence of the disrupted clearance of atherogenic lipoproteins by the liver, both models develop severe hypercholesterolemia and atherosclerosis when fed a high-fat diet, providing the background for investigating the role of a candidate gene in this disease. However, testing a new gene in atherosclerosis is highly

Dipak P. Ramji (ed.), *Atherosclerosis: Methods and Protocols*, Methods in Molecular Biology, vol. 2419,
https://doi.org/10.1007/978-1-0716-1924-7_42,
© The Author(s), under exclusive license to Springer Science+Business Media, LLC, part of Springer Nature 2022

time- and resource-consuming. First, a KO model for the gene of interest has to be generated. Then, extensive backcrossing to the *C57BL/6J* genetic background is required, followed by breeding to homozygosity with *Ldlr*- or *Apoe*-KO mice, before the actual experiment can begin [1]. This severely limits the rate at which candidate genes can be investigated and is further complicated when conditional alleles and reporter genes are required. Therefore, there is a compelling need to develop new, higher-throughput in vivo models that provide greater flexibility, lower costs and faster completion times to advance our understanding of this complex disease.

Adeno-associated viral (AAV) vectors are a leading platform for overexpressing transgenes as well as delivering the somatic genome editing tools to the liver, making them ideal for investigating candidate genes in lipid and atherosclerosis research [5]. Recombinant AAV are composed of a small, nonenveloped, single stranded DNA genome that can accommodate up to 4.9 kb of exogenous DNA, flanked on either side by hairpin like structures called inverted terminal repeats (ITRs). Following entry into the nucleus, the single stranded AAV genomes are converted to double-stranded episomes, which provide strong and stable expression of the transgene [6]. In addition to this, AAVs are well-tolerated and show no toxicity and modest immune response in mice, contrary to other commonly used viral vectors [5].

AAVs are currently being used to overexpress human or mouse proprotein convertase subtilisin/kexin type 9 (*PCSK9*) gain-of-function variants for generating atherosclerosis in mice. PCSK9 is secreted by the liver and promotes degradation of LDLR by preventing recycling to the cell surface [7]. As a consequence of the increased Ldlr turnover, this tool enables the rapid development of hypercholesterolemia in adult mice, bypassing the need of time-consuming crossing to *Ldlr* or *Apoe* KO background [8–10]. However, PCSK9 is overexpressed at supraphysiological levels by this method, which may not be ideal for all applications. For instance, it has been reported that at least a fraction of circulating PCSK9 resides on lipoprotein particles [11–13] and this could interfere if the gene of interest is expected to alter lipoprotein functions.

The clustered regularly interspaced short palindromic repeats (CRISPR)/Cas9 genome editing tool is derived from a naturally occurring bacteriophage defense system in bacteria [14]. This technology consists of a nuclease (Cas9) and a ~22-nucleotide synthetic guide RNA (gRNA), which guides the Cas9 to a complementary target sequence in genomic DNA, in immediate proximity to a protospacer adjacent motif (PAM). Cas9 induces a double-strand break (DSB) that, in mammalian cells, can be repaired by (1) non-homologous end-joining (NHEJ), which is the error-prone dominant repair pathway in nondividing cells that results in insertions and/or deletions of nucleotides (referred as “indels”), or

(2) homology directed repair (HDR), which uses a DNA template to repair DSB through homologous recombination, functioning most efficiently in dividing cells [15]. By providing an exogenous donor template with homology to the targeted site, it may eventually be possible to use CRISPR/Cas9 to correct a pathogenic mutation or insert a therapeutic transgene in a predetermined genomic site [16, 17]. On the other end, when an open reading frame is targeted, the NHEJ-derived indels induce frameshift mutations and premature stop codons that may be used for knocking out the gene of interest. Theoretically, any gene can be edited with CRISPR/Cas9 by simply modifying the gRNA design to be complementary to the targeted site.

The CRISPR/Cas9 system can be efficiently delivered to the liver for somatic genome editing. In this case, a double-stranded break introduces a myriad of mutations at a defined site in the genome. Although the liver will be mosaic with different mutations across alleles and target cells, the net effect is near complete ablation of expression of the target protein. One of the first in vivo applications of the CRISPR/Cas9 system in the setting of lipid and atherosclerosis research involved the somatic disruption of the *Pcsk9* gene. In the original study, adenovirus was used to deliver *Streptococcus pyogenes* (Sp) Cas9 to the liver, where increases in liver Ldlr and decreases in plasma cholesterol were observed [18]. However, adenovirus promotes undesirable immune responses and turnover of adeno-infected hepatocytes, unlike AAV particles. In a later study, Ran et al. used an AAV vector encoding the smaller *Staphylococcus aureus* (Sa) Cas9 and a gRNA targeting *Pcsk9*, which resulted in a high-rate of NHEJ-derived indels and significant reductions in circulating Pcsk9 and plasma cholesterol [19].

Recently, our group showed that the CRISPR/Cas9 system can be used for generating hypercholesterolemia and atherosclerosis in adult mice. First, we used AAVs to deliver two gRNAs targeting the *Ldlr* and *Apob* genes in the liver of adult Cas9-transgenic mice. We showed efficient disruption of *Ldlr* resulting in severe hypercholesterolemia and atherosclerosis, which could be rescued by the concomitant disruption of *Apob* [20]. Then, we used an all-in-one AAV-CRISPR system to deliver both SaCas9 and a gRNA targeting *Ldlr* in the liver of adult *C57BL/6J* mice (referred as *Ldlr* AAV-CRISPR). Similar to AAV-PCSK9, our *Ldlr* AAV-CRISPR tool induced severe hypercholesterolemia and atherosclerosis at extent comparable to *Ldlr* KO mice, but without requiring extensive crossing to *Ldlr* or *Apoe* KO background [21]. As a further example of application in lipid research, we recently exploited the AAV-CRISPR system for investigating the function of a branch point enzyme of the cholesterol biosynthetic pathway—dehydrodolichyl diphosphate synthase (DHDDS)—in the liver of adult mice, bypassing the need for generating new floxed animals [22].

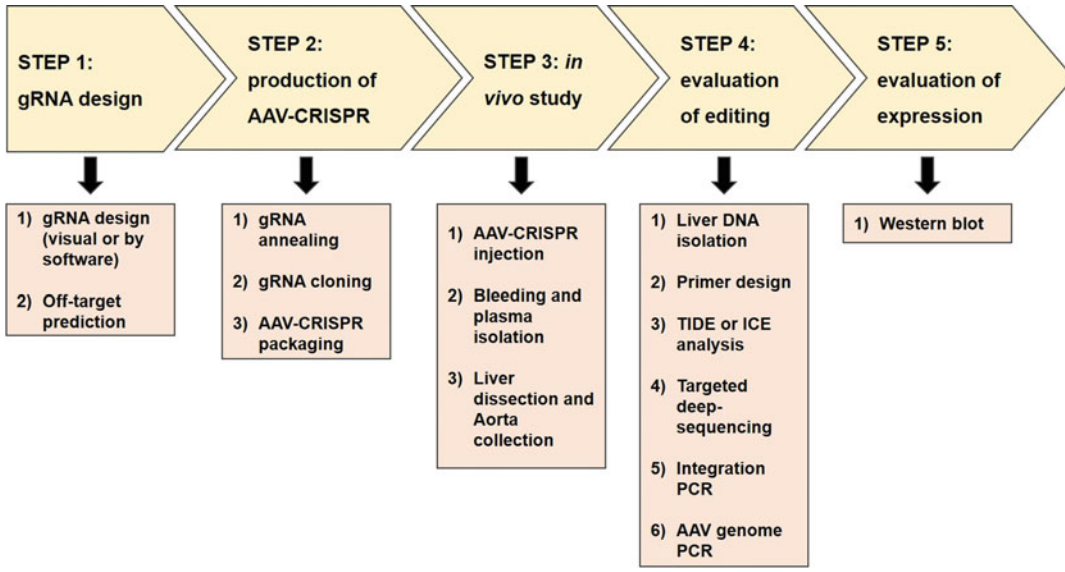

Fig. 1 Process flow diagram for somatically editing a gene in the liver using AAV-CRISPR. A flow diagram indicates the steps to follow for somatically editing a gene in the liver. The major methods covered in this Chapter are enlisted beneath the corresponding step

In this chapter, we provide a detailed protocol for using AAV-CRISPR for lipid and atherosclerosis research, through somatic editing of genes in the liver. Our protocol includes five general steps, as schematized in Fig. 1: (1) design of the gRNA for targeting the gene of interest; (2) generating AAV-CRISPR; (3) injection of AAV-CRISPR and in vivo study; (4) evaluation of editing at the targeted locus; (5) evaluation of expression level of the targeted gene. In this chapter, we do not cover methods for evaluating lipids and atherosclerosis, which can be found in other chapters of this book. We also do not cover AAV packaging, which can be performed by many academic or commercial cores, and has been published in a previous edition of Methods in Molecular Biology [6]. An overview of methods and expected outcomes is described in Subheadings 1.1 and 1.2.

1.1 AAV-CRISPR for Editing Candidate Genes in the Liver

gRNAs are designed manually or using CRISPOR for targeting the gene of interest. Off target analysis by COSMID or CRISPOR provides a list of potential off-target sites in the genome other than the targeted site that may be edited based on the gRNA sequence similarity and proximity to a PAM sequence (Fig. 2). gRNAs are annealed and cloned in 1313_pAAV-U6-SA-BbsI-MluI-gRNA-HLP-SACas9-HA-OLLAS-spA acceptor vector (Figs. 3 and 4) and the obtained plasmids need to be sequenced for verifying the insert and enzymatically digested for verifying that the ITRs are intact (Fig. 5). The final plasmids are used for generating AAVs based on serotype 8 for targeting the liver, by a triple

A

Excerpt from *Ldlr* Exon 14:

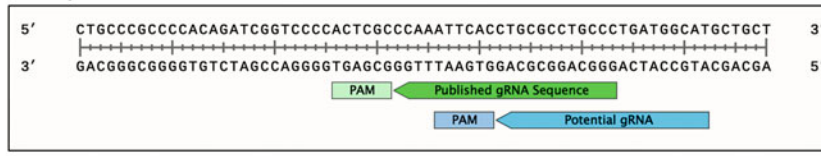

B

COSMID Output

Processing input tag: GGGCAGGCGCAGGTGAATTTGGNNGRR
Search in target database: mm10
Length: 27
searching for no indel hits allowing up to 3 mismatch(es) ... Done
searching for 1b-deletion hits allowing up to 2 mismatch(es) ..... Done
searching for 1b-insertion hits allowing up to 2 mismatch(es) ..... Done

Result	Query type	Mismatch	Hit ends in RG	chr position	Strand	Cut site	Score
GGGCAGGCGCAGGTGAATTTGGGCGAG -- hit NN RR -- query	No indel	0	Yes	Chr9:21744315-21744341	-	21744323	0
^GGCAGGCGCAGGTGAATTTGGGCGAG -- hit G NN RR -- query	Del 20, or Del 21, or Del 22	0	Yes	Chr9:21744315-21744340	-	21744323	0.61
GGC^AGGCGCAGGTGAATTTGGGCGAG -- hit GC NN RR -- query	Del 19	1	Yes	Chr9:21744315-21744340	-	21744323	0.76
GGCA^GGCGCAGGTGAATTTGGGCGAG -- hit GCA NN RR -- query	Del 18	2	Yes	Chr9:21744315-21744340	-	21744323	0.91
GGGCAGG^GCAGGTGAATTTCTGTGAG -- hit C GGNN RR -- query	Del 15	2	Yes	Chr2:126498613-126498638	+	126498630	11.72
GGGGAGGAGCA^GTGAATTTGGGGGAG -- hit C C G NN RR -- query	Del 10, or Del 11	2	Yes	ChrX:36067528-36067553	+	36067545	1.35
GGGCAGGCGCAGGTGAA^TTTGGGCGA -- hit T G NNGRR -- query	Del 3, or Del 4, or Del 5	2	No	Chr9:21744316-21744341	-	21744324	27.81

C

Predicted guide sequences for PAMs

Ranked by default from highest to lowest specificity score (Hsu et al., Nat Biot 2013). Click on a column title to rank by a score.
If you use this website, please cite our paper in NAR 2018. Too much information? Look at the CRISPOR manual.

Download as Excel tables: Guides / Off-targets / Saturating mutagenesis assistant

Position/ Strand	Guide Sequence + *PAM* + Restriction Enzymes + Variants Only G- Only GG- Only A-	MIT Specificity Score	Predicted Efficiency Najm 2018	Out-of-Frame	Off-targets for 0-1-2-3-4 mismatches + next to PAM	Genome Browser links to matches sorted by CFD off-target score exons only chr9 only
95 / rev	ATGCCATCAGGGCAGGCGCAG *GTGAAT* Enzymes: *HinP1I, AsuHPI, MluCI, XapI* **Cloning / PCR primers**	97	76	60	0 - 0 - 0 - 0 - 5 0 - 0 - 0 - 0 - 0 5 off-targets	4:intergenic:Schip1-Gm22073 4:intron:Klhl18 4:intron:Col14a1 show all...
85 / rev	GGCAGGCGCAGGTGAATTTGG *GCGAGT* Enzymes: *XapI* **Cloning / PCR primers**	60	82	71	0 - 0 - 0 - 2 - 94 0 - 0 - 0 - 0 - 0 96 off-targets	3:intergenic:Ccdc18-Dr1 3:intergenic:Swi5-Swi5/Golga2 4:intron:Ubac2 show all...

Fig. 2 gRNA design. (**a**) Excerpt of *Ldlr* Exon 14 with previously published gRNA and a second possible gRNA annotated. Sequence annotated in SnapGene. (**b**) Sample output from COSMID for the published gRNA sequence in (**a**). (**c**) Sample output from CRISPOR. Outputs for (**b**) and (**c**) were generated on 12-15-2020 and have been cropped for clarity

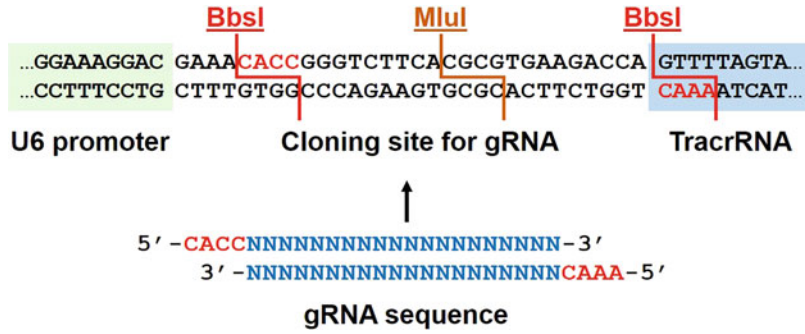

Fig. 3 Scheme of gRNA sequence and cloning. The gRNA sequence is composed of 20–22 double-strand nucleotides complementary to the targeted site, flanked by a BbsI restriction site overhang at each 5′ terminal. Annealed gRNAs are cloned into BbsI-linearized 1313 acceptor vector. The cloning site for gRNA in 1313 acceptor vector is shown with BbsI and MluI restriction sites indicated by elbow connectors

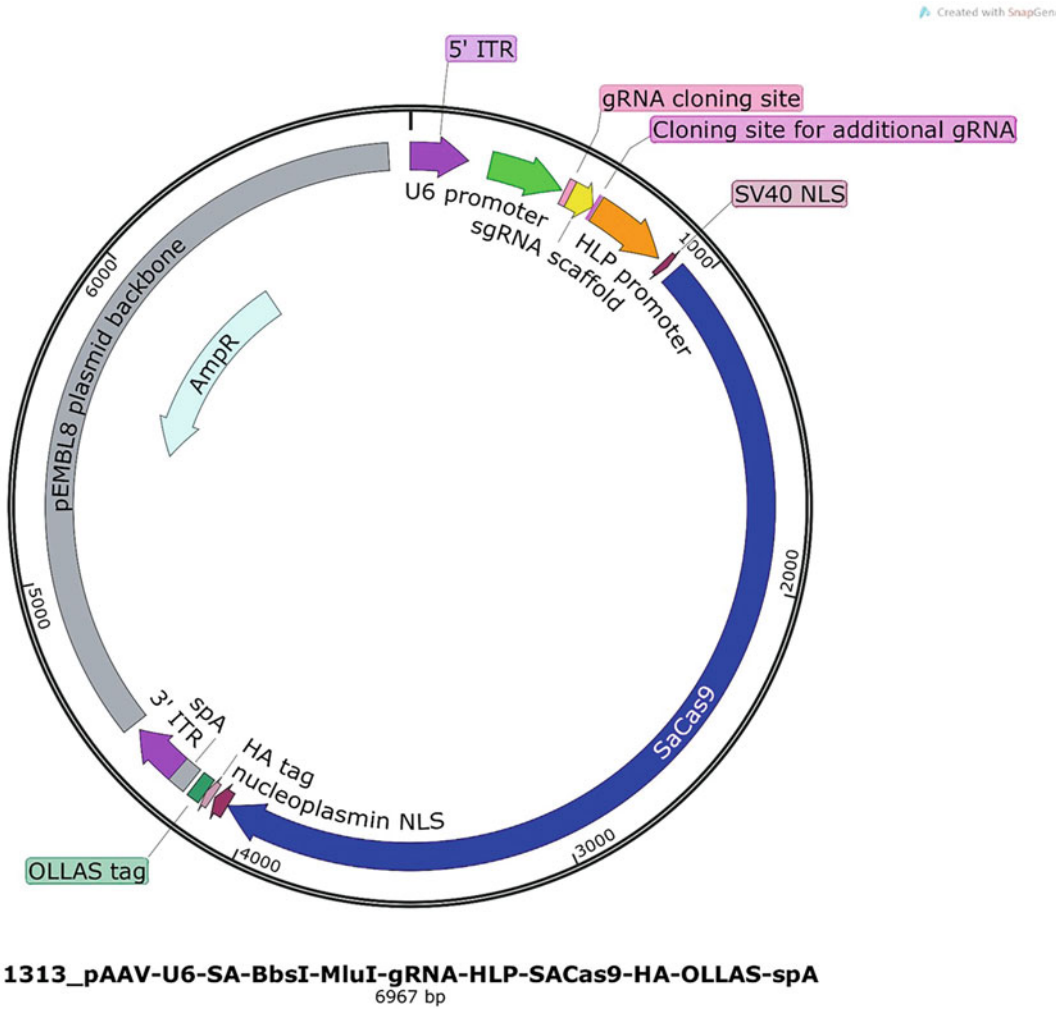

Fig. 4 Map of 1313 acceptor vector for gRNA cloning (Addgene 109,314). A gRNA cloning site is downstream of a U6 promoter and upstream of a sgRNA scaffold. The liver specific HLP promoter drives the expression of SaCas9. gRNA and SaCas9 expression cassettes are flanked by two complementary ITR sequences. Map generated with SnapGene

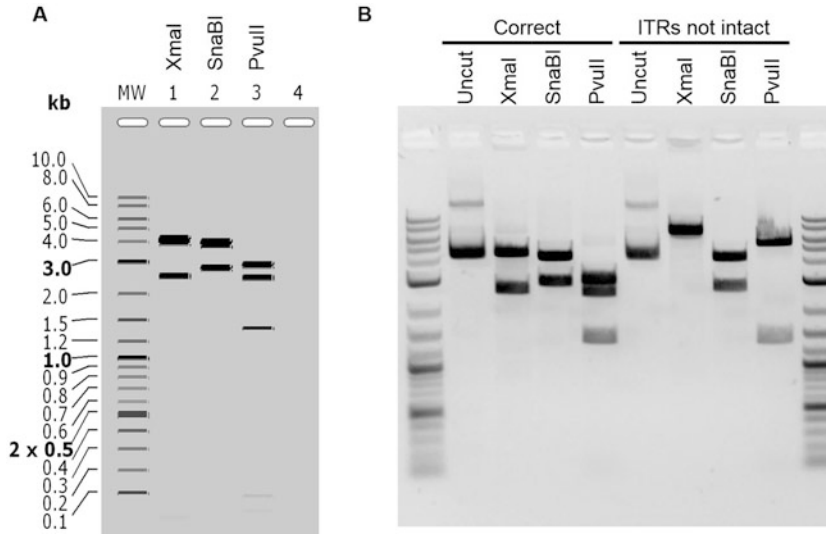

Fig. 5 Diagnostic enzymatic digestion of ITRs. (**a**) Prediction of diagnostic enzymatic digestions of ITRs in an AAV-CRISPR plasmid. Generated with SnapGene. (**b**) Gel electrophoresis of AAV-CRISPR plasmids digested with XmaI, SnaBI, and PvuII for checking the integrity of ITRs. Lanes 1 and 10 are loaded with a 1 kb DNA ladder. Lanes 2–5 represent a plasmid with intact ITRs, matching the predicted restriction patterns shown in (A). Lanes 6–9 represent a plasmid with damaged ITRs, where XmaI and PvuII show incorrect band sizes by restriction digest

transfection method. In our hands, an average yield in the order of 10^{12} to 10^{13} genome copies per lot is expected by using this method [6]. However, cores and companies can produce AAVs at a large scale. It is recommended to inject mice starting at 6–8 weeks of age. Editing is expected to be more efficient in adult mice, as a result of predominance of the error prone NHEJ-mediated repair in postmitotic tissues. A dose of 5×10^{11} genome copies is a good starting point for reaching high levels of editing at the desired locus [21–24]. However, a higher dose (up to 1×10^{12} genome copies) can be used for increasing editing levels, or when female mice are injected, due to the reported sexual dimorphism [21]. Based on our data, editing is detectable starting at 7 days postinjection. Integration PCR is the easiest method for qualitatively assessing editing, resulting in the PCR amplification of AAV-genome insertion events in the DSB site (Fig. 6). ICE and TIDE analyses, or deep sequencing provide the spectrum and frequency of indel formation (Fig. 6). It is important to amplify and analyze predicted off-target sites by deep sequencing to rule out any nonspecific effects on phenotype. When testing new gRNAs, a good gRNA candidate should show an indel frequency of at least 20–30% and no off target activity. The effects of gene editing on protein expression is verified by western blot on liver lysate or plasma. Ideally, efficient gene editing should result in undetectable protein expression levels of the targeted gene. The effects of gene editing are expected to be permanent if

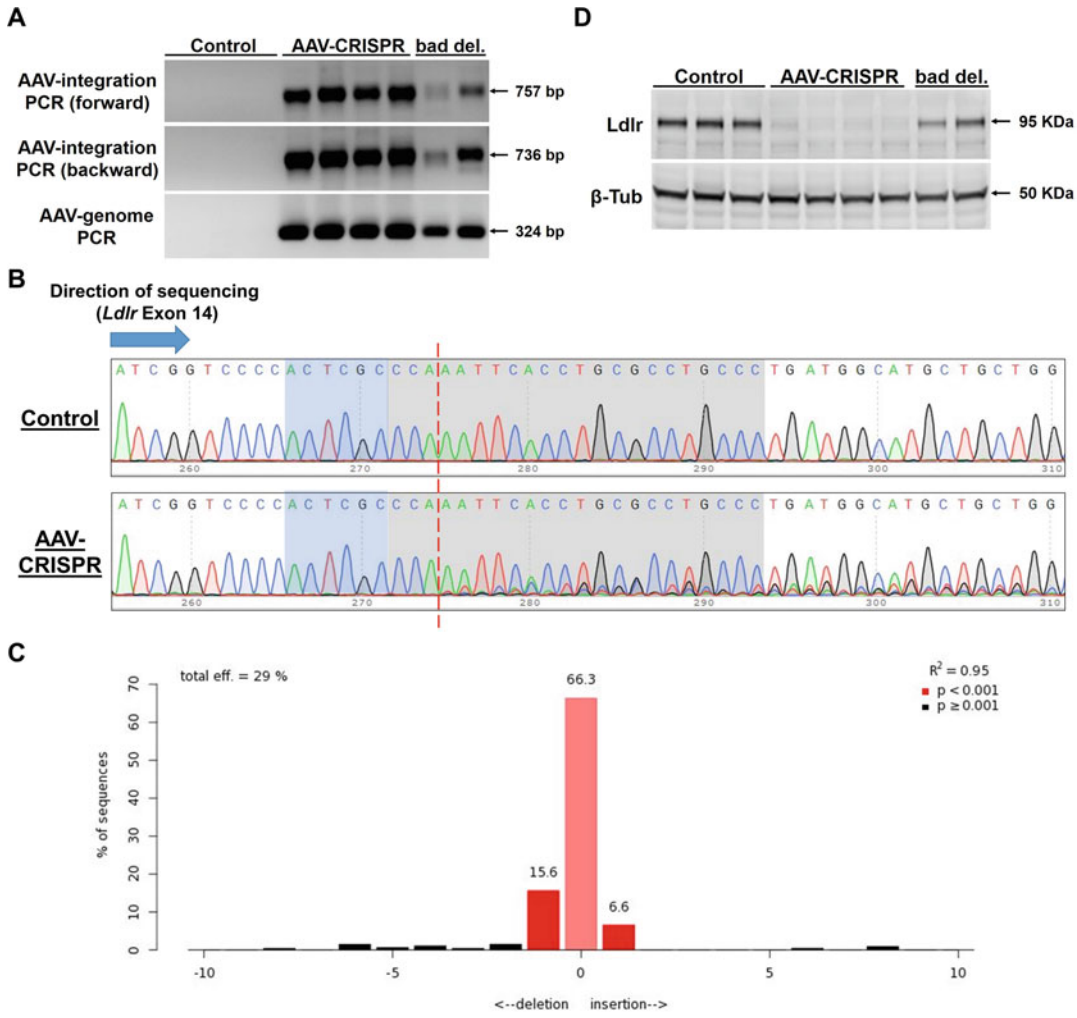

Fig. 6 Analysis of editing at the *Ldlr* locus and effects on Ldlr expression in the liver. (**a**) Integration PCRs detecting the AAV-genome forward and backward integration in the *Ldlr* locus by NHEJ in *Ldlr* AAV-CRISPR-injected mice. AAV genome PCR showing AAV genomes in the liver of AAV-CRISPR mice. Control mice were injected with sterile saline solution. Mice in the last two lanes show reduced delivery of AAVs to the liver, resulting in lower editing at the *Ldlr* locus (bad del.: bad delivery). (**b**) Representative DNA sequencing chromatograms showing multiple sequence traces in exon 14 of *Ldlr* in the liver from an *Ldlr* AAV-CRISPR-injected mouse compared to a control. The PAM and gRNA sequences are respectively highlighted in blue and grey. A dashed red line indicates the expected nuclease cut site. An arrow indicates the sequencing direction. (**c**) Indel spectrum by TIDE showing the relative percentage of unedited and edited sequences (with insertions or deletions) at the targeted locus. (**d**) Ldlr western blot on liver lysates with beta tubulin (β-Tub) used as loading control (1:500, mouse, University of Iowa Developmental Studies Hybridoma Bank E7). Mice in the last two lanes (bad del.) show marginally decreased Ldlr levels as a result of AAV bad delivery. A homemade antibody was used for detecting Ldlr at 1:5000 dilution (gift from Gene Ness)

the targeted gene is not essential for hepatocyte survival. In case of essential genes, cell death of targeted hepatocytes and regeneration of unedited hepatocytes may result in loss of the edited alleles over

time [22]. Moreover, the time frame between gene editing and protein knockdown along with phenotype development depends on the abundance and half-life of the targeted protein. Therefore, we recommend assessing editing and expression level of the candidate gene at different time points postinjection (e.g., at 2, 4, and 6 weeks). The effects of gene editing on lipid metabolism can be monitored by measuring plasma lipids at different time points and analyzing the liver at endpoint. Overall, AAV-CRISPR enables one to rapidly knock out genes in the liver, bypassing the need for floxed mice and complicated breeding schemes, and avoiding any developmental compensation.

1.2 AAV-CRISPR for Modeling Hypercholesterolemia and Atherosclerosis

A mouse model of hypercholesterolemia and atherosclerosis is generated by somatic editing of *Ldlr* in the liver of adult mice. A single dose of *Ldlr* AAV-CRISPR (5×10^{11} genome copies in male and 1×10^{12} genome copies in female mice injected at 6–8 weeks of age) is expected to edit exon 14 of *Ldlr* by NHEJ-mediated indel formation and AAV-genome insertion at the DSB site. AAV insertion events at the *Ldlr* locus can be easily detected by integration PCR as a first qualitative assessment of editing. An AAV genome PCR is useful for identifying mice with incomplete or failed delivery of AAV to the liver as a result of bad injection, and excluding them from the study (Fig. 6). TIDE and ICE analyses or deep sequencing provide quantitative information on the frequency of indels [21]. The genetic disruption of *Ldlr* is permanent resulting in near-complete loss of hepatic Ldlr throughout the atherosclerosis study. Mice with ~30% of indel formation rate are expected to show undetectable levels of Ldlr in liver lysates by western blot (Fig. 6). On the contrary, failed injections result in incomplete editing with only marginally decreased Ldlr levels (Fig. 6). *Ldlr* disruption is expected to gradually increase plasma cholesterol levels at extent comparable to the gold standard $Ldlr^{-/-}$ germline mouse model—for example, plasma cholesterol: 1408 ± 473 mg/dL versus 1966 ± 412 mg/dL in male mice after 20 weeks of western diet [21]. Measuring cholesterol at intermediate time points during the study can give an idea on the efficiency of *Ldlr* editing. Moreover, plasma cholesterol is expected to distribute mostly in the very low–density lipoprotein (VLDL), intermediate-density lipoprotein (IDL), and LDL fractions, similar to what was observed in $Ldlr^{-/-}$ mice. As a consequence of severe hypercholesterolemia, *Ldlr* AAV-CRISPR-injected mice fed a western diet develop severe atherosclerotic lesions, showing lesion area in the range of 6–10% by en face Oil Red O staining of aortae in male mice after 20 weeks of western diet feeding [21] (Fig. 7).

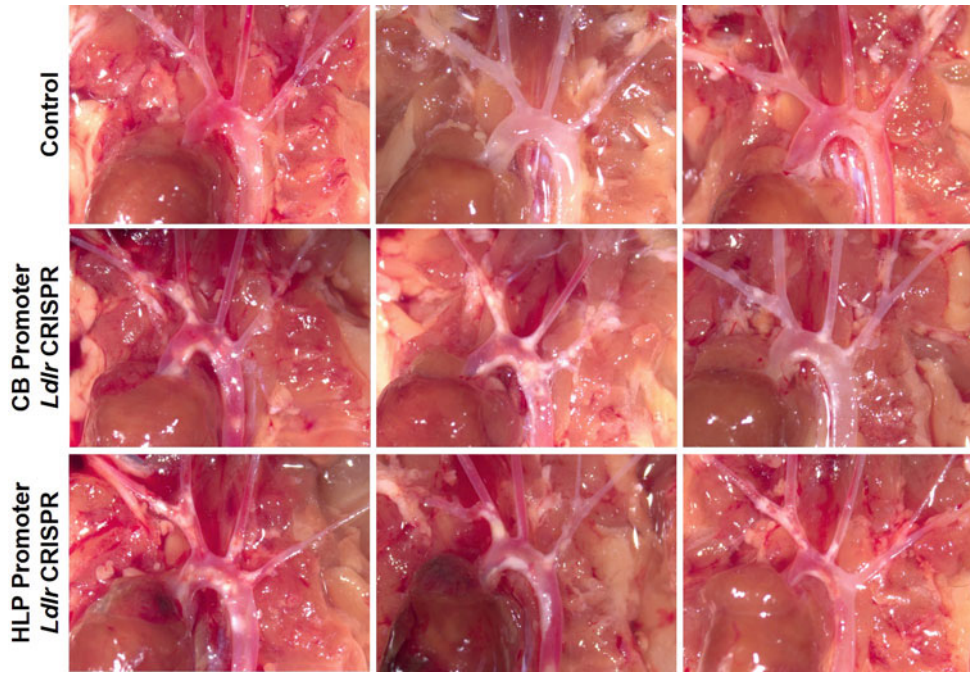

Fig. 7 Atherosclerosis development following *Ldlr* editing with *Ldlr* AAV-CRISPR. 8-week-old *C57BL/6 J* mice were injected with 5×10^{11} genome copies of *Ldlr* AAV-CRISPR expressing SaCas9 from the chicken β-actin (CB) promoter [21], *Ldlr* AAV-CRISPR expressing SaCas9 from the liver-specific HLP promoter or saline (control). Mice were placed on Western diet and followed for 20 weeks. Aortae were dissected and raw images were taken. The HLP vector results in atherosclerosis development at similar extent to the CB vector (*see* **Note 55**)

2 Materials

All buffers are made in Milli-Q double distilled water and stored at room temperature, unless stated otherwise.

2.1 General Materials and Equipment

1. Sterile PCR tubes.
2. Sterile 1.5 and 2 mL tubes.
3. Sterile 15 and 50 mL tubes.
4. Micropipettes.
5. Filtered tips.
6. Electronic pipettor.
7. Serological pipettes.
8. Heat block with 1.5 mL tube insert.
9. Thermocycler.
10. Molecular grade (nuclease-free) water.
11. Milli-Q double distilled water.

12. Oligonucleotides/primers (*see* **Note 1**).
13. Electrophoresis power supply.
14. Gel electrophoresis apparatus.
15. Gel tweezers.
16. Shaker.
17. Agarose, molecular biology grade: 1% (w/v) in 1× tris–acetate–EDTA (TAE) buffer (*see* **Note 2**).
18. 1× TAE buffer: 40 mM tris–acetate, 1 mM EDTA, pH 8.3.
19. Ethidium bromide, 10 mg/mL (*see* **Note 3**).
20. 1 kb DNA ladder for gel electrophoresis.
21. 6× DNA loading buffer for gel electrophoresis: 6× TAE buffer, 30% glycerol, 0.02% Bromophenol Blue.
22. Gel extraction kit (any commercially available kit).
23. UV transilluminator and gel imager (*see* **Note 4**).
24. Ice.
25. Tabletop centrifuge.
26. Centrifuge for 15, 50, and 250 mL centrifuge tubes.
27. Laboratory balances.
28. Bead mill homogenizer.
29. Steel beads.
30. UV-Vis spectrophotometer.
31. Vortex.
32. Sharp disposal container.
33. −80 °C freezer.
34. 70% ethanol.
35. 1× phosphate-buffered saline (PBS): 137 mM NaCl, 2.7 mM KCl, and 10 mM Na_2HPO_4, 1.8 mM KH_2PO_4.

2.2 gRNA Design

1. Gene annotation software (e.g., SnapGene) (*see* **Note 5**).
2. Genomic and mRNA sequence files for gene(s) of interest downloaded from NCBI Gene (https://www.ncbi.nlm.nih.gov/gene/) or UCSC Genome Browser (https://genome.ucsc.edu/) and edited in annotation software.
3. CRISPR Off-target Sites with Mismatches, Insertions and Deletions (COSMID) website for off-target prediction: https://crispr.bme.gatech.edu [25].
4. CRISPOR website for gRNA design and off-target prediction: http://crispor.tefor.net/ [26].

2.3 Plasmid Construction

1. Tris–EDTA (TE) buffer: 10 mM Tris–HCl pH 7.5, and 1 mM EDTA in molecular grade water.
2. 10× Annealing Buffer: 100 mM Tris–HCl pH 7.5, 1 M NaCl, and 10 mM EDTA in molecular grade water.
3. Plasmid 1313_pAAV-U6-SA-BbsI-MluI-gRNA-HLP-SACas9-HA-OLLAS-spA (Addgene 109314).
4. BbsI restriction enzyme.
5. 10× Enzyme buffer: 500 mM potassium acetate, 200 mM Tris–acetate, 100 mM magnesium acetate, 1 mg/mL BSA, pH 7.9. Store at −20 °C.
6. 2× Rapid Ligation Buffer: 132 mM Tris pH 7.6, 20 mM $MgCl_2$, 2 mM DTT, 2 mM ATP, 15% PEG. Store at −20 °C.
7. T4 DNA ligase.
8. Stable competent *E. coli* (NEB, C3040H): F′ *proA+B+ lacI*^{q} *Δ(lacZ)M15 zzf::Tn10* (Tet^R)*/Δ(ara-leu) 7697 araD139 fhuA ΔlacX74 galK16 galE15 e14- Φ80dlacZΔM15 recA1 relA1 endA1 nupG rpsL* (Str^R) *rph spoT1 Δ(mrr-hsdRMS-mcrBC)*.
9. 500 mL—1 L Erlenmeyer flasks.
10. LB (Luria–Bertani) broth: 25 g per L of Milli-Q double distilled water (*see* **Note 6**).
11. 50 mg/mL ampicillin, store at −20 °C.
12. LB Agar: 37 g per L in Milli-Q double distilled water (*see* **Note 7**).
13. 10 cm petri dish.
14. 42 °C water bath.
15. 37 °C incubator.
16. Laminar flow hood.
17. TE buffer: 10 mM Tris–HCl, pH 8.0. 1 mM EDTA.
18. 37 °C bacterial shaker equipped for 500 mL flasks and 15 mL tubes.
19. Miniprep kit (any commercially available kit).
20. Maxiprep kit (any commercially available kit).
21. XmaI restriction enzyme.
22. SnaBI restriction enzyme.
23. PvuII restriction enzyme.

2.4 In vivo Study

1. *C57BL/6J* mice.
2. Sterile PBS solution for injection.
3. Insulin syringes with 25–27G needles.
4. 10 mL syringes with 23G needles.

5. Isoflurane for animal use.
6. Anesthesia machine and charcoal filters.
7. Western diet containing 0.21% (w/w) cholesterol and 21% (w/w) fat.
8. Sterile heparinized capillary tubes.
9. Sterile gauze sponges.
10. Set of surgical instruments for animal dissection.
11. Razor blades.
12. Glass bead sterilizer.
13. 10% formalin.
14. Optimal cutting temperature (OCT) compound.
15. Specimen molds.
16. Liquid nitrogen.
17. Cryogenic microtubes.

2.5 Analysis of On-Target and Off-Target Nuclease Activity

1. DNA isolation kit (any commercially available kit).
2. Qubit 4 Fluorometer (Thermo Scientific).
3. 2 U/μL Phusion™ High-Fidelity DNA Polymerase (Thermo Scientific).
4. 10 mM Deoxynucleotide triphosphate (dNTPs).
5. Herculase II Fusion DNA Polymerase (Agilent Technologies).
6. Agencourt AmPure XP (Beckman Coulter).
7. Apex 2× Taq Red Master Mix (Genesee Scientific).
8. 96-well plates.
9. Primer 3 (http://bioinfo.ut.ee/primer3-0.4.0/).
10. Primer 3 Plus (http://www.bioinformatics.nl/cgi-bin/primer3plus/primer3plus.cgi).
11. Primer Blast (https://www.ncbi.nlm.nih.gov/tools/primer-blast/index.cgi).
12. Tracking of Indels by DEcomposition (TIDE) web-based tool (http://shinyapps.datacurators.nl/tide/) [27].
13. Inference of CRISPR Edits (ICE) web-based tool (https://ice.synthego.com/#/) [28].
14. CRISPResso2 web-based tool (https://crispresso.pinellolab.partners.org/submission) [29].

2.6 Evaluation of Gene Knockdown by Western Blot

1. RIPA buffer: 50 mM Tris pH 8.0, 1 mM EDTA, 1% Triton X-100, 0.1% sodium dodecyl sulfate, 0.5% sodium deoxycholate, and 150 mM sodium chloride. Store at −20 °C.
2. Protease inhibitor cocktail.

3. BCA protein assay kit.
4. 4× NuPAGE™ LDS Sample Buffer (Thermo Scientific) or equivalent.
5. Beta-mercaptoethanol.
6. XCell SureLock™ Mini-Cell (Thermo Scientific) or equivalent.
7. NuPAGE™ 4–12%, Bis-Tris, 1.0 mm, Mini Protein Gel (Thermo Scientific) or equivalent.
8. 20× NuPAGE™ MES SDS Running Buffer (Thermo Scientific) or equivalent.
9. Protein Marker.
10. 0.45 μm polyvinylidene fluoride (PDVF) membrane.
11. Tweezers.
12. Sponges.
13. 20× NuPAGE™ Transfer Buffer (Thermo Scientific) or equivalent.
14. Methanol.
15. XCell II™ Blot Module (Thermo Scientific) or equivalent.
16. Filter papers.
17. PBS-T: PBS supplemented with 0.05% Tween 20.
18. Western blot boxes.
19. Odyssey blocking buffer (PBS) (Licor): mix 2 parts of blocking buffer with 1 part of PBS-T.
20. Antibody buffer: 1% BSA in 0.05% PBS-T.
21. Anti Ldlr antibody (Abcam ab52818, 1:1000–1:2500).
22. Anti-housekeeping protein antibody (e.g., β-actin).
23. Goat anti-rabbit 680 nm (1:15000) (Rockland).
24. Goat anti-mouse 800 nm (1:15000) (Rockland).
25. Odyssey infrared imaging system (Licor).

3 Methods

3.1 gRNA Design

3.1.1 Target Gene Annotation

1. Navigate to NCBI Gene (https://www.ncbi.nlm.nih.gov/gene/) and search for your gene of interest (e.g., mouse *Ldlr*) (*see* **Note 8**).
2. Select the mouse ortholog of your gene of interest, scroll down to "NCBI Reference Sequences" and select the FASTA Genomic Build.
3. Select "Send to → Complete Record → File" and "GenBank (full)." Click "Create File" and open the downloaded file in SnapGene.

4. Repeat the process for any mRNA isoforms.
5. Using SnapGene, align mRNA sequences to confirm which exons are present in all mRNA isoforms. Annotate these exons in the mRNA and genomic files. Also note essential domains (*see* **Note 9**).

3.1.2 gRNA Design—Visual Selection

1. Open the sequence file for the target gene and search for 5′-NNGRRT-3′ (N is any nucleotide and R is A or G), which matches the PAM motif for SaCas9 (*see* **Note 10**). SnapGene will show PAM motifs on either strand. The gRNA will be 5′-(20-22N)NNGRRT-3′ (*see* Fig. 2a for example).
2. Highlight gRNA sequences 20–22 bp 5′ of the PAM. Annotate potential gRNAs early in the coding sequence and near important protein domains.
3. Note gRNAs for further consideration if they meet the following criteria (not including the PAM).
   (a) Melting temperature (Tm) between 55 and 70 °C.
   (b) Few repetitive bases (note that quadruple repeats of T will terminate U6 promoter expression).
   (c) 45–70% GC content.
   (d) The region within 3–5 bp from the PAM should be within the protein-coding region. Otherwise indel formation from editing may not knock out protein expression.
   (e) A gRNA starting with a G at the 5′ end is preferred for proper expression from the U6 promoter. Add a G at the 5′ when it is not present before proceeding to cloning.

3.1.3 Off-Target Prediction Using COSMID

1. Open the genomic sequence file for the target gene and copy the gRNA sequence to be assessed from 5′ to 3′. The PAM would be at the 3′ end of this sequence but should not be copied with the gRNA sequence. Make sure to copy the correct strand of the DNA. For example, if the gRNA is on the bottom strand, the sequence must be copied from the bottom strand from 5′ to 3′.
2. Navigate to https://crispr.bme.gatech.edu (*see* **Note 11**) and select the following parameters:
   (a) Target Genome: Mus Musculus GRCm38 (mm10).
   (b) Query Sequence: Paste the gRNA sequence 5′ to 3′, excluding the PAM.
   (c) Search Options:
   - Add PAM suffix NNGRR—exclude the T to allow the search to be slightly less stringent, returning more off-targets.

- Allowed indels and mismatch: Set to the least stringent search terms with the highest number of mismatches for each option: No Indels = 3, 1-base Del = 2 and 1-base Ins = 2.

(d) PCR Design Options: If you check the box, it will design a pair of primers for off-targets (*see* **Note 12**).

3. Hit submit. The page may take several minutes to load.
4. Analyze output:
   (a) Result: Shows the hit versus the sequence that was queried with mismatches from the hit in red text. These, minus ambiguous bases like "N" are totaled in the "Mismatch" column.
   (b) Query Type: The type of alteration required for binding (e.g., no indel, deletions or insertions in the gRNA or deletions or insertions in the PAM).
   (c) Hit ends in RG: This is for SpCas9 systems and is not applicable to the SaCas9 system that is being used here. Ignore this column.
   (d) Chr Position: This is the chromosomal location of the gRNA binding site for the on- or off-target. This is clickable and navigates to UCSC Genome Browser.
   (e) Score: The closer to 0 the score, the more likely the off-target site will be edited by that gRNA sequence. The on-target will ideally be the only site with a low score.
5. Download the Excel spreadsheet summary.
6. Duplicate the results tab and sort by chromosomal location. Some hits, especially for the on-target site, will be duplicates. Delete duplicates of the same site, keeping the lowest scoring duplicate. The final list should include any off-targets as well as your on-target.
7. Click the links for chromosomal position to determine if any off-targets reside in exons or near important gene regulatory regions. If off-targets are near these locations, do not choose this gRNA for testing. Choose final gRNAs with the fewest off-targets and preferably no predicted off-targets in exons. Off-targets with high scores are less likely to have off-target editing than those with lower scores. An example of COSMID output is shown in Fig. 2b.

3.1.4 gRNA Design and Off-Target Prediction Using CRISPOR

1. Open the genomic sequence file for the target gene and copy the region of interest, usually an early exon or essential region.
2. Navigate to http://crispor.tefor.net and paste the sequence into the text box (*see* **Note 13**).
3. Make the correct selections:

(a) For the genome, select Mus Musculus—Mouse (reference—UCSC Dec, 2011 (mm10 = C57BL/6J); and

(b) For the PAM, select 21 bp-NNG(A/G)(A/G)T—Cas9 S. Aureus.

4. Hit submit and review the outputs. The best gRNAs selected by CRISPOR will be noted with green to the left of the gRNA output (Fig. 2c) and do not consider gRNAs that are yellow or red. The parameters to look at are as follows

(a) Specificity score—How specific is the gRNA to the target? This is rated from 0–100, with 100 being the best, most specific score. gRNAs with a specificity score above 75 should be considered.

(b) Efficiency score—How quickly and effectively does the gRNA disrupt the target? Faster disruption is preferred. On the scale of 0–100, where 100 is the best, consider efficiency scores of greater than 75.

(c) Out of Frame—How likely is it that cutting with this gRNA will result in indel formation? Indels are needed both for loss of the protein of interest and for detection of editing, so higher Out of Frame scores are preferred. Select gRNAs with Out of Frame scores of greater than 50.

(d) Off-targets for 0-1-2-3-4 mismatches—This column lists how many off-targets are predicted for a given gRNA for 0–4 mismatches to the gRNA sequence. Off-targets that are perfect matches or have only single mismatches for the gRNA sequence exclude that gRNA from consideration. Select gRNAs that have the fewest number of off-targets and which have off-targets that have 3+ mismatches. There is a gray, second set of numbers in this column denoted as "+ next to PAM." These numbers show the number of off-targets with 0–4 mismatches that have no mismatches within 12 bp of the PAM. These gRNAs are more likely to have off-target effects at sites like these and should be avoided.

(e) Genome browser links to matches sorted by cutting frequency determination (CFD) off-target score—This is the list of off-targets predicted for a given gRNA. Select gRNAs with the lowest number of possible off-targets, but this list allows for further narrowing of gRNA candidates. Off-targets are listed as intron, intergenic or exon. Exclude gRNAs with off-targets in exons. The links for each off-target are clickable and direct to the UCSC Genome Browser to show the potential off-target cut site.

(f) Other points to consider:

- Pay attention to notes in the "Guide Sequence + PAM" column—CRISPOR notes gRNAs that have quadruple repeats of T, which halt transcription from the U6 promoter.
- Generally, try to avoid multiple repeats (3+) of the same base.
- Aim for gRNAs that have similar GC content across the gRNA sequence.
- If a gRNA does not start with a G at the 5′ end, one will need to be added before cloning for the gRNA to be properly expressed from the U6 promoter. Rerun the gRNA sequence of interest through COSMID with the G added.

5. Download the "Guides" and "Off-targets" files. The off-targets file will be necessary for primer design for assessing off-target editing later (*see* Subheadings 3.4.2 and 3.4.4).
6. Annotate and name gRNAs in the genomic and RNA files.
7. Repeat this process for other exons or regions of interest.
8. Check gRNAs as a final step using COSMID, which uses different off-target prediction algorithms compared to CRISPOR. Ideal gRNAs will have less than 10 off-targets for both COSMID and CRISPOR.
9. Select the top 2 to 5 gRNAs and proceed to Plasmid Construction (Subheading 3.2). An example of CRISPOR output is shown in Fig. 2c.

3.2 Plasmid Construction and AAV Production

3.2.1 Oligonucleotides Annealing

1. Each gRNA is designed as a ~20–22 double stranded nucleotide sequence complementary to the targeted gene, flanked by a BbsI restriction site overhang at each 5′ terminal. Do not include the PAM sequence in the gRNA sequence used for cloning. In order to generate annealed oligonucleotides that can be ligated into the sticky ends left by BbsI restriction, 5′-CACC-3′ must be added to the 5′ end of the top oligonucleotide sequence and 5′-AAAC-3′ must be added to the 5′ end of the bottom oligonucleotide (Fig. 3). Top and bottom oligonucleotides can be ordered from any commercial DNA synthesis company (*see* **Note 14**).
2. Dilute each oligonucleotide stock solution to 1 μM working solution in TE Buffer.
3. In a 1.5 mL tube, mix 10 μL of 10× Annealing Buffer, 8.3 μL of 1 μM top oligonucleotide solution, 8.3 μL of 1 μM bottom oligonucleotide solution, and 73.4 μL of molecular grade water so the final volume is 100 μL.
4. Vortex and then centrifuge at 2000 × *g* for 1 min.

5. Heat the annealing reactions at 100 °C for 2 min using a heat block.
6. Move the tubes on a bench and let them slowly cool down to room temperature for at least 30 min.
7. Centrifuge at 2000 × *g* for 1 min and place the tubes in ice (*see* **Note 15**).

3.2.2 Cloning and Analysis

1. To digest the 1313_pAAV-U6-SA-BbsI-MluI-gRNA-HLP-SACas9-HA-OLLAS-spA acceptor vector (Addgene 109314; *see* **Note 16** and Fig. 4), mix in a PCR tube 6 μg of 1313 vector, 8 μL of 10× Enzyme buffer, 2 μL of 20 U/μL BbsI, and molecular grade water to a final volume of 80 μL.
2. Set the following program in a thermocycler: 6 h at 37 °C; 15 min at 65 °C; and hold at 4 °C (*see* **Note 17**).
3. Prepare a 1% agarose gel containing ethidium bromide in a gel electrophoresis apparatus and load the whole volume of digestion from **step 2** supplemented with 1× DNA loading buffer. Include a lane loaded with 5 μL of 1 kb DNA ladder for estimating the size of concurrently analyzed samples.
4. Separate the digested vector by gel electrophoresis using 1× TAE buffer (150 V for 30 to 45 min). Check DNA ladder and digestions using an UV gel imager.
5. Cut out the digested vector with a pair of gel tweezers using a UV transilluminator for visualizing the DNA.
6. Gel purify the digested vector using a gel extraction kit, following the manufacturer's instructions.
7. Measure DNA concentration with a UV-Vis spectrophotometer.
8. Ligate the annealed gRNA in 50 ng of digested vector using a 10:1 (insert:vector) molar ratio. Include a mock-ligation reaction, which contains no insert. Use the following formula for calculating the amount of gRNA needed: ng gRNA = 50 ng vector × (kb insert/kb vector) × (10:1 ratio insert:vector). Set up ligations in a PCR tube with *X* μL of linearized 1313 vector (final amount of 50 ng), calculated *X* μL of gRNA, 10 μL of 2× Rapid ligation buffer, 1 μL of T4 DNA ligase and molecular grade water to a final volume of 21 μL total.
9. Mix and centrifuge at 2000 × *g* for 1 min.
10. Incubate at room temperature for 15 min.
11. Proceed to transformation or store at −20 °C.
12. For each transformation include the following plates as controls: (1) bacteria transformed with water as a negative control for ampicillin; (2) bacteria transformed with the mock-ligation as control for undigested or self-ligated vectors; and

(3) bacteria transformed with 5 ng of undigested vector, as positive control for transformation efficiency of the *E. coli*.

13. Thaw stable competent *E. coli* on ice.
14. Add 4 μL of ligation (or controls) to each aliquot of 50 μL bacteria and mix gently by pipetting.
15. Incubate in ice for 10 min.
16. Heat shock at 42 °C in a water bath for 45 s.
17. Incubate in ice for 2 min.
18. Add 500 μL of sterile LB medium to each tube and mix by pipetting.
19. Incubate 1 h in a 37 °C bacterial shaker at 200 rpm.
20. Seed 80 μL of bacteria on sterile LB agar plates containing ampicillin.
21. Incubate the plates at 37 °C for at least 14 h.
22. On the following day, proceed to colony screening. The water plate should show no colonies, whereas the positive control plate should show colonies in the order of 10^2 to 10^3. The mock-ligation plate should show no or very few colonies. If these conditions are met, pick three to five colonies from the ligation plate with sterile pipette tips and place each of them in 15 mL tubes filled with 5 mL of sterile LB medium supplemented with ampicillin (0.1 mg/mL; LB-Amp). Include a tube with LB-Amp medium only, as control of the correct functioning of the antibiotic. Store the agar plates at 4 °C for few weeks.
23. Incubate the 15 mL tubes from **step 22** in a shaker for 12–18 h (200 rpm at 37 °C). There should not be bacteria growth in the negative control medium after incubation. If this medium is turbid, discard all the tubes and repeat with fresh ampicillin stocks.
24. After overnight incubation, save 0.5 mL of culture from each tube and store at 4 °C for up to 1 week.
25. Centrifuge the remaining 4.5 mL of culture for 20 min at 3500 × *g*.
26. Purify recombinant DNA from the pellets using a miniprep kit, following the manufacturer's instructions. Elute plasmid DNA with 30–50 μL of molecular grade water or TE buffer.
27. Measure plasmid DNA concentration using a UV-Vis spectrophotometer.
28. Check whether ITRs are still intact by enzymatic digestion with XmaI, SnaBI and PvuII restriction enzymes (*see* **Note 18**). Include a reaction with no restriction enzymes (undigested control). In a PCR tube, mix 2 μg of plasmid DNA, 3 μL of

10x Enzyme buffer, 1 μL of 20 U/μL restriction enzyme, and molecular grade water to a final volume of 30 μL.

29. Set the following program in a thermocycler: 6 h at 37 °C; 15 min at 65 °C; and hold at 4 °C.
30. Prepare a 1% agarose gel containing ethidium bromide and load 1 kb DNA ladder and half volume of each digestion or undigested control supplemented with 1× DNA loading buffer. Perform gel electrophoresis using 1× TAE buffer (150 V for 30–35 min). Visualize DNA bands using an UV gel imager (*see* **steps 3** and **4**).
31. Compare the size of the observed bands with those predicted on SnapGene or other vector mapping software, as shown in Fig. 5.
32. If ITR integrity is verified, send plasmid DNA out for sequencing the gRNA insert using U6ForSeq primer: 5′- CCTTCA TATTTGCATATACGATACAAGGCTGTTAG-3′.
33. Select the clone that contains the gRNA insert and intact ITRs and proceed to maxiprep preparation.
34. Add the previously saved 0.5 mL of culture (**step 24**) to 250 mL of sterile LB-Amp medium and incubate in a shaker for 16–20 h (200 rpm at 37 °C).
35. The day after, centrifuge down the culture at 6000 × *g* for 30 min and isolate plasmid DNA using a maxiprep kit, following the manufacturer's instructions. Elute plasmid DNA with ~300 μL of molecular grade water or TE buffer.
36. Measure plasmid DNA concentration using a UV-Vis spectrophotometer.
37. Check gRNA and ITRs as described above (*see* **steps 28–32**) before proceeding to transfection.
38. Store plasmid DNA at −20 °C until use.

3.2.3 AAV Packaging

Use recombinant AAV vectors based on serotype 8 for targeting the liver. For the vast majority of academic labs, it is more cost- and labor-effective to have AAV packaged by an academic or commercial core. Therefore, AAV packaging will not be covered in this chapter. For reference, primers for determining AAV titers for these vectors are given in **Note 19**. For labs interested in performing their own AAV packaging, an excellent protocol exists in a previously published chapter [6]. AAV should be aliquoted and stored at −80 °C until ready for use. Avoid repeated freeze-thaw cycles.

3.3 In vivo Study

3.3.1 AAV Preparation and Injection

A protocol for AAV preparation and intraperitoneal injection in *C57BL/6J* mice is described below (*see* **Note 20**). During AAV preparation, work in sterile conditions under a laminal flow in a biosafety hood.

1. Calculate a master mix for injecting n mice (+10% of volume), each one with 5×10^{11} genome copies in a final volume of 300 μL of sterile PBS (*see* **Note 21**).
2. Thaw AAV on ice.
3. Dilute AAV in the calculated volume of sterile PBS in a 2 mL tube.
4. Slowly load a sterile insulin syringes (25 to 27G needle) with 300 μL of the specific AAV dilution. Avoid the formation of air bubbles.
5. Manually restrain the mouse in head-down position with the abdomen side up facing the operator (*see* **Note 22**).
6. Insert the needle in the animal's right abdominal quadrant at about 30° angle.
7. Aspirate to be sure that the needle has not penetrated a blood vessel, the intestines or the urinary bladder. If any fluid is aspirated, discard the needle and syringe and prepare a fresh injection. If no fluid is aspirated, slowly inject the AAV dilution or sterile PBS in control mice.
8. Dispose the syringe in a sharp container and place the animal back in the cage. Injection groups are randomly assigned within cages when experimental design allows.
9. For atherosclerosis studies, feed mice with a Western diet for ~20 weeks with free access to food and water, and standard light–dark cycles.

3.3.2 Bleeding and Plasma Isolation

To assess plasma lipids, blood is collected at time 0 (right before the injection) and every 4 weeks after 5 h of fasting (*see* **Note 23**). For retroorbital bleeding (*see* **Note 24**), follow these steps:

1. Induce anesthesia by delivering isoflurane in an isolated sealed chamber connected to a precision vaporized device, using a rate of 3–4% isoflurane in oxygen.
2. Place the anesthetized mouse on its side on a work surface and control the animal reactivity by toe pinch. If no reflexes are shown, open the eye so that the eyeball is slightly protruding. Insert the appropriate sterile heparinized capillary tube at the medial or lateral canthus of the eye, at a 45° angle and avoiding the eyeball.
3. Puncture the retroorbital plexus by gently rotating the capillary tube and applying light pressure.

4. Once blood is visualized entering the capillary tube, raise the mouse relative to the tube, which helps the blood flow into the tube.
5. Remove the capillary tube and ensure hemostasis by applying gentle pressure to the eye with a sterile gauze sponge.
6. Place blood in a 1.5 mL tube in ice.
7. Place the animal back in the cage and monitor its recovery postanesthesia.
8. For isolating plasma, centrifuge blood at 10,000 × *g* for 20 min at 4 °C. Carefully, collect plasma and store samples at −80 °C until further use (*see* **Note 25**).

3.3.3 Liver Dissection

To assess editing and expression levels of the targeted genes, collect liver samples at the endpoint of the experiment. This procedure takes approximately 30 min per mouse. For atherosclerosis studies, collect also heart and aorta (*see* **Note 26**).

1. Fast mice for at least 5 h or overnight before dissection.
2. Induce anesthesia by delivering isoflurane in an isolated sealed chamber connected to a precision vaporized device, using a rate of 4–5% isoflurane in oxygen.
3. Collect blood by retroorbital bleeding as described in Subheading 3.3.2.
4. Euthanize the mouse by cervical dislocation.
5. Sanitize the abdomen with 70% ethanol. Then, cut the skin and the underneath abdominal wall with scissors to expose the caudal surface of the diaphragm. Cut the diaphragm and open the thoracic cavity. After exposure of the heart, perfuse the left ventricle with 10 mL of sterile PBS using a syringe with a 23G needle. Apply a cut on the right atrium. After a good perfusion, the liver should pale considerably as it is cleared of blood.
6. Harvest the liver and measure liver weight with a laboratory balance.
7. Section the largest lobe with a razor blade for collecting the samples in cryogenic microtubes: a ~20, 10 and 50 mg piece provides enough material respectively for DNA, RNA and protein isolation and downstream analyses. Snap freeze the samples in liquid nitrogen.
8. Collect a transverse slice for OCT embedding. Soak the slice in a mold filled with OCT, avoiding bubble formation and freeze the OCT block in a −80 °C freezer.
9. Collect a transverse slice for formalin fixation and paraffin embedding for immunohistochemistry. Incubate the slice in 10% formalin shaking overnight at room temperature, then

dehydrate samples with 70% ethanol. Samples can be stored at room temperature until proceeding with immunohistochemistry.

10. Collect all the remainder liver in a cryogenic microtube for further analyses and snap freeze it in liquid nitrogen.
11. Store liver samples in a −80 °C freezer.

3.4 Analysis of On-Target and Off-Target Nuclease Activity

Genome editing can be evaluated by (1) Sanger sequencing-based methods, (2) targeted deep sequencing and (3) integration PCR. The first two methods enable the detection of small indels at the DSB site. The third method enables detection of large insertions derived from the NHEJ-mediated integration of viral genomes in the DSB site. Furthermore, an AAV-genome PCR can be performed for diagnostic detection of the AAV-CRISPR genome in the liver. All these methods require genomic DNA isolation, primer design and PCR-amplification.

3.4.1 Liver DNA Isolation and Quantification

To assess editing at *Ldlr*, other targeted loci, or predicted off-target sites, we isolate genomic DNA from the liver (*see* **Note 27**).

1. Homogenize a small piece of liver (~20 mg) in 180 μL of lysis buffer (provided with the DNA isolation kit) with 1 steel bead in the bead mill homogenizer (4 cycles at 2500 rpm, 30 s each).
2. Incubate the homogenate with proteinase K (provided with the DNA isolation kit) at 37 °C for 30 min.
3. Isolate and purify DNA using silica-based membranes following the manufacturer's instructions.
4. Quantify DNA using any UV-Vis spectrophotometer that reads absorbance at 260 nm (*see* **Note 28**).
5. DNA can be stored at −20 °C until further use.

3.4.2 Primers Design for Sanger Sequencing-Based Methods

The targeted locus needs to be PCR-amplified and then sequenced by Sanger sequencing.

For this, design PCR-primers with the help of primer design software tools, such as Primer 3 (http://bioinfo.ut.ee/primer3-0.4.0/) or Primer 3 Plus (http://www.bioinformatics.nl/cgi-bin/primer3plus/primer3plus.cgi) (*see* **Note 29**).

1. Select the targeted locus containing the gRNA cut-site flanked by around 400 bp of genomic DNA on each side.
2. Design the forward and reverse primer to anneal at least 200 bp from the guide RNA cut-site to allow for optimal sequencing quality across the edit.
3. Design the primers to have an amplicon ranging between 500 and 800 bp.

4. As general criteria for designing primers, select primers with a T_m of ~60 °C (range: 58–62 °C), length around 18–22 bp and about 50% of GC content.
5. Check the specificity of each primer pair by using Primer Blast (https://www.ncbi.nlm.nih.gov/tools/primer-blast/index.cgi).

3.4.3 TIDE and ICE Analyses

1. Amplify the targeted locus in control and edited DNA samples (*see* **Note 30**). Perform a PCR on 100 ng of genomic DNA in a total volume of 50 µL using 10 µL of 5× reaction buffer (for chosen Taq DNA polymerase), 1 µL of 10 mM dNTPs, 0.5 µM of forward primer, 0.5 µM of reverse primer, 0.5 µL of 2 U/µL Taq DNA polymerase, 100 ng of DNA, and molecular grade water to a final volume of 50 µL (*see* **Notes 31** and **32**).
2. Set the following program in a thermocycler: Initial denaturation for 1 cycle at 98 °C for 3 min; 35–40 cycles of denaturation (30 s at 98 °C), annealing at temperature dependent on the Tm of the primers (e.g., 60–62 °C) for 1 min and extension (1 min for amplicon <1 kb at 72 °C); final extension for 5 min at 72 °C and hold at 4 °C till required.
3. Perform agarose gel electrophoresis as described in **steps 3** and **4** of Subheading 3.2.2, loading the whole volume of each PCR reaction supplemented with 1× DNA loading buffer. Visualize PCR products by an UV gel imager (*see* **Note 33**).
4. Cut out the band of interest and purify the PCR product as described in **steps 5** and **6** of Subheading 3.2.2.
5. Measure DNA concentration using a UV-Vis spectrophotometer and prepare samples for Sanger sequencing as required by the sequencing company.
6. Once the sequencing chromatograms have been obtained, proceed using TIDE (http://shinyapps.datacurators.nl/tide/) or ICE (https://ice.synthego.com/#/) tool (*see* **Note 34**). Both tools require to insert the gRNA sequence without PAM and upload the control and edited chromatograms as .ab1 or .scf files. The analysis provides the spectrum and frequency of indels at the cut site. The R^2 value should be greater than 0.9 to ensure accurate estimation of CRISPR activity. An example of output from TIDE is shown in Fig. 6 (*see* **Note 35**).

3.4.4 Targeted Deep Sequencing

While Sanger sequencing-based methods successfully indicate on-target editing, deep sequencing is a highly sensitive and accurate method for qualitative and quantitative analysis of indels formation at both the targeted locus and at predicted off-target sites (*see* **Note 36**).For the Illumina system, this is how we have prepared DNA for deep sequencing editing analyses in the past.

1. Design primers for amplifying the targeted regions using primer design software tools following the general criteria described in **step 4** of Subheading 3.4.2. It is required that the gRNA target site is included at the center of the amplicon, whose length should be between 200 and 300 bp. Add the following adapter sequences to the 5′ of each primer pair.

   Forward primer adapter: 5′-TCTACAGTCCGACGATCA-3′.

   Reverse primer adapter: 5′-GACGTGTGCTCTTCCGATC-3′.

   Check each primer pair for specificity with Primer Blast (https://www.ncbi.nlm.nih.gov/tools/primer-blast/index.cgi) (*see* **Note 37**).

2. PCR-amplify the targeted locus and predicted off-target sites using a high-fidelity Taq Polymerase (*see* **Note 38**). For a single reaction, mix 100 ng of genomic DNA, 10 μL of 5× reaction buffer (for chosen DNA polymerase), 1.25 μL of 10 mM dNTPs, 0.25 μM of forward primer, 0.25 μM of reverse primer, 0.5 μL of 5 U/μL Herculase II Fusion DNA polymerase, and molecular grade water to a final volume of 50 μL total (*see* **Note 32**).

3. Set the following program in a thermocycler: Initial denaturation for 1 cycle at 95 °C for 3 min; 30–35 cycles of denaturation (30 s at 95 °C), annealing at temperature dependent on the Tm of the primers (e.g., 60–62 °C) for 30 s and extension (30 s at 72 °C); final extension for 3 min at 72 °C and hold at 4 °C till required.

4. Perform agarose gel electrophoresis as described in **steps 3** and **4** of Subheading 3.2.2, loading 5 μL of each PCR reaction supplemented with 1× DNA loading buffer. Visualize DNA using an UV gel imager (*see* **Notes 33** and **39**).

5. In case of successful PCR, use each PCR reaction as template for the barcoding PCR (*see* **Note 40**). For each experimental group, prepare a reaction mix using the specific P5 forward primer by mixing 10 μL of 5× reaction buffer (for chosen DNA polymerase), 1.25 μL of 10 mM dNTPs, 2.5 μL of 5 μM P5 forward primer (Cf: 0.25 μM), 0.5 μL of 5 U/μL Herculase II Fusion DNA polymerase and molecular grade water to a final volume of 45.5 μL total. For preparing multiple reactions, make a master mix by scaling up all the reagent volumes. Then, aliquot the master mix in a 96 well plate.

6. Add 2.5 μL of specific 5 μM P7 reverse primer to the appropriate well (Cf: 0.25 μM).

7. Add 2 μL of the appropriate PCR product (on- or off-target PCRs generated in **steps 2–4**). Include a reaction with no DNA as negative control for any reagent contamination.

8. Set a touch down PCR protocol in a thermocycler as follows: Initial denaturation for 1 cycle at 95 °C for 3 min; 7 cycles (delta −1 °C for annealing temperature at each cycle) of denaturation (30 s at 95 °C), annealing (30 s starting at 67 °C) and extension (30 s at 72 °C); then, 29 cycles of denaturation (30 s at 95 °C), annealing (30 s at 60 °C) and extension (30 s at 72 °C); final extension for 3 min at 72 °C and hold at 4 °C till required.
9. Perform agarose gel electrophoresis as described in **steps 3** and **4** of Subheading 3.2.2, loading 5 μL of each PCR reaction supplemented with 1× DNA loading buffer. Visualize DNA using an UV gel imager (*see* **Note 33**).
10. Purify each PCR reaction using Agencourt AmPure XP magnetic beads following the manufacturer's instructions.
11. Use Qubit fluorimeter for measuring the concentration of each purified DNA product (*see* **Note 41**).
12. Generate equimolar pools of the purified targets based on the requirements for the sequencing reaction (*see* **Note 42**).
13. Submit the equimolar, pooled barcoded DNA library to appropriate facility or company for sequencing (*see* **Note 43**).

3.4.5 Integration PCR

This method consists of PCR amplification of the targeted locus using a first primer complementary to a genomic region upstream or downstream of the targeted site and a second primer annealing to the ITR or other viral sequences (*see* **Note 44**). An example of integration PCRs at the *Ldlr* locus is shown in Fig. 6.

1. Design primers for amplifying the targeted locus using primer design software tools following the general criteria described in **step 4** of Subheading 3.4.2 (*see* **Note 45**).
2. Perform the PCR using 100 ng of genomic DNA using Apex 2× Taq Red Master Mix following the manufacturer's protocol. For a PCR reaction use 0.4 μM of each primer, 12.5 μL of 2× Taq Red Master Mix, 100 ng of genomic DNA, and molecular grade water to a final volume of 25 μL (*see* **Notes 32** and **46**).
3. Set the following program in a thermocycler: Initial denaturation for 1 cycle at 95 °C for 5 min; 35 cycles of denaturation (30 s at 95 °C), annealing at temperature dependent on the Tm of the primers (e.g., 60–62 °C) for 1 min and extension at 72 °C (1 min for <1 kb amplicon); final extension for 5 min at 72 °C; and hold at 4 °C till required.
4. Perform agarose gel electrophoresis as described in **steps 3** and **4** of Subheading 3.2.2, loading half volume of each PCR reaction supplemented with 1× DNA loading buffer. Visualize PCR products using an UV gel imager (*see* **Note 33**).

3.4.6 AAV Genome PCR

1. For an AAV genome PCR reaction (*see* **Note 47**) use 0.4 μM of primer WRL_0064 (5′ CCGTCGTGAAGAGAAGCTTCATC-3′), 0.4 μM of primer WRL_0070 (5′- CCACCTCATAGTT GAAGGGGTTG-3′), 12.5 μL of 2× Taq Red Master Mix, 100 ng of genomic DNA and molecular grade water to a final volume of 25 μL (*see* **Notes 32** and **46**).
2. Set the following program in a thermocycler: initial denaturation at 95 °C for 5 min; 35 cycles of denaturation (30 s at 95 °C), annealing (1 min at 62 °C) and extension (1 min at 72 °C); final extension at 72 °C for 5 min; and hold at 4 °C till required.
3. Perform agarose gel electrophoresis as described in **steps 3** and **4** of Subheading 3.2.2, loading half volume of each PCR reaction supplemented with 1× DNA loading buffer. Visualize PCR products using an UV gel imager (*see* **Note 33**).

3.5 Evaluation of Gene Knockdown by Western Blot

The effect of genome editing on the expression level of *Ldlr* or other targeted genes can be evaluated by western blot on liver lysates (or plasma if the protein is secreted) (*see* **Note 48**). An example of Ldlr western blot is shown in Fig. 6.

1. Thaw liver and plasma samples on ice.
2. For isolating liver proteins, add 10 volumes of RIPA buffer (supplemented with protease inhibitor cocktail) relative to liver weight (i.e., 500 μL for a 50 mg piece).
3. Add 1 steel bead to each tube.
4. Homogenize in a bead mill homogenizer (4 cycles at 2500 rpm, 30 s each).
5. Place lysed livers on ice for 30 min, and then vortex.
6. Centrifuge at 13,800 × *g* for 20 min at 4 °C.
7. Collect supernatant to a new 1.5 mL tube.
8. Dilute each sample 1:10 with Milli-Q double distilled water and use 2 μL of dilution in a final volume of 100 μL for measuring protein concentration (*see* **Note 49**). Once the concentration is determined, proceed to SDS-PAGE or store at −20 °C until further use.
9. Prepare liver lysates or plasma samples for SDS-PAGE in a final volume of 15 μL of loading mix per lane using 50–80 μg of liver lysate (or 1 μL of plasma sample), 3.75 μL of 4× LDS Sample Buffer, 0.75 μL of Beta-Mercaptoethanol (Cf: 5%) and water to 15 μL (*see* **Note 50**).
10. Heat samples to 95 °C for 10 min using a heat block or thermocycler, vortex, centrifuge at 2000 × *g* for 1 min to collect condensate and cool samples to room temperature before loading.

11. For most western blot applications, use 4–12% Bis-Tris gels with the appropriate number of lanes.
12. Dilute the 20× MES running buffer to 1× with Milli-Q double distilled water (*see* **Note 51**).
13. Assemble up to two gels in a mini-protein gel electrophoresis system.
14. Fill inner chamber with 1× running buffer and check for leaks.
15. Fill outer chamber about 80% with 1× running buffer.
16. Load the first lane with 3 μL of protein marker.
17. Load the following lanes with 15 μL of each sample.
18. Perform electrophoresis at 150 V (if desired gels can be run slower).
19. Shut off power supply when the dye front reaches about 1 cm from the bottom of the gel and proceed to transfer using the wet transfer method (*see* **Note 52**).
20. Dilute 20× transfer buffer to 1× with Milli-Q double distilled water and add methanol to 20% final concentration.
21. Soak 5 sponges and 4 filter papers per blot module in 1× transfer buffer.
22. Activate 0.45 μm PDVF membrane with 100% methanol for few minutes and then soak the membrane in 1× transfer buffer. Use gel tweezers for handling the membranes at each step.
23. Assemble the blot sandwich as following: FRONT (flat plate of the blot module); Sponge; Sponge; Filter paper; PDVF membrane 2; Gel 2; Filter paper; Sponge; Filter paper; PDVF Membrane 1; Gel 1; Filter paper; Sponge; Sponge; BACK (Deep plate of the blot module).
24. Avoid bubbles by rolling the sandwich with a serological pipette after the addition of each layer.
25. Put the sandwich in the blot module.
26. Close the blot module and place it in the mini-protein gel electrophoresis system, then secure with clamp.
27. Add 1× transfer buffer to the inner chamber.
28. Tap the gel box several times for removing any air bubbles.
29. Add ice water to the outer chamber.
30. Transfer at 35 V for 90 min.
31. Remove the membranes from transfer sandwich.
32. Block the membranes with blocking buffer by gently rocking for 2 h on a shaker (40 rpm at room temperature).

33. Dilute primary antibodies in antibody buffer following the dilution recommended by the manufacturer (*see* **Note 53**). Incubate on a shaker overnight (40 rpm at 4 °C).
34. The day after, wash membranes three times with PBS-T on a shaker, 10 min each (40 rpm at room temperature).
35. Dilute secondary antibodies, goat anti-rabbit 700 nm and goat anti-mouse 800 nm, 1:15,000 with antibody buffer (*see* **Note 54**). Incubate the membranes with the secondary antibodies gently rocking for 1 h at room temperature (40 rpm).
36. Wash membranes three times with PBS-T on a shaker, 10 min each (40 rpm at room temperature).
37. Image the membranes with Odyssey infrared imaging system using the following settings: Resolution: 169 μm; Quality: Low; Intensity for 700 nm channel: 5.0; Intensity for 800 nm channel: 5.0.

4 Notes

1. Resuspend oligonucleotides/primers in molecular grade water at a stock concentration of 100 μM. Store at −20 °C.
2. Bring the solution to boil by using a microwave oven for dissolving the agarose.
3. Add 3–4 μL per 150 mL of agarose in 1× TAE buffer, only after dissolving agarose. Handle ethidium bromide with caution because it is a mutagen.
4. Use a protective shield while using the UV transilluminator because UV radiation is harmful to both skin and eyes.
5. We use SnapGene (from Insightful Science; available at https://www.snapgene.com). SnapGene Viewer can also be used, but functionality is limited. However, other annotation software can be used.
6. Autoclave and store at room temperature for a short period.
7. Autoclave, cool down to 50 °C and add the 50 mg/mL Ampicillin stock to a final concentration of 0.1 mg/mL. Pour in 10 cm petri dishes and let it solidify. Store at 4 °C.
8. Before proceeding with gRNA design, a target file should be generated for both the genomic sequence and for the mRNA sequences for the target. The files should be annotated to highlight exons included in all mRNA isoforms, as well as essential domains or other regions of interest that would be detrimental to protein function if disrupted. gRNAs will be annotated in the files as they are generated. Later, primers for detection of editing can be added to these files. We use

SnapGene to annotate genomic, RNA and plasmid files, but other programs can be used.

9. We recommend designing gRNAs that target the first coding exons of the gene of interest when possible. Editing early exons is expected to increase the likelihood of frameshift mutations and premature stop codons resulting in aberrant proteins. If a target gene expresses multiple transcripts, we recommend targeting the exons conserved among the transcripts.
10. Until recently, most gRNA design tools did not include SaCas9, which has a 5′-NNGRRT-3′ PAM. Because of this, gRNAs were designed manually through visual inspection of the target genes. While tools that will be discussed later now exist (*see* Subheading 3.1.4), some gRNAs still need to be designed by in this way for complicated targets.
11. A limitation of the CRISPR/Cas9 system is the potential nuclease activity at genomic sites other than the targeted locus that show similarity with the gRNA sequence and are in close proximity to a PAM sequence (referred to as off-target sites). Off-target prediction allows selection of gRNAs that have the lowest probability for undesired edits at off-target sites. For predicting off-targets, we use the COSMID web-based tool that searches genomes for potential off-target sites (http://crispr.bme.gatech.edu) [25]. In addition, using COSMID website, both the gRNA target (on-target) and off-targets will be scored. The closer to zero this score is, the more likely there is to be cutting at the off-target site.
12. However, we generally download sequences for the off-targets for later primer design based on the chromosomal position (*see* Subheading 3.4.2).
13. Like COSMID, CRISPOR will predict off-targets though it uses different parameters and prediction algorithms, so the off-targets it predicts are slightly different. For details on the tool refer to Concordet et al. [26]. CRISPOR also selects potential gRNA sequences from a sequence input, so candidate gRNAs do not need to be designed by eye. CRISPOR ranks potential gRNAs, scores them based on specificity and efficiency and provides additional parameters for assessing gRNAs for the desired application. Using this tool is easier and faster than designing gRNAs by hand.
14. The oligonucleotide sequences for the *Ldlr* gRNA as follows: top: 5′-CACCGGGCAGGCGCAGGTGAATTTGG-3′ and bottom 5′-AAACCCAAATTCACCTGCGCCTGCCC-3′, with the gRNA sequence underlined.
15. Oligonucleotides are now annealed at a final concentration of 1.3 ng/μL (0.083 μM). Annealed oligonucleotides are ready

for direct ligation into the predigested acceptor vector or can be stored at −20 °C until further use.

16. Annealed gRNAs with BbsI overhangs are then cloned into BbsI-linearized 1313_pAAV-U6-SA-BbsI-MluI-gRNA-HLP-SACas9-HA-OLLAS-spA acceptor vector (Addgene 109314) [22, 23]. SnapGene or other vector mapping software can be used to design and map the vector, plan cloning, and predict enzymatic digestions. The 1313 acceptor vector contains the following components (Fig. 4).
    (a) Two complementary ITR sequences located at the 5′ and 3′ terminal ends of AAV genome, which are required for intermolecular recombination and circularization.
    (b) The U6 promoter, which drives the expression of the gRNA.
    (c) The gRNA cloning site containing BbsI and MluI restriction sites (Fig. 3).
    (d) A gRNA scaffold required for the Cas9:gRNA complex formation, composed of the crRNA direct repeat portion, a synthetic tetraloop and a Cas9 nuclease-recruiting sequence (TracrRNA).
    (e) A multiple cloning site, containing XbaI and HindIII restriction sites.
    (f) The hepatocyte specific hybrid liver promoter (HLP) [30], which enables a liver-restricted expression of Cas9, resulting in specific editing in the liver without any extrahepatic activity [22].
    (g) The SaCas9 coding sequence fused to the following elements: (a) the nuclear localization signal (NLS) from SV40 large T antigen in the 5′ end; (b) the bipartite NLS from nucleoplasmin in the 3′ end; (c) the human influenza hemagglutinin (HA) epitope tag in the 3′ end; (d) the *Escherichia coli* OmpF Linker and mouse Langerin fusion Sequence (OLLAS) epitope tag fused to the 3′ end upstream of the stop codon.
    (h) A synthetic polyadenylation signal (spA).
    (i) The pEMBL8 backbone including an ampicillin resistance gene (AmpR).
17. The dephosphorylation step is not required because BbsI generates sites that do not self-ligate as they are not complementary.
18. ITRs cannot be easily sequenced due to the repetitive nature and the hairpin structure. Hence, restriction digestions constitute the preferred diagnosis tool for checking the ITR integrity.

19. For determining the titer of AAV-CRISPR we recommend using primers WRL_0064 (5′-CCGTCGTGAAGAGAAGCTT CATC -3′) and WRL_0070 (5′- CCACCTCATAGTT GAAGGGGTTG -3′), which target the SaCas9 coding sequence generating a 324 bp product.
20. For *in vivo* studies, we use *C57BL/6J* mice, but the AAV-CRISPR tool can be applied to other mouse strains and genetic backgrounds. Somatic editing in mice on genetic backgrounds other than *C57BL/6J* may require a preliminary experiment for optimizing the dose of AAV-CRISPR. Older mice might also need a higher dose and different mouse models of liver disorders (e.g., liver steatosis or fibrosis) showing liver malfunction or toxicity may require dose optimization. We recommend titrating AAV-CRISPR from 5×10^{11} to 1×10^{12} genome copies per mouse for identifying the most efficient dose before starting the experiment. For targeting the liver, AAV8 vectors can be injected either intraperitoneally or intravenously. We generally practice intraperitoneal injection, which is highly effective in targeting the liver and is also easily executed with minimal training. When looking for editing a candidate gene, we find that an "n" of 6 to 8 age- and sex-matched mice per group is a good starting point. For atherosclerosis studies, we recommend enrolling 15 to 20 mice per group. Control mice will be injected with the same volume of sterile PBS or saline solution. Alternatively, control mice can be injected with an AAV-CRISPR with no gRNA. AAV injection can be performed only once because of the elicited immune response to the AAV capsid proteins and Cas9 [24, 31, 32].
21. In our experience, editing is more efficient in male *C57BL/6J* mice injected at an age of at least 6 to 8 week old. A dose of 5×10^{11} genome copies of *Ldlr* AAV-CRISPR enables efficient and permanent editing of the targeted gene [21]. We observed a sexual dimorphism in female mice injected with the same dose of *Ldlr* AAV-CRISPR, resulting in less efficient Ldlr knockdown and atherosclerosis development as compared to male mice [21]. In case of enrollment of female mice in a study, test 5×10^{11} and 1×10^{12} genome copies per mouse to ensure efficient editing of the target locus. The administered volume (300 μL) is much lower than 1.5 mL, which is the maximum volume allowed for a safe intraperitoneal injection to a ~20 g mouse.
22. Perform all the animal experiments in accordance with IACUC and institutional guidelines.
23. Fasting is important for clearance of food-derived lipids.

24. We collect blood from the retroorbital plexus, but other blood collection techniques can be applied. Seek training and ensure protocol approval before attempting blood collection. Mice have to be anesthetized during the procedure and the retroorbital puncture must be performed by skilled personnel for limiting the risk of injury to the eye and surrounding structures. In agreement with IACUC regulations, approximately 10% of the total blood volume can be safely removed every 2 to 4 weeks (around 110–140 μL of blood for a 20 g mouse).
25. For measuring plasma total cholesterol, we use a commercial kit (WAKO cholesterol E reagent) following the manufacturer protocol and 5 μL of 1:10 dilution of plasma samples. For measuring plasma triglycerides, we use a commercial kit (Infinity Triglycerides Reagent and Control Serum I) following the manufacturer protocol using 10 μL of plasma.
26. To quantify atherosclerosis development, the heart and aorta are collected for immunohistochemistry analysis of the aortic sinus and en face Oil Red O staining, respectively. These techniques enable to quantify the lipid burden and characterize the morphology, cellularity, and pathophysiology of the atherosclerosis lesions. For heart and aorta dissection and analysis protocols we refer to other relevant chapters of this book and to standard protocols already published [1, 33]. Wash and sterilize surgical instruments with a glass bead sterilizer after each dissection.
27. We use the DNeasy Blood and Tissue kit (Qiagen) following the manufacturer's protocol, though any other commercial kit can be used. Phenol–chloroform extraction can also be used.
28. For downstream analyses that require a more accurate and sensitive measurement, such as deep sequencing, we recommend using a fluorometric quantification (e.g., Qubit fluorometer). This method specifically quantifies DNA molecules via intercalating dyes resulting in higher specificity and sensitivity than absorbance-based methods, which do not discriminate DNA from RNA and nucleotide contaminants.
29. We recommend designing two to three primer pairs and test them for efficient amplification of the expected PCR product and absence of any nonspecific amplification. We use the same primers for sequencing the PCR-amplicon by Sanger sequencing. Otherwise, nested primers can be designed using the same primer design software tools.
30. We recommend using a high-fidelity Taq DNA polymerase for avoiding the generation of any random mutations that can bias the editing analysis. We use the Phusion High-Fidelity DNA Polymerase (Thermo-Scientific), following the manufacturer's protocol.

31. For amplifying the *Ldlr* locus, we recommend using primers *Ldlr* Ex14For1 (5′- CCGGAGGACATTGTCCTGTTC -3′) and *Ldlr* Ex14Rev1 (5′- CTCAGGGAATCTGCTTCAG CAAC-3′), which generate a PCR product of 638 bp.
32. For preparing multiple PCRs, make a master mix by scaling up all the reagent volumes except the template. Then, aliquot the master mix in the PCR tubes and finally add genomic DNA to each tube. Include a reaction with no DNA as negative control for any reagent contamination.
33. Discard tubes and repeat PCRs using new reagents if any amplification is detected in the negative control. Optimize the primer design or PCR protocol in case of no or multiple PCR products.
34. TIDE and ICE are free and easy-to-use web-based software tools that offer fast analysis of CRISPR editing data. Both methods require the PCR amplification of the targeted locus followed by Sanger sequencing. Moreover, both methods require an unedited sequence of the targeted site as a control sequence. TIDE aligns the control to the edited sequence, which shows a mixture of signals starting at the cut site and consisting of the unmodified DNA plus the sequences that are modified by insertions and deletions of nucleotides. Then, the TIDE software decomposes the composite sequence trace into its individual traces and estimates the relative abundance of every possible indel. Some parameters like the alignment and decomposition windows and the detected indel size range can be manually adjusted and optimized. Details on the algorithm are described in Brinkman et al. [27]. ICE has been generated by Synthego for implementing TIDE. Similarly to TIDE, ICE aligns the control to the edited sequence and quantifies the traces with indels. Distinct from TIDE, ICE enables multiple editing analyses at once and there is no requirement for parameter adjustments [28]. ICE and TIDE were designed for SpCas9 indel frequency calculation and do not allow specification of the PAM sequence. Because of this, when using ICE for SaCas9 gRNAs, there is often a notation that there is no PAM detected, which can be ignored. The editing results are still accurate. In our experience, TIDE and ICE result in comparable editing efficiency rates. The reliability of these methods depends on the purity of the PCR products and the quality of the sequence reads. Highly repetitive sequences around the target site can hamper the decomposition process. TIDE can detect indels with a sensitivity of ~1–2% across various targets [34].
35. In our experience, an editing frequency of at least 30% at the *Ldlr* locus is sufficient for reaching a ~90–95% knockdown

level [21]. The editing efficiency obtained by ICE, TIDE and deep sequencing underestimates actual editing. This is because analysis is performed using total liver DNA, which includes DNA derived from nonparenchymal cells (~15% of liver cells), which are not transduced by AAV. In addition, large insertions and deletions are not captured by sequencing-based methods, which involve small PCR amplicons. Finally, AAV-genome insertion at the DSB site is a recurring event and contributes to gene editing. For detecting AAV genome insertion at the DSB site, we perform an integration PCR as described in Subheading 3.4.5 in this chapter.

36. Deep sequencing can detect indels with a sensitivity of ~0.1% [23], making it ideal for assessing off-target editing events. The targeted locus and CRISPOR- or COSMID- predicted off-targets are amplified through two rounds of PCR, which add adaptors and barcoding sequences for sequencing by the Illumina system. Despite the high sensitivity of the method, the major limitations for this technique are the availability of Illumina system as well as the cost of the service. However, deep sequencing cores and companies can offer this service. Preparation of libraries of DNA samples may vary by facility, so confirm which barcoding paradigm they require for sequencing before proceeding.
37. If these barcode primers are used, for amplifying the *Ldlr* locus, we recommend using primers KEJ_0462 (5′-TCTACAGTCC GACGATCACTTGACTCTGCCCGTCATCA -3′) and KEJ_0463 (5′- GACGTGTGCTCTTCCGATCCTGGA CATCTGGTCAGCCTC-3′), which generates a PCR product of 318 bp.
38. We use the Herculase II Fusion DNA Polymerase (Agilent Technologies). However, other high-fidelity Taq Polymerases can be used.
39. Gel extraction can be performed for purifying the expected PCR product when multiple products of different size are detected.
40. The aim of this PCR reaction is to add barcodes to each PCR amplicon by using a unique combination of P5 forward and P7 reverse primers pair. A unique P5 forward primer (P5_1 or P5_2, etc.) is used for barcoding the specific experimental group. A unique P7 primer (P7_1 or P7_2, etc.) identifies a specific mouse in the experimental group. For instance, P5_1 and P5_2 are respectively used for barcoding “control” and “knockout” group. Then, each of the 3 “control” mice are barcoded combining P5_1 respectively with P7_1, P7_2 and P7_3. We use Herculase II Fusion DNA Polymerase (Agilent

Technologies) and 2 μL of the on- or off-target PCR reactions as template in a final 50 μL reaction.

41. Ideally the final concentration should be greater than 20 ng/μL.
42. For a previous sequencing reaction, we diluted the products to 40 nM and pooled equal volumes of all barcoded products to a final volume of greater than 200 μL.
43. Paired-end reads can be analyzed for genome editing using many different methods using Python or R, but extensive knowledge of computational methods is not required. Resources like CRISPResso2 (https://crispresso.pinellolab.partners.org/submission) allow direct submission of Fastq files, amplicon and gRNA information via a web form to determine editing efficiency [29]. CRISPResso2 is also open-source and can be run in the command line with no limitations (https://github.com/pinellolab/CRISPResso2).

    If needed CRISPResso2 can also filter low quality reads, trim adapters, and align reads. More information can be found here: https://crispresso.pinellolab.partners.org/help.

    For the web version of CRISPResso2, assign the center of the quantification window to −3, which is the most common SaCas9 cut site relative to the PAM. The Quantification Window Size determines how large the window around the cut site is for calling mutated bases. By default this is set to 1, but may need to be adjusted for different gRNA sequences.

    In the liver, because insertions and deletions larger than 2–3 bp are missed by standard editing pipelines, editing events greater than 25–30% suggest a large proportion of hepatocytes have been successfully edited.
44. ICE, TIDE, and deep sequencing enable detection of small editing events at the cut site. However, we and others have observed the NHEJ-mediated integration of partial or whole AAV genomes in the DSB site, which cannot be resolved with the sequencing-based methods due to their size [21–23, 35, 36]. Integration PCR is a simple and rapid method for detecting these large insertion events. We usually use this method as quick and qualitative assessment of genome editing at the targeted locus.
45. For detecting AAV integration at the DBS in exon 14 of *Ldlr*, we recommend using the following primers: *Ldlr* Ex14For1 (5′-CCGGAGGACATTGTCCTGTTC-3′) and U6RevSeq (5′-CTTTCAAGTTACGGTAAGCATATGATAG-3′) for detecting AAV forward integration (expected product size: 757 bp) or *Ldlr* Ex14For1 (5′-CCGGAGGACATTGTCCTGTTC-3′) and WRL_0067 (5′-CAGACATTCTGGGCAACCTGTA-3′) for detecting AAV backward integration (expected

product size: 736 bp). An example of integration PCRs at the *Ldlr* locus is shown in Fig. 6.

MDG_0151 (5′- GATAAGTAGCATGGCGGGTT -3′) primer anneals to the ITR sequence and can be used in pair with any other compatible primer for detecting integration of ITRs at the cut site, regardless of the viral genome orientation.

46. We use Apex 2X Taq Red Master Mix. However, other Taq Polymerases can be used. High-fidelity Taq Polymerases are not required for this PCR. It is recommended to perform an additional PCR in parallel using primer pairs already validated, as control of the DNA quality and PCR protocol.
47. When testing new gRNAs, it may be possible to observe low or no editing at the targeted locus. We recommend assessing in parallel, the expression of the targeted gene at protein level. Low levels of detectable editing levels due to high levels of AAV integration may still result in efficient protein knockdown. However, results showing low levels of both editing and knockdown may be explained by either poor design/specificity of the gRNA or a bad injection, which results in reduced or no delivery of the CRISPR/Cas9 tool to the liver. An AAV genome PCR on liver DNA provides rapid and qualitative information on the presence of AAVs in the liver, and therefore is very useful for troubleshooting. For detecting AAV genomes, we recommend using WRL_0064 (5′-CCGTCGTGAA GAGAAGCTTCATC -3′) and WRL_0070 (5′-CCACCTCATAGTTGAAGGGGTTG-3′) primers, which are designed to amplify the SaCas9 coding sequence generating a 324 bp PCR product. An example of AAV genome PCR is shown in Fig. 6.
48. Liver samples are mechanically homogenized producing liver lysates. Then, liver proteins (50–80 μg) are separated by SDS-PAGE, transferred to a PDVF membrane and probed for Ldlr (or the targeted protein), along with a constitutively expressed protein used as loading control. In the case of plasma, 1 μL of plasma is diluted in loading mix. As loading control for plasma samples, blots can be stained with Ponceau Red or probed for a constitutive expressed plasma protein (e.g., albumin, alpha-1 antitrypsin) [22]. We use an infrared-based detection system (Odyssey, Licor) that enables the simultaneous detection of two differently labeled proteins on a single blot. Other labeling and detection systems can be used. In the absence of working antibodies, qPCR analysis can be performed to investigate the knockdown of the targeted gene at RNA level [22].
49. We use a BCA assay following the manufacturer's protocol. Any other commercial kit can be used.

50. For preparing multiple loadings, make a master mix by scaling up LDS Sample Buffer and beta-mercaptoethanol. Then, aliquot the mix in 1.5 mL tubes and finally add the liver lysate or plasma dilution to each tube.
51. One mini-protein gel electrophoresis system requires about 800 mL of 1× running buffer.
52. Alternative transfer methods can be used.
53. For probing Ldlr, we recommend ab52818 (Abcam) at a 1:1000–1:2500 dilution.
54. Other secondary antibodies and labeling and detection systems can be used.
55. The *Ldlr* AAV-CRISPR described in Jarrett et al. [21] (1375_pAAV8-U6-SA-WTmLdlrEx14-gRNA2-N22-CB-SACas9-HA-OLLAS-spA, Addgene 109311) has been generated using 1255_ pAAV-U6-SA-BbsI-MluI-gRNA-CB-SACas9-HA-OLLAS-spA (Addgene 109320) as acceptor vector for the *Ldlr* gRNA. We recommend using 1313_pAAV-U6-SA-BbsI-MluI-gRNA-HLP-SACas9-HA-OLLAS-spA (Addgene 109314) as acceptor vector for the *Ldlr* gRNA, which implements 1255 vector by replacing the constitutive chicken β-actin (CB) promoter with the hepatocyte specific HLP promoter for driving the expression of SaCas9 (Fig. 3). We showed that the change of promoter does not affect *Ldlr* editing and disruption [24], as well as atherosclerosis development as documented in Fig. 7.

Acknowledgments

This work was supported by the National Institutes of Health (HL132840, DK124477, U42 OD026645 and UG3 HL151545 to W.R.L.; HL122677, DK119112, and DK118064 to T.Q. de A. V.; and T32HL069766 sponsoring K.E.J.) and the American Heart Association (19POST34430092 to M.D.G.).

References

1. Daugherty A, Tall AR, Daemen M, Falk E, Fisher EA, Garcia-Cardena G, Lusis AJ, Owens AP 3rd, Rosenfeld ME, Virmani R, American Heart Association Council on Arteriosclerosis T, Vascular B, Council on Basic Cardiovascular S (2017) Recommendation on design, execution, and reporting of animal atherosclerosis studies: a scientific statement from the American Heart Association. Arterioscler Thromb Vasc Biol 37(9): e131–e157. https://doi.org/10.1161/ATV.0000000000000062
2. Ishibashi S, Brown MS, Goldstein JL, Gerard RD, Hammer RE, Herz J (1993) Hypercholesterolemia in low density lipoprotein receptor knockout mice and its reversal by adenovirus-mediated gene delivery. J Clin Invest 92(2): 883–893. https://doi.org/10.1172/JCI116663
3. Defesche JC, Gidding SS, Harada-Shiba M, Hegele RA, Santos RD, Wierzbicki AS (2017)

Familial hypercholesterolaemia. Nat Rev Dis Primers 3:17093. https://doi.org/10.1038/nrdp.2017.93

4. Piedrahita JA, Zhang SH, Hagaman JR, Oliver PM, Maeda N (1992) Generation of mice carrying a mutant apolipoprotein E gene inactivated by gene targeting in embryonic stem cells. Proc Natl Acad Sci U S A 89(10): 4471–4475. https://doi.org/10.1073/pnas.89.10.4471
5. De Giorgi M, Lagor WR (2019) Gene delivery in lipid research and therapies. Methodist Debakey Cardiovasc J 15(1):62–69. https://doi.org/10.14797/mdcj-15-1-62
6. Lagor WR, Johnston JC, Lock M, Vandenberghe LH, Rader DJ (2013) Adeno-associated viruses as liver-directed gene delivery vehicles: focus on lipoprotein metabolism. Methods Mol Biol 1027:273–307. https://doi.org/10.1007/978-1-60327-369-5_13
7. Seidah NG, Awan Z, Chretien M, Mbikay M (2014) PCSK9: a key modulator of cardiovascular health. Circ Res 114(6):1022–1036. https://doi.org/10.1161/CIRCRESAHA.114.301621
8. Roche-Molina M, Sanz-Rosa D, Cruz FM, Garcia-Prieto J, Lopez S, Abia R, Muriana FJ, Fuster V, Ibanez B, Bernal JA (2015) Induction of sustained hypercholesterolemia by single adeno-associated virus-mediated gene transfer of mutant hPCSK9. Arterioscler Thromb Vasc Biol 35(1):50–59. https://doi.org/10.1161/ATVBAHA.114.303617
9. Goettsch C, Hutcheson JD, Hagita S, Rogers MA, Creager MD, Pham T, Choi J, Mlynarchik AK, Pieper B, Kjolby M, Aikawa M, Aikawa E (2016) A single injection of gain-of-function mutant PCSK9 adeno-associated virus vector induces cardiovascular calcification in mice with no genetic modification. Atherosclerosis 251:109–118. https://doi.org/10.1016/j.atherosclerosis.2016.06.011
10. Bjorklund MM, Hollensen AK, Hagensen MK, Dagnaes-Hansen F, Christoffersen C, Mikkelsen JG, Bentzon JF (2014) Induction of atherosclerosis in mice and hamsters without germline genetic engineering. Circ Res 114(11):1684–1689. https://doi.org/10.1161/CIRCRESAHA.114.302937
11. Kosenko T, Golder M, Leblond G, Weng W, Lagace TA (2013) Low density lipoprotein binds to proprotein convertase subtilisin/kexin type-9 (PCSK9) in human plasma and inhibits PCSK9-mediated low density lipoprotein receptor degradation. J Biol Chem 288(12):8279–8288. https://doi.org/10.1074/jbc.M112.421370
12. Sun H, Krauss RM, Chang JT, Teng BB (2018) PCSK9 deficiency reduces atherosclerosis, apolipoprotein B secretion, and endothelial dysfunction. J Lipid Res 59(2):207–223. https://doi.org/10.1194/jlr.M078360
13. Sun H, Samarghandi A, Zhang N, Yao Z, Xiong M, Teng BB (2012) Proprotein convertase subtilisin/kexin type 9 interacts with apolipoprotein B and prevents its intracellular degradation, irrespective of the low-density lipoprotein receptor. Arterioscler Thromb Vasc Biol 32(7):1585–1595. https://doi.org/10.1161/ATVBAHA.112.250043
14. Jinek M, Chylinski K, Fonfara I, Hauer M, Doudna JA, Charpentier E (2012) A programmable dual-RNA-guided DNA endonuclease in adaptive bacterial immunity. Science 337(6096):816–821. https://doi.org/10.1126/science.1225829
15. Pankowicz FP, Jarrett KE, Lagor WR, Bissig KD (2017) CRISPR/Cas9: at the cutting edge of hepatology. Gut 66(7):1329–1340. https://doi.org/10.1136/gutjnl-2016-313565
16. Yin H, Xue W, Chen S, Bogorad RL, Benedetti E, Grompe M, Koteliansky V, Sharp PA, Jacks T, Anderson DG (2014) Genome editing with Cas9 in adult mice corrects a disease mutation and phenotype. Nat Biotechnol 32(6):551–553. https://doi.org/10.1038/nbt.2884
17. Zhao H, Li Y, He L, Pu W, Yu W, Li Y, Wu YT, Xu C, Wei Y, Ding Q, Song BL, Huang H, Zhou B (2020) In vivo AAV-CRISPR/Cas9-mediated gene editing ameliorates atherosclerosis in familial hypercholesterolemia. Circulation 141(1):67–79. https://doi.org/10.1161/CIRCULATIONAHA.119.042476
18. Ding Q, Strong A, Patel KM, Ng SL, Gosis BS, Regan SN, Cowan CA, Rader DJ, Musunuru K (2014) Permanent alteration of PCSK9 with in vivo CRISPR-Cas9 genome editing. Circ Res 115(5):488–492. https://doi.org/10.1161/CIRCRESAHA.115.304351
19. Ran FA, Cong L, Yan WX, Scott DA, Gootenberg JS, Kriz AJ, Zetsche B, Shalem O, Wu X, Makarova KS, Koonin EV, Sharp PA, Zhang F (2015) In vivo genome editing using Staphylococcus aureus Cas9. Nature 520(7546): 186–191. https://doi.org/10.1038/nature14299
20. Jarrett KE, Lee CM, Yeh YH, Hsu RH, Gupta R, Zhang M, Rodriguez PJ, Lee CS, Gillard BK, Bissig KD, Pownall HJ, Martin JF, Bao G, Lagor WR (2017) Somatic genome editing with CRISPR/Cas9 generates and corrects a metabolic disease. Sci Rep 7:44624. https://doi.org/10.1038/srep44624

21. Jarrett KE, Lee C, De Giorgi M, Hurley A, Gillard BK, Doerfler AM, Li A, Pownall HJ, Bao G, Lagor WR (2018) Somatic editing of Ldlr with adeno-associated viral-Crispr is an efficient tool for atherosclerosis research. Arterioscler Thromb Vasc Biol 38(9):1997–2006. https://doi.org/10.1161/ATVBAHA.118.311221
22. De Giorgi M, Jarrett KE, Burton JC, Doerfler AM, Hurley A, Li A, Hsu RH, Furgurson M, Patel KR, Han J, Borchers CH, Lagor WR (2020) Depletion of essential isoprenoids and ER stress induction following acute liver-specific deletion of HMG-CoA reductase. J Lipid Res 61(12):1675–1686. https://doi.org/10.1194/jlr.RA120001006
23. Li A, Lee CM, Hurley AE, Jarrett KE, De Giorgi M, Lu W, Balderrama KS, Doerfler AM, Deshmukh H, Ray A, Bao G, Lagor WR (2019) A self-deleting AAV-CRISPR system for in vivo genome editing. Mol Ther Methods Clin Dev 12:111–122. https://doi.org/10.1016/j.omtm.2018.11.009
24. Li A, Tanner MR, Lee CM, Hurley AE, De Giorgi M, Jarrett KE, Davis TH, Doerfler AM, Bao G, Beeton C, Lagor WR (2020) AAV-CRISPR gene editing is negated by pre-existing immunity to Cas9. Mol Ther 28(6):1432–1441. https://doi.org/10.1016/j.ymthe.2020.04.017
25. Cradick TJ, Qiu P, Lee CM, Fine EJ, Bao G (2014) COSMID: a web-based tool for identifying and validating CRISPR/Cas off-target sites. Mol Ther Nucleic Acids 3:e214. https://doi.org/10.1038/mtna.2014.64
26. Concordet JP, Haeussler M (2018) CRISPOR: intuitive guide selection for CRISPR/Cas9 genome editing experiments and screens. Nucleic Acids Res 46(W1):W242–W245. https://doi.org/10.1093/nar/gky354
27. Brinkman EK, Chen T, Amendola M, van Steensel B (2014) Easy quantitative assessment of genome editing by sequence trace decomposition. Nucleic Acids Res 42(22):e168. https://doi.org/10.1093/nar/gku936
28. Hsiau T, Conant D, Rossi N, Maures T, Waite K, Yang J, Joshi S, Kelso R, Holden K, Enzmann BL, Stoner R (2019) Inference of CRISPR edits from sanger trace data. bioRxiv:251082. https://doi.org/10.1101/251082
29. Clement K, Rees H, Canver MC, Gehrke JM, Farouni R, Hsu JY, Cole MA, Liu DR, Joung JK, Bauer DE, Pinello L (2019) CRISPResso2 provides accurate and rapid genome editing sequence analysis. Nat Biotechnol 37(3):224–226. https://doi.org/10.1038/s41587-019-0032-3
30. McIntosh J, Lenting PJ, Rosales C, Lee D, Rabbanian S, Raj D, Patel N, Tuddenham EG, Christophe OD, McVey JH, Waddington S, Nienhuis AW, Gray JT, Fagone P, Mingozzi F, Zhou SZ, High KA, Cancio M, Ng CY, Zhou J, Morton CL, Davidoff AM, Nathwani AC (2013) Therapeutic levels of FVIII following a single peripheral vein administration of rAAV vector encoding a novel human factor VIII variant. Blood 121(17):3335–3344. https://doi.org/10.1182/blood-2012-10-462200
31. Boutin S, Monteilhet V, Veron P, Leborgne C, Benveniste O, Montus MF, Masurier C (2010) Prevalence of serum IgG and neutralizing factors against adeno-associated virus (AAV) types 1, 2, 5, 6, 8, and 9 in the healthy population: implications for gene therapy using AAV vectors. Hum Gene Ther 21(6):704–712. https://doi.org/10.1089/hum.2009.182
32. Leborgne C, Barbon E, Alexander JM, Hanby H, Delignat S, Cohen DM, Collaud F, Muraleetharan S, Lupo D, Silverberg J, Huang K, van Wittengerghe L, Marolleau B, Miranda A, Fabiano A, Daventure V, Beck H, Anguela XM, Ronzitti G, Armour SM, Lacroix-Desmazes S, Mingozzi F (2020) IgG-cleaving endopeptidase enables in vivo gene therapy in the presence of anti-AAV neutralizing antibodies. Nat Med 26(7):1096–1101. https://doi.org/10.1038/s41591-020-0911-7
33. Daugherty A, Whitman SC (2003) Quantification of atherosclerosis in mice. Methods Mol Biol 209:293–309. https://doi.org/10.1385/1-59259-340-2:293
34. Zischewski J, Fischer R, Bortesi L (2017) Detection of on-target and off-target mutations generated by CRISPR/Cas9 and other sequence-specific nucleases. Biotechnol Adv 35(1):95–104. https://doi.org/10.1016/j.biotechadv.2016.12.003
35. Hanlon KS, Kleinstiver BP, Garcia SP, Zaborowski MP, Volak A, Spirig SE, Muller A, Sousa AA, Tsai SQ, Bengtsson NE, Loov C, Ingelsson M, Chamberlain JS, Corey DP, Aryee MJ, Joung JK, Breakefield XO, Maguire CA, Gyorgy B (2019) High levels of AAV vector integration into CRISPR-induced DNA breaks. Nat Commun 10(1):4439. https://doi.org/10.1038/s41467-019-12449-2
36. Pan X, Philippen L, Lahiri SK, Lee C, Park SH, Word TA, Li N, Jarrett KE, Gupta R, Reynolds JO, Lin J, Bao G, Lagor WR, Wehrens XHT (2018) In vivo Ryr2 editing corrects catecholaminergic polymorphic ventricular tachycardia. Circ Res 123(8):953–963. https://doi.org/10.1161/CIRCRESAHA.118.313369

Chapter 43

Laser Capture Microdissection–Based mRNA Expression Microarrays and Single-Cell RNA Sequencing in Atherosclerosis Research

Xi Zhang, Zhihua Wang, Chuankai Zhang, Yutao Li, Shu Lu, Sabine Steffens, Sarajo Mohanta, Christian Weber, Andreas Habenicht, and Changjun Yin

Abstract

A major goal of methodologies related to large scale gene expression analyses is to initiate comprehensive information on transcript signatures in single cells within the tissue's anatomy. Until now, this could be achieved in a stepwise experimental approach: (1) identify the majority of transcripts in a single cell (single cell transcriptome); (2) provide information on transcripts on multiple cell subtypes in a complex sample (cell heterogeneity); and (3) give information on each cell's spatial location within the tissue (zonation transcriptomics). Such genetic information will allow construction of functionally relevant gene expression maps of single cells of a given anatomically defined tissue compartment and thus pave the way for subsequent analyses, including their epigenetic modifications. Until today these aims have not been achieved in the area of cardiovascular disease research though steps toward these goals become apparent: laser capture microdissection (LCM)-based mRNA expression microarrays of atherosclerotic plaques were applied to gain information on local gene expression changes during disease progression, providing limited spatial resolution. Moreover, while LCM-derived tissue RNA extracts have been shown to be highly sensitive and covers a range of 10–16,000 genes per array/small amount of RNA, its original promise to isolate single cells from a tissue section turned out not to be practicable because of the inherent contamination of the cell's RNA of interest with RNA from neighboring cells. Many shortcomings of LCM-based analyses have been overcome using single-cell RNA sequencing (scRNA-seq) technologies though scRNA-seq also has several limitations including low numbers of transcripts/cell and the complete loss of spatial information. Here, we describe a protocol toward combining advantages of both techniques while avoiding their flaws.

Key words Atherosclerosis, LCM-based microarrays; single-cell RNA sequencing (scRNA-seq), Transcriptome, Gene ontology

Andreas Habenicht and Changjun Yin contributed equally to this work.

Dipak P. Ramji (ed.), *Atherosclerosis: Methods and Protocols*, Methods in Molecular Biology, vol. 2419,
https://doi.org/10.1007/978-1-0716-1924-7_43,
© The Author(s), under exclusive license to Springer Science+Business Media, LLC, part of Springer Nature 2022

1 Introduction

Laser capture microdissection (LCM) technology has been applied to frozen samples with or without immunostaining, allowing the procurement of specific cell populations or structures for downstream genetic analysis [1, 2]. Combining LCM and whole-genome expression microarrays deciphered features related to cellular or structural information in atherosclerosis [3–5]. Single-cell RNA sequencing (scRNA-seq) was first reported a decade ago to obtain resolution at single cells [6]. In recent years, the drop- or well-based scRNA-seq techniques have been applied to atherosclerosis research [7, 8]. However, scRNA-seq is limited by several technical limitations and the complete loss of spatial information. The 10× Genomics platform can only analyze a maximum of 10,000 cells with an average of 1600 detected genes/cell. The well-based SMART-seq increases the gene coverage to 8000/cells and is capable of full-length sequencing, but the low throughput and high cost of this approach limit its widespread usage [9]. To overcome the lack of spatial information, several advanced methods such as LCM-seq, transcriptome in vivo analysis (TIVA) and geographical position sequencing (GEO-seq) have been developed in order to combine and integrate the principles of LCM with scRNA-seq. These advanced LCM-facilitated single-cell sequencing techniques have been successfully applied in the field of nervous system biology and cancer [10]. However, their potential in atherosclerosis research has yet to be demonstrated.

To investigate the immune response in the context of atherosclerosis, we employed both LCM-based microarray analysis and scRNA-seq analyses to delineate the regulation of inflammation in atherosclerosis. For microarray data, we compared large-scale transcriptomic information and determined differentially expressed genes (DEGs) of wild-type (WT) renal lymph nodes (RLNs), apolipoprotein E-deficient ($ApoE^{-/-}$) RLNs, $ApoE^{-/-}$ artery tertiary lymphoid organs (ATLOs) and $ApoE^{-/-}$ plaques [11–13]. These analyses yielded information on hundreds of upregulated or downregulated DEGs in different tissues in two genotypes of mice and largely were able to understand gene expression signatures in the three arterial wall layers, that is, the intima, the media and the adventitia. However, they fall short of an important emerging new technology termed zonation transcriptomics originally developed for zonated gene signatures in liver lobules [14, 15]. In our studies, DEGs were integrated into databases for functional enrichment analysis. Several inflammation-related Gene Ontology (GO) terms and genes were identified after enrichment. For the scRNA-seq data, we similarly determined DEGs and GO terms in the four tissues. Since the cell types were unambiguously

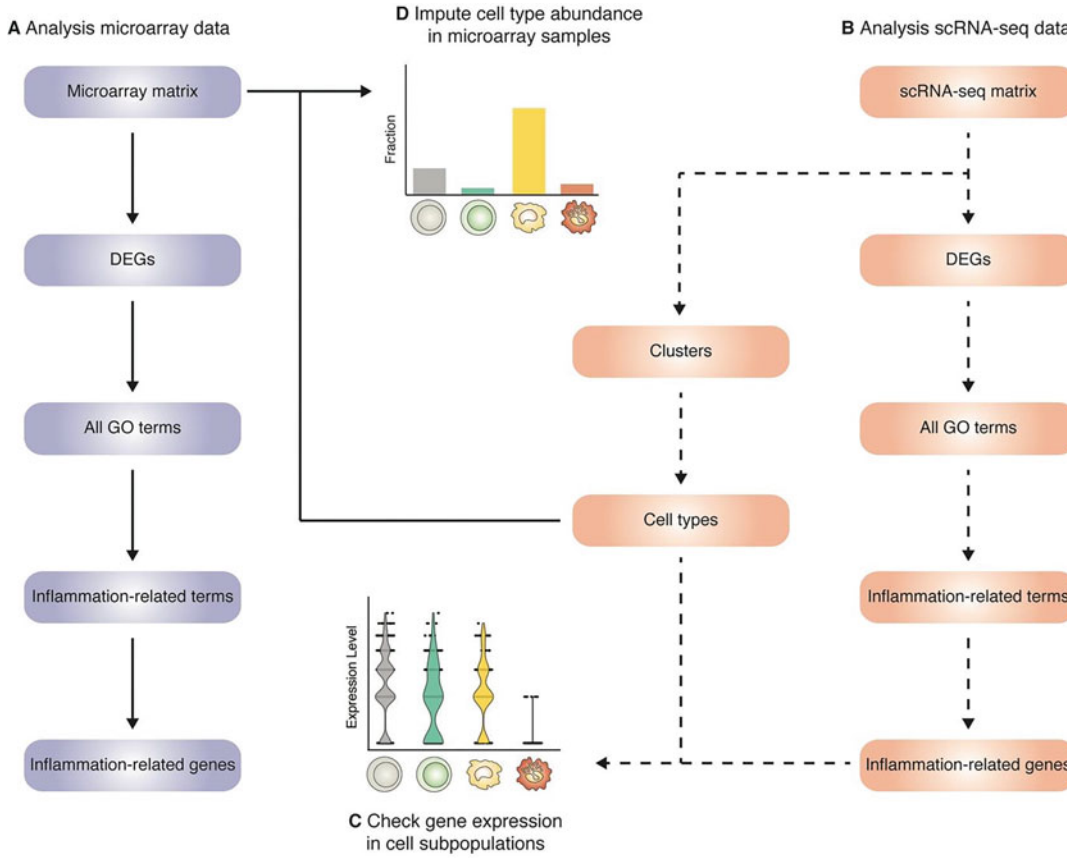

Fig. 1 Workflow for integrated analyses of microarray and scRNA-seq data. (**a**) Execute the microarray analysis to determine DEGs and inflammation-related GO terms. Based on the enriched GO terms, the inflammation-related genes involved in each term are identified. (**b**) Analyze the scRNA-seq data to obtain inflammation-related terms and genes, as well as decipher cellular heterogeneity in the samples. (**c**) The expression level of inflammation-related genes in distinct cell types is checked in scRNA-seq data. (**d**) The fraction of cell populations in microarray samples is inferred after constructing reference using the scRNA-seq result. The solid lines represent analysis in microarray data, and the dashed lines indicate analysis in scRNA-seq data. *DEGs* differentially expressed genes, *GO* gene ontology, *scRNA-seq* single-cell RNA sequencing

identifiable in the scRNA-seq data base via cell lineage markers, we applied the approach to expression analyses of inflammation-related genes in distinct cell populations. Furthermore, using scRNA-seq data, we were able to deduce the abundance of several cell populations in LCM-derived microarray data sets (Fig. 1). This combined analysis provided new insight into the pathobiology of atherosclerosis by integrating previous bulk technologies and the emerging single-cell technologies.

2 Materials

2.1 Data Acquisition

1. Microarray data of mouse WT RLNs, ApoE$^{-/-}$ RLNs, ApoE$^{-/-}$ ATLOs and ApoE$^{-/-}$ plaque downloaded from the gene expression omnibus (GEO) database at the National Center for Biotechnology Information (NCBI) https://www.ncbi.nlm.nih.gov/geo/ (accession number GSE40156).
2. scRNA-seq data of mouse WT RLNs, ApoE$^{-/-}$ RLNs, ApoE$^{-/-}$ ATLOs and ApoE$^{-/-}$ plaques generated in the laboratory (*see* **Note 1**).

2.2 Data Analysis

1. R (version 4.0.2) downloaded from https://www.r-project.org/ [16].
2. Rstudio (version 1.3.1093) downloaded from https://rstudio.com/ (*see* **Note 2**).
3. Bioconductor: https://www.bioconductor.org/ (*see* **Note 3**).
4. STRING: https://string-db.org/.
5. CIBERSORTx: https://cibersortx.stanford.edu/index.php (*see* **Note 4**).

3 Methods

3.1 Microarray Data Analysis

3.1.1 Microarray Data Preprocessing

1. Load CEL files containing information of probe intensities to the R workspace (*see* **Note 5**).
2. Remove microarray chips with low quality. Chips whose RNAs were highly degraded (the level of degradation in the 3′ end approached to the level of degradation in the 5′ end) or chips with higher background noise (>100) should be removed. Array chips that could not be successfully clustered with their replicants of 3–6 should also be discarded as outliers.
3. Convert probe intensities into the expression matrix and normalize the data using the "gcrma()" function built in the "gcrma" packages (*see* **Note 6**).
4. Filter probes with consistently low signals or probes with minimal variation across samples using the "nsFilter()" function in the "genefilter" package.
5. Load the "limma" package and fitting a linear model to the expression data, calculate the difference of gene expression between experimental group and control group using empirical Bayes moderated t-statistics test (*see* **Note 7**).
6. Annotate probe names into HGNC (HUGO Gene Nomenclature Committee) gene symbol and Entrez ID.
7. Remove probes that cannot be successfully annotated. For probe sets that share the common gene name, only keep one probe within that set.

3.1.2 Determination of DEGs and Inflammation-Related GO Terms

1. Compare gene expression between paired tissues in the R program: $ApoE^{-/-}$ RLNs vs WT RLNs; $ApoE^{-/-}$ ATLOs vs $ApoE^{-/-}$ RLNs; $ApoE^{-/-}$ ATLOs vs $ApoE^{-/-}$ plaque.
2. Determine DEGs in the R program with the following criteria: adjust p-value <0.05 and $|\log2 \text{ (fold change)}| > 2$. The fold change of expression and the adjusted *p*-values of individual genes can be visualized in a volcano plot.
3. Parse the DEGs referring to the STRING online database for functional enrichment analysis. In the biological process (BP) Gene Ontology (GO) category for example, the parent terms contain strings like "inflammatory" as an initial set of inflammation-related GO terms followed by daughter GO terms (*see* **Note 8**).
4. Visualize the expression of DEGs enriched in each inflammation-related GO term by using heatmaps in the R program.
5. Summarise all inflammation-related GO terms and DEGs.

3.2 scRNA-seq Data Analysis

3.2.1 scRNA-seq Data Preprocessing

1. Import the count matrix of each sample to the R workspace (*see* **Note 5**).
2. Load the "Seurat" package and create a seurat object suitable for the following analysis. When creating a seurat object, remove genes detected in less than three cells (*see* **Note 9**).
3. Discard cell doublets and cell debris based on the number of detected genes, the total count of genes and the proportion of mitochondrial genes (*see* **Note 10**).
4. Normalize the data based on the global-scaling normalization method and find highly variable genes using "Seurat" built on the "SCTransform()" function.
5. Integrate data across several samples and correct for the batch effect (*see* **Note 11**).
6. Perform principal component analysis (PCA) using "RunPCA ()" function to determine the number of PCs involved in reducing the expression dimensions. Visualize the expression profile of all cells and cluster cells with similar transcriptomes (*see* **Note 12**).
7. Use the "FindAllMarkers()" function to calculate specifically up-regulated genes in each cluster. The threshold of logarithmic fold changed is set to 0.25 as default.
8. Annotate clusters on the basis of canonical gene markers and highly up-regulated genes in each cluster.

3.2.2 Determination of DEGs and Inflammation-Related GO Terms

1. Compare gene expression between paired tissues in the R program: ApoE$^{-/-}$ RLNs vs WT RLNs; ApoE$^{-/-}$ ATLOs vs ApoE$^{-/-}$ RLNs; ApoE$^{-/-}$ ATLOs vs ApoE$^{-/-}$ plaques.
2. Determine DEGs in the R program with the criteria: adjust *p*-value <0.05 and $|\log2 \text{ (fold change)}| > 0.25$. The fold change of expression difference and adjusted *p*-values of individual genes can be visualized via a volcano plot.
3. Parse DEGs referring to the STRING online database for functional enrichment analysis. In the biological process (BP) Gene Ontology (GO) category, the terms containing strings like "inflammatory" are recognized as one set of inflammation-related GO terms.
4. Visualize expression of DEGs enriched in each inflammation-related GO term by using heatmaps in the R program.
5. Summarise all inflammation-related GO terms and DEGs.

3.3 Profiling Cellular Abundance in Microarray Data

1. Extract the expression matrix with cell-type annotation from the scRNA-seq data using "write.table()" function built in the R program (*see* **Note 13**).
2. Extract the expression matrix from the microarray data using "write.table()" function built in the R program(*see* **Note 13**).
3. Upload two matrix files to the CIBERSORTx website. The scRNA-seq matrix file is classified as "Single Cell Reference Matrix" file and the microarray matrix file is categorized to "Mixture" file.
4. In the CIBERSORTx online tool, select "Create Signature Matrix" module. By using of scRNA-seq matrix, create a reference file which can be used to determine cell types.
5. In the "Impute Cell Fractions" module, select the newly generated reference file as a signature matrix to estimate cellular composition and calculate the fraction in microarray matrix (*see* **Note 14**).

3.4 Comparing the Results Obtained from Microarray Analysis and scRNA-Seq Analysis

1. Compare the total number of DEGs and enriched GO terms obtained in the two methods using the VennDiagram package in the R.
2. Extract the inflammation-related GO terms obtained from each method. Compare the number of inflammation-related terms and genes (Fig. 2a).
3. Select several inflammation-related genes and compare their expression in microarray data vs. scRNA-seq data (Fig. 2b, c).
4. Visualize and compare the expression of inflammation-related DEGs in different cell types (Fig. 2d) (*see* **Note 15**).
5. Compare the fraction of cell subpopulations between the two datasets (Fig. 3).

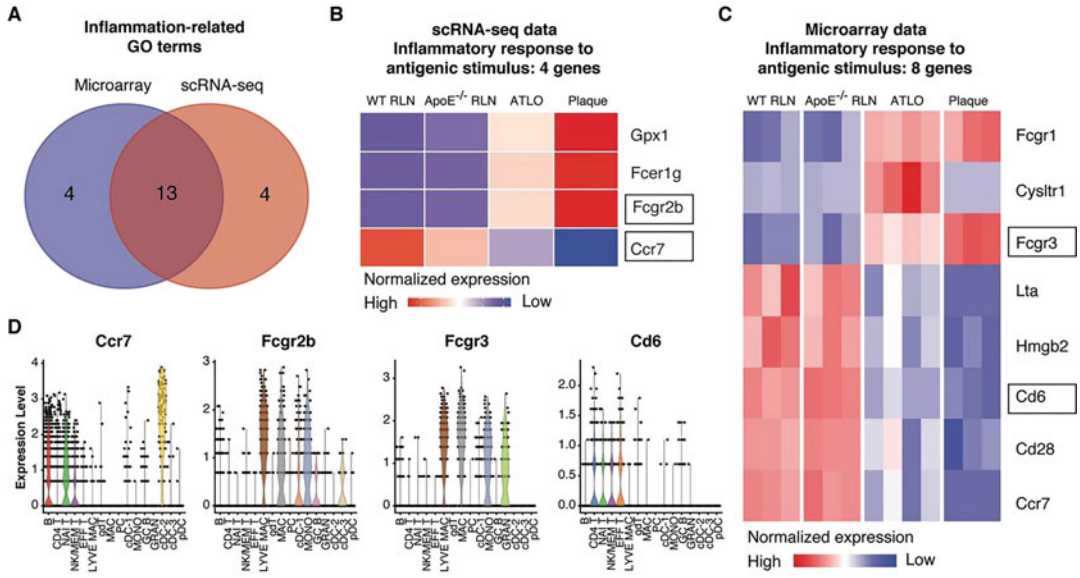

Fig. 2 Example of inflammation-related GO term and enriched inflammation-related DEGs. (**a**) Venn diagram shows the number of inflammation-related GO terms in each dataset. It also describes the number of terms shared by two datasets. (**b**) The heatmap displays the expression of DEGs enriched in one inflammation-related GO term obtained from the comparison of ATLOs and ApoE$^{-/-}$ RLNs in the scRNA-seq data. 2 DEGs were selected to check the cell type-specific expression in the single-cell data. (**c**) The heatmap displays the expression of DEGs enriched in one inflammation-related GO term obtained from the comparison of ATLOs and ApoE$^{-/-}$ RLNs in the microarray data. The scaled expression of enriched genes is displayed. 2 DEGs are selected to check the cell type-specific expression in the single-cell data. (**d**) The violin plot visualizes the normalized expression of 4 inflammation-related DEGs in different cell types. *GO* gene ontology, *scRNA-seq* single-cell RNA sequencing, *WT* wild type, *ApoE*$^{-/-}$ apolipoprotein-deficient, *RLN* renal lymph node, *ATLO* artery tertiary lymphoid organ, *NAI* naïve, *MEM* memory, *EFF* effector, *MAC* macrophage, *gdT* γδT, *PC* plasma cell, *cDC* conventional dendritic cell, *pDC* plasmacytoid dendritic cell, *MONO* monocyte, *GC* germinal center, *GRAN* granulocyte

4 Notes

1. As an example, we used the microarray data downloaded from NCBI database and scRNA-seq data generated following standard 10× Chromium protocol (Chromium Next GEM Single Cell 5′ Reagent Kits V2). However, the methods described here are applicable for other microarray and scRNA-seq data either obtained from the databases or generated in-house.
2. RStudio is an integrated development environment (IDE) for R. It connects with R installed locally and supports a more user-friendly implementation of R, including directly executing R code; easily managing scripts, plots, or packages; and quickly locating and debugging syntax errors [17].
3. The Bioconductor is an open-source container providing software and methods facilities for bioinformatic analysis of data

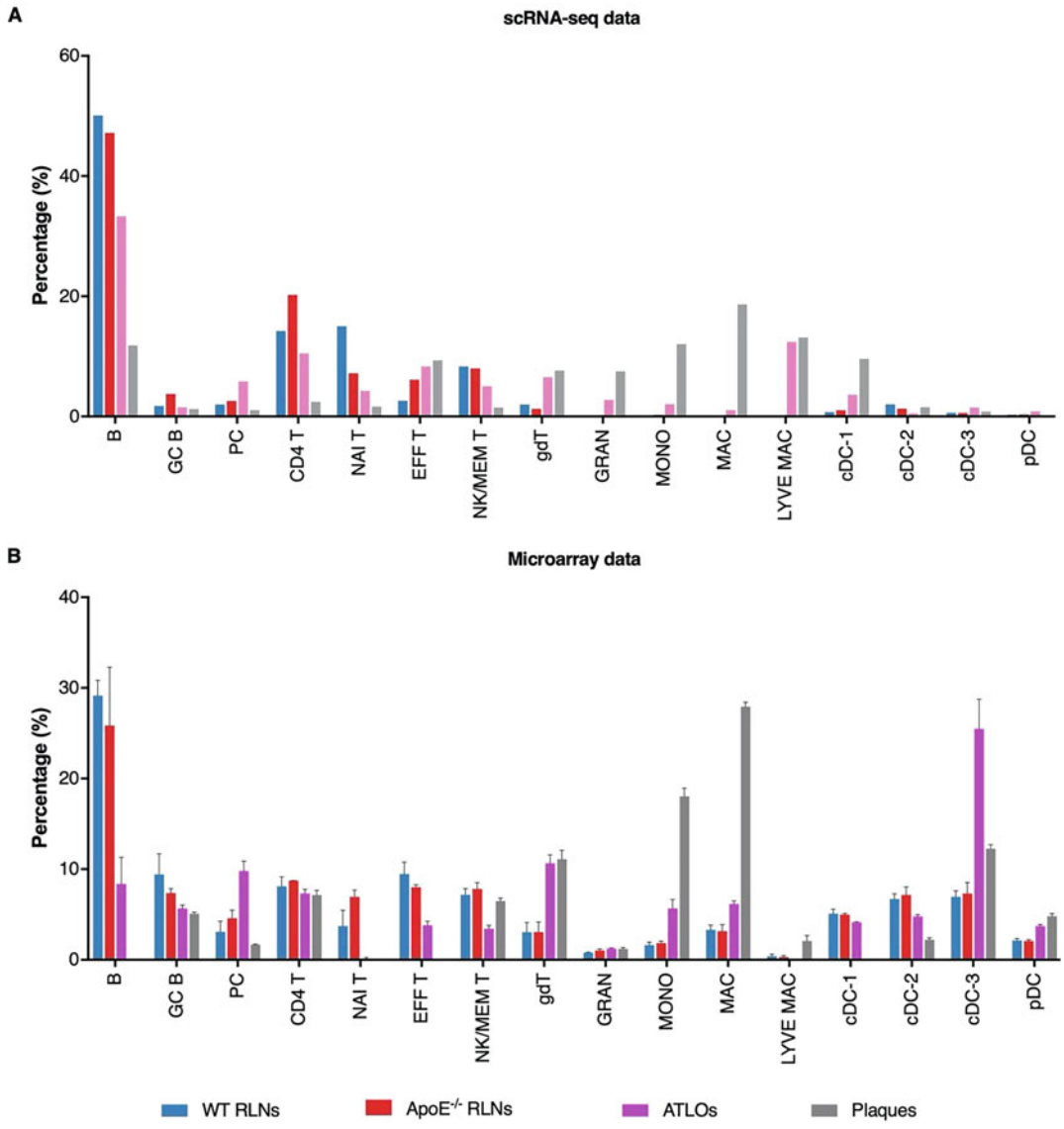

Fig. 3 The fraction of different cell types comprised in different tissues. The genetic deconvolution is applied to determine the cell components in the microarray data. The gene signature is constructed referring to single-cell data and the microarray data is introduced to dissect the cellular component. (**a**) The cellular abundance of four tissues in the scRNA-seq data. (**b**) The cellular abundance of four tissues in the microarray data. *scRNA-seq* single-cell RNA sequencing, *WT* wild type, *ApoE*$^{-/-}$ apolipoprotein deficient, *RLNs* renal lymph nodes, *ATLOs* artery tertiary lymphoid organs, *NAI* naïve, *MEM* memory, *EFF* effector, *MAC* macrophage, *gdT* γδT, *PC* plasma cell, *cDC* conventional dendritic cell, *pDC* plasmacytoid dendritic cell, *MONO* monocyte, *GC* germinal center, *GRAN* granulocyte

generated by microarray, RNA sequencing (RNA-seq) or other high-throughput sequencing technologies. The majority of software developed under Bioconductor project is rooted in R [18].

4. CIBERSORTx is a computational method developed by Newman et al. It works like a digital cytometry to mathematically deconvolute the sample admixture into its cellular composition based on the gene expression signature which defines the cell types, allowing estimation of the fraction of cell populations within one bulk-sequenced sample [19, 20].
5. All the analyses in Subheadings 3.1.1 and 3.2.1 are conducted using the R program.
6. The "gcrma()" function is capable of converting the probe intensities based on the robust multichip average (RMA) expression measure and scaling the value with logarithm calculation [21].
7. Normally, we fitted the expression data to "Y = β0 + β1A" linear model. The formula was ~0 + factor(s).
8. There are multiple platforms to execute functional enrichment analyses. For example, the "clusterProfiler" package in R, or online tools like "STRING" and "Metascape." Here, we selected the "STRING" online database, because it includes multiple resources to predict functions not be restricted to GO terms, but also covers Kyoto Encyclopedia of Genes and Genomes (KEGG) pathways, protein–protein interactions and multiple other types of information in public databases [22].
9. There are numerous software available for single-cell data analyses like the "Seurat" package, the "monocle" package or the "scater" packages developed by R language, or the Python-based "Scanpy" package. Here, we use the "Seurat" package for single-cell data analysis, using other packages will yield similar results.
10. In our protocol, cells containing less than 200 genes (i.e., derived from cell debris), or more than 4000 genes (i.e., double cells) were discarded. Cells which showed more than 5% of mitochondrial genes of total gene expression were also discarded [23]. The 5% thresholds should be uniquely considered based on cell types. For example, the percentage of mitochondrial genes is highly variable in different tissue types. It was previously reported that 30% of mRNA detected by sc-RNA seq are recognized as mitochondrial mRNA in heart muscle cells due to the high demand for energy [24].
11. Apart from real biological variance, the selection of reagents and protocols, the experimenters, as well as the environments to perform the experiment, will slightly impact the enzyme activities, which also result in gene expression variability of samples (referred to as batch effect). Therefore, in order to integrate and compare data obtained from different batches, it is essential to consider these technical confounds and repeat each experiment at least once. The integration and batch

correction could be achieved by using the "Seurat" package or other packages developed under R or Python. If the data is generated in the same batch using 10× Chromium protocols, they could also be integrated using the "aggr" function built in Cell Ranger software [25].

12. In order to identify cell types comprising the samples, it is necessary to cluster cells on the basis of their transcriptomic similarity, which is represented by their Euclidean distance in a plot. Each gene is considered as one dimension and the cells are assigned based on their expression of individual genes. However, it is unfeasible to visualize cell transcriptomes in a plot with thousands of dimensions. Since the expression of several genes correlates due to the alteration of biological status, multiple genes could be compressed into a single dimension. Consequently, the two-dimensional plot is constructed to describe the whole transcriptome and used for downstream analysis [26].
13. The expression matrix must be exported as a tab-delimited TXT file without quotations and missing values. For single-cell data, the first column contains gene symbols and the remaining columns are named by their phenotype, thus cells come from the same cell type should have the same column name. For microarray data, the first column contains gene symbols and the remaining columns are named by the sample name.
14. To further optimize the parameters, because the scRNA-seq data and the microarray data are sequenced by different platforms, it is recommended to enable batch correction and select "S-model." In addition, to execute microarray data, the quantile normalization should be activated.
15. scRNA-seq is capable of revealing the differences of gene expression within different samples similar to microarrays. Moreover, inasmuch as the cellular heterogeneity is elucidated in the scRNA-seq data, the detailed gene expression in the distinct tissue composition could also be compared, which offers the possibility to understand the disease-associated phenotypic variation.

Acknowledgments

This work was funded by the Deutsche Forschungsgemeinschaft (DFG) (YI 133/3-5), LMUexcellent 867949-0, Friedrich-Baur-Stiftung 39/20, Bayer Thrombosis Research Award to C.Y.; DFG HA 1083/15-4 and HA 1083/15-5 to A.J.R.H.; ERA-CVD (PL AQUEFIGHT) 01KL1808 to A.J.R.H.

References

1. Fend F, Emmert-Buck MR, Chuaqui R, Cole K, Lee J, Liotta LA, Raffeld M (1999) Immuno-LCM: laser capture microdissection of immunostained frozen sections for mRNA analysis. Am J Pathol 154(1):61–66. https://doi.org/10.1016/S0002-9440(10)65251-0
2. Espina V, Wulfkuhle JD, Calvert VS, VanMeter A, Zhou W, Coukos G, Geho DH, Petricoin EF 3rd, Liotta LA (2006) Laser-capture microdissection. Nat Protoc 1(2): 586–603. https://doi.org/10.1038/nprot.2006.85
3. Beer M, Doepping S, Hildner M, Weber G, Grabner R, Hu D, Mohanta SK, Srikakulapu P, Weih F, Habenicht AJ (2011) Laser-capture microdissection of hyperlipidemic/ApoE(−)/(−) mouse aorta atherosclerosis. Methods Mol Biol 755:417–428. https://doi.org/10.1007/978-1-61779-163-5_35
4. Yin C, Mohanta S, Ma Z, Weber C, Hu D, Weih F, Habenicht A (2015) Generation of aorta transcript atlases of wild-type and apolipoprotein E-null mice by laser capture microdissection-based mRNA expression microarrays. Methods Mol Biol 1339: 297–308. https://doi.org/10.1007/978-1-4939-2929-0_20
5. Stark R, Grzelak M, Hadfield J (2019) RNA sequencing: the teenage years. Nat Rev Genet 20(11):631–656. https://doi.org/10.1038/s41576-019-0150-2
6. Tang F, Barbacioru C, Wang Y, Nordman E, Lee C, Xu N, Wang X, Bodeau J, Tuch BB, Siddiqui A, Lao K, Surani MA (2009) mRNA-Seq whole-transcriptome analysis of a single cell. Nat Methods 6(5):377–382. https://doi.org/10.1038/nmeth.1315
7. Fernandez DM, Rahman AH, Fernandez NF, Chudnovskiy A, Amir ED, Amadori L, Khan NS, Wong CK, Shamailova R, Hill CA, Wang Z, Remark R, Li JR, Pina C, Faries C, Awad AJ, Moss N, Bjorkegren JLM, Kim-Schulze S, Gnjatic S, Ma'ayan A, Mocco J, Faries P, Merad M, Giannarelli C (2019) Single-cell immune landscape of human atherosclerotic plaques. Nat Med 25(10):1576–1588. https://doi.org/10.1038/s41591-019-0590-4
8. Zernecke A, Winkels H, Cochain C, Williams JW, Wolf D, Soehnlein O, Robbins CS, Monaco C, Park I, McNamara CA, Binder CJ, Cybulsky MI, Scipione CA, Hedrick CC, Galkina EV, Kyaw T, Ghosheh Y, Dinh HQ, Ley K (2020) Meta-analysis of leukocyte diversity in atherosclerotic mouse aortas. Circ Res 127(3):402–426. https://doi.org/10.1161/CIRCRESAHA.120.316903
9. Williams JW, Winkels H, Durant CP, Zaitsev K, Ghosheh Y, Ley K (2020) Single cell RNA sequencing in atherosclerosis research. Circ Res 126(9):1112–1126. https://doi.org/10.1161/CIRCRESAHA.119.315940
10. Liao J, Lu X, Shao X, Zhu L, Fan X (2021) Uncovering an organ's molecular architecture at single-cell resolution by spatially resolved transcriptomics. Trends Biotechnol 39(1): 43–58. https://doi.org/10.1016/j.tibtech.2020.05.006
11. Grabner R, Lotzer K, Dopping S, Hildner M, Radke D, Beer M, Spanbroek R, Lippert B, Reardon CA, Getz GS, Fu YX, Hehlgans T, Mebius RE, van der Wall M, Kruspe D, Englert C, Lovas A, Hu D, Randolph GJ, Weih F, Habenicht AJ (2009) Lymphotoxin beta receptor signaling promotes tertiary lymphoid organogenesis in the aorta adventitia of aged ApoE−/− mice. J Exp Med 206(1): 233–248. https://doi.org/10.1084/jem.20080752
12. Mohanta SK, Yin C, Peng L, Srikakulapu P, Bontha V, Hu D, Weih F, Weber C, Gerdes N, Habenicht AJ (2014) Artery tertiary lymphoid organs contribute to innate and adaptive immune responses in advanced mouse atherosclerosis. Circ Res 114(11): 1772–1787. https://doi.org/10.1161/CIRCRESAHA.114.301137
13. Hu D, Mohanta SK, Yin C, Peng L, Ma Z, Srikakulapu P, Grassia G, MacRitchie N, Dever G, Gordon P, Burton FL, Ialenti A, Sabir SR, McInnes IB, Brewer JM, Garside P, Weber C, Lehmann T, Teupser D, Habenicht L, Beer M, Grabner R, Maffia P, Weih F, Habenicht AJ (2015) Artery tertiary lymphoid organs control aorta immunity and protect against atherosclerosis via vascular smooth muscle cell lymphotoxin beta receptors. Immunity 42(6):1100–1115. https://doi.org/10.1016/j.immuni.2015.05.015
14. Halpern KB, Shenhav R, Matcovitch-Natan O, Tóth B, Lemze D, Golan M, Massasa EE, Baydatch S, Landen S, Moor AE, Brandis A, Giladi A, Stokar-Avihail A, David E, Amit I, Itzkovitz S (2017) Single-cell spatial reconstruction reveals global division of labour in the mammalian liver. Nature 542(7641): 352–356. https://doi.org/10.1038/nature21065
15. Ben-Moshe S, Itzkovitz S (2019) Spatial heterogeneity in the mammalian liver. Nat Rev

Gastroenterol 16(7):395–410. https://doi.org/10.1038/s41575-019-0134-x

16. Team RC (2019) R: A language and environment for statistical computing. https://www.R-project.org/
17. Team R (2020) RStudio: Integrated development for R. http://www.rstudio.com/
18. Gentleman RC, Carey VJ, Bates DM, Bolstad B, Dettling M, Dudoit S, Ellis B, Gautier L, Ge Y, Gentry J, Hornik K, Hothorn T, Huber W, Iacus S, Irizarry R, Leisch F, Li C, Maechler M, Rossini AJ, Sawitzki G, Smith C, Smyth G, Tierney L, Yang JY, Zhang J (2004) Bioconductor: open software development for computational biology and bioinformatics. Genome Biol 5(10): R80. https://doi.org/10.1186/gb-2004-5-10-r80
19. Newman AM, Steen CB, Liu CL, Gentles AJ, Chaudhuri AA, Scherer F, Khodadoust MS, Esfahani MS, Luca BA, Steiner D, Diehn M, Alizadeh AA (2019) Determining cell type abundance and expression from bulk tissues with digital cytometry. Nat Biotechnol 37(7): 773–782. https://doi.org/10.1038/s41587-019-0114-2
20. Steen CB, Liu CL, Alizadeh AA, Newman AM (2020) Profiling cell type abundance and expression in bulk tissues with CIBERSORTx. Methods Mol Biol 2117:135–157. https://doi.org/10.1007/978-1-0716-0301-7_7
21. Bolstad BM, Irizarry RA, Astrand M, Speed TP (2003) A comparison of normalization methods for high density oligonucleotide array data based on variance and bias. Bioinformatics 19(2):185–193. https://doi.org/10.1093/bioinformatics/19.2.185
22. Szklarczyk D, Gable AL, Lyon D, Junge A, Wyder S, Huerta-Cepas J, Simonovic M, Doncheva NT, Morris JH, Bork P, Jensen LJ, Mering CV (2019) STRING v11: protein-protein association networks with increased coverage, supporting functional discovery in genome-wide experimental datasets. Nucleic Acids Res 47(D1):D607–D613. https://doi.org/10.1093/nar/gky1131
23. Osorio D, Cai JJ (2020) Systematic determination of the mitochondrial proportion in human and mice tissues for single-cell RNA sequencing data quality control. Bioinformatics 37(7): 963–967. https://doi.org/10.1093/bioinformatics/btaa751
24. AlJanahi AA, Danielsen M, Dunbar CE (2018) An introduction to the analysis of single-cell RNA-sequencing data. Mol Ther Methods Clin Dev 10:189–196. https://doi.org/10.1016/j.omtm.2018.07.003
25. Tran HTN, Ang KS, Chevrier M, Zhang X, Lee NYS, Goh M, Chen J (2020) A benchmark of batch-effect correction methods for single-cell RNA sequencing data. Genome Biol 21(1):12. https://doi.org/10.1186/s13059-019-1850-9
26. Ding J, Condon A, Shah SP (2018) Interpretable dimensionality reduction of single cell transcriptome data with deep generative models. Nat Commun 9(1):2002. https://doi.org/10.1038/s41467-018-04368-5

Chapter 44

Combined Single-Cell RNA and Single-Cell α/β T Cell Receptor Sequencing of the Arterial Wall in Atherosclerosis

Zhihua Wang, Xi Zhang, Chuankai Zhang, Yutao Li, Shu Lu, Sarajo Mohanta, Christian Weber, Andreas Habenicht, and Changjun Yin

Abstract

Although various pro- and anti-inflammatory T cell subsets have been observed in murine and human atherosclerosis, principal issues of T cell immunity remain unanswered: Is atherosclerosis progression critically affected by aberrant T cell responses? Are tolerance checkpoints compromised during atherosclerosis progression? Answers to these questions will determine if we are at the cusp of developing T cell-dependent therapeutic strategies. Rapid advances in single cell RNA sequencing (scRNA-seq) and single cell α/β T cell receptor (TCR) (scTCR) sequencing allows to address these issues in unprecedented ways. The majority of T cells recognize peptide antigen-MHC complexes presented by antigen-presenting cells which, in turn, trigger activation and proliferation (clonal expansion) of cognate TCR-carrying T cells. Thus, clonal expansion and their corresponding transcriptome are two similarly important sides of T cell immunity and both will—as hypothesized—affect the outcome of atherosclerosis. Here, we combined scRNA-seq and scTCR-seq in single cells. Moreover, we provide single T cell transcriptomes and TCR maps of three important tissues involved in atherosclerosis This approach is anticipated to address principal questions concerning atherosclerosis autoimmunity that are likely to pave the long sought way to T cell-dependent therapeutic approaches.

Key words Atherosclerosis, Single-cell sequencing, Transcriptome, TCR repertoire

1 Introduction

T cells are involved in almost all types of diseases ranging from autoimmune diseases, cancers, infectious diseases, neurodegenerative diseases and cardiovascular diseases [1–3]. The *naïve T cell repertoire* emerges during embryogenesis and early life in the thymus. Progenitor T cells are produced in the bone marrow and then migrate to the thymus, where precursor T cells emerge to express various types of T cell receptors (TCRs) [4, 5]. αβ TCRs determine

Zhihua Wang, Xi Zhang, Andreas Habenicht and Changjun Yin contributed equally to this work.

Dipak P. Ramji (ed.), *Atherosclerosis: Methods and Protocols*, Methods in Molecular Biology, vol. 2419,
https://doi.org/10.1007/978-1-0716-1924-7_44,
© The Author(s), under exclusive license to Springer Science+Business Media, LLC, part of Springer Nature 2022

the binding affinity for major histocompatibility complex (MHC)-peptide complexes, which in turn determine T cell development and maturation pathways in the thymus. Here most αβ T cells with too weak or too strong affinity self-reactivity are eliminated—under conditions of physiological tissue homeostasis—at central tolerance checkpoints: (1) TCRs which do not bind or bind at low-affinity die by neglect; and (2) TCRs which bind at high-affinity are eliminated by multiple additional mechanisms [4, 5]. In contrast, γδ T cells do not undergo a similar selection and express a small set of recurrent families of germ line–encoded TCRs [6]. The large majority of T cells expressing the αβ TCRs that survive central tolerance elimination, emigrate from the thymus to patrol secondary lymphoid organs, the circulation and all peripheral tissues. During their life in peripheral tissues, T cells are confronted with multiple further tolerance checkpoints to participate in diverse tasks of T cell and B cell immunity. Compromised central and peripheral tolerance checkpoints have been observed in various autoimmune diseases and cancers though little is known in atherosclerosis [7–10].

Various pro- and anti-inflammatory T cell subsets have been studied in atherosclerosis using transgenic mouse models in which broad T cell subsets have been targeted [11–13]. Dendritic cell subsets in atherosclerotic plaques may process atherosclerosis-relevant T cell peptide antigens in plaques or migrate to draining secondary lymphoid organs to trigger T cell activation and expansion. These possibilities have not been discriminated in atherosclerosis. In addition to T cell activation and maturation in secondary lymphoid organs, leukocyte aggregates in the lamina adventitia form artery tertiary lymphoid organs (ATLOs) in mice [14–16] and humans [17]. These data raised another so far ignored possibility that atherosclerosis-relevant adaptive T cell responses may be organized in ATLOs [15, 18]. Comparing atherosclerotic plaques, adventitia leukocyte aggregates including ATLOs, and the aorta-draining renal lymph nodes (LNs) at the single cell resolution in aged WT and ApoE$^{-/-}$ mice may therefore be of considerable interest to understand T cell immunity in atherosclerosis.

Single cell RNA sequencing (scRNA-seq) technologies allow—until today—detection of 1000–2000 transcripts per cell but new platforms allowing detection of more transcripts per cell are under development. The resulting transcript signatures can be used as fingerprints of single T cells to define their biological impacts in tissue homeostasis and disease conditions and to group T cells into its T cell subset or discover new subsets. Various scRNA-seq technologies are emerging, including the unique molecular identifiers (UMIs)-based methods (Drop-seq, CEL-seq2, MARS-seq, and SCRB-seq) and full-length coverage based methods (Smart-seq2 and Smart-seq/C1) [19]. Recently, Drop-seq based scRNA-seq technology (10x Genomic platform) applied to explore atherosclerosis pathologies at the single cell level revealed the heterogeneity

of myeloid and T-cell subsets [20–25]. However, these studies fall short to provide the TCR information of individual T cells. The TCRα gene locus contains a variable (V) gene segment, a joining (J) segment, and a constant (C) segment; the TCRβ gene locus adds additional diversity (D) segments. During T cell development and maturation in the thymus, the TCR α/β chains undergo VJ/VDJ recombination events, which result in the diversity of theoretically $>10^{15}$ individual TCR sequences (the TCR repertoire) of an individual [26]. The binding of TCRα/β and peptide antigen-MHC complexes triggers activation and proliferation (clonal expansion) of cognate TCR-carrying T cells. Importantly and relevant for the protocol outlined below, during activation and antigen-triggered clonal expansion, T cells of various subsets thereof undergo major changes in their transcriptome signature, which ultimately determines its impact within the immune response. It follows that it is highly informative and desirable to combine α/β TCR sequencing and transcriptome analyses in each T cell in various localization in atherosclerosis. Here, we describe a protocol of combining scRNA-seq and single cell α/β TCR sequencing (scTCR-seq) (Fig. 1a). The protocol will be valuable to address unanswered fundamental issues of the role of T cells in atherosclerosis, including clonal expansion, the relation between activation and metabolic reprogramming in each T cell and the territoriality of distinct T cell subsets and their expansion in the diseased arterial wall and secondary and tertiary lymphoid organs. Our approach will also allow answers to the important question of T cell tolerance in the periphery and whether potential autoimmune T cells are generated.

2 Materials

2.1 Aorta Dissection and Single-Cell Suspension Preparation

1. 115.4 mg/mL stock of Ketamine hydrochloride.
2. 20 mg/mL stock of Xylazine hydrochloride.
3. PBS: 137 mM NaCl, 2.7 mM KCl, 8 mM Na_2HPO_4, 2 mM KH_2PO_4.
4. Dulbecco's phosphate buffered saline (DPBS).
5. 5 mM EDTA in PBS.
6. FACS buffer: PBS, 2% fetal bovine serum (FBS).
7. Enzyme cocktail: 400 U/mL collagenase type I, 120 U/mL collagenase XI, 60 U/mL hyaluronidase, 60 U/mL DNase I, 20 mM HEPES in DPBS.
8. 75% and 80% ethanol.
9. Anti-mouse CD45 antibody.
10. Fixable viability dye (FVD).

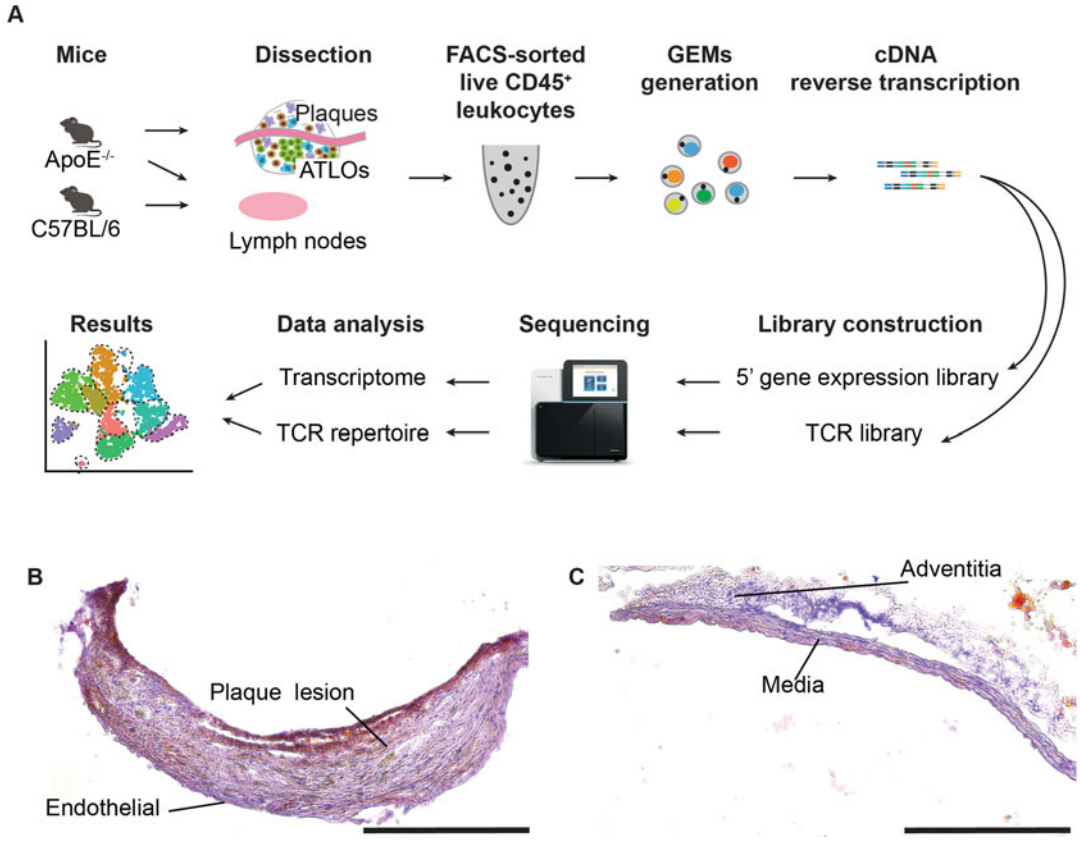

Fig. 1 Experimental design. (**a**) Experimental design to simultaneously establish single-cell RNA sequencing and single-cell TCR sequencing of the diseased atherosclerotic arterial wall. (**b**, **c**) Isolated atherosclerotic plaque (**b**) from the diseased aorta. The remaining media and adventitia are shown in (**c**). Tissue sections are stained with oil red O for lipid (red) and hematoxylin for nuclei (blue). Bar = 500 μm. *ATLO* artery tertiary lymph organ, *GEM* Gel Bead-in-Emulsion, *TCR* T cell receptor

11. Evan's blue dye solution.
12. Curved forceps (Fine Science Tools, Dumont #5/45 Forceps).
13. 1 mL and 10 mL syringes.
14. Automated cell counter.
15. FACS single cell sorter.
16. Cell culture dish.
17. Tube (0.2 mL, 1.5 mL, 15 mL, 50 mL FACS tube and tubes for collecting blood).
18. Centrifuge with cooling system.
19. Dissecting scissors.
20. Incubator with shaker.
21. 100 μm cell strainer.
22. 96-well v-bottom plate.

23. 100 μm filter membrane.
24. Stereo dissecting microscope.
25. Foam plate.
26. Ice.

2.2 Single-Cell Library Construction

2.2.1 Equipment and Reagents

1. 8-tube strip, 0.2 mL pipette and wide-bore tips.
2. Qubit assay tubes (Thermo Fisher Scientific, Q32856).
3. 10× Chromium controller and accessories (holder, vortex adapter, magnetic separator).
4. The thermal cycler with deep wells.
5. Automated electrophoresis system (Fragment analyzer).
6. Qubit fluorometer (Thermo Fisher Scientific).
7. Chromium chip A single cell kit: Contains chip A, gasket, partitioning oil and recovery agent (10× Genomics, 1000009).
8. Chromium single cell 5′ library and gel bead kit: Contains single cell 5′ gel beads, RT reagent mix, RT enzyme mix B, additive A, poly-dT RT primer, buffer sample cleanup 1, amplification master mix, cDNA primer mix, cDNA additive, fragmentation enzyme blend, fragmentation buffer, ligation buffer, DNA ligase, adapter mix, and SI-PCR primer (10× Genomics, 1000014).
9. Dynabeads™ MyOne™ SILANE kit (10× Genomics, 2000048).
10. Chromium single cell 5′ library construction kit: contains cDNA additive, fragmentation enzyme blend, fragmentation buffer, ligation buffer, DNA ligase, adapter mix, and SI-PCR primer (10× Genomics, 1000020).
11. Chromium single cell V(D)J enrichment kit, mouse T cell: contains mouse T cell mix 1 and mouse T cell mix 2 (10× Genomics, 1000071).
12. Chromium i7 multiplex kit: contains individual Chromium i7 sample index (10× Genomics, 120262).
13. SPRIselect reagent: contains magnetic beads (Beckman Coulter, B23317).
14. Qubit dsDNA HS Assay Kit: Contains working solution, standard 1 and standard 2 (Thermo Fisher Scientific, Q33230).
15. Library quantitation kit for Illumina.
16. Nuclease-free water.

2.2.2 PCR Reaction Mixture

1. Master mix (reagents in Chromium single cell 5′ library and gel bead kit): 50 μL RT reagent mix, 5.9 μL poly-dT RT primer, 2.4 μL additive A, 10 μL RT enzyme mix B (*see* **Note 1**).
2. Dynabeads cleanup mix (reagents in Chromium single cell 5′ library and gel bead kit): 182 μL buffer sample cleanup 1, 1.8 μL Dynabeads, 5 μL additive A, 5 μL nuclease-free water.
3. Elution solution I (reagents in Chromium single cell 5′ library and gel bead kit): 98 μL buffer EB, 1 μL 10% Tween 20, 1 μL additive A.
4. cDNA amplification mix (reagents in Chromium single cell 5′ library and gel bead kit): 8 μL nuclease-free water, 50 μL amplification master mix, 5 μL cDNA additive, 2 μL cDNA primer mix.
5. Fragmentation mix (reagents in Chromium single cell 5′ library and gel bead kit or Chromium single-cell 5′ library construction kit): 15 μL nuclease-free water, 5 μL fragmentation buffer, 10 μL fragmentation enzyme blend.
6. Adaptor ligation mix (reagents in Chromium single cell 5′ library and gel bead kit or Chromium single-cell 5′ library construction kit): 17.5 μL nuclease-free water, 20 μL ligation buffer, 10 μL DNA ligase, 2.5 μL adaptor mix.
7. Sample index PCR mix (reagents in Chromium single-cell 5′ library and gel bead kit or Chromium single-cell 5′ library construction kit and Chromium i7 multiplex kit): 8 μL nuclease-free water, 50 μL amplification master mix, 2 μL SI-PCR primer.
8. Target enrichment 1 reaction mix (reagents in Chromium single-cell 5′ library construction kit and Chromium single cell V(D)J enrichment kit): 5 μL nuclease-free water, 50 μL amplification master mix, 5 μL cDNA additive, 5 μL T cell mix 1.
9. Target enrichment 2 reaction mix (reagents in Chromium single-cell 5′ library construction kit and Chromium single cell V(D)J enrichment kit): 5 μL nuclease-free water, 50 μL amplification master mix, 5 μL cDNA additive, 5 μL LT cell mix 2.

2.3 Sequencing

1. NextSeq 500 system.
2. PhiX control library.

2.4 Data Analysis

1. Computer (Linux and Windows system, minimum with 8+ cores, 64GB RAM).
2. R (version 4.0.3), https://www.r-project.org/; RStudio (version 3.6.0), https://rstudio.com/.

3. Cell Ranger (version 3.1.0): https://support.10xgenomics.com/single-cell-vdj/software/downloads/latest.
4. Loup Cell Browser (version 5.0.1): https://support.10xgenomics.com/single-cell-gene-expression/software/downloads/latest
5. Loup V(D)J Browser (version 4.0.0): https://support.10xgenomics.com/single-cell-vdj/software/downloads/latest.
6. Seurat package (version 3.0).
7. clusterProfiler package (version 3.12.0).
8. Philentropy package (version 0.4.0).
9. edgeR package (version 3.26.8).
10. vegan package (version 2.5-6).
11. circlize package (version 0.4.11).

2.5 Mice

78 weeks old C57BL/6J WT and ApoE$^{-/-}$ mice fed a chow diet under pathogen-free animal facilities. All animal procedures should be carried out according to local and national guidelines (e.g., those presented in this chapter were approved by Regierung von Oberbayern Animal Use and Care Committee).

3 Methods

3.1 Dissection of Atherosclerotic Plaques and ATLOs from the Diseased Aorta

1. Anesthetize aged WT and ApoE$^{-/-}$ mice with 120 mg/kg ketamine hydrochloride and 8 mg/kg xylazine hydrochloride in 500 μL of DPBS per mouse by intraperitoneal injection.
2. After anesthesia, place the mouse in the supine position and fix on a foam plate. Spray with 75% ethanol on the abdominal fur and draw blood by cardiac puncture using a 1 mL syringe. Then fully perfuse aorta from the left ventricle to remove remaining blood with 10 mL of 5 mM EDTA buffer followed with 20 mL of PBS and 20 mL of FACS buffer, respectively.
3. Remove other tissues and collect the renal lymph nodes under the stereo dissecting microscope of both aged WT and ApoE$^{-/-}$ mice.
4. Carefully dissect the whole aorta out from aged ApoE$^{-/-}$ mice and place the aorta in a cell culture dish covered with 1 mL of precooled FACS buffer. Maintain cell culture dish and the aorta ice-cold during the isolation of plaque tissues. Clean the aorta from the surrounding adipose tissues and lymph nodes under the dissection microscope to avoid contamination of lymphocytes from adipose tissues and small lymph nodes (Fig. 1b, c) (*see* **Note 2**).

5. Place the aorta into a new dish with precooled FACS buffer and open the aorta in the longitudinal direction with a fine dissecting scissors. Atherosclerotic plaques with the white color and bulged shape can be clearly recognized under the microscope.
6. Carefully remove all visible plaque lesions with curved forceps from the diseased aorta and collect the plaque tissues into a 15 mL tube with precooled FACS buffer (Fig. 1b, c) (*see* **Note 2**). Also collect the supernatants containing the plaque constituents into the same 15 mL tube.
7. Rinse the remaining aorta with FACS buffer in a new dish and collect the aorta without plaques into a 1.5 mL tube with precooled FACS buffer.

3.2 Preparation of Single-Cell Suspension of Plaques, ATLOs, and LNs

1. Centrifuge plaque tissues with supernatants and the remaining aorta samples at 400 × *g* for 5 min at 4 °C and discard the supernatant.
2. Resuspend samples with cold PBS buffer and centrifuge as **step 1**.
3. Repeat **step 2** and then discard the supernatant.
4. Cut tissues with dissecting scissors into small pieces while keeping them on ice.
5. Add 1 mL of Enzyme cocktail and incubate at 37 °C with slow shaking for 40 min (*see* **Note 3**).
6. Filter the digested cell suspensions through a 100 μm strainer, mash tissues with syringe plunger gently, and rinse with 5 mL of ice-cold FACS buffer.
7. Centrifuge the samples at 400 × *g* for 5 min at 4 °C and discard the supernatant. Resuspend the cells with 5 mL of ice-cold FACS buffer.
8. Repeat the **step 7** for washing purpose and then resuspend the single cell pellets in 200 μL of FACS buffer and transfer to a 96-well v-bottom plate for Subheading 3.3.
9. For lymph node samples, cut tissues with dissecting scissors, perform **steps 6–8** and transfer samples to the 96-well v-bottom plate for Subheading 3.3.

3.3 Single-Cell Sorting

1. Centrifuge cell suspensions in 96-well plate at 400 × *g* for 5 min at 4 °C and discard the supernatant.
2. Resuspend cell pellets in 100 μL of FVD (1:1000 dilution) in PBS at 4 °C for 20 min.
3. Perform the washing steps twice as described above in Subheading 3.2, **steps 2** and **3**.
4. Stain the samples with 100 μL of anti-CD45 antibody (1:200 dilution) and incubate at 4 °C for 25 min.

5. Wash twice as described in **step 3**.
6. Resuspend cells with 200 μL of FACS buffer and transfer into FACS tube by filtering through 100 μm filter membrane.
7. Sort $FVD^{-}CD45^{+}$ leukocytes into a 1.5 mL precooled tube by single cell sorter (e.g., BD FACSAria™ III) (*see* **Note 4**). Samples should be kept on ice during all operations.

3.4 Gel Bead Emulsions (GEMs) Generation and Reverse Transcription

1. After sorting from Subheading 3.3, immediately examine the single cell suspension with automated cell counter to check the cell density and the percentages of live cells. Adjust cell concentration to 700–1200 cells/μL with FACS buffer (*see* **Note 5**).
2. According to the calculator table appended in the 10× Chromium™ 5′ Reagent Kits User Guide, calculate the number of input cells and the volume of nuclease-free water based on how many cells per sample (from 1000 cells to 10,000 cells per sample) will be used. Mix nuclease-free water, cell suspension and 68.3 μL of master mix (Subheading 2.2.2, **step 1**) in 0.2 mL 8-strip tube.
3. Load 90 μL of sample from **step 2**, 40 μL of gel beads (Subheading 2.2.1, **step 8**) and 270 μL of partitioning oil (Subheading 2.2.1, **step 7**) to the Chromium chip A. Cover the chip with gasket (Subheading 2.2.1, **step 7**) and place the chip in the Chromium controller to generate GEMs.
4. Transfer 100 μL of GEMs to a 0.2 mL eight-strip tube and carry out the reverse transcription reaction at 53 °C for 45 min followed by 85 °C for 5 min using the thermal cycler (Subheading 2.2.1, **step 4**). Keep at 4 °C.
5. Add 125 μL of recovery agent (Subheading 2.2.1, **step 7**) to the top of the sample and wait for 1 min at room temperature (RT). Slowly remove 125 μL of recovery agent from the bottom of the tube.
6. Add 200 μL of Dynabeads cleanup mix (Subheading 2.2.2, **step 2**) and incubate for 10 min at RT. Place the tube on the 10× magnetic separator (Subheading 2.2.1, **step 3**) and remove the supernatant. Wash the tube twice with 80% ethanol. Remove the tube from the separator, add 35.5 μL of elution solution I (Subheading 2.2.2, **step 3**) and incubate for 2 min to elute the products. Place the tube back to the separator and transfer 35 μL of samples to a 0.2 mL eight-strip tube (*see* **Note 6**).
7. Add 65 μL of cDNA amplification mix (Subheading 2.2.2, **step 4**) to the purified products. Set the PCR condition as: 98 °C for 45 s; 98 °C for 20 s, 67 °C for 30 s, 72 °C for 1 min, 11–18 PCR cycles (*see* **Note 7**).

8. Purify the PCR products using the SPRIselect beads (Subheading 2.2.1, **step 13**). Conduct the single-sided size selection by adding 60 μL (0.6×) of SPRIselect beads and incubate for 5 min at room temperature. Place the tube on the 10× magnetic separator and remove supernatant. Wash the tube twice with 200 μL of 80% ethanol each time. Remove the tube from the separator, add 45.5 μL of buffer EB and incubate for 2 min to elute the products. Place the tube back to the separator and transfer 45 μL of sample to a 0.2 mL eight-strip tube (*see* **Note 6**).
9. Quantify the concentration of products using Qubit fluorometer with Qubit dsDNA HS Assay Kit (Subheading 2.2.1, **step 14**).

3.5 5′ Gene Expression Library Construction

1. Use 50 ng of purified GEM-RT products for the 5′ gene expression library construction. If the volume of 50 ng products exceeds 20 μL, only take 20 μL products for subsequent library construction.
2. Add 30 μL of fragmentation mix (Subheading 2.2.2, **step 5**) into each 50 ng of sample. Load the tube into the thermal cycler and set up the following parameters: 32 °C for 5 min; 65 °C for 30 min; keep on 4 °C (*see* **Note 8**).
3. Purify the PCR products using SPRIselect beads (Subheading 2.2.1, **step 13**). Conduct the double-sided size selection by firstly adding 30 μL (0.6×) of SPRIselect beads, and incubate for 5 min at RT Place the tube on the 10× magnetic separator and transfer the supernatant to a 0.2 mL 8-strip tube. Then, add 10 μL (0.8×) of SPRIselect beads to the supernatant and incubate for 5 min. Place the tube on the separator and remove the supernatant. Wash the tube using 125 μL of 80% ethanol twice. Remove the tube from the separator, add 50.5 μL of EB buffer and incubate for 2 min to elute the products. Place the tube back to the separator and transfer 50 μL of sample to a 0.2 mL 8-strip tube (*see* **Note 6**).
4. Add 50 μL of adaptor ligation mix (Subheading 2.2.2, **step 6**) to the purified products, set the thermal cycler condition as: 20 °C for 15 min; keep on 4 °C.
5. Purify the ligation products with single-sided size selection by adding 80 μL (0.8×) of SPRIselect beads. After purification as Subheading 3.4, **step 8**, elute the magnetic beads with 30 μL EB buffer into a 0.2 mL tube.
6. Add 60 μL of sample index PCR mix (Subheading 2.2.2, **step 7**) to the purified products followed by 10 μL of Chromium i7 sample index primer (Chromium i7 multiplex kit). Load the tube into the thermal cycler and set the PCR reaction as: 98 °C

for 45 s; 98 °C for 20 s, 54 °C for 30 s, 72 °C for 20 s. After 14 PCR cycles, set 72 °C for 1 min; keep at 4 °C (*see* **Note 9**).

7. Purify the PCR products with double-sided size selection as described in **step 3**. In brief, firstly add 60 μL (0.6×) of SPRIselectbeads followed by separations. Then add 20 μL (0.8×) of SPRIselect beads into the supernatant. After purification, wash the beads with 200 μL of 80% ethanol twice, elute the magnetic beads with 35.5 μL of EB buffer and transfer 35 μL of sample to a 0.2 mL 8-strip tube.
8. Check the size of the purified product and determine the average size of each sample using the Fragment analyzer (Subheading 2.2.1, **step 5**). The size of the products mainly ranges from 300 to 700 bp.
9. Quantify the concentration of each sample using the NEBNext® library quant kit (Subheading 2.2.1, **step 15**). In order to get enough products for sequencing, the concentration of each sample should exceed 4 nM.
10. Pool the samples as one ready-for-sequencing library with equal mass.

3.6 TCR Enrichment and Library Construction

1. Add 33 μL of nuclease-free water to 2 μL sample of Subheading 3.4, **step 8** in a 0.2 mL 8-strip tube. Combine with 65 μL of target enrichment 1 reaction mix (Subheading 2.2.2, **step 8**). Load the tube into the thermal cycler and set the PCR condition as: 98 °C for 45 s; 98 °C for 20 s, 67 °C for 30 s, 72 °C for 1 min; followed by 9 cycles, then 72 °C for 1 min; keep on 4 °C (*see* **Note 10**).
2. Cleanup the PCR products with single-sided size selection by adding 80 μL (0.8×) of SPRIselect beads as described in Subheading 3.4, **step 8**. After purification, elute the product with 35.5 μL of EB buffer to obtain 35 μL of sample in a 0.2 mL 8-strip tube.
3. Add 65 μL of target enrichment 2 reaction mixture (Subheading 2.2.2, **step 9**) to the purified PCR products. Set the PCR condition as: 9 °C for 45 s; 98 °C for 20 s, 67 °C for 30 s, 72 °C for 1 min; followed by 9 cycles, then 72 °C for 1 min; keep on 4 °C.
4. Purify the PCR products with double-sided size selection as described in Subheading 3.5, **step 3**. Briefly, add 50 μL (0.5×) of SPRIselect beads in first round, followed with 30 μL (0.8×) of SPRIselect beads in second round. After purification and wash steps, elute the magnetic beads with 45.5 μL of EB buffer. Then, collect 45 μL of sample into a 0.2 mL 8-strip tube. Quantify the concentration of products using Qubit. Carry 50 ng of enriched TCR products for the following library

construction. If the volume of 50 ng products exceeds 20 μL then only include 20 μL of products.

5. Follow all the steps in Subheading 3.5 for enriched TCR library construction. The only changes are in the Subheading 3.5, **step 2**, 32 °C for 2 min; skip **step 3**; **step 6**, set the PCR with 8 cycles; **step 7**, add 80 μL SPRIselect beads for single-sided size selection.

3.7 Sequencing

1. Add 1% of PhiX control library to the 5′ gene expression library from Subheading 3.5, **step 10** and perform the 26 + 91 bp pair-end sequencing using the Nextseq 500 system following the manufacturer's instructions (*see* **Note 11**).
2. Add 1% PhiX control library to the enriched TCR library constructed in Subheading 3.6 and perform the 150 + 150 bp pair-end sequencing using the Nextseq 500 system (*see* **Note 11**).

3.8 Data Analysis

3.8.1 Sequencing Alignment

1. Demultiplex the sequencing raw binary base call (BCL) files into individual FASTQ files with the "mkfastq" function built in the Cell Ranger (version 3.1.0). (Fig. 2) (*see* **Note 12**).
2. For the 5′ gene expression libraries, download mm10 reference from 10× Genomics (https://support.10xgenomics.com/single-cell-gene-expression/software/downloads/latest). Then, align reads referring to mm10 reference using the built-in "count" function of STAR aligner (the default alignment method in Cell Ranger) to generate data matrix for transcriptome.
3. For the T cell V(D)J libraries, download GRCm38 reference from 10× Genomics (https://support.10xgenomics.com/single-cell-vdj/software/downloads/latest). Then map the reads to the "GRCm38 reference-3.1.0" using the built-in "vdj" function in the Cell Ranger to annotate V(D)J information of T cells.
4. Visualize the output ".cloupe" and ".vloupe" files in the Loupe Cell Browser and Loupe V(D)J Browser, respectively (Fig. 2), which are free software provided by 10× Genomics.

3.8.2 Single Cell Transcriptome Analysis in RStudio

1. Load Seurat package into RStudio (Fig. 2).
2. Load the output raw barcodes, features and matrix files of each sample (Subheading 3.8.1, **step 2**) into RStudio.
3. Create Seurat object of each sample by "CreateSeuratObject()" function, and remove cells with less than 200 genes and genes detected in less than 3 cells.
4. Filter out low quality and duplicated cells based on the counts of detected genes and the percentage of mitochondrial genes in each cell (*see* **Note 13**).

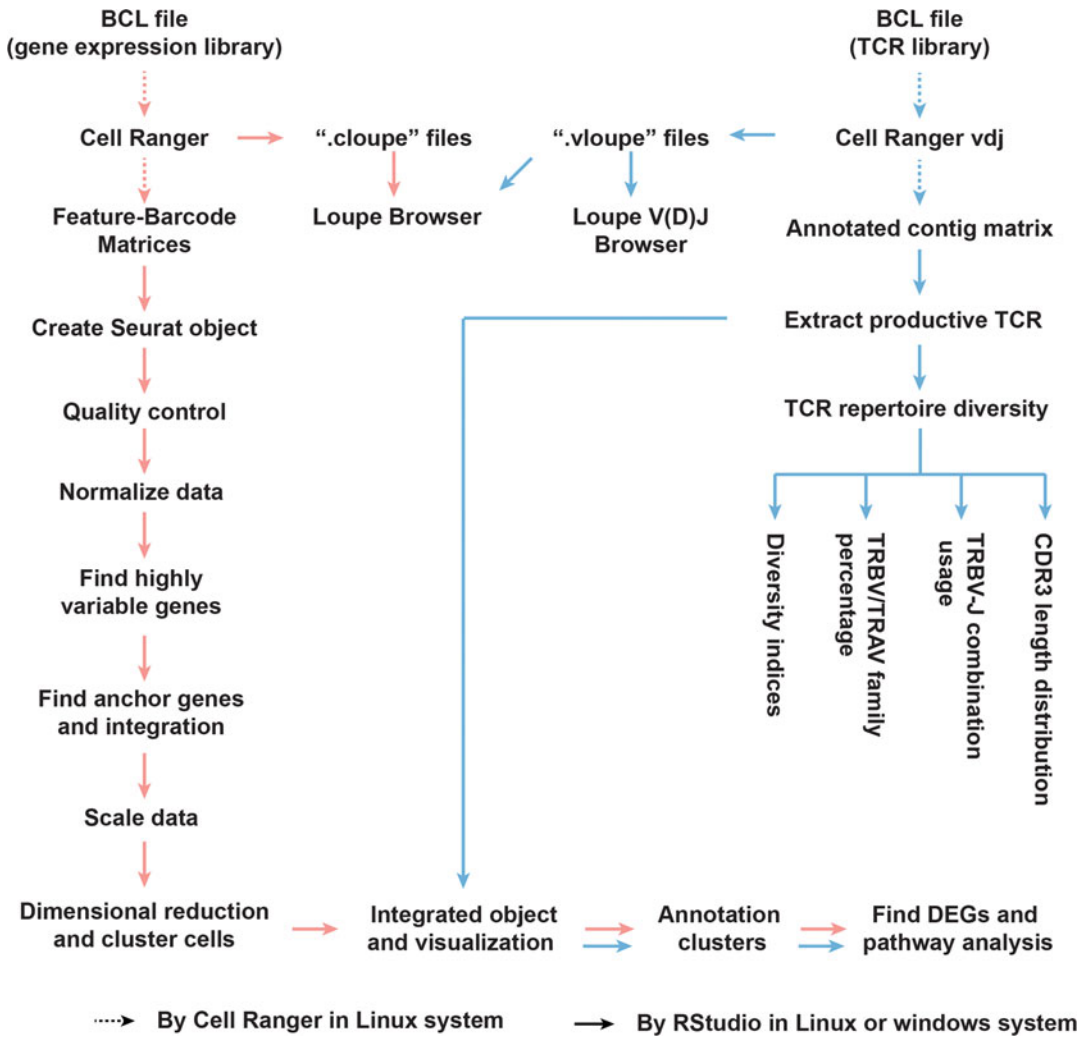

Fig. 2 Workflow for integrated analyses of scRNA-seq and scTCR-seq data. Subsequent to the generation of high-quality cDNA from a given sample, the transcriptome and the TCR repertoire libraries are generated from the same cDNA. The raw data in BCL format of two libraries are analyzed independently (*see* lines in orange and blue, respectively). The transcriptome and TCR sequences share identical cell-specific barcodes in each T cell allowing to integrate the two specific libraries in single T cells

5. Normalize the gene expression for each cell using "NormalizeData()" function in Seurat package.
6. Identify 2000 cell-to-cell highly variable genes by "FindVariableFeatures()" function (selection.method="vst") in Seurat package.
7. Integrate data of four samples based on the anchor genes identified by "FindIntegrationAnchors()" function (dims=20) in Seurat package.

8. Switch the default assay into "integrated" using the "DefaultAssay()" function for integrated analysis. Scale the data to get rid of the effect of highly expressed genes using Seurat package.
9. Perform the principal component analysis (PCA) to reduce the dimension. The significant PCs are used to construct shared nearest neighbor graph in Seurat package. Then, cluster cells by "FindClusters()" function in Seurat package with an appropriate resolution value (*see* **Note 14**).
10. Visualize the cell distribution by nonlinear dimensional reduction (tSNE or UMAP) plot.
11. Identify differentially expressed genes among clusters by using Wilcoxon rank-sum test in "FindAllMarkers()" function in Seurat package. Genes expressed in less than 10% of cells should be excluded from testing.
12. Annotate cell clusters in Seurat package by using canonical lineage-specific markers like *Cd3e*, *Cd79a*, *Cd19*, and *Cd68* to categorize the populations of T cells, B cells and myeloid cells, respectively.
13. Perform gene enrichment analysis using "clusterProfiler" (Subheading 2.4, **step 7**) to validate each cluster's phenotypes and functions.
14. Extract the T cell population from the total $CD45^+$ cells by cluster numbers using "subset()" function in R package.
15. Reanalyze T cell subsets following the Subheading 3.8.2, **steps 8–13**.
16. Annotate each T cell subtypes as described in Subheading 3.8.2, **step 12** by using more T cell subpopulation linage markers, that is, *Cd4*, *Cd8a*, *Cd44*, *Sell*, *Ccr7*, *Foxp3*, *Trdc*, *Klrb1c*, *Cxcr5,* and other known cell lineage markers.
17. Perform gene enrichment analysis using "clusterProfiler" package to validate each T-cell subcluster.

3.8.3 TCR Repertoire Analysis in RStudio

1. Load the output file of "filtered_contig_annotations.csv" of Subheading 3.8.1, **step 3** into RStudio (Fig. 2).
2. Extract the productive TCR using "subset()" function in R package for TCR repertoire analysis (*see* **Note 15**).
3. Integrate the productive TCR information into the metadata of single-cell transcriptome Seurat object created in Subheading 3.8.2, **step 16** by the unique cell barcode.
4. Filter out the TCRs which cannot integrate with the existing T cells in the Seurat object.
5. Add TCR expansion character into metadata based on their TCR sequences. At least two T cells with the same V family and identical CDR3 amino acid (aa) sequence of paired αβ chains

should be considered as expanded T cells (or clonally expanded T cells). Cells without detected TCR are considered as non-detected T cells. Cells with unique paired αβ chains or with single α or β chain are categorized as nonexpanded T cells (*see* **Note 16**).

6. Calculate the canonical Shannon entropy, Gini index and inverse Simpson diversity to assess TCR diversity using "H()" function, "gini()" function, "diversity()" function in philanthropy, edgeR and vegan packages, respectively [27] (*see* **Note 17**).
7. Calculate the percentage of different V family of β chain and CDR3 length distribution in total T cells, expanded T cells and nonexpanded T cells of each sample.
8. Calculate the frequency of TCR V-J combination usage in each tissue. Use a circular plot to display the combination.
9. Summarize the shared clonally expanded CDR3 among different tissues and present it by circular plot.

3.8.4 Combined Transcriptome and TCR Repertoire Analysis in RStudio

1. Calculate the percentage of expanded T cells in each T cell cluster based on the TCR sequences, which have already been added into the metadata of Seurat object created in Subheading 3.8.3, **step 5** (Fig. 2).
2. Visualize the distribution of expanded T cells in tSNE plot.
3. Identify the differentially expressed genes between expanded T cells and nonexpanded T cells using the "FindMarkers()" function in Seurat. Genes expressed in less than 10% of cells are excluded for testing.
4. Perform gene enrichment analysis using "clusterProfiler" (Subheading 2.4, **step 7**) to find the function-correlated pathways between expanded and nonexpanded T cells.

4 Notes

1. The reagents used in Subheading 2.2.2 are included in Chromium kits. The given volume of each mixture is applied to one sample.
2. In the present protocol, it takes around half an hour to dissect one aorta and to remove plaque lesions. In order to obtain enough immune cells from plaques for scRNA-seq, it is important to mix the plaque tissues collected from 3 to 5 aged $ApoE^{-/-}$ mice. Drop cold FACS buffer to cover the aorta to avoid dry surface and keep the dish on ice during operation. The following should be considered during sample collection to avoid cross contamination of leukocytes from different

sources: (1) the appropriate perfusion step following with the order of EDTA, PBS, and FACS buffers is important to avoid blood-derived leukocyte contamination; (2) the major leukocyte sources of the diseased aorta are ATLOs, thus, it is important to avoid ATLO-derived leucocytes contaminating plaque leukocytes; (3) Para-aortic lymph nodes and adipose tissues should be carefully removed under microscope.

3. We use enzyme digestion to digest plaques and aorta samples. It is known that the digestion procedure can induce the upregulation of expression of some transcripts [28] and also reduce the expression of some cell surface markers [29]. It is therefore important to cut the large piece of tissues into small parts and to optimize the digestion time. We recommend using 40-min digestion time.
4. High quality single cell suspension is crucial for high quality scRNA-Seq experiments. Different single cell sorting strategies can be applied to obtain plaque T cells (i.e., total live cells, total $CD45^+$ cells, $CD3^+$ cells, $TCR\beta^+$ cells, $CD4^+$ cells, $CD8^+$ cells). To obtain the T cell landscape within plaques, single cell sorting of $CD45^+$ cells is recommended. For some rare cell types, it is strongly recommended to perform enrichment steps to elaborate its abundance. Using cell viability dye to eliminate dead cells during cell sorting is necessary.
5. High cell viability should be maintained before loading into the Chromium controller. For lymphoid organs, it is easy to separate single cells from tissue blocks and >95% cell viability can be obtained after single cell sorting. For plaques, it is more challenging to separate single cells from tissue blocks, thus, 70–80% cell viability of plaque leukocytes is realistic. It is recommended to filter the Evan's blue dye solution before loading to the automate cell counter to obtain accurate cell viability. Few recommendations to maintain cell viability: (1) precool the collection tubes at the single cell sorting step; (2) load the cell suspension within 30 min after the single cell sorting; (3) treat the cells gently with wide-bore tips to reduce cell lysis; and (4) keep the whole procedure under ice-cold condition. If the cell density is too low, concentration by centrifugation is required.
6. After removing the ethanol, the elution buffer should be added to the products within 2 min to prevent from over-drying.
7. Repeat cycles are determined by the sample types and targeted cell numbers. Primary cells need more cycles than cell lines. Reduce cell cycles if more cells are used. For example, we set 14 cycles to for 3000 targeted primary $CD45^+$ cells. 10× Chromium™ 5′ Reagent Kits User Guide also provide recommendations of cycle-setting.

8. The block of the thermocycler needs to be precooled at 4 °C before transferring the sample to the thermal cycler.
9. If the range mass of input products is 26–50 ng, set the repeat as 14 cycles. However, if the mass is less than 50 ng then set at 16 cycles.
10. It is important to estimate the T cell percentages of the total cells. If there are too few T cells (i.e., <10%) in the samples, it will be difficult to obtain TCR libraries. If the T cell content in the sample is unknown, it is recommended to keep the cDNA at −20 °C for 1–2 weeks and then sequence the 5′ expression libraries to obtain an accurate T cell percentage first. Then, the TCR libraries can be constructed and sequenced later (*see* Subheading 3.6).
11. NextSeq 500 sequencing platform is not obligatory, other Illumina sequencers can be used (i.e., NovaSeq 6000, HiSeq 2500). It is recommended to sequence the gene expression libraries and TCR libraries using the same platform.
12. The 10× Genomics platform is used to prepare the library as described in Subheadings 3.4–3.6. We use the Cell Ranger pipeline to demultiplex the raw base call files of next generation sequencing, align reads and generate a gene-barcode count matrix. All the steps in this section are conducted with the Cell Ranger software in Linux system.
13. After loading data into Seurat, it returns a unique molecular identified (UMI) count matrix, which provides the counts of genes (feature; row) detected in individual cell (barcode; column). Low quality, cell debris and duplicated cells in the single-cell sequencing data should be filter out. Three parameters are used to control the data quality in Seurat: the total number of genes detected in each cell (nFeature_RNA); the number of UMIs detected in each cell (nCount_RNA); and the mitochondrial percentage (percent.mt). We filter out cells with nFeature_RNA <200 and nFeature_RNA >4000 in lymphoid organ samples and cells with nFeature_RNA <200 and nFeature_RNA >5000 in plaque samples. Cells with high percentage of mitochondrial genes (i.e., > 8% of total RNA) were also filtered out.
14. The number of clusters can be changed by adjusting the resolution and the number of PCs in the "FindClusters" function and the "FindNeighbors" function. Seurat provides other methods like "ElbowPlot()" and "JackStraw()" to help to determine the proper PCs for dimensional reduction. We use the top 12 PCs for dimensional reduction with the resolution value at 0.8 for clustering.

15. The "filtered_contig_annotaions.csv" file contains TCR V, D, J, and C gene families, CDR3 nt/aa sequence, clonetype number, and frequency of each TCR clone.
16. The mouse TCR V(D)J Enrichment Kit contains the primers to target TCRα and TCRβ chains. In order to obtain the TCR sequences of γδ T cells, the custom designed primers to target TCRγ and TCRδ chains are required [30].
17. In order to compare TCR repertoire diversity and clonality, downsampling all tissues into the same sample depth is required. The Shannon entropy (function: H(x)), Gini index (function: gini(x)), and inverse Simpson diversity index (function: diversity(x, "invsimpson")) are calculated by randomly downsampling into the sample depth. The downsampling is repeated 1000 times.

Acknowledgments

This work was funded by the Deutsche Forschungsgemeinschaft (DFG) (YI 133/3-5), LMUexcellent 867949-0, Friedrich-Baur-Stiftung 39/20, Bayer Thrombosis Research Award to C.Y.; DFG HA 1083/15-4 and HA 1083/15-5 to A.J.R.H.; and ERA-CVD (PLAQUEFIGHT) 01KL1808 to A.J.R.H.

References

1. Farber DL (2020) Form and function for T cells in health and disease. Nat Rev Immunol 20(2):83–84. https://doi.org/10.1038/s41577-019-0267-8
2. Ketelhuth DF, Hansson GK (2016) Adaptive response of T and B cells in atherosclerosis. Circ Res 118(4):668–678. https://doi.org/10.1161/circresaha.115.306427
3. Weyand CM, Younge BR, Goronzy JJ (2008) T cells in arthritis and atherosclerosis. Curr Opin Lipidol 19(5):469–477. https://doi.org/10.1097/mol.0b013e32830bfdc2
4. Xing Y, Hogquist KA (2012) T-cell tolerance: central and peripheral. Cold Spring Harb Perspect Biol 4(6):a006957. https://doi.org/10.1101/cshperspect.a006957
5. Klein L, Robey EA, Hsieh C-S (2019) Central CD4+ T cell tolerance: deletion versus regulatory T cell differentiation. Nat Rev Immunol 19(1):7–18. https://doi.org/10.1038/s41577-018-0083-6
6. Bendelac A, Bonneville M, Kearney JF (2001) Autoreactivity by design: innate B and T lymphocytes. Nat Rev Immunol 1(3):177–186. https://doi.org/10.1038/35105052
7. von Boehmer H, Melchers F (2010) Checkpoints in lymphocyte development and autoimmune disease. Nat Immunol 11(1):14–20. https://doi.org/10.1038/ni.1794
8. Handel AE, Irani SR, Holländer GA (2018) The role of thymic tolerance in CNS autoimmune disease. Nat Rev Neurol 14(12):723–734. https://doi.org/10.1038/s41582-018-0095-7
9. Waldman AD, Fritz JM, Lenardo MJ (2020) A guide to cancer immunotherapy: from T cell basic science to clinical practice. Nat Rev Immunol 20(11):651–668. https://doi.org/10.1038/s41577-020-0306-5
10. Goronzy JJ, Weyand CM (2017) Successful and maladaptive T cell aging. Immunity 46(3):364–378. https://doi.org/10.1016/j.immuni.2017.03.010
11. Wolf D, Ley K (2019) Immunity and inflammation in atherosclerosis. Circ Res 124(2):315–327. https://doi.org/10.1161/circresaha.118.313591
12. Witztum JL, Lichtman AH (2014) The influence of innate and adaptive immune responses on atherosclerosis. Annu Rev Pathol 9:73–102.

https://doi.org/10.1146/annurev-pathol-020712-163936

13. Tabas I, Lichtman AH (2017) Monocyte-macrophages and T cells in atherosclerosis. Immunity 47(4):621–634. https://doi.org/10.1016/j.immuni.2017.09.008
14. Hu D, Mohanta SK, Yin C, Peng L, Ma Z, Srikakulapu P, Grassia G, MacRitchie N, Dever G, Gordon P, Burton FL, Lalenti A, Sabir SR, McInnes IB, Brewer JM, Garside P, Weber C, Lehmann T, Teupser D, Habenicht L, Beer M, Grabner R, Maffia P, Weih F, Habenicht AJ (2015) Artery tertiary lymphoid organs control aorta immunity and protect against atherosclerosis via vascular smooth muscle cell lymphotoxin β receptors. Immunity 42(6):1100–1115. https://doi.org/10.1016/j.immuni.2015.05.015
15. Mohanta SK, Yin C, Peng L, Srikakulapu P, Bontha V, Hu D, Weih F, Weber C, Gerdes N, Habenicht AJ (2014) Artery tertiary lymphoid organs contribute to innate and adaptive immune responses in advanced mouse atherosclerosis. Circ Res 114(11): 1772–1787. https://doi.org/10.1161/CIRCRESAHA.114.301137
16. Grabner R, Lotzer K, Dopping S, Hildner M, Radke D, Beer M, Spanbroek R, Lippert B, Reardon CA, Getz GS, Fu YX, Hehlgans T, Mebius RE, van der Wall M, Kruspe D, Englert C, Lovas A, Hu D, Randolph GJ, Weih F, Habenicht AJ (2009) Lymphotoxin beta receptor signaling promotes tertiary lymphoid organogenesis in the aorta adventitia of aged ApoE$^{-/-}$ mice. J Exp Med 206(1): 233–248. https://doi.org/10.1084/jem.20080752
17. Gewaltig J, Kummer M, Koella C, Cathomas G, Biedermann BC (2008) Requirements for CD8 T-cell migration into the human arterial wall. Hum Pathol 39(12): 1756–1762. https://doi.org/10.1016/j.humpath.2008.04.018
18. Yin C, Mohanta SK, Srikakulapu P, Weber C, Habenicht AJR (2016) Artery tertiary lymphoid organs: powerhouses of atherosclerosis immunity. Front Immunol 7:387. https://doi.org/10.3389/fimmu.2016.00387
19. Ziegenhain C, Vieth B, Parekh S, Reinius B, Guillaumet-Adkins A, Smets M, Leonhardt H, Heyn H, Hellmann I, Enard W (2017) Comparative analysis of single-cell RNA sequencing methods. Mol Cell 65(4):631–643.e634. https://doi.org/10.1016/j.molcel.2017.01.023
20. Cochain C, Vafadarnejad E, Arampatzi P, Pelisek J, Winkels H, Ley K, Wolf D, Saliba AE, Zernecke A (2018) Single-cell RNA-seq reveals the transcriptional landscape and heterogeneity of aortic macrophages in murine atherosclerosis. Circ Res 122(12):1661–1674. https://doi.org/10.1161/circresaha.117.312509
21. Winkels H, Ehinger E, Vassallo M, Buscher K, Dinh HQ, Kobiyama K, Hamers AAJ, Cochain C, Vafadarnejad E, Saliba AE, Zernecke A, Pramod AB, Ghosh AK, Anto Michel N, Hoppe N, Hilgendorf I, Zirlik A, Hedrick CC, Ley K, Wolf D (2018) Atlas of the immune cell repertoire in mouse atherosclerosis defined by single-cell RNA-sequencing and mass cytometry. Circ Res 122(12):1675–1688. https://doi.org/10.1161/CIRCRESAHA.117.312513
22. Lin JD, Nishi H, Poles J, Niu X, McCauley C, Rahman K, Brown EJ, Yeung ST, Vozhilla N, Weinstock A, Ramsey SA, Fisher EA, Loke P (2019) Single-cell analysis of fate-mapped macrophages reveals heterogeneity, including stem-like properties, during atherosclerosis progression and regression. JCI Insight 4(4): e124574. https://doi.org/10.1172/jci.insight.124574
23. Depuydt MAC, Prange KHM, Slenders L, Ord T, Elbersen D, Boltjes A, de Jager SCA, Asselbergs FW, de Borst GJ, Aavik E, Lonnberg T, Lutgens E, Glass CK, den Ruijter HM, Kaikkonen MU, Bot I, Slutter B, van der Laan SW, Yla-Herttuala S, Mokry M, Kuiper J, de Winther MPJ, Pasterkamp G (2020) Microanatomy of the human atherosclerotic plaque by single-cell transcriptomics. Circ Res 127(11):1437–1455. https://doi.org/10.1161/CIRCRESAHA.120.316770
24. Fernandez DM, Rahman AH, Fernandez NF, Chudnovskiy A, Amir ED, Amadori L, Khan NS, Wong CK, Shamailova R, Hill CA, Wang Z, Remark R, Li JR, Pina C, Faries C, Awad AJ, Moss N, Bjorkegren JLM, Kim-Schulze S, Gnjatic S, Ma'ayan A, Mocco J, Faries P, Merad M, Giannarelli C (2019) Single-cell immune landscape of human atherosclerotic plaques. Nat Med 25(10):1576–1588. https://doi.org/10.1038/s41591-019-0590-4
25. Pan H, Xue C, Auerbach BJ, Fan J, Bashore AC, Cui J, Yang DY, Trignano SB, Liu W, Shi J, Ihuegbu CO, Bush EC, Worley J, Vlahos L, Laise P, Solomon RA, Connolly ES, Califano A, Sims PA, Zhang H, Li M, Reilly MP (2020) Single-cell genomics reveals a novel cell state during smooth muscle cell phenotypic switching and potential therapeutic targets for atherosclerosis in mouse and human. Circulation 142(21):2060–2075. https://doi.org/10.1161/circulationaha.120.048378

26. Nikolich-Zugich J, Slifka MK, Messaoudi I (2004) The many important facets of T-cell repertoire diversity. Nat Rev Immunol 4(2): 123–132.https://doi.org/10.1038/nri1292
27. Heather JM, Best K, Oakes T, Gray ER, Roe JK, Thomas N, Friedman N, Heather JM, Best K, Oakes T, Gray ER,Roe JK, Thomas N, Friedman N, Noursadeghi M, Chain B (2016) Dynamic perturbations of the T-cell receptor-repertoire in chronic HIV infection and following antiretroviral therapy. Front Immunol 6:644. https://doi.org/10.3389/fimmu.2015.00644
28. Li Y, Ren P, Dawson A, Vasquez HG, Ageedi W, Zhang C, Luo W, Chen R, Li Y, Kim S, Lu HS, Cassis LA, Coselli JS, Daugherty A, Shen YH, LeMaire SA (2020) Single-cell transcriptome analysis reveals dynamic cell populations and differential gene expression patterns in control and aneurysmal human aortic tissue. Circulation 142(14): 1374–1388. https://doi.org/10.1161/CIRCULATIONAHA.120.046528
29. Srikakulapu P, Hu D, Yin C, Mohanta SK, Bontha SV, Peng L, Beer M, Weber C, McNamara CA, Grassia G, Maffia P, Manz RA, Habenicht AJ (2016) Artery tertiary lymphoid organs control multilayered territorialized atherosclerosis B-cell responses in aged ApoE−/− mice. Arterioscler Thromb Vasc Biol 36(6): 1174–1185. https://doi.org/10.1161/ATVBAHA.115.306983
30. Lee M, Lee E, Han SK, Choi YH, D-I K, Choi H, Lee K, Park ES, Rha M-S, Joo DJ, Shin E-C, Kim S, Kim JK, Lee YJ (2020) Single-cell RNA sequencing identifies shared differentiation paths of mouse thymic innate T cells. Nat Commun 11(1):4367. https://doi.org/10.1038/s41467-020-18155-8

Chapter 45

Tissue Clearing Approaches in Atherosclerosis

Ting Sun, Yuanfang Li, Benjamin Förstera, Karen Stanic, Shu Lu, Sabine Steffens, Changjun Yin, Ali Ertürk, Remco T. A. Megens, Christian Weber, Andreas Habenicht, and Sarajo K. Mohanta

Abstract

Recent advances in cardiovascular research have led to a more comprehensive understanding of molecular mechanisms of atherosclerosis. It has become apparent that the disease involves three layers of the arterial wall: the intima, the media, and a connective tissue coat termed the adventitia. It is also now appreciated that arteries are surrounded by adipose and neuronal tissues. In addition, adjacent to and within the adventitia, arteries are embedded in a loose connective tissue containing blood vessels (*vasa vasora*) and lymph vessels, artery-draining lymph nodes and components of the peripheral nervous system, including periarterial nerves and ganglia. During atherogenesis, each of these tissues undergoes marked structural and cellular alterations. We propose that a better understanding of these cell–cell and cell–tissue interactions may considerably advance our understanding of cardiovascular disease pathogenesis. Methods to acquire subcellular optical access to the intact tissues surrounding healthy and diseased arteries are urgently needed to achieve these aims. Tissue clearing is a landmark next-generation, three-dimensional (3D) microscopy technique that allows to image large-scale hitherto inaccessible intact deep tissue compartments. It allows for detailed reconstructions of arteries by a combination of labelling, clearing, advanced microscopies and other imaging and data-analysis tools. Here, we describe two distinct tissue clearing protocols; solvent-based modified three-dimensional imaging of solvent-cleared organs (3DISCO) clearing and another using aqueous-based 2,2′-thiodiethanol (TDE) clearing, both of which complement each other.

Key words Atherosclerosis, Fluorescence imaging, DISCO clearing, TDE clearing, Light-sheet microscopy; multiphoton microscopy, Confocal microscopy, Image processing

1 Introduction

High-resolution deep tissue imaging has been challenging in the past as tissues are intrinsically opaque, thereby unavoidably generating severe light scattering and spherical aberrations. Recently developed tissue-clearing approaches have been shown to overcome these limitations leading to unprecedented insights into the

Ting Sun, Yuanfang Li, Andreas Habenicht and Sarajo K. Mohanta contributed equally to this work.

Dipak P. Ramji (ed.), *Atherosclerosis: Methods and Protocols*, Methods in Molecular Biology, vol. 2419,
https://doi.org/10.1007/978-1-0716-1924-7_45,
© The Author(s), under exclusive license to Springer Science+Business Media, LLC, part of Springer Nature 2022

structure and cellularity of whole tissues and organs, hence allowing definition of the connectivity of tissues and indeed cells with their neighbors and adjacent tissues.

Atherosclerosis involves three layers of the arterial wall, which is surrounded by both adipose and neuronal tissues [1, 2]. Moreover, the outer connective tissue coat of arteries (i.e., the lamina adventitia) is used by the nervous system as its principal conduit to reach peripheral tissues [3]. Arteries are located within a loose connective tissue containing blood vessels (*vasa vasora*) and lymph vessels, lymph nodes, adipose tissue and components of the peripheral nervous system, including axons, axon bundles, large nerves and ganglia [3]. During atherosclerosis progression, the connective tissue and indeed each single cell of the artery undergoes major changes in structure, transcriptome signatures, epigenetic modifications along with other changes referred to as remodeling [4, 5]. As conventional histological techniques cannot comprehensively delineate these changes in 3D, new methods are required. For in-depth understanding of biological mechanisms in health and disease, unbiased approaches are urgently needed for 3D high-resolution imaging of the whole intact artery [6]. However, high-resolution imaging deep inside the intact tissues has been challenging as these are opaque with severe light scattering and spherical aberrations [7, 8]. Tissue-clearing approaches have overcome the major limitations of standard histology approaches [9, 10]. Clearing protocols dramatically reduce light scattering, making large tissue compartments and indeed whole organs or small mammals transparent by homogenously adjusting the refractive index, leading to excellent resolution imaging at high penetration depths with reduced acquisition time [11–13]. Using relatively simple immersion procedures, the refractive indices (RIs) of samples can be matched either to that of immersion oil (RI 1.52) or glycerol (RI 1.46), thus greatly minimizing light scattering and spherical aberrations. Recent advances in whole-body or whole-mount tissue clearing techniques, including 3D imaging of solvent-cleared organs (3DISCO), aqueous-based 2,2-′-thiodiethanol (TDE) cleared organs coupled to down-stream volumetric imaging techniques, including light-sheet imaging, multiphoton and confocal imaging, allow detailed reconstructions of the microanatomy of arteries by preserving the miniscule morphology of the vascular architecture and various fluorescently labeled cells and structures [6, 14–17]. When coupled to fluorescent immunolabeling, the connectivity of cells, tissues and organs with their neighbors can be imaged, yielding new important answers to decade-long questions. Both tissue clearing approaches described here are needed as 3DISCO leads to tissue shrinking and includes delipidation steps, whereas TDE clearing does not involve shrinking and can image lipids (Fig. 1).

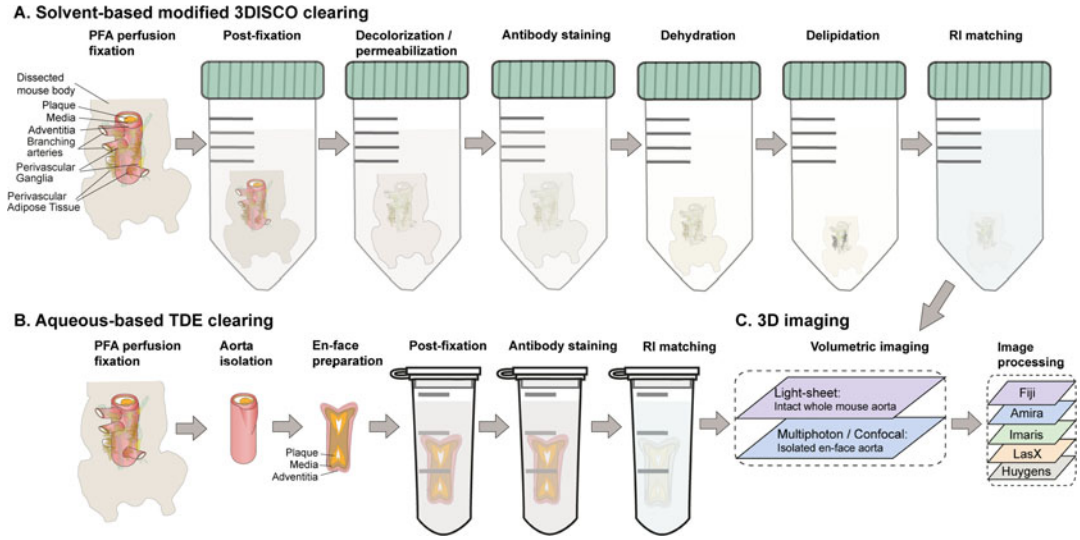

Fig. 1 Workflow for immunostaining-based tissue clearing approaches of diseased aorta. (**a**) Solvent-based modified 3DISCO clearing of whole mouse aorta. (**b**) Aqueous-based TDE clearing of isolated aorta. (**c**) 3D imaging of optically cleared aorta samples

To study the architecture of the intact healthy and diseased aorta in murine atherosclerosis, we used a modified version of 3DISCO clearing. The modified 3DISCO clearing involves decolorization and permeabilization prior to antibody labelling, followed by dehydration, delipidation, and refractive index matching (RI 1.56) using different hydrophobic organic solvents, leading to tissue shrinkage that allows visualization of large tissue (surface/volume) by a light-sheet microscope [18, 19]. Thus, 3DISCO clearing followed by light-sheet imaging allows for the visualization of intact arteries with perivascular adipose and neuronal tissues in the whole mouse. However, tissue shrinkage and delipidation during the clearing is a disadvantage for lipid-rich atherosclerotic tissues. In addition, light-sheet microscopy falls short of imaging subcellular details at the submicron level and visualizing small diameter neuronal projections, such as single axons and their connections and other very small tissue components. To overcome these problems, we used aqueous-based TDE clearing that involves refractive index matching (RI 1.4–1.5 depending on TDE concentrations) using different concentrations of hydrophilic TDE working solutions after whole mount immunostaining of the en face aorta, thereby making the optically opaque aortic tissue transparent without altering its volume [17, 20]. TDE clearing followed by multiphoton or confocal imaging of the whole-mount en face aorta allows for visualization of plaque or adventitia cellularity, and the territoriality of adventitial neuronal projections among other structures.

2 Materials

2.1 Mice

Seventy-eight weeks aged C57BL/6J WT and ApoE$^{-/-}$ mice maintained on a standard rodent chow diet under pathogen-free conditions according to local and national guidelines (*see* **Note 1**). All data are reported according to the ARRIVE criteria [21].

2.2 Reagents

2.2.1 Perfusion and Fixation Reagents

1. 115.4 mg/mL ketamine hydrochloride.
2. 20 mg/mL xylazine hydrochloride.
3. Phosphate buffer saline (PBS): 137 mM NaCl, 2.7 mM KCl, 8 mM Na_2HPO_4, and 2 mM KH_2PO_4, pH 7.4.
4. 5 mM Ethylenediaminetetraacetic acid (EDTA) in distilled water: Mix 14.612 g of EDTA with 80 mL of distilled water to prepare 50 mM EDTA. Stir the solution vigorously using a magnetic stirrer. Adjust pH to 8.0 using NaOH. Adjust volume to 100 mL with distilled water. Add 10 mL of 50 mM EDTA stock solution to 90 mL of distilled water to prepare 5 mM EDTA.
5. 75% ethanol in distilled water.
6. 4% Paraformaldehyde (PFA) in PBS. Mix 40 g of PFA with 800 mL of 0.1 M PBS. Stir the solution at 62 °C (avoid boiling) under a fume hood. Add 1/500–1/1000 volume of 1 M NaOH to help dissolving PFA faster. After complete dissolution, adjust the pH to 7.4 using HCl. Add distilled water make up the solution to 1000 mL (*see* **Note 2**).
7. 0.05% sodium azide in PBS: Dissolve 0.5 g of sodium azide in 1 L of PBS (*see* **Note 2**).
8. 1 M NaoH (*see* **Note 2**).
9. 1 M HCl (*see* **Note 2**).

2.2.2 Decolorization and Permeabilization Reagents

1. Urea (99–100%).
2. 98% *N*,*N*,*N*′,*N*′-tetrakis (2-hydroxypropyl) ethylenediamine (Quadrol).
3. Triton X-100 (100%).
4. 50 mg/mL porcine skin gelatin.
5. 60 mg/mL serum (goat and donkey).
6. 0.5 mg/mL CD16/32 Fc blocking antibody.
7. 10% bovine serum albumin (BSA).
8. 20% CUBIC reagent: Dissolve 125 g of urea and 140 mL of 98% Quadrol in 160 mL of PBS and add 75 mL of Triton X-100. Dilute the solution with PBS to 500 mL.
9. PBS–gelatin–Triton X-100–serum (PGTS) solution: 0.2% porcine skin gelatin, 0.5% Triton X-100, 5% goat serum in PBS.

10. Blocking solution: 10% normal donkey serum, 1% BSA, 0.5% Triton X-100 in PBS.

2.2.3 Antibodies

1. Primary antibody: 0.5 mg/mL affinity purified hamster anti-mouse CD3e (clone 145) (*see* **Note 3**).
2. Primary antibody: 0.2 mg/mL affinity purified rat anti-mouse B220 (clone RA3-6B2) (*see* **Note 3**).
3. Secondary antibody: 1.5 mg/mL donkey anti-hamster IgG conjugated with Cy3.
4. Secondary antibody: 1.5 mg/mL donkey anti-rat IgG conjugating with Cy5.
5. 25 mg/mL 4′,6-Diamidine-2′-phenylindole dihydrochloride (DAPI).
6. Antibody solution: 1% BSA, 0.5% Triton-X 100 in 0.1 M PBS.

2.2.4 Clearing Reagents

1. Tetrahydrofuran (THF) (99–100%).
2. 50%, 70% and 80% only THF in distilled water: Prepare in a 100 mL glass bottle in a fume hood (*see* **Note 4**).
3. Dichloromethane (DCM) (99–100%).
4. Benzyl-alcohol (99–100%).
5. Benzyl-benzoate (99%).
6. Benzyl-alcohol-Benzyl-benzoate (BABB) solution: Mix 50 mL of benzyl alcohol and 100 mL of benzyl benzoate in a 250 mL glass bottle on a shaker (or stirrer) for 5 min in a fume hood.
7. 2,2′ Thiodiethanol (TDE) (100%).
8. 20%, 47%, 60%, and 80% TDE working solutions in Dulbecco's phosphate-buffered saline (DPBS): For preparing 80% TDE working solution, mix 40 mL of TDE and 10 mL of DPBS in a 50-mL tube with gentle shaking.
9. 1.5% agarose gel in PBS: Dissolve 1.5 g agarose in 100 mL of PBS at 37 °C in an incubator.

2.3 Equipment and Other Material

1. Foam plate.
2. 1, 2, and 5 mL safe-lock tubes.
3. 15, 30, and 50 mL centrifuge tubes.
4. Perfusion pump.
5. 1, 10, and 20 mL disposable syringes.
6. Scissors: Dissection, fine iris, and spring scissors.
7. Forceps: curved fine forceps, narrow pattern, and blunt forceps.
8. Dissecting stereomicroscope.
9. Rotator.

10. Shaker.
11. Incubator.
12. 4 °C refrigerator.
13. Magnetic stirrer.
14. pH meter.
15. Glass vials.
16. Aluminum foil.
17. Microscopy glass slides.
18. Coverslips.
19. Glass petri dish.
20. Glass waste containers.
21. 5 and 10 mL Pasteur pipette.
22. Paper cloth.
23. Fume hood.
24. Adhesive tape.
25. Super glue.
26. Immersion oil (with glycerol).

2.3.1 Imaging Microscopes

1. LaVision ultramicroscope II: This is equipped with 1× Olympus air objective (Olympus MV PLAPO × 1/0.25 NA; working distance = 65 mm), or a 2× objectives (Olympus MVPLAPO2XC/0.5 NA; working distance = 6 mm) or a 4× objective (Olympus XLFLUOR 4× corrected/0.28 NA; working distance = 10 mm) for light-sheet microscopy (*see* **Note 5**).
2. Upright multiphoton laser scanning microscope (Leica TCS SP5II MP): This is equipped with a Ti:Sa pulsed laser (Spectra-Physics MaiTai DeepSee) equipped with 20× 1.00 water dipping objective (Leica HCX APO L 20×/1.00 W; working distance = 2 mm), and with a tunable laser (up to 900 nm excitation) for multiphoton microscopy (*see* **Note 6**).
3. Inverted confocal laser scanning microscope (TCS-SP8 3×): This is equipped with 20× immersion objective (Leica HC PL APO 20×/0.75 IMM; working distance = 0.68 mm), and with a tunable white light laser source, for confocal microscopy (*see* **Note 7**).

2.3.2 Image Analyses Tools

1. High power image processing workstation: MIFCOM X5 workstation equipped with AMD Ryzen Threadripper 3970X processor, 32GB DDR4–3000 RAM, and NVIDIA Titan RTX, 24GB graphics card.
2. Fiji (ImageJ2) downloaded from https://imagej.net/Fiji (*see* **Note 8**).

3. Amira software for 3D visualization and manual tracing (Thermo Fisher, https://www.thermofisher.com/de/de/home/industrial/electron-microscopy/electron-microscopy-instruments-workflow-solutions/3d-visualization-analysis-software/amira-life-sciences-biomedical.html).
4. Imaris 8.4 for 3D reconstruction of Z-stacks (Bitplane, http://www.bitplane.com/imaris/imaris).
5. Leica Application Suite X (LasX, v.3.1 Leica Microsystems, Germany) for 2D and 3D visualization.
6. Huygens Professional for deconvolution of 3D stacks (V.19.10, Scientific Volume Imaging, https://svi.nl/Huygens-Professional).

3 Methods

3.1 Whole-Body Immunostaining and 3DISCO Tissue Clearing

3.1.1 Tissue Preparation

1. Deeply anesthetize mice with 120 mg/kg of Ketamine and 8 mg/kg of Xylazine per mouse by intraperitoneal injection. Confirm death by lack of respiration and motility.
2. Lay down the mouse in a supine position and fix arms and legs on a foam plate. Disinfect the ventral side with 75% ethanol and take blood through the left ventricle with a 1 mL disposable syringe to remove the blood for better perfusion.
3. Perfuse the mice transcardially with 5 mM EDTA in PBS for 5 min with perfusion pump with 100–125 mm Hg pressure, followed by PBS for 5–10 min at room temperature (RT) until the blood is washed out. Finally, perfuse with 4% PFA for 20 min.
4. Deskin the mice with dissection scissors and narrow pattern forceps.
5. Remove organs, including lung, liver, spleen, and gastrointestinal and reproductive organs, while leaving heart, aorta, and kidneys intact in situ using dissection scissors, fine iris scissors, blunt forceps, and curved forceps.
6. Dissect the mouse above the diaphragm level using dissection scissors and blunt forceps.
7. Postfix the lower body part containing abdominal aorta, aortic branches, perivascular adipose tissue, and ganglia (referred below as sample) in 4% PFA for 1–2 day(s) at 4 °C in the refrigerator in a 50 mL tube.
8. Wash samples three times with PBS (10 min per wash) at RT.
9. Incubate the sample in 20% CUBIC reagent for 48 h for decolorization.
10. Wash the sample three times in PBS (1.5 h per wash) at RT.

11. Incubate the sample in PGTS solution with gentle shaking at RT for overnight for permeabilization and blocking.
12. Incubate the sample in PGTS solution containing primary antibodies [e.g., CD3e (1:100 dilution), B220 (1:200 dilution) (*see* **Note 3**), and 0.05% sodium azide] for 10–12 days with gentle shaking at RT.
13. Wash the sample three times in PGTS solution (1.5 h per wash) at RT.
14. Incubate with appropriate secondary antibody (1:300 dilution) (*see* **Note 9**) in PGST containing 0.05% sodium azide with gentle shaking at RT for 7 days.
15. Wash the sample three times in PGTS solution (1.5 h per wash) at RT.
16. Transfer the sample into PBS in a 50 mL centrifuge tube, cover it with aluminum foil and store at 4 °C until tissue clearing in **step 1** in Subheading 3.1.2.

3.1.2 Tissue Clearing

All organic solvents used in DISCO clearing reagents are hazardous. All clearing steps should be at RT with gentle shaking in a fume hood due to the volatile nature of the chemicals used for clearing. During all clearing steps, wrap the tubes with aluminum foil to keep them in dark to avoid bleaching/quenching by direct light exposure. Use a lab coat, proper gloves and a mask when handling them, and perform all the experiments in a fume hood except the imaging step. Avoid using the same working solutions for more than 2 weeks and avoid inhalation or contact with skin and eyes. Collect the clearing waste into glass waste containers that are kept in a hood. All storage containers, including the waste containers, should be glass and stored in the dark.

1. Immerse the stained samples from **step 16** in Subheading 3.1.1 into 50 mL centrifuge tubes with series of increased concentrations, that is, 50%, 70%, 90%, and 100% (two times 100%) THF working solution for 12 h per concentration to dehydrate the tissue.
2. Transfer the sample to DCM solution for 3 h to remove lipids. Each time use a new Pasteur pipette when a new clearing solution is added (e.g., changing from THF to DCM).
3. Incubate the sample in BABB solution for matching the refractive index (*see* **Note 10**) for 3–6 h until the samples become transparent in visible light (i.e., yellowish/transparent for large tissue like whole intact aorta) (Fig. 2a) (*see* **Note 11**).

3.1.3 Imaging 3DISCO Cleared Tissue

1. Image the cleared sample from **step 3** in Subheading 3.1.2 as soon as a complete clearing is achieved.

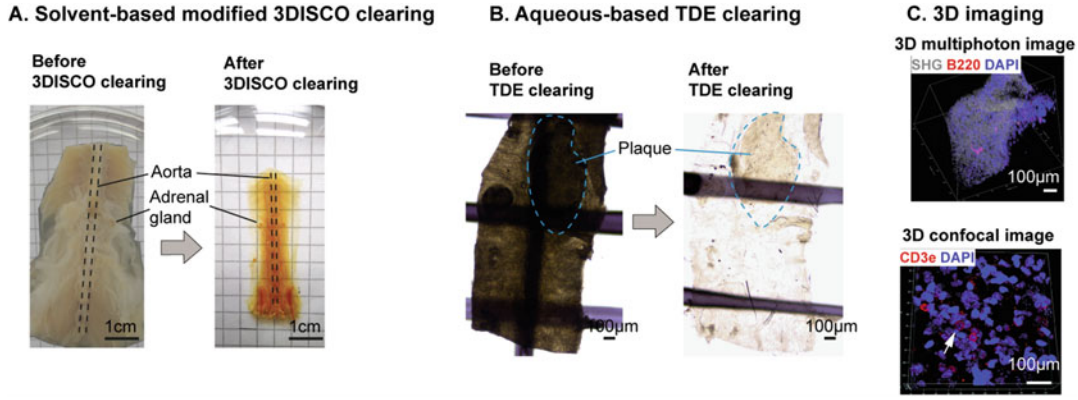

Fig. 2 Example of modified 3DISCO and TDE clearing and subsequent imaging. (**a**) Images of aorta with whole mouse abdominal segment before and after 3DISCO clearing. (**b**) Images of en face opened aorta before and after TDE clearing. (**c**) 3D imaging of TDE cleared aorta. Upper panel: Multiphoton aorta image obtained from the abluminal side showed adventitial collagen-derived second harmonic generation (white), B220 stained B cells (red) and DAPI stained nuclei (blue) in atherosclerotic aorta adventitia of 78-week-old ApoE$^{-/-}$ mice; Lower panel: Confocal image showed CD3e stained T cells (red) and DAPI stained nuclei in atherosclerotic aorta adventitia

2. Use light-sheet microscope, for example, LaVision ultramicroscope II, to image the samples.
3. Fill the imaging reservoir with the final clearing solution (i.e., BABB solution).
4. Remove the sample from the storage vial with blunt forceps.
5. Gently dry the sample shortly by placing it on a paper cloth.
6. Mount the sample on the correctly sized sample holder of the microscope using super glue.
7. Place the sample holder with the sample into the imaging reservoir of the light-sheet microscope that is filled with BABB solution (*see* **Note 12**).
8. Orient the sample mount in the reservoir to ensure that the sample is perpendicular to the light sheet.
9. Move the sample using the joystick until the light sheet illuminates the sample, then lower the objective to focus the sample.
10. Use a 1× Olympus air objective for low-magnification images covering the entire width of the whole sample.
11. Adjust the display settings while focusing to properly view the sample (i.e., until a clear focus is seen through the eyepiece of the microscope).
12. In the light-sheet microscope software, select which light sheet (s) will be used (this will depend on the specific instrument), and adjust the width of the light sheet to evenly illuminate the entire view field (*see* **Note 13**).

13. Select the lasers and adjust the focus for each channel individually for using multiple wavelengths. Adjust the laser power and exposure time to ensure a nonsaturated signal.
14. Save user settings to ensure consistency between imaging sessions.
15. Next, define the scan field in *x*-*y*-*z* mode: set the tile scans with 20–50% overlap along the longitudinal *y* axis covering the entire area of the sample, and set the z-scan with a z-step of 2–8 μm covering the entire volume of the sample.
16. Acquire tiled mosaic images (16 bit) on z-scan at the best resolution that the microscope can deliver and obtain images from ventral and dorsal surfaces up to 6–8 mm in depth to cover the entire volume of the sample.
17. Name the scan and save the data (*see* **Note 14**).
18. After low-magnification imaging of the whole sample, use a 2× objectives or a 4× objective with zoom-in/out functions to perform high-magnification imaging of specific body regions of interest.
19. Move the dipping objective slowly toward the imaging reservoir until it touches the surface of the BABB to prevent accidentally hitting the sample or holder.
20. Follow **steps 11–17** above for imaging and saving the data.

3.2 Whole-Mount Imaging of Isolated Aorta and TDE Clearing

3.2.1 Tissue Preparation

1. Follow **steps 1–5** in Subheading 3.1.1 for anesthesia, fixing the mouse, perfusion, and removal of organs without deskinning the mouse (except **step 4**).
2. Expose aorta from heart onto the level below the iliac bifurcation. Under a dissecting stereomicroscope equipped with fiber-optic light source at 30–40× magnification, carefully dissect out the thymus and adipose tissue using fine iris scissors, spring scissors, and curved fine forceps. Caution should be taken to prevent aorta injury during removal of liver, mesentery, thymus, kidney, and adipose tissue (*see* **Note 15**).
3. Harvest the abdominal aorta from the level above celiac artery to the level of iliac bifurcation.
4. Put the aorta onto a petri dish containing PBS.
5. Split the aorta longitudinally from the common iliac artery using spring scissors and proceed anteriorly until the end.
6. Postfix the aorta in 4% PFA overnight at 4 °C in a 2 mL safe-lock tube.
7. Thoroughly wash the separated aorta segments in different tubes with PBS for 5 min for five times at RT on a rotating shaker.

8. Incubate the sample in blocking solution on a rotating shaker for 2 h at RT for blocking and permeabilization.
9. Incubate the sample in antibody solution containing the primary antibody, for example, CD3e (1:100 dilution), B220 (1:200 dilution) (*see* **Note 3**) on a rotating shaker for 24 h at RT.
10. Wash the sample five times in PBS (5 min per wash) at RT on a rotating shaker.
11. Incubate the sample in antibody solution containing corresponding secondary antibodies (1:300 dilution) and DAPI (1 mg/mL) for nuclear staining (*see* **Note 9**) on a rotating shaker overnight at RT.
12. Wash the sample five times in PBS (5 min per wash) at RT on a rotating shaker.
13. Transfer the sample into PBS.
14. Cover the tubes with aluminum foil and store at 4 °C until tissue clearing in **step 1** in Subheading 3.2.2.

3.2.2 Tissue Clearing

1. Immerse the stained samples from **step 14** in Subheading 3.2.1 in a 2 mL safe-lock tube with 20% TDE working solutions for 1 h at 37 °C in the incubator.
2. Transfer the sample to 47% TDE working solutions for 12 h at RT on a rotating shaker.
3. Incubate the sample in 60% TDE working solutions solution for 24–36 h on a rotating shaker for matching the refractive index (*see* **Note 10**) until the samples became transparent in visible light (Fig. 2b).
4. Collect the clearing waste into glass waste containers that are kept in a hood.
5. Follow **step 14** in Subheading 3.2.1 for wrapping and storing the cleared samples.

3.2.3 Imaging of TDE Cleared Sample Using Multiphoton Laser Scanning Microscope (MPLSM)

1. Image the cleared aorta from **step 5** in Subheading 3.2.2 as soon as possible.
2. Use an upright multiphoton laser scanning microscope (MPLSM), for example a Leica TCS SP5II MP (Leica), equipped with a water-dipping objective with sufficient working distance (20× 1.00; working distance = 2 mm) for volumetric imaging up to 1.5 mm deep.
3. For MPLSM imaging, embed the sample in prewarmed 1.5% agarose gel before imaging.
4. Place the embedded sample with abluminal side of the en face aorta on the top into a petri dish filled with PBS (*see* **Note 16**).

5. Move the 20× dipping objective slowly toward the sample until it touches the surface of the PBS to prevent accidentally hitting the sample.
6. Adjust the focus to visualize the sample (i.e., change the z-position until a clear and sharp focus is detectable through the eyepiece of the microscope).
7. Tune MPLSM excitation at 800 nm to maximize fluorophore excitation/emission.
8. Adjust the spectral range of the (four) hybrid diode detectors to detect the signals deriving from the dyes, autofluorescent structures, and second harmonic generation (SHG) of collagen.
9. To allow simultaneous collection of different spectra while minimizing color spillover and maximizing contrast, tune the spectral detection range of the hybrid diode detectors (i.e., the collection channels) as follows: 395–405 nm for collagen SHG, 430–500 nm for adipocyte-derived autofluorescent signal, 600–650 nm for Cy3 and 660–770 nm for Cy5.
10. Acquire Z-stacks from abluminal side of the en face aorta at 10–15 μm step-size of 1024 × 1024 pixel XY images (740 × 740 μm^2) up to 700 μm depth.
11. Follow **step 16** in Subheading 3.1.3 for naming and saving the data.

3.2.4 Imaging of TDE Cleared Sample Using CLSM

1. Use an inverted confocal laser scanning microscope (CLSM, Leica, TCS-SP8 3X) equipped with 20× objective (NA: 0.75, working distance = 100 μm) for volumetric imaging up to 70 μm deep, and for imaging cells/structures that are close to the sample surface, particularly when a higher resolution is needed such as for analyses of nerve diameter or nerve contacts.
2. If MPLSM and CLSM where imaging needs to be performed in the same samples, do the confocal imaging last due to the increased risk of sample bleaching.
3. Mount the sample in final clearing solution on a clean glass slide and coverslip carefully avoiding air bubbles between the sample and the coverslip. Make sure to put abluminal side of the en face aorta toward the coverslip.
4. Move the 20× objective slowly toward the sample after putting immersion oil (with glycerol) until it touches the surface of the coverslip.
5. Adjust display settings and tune the hybrid diode detectors for detecting the signals deriving from autofluorescent structures and stained dyes.

6. Acquire Z-stacks from abluminal side of the en face aorta at 2–4 μm step-size of 1024 × 1024 pixel XY images up to 60 μm depth.
7. Follow **step 16** in Subheading 3.1.3 for naming and saving the data.

3.3 Image Processing and Analyses

3.3.1 Image Processing of Light-Sheet Images

1. Move the acquired Z-stacked tiled images to the high-power image processing workstation [15, 18]. We used MIFCOM X5 workstation equipped with AMD Ryzen Threadripper 3970X processor, 32GB DDR4-3000 RAM, and NVIDIA Titan RTX, 24GB graphics card.
2. Systematically and carefully perform image collection, storage, and data backup due to enormous size of the clearing data generated over time. Make sure to always keep the data backed up. Files generated by multiphoton or light-sheet microscopy are large (5–100 GB per image), so make a plan for long-term data storage.
3. Load the TIFF image series to software Fiji, and stitch the tile scans of light-sheet images using Fiji's stitching plugin [18, 22].
4. Save the stitched images in TIFF format and compressed in LZW format (if required) to enable fast processing using different software.
5. Analyze the data with free software such as Fiji or with commercially available 3D image processing software including Amira or Imaris for visualization, segmentation and quantification.
6. Load the preprocessed data into Amira for segmentation and manual tracing of different tissues and neuronal structures [19].
7. Load the preprocessed data into Imaris 8.4 (Bitplane), and Fiji for 2D and 3D image visualizations, and video generation.
8. In Amira and Imaris, visualize the sample by browsing the slices in different 2D orientations and using crop-corner module or 3D view module in 3D views respectively [15, 18].

3.3.2 Image Processing of MPLSM and CLSM Images

1. Follow **steps 1** and **2** in Subheading 3.3.1 for image processing workstation and data storage.
2. Visualize the Z-stacks generated from MPLSM/CLSM microscope in 3D using the LasX software (Leica) [23, 24].
3. Analyze the data with free software such as Fiji or with commercially available 3D image processing software including Imaris, Las X, and Huygens for visualization, segmentation, and quantification (Fig. 2c).

4. For volumetric depth-color coding of cells or structures, deconvolve the raw images with Huygens Professional and generate maximum intensity projections of deconvolved data with the Las X or with temporal-color code in Fiji.

4 Notes

1. C57BL/6J wild-type and ApoE$^{-/-}$ mice were maintained on a standard rodent chow under pathogen-free conditions until 1 year 6 months (78 weeks) according to local and national guidelines. ApoE$^{-/-}$ mice fed with chow diet are hyperlipidemic and spontaneously develop atherosclerosis during aging.
2. PFA, sodium azide, NaOH, and HCl are toxic. Perform all procedures in a fume hood.
3. CD3e is a pan-T cell marker and B220 is a pan-B cell marker.
4. Prepare each THF working solution in a different glass bottle in a fume hood, label them, and store in the dark at RT. Order the highest purity stock solution as small-volume units (e.g., 100-mL bottles to use 1–2 times per bottle).
5. Light-sheet microscopy is an imaging technique that allows fast, high-resolution imaging of large biological specimens with low light exposure by rapidly acquiring images of thin optical sections illuminated by laser light sheets.
6. Multiphoton microscopy is a laser scanning microscopic modality and imaging technique that allows fast, multidimensional high-resolution imaging of intact and viable biological tissues on length scales at (sub)cellular and molecular level over prolonged periods of time, deep in the sample and with minimal invasion.
7. Confocal laser scanning microscopy is an imaging technique that allows multidimensional high-resolution imaging of intact biological tissues or sections with high specificity and at subcellular resolution.
8. Fiji (ImageJ2) is a freeware from the US National Institutes of Health (NIH) for 2D and 3D image analyses.
9. Use secondary antibody raised against the host of the primary antibody (e.g., for rat anti-mouse B220, use donkey or goat anti-rat secondary antibody). It is recommended to change the secondary antibody once after incubation for 3 days. It is recommended to use red (Cy3 or Alexa 594) or far-red (Cy5 or Alexa 633) secondary antibodies because tissue autofluorescence might interfere with shorter wavelengths antibodies like FITC or Alexa 488. Use DAPI for staining the cell nuclei.

10. Refractive index is the ratio of the speed of light in a vacuum to its speed in a specified medium. The refractive index (RI) of a vacuum is 1 by definition, whereas water RI is ~1.33, BABB RI is 1.56, 47% TDE RI is 1.43 and 60% TDE RI is 1.45.
11. Always store the cleared sample in the final BABB clearing solution, including the imaging steps.
12. Take care not to spill BABB on the instrument and clean any spills immediately with methanol. Replace gloves contaminated with BABB before handling any instrument or equipment to avoid damage.
13. For example, in an ultramicroscope system with both-side laser illumination, align the left and right laser by selecting and focusing one side first. Then, activate both side lasers to see a merged scan image coming from both scans. In case of uneven illumination of both sides of the sample, adjust the focus and width of the light sheet to evenly illuminate the entire sample.
14. For convenience during image analysis, include the following in the title: Sample name, objective, zoom factor, z-steps, antibody used, laser line used, and date of the scan. For example, WT 1_ 2x_4p5x_5μm_NF200 594_08.09.2019.
15. Under dissection microscope, it is possible to distinguish the compact aorta adventitia from loose light yellow-colored brown adipose tissue in the thorax and loose pale white-colored white adipose tissue in abdomen as well as from solid light yellow/brown paraaortic lymph nodes in situ.
16. Take care not to spill PBS on the instrument and dry any spills immediately.

Acknowledgments

This work was funded by the Deutsche Forschungsgemeinschaft (DFG) (MO 3054/1-1) to S.M.; DFG HA 1083/15-4, HA 1083/15-5, and ERA-CVD (PLAQUEFIGHT) 01KL1808 to A. H; and SFB1123/A1, A10 and Z1, INST 409/97-1 FUGG, INST 409/150-1 to C.W. and R.T.A.M.

References

1. Mohanta SK, Yin C, Peng L, Srikakulapu P, Bontha V, Hu D, Weih F, Weber C, Gerdes N, Habenicht AJ (2014) Artery tertiary lymphoid organs contribute to innate and adaptive immune responses in advanced mouse atherosclerosis. Circ Res 114(11): 1772–1787. https://doi.org/10.1161/CIRCRESAHA.114.301137
2. Newland SA, Mohanta S, Clement M, Taleb S, Walker JA, Nus M, Sage AP, Yin C, Hu D, Kitt LL, Finigan AJ, Rodewald HR, Binder CJ, McKenzie ANJ, Habenicht AJ, Mallat Z (2017) Type-2 innate lymphoid cells control the development of atherosclerosis in mice. Nat Commun 8:15781. https://doi.org/10.1038/ncomms15781

3. Yin C, Mohanta SK, Srikakulapu P, Weber C, Habenicht AJ (2016) Artery tertiary lymphoid organs: powerhouses of atherosclerosis immunity. Front Immunol 7:387. https://doi.org/10.3389/fimmu.2016.00387
4. Mohanta S, Yin C, Weber C, Hu D, Habenicht AJ (2016) Aorta atherosclerosis lesion analysis in hyperlipidemic mice. Bio Protoc 6(11): e1833. https://doi.org/10.21769/bioprotoc.1833
5. Hu D, Yin C, Luo S, Habenicht AJR, Mohanta SK (2019) Vascular smooth muscle cells contribute to atherosclerosis immunity. Front Immunol 10:1101. https://doi.org/10.3389/fimmu.2019.01101
6. Becher T, Riascos-Bernal DF, Kramer DJ, Almonte VM, Chi J, Tong T, Oliveira-Paula GH, Koleilat I, Chen W, Cohen P, Sibinga NES (2020) Three-dimensional imaging provides detailed atherosclerotic plaque morphology and reveals angiogenesis after carotid artery ligation. Circ Res 126(5):619–632. https://doi.org/10.1161/CIRCRESAHA.119.315804
7. Ueda HR, Erturk A, Chung K, Gradinaru V, Chedotal A, Tomancak P, Keller PJ (2020) Tissue clearing and its applications in neuroscience. Nat Rev Neurosci 21(2):61–79. https://doi.org/10.1038/s41583-019-0250-1
8. Zhao J, Lai HM, Qi Y, He D, Sun H (2021) Current status of tissue clearing and the path forward in neuroscience. ACS Chem Neurosci 12(1):5–29. https://doi.org/10.1021/acschemneuro.0c00563
9. Richardson DS, Lichtman JW (2015) Clarifying tissue clearing. Cell 162(2):246–257. https://doi.org/10.1016/j.cell.2015.06.067
10. Ariel P (2017) A beginner's guide to tissue clearing. Int J Biochem Cell Biol 84:35–39. https://doi.org/10.1016/j.biocel.2016.12.009
11. Seo J, Choe M, Kim SY (2016) Clearing and labeling techniques for large-scale biological tissues. Mol Cells 39(6):439–446. https://doi.org/10.14348/molcells.2016.0088
12. Orlich M, Kiefer F (2018) A qualitative comparison of ten tissue clearing techniques. Histol Histopath 33(2):181–199. https://doi.org/10.14670/HH-11-903
13. Yu T, Zhu J, Li D, Zhu D (2021) Physical and chemical mechanisms of tissue optical clearing. iScience 24(3):102178. https://doi.org/10.1016/j.isci.2021.102178
14. Zhao S, Todorov MI, Cai R, Maskari RA, Steinke H, Kemter E, Mai H, Rong Z, Warmer M, Stanic K, Schoppe O, Paetzold JC, Gesierich B, Wong MN, Huber TB, Duering M, Bruns OT, Menze B, Lipfert J, Puelles VG, Wolf E, Bechmann I, Erturk A (2020) Cellular and molecular probing of intact human organs. Cell 180(4):796–812. e719. https://doi.org/10.1016/j.cell.2020.01.030
15. Cai R, Pan C, Ghasemigharagoz A, Todorov MI, Forstera B, Zhao S, Bhatia HS, Parra-Damas A, Mrowka L, Theodorou D, Rempfler M, Xavier ALR, Kress BT, Benakis C, Steinke H, Liebscher S, Bechmann I, Liesz A, Menze B, Kerschensteiner M, Nedergaard M, Erturk A (2019) Panoptic imaging of transparent mice reveals whole-body neuronal projections and skull-meninges connections. Nat Neurosci 22(2):317–327. https://doi.org/10.1038/s41593-018-0301-3
16. Liebmann T, Renier N, Bettayeb K, Greengard P, Tessier-Lavigne M, Flajolet M (2016) Three-dimensional study of Alzheimer's disease hallmarks using the iDISCO clearing method. Cell Rep 16(4):1138–1152. https://doi.org/10.1016/j.celrep.2016.06.060
17. Costantini I, Ghobril JP, Di Giovanna AP, Allegra Mascaro AL, Silvestri L, Mullenbroich MC, Onofri L, Conti V, Vanzi F, Sacconi L, Guerrini R, Markram H, Iannello G, Pavone FS (2015) A versatile clearing agent for multimodal brain imaging. Sci Rep 5:9808. https://doi.org/10.1038/srep09808
18. Pan C, Cai R, Quacquarelli FP, Ghasemigharagoz A, Lourbopoulos A, Matryba P, Plesnila N, Dichgans M, Hellal F, Erturk A (2016) Shrinkage-mediated imaging of entire organs and organisms using uDISCO. Nat Methods 13(10):859–867. https://doi.org/10.1038/nmeth.3964
19. Erturk A, Becker K, Jahrling N, Mauch CP, Hojer CD, Egen JG, Hellal F, Bradke F, Sheng M, Dodt HU (2012) Three-dimensional imaging of solvent-cleared organs using 3DISCO. Nat Protoc 7(11):1983–1995. https://doi.org/10.1038/nprot.2012.119
20. Staudt T, Lang MC, Medda R, Engelhardt J, Hell SW (2007) 2,2′-thiodiethanol: a new water soluble mounting medium for high resolution optical microscopy. Microsc Res Tech 70(1):1–9. https://doi.org/10.1002/jemt.20396
21. Kilkenny C, Browne WJ, Cuthill IC, Emerson M, Altman DG (2010) Improving bioscience research reporting: the ARRIVE guidelines for reporting animal research. PLoS Biol 8(6):e1000412. https://doi.org/10.1371/journal.pbio.1000412

22. Preibisch S, Saalfeld S, Tomancak P (2009) Globally optimal stitching of tiled 3D microscopic image acquisitions. Bioinformatics 25(11):1463–1465. https://doi.org/10.1093/bioinformatics/btp184
23. Bianchini M, Duchene J, Santovito D, Schloss MJ, Evrard M, Winkels H, Aslani M, Mohanta SK, Horckmans M, Blanchet X, Lacy M, von Hundelshausen P, Atzler D, Habenicht A, Gerdes N, Pelisek J, Ng LG, Steffens S, Weber C, Megens RTA (2019) PD-L1 expression on nonclassical monocytes reveals their origin and immunoregulatory function. Sci Immunol 4(36):eaar3054. https://doi.org/10.1126/sciimmunol.aar3054
24. Hu D, Mohanta SK, Yin C, Peng L, Ma Z, Srikakulapu P, Grassia G, MacRitchie N, Dever G, Gordon P, Burton FL, Ialenti A, Sabir SR, McInnes IB, Brewer JM, Garside P, Weber C, Lehmann T, Teupser D, Habenicht L, Beer M, Grabner R, Maffia P, Weih F, Habenicht AJ (2015) Artery tertiary lymphoid organs control aorta immunity and protect against atherosclerosis via vascular smooth muscle cell lymphotoxin beta receptors. Immunity 42(6):1100–1115. https://doi.org/10.1016/j.immuni.2015.05.015

Chapter 46

Single-Cell Antibody Sequencing in Atherosclerosis Research

Ryosuke Saigusa, Christopher P. Durant, Vasantika Suryawanshi, and Klaus Ley

Abstract

The transcriptomic information obtained by single cell RNA sequencing (scRNA-seq) can be supplemented by information on the cell surface phenotype by using oligonucleotide-tagged monoclonal antibodies (scAb-Seq). This is of particular importance in immune cells, where the correlation between mRNA and cell surface expression is very weak. scAb-Seq is facilitated by the availability of commercial antibodies and antibody mixes. Now panels of up to 200 antibodies are available for human and mouse cells. Proteins are detected by antibodies conjugated to a tripartite DNA sequence that contains a primer for amplification and sequencing, a unique oligonucleotide that acts as an antibody barcode and a poly(dA) sequence, simultaneously detecting extension of antibody-specific DNA sequences and cDNAs in the same poly(dT)-primed reaction. For each cell, surface protein expression is captured and sequenced along with the cell's transcriptome. Here, we list the steps needed to produce antibody sequencing data from tissue or blood cells.

Key words Cellular indexing of transcriptomes and epitopes by sequencing (CITE-seq), AbSeq, TotalSeq, RNA expression and protein sequencing assay (REAP-seq), Surface markers

1 Introduction

Atherosclerosis is the most common underlying pathology of peripheral artery disease, coronary artery disease and cerebrovascular disease. Recent approaches, including clinical interventional studies, lineage tracking and knockout mouse studies, in vivo imaging and mRNA sequencing techniques have drawn much attention to the critical role of immune cells in the development of atherosclerosis [1, 2]. The immune cell composition of blood is commonly determined by flow cytometry. For immune cells in tissues like atherosclerotic mouse aortas, digestion protocols have been developed [3] and refined [2]. The development of massively parallel single cell RNA sequencing (scRNA-seq) and mass cytometry (CyTOF) have given us new insights into immune cell subsets in a

Dipak P. Ramji (ed.), *Atherosclerosis: Methods and Protocols*, Methods in Molecular Biology, vol. 2419,
https://doi.org/10.1007/978-1-0716-1924-7_46,
© The Author(s), under exclusive license to Springer Science+Business Media, LLC, part of Springer Nature 2022

variety of diseases, including atherosclerosis [4]. However, combining CyTOF with scRNA-Seq cannot link the transcriptome to the cell surface phenotype of the same cell, because CyTOF is a destructive method (cells are vaporized). Human plaque immune composition has been inferred using deconvolution methods on bulk RNA-seq data from atherosclerotic tissue and CyTOF analysis of an individual plaque [5]. Conventional bulk RNA-seq approaches are limited because they average gene expression patterns across whole tissues. Single-cell technologies allow measurements of individual cell functional and phenotypical variations that have the potential to improve the understanding of atherosclerosis [6].

1.1 The Development of Single-Cell Technology

The commercialization of gel-bead–based approaches has revolutionized the assessment of the immune landscape of blood and solid tissues by allowing the analysis of thousands of single-cell transcriptomes in parallel. In the field of atherosclerosis research, scRNA-seq enables a better understanding of the function of aortic wall cells and particularly leukocytes [1, 5, 7–11]. On the basis of transcriptomic data, the functionality of immune cell subsets can be predicted [12], the developmental ontogeny of individual cell clusters can be assessed with trajectory algorithms [13] and the cellular interaction partners within a tissue can be identified on the basis of the expression of receptor–ligand pairs [14–16]. Gene expression and cell surface phenotypes can be assessed in the same single cell with the use of antibodies conjugated with barcoded oligonucleotides, such as with the cellular indexing of transcriptomes and epitopes by sequencing (CITE-seq) [17] or RNA expression and protein sequencing assay (REAP-seq) [18] methods. Both CITE-seq, developed by the New York Genome Center group, and REAP-seq, designed by the Merck group, use a similar approach [19]. The two approaches differ in how the DNA barcode is conjugated to the antibody. While antibodies used in CITE-seq are conjugated to streptavidin that is noncovalently bound to biotinylated DNA barcodes, REAP-seq relies on covalent bonds between the antibody and aminated DNA barcode. Variations of CITE-seq and REAP-seq are now available as commercial products from BD (AbSeq) [20, 21] or BioLegend/10× Genomics (TotalSeq) [17].

1.2 Why Surface Phenotype Matters

scRNA-seq has become a popular method in many areas of biomedical research, including cardiovascular research. The transcriptomic information obtained can be supplemented by information on the cell surface phenotype by using oligonucleotide-tagged monoclonal antibodies. This provides valuable information as cell surface information builds on over 30 years of experience with immune cell identification. In immunology, surface markers have been used for decades to define and distinguish cell types [7, 22, 23]. Flow cytometry, which measures expression of surface

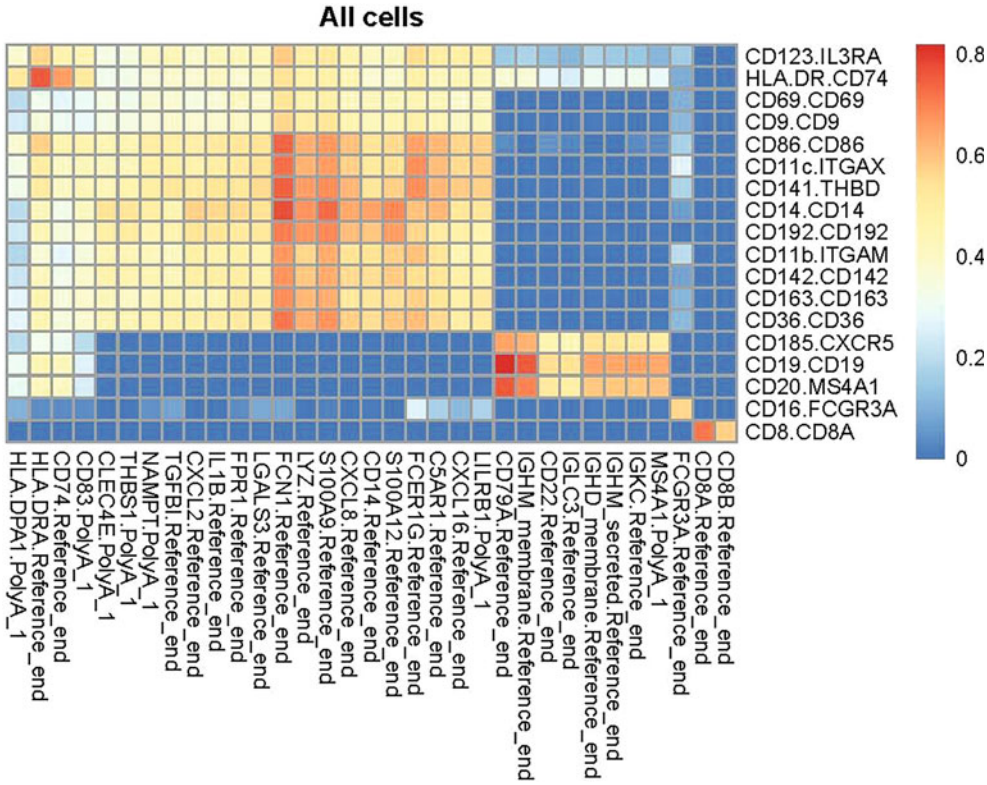

Fig. 1 Positive correlations between gene (*x* axis) and protein surface (*y* axis) expression. (Data from ~42,000 human PBMCs [27]). The correlation is indicated in the color scale shown in the color bar (right). Negative correlations are not shown

markers, is the discipline-defining method of immunology [24]. The correlation between cell surface protein and mRNA expression is known to be quite weak [25]. Therefore, scRNA-seq without surface phenotype fails to identify immune cell types based just on mRNA information. This has led to much frustration in this field because the expression of genes encoding even major cell surface markers are not detected [7, 8, 26]. As such, it is still difficult to call cell types based on gene expression data alone, which emphasizes the need for cell surface phenotypes in addition to transcriptomes. Recently, Vallejo et al. [27] correlated gene expression with cell surface expression for 41 pairs of genes and proteins in and AbSeq study based on BD Rhapsody [20, 21]. Fewer than half of the surface markers measured were reasonably well correlated with the mRNA of their encoding genes (Fig. 1). This also illustrates how monitoring cell surface phenotype by antibodies adds enormous value to scRNA-seq.

An alternative approach is to search for genes whose expression is correlated with surface markers. Using the human peripheral blood mononuclear cells (PBMC) data set in [27], we correlated

the expression of 485 genes with the expression of 40 surface markers as detected by AbSeq in order to find markers that can be used in experiments where information on cell surface expression is not available. Correlations between all genes and all surface markers were calculated and filtered for those that were statistically significant and whose $|r| > 0.5$ for all cells. Across all cells, the gene expression of FCN1, which encodes Ficolin-1, is highly correlated with cluster of differentiation (CD)11c and CD86 surface expression ($r = 0.8$) and well correlated with CD11b, CD192 (CCR2), CD142 (tissue factor) and CD163 (hemoglobin-haptoglobin receptor). Also, immunoglobulin heavy constant Mu (IGHM) membrane and CD79A gene expression are excellent surrogates for CD19 and CD20 cell surface expression because they all define B cells. Other immunoglobulin genes are also well correlated [IGHD (Immunoglobulin Heavy Constant Delta), IGHM secreted (Immunoglobulin Heavy Constant Mu secreted), IGKC (Immunoglobulin Kappa Constant)]. Surprisingly, only 33 of 485 genes and 18 of 40 antibodies survived this analysis, indicating that the chance of finding surrogate mRNA markers substituting for surface markers is limited. This further emphasizes the need to assess cell surface phenotype.

1.3 Assessing Cell Surface Phenotype

Assessing cell surface phenotype by sequencing oligonucleotide-tagged antibodies is facilitated by the availability of commercial antibodies and antibody mixes from BioLegend and Becton Dickinson. The BioLegend antibodies are designed for the 10× Genomics platform (TotalSeq) [17] and the Becton Dickinson antibodies are designed for the Rhapsody platform (AbSeq) [20, 21]. In both cases, now panels of up to 200 antibodies are available for human and mouse cells. Proteins are detected by antibodies conjugated to a tripartite DNA sequence that contains a primer for amplification and sequencing, a unique oligonucleotide that acts as an antibody barcode and a poly(dA) sequence. The poly(dA) sequence allows simultaneous extension of antibody-specific DNA sequences and cDNAs in the same poly(dT)-primed reaction. Antibody tags are captured and sequenced along with each cell's transcriptome.

1.3.1 TotalSeq

This BioLegend brand of TotalSeq uses poly(dT) oligos and Drop-seq approaches utilizing 3′ or 5′ sequencing. Cell Ranger is used as a set of analysis pipelines that process 10× single-cell RNA-seq output to align reads, generate feature-barcode matrices and perform clustering and gene expression analysis. The performance of Cell-Ranger was recently improved by introducing a cloud-based version (www.10xgenomics.com). Alternative pipelines are available [28].

1.3.2 AbSeq

Originally, the BD Rhapsody was designed to detect the expression of ~500 known target genes. A newly developed Rhapsody method has been designed to provide full (not targeted) transcriptomes [20, 21]. Several gene panels are now available. Rhapsody performs paired barcoding in microwells with magnetic beads, whereas 10× Genomics uses gel beads encapsulated in silicone oil [17]. Beads and attached mRNA are retrieved and synthesized into cDNA, which is then amplified using targeted primers to specific genes and labeled with library index barcodes. Amplified cDNAs are sequenced, and the libraries are prepared for assessment of target gene expression. Rhapsody is compatible with the detection of surface antigens by AbSeq and provides protein information at the same single cell level. Seven Bridges is an analysis pipeline that processes the BD Rhapsody RNA-seq and AbSeq output. We used this platform on 32 clinical PBMC samples, measuring the expression of 40 surface markers and 485 genes [27]. The cell surface phenotype alone, without even considering the transcriptome, enabled detailed analysis of all major cell types (B cells, CD4 and CD8 T cells, monocytes, NK cells), resolving 58 clusters in almost 42,000 single cells [27].

1.4 Challenges

scRNA-seq, CITE-seq, and REAP-seq as well as flow cytometry and CyTOF all require mechanical dissociation and enzymatic tissue digestion to prepare single-cell suspensions [6]. The enzymes used for tissue digestion can alter cell surface molecules by proteolytic cleavage and the cellular processes that take place during digestion and isolation can alter single-cell transcriptomes. Moreover, the proportion of different cell types can be affected and skewed by the isolation procedures. For example, T cells, which are small, round, and mechanically robust, can survive the isolation procedure better than macrophages or dendritic cells, which are large, branched, and fragile. Kim et al. [10] developed a lipid staining-based flow cytometric method for analyzing the lipid-laden foam cells of atherosclerotic aortas by scRNA-seq, greatly enhancing the identification of foam cells without depending on surface phenotypes.

The scRNA-seq and antibody-Seq datasets comprise thousands to millions of cells, each with hundreds to thousands of features in a single experiment, presenting new challenges for computational and statistical analyses. At the single cell resolution, data sparsity (aka missing data) exacerbates the uncertainty of measured signals in comparison to bulk sequencing methods. Two unique challenges are posed by single cell data at the analytical level. First, scalable methods must be developed for increasingly high dimensional data. Second, it is challenging but often necessary to integrate data across varied modalities such as RNA and proteins [29, 30], across samples [2, 31], time points [32], or even species [33].

Other challenges include doublet or multiplet removal [34], dead cell removal [35], and correction for batch effects [36]. In combined protein and transcript panel single cell sequencing, as in flow cytometry, nonspecific binding contributes to the antibody signal. Additional nonspecific background staining is caused by oligonucleotide-tagged antibody being trapped in the drop or nanowell [17].

1.5 Flow of Antibody Sequencing and Analysis

The wet lab work starts with isolating cells from blood or tissues or thawing frozen PBMCs and viability assessment for initial quality control (Fig. 2). The cells are aliquoted to an appropriate count (typically around one million) and incubated with Fc Block to limit nonspecific antibody binding to Fc receptors. After washing, cells are resuspended in a cocktail of surface antibodies according to the manufacturer's recommendations (BioLegend and Becton Dickinson). Once the cells are suspended at the correct loading concentration, the primed microwell plate (BD Rhapsody) or silicone oil–based microfluidics device (10× Genomics Chromium controller) are loaded. Then, oligo-tagged cDNA is amplified by PCR reactions and libraries are constructed. The samples are pooled and sequenced to a nominal depth of as follows: 20,000 read pairs per cell for transcriptomes and 1000 × "n" read pairs per cell for antibodies (n = number of antibodies used in the experiment) (BD Rhapsody), and 50,000 read pairs per cell for transcriptomes and 10,000 read pairs per cell for antibodies (10× Genomics).

The bioinformatics workflow starts with the FASTQ files generated by the sequencer, in our case Illumina NovaSeq. They are uploaded to pipelines like Seven Bridges for BD Rhapsody or CellRanger for 10× Genomics, where the data is demultiplexed, filtered and csv files are generated. Before analyzing the data, low-quality transcriptomes, doublets, dead cells, and proliferating cells must be tagged so they can be removed or analyzed separately (proliferating cells). For doublet removal, the Doublet Finder package on R, with the default doublet formation rate (7.5%), is often used. Clustering is performed using UMAP (Uniform Manifold Approximation and Projection) [37] and Louvain clustering [38]. UMAP is a manifold learning technique for dimensionality reduction. It is based on the neighborhood graphs, which captures local relationship in the data.

From here, we list the reagents and steps needed to produce antibody sequencing data from tissue or blood cells. We do not describe the process of obtaining suspended cells from tissues or blood and the common process with scRNA-seq, including cell loading to the machines for scRNA-seq.

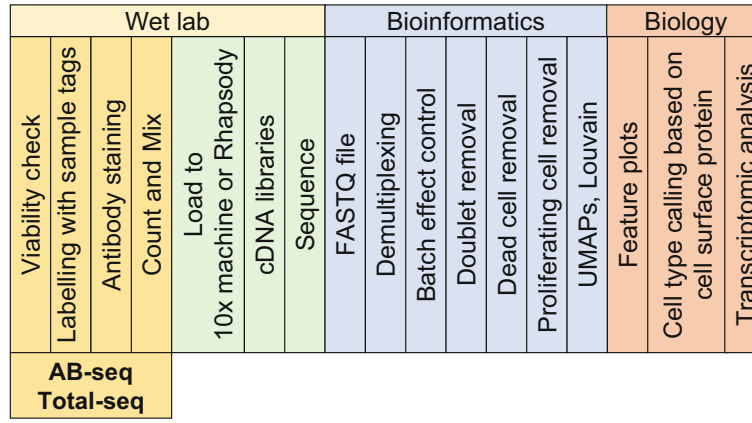

Fig. 2 scAb-seq workflow. Antibody staining panels of up to 200 antibodies are available for human and mouse cells (yellow). After staining and counting, cells are loaded into the 10× Chromium controller or the Rhapsody Cartridge for single cell sequencing (green). After bioinformatics processing (blue), cell types are based on cell surface protein. Transcriptomic analysis finds differentially expressed genes in each cell type

2 Materials

Prepare all the reagents in advance of the experiment.

2.1 Materials for both TotalSeq and AbSeq

1. PBS: 137 mM NaCl, 2.7 mM KCl, 8 mM Na_2HPO_4, 2 mM KH_2PO_4.
2. Staining buffer (SB): 2% FBS in PBS.
3. Trypan Blue solution: 0.4% solution in 0.81% sodium chloride, 0.06% potassium phosphate, dibasic.
4. 0.5 mg/mL human Fc Block reagent (BD Pharmingen).
5. Ice in an insulated container.
6. 1.5 mL or 2 mL Eppendorf low-binding (RNase free) tubes.
7. Clean lint-free paper towel.
8. Vortex mixer.
9. Centrifuge.
10. Microcentrifuge.
11. 15 mL Corning tubes.
12. 96-well plate.

2.2 Materials for TotalSeq

1. Hemocytometer.
2. 5 mL Eppendorf tubes.
3. Moxi Z Mini Automated Cell Counter (ORFLO Technologies): Type M chips with the gate set to >7 μm.

4. TotalSeq-C oligonucleotide antibodies (BioLegend).
5. TotalSeq-C 200-Plex Lyophilized Antibody Staining (BioLegend): Before use, briefly centrifuge down the lyophilized antibody cocktail in a microcentrifuge and add 50 μL of SB to make the antibody cocktail.
6. 0.5 mg/mL Unique Hashtag oligonucleotides: 1:1 ratio of β2-microglobulin and CD298.
7. 10× Genomics chip: Depending on the protocol that is being followed, 10× defines chip G, H, K and J. For example, Chip A is used with v1.0 of the 5′ 10× method whereas Chip K is used with v2.0 of the 5′ method. If the goal of an experiment is to capture T cell receptor (TCR) or B cell receptor (BCR) then the 5′ method is required, otherwise the 3′ capture method could be used in which case a different chip would be required. 10× Genomics is continuously updating their reagents, kits and chips.

2.3 Materials for AbSeq

1. Rhapsody scanner (BD Biosciences).
2. Calcein and Draq 7 (BD Biosciences) (*see* **Note 1**).
3. DMSO.
4. Sample Multiplexing Kit (BD Biosciences): This contains oligonucleotide cell labeling (Sample Tags) pretitrated and prepared by BD Biosciences. This should be at room temperature (RT) before use.
5. 5 mL polystyrene tubes with blue lid using 35 μm cell strainer lids.
6. AbSeq antibodies (BD Biosciences): Pretitrated oligonucleotide antibodies for 3' RNA sequencing.
7. 5 mL polystyrene tubes.
8. BD Rhapsody Cartridge for loading cells for scRNAseq capture: Contains 250,000 microwells in the plate. Uses controlled fluid dynamics for equal distribution of cells, beads and reagents onto the plate.

3 Methods

3.1 TotalSeq

3.1.1 Viability Check

1. Resuspend cell samples processed from tissues or blood in 0.5 mL of SB for every anticipated one million cells in a 15 mL Corning tubes (*see* **Note 2**).
2. Pipette 10 μL of well-suspended sample into a well of a new 96-well plate. Pipette 10 μL of Trypan Blue solution. Mix the sample gently with pipette set to 10 μL. Pipette 10 μL of the mixture onto a hemocytometer (*see* **Notes 2** and **3**).

3. Using the hemocytometer, count the living and dead cells respectively in each 16-square quadrant. Ensure that there are at least 100 total cells but no more than 400 total cells. Take note of the volume used to resuspend the sample.
4. Confirm that each of the duplicates for live and dead cell counts are within 10% variance of each other and that the viability is greater than 80%.

3.1.2 Labeling with Sample Tags and Mixing

1. Begin with no more than one million cells per sample, each suspended in 50 μL of SB.
2. Incubate at room temperature (RT) with human Fc Block reagent (2.5 μg in 50–100 μL of SB) for 10 min.
3. Whilst the incubation in **step 2** is taking place, centrifuge each of the TotalSeq-C oligonucleotide antibodies at 14,000 × *g* for 10 min at 4 °C.
4. Being careful not to place the pipette tip on the bottom of the tube, add 2 μL of 0.5 mg/mL of unique hashtag oligonucleotide to each sample and mix gently by pipetting.
5. Incubate the samples on ice for 20 min.
6. Transfer the cells to their own unique (not sharing with other samples) 5 mL Eppendorf tube. Add 500 μL of SB to the tube the sample was stained in, mix and transfer to the 5 mL Eppendorf tube. Then, add an additional 1000 μL of SB to the walls of the same tube to ensure all the cells are collected. Then, add 2000 μL of SB to the 5 mL Eppendorf tube to bring the total washing volume to 3.5 mL.
7. Centrifuge at 400 × *g* for 5 min at 4 °C.
8. Add 3.5 mL of SB to the 5 mL Eppendorf tube and mix gently by pipetting.
9. Centrifuge at 400 × *g* for 5 min at 4 °C.
10. Repeat **steps 8** and **9** once more for a total of three times with 3.5 mL washes.
11. Decant the supernatant by dabbing the top of the tube on a clean lint-free paper towel.
12. Resuspend each sample in 500 μL of SB.
13. Count the samples with the Moxi Z Mini Automated Cell Counter.
14. Combine each unique sample to a maximum total of one million cells, in equal proportions, based on the concentrations.
15. Centrifuge the samples at 400 × *g* for 5 min at 4 °C.

16. Decant the supernatant and dab the top of the tube on a clean lint-free paper towel.
17. Resuspend the cells in 50 μL of SB.

3.1.3 Antibody Staining

1. Vortex the antibody cocktail (TotalSeq-C 200-Plex Lyophilized Antibody Staining) for 10 s.
2. Incubate the cocktail for 5 min at room temperature to ensure that the cocktail is fully resuspended.
3. Add 50 μL of antibody cocktail to 50 μL of cell suspension.
4. Incubate the sample on ice for 20 min.
5. Transfer the cells to a 5 mL Eppendorf tube and wash as in **steps 7** and **8** in Subheading 3.1.2.
6. Decant the supernatant by dabbing the top of the tube on a clean lint-free paper towel.
7. Resuspend each sample in 500 μL of SB.
8. Perform a final count using the Moxi Z Mini Automated Cell Counter.
9. Prepare the loading concentration by a final centrifugation at 400 × *g* for 5 min at 4 °C.
10. Decant the supernatant by dabbing the top of the tube on a clean lint-free paper towel.
11. Resuspend the cells in a volume that results ~1000 cells/μL.
12. Load the cells into the 10× Genomics chip as per the manufacturer's protocol.

3.2 AbSeq

3.2.1 Viability Check

1. Resuspend cell samples processed from tissues or blood in 0.5 mL of SB for every anticipated one million cells in a 15 mL Corning tubes (*see* **Note 2**).
2. Count the cells using the Rhapsody scanner (*see* **Note 4**).
3. Additionally, count the cells using Trypan Blue, because cell count should be as accurate as possible for the later steps. Before Calcein and Draq 7 are added, take a small aliquot from each of the samples for this method of counting.
4. Continue with those samples whose viability is above 70% (*see* **Note 5**).
5. Centrifuge the samples for 5 min at 400 × *g* and resuspend the samples in 200 μL of SB.

3.2.2 Labeling with Sample Tags and Mixing

1. Resuspend one million cells in 100 μL of SB with human Fc block reagent (2.5 μg in 50–100 μL of SB) and incubate for 15 min at RT.

2. Transfer one million cells to Eppendorf tubes (*see* **Note 6**). Centrifuge the samples for 5 min at 400 × *g* and discard the supernatant by dabbing on lint-free paper towel.
3. Resuspend the pellet in 170 μL of SB so that the final volume is 180 μL given that some volume will be left in the tube after decanting.
4. Centrifuge the Sample Tag tubes in Sample Multiplexing Kit for 10 s in a microcentrifuge (Do not vortex). Transfer the entire volume (approximately 180 μL) of each 5 sample to Sample Tag tubes, which contains about 20 μL of sample tag.
5. Incubate the sample tag tubes with the samples for 20 min at RT.
6. Transfer the cell suspension to 5 mL polystyrene tubes with blue lid using cell strainer lids if desired.
7. Add 2 mL of SB to labeled cells, mix by pipetting and centrifuge at 400 × *g* for 5 min. Decant the supernatant followed by dabbing on lint-free paper towel.
8. Repeat **step 7** twice (i.e., total of three times).
9. Resuspend the pellet in 500 μL of cold SB (*see* **Note 7**).
10. Count the cells using Rhapsody scanner (*see* **Note 4**).
11. Pool the appropriate volumes of each of the samples in one tube (*see* **Note 8**).
12. Centrifuge the tube for 5 min at 400 × *g* and 4 °C.
13. Decant the supernatant by dabbing on lint-free paper towel and resuspend in 102 μL of the antibody cocktail that will be made in the next step.

3.2.3 Antibody Staining

1. Centrifuge AbSeq antibodies for 10 min at 500 × *g* and 4 °C before using them. You need to use 2.4 μL of each antibody (include 20% extra) for each plate. Keep everything on ice.
2. Resuspend the cells in 102 μL of the mix of all the antibodies in 5 mL polystyrene tubes. Incubate on ice for 30–60 min.
3. Add 2 mL of SB to labeled cells, mix by pipetting and centrifuge at 400 × *g* for 5 min at 4 °C.
4. Decant the supernatant by dabbing on lint-free paper towel, and repeat **step 3** twice (i.e., total three times).
5. Resuspend the pellet of each of the tube in 400 μL of SB (*see* **Note 9**).
6. Count the cells using Rhapsody scanner (*see* **Note 4**).
7. Additionally, count the cells using Trypan Blue in a hemocytometer (*see* **Note 1**).

8. Leave the cells on ice (*see* **Note 10**) and prepare for loading the cells in the tube into the BD Rhapsody Cartridge as per the manufacturer's protocol.

4 Notes

1. This should be used in <1 year after opening. For the calculations, we use dilution factor of 2, achieved by adding the same volume of a sample and the trypan blue. For an accurate measurement, one should not have more than 200–400 cells when using hemocytometer. An appropriate dilution should be prepared if the suspension is highly concentrated.
2. It is optimal to begin with no fewer than one million cells. However, 500,000 cells can also work. You can refer to the references 5, 27 for the preparation of cell samples from atherosclerotic plaques and PBMCs from human blood.
3. This should be performed in duplicate. Adjust cell concentration as needed, either by centrifugation and resuspension (too few cells) or adding more media (too many cells).
4. To determine cell viability and cell count, add Calcein and Draq 7 (BD) to the samples in a dilution of 1:200. Calcein and Draq7 should be kept cold and in dark. Calcein is prepared by adding 503 μL of DMSO to the stock solution. Incubate the samples in the dark at room temperature for 5 min before measurement. It is important to measure viability twice for each sample to ensure accuracy.
5. If needed, use Easy Sep Dead Cell removal kit (based on annexin V, Stem Cell Technologies), Dead Cell Removal Kit (Miltenyi Biotec), or any other dead cell removal kits, following the manufacturer's instruction to improve the quality of the cells.
6. You may use 1.5 mL tubes though 2 mL tubes are better.
7. For those samples with low concentration of cells (based on previous measurements), resuspend in 200 μL of SB instead. If too concentrated, resuspend in 750 μL to 1 mL.
8. If some of the samples have a concentration above 1000 cells/μL, dilute more as it is better to have a concentration closer to 800 cells/μL. Each plate cannot exceed one million cells in total. A sample for batch effect control should be 10% of the total cells.
9. If the tube had a low concentration, resuspend in 200 μL of SB instead. Important to have the number of cells between 700 and 800 cells/μL.

10. Do not leave the cells for more than 1 h. Go to the next step as soon as possible.

Acknowledgments

This study was supported by Uehara Memorial foundation fellowship to R.S., NIH HL 136275, 145241, and 148094 to K.L.

References

1. Saigusa R, Winkels H, Ley K (2020) T cell subsets and functions in atherosclerosis. Nat Rev Cardiol 17:387–401
2. Zernecke A, Winkels H, Cochain C et al (2020) Meta-analysis of leukocyte diversity in atherosclerotic mouse aortas. Circ Res 127: 402–426
3. Galkina E, Kadl A, Sanders J, Varughese D, Sarembock IJ, Ley K (2006) Lymphocyte recruitment into the aortic wall before and during development of atherosclerosis is partially L-selectin dependent. J Exp Med 203: 1273–1282
4. Winkels H, Ehinger E, Goshesh Y, Wolf D, Ley K (2018) Atherosclerosis in the single-cell era. Curr Opin Lipidol 29:389–396
5. Fernandez DM, Rahman AH, Fernandez NF et al (2019) Single-cell immune landscape of human atherosclerotic plaques. Nat Med 25: 1576–1588
6. Williams JW, Winkels H, Durant CP, Zaitsev K, Ghosheh Y, Ley K (2020) Single cell RNA sequencing in atherosclerosis research. Circ Res 126:1112–1126
7. Winkels H, Ehinger E, Vassallo M et al (2018) Atlas of the immune cell repertoire in mouse atherosclerosis defined by single-cell RNA-sequencing and mass cytometry. Circ Res 122: 1675–1688
8. Cochain C, Vafadarnejad E, Arampatzi P, Pelisek J, Winkels H, Ley K, Wolf D, Saliba A-E, Zernecke A (2018) Single-cell RNA-seq reveals the transcriptional landscape and heterogeneity of aortic macrophages in murine atherosclerosis. Circ Res 122:1661–1674
9. Gu W, Ni Z, Tan Y-Q et al (2019) Adventitial cell atlas of wt (wild type) and ApoE (apolipoprotein E)-deficient mice defined by single-cell RNA sequencing. Arterioscler Thromb Vasc Biol 39:1055–1071
10. Kim K, Shim D, Lee JS et al (2018) Transcriptome analysis reveals nonfoamy rather than foamy plaque macrophages are proinflammatory in atherosclerotic murine models. Circ Res 123:1127–1142
11. Wirka RC, Wagh D, Paik DT et al (2019) Atheroprotective roles of smooth muscle cell phenotypic modulation and the TCF21 disease gene as revealed by single-cell analysis. Nat Med 25:1280–1289
12. Krämer A, Green J, Pollard J, Tugendreich S (2014) Causal analysis approaches in ingenuity pathway analysis. Bioinformatics 30:523–530
13. Qiu X, Hill A, Packer J, Lin D, Ma Y-A, Trapnell C (2017) Single-cell mRNA quantification and differential analysis with census. Nat Methods 14:309–315
14. Cohen M, Giladi A, Gorki A-D et al (2018) Lung single-cell signaling interaction map reveals basophil role in macrophage imprinting. Cell 175:1031–1044
15. Kumar MP, Du J, Lagoudas G, Jiao Y, Sawyer A, Drummond DC, Lauffenburger DA, Raue A (2018) Analysis of single-cell RNA-seq identifies cell-cell communication associated with tumor characteristics. Cell Rep 25:1458–1468.e4
16. Efremova M, Vento-Tormo M, Teichmann SA, Vento-Tormo R (2020) CellPhoneDB: inferring cell-cell communication from combined expression of multi-subunit ligand-receptor complexes. Nat Protoc 15:1484–1506
17. Stoeckius M, Hafemeister C, Stephenson W, Houck-Loomis B, Chattopadhyay PK, Swerdlow H, Satija R, Smibert P (2017) Simultaneous epitope and transcriptome measurement in single cells. Nat Methods 14:865–868
18. Peterson VM, Zhang KX, Kumar N, Wong J, Li L, Wilson DC, Moore R, McClanahan TK, Sadekova S, Klappenbach JA (2017) Multiplexed quantification of proteins and transcripts in single cells. Nat Biotechnol 35: 936–939
19. Todorovic V (2017) Single-cell RNA-seq—now with protein. Nat Methods 14: 1028–1029

20. Fan HC, Fu GK, Fodor SPA (2015) Combinatorial labeling of single cells for gene expression cytometry. Science 347:1258367
21. Mair F, Erickson JR, Voillet V, Simoni Y, Bi T, Tyznik AJ, Martin J, Gottardo R, Newell EW, Prlic M (2020) A targeted multi-omic analysis approach measures protein expression and low-abundance transcripts on the single-cell level. Cell Rep 31:107499
22. Cole JE, Park I, Ahern DJ, Kassiteridi C, Danso Abeam D, Goddard ME, Green P, Maffia P, Monaco C (2018) Immune cell census in murine atherosclerosis: cytometry by time of flight illuminates vascular myeloid cell diversity. Cardiovasc Res 114:1360–1371
23. Spitzer MH, Nolan GP (2016) Mass cytometry: single cells, many features. Cell 165: 780–791
24. Robinson JP, Roederer M (2015) History of science. Flow cytometry strikes gold. Science 350:739–740
25. Liu Y, Beyer A, Aebersold R (2016) On the dependency of cellular protein levels on mRNA abundance. Cell 165:535–550
26. Lundberg E, Fagerberg L, Klevebring D, Matic I, Geiger T, Cox J, Algenäs C, Lundeberg J, Mann M, Uhlen M (2010) Defining the transcriptome and proteome in three functionally different human cell lines. Mol Syst Biol 6:450
27. Vallejo J, Saigusa R, Gulati R, et al (2020) Combined protein and transcript single cell RNA sequencing reveals cardiovascular disease and HIV signatures bioRxiv 2020.09.10.292086
28. Melsted P, Booeshaghi AS, Gao F, Beltrame E, Lu L, Hjorleifsson KE, Gehring J, Pachter L (2019) Modular and efficient pre-processing of single-cell RNA-seq bioRxiv 673285
29. Hao Y, Hao S, Andersen-Nissen E, et al (2020) Integrated analysis of multimodal single-cell data. bioRxiv 2020.10.12.335331
30. Butler A, Hoffman P, Smibert P, Papalexi E, Satija R (2018) Integrating single-cell transcriptomic data across different conditions, technologies, and species. Nat Biotechnol 36: 411–420
31. Korsunsky I (2019) Fast, sensitive and accurate integration of single-cell data with harmony. Nat Methods 16:16
32. Hwang B, Lee JH, Bang D (2018) Single-cell RNA sequencing technologies and bioinformatics pipelines. Exp Mol Med 50:1–14
33. Efremova M, Teichmann SA (2020) Computational methods for single-cell omics across modalities. Nat Methods 17:14–17
34. Xi NM, Li JJ (2021) Benchmarking computational doublet-detection methods for single-cell RNA sequencing data. Cell Syst 12: 176–194.e6
35. Ilicic T, Kim JK, Kolodziejczyk AA, Bagger FO, McCarthy DJ, Marioni JC, Teichmann SA (2016) Classification of low quality cells from single-cell RNA-seq data. Genome Biol 17:29
36. Tran HTN, Ang KS, Chevrier M, Zhang X, Lee NYS, Goh M, Chen J (2020) A benchmark of batch-effect correction methods for single-cell RNA sequencing data. Genome Biol 21:12
37. Becht E, McInnes L, Healy J, Dutertre C-A, Kwok IWH, Ng LG, Ginhoux F, Newell EW (2019) Dimensionality reduction for visualizing single-cell data using UMAP. Nat Biotechnol 37:38–44
38. Emmons S, Kobourov S, Gallant M, Börner K (2016) Analysis of network clustering algorithms and cluster quality metrics at scale. PLoS One 11:e0159161

Chapter 47

Flow Cytometry and Mass Cytometry for Measuring the Immune Cell Infiltrate in Atherosclerotic Arteries

Marco Orecchioni, Melissa A. Meyer, Catherine C. Hedrick, and Klaus Ley

Abstract

Atherosclerosis is characterized by the abundant infiltration of immune cells starting at early stages and progressing to late stages of the disease. The study and characterization of immune cells infiltrating and residing in the aorta has being tackled by several methodologies such as flow cytometry and mass cytometry (CyTOF). Flow cytometry has been primarily used to address the aortic leukocyte composition; however, only a limited number of markers can be analyzed simultaneously. CyTOF started to overcome these limitations by employing rare element-tagged antibodies and combines mass spectrometry with the ease and precision of flow cytometry. CyTOF currently allows for the simultaneous measurement of more than 40 cellular parameters at single-cell resolution.

In this chapter, we describe the methodology used to isolate single immune cells from mouse aortas, followed by protocols for flow cytometry and CyTOF for aortic immune cell characterization.

Key words Atherosclerosis, Aorta, Immune cells, Leukocytes, Flow cytometry, Mass cytometry, CyTOF

1 Introduction

Atherosclerosis is a chronic inflammatory disease of the arterial wall characterized by lipid deposition. Innate and adaptive immune cells infiltrate the aorta of atherosclerotic mice during the development of the disease [1]. Common animal models used in cardiovascular research include genetically modified mice with altered lipid levels such as apolipoprotein E gene knockout and low-density lipoprotein receptor gene knockout mice [2].

In early studies, the immune cell infiltrate was characterized by immunohistochemistry [3]. Later, methods were developed to generate single-cell suspensions from the mouse aorta for flow cytometry analysis [4]. Recently, improvement in flow cytometry

Marco Orecchioni and Melissa A. Meyer contributed equally to this work.

Dipak P. Ramji (ed.), *Atherosclerosis: Methods and Protocols*, Methods in Molecular Biology, vol. 2419,
https://doi.org/10.1007/978-1-0716-1924-7_47,
© The Author(s), under exclusive license to Springer Science+Business Media, LLC, part of Springer Nature 2022

allowed the detection of 16 to 20 markers simultaneously. Mass cytometry (CyTOF) uses rare earth metal tags instead of fluorochromes, further expanding the range of markers up to 50 [5].

To study the immune cell composition of the artery wall by flow cytometry or CyTOF, single-cell suspensions must be made. Most of our knowledge is derived from animals, usually mouse models. The majority of methods to evaluate mechanisms of disease and efficacy of therapy would include the isolation and excision of the aorta. Analogous protocols can be used for other arteries (not described here).

The yield, viability, and composition of the single-cell suspensions depend on the diet, age and sex of the animals, harvesting practices, and the protocol used to obtain single-cell suspensions [4, 6–12]. The number of immune cells in the aorta differs significantly using different protocols [12–16].

This chapter provides an overview of the methods used for aortic immune cell characterization, from aortic leukocyte harvesting to flow cytometry and CyTOF analysis.

2 Materials

2.1 Mouse aorta Harvesting

1. Microdissection tools: two blunt curved forceps, iris scissors.
2. Surgical dissecting microscope.
3. Foam plate.
4. 1× Phosphate buffered saline (PBS): 137 mM NaCl, 2.7 mM KCl, 8 mM Na_2HPO_4, and 2 mM KH_2PO_4.
5. 1 mL syringes with 25G Needle.
6. 10 mL syringes with 25G Needle and Luer-Lok Tip.
7. 70% ethanol.
8. CO_2.
9. Ketamine.
10. Perfusion Buffer: 2% heparin diluted in PBS.
11. Fetal bovine serum (FBS).
12. RPMI 1640 Media.
13. Penicillin–streptomycin solution.
14. 0.5 M sterile ethylenediaminetetraacetic acid (EDTA).
15. 15 mL conical tubes.

2.2 Aorta Digestion

1. Microdissection tools: two blunt curved forceps, iris scissors.
2. 1× PBS.
3. FBS.
4. 1× HBSS with Ca^{2+} and Mg^{2+}.

5. Collagenase, Type I.
6. Collagenase, Type XI.
7. Deoxyribonuclease I (DNase) from bovine pancreas, type I.
8. Hyaluronidase from bovine testes, type 1-s.
9. Penicillin–streptomycin solution.
10. Completed RPMI Media: RPMI 1640 containing 10% FBS and 1% penicillin–streptomycin solution.
11. 15 mL conical tubes.
12. 70 μm nylon mesh strainers.
13. Thermally controlled circular shaker.
14. Thermally controlled 15/50 mL conical tubes centrifuge.
15. Ice.

2.3 Flow Cytometry (FACS)

1. Cell counting tool (e.g., hemocytometer or automatic cell counter).
2. Fc blocking antibodies (CD16/CD32 solution).
3. Antibodies as per panel (*see* Table 1).
4. Fixable viability dye.
5. 2% paraformaldehyde (PFA).
6. 1× PBS.
7. FBS.
8. 5% sodium azide (NaN_3).
9. FACS Buffer: PBS, 0.5–1% BSA or 4% FBS, 0.1% NaN_3.
10. Fc blocking buffer: FACS buffer, Fc blocking antibodies.
11. Flow cytometry acquisition instrument (e.g., BD LSR 2 II, BD Fortessa).
12. Compensation beads.
13. FACS tubes.
14. Table top centrifuge able to accommodate 15 mL conical tubes.
15. Flow cytometry analysis software (e.g., FlowJo).

2.4 Mass Cytometry (CyTOF)

1. CyPBS: 1× PBS free from heavy metal contaminates.
2. Cell Freezing Media: 5% DMSO in FBS.
3. CyFACS: 2 mM EDTA, 0.1% BSA, 0.05% NaN_3 in CyPBS. Filter-sterilize and store at 4 °C.
4. Purified CD16/32 Antibody.
5. Liquid nitrogen.

Table 1
Aortic panleukocyte panel example for flow cytometry

Antigen	Color	Dilution	Clone	Source
CD5	PerCP Cy5.5	1 to 200	54-7.3	BioLegend
CD11b	PE-Cy7	1 to 200	M1/70	BioLegend
CD64	APC	1 to 200	X54-5/7.1	BioLegend
CD19	APC-Cy7	1 to 200	6D5	BioLegend
CD45	AF700	1 to 400	30-F11	BioLegend
CD11c	BV605	1 to 200	N418	BioLegend
CD127	BV570	1 to 200	A7R34	BioLegend
TCR-y/d	FITC	1 to 200	GL3	BioLegend
CD8a	BV421	1 to 400	53-6.7	BioLegend
NK1.1	BV650	1 to 200	PK139	BD Biosciences
TCR-β	BV711	1 to 400	H57-597	BioLegend
Ly6C	BV786	1 to 200	RB6-8C5	BD Biosciences
CD4	PE/Dazzle 594	1 to 400	RM4-5	BioLegend
CD25	PE	1 to 200	PC61	BioLegend
LD	AQUA	1 to 1000	N/A	Thermo Scientific

6. Conjugated antibody: extracellular, intracellular, spike-in (will vary depending on designed panel, *see* Table 2).
7. Cell counting tool (e.g., hemocytometer or automatic cell counter).
8. Table top centrifuge able to accommodate 15 mL conical tubes.
9. Live/Dead Stain: 5 μM Cell ID Cisplatin (Fluidigm) in CyPBS. Prepare fresh each day.
10. 2% PFA: 16% methanol-free formaldehyde diluted to 2% in CyPBS. Store aliquots at −20 °C, protected from light.
11. Fixation/Permeabilization Buffer from FoxP3/Transcription Buffer Set (eBioscience). Working solution as described in the manufacturer's protocol: 4× Fixation/Permeabilization Concentrate diluted to 1× in Fixation/Perm Diluent. Prepare fresh each day.
12. Permeabilization Buffer from FoxP3/Transcription Buffer Set (eBioscience): 10× Permeabilization Buffer diluted to 1× with Milli-Q water. Prepare fresh each day.
13. Intercalator Solution: Cell ID Intercalator-IR, which contains natural-abundance iridium, 191Ir and 193Ir (Fluidigm)

Table 2
CyTOF panel as published in Winkels et al. [9]

Antigen	Label	Clone	Source	Catalog number	Conjugation
CD45	89Y	30-F11	Fluidigm	3089005B	Commercial
Ly-6C	141Pr	HK1.4	BioLegend	128002	In-house
CD11c	142Nd	N418	Fluidigm	3142003B	Commercial
TCR-β	143Nd	H57-597	Fluidigm	3143010B	Commercial
CD41	144Nd	MWReg30	BioLegend	133902	In-house
CD45 (Spike In)	145Nd	A20	BioLegend	110702	In-house
CD5	146Nd	53-7.3	Fluidigm	3146012B	Commercial
CD11b	148Nd	M1/70	Fluidigm	3148003B	Commercial
CD19	149Sm	6D5	Fluidigm	3149002B	Commercial
CD64	150Nd	X54-5/7.1	BioLegend	139302	In-house
CD25	151Eu	3C7	Fluidigm	3151007B	Commercial
Siglec-F	152Sm	1RNM44N	eBioscience	14-1702-82	In-house
CD8a	153Eu	53-6.7	Fluidigm	3153012B	Commercial
TER-119	154Sm	TER-119	Fluidigm	3154005B	Commercial
FR4	155Gd	TH6	BioLegend	125102	In-house
CD103	156Gd	2E7	BioLegend	121402	In-house
TCR-γ/δ	159Tb	GL3	Fluidigm	3159012B	Commercial
B220	160Gd	RA3-6B2	Fluidigm	3160012B	Commercial

diluted 1:2000 in permeabilization buffer. Prepare fresh each day.

14. Cell Acquisition Solution (Fluidigm).
15. Washing Solution (Fluidigm).
16. Cell Acquisition Solution and Beads: EQ Four Element Calibration Beads (Fluidigm) diluted 1:10 in Cell Acquisition Solution (Fluidigm). Prepare fresh each day.
17. 70 um filters.
18. FACS tubes.
19. CyTOF Helios (Fluidigm).
20. Normalizer (https://github.com/nolanlab/bead-normalization/releases, [17]).
21. CyTOF analysis software (e.g., FlowJo, Cytobank, Omiq).

3 Methods

3.1 Mouse Aorta Harvesting

1. Euthanize mouse by CO_2 inhalation or by exposing the animal to a supratherapeutic dose of anesthetics, such as 100–200 mg/kg of ketamine by intraperitoneal injection. The method used needs to be in accordance with the approved protocol of the appropriate Animal Care and Use Committee.
2. Verify primary euthanasia via toe pinch as a noxious stimulus.
3. Use a secondary method of euthanasia for confirmation (diaphragm cutting or heart puncture). Avoid cervical dislocation due to possible mechanical aortic damage.
4. After euthanasia, spray the mice with 70% ethanol and place in supine position with all 4 legs fixed onto a foam plate.
5. Puncture the heart with a 1 mL syringe with 25G needle to harvest blood, if desired.
6. To remove the remaining blood, use a 10 mL syringe with 25G needle to perfuse the aorta by puncture of the left ventricle with 5 to 10 mL of sterile cold (4 °C) perfusion buffer to avoid blood clots. The aorta will appear white after perfusion.
7. Using microdissection tools, remove the intestines, spleen, liver, and lung, keeping the heart, kidneys, and aorta in situ (*see* **Note 1**).
8. Remove the aorta under a dissecting microscope (*see* **Note 2**), carefully cleaning it from the periaortic fat.
9. Leave the main artery branches intact (0.5 cm from their branching location): Innominate artery, left carotid artery, left subclavian artery, renal arteries, celiac artery, and the common iliac artery.
10. Place the harvested aorta in a 15 mL conical tube containing PBS supplemented with 2% FBS and 2 mM EDTA or RPMI 1640 media supplemented with 10% FBS.

3.2 Aorta Digestion

1. Prepare enzyme digestion solution (diluted in HBSS containing Ca^{2+} and Mg^{2+}) with the following enzymes: 675–450 U/mL collagenase type I; 250–125 U/mL collagenase type XI; 120–60 U/mL hyaluronidase type I-s; and 60 U/mL DNase-I (to establish the exact enzyme concentration for the specific experimental settings *see* **Notes 3–6**).
2. Place 5 mL of the enzyme digestion solution in a 15 mL conical tube containing the aorta. Aortas can be cut into small pieces to improve digestion of the tissues.
3. Incubate at 37 °C for 40–70 min in agitation at 160–180 rpm In a thermally controlled circular shaker (*see* **Note 3**).

4. After incubation, filter through 70 μm nylon mesh strainers, and add 10 mL of cold PBS.
5. Wash by centrifugation at 400 × *g* at 4 °C for 5 min and then decant supernatant.
6. Resuspend in 2 mL of completed RPMI media and incubate at 37 °C for antigen recovery (*see* **Note 5**).
7. Wash by centrifugation at 400 × *g* at 4 °C for 5 min and then decant supernatant.
8. Add 1 mL of FACS buffer and place on ice and proceed with the chosen next steps (Flow Cytometry or CyTOF).

3.3 Flow Cytometry (FACS)

3.3.1 FACS Panel Design

Panel design is the most important step in designing a flow cytometry experiment. One of the most commonly available Flow Cytometers are the BD LSR II and the BD Fortessa. Both are capable of detecting from 15 to 20 markers including nuclear markers. For the design and optimization of an effective multi colorimetric flow cytometric panel, several steps are required such as correct fluorophore selection (*see* **Notes 7** and **8**), titration (*see* **Note 9**), live–dead cell staining (*see* **Note 10**), and validation with Fluorescence Minus One (FMO) control (*see* **Note 11**).

3.3.2 FACS Extracellular Staining

1. Perform extracellular marker staining on aortic cell suspension using a standard flow cytometry protocol as described below.
2. Count the cells with the desired method (e.g., hemocytometer or automatic cell counter) and incubate 1.0–1.5 × 10^6 of aortic cell suspension with 50 μL of 10 μg/mL of Fc blocking buffer for 10 min at room temperature to inhibit nonspecific binding of antibodies.
3. Add 50 μL of antibodies as per panel (*see* **Note 12** and Table 1) prepared in 10 μg/mL of Fc blocking buffer.
4. The extracellular antibody staining can be combined with the viability stain (*see* **Note 10**).
5. Incubate samples in the dark for 20–30 min at room temperature or 40 min on ice.
6. After the antibody incubation, add 1 mL of PBS to wash.
7. Centrifuge at 400 × *g* at 4 °C for 5 min and decant the supernatant.
8. Repeat **steps 6** and **7**.
9. After washing, fix the cells in 100 μL of 2% PFA for 30 min.
10. Repeat **steps 6** and **7**.
11. Resuspend the cell pellet in 200 to 300 μL of FACS buffer.
12. Proceed to data acquisition using the flow cytometer or store overnight at 4 °C in the dark.

3.3.3 FACS Sample Acquisition

1. Before sample acquisition, set up the flow cytometer and settings according to the manufacturer's protocol.
2. Set up voltages and run compensation controls for each fluorophore by using compensation beads or single fluorophore stained cells and apply to the experiment (*see* **Note 13**).
3. Use unstained and FMO controls (*see* **Note 11**) to set the appropriate forward (FSC) and side (SSC) scatter as well as gates for the fluorescent channels to depict clear negative and positive populations for each fluorophore used. Then, begin collecting control samples.
4. Run samples from Subheading 3.3.2, **step 12**.

3.3.4 FACS Data Analysis

For multiparametric flow cytometry analysis, often the software installed in the Flow Cytometer are not the best tools, being inherently slow and poorly intuitive. To overcome these problems, other software can be used (e.g., FlowJo and Cytobank). Both FlowJo and Cytobank allow processing of data from initial compensation and doublet removal (*see* **Notes 13** and **14**) to figure editing, providing all the tools required. Recently, these programs also include a user-friendly interface for biaxial analysis such as viSNE that allows the two dimensional visualization of high-dimensional single-cell data based on the t-Distributed Stochastic Neighbor Embedding (t-SNE) [18] and Uniform Manifold Approximation and Projection method (UMAPs) allowing a full characterization and visualization of multiparametric data as recently shown by McArdle and colleagues [15].

3.4 Mass Cytometry (CyTOF)

3.4.1 CyTOF Panel Design

The most widely available CyTOF, the Helios, is capable of detecting ions atomic masses from 75 to 209 Da [19]. *See* **Notes 15** and **16** for extensive description of the procedures needed for panel design, antibody conjugation, antibody titration, and required controls.

3.4.2 CyTOF Internal Controls (See **Notes 17–20**)

1. Prepare aliquots of spike-in control by isolating a single cell suspension of aorta or spleen.
2. Wash with CyPBS, resuspend in Cell Freezing Media, and slow freeze at −80 °C. Store at −80 °C or in liquid nitrogen until use. Prepare at least one vial per day of staining.

3.4.3 CyTOF Antibody Cocktails (See **Note 21**)

1. Prepare IgG FC Receptor block by diluting purified CD16/32 in CyFACS at 1:200 (*see* **Note 22**).
2. Prepare CD45 Sample Cocktail by diluting sample-specific antibody (89Y-CD45 in example panel, Table 2) in CyFACS at determined titration.

3. Prepare CD45 Spike-In Cocktail by diluting spike-in-specific antibody (145Nd-CD45 in example panel, Table 2) in CyFACS at determined titration.
4. Prepare Extracellular Antibody Cocktail by diluting all extracellular antibodies except CD45 in CyFACS at determined titrations (*see* **Note 23**).
5. Prepare Intracellular Antibody Cocktail by diluting all intracellular antibodies in Permeabilization Buffer at determined titrations (*see* **Note 24**).

3.4.4 CyTOF Live/Dead Staining

1. Proceed from the isolation of single cells from the aorta (Subheading 3.2, **step 8**). Use the entire aorta digestion for each sample. Note a cell count for each sample using desired method.
2. Thaw a vial of spike-in control into 5 mL of CyPBS. Centrifuge 350 × *g* at 4 °C for 5 min. Aspirate (*see* **Note 25**).
3. For each sample and the spike-in control, wash cells with 5 mL of CyPBS.
4. Centrifuge 350 × *g* at 4 °C for 5 min. Aspirate.
5. Resuspend in 1 mL of Live/Dead stain (*see* **Note 26**).
6. Incubate at 4 °C for 5 min.
7. Quench with 1.5 mL of CyFACS.
8. Centrifuge 350 × *g* at 4 °C for 5 min. Aspirate.
9. Resuspend in 1 mL of CyFACS.
10. Centrifuge 350 × *g* at 4 °C for 5 min. Aspirate.

3.4.5 CyTOF Cell Staining

1. Resuspend in 100 μL of IgG FC Receptor Block. Incubate at 4 °C for 10 min.
2. Centrifuge 350 × *g* at 4 °C for 5 min. Aspirate.
3. Resuspend each sample in 100 μL of CD45 Sample Cocktail. Resuspend spike-in in 100 μL of CD45 Spike-In Cocktail (*see* **Note 17**). Incubate at 4 °C for 30 min.
4. Add 1 mL of CyFACS. Resuspend samples and spike-in in 100 μL extracellular antibody cocktail (*see* **Note 16**). Add appropriate volume of spike-in control suspension to each sample.
5. Incubate at 4 °C for 30 min.
6. Add 1 mL of CyFACS.
7. Centrifuge 350 × *g* at 4 °C for 5 min. Aspirate.

3.4.6 CyTOF Cell Fixation

1. Resuspend in 100 μL of 2% PFA. Incubate overnight at 4 °C (*see* **Note 27**).

2. Add 1 mL of CyFACS.
3. Centrifuge 800 × *g* at 4 °C for 5 min. Aspirate (*see* **Note 28**).

3.4.7 CyTOF Intercalator Stain and Intracellular Staining

Intracellular staining is not necessary for all panels. If no intracellular antibodies are used, skip **steps 6–11**.

1. Resuspend in 1 mL of Fixation/Permeabilization Buffer. Incubate at 4 °C for 30 min.
2. Add 1 mL of Permeabilization Buffer.
3. Centrifuge 800 × *g* at 4 °C for 5 min. Aspirate.
4. Resuspend in 1 mL of Permeabilization Buffer.
5. Centrifuge 800 × *g* at 4 °C for 5 min. Aspirate.
6. Resuspend in 100 μL of Intracellular Antibody Cocktail (*see* **Note 16**).
7. Incubate at 4 °C for 30 min.
8. Add 1 mL of CyFACS.
9. Centrifuge 800 × *g* at 4 °C for 5 min. Aspirate.
10. Resuspend in 1 mL of CyFACS.
11. Centrifuge 800 × *g* at 4 °C for 5 min. Aspirate.
12. Resuspend in 100 μL of intercalator solution (*see* **Note 29**).
13. Incubate at room temperature for 30 min.
14. Add 1 mL of CyFACS.
15. Centrifuge 800 × *g* at 4 °C for 5 min. Aspirate.
16. Resuspend in 1 mL of CyFACS.
17. Store at 4 °C until prepared to acquire samples (*see* following sections and **Note 30**).

3.4.8 CyTOF Acquisition

1. Warm up, tune and inspect make-up gas each day of use of CyTOF Helios in addition to regular maintenance (*see* **Note 31**).
2. Prepare for acquisition in the software by input of your panel and setting the run time or event count for each sample.
3. Clean the CyTOF Helios by running 5 min of Washing Solution followed by 5 min of Cell Acquisition Solution.
4. Prepare sample by first centrifugation at 800 × *g* at 4 °C for 5 min. Aspirate (*see* **Note 32**).
5. Resuspend in 1 mL of Cell Acquisition Solution.
6. Centrifuge 800 × *g* at 4 °C for 5 min. Aspirate.
7. Resuspend in 1 mL Cell Acquisition Solution + Beads.
8. Filter through 70 μm filter into a FACS tube (*see* **Note 33**).

9. Analyze sample on CyTOF Helios. Acquire one million cells or the entire samples, whichever occurs first. The event rate should be no greater than 500 events/s.

3.4.9 CyTOF Cleaning Data

The following process will normalize data using the four element beads and remove debris, doublet, and dead cells using FlowJo. Further gating in FlowJo may be necessary to select for subpopulations of cells or to separate out the spike-in control. Many computational pipelines or user-friendly software packages are capable of cleaning the data and/or normalizing with beads, spike-in controls and barcoding independent of FlowJo manipulation.

1. Normalize to and remove beads using Normalizer (https://github.com/nolanlab/bead-normalization/releases [17]).
2. Import normalized files into FlowJo.
3. Select singlets (*see* **Note 34**).
4. Select live cells.
5. Export live cells as a new FCS file (*see* **Notes 35** and **36**).

3.4.10 CyTOF Analysis

CyTOF analysis can be accomplished in many different ways and is dependent on the skill sets available and the biological question. Many user-friendly platforms for high-dimensional cytometry analysis are now available, including Cytobank, Omiq, and FlowJo. Pay for service analyses are also available including the Astrolabe Cytometry Platform. The most flexible type of analysis is the use of computational pipelines, though they require computational expertise.

4 Notes

1. To avoid contamination of the aorta, all tools (scissors, forceps) must be clean and sterile by autoclaving.
2. To avoid cell death, aorta harvesting steps need to be performed in a timely manner, avoiding leaving the aorta sitting for a long time. The average time for aorta harvest from mouse euthanasia should not exceed 15 min. Moreover, during harvesting, aorta should be always kept moist with cold perfusion solution.
3. Enzyme concentration, as well as incubation time, are the key factor in the quality and quantity of the aortic single-cell recovered. Lower concentration of collagenase XI and hyaluronidase (e.g., 125 U/mL, and 60 U/mL respectively), followed by a reduced incubation time (e.g., 40-min), is preferred for a good representation of myeloid cells in the single-cell pool. Higher enzyme concentration (e.g., 250 U/mL of collagenase XI, and

120 U/mL of hyaluronidase) followed by at least 60-min incubation provides a better representation of T cells and B cells, with fewer macrophages and foam cells [12]. The best recovery of myeloid cells and foam cells so far obtained has been achieved by Kim and Lin et al. [11, 20]. Kim and colleagues applied a double digestion method using an initial short incubation time with Collagenase type II followed by a long 70-min incubation time that included all classical enzymes [11]. This approach provided a good amount of foam cells but lost all the other major cell populations. Similarly, McArdle et al. used a 45 + 45 min incubation with the same enzymatic pool described above to achieve macrophage isolation that was used for bulk RNA seq analysis [15].

4. Enzymatic digestion is necessary to retrieve single-cell suspension especially for studying tissue cell composition and describing new players in diseases like atherosclerosis. The methods used until now are far from being perfect, the high variability in the cell quality and quantity still require adjustment based on the focus of the study. Moreover, collagenase-based enzymes are known to induce changes in the cell transcriptomic profile. Often, the expression of stress response and cell death genes are induced. Due to continuous advancements in the sensitivity of high throughput technologies, small changes in gene expression can dramatically influence the interpretation of biological data. Transcription is active at 37 °C, and extended incubation at high temperatures may introduce gene expression artifacts, independent of the biology at the time of harvest [21].
5. Another example of the effect of digestion on the cells is the loss of some antigen expression like CD4. Rescue methods can be applied to retrieve the expression of some such markers. This requires incubation in complete media like RPMI containing 10% fetal bovine serum at 37 °C for 30–40 min [9].
6. Recently, a serine protease (subtilisin A) isolated from a Himalayan glacier–resident bacterium, *Bacillus licheniformis*, has been shown suitable for dissociation of tissues such as kidney and solid tumors at 4–6 °C. Its application reduced artifacts, including global and single-cell gene expression changes compared to classical collagenase-based digestion [22]. Cold enzymatic digestion has not been applied yet for the aorta; however, its application could provide improvement in cell viability with the cold incubation allowing the maintaining of the cell pool diversity in tissues, finally achieving a complete overview of the population habiting tissues in a healthy or disease state.
7. Not all fluorophores work the same. It is critical to study the absorption spectra (to select the laser) and the emission spectra. You must select the right fluorophore for the right marker. You

may use a less efficient marker for the dump channel (cell types you are not studying). The number of fluorophores available has increased significantly thanks to the development of new tandem dyes and dyes with large Stokes's shift. Each fluorophore, other than a specific excitation and emission wavelength, can also be ranked for its brightness and stability in the buffer. The relative abundance of a marker in the cells of interest is what should guide the selection of the fluorophore; CD45, for example, is abundant in leukocytes and should be always used in dim fluorophores such as FITC or PerCP. Conversely, rare markers will preferentially require bright fluorophores like PE or Alexa Fluor 647.

8. Tandem dyes contain chemically linked donor and acceptor molecules. The donor molecule is generally a dye with a large extinction coefficient, and the acceptor molecule absorbs energy emitted by the donor molecule through a phenomenon called fluorescence-resonance energy transfer (FRET). Tandem dyes have substantially increased the fluorophore choice. However, the stability of these dyes is limited. The decoupling of the donor from the acceptor can change substantially the emission wavelength, causing emission to erroneously fall into the channel of another fluorophore. For example, when PE-Cy7 disintegrates over time, the signal will fall in the PE channels giving false positive signals. Tandem dyes must be stored strictly according to the manufacturer's specifications.
9. Titration is required for optimizing the resolution and obtaining robust results for population identification and expression level measurements. It requires little effort and can save time, money, and problems in the long run. Titration means to test different concentrations of an antibody, for example, from 1:50 to 1:1000, and check which concentration will provide the best separation index between positive and negative events. When this is set, that concentration can be used among all the experiments.
10. Due to the elevated cell death caused by the digestion protocols, effective and correct aortic leukocyte characterization require the use of specific live–dead markers to assess cell viability and avoid false-positive signals. When cells die, they lose their membrane integrity and become "leaky." This is what causes the nonspecific binding. In our laboratory, we reject samples with leukocyte viability below 60%. Live–dead markers can be added to the staining mix or used before the antibody staining by incubation for 15 min in the dark. There are two main live–dead markers used in flow cytometry: DNA binding dyes and protein binding dyes. DNA binding dyes, such as propidium iodide (PI), DAPI, or 7-AAD only enter the cells when the membranes have been compromised. Once they do,

they bind the DNA and fluoresce. A range of these dyes with different excitation and emission characteristics exists. However, they should be avoided if the protocol requires a final fixation of the cells. Protein binding dyes, also known as amine-reactive dyes or live/dead fixable dyes, are still based on the principle that dead cells have compromised membranes but instead of binding DNA, they bind specific intracellular proteins. Moreover, this dye can be used also in protocols that require cell fixation.

11. Fluorescence minus one (FMO) controls are important when optimizing multicolor flow cytometry panels as they will help to determine where the gates delineating negative with positive events should be set. They are needed because of the so-called fluorescent spread, which is most pronounced with the brighter fluorophores. That is why the unstained control is not sufficient to correctly set the gates. FMOs consume a lot of cells, because you would have 20 different FMO tubes in a 20-flurophore panel. FMO controls are highly recommended when accurate identification between a positive and negative population is vital in the correct characterization of such population. FMOs can be omitted for abundant markers such as CD45, CD4, CD8, and CD19.
12. Aortic leukocyte panel design: In 2018, Winkels et al. applied a 13-marker panel for the discrimination of aortic leukocytes including: CD45, CD11b, F4/80, TCRγδ, CD117 (c-kit), CD19, FceR1, CD11c, NK1.1, TCR-b, Ly6C/G (Gr-1), CD4, and CD8 [9]. With this set of markers, they were able to successfully identify 12 leukocyte populations from the aorta of $ApoE^{-/-}$ mice fed 12 weeks western diet (WD), including mast cells, γδ T Cells, CD4+ T cells, CD8+ T cells, NK cells, NK T cells, macrophages, CD11c+ macrophages, DCs and myeloid DCs, and CD11b+ and CD11b- B cells acquired with an LSRII flow cytometer. However, 17% of cells remained unidentified, suggesting that other leukocyte populations are present in the aorta and the markers used are not sufficient for their detection. The panleukocyte panel currently used and validated in our laboratory did change with the addition of few specific markers, increasing the limit to currently 15 or 16 markers designed for the LSRII configuration (panel example in Table 1) and includes: (1) CD127 and CD25 for the identification of CD4+ T regs (TCRβ+, CD4+, CD25+ CD127 low); (2) Ly6C (instead of GR1) for the identification of classical and nonclassical monocytes; (3) CD5 recently used together with CD19 and CD11b to identify B1a (CD19+, CD11b+, CD5+) and B1b (CD19+, CD11b+, CD5+) B Cells subpopulations; and (4) CD64 to improve macrophage detection given that some DCs also express F4/80

[23]. Thanks to the new single cell RNA sequencing and CyTOF studies [9, 8, 12], new knowledge on the leukocytes subsets such as macrophages inhabiting the aorta are available. New panels are currently being developed with a combination of markers like CD45, CD64, CD206, CD169, CD11c, CD11b, MHCII, F4/80, Ly6C, and CD9/TREM2 for the identification of the newly defined subsets.

13. Compensation is always required because a fluorophore can bleed into a channel applied for the detection of another dye. This spillover can be extensive for fluorophore with close emission spectra such as FITC and PE resulting in false double-positive events. The spillover fluorescence can be defined as a linear function of the fluorescence intensity at the same photomultiplier tube (PMTs) voltages and filter sets. Introducing a spillover coefficient for each channel is sufficient for the flow cytometry software to calculate the compensated data [24]. Thus, voltage and spillovers among fluorophores in the same PMT should be carefully checked before the acquisition, aiming to keep the spillover below 30%. When using a large multicolor panel, further compensation might be required with third-party software like FlowJo, which allows manual correction of the automatic compensation generated by the flow cytometry software. This will help in improving the quality of the final data.
14. Another crucial aspect in the flow cytometric data analysis is the removal of doublet events (two cells passing the laser at the same time) as this can lead to false discovery especially when, as in atherosclerosis research, the goal is to define new populations inhabiting the aorta. Any "new" cell type is initially suspect of being a doublet unless proven otherwise. Several strategies are applied to exclude cell doublets from the data: (1) The most common is to exclude the events that deviate from the linear correlation between the forward scatter area (FSC-A) and the FSC height (FSC-H) parameters; and (2) To be more restrictive, two more filtering steps can be done with FSC-A by FSC width (FSC-W) and side scatter area (SSC-A) by SSC width (SSC-W) utilizing the low pulse width signal indicative of single cells [25]. The method indicated will remove the majority of cell doublets; however, some are not fully removed, which needs to be always considered when performing the analysis. Not all doublets are technical. There is mounting evidence that some doublets may have functional and biological meaning suggesting true cell-cell interactions [26].
15. CyTOF allows for the analysis of many cell populations and phenotypes in a single experiment. It is important to consider each cell type you would like to identify, as well as the cell types that need to be excluded. Markers for each should be included

in the panel. It is acceptable to use "dump" channels, where multiple antibodies are stained in the same channel and all positive cells are excluded from the analysis. Table 2 displays a CyTOF panel similar to the one used in Winkels et al. [9]. This panel allowed for the identification of 28 clusters or cell populations in the mouse aorta across healthy and atherosclerotic mice. Generally, panel design for CyTOF is more forgiving than panel design for flow cytometry. Because heavy metals are utilized rather than fluorophores, spectral overlap and compensation are not an issue like in flow cytometry. Yet there are a few considerations to be aware of in assigning antibodies against specific antigens to certain heavy metals. Like flow cytometry fluorophores, some heavy metals are "brighter" than others. Metals near the middle of the detection range (~147Gd to 170Er) provide a stronger signal than those metals on the ends of the range [27]. Low abundance markers should be assigned to the "brighter" metals to ensure detection. Next, a small amount of metal impurity can occur. This leads to spillover in the channel the next mass higher or the next mass lower (M + 1 or M − 1). The Maxpar labeling kits and commercially conjugated antibodies guarantee the purity of 98% or higher and rarely lead to enough rogue signal to require compensation [28]. Another source of spillover is oxidation. Oxidation can occur during the acquisition of the sample on the Helios leading to additional signals in the M + 16 channel. Careful warm-up, tuning, and adjusting of the make-up gas on the Helios each day can keep oxidation to a minimum (<3% of the signal) [28]. If issues from spillover arise, it would be prudent to consider using antibodies against antigens that are relatively low in abundance for the channel in question, to reduce the magnitude of the spillover.

16. Many antibodies can be purchased commercially from Fluidigm already conjugated to heavy metal isotopes. In the case that a commercial reagent is not available, purified antibodies can be conjugated to the heavy metal isotope of choice using the Maxpar antibody labeling kits available from Fluidigm. Purified antibody preparations should be free of carrier proteins. The antibody labeling kits work best with IgG isotypes and also work with affinity-purified polyclonal antibodies, but are not useful for conjugation to IgM isotypes. Once antibodies are obtained from Fluidigm and/or conjugated using the Maxpar antibody labeling kit, it is prudent to validate the antibodies using titration. The best method is to use the tissue of interest to perform titrations, but another tissue (such as the spleen) is acceptable if the material is limited (as it is for the aorta). Titrations should be performed on a similar number of cells to match expected staining conditions, or on ten million

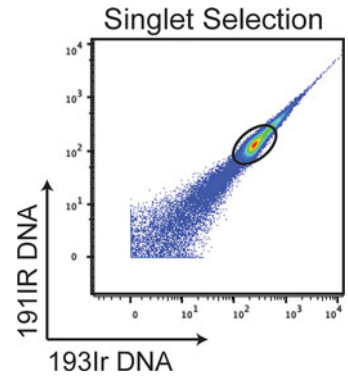

Fig. 1 Example of FlowJo-based sample cleaning. Singlet selection is preformed first by inspecting 191IR vs. 193IR to look at cellular DNA content. An oval shaped, concentrated bulge is selected as shown. Selected singlets are suitable for export and use in further downstream analysis

cells if the staining conditions are unknown. The full CyTOF staining protocol should be performed in the same way as is expected for the final experiment. Titration of 1:400, 1:200, 1:100, and 1:50 are suggested but could be adjusted based on the user's experience. An unstained control is necessary for comparison. Unlike flow cytometry, titration for multiple antibodies can be performed using a single tube for a single dilution (i.e., if four antibodies need to be titrated, they could be combined at 1:400, a second tube at 1:200, a third tube at 1:100, a fourth tube at 1:50, and an unstained control for a total of only 5 samples). Titration can be analyzed simply using Flowjo. After the selection of single (Fig. 1) and live cells, titrations can be inspected as shown in Fig. 2. In the case of Fig. 2, a dilution of 1:100 would be chosen because it shows distinct staining and higher dilutions do not provide additional resolution. All antibodies in a "dump" channel need to be titrated independently to ensure each is staining. In this case, more than five tubes would be necessary. In CyTOF, we generally do not perform control similar to fluorescence minus one. Instead, it is prudent to use knowledge of biology to inspect for artifacts or nonspecific staining. For example, CD4 and CD8 are not expected to be coexpressed on T cells outside of the thymus, so coexpression might suggest a problem with staining. It is important to remember that CyTOF data may need to be validated using an additional method like FACS if a novel or unexpected population of cells is identified.

17. One limitation of CyTOF is the degradation of the signal on the CyTOF Helios across a day of acquisitions and the inconsistency in detection and staining from day to day, or month to month for longitudinal studies. Two methods of internal

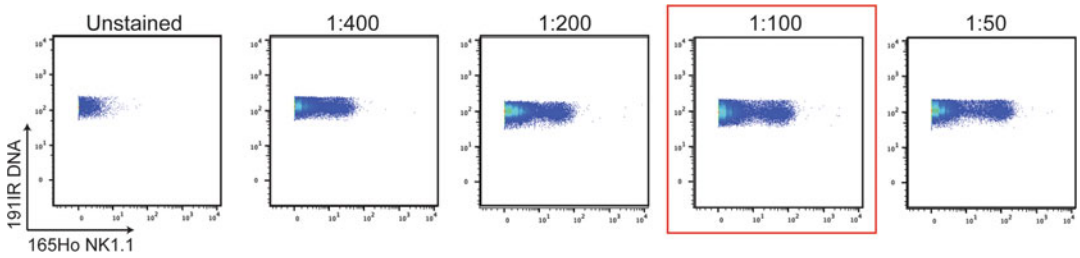

Fig. 2 Example of antibody titration. Blood cells were stained with anti-mouse NK1.1 tagged with 165Ho at dilutions of 1:400, 1:200, 1:100, and 1:50. An unstained sample was also collected. Decreasing dilutions of antibody showed increased staining and better separation between the positive and negative populations. Separation and staining plateau at 1:100. Therefore, this dilution is chosen

control can be used to ensure consistency after normalization. The first is a spike-in control. In this case, a control sample of the tissue in question or another tissue that also expresses all of the incorporated markers such as the spleen, is collected, processed into single cells, and frozen using cell freezing media, aliquoting enough vials to have sufficient supply to thaw one vial each time staining occurs. Each staining day, a vial is thawed and first stained with a CD45 antibody tagged with a unique metal. This is considered the spike-in control. In parallel, the sample of interest is stained with a CD45 antibody tagged with a different metal. Once washed, the cells are mixed before proceeding with additional staining and acquisition. During the analysis, the spike-in is separated and used as a reference to normalize all samples.

If samples are stained all on the same day, barcoding is the best internal control method to use. Recent advances have provided a cadmium-based barcoding system available from Fluidigm [29]. In this protocol, each sample is labeled with a different combination of the seven available cadmium isotopes tagged to a CD45 antibody, before mixing and proceeding with further staining and acquisition. Before analysis, samples are de-barcoded using available open-source software packages or user-friendly software programs such as Cytobank. In addition to these optional internal controls, all samples are acquired on the Helios with EQ 4 Element Beads from Fluidigm. These polystyrene beads are tagged with 140/142Ce, 151/153Eu, 165Ho and 175/176Lu and are added to the sample during the final resuspension before the acquisition. Like a spike-in control, these beads provide a consistent signal that is used to normalize signal variation that can occur over time especially if the machine is run for hours or across days. It is important to make sure that signals from these channels are collected, but do not exclude their use for other markers. Beads are easily distinguished from cells due to their coexpression of all four metals

and the bright signal. Normalizing software is available to correct the data and remove the beads [17]. Normalizer v0.3 from the Nolan laboratory is available for download from github (https://github.com/nolanlab/bead-normalization/releases).

18. Reagents and samples should be kept cool throughout the procedure unless otherwise noted. Samples and reagents can be incubated, centrifuged, and stored at 4 °C. Samples can be quickly manipulated at the bench before returning to 4 °C or work can be done on ice.
19. Reagents need to be clean of heavy metal contamination. Common contaminants include barium, lead and iodine. Barium can be present on some laboratory materials and in laboratory soap. To avoid barium, it is suggested to use new plastics rather than washed reusable containers. Iodine can be present on some laboratory materials. Lead can be found in some municipal water supplies. To avoid lead, it is suggested that Milli-Q water be used for diluting reagents. To test for contamination, process a sample without antibody staining and look for contamination.
20. The protocol details a spike-in internal control. For protocols defining barcoding, *see* reference of Zivanovic et al. [30].
21. Prepare antibody cocktails before beginning an experiment. Antibody cocktails can be prepared a day prior to an experiment and stored at 4 °C.
22. If CD16/32 is part of the panel design, use the conjugated CD16/32 antibody at the tested dilution in the IgG block. This step will block any nonspecific antibody interactions.
23. Do account for antibody volume when preparing dilutions of the extracellular antibody cocktail.
24. If all antibodies are extracellular, skip intracellular staining. Prepare the intracellular antibody cocktail the day it is used.
25. Spike-in should account for 10–20% of each sample. Make sure enough spike-in is processed to cover all samples.
26. Cisplatin is used to detect dead cells. Cisplatin is excluded from live cells but penetrates dead cells during a short incubation.
27. Cells are acquired in a hypotonic solution. Fixation is imperative to stabilize cells.
28. After fixation, increase centrifuge speed to 800 × *g* to increase cell recovery.
29. The cell structure is not maintained or recorded as cells pass through the CyTOF. Instead, a DNA intercalator is used to identify cells and exclude doublets.

30. Sample can be stored up to 2 days before the acquisition. Cell integrity will be maintained better the sooner samples are acquired.
31. This is usually performed by staff in a core facility. If you are to operate the CyTOF independently, ask for training from your institution.
32. Prepare a single sample at a time for acquisition. Once a sample is washed into Cell Acquisition Solution, it cannot go back into CyFACS. If problems with the CyTOF Helios arise, the washed but unacquired sample will be lost.
33. The CyTOF Helios is prone to clogs. It is prudent to filter the sample before the acquisition. It is also useful to add an in-line filter to the CyTOF sampler before applying a sample.
34. The singlet gate may move up and down the plot along the diagonal day to day and even sample to sample. The gate should encompass a single cluster and, usually, the cluster that is the largest.
35. If two acquisitions were used for a single sample (i.e., after the machine clogs), concatenate for a single FCS file at the point of export after cleaning the data. Export and concatenation can both be accomplished by right-clicking on the population you would like to export in the workspace and selecting "export/concatenate." Many naming and file location selection options are available.
36. For many analyses, the spike-in control should be separated from the sample at this point. To do this in FlowJo, select each population using the two CD45-labeled channels. Export each population separately.

Acknowledgments

This work was supported by grants to M.O. from the American Heart Association (AHA18POST34060251), and from The Conrad Prebys Foundation Award. M.A.M acknowledges support from the American Cancer Society Postdoctoral Fellowship (PF-20-132-01-LIB) and the National Institute of Health (2T32AR064194). C. C. H. Acknowledges support from NIH grants U01 CA224766, R01 CA202987, R01 HL134236, and P01 HL136275. K. L. was supported by grants NIH HL 115232, 145241, and HL088093.

References

1. Weber C, Zernecke A, Libby P (2008) The multifaceted contributions of leukocyte subsets to atherosclerosis: lessons from mouse models. Nat Rev Immunol 8(10):802–815. https://doi.org/10.1038/nri2415
2. Getz GS, Reardon CA (2012) Animal models of atherosclerosis. Arterioscler Thromb Vasc Biol 32(5):1104–1115. https://doi.org/10.1161/ATVBAHA.111.237693
3. Jonasson L, Holm J, Skalli O, Bondjers G, Hansson GK (1986) Regional accumulations of T cells, macrophages, and smooth muscle cells in the human atherosclerotic plaque. Arteriosclerosis 6(2):131–138. https://doi.org/10.1161/01.atv.6.2.131
4. Galkina E, Kadl A, Sanders J, Varughese D, Sarembock IJ, Ley K (2006) Lymphocyte recruitment into the aortic wall before and during development of atherosclerosis is partially L-selectin dependent. J Exp Med 203(5):1273–1282. https://doi.org/10.1084/jem.20052205
5. Hamers AAJ, Dinh HQ, Thomas GD, Marcovecchio P, Blatchley A, Nakao CS, Kim C, McSkimming C, Taylor AM, Nguyen AT, McNamara CA, Hedrick CC (2019) Human monocyte heterogeneity as revealed by high-dimensional mass cytometry. Arterioscler Thromb Vasc Biol 39(1):25–36. https://doi.org/10.1161/ATVBAHA.118.311022
6. Clement M, Raffort J, Lareyre F, Tsiantoulas D, Newland S, Lu Y, Masters L, Harrison J, Saveljeva S, Ma MKL, Ozsvar-Kozma M, Lam BYH, Yeo GSH, Binder CJ, Kaser A, Mallat Z (2019) Impaired autophagy in CD11b(+) dendritic cells expands CD4(+) regulatory T cells and limits atherosclerosis in mice. Circ Res 125(11):1019–1034. https://doi.org/10.1161/CIRCRESAHA.119.315248
7. Campbell LA, Rosenfeld ME (2015) Infection and atherosclerosis development. Arch Med Res 46(5):339–350. https://doi.org/10.1016/j.arcmed.2015.05.006
8. Cole JE, Park I, Ahern DJ, Kassiteridi C, Danso Abeam D, Goddard ME, Green P, Maffia P, Monaco C (2018) Immune cell census in murine atherosclerosis: cytometry by time of flight illuminates vascular myeloid cell diversity. Cardiovasc Res 114(10):1360–1371. https://doi.org/10.1093/cvr/cvy109
9. Winkels H, Ehinger E, Vassallo M, Buscher K, Dinh HQ, Kobiyama K, Hamers AAJ, Cochain C, Vafadarnejad E, Saliba AE, Zernecke A, Pramod AB, Ghosh AK, Anto Michel N, Hoppe N, Hilgendorf I, Zirlik A, Hedrick CC, Ley K, Wolf D (2018) Atlas of the immune cell repertoire in mouse atherosclerosis defined by single-cell RNA-sequencing and mass cytometry. Circ Res 122(12):1675–1688. https://doi.org/10.1161/CIRCRESAHA.117.312513
10. Cochain C, Vafadarnejad E, Arampatzi P, Pelisek J, Winkels H, Ley K, Wolf D, Saliba AE, Zernecke A (2018) Single-cell RNA-seq reveals the transcriptional landscape and heterogeneity of aortic macrophages in murine atherosclerosis. Circ Res 122(12):1661–1674. https://doi.org/10.1161/CIRCRESAHA.117.312509
11. Kim K, Shim D, Lee JS, Zaitsev K, Williams JW, Kim KW, Jang MY, Seok Jang H, Yun TJ, Lee SH, Yoon WK, Prat A, Seidah NG, Choi J, Lee SP, Yoon SH, Nam JW, Seong JK, Oh GT, Randolph GJ, Artyomov MN, Cheong C, Choi JH (2018) Transcriptome analysis reveals nonfoamy rather than foamy plaque macrophages are proinflammatory in atherosclerotic murine models. Circ Res 123(10):1127–1142. https://doi.org/10.1161/CIRCRESAHA.118.312804
12. Zernecke A, Winkels H, Cochain C, Williams JW, Wolf D, Soehnlein O, Robbins CS, Monaco C, Park I, McNamara CA, Binder CJ, Cybulsky MI, Scipione CA, Hedrick CC, Galkina EV, Kyaw T, Ghosheh Y, Dinh HQ, Ley K (2020) Meta-analysis of leukocyte diversity in atherosclerotic mouse aortas. Circ Res 127(3):402–426. https://doi.org/10.1161/CIRCRESAHA.120.316903
13. Butcher MJ, Galkina EV (2012) Phenotypic and functional heterogeneity of macrophages and dendritic cell subsets in the healthy and atherosclerosis-prone aorta. Front Physiol 3:44. https://doi.org/10.3389/fphys.2012.00044
14. Gjurich BN, Taghavie-Moghadam PL, Galkina EV (2015) Flow cytometric analysis of immune cells within murine aorta. Methods Mol Biol 1339:161–175. https://doi.org/10.1007/978-1-4939-2929-0_11
15. McArdle S, Buscher K, Ghosheh Y, Pramod AB, Miller J, Winkels H, Wolf D, Ley K (2019) Migratory and dancing macrophage subsets in atherosclerotic lesions. Circ Res 125(12):1038–1051. https://doi.org/10.1161/CIRCRESAHA.119.315175
16. Hu D, Mohanta SK, Yin C, Peng L, Ma Z, Srikakulapu P, Grassia G, MacRitchie N, Dever G, Gordon P, Burton FL, Ialenti A, Sabir SR, McInnes IB, Brewer JM, Garside P, Weber C, Lehmann T, Teupser D,

Habenicht L, Beer M, Grabner R, Maffia P, Weih F, Habenicht AJ (2015) Artery tertiary lymphoid organs control aorta immunity and protect against atherosclerosis via vascular smooth muscle cell lymphotoxin beta receptors. Immunity 42(6):1100–1115. https://doi.org/10.1016/j.immuni.2015.05.015

17. Finck R, Simonds EF, Jager A, Krishnaswamy S, Sachs K, Fantl W, Pe'er D, Nolan GP, Bendall SC (2013) Normalization of mass cytometry data with bead standards. Cytometry A 83(5):483–494. https://doi.org/10.1002/cyto.a.22271
18. el AD A, Davis KL, Tadmor MD, Simonds EF, Levine JH, Bendall SC, Shenfeld DK, Krishnaswamy S, Nolan GP, Pe'er D (2013) viSNE enables visualization of high dimensional single-cell data and reveals phenotypic heterogeneity of leukemia. Nat Biotechnol 31(6):545–552. https://doi.org/10.1038/nbt.2594
19. Hartmann FJ, Simonds EF, Vivanco N, Bruce T, Borges L, Nolan GP, Spitzer MH, Bendall SC (2019) Scalable conjugation and characterization of immunoglobulins with stable mass isotope reporters for single-cell mass cytometry analysis. Methods Mol Biol 1989:55–81. https://doi.org/10.1007/978-1-4939-9454-0_5
20. Lin JD, Nishi H, Poles J, Niu X, McCauley C, Rahman K, Brown EJ, Yeung ST, Vozhilla N, Weinstock A, Ramsey SA, Fisher EA, Loke P (2019) Single-cell analysis of fate-mapped macrophages reveals heterogeneity, including stem-like properties, during atherosclerosis progression and regression. JCI Insight 4(4). https://doi.org/10.1172/jci.insight.124574
21. O'Flanagan CH, Campbell KR, Zhang AW, Kabeer F, Lim JLP, Biele J, Eirew P, Lai D, McPherson A, Kong E, Bates C, Borkowski K, Wiens M, Hewitson B, Hopkins J, Pham J, Ceglia N, Moore R, Mungall AJ, McAlpine JN, Team CIGC, Shah SP, Aparicio S (2019) Dissociation of solid tumor tissues with cold active protease for single-cell RNA-seq minimizes conserved collagenase-associated stress responses. Genome Biol 20(1):210. https://doi.org/10.1186/s13059-019-1830-0
22. Adam M, Potter AS, Potter SS (2017) Psychrophilic proteases dramatically reduce single-cell RNA-seq artifacts: a molecular atlas of kidney development. Development 144(19):3625–3632. https://doi.org/10.1242/dev.151142
23. Randolph GJ, Inaba K, Robbiani DF, Steinman RM, Muller WA (1999) Differentiation of phagocytic monocytes into lymph node dendritic cells in vivo. Immunity 11(6):753–761. https://doi.org/10.1016/s1074-7613(00)80149-1
24. Szaloki G, Goda K (2015) Compensation in multicolor flow cytometry. Cytometry A 87(11):982–985. https://doi.org/10.1002/cyto.a.22736
25. Stadinski BD, Huseby ES (2020) How to prevent yourself from seeing double. Cytometry A 97(11):1102–1104. https://doi.org/10.1002/cyto.a.24045
26. Burel JG, Pomaznoy M, Lindestam Arlehamn CS, Weiskopf D, da Silva AR, Jung Y, Babor M, Schulten V, Seumois G, Greenbaum JA, Premawansa S, Premawansa G, Wijewickrama A, Vidanagama D, Gunasena B, Tippalagama R, deSilva AD, Gilman RH, Saito M, Taplitz R, Ley K, Vijayanand P, Sette A, Peters B (2019) Circulating T cell-monocyte complexes are markers of immune perturbations. Elife 8:e46045. https://doi.org/10.7554/eLife.46045
27. Gonder S, Fernandez Botana I, Wierz M, Pagano G, Gargiulo E, Cosma A, Moussay E, Paggetti J, Largeot A (2020) Method for the analysis of the tumor microenvironment by mass cytometry: application to chronic lymphocytic leukemia. Front Immunol 11:578176. https://doi.org/10.3389/fimmu.2020.578176
28. Leipold MD, Newell EW, Maecker HT (2015) Multiparameter phenotyping of human PBMCs using mass cytometry. Methods Mol Biol 1343:81–95. https://doi.org/10.1007/978-1-4939-2963-4_7
29. Lai L, Ong R, Li J, Albani S (2015) A CD45-based barcoding approach to multiplex mass-cytometry (CyTOF). Cytometry A 87(4):369–374. https://doi.org/10.1002/cyto.a.22640
30. Zivanovic N, Jacobs A, Bodenmiller B (2014) A practical guide to multiplexed mass cytometry. Curr Top Microbiol Immunol 377:95–109. https://doi.org/10.1007/82_2013_335

Chapter 48

Contrast-Enhanced Ultrasound Molecular Imaging in Atherosclerosis Research

The Anh Nguyen and Jonathan R. Lindner

Abstract

The management of cardiovascular conditions will likely be improved by noninvasive in vivo molecular imaging technologies that can provide earlier or more accurate diagnosis. These techniques are already having a positive impact in preclinical research by providing insight into disease pathobiology or efficacy of new therapies. Contrast enhanced ultrasound (CEU) molecular imaging is a technique that relies on the ultrasound detection of targeted microbubble contrast agents to examine molecular or cellular events that occur at the blood pool-endothelial interface. For the most part, targeted contrast agents are composed of encapsulated gas microbubbles (MBs) that are 2–4 μm in diameter, or other acoustically active micro- or nanoparticles. These agents bear several tens of thousands of binding molecules per particle. Because nonadhered agent is cleared rapidly, CEU molecular imaging can be performed in a matter of minutes. MBs are detected using contrast-specific techniques that generate and receive nonlinear signals produced by MB cavitation, thereby increasing signal-to-noise ratio. Dedicated kinetic models for molecular imaging have been generated that permit the elimination of signal from nonadherent agent.

Key words Cavitation, Contrast-enhanced ultrasound, Microbubbles, Molecular imaging, Atherosclerosis

1 Introduction

Contrast enhanced ultrasound (CEU) imaging relies on receiving signal generated by encapsulated gas microbubbles (MBs) that undergo volumetric oscillation [1]. Because they are highly compressible, MBs can undergo steady expansion and contraction, termed stable cavitation, in a low-pressure ultrasound field. If power is sufficiently high (e.g., mechanical index [MI] of 0.10 to 0.25) and ultrasound is applied within the ideal resonant frequency range for the MBs (which for conventional agents corresponds to diagnostic ultrasound frequencies), cavitation will be nonlinear with regards to the relationship between pressure and volume [2]. At very high power (MI > 0.8), destruction of microbubbles can occur from exaggerated oscillation, also known as inertial

Dipak P. Ramji (ed.), *Atherosclerosis: Methods and Protocols*, Methods in Molecular Biology, vol. 2419,
https://doi.org/10.1007/978-1-0716-1924-7_48,
© The Author(s), under exclusive license to Springer Science+Business Media, LLC, part of Springer Nature 2022

cavitation [3]. Both inertial cavitation and nonlinear stable cavitation result in emission of broad band ultrasound signals and ultrasound energy peaks at harmonic frequencies, thereby producing a unique acoustic signature that can be detected and isolated from background tissue signal [1, 4]. Conventional MB agents used in humans and in animal models are between 1 and 5 μm in diameter, have a core composed of a high-molecular-weight inert gas such as perfluorocarbons or sulfur hexafluoride and a shell composed of lipids or proteins such as albumin. These MBs are smaller than erythrocytes and have a microvascular rheology similar to that of erythrocytes [5]. Accordingly, they normally pass unimpeded through capillaries, which is important for both safety considerations and their use as flow tracers [6]. Lipid MBs also often contain surface "coats" composed of biocompatible polymers such as polyethylene glycol (PEG), which prevent their interaction with cells and plasma proteins [7, 8].

Molecular imaging with CEU is performed by diagnostic ultrasound imaging which detects targeted MBs that have been retained by virtue of their attachment to specific molecular processes within the vascular compartment [9, 10]. There are many different approaches to targeting of MBs. This chapter focuses on a flexible molecular imaging platform by which biotinylated antibodies proteins or small molecule ligands can readily be conjugated in a multivalent fashion to the same MB platform. Ligand–target interaction is encouraged by placing the ligand at the end of a molecular spacer. With respect to targeted imaging protocols, it is recommended that any multipulse contrast-specific ultrasound regime be used (e.g., pulse inversion, power modulation) [1]. For quantification of signal, tracer kinetic models have been developed that take differences in perfusion into account in order to derive a retention fraction [11]. However, these complex models are not required and do not apply to basic molecular imaging of vascular surfaces. The short duration (approximately 8 min) required for imaging and the ability to completely null the signal from targeted microbubbles after registering their signal allows us to noninvasively evaluate multiple targets sequentially in a single imaging session [12, 13].

2 Materials

1. Phosphate-buffered saline (PBS): 137 mM NaCl, 2.7 mM KCl, 8 mM Na_2HPO_4, and 2 mM KH_2PO_4.
2. Sterile normal saline solution.
3. Distearoylphosphocholine. Store at −4 °C.
4. Distearoylphosphatidylethanolamine-PEG(2000)biotin. Store at −4 °C.

5. Polyoxyethylene-40-stearate (PEG-stearate). Store at −4 °C.
6. Streptavidin.
7. 3 mL syringes (Luer lock).
8. 1 mL syringe.
9. 23G blunted needle.
10. 3-way stopcocks.
11. Decafluorobutane (DFB) or octafluoropropane (OFP) gas.
12. Sonicator with sonicating horn.
13. 50 mL beakers.
14. Ice.
15. 24 mL glass scintillation vial with screw caps.
16. PE 50 tubing.
17. Biotinylated monoclonal antibody (mAb) or small molecule ligand.
18. Surgical instruments for murine experiments (micro Vannas scissors, micro-curved forceps, scissors).
19. Multisize (1–20 μm) particle analyzer for concentration and size distribution.
20. Ultrasound Imaging System contrast-specific detection algorithms and transducers.
21. Ultrasound coupling gel.
22. Hot bead sterilizer.
23. pH meter.
24. Coulter counter or hemocytometer.
25. Centrifuge.

3 Methods

All procedures should be performed at room temperature, unless advised otherwise.

3.1 Biotinylated Microbubble Preparation

1. In a 24 mL glass scintillation vial, add 10 mL of PBS and measure pH.
2. To the PBS, add 20 mg of distearoylphosphocholine, 1 mg of distearoylphosphatidylethanolamine-PEG(2000)biotin and 10 mg of polyoxyethylene-40-stearate. Lipids will not be immediately soluble.
3. Sonicate the solution for 3–5 min or until all the reagents have dissolved into a homogeneous solution.

4. Bubble DFB or OFP into the solution. Sonicate for an additional 5–10 s until the solution becomes opaque due to MB formation. Let the solution cool to room temperature or place on ice, making sure not to cap the vial.
5. Once the MB suspension reaches room temperature, layer the vial with DFB or OFP gas, tighten the cap and store the stock suspension at 4 °C for as long as 4 weeks (*see* **Note 1**).
6. Prior to use, hand agitate the solution to resuspend the MBs from the flotation cake phase back into a homogeneous solution.
7. Count MB using a Coulter counter. A hemocytometer can be used as a second but less desirable option.

3.2 Microbubble Conjugation

1. Resuspend biotinylated MBs by gently swirling and inverting the stock solution vial for 30 s.
2. Pipet 2 mL of MB into 3 mL syringe with plunger removed and with attached stopcock closed to the syringe.
3. Centrifuge at 500 × *g* for 1 min to form a MB cake on top. Then, slowly remove the subnatant lower fraction of MB-cake-free PBS by opening the stopcock and controlling ambient air pressure at the top of the syringe.
4. Wash MB by adding 1 mL of PBS to the MB cake, resuspending MB by gentle agitation, and centrifuging with subsequent removal of the PBS subnatant as **step 3**.
5. Repeat **step 4**.
6. Reconstitute MBs by adding 1 mL of normal saline and count using Coulter counter or hemocytometer.
7. For each 1×10^8 MBs, add 30 μg of streptavidin and incubate on ice for 30 min or at room temperature for 10 min.
8. Perform **steps 3–6** on streptavidin-conjugated MB.
9. For each 1×10^8 MBs, add 30 μg of biotinylated monoclonal antibody (mAb) or equivalent molar amount of small molecule ligand. Incubate on ice for 30 min or at room temperature for 10 min.
10. Perform **steps 3–6** on targeted MBs to wash free ligand.
11. Evaluate MB concentration using Coulter counter or hemocytometer. Keep MB on ice and use on same day.

3.3 Surgery for Intravenous Injection in Anesthetized Mice

1. Shave or depilate, clean, and drape the neck of the mouse in sterile fashion (*see* **Note 2**).
2. Perform skin cephalad–caudal oriented skin incision and expose a jugular vein using blunt dissection.

3. Place several sterile sutures around the mid portion of the vein. Tie into a single knot but do not tighten. Ligate any posterior branch veins.
4. Attach a 10–15 cm segment of sterile PE50 tubing to a syringe containing sterile saline using a 23G blunted needle. Flush the line with the sterile saline. Cut a bevel in the PE 50 tubing at the end to be inserted into the vein (*see* **Notes 3** and **4**).
5. Cut a small incision in the jugular vein between two sutures, retract the cephalad-most suture to maintain hemostasis, and insert the PE50 tubing beyond the caudal-most suture. Flush with sterile saline to ensure catheter is in an intravenous position and secure sutures around the cannula (*see* **Note 5**).

3.4 CEU Molecular Imaging

1. Match the targeted MB dose to the signal-to-noise capability of the ultrasound imaging system.
2. Draw targeted MBs (or control MB) into a 1 mL syringe and dilute with sterile saline to a total volume of 75–100 μL.
3. Depilated the area of imaging and position the ultrasound probe to image the vessel of interest (ascending aorta, descending aorta, carotid artery) using gel as an acoustic interface.
4. Record 2D B-mode images using the highest-resolution mode (high frequency, short pulse duration) as an anatomic map.
5. Switch imaging to a contrast-specific mode (pulse inversion, amplitude modulation, pulse inversion/power modulation). Set mechanical index at <0.2 and optimize gain settings to just eliminate background scatter. Place the acoustic focus at the level of the vessel of interest.
6. Inject targeted or control MB as a slow intravenous bolus over 10–20 s followed by a small 50–75 μL flush with sterile saline (*see* **Note 6**).
7. Visualize intense MB contrast signal by ultrasound to confirm successful injection.
8. Pause the ultrasound imaging and allow MBs to circulate for 8 min to allow attachment and clearance of freely circulating MBs from the blood pool.
9. At 8 min, resume low-power imaging at a mechanical index (power display of ultrasound systems) of <0.2. Triggered imaging gated to diastole on the electrocardiogram (ECG) is preferable to reduce nonlinear flow artifact and to reduce total file size. Begin image acquisition and acquire at least five "predestruction" frames at MI <0.2. Then destroy MBs by increasing MI to 1.0 or greater for least 5 frames. Reduce MI back to its original low MI for acquisition of at least five additional "postdestruction" frames.

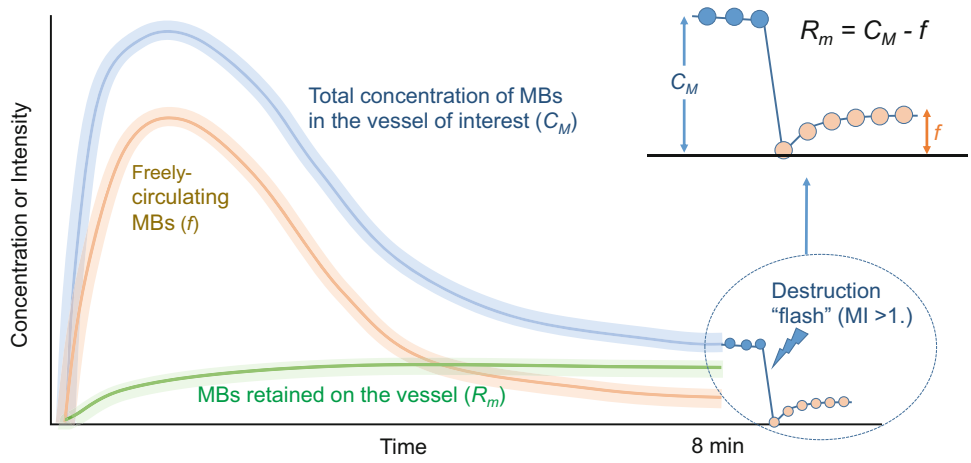

Fig. 1 Simplified kinetic model for measuring retained targeted MB signal. Most MB retention occurs when circulating MB concentration is high. MBs are injected as a bolus injection. Most but not all MBs are cleared by 8 min. To derive signal only from retained MB (R_m), signal 8 min after IV injection is measured by several frames (blue dots). Free and retained MBs are then destroyed by high MI "flash" exposure for several frames. Signal recovery immediately after the flash represents only that from freely circulating MBs that have returned back into the sector from flow. Averaging the signal from this signal recovery (f) from the predestruction frames yield signal from retained agent only

10. Before injection of the next agent, destroy all MBs (free and attached) by 10–15 s of continuous high MI (MI > 1.0) imaging.

3.5 Image Analysis

1. Transfer digital image sets to an image analysis program capable of frame selection, frame classification, digital subtraction, and intensity quantification.
2. The model for quantification based on the frames acquired is illustrated in Fig. 1. Select, align, and average several frames obtained prior to the high MI destructive burst sequence. These frames contain signal from retained and freely circulating MBs. Similarly, select, align, and average several frames after the high MI destructive burst. These frames contain signal from freely circulating MBs only. Digitally subtract postdestructive from predestructive frames to yield signal from retained MBs only (*see* **Note 7**).
3. Draw a standardized constant region-of-interest that is determined a priori based on anatomic landmarks for measurement of signal from retained agent.

4 Notes

1. For targeted agent preparation and storage, the stock suspension of biotinylated MBs can be stored for as long as 1 month.

Preservation of the agent is facilitated by replacing DFB or OFP in the headspace of vials after each sampling of the stock solution.

2. For the "Surgical Preparation of Mice," all surgery on animals that survive after molecular imaging require provisions for sterile surgical technique, sterile gloves, hemostasis, eye protection, and wound closure in layers. Instruments should be sterile at the procedure onset and periodic placement in a hot bead sterilizer should be performed.
3. For Molecular Imaging Methods, mice are extremely sensitive to even small venous air emboli. It is imperative to avoid any air in the line during MB injection and flush. The use of a Y-connector between MB and flush syringes is helpful for avoiding air embolism and a curved hemostat can be placed on the line between injections to prevent blood from backing into the PE50 line.
4. For molecular imaging methods and contrast injection, the PE50 lines should be as short as reasonably possible to reduce volume of injection.
5. For animal preparation, laboratories that are highly skilled in placing tail vein cannulas may choose to use this route for intravenous injection. Because partial extravasation frequently occurs with this technique, we recommend injection through an internal jugular catheter.
6. With respect to Molecular Imaging Protocols, all experiments should include provisions for control MB agent. Control agents are often composed of those that contain a nonspecific mAb or scrambled peptide.
7. With respect to Image analysis, it is important to realize that most intense measurements from ultrasound are expressed on a log-compressed scale and are further altered by postprocessing algorithms. The former can be corrected, if desired, by antilog conversion. The recommended program for analysis is freeware for use on tablet-based devices from Narnar LLC (Narnar v2.0).

References

1. Kaufmann BA, Wei K, Lindner JR (2007) Contrast echocardiography. Curr Probl Cardiol 32(2):51–96
2. Overvelde M, Garbin V, Sijl J, Dollet B, de Jong N, Lohse D, Versluis M (2010) Nonlinear shell behavior of phospholipid-coated microbubbles. Ultrasound Med Biol 36(12): 2080–2092. https://doi.org/10.1016/j.ultrasmedbio.2010.08.015
3. Shi WT, Forsberg F, Tornes A, Ostensen J, Goldberg BB (2000) Destruction of contrast microbubbles and the association with inertial cavitation. Ultrasound Med Biol 26(6): 1009–1019. https://doi.org/10.1016/s0301-5629(00)00223-4
4. Simpson DH, Chin CT, Burns PN (1999) Pulse inversion Doppler: a new method for detecting nonlinear echoes from microbubble

contrast agents. IEEE Trans Ultrason Ferroelectr Freq Control 46(2):372–382. https://doi.org/10.1109/58.753026

5. Lindner JR, Song J, Jayaweera AR, Sklenar J, Kaul S (2002) Microvascular rheology of Definity microbubbles after intra-arterial and intravenous administration. J Am Soc Echocardiogr 15(5):396–403
6. Porter TR, Mulvagh SL, Abdelmoneim SS, Becher H, Belcik JT, Bierig M, Choy J, Gaibazzi N, Gillam LD, Janardhanan R, Kutty S, Leong-Poi H, Lindner JR, Main ML, Mathias W Jr, Park MM, Senior R, Villanueva F (2018) Clinical applications of ultrasonic enhancing agents in echocardiography: 2018 American Society of Echocardiography guidelines update. J Am Soc Echocardiogr 31(3):241–274. https://doi.org/10.1016/j.echo.2017.11.013
7. Du H, Chandaroy P, Hui SW (1997) Grafted poly-(ethylene glycol) on lipid surfaces inhibits protein adsorption and cell adhesion. Biochim Biophys Acta 1326(2):236–248. https://doi.org/10.1016/s0005-2736(97)00027-8
8. Fisher NG, Christiansen JP, Klibanov A, Taylor RP, Kaul S, Lindner JR (2002) Influence of microbubble surface charge on capillary transit and myocardial contrast enhancement. J Am Coll Cardiol 40(4):811–819
9. Lindner JR (2010) Molecular imaging of vascular phenotype in cardiovascular disease: new diagnostic opportunities on the horizon. J Am Soc Echocardiogr 23(4):343–350.; ; quiz 450-342. https://doi.org/10.1016/j.echo.2010.01.025
10. Lindner JR (2009) Molecular imaging of cardiovascular disease with contrast-enhanced ultrasonography. Nat Rev Cardiol 6(7):475–481
11. Carr CL, Qi Y, Davidson B, Chadderdon S, Jayaweera AR, Belcik JT, Benner C, Xie A, Lindner JR (2011) Dysregulated selectin expression and monocyte recruitment during ischemia-related vascular remodeling in diabetes mellitus. Arterioscler Thromb Vasc Biol 31(11):2526–2533
12. Moccetti F, Brown E, Xie A, Packwood W, Qi Y, Ruggeri Z, Shentu W, Chen J, Lopez JA, Lindner JR (2018) Myocardial infarction produces sustained proinflammatory endothelial activation in remote arteries. J Am Coll Cardiol 72(9):1015–1026. https://doi.org/10.1016/j.jacc.2018.06.044
13. Kaufmann BA, Carr CL, Belcik JT, Xie A, Yue Q, Chadderdon S, Caplan ES, Khangura J, Bullens S, Bunting S, Lindner JR (2010) Molecular imaging of the initial inflammatory response in atherosclerosis: implications for early detection of disease. Arterioscler Thromb Vasc Biol 30(1):54–59. https://doi.org/10.1161/ATVBAHA.109.196386

Chapter 49

Nanoprobes for Computed Tomography and Magnetic Resonance Imaging in Atherosclerosis Research

Ketan B. Ghaghada, Rohan Bhavane, Andrew Badachhape, Eric Tanifum, and Ananth Annapragada

Abstract

Atheromatous lesions are characterized by intrusion into the vascular lumen, resulting in morphological changes to the blood compartment and into the vessel wall, resulting in characteristic molecular and cellular signatures in the solid tissue of the intima, tunica media, adventitia and surrounding tissue. Nanoprobes can be easily formulated to provide long blood-pool residence and molecular targeting, facilitating the imaging of atheromatous changes. Detection of nanoprobes can be accomplished by a variety of methods. We focus in this chapter on the use of cross-sectional imaging techniques, computed tomography (CT) and magnetic resonance imaging (MRI), that facilitate in vivo, noninvasive imaging of the vascular morphology and molecular/cellular signatures of the atheroma. The methods described are suitable for use in animal models, although versions of the probes are being readied for clinical trials, potentially facilitating clinical use in the future.

Key words Liposome, Nanoprobe, Macrophage, Blood pool, Alpha-4 integrin, CT, MRI, Mouse model

1 Introduction

In studying atheromatous lesions in animal models, there is often a need to study (1) the extent of occlusion of the vascular lumen, (2) the molecular profile of the lesion surface, in particular the presence of adhesion molecules that serve to recruit circulatory immune cells, and (3) the cellular makeup of the lesion itself. While these can all be studied ex vivo by histopathological examination, in vivo characterization yields information that can be directly correlated with physiological conditions, and further can follow longitudinal trends following some form of intervention.

Ketan B. Ghaghada, Rohan Bhavane, Andrew Badachhape and Eric Tanifum contributed equally to this work.

Dipak P. Ramji (ed.), *Atherosclerosis: Methods and Protocols*, Methods in Molecular Biology, vol. 2419,
https://doi.org/10.1007/978-1-0716-1924-7_49,
© The Author(s), under exclusive license to Springer Science+Business Media, LLC, part of Springer Nature 2022

Additionally, multislice or volumetric imaging provides a 3D view of both morphological and molecular/cellular profiles.

Blood pool imaging, by either magnetic resonance imaging (MRI) or computed tomography (CT), using long circulating nanoprobes provides excellent high-resolution visualization of vascular dimensions, vessel tortuosity, and stenosis [1, 2]. Coupled with simultaneous respiratory and cardiac gating, motion artifacts even within the highly mobile heart can be corrected [3–5]. Liposomes loaded with nonionic iodine compounds (for CT) and conjugated with gadolinium (Gd) chelates on their surface (for spin-lattice (T1) relaxation-weighted MR) have proven to be excellent blood pool contrast agents for these purposes. Other nanoparticle formats, including metals and various polymers have been evaluated, but none have achieved the versatility, safety, and complete blood pool retention of polyethylene glycol (PEG)ylated liposomes, even demonstrating retention by the placental barrier [6–8], enabling studies in pregnant dams while isolating the fetus from the contrast agent.

Imaging molecular profiles has generally been the realm of nuclear medicine, particularly positron emission tomography (PET), because of the dramatically high signal-to-noise ratio (SNR) achievable with radioactive probes. Background radiation at the wavelengths used in nuclear medicine is generally very low, and PET further takes advantage of the unique dichotomous phase-opposed generation of photons that is the result of positron annihilation, to additionally discriminate true signal from background noise. As a result, PET typically exhibits picomolar sensitivity, while conventional gamma radiography has nanomolar sensitivity. Both these techniques, however, suffer from poor spatial resolution and expose the subject to radiation. A molecular imaging agent that does not expose the subject to radiation, has comparable sensitivity to nuclear imaging and higher spatial resolution is therefore highly desirable. It has been shown [9] that associating Gd chelates with slow diffusing nanoparticles can dramatically increase the effective T1 relaxivity by virtue of a retarded rotational correlation. Liposomal nanoparticles with surface conjugated Gd chelates have therefore been constructed, and when targeted to molecular targets by suitable ligands, have demonstrated facile molecular imaging in small animal models [10–12]. Of particular note, these nanoparticle T1 agents have maximum relaxivity at moderate magnetic resonance (MR) field strengths (1–3 Tesla). Consequently, low-cost permanent magnet MRI instruments within the reach of most laboratories can be used for these studies. Furthermore, the results are directly translatable to clinical use since the majority of clinical MRI scanners operate in the same field strength range. In this chapter, we present methods to prepare both CT and MRI liposome-based nanoprobes and methods to use them for blood pool imaging, probing vascular permeability and molecular imaging for applications in preclinical atherosclerotic research.

2 Materials

Common names are provided for all materials below. CAS numbers, where available, are also provided in parentheses as unique identifiers.

1. Argon gas (Cas# 7440-37-1.
2. 1,2-Dipalmitoyl-sn-glycero-3-phosphatidylcholine (DPPC) (Cas# 63-89-8).
3. Cholesterol (Chol) (Cas# 57-88-5).
4. *N*-(carbonyl-methoxy polyethylene glycol 2000)-1,2-distearoyl-*sn*-glycero-3 phosphoethanolamine (MPEG2000-DSPE or MPEG-DSPE) (Cas# 474922-77-5).
5. Bis(stearylamide) Gd- diethylenetriamine pentaacetic acid gadolinium (BSA-DTPA-Gd) (Cas# 186796-30-5).
6. 1,2-Distearoyl-*sn*-Glycero-3 phosphoethanolamine 1,4,7,10-Tetraazacyclododecane-1,4,7,10-tetraacetic acid Gadolinium (DSPE-DOTA-Gd).
7. 1,2-Distearoyl-*sn*-glycero-3-phosphoethanolamine-*N*-[amino (polyethylene glycol 3400)] (DSPE-PEG3400-NH_2).
8. Carboxy-functionalized targeting ligand.
9. Iodixanol (Cas# 92339-11-2).
10. Dimethylformamide (DMF) (Cas# 4637-24-5).
11. *N*,*N*-Diisopropylethylamine (DIPEA) (Cas# 7087-68-5).
12. Dichloromethane (DCM) (Cas# 75-09-2).
13. *N*,*N*,*N*′,*N*′-tetramethyl-*O*-(*N*-succinimidyl)uranium tetrafluoroborate (TSTU) (Cas# 105832-38-0).
14. Acetonitrile (Cas# 75-05-8).
15. Methanol (Cas# 67-56-1).
16. Trifluoroacetic acid (Cas# 76-05-1).
17. 10% (w/v) phosphomolybdic acid (PMA) (Cas# 51429-74-4) stain in ethanol.
18. Absolute ethanol (64-17-5).
19. Deionized (DI) water.
20. Phosphate buffered saline (PBS): 137 mM NaCl (Cas# 7647-14-5), 2.7 mM KCl (Cas# 7447-40-7), 8 mM Na_2HPO_4, (Cas# 7558-79-4), and 2 mM KH_2PO_4 (Cas# 7778-77-0).
21. Tris (tromethamine) buffered saline (TBS): 50 mM Tris–HCl, (Cas# 1185-53-1), pH 7.6, 150 mM NaCl.
22. Histidine buffered saline (HBS): 10 mM L-histidine (Cas# 71-00-1), 150 mM NaCl, pH 7.4.

23. 2% (v/v) Nitric acid (HNO_3) (Cas# 7697-37-2) solution prepared in DI water.
24. Graduated pipettes and pipette tips.
25. Graduated measuring cylinders.
26. Glass beakers.
27. 20 mL glass scintillation vials.
28. Stir bars.
29. Magnetic stir-plate with heating.
30. Heated water bath sonicator.
31. Ice bath.
32. Refrigerator.
33. Tabletop vortexer.
34. Size-exclusion chromatography system (e.g., Sephadex LH-20).
35. Thin-layer chromatography (TLC) plates.
36. Ultraviolet (UV) light source.
37. UV spectrometer.
38. Rotary evaporator.
39. Lyophilizer.
40. Circulating water heating bath with temperature control capable of maintaining up to 75 °C.
41. Matrix-assisted laser desorption/ionization (MALDI) instrument.
42. Heating water bath with temperature control capable of maintaining up to 75 °C.
43. Liposome extruder (e.g., 10 mL Lipex membrane extruder [Evonik, Vancouver, BC, Canada]).
44. Nuclepore track-etch polycarbonate membranes (100 nm, 200 nm and 400 nm pore size).
45. Tangential flow diafiltration system (hollow fiber filter modules) with 500 kDa molecular weight cutoff (MWCO).
46. Dialysis tubing with 500 kDa MWCO.
47. Inductively coupled plasma atomic emission spectroscopy (ICP-AES).
48. ICP standard stock solutions for phosphorus (P) and gadolinium (Gd) at 1000 parts per million (ppm).
49. Dynamic light scattering (DLS) instrument for nanoparticle size analysis.
50. Animal model of atherosclerosis.
51. Isoflurane (Cas# 26675-46-7).

52. Syringe.
53. 28 or 30G needle.
54. 1 to 4.7 T small animal MRI scanner.
55. Small animal micro-CT system.
56. Image analysis software.

3 Methods

3.1 Preparation of Lipid Anchored Targeting Ligand

A detailed example is provided in the literature [11] and the relevant details are reproduced here.

1. Dissolve carboxy-functionalized ligand (0.585 mmol) in DMF (5.9 mL) at room temperature (*see* **Note 1**).
2. Under an argon environment, add 0.38 mL of DIPEA (2.19 mmol) and 283 mg of *N,N,N′,N′*-tetramethyl-*O*-(*N-succinimidyl*)uronium tetrafluoroborate (TSTU) (0.73 mmol) to the solution in **step 1**.
3. Stir the resulting mixture for 1.5 h.
4. Dissolve 616 mg of DSPE-PEG3400-NH_2 (approximately 0.146 mmol) in 2 mL of DMF at room temperature.
5. Under an argon environment, cannulate and transfer the mixture in **step 3** into a solution of DSPE-PEG3400-NH_2 in **step 4**.
6. Stir the resulting mixture for 2.5 days and subsequently concentrate under reduced pressure using a rotary evaporator at 50 °C.
7. Use a 1:1 (v/v) mixture of acetonitrile and water (6 mL) to recover the residue.
8. Remove the acetonitrile by rotary evaporation on a rotary evaporator with bath temperature maintained at 50 °C until the solution is slightly cloudy.
9. Add acetonitrile dropwise until a clear solution is seen.
10. Lyophilize the mixture.
11. Dissolve the lyophilized powder in 1 mL of methanol and purify by size-exclusion chromatography on Sephadex LH-20, eluting with methanol. Spot individual fractions on TLC plates (with UV indicator) and visualize by UV light as well as a 10% PMA stain in ethanol. The material that is both UV and PMA active comes off the column in two bands. The first band contains the desired product and fractions from this band can be combined and concentrated under reduced pressure using a rotary evaporator to yield the *t*-BOC protected conjugate (680 mg) as a tan-yellow glass.

12. Dissolve t-BOC protected conjugate (680 mg, approximately 0.13 mmol) in 9 mL of DCM.
13. Add 9 mL of trifluoroacetic acid to the solution from **step 12**.
14. Stir the mixture at room temperature for 4 h and then concentrate by rotary evaporation.
15. Dissolve the residue in 10 mL of dichloromethane and concentrate by rotary evaporation. Repeat the process five times or until a residue is obtained.
16. Dissolve the ensuing residue in a 1:3 (v/v) mixture of acetonitrile and water.
17. Lyophilize the mixture and purify the lyophilized powder by size-exclusion chromatography on Sephadex LH-20, eluting with methanol.
18. Spot individual fractions on TLC plates (with UV indicator) and visualize by UV light as well as 10% (w/v) PMA stain in ethanol.
19. Combine fractions containing material that is both UV and PMA active.
20. Concentrate the combined fractions by rotary evaporation and redissolve the residue in 10 mL of a 1:3 (v/v) mixture of acetonitrile and water.
21. Lyophilize the solution to obtain the desired product (572 mg) as an off-white solid.
22. Perform product characterization using MALDI (*see* **Note 2**).
23. These procedures can be adapted as appropriate to the specific targeting ligand desired by the experimenter (*see* **Note 3**).

3.2 Preparation and Characterization of CT Nanoprobes

3.2.1 Preparation of Iodixanol Solution (10 mL, 400 mg Iodine/mL)

1. Dissolve 8.2 g of iodixanol powder in 6.62 mL of TBS. Heat the solution at 65–70 °C (*see* **Note 4**).
2. Perform intermittent vortexing and sonication in a heated water bath sonicator (65–70 °C) to facilitate dissolution of iodixanol. A viscous and clear solution is obtained upon complete dissolution of iodixanol.

3.2.2 Preparation of Liposomal-Iodine CT Nanoprobe Formulations

1. The method described below is for the preparation of 10 mL of CT nanoprobe formulation (*see* **Note 5**).
2. Weigh DPPC, Chol, and MPEG-DSPE (55:40:5 molar ratio) for a 100 mM total lipid concentration and a 10 mL volume. Transfer the lipids into a glass scintillation vial.
3. Dissolve the above lipid mixture (**step 2**) in 1 mL of absolute ethanol at 60–65 °C under constant magnetic stirring (*see* **Note 6**).
4. In another glass vial, heat 10 mL of iodixanol solution at 65 °C.

5. Once all lipids have dissolved, add 9 mL of heated iodixanol solution (**step 4**) to the lipid solution (**step 3**) under constant stirring. Maintain the suspension at 60–65 °C under constant mixing for 30–60 min.
6. Extrude the suspension through Nuclepore polycarbonate track-etch membranes using a high-pressure extruder that is maintained at 65 °C. Extrude the suspension three times through a 400 nm membrane. Replace the membrane and extrude five times through a 200 nm membrane. Replace the membrane and extrude five times through a 100 nm membrane (*see* **Note 7**).
7. At the end of the extrusion process, measure liposomal nanoparticle size in the extruded solution using a DLS instrument (*see* **Note 8**).
8. Rapidly cool the liposomal suspension to room temperature in an ice bath.
9. Remove the nonencapsulated iodixanol from the liposomal suspension by diafiltration using a 500 kDa molecular weight cutoff (MWCO) hollow fiber filter module. Use fresh TBS to replenish the volume of formulation during the diafiltration process (*see* **Note 9**).
10. Store the suspension under refrigerated conditions (2–8 °C) until ready for use. Agent is usually stable for 6 months or more.

3.2.3 Determination of Iodine Content in CT Nanoprobe Formulations

The iodine concentration is determined by UV spectrometry ($\lambda_{abs} = 245$ nm) using a standard curve generated from measuring absorbance of known iodine standards.

1. Prepare iodine standards by dissolving iodixanol in DI water with concentrations ranging from 1 to 50 μg/mL of iodine.
2. For determining the iodine content of CT nanoprobe formulation, dilute the iodixanol liposomes 10× in water followed by a further 10× dilution in water with 30% by volume of ethanol (*see* **Note 10**). Perform an additional 100× dilution in water.
3. Measure UV absorbance and determine iodine concentration using standard curve.

3.3 Preparation and Characterization of MR Nanoprobes

3.3.1 Preparation of Liposomal-Gadolinium MR Nanoprobe Formulations

1. The method described below is for the preparation of 10 mL of MR nanoprobe formulation (*see* **Note 11**).
2. Weigh and transfer into a glass scintillation vial DPPC, Chol, MPEG-DSPE, and BSA-DTPA-Gd (or DSPE-DOTA-Gd) (50:25:5:20 molar ratio) for a 50 mM total lipid concentration and a 10 mL volume. For preparation of a molecular targeted MR nanoprobe, use a lipid ratio of DPPC:Chol:MPEG-DSPE:BSA-DTPA-Gd:DSPE-PEG_{3400}-Ligand 50:25:5-x:20:x, where x is the desired mole % of the targeting ligand (*see* **Note 12**).

3. Dissolve the above lipid mixture (**step 2**) in 1 mL of absolute ethanol at 60–65 °C under constant magnetic stirring (*see* **Note 6**).
4. In another glass scintillation vial, heat 10–12 mL of HBS at 65 °C.
5. Once all the lipids are dissolved, add 9 mL of the heated HBS solution (**step 4**) to the lipid solution (**step 3**) under constant stirring. Maintain the suspension at 60–65 °C with constant mixing for 30–60 min.
6. Extrude the suspension as described in **step 6** of Subheading 3.2.2 above. Measure the nanoparticle size as described in **step 7** of Subheading 3.2.2 above.
7. After cooling the liposomes, dialyze against a large excess (50–100×) of HBS for 24 h to remove ethanol.
8. Store the final product under refrigerated conditions (2–8 °C) until ready for use. Agent is usually stable for 6 months or more.

3.3.2 Determination of Gadolinium and Lipid Content in MR Nanoprobes

1. Perform 100× dilution of MR nanoprobe formulation in 2% nitric acid.
2. Make ICP standards of phosphorus (P) and gadolinium (Gd) from 0 to 100 ppm in 2% HNO_3 using the stock standard solutions. Analyze the standards, using an inductively coupled plasma atomic emission spectroscopy (ICP-AES) instrument, to generate standard curves.
3. Determine the phospholipid concentration (by measuring P) and Gd concentration (MR formulation only) by analyzing the liposomal formulations prepared in **step 1** above using ICP-AES.

3.4 In Vivo MR Imaging

1. Use a mouse MRI body coil (~35 mm volume coil) for volumetric imaging.
2. Sedate the animal by placing it in an induction chamber maintained under 3–4% isoflurane (*see* **Note 13**).
3. Transfer the sedated animal onto the MRI bed with a built-in face-cone for delivering gas anesthesia. The animal is generally positioned prone on the MRI bed and imaged while free breathing under anesthesia of 1.5–2.5% isoflurane.
4. Place a pressure-pad underneath the animal in the abdominal region to monitor the respiratory rate and well-being of the animal during the imaging session.
5. Acquire axial, coronal, and sagittal scout to ensure proper positioning of the animal. Align center of field of view (FOV) over thoracic cavity.

6. Acquire baseline, precontrast T1-weighted images. Use a T1-weighted gradient recalled echo (T1w-GRE) sequence for acquiring MR images. Use the following T1w-GRE parameter ranges for mouse body imaging: repetition time (TR) 20–30 ms; echo time (TE) = 2.5–4.0 ms; flip angle = 70°; voxel size = 0.3 mm × 0.3 mm × 0.3 mm; acquisition plane = coronal; slices = 60–70; and scan time ~5–6 min.
7. Prefill a syringe of MR nanoprobe for desired dose of administration. For applications described in this section, dose ranges from 0.10 to 0.20 mmol Gd/kg.
8. Inject liposomal-Gd for postcontrast imaging. Intravenous tail-vein injection (using a 28 or 30G needle) is the preferred route for MR nanoprobe administration. Injection can be performed in restrained or anesthetized animal (*see* **Note 14**). Equilibrate the MR nanoprobe formulation to room temperature before injection in animals (*see* **Note 15**). Inject as a slow manual bolus over 45–60 s (*see* **Note 16**).
9. Perform acute postcontrast imaging (~1 h postinjection) for vascular interrogation using scan parameters described in **step 6** (*see* **Note 17**) (Fig. 1).

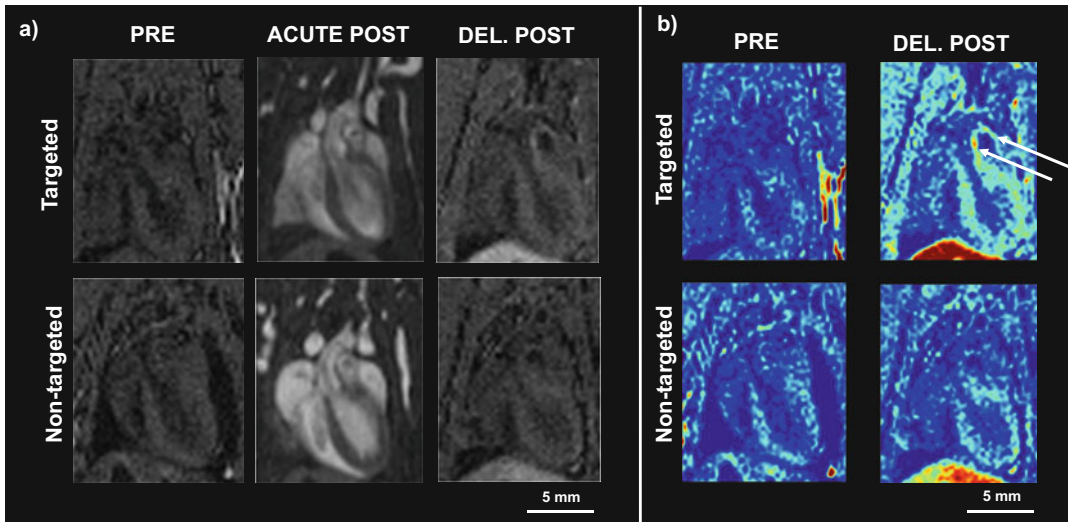

Fig. 1 Example cardiovascular imaging application in a mouse of contrast-enhanced MRI using a liposomal-gadolinium MR nanoprobe platform. (**a**) ApoE$^{-/-}$ mice (12–14 weeks old) were fed a high-fat diet for ~10 weeks and then underwent CE-MRI at precontrast (PRE), acute postcontrast (ACUTE POST) ~1 h after contrast administration, and delayed postcontrast (DEL. POST) 72 h after contrast administration. Representative coronal T1-weighted gray-scale MR images of the aortic arch from a THI0567-targeted liposomal-Gd treated mouse (top row) and a nontargeted liposomal-Gd-treated mouse (bottom row) are shown. (**b**) Coronal T1-weighted pseudocolored MR images are shown for precontrast and delayed postcontrast time points to better demonstrate enhancement in the aortic arch (white arrows) between targeted and nontargeted treated mice

10. Perform delayed postcontrast imaging (~72–96 h postinjection) for target interrogation using scan parameters described in **step 6** (*see* **Note 18**) (Fig. 1).
11. Perform quantitative and qualitative image analysis using an image analysis software.
12. Analyze precontrast and postcontrast images for signal intensity (SI) changes in regions of interest (ROI) such as the aortic vessel wall in cardiovascular applications.
13. Calculate signal-to-noise ratio (SNR) as SI_{ROI}/SI_{noise} where SI_{ROI} describes signal in the ROI and SI_{noise} describes standard deviation for signal in an area outside the animal.
14. Calculate % signal change to compare precontrast ROI (*ROI Pre*) and postcontrast ROI (*ROI Post*) (*see* **Note 19**):

$$\text{Signal change } (\%) = 100 \times \frac{SI_{ROI\ \ Post} - SI_{ROI\ Pre}}{SI_{ROI\ Pre}}$$

15. Figure 1 shows an example of using an α_4 integrin targeted MRI contrast nanoparticle agent to image atherosclerotic plaques in the ApoE knockout mouse model [11]. Other examples of MRI nanoparticle enhanced imaging are described in the literature [7, 8, 10].

3.5 In Vivo CT Imaging

1. Sedate the animal by placing it in an induction chamber maintained under 3–4% isoflurane.
2. Transfer the sedated animal onto CT bed. Position the animal prone on CT scanner bed and image while free breathing under anesthesia using 1.5–2.5% isoflurane delivered by a face cone (*see* **Note 20**).
3. Place a pressure-pad underneath the animal in the abdominal region to monitor the respiratory rate and well-being of the animal during the imaging session.
4. Acquire a scout scan to ensure proper positioning of the animal. Review scout images in axial and coronal plane to ensure that the thoracic cavity is centered within the field of view (FOV) in order to include the heart, ascending and descending thoracic segments of the aorta.
5. Acquire baseline, precontrast images. A typical scan protocol contains the following scan parameters: 50 kVp peak voltage; 0.5 mA tube current; 400 ms X-ray exposure time; 540 projections over a 360° rotation; 70 μm voxel size; and 10 min scan time. The estimated radiation dose associated with this scan protocol is about 30 cGy (*see* **Note 21**).
6. Inject the nanoprobe for postcontrast CT imaging. Intravenous tail-vein injection (using a 28 or 30G needle) is the preferred route for nanoprobe administration. Injection of nanoprobe can be performed in awake (held in a restrainer)

or anesthetized animal (*see* **Note 14**). Equilibrate the formulations to room temperature before injection in animals (*see* **Note 15**).

7. For the injection of nanoprobe, prefill a syringe with the desired nanoprobe dose. Typical iodine dose of CT nanoprobes ranges between 1 and 2 mg/g of body weight. The nanoprobe is injected as a slow manual bolus over 45–60 s (*see* **Note 16**). An equivalent molar weight of alternate high atomic weight element-based CT nanoprobes can also be used.
8. Perform CT angiography (~1 h postinjection) for vascular interrogation using scan parameter described in **step 5** (*see* **Notes 22** and **23**) (Fig. 2).
9. Perform CT delayed (CTD) imaging (~72–96 h postinjection) for target interrogation using scan parameter described in **step 5** (*see* **Notes 22–24**).
10. Reconstruct X-ray projection images using vendor-provided image reconstruction software. Filtered back projection is a common reconstruction method for converting projection images into 3D CT images. Additionally, CT images should be calibrated for Hounsfield Units (HU) (*see* **Note 25**).
11. Analyze CT images using a standard image analysis software (*see* **Note 26**).
12. Figure 2 shows an example of vascular imaging using a CT nanoprobe.

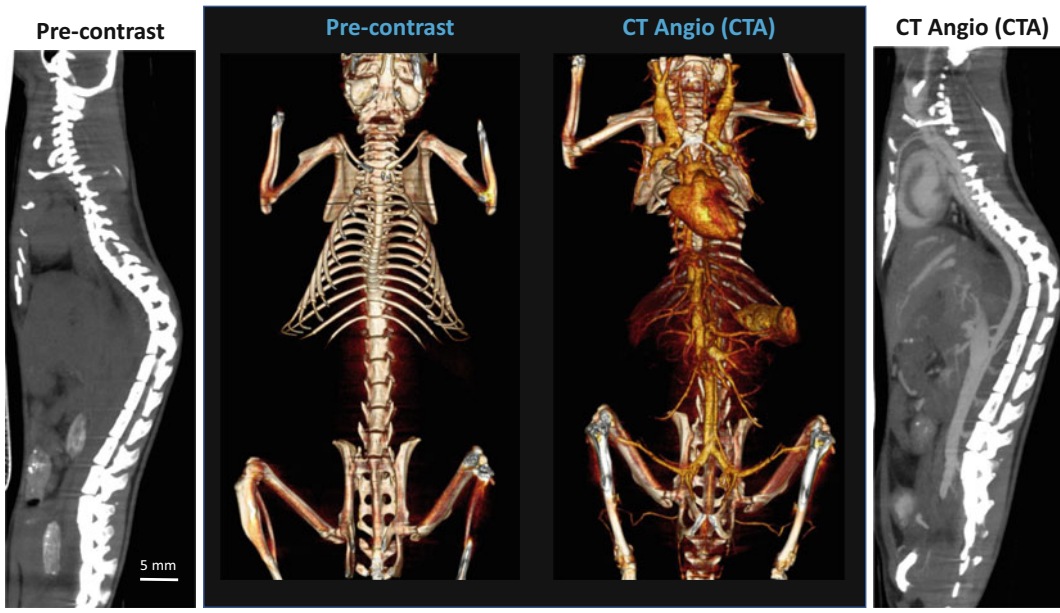

Fig. 2 Whole-body CT imaging of a mouse using a liposomal-iodine CT nanoprobe demonstrates facile visualization of the cardiovascular and blood circulatory system after intravenous administration of a CT nanoprobe. In comparison, precontrast 3D volume-rendered image only shows the skeletal system

4 Notes

1. Ligands with activatable carboxyl groups are best conjugated to DSPE-PEG3400-NH_2 in organic medium.
2. MALDI characterization of lipid-PEG-anchored targeting ligand conjugate is carried out in positive mode using sinapic acid as matrix material. The central mass of distribution for final product is 4867.8.
3. Ligand conjugation steps described in Subheading 3.1 are applicable for conjugating carboxy-functionalized small and large molecules (antibodies) to the distal end of DSPE-PEG-NH_2 construct. Depending on the scale of production, the amount of individual reagents will change. However, it is suggested that the molar ratios of reagents be maintained as described in Subheading 3.1.
4. Use of a stir bar is not recommended for this dissolution step due to the high solute content.
5. 10 mL of CT nanoprobe is adequate for ~40 doses in mice.
6. Use absolute ethanol without any denaturing agents.
7. At high lipid concentrations, membrane clogging is common and the suspension may not pass through the extruder. If this occurs, replace membrane and continue the extrusion process.
8. Mean hydrodynamic diameter of liposomes is generally between 100 and 120 nm.
9. During liposome formation, iodixanol molecules are present in the interior core of the liposomes (encapsulated fraction) and in the external volume outside the liposomes (nonencapsulated fraction). The diafiltration step removes the non-encapsulated fraction. In order to remove >99% of nonencapsulated fraction, the diafiltration process is performed by exchanging 16 volumes of the liposomal suspension with fresh TBS. Alternatively, conventional dialysis against a large excess of TBS can be used to remove nonencapsulated iodixanol. Perform the dialysis over 3 days with a total six changes of the external buffer every ~12 h.
10. Ethanol is used to rupture the liposomes and release the encapsulated contents.
11. 10 mL of MR nanoprobe is adequate for ~50 doses in mice.
12. Use of 1–2 mole% of targeting ligand conjugate during preparation of targeted nanoprobe yields ~1000–2000 molecules on the outer surface of the liposome. This number of molecules per nanoparticle is sufficient to ensure a strong and stable interaction between nanoparticle and its target cell.

13. All animal studies should be carried out under a protocol approved by the Institutional Animal Care and Use Committee.
14. A successful intravenous (IV) injection is important in order to achieve adequate opacification of vascular compartment during acute postcontrast scans. Tail vein injections in mice can be challenging. Consider additional volume of administration if adequate vascular signal is not observed in images.
15. It is important to ensure that the nanoprobe formulation has been equilibrated at room temperature prior to injection in animals. Injection of large volume of cold nanoprobe solution can be detrimental to the health of the animal.
16. Do not attempt a rapid bolus injection of nanoprobe. A rapid injection of a viscous nanoprobe solution can damage the tail vein.
17. Liposomal MR nanoprobes have a long blood half-life of 24–48 h in mice [13]. The long blood half-life of nanoprobes allows two modes for post-contrast imaging: acute postcontrast imaging (~1 h postinjection) for vascular interrogation and delayed postcontrast imaging (~72–96 h postinjection) for target interrogation. In acute postcontrast imaging phase (~1 h postinjection), the nanoprobe is predominantly present, and equilibrated, in the blood-pool compartment. This enables acquisition of angiograms for morphometric analysis of vascular compartments in the anatomy of interest. In the delayed postcontrast imaging phase (~72–96 h postinjection), the agent is bound to its target and unbound fraction cleared from systemic circulation, thereby enabling visualization of targeted biomarkers.
18. Acute postcontrast imaging is not necessary if vascular imaging is not the desired application. However, acute postcontrast imaging is helpful to confirm a successful intravenous administration of the nanoprobe.
19. Enhancement above a certain cutoff threshold, determined through composite analysis of SNR variation among the cohort, positively identifies an animal for the targeted pathology.
20. It is important to maintain the animal under deep anesthesia to minimize motion-induced artifacts in CT images. Adjust the level of isoflurane anesthesia to achieve a respiratory rate of 25–40 breaths per minute.
21. Higher spatial resolution in CT images often necessitates higher radiation dose in order to achieve adequate signal to noise ratio. Several factors should be considered during the selection of scan parameters, including the size of vascular

and atherosclerotic features to be imaged, number of imaging sessions per animal, effect of anesthesia duration on health of the animal and potential effects of radiation dose on the atherosclerotic biology.

22. Liposomal CT nanoprobes have a long blood half-life of 24–48 h in mice [13]. As such, nanoparticle contrast-enhanced CT (n-CECT) using a nontargeted nanoprobe provides two modes for imaging of atherosclerotic lesions (Fig. 2). Images acquired within 1–2 h after injection of nontargeted nanoprobe enables acquisition of high-resolution images of the vascular compartment for the interrogation of vessel diameter at sites of pathology. This imaging mode is referred as CT angiography (CTA). Images acquired 72–96 h after injection of nontargeted nanoprobe enables imaging of atherosclerotic lesions due to increased vascular permeability. This imaging mode is referred to as CT delayed (CTD) imaging. CTD scans should generally be acquired after the nanoprobe has cleared from vascular compartment. This is carried out to eliminate confounding residual blood pool signal and to boost contrast-to-noise ratio of intramural signal associated with accumulation of nanoprobe within the wall.
23. Cardiorespiratory gated imaging is recommended for imaging small vascular features, such as mouse coronaries. However, gated imaging will generally result in longer scan times.
24. Acute postcontrast imaging is not necessary if vascular imaging is not the desired application. However, acute postcontrast imaging is helpful to confirm a successful intravenous administration of the nanoprobe. Alternatively, since nanoprobes are systemically cleared via liver and spleen, CT signal in these organs can be used to assess success of IV injection when only CTD imaging is performed. For instance, if CTD images show poor enhancement of liver and spleen, it is likely that IV injection was not successful. This could result in little to no wall signal at sites of atherosclerotic lesions.
25. Since CT attenuation (Hounsfield Units, HU) is directly proportional to contrast agent concentration, HU-calibrated CT images can be converted into iodine maps. Tube phantoms of known iodine concentrations (0, 2.5, 5, 7.5, and 10 mg /mL) can be placed underneath the CT animal bed and included within the field of view to generate HU-iodine concentration curve and for conversion of HU values into iodine maps.
26. The file size of CT datasets increases exponentially with image spatial resolution. A high-end workstation ($\geq$32 GB RAM, GPU workstation, $\geq$500 GB storage space) is recommended for analysis and processing of CT datasets.

Acknowledgments

Methods described in this paper were developed in part with funding from the National Institutes of Health (R01CA159042, R01DE024932, R01HD094347, R44AG051292, U01DE028233), The American Heart Association (19CSLOI34660145), and the Gillson Longenbaugh Foundation who have continuously supported AA from 2009 to 2020. The authors also gratefully acknowledge support of the Small Animal Imaging Facility at Texas Children's Hospital, that houses the micro-CT and small animal MRI instruments used in the acquisition of images shown in this chapter.

Conflict of Interest: KBG is a consultant for Alzeca Inc. RB owns stock in Sensulin LLC. ET owns stock and is a consultant for Alzeca Inc. AA owns stock in Alzeca Inc. and Sensulin LLC, and is a consultant for Alzeca Inc.

References

1. Starosolski Z, Villamizar CA, Rendon D et al (2015) Ultra high-resolution in vivo computed tomography imaging of mouse cerebrovasculature using a long circulating blood pool contrast agent. Sci Rep 5:10178
2. Luo W, Wang Y, Zhang L et al (2020) Critical role of cytosolic DNA and its sensing adaptor STING in aortic degeneration, dissection, and rupture. Circulation 141:42–66
3. Howles GP, Ghaghada KB, Qi Y et al (2009) High-resolution magnetic resonance angiography in the mouse using a nanoparticle blood-pool contrast agent. Magn Reson Med 62:1447–1456
4. Mukundan S Jr, Ghaghada KB, Badea CT et al (2006) A liposomal nanoscale contrast agent for preclinical CT in mice. AJR Am J Roentgenol 186:300–307
5. Bucholz E, Ghaghada K, Qi Y et al (2008) Four-dimensional MR microscopy of the mouse heart using radial acquisition and liposomal gadolinium contrast agent. Magn Reson Med 60:111–118
6. Ghaghada KB, Starosolski ZA, Bhayana S et al (2017) Pre-clinical evaluation of a nanoparticle-based blood-pool contrast agent for MR imaging of the placenta. Placenta 57:60–70
7. Badachhape AA, Kumar A, Ghaghada KB et al (2019) Pre-clinical magnetic resonance imaging of retroplacental clear space throughout gestation. Placenta 77:1–7
8. Badachhape AA, Devkota L, Stupin IV et al (2019) Nanoparticle contrast-enhanced T1-mapping enables estimation of placental fractional blood volume in a pregnant mouse model. Sci Rep 9:18707
9. Caravan P, Ellison JJ, McMurry TJ et al (1999) Gadolinium(III) chelates as MRI contrast agents: structure, dynamics, and applications. Chem Rev 99:2293–2352
10. Tanifum EA, Ghaghada K, Vollert C et al (2016) A novel liposomal nanoparticle for the imaging of amyloid plaque by magnetic resonance imaging. J Alzheimers Dis 52:731–745
11. Woodside DG, Tanifum EA, Ghaghada KB et al (2018) Magnetic resonance imaging of atherosclerotic plaque at clinically relevant field strengths (1T) by targeting the integrin $\alpha 4\beta 1$. Sci Rep 8:3733
12. Badachhape AA, Working PK, Srivastava M et al (2020) Pre-clinical dose-ranging efficacy, pharmacokinetics, tissue biodistribution, and toxicity of a targeted contrast agent for MRI of amyloid deposition in Alzheimer's disease. Sci Rep 10:16185
13. Ghaghada KB, Badea CT, Karumbaiah L et al (2011) Evaluation of tumor microenvironment in an animal model using a nanoparticle contrast agent in computed tomography imaging. Acad Radiol 18:20–30

Chapter 50

Positron Emission Tomography in Atherosclerosis Research

Anne Roivainen, Mia Ståhle, and Antti Saraste

Abstract

Positron emission tomography (PET) is a quantitative imaging technique that uses molecules labeled with positron-emitting radionuclides to visualize and measure biochemical processes in the tissues of living subjects. In recent years, different PET tracers have been evaluated for their ability to characterize the atherosclerotic process in order to study the activity of the disease. Here, we describe detailed PET methods for preclinical studies of atherosclerosis and summarize the key methodological aspects of PET imaging in clinical studies of atherosclerosis.

Key words Autoradiography, ^{18}F-FDG, In vivo positron emission tomography/computed tomography

1 Introduction

Minimally invasive positron emission tomography/computed tomography (PET/CT) allows highly sensitive detection of radiolabeled compounds (tracers). In addition to in vivo imaging, ex vivo (postmortem) PET methods can be used in animal research to allow even more detailed examinations.

Cardiovascular PET imaging has the potential to provide information on disease activity, information that is complementary to that obtained from the anatomical assessment of atherosclerotic plaques offered by CT or magnetic resonance imaging (MRI). As inflammatory cells are the most abundant cell type in high-risk atherosclerotic lesions, they represent an attractive target for the identification of active disease [1]. The glucose analog 2-deoxy-2-[^{18}F]-fluoro-*D*-glucose (^{18}F-FDG) is still the most commonly used tracer, especially in large vessels such as the aorta and carotids. ^{18}F-FDG reflects the real-time glucose utilization of tissues, and therefore the uptake of ^{18}F-FDG is increased in the metabolically active cells found in pathological processes such as cancer and inflammation, including the inflammatory cells present in atherosclerotic lesions. Several studies have confirmed that ^{18}F-FDG

Dipak P. Ramji (ed.), *Atherosclerosis: Methods and Protocols*, Methods in Molecular Biology, vol. 2419,
https://doi.org/10.1007/978-1-0716-1924-7_50,
© The Author(s), under exclusive license to Springer Science+Business Media, LLC, part of Springer Nature 2022

uptake in plaques correlates with the histological degree of macrophages, but other metabolically active cells such as smooth muscle cells, fibroblasts and endothelial cells may also contribute to the uptake. Vascular ^{18}F-FDG PET imaging is a highly reproducible and sensitive method, with high arterial ^{18}F-FDG uptake being associated with cardiovascular risk factors, and it is increasingly being used as a surrogate marker to evaluate the effects of novel therapies on atherosclerotic inflammation. However, the high physiological uptake in the myocardium makes coronary imaging challenging [2].

Several new PET tracers have been evaluated for the imaging of atherosclerosis, with the molecular targets including macrophage surface receptors, adhesion molecules, integrins, and microcalcifications (Table 1). Compared with ^{18}F-FDG, some of these new tracers have the advantage of lower physiological uptake in the myocardium and more specific detection of particular inflammatory cell populations. In addition, new tracers may provide new pathological insights and allow evaluation of new targets for future diagnostic and therapeutic approaches. One of the strengths of PET/CT imaging of atherosclerosis is that changes in atherosclerotic plaque biology underlying structural changes in the vessel wall can be evaluated in vivo.

As ^{18}F-FDG is the most commonly used PET tracer for the imaging of atherosclerosis in mice and clinical studies, the PET methods mentioned here describe ^{18}F-FDG studies, whereas other tracers and animal models may use different protocols. A more detailed discussion of what to consider in animal PET studies can be found in the publications by Cicone et al. and Meester et al. [3, 4].

In an effort to acknowledge some of the clinical challenges and to standardize arterial PET imaging using ^{18}F-FDG PET in patients, a position paper was published by the Cardiovascular Committee of the European Association of Nuclear Medicine (EANM) in 2016 [5]. This position paper, as well as some more recent documents on PET imaging in inflammatory conditions [6, 7], addresses some central aspects regarding patient preparation, imaging protocol, and data analysis when applying ^{18}F-FDG to the assessment of atherosclerosis.

2 Materials

1. Animal model of atherosclerosis (e.g., high-fat fed, low-density lipoprotein receptor deficient mice, which express only apolipoprotein B100 [LDLR$^{-/-}$ApoB$^{100/100}$]).
2. Timer or clock.
3. Scales (precision scales and analysis scales).

Table 1
PET tracers evaluated for the imaging of inflammation in atherosclerosis

Target	Tracer	Development stage	References
Inflammatory cells (macrophages)			
Glucose metabolism	^{18}F-FDG	Clinical and preclinical Applications	[8–11]
Somatostatin receptor 2	^{68}Ga-DOTATATE	Clinical	[12–15]
		Mouse	
	^{64}Cu-DOTATATE	Clinical	
	^{68}Ga-DOTANOC	Mouse	
Chemokine receptor 4	^{68}Ga-Pentixafor	Clinical	[16–18]
		Rabbit	
Phospholipid metabolism	^{18}F-FCH	Clinical	[19–21]
	^{18}F-FMC	Mouse	
	^{11}C-Choline	Mouse	
18 kD translocator protein	^{11}C-PK11195	Clinical	[22–24]
	^{18}F-FEMPA	Mouse	
	^{18}F-GE-180	Mouse	
Mannose receptor	^{68}Ga-NOTA-MSA	Rabbit	[25, 26]
	^{18}F-FDM	Rabbit	
Folate receptor β	^{18}F-FOL	Mouse, rabbit	[27]
Cannabinoid receptor 2	^{11}C-RS-016	Mouse	[28]
Scavenger receptor CD68	^{64}Cu-CD68-Fc	Mouse	[29]
Leukocyte proliferation	^{18}F-FLT	Patients	[30]
		Mouse, rabbit	
Adhesion molecules			
VCAM-1	^{18}F-4V	Mouse	[31]
P-selectin	^{64}Cu-DOTA-anti-P-selectin mAb	Mouse	[32, 33]
	^{68}Ga-Fucoidan	Mouse	
VAP-1	^{68}Ga-DOTA-Siglec-9	Mouse	[34]
Integrins			
$\alpha_v\beta_3$	^{18}F-Fluciclatide	Clinical	[35–40]
	^{18}F-Galacto-RGD	Clinical	
		Mouse	
	^{18}F-Flotegatide	Mouse	
	^{68}Ga-NOTA-RGD	Mouse	

(continued)

Table 1
(continued)

Target	Tracer	Development stage	References
Matrix metalloproteinases			
MMP-2/9	^{68}Ga-DOTA-TCTP-1	Mouse	[41]
Microcalcifications			
Hydroxyapatite	^{18}F-NaF	Clinical	[42, 43]

VCAM-1 vascular cell adhesion protein 1, *VAP-1* vascular adhesion protein 1, *MMP-2/9* matrix metalloproteinase 2/9

4. PET tracer (e.g., ^{18}F-FDG with molar activity of typically ≥74 GBq/μmol at the end of radiosynthesis).
5. CT contrast agent [e.g., iodine-based eXIATM160XL (stock 160 mg/mL)].
6. Dose calibrator (e.g., VDC-404).
7. Glucometer (e.g., Bayer Contour).
8. Centrifuge.
9. PET/CT device (e.g., Inveon Multimodality with Inveon Acquisition Workplace software for image reconstruction or β/X-CUBE with Molecubes software for image reconstruction).
10. Gamma counter (e.g., Triathler 3″).
11. Isoflurane anesthesia unit (if isoflurane anesthesia is used.)
12. Cryomicrotome.
13. Autoradiography scanner (e.g., Fuji Analyzer BAS-5000).
14. Digital slide scanner (e.g., Pannoramic 250 Flash).
15. Injection equipment [catheter (PE10 polyethylene tubing, OD 0.61 mm, ID 0.28 mm), 25G/30G needle and 1 mL syringe].
16. Tubes for blood samples (e.g., heparinized 100 μL Microvette 100 tubes).
17. Anesthetic(s) (e.g., isoflurane [stock 1000 mg/g; 100%], ketamine [stock 50 mg/mL], xylazine [stock 20 mg/mL]).
18. Heating pad.
19. Instruments for dissection (e.g., Iris T/C (tungsten carbide) 11.5 cm scissors; VANNAS spring 8.5 mm scissors; Graefe Iris 10–12 cm tweezers).
20. Vials for tissues (e.g., 5 mL plastic tubes).
21. Optimal cutting temperature (OCT) compound (e.g., TissueTek).
22. Microscope slides (e.g., positively charged Superfrost Ultra Plus slides).

23. Hair dryer.
24. Imaging plate (e.g., Fuji Imaging Plate BAS-TR2025).
25. PET/CT image analysis software (e.g., freely available Carimas software; Turku PET Centre, Turku, Finland, www.turkupetcentre.fi/carimas).
26. Autoradiography image analysis software (e.g., TINA or AIDA software).
27. Pannoramic viewer software (Pannoramic 250 Flash).
28. Sterile saline (0.9% sodium chloride).
29. Isopentane (stock ≥99%).
30. Dry-ice.
31. Hematoxylin (e.g., Mayer's hematoxylin, stock 1 g/L).
32. 0.1% Eosin.
33. Image editing software (e.g., freely available Gimp software).
34. Microsoft Excel.

3 Methods

3.1 In Vivo PET/CT of Small Animals

1. Preconditioning: Fast animal for at least 4 h prior to ^{18}F-FDG imaging.
2. Weigh the animal.
3. Anesthetize the animal with isoflurane (3–4% for induction, 1–2% for maintenance) or injectable anesthetics (e.g., intraperitoneal ketamine [80 mg/kg]/xylazine [10 mg/kg]). Keep the animal warm using a heating pad (*see* **Note 1**).
4. Take a blood sample from the saphenous vein to determine blood glucose level using a glucometer.
5. Insert catheter into the tail vein for injection of ^{18}F-FDG and contrast agent.
6. Place animal on the PET/CT scanner and keep the body temperature steady using a heating pad.
7. Perform a low-dose CT scan for attenuation correction.
8. Inject 5–10 MBq of ^{18}F-FDG (maximum 5 mL/kg in saline) via the tail vein catheter (*see* **Note 2**).
9. At the time of injection, start a 90-min dynamic PET data acquisition or perform a 20 min static acquisition starting at 70 min post-injection.
10. After PET, inject 100 μL iodinated contrast agent (e.g., eXIATM160XL) via the tail vein catheter and acquire high-resolution CT.

11. After imaging, take a blood sample to determine the blood glucose level (*see* **Note 3**).
12. Reconstruct the image data, with example algorithms being:
    (a) PET images: iterative reconstruction with an ordered-subsets expectation maximization 2D algorithm (OSEM2D with two iterations). Reconstructed into 5 × 60 s, 3 × 300 s, 1 × 600 s and 2 × 1800 s time frames (matrix size: 128 × 128 × 159; pixel size: 0.776 × 0.776 × 0.796 mm).
    (b) Contrast-enhanced CT images: a Feldkamp based algorithm (matrix size: 768 × 768 × 923; pixel size: 0.094 × 0.094 × 0.094 mm).
13. Coregister the PET and CT images and analyze them using appropriate software [e.g., the free Carimas software (Turku PET Centre; Turku, Finland, www.turkupetcentre.fi/carimas/].
14. Define regions of interest (ROIs) for the aortic arch, vena cava (representing the blood pool) and myocardium in the coronal or transaxial PET/CT image, using the contrast-enhanced CT images for anatomical reference. Ensure the correct ROI placement in coronal, transaxial, and sagittal views (*see* **Note 4**).
15. The radioactivity in tissues is dependent on the injected radioactivity dose and the animal weight, and these can be standardized to obtain more comparable results between different animals. To do this, export the mean and/or maximum radioactivity concentrations (Bq/mL) within the ROIs; choose the most suitable time frames if dynamic imaging was performed; and calculate the results as percentage injected radioactivity dose per gram of tissue (%ID/g), standardized uptake value (SUV) or target-to-background ratio (TBR). The formulas for %ID/g and SUV are as follows:

$$\%\mathrm{ID/g} = \frac{\mathrm{Tissue\_radioactivity}\ (kBq)/\mathrm{Tissue\_weight}\ (\mathrm{g})}{\mathrm{Injected\_dose}\ (kBq)} \times 100\%$$

$$\mathrm{SUV} = \frac{\mathrm{Tissue\_radioactivity}\ (kBq)/\mathrm{Tissue\_weight}\ (\mathrm{g})}{\mathrm{Injected\_dose}\ (kBq)/\mathrm{Animal\_weight(g)}}$$

Note that the weight (g) can be considered as volume in mL (or cm^3, cubic centimeter; 1 mL = 1 cm^3) in PET images. The plaque-to-blood pool ratio is usually a useful TBR in the imaging of atherosclerosis and can be calculated as $SUV_{max,\ aortic\ arch}/SUV_{mean,\ blood}$ (*see* **Note 5**).

3.2 Ex Vivo Digital Autoradiography

1. After imaging, euthanize the animal by cardiac puncture (to remove blood) under deep isoflurane anesthesia, followed by cervical dislocation. Open the thorax and inject saline into the left ventricle to remove the remaining blood from the aorta.

Excise the thoracic aorta from the sinotubular junction to the level of the diaphragm and rinse with saline. Carefully remove the surrounding adventitial tissue and place the excised aorta in an anatomically relevant position (*see* **Note 6**).

2. At this point, the aorta can be weighed and measured for total radioactivity using a gamma counter, if required.
3. Embed the aorta in optimal cutting temperature (OCT) compound, freeze in dry ice–cooled isopentane and cut into sequential longitudinal cryosections of 20 and 8 μm using a microtome. Place the sections on microscopy slides such that one slide consists of 6–8 sections through the aorta (Fig. 1). With mice, there are typically enough sections for 4 × 20 μm and 5 × 8 μm slides.
4. Air dry the cryosections with a gently blowing of an ordinary hair dryer for 1–2 min and place the slides under a radiation-sensitive imaging plate for a specific time, depending on the radionuclide decay (typically two physical half-lives, i.e., 4 h for ^{18}F-FDG).
5. Scan the imaging plate with a Fuji Analyzer BAS-5000 (internal resolution of 25 μm) and save the images as original .inf files.
6. Stain the 20 μm sections with hematoxylin and eosin (H&E) for general histology (*see* **Note 7**). The most convenient way to create images from histological sections is to scan the slides with a digital slide scanner. This allows the simultaneous analysis of all sections on a single slide. Images of the histology staining can also be obtained using a microscope camera.
7. Define ROIs on the autoradiography image on the basis of the histology findings. Determine ROI categories (which areas are defined as ROIs and how) in a prespecified manner before starting the analysis.
8. Analyse throughout the aorta, not only on single sections. It is recommended to analyze a minimum of six sections of the aorta (*see* **Note 8**).
9. A so-called contour image can be produced to make the analysis easier to perform and improve reliability. Mark the outlines of the aorta; choose the areas where the ROIs are going to be defined in the histology image; move the alignment of contour lines to the autoradiography image (Fig. 1). This can be easily performed with image editing software (e.g., the freely available Gimp software; *see* **Note 9**).
10. Open the original or contour autoradiography image (e.g., with AIDA or TINA image analysis software). Keep the colors as black and white or adjust to rainbow colors (*see* **Note 10**). Using a freehand ROI-tool (pen) or other tools, draw the ROIs on atherosclerotic lesions and on vessel walls without

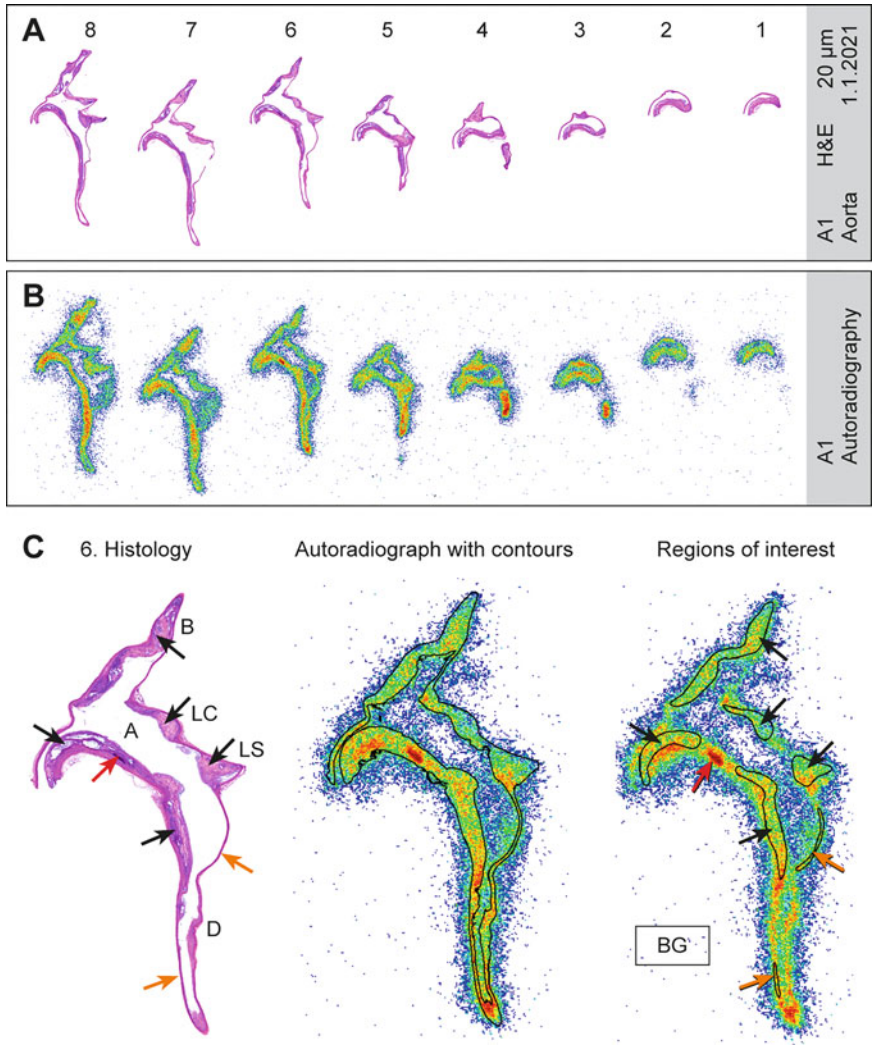

Fig. 1 Digital autoradiography analysis. Hematoxylin and eosin (H&E)-stained longitudinal cryosections throughout the aorta (**a**) and the corresponding autoradiographs (**b**). An example of the definition of regions of interest (ROIs) in the autoradiograph (**c**). Addition of aortic contours from the H&E image to the autoradiograph may help to distinguish between atherosclerotic lesions and the vessel wall. ROIs should be carefully drawn in the atherosclerotic lesions (black arrows) and lesion-free vessel walls (orange arrows). Calcified areas should be avoided (red arrow) and a background (BG) ROI should be added. A minimum of six sections throughout the aorta should be analyzed (e.g., sections 3 to 8). For panel C, A: aortic arch, B: brachiocephalic artery, D: descending thoracic aorta, LC: left common carotid artery, LS: left subclavian artery

lesions (*see* **Note 11**). One ROI should also be defined for the background. Check the histology for every ROI drawn to make sure that the ROI is in the right position and to avoid sites showing artifacts. The drawn ROIs can be saved as a separate template for later analysis (*see* **Note 12**).

11. Select the region report window, choose the background ROI and label it as the background. This will allow automatic subtraction of the background radioactivity from the tissue data. Export the data to Microsoft Excel. The column that should be used is photostimulated luminescence per square millimeter, background (Bkg) subtracted ([PSL-Bkg]/mm^2).
12. For every animal, calculate the mean (PSL-Bkg)/mm^2 value for each different ROI category. For example, the typical number of ROIs drawn for a mouse is 20–25 for atherosclerotic lesions and 15–20 for lesion-free vessel walls. When the mean values are calculated, there will be one data value for the lesions and one for the vessel walls for each mouse. From these mean values, the TBR (i.e., the lesion-to-wall ratio) can be calculated for each mouse.
13. Compare the resulting (PSL-Bkg)/mm^2 values and/or TBR values between study groups. If absolute (PSL-Bkg)/mm^2 values are compared between groups, it is good practice to decay-correct the results to injection time and exposure time and normalize the results for the injected radioactivity dose per animal weight (*see* **Note 13**).

3.3 Clinical PET

1. Check that the prescan blood glucose level is <7.0–7.2 mmol/L (*see* **Note 14**).
2. Inject ^{18}F-FDG as a bolus of 3–4 MBq/kg of body weight (*see* **Note 15**).
3. Keep the delay between ^{18}F-FDG injection and PET acquisition at 2 h, as recommended (*see* **Note 16**).
4. Follow the recommended scan and reconstruction parameters whenever possible: Measurement of radiotracer uptake in arterial lesions is challenging because of the small size of the lesions. Optimize patient positioning to avoid motion artifacts. Partial volume effects cause underestimation in structures that are smaller than the spatial resolution of the scanner. To reduce such errors in radioactivity measurement, the following parameters have been proposed: acquisition of 8 min, reconstruction using a point spread function, $1 \times 1 \times 1$ mm voxel size, no post filtering and at least 120 iterations using OSEM.
5. Quantification of ^{18}F-FDG uptake: For atherosclerosis imaging, the TBR is recommended over the SUV to correct for blood-pool radioactivity. Calculate the TBR as the ratio of the maximum SUV_{max} measured in atherosclerotic plaques or the arterial vessel wall to the venous blood-pool mean SUV_{mean} (*see* **Note 17**). Depending on the aim of the study, three different approaches for the quantitative assessment of ^{18}F-FDG uptake in a target vessel can be used: measurement of the average TBR (either TBR_{mean} or TBR_{max}) along all the axial segments that

comprise the target vessel; measurement of the average TBR_{max} in a small segment of the index vessel with the highest ^{18}F-FDG uptake (the most diseased segment, MDS); and measurement of the ^{18}F-FDG uptake only in arterial locations meeting a predefined ^{18}F-FDG uptake (active segment, AS).

4 Notes

1. Keep the preconditions and animal handling (e.g., fasted, warmed, anesthetized) standardized throughout the study as these variables have a major effect on the ^{18}F-FDG biodistribution [44]. The choice of anesthetic can also have profound effects on cardiomyocyte ^{18}F-FDG uptake (i.e., ^{18}F-FDG uptake can be higher under continuous isoflurane anesthesia than after ketamine–xylazine administration) [45].
2. Attention must be paid to avoid bubbles and to not inject excessive volumes at high speed. Aim for a bolus injection with a low volume. The intraperitoneal injection route is also possible, but slower tracer kinetics need to be taken into account.
3. If the blood glucose values vary a lot between animals, the imaging results can be normalized to the mean glucose value of the study group.
4. The blood-pool ROI can be defined according to the tracer used (e.g., from the vena cava or left ventricle cavity).
5. If all the studied animals are about the same weight, then %ID/g can be used. SUV is better when animals show a lot of variation in their weight (e.g., when using both genders and/or animals of different ages). When imaging structures with sizes around or below the resolution of the scanner, such as plaques, it is important to realize that partial volume effects can cause a substantial underestimation of the true value. Recent technical developments allow echocardiogram (ECG)-gating in preclinical imaging, which may improve the quality of images of moving structures like the heart.
6. Keep the aorta wet all the time with saline to avoid drying. If the tissue dries, it causes artifacts/overestimation of the tracer signal in the autoradiography image.
7. The parallel 8 μm sections can be used for immunohistochemical or immunofluorescence staining (e.g., for macrophage staining).
8. Both 20 μm and 8 μm sections can be used for autoradiography image analysis, but 20 μm sections produce more signal.

9. Open the original autoradiography file (e.g., with AIDA or TINA image analysis software) and save the slide you wish to use in the analysis as .TIFF and .pcb files. It is important that the .TIFF and .pcb represent exactly the same original autoradiography file. The contour lines are added to the .TIFF autoradiography image.
10. It is a good idea to maintain the black-and-white color scale, as a rainbow color scale can sometimes bias the selection and drawing toward hot-spot areas.
11. Select and draw ROIs in all representative atherosclerotic lesions throughout the sections, with the exception of those with calcification. If the lesion is big, it is possible to exclude calcified areas (spill-over effect) by leaving a "safety margin" (Fig. 1). Select the lesion-free vessel wall areas ensuring that they are separate from the lesions.
12. If the contour autoradiography image is used, the ROIs are drawn on the .TIFF image, saved as a template and then opened again in the .pcb file to export the results as (PSL-Bkg)/mm^2 values.
13. For technical reasons, the time spent cutting the aorta can sometimes vary between mice, and this can be taken into account by calculating a decay correction. Furthermore, if the weights of the mice differ and they have been injected with the same amount of tracer, it is recommended to normalize the results according to animal weight. If only TBR values are used, no corrections are needed.
14. Higher blood glucose levels are associated with increased ^{18}F-FDG blood-pool radioactivity, which is used as a denominator when quantifying ^{18}F-FDG uptake. In patients with high blood glucose levels, administration of rapid-acting insulin may be considered to lower blood glucose levels. Alternatively, correction of vascular ^{18}F-FDG uptake according to EANM recommendations for oncological PET imaging may be considered.
15. Lower ^{18}F-FDG activities may be considered for repeated PET studies and when using sensitive PET scanners.
16. Longer delays than those used for oncology are recommended to allow sufficient ^{18}F-FDG accumulation in the arterial wall and to reduce the intensity of the ^{18}F-FDG signal in the blood.
17. For region-of-interest (ROI) definition, anatomical reference images such as CT or MRI are needed, and care should be taken to avoid any interference from high ^{18}F-FDG uptake in tissues adjacent to the vessel wall or blood pool, such as myocardium or lymph nodes. ^{18}F-FDG blood-pool radioactivity should be measured in a venous structure close to the target

artery, allowing data acquisition in the same bed position of the PET scan.

Acknowledgments

This work was supported by the Jane and Aatos Erkko Foundation and the Finnish Foundation for Cardiovascular Research.

References

1. Dweck MR, Aikawa E, Newby DE, Tarkin JM, Rudd JHF, Narula J, Fayad ZA (2016) Noninvasive molecular imaging of disease activity in atherosclerosis. Circ Res 119:330–340
2. Hyafil F, Vigne J (2019) Nuclear imaging focus on vascular probes. Arterioscler Thromb Vasc Biol 39:1369–1378
3. Cicone F, Viertl D, Quintela Pousa AM, Denoël T, Gnesin S, Scopinaro F, Vozenin M-C, Prior JO (2017) Cardiac radionuclide imaging in rodents: a review of methods, results, and factors at play. Front Med 4:35
4. Meester EJ, Krenning BJ, de Swart J, Segbers M, Barrett HE, Bernsen MR, Van der Heiden K, de Jong M (2019) Perspectives on small animal radionuclide imaging; considerations and advances in atherosclerosis. Front Med 6:39
5. Bucerius J, Hyafil F, Verberne HJ, Slart RH, Lindner O, Sciagra R, Agostini D, Übleis C, Gimelli A, Hacker M, Cardiovascular Committee of the European Association of Nuclear Medicine (EANM) (2016) Position paper of the Cardiovascular Committee of the European Association of Nuclear Medicine (EANM) on PET imaging of atherosclerosis. Eur J Nucl Med Mol Imaging 43:780–792
6. Slart RHJA, Writing group; Reviewer group; Members of EANM Cardiovascular; Members of EANM Infection & Inflammation; Members of Committees, SNMMI Cardiovascular; Members of Council, PET Interest Group; Members of ASNC; EANM Committee Coordinator (2018) FDG-PET/CT(A) imaging in large vessel vasculitis and polymyalgia rheumatica: joint procedural recommendation of the EANM, SNMMI, and the PET Interest Group (PIG), and endorsed by the ASNC. Eur J Nucl Med Mol Imaging 45:1250–1269
7. RHJA S, AWJM G, Gheysens O, Lubberink M, Kero T, Dweck MR, Habib G, Gaemperli O, Saraste A, Gimelli A, Georgoulias P, Verberne HJ, Bucerius J, Rischpler C, Hyafil F, Erba PA, 4Is Cardiovascular Imaging: a joint initiative of the European Association of Cardiovascular Imaging (EACVI); European Association of Nuclear Medicine (EANM) (2020) Procedural recommendations of cardiac PET/CT imaging: standardization in inflammatory-, infective-, infiltrative-, and innervation (4Is)-related cardiovascular diseases: a joint collaboration of the EACVI and the EANM. Eur J Nucl Med Mol Imaging 21:1320–1330
8. Rudd JHF, Warburton TD, Fryer HA, Jones JC, Clark N, Antoun P, Johnström AP, Davenport PJ, Kirkpatrick BN, Arch JDP, Weissberg PL (2002) Imaging atherosclerotic plaque inflammation with [^{18}F]-fluorodeoxyglucose positron emission tomography. Circulation 105:2708–2711
9. Rudd JHF, Myers KS, Bansilal S, Machac J, Woodward M, Fuster V, Farkouh ME, Fayad ZA (2009) Relationships among regional arterial inflammation, calcification, risk factors, and biomarkers: A prospective fluorodeoxyglucose positron-emission tomography/computed tomography imaging study. Circ Cardiovasc Imaging 2:107–115
10. Silvola JMU, Saraste A, Laitinen I, Savisto N, Laine VJO, Heinonen SE, Ylä-Herttuala S, Saukko P, Nuutila P, Roivainen A, Knuuti J (2011) Effects of age, diet, and type 2 diabetes on the development and FDG uptake of atherosclerotic plaques. JACC Cardiovasc Imaging 4:1294–1301
11. Tawakol A, Migrino RQ, Hoffmann U, Abbara S, Houser S, Gewirz H, Muller JE, Brady TJ, Fischman AJ (2005) Noninvasive in vivo measurement of vascular inflammation with F-18 fluorodeoxyglucose positron emission tomography. J Nucl Cardiol 12:294–301
12. Tarkin JM, Joshi FR, Evans NR, Chowdhury MM, Figg NL, Shah AV, Starks LT, Martin-Garrido A, Manavaki R, Yu E, Kuc RE, Grassi L, Kreuzhuber R, Kostadima MA, Frontini M, Kirkpatrick PJ, Coughlin PA, Gopalan D, Fryer TD, Buscombe JR, Groves AM, Ouwehand WH, Bennett MR, Warburton EA, Davenport AP, Rudd JHF (2017)

Detection of atherosclerotic inflammation by ^{68}Ga-DOTATATE PET compared to [^{18}F] FDG PET imaging. J Am Coll Cardiol 69: 1774–1791

13. Li X, Bauer W, Kreissl MC, Weirather J, Bauer E, Israel I, Richter D, Riehl G, Buck A, Samnick S (2013) Specific somatostatin receptor II expression in arterial plaque: ^{68}Ga-DOTATATE autoradiographic, immunohistochemical and flow cytometric studies in apoE-deficient mice. Atherosclerosis 230:33–39
14. Pedersen SF, Sandholt BV, Keller SH, Hansen AE, Clemmensen AE, Sillesen H, Højgaard L, Sejersten Ripa R, Kjær A (2015) ^{64}Cu-DOTATATE PET/MRI for detection of activated macrophages in carotid atherosclerotic plaques: studies in patients undergoing endarterectomy. Arterioscler Thromb Vasc Biol 35: 1696–1703
15. Rinne P, Hellberg S, Kiugel M, Virta J, Li XG, Käkelä M, Helariutta K, Luoto P, Liljenbäck H, Hakovirta H, Gardberg M, Airaksinen AJ, Knuuti J, Saraste A, Roivainen A (2015) Comparison of somatostatin receptor 2-targeting PET tracers in the detection of mouse atherosclerotic plaques. Mol Imaging Biol 18:99–108
16. Derlin T, Sedding DG, Dutzmann J, Haghikia A, König T, Napp LC, Schütze C, Owsianski-Hille N, Wester HJ, Kropf S, Thackeray JT, Bankstahl JP, Geworski L, Ross TL, Bauersachs J, Bengel FM (2018) Imaging of chemokine receptor CXCR4 expression in culprit and nonculprit coronary atherosclerotic plaque using motion-corrected [^{68}Ga]pentixafor PET/CT. Eur J Nucl Med Mol Imaging 45:1934–1944
17. Li X, Heber D, Leike T, Beitzke D, Lu X, Zhang X, Wei Y, Mitterhauser M, Wadsak W, Kropf S, Wester HJ, Loewe C, Hacker M, Haug AR (2018) [^{68}Ga]Pentixafor-PET/MRI for the detection of chemokine receptor 4 expression in atherosclerotic plaques. Eur J Nucl Med Mol Imaging 45:558–566
18. Hyafil F, Pelisek J, Laitinen I, Schottelius M, Mohring M, Döring Y, van der Vorst EPC, Kallmayer M, Steiger K, Poschenrieder A, Notni J, Fischer J, Baumgartner C, Rischpler C, Nekolla SG, Weber C, Eckstein HH, Wester HJ, Schwaiger M (2017) Imaging the cytokine receptor CXCR4 in atherosclerotic plaques with the radiotracer ^{68}Ga-Pentixafor for PET. J Nucl Med 58:499–506
19. Vöö S, Kwee RM, Sluimer JC, Schreuder FHBM, Wierts R, Bauwens M, Heeneman S, Cleutjens JPM, Van Oostenbrugge RJ, Daemen JWH, Daemen MJAP, Mottaghy FM, Kooi ME (2016) Imaging intraplaque inflammation in carotid atherosclerosis with ^{18}F-fluorocholine positron emission tomography-computed tomography. Circ Cardiovasc Imaging 9:e004467
20. Hellberg S, Silvola JMU, Kiugel M, Liljenbäck H, Metsälä O, Viljanen T, Metso J, Jauhiainen M, Saukko P, Nuutila P, Ylä-Herttuala S, Knuuti J, Roivainen A, Saraste A (2016) Type 2 diabetes enhances arterial uptake of choline in atherosclerotic mice: an imaging study with positron emission tomography tracer ^{18}F-fluoromethylcholine. Cardiovasc Diabetol 15:26
21. Laitinen IEK, Luoto P, Någren K, Marjamäki PM, Silvola JMU, Hellberg S, Laine VJO, Ylä-Herttuala S, Knuuti J, Roivainen A (2010) Uptake of ^{11}C-choline in mouse atherosclerotic plaques. J Nucl Med 51:798–802
22. Gaemperli O, Shalhoub J, Owen DRJ, Lamare F, Johansson S, Fouladi N, Davies AH, Rimoldi OE, Camici PG (2012) Imaging intraplaque inflammation in carotid atherosclerosis with ^{11}C-PK11195 positron emission tomography/computed tomography. Eur Heart J 33:1902–1910
23. Hellberg S, Silvola JMU, Kiugel M, Liljenbäck H, Savisto N, Li XG, Thiele A, Lehmann L, Heinrich T, Vollmer S, Hakovirta H, Laine VJO, Ylä-Herttuala S, Knuuti J, Roivainen A, Saraste A (2017) 18-kDa translocator protein ligand ^{18}F-FEMPA: biodistribution and uptake into atherosclerotic plaques in mice. J Nucl Cardiol 24:862–871
24. Hellberg S, Liljenbäck H, Eskola O, Morisson-Iveson V, Morrison M, Trigg W, Saukko P, Ylä-Herttuala S, Knuuti J, Saraste A, Roivainen A (2018) Positron emission tomography imaging of macrophages in atherosclerosis with ^{18}F-GE-180, a radiotracer for translocator protein (TSPO). Contrast Media Mol Imaging 2018:9186902
25. Kim EJ, Kim S, Seo HS, Lee YJ, Eo JS, Jeong JM, Lee B, Kim JY, Park YM, Jeong M (2016) Novel PET imaging of atherosclerosis with ^{68}Ga-labeled NOTA-Neomannosylated human serum albumin. J Nucl Med 57: 1792–1797
26. Tahara N, Mukherjee J, De Haas HJ, Petrov AD, Tawakol A, Haider N, Tahara A, Constantinescu CC, Zhou J, Boersma HH, Imaizumi T, Nakano M, Finn A, Fayad Z, Virmani R, Fuster V, Bosca L, Narula J (2014) 2-deoxy-2-[^{18}F]fluoro-D-mannose positron emission tomography imaging in atherosclerosis. Nat Med 20:215–219
27. Silvola JMU, Li XG, Virta J, Marjamäki P, Liljenbäck H, Hytönen JP, Tarkia M, Saunavaara V, Hurme S, Palani S,

Hakovirta H, Ylä-Herttuala S, Saukko P, Chen Q, Low PS, Knuuti J, Saraste A, Roivainen A (2018) Aluminum fluoride-18 labeled folate enables in vivo detection of atherosclerotic plaque inflammation by positron emission tomography. Sci Rep 8:9720

28. Meletta R, Slavik R, Mu L, Rancic Z, Borel N, Schibli R, Ametamey SM, Krämer SD, Müller HA (2017) Cannabinoid receptor type 2 (CB2) as one of the candidate genes in human carotid plaque imaging: evaluation of the novel radiotracer [^{11}C]RS-016 targeting CB2 in atherosclerosis. Nucl Med Biol 47: 31–43
29. Bigalke B, Phinikaridou A, Andia ME, Cooper MS, Schuster A, Wurster T, Onthank D, Münch G, Blower P, Gawaz M, Nagel E, Botnar RM (2014) PET/CT and MR imaging biomarker of lipid-rich plaques using [^{64}Cu]-labeled scavenger receptor (CD68-Fc). Int J Cardiol 177:287–291
30. Ye YX, Calcagno C, Binderup T, Courties G, Keliher EJ, Wojtkiewicz GR, Iwamoto Y, Tang J, Pérez-Medina C, Mani V, Ishino S, Johnbeck CB, Knigge U, Fayad ZA, Libby P, Weissleder R, Tawakol A, Dubey S, Belanger AP, Di Carli MF, Swirski FK, Kjaer A, Mulder WJM, Nahrendorf M (2015) Imaging macrophage and hematopoietic progenitor proliferation in atherosclerosis. Circ Res 117:835–845
31. Nahrendorf M, Keliher E, Panizzi P, Zhang H, Hembrador S, Figueiredo JL, Aikawa E, Kelly K, Libby P, Weissleder R (2009) ^{18}F-4V for PET-CT Iiaging of VCAM-1 expression in atherosclerosis. JACC Cardiovasc Imaging, 2: 1213–1222
32. Nakamura I, Hasegawa K, Wada Y, Hirase T, Node K, Watanabe Y (2013) Detection of early stage atherosclerotic plaques using PET and CT fusion imaging targeting P-selectin in low density lipoprotein receptor-deficient mice. Biochem Biophys Res Commun 433:47–51
33. Li X, Bauer W, Israel I, Kreissl MC, Weirather J, Richter D, Bauer E, Herold V, Jakob P, Buck A, Frantz S, Samnick S (2014) Targeting p-selectin by gallium-68-labeled fucoidan positron emission tomography for noninvasive characterization of vulnerable plaques: correlation with in vivo 17.6t mri. Arterioscler Thromb Vasc Biol 34:1661–1667
34. Silvola JMU, Virtanen H, Siitonen R, Hellberg S, Liljenbäck H, Metsälä O, Ståhle M, Saanijoki T, Käkelä M, Hakovirta H, Ylä-Herttuala S, Saukko P, Jauhiainen M, Veres TZ, Jalkanen S, Knuuti J, Saraste A, Roivainen A (2016) Leukocyte trafficking-associated vascular adhesion protein 1 is expressed and functionally active in atherosclerotic plaques. Sci Rep 6:35089
35. Jenkins WS, Vesey AT, Vickers A, Neale A, Moles C, Connell M, Joshi NV, Lucatelli C, Fletcher AM, Spratt JC, Mirsadraee S, Van Beek EJR, Rudd JHF, Newby DE, Dweck MR (2019) In vivo alpha-V beta-3 integrin expression in human aortic atherosclerosis. Heart 105:1868–1875
36. Beer AJ, Pelisek J, Heider P, Saraste A, Reeps C, Metz S, Seidl S, Kessler H, Wester HJ, Eckstein HH, Schwaiger M (2014) PET/CT imaging of integrin αvβ3 expression in human carotid atherosclerosis. JACC Cardiovasc Imaging 7:178–187
37. Laitinen I, Saraste A, Weidl E, Poethko T, Weber AW, Nekolla SG, Leppänen P, Ylä-Herttuala S, Hölzlwimmer G, Walch A, Esposito I, Wester HJ, Knuuti J, Schwaiger M (2009) Evaluation of alphavbeta3 integrin-targeted positron emission tomography tracer ^{18}F-galacto-RGD for imaging of vascular inflammation in atherosclerotic mice. Circ Cardiovasc Imaging 2:331–338
38. Su H, Gorodny N, Gomez LF, Gangadharmath UB, Mu F, Chen G, Walsh JC, Szardenings K, Berman DS, Kolb HC, Tamarappoo BK (2014) Atherosclerotic plaque uptake of a novel integrin tracer ^{18}F-Flotegatide in a mouse model of atherosclerosis. J Nucl Cardiol 21:553–562
39. Haukkala J, Laitinen I, Luoto P, Iveson P, Wilson I, Karlsen H, Cuthbertson A, Laine J, Leppänen P, Ylä-Herttula S, Knuuti J, Roivainen A (2009) ^{68}Ga-DOTA-RGD peptide: biodistribution and binding into atherosclerotic plaques in mice. Eur J Nucl Med Mol Imaging 36:2058–2067
40. Paeng JC, Lee YS, Lee JS, Jeong JM, Kim KB, Chung JK, Lee DS (2013) Feasibility and kinetic characteristics of ^{68}Ga-NOTA-RGD PET for in vivo atherosclerosis imaging. Ann Nucl Med 27:847–854
41. Kiugel M, Hellberg S, Käkelä M, Liljenbäck H, Saanijoki T, Li XG, Tuomela J, Knuuti J, Saraste A, Roivainen A (2018) Evaluation of [^{68}Ga]Ga-DOTA-TCTP-1 for the detection of metalloproteinase 2/9 expression in mouse atherosclerotic plaques. Molecules 23:3168
42. Dweck MR, Chow MW, Joshi NV, Williams MC, Jones C, Fletcher AM, Richardson H, White A, McKillop G, van Beek EJ, Boon NA, Rudd JH, Newby DE (2012) Coronary arterial ^{18}F-sodium fluoride uptake: a novel marker of plaque biology. J Am Coll Cardiol 59: 1539–1548
43. Joshi NV, Vesey AT, Williams MC, Shah ASV, Calvert PA, Craighead FHM, Yeoh SE,

Wallace W, Salter D, Fletcher AM, Van Beek EJR, Flapan AD, Uren NG, Behan MWH, Cruden NLM, Mills NL, Fox KAA, Rudd JH F, Dweck MR, Newby DE (2014) ^{18}F-fluoride positron emission tomography for identification of ruptured and high-risk coronary atherosclerotic plaques: A prospective clinical trial. Lancet 383:705–713

44. Fueger BJ, Czernin J, Hildebrandt I, Tran C, Halpern BS, Stout D, Phelps ME, Weber WA (2006) Impact of animal handling on the results of ^{18}F-FDG PET studies in mice. J Nucl Med 47:999–1006
45. Thackeray JT, Bankstahl JP, Wang Y, Wollert KC, Bengel FM (2015) Clinically relevant strategies for lowering cardiomyocyte glucose uptake for ^{18}F-FDG imaging of myocardial inflammation in mice. Eur J Nucl Med Mol Imaging 42:771–780

Chapter 51

Three-Dimensional Visualization of Atherosclerotic Vessels by Tissue Clearing and Light-Sheet Fluorescence Microscopy

Tobias Becher, Dario F. Riascos-Bernal, Jingyi Chi, Paul Cohen, and Nicholas E. S. Sibinga

Abstract

Although arteries and atherosclerotic plaques are three-dimensional structures, the evaluation of plaque size and morphology in preclinical models of atherosclerosis is typically performed in two dimensions by histological analysis. Here, we describe a method to visualize arteries and atherosclerotic plaques in three dimensions. This method combines AdipoClear, a procedure that achieves whole tissue immunolabeling and clearing, and light-sheet fluorescence microscopy, which generates a three-dimensional reconstruction of vessel architecture including atherosclerotic lesions if present. This approach reveals the volume, geometry, acellular component and surface of atherosclerotic plaques as well as the spatial position of the lesion in relation to the affected artery.

Key words 3D imaging, Atherosclerosis, Tissue clearing, Light-sheet microscopy, Endothelium

1 Introduction

Atherosclerosis is a multifactorial chronic disease of the arterial wall and understanding of its pathogenesis is incomplete [1]. Preclinical models of this disease, particularly those based on genetically modified mice, provide important tools to evaluate molecular cause-effect mechanisms involved in atherosclerosis initiation and progression. Scoring the atherosclerotic phenotype in preclinical models typically entails the use of histological techniques that allow evaluation of lesion size and morphology in two dimensions at specific regions of an artery, usually the brachiocephalic artery or the aortic root [2, 3]. Although serial cutting and assessment of multiple arterial sections can be performed, every section is not

Tobias Becher and Dario F. Riascos-Bernal contributed equally to this work.

Dipak P. Ramji (ed.), *Atherosclerosis: Methods and Protocols*, Methods in Molecular Biology, vol. 2419,
https://doi.org/10.1007/978-1-0716-1924-7_51,
© The Author(s), under exclusive license to Springer Science+Business Media, LLC, part of Springer Nature 2022

stained and accounted for when scoring the phenotype. Another two-dimensional approach routinely performed to assess the extent of atherosclerosis is the en face preparation of the aorta [4], which quantifies the aortic area affected by the disease. None of these methods, however, reveal the overall three-dimensional geometry, volume, topology, and luminal surface of atherosclerotic lesions within the intact vessel.

Here, we describe a method that we have recently developed to generate three-dimensional reconstructions of arteries with and without atherosclerosis [5]. Our approach combines AdipoClear, a procedure that allows immunolabeling and clearing of intact tissue [6] and light-sheet fluorescence microscopy to visualize the three dimensional architecture of the vessel. This method provides information required to derive and observe the overall geometry, volume, topology and luminal surface of atherosclerotic lesions within the affected artery. Our method follows four major steps: vessel harvesting and fixation; tissue immunolabeling and clearing; light-sheet fluorescence microscopy; and image processing and analysis. These steps will be described in detail below for the evaluation of brachiocephalic arteries from mouse models of atherosclerosis such as Apolipoprotein E deficient mice ($Apoe^{-/-}$) fed with a high fat diet, but they can be easily adapted to test other arteries or samples from different models of atherosclerosis.

2 Materials

2.1 Vessel Harvesting and Fixation

1. Phosphate-buffered saline (PBS).
2. General anesthesia: mixture of ketamine (90 mg/kg) and xylazine (10 mg/kg) in PBS or other anesthetic approved by the Institutional Animal Care and Use Committee (*see* **Note 1**).
3. 10% buffered formalin phosphate.
4. PBS containing 0.02% NaN_3 (*see* **Note 2**).
5. 26G needles and 1 mL syringes.
6. 23G butterfly needles.
7. Stereomicroscope for animal surgery and dissection.
8. Dissecting scissors and forceps.
9. Electrical clippers.
10. 1.5 mL tubes.
11. Infusion apparatus.
12. Horizontal shaker.

2.2 Adipo-Clear

1. 2 mL safe-lock tubes.
2. UltraPure agarose.

3. Weighing dish.
4. Triton X-100.
5. Glycine.
6. 10 M NaOH solution.
7. 20% NaN_3 stock solution (*see* **Note 2**).
8. Tween 20.
9. 20 mg/mL heparin sodium salt solution in water.
10. Milli-Q water.
11. PBS.
12. Dichloromethane (DCM).
13. Dibenzyl ether (DBE).
14. Methanol.
15. TO-PRO-3 Iodide.
16. Goat polyclonal antibody against mouse CD31/PECAM-1 IgG (R&D AF3628).
17. Rat monoclonal antibody against mouse CD68 (Bio-Rad MCA 1957T).
18. Donkey anti-goat Alexa Fluor 568 (Invitrogen A-11057).
19. Donkey anti-rat Alexa Fluor 790 (Jackson Immuno Research 712-655-153).
20. B1N buffer: 1 mL Triton X-100, 22.6 g glycine, 0.1 mL NaOH, 0.5 mL NaN_3. Add Milli-Q water to a final volume of 1000 mL, pH 7.0–7.4. Store at room temperature (RT).
21. PTxwH Buffer: 1.0 mL Triton X-100, 0.5 mL Tween 20, 0.1 mL heparin sodium salt (from 20 mg/mL stock solution), 1.0 mL NaN_3. Add PBS to 1000 mL, pH 7.4. Store at RT.
22. Container filled with crushed ice.

2.3 Light Sheet Fluorescence Microscopy

1. Ultramicroscope II (LaVision Biotec, Bielefeld, Germany).
2. sCMOS camera (Andor Neo, Oxford Instruments Group, Belfast, UK).
3. LVMI-Fluor 1.3×/0.1 (LaVision Biotec, Bielefeld, Germany).
4. LVMI-Fluor 4×/0.3 (LaVision Biotec, Bielefeld, Germany).
5. ImspectorPro software (LaVision Biotec, Bielefeld, Germany).

2.4 Image Processing and Analysis

1. Imaris File Converter (version 9.1.1, Bitplane, Belfast, UK).
2. Imaris software (version 9.2.1, Bitplane, Belfast, UK).

3 Methods

3.1 Vessel Harvesting and Fixation

1. Anesthetize a mouse by intraperitoneal injection of ketamine and xylazine, 90 mg/kg and 10 mg/kg respectively and wait until the animal reaches a surgical plane of anesthesia (*see* **Notes 1** and **3**). Remove hair across the thorax and abdomen with electric clippers.
2. With the mouse in supine position, incise the abdominal wall along the midline 1 cm below the xiphoid process, open the peritoneal cavity without damaging internal organs and then extend the incision transversely toward both flanks.
3. Gently pull up the xiphoid process, visualize the diaphragm, make a small incision in the diaphragm, wait for the lungs to collapse, and extend the incision toward both flanks.
4. Cut the ribcage at both parasternal lines, grasp the xiphoid process, and lift and flip over the sternum to visualize the beating heart.
5. Under the dissecting stereomicroscope, make a small nick on the right atrium and introduce into the left ventricle, following an apex-to-base direction, a 23G butterfly needle connected to an infusion apparatus to perfuse the circulatory system with PBS at physiological pressure (*see* **Note 4**). Continue PBS infusion until the circulation is cleared of blood, which usually takes between 1 and 2 min.
6. Using the same 23G butterfly needle and the infusion apparatus, perfuse the circulatory system with 10% buffered formalin phosphate at physiological pressure for 7 min to achieve fixation in situ (*see* **Note 5**).
7. In order to obtain the brachiocephalic artery, under the stereomicroscope, dissect and visualize the aortic arch, brachiocephalic artery, the proximal region of the right subclavian artery, and the proximal region of the right common carotid artery. Harvest the brachiocephalic artery from its origin in the aortic arch to its bifurcation (*see* **Note 6**) and place it in a 1.5 mL tube containing 10% buffered formalin phosphate for further fixation at 4 °C overnight.
8. Gently wash the artery with PBS three times for 1 h each on a horizontal shaker to remove fixative. The fixed sample is now ready for the next step.
9. If the artery cannot be immediately processed, it can be stored in PBS containing 0.02% NaN_3 at 4 °C in the dark.

3.2 Adipo-Clear

An overview of sample preparation, image acquisition and analysis are depicted in Fig. 1.

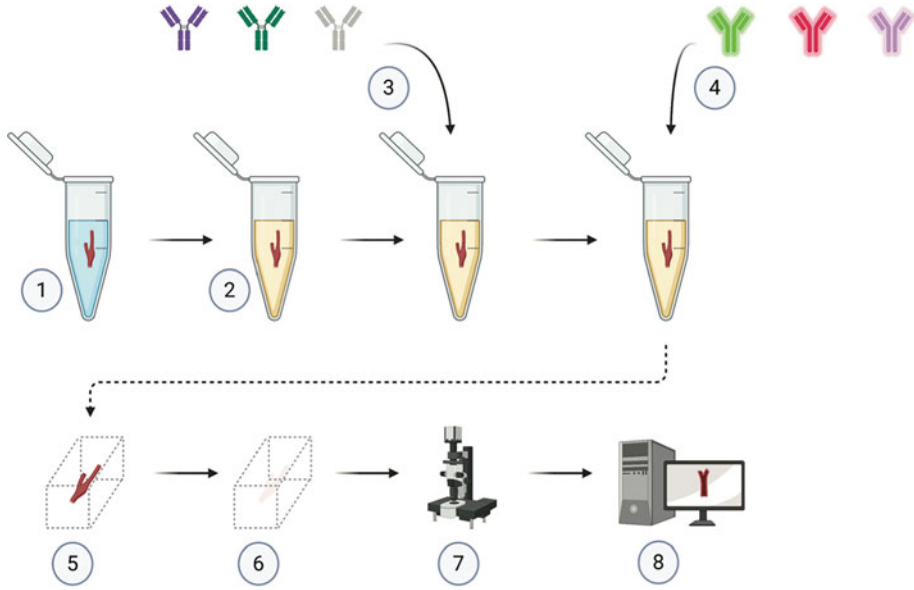

Fig. 1 Overview of sample preparation and image acquisition. These steps include delipidation and rehydration (1), incubation in staining buffer (2), addition of primary (3) and secondary antibodies plus molecular probes such as nuclear stain (4), embedding in agarose (5), clearing (6), light-sheet microscopy (7), and image analysis (8) (Created with BioRender.com)

1. Remove any hair and lint that may be attached to the sample and trim excess perivascular fat using fine scissors and tweezers under a dissection microscope.
2. Depending on vessel size and purpose of imaging, trim vessel to the desired size (*see* **Note 7**). Place vessel in a 2 mL safe-lock tube. All subsequent solutions should be added at a volume of 1.6 mL unless stated otherwise.
3. Begin delipidation by adding 20% methanol and 80% B1N buffer. Place tubes horizontally on top of a container filled with crushed ice. Place the container on top of a horizontal shaker, the vessel should move freely in the liquid during the shaking process. Incubate for 30 min (*see* **Note 8**).
4. Change the solution subsequently to 40% methanol and 60% B1N buffer, 60% methanol and 40% B1N buffer, 80% methanol and 20% B1N buffer and 100% methanol and incubate while shaking for 30 min each on ice (*see* **Note 9**).
5. Change the solution to 1.0 mL DCM and incubate for 30 min while shaking followed by 1 h in 1.6 mL of fresh DCM and another 30 min in 1.6 mL fresh DCM (*see* **Note 10**).
6. Rehydrate the sample in 100% methanol (twice); 80% methanol and 20% B1N buffer; 60% methanol and 40% B1N buffer; 40% methanol and 60% B1N buffer; 20% methanol and 80% B1N

buffer; and 100% B1N buffer for 30 min each. All incubation steps should be performed on ice until changing to 20% methanol and 80% B1N buffer from where all subsequent steps may be carried out at RT.

7. Change the 100% B1N buffer after 30 min and incubate in fresh B1N buffer overnight at RT while shaking.
8. Change to PTxwH buffer and incubate overnight. Samples may be stored in this buffer for multiple weeks to months at 4 °C.
9. Incubate samples in PTxwH buffer containing primary antibodies diluted at the desired concentrations and protected from light for 4 days at RT with shaking. For CD31/PECAM-1, dilute the antibody to a final concentration of 2 μg/mL in 1.6 mL PTxwH. For CD68, dilute to a final concentration of 5 μg/mL in 1.6 mL PTxwH (*see* **Note 11**).
10. After the incubation period, wash the sample in PTxwH buffer for increasing periods of time starting at 5 min and proceed with washes of 10 min, 15 min, 20 min, 1 h, 2 h, 4 h and overnight incubation at RT.
11. Incubate samples in PTxwH buffer containing secondary antibodies diluted at the desired concentrations and protected from light for 4 days at RT while shaking. For donkey anti-goat Alexa Fluor 568–conjugated antibody and donkey anti-rat Alexa Fluor 790–conjugated antibody, dilute to a final concentration of 10 μg/mL. For TO-PRO-3 iodide dilute 1:5000.
12. After this incubation step, wash the sample in PTwxH buffer as outlined in **step 10**.
13. Before embedding, wash samples in PBS for 5 min, 10 min and 30 min each (*see* **Note 12**).
14. Dissolve 0.9% agarose in PBS. Check meticulously that the agarose has dissolved completely and let it cool to approximately 50 °C. Place the sample in a weighing dish and pour the agarose over the sample, making sure that the sample stays at the bottom of the dish. Confirm correct positioning of the sample under the dissection scope and let the agarose cool. Trim the agarose block with the sample so that it fits into a 2 mL safe-lock tube (*see* **Note 13**).
15. Transfer the embedded sample into a new 2 mL safe-lock tube and incubate with 25% methanol and 75% H_2O, 50% methanol and 50% H_2O, 75% methanol and 25% H_2O and 100% methanol (2×) for 30 min each at RT while shaking.
16. Incubate the sample while shaking with 100% DCM for 30 min and switch to 100% DCM for another 1 h. The sample should sink to the bottom (*see* **Note 14**).

17. Switch to DBE and incubate overnight. Change DBE to fresh DBE for storage (*see* **Note 15**).

3.3 Light Sheet Fluorescence Microscopy

1. Mount the sample in an appropriate sample holder and place it in the microscope reservoir filled with DBE. Position the sample so that the laser beam from the light sheet hits the sample along its longitudinal axis.
2. Use the 1.3× lens for larger samples (e.g., the mouse thoracic aorta) and the 4× lens for smaller samples that require imaging with higher resolution such as the brachiocephalic artery. Use wavelengths of 488 nm to reveal tissue autofluorescence (independent of any stain) and 639 nm to elicit nuclear signals from TO-PRO-3. For the suggested secondary antibodies and their respective fluorophores, use excitation wavelengths 561 nm (CD31/PECAM-1) and 785 nm (CD68). Focus on the sample and adjust the acquisition settings of the light sheet microscope. When using the 785 nm laser, chromatic adjustment may be necessary to acquire in-focus images for all lasers. Adjust laser transmission control percentage for each laser individually. Set scan range to define the depth of the z-stack of your samples. Use the following settings in the Imspector Pro GUI for image acquisition: set zoom to 1.3 or 4.0× respectively; sample liquid DBE; step size 2.5 μm (*see* **Note 16**).

3.4 Image Processing and Analysis

1. Save the images obtained through the ImSpector Pro software in the OME-TIFF format. To facilitate data handling and storage, transform files into Imaris file format *.ims using the Imaris File Converter software (Bitplane, Belfast, UK; https://imaris.oxinst.com/downloads).
2. Open the *.ims file in the Imaris software, adjust gain settings for each channel individually and choose appropriate color settings.
3. Use the auto-fluorescence signal, CD31/PECAM-1 and TO-PRO-3 staining to identify the vessel wall (auto-fluorescence and TO-PRO-3 signal), the endothelial layer (CD31/PECAM-1 signal), the plaque (both cellular and acellular region using the auto-fluorescence, CD31/PECAM-1 and TO-PRO-3 signal) and macrophages (CD68).
4. To characterize plaque composition and volume, use the contour surface tool to manually segment the necrotic core (area inside the plaque without TO-PRO-3 staining) and the entire plaque (area between the CD31/PECAM-1 positive endothelial layer and vessel wall as identified by auto-fluorescence/TO-PRO-3) in regular intervals along the longitudinal axis of the vessel in order to create two 3D objects. Finally, create a 3D

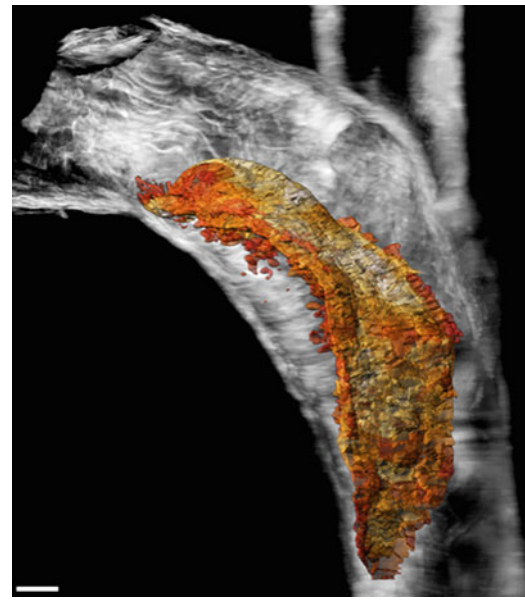

Fig. 2 Color-coded endothelial surface of plaque located in the inner curvature of the brachiocephalic artery. CD31 staining was used to identify the endothelium and create a plaque surface with lighter-red areas to depict more intensive CD31 expression and darker red areas to indicate less intense CD31 expression. Vessel outline based on autofluorescence is depicted in gray (scale bar 200 μm)

object of the vessel wall using the same approach by applying the auto-fluorescence layer as vessel outline. The volumes of each object can be derived from the statistics tool.

5. To measure the degree of stenosis at different positions along the longitudinal axis of the vessel starting at the brachiocephalic bifurcation, create two 3D objects using the contour surface tool on the same slice. The first 3D object is designed to fit the actual lumen (representing the stenotic lumen), while the second 3D object should fit within the inside of the inner border of the media (this is the expected vessel lumen without the plaque). The volume of each 3D object can be derived from the statistics tool. The degree of stenosis can then be obtained as percentage of expected vessel lumen volume occupied by the plaque.
6. To characterize the endothelial surface, use the surface tool with the region growing option enabled for the CD31/PECAM-1 channel. This will create a segmented surface of the CD31/PECAM-1 positive endothelial layer. Use color-coding based on mean CD31/PECAM-1 fluorescence intensity to characterize differences in CD31/PECAM-1 expression across the plaque surface (Fig. 2).

4 Notes

1. Prepare a ketamine and xylazine solution in sterile PBS such that 90 mg/kg of ketamine and 10 mg/kg of xylazine can be administered to a mouse by intraperitoneal injection in a volume no larger than 500 μL.
2. NaN_3 is a powerful bacteriostatic that inhibits cytochrome oxidase in gram-negative bacteria and can thus be used as a preservative. It is also highly toxic and may be fatal in contact with skin or if swallowed. All necessary precautions should be observed when handling this chemical, including proper disposal.
3. The mouse is unconscious and neither fights the supine position nor moves in response to a noxious stimulus such as a firm toe pinch.
4. The infusion apparatus can be assembled using parts from medical intravenous infusion systems, 60 mL syringes and three-way stopcocks. Physiological perfusion pressure can be achieved by placing the reservoirs (60 mL syringes) for PBS or 10% buffered formalin to the appropriate height relative to the mouse to deliver a pressure around 115 mmHg or 156 cm of water.
5. If the systemic perfusion of fixative is successful, an obvious tissue reaction can be observed in the tail and fore and hind limbs.
6. Make sure to include portions of the proximal regions of the right subclavian and common carotid arteries such that the final sample is a Y-shaped vessel. Avoid touching the brachiocephalic artery itself, always manipulate the sample using the edges of its branches from a region distant from any visible atherosclerotic lesion.
7. We use both 2 mL and 5 mL safe-lock Eppendorf tubes for tissue processing for murine carotid vessels and the entire thoracic and abdominal aorta respectively. In theory, all sizes of tubes work, but larger tubes will require larger quantities of antibodies during the immunolabeling steps. The volume of all solutions will need to be adapted to the tube size. Care has to be taken that the sample can move freely during the incubation on the horizontal shaker.
8. We label the tubes on top and on the side. All solutions used throughout the procedure may remove ink and care should be taken to retain the labeling.
9. The tissue will shrink during the delipidation process and care must be taken to avoid losing the sample when changing the buffers. The buffers may be stored at 4 °C for multiple months.

Glycine will start to precipitate when B1N buffer exceeds 60% of the solution but this will not impair the delipidation process.

10. The tissue should sink to the bottom after the 1 h incubation step and after the last incubation with DCM. This ensures complete removal of lipids. DCM is a polar organochloride compound that is highly volatile, dissolves certain plastics and can be absorbed through inhalation and skin contact. All necessary precautions should be observed when handling this chemical, including proper disposal.
11. Incubation time depends on sample characteristics such as tissue size and antigen density. We have successfully used incubation times as little as 2 days. A list of validated antibodies compatible with methanol based clearing techniques and a protocol to test new antibodies may be found under https://idisco.info. We usually start with a 1:200 dilution when testing new antibodies.
12. Before proceeding with embedding in agarose, examine the samples under a dissection microscope to check that they do not have hair or lint attached. Remove if necessary.
13. Once the sample is embedded in agarose, repositioning is no longer possible. It is thus important to position the sample correctly. We try to make sure that the sample stays at the bottom of the weighing dish. During light-sheet microscopy, this side of the block will face up and therefore face away from the sample holder. Additionally, agarose becomes very brittle during the clearing process, which makes it difficult to trim. Care should be taken that the size of the agarose block with the sample fits the sample holder of the light sheet microscope.
14. If the sample does not sink to the bottom, incubate for a longer period of time until sinking is observed.
15. DBE is a benzyl ether. All necessary precautions should be observed when handling this chemical, including proper disposal.
16. We check image quality immediately after image acquisition using Imaris. If initial image quality is not satisfactory, acquisition may be repeated with adjusted settings. Samples may be stored in DBE for a number of weeks and imaging may be repeated. We have however not tested stability systematically.

Acknowledgments

This work was supported in part by the National Center for Advancing Translational Sciences, National Institutes of Health (NIH), through Rockefeller University (grant number UL1TR001866). D.F. Riascos-Bernal was supported by a Career

Development Award from the American Heart Association (19CDA34660217). P. Cohen was supported by the NIH Research Project Grant Program Award R01DK120649. N.E.S. Sibinga was supported by NIH Research Project Grant Program Awards R01HL128066 and R01HL133861.

References

1. Libby P, Hansson GK (2019) From focal lipid storage to systemic inflammation: JACC review topic of the week. J Am Coll Cardiol 74(12): 1594–1607. https://doi.org/10.1016/j.jacc.2019.07.061
2. Whitman SC (2004) A practical approach to using mice in atherosclerosis research. Clin Biochem Rev 25(1):81–93
3. Paigen B, Morrow A, Holmes PA, Mitchell D, Williams RA (1987) Quantitative assessment of atherosclerotic lesions in mice. Atherosclerosis 68(3):231–240
4. Ko KA, Fujiwara K, Krishnan S, Abe J-I (2017) En face preparation of mouse blood vessels. J Vis Exp 123:55460. https://doi.org/10.3791/55460
5. Becher T, Riascos-Bernal DF, Kramer DJ, Almonte VM, Chi J, Tong T, Oliveira-Paula GH, Koleilat I, Chen W, Cohen P, Sibinga NES (2020) Three-dimensional imaging provides detailed atherosclerotic plaque morphology and reveals angiogenesis after carotid artery ligation. Circ Res 126(5):619–632. https://doi.org/10.1161/circresaha.119.315804
6. Chi J, Wu Z, Choi CHJ, Nguyen L, Tegegne S, Ackerman SE, Crane A, Marchildon F, Tessier-Lavigne M, Cohen P (2018) Three-dimensional adipose tissue imaging reveals regional variation in beige fat biogenesis and PRDM16-dependent sympathetic neurite density. Cell Metabol 27(1): 226–236.e223. https://doi.org/10.1016/j.cmet.2017.12.011

Chapter 52

Intravascular Fluorescence Molecular Imaging of Atherosclerosis

Mohammed M. Chowdhury, Zhonglie Piao, Mazen S. Albaghdadi, Patrick A. Coughlin, James H. F. Rudd, Guillermo J. Tearney, and Farouc A. Jaffer

Abstract

Optical molecular imaging using near-infrared fluorescence (NIRF) light is an emerging high-resolution imaging approach to image a wide range of molecular and cellular species in vivo. Imaging using NIR wavelengths (650–900 nm) enables deeper photon penetration into tissue and reduced tissue autofluorescence, resulting in higher sensitivity to detect exogenously administered NIR fluorophores (injectable molecular imaging agents). Greater imaging depth of several centimeters is further achievable in the NIR window as blood absorption is as an order of magnitude lower than in the visible range. Furthermore, as optical imaging is routinely performed in the cardiac catheterization laboratory (e.g., optical coherence tomography), intravascular NIRF offers a promising translational approach for clinical coronary and peripheral arterial imaging. To this point, the first human intravascular NIRF imaging study recently demonstrated the ability to detect NIR autofluorescence in patients with coronary atherosclerosis. This study provides a foundation for targeted intravascular NIRF molecular imaging studies in coronary patients. In this chapter, we detail system engineering, imaging agents and translational applications of intravascular NIRF molecular imaging.

Key words Atherosclerosis, Inflammation, Drug-coated balloon, Peripheral arterial disease, Imaging, Near-infrared fluorescence, Optical coherence tomography, Intravascular ultrasound

1 Introduction

Atherosclerosis is the dominant form of coronary artery disease (CAD) and the major cause of death worldwide. Clinically, noninvasive imaging modalities such as computed tomography (CT), magnetic resonance imaging (MRI), and ultrasound (US) are widely used for diagnosis of atherosclerosis in larger vessels, and in the case of CT, both in coronary arteries and larger arteries. Nonetheless, these techniques have limited ability to provide specific biological and molecular information underlying

Dipak P. Ramji (ed.), *Atherosclerosis: Methods and Protocols*, Methods in Molecular Biology, vol. 2419,
https://doi.org/10.1007/978-1-0716-1924-7_52,
© The Author(s), under exclusive license to Springer Science+Business Media, LLC, part of Springer Nature 2022

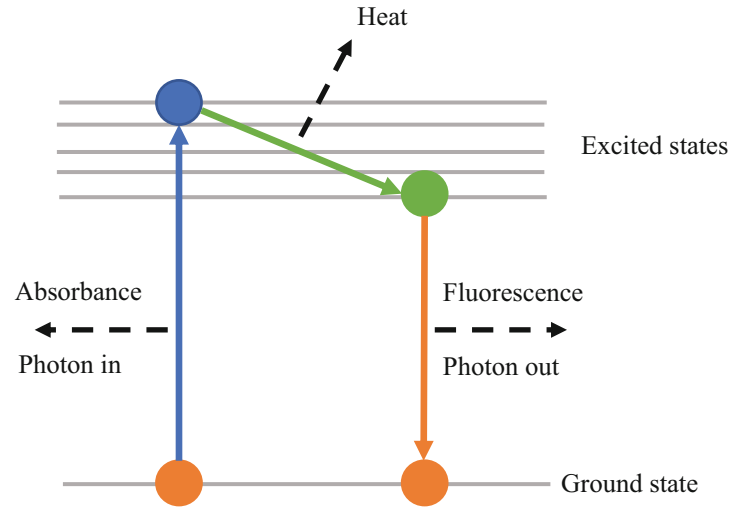

Fig. 1 Jablonski diagram of the fluorescence mechanism. A photon is absorbed causing the molecule to move to an excited electronic state (blue line). The molecule loses some energy to heat as it moves to the lowest excited state (green). A photon is spontaneously emitted allowing the molecule to return to the ground state (red line)

atherosclerosis progression and complications. Intravascular near-infrared fluorescence (NIRF) molecular imaging is a promising approach for comprehensively understanding coronary atherosclerosis on cellular and molecular level [1–3].

Fluorescence spectroscopy is the optical detection of molecules that absorb a particular spectrum of electromagnetic radiation (light) and then reemit electromagnetic radiation at another lower energy level. Figure 1 illustrates a simplified Jablonski diagram [4] that demonstrates the fluorescence mechanism. The absorption of a single photon at an appropriate frequency, and this energy, causes an electron to move from the electronic ground state to a high-energy state. Over a very short period of time (i.e., 10^{-12} s) [5], the electron loses some energy to the environment (in the form of heat) which returns the electron to the lowest singlet excited state. After some time in this state (i.e., 10^{-8} s) [5], the electron is then able to return back to the electronic ground state by emitting the remaining energy as another single photon at a lower frequency (longer wavelength).

The optical detection of this process, known as fluorescence spectroscopy, is conducted by exciting the fluorophore with a light source at an appropriate wavelength (ideally tuned to the peak absorption of the fluorophore) and collecting the emission light that is released at a longer wavelength. The excitation source can be a laser, light-emitting diode or a broadband filament bulb with an appropriate filter in place. The difference between the wavelength of maximum absorption and the wavelength of maximum emission

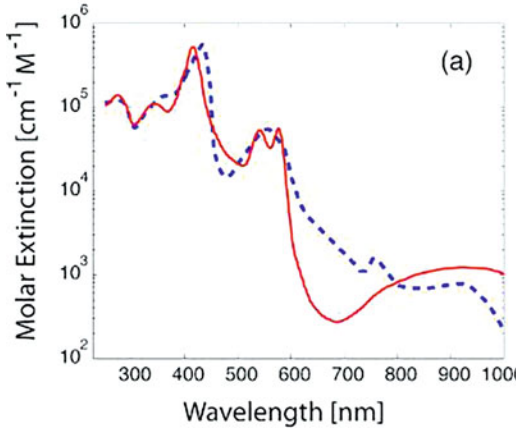

Fig. 2 Molar extinction coefficients of oxy- (red)/deoxy- (blue) haemoglobin over a large spectral range. (Reproduced from permission from Ref. 8)

is known as the Stokes's shift. The larger the Stokes's shift, the easier it is to resolve the emission light from the excitation light. It is common for an organic fluorophore to have a Stokes's shift of approximately 10–20 nm.

Near-infrared fluorescence (NIRF) imaging detects fluorophores that absorb and emit light in the wavelength range of 650–900 nm. NIR fluorescence detection is more efficient than visible fluorescence detection due to reduced scatter [6] and lower autofluorescence [7] of common catheter substrates such as nitrocellulose, polyvinylidene difluoride (PVDF), poly(methylmethacrylate) (PMMA) and polydimethylsiloxane (PDMS). NIR fluorescence is also useful for in vivo imaging due to its deeper penetration into tissue and reduced tissue autofluorescence, as compared to visible light. The deeper penetration is mostly enabled due to the relatively lower absorption and scatter of NIR light by hemoglobin (oxygenated and deoxygenated) and water. Figure 2 illustrates the extinction coefficient of deoxygenated hemoglobin and oxygenated hemoglobin in the wavelength range of 400 to 1000 nm [8]. The extinction coefficient of a material is the amount of light attenuation per mole of the material, per unit length of depth. In addition to the increased depth of penetration, the lower absorption and scatter of biological materials in the NIR also reduces the autofluorescence and total background signal, which ultimately leads to improved signal-to-noise ratio. The advantages of NIR fluorescence for in vivo imaging of animals and humans has led to applications, including imaging of normal and disease vasculature, tissue perfusion, protease activity, hydroxyapatite, and malignancy [9].

Given the favorable high sensitivity in the NIR range, NIRF imaging can further enable signal detection through blood, without the need for flushing. The first real-time intravascular catheter

molecular sensing probe was described by Jaffer et al. [10], who detected in vivo inflammatory cysteine protease activity in experimental atheroma of human-sized arteries of the aorta of rabbits. The first rotational, automated 2D imaging catheter was engineered by Jaffer et al. [11] who performed intra-arterial imaging of stented rabbit aortas and coronary bare-metal stents, and demonstrated excellent nanomolar sensitivity to fluorophores resident within plaque and stent injury-induced arterial inflammation. Further research into this novel imaging approach will also employ new tagged-monoclonal autoantibodies implicated in atherosclerosis (i.e., oxidized LDL [oxLDL], acetylated LDL, matrix metalloproteinases). Indeed, Khamis et al. [12] have developed a quantitative antibody-based NIRF approach for targeting oxLDL in vivo—providing new potential avenues for exploring molecular compositions of atheroma oxidative stress longitudinally. In addition, Food and Drug Administration (FDA)-approved indocyanine green is a promising translational NIR fluorophore for plaque imaging [13], and has recently been shown to be a marker of impaired endothelial barrier function in human plaques [14].

Intravascular NIRF imaging was introduced by engineering an optical fiber–based catheter to excite NIR fluorophores to sense molecular information within the arterial wall. After initial studies of standalone NIRF systems [10, 11], it became apparent that standalone NIRF imaging was limited by the lack of coregistered anatomic information. Therefore, a dual-modality NIRF catheter incorporating the high-resolution clinical structural imaging method, optical coherence tomography (OCT), was developed for acquiring coregistered structural–molecular information simultaneously. Intravascular OCT is a highly sensitive, minimally invasive imaging modality that provides high resolution (~10 μm) cross-sectional views of the tissues, enables a real-time in vivo optical "biopsy" of arterial wall to identify the morphological features of the plaque such as thin cap fibroatheroma (TCFA), macrophages, calcifications, thrombi, and cholesterol crystals. Combination of NIRF with OCT (NIRF-OCT) is technically straightforward compared to the combination of NIRF with intravascular ultrasound (IVUS), as with NIRF-OCT, the two modalities share the same optical components to deliver and receive light at the catheter tip. In order to acquire coregistered NIRF and OCT simultaneously, simultaneous light delivery and reception is enabled by use of a dual-channel rotary junction and a double-clad fiber (DCF) based catheter (Fig. 3) [15].

Intravascular NIRF-OCT was demonstrated for in vivo characterization of inflammatory cells using OCT and quantify molecular activity using cathepsin protease-activated NIR molecular beacons. Furthermore, stent-induced injury and healing, as reflected by fibrin deposition, can be quantified in vivo and investigated using this single pullback technology to resolve different stent healing

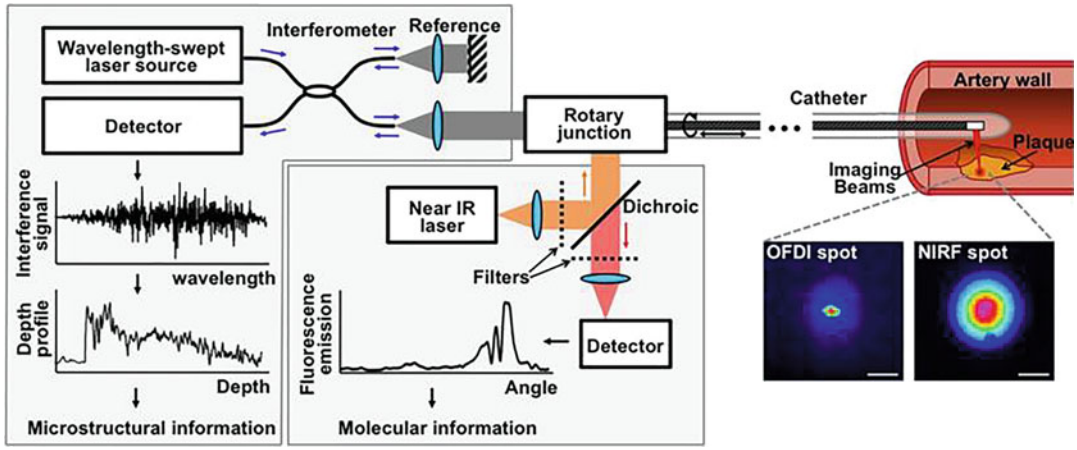

Fig. 3 Dual-modality intravascular NIRF-OCT imaging system and catheter. (Reproduced from Ref. 15 with permission)

profiles [16]. The translational potential of NIRF-OCT is evident by the recent development of an intravascular NIRF-OCT system allowing reporting on NIR autofluorescence in the coronary arteries of patients, a new signature of coronary CAD that may indicate intraplaque hemorrhage and oxidative stress [17].

This chapter details the methodology of the use of intravascular NIRF molecular imaging to assess the effect of interventions on atheroma inflammation in coronary-sized arteries in vivo. We highlight a specific application of assessing paclitaxel drug-coated balloon angioplasty on plaque inflammation and progression in rabbit atherosclerosis in vivo and compare to animals treated with conventional angioplasty or sham-angioplasty. Methods described in this chapter include creation of atherosclerosis in the aorta of rabbits, in vivo intravascular imaging harnessing intravascular ultrasound and the novel serial intravascular near-infrared fluorescence-optical coherence tomography (NIRF-OCT) molecular-structural imaging of inflammatory protease activity. Furthermore, methods used to elucidate mechanisms underlying the in vivo findings are described, including histological and molecular assays of resected lesions.

2 Materials

2.1 NIRF-OCT Imaging System and Catheter

A prototypical intravascular NIRF-OCT system consists of an OCT console, a NIRF console, a dual-channel optical rotary junction and a catheter (Fig. 3).

2.2 OCT Console

The OCT console comprises the following setup.

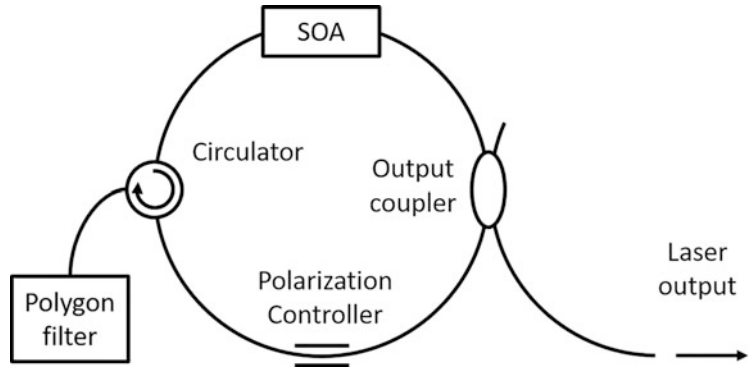

Fig. 4 Wavelength-swept laser. (Reproduced from Ref. 18 with permission)

1. A wavelength-swept laser cavity comprises of three components: a gain medium, wavelength scanning filter and an output coupler (Fig. 4) [18].
2. A semiconductor optical amplifier (SOA) used as a gain medium, typically having a >15 dB gain at a broad wavelength range from 1240 nm to 1360 nm.
3. A polygon filter is used as a wavelength scanning filter. The wavelength tuning repetition rate is determined by the number of mirror facets (72) and the spinning frequency (52,000 rpm) of the polygon scanning mirror.
4. A 50/50 power splitting directional fiber coupler is employed as an output coupler. A wavelength-swept laser with center wavelength at 1310 nm, a bandwidth of >100 nm and average output power up to 60 mW can be achieved. This source can provide an axial resolution below 10 μm in air and ranging depth of 4.5 mm along the axial direction.
5. The wavelength swept laser has a repetition rate of 50 kHz, capable for cross-sectional imaging with frame rate of 50 Hz (1024 A-lines) or 25 Hz (2048 A-lines).
6. Light from the wavelength swept laser source is coupled into a fiber-based interferometer. A 90/10 fiber coupler (Gould Fiber Optics, 90/101310 nm splitter) is used to divide the light into a sample arm (90%) towards the imaging catheter and a reference arm (10%) with a fixed mirror.
7. Backscattered light from sample/reference arms are combined by a 50/50 fiber coupler (Gould Fiber Optics, 50/50 1310 nm splitter) and interferes at the interferometer.
8. The balanced detector (New Focus, 80 MHz Balanced Receiver) has a dual optical input, and before signal amplification, subtract the signal from the second input to reduce the common-mode noise, thus eliminating the autocorrelation signal and enhancing the interference signal.

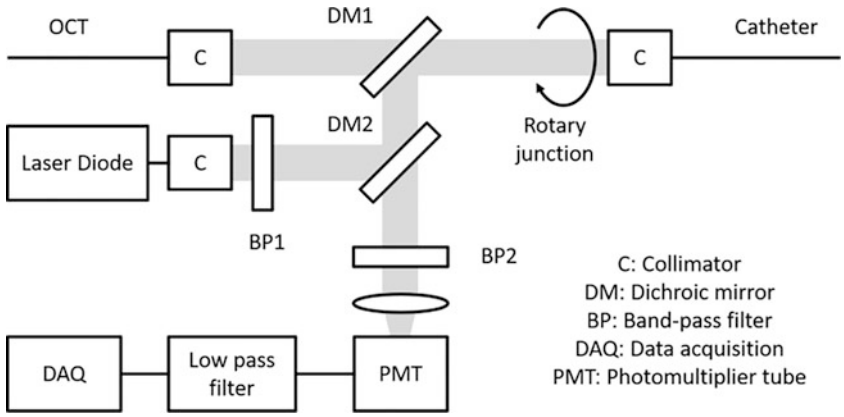

Fig. 5 NIRF console and rotary junction. Reproduced from Ref. 15 with permission)

9. Polarization-diverse detection is applied for eliminating artifacts that can arise from birefringent tissues such as collagen and muscle, as well as the system and optical fibers.
10. The analog signal from the photoreceivers is digitized and captured by two channels at 200 MS/s with 14-bit resolution. The data is streamed to a 5 TB RAID hard drive array.
11. A Fourier transform is utilized to reconstruct the backscattering as a function of depth (A-line) that reveals the depth-resolved tissue microstructure.

2.3 NIRF Console

This NIRF console consists of the following items:

1. In the NIRF console (Fig. 5) [15], a multimode fiber-coupled continuous wave NIR laser diode at 750 nm (LDX-3110-750-FC) is used to excite NIR fluorophores resident within the arterial wall.
2. A narrow band laser cleanup band-pass filter (zet750/20X) is used for suppressing ambient light.
3. A specialized catheter (Subheading 2.4) transmits the NIR excitation light to the tissue via a rotary junction (Subheading 2.5). Then, the collected NIRF signal from the sample is detected by a photomultiplier tube.
4. The NIRF signal is next filtered by a DC coupled low-pass filter (50 kHz).
5. The filtered NIRF signal is then amplified and acquired by a data acquisition board.

2.4 NIRF-OCT Catheter

The catheter has the following setup.

1. A dual-modality NIRF-OCT imaging probe (Fig. 6) consists of a double-clad fiber (DCF, FUD-4305)-based catheter with outer diameter of 0.55 mm, allowing it to fit into a commercial

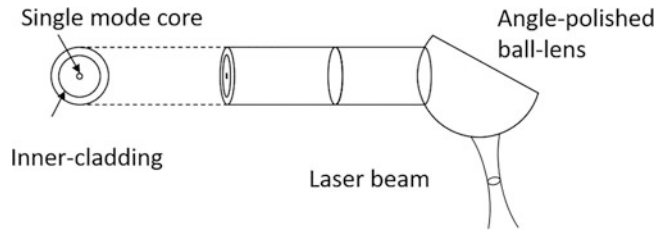

Fig. 6 Dual-modality NIRF-OCT catheter. (Reproduced from Ref. 15 with permission)

OCT housing sheath of 2.4 French (0.79 mm) full outer diameter.

2. The DCF has a single mode fiber core (diameter: 7.8 μm; NA: 0.130) that transmits the OCT light at center frequency 1.3 μm.
3. In order to improve light collection efficiency, the inner cladding (diameter: 125 μm; NA: 0.46) of the DCF is used for propagating the NIRF excitation and emission signal.
4. At the distal end of the DCF, a ball lens (diameter: 320 μm) is equipped to focus the light on the arterial wall.
5. The ball lens can be fabricated by an automatic CO_2 laser splicing station (LZM-100) from a coreless fiber, which is spliced to DCF and melted on the other side by laser ablation to form a spherical shape with demanded diameter.
6. The ball-lens is subsequently polished to a 38-degree angle by a polishing machine to achieve side-view imaging.
7. The polished ball-lens is next assembled into a driveshaft and inserted into a protective sheath with transparent imaging window at the distal portion.
8. The lateral resolution is defined by the optical focus of the ball-lens, and typically has a focal spot of ~30 μm obtained at a working distance of 1.5 mm.
9. The maximum power output from the imaging window is set to 20 mW.

2.5 Dual-Channel Rotary Junction

The rotary junction has the following setup.

1. A dual-channel rotary junction is used to combine and transmit the NIRF and OCT light between the rotating probe and static system. Lens-based collimators are used to collimate the light from both sides, as shown in Fig. 5.
2. The NIR light (excitation 750 nm) is reflected by dichroic mirror-1 (T770LPXR), and then reflected by dichroic mirror-2 (T1000LP, R: 750–860 nm, T: 1200–1400 nm) into the

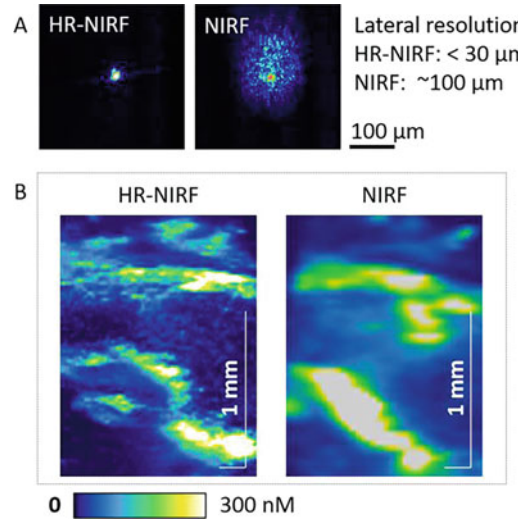

Fig. 7 High-resolution NIRF-OCT imaging. (Reproduced from Ref. 19 with permission)

dual-clad fiber (DCF) catheter, while the OCT light is transmitted and directly coupled to the core of the DCF catheter.

3. The collected NIRF emission from the catheter is reflected by the same dichroic mirror (T1000LP) and filtered by an emission filter (ET810/90 nm and then focused by a planoconvex lens (LA1805-B) into the PMT.
4. The rotary junction rotates at a constant speed (e.g., 25 Hz or 50 Hz) corresponding to 2048 or 1024 A-lines per rotation.
5. Simultaneously, three-dimensional NIRF-OCT images are acquired by helical scanning of the catheter by the rotary junction.
6. The catheter pullback rate can be adjusted from 1–10 mm/s. The trade-off for a faster pullback rate is lower spatial resolution.
7. An alternative high-resolution (HR)-NIRF-OCT imaging design uses a single mode laser diode (FIDL-30S-750X) with a high-throughput DCF rotary junction (throughput >92%) to precisely transmit the NIRF excitation light to the core of a DCF catheter. These advances enable three times higher lateral NIRF resolution (<30 µm) compared to first-generation NIRF-OCT imaging systems (Fig. 7a) [19].
8. The HR-NIRF-OCT imaging system enables high-resolution visualization of atherosclerosis inflammation and demonstrates greater spatial detail of inflammatory cathepsin activity (Fig. 7b) [19], and can enhance the effectiveness of NIRF-

OCT for molecular phenotyping of atherosclerosis and stent-induced vascular injury.

2.6 NIRF Calibration and Data Processing

1. To achieve quantitative NIRF information from the vessel wall, the NIRF console and catheters should be calibrated by using saline-based solutions comprising a range of concentrations (1–1000 nM) of an NIR fluorophore (i.e., Alexa Fluor 750).
2. The intravascular NIRF signal intensity decays as a function on the distance between the imaging probe and the arterial wall. NIRF distance calibration is therefore performed with a glass tube filled with NIR fluorescent dye (AF 750) with concentration of 1 μM. A plot of NIRF signal intensity vs distance (mm) is then generated. The plot is used to calculate the linear curve for fitting the distance function use for further distance correction in NIRF-OCT imaging.
3. The NIRF-OCT pullback is performed and the coregistered OCT and NIRF datasets are acquired simultaneously. First the vessel wall on the OCT image is segmented, subsequently, NIRF data is calibrated by the distance of the segmented vessel wall to the sheath surface.
4. The calibration procedure runs automatically in MATLAB code. The distance corrected NIRF intensity profile along the pullback direction, a two-dimensional NIRF map (carpet view), coregistered NIRF over the OCT frames, and three-dimensional volume image are reconstructed and displayed.

2.7 Experimental Rabbit Atherosclerosis Model

1. New Zealand white rabbits (weight 3–4 kg). Lipid-rich lesions developed by 1% high-cholesterol diet (1% cholesterol, 5% peanut oil, Research Diets) for total of 6 weeks. This is followed by 4 weeks of normal chow.
2. Anesthesia: intramuscular ketamine (35 mg/kg) and xylazine (5 mg/kg) with a total of 0.01 mg/kg of buprenorphine. Inhaled anesthesia with 1–5% (v/v) of isoflurane Novaplus and supplemental carrier oxygen at 1 L/min.
3. Electric razor.
4. Artificial tears (over the counter pharmacy).
5. Scalpel 15 blade.
6. 28G, 30G, and 32G needles.
7. Dissecting scissors, forceps, 3-0 nylon sutures for slings, 3-0 vicryl suture.
8. 4F intravascular sheath (Avanti Sheath introducer, Cordis).
9. 50% saline and 50% iopamidol contrast media (Bracco).
10. 3F Fogarty embolectomy catheter (Edwards).
11. Hard E-collar for rabbit neck.

12. Saline.
13. Dissecting board.
14. Dry ice.
15. 2-methyl butane.
16. RNAlater.

2.8 Angioplasty Balloons

1. 4.0 × 40 mm drug-coated balloon angioplasty device with 3.5 μg/mm^2 of paclitaxel coating on balloon (IN.PACT Admiral Balloon, Medtronic).
2. 4.0 × 40 mm plain angioplasty balloon device (Medtronic).

2.9 Intravascular Ultrasound Imaging

1. Intravascular ultrasound (IVUS) clinical console [iLab2, Polaris2 Software Imaging System (Boston Scientific)].
2. OsiriX imaging platform and Fiji ImageJ v2.0.0.
3. USB drive.

2.10 NIRF-OCT Imaging

1. ProSense750 VM110 (PerkinElmer, Waltham, MA).
2. Butterfly needle 25G.
3. NIRF-OCT imaging console.

2.11 Molecular Analysis of Tissue

1. RNase-free water.
2. RNeasy kit (Qiagen): Contains buffers RLT, RPE, and RW1, RNAeasy spin column.
3. 1.5 mL microcentrifuge tubes.
4. Microcentrifuge.
5. 70% ethanol.
6. Nanodrop spectrophotometer.
7. Rotar-stator homogenizer.
8. Reagents for cDNA synthesis: 10× reverse transcriptase, 10 nM dNTPs, 10× random hexamers, Multiscribe, water.
9. Thermocycler or heating block at different temperatures.
10. Basic Local Alignment Search Tool (BLAST).
11. Cathepsin B primer: F, TTCTTGCGACTCTTGGGACTTC ; R, TGACGAGGATGACAGGGAACTA.
12. Cathepsin L primer: F, AGGGTCAGTGTGGTTCTTGTTG ; R, TGAGATAAGCCTCCCAGTTTTC.
13. Cathepsin S primer: F, TGTTCACACTTTGCCCTATGAC ; R, AGGGGCTCCATAAGGAAATAAA.
14. GAPDH primer: F, GGGGCTGGCATTGCCCTCAA; R, G GCTGGTGGTCCAGGGGTCT.
15. 96 well plate.

16. SYBR Green real-time PCR reagents.
17. QuantStudio 3 Real-Time PCR System or equivalent.

2.12 Histology

1. Optimal cutting temperature embedding medium.

3 Methods

3.1 Experimental Atherosclerosis Lesion Generation in Rabbits

1. Induce macrophage- and lipid-rich atherosclerosis in the aortas of male or female New Zealand white rabbits (weight 3–4 kg) by local balloon endothelial injury and high-cholesterol diet as detailed in steps below.
2. Feed that rabbits the atherogenic diet and subject the infrarenal abdominal aorta to balloon injury (e.g., with standard angioplasty balloon or a 3F Fogarty balloon which is capable of greater endothelial denudation and injury) (*see* **Note 1**).
3. Induce anesthesia with appropriate agent(s) (*see* **step 3** in Subheading 2.7) and continue with inhalational anesthetic.
4. In preparation for intravascular NIRF-OCT via the femoral artery, shave and clean the overlying rabbit skin in a sterile manner using the electric razor.
5. Lubricate the eyes with artificial tears.
6. Make a small incision (approximately 1.5 cm) in the oblique groin over the natural lie of the common femoral artery.
7. Dissect and slung the artery with an absorbable suture and ligate the distal end.
8. Make a small arteriotomy and introduce a 4 French (F) sheath into the vessel.
9. At this point, blood can be aspirated and stored for later analysis (*see* **Note 2**).
10. Take an angiogram using 50% saline and 50% iopamidol contrast media.
11. Advance a 3F Fogarty arterial embolectomy catheter through a 4F sheath into the infrarenal aorta, approximately 15 mm below the lowest renal artery. Fill the balloon with a 0.9% saline/contrast 50:50 mix to a volume of 0.3 mL. Injure the aorta by three sequential manual pullbacks of a nominally inflated 3F Fogarty under x-ray angiographic guidance over a distance of approximately 60 mm.
12. Ligate the femoral artery and close the muscle and skin closure with 3-0 vicryl suture (*see* **Note 3**).
13. Recover the rabbits and place in a neck E-collar for 1 week to prevent any manual disruption of the wound.

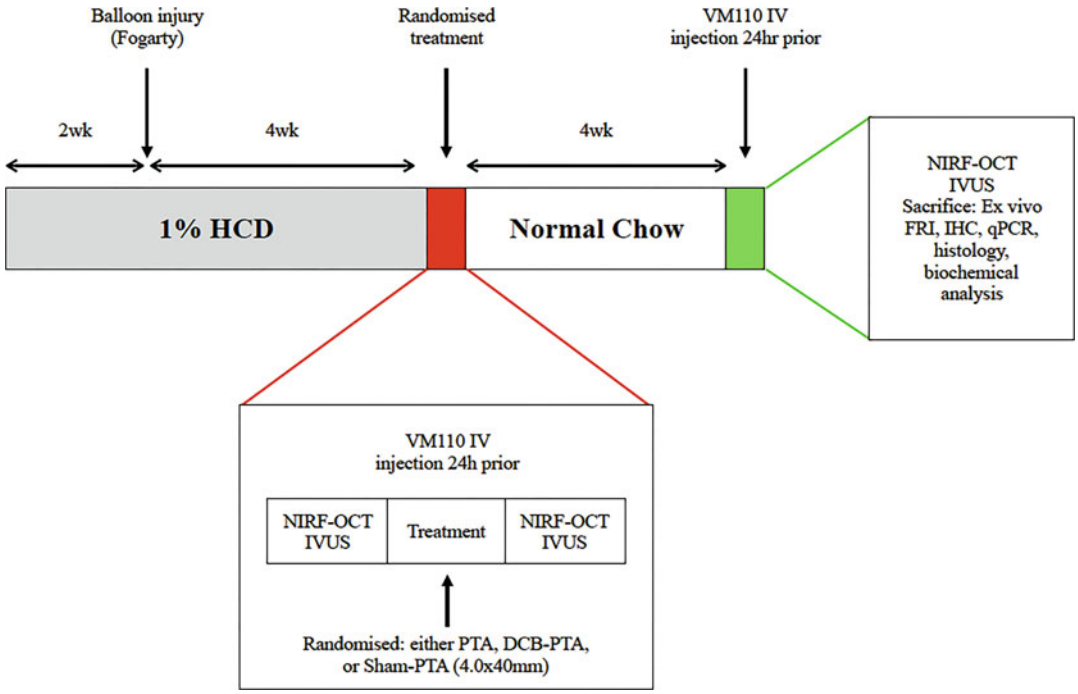

Fig. 8 Experimental Study Design. All 25 rabbits received 1.0% high-cholesterol diet (HCD) 2 weeks before aorta balloon injury, and for 4 weeks thereafter, followed by normal chow for the final 4 weeks. At 4 weeks after balloon injury, rabbits were intravenously injected with ProSense VM110 (400 nmol/kg). Rabbits underwent in vivo multimodal survival near-infrared fluorescence-optical coherence tomography (NIRF-OCT), intravascular ultrasound (IVUS), and X-ray angiography 24 h later. Then, the animals randomly underwent drug-coated balloon percutaneous transluminal angioplasty (DCB-PTA) ($n = 10$), PTA ($n = 10$) or sham-PTA ($n = 5$) therapy. Four weeks later at week 10, multimodal imaging NIRF-OCT and IVUS imaging were repeated, followed by sacrifice and ex vivo fluorescence imaging, as well as RNA and histopathological analysis. *FRI* fluorescence reflectance imaging, *IHC* immunohistochemistry, *qPCR* quantitative polymerase chain reaction. (Reproduced by permission from Ref 25)

14. Continue feeding the rabbits a 1% high-cholesterol diet until week six, followed by a normal chow diet for the remainder of the study (typically four additional weeks; Fig. 8).

3.2 Randomization of Angioplasty Therapy

1. After survival intravascular NIRF-OCT and IVUS imaging (Subheading 3.3) at baseline 6-weeks after balloon-injury, randomize rabbits to one of three treatments (*see* **Note 4**): paclitaxel drug-coated balloon percutaneous transluminal angioplasty (DCB-PTA, $n = 10$, 3.5 μg/mm^2 of drug coated concentration with urea excipient) or conventional PTA ($n = 10$) or sham PTA ($n = 5$, placement of a balloon without inflation), followed by imaging and sacrifice 4 weeks later at week 10 (*see* **Note 5**). As explained in the note, this protocol is specific to angioplasty interventions, but the same protocol can be used when examining other types of intervention (e.g., pharmacotherapeutics, stents).

3.3 Intravascular Ultrasound (IVUS) Imaging

1. Acquire IVUS images of the abdominal aorta with a 40 mega-Hertz (MHz) clinical catheter by automated 0.5 mm/s pullback.
2. Commence imaging from the abdominal aorta at the level of the lowest renal artery until into the common iliac vessel.
3. Perform IVUS at serial timepoints 6 weeks and 10 weeks. IVUS should be performed both pre- and postangioplasty, and the data recorded and stored.
4. Manually coregister the IVUS datasets at 6 and 10 weeks to each other using anatomical landmarks including side branches as fiducial markers and the known pullback rates of the imaging systems, and then analyze further by manual segmentation [20], in accordance to expert consensus IVUS recommendations [21].
5. Measure the external elastic membrane (EEM) and vessel lumen every 0.4 mm from axial IVUS images for each rabbit at 6 and 10 weeks, across the area that has undergone angioplasty (total 40 mm length, 200 images per animal [100 images per timepoint]). These measurements permit calculation of the atheroma cross-sectional area (CSA) and plaque burden (PB) for each IVUS slice. All cross-sectional slices obtained can be analyzed and included in the image analysis results. On a per slice basis every 0.4 mm, atheroma progression is quantified as the change in IVUS PB (ΔPB) between 6 and 10 weeks.
6. IVUS formulae include:
   (a) $\text{Atheroma}_{CSA}\ (mm^2) = \text{EEM}_{CSA} - \text{Lumen}_{CSA}$.
   (b) $\text{PB (plaque burden) (\%)} = (\text{Atheroma}_{CSA} \div \text{EEM}_{CSA}) \times 100\%$.
   (c) $\Delta\text{PB (plaque burden) (\%)} = \text{PB}_{\text{follow-up}} - \text{PB}_{\text{baseline}}$.
   (d) $\text{PAV (percent atheroma volume) (\%)} = (\Sigma\text{Atheroma}_{CSA} \div \Sigma\text{EEM}_{CSA}) \times 100\%$.
   (e) Percentage Maximum Stenosis (%) = (1 − (MLA/reference luminal area)) × 100%.

3.4 Intravascular NIRF-OCT Imaging of Plaque Inflammation and Structure

1. To image plaque inflammation, 24 h before NIRF-OCT imaging sessions, intravenously inject the rabbits inflammatory protease NIRF imaging agent ProSense750 VM110 (a quenched sensor engineered to generate fluorescence following protease activation by cathepsins B, L, or S) [15].
2. Perform automated reconstruction of dual-modal NIRF-OCT pullbacks [17]. Generate quantitative NIRF by using coregistered OCT images to correct the NIRF signal according to the distance between the catheter and the lumen surface, and express as both the NIRF concentration (nanomolar; nM)

averaged over all the slices comprising the plaque and the average NIRF concentration per OCT slice at 0.4 mm intervals [15]. Calculate the change in NIRF concentration (ΔNIRF, in nM) on a per slice basis as the difference between the NIRF concentration at 6 and 10 weeks. All IVUS and NIRF image analyses should be performed in a blinded fashion in terms of group assignment of each animal (*see* **Note 6**).

3.5 Randomization of Angioplasty Therapy: Experimental Setup

1. At the baseline first imaging timepoint of 6 weeks (Fig. 7) [22], to image arterial inflammation (cathepsin protease activity) in vivo, inject rabbits with ProSense VM110 24 h prior to imaging (400 nmol/kg via ear vein intravenous injection) [11, 15].
2. The next day, carry out the same surgical preparation and anesthetic protocol as at week two (Subheading 3.1; **steps 3–10**) on the rabbits, and secure the femoral and carotid artery access using open surgical cutdown.
3. Next using NIRF-OCT, IVUS, and X-ray angiographic guidance, inflate a single paclitaxel-coated angioplasty balloon of size 4.0 × 40 mm or a single plain angioplasty balloon 4.0 × 40 mm to a maximal pressure of 8 atmospheres (atm) for a period of 120 s.
4. For the control sham-PTA group, place a plain PTA balloon with the same 4.0 × 40 mm dimension in the aorta and inflate to 0 atm for a period of 120 s. The average aortic diameter in the rabbit is 3.25 mm correlating with a balloon overdistention ratio of 1.2:1 [23].
5. Only the approximate distal 40 mm of the Fogarty-balloon injured area is subject to angioplasty. Take care not to disrupt the drug-coated balloon once out of packaging (no direct handling) and to work as swiftly as possible. Follow the IFU for the use of both balloons; predilate the planned region of angioplasty with a plain balloon before drug-coated balloon use.
6. Calculate the area subject to angioplasty using a combination of the angiogram, IVUS and OCT to ensure the coregistration is accurate. This involves a combination of distance from renal arteries, side branches and fiducial markers.

3.6 Sacrifice and End of Study: Experimental Setup

1. One day prior to final 10-week imaging timepoint, inject rabbits again with ProSense VM110 24 h prior to imaging (400 nmol/kg via ear vein intravenous injection).
2. The next day (Fig. 8), perform the same surgical preparation and anesthetic protocol as in week 2 (Subheading 3.1; **steps 3–10**) with femoral and contralateral carotid access secured with surgical cut down.

3.7 Molecular Analysis: Aortic Tissue

1. Following sacrifice, perfuse rabbit aortas with cold saline and harvest.
2. Measure the explanted aorta out to its in vivo size and pin to measuring board. Create sections every 0.5 mm, with selected tissue from three regions stored in RNAlater for subsequent RNA analysis. The three regions include (1) normal aorta (no balloon injury), (2) PTA or DCB-PTA segment and (3) Fogarty balloon-injured region without additional PTA (*see* **Note 7**).
3. Snap-freeze the remaining tissue using dry ice and 2-methylbutane, placed in Optimal Cutting Temperature compound medium and store in −80 °C for later sectioning and histopathology as desired.

3.8 Molecular Analysis: RNA Extraction and cDNA Synthesis

1. Extract RNA by homogenization of the tissue sample in question using a rotor-stator homogenizer. Use the RNeasy mini-kit to extract RNA from the tissue.
2. Cut the RNAlater-stabilized tissue into small pieces and place in 600 μL of RLT buffer provided in the kit. Homogenize until the solution is uniformly homogenous.
3. Centrifuge the solution at 12,000 × *g* for 3 min.
4. Transfer the resultant supernatant into a new microcentrifuge tubes, add 600 μL of 70% ethanol and pipette multiple times to mix the solution.
5. Add 700 μL of this solution to the RNeasy spin column and centrifuge for 15 s at 8000 × *g*.
6. Discard the flow through, add 700 μL of buffer RW1 provided in the kit to the spin column and centrifuge for 15 s at 8000 × *g*.
7. Discard the flow through, add 500 μL of buffer RPE to the column and centrifuge for 15 s at 8000 × *g*.
8. Repeat **step 7** but centrifuge the column for 2 min at 8000 × *g*.
9. Change the collection tube and centrifuge further in a microcentrifuge at maximum speed for 1 min to dry the membrane.
10. Place the spin column in a 1.5 mL collection microcentrifuge tube, add 30 μL of RNase-free water directly to the center of the column and centrifuge for 1 min at 8000 × *g*.
11. Place samples immediately on ice and determine RNA concentration (ng/μL) using the Nanodrop Spectrophotometer.
12. Synthesize complementary DNA (cDNA) from 1 μg of total RNA using a reaction mix with a final volume of 20 μL containing 2 μL of 10× reverse transcriptase buffer, 0.8 μL of 10 nM dNTP, 2 μL of 10× random hexamers, 1 μL of Multiscribe, and 14.2 μL of RNase-free water and mix.

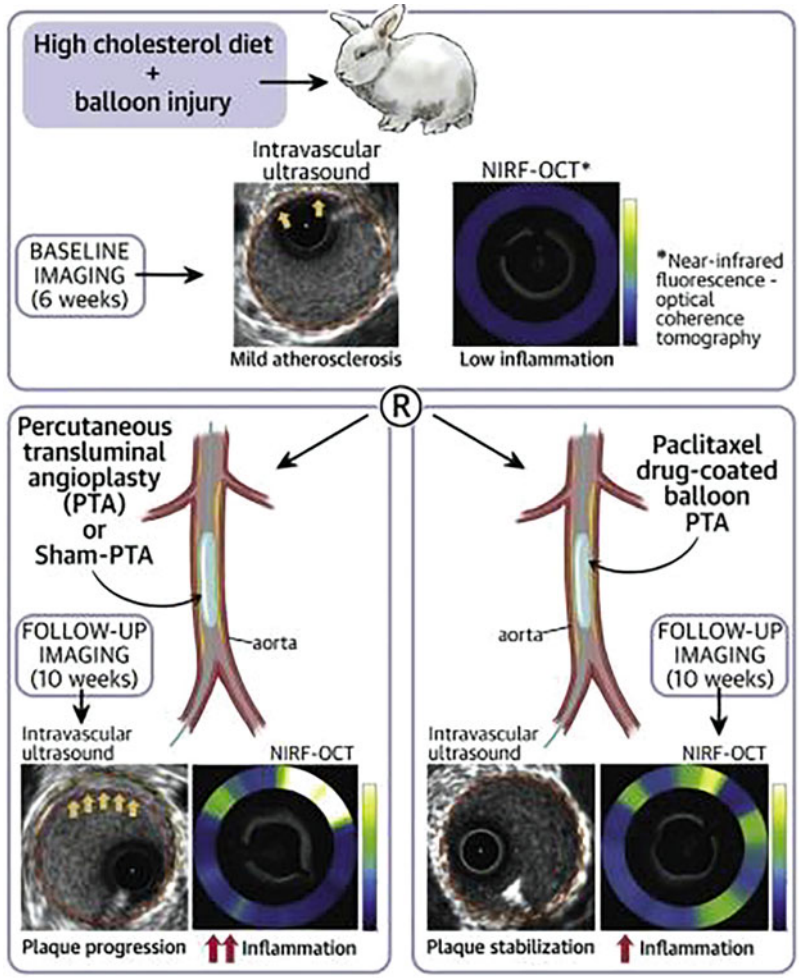

Fig. 9 Experimental Study Design. Paclitaxel drug-coated balloons (DCBs) reduce restenosis, but their overall safety has recently raised concerns. Previous research has hypothesized that DCBs could lessen inflammation and reduce plaque progression. Using 25 rabbits with cholesterol feeding– and balloon injury–induced lesions, DCB-percutaneous transluminal angioplasty (PTA), plain PTA or sham-PTA (balloon inserted without inflation), was investigated using serial intravascular near-infrared fluorescence-optical coherence tomography and serial intravascular ultrasound. In these experiments, DCB-PTA reduced inflammation and plaque burden in nonobstructive lesions compared with PTA or sham-PTA. These findings indicated the potential for DCBs to serve safely as regional antiatherosclerosis therapy (as evidenced in Fig. 5). (Reproduced by permission from Ref. 25)

13. Perform reaction for 10 min at 25 °C, 120 min at 37 °C, 5 min at 85 °C and hold at 4 °C to produce cDNA.
14. Dilute the cDNA to 25 ng/μL and store at −20 °C until further use.
15. Assess cathepsin B, cathepsin L and cathepsin S expression using SYBR Green real-time PCR using primer sequences designed using appropriate software (e.g., Primer Express™,

ver. 3.0.1, ThermoFisher Scientific). Verify gene specificity of all primer sequences by BLAST (Basic Local Alignment Search Tool) searches.

16. Perform q-RT-PCR using the QuantStudio 3 Real-Time PCR System (ThermoFisher Scientific) in a 96-well plate format using following cycle parameters: initial denaturation at 95 °C for 4 min followed by 40 cycles of denaturation at 95 °C for 10 s, annealing at 60 °C for 30 s and elongation at 72 °C for 5–30 s.
17. Analyze data using the QuantStudio 3 Sequence Detection System 2.2.1 software (v20040907-2, 2004, ThermoFisher Scientific) with the detection threshold set manually at 0.05 for all the assays. Normalize all transcripts to GAPDH housekeeping gene) and determine relative gene expression by using the comparative C_t method ($2^{-\Delta\Delta Ct}$) (Fig. 9).

4 Notes

1. Regarding balloon injury of the rabbit aorta, care is taken to ensure pre– and post–balloon injury points are taken fluoroscopically with the exact placement of the radiopaque Fogarty catheter. This enables accurate coregistration of length of injury and can aid where intervention PTA occurs.
2. Once access has been secured in the femoral artery with the 4F sheath, blood can be aspirated via the sheath and stored in a microcentrifuge tube on ice for later serum analysis. Ensure that a few milliliters are first aspirated and disposed of prior to taking formal sample.
3. For skin closure after arterial cutdown, use two techniques of both subcuticular and interrupted vicryl and glue to ensure wound dehiscence is kept to a minimum.
4. The atherosclerosis generation timeline (Fig. 8) is sufficient to reproduce acceptable atherosclerosis generation in rabbits for an "intervention" study (be that endovascular or pharmacotherapeutics).
5. When using drug-eluting balloons, strict adherence to IFU is required. Always ensure there is a predilatation with a plain angioplasty balloon and endeavor not to handle the drug-eluting balloon directly when placing into the sheath over the wire.
6. For all IVUS and NIRF-OCT measurements during each imaging session, always take single shot fluoroscopic images to clearly delineate starting and finishing points of each catheter, to aid with coregistration.

7. At the time of harvest, aortic tissue does not need to be placed in RNAlater® immediately; a period of 12 h in saline can be stored at 4 °C and placed in RNA stabilizing solution later. Comparisons of RNA quality and yield were made for both of these with no significant difference.

Acknowledgments

This work was supported by NIH R01 HL150538 and R01 HL137913 grants to F.A.J.

References

1. Bourantas CV, Jaffer FA, Gijsen FJ, van Soest G, Madden SP, Courtney BK, Fard AM, Tenekecioglu E, Zeng Y, van der Steen AFW, Emelianov S, Muller J, Stone PH, Marcu L, Tearney GJ, Serruys PW (2017) Hybrid intravascular imaging: recent advances, technical considerations, and current applications in the study of plaque pathophysiology. Eur Heart J 38:400–412. https://doi.org/10.1093/eurheartj/ehw097
2. Chowdhury MM, Tawakol A, Jaffer FA (2017) Molecular imaging of atherosclerosis: a clinical focus. Curr Cardiovasc Imaging Rep 10:2. https://doi.org/10.1007/s12410-017-9397-1
3. Khraishah H, Jaffer FA (2020) Intravascular molecular imaging: near-infrared fluorescence as a new frontier. Front Cardiovasc Med 7:587100. https://doi.org/10.3389/fcvm.2020.587100
4. Jablonski A (1933) Efficiency of anti-stokes fluorescence in dyes. Nature 131:839–840. https://doi.org/10.1038/131839b0
5. Lakowicz JR (2006) Principles of fluorescence spectroscopy. Springer US, Boston, MA
6. Middendorf L, Amen J, Bruce R, Draney D, DeGraff D, Gewecke J, Grone D, Humphrey P, Little G, Lugade A, Narayanan N, Oommen A, Osterman H, Peterson R, Rada J, Raghavachari R, Roemer S (1998) Near-infrared fluorescence instrumentation for DNA analysis. In: Near-infrared dyes for high technology applications. Springer Netherlands, Dordrecht, pp 21–53
7. Piruska A, Nikcevic I, Lee SH, Ahn C, Heineman WR, Limbach PA, Seliskar CJ (2005) The autofluorescence of plastic materials and chips measured under laser irradiation. Lab Chip 5:1348–1354. https://doi.org/10.1039/b508288a
8. Robles FE, Chowdhury S, Wax A (2010) Assessing hemoglobin concentration using spectroscopic optical coherence tomography for feasibility of tissue diagnostics. Biomed Opt Express 1:310–317. https://doi.org/10.1364/boe.1.000310/
9. Frangioni JV (2003) In vivo near-infrared fluorescence imaging. Curr Opin Chem Biol 7:626–634
10. Jaffer FA, Vinegoni C, John MC, Aikawa E, Gold HK, Finn AV, Ntziachristos V, Libby P, Weissleder R (2008) Real-time catheter molecular sensing of inflammation in proteolytically active atherosclerosis. Circulation 118:1802–1809. https://doi.org/10.1161/CIRCULATIONAHA.108.785881
11. Jaffer FA, Calfon MA, Rosenthal A, Mallas G, Razansky RN, Mauskapf A, Weissleder R, Libby P, Ntziachristos V (2011) Two-dimensional intravascular near-infrared fluorescence molecular imaging of inflammation in atherosclerosis and stent-induced vascular injury. J Am Coll Cardiol 57:2516–2526. https://doi.org/10.1016/j.jacc.2011.02.036
12. Khamis RY, Woollard KJ, Hyde GD, Boyle JJ, Bicknell C, Chang S-H, Malik TH, Hara T, Mauskapf A, Granger DW, Johnson JL, Ntziachristos V, Matthews PM, Jaffer FA, Haskard DO (2016) Near infrared fluorescence (NIRF) molecular imaging of oxidized LDL with an autoantibody in experimental atherosclerosis. Sci Rep 6:21785. https://doi.org/10.1038/srep21785
13. Vinegoni C, Botnaru I, Aikawa E, Calfon MA, Iwamoto Y, Folco EJ, Ntziachristos V, Weissleder R, Libby P, Jaffer FA (2011) Indocyanine green enables near-infrared fluorescence imaging of lipid-rich, inflamed atherosclerotic plaques. Sci Transl Med 3:84ra45. https://doi.org/10.1126/scitranslmed.3001577

14. Verjans JW, Osborn EA, Ughi GJ, Calfon Press MA, Hamidi E, Antoniadis AP, Papafaklis MI, Conrad MF, Libby P, Stone PH, Cambria RP, Tearney GJ, Jaffer FA (2016) Targeted near-infrared fluorescence imaging of atherosclerosis: clinical and intracoronary evaluation of Indocyanine green. JACC Cardiovasc Imaging 9:1087–1095. https://doi.org/10.1016/j.jcmg.2016.01.034
15. Yoo H, Kim JW, Shishkov M, Namati E, Morse T, Shubochkin R, McCarthy JR, Ntziachristos V, Bouma BE, Jaffer FA, Tearney GJ (2011) Intra-arterial catheter for simultaneous microstructural and molecular imaging in vivo. Nat Med 17:1680–1684. https://doi.org/10.1038/nm.2555
16. Hara T, Ughi GJ, McCarthy JR, Erdem SS, Mauskapf A, Lyon SC, Fard AM, Edelman ER, Tearney GJ, Jaffer FA (2017) Intravascular fibrin molecular imaging improves the detection of unhealed stents assessed by optical coherence tomography in vivo. Eur Heart J 38:447–455. https://doi.org/10.1093/eurheartj/ehv677
17. Ughi GJ, Verjans J, Fard AM, Wang H, Osborn E, Hara T, Mauskapf A, Jaffer FA, Tearney GJ (2015) Dual modality intravascular optical coherence tomography (OCT) and near-infrared fluorescence (NIRF) imaging: a fully automated algorithm for the distance-calibration of NIRF signal intensity for quantitative molecular imaging. Int J Cardiovasc Imaging 31:259–268. https://doi.org/10.1007/s10554-014-0556-z
18. Yun SH, Boudoux C, Tearney GJ, Bouma BE (2003) High-speed wavelength-swept semiconductor laser with a polygon-scanner-based wavelength filter. Opt Lett 28:1981–1983
19. Piao Z, Singh K, Chowdhury M, Gardecki J, Nishimiya K, Yin B, Beatty M, Bablouzian A, Giddings S, Mauskapf A, Jaffer FA, Tearney G (2018) TCT-56 high-resolution intravascular OCT-NIRF molecular imaging for in vivo assessment of inflammation in atherosclerosis and vascular injury. J Am Coll Cardiol 72:B25. https://doi.org/10.1016/j.jacc.2018.08.1143
20. Schindelin J, Arganda-Carreras I, Frise E, Kaynig V, Longair M, Pietzsch T, Preibisch S, Rueden C, Saalfeld S, Schmid B, Tinevez J-Y, White DJ, Hartenstein V, Eliceiri K, Tomancak P, Cardona A (2012) Fiji: an open-source platform for biological-image analysis. Nat Methods 9:676–682. https://doi.org/10.1038/nmeth.2019
21. Mintz GS, Nissen SE, Anderson WD, Bailey SR, Erbel R, Fitzgerald PJ, Pinto FJ, Rosenfield K, Siegel RJ, Tuzcu EM, Yock PG (2001) American College of Cardiology Clinical Expert Consensus Document on standards for acquisition, measurement and reporting of intravascular ultrasound studies (IVUS). A report of the American College of Cardiology Task Force on Clinical Expert Consensus Documents. J Am Coll Cardiol 37:1478–1492
22. Chowdhury MM, Singh K, Albaghdadi MS, Khraishah H, Mauskapf A, Kessinger CW, Osborn EA, Kellnberger S, Piao Z, Lino Cardenas CL, Grau MS, Jaff MR, Rosenfield K, Libby P, Edelman ER, Lindsay ME, Tearney GJ, Jaffer FA (2020) Paclitaxel drug-coated balloon angioplasty suppresses progression and inflammation of experimental atherosclerosis in rabbits. JACC Basic Transl Sci 5:685–695. https://doi.org/10.1016/j.jacbts.2020.04.007
23. Schwartz RS, Chronos NA, Virmani R (2004) Preclinical restenosis models and drug-eluting stents: still important, still much to learn. J Am Coll Cardiol 44:1373–1385. https://doi.org/10.1016/j.jacc.2004.04.060

INDEX

A

Dipak P. Ramji (ed.), *Atherosclerosis: Methods and Protocols*, Methods in Molecular Biology, vol. 2419,
https://doi.org/10.1007/978-1-0716-1924-7,

© The Author(s), under exclusive license to Springer Science+Business Media, LLC, part of Springer Nature 2022

B

C

D

E

F

G

H

I

J

L

M

N

O

P

Q

R

S

T

U

V

W

Z